

Proceedings of
**The Second Asian-Australasian
Conference on Composite Materials (ACCM-2000)**

***“Composites Technologies
for the New Millennium”***

VOLUME I

Edited by
Chang-Sun Hong and Chun-Gon Kim
(KAIST)

18-20 August 2000
Kyongju, Korea

DISTRIBUTION STATEMENT
Approved for Public Release
Distribution Unlimited

Organized by
The Asian-Australasian Association for Composite Materials (AACM)
The Korean Society for Composite Materials (KSCM)

DTIC QUALITY INSPECTED 4

20000915 142

Published by

The Korean Society for Composite Materials
373-1, Kusong-dong, Yusong-gu, Taejon 305-701, Korea
Tel : +82-42-869-3752 • Fax : +82-42-869-3710

Copyright © 2000, The Korean Society for Composite Materials
All rights reserved

No part of this publication may be reproduced, stored in a retrieval system,
or transmitted in any form or by means, electronic, mechanical
photocopying or otherwise, without permission in writing from the publisher.

ISBN 89-951567-0-8 for 2 Volume Set
ISBN 89-951567-1-6 94550 for Volume I
ISBN 89-951567-2-4 94550 for Volume II

Printed in Korea

How to order this book

Order to the Korean Society for Composite Materials by Credit Card using a
copy of this page.

KSCM (Prof. C. S. Hong)

By Fax : +82-42-869-3710

By Mail : Dept. of Aerospace Engineering, KAIST 373-1, Kusong-dong,
Yusong-gu, Taejon 305-701, Korea

Post Conference Price : \$150 (Volume I, II) with shipping per each set

By Credit Card : American Express, VISA, MasterCard

(Information of ACCM-2000 : <http://accm.kaist.ac.kr>)

Your Name (Print) : _____

Your Address :

Date : Your Credit Card : Exp. Date :

No. : □□□□ □□□□ □□□□ □□□□ □□□□ □□□□

Signature : _____

REPORT DOCUMENTATION PAGE				Form Approved OMB No. 0704-0188	
<p>The public reporting burden for this collection of information is estimated to average 1 hour per response, including the time for reviewing instructions, searching existing data sources, gathering and maintaining the data needed, and completing and reviewing the collection of information. Send comments regarding this burden estimate or any other aspect of this collection of information, including suggestions for reducing the burden, to Department of Defense, Washington Headquarters Services, Directorate for Information Operations and Reports (0704-0188), 1215 Jefferson Davis Highway, Suite 1204, Arlington, VA 22202-4302. Respondents should be aware that notwithstanding any other provision of law, no person shall be subject to any penalty for failing to comply with a collection of information if it does not display a currently valid OMB control number.</p> <p>PLEASE DO NOT RETURN YOUR FORM TO THE ABOVE ADDRESS.</p>					
1. REPORT DATE (DD-MM-YYYY) 07-09-2000		2. REPORT TYPE Conference Proceedings		3. DATES COVERED (From - To) 18-20 August 2000	
4. TITLE AND SUBTITLE The 2nd Asian-Australasian Conference on Composite Materials (ACCM-2000), 18-20 August 2000, Kyongju, Korea				5a. CONTRACT NUMBER F6256200M9036	
				5b. GRANT NUMBER	
				5c. PROGRAM ELEMENT NUMBER	
6. AUTHOR(S) Conference Committee Edited by: Chang-Sun Hong and Chun-Gon Kim				5d. PROJECT NUMBER	
				5e. TASK NUMBER	
				5f. WORK UNIT NUMBER	
7. PERFORMING ORGANIZATION NAME(S) AND ADDRESS(ES) Korea Advanced Institute of Science & Technology Dept. of Materials Science and Engr., 373-1 Kusung-dong, Yusung-gu Taejon 305-701 Korea (South)				8. PERFORMING ORGANIZATION REPORT NUMBER N/A	
9. SPONSORING/MONITORING AGENCY NAME(S) AND ADDRESS(ES) AOARD UNIT 45002 APO AP 96337-5002				10. SPONSOR/MONITOR'S ACRONYM(S) AOARD	
				11. SPONSOR/MONITOR'S REPORT NUMBER(S) CSP-99-17	
12. DISTRIBUTION/AVAILABILITY STATEMENT Approved for public release; distribution is unlimited.					
13. SUPPLEMENTARY NOTES					
14. ABSTRACT Conference Proceedings, Volume I : Plenary Lectures; Keynote Lectures; Session 1: Design; Session 2: Application(1); Session 3: SMC/RTM; Session 4: Textile Composites; Session 5: Processing(1); Session 6: Processing(2); Session 7: MMC(1); Session 8: MMC(2); Session 9: MMC(3); Session 10: Adhesion & Coating; Session 11: Interface(1); Session 12: Interface(2); Session 13: Polymer(1); Session 14: Polymer(2); Session 15: Analysis(1); Session 16: Fatigue & Fracture(1); Session 17: Fatigue & Fracture(2) Session 18: Fatigue & Fracture(3); Volume II : Session 19: C/C & CMC(1); Session 20: C/C & CMC(2); Session 21: C/C & CMC(3); Session 22: NDE/NDT; Session 23: Vibration(1); Session 24: Vibration(2); Session 25: Analysis(2); Session 26: Analysis(3); Session 27: Fatigue & Fracture(4); Session 28: Fatigue & Fracture(5); Session 29: Smart Materials & Structures(1); Session 30: Smart Materials & Structures(2); Session 31: Smart Materials & Structures(3); Session 32: Environment; Session 33: Testing (1); Session 34: Testing(2); Session A: Application(2); Late Paper					
15. SUBJECT TERMS Composite Materials					
16. SECURITY CLASSIFICATION OF:			17. LIMITATION OF ABSTRACT	NUMBER OF PAGES	19a. NAME OF RESPONSIBLE PERSON
a. REPORT	b. ABSTRACT	c. THIS PAGE			Thomas D. Kim
U	U	U	UU	1,323	19b. TELEPHONE NUMBER (Include area code) +81-3-5410-4409

Preface

There has been active discussion about the formation of the so-called "*Asian-Australasian Association for Composite Materials (AACM)*" as an equivalent ICCM in the Asian-Australasian region. The AACM was established after active discussion during ICCM-11 meeting in Gold Coast. The objective of the AACM is to encourage the free interchange of information on all aspects related to composite materials, which are of interest to the scientific and engineering community. Therefore, the ACCM (Asian-Australasian Conference on Composite Materials) is organized to provide an Asian-Australian-wide forum for the discussion of such topics.

Following the success of the first Conference held in Osaka, Japan, The ACCM will be held biannually as an exciting forum for reporting and discussing the latest progress in composite technologies. This series of ACCM meetings will provide high quality technical programs related with manufacturing and design based on polymer, metal, and ceramic composite materials. As noted in the conference title of ACCM-2000, this conference will focus on the applications of composite materials and structures for the new millennium.

The Proceedings of the Second Asian-Australasian Conference on Composite Materials contains over 200 technical papers that are to be presented at the conference. With over 15 countries represented by authors and delegates, the present conference is truly an international forum for specialists in this important area of technology for the new millennium. We would like to keep up the good tradition and create a welcome environment for a pleasant get-together.

Appreciation is hereby expressed to the plenary speakers: Professor H. T. Hahn, Professor S. W. Tsai, Dr. E. J. Jun, and Dr. N. Sato. We would like to take this opportunity to thank the invited speakers, and authors for their efforts devoted to their papers and presentations. In particular, our thanks are due to members of Organizing Committee, Scientific Committee, and Local Executive Committee.

Chang-Sun Hong and Chun-Gon Kim
Korea Advanced Institute of Science and Technology

August 2000

Preceding Page's Blank

Conference Organization

1. AACM Council

President	I. Kimpara	The University of Tokyo
Vice President	C. S. Hong	Korea Advanced Institute of Science and Technology
General Secretary	J. K. Kim	Hong Kong University of Science and Technology
Immediate Past President	Y. W. Mai	University of Sydney
Immediate Past Vice President	M. Zako	Osaka University

2. ACCM-2000 Conference Organization

Chairman	C. S. Hong	Korea Advanced Institute of Science and Technology
Vice Chairman	E. J. Jun	Ministry of Science and Technology, Korea
	T. Fukuda	Osaka City University
	M. S. Cho	Hankook Fiber Glass Co.
	Ren-Jie Wu	Shanghai Jiao Tong University
Treasurer	S. H. Hong	Korea Advanced Institute of Science and Technology
	T. J. Kang	Seoul National University
Secretary General	D. G. Lee	Korea Advanced Institute of Science and Technology
Secretary	C. G. Kim	Korea Advanced Institute of Science and Technology

3. International Advisory Committee

D. Bhattacharyya	University of Auckland
H. R. Daghyani	Amirkabir University of Technology
T. Fujii	Doshisha Univ
H. Fukuda	Science University of Tokyo
K. S. Han	Pohang University of Science & Technology
I. Herszberg	Royal Melbourne Institute of Technology
S. H. Hong	Korea Advanced Institute of Science and Technology
D.A.L. Juwono-Soenarso	University of Indonesia
W. I. Lee	Seoul National University
C. C. M. Ma	National Tsing Hua University
Y. Miyano	Kanazawa Institute of Technology
M. Nasir	University of Sains Malaysia
V.A. Phan	Institute of New Technologies Promotion of Vietnam
S. Ramakrishna	National University of Singapore
N. Takeda	The University of Tokyo
D. Z. Wo	Nanjing University of Aeronautics & Astronautics
C. Y. Yue	Nanyang Technological University
M. Zako	Osaka University
H. M. Zeng	Zhongshan University

4. Conference Organizing Committee

Goichi Ben	Nihon University
N. S. Choi	Hanyang University
L. Choi	Ssangyong Industrial Co.
S. Y. Du	Harbin Institute of Technology
M. Iwamoto	Kyoto Institute of Technology
B. S. Kim	Korea Institute of Machinery and Materials
K. S. Kim	Korea Aerospace Industries, LTD.
S. J. Kim	Seoul National University
J. H. Lee	Pusan National University
J. R. Lee	Korea Research Institute of Chemical Technology
Y. S. Lee	Chungnam National University
J. W. Lee	Samsung Heavy Industries
T. X. Mao	Beijing Institute of Mechanics
K. Takahashi	Kyushu University
S. Y. Yoo	Korean Air
J. R. Youn	Seoul National University

5. Scientific Committee

Chairman	C. S. Hong	Korea Advanced Institute of Science and Technology
Members	In Lee	Korea Advanced Institute of Science and Technology
	T. Ishikawa	National Aerospace Laboratory
	W. I. Lee	Seoul National University
	J. K. Kim	Hong Kong University of Science and Technology
	J. R. Youn	Seoul National University

6. Local Executive Committee

Chairman	D. G. Lee	Korea Advanced Institute of Science and Technology
Secretariat	C. G. Kim	Korea Advanced Institute of Science and Technology
Members	J. M. Cho	Hankook Fiber Glass Co. Ltd
	H. J. Chun	Yonsei University
	B. K. Han	Hongik University
	Y. M. Han	Agency for Defense Development
	W. B. Hwang	Pohang University of Science and Technology
	H. S. Kang	Taekwang Ind. Co., Ltd.
	B. G. Min	Chungju National University
	K. J. Yoon	Konkuk University
	T. H. Yoon	Kwangju Institute of Science and Technology

Co-Sponsors

Co-Sponsored by

Asian Office of Aerospace Research and Development/Air force

Office of Scientific Research (AOARD/AFOSR)

FiberPro

Hankuk Carbon Co., Ltd.

Hyundai Motor Company

ICES Co., Ltd.

Korea Advanced Institute of Science and Technology (KAIST)

Korea Federation of Science and Technology (KOFST)

Korea Research Foundation (KRF)

Korea Science and Engineering Foundation (KOSEF)

Korean Air

In Cooperation with

Composite Division of the Society of Materials Science, Japan (JSMS)

The Japan Society for Composite Materials (JSCM)

The Korean Institute of Metals and Materials (KIMM)

The Korean Society for Precision Engineering (KSPE)

Contents

VOLUME I

Plenary Lectures

Information Systems for Composites <i>Hahn, H. T.</i>	1
Low-Cost Interlocked Composite Grids <i>Tsai, S. W., Liu, K. K. S. Han, D. Y. and Wang, J.</i>	11
National Science & Technology Policy in Korea <i>Jun, E. J.</i>	17
Recycling of Polymer Materials for Automobile <i>Sato, N.</i>	23

Keynote Lectures

Thermochemical Response (Microcracking) of Lamonates at Cryogenic Temperatures <i>Kim, R. Y. and Crasto, A. S.</i>	33
A New Approach to the EMI Shielding Composite Materials <i>Choe, C. R., Park, M., and Mironov, V.</i>	41
Damage and Fracture of Infiltrated Particle Reinforced Aluminium Composites <i>Kouzeli, M., Miserez, A., Rossoli, A., Marchi, C. S., Weber, L. and Mortensen, A.</i>	47
Evaluation of Interface Propertise from a Fibre Fragmentation Test <i>Liu, H. Y. and Mai, Y. W.</i>	57
Mechanical Identification of Composite Materials and Structures <i>Vautrin, A.</i>	63
The Proper Use of Fracture Mechanics in the Analysis of Composites Materials and Laminates <i>Sun, C. T.</i>	65
An Overview of Cure Monitoring in Composites Molding Process <i>Fukuda, T. and Kosaka, T.</i>	77
An Experimental/Analytical Correlation of the Micromechanical Elastic Response of a Unidirectional Composite Under Transverse Tension <i>Mollenhauer, D. H.</i>	87

Session 1 : Design

Elastic Buckling Behavior of Orthotropic Web Plate with a Longitudinal Stiffener <i>Yoon, S. J., Jung, J. H. and Ahn, D. J.</i>	95
--	----

Stacking Sequence Optimization for Buckling of Laminated Plates by The Complex Method <i>Zhao, X. and Narita, Y.</i>	101
Optimal Design for the Maximum Frequency of a Rectangular Plate with Additional FRP Sheets <i>Narita, Y., Ohta, Y. and Kakudate, T.</i>	109
Optimal Design of Laminate Composites with Gradient Structure for Weight Reduction <i>Back, S. K., Kang, T. K. and Lee, K. W.</i>	113
Property Tailoring of CFRP Laminates by Interleaving <i>Tanimoto, T.</i>	119
The Effect of Neglecting the Longitudinal Moment Terms in Analyzing [90,0,90] _s Type Laminates with Increasing Aspect Ratio <i>Kim, D. H., Han, B. K., Park, J. H. and Lee, D. H.</i>	125

Session 2 : Application(1)

Optimal Design of The Composite Aerostatic Spindle <i>Bang, K. G., Kim, P. J. and Lee, D. G.</i>	135
Health Monitoring System of Composite Laminated Structures using Vibration Data <i>Inada, T., Shimamura, Y., Todoroki, A., Kobayashi, H. and Nakamura, H.</i>	141
Design Strength of Pultruded Universal Section Columns <i>Yoon, S. J., Jeong, S. K. and Cho, S. K.</i>	147
Correlation between Damage Behavior and Electrical Resistance Change in CFRP and CFGFRP Composites <i>Song, D. Y., Park, J. B., Yamane, T., Takeda, N. and Kitano, A.</i>	153
Design and Manufacture of a Composite End Effector for Large LCD Glass Handling Robots <i>Oh, J. H., Lee, D. G. and Kim, H. S.</i>	159
Temperature Effect on Impact Responses of Carbon Fibre/Epoxy Composite Laminates <i>Sohn, M. S., Hu, X. Z. and Kim, J. K.</i>	165

Session 3 : SMC/RTM

Effect of Boundary Condition Type on Mold Filling in RTM Process <i>Shojaei, A., Ghaffarian, S. R. and Karimian, S. M. H.</i>	173
A New Technique to Determine In-Plane Permeability of Fiber Preforms <i>Hwang, B. S., Um, M. K. and Daniel, I. M.</i>	179
Modeling of Void Formation during Resin Transfer Molding Process <i>Lim, S. T., Kang, M. K. and Lee, W. I.</i>	185
Novel Sensor Development for Resin Front Detection in RTM <i>Motogi, S., Yamagishi, Y. and Fukuda, T.</i>	191

A Study on the Manufacturing of Screw Rotors using RTM Process <i>Choi, J. H., Suh, J. D. and Lee, D. G.</i>	197
---	-----

Session 4 : Textile Composites

Prediction of Elastic Moduli of Woven Composite by Using Artificial Neural Network <i>Ding, X., and Yi, H. L.</i>	205
Inter-Laced Fibers/Light-Curing Resin Composite Structures <i>Akkus, N., Verchery, G., Kanemoto, Y., Kawahara, M. and Hurez, A.</i>	211
Deep-drawing Simulation of Knitted Fabric Composite Materials by the Homogenization Method Considering Micro-Macro Coupling Effect <i>Takano, N. and Zako, M.</i>	223

Session 5 : Processing(1)

Silica Nanoparticles Filled Polypropylene: Effects of Irradiation Grafting of Silica on the Tensile Properties of Composites <i>Rong, M. Z., Zhang, M. Q., Zheng, Y. X. and Zeng, H. M.</i>	231
The Deciding Method of Drill Tool Life based on Estimation of Hole Damage in PWB made of GFRP <i>Inoue, H., Hirogaki, T., Aoyama, E. and Katayama, T.</i>	237
Kinetic Study on the Thermal Degradation of Phenolic Resin/Silica Hybrid Ceramer Nanocomposites <i>Ma, C. C. M., Lin, J. M. and Chen, C. Y.</i>	243
Effects of Packing on the Fiber Orientation during Injection Molding of Short Fiber Composites <i>Lee, S. W. and Youn, J. R.</i>	249
Numerical and Experimental Analysis of Roll Forming Fibre Reinforced Thermoplastic Sheets <i>Bhattacharyya, D., Dykes, R. J. and Hunter, P. J.</i>	251

Session 6 : Processing(2)

Particulate Composites Based on Ground Rubber Tire and Polyethylene: Manufacturing of Porous Pipe and Effects of Different PEs on Mechanical Properties and Leak Rate <i>Motlagh, G. H., Ghaffarian, S. R., Mohammadi, N., Nazokdast, H. and Mahdavian, M. H.</i>	259
Resistance Welding of Carbon Fibre Reinforced Thermoplastic Composite <i>Yuan, Q., Hou, M., Mai, Y. W. and Ye, L.</i>	265
Cure Monitoring of FW Pipe by using EFPI Fiber Optic Sensors <i>Kosaka, T., Osaka, K., Sando, M. and Fukuda, T.</i>	271
Numerical Simulation of Sheet Molding Compound in Compression Molding Process <i>Yan, S. L., Tang, Z. G. and Liu, M.</i>	277

Study on the Non-linear Creep Behavior of BMC <i>Somiya, S. and Shirata, Y.</i>	283
--	-----

Session 7 : MMC(1)

Fabrication of TiAl Matrix Composite by Reactive Forming Process <i>Kobashi, M., Muto, H., Kanetake, N. and Choh, T.</i>	291
2-D Simulation of Fiber Orientation in Short Fiber Preform <i>Jung, S. W., Nam, J. B., Nam, H. W. and Han, K. S.</i>	297
Investigation on Corrosion Behavior of Aluminum Metal Matrix Composite <i>Hadianfard, M. J. and Jafari, S.</i>	303
Induction Heating of Metal Matrix Composites for Thixoforming <i>Ahn, S. S., Kang, C. G. and Jo, H. H.</i>	309
Effect of SiC Whiskers on the Elastic Constants of SiC _w /2124Al Metal Matrix Composites <i>Jung, H. K., Cheong, Y. M., Kim, S. H., Ryu, H. J. and Hong, S. H.</i>	315

Session 8 : MMC(2)

Processing and Microstructure of Magnesium Alloy Matrix Composites <i>Sasaki, G., Hara, S., Yoshida, M., Pan, J., Fuyama, N., Fujii, T. and Fukunaga, H.</i>	323
Synthesis of a Copper Matrix Composite and Simultaneous Bonding with Aluminum via Combustion Reaction in Ti-B System <i>Kwon, Y. J., Kobashi, M., Kanetake, N. and Choh, T.</i>	329
Study on Technology for Manufacturing MMC by V-EPC Method <i>Cui, Y. H., Tao, J. and Wo, D.</i>	335
Thermal Properties of High Volume Fraction SiC Particle Reinforced Al Metal Matrix Composites <i>Lee, H. S. and Hong, S. H.</i>	341
Strengthening of Particulate Metal Matrix Composites due to Grain Boundaries <i>Hadianfard, M. J.</i>	347
Evaluation of Hot Corrosion Resistance of Al ₂ O ₃ and YAG by Computer Simulation <i>Otsuka, A., Waku, Y., Kitagawa, K. and Arai, N.</i>	353

Session 9 : MMC(3)

A Study on the Impact Abrasion Performance of the Al ₂ O ₃ F/Al-9Si MMC and its Speed-dependency by Single Pendulum Scratch Method <i>Bai, X. J., Sha, J. B., Zhu, H. X., Yuan, G. C., Li, Z. J. and Zeng, Q.</i>	361
Fabrication of A356 Aluminum Alloy Composites Reinforced with SiC Particulates by Vacuum Compo-Casting Process <i>Euh, K. J., Kim, W. S. and Lee, S. H.</i>	367

Cavity Nucleation at Interfaces in Superplastic Metal Matrix Composites <i>Hosokawa, H., Iwasaki, H. and Higashi, K.</i>	373
---	-----

Application of Composite Materials in Hyundai Motor Company <i>Kim, S. C., Choi, C. H., Hwang, T. W. and Cho, W. S.</i>	379
--	-----

Session 10 : Adhesion & Coating

A Study on Ice Adhesiveness to Newly-developed Water-repellent Coating <i>Saito, H., Yamauchi, G., Takai, K., Nishi, C. and Ueda, T.</i>	389
---	-----

A Study on the Tensile Load Bearing Capacities of a Co-cured double Lap Joint <i>Shin, K. C. and Lee, J. J.</i>	395
--	-----

Effects of Strain Rates on Stress-Strain Behaviors in Adhesively Bonded Joints <i>Osaka, K., Fujinami, A., Wada, T., Fukuda, T. and Imanaka, M.</i>	399
--	-----

Effect of Microstructure on the Anodic Surface Modification of Carbon Blacks <i>Park, S. J., Kim, J. S. and Lee, J. R.</i>	405
---	-----

Session 11 : Interface(1)

Rheological Characterization of Interfacial Interaction in PP/BaSO ₄ Composites <i>Wang, K., Wu, J. S. and Zeng, H. M.</i>	413
--	-----

The Influence of Interphase Condition and Fiber Shape on the Tensile Properties of Short-fiber Reinforced Rubber <i>Ryu, S. R. and Lee, D. J.</i>	419
--	-----

Comparison of Interfacial Properties for Electrodeposited Carbon Fiber/Epoxy Composites by Tensile/Compressive Fragmentation Tests and Acoustic Emission (AE) <i>Park, J. M., Kim, J. W., Kim, Y. M. and Yoon, D. J.</i>	425
---	-----

Biomedical Applications of Polymer Composite Materials <i>Ramakrishna, S.</i>	431
--	-----

Silane Treatment of Glass Fiber to Improve Interfacial Adhesion Between Glass Fiber and Unsaturated Polyester <i>Jin, J. S., Park, S. J., Lee, J. R. and Kim, Y. K.</i>	437
--	-----

Session 12 : Interface(2)

Effect of Interdiffusion on the Interfacial Adhesion of Polymer Coated Carbon Fibers <i>Kang, H. M. and Yoon, T. H.</i>	445
--	-----

Measurement of Interphase Thickness in Glass Fibre Composites <i>Kim, J. K., Sham, M. L. and Wu, J. S.</i>	451
---	-----

Roles of Chemically Modified Carbon Black Surfaces to Enhance interfacial Adhesion Between Carbon Black and Elastomer <i>Kim, J. S., Park, S. J. and Lee, J. R.</i>	457
--	-----

Microanalysis of the Interface in Glass Fibre-Polymer Matrix Systems <i>Stachurski, Z. H., Hodzic, A. and Kim, J. K.</i>	463
---	-----

Effect of Sizing Agent on Glass Fiber/Polymer Matrix Interfacial Adhesion of Composites <i>Kim, T. J., Park, S. J. and Lee, J. R.</i>	469
--	-----

Session 13 : Polymer(1)

Silica Nanoparticles Filled Polypropylene: Brittle-Ductile Transition and Double Percolation Mechanism <i>Rong, M. Z., Zhang, M. Q., Zheng, Y. X. and Zeng, H. M.</i>	477
--	-----

Thermal Stability and Mechanical Properties of DGEBA/Trimethylolpropane Triglycidylether Epoxy Blends Initiated by Cationic Latent Catalyst <i>Kim, T. J., Park, S. J., Lee, J. R. and Hong, S. K.</i>	483
---	-----

Thermal and Mechanical Properties of Poly-(dimethyl-siloxane-adiamide) Toughened Novolac Type Phenolic Resin <i>Wang, F. Y., Ma, C. C. M. and Lee, C. C.</i>	489
---	-----

A Mechanistic Modeling of the Glass Transition Temperature of a Thermoset Polymer <i>Min, B. G.</i>	495
--	-----

Session 14 : Polymer(2)

Epoxy Resin Cured by Cationic Latent Thermal Catalyst: Effect of Catalyst on the Physical, Thermal and Mechanical Properties <i>Seo, M. K., Park, S. J., Lee, J. R. and Lee, D. R.</i>	503
---	-----

Thermal Stability and Cure Behavior on Epoxy /Polyurethane Blend System <i>Park, S. J., Jin, J. S., Lee, J. R. and Pak, P. K.</i>	509
--	-----

Enhancing the Fracture Toughness of Epoxy Resins with Amine terminated PES-CTBN-PES Triblock Copolymers <i>Kim, H. R., Myoung, B. Y., Yuck, J. I. and Yoon, T. H.</i>	515
--	-----

Session 15 : Analysis(1)

Crippling Behavior of Graphite/Epoxy Composite Stringers <i>Kweon, J. H.</i>	523
---	-----

Prediction of Damage Growth in Composite Laminates by Fracture Simulation Method Based on FEM <i>Shimamura, Y., Todoroki, A., Kobayashi, H. and Nakamura, H.</i>	529
---	-----

Prediction of Damage Growth in Composite Laminates by Fracture Simulation Method Based on FEM <i>Todoroki, A., Kobayashi, H. and Nakamura, H.</i>	539
--	-----

Effects of Mechanical Properties of Unidirectional Plies on Stress Analysis of Composite Structures <i>Shokrieh, M. M. and Bohlool, A.</i>	535
---	-----

Nonlinear Analysis of Postbuckled Stiffened Panels Made of Heat Resistant Thermoplastic Composites (CF/PIXA) and Comparison with Experiments for Supersonic Commercial Transport
Ishikawa, T., Matsushima, M. and Hayashi, Y. 543

Three Dimensional Analysis of Adhesively Bonded Composite Lap Joint
Kim, S. J., Yeo, H. J., Chung, S. W. and Han, W. S. 549

Session 16 : Fatigue & Fracture(1)

Fatigue Life Assessment of Repaired Panels with Adhesively Bonded Composite Plates
Toudeshky, H. H., Shahverdi, H. and Daghyani, H. R. 557

Complementarity of the Eigenvalues in the three Dimensional Wedges
Lee, Y. W. and Im, S. Y. 555

Computational Analysis of Crack Growth in SiC/SiC Composite caused by Creep of Bridging Fibers
Serizawa, H., Ando, M., Lewinsohn, C. A. and Murakawa, H. 571

Fracture Analysis of Repaired Panels with Adhesively Bonded Composite Plates
Daghyani, H. R., Eshaghi, S., and Toudeshky, H. H. 577

Effects of Fiber Content on Strength and Damage for Notched FRP Plates under Static Load
Yamamoto, T. and Hyakutake, H. 583

Characterization of Low Cycle Fatigue for Woven Fabric Composites (Below the Freezing Point)
Zako, M., Takano, N., Kurashiki, T. and Moriki, H. 589

Session 17 : Fatigue & Fracture(2)

Modeling of the Closure Effect in Anisotropic Damaged Material Using the Concept of Loading Mode in the Framework of Damage Mechanics
Thionnet, A. and Renard, J. 597

Effect of Circular Hole Notch on Notched Strength Characteristics of Al7075/CFRP Layered Composites
Park, J. S., Yoon, H. K., Lee, S. P. and Kohyama, A. 605

Fracture Toughness and Interfacial Structure of PP/Wood Composites
Li, T. Q., Li, R. K. Y. and Zeng, H. M. 611

Mixed Mode Impact Fracture Toughness and Rate Dependent Fracture Behavior of Interlayer-Toughened Carbon-Fiber/Epoxy Composite Laminates
Horikawa, N., Kusaka, T., Masuda, M. and Adachi, S. 617

Composite Patching Technique for the Extension of Fatigue Life of Aircraft
Kim, W. D., Yoon, K. D. and Sun, C. T. 623

Morphological Aspects of Cracking under Cyclic Loading
El-Sheikhy, R. A. I. 629

Session 18 : Fatigue & Fracture(3)

Fatigue Strength of Fiber-Metal Laminate: GLARE-3 <i>Kawai, M., Hachinohe, A., Takakura, H. and Kato, K.</i>	639
Interactive Calculation of Stress Intensity Factors of Radial Cracks in Composite Plate by Mapping-Collocation Method <i>Cheong, S. K., Kim, Y. B. and Yong, H. T.</i>	645
Microstructures and Fracture Characteristics of Reaction Sintered SiC/SiC Composites <i>Lee, S. P., Katoh, Y., Zhang, W., Kotani, M., Kohyama, A. and Suyama, S.</i>	651
Interlaminar Fracture of CF/EP Composite Laminates with Different Rubber Tougheners <i>Ye, L., and Xiao, K.</i>	657
Effect of Particle Dispersibility on the Fracture Behavior of ZrO ₂ /Ni Composite Materials <i>Hanada, N., Arakawa, K. and Takahashi, K.</i>	663
Shear Deformation Behavior in Semi-Solid State of a High Strain Rate Superplastic Si ₃ N ₄ /Al-Mg-Si Composite <i>Iwasaki, H., Mori, T., Mabuchi, M. and Higashi, K.</i>	669

VOLUME II

Session 19 : C/C & CMC(1)

- The Mechanical Properties of Carbon/Carbon Composites Prepared by Rapid CVI
Luo, R. 677
- High Heat Flux Tests of Carbon Fiber Reinforced Carbon Composites for KSTAR
Park, H. C., Choi, W. C., Kim, K. S., Nygren, R. E., Youchision, D. L. and Im, K. H. 683
- PIP Process Optimization and Mechanical Properties of SiCf/SiC Composites
Kotani, M., Kohyama, A., Katoh, Y. and Okamura, K. 689
- On Research of Co-deposited Mechanism and Characteristics of Amorphous Ni-P-SiC Composites
Wu, Y. C., Zhang, L., Li, G. H. and Ye, M. 695
- Effects of Contact Pressure and Reciprocation Number on the Coefficients of Friction of Carbon/Carbon Composites with Metal Impregnation
Matsubara, T., Takao, Y., Wang, W. X. and Hanzawa, S. 701
- Effects of Oxide Inclusions on the CREEP of P/M Al-2014 Alloy and Composites
Kang, Y. C. and Chan, S. L. I. 707

Session 20 : C/C & CMC(2)

- Mechanical Strength Experiments of Carbon/Carbon Brake Disk
Yoo, J. S., Sung, D. U., Kim, C. G., Hong, C. S. and Kim, K. S. 715
- Effect of Specimen Geometry on Tensile Properties of SiC/SiC Composites
Nozawa, T., Hinoki, T., Katoh, Y., Kohyama, A., Lara-Curzio, E. and Lee, S. P. 721
- Anti-Oxidation Properties of Carbon/MoSi₂/Carbon Composites
Seo, M. K., Park, S. J., and Lee, J. R. 727
- The Influence of Dual-ion Irradiation and High Temperature Annealing in SiC/SiC Composites
Kishimoto, H., Katoh, Y., Kohyama, A. and Ando, M. 733
- Controlling Fiber-Matrix Interfacial Properties of SiC/SiC Composites by Simple Fiber Pre-Treatment
Hinoki, T., Yang, W., Nozawa, T., Katoh, Y. and Kohyama, A. 739

Session 21 : C/C & CMC(3)

- Characterization of the Milliwave-PIP SiC/SiC Composites
Dong, S., Zhang, W., Nozawa, T., Katoh, Y., Kohyama, A., Schwab, S. T. and Snead, L. L. 747

Ultra-Fine Cement Matrix of The Continuous Fiber Reinforced Composite <i>Kim, T. J., Yang, J., Kim, K. S. and Choi, L.</i>	753
The Evaluation of the Interfacial Properties in SiCf/SiC Composites by PIP <i>Zhang, W., Kato, Y. and Kohyama, A.</i>	759
The Fast Manufacturing Process of Carbon Composites for Plasma Facing Component (PFC) <i>Choi, W. C., Park, S. H. and Kim, K. S.</i>	765
Mechanical Properties of Multi-Layer 3D Fabric C/C Composites <i>Suwa, H., Xia, M. and Kemmochi, K.</i>	771

Session 22 : NDE/NDT

A Study on Microscopic Damage Behavior of Carbon Fiber Sheet Reinforced Concrete using Acoustic Emission Technique <i>LEE, J. K., Lee, J. H. and Jeong, S. R.</i>	781
The Analysis on Electromagnetism Properties of Composite Materials in Theory <i>Zhu, Z. H. and Hu, W. Y.</i>	787
Short-Time Fourier Transform for AE Signals in CFRP Composites <i>Ni, Q. Q., Kurashiki, K. and Iwamoto, M.</i>	793
Ultrasonic Wave Propagation in Composites with Fiber Waviness <i>Chun, H. J. and Jang, P. S.</i>	799
Quantitative Evaluation of CFRP Composites by Ultrasonic Wave Propagation Characteristics <i>Okabe, Y. and Takeda, N.</i>	805
Electromagnetic Acoustic Transducer for Nonconductive FRP <i>Yamasaki, T., Nishiwaki, M. and Motogi, S.</i>	811

Session 23 : Vibration(1)

Vibration and Noise Control of a Smart Plate Featuring Electro-Rheological Fluids <i>Choi, S. B., Seo, J. W. and Kim, J. H.</i>	819
Electrical and Dynamic Mechanical Behavior of BaTiO ₃ /VGCF/CPE Composites <i>Yan, X., Zhang, H. and Sumita, M.</i>	825
A Closed-form Solution of Natural Frequency for Composite Cantilever Cylindrical Shells <i>Kim, C. W., Han, B. K. and Kim, C. K.</i>	831
Optimization of FRP Laminated Circular Cylindrical Shells by Genetic Algorithm <i>Ohta, Y.</i>	837
Flutter Suppression of a Lifting Surface using Piezoelectric Actuation <i>Han, J. H., Tani, J. and Lee, I.</i>	843
Fatigue Damage Detection and Vibration Sensing Using Optical Fiber Sensor <i>Yang, Y. C., Jeon, H. C. and Han, K. S.</i>	849

Session 24 : Vibration(2)

The Active Vibration Control Performance of the LICIT Actuator <i>Kwak, M. K. and Yoon, K. J.</i>	857
Vibration Control of Laminated Composite Plates using Piezoceramic Sensor/Actuators and Viscoelastic Materials <i>Kang, Y. K., Seo, K. M. and Lee, S. B.</i>	863
Free Vibration Analysis of Stiffened, Laminated Composite Plates <i>Ohta, Y., Narita, Y. and Wakayama, Y.</i>	869
Transonic and Supersonic Static Aeroelastic Characteristics of a Composite Wing <i>Kim, D. H., Lee, G. S. and Lee, I.</i>	875
Thermopiezoelectric Postbuckling and Vibration Analysis of Piezolaminated Plate using Layerwise Theory <i>Oh, I. K., Han, J. H. and Lee, I.</i>	881
Fuzzy Controller Design and Stability Analysis for Vibration of A Smart CFRP Composite Beam <i>Takawa, T., Fukuda, T. and Ofuji, K.</i>	887

Session 25 : Analysis(2)

Static and Dynamic Response of Sandwich Panels <i>Sadighi, M.</i>	895
A Method of Predicting the Nonlinear and Plastic Behavior of Fiber-reinforced Composite Lamiantes <i>Lin, W. P. and Hu, H. T.</i>	901
Nonlinear Flexural Behavior of Initially Curved Thick Composites with Fiber Waviness <i>Chun, H. J. and Lee, S. W.</i>	909
A Study on Stress Analysis of Composite Cylindrical Shells With a Circular or Elliptical Cutout <i>Ryu, C. H., Lee, Y. S., Choi, M. H. and Kim, Y. W.</i>	915
Elasticity Solution for Thick Laminated Shallow Circular Cylindrical Panels Under Dynamic Patch Load <i>Shakeri, M., Eslami, M. R. and Alibiglu, A.</i>	921
Design of Composite Squirrel Cage Rotor for High Speed Induction Motors <i>Chang, S. H., Lee, D. G. and Choi, J. K.</i>	929

Session 26 : Analysis(3)

Theoretical Analysis and Evaluation of Stress Concentration at Surface of Fiber Inclusions by Considering Global Anisotropy of Composite <i>Wu, Y. D. and Nakagaki, M.</i>	937
Analysis of Filament Wound Pressure Tanks Considering Fiber Angle Variation in Thickness Direction <i>Park, J. S., Kim, C. U., Hong, C. S., Kim, C. G. and Hwang, T. K.</i>	943

Postbuckling Behavior of Composite Beams with Multiple Delaminations <i>Kondo, K., Lee, C. H. and Makuta, Y.</i>	949
Low-Velocity Impact Characterization of Composite Plate by Direct Numerical Simulation (DNS) <i>Kim, S. J., Ji, K. H. and Goo, N. S.</i>	955
Finite Element Modeling of Fractured Bones Fixed with Composite Plates <i>Daghyani, H. R., Farmanzad, F. and Jabbari, E.</i>	961
Nonlinear Analysis of the Curvature Shapes of Unsymmetric Laminates including Slippage Effects <i>Cho, M. H. and Roh, H. Y.</i>	965

Session 27 : Fatigue & Fracture(4)

On The Fracture in Biaxial Fields with a New Technique <i>El-Sheikhy, R. A. I.</i>	973
Microscopic Damage Progress in High Temperature CFRP Cross-Ply Laminates under Thermal Cycling <i>Terada, K., Kobayashi, S. and Takeda, N.</i>	981
Mode II Static and Fatigue Delamination of Interlayer-Toughened CFRP in Air and in Water <i>Hojo, M., Matsuda, S., Ochiai, S. and Murakami, A.</i>	987
Factor Analysis of Lamina Combination for Flexural Fracture of CFRP <i>Kanemitsu, M. and Nakayasu, H.</i>	993
Bearing Creep Property of a Carbon /Bismaleimide Composite Material for Next-Generation SST Structures <i>Kato, H., Shimokawa, T., Tsuda, H., Sakai, A. and Asagumo, R.</i>	999

Session 28 : Fatigue & Fracture(5)

Repaired Efficiency in a Notched Steel Beam Reinforced with CFRP Patches under Static and Fatigue Loading <i>Yamaguchi, K., Kimpura, I. and Kageyama, K.</i>	1007
Effects of Elongation Property of Matrix Resin and Fiber Content on Fatigue Temperature Rise of GFRP <i>Kurashiki, K., Hirata, Y., Ni, Q. Q. and Iwamoto, M.</i>	1013
Interlaminar Fracture Toughness of Laminated Composites under Realistic Interfaces <i>Hwang, J. H., Hwang, W., Park, H. C. and Han, K. S.</i>	1019
Fatigue of a Plain Weave Glass Fabric Composite under Combined Stress-Effects of Loading Path and Temperature on Low Cyclic Fatigue Damage Process <i>Okubo, K., Fujii, T., Inoue, A. and Kawakami, H.</i>	1027
Prediction of Delamination Growth in Laminated Composites <i>Tay, T. E. and Shen, K318 F.</i>	1033

Session 29 : Smart Materials & Structures(1)

- Smart Delamination Monitoring of Graphite/Epoxy Laminates Using Electric Resistance Change with Response Surfaces
Todoroki, A., Tanaka, Y. and Shimamura, Y. 1041
- Plug & Monitor System for Smart Detection of Damage of Composite Structures
Todoroki, A., Shimamura, Y., Iwasaki, A., Inada, T. and Moriki, H. 1047
- Control of Wing Shape Using Smart Materials
Oh, J. T., Park, H. C. and Hwang, W. 1053
- Application of Health Monitoring Technology Using Fiber Optic Distributed Strain Sensors to IACC Yachts
Murayama, H., Kageyama, K., Kimpara, I., Shimada, A. and Naruse, H. 1059
- Mechanical Properties of CFRP Laminates with Embedded SMA Foils
Kobayashi, M., Song, D. Y., Ogisu, T. and Takeda, N. 1065
- Detection of Transverse Cracks in Composites Using Fiber Bragg Grating Sensors
Yashiro, S., Okabe, Y., Kosaka, T. and Takeda, N. 1071

Session 30 : Smart Materials & Structures(2)

- Structural Integrity Measurement of Reinforced Concrete Beams with CFRP Plates using Fiber Optics Michelson Sensors
Kwon, I. B., Kim, M. S., Cho, H. D., Hong, K. N. and Han, S. H. 1079
- Tuned Sloshing Damper Using Electro-rheological Fluid
Sakamoto, D., Oshima, N. and Fukuda, T. 1085
- Monitoring Thermal Behavior of Composite Materials Using Embedded Fiber Bragg Grating Sensor
Choi, H. S., Chun, H. J. and Kim, S. T. 1091
- Effects of Discrepancy of Optical Axis in EFPI Sensors on Measurement of Strains in GFRP Laminates
Osaka, K., Kosaka, T., Kawasaki, Y. and Fukuda, T. 1097
- Lightweight Curved Actuator with Piezoelectric Ceramic Layer and Fiber Composite Layers
Yoon, K. J., Shin, S. J., Park, H. C. and Kwak, M. K. 1103
- Fundamental Study of Used Optical Fibers as the Reinforcement in FRP
Ohsawa, I., Kimpara, I., Kageyama, K., Suzuki, T. and Kanai, M. 1109

Session 31 : Smart Materials & Structures(3)

- Measurement of Internal Strains in FRP Laminate with EFPI Optical Fiber Sensor during Autoclave Molding; Measurement in Off-axis Directions
Osaka, K., Kosaka, T., Asano, Y. and Fukuda, T. 1117
- Impact Monitoring Techniques for Smart Composite Laminates
Sung, D. U., Oh, J. H., Kim, C. G. and Hong, C. S. 1123

Cure Monitoring of Fiber Reinforced Plastics by Piezoelectric Ceramics <i>Oshima, N., Aoki, K., Motogi, S. and Fukuda, T.</i>	1129
A Study on the Discontinuous Effect of the Shape Memory Alloy Fiber in the Plane Stress Distributions of the Intelligent Composites <i>Hawong, J. S., Lee, H. J. and Back, U. C.</i>	1135
Detection of Damage in GFRP Laminates using Multi-Mode Optical Fiber <i>Kawada, H., Takashima, M. and Lee, G. W.</i>	1141
Vibration and Mode Sensing of a Composite Beam Using Fiber Bragg Grating Sensor Arrays <i>Koo, B. Y., Ryu, C. Y., Hong, C. S. and Kim, C. G.</i>	1147

Session 32 : Environment

Thermo-Acoustic Emission from Free Edge Damage in Composite Laminates <i>Lee, S. H. and Choi, N. S.</i>	1155
Long Term Prediction of Fatigue Life for FRP Joint Systems <i>Miyano, Y., Nakada, M., Yonemori, T., Sekine, N. and Tsai, S. W.</i>	1161
Correlation of Accelerated Exposure test with Outdoor one for Weatherability Flexural Properties of CFRP <i>Byon, O. I., Kudo, A., Motogi, S. and Motoyama, T.</i>	1167
Eco-friendly Composite Materials for Automotive Use <i>Jayaraman, K.</i>	1173
Modeling and Ultrasonic Evaluation of Interfacial Cracking Damage in Random Particulate Composites <i>Motogi, S. and Motoyama, T.</i>	1179

Session 33 : Testing(1)

Compression Bending Test Method For CFRP Pipe <i>Fukuda, H., Watanabe, T. and Itabashi, M.</i>	1187
Strain Field Measurement of Woven Fabric Composites <i>Pandita, S. D., Nishiyabu, K., Huysmans, G. and Verpoest, I.</i>	1193
Stitching Effect on Textile Composites <i>Suh, S. S., Park, J. H. and Hahn, H. T.</i>	1199
Improvement of three Rails Shear Test Method for Advanced Composite Materials <i>Soemardi, T. P. and Setiawan, K.</i>	1205
Thermal Properties of Polymer Gradient Composites of Epoxy Resin Filled with Nickel Particles <i>Funabashi, M.</i>	1213
Mechanical Strengths of Graphite/Peek Laminates Repaired after Low-Energy Impact <i>Yeh, M. K., Tai, N. H. and Chou, S. S.</i>	1219

Session 34 : Testing(2)

- Quantitative Characterization of Damage Development in Carbon Fabric Composites by Using an Enhanced Thermoelastic Technique
Uenoya, T. and Fujii, T. 1227
- Time-Dependent Off-Axis Behavior of Unidirectional Carbon Fiber Composites at High Temperature
Kawai, M., Kazama, T., Masuko, Y. and Shinbo, S. 1233
- Properties and Mechanism of Acoustic Attenuation in SiC Particle Reinforced Polyethylene Matrix Composites
Kim, K. S., Jung, H. K. and Hong, S. H. 1239
- Degradation of High-Temperature Polymer Composite Materials for the Next-Generation SST Structures by Thermal Cycling
Shimokawa, T., Katoh, H., Hamaguchi, Y., Sanbongi, S., Mizuno, H., Nakamura, H., Asagumo, R. and Tamura, H. 1245
- Ultimate Deformation of Glass Knitted Fabrics Under Biaxial Tension
Luo, Y. W. and Verpoest, I. 1251
- Bolted Joint Damages of Heat-Resistant Composite under Static Loading
Susuki, I., Hamaguchi, Y., Xiao, Y. and Sato, Y. 1257

Session A : Application(2)

- Property Optimization of Composite Coil Springs Processed by RTM
Kim, B. S., Byun, J. H. and Kim, B. H. 1265
- Appraisalment of Applications of Composite Material to Railway Vehicle
Ju, J. S., Cho, S. H., Park, B. J. and Cho, J. M. 1271
- The Static and Dynamic Behaviors and the Applications of the Stitched Sandwich Composites
Cho, J. M., Park, B. J., Cho, S. H. and Lee, S. J. 1277
- Design of a Train Seat in Composite Materials
Avril, S., Han, W. S. and Vautrin, A. 1283
- Study on the Interfacial Behavior of Polypropylene(PP) Fiber Reinforced Cement-Single Fiber Pull-Out Test
Zhao, M., Liu, J. S., Guo, H. Y. and Wang, Y. M. 1289
- Development of High Performance Composite Propulsion Shaft for High Speed Vessels
Lee, J. W., Shon, M. Y., Park, S. S. and Rew, Y. H. 1295

Late Paper

- Effects of the Residual Stresses on the Performance of the Hybrid Composite Flywheel Rotor
Ha, S. K. and Yoon, Y. B. 1303
- Mechanical Identification of Composite Materials and Structures
Vautrin, A. 1305

Plenary Lectures

INFORMATION SYSTEMS FOR COMPOSITES

H. Thomas Hahn

*Mechanical and Aerospace Engineering Department, University of California
Los Angeles, California 90095-1597 USA: hahn@seas.ucla.edu*

SUMMARY: As information technology tools become more powerful and convenient to use, they can be used to accelerate the transfer of composites technology from research to application. An efficient utilization of the literature data through the use of an information system will lead to a more timely and wider application of composite materials. As an illustration, the present paper discusses the development of databases to facilitate certification of composite structures for damage tolerance and durability.

KEYWORDS: information technology, relational databases, expert systems, composites design, damage tolerance, durability

INTRODUCTION

IT (information technology) is a term that encompasses all forms of technology used to create, store, process, exchange, and use various forms of information, such as business data, voice conversations, still images, motion pictures, multimedia presentations, and others not yet conceived. Information systems are developed using these technologies for the purpose of collecting, storing, synthesizing, and disseminating information from an environment in order to support decision making, communication, coordination, control, analysis, and visualization. Some of the common information systems are knowledge work systems, decision support systems, management information systems, transaction processing systems also known as databases, and artificial intelligence tools such as expert systems and neural networks. In the present paper we discuss the development of databases for the purpose of facilitating certification of composite structures for damage tolerance and durability.

Certification of composite structures for damage resistance, damage tolerance, and durability usually requires lengthy experimental effort. Although a fair amount of data as well as a number of mechanistic models is already available as a result of much research done so far, a truly generic model to use in lieu of experimental verification is not available yet because of the many parameters involved. An alternative is to develop a database that would complement traditional mechanistic models to reach a certification decision in shorter time. Such a database should be able to synthesize a variety of data from different sources to discern underlying information.

In the information systems we have developed most of the parameters that control damage tolerance and durability have been identified and are provided for the user to choose as input.

The output contains critical performance parameters such residual strength, life, and extent of damage. The information systems are constituted in a relational database platform Microsoft Access. Tools from expert system technology are incorporated so that low confidence input can be accommodated and flexibility can be maintained in similarity assessments. Using these systems, users can easily conduct parametric studies to determine the effect of each design parameter or a combination of parameters on damage tolerance and durability. In addition, graphical user interfaces have been developed to render the systems user friendly.

BACKGROUND

Engineering community is familiar with knowledge work systems such as computer aided design (CAD) and finite element analysis (FEA) software packages. These knowledge-level systems have seen growing applications over the last three decades. In recent years, decision support systems (DSS) have emerged to complement knowledge-level systems. The DSS help engineers make decisions in situations that are semi-structured and difficult to model in a traditional way. Thus, the DSS are either integrated with databases or built around a database structure. The analytical capabilities of DSS may be enhanced by the incorporation of artificial intelligence (AI) tools. The AI tools are used to improve human expertise and decision-making. One form of AI is expert systems, i.e., computer programs that apply the knowledge and reasoning used by human experts to solve difficult problems.

Although databases and expert systems have some similarities, the approaches they take are conceptually different. Both are developed and used to enhance information processing. Databases store large amounts of facts extensionally. The user must supply intentional definitions to retrieve the data that is wanted. An expert system, on the other hand, stores a number of intentional definitions and the user must supply specific information about a particular case to which these definitions can be applied. Thus the two technologies complement each other [1].

Because of their heterogeneity and anisotropy, composites tend to require more extensive databases than traditional materials do [2]. Civil aviation certification agencies encourage the development and use of databases in material and fabrication development [3]. The existence of a database is one of the criteria in determining the extent of testing and is crucial to addressing similarity between designs and material systems.

A large amount of data on composites has been accumulated in the past three decades to satisfy certification procedures [4]. Recently, two databases were developed under the NASA's Advanced Composites Technology (ACT) program: the Composites Information System (COINS) [5] and the Mechanical Properties of Textile Composites Database (MPTCD) [6]. The COINS contains not only material property data but also fabrication, service, maintenance, and cost data for all types of composite airframe structures. Its goal is to provide future airframe preliminary design and fabrication teams with a tool that can predict production cost during the design phase. The MPTCD, on the other hand, contains property data on textile composites. All data in the latter database come from individual coupon tests, and panel, subcomponent, and component level data are excluded. Nevertheless, manufacturing and testing specific information is also included in the MPTCD. Both databases provide NASA customers with a single source of information, facilitating data sharing. However, neither the COINS nor the TMPTCD has information on impact damage and durability behavior of composites.

The early use of expert systems for composites was mostly in the area of processing and material selection perhaps because of the difficulty of using deterministic models. A number of researchers proposed expert systems to develop and control cure cycles in autoclave and hot press molding [7, 8]. An expert system, the DSSPreform, assists in the selection of preforms used in the infiltration processing of ceramic and metal matrix composites [9]. Another system, the composites design and manufacturing critiquing system, evaluates designs and offers suggestions on the process selection [10]. The design of composites has also been an area of expert system development because of the complexity involved. Some expert systems introduce a heuristic method for the stiffness effective design optimization of composite plates under multiple loading [11, 12]. In these systems, laminate stacking sequence and the total number of plies are optimized according to the built-in design heuristics. Another example is the assistant composite laminate designer (ACOLADE), which combines classical lamination analysis with design heuristics [13]. An approach to the knowledge representation and inference strategies required for the conceptual design of polymer composite assemblies was discussed in [14]. Further, activity-based costing models have been incorporated to enable for cost estimation in composites manufacturing [15].

No expert systems have been developed yet to aid design for durability and damage tolerance of composites. The present study is a first step toward developing such expert systems to facilitate design and certification.

DATABASES FOR DAMAGE TOLERANCE AND DURABILITY OF COMPOSITES

In aerospace applications, damage tolerance refers to a safety of flight issue where the structure must be able to sustain design limit loads in the presence of damage and return to base safely. Durability, on the other hand, is an economic issue where the structure must be able to survive a certain life before the initiation of observable damage. In both cases, ply cracking and delamination are usually the dominant damage modes in composites. The growth and accumulation of these damages is usually the sequence of events that leads to failure and loss of structural integrity.

Damage Tolerance

Damage tolerance in a broader sense is the ability of a material to resist the incidence of damage as well as to tolerate the presence of damage. The present study is limited to the damage tolerance under impact since composites are known to be weak when impacted by a foreign object. Parameters affecting damage tolerance are too numerous to allow a simple comparison [16]. Therefore, a well-structured database is needed to make efficient use of the available data. The damage resistance may be measured by dent depth and/or damage area whereas the damage tolerance is usually measured by the residual strength. Both issues are of equal importance and play interdependent roles in design. Thus, these properties are the key properties to be included in a database.

Durability

Durability is the ability of a material to perform as intended for an extended period of time. Typical service environments are not only of mechanical nature but also thermo-chemical. However, the present study is limited to mechanical fatigue where damage is initiated and grows under repeated mechanical loading. While the critical fatigue damage in homogeneous

materials is in the form of a single crack, such is not the case in composites. A multitude of cracks of different shapes characterizes the fatigue damage in composites.

Many studies have been conducted over the years to determine the fatigue behavior of composites, resulting in a fair amount of data. However, the complexity in the damage mode does not allow the development of a generic model that can be used under different conditions. Most of the existing models tend to work only under the specific conditions they are intended for. Thus, there is a need to develop a database that can complement these models. The present database contains information on the subcritical damage growth under constant-amplitude and spectrum fatigue.

Databases

Two databases have been developed using the Microsoft Access Relational Database Management System (RDMS): the *DamTol* database and the *Durability* database. Visual Basic for Applications subroutines and SQL commands have been used for the data retrieval and expert solution interfaces. The use of the MS Access makes the databases easy to use and improve, and easily transferable.

Both databases have two tiers of tables. The first tier has information about the source of the data being input including the data enterer. The second tier has actual property data together with the appropriate fabrication methods and experimental conditions. Tables in those two tiers are connected through the Main table.

The hierarchical architectures of the DamTol and Durability databases are shown in Figures 1 and 2, respectively. In both databases, tables describing the sources of data (Tier 1) and the types of material have the same parameters. However, the remaining tables in the two databases have different parameters that are specific to the type of property in question.

Once a database is launched, the user is presented with a switchboard having three options: Data Entry, Data Retrieval and Expert Solution. Data Entry is a form to guide and facilitate the process of entering or modifying data. Data Entry is divided into two pages: page one for the Tier 1 information and page two for the Tier 2 information. The *Notes* section in Data Entry allows recording of any important information that is not directly related to damage tolerance or durability. The second page facilitates inputting the second tier information by providing cascaded folders that together describe a particular set of test results reported in a reference. Within each folder, the user assigns values for pertinent parameters either by selecting previous entries displayed or by typing in new values, Figure 3.

Data Retrieval allows the user to query the database for the needed information. As the user specifies values for the pertinent parameters and uses logical operators "AND" and "OR" to relate these parameters, a search string based on Structured Query Language (SQL) is generated automatically by the system. Operators "=", "Like", "<", ">", "<=" and ">=" can be used to define a range of values, Figure 4. Once the appropriate search string is created, the system finds results from the database that satisfy the search string. Results can be viewed either in tabular form or as plots, and detailed information about any record can also be obtained on the screen. The database thus makes it very easy to do parametric studies.

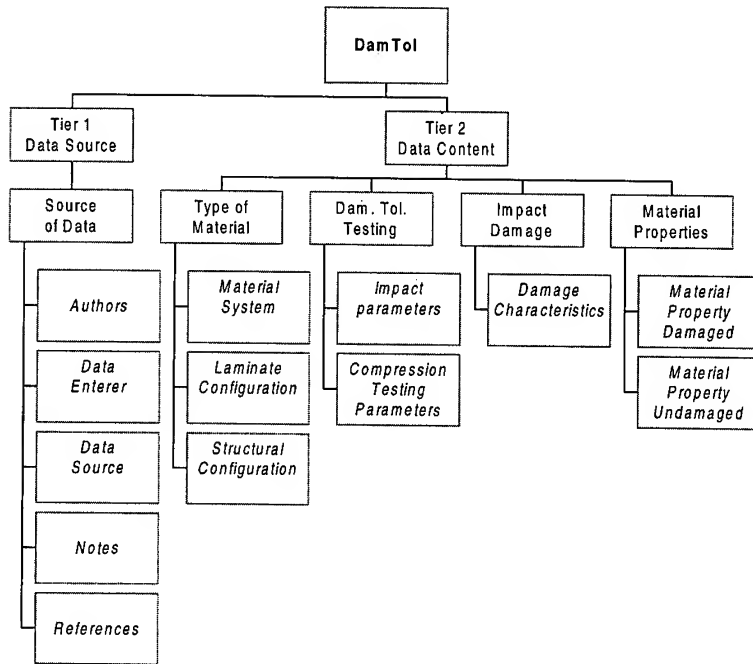


Fig. 1 Tables (in *italic*) in the DamTol database

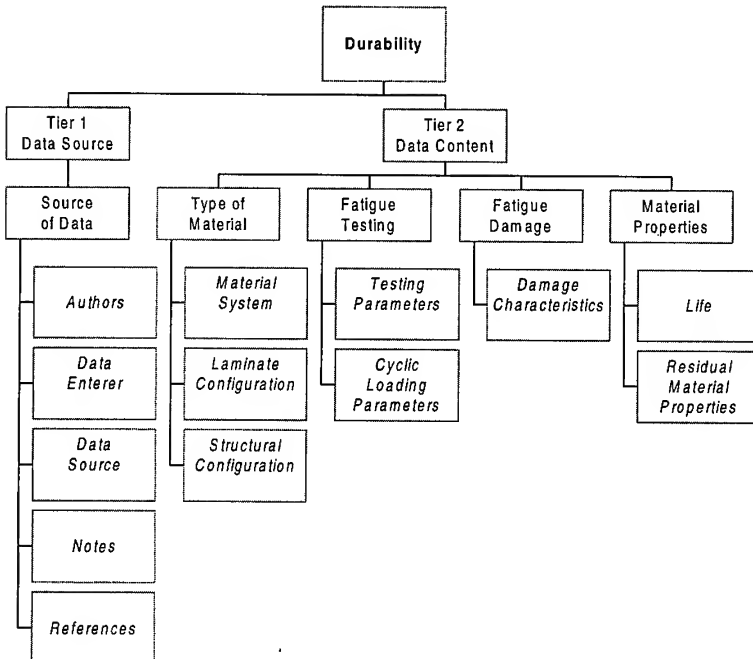


Fig. 2 Tables (in *italic*) in the Durability Database

Microsoft Access - [Data Entry]

File Edit View Insert Format Records Tools Window Help

Cyclic Loading Parameters | Residual Material Properties | Damage | Mechanical Testing Parameters | Life

Material System | Material Properties (Baseline) | Laminite Configuration | Structure

Preform Type: Ply Percentage:

LayUp Type: Laminate Thickness (in):

Stacking Sequence: Fiber Volume Fraction:

Number of Plies: Manufacturing Method:

Record: 14 | 4 | 2 | 1 | 2 | 3 of 3

New Test Delete Test

Paper Number: 1 Test Number: 39 < Previous Page 2

Form View

Fig. 2 Data Entry Interface for Durability information system

The third option Expert Solution is intended to assist the user to estimate the damage tolerance, damage extent or fatigue life when the data is not available for a specific requirement. To this end, the system compares the user requirement with that in the database and presents possible solutions with a ranking by using an embedded reasoning mechanism.

For each pertinent parameter the user chooses from the drop-down menu a value that is closest to the required. Then, a weight (W_i) and a confidence level (C_i) are assigned additionally to the chosen parameter and its value, respectively. W_i is a measure of how relevant the parameter i is in satisfying the user requirement, and C_i is a measure of how well the chosen value matches the user requirement. Both W_i and C_i can have a value ranging from 0 to 10, where 10 is the maximum. This way the user's knowledge and judgment are utilized in selecting the best solutions.

For every record which has at least one of its parameters specified an average probability of satisfying the user requirement is calculated from W_i 's and C_i 's using the weighted average method [17]. The records are then presented in the order of decreasing probability. The user may finally select the record with the highest probability as the most probable solution.

SOL Command Line ☐ AND ☐ OR

Industrial Name: Test Fixture BCs:

Structural Config: UTS: Load Dominance:

Structure Length: Load Type:

Structure Width: Max. Cyclic Stress:

Damage Type: Mean Stress:

Damage Location: Stress Ratio:

Lay-up Type: Frequency:

Stacking Sequence: No. of Cycles (log):

Number of Plies: Crack Density Ply:

Fiber Vol. Fraction: Crack Density:

Ply Percentages: Split Length:

Laminate Thickness: Delamination Area:

Preform Type: Fatigue Life:

Gege Length: Gege Width:

Table

Split Length	Industrial Name	Source	Primary Author Last Name	Primary Author First Name
0.31975	AS4/3501-6	Effect of loading parameters on Fatigue Damage Development in Notched Composite Laminates	Choi	Sung Won
0.6015	AS4/3501-6	Effect of loading parameters on Fatigue Damage Development in Notched Composite Laminates	Choi	Sung Won
1.3345	AS4/3501-6	Effect of loading parameters on Fatigue Damage Development in Notched Composite Laminates	Choi	Sung Won
1.09025	AS4/3501-6	Effect of loading parameters on Fatigue Damage Development in Notched Composite Laminates	Choi	Sung Won
2.9025	AS4/3501-6	Effect of loading parameters on Fatigue Damage Development in Notched Composite Laminates	Choi	Sung Won
1.44475	AS4/3501-6	Effect of loading parameters on Fatigue Damage Development in Notched Composite Laminates	Choi	Sung Won
1.695	AS4/3501-6	Effect of loading parameters on Fatigue Damage Development in Notched Composite Laminates	Choi	Sung Won

Records: 14 of 43

Fig. 4 Data Retrieval for the Durability information system

DISCUSSION

An advantage of using a structured database for non-standardized data is that any new piece of data can be used as soon as it becomes available without having to wait for standardization to take over. The database offers a solution by providing the user with multiple results and freedom to make a choice. Also, by facilitating comparison of various data sets, it can identify outliers easily and point to the direction of standardization objectively. Furthermore, searching for data takes considerable amount of time and the needed documents may not be readily available. As a PC-based application, the present database can conveniently be used wherever a Microsoft Access is available.

For easy reference the same terminology as in the Military Handbook 17 was used in the present databases [18]. Users are expected to be somewhat familiar with the damage tolerance and durability design of composites. The data contained in the DamTol and Durability is far from complete. Efforts are underway to expand the database to include not only more property data but also other types of composites [19].

While well-structured comprehensive databases are necessary to take advantage of the results of many years of efforts, they alone are not sufficient to enable timely and wide applications of composites. A true information system should be based on a synergistic combination of

databases, traditional analytical models, and other artificial intelligence tools such as expert systems and neural networks. The present effort is a first step toward developing such a comprehensive information system for composites.

Parameter	Value Boundary	User Confidence	Parameter Weight
Industrial Name		10	0
Structural Configuration		10	0
L-Structure		10	0
W-Structure		10	0
Structure Type		10	0
Stiffener web spacing		10	0
Lay-up Type		10	0
Stacking Sequence		10	0
Number of Plies	10/45/0/45/30/45/0/45/0/8	10	0
Fiber Volume Fraction	145/45/0/0/25	10	0
LMN Percentages	145/45/0/45/45/2/30/5	10	0
Laminale Thickness	145/45/0/45/90/45/0/45/45	10	0
UCS	145/45/0/25	10	0
Ec		10	0
Failure Strain		10	0
Failure Load		10	0
Compression Fixture		10	0
Comp. Fixture L		10	0
Comp. Fixture W		10	0
Comp. Fixture BCs		10	0
Impact Type		10	0
Impact Fixture		10	0
Impact Fixture L		10	0
Impact Fixture W		10	0
Impact Fixture BCs		10	0

Fig. 3 Expert Solution Interface for DamTol information system

CONCLUSIONS

As information technology tools become more powerful and easy to use, they can be used to transfer a wealth of literature information to the design, manufacture and certification of composites. An information system consisting of a database, mechanistic models and artificial intelligence tools would certainly facilitate a more timely and wider application of composites. The databases developed in the present study, the DamTol and Durability, are a first step toward this goal.

Damage tolerance and durability were the properties chosen for the databases in the present study because they are difficult to describe using mechanistic models alone. Appropriate database structure was then identified and implemented using a Microsoft Access. These databases make it easy to retrieve, compare and synthesize pertinent data from different sources.

At present, the data stored in the DamTol and Durability is rather limited. Efforts are underway to expand these databases. Planned for the future is a synergistic combination of these databases with mechanistic models and artificial intelligence tools to develop a comprehensive information system for composites.

REFERENCES

1. T.J.M. Bench-Capon, "Why Database AND Expert Systems?" *Proc. of the Eighth International Workshop on Database and Expert Systems Applications*, (1997), pp.2-5.
2. W.J. Rasdorf, "Composite Materials Design Database and Data Retrieval System Requirements," *Journal of Mechanical Design, Transactions of the ASME* Vol 116, 1994, pp. 531-538.
3. *Composite Aircraft Structure*, Federal Aviation Administration Advisory Circular (AC) 20-107A. (1984).
4. R.S. Whitehead, "Certification of Primary Aircraft Structures," *Proc. of the 14th Symposium of the International Committee on Aeronautical Fatigue*, Ottawa, Canada, June 1987, p. 585-617.
5. S. Siddiqi, L. F. Vosteen, R. Edlow, T. Kwa, "COINS: A Composites Information Database System," *Proc. of the Second NASA Advanced Composites Technology Conference*, NASA Conference Publication 3154, Nov. 1991, pp. 47-55.
6. Delbrey, J., *Database of Mechanical Properties of Textile Composites*, NASA CP-4747, (1996).
7. Ciriscioli, P.R., G.S. Springer, and W. I. Lee, "Expert System for Autoclave Curing of Composites," *Journal of Composite Materials*, **25**, (1991), pp. 1542-1587.
8. D.D. Shin, L.L. Lai, and H.T. Hahn, "Thermal Control System for Thick Composite Laminates Based on Forecasting," *Proc. of the 12th Tech. Conf. of American Society of Composites*, eds. Gibson and Newaz, Dearborn, MI, 1997, pp. 882-891.
9. R. Pitchumani, and V.M. Karbhari, "Knowledge-based Decision-Support Systems for Rapid and Efficient Production Planning in CMC Fabrication," *Proc. of the 18th Annual Conference on Composites and Advanced Ceramic Materials - B. Part 2*, Cocoa Beach, FL, USA. Sep. 1994, pp. 932-939.
10. S.L. Messimer, J. M. Henshaw, J. Montgomery, and J. Rogers, "Composite Design and Manufacturing Critiquing System," *Artificial Intelligence for Engineering Design, Analysis and Manufacturing: AIEDAM* Vol 10 (1), (1996), pp. 65-79.
11. S.K. Morton, and J.P.H. Webber, "Heuristic Design of Composite Laminates for Strength, Stiffness and Multiple Load Cases," *Aeronautical Journal*, Vol.101 (1001), 1997, pp. 35-45.
12. J.S. Kim, C.G. Kim, C.S. Hong, "Knowledge-based Expert System for Optimal Stacking Sequence Design of Composite Structures," *Journal of Composite Materials* Vol.33 n 13, 1999, pp. 1244-1274.
13. Allen, R. H. and A. Bose "ACOLADE: A Hybrid Knowledge-Based System for Preliminary Composite Laminate Design," *Proc. of the 1987 ASME International*

-
- Computers in Engineering Conference and Exhibition*, New York, Vol. 1, New York, NY, USA, 1987, pp 51-57.
14. T.J. Lenz, M.C. Hawley, C. Martin, J. Sticklen, J.K. McDowell, J.F. Scanlon, G.A. Wigell, "Virtual Prototyping in Polymer Composites," *Journal of Thermoplastic Composite Materials*, Vol.11 n 5, Sep 1998, pp. 394-416.
 15. M.A. Eaglesham and M.P. Deisenroth, "Advanced Composites Manufacturing Cost Estimation Decision Support System," *Proc. of the 1997 6th Annual Industrial Engineering Research Conference*, IERC, Miami Beach, FL, USA., 1997. Pp. 632-637.
 16. H.P. Kan, "Advanced Reliability Prediction Methodology for Impact Damaged Composite Structures," Final Report, DOT/FAA/AR-97/79, November 1997.
 17. O. Turkgenç, R. Dianati, M. Mitrovic, H.T. Hahn, and P. Shyprykevich, "An Information System for Damage Tolerance of Polymer Matrix Composites," *Journal of Engineering Materials and Technology, Transactions of the ASME* Vol.121 (4), 524-529.
 18. *Military Handbook: Polymer Matrix Composites*, MIL-HDBK-17-3E, Department of Defense, August 1996.
 19. M. A. Mahler, *Bonded Composite Repair of Composite Structures*, Ph.D. Dissertation, University of California, 1999.

LOW-COST INTERLOCKED COMPOSITE GRIDS

Stephen W. Tsai¹, Kevin K.S. Liu², Dongyup Han³ and Julie Wang⁴

*Department of Aeronautics & Astronautics
Stanford University*

Stanford, CA 90305-4035 USA

*¹stsai@structure.stanford.edu, ²ks-liu@pacbell.net
³dyhan@leland.stanford.edu, ⁴qlwang@structure.stanford.edu*

SUMMARY: Grids made of composite materials offer high stiffness and strength at low weight. Being fundamentally different from composite laminates, grids derive their global stiffness and strength from their ribs. Tridirectional grids have balanced Young's and shear moduli, but bidirectional or square grids are simpler because the rib intersections are simpler to design, manufacture and assemble. Such grids can be made from pultruded sections which are readily available and intrinsically low cost. The slotted joint grids in particular offer many advantages that include automatable fabrication and easy assembly without assembly jig. One key step of this simple grid is the use of rib caps that would alleviate stress concentrations around the machined slots. The bonded cap can restore the properties of the rib to those without slots. GFRP grids have been made and tested. The results are compared with predictions. Remarkable plastic strains were observed. Grids may soon emerge as one of the common structural configurations along with solid, stiffened and sandwich panels.

KEYWORDS: pultrusion, composite grids, interlocked grid, low-cost manufacturing, test data, reinforced concrete.

INTRODUCTION

There are at least two fundamental aspects of making a competitive structure. One is to maximize the stiffness and strength for a given materials; the other is to keep the lowest cost of fabrication and assembly.

In Fig. 1 we show the difference in stiffness and strength of unidirectional versus "fabric" glass/organic matrix composites. When fibers are kept straight two benefits are derived: 1) higher properties and 2) higher fiber volume packing. Thus unidirectional composites are many time higher than any other architectures that include preforms for RTM, braiding and even multidirectional laminates.

The other fundamental aspect is low cost. Ribs of a grid structure can be made by pultrusion. The result will lead to by far the lowest cost of any automated process, comparable to filament winding. The process of pultrusion is fast, widely available around the world, and attains a fiber volume fractions over 70 percent (represented by the highest

points in Fig. 1, over 50 GPa and 1500 MPa!) For carbon composites a similar difference exists between nonwoven and woven fibers.

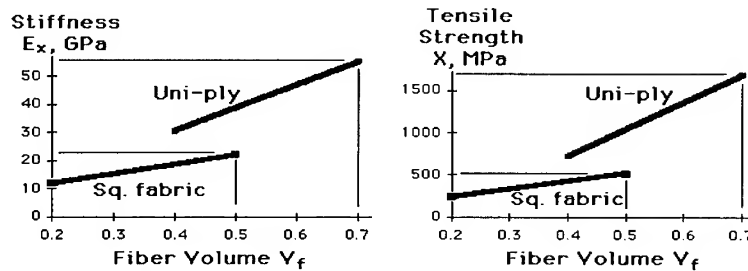


Fig. 1 Stiffness and strength of uni-ply versus square fabric.

Large volume production of pultrusion is possible. Each machine can produce simple structural shapes up to 1 meter/minute or 1.44 km/day. It is therefore possible to use unidirectional ribs to form a large, continuous square grid that would give us the most competitive composite panels not possible with any other existing process.

The weakness of a slotted joint grid, however, is the discontinuous ribs in opposite directions on the top and bottom of the grid shown in Fig. 2.

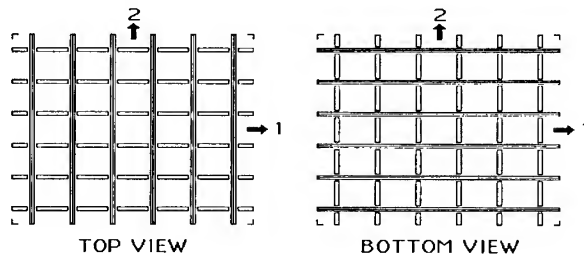


Fig. 2 Top and bottom views of a slotted joint square grid.
Note the continuous and discontinuous ribs.

Although the ribs are interlocked, the slots weaken the grid. This weakness is shown in Fig. 3 where the slots cause: 1) stress concentration under tension at the root of the slot, and 2) softening in compression from the presence of [90] rib that interrupt the otherwise all [0] rib. Both lead to lower performance of the slotted joint grid.

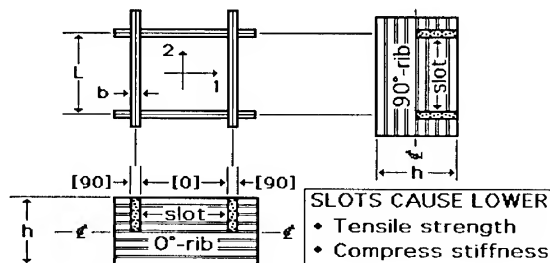


Fig. 3 Slots cut into 0 and 90 degree ribs cause lower tensile and flexural strengths and lower stiffness in compressive stiffness.

One easy way to overcome this weakness is to install a rib cap that would provide a continuous load path thereby offsetting the damaging effect of slots. The high stiffness and strength of ribs without slots can thus be recovered and restored. The sequence of assembly of the ribs to form a slotted joint grid and subsequent bonding of rib caps are shown in Fig. 4.

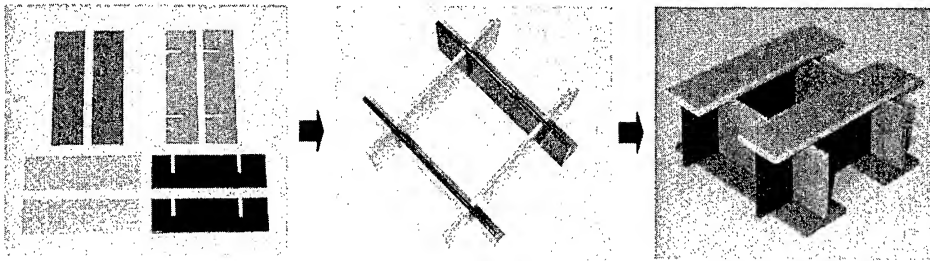


Fig. 4 Assembly sequence of slotted joint grid and bonding of rib caps

Fig. 5 shows one of the finite element analyses that models a slotted rib reinforced by a bonded rib cap. For the example shown below, rib height is 2 inch, rib and cap thicknesses are 0.25 inch and the cap width is 0.25 inch. The stiffness of the rib without slots and rib caps is fully recovered (labeled as Ideal in Fig. 5) and becomes even stiffer as you increase the distance between the slots. For this case, there is no rib cap. The finite element analysis shows that for this case a ratio of unity between the slot distance and rib height (the abscissa axis), the rib stiffness can be fully recovered; i.e., the bending stiffness of a rib with slots and rib cap equals a solid rib without slots (the Ideal case).

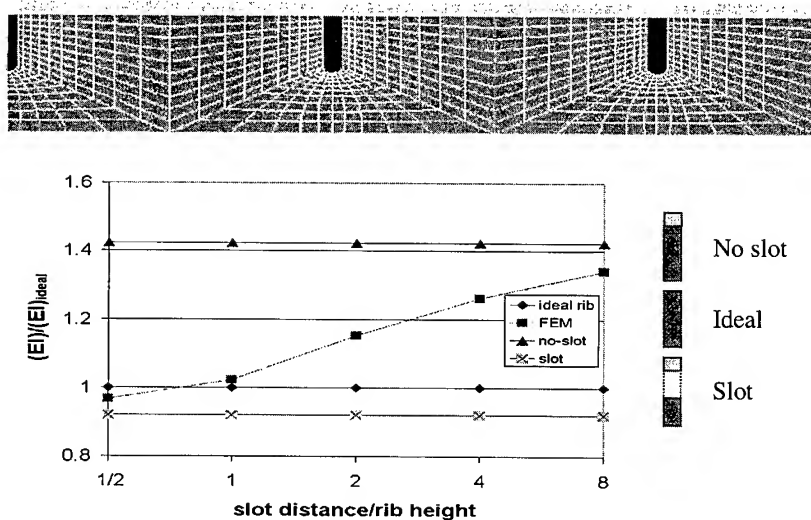
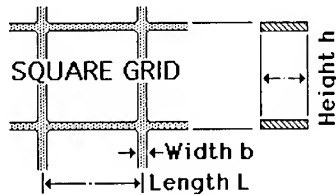


Fig. 5 Finite element model for a cap reinforced rib and rib stiffness recovery from use of rib caps.

If the rib stiffness is fully recovered there are exceptionally simple relations between the rib and grid stiffness. The relations are shown in Fig. 6. A key parameter is the rib volume fraction f that is inversely proportional to the rib aspect ratio L/b . These relations give confidence to designers and permit instant the back-of-the-envelope calculations. [1]



$$\text{Rib Fraction } f = \frac{2}{L/b}$$

$$E_x = E_y = \frac{b E_{\text{rib}}}{L} = \frac{f E_{\text{rib}}}{2}$$

$$\nu_x = 0$$

$$G_x = 0$$

Fig. 6 Elastic constants of square grids as functions of f and L/b .

The actual stiffness of an interlocked grid in terms of the rib stiffness is more complicated than those shown in Fig. 6 because the slots and rib caps are unsymmetric. A more detailed modeling that takes into account of the asymmetry will be needed.

In conclusion, slotted joint grids can now be made to perform as if the slots are no longer the source of stress concentration. The remarkable stiffness and strength of unidirectional ribs are directly translated to the grid properties. Yet the low cost of pultrusion is utilized to the maximum degree. It is our plan to have a slot cut by saw or waterjet as soon as the pultruded section is cured. The cutting can also be done in the field. Then field assembly of the grid can be done without additional assembly jig. The use of ribs with slotted joints can be used for grid assembly. Being able to have the grid assembled in plant or construction site is a huge advantage. The cycle time is the curing time for the adhesive, which can be as low as one minute.

PRELIMINARY RESULTS

Using the concept introduced above, we built and tested several 'Interlocked Composite Grids' and Fig. 7 shows pictures of a 10' x 10' x 6" grid in two stages of assembly. This grid was assembled manually in a matter of minutes. No special fixturing or tooling was used.

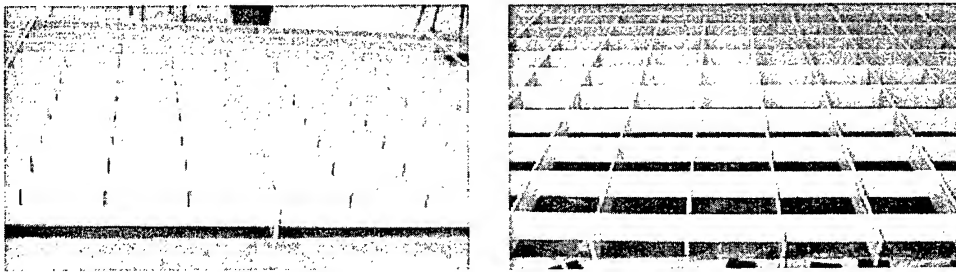


Fig. 7 A square grid of partial (left) and complete assembly (right).

Fig. 8 shows the finished grid with rib caps bonded to the unreinforced grid shown in Fig. 7, and the load-deflection curve of the grid subjected to a central load with panel edges simply supported. Testing the grid shown in Fig. 8 revealed remarkable resilience. Loading, unloading and reloading showed essentially no permanent strain or hysteresis. As expected, failure initiates from the root of the slots. Cracks propagate along the fiber direction, growing slowly and predictably, not catastrophically. The rib cap bonding does not fail until after cracks from the slots are clearly visible. The ultimate failure strain was many times the initial failure strain, yielding a highly ductile overall behavior. Thus the grid is tough and damage tolerant and well suited for bridge decks and other critical applications.

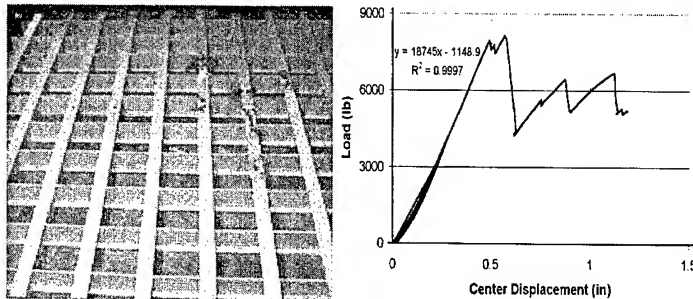


Fig. 8 A completed grid and its performance under centrally applied load.

GRID REINFORCED CONCRETE

There are numerous potential applications. Grids without skin can be a reinforcement for concrete walls and decks. Panels with one skin can be used as skins for aircraft and spacecraft, bridge decks, floor panels for buses, trains and trailers. Panels with two skins can be used for building walls.

Among these, the following discussion concentrates on composite grids as concrete reinforcements. Composite grids have unique characteristics when used as reinforcement in concrete. Carbon fibers instead of glass fibers must be used since the carbon fibers can resist alkaline attack in concrete that glass fibers cannot. The volume of fibers required to reinforce concrete is proportional to the fiber stiffness; carbon fibers are more than three times the stiffness of glass fibers. The increased stiffness and alkaline resistance offset nearly ten times the cost of carbon over glass fibers. Outstanding properties of carbon-grid reinforced concrete structures are listed below.

- 1) **SYNERGISM:** Concrete stabilizes ribs and provides in-plane shear rigidity; grid provides tensile strength and prevents macro cracks. Decks, floors, roads and sidewalks without macro cracks not only enhance appearance but also save maintenance cost.
- 2) **LOAD TRANSFER:** Instead of friction between rebars and concrete, load transfer between grid and concrete is through interlocking. Fig. 9 illustrates the difference. Grid is bi-directional. It is particularly suited for decks and panels. Non uniform foundation support can be bridged by such decks and panels making macro cracking more difficult. Interlocked grids can blunt such cracks.

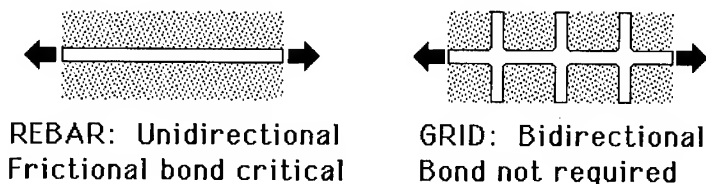


Fig. 9 Comparison of reinforcing mechanisms in concrete.

- 3) **THERMAL EXPANSION:** Carbon ribs have zero thermal expansion. Grid in concrete can hold concrete to zero expansion. Expansion joints can be eliminated making continuous concrete possible. Being sources of water penetration and spallation continuous concrete requires less maintenance. Continuous decks are more efficient – several times stiffer than bridge decks made of individual decks

between support, and many times stronger against earthquake. Individual decks are more likely to fall down than a continuous deck.

- 4) **SELF-SUPPORTING FORMS:** Grid has sufficient stiffness and strength to carry wet concrete and requires minimal or no support. Special, soaring architectural forms that may be impossible to build using conventional forms that require support can now be built with our grid. Rapid construction with minimum traffic disruption is possible. There is also enhanced safety for workers – wet concrete collapse can be avoided.
- 5) **FIRE PROTECTION:** Grid is protected from fire by fire proofing. Polyester instead of epoxy may be an acceptable matrix. Polyester is lower cost and makes pultrusion process easier and faster than epoxy. A new generation decking, in place of grating, is now possible. Solid decking is safer in case of fire because flame must go around the deck.
- 6) **HIGH STRENGTH VENEER:** Grid can also support brick and stone veneer for building. Bricks and cut stone can be inserted and bonded in grid cells. Such construction can save labor (with lower level skill and quicker installation) and improve explosion and earthquake resistance.

Preliminary test result of a grid with and without concrete is shown in Fig. 10. Glass fiber is used for the test. There is a 7-fold increase in stiffness and strength. Substantial “plastic strain” was exhibited. The glass ribs are 2” high x 3/16” thick. The cells are 4” square. If carbon grids are used, 1/16” thick ribs will provide the same reinforcement.

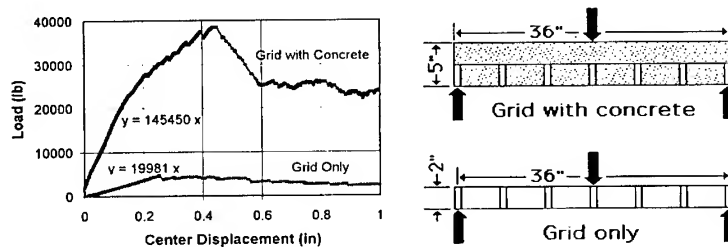


Fig. 10 Load-deflection curves of grid with and without concrete.

CONCLUSION

The new concept of making composite grid structures is proposed. The ‘Interlocked Composite Grid’ uses the slotted unidirectional composite ribs and slot reinforcing rib caps. All the ribs and caps are manufactured by pultrusion process. The material cost and fabrication cost are low while the performance of the final product is outstanding. The preliminary test results of the interlocked grid and grid reinforced concrete slab are presented. Finally, the superior characteristics of the grid reinforced concrete compared to conventional rebar reinforced concrete have been reviewed.

The information contained in this document is Stanford University proprietary.

REFERENCE

1. S.W. Tsai, K.S. Liu, and P. M. Manne, "Manufacture and Design of Composite Grids," 3-D Textile Reinforcements in Composite Materials, Antonio Miravete, ed. Chapter 5 (1999), pp. 151-179.

NATIONAL SCIENCE & TECHNOLOGY POLICY IN KOREA

Eui Jin, Jun

*Deputy Minister, Ministry of Science and Technology,
Government Complex, Jungnang-dong 1, Kwachon, Kyunggi-do, Korea
E-mail : ejjun@most.go.kr*

SUMMARY: The direction of Korea's S&T policy for the 21st century and major tasks to be implemented are introduced. In the Long-term Plan for S&T Development, which formulates the vision and direction of S&T development for the 1st quarter of 21st century, the goal of S&T development is addressed. To achieve the goal of the long-term plan, the government is pursuing the following policy tasks; measures to increase investment and efficiency of the national R&D, the 21st Century Frontier R&D Project, the National Research Laboratory project, R&D projects on the future core technologies, measures to support technology innovation of the private sector, measures to stimulate basic science and foster creative manpower.

KEYWORDS: MOST, NSTC, the long-term plan for S&T development, 21C frontier R&D project, NRL, space technology development project, biotechnology project, diffusion of R&D results, the advancement of basic science, fostering the creative workforce

INTRODUCTION

The future society of the 21st century will witness radical changes which have been unprecedented in history. We will experience an information and knowledge-based society where the source of wealth and growth is no longer material resource, but knowledge, information and S&T instead. In the coming century, splendid achievements will have been made in science and technology. Science and Technology will be a driving force leading economic and social developments as well as restructuring the overall social system. As a result, the society will be increasingly driven by the S&T development.

1. Administrative Reform in S&T Policy of Korea

The 1990s was a period of change and challenge for S&T of Korea. The main focus of the S&T policy was to devise and implement an overall policy embracing the great changes of the 21st century. To support the government's policy, the "Special Law for Scientific and Technological Innovation" was enacted in April, 1999. In January 1999, the "Law on Foundation, Management, and Support of Government Research Institutions(GRIs)" was enacted, designating the Prime Minister as an overseer of GRIs. To strengthen the overall coordination of

national S&T policy, the National Science and Technology Council (NSTC) was established. Its main role is to coordinate major policies and overall plans for promoting S&T, expand the S&T-related investments and set the priority on national R&D programs and so on. NSTC consists of 19 members, including President as chairman, major cabinet members, and civil experts related to S&T.

S&T of Korea have developed dramatically during the last 30 years, especially in the volume of investments and organizations. R&D investment has expanded to 2.52% of GDP, with R&D manpower reaching 130,000 persons in 1998. However, compared with advanced countries as the U.S. and Japan, Korea is still far behind; in terms of the size of the investments, Korea stands at only a twenty-eighth of the U.S. and a fifteenth of Japan.

2. The Vision and Objective of Science and Technology of the 21st Century

A "Long-term Plan for National Science and Technology Development" was established in 1999. According to the plan, Korea is to surpass its rivalling Asian countries by the year 2005. Korea will have become the center of research in the Asian Pacific region by the year 2015, and one of the top 7 countries by the year 2025.

If everything goes as planned, by 2025, Korea will have secured technological initiative in specific areas and become the top 5th country in the world in terms of informization index. Furthermore, S&T will have contributed to 30% of the total national economic growth, up from 19% of the present. Thus, Korea will finally join the ranks of industrially advanced countries, with import and export of technology well balanced.

In an effort to achieve the long-term goal, the government established the direction of a new policy which is designed to strengthen the potential of a National S&T Innovation System.

First, to accommodate the radically changing scientific and technological environments, the government will encourage technological innovation driven by the private sector rather than by the government.

Second, to ensure effective investments into R&D, the government will place emphasis on the efficiency of resource allocation along with steady efforts in increasing investments.

Third, to overcome the limitation of domestic R&D resources, globally networked R&D activities will be pursued instead of domestically-driven R&D.

Lastly, technology innovation will be geared towards market-creation from a long-term point of view instead of responding to short-term demands.

With such efforts, Korea will be able to acquire the knowledge creation capability which will eventually enable itself to explore a new industry, no longer adopting or imitating the advanced technologies of developed countries.

Table 1. Key S&T Indexes

Classification			1998	2005	2015	2025
In-put	Investment	R&D Investment	\$8.1 billion	\$20 billion	\$47billion	\$80billion
		rate to GDP	2.52%	3.0%	3.5%	4.0%
		rate to Governments Budget	3.6%	5.0%	5.0%	5.0%
		Government : Private	27:73	27:73	30:70	30:70
	Work-force	Number of Researchers By 10,000 heads	129,767 27.9	196,000 40	258,000 50	314,000 60
Out put	Patent	Domestic	35,900	128,600	333,600	535,500
		Overseas	3,391 ('96)	17,500	45,400	74,000
	Papers	SCI	11,514	41,000	107,000	174,000
		World Ranking	16	12	8	5
		The number of being quoted in recent 5 years	60	40	20	10
	Technology Export/Import		0.07('97)	0.3	0.7	1.0
Others	S&T Competitiveness(IMD) World Ranking		22('00)	12	10	7
	S&T's Contribution to Economic Growth		19%('97)	23%	26%	30%
	Technology Management, World Ranking		27('00)	25	15	7
	Scientific Environment, World Ranking		25('00)	20	12	3

3. Expansion of R&D Investments

Korea's R&D investments have steadily grown by 20% in annual average since 1990 through 1997 thanks to the efforts made by the government as well as by industry. In 1998, however, for the first time, R&D investments have declined 10.4% due to the drastic restructuring efforts of industry to cope with the financial crisis which struck the nation. To make up the reduction in R&D investments, the government had to raise its share of financial burden; the share of financial burden by the government versus private sector went up to 27:73 in 1998 from 23:77 of 1997. In the long-run, we planned to expand R&D investments from \$ 12.8 billion in 1997 to \$ 80 billion by 2025.

4. National R&D Projects

Key R&D Programs of MOST, of which budget amounts is about \$ 750 million - about 21 % of total government R&D Budget- in Fiscal Year 2000, are as follows.

Table 2. R&D Programs of MOST (F.Y.2000)

(Unit: million \$)

R&D Programs	Amounts
O Highly Advanced National Project	62.7
O National R&D Program for Critical Technologies	72.5
O Dual-use Technology Program	19.4
O 21st Century Frontier R&D Program	45.5
O Space Technology Development Program	46.4
O The Creative Research Program(CRI)	25.0
O The National Research Laboratory Program(NRL)	68.2
O Promotion of Basic Research	218.3
O Nuclear R&D Program	140.5
O International S&T Cooperation	18.0
O Others	34.2
Total	750.6

Highly Advanced National Projects (HAN) is a large scale R&D projects carried out with funding from government and industries under 9-year project management system. A total of \$ 1896.4 million had been invested over the period from 1992 to 1997. The HAN project is composed of two categories. Product technology development projects focus on ISDN, HDTV, ASIC, flat panel displays, biomedical, micromachine, which Korea has the potential to compete with the advanced countries. Fundamental technology projects emphasize core technologies such as environment technology, next generation energy problem, human sensibility, functional materials and etc.

The 21st Century Frontier R&D Project is being carried out with an objective of enhancing the nation's competitiveness in strategic technology, thereby joining the ranks of advanced countries and realizing the living standards of advanced countries. By the year 2002, about 20 projects will have been launched, including two model projects launched in 1999 along with three projects to be launched this year. Every projects will be funded about \$ 9 million for ten years and project managers will have autonomy on his projects.

The National Research Laboratory(NRL) project is being carried out with an objective of picking out and nurturing promising research laboratories working on the core technologies to grow up to represent the nation. First of all, the excellent research projects on core technologies are selected, and then supported for the maximum of 5 years. In 1999, 140 research laboratories were selected and supported and about 150 research laboratories of industry and academia will be

picked out and supported this year and next year. Thus, \$ 41 million in all (\$ 2.7 million per a research laboratory and 150 labs) will be supported in every year.

The Promotion of Creative Research Projects has been carried out since 1997 with an objective of pushing back the frontier of existing technologies and creating new knowledge through planting and nurturing the new seeds of technology. The research projects will be evaluated every 3 years and be supported for a maximum of 9 years. This year the government will steadily support a total of 51 projects selected during a period of 1997 through 1999 with \$ 25 million.

The Space Development Project will be carried out in full scale. The development of a communication satellite (Mookungwha #4) will be launched earlier than planned. By 2005 a space center with launching facility will be constructed. By 2006 the multi-purpose satellite and communication satellite will be completed with our own technology.

Master Plans for Biotechnology and Plan for Brain Research Promotion will be carried out with an objective of securing the most advanced level of biotechnology in the world. 7 ministries including MOST have already invested \$ 600 million into 7 core technologies since 1994 through 1999. This year, 7 ministries will invest \$ 203 million into the projects such as the development of the state-of-the art biological material, brain research which might lead to the development of new medicine and new treatment of diseases, even with the possibility of conquering such incurable diseases as stroke and senility. Furthermore, laws regarding safety of biotechnology and ethical issues involved will be continuously improved.

5. Encouraging technology innovation by the private sector and diffusing research results

The government will support the research conducted by the private sector. Private research institutes have grown these days with the number exceeding 5000, taking up 80% of the total national R&D investment and 55% of total research manpower. In 1981, there were only 46 private research institutes which were licensed by MOST, however, the number has escalated to 1,000 by 1991, 3000 by 1997 and 5,000 by Feb. 2000. Furthermore, the number of venture companies has already exceeded 5,000 by March 2000.

To effectively support the growing R&D activities, Daeduk research complex which were originally developed for academic and research purpose will be reinforced to develop into a venture valley. The existing Start-ups Incubator in the KAIST will reemerge to serve as a base for supporting venture companies. Besides, to promote commercialization of excellent research results, the government will establish more Start-ups Incubators in government-supported research institutes.

6. Expansion of Investment in Basic Science

It has been acknowledged that Korea is lagging far behind in basic science not just in terms of investments but also in performance. With an objective of raising the nation's level of basic science to the 10th from 16th of 1999, the government will increase investments in basic science; the percentage of basic research budget out of the government's total R&D budget will rise to 20% in 2002 from 16.8% of 1998. For this, \$ 154 million was allocated to basic science projects, 7.4% up from that of 1999.

The government established two types of research centers in universities: Center of Excellence (SRC/ERC) and Regional Research Centers (RRC). 61 centers have been set up at major universities as of 1999. The research paper publications of these centers account for 20 % of all Korean papers in SCI journals. 37 RRCs were located in regional universities nationwide. These RRCs help local industries strengthen their international competitiveness. The government supports research funds to these centers for 9 years.

7. International S&T Cooperation

As a newly industrialized country facing a competitive global economy, Korea recognizes the need for a new approach to international cooperation. Korea is seeking a more active role in the international science and technology community, not only to contribute to scientific advancement but also to harness new knowledge for the nation's social and economic development. To this end, it is actively pursuing both bilateral and multilateral cooperation. In bilateral cooperation, although the United States, Japan, and European countries have been major partners, cooperation with Eastern European countries has increased in recent years. Annual S&T minister level joint committees with these countries are held at home and abroad in turn. In multilateral cooperation, Korea has been endeavoring to strengthen the relationship with international organizations such as APEC(Asia Pacific Economic Cooperation), OECD(Organization for Economic Cooperation and Development), EU(European Union), ISTC(International Science and Technology Center) in Russia and etc.

The government supported about 1,100 international joint research programs since 1985. The government established research centers in several countries. KIST-Europe in Germany, 5 centers in Russia, two in China, each one in U.K. and U.S.A.

REFERENCES

1. Ministry of Science and Technology, "Long-term Vision for S&T Development toward the year 2025", 1999.12, pp.23-153.
2. Ministry of Science and Technology, "Science and Technology Annual 1998", 1999.3, pp.1-73, 145-239.
3. Science and Technology Policy Office, Ministry of Science and Technology, "Report on IMD's National Competitiveness Ranking Appraisal", 2000.4, pp.2-14.

Recycling of Polymer Materials for Automobile

Norio Sato

*Toyota Central Research and Development Laboratories, Inc.
Nagakute, Aichi, 480-1192, Japan*

SUMMARY: Toyota Central R&D Labs., Inc. has been conducting "Material Recycling Project" in order to develop fundamental technology for automotive plastics recycling. The project has developed bumper-to-bumper recycling technology for painted thermoplastic bumper. Toyota Motor Corporation has developed the recycling system based on the technology and started post consumer bumper recycling. Furthermore, the project has developed new technologies for polyurethane bumper recycling, rubber recycling, floor carpet recycling, and plastics identification. This paper describes briefly the technology for the plastics recycling which is based on "Reactive Extrusion Processing".

INTRODUCTION

The necessity to develop an appropriate technology for recycling of automotive plastics parts has been intensified in recent years, in terms of environmental protection and preservation of resources. Toyota Central R&D Labs., Inc. has been conducting "Material Recycling Project" in order to provide fundamental technology for material recycling, in particular for plastics recycling. The project is composed of five research teams of mechanical recycling, chemical recycling, biochemical recycling, electrolysis recycling, and life cycle assessment. This paper describes an overview of the project and presents "Reactive Extrusion Processing" using screw extruder as key technology of plastics recycling.

THERMOPLASTIC BUMPER-TO-BUMPER RECYCLING

Thermoplastic (elastomer modified polypropylene (PP) and Toyota Super Olefin Polymer (TSOP); hereafter referred to as "TP") bumper-to-bumper recycling is the most important target for automotive plastics recycling. Figure 1 shows an example of comparison of mechanical properties between virgin material and recycled material obtained by remelting of crushed bumper. In the case of such simply recycled material, impact strength and brittleness temperature in particular, which are critical characteristics of bumper, tend to deteriorate. The cause for the deterioration of mechanical properties is relatively large size of paint fragments dispersed in TP resin as foreign substances, that give adverse effects to mechanical properties in general and impact resistance in particular. Figure 2 shows a magnified view of fracture surface of simply-recycled material, which shows a coarse paint fragment as an initiation of fracture. If such coarse paint fragments exist in a molded product, the surface appearance will be also affected adversely. Therefore, the elimination of adverse effects is necessary in order to allow the recycled material into the original form of bumpers.

Several methods for eliminating the paint film have been developed. However, they have some disadvantages in quality of recycled material, recycling productivity and economical point. The authors et al. have developed a new recycling technology based on pressured hydrolysis of the paint film. In the pressured hydrolysis technology, water under high temperature and high pressure is used to hydrolyze and break crosslinks of the paint film and the decomposed paint film is dispersed in the TP resin by kneading. Major component of the paint resin is alkyd-melamine resin or acrylic-melamine resin, which can be decomposed by hydrolysis under such severe conditions. Two types of processing systems have been developed. One is autoclave/screw-extrusion processing system (batch system)[1-3], and the other is twin screw reactive extrusion processing system (continuous system)[4,5]. Figure 3 shows the twin screw reactive extrusion processing system. The crushed bumper is subjected to the twin screw reactive extruder whose cylinder is divided into three zones of melting, hydrolysis reaction, and mixing. In the melting zone, the crushed TP bumper is melted down and kneaded. The paint film on the TP resin is torn into fragments by shear stress of kneading. In the next hydrolysis reaction zone, water is injected into the cylinder and vapor of water is mixed with melted resin at a temperature of 250°C. The paint film in the melt TP resin is hydrolyzed in a short time by the pressured vapor of water. In the next mixing zone, decomposed paint film is dispersed in the TP resin in the form of very small particle. The volatile fraction of decomposed paint film and vapor of water are evacuated from a vent. Finally the TP resin is extruded from head of the extruder and cut to pellet. This system is a continuous process of melting, hydrolysis reaction, mixing, and pelletizing, so it is of great advantage for environment and economy.

Figure 4 shows a SEM observation of decomposed paint film on fracture surface of the recycled material. The size of non-decomposed paint film shown in Fig. 2 is as large as 200 μm or greater with the complete separation at the interface between TP resin, resulting in the deterioration of impact resistance. The size of decomposed paint film in Fig. 4, on the other hand, is reduced to about 15 μm , and the interface between TP resin is not separated. It indicates that compatibility and adhesion performance at the interface are improved. Figure 5 shows mechanical properties of 100% recycled material obtained by the reactive extrusion compared with those of the virgin material. Izot impact strength at low temperature, brittleness temperature, and other fundamental characteristics such as weather durability, are nearly equal to those of the virgin material. The quality of appearance is not different from that of the virgin material. Very fine particle of decomposed paint film and of the compatibility of the TP resin interface described above are considered to be elimination of the adverse effects of the paint film in the recycled material.

POLYURETHANE BUMPER RECYCLING

Polyurethane bumper recycling has been studied for a long time. Various technologies for mechanical and chemical recycling have been proposed. Toyota Motor Corporation has performed recycling to automotive mud guard. Because of limitation of the amount of recycled material, other recycling technology is required. The authors et al. have developed two recycling technologies. One is a pressured glycolysis as chemical recycling. The pressured glycolysis has been performed with an autoclave under a pressure of 0.3 MPa and a temperature of 240 °C. The benefits of the pressured glycolysis compared with the conventional glycolysis which is performed under atmosphere are that the reaction time becomes shorter from 8 hours to 30 minutes and that viscosity of the recycled material becomes lower as that of the virgin one. The recycled material is available for forming by RIM. The mechanical property and surface appearance, however, must be improved for

automotive bumper application. Other parts application of the recycled material has been undertaken.

The other is a blend of polyurethane and thermoplastics as mechanical recycling. The blending of crashed polyurethane bumper with polypropylene has been performed by reactive extruder. Polyurethane is thermoset resin and polypropylene is thermoplastic resin. They are incompatible, so that obtained blend is inhomogeneous as shown in Fig. 6(a). Adding water into the extruder to promote chemical decomposition of polyurethane, hydrolysis of polyurethane occurs in melt polypropylene, so that homogeneous blend can be obtained as shown in Fig. 6(b). The blend is available for conventional injection molding. The blend has been used as automotive plastics parts. This technology is considered to be useful for polyurethane recycling from viewpoint of economy.

RUBBER RECYCLING

Rubber recycling technology has been already developed and used in practice in industrial fields. One of the typical technologies is a chemical recycling called "Pan method", where crosslinks of the rubber is broken using steam autoclave under a temperature of about 200°C, and a pressure of about 2MPa for more than 10 hours. It is considered to be difficult to apply the technology for automotive industry because its productivity is very low. The authors et al. have developed a new system using a screw reactive extruder which permits high productivity and high quality of the recycled rubber[7]. Figure 7 shows the extruder where crushed rubber is fed with some amount of decrosslinking agent and the recycled rubber is extruded from head of the extruder as shown in Fig. 8. The productivity is 200kg/hour in the case of the screw diameter of 55 mm. The recycled rubber shows excellent mechanical properties equivalent to the virgin one as shown in Fig. 9. This technology has been using for in-plant recycling of waste of weather strip of EPDM rubber as the first step of the automotive rubber parts recycling.

FLOOR CARPET RECYCLING

In the fabrication of the floor carpet, a large amount of trimming waste is generated, so that the waste is required to be recycled. The authors et al. have developed recycling technology for the carpet waste. The waste has been recycled to backing material of the carpet[8]. Two important technologies have developed for the recycling. The carpet waste is too bulky to be fed to melt-extruder. In order to make the waste compact, a rotating friction disc machine has been developed. The bulky waste becomes granule by half-melt. The granule is available to be fed to extruder. The other is how to improve mechanical properties of recycled material. Since the carpet is composed of polyester fiber of base fabric, nylon fiber of pile, and polyethylene resin of backing material, the melt-compound is incompatible. In order to improve the compatibility of the compound, a reactive compatibilizer is added to the melt-extrusion processing. Due to chemical reaction among three components, mechanical property of the compound was remarkably improved. This technology has been used for in-plant recycling in a Toyota cooperative company since 1990, which permits tremendous reduction of the landfill of the waste.

PLASTICS IDENTIFICATION

Plastics identification is very important for plastics recycling. Reflection infrared spectrometer has been used for the identification. Its precision is very high, but the surface of plastics must be ground and put on the window in the spectrometer. The authors et al. have

developed an identification method using pyrolysis infrared spectrometer as shown in Fig. 10. A special prove has been developed in which the surface of plastics is heated by infrared heat beam and induced pyrolysis gas is introduced into gas cell of the spectrometer through a flexible heat tube. The precision of identification is excellent as compared with that using the reflection infrared spectrometer. The advantages of this method are that there is no limitation of the surface condition of plastics and that the prove is flexible and attachable to any shape of plastics parts. This technology has been now applying for the identification of automotive rubber parts and thermoplastic bumpers.

SUMMARY

In order to realize the plastics recycling, recycling technology must be simple and must be available for various kinds of plastics. Furthermore, the technology must provide high grade recycled materials. "Reactive Extrusion Processing" proposed here for TP bumper recycling, polyurethane bumper recycling, rubber recycling, and floor carpet recycling is considered to satisfy above demands for recycling [9]. The processing is applicable not only for thermoplastics but also for thermosets and also for their mixture. The reactive extrusion processing is considered to become a real plastics recycling technology. Toyota Central R&D Labs., Inc. has been actively developing the reactive extrusion processing as a key technology of automotive plastics recycling.

REFERENCE

- [1] T. Ohta, N. Sato, S. Sugiyama, and M. Matsushita; Polymer Preprints, Japan, Vol. 42, No. 11, 4858 (1993)
- [2] T. Ikai, H. Iwai, I. Sakata, S. Ikeda, and N. Sato; SAE preprints, Japan, Vol. 931, 137 (1993)
- [3] T. Ikai, H. Iwai, I. Sakata, S. Ikeda, and N. Sato; Trans. Mat. Res. Soc. Japan, Vol. 18A, 763 (1993)
- [4] S. Ikeda, T. Kato, S. Inoue, and N. Sato; SAE Preprints, Japan, Vol. 946, 205 (1994)
- [5] N. Tatsuda, K. Fukumori, T. Ohta, N. Sato, T. Takahashi; Polymer Preprints, Japan, Vol. 44, No. 12, 3112 (1995)
- [6] J. Handa, H. Iwai, S. Ikeda, T. Suzuki, N. Sato, T. Ohta, M. Matsushita, and S. Sugiyama; SAE Preprints, Japan, Vol. 952, 129 (1995)
- [7] T. Mouri, A. Usuki, A. Murase, and N. Sato; Polymer Preprint, Japan, Vol. 44, No. 12, 3114 (1995)
- [8] K. Fukumori, S. Sugiyama, N. Tatsuda, N. Sato, H. Takahashi, Polymer Preprints, Japan. Vol. 43, No. 9, 2976 (1994)
- [9] N. Sato; Soc. Polym. Sci., Japan, Proceedings of 43rd Summer Seminar, 98 (1995)

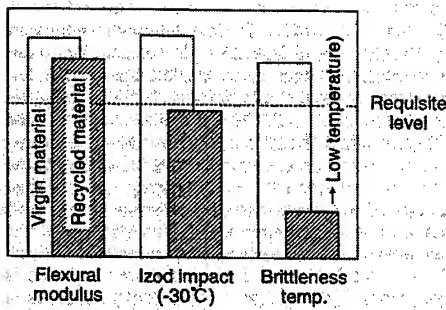


Fig. 1 Mechanical properties of simply-recycled material and virgin one for bumper

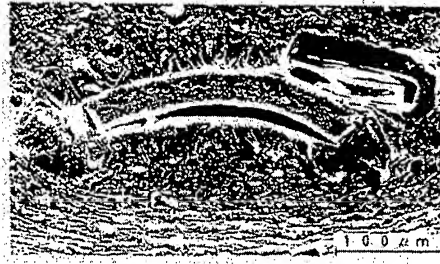


Fig. 2 SEM observation of paint fragment in simply-recycled material for bumper

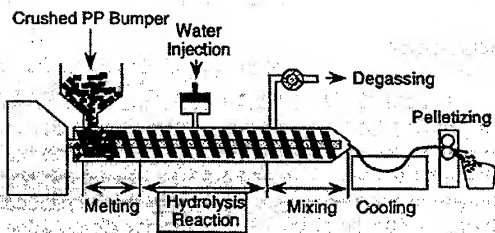


Fig. 3 Twin screw reactive extrusion system for thermoplastic bumper recycling

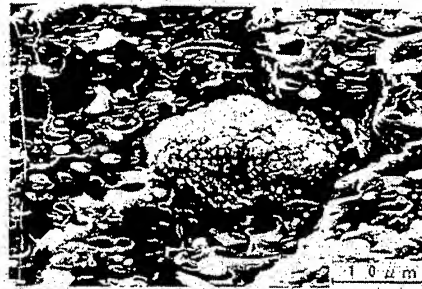


Fig. 4 SEM observation of decomposed paint film in reactive-recycled material for bumper

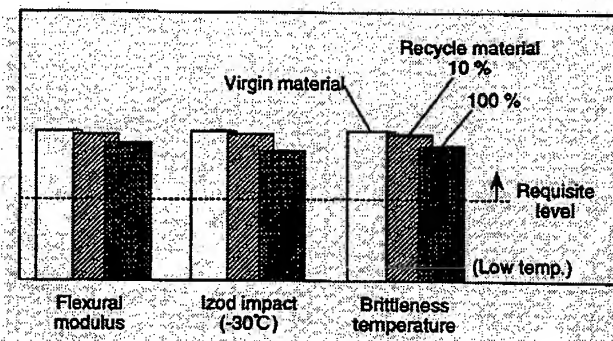


Fig. 5 Mechanical properties of reactive-recycled material for bumper

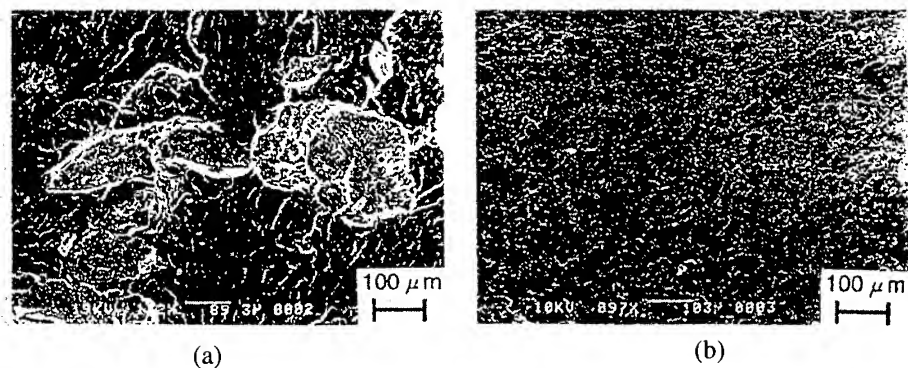


Fig. 6 Recycled material of polyurethane/polypropylene blend
(a) without reaction
(b) with reaction

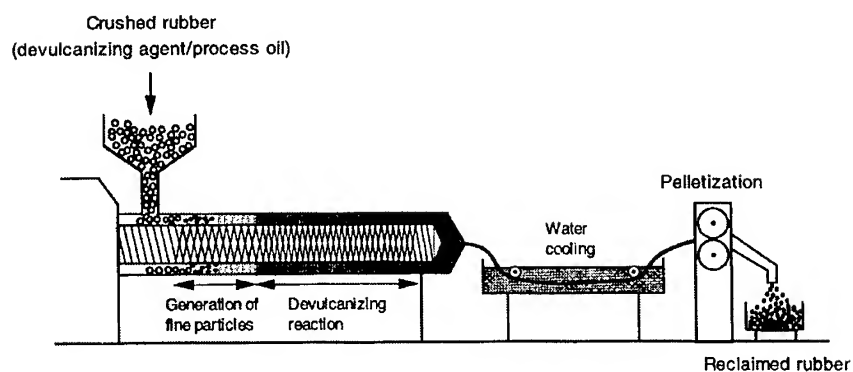


Fig. 7 Reactive extruder for rubber recycling

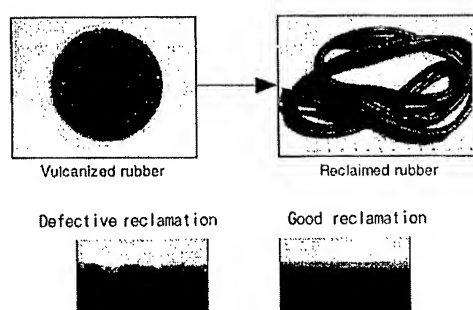


Fig. 8 Crushed rubber and recycled rubber obtained by reactive extruder

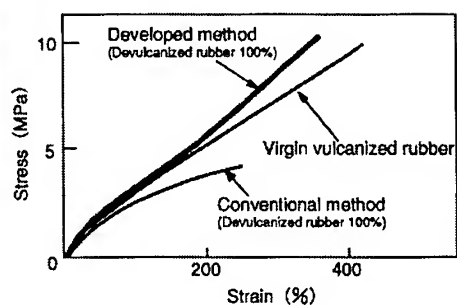


Fig. 9 Mechanical property of recycled rubber obtained by reactive extruder

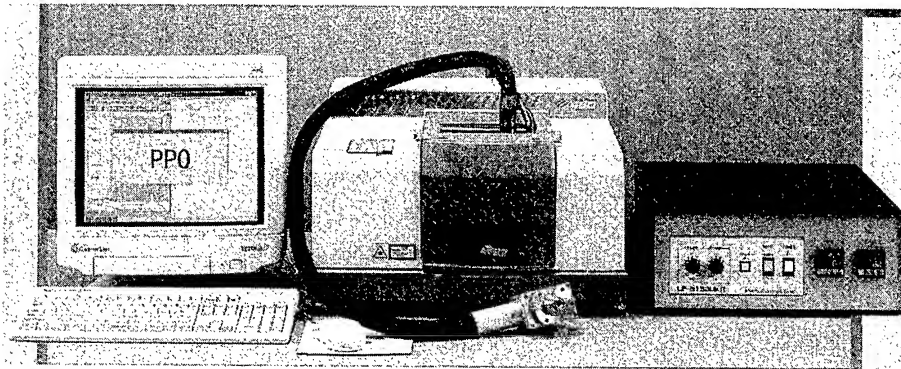


Fig. 10 Plastics identification system using pyrolysis IR spectrometer

Keynote Lectures

THERMOMECHANICAL RESPONSE (MICROCRACKING) OF LAMINATES AT CRYOGENIC TEMPERATURES

Ran Y. Kim¹ and Allan S. Crasto¹

¹ *University of Dayton Research Institute, 300 College Park, Dayton, Ohio, USA 45469
ran.kim@afrl.af.mil*

SUMMARY: The application of composites in space structures such as reusable launch vehicles requires a detailed understanding of their mechanical behavior and damage resistance in the service environment. Experimental and analytical studies were conducted on IM7/977-3, a toughened graphite/epoxy, to characterize the influence of cryogenic service temperatures on the strength and modulus of this material system and on transverse crack initiation in cross-ply laminates at 23, -129, and -196°C. Transverse tensile and shear strengths and moduli increased at the cryogenic test temperatures while strain to failure decreased, denoting increased brittleness. The stress for the onset of transverse cracking decreased substantially at cryogenic temperatures, due primarily to an increase in the curing residual stresses. Laminated plate theory, in conjunction with maximum stress criteria, appears to overestimate the onset of the transverse cracking in this laminate.

KEYWORDS: cryogenic temperature, strength, modulus, transverse cracking, residual stress, coefficient of thermal expansion, thermal strain

INTRODUCTION

Advanced polymer composites are being explored for structural applications at extremely low temperatures, for example in large cryogenic fuel tanks on NASA's Reusable Launch Vehicle and on the U.S. Air Force's Space Operations Vehicle [1]. Exposure to these cryogenic temperatures can cause transverse microcracking in these composites due to thermal residual stresses that arise from the anisotropy in the composite ply coefficient of thermal expansion (CTE). Transverse cracking often results in a reduction in laminate stiffness and strength and changes in laminate CTE, and provides a pathway for the ingress of moisture or corrosive chemicals; in cryotanks, transverse cracking can cause leakage of the pressurized liquid fuel.

Very little work has been reported in the technical literature [2-4] on the mechanical performance of and damage development in polymer composites at cryogenic temperatures. The main objective of this work was to understand the mechanical behavior and damage processes in composites at cryogenic temperatures, and to develop a predictive capability for the onset of transverse cracking in composite laminates subjected to isolated or combined thermal and mechanical loads. The material system investigated was a carbon fiber-reinforced toughened epoxy composite, IM7/977-3. The thermomechanical properties required for the analysis were obtained from tests on $[0]_{8T}$, $[90]_{8T}$, and $[\pm 45]_{2S}$ laminates. These laminates were tested at a number of temperatures, ranging from ambient down to -196°C , using a custom-built cryogenic chamber installed on a mechanical test machine. Cross-ply laminates were used to experimentally determine the onset of transverse cracking under isolated or combined mechanical and thermal loads. Transverse cracking was detected from acoustic emission and incremental loading and unloading, and confirmed from microscopic examination of polished specimen edges. Ply stresses were calculated for the corresponding conditions from laminated plate theory, using the appropriate experimentally generated thermomechanical properties and the applied load. The maximum stress failure theory was applied to predict failure. Analytical predictions were then compared with experimental results at temperatures of 23, -129 , and -196°C , and the results are reported here.

EXPERIMENTAL

The material system used in this study was a carbon fiber-reinforced toughened epoxy, IM7/977-3, supplied as a unitape prepreg by the manufacturer. Unidirectional ($[0]_{8T}$ and $[90]_{8T}$) and multidirectional ($[\pm 45]_{2S}$ and $[0_2/90_2]_S$) laminates were fabricated in an autoclave in accordance with the manufacturer's recommended cure cycle. Cured composite panels were postcured for 7 hours at 232°C in an oven. The $[0]_{8T}$, $[90]_{8T}$ and $[\pm 45]_{2S}$ laminates were used to characterize this composite material at cryogenic temperatures and provide the thermomechanical properties required for analytical calculation. The $[0_2/90_2]_S$ laminate was used to investigate transverse crack initiation in this composite system at cryogenic temperatures. Rectangular coupons were sectioned from the panels using a diamond-impregnated saw blade. All $[0]_{8T}$ specimens, as well as all specimens tested at -196°C , were 1.25 cm wide with a gage length of 10 cm due to limitations imposed by the test fixture. All the remaining specimens had a width of 2.5 cm. Fiberglass/epoxy end-tabs were bonded to $[0]_{8T}$ and $[\pm 45]_{2S}$ specimens tested at 23 and -129°C ; no end-tabs were used for specimens tested at -196°C . An axial strain gage was used to determine the elastic modulus and strain to failure at all test temperatures. The edges of the $[0_2/90_2]_S$ specimens were first ground with sandpaper and then polished with 5-micron and 1-micron polishing powder to enhance microscopic imaging for crack detection. Prior to testing, all specimen edges were examined under a microscope to determine if specimen sectioning and handling induced any damage. No damage was observed in any specimen prior to testing.

A special mechanical grip (17.8 kN load capacity) was designed and built for tests at cryogenic temperatures. The clamping face of each grip was coated using a Surfalloy process to enhance the gripping action without damaging the specimen surface by grip force. This grip can accommodate specimens with a width up to 1.25 cm. All specimens were tested on an MTS test machine using a commercial temperature chamber for tests at -129°C and a stainless-steel container, designed and built in-house, for tests at liquid nitrogen temperature (-196°C). Specimens, mounted on the test machine, were cooled to the desired test temperature by immersion in liquid nitrogen in the insulated stainless-steel container and allowed to equilibrate for 20 minutes. They were then loaded in tension at a strain rate of 0.02/min. Acoustic emission was employed to detect the onset of microcracking in tests conducted under ambient conditions. When a sudden acoustic emission event was observed, the specimen was unloaded and examined in a microscope to confirm the presence of transverse cracking. Fig. 1 shows the acoustic emission record for a specimen tested at 23°C , indicating the occurrence of transverse cracking.

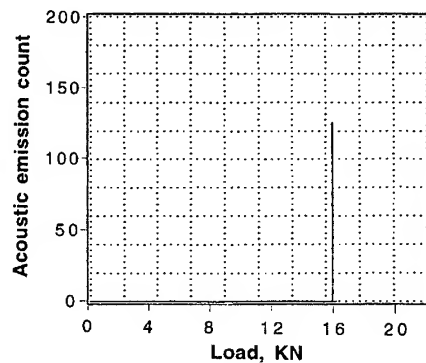


Fig. 1 Acoustic emission record for $[0_2/90_2]_S$ laminate at 23°C .

It should be noted that no other acoustic events were recorded in Fig. 1, indicating no ambient noise during the test. The use of acoustic emission to detect microcracking was unsuccessful at -129°C , because of relatively high background noise, and at -196°C , because of limitations of the transducer. Transverse crack initiation was therefore determined by microscopic examination of the polished specimen free edges after a series of incremental loading and unloading experiments. In this procedure a specimen is loaded to a stress level slightly lower than that at which microcracking is expected, then unloaded and the free edges examined in a microscope. If no microcracks are observed, the specimen is reloaded to a stress incrementally higher than before, unloaded, and examined again. This procedure is repeated until the first crack is observed, which is usually accomplished in two to five iterations. The average value of the last two consecutive loads is then used to compute the stress required to initiate transverse cracking. With this procedure, the error in the computed stress for crack initiation is less than 5%.

Composite CTEs were measured using strain gages, in conjunction with a computer-controlled temperature chamber and data acquisition system, continuously over the temperature range of 149 to -129°C, and then immersed in liquid nitrogen (-196°C) and liquid helium (-269°C) to record thermal strains at the corresponding temperatures. Ultra-low-expansion titanium silicate was used as the reference material for completion of the strain gage bridge circuit. The details of this technique of CTE measurement using strain gages may be found elsewhere [5].

RESULTS

Strength and Modulus

The results of composite modulus and strength measurements are summarized in Table 1.

Table 1 Variation of strength and modulus at various temperature.

Laminate	Temperature C	Strength MPa	Coefficient of Variation, %	Modulus GPa
Longitudinal [0] _{8T}	23	2,599	4.2	180
	-129	2,425	10.1	183
	-196	x	x	x
Transverse [90] _{8T}	23	66.1	6.7	9.8
	-129	76.3	22.1	13
	-196	94.6	5.6	13.2
Shear [±45] _{2S}	23	113.3	5.6	6.1
	-129	130.5	3.1	8.1
	-196	132.1	5.4	9.2

There is a considerable variation in modulus and strength, especially in matrix-dominated directions, over the temperature range of 23 to -196°C. The longitudinal modulus, from [0]_{8T} specimens, did not change in the temperature range, but longitudinal strength decreased by 7% at -129°C. Both moduli and strengths for the [90]_{8T} and [±45]_{2S} orientations increase significantly at the lower test temperatures, as seen in Table 1. Analysis of the fracture modes indicated increasingly brittle failure at the lower temperatures. Fig. 2 and 3 show photographs of failed [90]_{8T} and [±45]_{2S} specimens tested at 23 and -196°C. Multiple failures were observed in some [90]_{8T} specimens at -129 and -196°C, whereas each specimen tested at 23°C exhibited a single failure. The failure modes of the [±45]_{2S} specimens also clearly showed the increased brittleness at -196°C.

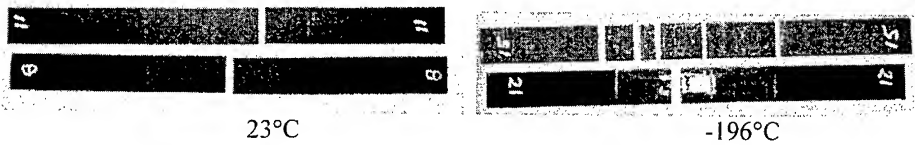


Fig. 2 Photograph showing failure of $[90]_{8T}$ laminate

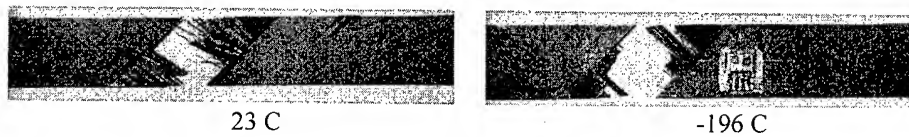


Fig. 3 Photograph showing failure of $[\pm 45]_{2S}$ laminate

The longitudinal stress-strain curves at 23 and -129°C shown in Fig. 4 are linear and practically coincide. The transverse stress-strain curves for the test temperatures 23, -129 , and -196°C , shown in Fig. 5, indicate an increase in modulus at lower temperatures.

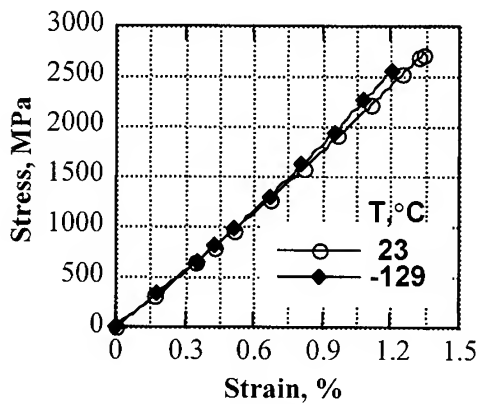


Fig. 4 Stress-strain curves for $[0]_{8T}$

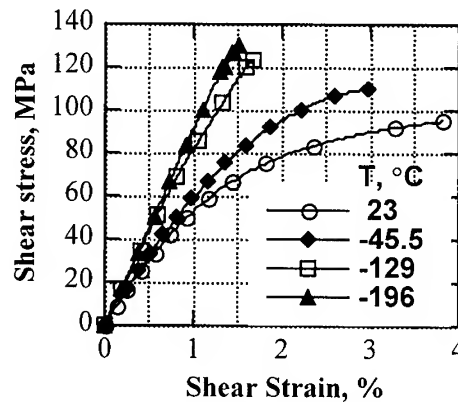


Fig. 5 Stress-strain curves for $[90]_{8T}$

The stress-strain behavior of the $[\pm 45]_{2S}$ laminate shows a wide range of nonlinearity over the range of test temperatures; the nonlinearity gradually decreases with test temperature until the plot is almost linear (up to failure) at the lowest temperature as shown in Fig. 6.

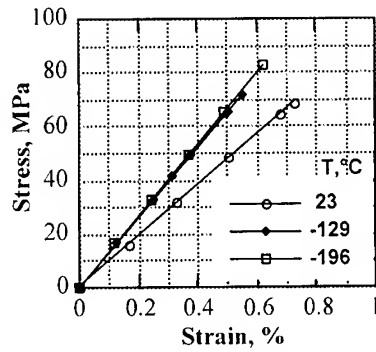


Fig. 6 Shear stress-strain curves

Onset of Transverse Cracking

All the transverse cracks observed on the specimen edge extended through the entire thickness of the 90° plies as shown in Fig. 7. There was a one-to-one mapping of cracks on both edges of the same specimen, suggesting that these transverse cracks traversed the full specimen width.

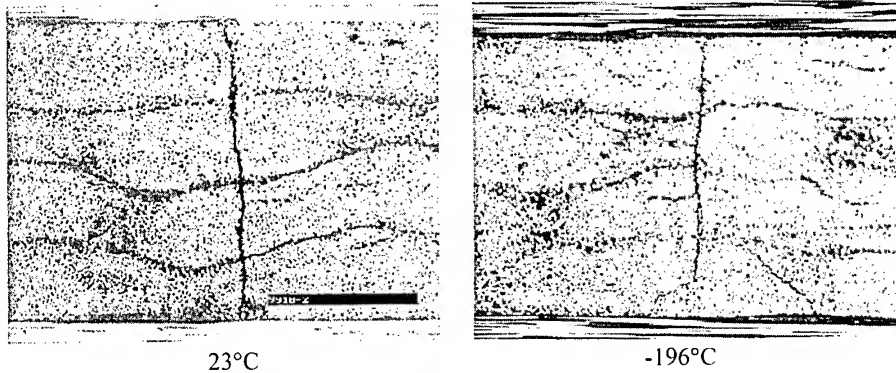


Fig. 7 Transverse cracks in $[0_2/90_2]_S$ laminate.

In specimens tested at -196°C , a slanted partial crack was also observed near the major transverse crack (Fig. 6); this damage was not observed in specimens tested at 23°C and -129°C . The stress in the 90° plies of the $[0_2/90_2]_S$ laminate, at the onset of transverse cracking, was calculated from the applied stress using classical laminated plate theory for comparison with the transverse strength obtained from tensile tests on $[90]_{8T}$ specimens. The curing residual stress, taking into account the influence of water absorbed under ambient storage conditions, was calculated with the assumption of a stress-free temperature of 163°C (cure temperature 177°C). The moisture content of the composite, absorbed during storage between fabrication and testing,

was determined to be 0.15%. Table 2 shows the 90° ply stresses calculated for the $[0_2/90_2]_s$ laminate at the onset of transverse cracking, and the measured composite transverse strength.

Table 2 Calculated 90° ply stress and strength.

Temperature	*Curing residual stress	Mechanical stress at cracking load	Total stress	90° ply strength
°C	MPa	MPa	MPa	MPa
23	21.55	58.74	80.29	66.19
-129	45.24	44.06	89.30	76.53
-196	55.68	34.11	89.79	94.46

The total stress represents the stress calculated from the laminate stress (applied load) at the onset of transverse cracking and the curing residual stress. It can be seen that the predictions, based on a maximum stress failure criterion from lamination theory, are considerably overestimated especially for tests conducted at -129°C. A number of factors such as the constraining effect of neighboring plies, ply thickness, inadequacy of the failure criteria, inaccuracies in the estimation of residual stress, insufficient data on transverse strengths and stress for the onset of transverse crack initiation may contribute to the discrepancy between prediction and experiment. A fracture mechanics approach, which accounts for some of the above factors, is currently being explored using analytical models [6,7] in conjunction with additional experimental data.

CONCLUSIONS

Experimental and analytical studies were conducted to determine the influence of cryogenic temperatures on the strength and modulus of IM7/977-3, a graphite/toughened epoxy composite, and the initiation of transverse cracking in cross-ply laminates. Based on the results, the following conclusions are drawn:

1. Transverse tensile and shear strengths and moduli increased at lower temperatures while strain to failure decreased (indicating increased brittleness).
2. The nonlinearity of the shear stress-strain curve decreased significantly at lower temperatures.
3. The stress level at the onset of transverse cracking decreased significantly at lower temperatures, mainly due to an increase in the curing residual stresses. Residual stress relief due to absorbed moisture was taken into account.

4. Lamination theory in conjunction with the maximum stress failure criterion appears to overestimate the onset of the transverse cracking in this laminate.
5. The strain gage technique is an easy and accurate means of measuring composite CTE at cryogenic temperatures.
6. Specimen alignment, especially for transverse loading, is critical, due to specimen embrittlement at cryogenic temperatures.

ACKNOWLEDGEMENT

The assistance of Ron Esterline of the University of Dayton Research Institute is greatly appreciated for conducting the experimental tests. This work was funded by the Air Force Research Laboratory and NASA Marshall.

REFERENCES

1. R. Heydenreich, "Cryotanks in Future Vehicles," *Cryogenics*, v. 38, 1998, pp.125-130.
2. R. P. Reed and M. Golda, "Cryogenic Properties of Unidirectional Composites," *Cryogenics*, v. 34, 1994, pp. 909-928.
3. J. B. Schutz, "Properties of Composite Materials for Cryogenic Applications," *Cryogenics*, v. 38, 1998, pp. 3-12.
4. T. Ishikawa, H. Kumazawa, Y. Morino, and Y. Hayashi, "Cryogenic Strength Behavior of Toughened Composites for Propellant Tank of Reusable Launch Vehicle," ACCM 1, 1998.
5. R. Y. Kim, A. S. Crasto and G. A. Schoeppner, "Measured and Predicted Variation in Laminate CTE due to Microcracking," *Proc. of American Society for Composites*, v.12, 1997, pp. 1103-1112.
6. S. C. Lim and C. S. Hong, "Prediction of Transverse Cracking and Stiffness Reduction in Cross-Ply Laminated Composites," *J. Compos. Mater.*, v. 23, 1989, pp. 695-713.
7. N. J. Pagano, G. A. Schoeppner, R. Y. Kim and F. L. Abrams, "Steady-State Cracking and Edge Effects in Thermomechanical Transverse Cracking of Cross-Ply Laminates," *Composite Science and Technology*, v. 58, 1998, pp.1811-1823.

A NEW APPROACH TO THE EMI SHIELDING COMPOSITE MATERIALS

*Chul Rim Choe, Min Park and V. Mironov
Polymer Hybrids Research Center, KIST*

39-1 Hawolkokdong, Sungbukgu, Seoul, Korea: E-mail crchoe@kist.re.kr

SUMMARY: EMI Shielding materials have been recently a key issue with the dramatic change of information and communication technologies. In terms of cost/performance balance metallic coatings and conductive plastics have been intensively applied for achieving acceptable attenuation of incident electromagnetic waves. Conductive plastics are produced normally by compounding metallic fibers with plastics, where the high volume of fillers can not be avoided for effective shielding since the original form of fillers is damaged due to the high shear force exerted during processing. In this paper the possibility of a new processing technique is reported to produce EMI shielding composite materials including discontinuous carbon fibers as conductive filler, where the length of fibers can be maintained intact and hence relatively lower fiber volume is expected to achieve high shielding effectiveness.

KEYWORDS: EMI shielding, conductive plastics, composite films, resistivity

INTRODUCTION

As electronic products represented by cellular phones and personal computers tend to be thinner, lighter and smaller complying with customer's demand, they become more susceptible to incoming electromagnetic interference (EMI) waves from outside as well as generate high frequency EMI waves. These unwanted EMI waves are apt to cause malfunction of other important electronics such as electronic aviation systems in aircraft and medical related electronics. Further, these unwanted EMI waves have been being suspected to

threaten the health of mankind. These have been driving forces for searching for new materials and processes for better EMI shielding for last two decades since the first step toward the regulation of EMI for electronic products was made by Federal Communications Commission (FCC) of USA in 1983.

Thermoplastic materials have been widely used as housings of a variety of electronic devices over metallic sheets mainly due to its lightweight, corrosion resistance, ease of processing and versatility for design. However, as they are electrically insulators that are transparent to any electromagnetic waves, some means to make them conductive are required so as to prevent any transmission of electromagnetic waves through the housings. There are, of course, many ways other than the use of shielding materials to solve EMI problems for information-related apparatus such as improved circuit design, the use of noise filters and shielding cables and proper grounding. But the use of shielding materials has proven to be the most immediate as well as the simplest way among many EMI shielding countermeasures.

In this paper, after brief introduction on fundamental aspects of EMI shielding, traditional EMI shielding materials will be mentioned. Special attention will be focused on highly conductive polyethylene/carbon fiber composite films fabricated under high intensive electric fields.

FUNDAMENTALS OF EMI SHIELDING

EMI shielding means the spatial isolation of EMI sources or sophisticated electronic circuits susceptible to EMI waves by the use of conductive materials. When EMI waves impinge on the conductive materials, most of its energy will reflect off due to large mismatch in impedance of free space (377Ω) and conductive materials. The shielding capability or effectiveness is expressed in decibel (dB) by the attenuation of incident wave after transmission as Eqn 1.

$$SE = 20 \log (E_i / E_t) \quad (1)$$

Where SE : shielding effectiveness, in dB

E_i : electric field intensity of incident wave, in V/cm

E_t : electric field intensity of transmitted wave, in V/cm

There was an attempt to set some criteria of SE levels for comparison of different shielding materials as shown in Table 1[1].

According to Schelkunoff's theory [2] on the shielding effect exerted by a metallic sheet, SE is the sum of three contributions, i.e., absorption loss (A), reflection loss (R), and multiple reflection loss (M). Because M is usually negligible when a high frequency is applied, SE can

Table 1. EMI shielding levels

SE (dB)	
0 ~ 10	No expectation for shielding
10 ~ 30	Marginal shielding
30 ~ 60	Normal shielding
60 ~ 90	Sufficient shielding
90 ~ 120	Almost perfect shielding
120 ~	Maximum shielding

be simply expressed as the sum of A and R. Here, A is related to material constants such as specific electric conductivity (σ_r) and specific permeability (μ_r) to copper, material thickness (t) in m, and frequency of waves (f) in Hz as Eqn 2.

$$A \text{ (dB)} = 131.4 t (f \sigma_r \mu_r)^{1/2} \quad (2)$$

Similarly, R is denoted in case of a plane wave or in a far field as Eqn 3.

$$R \text{ (dB)} = 108.2 - 10 \log f/10^6 + 20 \log (\sigma_r / \mu_r)^{1/2} \quad (3)$$

Generally μ_r is equal to unity as long as magnetic materials are not employed. Thus, SE of metallic materials are conveniently estimated from Eqn 4 when we replace σ_r with volumetric resistivity (ρ) in $\Omega \cdot \text{cm}$ and are using MHz instead of Hz as a unit of frequency.

$$SE = 50 + 10 \log (1/f\rho) + 1.7 t (f/\rho)^{1/2} \quad (4)$$

Though Eqn 4 was derived to predict EMI SE for metallic bodies, it can also be of value for non-metallic materials including conductive plastics as long as conductive fillers are 'well' dispersed in the matrix resin. According to Table 1, materials with more than SE of 30 dB can be considered valuable as EMI shielding materials, which can be obtained by 16 μm thick copper foil. Table 2 demonstrates SE values calculated according to Eqn 4 for various frequency and volumetric resistivity at fixed thickness ($t = 0.3 \text{ cm}$).

Table 2. Relationships between volumetric resistivity and frequency

ρ $\Omega \cdot \text{cm}$	SE			
	10 MHz	100 MHz	500 MHz	1000 MHz
0.1	55	56	69	81
1	42	35	34	36
10	31	22	17	15
100	21	10	4	2

Table 2 indicates that materials should have volumetric resistivity less than $1 \Omega \cdot \text{cm}$ to be useful as a EMI shielding material and that the lower resistivity of materials gives the better shielding capability at high frequencies.

TRADITIONAL TECHNIQUE FOR EMI SHIELDING

Metallic surface coating: A number of methods have been suggested and commercialized to impart conductivity to plastic surfaces, i.e., nickel/copper electroless plating, zinc melt spraying, aluminum vacuum plating, ion plating and the use of conductive paints [3]. Electroless plating produces thin metallic layer on thermoplastic molded products. This technique is widely utilized currently and well known to give superior shielding capability and reliability compared with any other shielding methods in spite of high cost burden for an etching step required to assure adhesion between plastics and metals. Though cheaper zinc melt spraying provides intermediate shielding effect between electroless plating and conductive painting, its use is now declining because of the toxicity of zinc metal vapor. Vacuum plating has attracted much attention due to the formation of thick aluminum layer of $2.5 \sim 5 \mu\text{m}$ on a plastic substrate. Ion plating is an emerging technology that enables the formation of various functional coatings on plastics substrates by combining vacuum plating and plasma technique. Unlike vacuum plating where vaporized neutral molecules with low energy form coating, energetic species such as ions, excited molecules and radicals involve in the formation of compact surface coating. This technique is now receiving great attention due to its nature of dry process and excellent properties. Finally, conductive paints composed of binders such as acrylic, acrylic-urethane resins and conductive fillers such as nickel, copper, silver, or graphite powders exhibited shielding capability inferior to metallic surface coatings and very dependent on coating thickness.

Conductive plastics: Generally, conductive plastics in which conductive fillers are dispersed in thermoplastic matrix can be molded by injection or compression technique using electroconductive thermoplastic molding compounds as a feedstock. Unlike conductive coating approaches, this method attempts to make whole plastics conductive, otherwise insulating plastics, by incorporating various conductive fillers ranging from metallic fibers to carbon blacks during compounding step. As a result, the absence of costly secondary process encountered in the metallic surface coating techniques render this approach viable for mass production offering the best competitiveness in terms of cost. Typical conductive molding compounds filled with few volume percent of metallic fibers usually exhibit low volumetric resistivity of less than $10 \Omega \cdot \text{cm}$. Since there are many possible combinations of thermoplastics and metallic fibers enabling the selection of properties for specific EMI shielding applications [4]. However, extensive use of conductive plastics is still away due to several significant problems to be solved for these materials to be widely accepted in high

volume markets. First, a large difference in specific gravity between metallic fillers and resin matrix may lead to uneven distribution of fillers in the injection molded parts because of their different flow responses to high shearing forces during injection process. Second, severe fiber breakage during compounding and injection may greatly reduce the final aspect ratio in molded products, requiring high levels of filler loading to ensure EMI shielding capability. Finally, thermal mismatch between metallic fillers and resin matrix often causes instability of conductivity because more expansion of resin will adversely affect the conducting network during thermal excursion in use. Some of problems mentioned can be solved through the improvement of processing conditions, the addition of processing aids or the formation of fixed contact points in the network by adding the low melting metals [5]. However, there remains much to be improved in conductive plastics to increase EMI SE and to ensure the materials' reliability, which inevitably drives the search for new EMI shielding materials and processes.

COMPOSITE FILMS FABRICATED BY THE EIT

Recently, novel methods to fabricate carbon fiber reinforced plastics (CFRP) films for EMI shielding have been proposed and come into market [6]. One of them is so-called electron-ion technology (EIT) of CFRP films based on powder technology, short-chopped fiber flocking and thermoforming [7]. Figure 1 depicts the schematic diagram of the process. First, molten thin layer of polyethylene (PE) applied to the substrate by fluidized bed coating is formed. Second, discontinuous carbon fiber (CF) from fiber feeder is electrodeposited onto the molten PE layer. In this step, CF is uniformly distributed on the adhesive PE layer under the influence of high electric fields. Third, additional PE powders either charged or uncharged are deposited in a controlled manner onto the CF flocked PE film. Final step is a thermo-mechanical forming by heated rollers to obtain CFRP film, where CF will adapt the orientation of rolling direction. In this process, the control of charging and motion of CF flocks in the second step is important to ensure the fabrication of quality films [8] and can be achieved by a variety of surface treatment of CF flocks. In this process, variables such as CF content of the film, CF layer density in flocking step and thickness of adhesive PE layer are all inter-related and by adjusting these variables we can fabricate PE/CF films with low resistivity less than $0.1 \Omega \cdot \text{cm}$ as well as high tensile strength about 35 MPa [9].

CONCLUSION

Considering the significance of EMI problems, more reliable shielding materials and processes to make them are being actively sought for many demanding applications. In this situation, the EIT can be a potentially viable process to fabricate conductive PE/CF films with wide property spectrum in terms of resistivity and tensile strength by combining existing flocking and thermoforming technology.

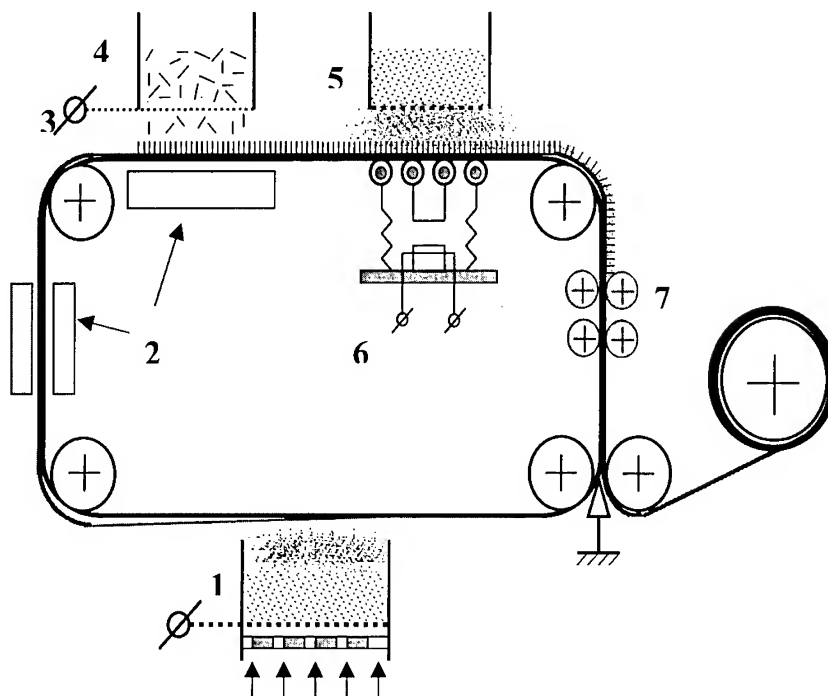


Fig. 1 Schematic diagram of the EIT process (1: fluidized bed coater, 2: infra-red heaters, 3: high voltage source, 4: fiber feeder, 5: powder feeder, 6: vibrator, 7: heated roller).

REFERENCES

1. M. Morita and H. Iwamoto, "Composite Materials for Electronic Engineering", Information and Communication Engineers in Japan, 1986, pp.155.
2. M. Endo, "Advanced Materials and Materials for EMC, CMC, 1998, pp.83.
3. S. Yasufuku, "Technical Progress of EMI Shielding Materials in Japan", *IEEE Electrical Insulation Magazine*, Vol.6, 1990, pp.21.
4. R. P. Kusy, "Metal-Filled Polymers", Marcel Dekker, New York, 1986, pp. 68.
5. M. Endo, "Advanced Materials and Materials for EMC, CMC, 1998, pp.90
6. M. Sugino, "Long Carbon Fiber Reinforced Plastics", *Kino Zairyo*, Vol. 19, 1999, pp.5.
7. V. Mironov and M. Park, "Electroflocking Technique in The Fabrication and Performance Enhancement of Fiber-Reinforced Polymer Composites", *Composite Science and Technology* (in press)
8. M. Park, C. R. Choe, and V. Mironov, "Charging Behavior of Chopped Carbon Fibers under High Intensity Electric Fields", *Korea Polymer Journal*, Vol.8, 2000, pp.6.
9. M. Park, C. R. Choe, and V. Mironov, "Fabrication and Properties of Conductive Carbon Fiber/Polyethylene Films Fabricated under High Intensity Electric Fields: Effect of Polymer Sublayer", *Polymer (Korea)*, Vol. 24, 2000, pp.268.

DAMAGE AND FRACTURE OF INFILTRATED PARTICLE REINFORCED ALUMINIUM COMPOSITES

M. Kouzeli, A. Miserez, A. Rossoll, C. San Marchi, L. Weber and A. Mortensen

*Laboratory for Mechanical Metallurgy, Department of Materials
Swiss Federal Institute of Technology in Lausanne (EPFL), CH-1015, Lausanne, Switzerland
Email: <andreas.mortensen@epfl.ch>*

SUMMARY: Particle reinforced materials can be produced by infiltrating ceramic particle beds with a metallic melt. Resulting composites feature a homogeneous particle distribution, making them attractive for the study of damage and fracture processes in particle reinforced metals. We provide here an overview of current research at EPFL on the mechanical behaviour of this class of composites.

The composites investigated consist of close-packed particles of either alumina or boron carbide in high purity aluminium (99.99 %). The volume fraction ceramic ranges between 40 and 55 vol pct, depending on the type of powder and the average particle size. Pore-free and homogeneous microstructures are achieved with most systems. These composites are characterized in terms of tensile behaviour and fracture toughness. Reinforcement type and size are shown to exert a significant influence on damage and fracture processes within these materials; preliminary micromechanical simulation of these composites is presented.

KEYWORDS: aluminium, alumina, boron carbide, infiltration, ductility, damage, toughness, fracture.

INTRODUCTION

Several processes have been used for the production of composites with aluminum matrices reinforced with ceramic particles [1-3]. Powder metallurgy, stir casting, and spray casting are commonly employed to produce composites with less than about 40 vol pct reinforcement. Infiltration, on the other hand, is better-suited for the fabrication of composites with a relatively high volume fraction ceramic because, contrary to the first three processes, the reinforcement exists as a preform of a packed powder prior to infiltration. For narrow size distributions of powder, therefore, the volume fraction reinforcement in the infiltrated composite is approximately equivalent to the tap density of the powder, generally in the range 40 to 55 vol pct. Multimodal powder blends, such that finer particles fill the space between larger touching ones, can be used to produce composites with higher reinforcements densities, near 75 vol pct; these are highly attractive for electronic substrate applications.

With appropriate procedures, infiltration can produce particle reinforced metal matrix composites that feature homogeneously distributed and percolating particles embedded in a pore-free metal matrix. Because the reinforcement is densely packed in these composites, there are no spatial variations in reinforcement volume fraction (often called clustering or banding) typical of composites with lower ceramic loadings; therefore, complications in micromechanical analysis and interpretation introduced by this phenomenon can be avoided. As composites which feature metallurgically simple matrices and compatible reinforcements can easily be produced by infiltration, these materials are attractive for the study of micromechanical damage and fracture and their links to macroscopic composite properties.

Compared to low particle fraction composites, these materials are attractive because the higher volume fractions of reinforcement maximize the influence of the ceramic on the mechanical behaviour of the matrix, both for good and for bad. Compared with conventional particle reinforced metals, infiltrated particle reinforced composites are stiffer and their thermal expansion is lower; on the other hand, their fracture toughness and ductility are expected to be far lower than those of the matrix for two well-documented reasons:

- (i) damage develops within the material substantially lowering its work hardening rate and accelerating the onset of tensile instability,
- (ii) fracture toughness of these materials is often sufficiently low for samples to fail by brittle rupture prior to tensile instability (*e.g.*, [4, 5]).

These phenomena depend on the morphology and microstructure of the composite; this is evident in the wide range of properties found in work on infiltrated ceramic particle reinforced metals *e.g.*, [5-17]. We present in what follows an overview of an ongoing study of the mechanical behaviour of composites made by gas-pressure infiltration, focussing, on (i) quantification of damage during uniaxial tension and (ii) fracture toughness. The composites are as microstructurally simple as possible: pure aluminium reinforced with particles of aluminium oxide or boron carbide of varying average size. We seek to address the role of two principal microstructural parameters, namely the type of particle and the average particle diameter.

THE MATERIALS: PROCESSING AND MICROSTRUCTURE

The reinforcements are alpha-alumina and boron carbide particles, both purchased from Tracomme (Adliswil, Switzerland). These particles have an angular morphology, and feature an aspect ratio, on average, near one. The average particle diameter was varied between 5 and 50 μm . The matrix of the composites is 99.99 % pure aluminium. Details of the gas-pressure infiltration process are discussed elsewhere [18]. It is sufficient to note here that preforms were prepared by tapping dry powder into graphite-coated alumina crucibles in air; these preforms were then evacuated prior to heating isothermally with the aluminum to 750 $^{\circ}\text{C}$. Pressurized argon at 8 MPa was used for infiltration, after which the composite was directionally solidified.

Example microstructures of the as-produced composites are given in Fig. 1: the homogeneous distribution of the reinforcing phase is evident, as are its high volume fraction and the lack of microstructural defects such as porosity. With alumina particles, only two phases were present: the pure aluminium matrix and the unreacted particles. Variable amounts of the reaction products, AlB_2 and Al_3BC , were found in the boron carbide reinforced composites depending on the time of contact between the molten matrix and the reinforcement. These reaction products are expected based on the thermodynamics of the $\text{Al-B}_4\text{C}$ system [19]; however, the extent of reaction can be significantly reduced with short processing times.

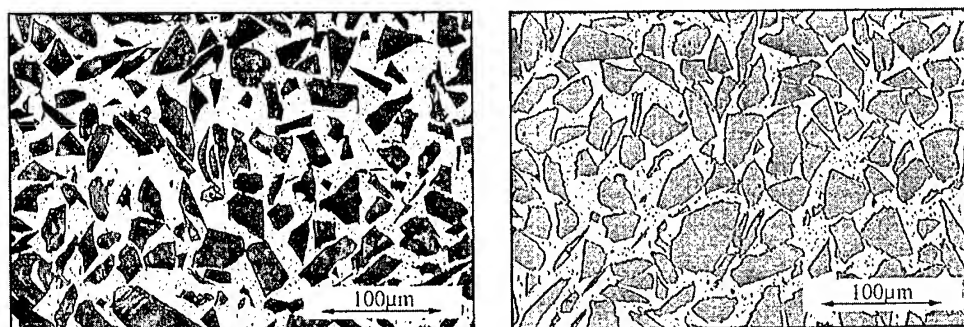


Fig. 1: Optical micrographs of as-cast $\text{Al-Al}_2\text{O}_3$ (left) and as-cast $\text{Al-B}_4\text{C}$ (right) composites.

Considerable care during processing is also required to avoid the formation of macro-defects in the form of bands or "veins" of unreinforced matrix, generally visible to the naked eye on composite cross-sections. These defects have been observed in prior studies as well (*e.g.*, [16]), but they have been eliminated in most, but not all, of the composites processed in this work.

TENSILE BEHAVIOUR

Experimental Procedures

Electro-discharge machining was employed to machine the samples from the composite castings: the specimen geometry was subsized dog-bone, according to ASTM Standard B557M-84. Tensile testing of the composites was conducted on a 10 kN screw-driven testing frame under displacement control with an initial strain rate of 10^{-4} s^{-1} . Longitudinal strains were measured over a gauge length of 10 mm using a clip-on extensometer.

Damage evolution during tensile straining was monitored through Young's modulus and density measurements. The first technique is realised using load-unload cycles during the tensile tests, while the second involves high precision measurement of density after incremental plastic straining. Observation and quantification of damage was also conducted microscopically by means of optical and Scanning Electron Microscopy (SEM). Polishing of longitudinal cuts to the fracture surface of failed tensile samples was finished by a brief electrolytic polishing step; this served to remove the smeared layer of aluminium introduced during mechanical polishing, thus unequivocally revealing any matrix voids.

Results

Tensile properties of the composites are summarised in Table 1: the values listed represent the average of at least three tensile tests. The subscript (v) denotes samples from castings that contain the unreinforced metal "veins" mentioned earlier; hence the measured mechanical properties should not be taken as indicative of intrinsic material properties, particularly with regard to tensile elongation. The volume fraction ceramic was determined by means of precision density measurements; the evident variation in values is mainly due to differences in packing characteristics of the starting powders.

Table 1: Basic Mechanical Properties of the Pressure-Cast Composites.

Reinforcement	d_{50} (μm)	V_f (pct)	E (GPa)	UTS (MPa)	e_f (%)
Al_2O_3	50	47.5	145	99	2.2
	30	46.1	143.5	123.5	3.2
	10(v)	53	162	195	1.8
	5	40	129	236	2.8
B_4C	50	50	170	129.5	3.2
	30	53.6	183	195	3.5
	10(v)	49	183	265	1.4
	5(v)	50	173	258	1

The incidence of the type and average size of the reinforcing particles on the tensile properties is manifest both in the elastic modulus and the ultimate tensile strength (UTS) of the composites. Decreasing particle size enhances the initial work-hardening rate, resulting in composites that are stronger for both types of particles. Moreover, B_4C particle reinforced composites are both stiffer and stronger. In terms of ductility, defect-free materials fail in a ductile manner exceeding elongations of 2 percent. Their failure is generally determined by the onset of tensile instability (the point of intersection between the flow curve and its derivative, as shown in Fig. 2); however, in composites with the smallest particles size, fracture seems to be defect controlled. Fig. 2 also gives an example of such failure.

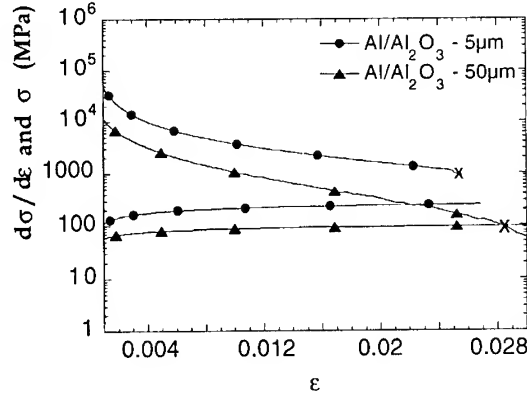


Fig. 2. Tensile instability and fracture toughness controlled fracture.

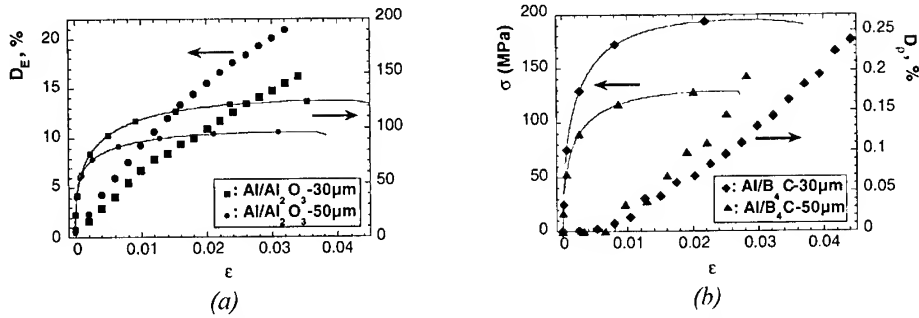


Fig. 3: Flow curves and damage evolution for (a): Al-Al₂O₃ and (b): Al-B₄C composites.

Two typical flow curves of Al-Al₂O₃ composites together with the evolution of the modulus-based damage parameter $D_E (= 1 - E/E_0)$, where E_0 is the initial Young's modulus and E is the modulus after strain ϵ are shown in Fig. 3-a. Damage accumulation as described by this parameter becomes important from the very early stages of plastic deformation. Also, the rate of damage accumulation is higher in the composite reinforced with the larger Al₂O₃ particles; this behaviour is illustrative for the whole spectrum of the composites studied. Similar trends are revealed in Fig. 3-b, which depicts the evolution of the density-based damage parameter D_p with strain for two B₄C composites together with their representative flow curves. The D_p parameter represents damage as measured through the increase in volume during tensile straining and is defined as $D_p = 1 - \rho/\rho_0$, where ρ_0 is the initial density and ρ is the density at strain ϵ . Damage accumulates faster for the Al-B₄C composite with the larger average particle size. Contrary to the evolution of D_E , though, there is a threshold of strain before a significant amount of void growth in the material becomes apparent; this was also observed for alumina-reinforced composites.

Microscopic observations reveal significant differences in the micromechanisms of damage in the various composites. In Al₂O₃ reinforced composites, particle fracture is primarily responsible for damage accumulation with strain. Even at very low strains, particle cracking occurs, as is also manifest by the increase of D_E . An interesting observation is that particle fracture is dominated by particle-particle interactions within the composite. The cracked particle faces open up through subsequent plastic straining of the matrix, producing an increase in volume, Fig. 4-a. This mechanism was observed to be operative in alumina-reinforced composites for all particle sizes studied. In contrast to the Al-Al₂O₃ composites, two concurrent damage mechanisms can be found in the Al-B₄C composites: matrix voiding and particle cracking. Matrix voids in these composites develop in regions of high matrix

constraint between closely spaced particles, Fig. 5-b. Nevertheless, particle cracking also occurs with an increasing tendency as the average particle diameter increases.

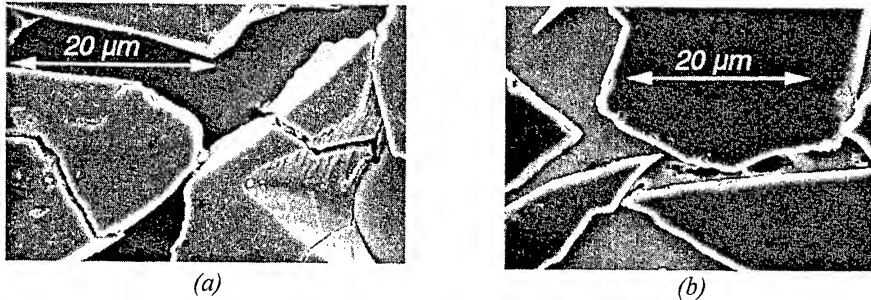


Fig. 4: Damage mechanisms in (a) Al-Al₂O₃ (b) Al-B₄C composites.

FRACTURE BEHAVIOUR

Experimental

Initial experiments have shown that, despite the high volume fraction of ceramic particles, stable fatigue crack growth can be obtained in these materials. The J -integral single specimen technique (ASTM E-1737) was employed to characterize the fracture behaviour. Specimens were initially fatigue pre-cracked to a crack length of 1 mm, on a hydraulic testing machine at ΔK between 8 and 12 MPa $\sqrt{\text{m}}$. Fracture tests were conducted on 13 mm thick compact tension (CT) specimens using a screw-driven universal testing machine, under displacement control at a rate of 0.05 mm/min. Crack length and crack extension were determined from elastic compliance measurements during unload-reload cycles. The J - R curves were computed based on "deformation theory" as described in the ASTM standard and in Ref. [20]. In order to identify fracture micromechanisms, chevron notch specimens were also tested. These tests were interrupted prior to final fracture: rapidly bonding adhesive was then introduced into the crack while the specimen remained under load. Glued samples were cut perpendicularly to the crack front, polished and observed using optical microscopy.

Results

Load-displacement curves and related R -curves are shown in Figs 5 and 6, for J -integral fracture tests conducted on B₄C and Al₂O₃ reinforced composites with 30 and 5 μm average particle sizes. Stable crack growth was observed in 30 μm particle reinforced composites with significant plastic deformation prior to maximum load; while, the 5 μm particle reinforced composites exhibit unstable crack propagation at maximum load (with B₄C) or soon thereafter (with Al₂O₃).

The J_{Ic} crack initiation resistance as defined in the standard is based on the intersection of the measured R -curve with an 0.2 mm offset line having a slope corresponding to the amount of crack extension due to crack tip blunting. This definition requires a highly precise measurement of the crack length, since J_{Ic} thus defined is dependent on the initial crack length. In the present experiments, crack closure effects are evident in the decrease of specimen compliance during the first unloading steps. The initial crack length was therefore defined from the minimum compliance measured during unloading cycles; this choice affects the computed value of J at 0.2 mm of crack extension ($J_{0.2\text{ mm}}$), given in Table 2. In order to compare quantitatively the resistance to crack growth, the values of J at maximum load (J_{Fmax}), are also given in Table 2 (together with converted equivalent K values). These J -values are less dependent on the crack closure effect and still within the validity limits of J -integral testing. We emphasize that curves and toughness values reported here are preliminary, and that further work will be needed to confirm both their experimental and their physical validity.

Table-2: Measured toughness of the composites, expressed in terms of J for 0.2 mm crack extension ($J_{0.2 \text{ mm}}$) and at maximum load ($J_{F_{\max}}$); these values are converted to equivalent K values via the relation $K = \sqrt{J \cdot E / (1 - \nu^2)}$ where E is Young's modulus and ν is Poisson's ratio.

	$J_{0.2 \text{ mm}}$ [kJ/m ²]	$K_{0.2 \text{ mm}}$ [MPa√m]	$J_{F_{\max}}$ [kJ/m ²]	$K_{F_{\max}}$ [MPa√m]
Al- B ₄ C 30 μm	2.5	22	4.9	31
Al- B ₄ C 5 μm	1.6	17	1.8	18
Al- Al ₂ O ₃ 30 μm	1.2	14	3.9	25
Al- Al ₂ O ₃ 5 μm	2.3	19	2.3	19

Overall, several features are apparent: (i) crack initiation toughness ($J_{0.2 \text{ mm}}$) is relatively high for materials that contain about 50 vol pct ceramic (with the consequence that specimen size requirements for LEFM testing would be prohibitive); (ii) there is significant R -curve behaviour with 30 μm particle-reinforced composites. For example, with 30 μm particles, the toughness of the B₄C-reinforced aluminum is higher than with Al₂O₃ particles. With 5 μm particles, one can see that the situation is reversed, *i.e.*, the toughness of the Al₂O₃-reinforced composite is higher than that of B₄C composites.

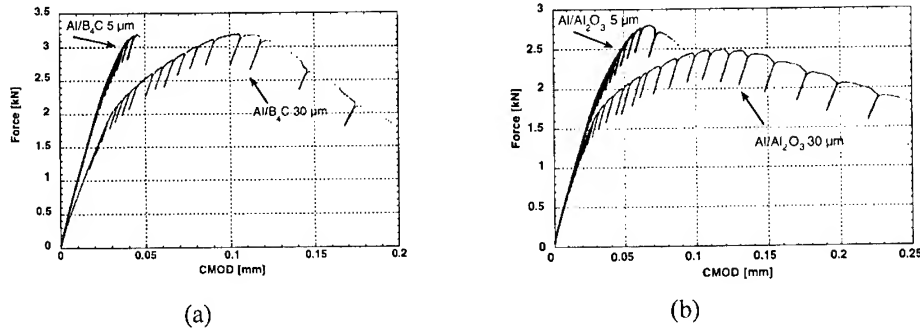


Fig.5: Load-displacements curves of (a) Al-B₄C, 30 and 5 μm particle size and (b) Al-Al₂O₃ 30 and 5 μm particle size

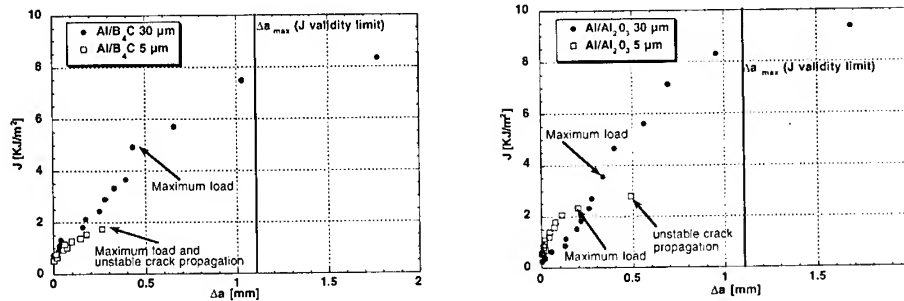


Fig. 6: R -curves corresponding to fracture testing curves of Fig 5.

Fracture micromechanisms observed near the crack tip of arrested chevron notch specimens, Fig. 7, show that the dominant failure micromechanism in the 30 μm Al-Al₂O₃ composite is particle fracture. Comparatively, the crack advances in 30 μm Al-B₄C composites mainly by

the nucleation, growth and coalescence of voids in the matrix. With 5 μm particles, SEM pictures of the crack path showed that almost no particle fracture occurred in either system.

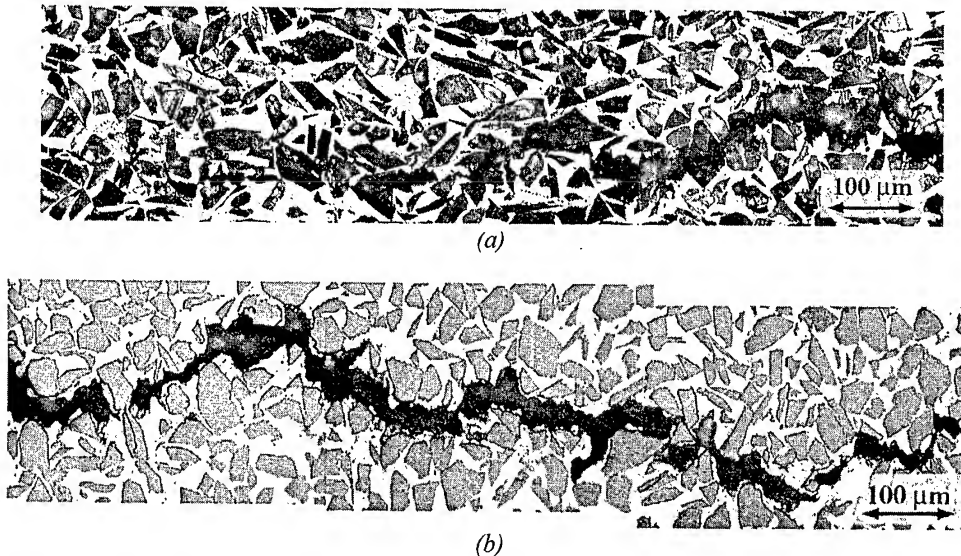


Fig. 7: Optical micrographs near the crack tip of interrupted chevron notched tests. (a) Al-Al₂O₃, 30 μm particle size. (b) Al-B₄C, 30 μm particle size

DISCUSSION AND CONCLUSIONS

Considering that these materials contain about fifty percent brittle ceramic, measured tensile ductility and toughness values are quite high: in defect-free material. Tensile failure occurs by geometric instability after a few percent of elongation. Equivalent values of crack initiation toughness computed from measured J -values range between 15 and 20 $\text{MPa}\sqrt{\text{m}}$. Clearly, these characteristics result from the soft and ductile matrix. This choice of matrix also has the consequence that the flow stress of these composites is relatively low, in the range of 100 to 250 MPa. Damage micromechanisms observed in tensile specimens, namely particle fracture and matrix voiding, Fig. 4, also occur near crack tips in fracture specimens with the same variations in relative importance from material to material, Fig. 7. In particular, for both composite systems the tendency for particle cracking increases as the particle size increases, in agreement with prior investigations on the behaviour of particle reinforced metals. The two measures of damage, namely the modulus- and density-based parameters D_E and D_ρ , provide clear and different measures of the progression of internal damage within these materials: the former is highly sensitive to particle fracture while the latter measures matrix void growth.

As the particle size increases, we observe that: (i) the flow stress of the composites decreases, (ii) the rate of damage nucleation and growth increases, and (iii) the crack growth resistance increases. Underlying causes are, respectively, (i) increased matrix dislocational hardening in composites with smaller particle size (probably augmented by hardening due to reaction in the Al-B₄C composites), (ii) the increased role of internal defects in larger particles, and (iii) the increased work of fracture in the crack-tip process zone, together with a decreasing flow stress, in the larger particle reinforced composites (we refer to Eq. (6) and the discussion in Ref. [21] as a simple proof). As was suggested by observation of the tensile behaviour of analogous (but more brittle) composites in Ref. [4], the trade-off between properties indicates that the particle size in these composites can be optimized.

Composites reinforced with boron carbide tend to have better properties than the alumina reinforced composites; for example, in the composites reinforced with 30 μm particles, the

boron carbide reinforced material has superior stiffness, flow stress and fracture toughness, with an equivalent ductility. This is due to a higher volume fraction ceramic in the B_4C containing composites, as well as to the lower rate of particle fracture compared to fracture of Al_2O_3 particles. The latter lowers the rate of damage accumulation and increases the local work of fracture within the crack-tip process zone. The limited particle fracture observed in both $5\text{ }\mu\text{m}$ particle composites coupled with the lower flow stress in the Al_2O_3 -containing composite explain the greater toughness of this material compared to that reinforced with B_4C .

Overall, particle reinforced composites produced by infiltration thus provide insight into the local phenomena that determine the mechanical performance of ceramic particle reinforced metals. Trends in composite properties with variations of the type of particle and the size are evident, at both microscopic and macroscopic levels. Quantification of these trends is currently being investigated, involving in particular the construction of finite-element (FEM) models that “realistically” simulate these composites on the microstructural scale, following the procedure pioneered by Fischmeister *et al.* [22]. The main advantage of these models, as compared with simple “unit-cell” approaches containing a single cylindrical or ellipsoidal particle, is that damage can be studied more realistically. This is important because damage is a highly localized phenomenon and thus very much dependent on the local arrangement of the two phases.

Commonly, such models of “realistic” microstructures are limited to two dimensions, because the generation of three-dimensional models is very difficult and their numerical solution is impractical from a computation standpoint. Consequently, these models are based on a (generalized) plane strain assumption. This, however, overconstrains the soft phase and induces strong strain localization together with premature matrix damage, notably if the matrix phase is much softer than the reinforcement. We therefore use a somewhat different approach: we solve for the two-dimensional deformation of a (complex) composite unit cell which, experiences locally the same stress perpendicular to the plane of deformation as if layered with an equally thick identical mesh of a homogeneous damage-free “background” material. This is accomplished by adding constraint equations that are imposed on the “additional” nodes (one for each generalized plane strain element) that describe the thickness degree of freedom. These equations are designed such that the overall deformation of the composite-background material sandwich is homogeneous in the thickness direction, whereas the partitioning of deformation between composite and background material produces local lateral stress equilibrium in each pair of elements. The properties of the background material are chosen identical to those of the matrix, but without damage. Of course, this “relaxed-constraint” approach is not rigorous from a mechanics point of view; however, checks on load-partitioning between ceramic and metal phase, as well as global and local stress and strain fields, show that a noticeable improvement in simulating a three-dimensional constraint situation is obtained. Periodic boundary conditions are employed for the in-plane nodes and about 30000 (first order quadrilateral) finite elements are used.

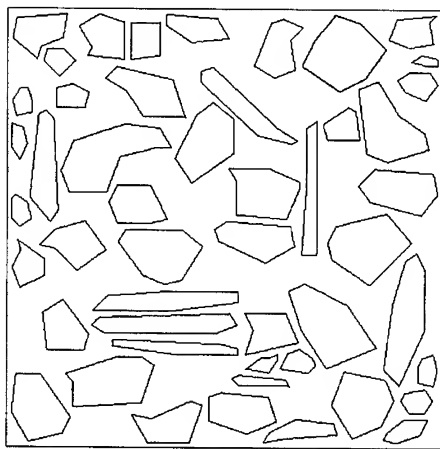
An example of such a model microstructure is given in Fig. 8-a, and Fig. 8-b shows preliminary computational results. Ductile matrix damage is simulated with a rate-dependent modification of the well-known GTN model [23-25]. The flow potential reads

$$\phi = \left(\frac{\sigma_{eq}}{\sigma_d} \right)^2 + 2 q_1 f^* \cosh \left(\frac{3 q_2 \sigma_h}{2 \sigma_d} \right) - (1 + q_3 f^2)$$

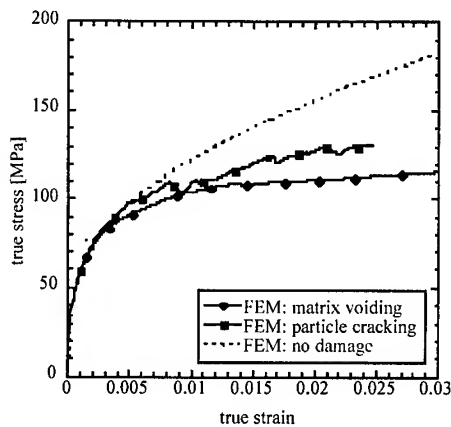
where σ_{eq} is the von Mises equivalent stress, σ_d the “dynamic” flow stress in the (void-free) matrix, σ_h the hydrostatic pressure, f^* the modified void volume fraction as described in [25], and q_1 , q_2 and q_3 parameters introduced by Tvergaard [24]. Nucleation of voids in the originally dense matrix material was taken to be strain-induced (*e.g.*, Ref. [25]) with a nucleation strain of 0.3 and a standard deviation of 0.1. Perfect interfaces have been assumed, *i.e.* debonding is not considered. Brittle failure in the particles follows a critical stress criterion, with a critical cracking stress of 1000 MPa. The flow stress curve of aluminium taken as input for the simulation was derived from literature data coupled with tests of the unreinforced matrix. Matrix hardening due to thermal stresses is not taken into account in the simulation.

and no attempt has been made to account for the dependence of the observed flow stress on particle size.

While choices made for the damage parameters are still arbitrary, it is evident that damage must be accounted for in the model to describe the steep drop of the work hardening rate that is experimentally observed, and which dictates the tensile ductility of the materials (*cf.* Figs 3.). The fact that the computed curve for a composite damaging by particle cracking lies above that derived for matrix voiding is a simple result of the choice of parameters, and that matrix voiding concomitant with particle fracture was not considered in the former simulation. These results highlight the importance of micromechanical parameters chosen to simulate the composite material flow behaviour and the measured progression of internal damage. Future work will aim to fit predictions from the model with experimental data and to derive, from these comparisons, an assessment of the intrinsic properties of the microstructural constituents.



a)



b)

Fig 8 a) FEM model showing the contours of the particles (50 vol pct).
b) Influence of damage on the computed composite stress-strain curves.

ACKNOWLEDGMENTS

The authors acknowledge funding from the Swiss National Science Foundation, project No. 20-55291.98, and from core laboratory funding within EPFL.

REFERENCES

1. A. Mortensen and I. Jin: *Intern. Mater. Rev.*, 1992, vol. 37, pp.101-128.
2. T.W. Clyne and P.J. Withers: *An Introduction to Metal Matrix Composites*, Cambridge University Press, Cambridge, U.K., 1993.
3. V.J. Michaud: in *Fundamentals of Metal Matrix Composites*, S. Suresh, A. Mortensen, and A. Needleman, ed., Butterworth-Heinemann, Stoneham, Mass, 1993, pp.3-22.
4. J.Y. Yang, F.W. Zok, and C.G. Levi: in *Processing, Properties and Applications of Cast Metal Matrix Composites*, Proc. Conf., Cincinnati, OH, 1996, P.K. Rohatgi, ed., TMS, Warrendale, PA, pp.77-92.

5. M.S. Hu: *Scripta Metall. et Mater.*, 1991, vol. 25, pp.695-700.
6. S.W. Lai and D.D.L. Chung: *J. Mater. Sci.*, 1994, vol. 29, pp.3128-3150.
7. J. Yang, S.M. Pickard, C. Cady, A.G. Evans, and R. Mehrabian: *Acta Metall. et Mater.*, 1991, vol. 39, pp.1863-1869.
8. S.M. Pickard, S. Schmauder, D.B. Zahl, and A.G. Evans: *Acta Metall. et Mater.*, 1992, vol. 40, pp.3113-3119.
9. R.H. Pestes, S.V. Kamat, and J.P. Hirth: *Mater. Sci. & Eng.*, 1994, vol. A189, pp.9-14.
10. W.R. Blumenthal, G.T. Gray, and T.N. Claytor: *J. Mater. Sci.*, 1994, vol. 29, pp.4567-4576.
11. K.T. Ramesh and G. Ravichandran: *Mech. of Mater.*, 1990, vol. 10, pp.19-29.
12. B.K. Hwu, S.J. Lin, and M.T. Jahn: *Mater. Sci. & Eng.*, 1996, vol. A207, pp.135-141.
13. D. Muscat, K. Shanker, and R.A.L. Drew: *Mater. Sci. and Technol.*, 1992, vol. 8, pp.971-976.
14. K. Shanker, L.T. Mavropoulos, R.A.L. Drew, and P.G. Tsantrizos: *Composites*, 1992, vol. 23, pp.47-53.
15. A. Redsten and D.C. Dunand: in *Light Weight Alloys for Aerospace Applications III*, Proc. Conf., 1995, E.W. Lee, N.J. Kim, K.V. Jata, and W.E. Frazier, ed., TMS, Warrendale, PA, USA, pp.545-558.
16. S. Cardinal, M. R'Mili and P. Merle, *Composites – A*, 1998, vol. 29A, pp.1433-1441.
17. V. Massardier, R. Fougères, and P. Merle: *Mater. Sci. & Eng.*, 1995, vol. A203, pp.93-104.
18. J.A. Isaacs, F. Taricco, V.J. Michaud, and A. Mortensen: *Metall. Trans.*, 1991, vol. 22A, pp.2855-2862.
19. J.C. Viala, J. Bouix, G. Gonzalez, and C. Esnouf: *J. Mater. Sci.*, 1997, vol. 32, pp.4559-4573.
20. T.L. Anderson: *Fracture Mechanics, Second Edition*, CRC Press, Boca Raton, USA, 1995, Chapters 3, 5 and 7.
21. A. Mortensen: in *Fabrication of Particulate Reinforced Metal Composites*, Proc. Conf., Montréal, Canada, 1990, J. Masounave and F.G. Hamel, eds., ASM Int., pp.217-233.
22. J. Wulf, T. Steinkopf and H.F. Fischmeister, *Acta Mater.*, 1996, vol. 44, pp.1765-1779.
23. A.L. Gurson, *J. Engng. Mat. Techn.*, 1977, vol. 99, pp.2-15.
24. V. Tvergaard, *Int. J. Fracture*, 1982, vol. 18, pp.237-252.
25. V. Tvergaard and A. Needleman, *Acta Met.*, 1984, vol. 32, pp.157-169.

EVALUATION OF INTERFACE PROPERTIES FROM A FIBRE FRAGMENTATION TEST

Hong-Yuan Liu and Yiu-Wing Mai

*Centre for Advanced Materials Technology,
Department of Mechanical and Mechatronic Engineering J07,
The University of Sydney, Sydney, NSW 2006, Australia*

SUMMARY: A new theoretical model is presented for the evaluation of interface properties from a single fibre test. With only very few assumptions, the solution of the stress field can be obtained satisfying all equilibrium equations, boundary conditions and continuity at the fibre/matrix interface. Considering the thermal residual strains of both fibre and matrix in the basic equations, the interfacial shear strength τ_s can be solved by a simple equation with three measured experimental data: fibre fragment length, debonding length and the corresponding applied stress. After the solution of the interfacial shear strength, another interfacial parameter, interfacial friction coefficient μ , can also be obtained by solving a non-linear equation or by a simple computer simulation program.

KEYWORDS: Interface properties, fibre fragmentation, theoretical model, debonding length, interfacial shear strength, interfacial friction.

INTRODUCTION

It is well recognized that the mechanical properties of fibre composites are highly dependent on the integrity of the interface. Interface debonding and post-debonding friction are two important mechanisms of energy absorption during the failure of a composite interface [1]. Therefore, evaluation of interface properties, bonding strength and friction coefficient, has attracted special attentions in recent years. Single fibre fragmentation test is commonly considered as one of the most powerful tools to evaluate the interface properties. The traditional approach to evaluate the interface shear strength from a single fibre fragmentation test is presented by Kelly & Tyson in 1965 [2]. In their model, a simple formula was derived to relate the interfacial shear strength τ_s to the average fibre fragment length l_c at saturation, that is

$$\tau_s = \frac{\sigma_{TS} d}{2l_c} \quad (1)$$

where, d and σ_{TS} are fibre diameter and tensile strength, respectively. This model is based on an elastic-plastic assumption that the interfacial shear stress is constant and equals to the interfacial shear strength. In recent years, more and more theoretical and FEA investigations have proven that the interfacial shear stress varies with the axial distance. When the maximum shear stress reaches the shear strength, interface debonding propagates. Therefore, for the same fibre tensile strength and fragment length, the interface shear strength evaluated by Kelly's model may be lower than the real value. In 1995, Zhou and his co-workers presented a theoretical model for fibre fragmentation test [3]. In their study, the stress field was solved by the extending Lamé's solution. Griffith's fracture mechanics approach was used to derive the interface debonding criterion. Since the thermal residual strains in the fibre/matrix system were not included in their basic strain-stress equations, therefore, the unknown parameters, interfacial fracture toughness, friction coefficient and radial clamping stress, cannot be evaluated independently by two available equations. As discussed in a recent review [4], though various theoretical models have been presented to study the stress field and debonding behaviour in the fibre fragmentation test, up to now, there is no satisfactory method presented for the evaluation of the interface properties.

The aim of this paper is to present an improved model of a fibre fragmentation test. Including the thermal residual strains in the basic equations, the unknown interface parameters, interfacial shear strength and interfacial friction coefficient, can be solved by two independent equations: fibre breaking criterion and interface debonding criterion. Compared with other previous methods, the advantages of this model are its modification and simplification in the methodology of the evaluation.

BASIC EQUATIONS

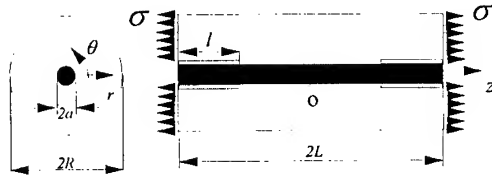


Figure 1 Schematic diagram of the fibre/matrix cylinder with a length $2L$ and a debonded region of length l at each end. The radii of the fibre and matrix are a and R , respectively. The applied stress is σ .

A mechanics model of a fibre fragment is shown in Fig. 1. The boundary conditions at the two ends are:

$$\sigma_f^z(\pm L) = 0, \quad \sigma_m^z(\pm L) = \sigma \quad (2)$$

in which, the superscripts denote the coordinates and subscripts f, m refer to the fibre and matrix, respectively. The equilibria between the axial stresses and interfacial shear stress, τ_a , are

$$\frac{d\sigma_f^z}{dz} = -\frac{2}{a}\tau_a, \quad \frac{d\sigma_m^z}{dz} = \frac{2\gamma}{a}\tau_a, \quad \gamma = \frac{a^2}{R^2 - a^2} \quad (3)$$

Here, we assume that the axial stresses are independent of r -coordinate [4].

The matrix is considered as isotropic, i.e.

$$\begin{aligned}\varepsilon_m^r &= \frac{1}{E_m} [\sigma_m^r - \nu_m (\sigma_m^\theta + \sigma_m^z)] + \varepsilon_m^{tr} \\ \varepsilon_m^\theta &= \frac{1}{E_m} [\sigma_m^\theta - \nu_m (\sigma_m^r + \sigma_m^z)] + \varepsilon_m^{tr} \\ \varepsilon_m^z &= \frac{1}{E_m} [\sigma_m^z - \nu_m (\sigma_m^r + \sigma_m^\theta)] + \varepsilon_m^t\end{aligned}\quad (4)$$

The fibre is transversely isotropic, i.e.

$$\begin{aligned}\varepsilon_f^r &= \frac{1}{E_f} (\sigma_f^r - \nu_f^r \sigma_f^\theta) - \frac{\nu_f}{E_f} \sigma_f^z + \varepsilon_f^{tr} \\ \varepsilon_f^\theta &= \frac{1}{E_f} (\sigma_f^\theta - \nu_f^r \sigma_f^r) - \frac{\nu_f}{E_f} \sigma_f^z + \varepsilon_f^{tr} \\ \varepsilon_f^z &= \frac{1}{E_f} \sigma_f^z - \frac{\nu_f^r}{E_f} (\sigma_f^r + \sigma_f^\theta) + \varepsilon_f^t\end{aligned}\quad (5)$$

where, ε^t and ε^{tr} are axial and radial thermal residual strains and equal to the product of the thermal expansion coefficient (α_f , α_f^r , and α_m) and the temperature change (ΔT). E (E^r) and ν (ν^r) denote Young's modulus and Poisson's ratio in axial (transverse) direction.

The outer boundary conditions of the matrix are given by

$$\sigma_m^r|_{r=R} = 0, \quad \tau_m^{rz}|_{r=R} = 0 \quad (6)$$

At the interface, the radial stresses and displacements of the fibre and matrix satisfy

$$\sigma_m^r|_{r=a} = \sigma_f^r|_{r=a} = q_i, \quad u_m^r|_{r=a} = u_f^r|_{r=a} \quad (7)$$

where, q_i is the interfacial radial stress including thermal residual stress and Poisson contraction.

At the bonded interface ($0 \leq z \leq L-l$), the continuity of axial deformations requires that

$$u_m^z|_{r=a} = u_f^z|_{r=a} \quad (8)$$

At the debonded interface ($L-l \leq z \leq L$), the interfacial shear stress is determined by the Columob's friction law with a constant friction coefficient, μ , that is

$$\tau_a = -\mu q_i \quad (9)$$

Combining Eqns (2)-(9) with the basic equations of elasticity and following the same procedure and assumptions as that in our early work [5,6], the fibre axial stress, σ_f^z , is obtained as

$$\sigma_f^z = (\sigma_f^l + \frac{A_2\sigma}{A_1} - \frac{A_3\sigma^T}{A_1}) \frac{\cosh \sqrt{A_1} z}{\cosh \sqrt{A_1} (L-l)} - \frac{A_2\sigma}{A_1} + \frac{A_3\sigma^T}{A_1} \quad (0 \leq z \leq L-l) \quad (10)$$

$$\sigma_f^z = (\frac{B_3\sigma}{B_2} + \frac{B_4\sigma^T}{B_2}) [\frac{e^{\lambda_1 z} \sinh \lambda_2 L - e^{\lambda_2 z} \sinh \lambda_1 L}{\sinh(\lambda_2 - \lambda_1)L} - 1] \quad (L-l \leq z \leq L) \quad (11)$$

$$\sigma_f^l = (\frac{B_3\sigma}{B_2} + \frac{B_4\sigma^T}{B_2}) [\frac{e^{\lambda_1(L-l)} \sinh \lambda_2 L - e^{\lambda_2(L-l)} \sinh \lambda_1 L}{\sinh(\lambda_2 - \lambda_1)L} - 1] \quad (12)$$

in which, the parameters A_i , B_i and λ_i are given in Appendix A.

EVALUATION OF INTERFACE PROPERTIES

When the maximum fibre axial stress (at $z=0$) reaches its strength, $\sigma^{TS}(2L_0)$ [3], fibre breaks. From Eqns. (10) and (12), the maximum fibre stress can be obtained as

$$\sigma_{f,max} = \frac{\sigma_f^l}{\cosh \sqrt{A_1} (L-l)} - (\frac{A_2\sigma}{A_1} - \frac{A_3\sigma^T}{A_1}) [1 - \frac{1}{\cosh \sqrt{A_1} (L-l)}] = \sigma_f^{TS}(2L) \quad (13)$$

During the interface debonding, the interfacial shear stress at the debonding tip equals the interface shear strength, τ_s . From Eqns. (3) and (10), we have

$$\tau_s = \tau_a(L-l)^- = -\frac{a\sqrt{A_1}}{2} (\sigma_f^l + \frac{A_2\sigma}{A_1} - \frac{A_3\sigma^T}{A_1}) \frac{\sinh \sqrt{A_1} (L-l)}{\cosh \sqrt{A_1} (L-l)} \quad (14)$$

In a fibre fragmentation test, if the fibre fragment of length $2L_i$ breaks at the stress level σ_i , the interfacial shear strength can be evaluated from Eqns. (13) and (14), i.e.

$$\tau_s = -\frac{a\sqrt{A_1}}{2} [\sigma^{TS}(2L_i) + \frac{A_2\sigma_i}{A_1} - \frac{A_3\sigma^T}{A_1}] \sinh \sqrt{A_1} (L_i - l_i) \quad (15)$$

Substituting Eqn. (12) into Eqn. (14), another interfacial parameter: friction coefficient μ , can be easily solved by a numerical method.

Table 1 Evaluation of interface properties from single fibre tests.

	σ_i (GPa)	σ_f^{TS} (GPa)	a (mm)	R (mm)	L_i (mm)	$l/L=0.55$ τ_s (GPa), μ	$l/L=0.6$ τ_s (GPa), μ	$l/L=0.65$ τ_s (GPa), μ
G34-700/Araldite-F (treated/sized)	0.054	5	0.0035	1.5	0.4	0.113, 0.12	0.094, 0.9	0.076, >2.0
T700/Araldite-F (sized)	0.059	8	0.003	1.5	0.62	0.110, 0.55	0.08, 1.4	0.058, >2.0

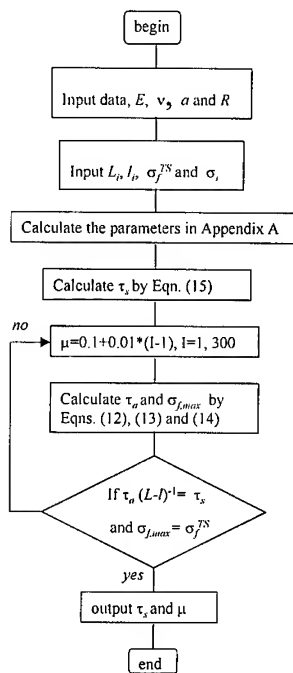


Figure 2 Flowchart of evaluation program.

The experimental data are given in Table 1 [7], in which $E_f=240$ GPa, $E_m=1.6$ GPa and $\nu_f=0.2$, $\nu_m=0.3$. Since the debonding length was not measured by the test, three different debonding lengths are assumed for each specimen. In a fibre fragmentation test without thermal residual stress, the fibre axial stress

should be in tension. From Eqn. (13), the minimum debonding length to ensure this condition can be obtained. Therefore, the debonding lengths assumed in the examples are equal to or larger than the minimum debonding length. Following the process given in Fig. 2, the evaluated values of interfacial shear strength and friction coefficient for different debonding lengths are given in Table 1. As we mentioned in our previous paper [4] the debonding length is a very important factor in the evaluation of the interfacial properties. It is also shown in Table 1, that different assumptions of the debonding length can make a significant difference in both the interfacial shear strength and friction coefficient.

CONCLUSIONS

A closed-form model has been introduced to evaluate the interfacial properties from a single fibre fragmentation test. The interfacial shear strength can be calculated by a simple formula. The interfacial friction coefficient can be obtained by solving a non-linear equation or numerical simulation. It is proven that the debonding length is an essential factor for the determination of interfacial properties.

ACKNOWLEDGMENT

The authors would like to thank the Australia Research Council (ARC) for the continuing support of this project. Hong-Yuan Liu is supported by an ARC Postdoctoral Fellowship tenable at the CAMT of the University of Sydney.

REFERENCES

1. Kim, J.-K. and Mai, Y.-W., *Engineered interfaces in fibre-reinforced composites*, Elsevier, Oxford, (1998).
2. Kelly, A. and Tyson, W.R., "Tensile properties of fibre-reinforced metals: copper/tungsten and copper/molybdenum", *J. Mech. Phys. Solids*, **13**, 1965, pp. 329-350.
3. Zhou, L.-M., Kim, J.-K., Baillie, C. and Mai, Y.-Y., "Fracture mechanics analysis of the fibre fragmentation test", *J. comp. Mater.*, **29**, 1995, pp. 881-902.
4. Liu, H.-Y. and Mai, Y.-W., "An appraisal of composite interface mechanics models and some challenging problems", *Comp. Interfaces*, **6**, 1999, pp. 343-362.
5. Zhang, X., Liu, H.-Y., Mai, Y.-W. and Diao, X.-X., "On steady-state fibre pull-out part I: the stress field", *Comp. Sci. and Technol.*, **59**, 1999, pp. 2179-2189.
6. Liu, H.-Y., Zhang, X., Mai, Y.-W. and Diao, X.-X., "On steady-state fibre pull-out part II: computer simulation", *Comp. Sci. and Technol.*, **59**, 1999, pp. 2191-2199.
7. Deng, S., Ye, L., Mai, Y.-W. and Liu, H.-Y., "Evaluation of fibre tensile strength and fibre/matrix adhesion using single fibre fragmentation tests", *Comp. Part A*, **29**, 1998, pp. 423-434.

APPENDIX A

$$A_1 = \frac{\beta + \gamma - 2k(\beta v_f + \gamma v_m)}{C_1(v_m - 2k)}, \quad \beta = \frac{E_m}{E_f}, \quad \beta' = \frac{E_m}{E_f'} \quad (A1)$$

$$A_2 = \frac{2k v_m - 1}{C_1(v_m - 2k)}, \quad A_3 \sigma^T = \frac{E_m \Delta T [\alpha_m - \alpha_f + 2k(\alpha_m - \alpha_f')]}{C_1(v_m - 2k)} \quad (A2)$$

$$k = \frac{\beta' v_f + \gamma v_m}{\beta' (1 - v_f') + 1 + 2\gamma + v_m}, \quad C_1 = \frac{a}{2} \{F(R) - F_1(a) - (1 + 2\gamma)[F(a) - F(R)]\} \quad (A3)$$

$$F(r) = \frac{\gamma}{a} \left\{ \frac{R^2}{2} - \frac{r^2}{4} + \frac{2(1 + v_m)}{v_m} \left[\frac{R^2}{2} \left(\ln r - \frac{1}{2} \right) - \frac{r^2}{8} \right] \right\} \quad (A4)$$

$$F_1(r) = \frac{2(1 + v_m)}{v_m} \frac{\gamma}{a} \left(R^2 \ln r - \frac{r^2}{2} \right) - F(r) \quad (A5)$$

$$\lambda_{1,2} = \frac{-B_1 \pm \sqrt{B_1^2 + 4B_2}}{2}, \quad B_1 = \frac{a(\beta' v_f' + \gamma v_m)}{2\mu C_1 k}, \quad B_2 = \frac{\beta v_f + \gamma v_m}{C_1} \quad (A6)$$

$$B_3 = -\frac{v_m}{C_1}, \quad B_4 \sigma^T = \frac{E_m \Delta T (\alpha_m - \alpha_f')}{C_1} \quad (A7)$$

MECHANICAL IDENTIFICATION OF COMPOSITE MATERIALS AND STRUCTURES

Alain Vautrin

*Mechanical and Materials Engineering Department
Ecole Nationale Supérieure des Mines de Saint-Etienne
158, cours Fauriel, 42023 Saint-Etienne cedex 2, France:vautrin@emse.fr*

late paper (pp. 1305)

THE PROPER USE OF FRACTURE MECHANICS IN THE ANALYSIS OF COMPOSITE MATERIALS AND LAMINATES

C. T. Sun

*School of Aeronautics and Astronautics
Purdue University
West Lafayette, Indiana 47907-1282, USA, :sun@ecn.purdue.edu*

SUMMARY: Fracture mechanics has been used by many researchers to study matrix cracking, fiber/matrix debonding, laminate delamination, and many other failure modes in composites. Due to their complexities, composites present great challenges to researchers in applications of fracture mechanics. In this paper, many pitfalls are presented and discussed. First, the concept of energy release rate is revisited, and its meaning in the presence of other energy dissipative mechanisms discussed. Interfacial cracks are common in composite materials and laminates. The conventional treatment of fracture of interfacial cracks are reviewed. Effects of crack surface contacts and friction on the near tip stress field are examined. The commonly used test methods with DCB and ENF specimens for determining interlaminar fracture toughness of composites may give different toughness values depending on a number of testing conditions. Finally, there are situations where the singular stress field is not dominant and, as a result, the stress intensity factor cannot be used for fracture predictions.

KEYWORDS: energy release rate, stress intensity factor, interface crack, debonding, delamination, friction, fracture toughness

INTRODUCTION

Fracture mechanics has been developed into a major tool for analysis and design of failure in structures and materials over the past fifty years. It has been used in composite materials and laminates on many aspects including characterizing toughness, interfacial properties of fiber/matrix interface, matrix cracking and interlaminar delamination, etc. Because of the complexities of the composites architectures, the application of fracture mechanics has been stretched to the extent that the validity of its application is in serious question.

Two parameters have been used for fracture prediction, i. e., stress intensity factor and energy release rate. In most situations, these two parameters are uniquely related and, theoretically, can be interchanged in applications. It appears that energy release rate has been more popular in the composites community because, perhaps, it is much easier to calculate energy release rate than the stress intensity factor. Although energy release rate was introduced first by Griffith [1] to explain fracture of solids, it has some shortcomings in

certain applications such as elastic-perfectly plastic analysis and frictional contact of crack surfaces, in which energy release rate vanishes.

In this paper, the problems where the use of energy release rate is not proper are discussed. Discussion also includes problems arising from situations where the K-field near the crack tip is not dominant. Finally, comments on the conventional interlaminar fracture toughness testing using DCB and ENF specimens are presented.

ENERGY RELEASE RATE

The explanation of fracture in terms of an energy balance for the extension of a pre-existing crack began with the classic work of Griffith [1]. He obtained a criterion of brittle fracture by equating the decrease in potential energy of a linearly elastic body, due to crack extension, to the surface energy of the newly created crack surfaces. The Griffith fracture theory in its original form fails to account for the great discrepancy between the magnitude of actual fracture energy and surface energy. This led to the generalization that surface energy includes the crack tip plastic work dissipation as proposed by Irwin [2] and Orowan [3]. They equated the decrease in the potential energy due to crack extension to the sum of the energy in creating new crack surfaces and plastic dissipation. In 1966, Rice [4] gave an analytical examination and discussion of fracture energy balance, attempting to seek conclusions which follow from the more general theorems of continuum mechanics and broad classifications of solids. For elastic/perfectly plastic solids, paradoxical results obtained by Rice [4] indicated that such solids provide no energy surplus to drive the continuous crack extension. Later, using the finite element method, Kfoury and Miller [5] and Kfoury and Rice [6] confirmed the vanishing strain energy release rate result obtained in [4]. However, they attempted to attain a nontrivial energy surplus (strain energy release rate) in order to facilitate the use of Griffith theory. They suggested a so-called finite crack extension zone to calculate the strain energy release rate that, due to a faulty numerical procedure, was shown to be of nonzero value.

Another paradox related to the concept of strain energy release rate in elastic solids exists. Within the framework of classical elasticity, there is no mechanism to store surface energy. Therefore, released strain energy is absent from the body after crack extension, and the energy balance requirement during crack extension cannot be satisfied. From the consideration of energy balance, the vanishing surplus energy during crack extension is, in fact, more consistent with the theory of continuum mechanics. In a recent study, Sun and Wang [7] used a finite element based numerical procedure to calculate the variation of energies during crack extension in a plane stress elastic/perfectly plastic solid. The FEM results are shown in Fig. 1. First, we note that separation work vanishes independent of the plastic zone size r_p . As the plastic zone size increases, the plastic work rate G_p increases while the rate of elastic energy increment G_e decreases. It is interesting to note that, as r_p approaches zero, both G_e/G_w and G_p/G_w approach 1/2. This means that the elastic strain energy release rate G is equal to the rate of plastic work when an elastic solid is considered as a limiting case of an elastic/perfectly plastic solid by taking $r_p \rightarrow 0$. The difference between G_p and G may be used as a quantitative measure of the validity of the small scale yielding concept. It is shown that the elastic strain energy release rate always vanishes without regard to assumed crack extensions. It is also shown that the strain energy release rate in elastic solids is the same as the plastic work dissipation rate taken in the limit as the yield stress approaches infinity.

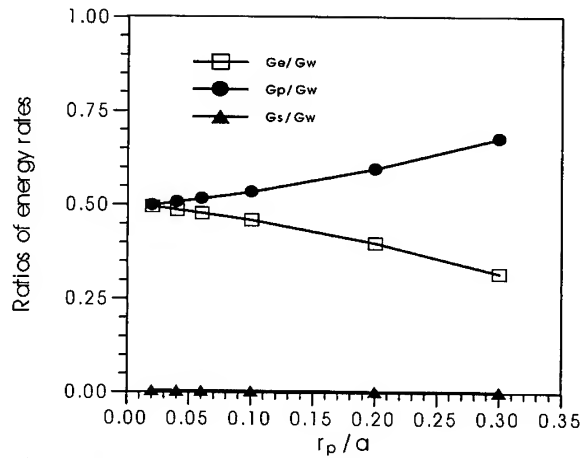


Fig. 1 Effect of plastic zone size on ratios of the energy rates

OPEN INTERFACIAL CRACK

Interfacial cracks are common in composites; they exist between fiber and matrix, between laminas in laminates. The basic nature of interfacial cracks can be illustrated with isotropic solids. Consider the near-tip stress fields for a two-dimensional bimaterial infinite medium with an interfacial center crack of size $2a$ subject to remotely uniform tensile stress σ_{yy}^{∞} for which the solution was given by Rice and Sih [8]. The asymptotic crack tip stresses along the interface ahead of the crack tip from the oscillatory solution are

$$\sigma_{yy} = \frac{\sigma_{yy}^{\infty}}{\sqrt{2x/a}} \left[\cos\left(\epsilon \ln \frac{x}{2a}\right) - 2\epsilon \sin\left(\epsilon \ln \frac{x}{2a}\right) \right] \quad (1)$$

$$\sigma_{xy} = \frac{\sigma_{yy}^{\infty}}{\sqrt{2x/a}} \left[\cos\left(\epsilon \ln \frac{x}{2a}\right) + 2\epsilon \cos\left(\epsilon \ln \frac{x}{2a}\right) \right] \quad (2)$$

where

$$\epsilon = \frac{1}{2\pi} \left[\left(\frac{\kappa_1}{\mu_1} + \frac{1}{\mu_2} \right) / \left(\frac{\kappa_2}{\mu_2} + \frac{1}{\mu_1} \right) \right], \quad \kappa_j = \begin{cases} 3 - 4\nu_j & \text{for plane strain} \\ 3 - \nu_j & \text{for plane stress} \end{cases} \quad (3)$$

Here μ is shear modulus, ν is Poisson's ratio, and subscripts 1 and 2 denote upper and lower materials, respectively. This solution exhibits the well known violent oscillatory stresses when approaching the crack tip. Moreover, the crack surfaces display the physically impossible interpenetration phenomenon near the crack tip. An exact solution which satisfies the crack surface contact condition was given by Gausen and Dundurs [9] which is mathematically much more involved than the oscillatory solution. However, the contact zone size (or the oscillatory zone size) is usually very small as compared to the crack size and, thus, has been commonly ignored and the simpler oscillatory solution adopted for applications.

The main dilemma caused by the oscillatory stress and displacement fields in an interfacial crack is the nonexistence of the individual mode I and mode II energy release rates. For a finite crack extension Δa , Sun and Jih [10] obtained

$$\hat{G}_I(\Delta a) = \frac{1}{2}G + C[A_R(K_I^2 - K_{II}^2) - 2A_I K_I K_{II}] \quad (4)$$

$$\hat{G}_{II}(\Delta a) = \frac{1}{2}G - C[A_R(K_I^2 - K_{II}^2) - 2A_I K_I K_{II}] \quad (5)$$

where

$$G = D(K_I^2 + K_{II}^2) \quad (6)$$

is the total strain energy release rate, B and C are two complex constants, and

$$A_R = \text{Re}(A), \quad A_I = -\text{Im}(A), \quad A = B \left[\frac{\Delta a}{4a} \right]^{-2ie}, \quad D = \frac{1}{16} \left[\frac{\kappa_1 + 1}{\mu_1} + \frac{\kappa_2 + 1}{\mu_2} \right]$$

From the above expressions, it is evident that the limits as $\Delta a \rightarrow 0$ do not exist. There was some effort to redefine G_I and G_{II} [11] to remove their oscillatory behavior. However, the more practical approach in establishing a fracture criterion for interfacial cracks has been either going back to the use of the stress intensity factors or simply using the total energy release rate in conjunction with the mode mixity $\tan^{-1}(K_{II}/K_I)$ as suggested by Hutchinson [12].

INTERFACIAL CRACK WITH FRICTIONAL CONTACT

The development of classical fracture mechanics is based on the open crack assumption, i.e., the crack surfaces are not in contact. That assumption leads to, in linear elastic solids, stress singularity of inverse square root that enables one to employ either strain energy release rate or stress intensity factor to characterize fracture toughness and predict crack movement.

For bimaterial cracks under combined compression and/or shear, the effect of sliding frictional stresses on the crack surfaces cannot always be ignored. Only in the case in which the neartip contact zone is extremely small, the K-dominated field basically agrees with that of the open crack solution. This was discussed in detail by Sun and Qian [11] for bimaterial interfacial cracks under "Mode I" loading. On the other hand, if the contact zone is finite, frictional contact of the crack surfaces can no longer be neglected. Most importantly, the frictional contact alters the stress singularity to weak singularities [13]. Consequently, the strain energy release rate as conventionally defined vanishes and cannot be used as a fracture parameter.

Many researchers have attempted to extend the fracture mechanics approach to treat various engineering problems involving interfacial cracks with frictional contact. Fiber pull-out and push-out problems have attracted the most attention [14-17]. Various methods were proposed by these authors to derive the energy release rate or to employ different parameters for characterizing the interfacial crack toughness. Many of these approaches suffer deficiencies mainly due to the weak singularity and the energy dissipation associated with the frictional sliding of crack surfaces.

Near Tip Field and Strain Energy Release Rate

For a crack in homogenous media with friction or an interface crack without friction, there is always square root singularity associated with the near tip field. However, it was originally shown by Comninou [13] for an interface crack between two dissimilar isotropic media with

friction and later confirmed and extended by Deng [18] for an interface crack between two dissimilar anisotropic media that the stress singularity $r^{-\lambda}$ is always weak ($\lambda < 0.5$) for a stationary crack under monotonic loading. The singularity index λ is related to the coefficient of friction μ as [2]

$$\cot \lambda \pi = \mu \beta \quad (7)$$

where

$$\beta = \frac{\mu_1(\kappa_2 - 1) - \mu_2(\kappa_1 - 1)}{\mu_1(\kappa_2 + 1) + \mu_2(\kappa_1 + 1)} \quad (8)$$

is a Dundurs parameter. In (8), subscripts 1 and 2 stand for upper and lower materials, respectively, $\mu_i (i = 1, 2)$ are the corresponding shear moduli.

The near tip stress field along the bimaterial interface and the relative crack surface sliding displacement in plane strain condition are

$$\begin{aligned} \sigma_{xy}(r, 0) &= K_{II}(2\pi r)^{-\lambda} \\ \sigma_{xy}(r, \pm\pi) &= K_{II} \cos \lambda \pi (2\pi r)^{-\lambda} \\ \sigma_{yy}(r, \pm\pi) &= -K_{II} \beta \sin \lambda \pi (2\pi r)^{-\lambda} \end{aligned} \quad (9)$$

and

$$\Delta u_x(r) = u_x(r, \pi) - u_x(r, -\pi) = \left[K_{II} \gamma \sin \lambda \pi / 2(1 - \lambda)(2\pi)^\lambda \right] r^{1-\lambda} \quad (10)$$

respectively, where the generalized stress intensity factor K_{II} is defined as

$$K_{II} = \lim_{r \rightarrow 0} (2\pi r)^\lambda \sigma_{xy}(r, 0) \quad (11)$$

and

$$\gamma = \left[\frac{((3 - 4\nu_1)(1 - \beta) + (1 + \beta))}{2\mu_1} \right] + \left[\frac{((3 - 4\nu_2)(1 + \beta) + (1 - \beta))}{2\mu_2} \right] \quad (12)$$

The solutions above are obtained with the assumptions that the crack surfaces slide and the normal and shear stresses behind the crack tip follow the Coulomb frictional law.

Because of the contact of crack surfaces, only mode II fracture mode is present. The strain energy released for a crack extension Δa was obtained using Irwin's crack closure integral by Sun and Qian [20] as

$$\begin{aligned} \hat{G}(\Delta a) &= \frac{1}{2\Delta a} \int_0^{\Delta a} [\sigma_{xy}(r, 0) - \sigma_{xy}(\Delta a - r, \pi)] \Delta u_x(\Delta a - r) dr \\ &= \frac{K_{II}^2 \gamma \sin \lambda \pi}{4(1 - \lambda)(2\pi)^{2\lambda}} \Delta a^{1-2\lambda} \left[\frac{\Gamma(2 - \lambda)\Gamma(1 - \lambda)}{\Gamma(3 - 2\lambda)} - \frac{\cos \lambda \pi}{2(1 - \lambda)} \right] \end{aligned} \quad (13)$$

in which Γ is the gamma function. The conventional strain energy release rate is defined as $G = \lim_{\Delta a \rightarrow 0} \hat{G}(\Delta a)$. In the crack closure integral of (11), the term $\sigma_{xy}(r, 0)$ is the interfacial shear stress ahead of the crack tip, and $\sigma_{xy}(\Delta a - r, \pi)$ is the frictional shear stress behind the crack tip. During the crack extension of Δa , the shear stress initially ahead of the crack tip reduces to that of the frictional shear stress behind the crack tip after the assumed crack extension. Thus, the strain energy release rate of (13) can be interpreted as the total energy release rate less the frictional energy dissipation rate.

It is seen from (13) that the strain energy release rate \hat{G} vanishes as $\Delta a \rightarrow 0$ due to the fact that $\lambda < 0.5$ in the presence of friction. Consequently, G cannot be used as a parameter in the fracture criterion. On the other hand, for $\Delta a = \Delta a_0 \neq 0$, $\hat{G}(\Delta a_0)$ is uniquely related to the stress intensity factor K_{II} and, thus, to the near tip stress field. By selecting a proper characteristic crack closure distance Δa_0 , it seems possible to use $\hat{G}(\Delta a_0)$ as a fracture parameter when friction is present.

A Fracture Criterion

In view of the foregoing, Sun and Qian [20] proposed a fracture criterion using the strain energy release rate \hat{G} of a characteristic crack extension Δa_0 as a fracture toughness parameter:

$$\hat{G}(\Delta a_0) = \frac{\Delta W_e}{\Delta a} - G_d(\Delta a_0) - \frac{\Delta U}{\Delta a} = \hat{G}_c \quad (14)$$

where ΔW_e , ΔU and $G_d(\Delta a_0)$ are the external work done, strain energy change and the dissipation energy rate for a crack extension of Δa_0 , respectively. From (13), it is seen that, for a fixed Δa_0 the finite extension strain energy release rate \hat{G} has a unique relation with the generalized stress intensity factor K_{II} . The fracture criterion given by (14) states that the interfacial crack would grow if the near tip stress field reaches a certain critical state.

Fiber Pull-out and Fiber Push-out

The properties of the fiber/matrix interface are important in determining the mechanical behavior of fibrous composites. The local response of the fiber-matrix interface during fracture has pronounced effects on the mechanical performance and structural integrity of the composite. Fiber pull-out as well as fiber push-out are two methods to determine the fiber/matrix interfacial properties as well as to understand the toughening effect of fiber composites due to frictional sliding after debonding.

There have been numerous theoretical models based on fracture mechanics to analyze the fiber-matrix interface toughness and toughening effect due to fiber sliding. A comprehensive review of the subject was given by Deng [21]. In these studies, the classical strain energy release rate was the key fracture parameter in determining the debonding initiation and debonding progression. However, most researchers did not account for the effect of the weak interfacial stress singularity due to friction. Some researchers used approximate interfacial shear stress distributions to calculate the “strain energy release rate” assuming $G = dU/da$, e.g., [14] and [16]. Consequently, these models cannot accurately characterize the intrinsic interfacial toughness.

An axisymmetric section of the composite model shown in Fig. 2 was used by Sun and Qian [20] for fiber pull-out and push-out study. The four-noded axisymmetric element CAX4 and the interface element INTER2 in ABAQUS were used in the simulation. The debonding crack a was assumed to initiate from the top as shown in Fig. 2. The fiber, matrix, and the “composite” regions were assumed to be isotropic. The characteristic length Δa_0 was taken to be $0.01a$ throughout the debonding process.

For fiber pull-out, a constant tensile stress σ is applied at the ending of the fiber. An open debonding crack tip results from this pulling action. In this case, the interfacial crack between the fiber and matrix should be treated as the classical open interfacial crack with oscillatory stress field [11], and the frictional effect is negligible. Figure 3 shows mode I and mode II strain energy release rates, \hat{G}_I and \hat{G}_{II} calculated with the finite crack extension $\Delta a/a = 0.01$. Note that the total strain energy release rate $G = \hat{G}_I + \hat{G}_{II}$ is well defined. For the open crack, the critical strain energy release G_c with the mode mixity must be determined for fracture prediction.

For fiber push-out under a compressive constant load σ , the debonding crack surfaces are completely closed, and the frictional effect is significant. Figure 4 shows the finite extension strain energy release rate, dissipation energy rate, and total energy rate for various debonding lengths.

The "fracture toughness" obtained from these two types of testing are different and cannot be compared because the pull-out test produces an open interfacial crack and the push-out test produces a closed crack. Moreover, their toughness is measured with different parameters. In the case of fiber push-out, the work resulting from the frictional contact of crack surfaces must be removed in order to obtain the intrinsic fiber/matrix interfacial toughness.

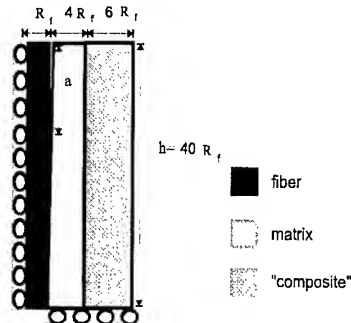


Fig. 2 The axisymmetric section of the fiber pull-out and push-out model

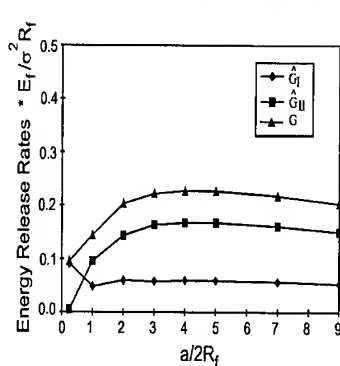


Fig. 3 Finite extension energy release rates for fiber pull-out under tensile load σ

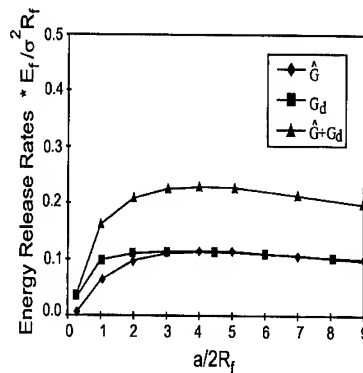


Fig. 4 Finite extension energy release rates for fiber push-out under compressive load σ

K-DOMINANCE ZONE

In the vicinity of the crack tip, the magnitude of the nonsingular terms of the stress field is negligible as compared to the singular term. This defines the region of K-dominance. As the distance from the crack tip increases, the relative magnitude of the nonsingular terms increases and the stress field will no longer be well-characterized by the K-dominance field.

In applications, composite laminates are thin, and the region of K-dominance near the crack tip could become very small. There are at least three important consequences of the small K-dominance zone. First, very fine meshes (if the finite element method is used for analysis) are required to calculate the strain energy release rate or stress intensity factor. Second, the singular term alone may not be sufficient to characterize the stress field in the fracture process zone and it may be necessary to include nonsingular stress terms. Third, the technique of smearing the thickness-wise laminate properties may not be valid for the analysis of stress intensity factors.

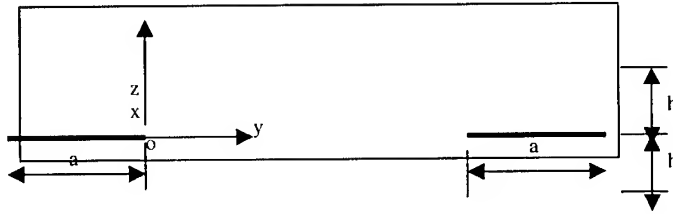


Fig. 5 Cross-section of laminate with edge cracks.

For convenience, let's consider the Mode I linear-elastic fracture mechanics solution for the stress field ahead of the crack tip. The crack opening stress (see Fig. 5) is given by

$$\sigma_{zz} = \frac{K_I}{\sqrt{2\pi y}} + \text{Non-singular term} \quad (15)$$

The degree of K-dominance at a distance y is defined as

$$D = \frac{\text{Singular Stress}}{\text{Singular Stress} + |\text{Non-singular Stress}|} = \frac{K_I}{K_I + |\sigma_{zz}\sqrt{2\pi y} - K_I|} \quad (16)$$

The parameter "D" measures the percentage of the singular stress against the total stress. At the crack tip, $D=1$. If we set, say, $D=0.9$ as the criterion of K-dominance, then the K-dominance region (the distance R_0 from the crack tip) can be determined from Eq. (16).

As an illustration, consider cross-ply laminates with two free edge cracks located at the mid-plane as shown in Fig. 5. The composite is AS4/3501-6 carbon/epoxy. Two types of loads are considered, i.e., opening line loads applied along the edges of the laminate, and a uniform axial strain applied in the x -direction. For convenience, we assume that the lamina thickness can assume arbitrary values. Table 1 presents the results for the K-dominant size R_0 of the edge crack in the thin laminate with $h/a = 0.1$ and in the thicker laminate with $h/a = 1$. It is evident that the K-dominance size is very small for thin laminates. If the finite element method is employed to perform the analysis of stress intensity factors or strain energy release rates in thin laminates, the meshes must be very fine in order to obtain accurate values. Moreover, the validity of the small scale yielding concept commonly adopted in LEFM may

be questionable because the K-dominance region may be completely engulfed by the plastic zone. Another implication of this result is that a thin laminate cannot be represented by an equivalent continuum by using the smearing technique.

Table 1 The relation between K-dominant size, R_o , for $D = 0.9$, and laminate thickness.

Load	Line Load				Axial Strain $\epsilon_x = 0.001$	
Laminate	[0/90] _s	[0/90] _s	[90/0] _s	[90/0] _s	[0/90] _s	[0/90] _s
h/a	1	0.1	1	0.1	1	0.1
R_o/a	0.041	0.0034	0.046	0.0036	0.025	0.0034

TESTING INTERLAMINAR TOUGHNESS

The double cantilever beam (DCB) and the end-notched flexural (ENF) specimens are the most popular specimen configurations in the experimental determination of mode I and mode II interlaminar fracture toughnesses. Common procedures for data reduction of DCB test are to use a compliance calibration technique known as Berry's method [22]. The area method is also very popular because of its simplicity [23]. Alternatively, beam theories are employed to calculate interlaminar toughness based on the experimental critical load.

In a general laminated DCB or ENF specimen, the strain energy release rate at the crack front varies (and may be skewed) across the specimen width. Consequently, the crack front is also curved and skewed. Thus, before beam theories are used to reduce experimental data, we must evaluate the validity of the beam-based solutions and provide proper interpretations of these solutions.

The behavior of strain energy release rate at the crack front of DCB and ENF specimens has been investigated by a number of researchers. Among them, Davidson [24], Davidson and Shapery [25], and Nilsson [26] analyzed the growth of the DCB crack front and found the crack front to be curved and of a thumb-shape. Sun and Zheng [27] used a double plate model to perform the delamination crack analysis for various laminates and showed that the delamination crack front in a DCB specimen was convex (the thumb shape), and that in an ENF specimen it was concave. Thus, the crack length measured from the edges of the specimen is not accurate. In fact, for the DCB specimen, the measurement is underestimated, while for the ENF specimen it is overestimated.

Recently, Yang and Sun [28] have conducted an experimental investigation on interlaminar fracture behavior and fracture toughness of multidirectional composite laminates is presented using end-notched flexure specimens. The $0/\theta$ interfaces are considered. The interlaminar fracture toughness is obtained and compared using three data reduction methods, *i. e.*, the area method, the classical laminated plate (beam) theory, and the 2D finite element analysis. Results show that the toughness value significantly depends on the data reduction method used. Two different crack-length-to-span ratios are chosen to study how the stable or unstable crack extension influences the toughness measurement. It is observed that the toughness obtained from the tests of stable crack extension is appreciably higher than that from the tests of unstable crack extension. It is also seen that friction resulting from contact of crack surfaces greatly affects the measured toughness in the case of stable crack extension.

CONCLUSIONS

Fracture mechanics is a powerful tool for analyzing and characterizing failure in solids containing crack-like flaws or failure modes. While fracture parameters such as energy release rate have been commonly considered as exact alternate to the stress intensity factor, there are situations where energy release rate as conventionally defined may not exist and, thus, cannot be used in fracture criteria. Examples include fiber/matrix debonding and delamination in composite laminates. The use of stress intensity factor or energy release rate for fracture predictions is based on the assumption that in the fracture process zone, the singular stress field is much greater as compared to the non-singular terms. In thin composite laminates, this assumption may not be always true, and the K-dominance field may be too small for invoking the classical LEFM.

ACKNOWLEDGMENT

This work was supported by an Office of Naval Research Grant No. N00014-96-1-0822 awarded to Purdue University. The grant monitor was Dr. Yapa D.S. Rajapakse.

REFERENCES

1. A. A. Griffith, "The phenomena of flow and rupture in solids," *Philosophical Transactions Royal Society of London*, Vol. A221, 1921, pp. 163-197.
2. G. R. Irwin, Fracture. In S. Flugge (ed.), *Hanbuch der Physik*. Springer-Verlag, Berlin, Vol. 6, 1958, pp. 551-590.
3. E. Orowan, "Energy criteria of fracture," *Welding Journal. Res. Suppl.*, Vol. 34, 1955, pp. 157-160.
4. J. R. Rice, "An examination of the fracture mechanics energy balance from the point of view of continuum mechanics," *Proceedings First International Conference on Fracture*, Sendai, Japan (T. Yokobori, ed.), Vol. 1, 1966, pp. 309-337.
5. A. P. Kfoury, and K. J. Miller, "Crack separation energy rates in elastic-plastic fracture mechanics," *Proceedings of the Institute of Mechanical Engineering*, Vol. 190, 1976, pp. 571-584.
6. A. P. Kfoury and J. R. Rice, "Elastic/plastic separation energy rate for crack advance in finite growth steps," *Proceedings fourth international conference on fracture*, University of Waterloo, Canada (D. M. R. Taplin, ed., Pergamon press, New York, 1977, pp. 43-59.
7. C. T. Sun and C. Wang, "A new look at strain energy release rate," submitted for publication.
8. J. R. Rice and G. C. Sih, "Plane problems of cracks in dissimilar media," *J. Appl. Mech.*, Vol 32, 1965, pp. 418-423.
9. A. K. Gautsen and J. Dundurs, "The interface crack in a tension field," *J. Appl. Mech.*, Vol. 54, 1987, pp. 93-98.
10. C. T. Sun and C. J. Jih, "On strain energy release rate for interfacial cracks in bimaterial media," *Enging. Fracture Mech.*, Vol. 28, 1987, pp. 13-20.
11. C. T. Sun and W. Qian, "The use of finite extension strain energy release rates for fracture in interface cracks," *International Journal of Solids and Structures*, Vol. 34, No. 20, 1997, pp. 2595-2609.
12. J. W. Hutchinson, "Mixed mode fracture mechanics of interfaces," *Metal-Ceramic Interface, Acta-Scripta Metallurgica*, Vol. 4, 1990, pp. 295-306.
13. M. Comninou, "Interface crack with friction in the contact zone," *Journal of Applied Mechanics*, Vol. 44, 1977, pp. 780-781.

14. Y. C. Gao, Y.W. Mai and B. Cotterell, "Fracture of fiber reinforced materials," *Journal of Applied Mathematics and Physics. (ZAMP)*, Vol. 39, 1988, pp. 550-572.
15. L. S. Sigl, and A. G. Evans, "Effects of residual stress and frictional sliding on cracking and pullout in brittle matrix composites," *Mechanics of Materials*, Vol. 8, 1989, pp. 1-12.
16. R. J. Kerans, and T. A. Parthasarathy, "Theoretical analysis of the fiber pullout and pushout tests," *Journal of the American Ceramics Society*, Vol. 74, 1991, pp. 1585-1596.
17. J. W. Hutchinson, and H. M. Jensen, "Models of fiber debonding and pullout in brittle composites with friction," *Mechanics of Materials*, Vol. 9, 1990, pp. 139-163.
18. X. Deng, "An asymptotic analysis of stationary and moving cracks with frictional contact along bimaterial interfaces and in homogeneous solids," *International Journal of Solids and Structures*, Vol. 31, No. 17, 1994, pp. 2407-2429.
19. M. Comninou and J. Dundurs, "Effect of friction on the interface crack loaded in shear," *Journal of Elasticity*, Vol. 10, No. 2, 1980, pp. 203-212.
20. C. T. Sun and W. Qian, "A treatment of interfacial cracks in the presence of friction," *International Journal of Fracture*, Vol. 32, No. 1, 1998, pp. 371-382.
21. X. Deng, "Mechanics of debonding and delamination in composites: Asymptotic studies," *Composites Engineering*, Vol. 5, No. 11, 1995, pp. 1299-1315.
22. J. P. Berry, "Determination of fracture surface energies by the cleavage technique," *Journal of Applied Physics*, Vol. 34, No.1, 1963, pp. 62-68.
23. J. M. Whitney, D. E. Browning, and W. Hoogsteden, "A double cantilever beam test for characterizing Mode I delamination of composite materials," *Journal of Reinforced Plastic Composites*, Vol. 1, 1982, pp. 297-313.
24. B. D. Davidson, "An analytical investigation of delamination front curvature in double cantilever beam specimens," *Journal of Composite Materials*, Vol. 24, 1990, pp. 1124-1137.
25. B. D. Davidson and R. A. Schapery, "Effect of finite width on deflection and energy release rate of an orthotropic double cantilever specimen," *Journal of Composite Materials*, Vol. 22, 1988, pp. 641-656.
26. K. F. Nilsson, "On growth of crack fronts in the DCB test," *Composites Engineering*, Vol. 3, No. 6, 1993, pp. 527-546.
27. C. T. Sun and S. Zheng, "Delamination characteristics of double-cantilever beam and end-notched flexure composite specimens," *Composites Science & Technology*, Vol.56, 1996, pp. 451-459.
28. Z. Yang and C. T. Sun, "Interlaminar fracture toughness of multidirectional composites," to be published.

An Overview of Cure Monitoring in Composites Molding Process

Takehito Fukuda and Tatsuro Kosaka

*Department of Intelligent Materials Engineering, Osaka City University,
Sugimoto 3, Sumiyoshi, Osaka, 558-8585, Japan
takehito@mech.eng.osaka-cu.ac.jp: kosaka@mech.eng.osaka-cu.ac.jp*

SUMMARY:

The monitoring techniques in smart materials and structures have mainly two practical and commercial targets. One is the cure monitoring, which monitors the manufacturing process of thermosetting polymers and polymer matrix composites (PMCs), and another is the health monitoring, which monitors health condition of materials and structures. In the present paper, the former technique is focused and described from the viewpoint based on several kinds of sensors including optical fiber sensors, dielectric sensors, piezoelectric sensors and ultrasonic measurements.

KEYWORDS: Cure monitoring, Optical fiber sensor, Dielectric sensor, Piezoelectric sensor, Ultrasonic measurement

INTRODUCTION

Engineering plastics and PMCs have been widely used in consumer and leisure products as diverse as golf clubs, fishing rods, skis, tennis rackets. They have been also used in advanced engineering products such as airplanes, space structures and military ships. The molding process of thermosetting resins includes the curing process, in which liquid monomeric resin becomes a rigid solid by chemical cross-linking under proper conditions. Since the curing process of the thermosetting polymers governs mechanical properties and integrity of the final products, it is very important to determine optimum conditions of temperature and pressure in the molding process. These conditions have been obtained mainly by trial and error and thereby it makes the curing process inefficient. The inefficiency increases the manufacturing cost of PMCs. Therefore, the efficient (short time) and optimally controlled cure processing techniques of polymers and composites need to be introduced. The cure monitoring is performed to monitor chemical or mechanical properties in the curing process of thermosetting resin. The collected data from cure monitoring sensors can be used for estimation of the curing state and optimal control.

Cure monitoring technology has an older history than smart materials and structures technology. The traditional methods of cure monitoring are differential scanning calorimeter (DSC), dynamic mechanical analysis (DMA), infrared spectroscopy (IRS) and dielectric measurement. DSC and DMA cannot be used in the molding of real products. DSC method measures the heat of calorific reaction in the curing process. The degree of cure (DOC) of the resin is generally defined as a ratio of heat from the beginning to total heat of the curing reaction. The thermo-chemical for prediction of DOC was presented by Springer and Loos [1]. They also proposed resin flow model to predict the behavior of resin flow in the curing process of laminates. DMA is the technique measuring variation of mechanical

viscosity of the resin at various temperatures. The IRS can be used to measure variation of chemical constitution of resin. The changes in electrical properties of resin in the curing process can be measured using dielectric sensor. IRS with optical fibers and dielectric measurements with micro film-type sensors can be categorized in the technologies of smart materials and structures. In smart materials and structures, these indirect techniques are employed to develop analytical models and supplement data measured by smart sensors. Thermocouples and pressure sensors are also used to monitor the curing conditions, and the collected data are used for the feedback control.

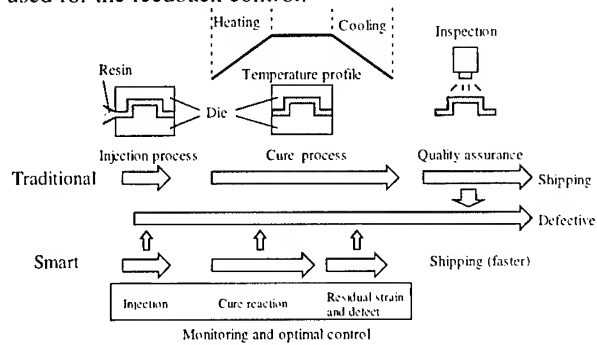


Fig.1 Comparison of traditional manufacturing process and smart manufacturing process

The traditional techniques of cure monitoring are in a sense effective. However, the “smart” manufacturing process, which is a more effective approach, has been proposed in recent twenty years. In the present paper, a manufacturing process is defined as the process including set-up process, curing process and quality inspection process. The smart manufacturing process monitors the state of products for the three processes (Fig.1). In the set-up process, resin flow in liquid molding or vacuum packaging in autoclave molding is monitored by *in situ* sensors. In the curing process, the *in situ* sensors monitor changes in chemical constitution, viscosity, elasticity, conductivity and temperature to know DOC. At the cooling stage in the curing process, residual stresses and imperfection in products are monitored to assure the quality of products because the residual stresses effect on the strength or durability of polymers and PMCs. The smart manufacturing process does not need quality inspection process after curing process because the quality is already assured at the end of curing process. This technique is cost-effective because the time of manufacturing process can be minimized. In this paper, cure monitoring techniques are focused, while the monitoring technique in the set-up process are also described in the following section.

Several kinds of micro sensors, optical fiber sensors, dielectric sensors, piezoelectric sensors and ultrasonic sensors, have been investigated to monitor the processing state in the manufacturing of polymers and PMCs. Some of the techniques use downsized sensors based on traditional sensing techniques like fiber optic spectroscopy and micro embeddable dielectric sensors, and some are new sensing techniques. In the following sections, smart manufacturing techniques with optical fiber sensors, dielectric sensors, piezoelectric sensors and ultrasonic sensors are described in detail with being classified by kinds of sensor elements.

OPTICAL FIBER SENSORS

Cure monitoring technique with optical fiber sensors is a most promising one, and has been developed in the last decade. The advantages of utilization of optical fiber sensors in cure monitoring are small size, high temperature resistance and capability of the embedding. In addition, embedded optical fiber sensors can be used in operation after implementation of

products. Most of optical cure-monitoring techniques are possible to be applied with optical fibers. In this section, four types of optical fiber sensors, spectroscopy-based sensor, fluorimetry-based sensor, refractive index-based sensor and strain/temperature sensor have been mainly addressed. Near-infrared spectroscopy (NIRS)-based sensor and fluorimetry-based sensor can be used for monitoring of chemical state of resin [2]. Refractive index-based sensor is utilized for measurement of optical properties of resin. Embedded temperature sensor monitors local temperature in polymers and PMCs. The measurement of residual strains in polymers and PMCs can be conducted by using embedded strain sensor.

Near-infrared spectroscopy-based sensor

NIRS-based sensing is based on the phenomena that the transmitted light in a sample is absorbed at some wavelength in a range of NIR due to resonance vibration with the molecules. In the curing process of thermosetting polymers, generation or disappear of molecule groups change behavior of the absorbency at the characteristic wavelength. Therefore, this sensor can measure directly the variation of chemical constitution. NIRS-based optical fiber sensor is an application of the technique

using optical fiber. The system has a white light source, a modified optical fiber and measuring device of optical spectrum. The wavelength used for cure monitoring is in a range of 1300-2300 nm wavelength (from visible light to NIR light). The optical fibers have peculiar transmission properties in wavelength domain as shown in Fig. 2 [3]. Silica fibers are very cheap and have good transmission properties in range from UV to NIR. Sapphire and fluoride fibers have better transmission properties than silica fibers. Since a silica fiber is cheapest, silica fibers have been widely employed for cure monitoring. Optical spectrum analyzing device has also range of measurable wavelength. For example, the range of general optical spectrum analyzer (typically visible to 1600 nm) is different from that of FT-IR (Fourier Transform Infrared Spectroscopy, The range is in IR). Since the targeted wavelengths for cure monitoring depend on the kind of polymer, it is important to know the properties of optical absorption in polymer to design appropriate measurement system. For instance, the cure monitoring of epoxy-amine resin system needs 1500-1700nm range, which includes absorption bands of epoxy groups, amine groups, C-H groups or O-H groups [4, 5].

The sensing part of optical fiber is fabricated so that a propagating light must be leaked from the core to transmit the light through the polymer region. Two types of the configuration are suggested [3-7]. One is a transmission type and another is an evanescent type. Transmission type sensor has a simple structure as shown in Fig. 3 (a). The two fibers are fixed with the bore metal capillary with the exposed side. When the sensor placed in liquid polymer, the gap is filled with it.

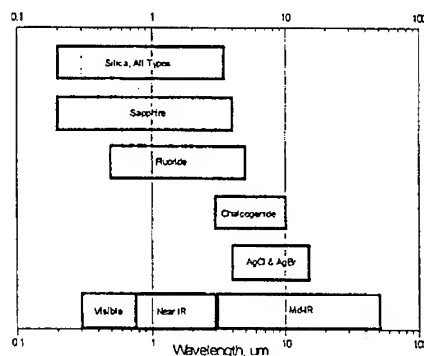


Fig.2 Transmission properties of optical fibers (J.M. Fildes et al. 1999, [3])

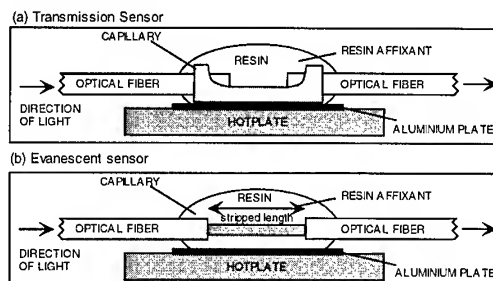


Fig.3 Schematic of spectroscopy-based sensor (C. Doyle et al. 1998 [6])

Then, the light propagates through the polymer in the gap. Evanescent type sensor consists of a fiber, which has the stripped cladding region as shown in Fig. 3 (b). An evanescent wave is a light transmitting in a clad of fiber. Therefore, the refractive index of fiber core must be larger than that of resin. In the stripped region of the evanescent type sensor, the evanescent wave transmits in the matrix resin instead of the silica clad of fiber. The representative experimental results are shown in Fig. 4. It shows that the absorption peak of epoxy is decreasing with progress of the cure reaction due to the cross-link in epoxy-amine resin system [6]. It is noted that the behavior of absorption peaks is sometimes complex due to the overlaps of peaks related to different molecules. To improve the difficulty of quantitative analysis of the spectra, a neural network analysis has been applied [3].

Fluorimetry-based sensor

Fluorimetry is one of optical spectroscopy-based techniques, and measures molecular (by ultraviolet (UV) light) or atom (by X-ray) composition of liquid, gas and solid. This technique is based on a photoluminescence phenomenon that visible light or UV light irradiates fluorescent materials. Fluorimetry-based optical fiber sensor uses this method for cure monitoring of resin, which is cured with a fluorescent curing agent [8-10]. When UV light is incident in the liquid resin mixed with fluorescent curing agent, the curing agent absorbs in the ultraviolet (up to 400nm) and emits in the short-wavelength visible region (400-600nm). Fluorimetry system has UV light source and two wavelength scanning filters for excitation light and emission light, and a photo detector. Emission spectra are scanned with fixed excitation wavelength to the absorption wavelength of fluorescent material, and excitation spectra are done with fixed emission wavelength, which has maximum emission intensity. In the curing process, the peak position of spectra shift and the intensity is changed due to the changes in the chemical structure of the fluorescent curing agent. The capability of quantitative measurement by peak shift of spectra is an advantage against NIRS-based sensor. The structures of sensors are similar to those used in NIRS-based sensors, that is, transmission type and evanescent type [8-10]. The utilization of sapphire optical fiber for evanescent type sensing has been reported [9]. The example of cure monitoring results with fluorimetry-based optical fiber sensor is shown in Fig. 5. The figure shows the peak shift of

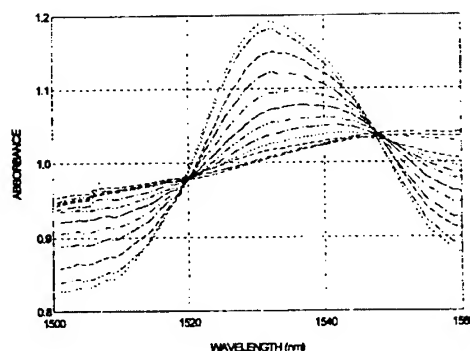


Fig.4 Overlaid optical fibre evanescent wave spectra obtained during cure of Epikote 828 + hexanediamine at 40°C (C. Doyle et al. 1998 [6])

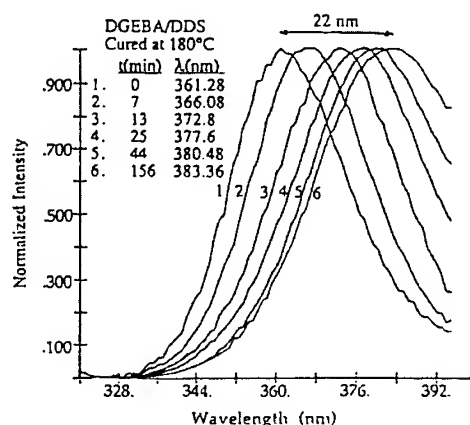


Fig. 5 Excitation spectra of DGEBA-DDS epoxy obtained *in-situ* at 180 °C as a function of cure time (Spectra plotted without regard to intensity) (H.J. Paik et al. 1994 [10])

excitation spectra in the curing process.

Refractive index-based sensor

Refractive index-based sensor measures changes in refractive index of the matrix resin from the intensity of light. There are two types of sensors, transmission type sensor and a reflection type sensor [5,6]. Transmission type sensor has a region where the clad of fiber is stripped. It is similar to evanescent type sensor used in NIRS-based sensor and fluorimetry-based sensor [4-6]. The transmission type sensor using polymer core fiber has been also proposed since the late 1980s [2].

The light propagates in the fiber core with reflecting at the boundary between fiber core and resin in the stripped region. Reflection type sensor monitors Fresnel reflection at the cut end of fiber, which contact with a matrix resin [5,6,11,12]. The intensity of reflected/transmitted light changes due to changes in reflection rate at the boundary between fiber core and resin. Since this type of sensor has a simple construction and does not require optical spectrum analyzing device, the cost is lower than spectroscopy-based monitoring method. However, it should be noted that the long-time stability of a laser output and a detector is very important for the stable and low S/N measurement. Figure 6 shows the experimental results measured by the refractive index-based sensor comparing with that by the evanescent type sensor during cure [6]. The figure shows that the curve of the refractive index-based sensor is proportional inversely to that of the transmission type sensor.

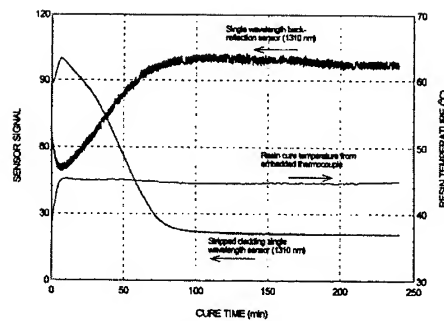


Fig. 6 Cure data obtained from reflection type and transmission type sensors during cure of Epikote 828 and hexanediamine at 45°C (C. Doyle et al. 1998 [6])

Optical fiber strain/temperature sensors

Optical fiber strain/temperature sensors can be utilized to measure the strain or temperature of optical fiber itself in manufacturing process as well as in operation. Polymers and PMCs molded to three-dimensional shape have complicated temperature distribution, and thick composite laminates have a large slop of temperature in curing process. Therefore, measurement of local temperatures in materials can improve quality of final products by controlling temperature condition. On the other hand, it is important that residual strains/stresses are certified to assure the quality because the unexpected residual strains cause defects of product and damages in operation such as warping, matrix cracks and delamination. Since residual strains are produced by inadequate cooling process, the complex interactions of matrix and reinforcement of PMCs and thermal anisotropy of plies of composite laminates, they should be monitored in cooling process. Here, applications of extrinsic Fabry-Perot interferometer (EFPI) sensor, fiber Bragg grating (FBG) sensor and interferometric sensors are described in brief. It should be noted that many types of strain/temperature sensors have capability of utilization for process monitoring.

EFPI sensor is constructed from two optical fibers, which are fixed with a capillary tube and have half mirrors at the ends of fibers as shown in Fig.7. The two mirrors compose a Fabry-Perot interferometer. There are two measurement systems for EFPI sensors. One uses narrow-band light and another uses broadband light. The former is cheaper and used at high-speed measurement, but affected by optical power loss in fiberoptic guide. The loss in optical fiber guide is a problem because high pressure is applied to PMCs in manufacturing

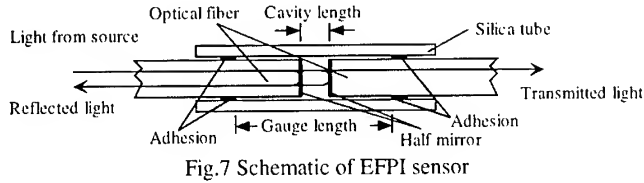


Fig.7 Schematic of EFPI sensor

process. The latter is independent on the optical power loss due to the capability of absolute measurement of cavity length [14]. Most of commercial EFPI strain sensors have low thermal sensitivity because the gauge length is about 20 times as long as the cavity length. The thermal sensitivity of the sensor can be maximized by bonding the capillary tube to the high CTE (Coefficient of Thermal Expansion) material such as aluminum for temperature measurement [13]. The evaluations of residual strains have been conducted [14,15].

FBG sensor has a longitudinal periodic variation of the refractive index in the core of the single mode fiber. The wavelength shift of the reflected light from the Bragg grating is proportional to the strain variation. This absolute measurement technique is affected by strain and temperature change. FBG sensor can be manufactured to be sensitive only to temperature by making a sensing part free from strains as shown in Fig. 8 [17]. Multi-functional sensor with combination of FBG temperature sensor and NIRS-based sensor was proposed [18]. To evaluate real strains by FBG sensor in curing process, local temperature in sensor must be monitored due to the high-sensitivity to temperature. It was reported that FBG sensors embedded in CFRP and GFRP composites could detect the onset of vitrification of the resin during cure [16].



Fig.8 Cross section of embedded FBG temperature sensor (R.C. Foedinger et al. 1999 [17])

DIELECTRIC SENSORS

Dielectric sensor is used to obtain the dielectric parameters related to the viscosity of the polymers and PMCs in cure process. Dielectric measurement techniques of polymers have been investigated since 1960s. The study on the use for cure monitoring started at 1980s, and micro-dielectric sensors have been developed for the *in situ* monitoring of the cure process of polymers and PMCs [19]. This measurement technique is based on the method to measure the complex dielectric constant of dielectric materials. The real part ϵ' and the imaginary part ϵ'' are called a relative permittivity and a loss factor, respectively. The basic components of dielectric sensing are a voltage source and two electrodes. Micro dielectric sensor has an electrode pattern printed on a small and thin base plate [20]. When the sensor is covered with resin, it can be assumed that the sensor and the resin compose an equivalent RC electric circuit. Consequently, when a sinusoidal voltage is applied to the circuit, the sinusoidal current generates with a lag of phase angle δ . Then, the resin capacitance C , the resin resistance R and $\tan\delta$ can be obtained simply from the current output. The complex dielectric constant is represented by following simple form, $\epsilon' = C/C_0$ and $\epsilon'' = 1/R\omega C_0$, where C_0 is capacitance of a free space capacitor and ω is an angular frequency of a voltage source. The above relations indicate that the loss factor has dependency of the frequency. Loss factor is contributed by both dipole orientation and free charge migration. Hence, loss factor is expressed as a linear combination of contribution of dipole polarization $(\epsilon_r - \epsilon_0)(\epsilon\tau)/(1 + \omega^2\tau^2)$,

and contribution of free charge migration $\sigma/\omega\epsilon_0$. Here, ϵ_r is relaxed permittivity, ϵ_u is unrelaxed permittivity, ϵ_0 is permittivity in vacuum, τ is relaxation time and σ is ionic conductivity defined as $\sigma = \epsilon_0 G / C_0$. The contribution of dipole polarization is negligible when $\omega\tau \ll 1$ at the low frequency which is generally less than 1kHz [21] and then ionic conductivity can be calculated from the equation of $\sigma = \omega\epsilon_0\epsilon''$. The ionic conductivity is practically convenient to estimate the degree of cure or viscosity since it has the strong relation with the mobility of ions in

polymers. The resistance $1/\sigma$ is called an ion viscosity and the logarithmic value is used for the estimation. Figure 9 shows that the behavior of log ion viscosity of graphite/epoxy composite is qualitatively similar to that of mechanical viscosity up to gel point, but the difference increases after gel point [19]. A comparison of DOC from DSC and from dielectric measurement is shown in Fig.10. It is evident that the DOC from DSC is different from that obtained by dielectric measurement. The above theory and history are described in detail on the paper by Mijovic [19].

Several new systems, new sensors and new applications have been proposed for *in situ* cure monitoring by dielectric sensors in recent years. The comparative study among three types of commercial dielectric sensors and viscosity was conducted [22]. It was demonstrated that the dielectric sensors used for cure monitoring of polymer coating could monitor the degradation of the performance properties [23]. It implies the feasibility of the utilization of embedded dielectric sensors in both cure and use. Dielectric measurements at a high frequency range (kHz-MHz) have been carried out to monitor the dipole rotational mobility [21,29]. The new parameter was introduced for estimation of the degree of cure from the measured dielectric parameters, and the experimental data had good agreement with simulation by using an analytical model and DSC data under the various temperature profiles [20]. It was shown that the dielectric sensor could be applied to monitoring of the impregnation of liquid resin in resin

infusion molding [24] or in RTM molding (Fig. 11) [21,25]. Dielectric sensing technique was applied to process monitoring of SMC/BMC (Sheet Molding Compound / Bulk Molding Compound) industry involving cure monitoring, quality assurance / quality control [28].

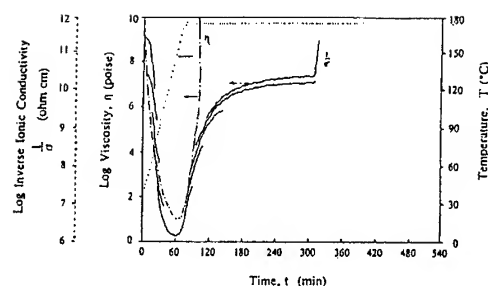


Fig. 9 Measured resistivity and viscosity as a function of time during cure of a graphite/epoxy composite (J. Mijovic et al. 1993 [19])

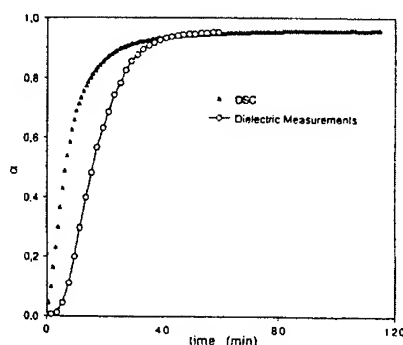


Fig. 10 A comparison of degree of cure from DSC and from dielectric measurements as a function of time during cure of an epoxy resin at 200°C (J. Mijovic et al. 1993 [19])

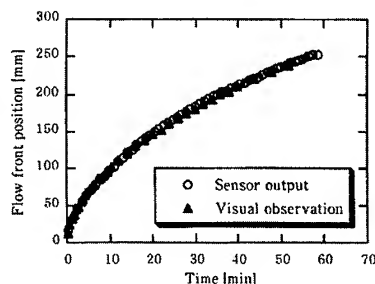


Fig.11 Flow-front position measured by long-gage dielectric sensor in the RTM molding process (S.Motogi, 1999 [25])

The new methods of prediction of DOC and process control with a dielectric sensor system by using artificial intelligence [26] or finite element analysis [27] were reported.

PIEZOELECTRIC SENSORS

Piezoelectric ceramics wafers have been employed as sensors/actuators for structural monitoring and control of structural vibration. The cure monitoring using a piezoelectric wafer actuator/sensor was referred by X. Wang et. al. in 1997 [32]. This is based on the measurement of electric resonance response of the piezoelectric wafer placed in the resin. The system composed of the piezoelectric wafer and resin can be modeled by a series of mass-spring-damper system, which is an equivalent electric circuit (Fig. 12) [30]. In curing process of resin, changes in the mechanical properties of shear modulus (spring) and viscosity (damper) affect an electric response of piezoelectric wafer. The measurement of electric response at a resonant frequency region is carried out to monitor changes in electric admittance at the resonant frequency and the anti-resonant frequency. The increase of modulus and viscosity of the resin reduces the amplitude of transfer function, which is the peak-to-peak value. The example of transfer functions of epoxy resin measured at different curing times is shown in Fig.13 [30]. The temperature influences on the capacitance of piezoelectric wafer, consequently, the magnitude of the transfer function. However, the peak-to-peak amplitude of the transfer function is more sensitive to changes in mechanical properties in liquid-state resin [31]. Therefore, the measurement before the gelation of resin is available. It is found that the resonance peak amplitudes of the transfer function of the piezoelectric wafer have a good relationship with viscosity of the resin before the gelation, while the resonance response is suppressed after the gelation of the resin. Thereby, this sensor can be used only as internal temperature sensor after the gelation. This technique has an advantage of usability of embedded piezoelectric ceramics in operation as well as in cure. Since the peak-to-peak amplitude of the transfer function changes with regard to the contact area with liquid, it can be used for detecting the injection of liquid resin in liquid molding manufacturing such as RTM [31].

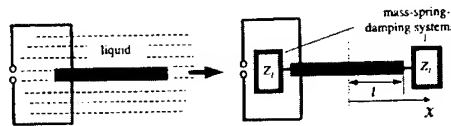


Fig.12 The simplified model of a piezoelectric wafer in a viscous liquid (X. Wang et al. 1998 [30])

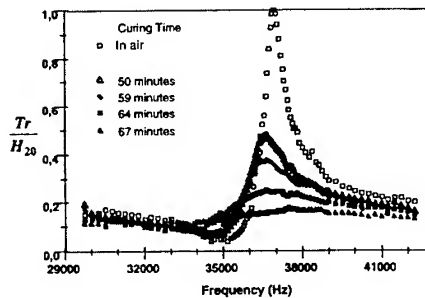


Fig.13 The transfer functions of the piezoelectric wafer embedded in epoxy at different curing times (X. Wang et al. 1998 [30])

ULTRASONIC MEASUREMENTS

The technique using an ultrasonic wave propagating in a material is a traditional non-destructive technique for measurement of the mechanical properties, and it can be also to detect of internal defects or damages in materials. The ultrasonic measurement has been applied to in-process health monitoring of polymer and PMCs since the late 1980s. The cure monitoring technique using ultrasonic is based on wave propagation analysis in viscoelastic and anisotropic materials [33]. The behavior of elastic waves propagation is affected by changes of modulus, density, and viscosity of the polymers and PMCs in the curing process.

In most cases, the size of reinforcements of composites is so small than the wavelength of propagating elastic waves that the composites can be treated as homogenous materials. There are two methods to propagate ultrasonic wave into a material in mold at curing stage. One locates ultrasonic transmitters and receivers in or on the mold, and thereby, this configuration has an advantage of unnecessary of internal sensors [34]. Another method uses an acoustic waveguide, which propagates an ultrasonic elastic wave [33,35]. The parameters of propagating wave such as wave velocity, attenuation and reflection factor can be used for the estimation of the DOC.

The sound velocity increases with an increase of the elastic modulus of resin from liquid to solid in the curing process, while the attenuation associated with viscoelastic relaxation and scattering factor decreases. Sound velocity is a convenient parameter to evaluate the degree of cure because the influence of molding pressure on the sound velocity is small. The example data of measurement of longitudinal sound velocity and relative attenuation in the cure of thermoset resin are shown in Fig. 14 [35].

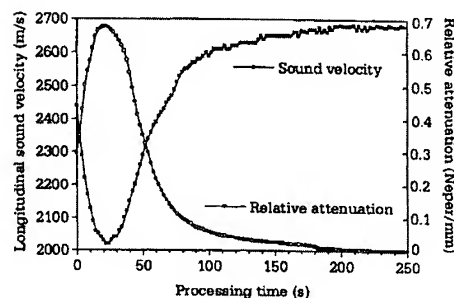


Fig.14 Longitudinal sound velocity and relative attenuation as a function of processing time. Phenolic-formaldehyde moulding compound PF31 (M. Rath et al. 2000 [35]).

CONCLUSION

In the present paper, recent studies of cure monitoring of thermosetting polymers and PMCs were reviewed. It is considered that the smart manufacturing technology can be applied to thermoplastic resin or other kinds of composites. However, this technology is just in laboratory study because the devices are expensive. For the practical use, it is necessary to develop cheap, simple and reliable devices. The cure monitoring technique promises to dramatically reduce the manufacturing cost for advanced composites.

REFERENCES

1. A.C. Loos and G.S. Springer, Curing of Epoxy Matrix Composites, *J. Compos. Mater.*, 17, 1983, pp.135-169
2. S.S.J. Roberts & R. Davidson, *Compos. Sci. Tech.*, 49, 1993, pp.265-276
3. J.M. Fildes, S.M. Milkovich, R. Altkorn, R. Haidle and J. Neatrou, *25th Int'l SAMPE Tech. Conf.*, 1993, pp.26-28
4. G.R. Powerll, P.A. Crosby, D.N. Waters, C.M. France, R.C. Spooncer and G.F. Fernando, *Smart Mater. Struct.*, 7, 1998, pp.557-568
5. P.A. Crosby, G.R. Powerll, G.F. Fernando, C.M. France, R.C. Spooncer and D.N. Waters, *Smart Mater. Struct.*, 5, 1996, pp.415-428
6. C. Doyle, A. Martin, T. Liu, M. Wu, S. Hayes, P.A. Crosby, G.R. Powerll, D. Books and G.F. Fernando, *Smart Mater. Struct.*, 7, 1998, pp.145-158
7. B.P. Rice, *38th Int'l SAMPE Symp.*, 1993, pp.1346-1356
8. D.L. Woerdenman and R.S. Parnas, *Plastics Engineering* 51(10), 1995, pp.25-27
9. A. Fuchs and N.H. Sung, *53rd Soc. Plast. Eng. Annu. Tech. Conf., ANTEC'95*, 1995, 2, 2437-2441
10. H.J. Paik and N.H. Sung, *Polymer Engineering and Science*, 34(12), 1994, pp.1025-1032
11. J.P.H. Steele, D. Mishra and C. Ganesh, Intelligent Process Monitoring for Carbon Fiber/Epoxy Composite Manufacturing, *Proc. of the ASME Materials Division*, 69(2),

- 1995, pp.899-909
12. Y.M Liu, C. Ganesh, J.P.H. Steele and J.E. Jones, *J. Compos. Mater.*, 31(1), 1997, pp.87-102
13. L. Lai, G. Carman, S.Chiou, P. Kukuchek and D. Echternach, *Smart Mater. Struct.*, 4, pp.118-125 (1995)
14. A.L. Kalamkarov, S.B. Fitzgerald, D.O. MacDonald, *Composites: Part B*, 30, 1999, pp.167-175
15. K.Osaka and T.Fukuda, *Proc.of 44th Int'l SAMPE Symp.* 1999, pp.1993-2004.
16. V.M. Murukeshan, P.Y. Chan, L.S. Ong, L.K. Seah, *Sensors and Actuators: A*, 79, 2000, pp.153-161
17. R.C. Foedinger, D.L. Rea, J.S. Sirkis, C.S. Baldwin and J.R. Troll, *Proc SPIE*, 3670, 1999, pp.289-301
18. P.A. Crosby, C.Doyle, C. Tuck, M. Singh and G.F. Fernando, *Proc SPIE*, 3670, 1999, pp.144-152
19. J. Mijovic, J.M. Kenny, A. Maffezzoli, A. Trivisano, F. Bellucci and L. Nicolais, *Compos. Sci. Tech.*, 49, 1993, pp.277-290
20. J.S. Kim and D.G. Lee, *J. Compos. Mater.*, 30(13), 1996, pp.1436-1457
21. D.E. Kranbuehl, P. Kingsley and S. Hart, *Polymer Composites*, 15(4), 1994, pp.299-305
22. M.B. Buczek and C.W. Lee, *Int'l SAMPE Symp.*, 40(1), 1995, pp.696-702
23. D. Kranbuehl, D. Hood, J. Rogozinski, A. Meyer and M. Neag, *Progress in Organic Coatings*, 35, 1999, pp.101-107
24. T. Krusche and W. Michaeli, *Int'l SAMPE Symp.* 41(2), 1996, pp.1542-1550
25. S. Motogi, T. Itoh, T. Fukuda, K. Yamagishi, S. Kitade and H. Morita. 12th Int'l Conf. *Compos. Mater.*, Paris, France, 1999, Pap1260 (PDF)
26. J.F. Maguire, M.A. Miller, S. Venketesan, *Engineering Applications of Artificial Intelligence*, 11, 1998, pp.605-618
27. J.S. Kim and D.G. Lee, *Sensors and Actuators B: Chemical*, 30(2), 1996, pp.159-164
28. D.D. Shepard, D.R. Day and K.J. Craven, *Journal of Reinforced Plastics and Composites*, 14, 1995, pp.297-308
29. D. Kranbuehl, D. Hood, Y. Wang, G. Boiteux, F. Stephan, C. Mathieu, G. Seytre, A. Loos and D. McRae, *Polymers for Advanced Technologies*, 8, 1997, pp.93-99
30. X. Wang, C. Ehlers, C. Kissinger, M. Neitzel, L. Ye and Y.W. Mai, *Smart Mater. Struct.*, 7, 1998, pp.113-120
31. X. Wang, C. Ehlers, C. Kissinger, M. Neitzel, L. Ye and Y.W. Mai, *Smart Mater. Struct.*, 7, 1998, pp.121-127
32. X. Wang, L. Ye and Y.W. Mai, *Journal of Intelligent Material Systems and Structures*, 8, 1997, pp.1073-1078
33. J.E. Eder and J.L. Rose, *Wave Propagation and Emerging Technologies*, ASME, 188, 1994, pp.179-186
34. N. Legros, C. -K. Jen and I. Ihara, *Ultrasonics*, 37(4), 1999, pp.291-297
35. M. Rath, J. Döring, W. Stark and G. Hinrichsen, *NDT & E International*, 33(2), 2000, pp.123-130

An Experimental/Analytical Correlation of the Micromechanical Elastic Response of a Unidirectional Composite Under Transverse Tension

David H. Mollenhauer

*Nonmetallic Materials Division, United States Air Force Research Laboratory
AFRL/MLBC, 2941 P St Rm 136
Wright-Patterson AFB, Ohio 45433-7750, USA
david.mollenhauer@afrl.af.mil*

SUMMARY: The elastic surface strain distribution of a model composite made from silicon carbide fibers and epoxy was quantified using moiré interferometry. The specimen had a cruciform geometry with two rows of fibers perpendicular to the loading direction. The fibers spanned the width of the specimen parallel to and in the center of the unloaded arms of the cruciform geometry. Moiré measurements were obtained at three load levels. A finite element model (FEM) of the specimen was constructed and analyzed. The experiment and modeling were repeated on a cruciform specimen without fibers. In all cases, comparison between the moiré and FEM strain distributions showed excellent agreement in both the distribution shape and the magnitude of obtained strain data. This agreement is important to establish the veracity of micromechanical calculations for structural graphite-resin composites, where the influence of the small fiber diameters (0.007 mm) may not be measurable with the moiré technique.

KEYWORDS: Model composite, interlaminar tension, moiré interferometry, silicon carbide fibers, cruciform specimen, finite element modeling

INTRODUCTION

In their 1974 work, Pagano and Rybicki [1] considered a variety of free edge problems for fiber-reinforced composite materials. They demonstrated that a significant difference existed in the predicted stress distributions at a free edge ply interface between micro-scale and macro-scale (effective modulus theory) modeling methods. In a recent paper [2] and an ongoing research effort, Pagano and Yuan revisit the free edge problem. Their main concern is the geometric scale necessary to properly model the free edge problem for a composite with complex macroscopic (ply-level) stress gradients. Their work is oriented toward establishing the proper methodologies for predicting damage in composite materials subject to complex loading.

In support of the work of Pagano, Yuan, and their associates, direct experimental validation of deformation predictions made using FE modeling was attempted. A free edge problem was considered for a composite laminate with two rows (layers) of fibers. The specimen was loaded in tension such that the load direction was transverse to the fibers. A cruciform specimen geometry, with the fiber rows running along the transverse specimen

arms, was chosen to avoid singular effects associated with the intersection of a fiber with the free edge by reducing the load delivered to the free edge regions.

Specifically, this work presents the results from two specimens examined experimentally and modeled numerically. Both specimens had a cruciform geometry. One specimen contained two rows of fibers perpendicular to the loading direction. The other specimen contained no fibers. This research focused on the use of the experimental displacement measuring technique known as moiré interferometry to obtain accurate deformation measurements on the surface of the cruciform geometry specimens. Moiré interferometry is an optical technique that yields full-field, high fidelity displacement information on the surface of a specimen. Further details concerning moiré interferometry can be obtained in Ref. 3. Results from the moiré interferometry testing were compared with numerical results obtained with FE modeling.

EXPERIMENTAL PROCEDURE

Two cruciform specimens were manufactured for this research. Scale drawings and dimensions of the specimens are shown in Figure 1. One specimen was manufactured entirely from Epon 828 epoxy resin. The other specimen contained two rows of SCS-6 silicon carbide fibers with a matrix of Epon 828 epoxy. The Young's modulus and Poisson's ratio of the matrix and fibers were $E_m=3.3$ GPa and $\nu_m=0.35$ and $E_f=375$ GPa and $\nu_f=0.22$, respectively. The fibers of the second specimen spanned the width of the specimen parallel to and approximately in the center of the unloaded arms of the cruciform geometry. Each row of fibers ideally consisted of 12 fibers perfectly distributed in a straight line through the specimen thickness. An error in specimen manufacturing resulted in 12 fibers in one row and 11 fibers in another. The distribution of fibers through the specimen thickness was also non-uniform. A cross-section of the specimen was obtained by sectioning the specimen with fibers after the moiré testing was completed. Figure 2 is a close-up of the central portion of the specimen cross-section showing the non-uniform fiber distribution. Note also that the average fiber row locations were not symmetrically placed with respect to the specimen centerline. The fibers had diameters of 0.14 mm, and the fiber rows were separated by approximately 0.9 mm.

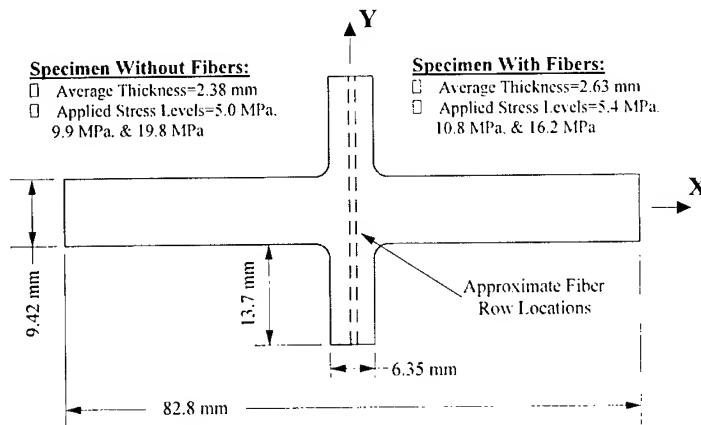


Fig. 1: Specimen geometry and loading levels.

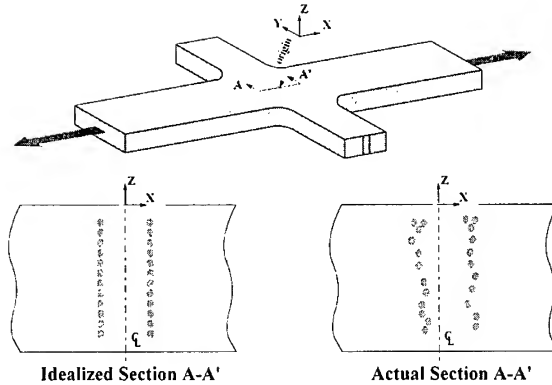


Fig. 2: Idealized and actual fiber distribution at the centerline of the specimen.

A 1200 line/mm crossed-line diffraction grating was applied to the gage section of each of the specimens. Each specimen was loaded in tension to three levels as shown in Figure 1. An interferometer of the type described in Ref. 4 was used to record fringe patterns for the components of x-displacement (U_x) and y-displacement (U_y) at the initial zero load and at each applied traction. After these data were gathered, U_x and U_y fringe patterns were obtained at zero load for both specimens as a check for inelastic deformation behavior. Because of the expected low level of displacement variation, a digital phase-shifting technique [5] was used to enhance the accuracy of the experimentally obtained displacement information. Displacement data was gathered for both specimens on a 2.4 mm by 1.8 mm rectangular area near the center of the cruciform geometry. A representative U_x fringe pattern from the specimen with fibers is shown in Figure 3. For enhanced visibility of the influence of the fiber rows, the fringe pattern contains a carrier of rotation (a rigid body rotation about the z-axis).

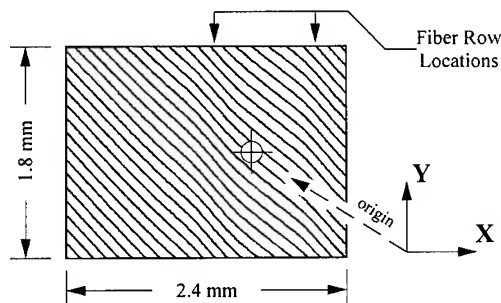


Fig. 3: U_x fringe pattern from the specimen containing fibers. The fringe pattern contains a carrier of rotation. The applied traction was 16.2 MPa.

The digital displacement data obtained from the moiré interferometry experiments were manipulated to produce in-plane strain distributions over the region of interest. These data consisted of matrices of more than 100,000 displacement values for each traction level and displacement component. The null-field data was first subtracted from each of the loaded data sets. As is typical of phase-shifted moiré data, each resulting displacement data set was smoothed to remove roughness so that numerical differentiation does not produce overly noisy results. The smoothing consisted of many passes (less than 50) of a central point

smoothing function. This method averages a data point with the eight surrounding values for each smoothing pass. It has been shown that this method is effective at local smoothing without producing significant over-smoothing error [6]. Strains were then obtained using a central difference numerical differentiation scheme. For comparison with numerical results, a strip 2.4 mm in the x-direction by 0.6 mm in the y-direction was cut from each strain data set. These strips were averaged in the y-direction to produce line plots of the variation of each strain component with respect to position in the x-direction.

NUMERICAL MODELING

Finite element models of the specimens examined experimentally were constructed and analyzed. Pre- and post-processing was accomplished with MSC/PATRAN and the analysis package ABAQUS was used to analyze the constructed FE models. Each specimen was represented using 8-node solid brick elements. A relatively coarse mesh was used for both models. The fibers were modeled using 2820 elements and the surrounding matrix was represented by 8446 elements for a total of 11266 elements. The density of elements was concentrated near the central portion of the cruciform geometry. The specimen without fibers had the same mesh as the specimen with fibers. Both models were assigned symmetry conditions on the x-z plane along the specimen centerline. Tensile load was introduced through symmetric end displacements of the loading arms of the cruciform geometry. Strain data was averaged (in the y-direction) from a 2.4 mm by 0.6 mm region to produce line plots for comparison with the moiré interferometry results. A more refined model of the fiber specimen with 67100 elements was analyzed to examine convergence of strain in the region of interest. Very little difference in the data was discernable between the refined and unrefined models.

These FE models represented the actual specimens as closely as possible. Three differences between reality and model are noteworthy. For the specimen with fibers, the fibers were assumed to be straight. This was not the case since the distribution of fibers at the ends of the cruciform arms were not the same as shown in Figure 2. Also, the fibers were modeled as a homogeneous isotropic material of constant 0.14 mm diameter. The carbon coating and carbon central core of SCS-6 fibers were not explicitly modeled, and the constancy of the diameter of the actual fibers was not verified. Finally, neither specimen had a constant thickness. The thickness variations in the actual specimen were only significant, although small, in the x-direction. An average thickness was assumed in the FE modeling.

RESULTS AND DISCUSSION

The strain distributions obtained through analysis were compared with those obtained with moiré interferometry. All strain data was divided by the far-field stress. Experimental data from only one load level for each specimen is presented in the following sections.

An experimental/analytical comparison of the distribution of ϵ_x at $y=0$ (the specimen centerline) along the x-axis from -1.6 mm to 0.8 mm from both specimens is plotted in Figure 4. The strain from the specimen without fibers is nearly constant with a gradual rise near the center. Moiré and numerical data match relatively closely, especially in the gradual trend. The magnitude of the moiré data is, however, lower than predicted by the FE model. In contrast, the strain distribution from the specimen containing the fibers shows marked variation across the region of interest. Two large peaks dominate the central section of the distribution. These peaks correspond precisely with the locations of the underlying fiber rows. The numerical and experimental data compare very well with the moiré data again being generally lower in magnitude than the prediction.

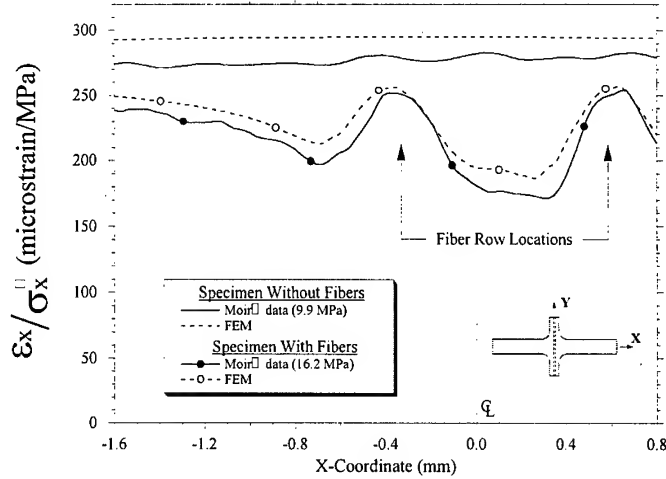


Fig. 4: Distribution of ϵ_x at $y=0$ measured with moiré interferometry and predicted by FE modeling for both specimens.

Figure 5 shows a similar comparison for ϵ_y . Note that the data scale is one half that presented for ϵ_x . In both cases, the experimental/analytical match is extremely close. The moiré data shows the gradual decrease in strain toward the center of the fiberless specimen predicted by the FE model. It also shows the more rapid increase in strain predicted by the FE model for the specimen containing fibers. A local effect of the fiber rows is apparent in the FE model. It is evident as a slight decrease in the strain in the locations of the underlying fiber rows. This trend is not present in the moiré data.

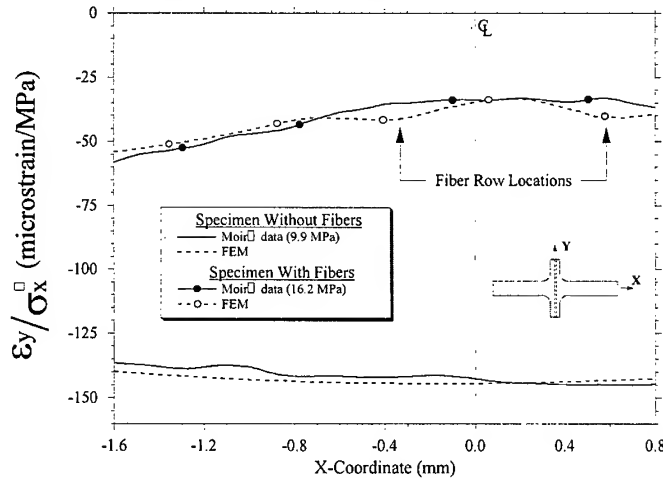


Fig. 5: Distribution of ϵ_y at $y=0$ measured with moiré interferometry and predicted by FE modeling for both specimens.

There are several possible sources for the differences in experimentally and numerically obtained strain distributions presented in this research. Inelastic behavior was considered to be a possible source of discrepancy. When the two sets of zero load moiré interferometry data were compared, no significant evidence of permanent deformation

behavior was found. Other sources of error include the model departures from reality previously identified, load-cell errors in the experimental procedure, and material property assignment errors in the FE modeling.

CONCLUDING REMARKS

In this work, it was demonstrated that finite element modeling accurately predicts the surface deformation behavior of a "multi-layer" composite on a scale of the order of a fiber diameter of 0.14 mm. This verification is a necessary component in developing methodologies for realistic failure prediction in composites in which a macroscopic (ply-level) complex stress gradient is present. Establishing modeling techniques that are effective at various scales is one piece of the puzzle in the determination of the proper scale(s) of observation necessary for the composite failure problem. It is important to note that in this work only the surface deformation predictions were validated. No serious attempt to examine model convergence in the vicinity of individual fibers was pursued. Future efforts must and will include such local convergence studies to properly address the development of realistic failure predictions.

ACKNOWLEDGMENTS

The author would like to thank the Metals and Ceramics Division of the Air Force Research Laboratory, Materials and Manufacturing Directorate for providing the test specimens. The advice and fruitful discussion provided by Dr. Nick Pagano and Dr. Vernon Bechel are greatly appreciated.

REFERENCES

1. N.J. Pagano and E.F. Rybicki, "On the Significance of Effective Modulus Solutions for Fibrous Composites," *J. of Composite Materials*, Vol. 8, 1974, pp. 214-228.
2. N.J. Pagano and F.G. Yuan, "Significance of Effective Modulus Theory (Homogenization) in Composite Laminate Mechanics," Submitted for publication in *J. of Composite Science and Technology*, 2000.
3. D. Post, B. Han, and P. Ifju, High Sensitivity Moiré: Experimental Analysis for Mechanics and Materials, Springer-Verlag Inc., New York, 1994.
4. D. Mollenhauer, P. Ifju, and B. Han, "A Compact, Robust, and Versatile Moiré Interferometer," *Optics and Lasers in Engineering*, Vol. 22, 1994, pp. 29-40.
5. G. Lassahn, P. Taylor, V. Deason, and J. Lassahn, "Multiphase Fringe Analysis with Unknown Phase Shifts," *Optical Engineering*, Vol. 33, No. 6, 1994, pp. 2039-44.
6. D. Mollenhauer, "A Comparison of Experimental and Analytical Strains in the Vicinity of a Hole," Project for Scientific Visual Analysis with Multimedia, Virginia Polytechnic Institute and State University, full project available for download at <ftp://ftp.sv.vt.edu/pub/projects95>, summary project available at <http://www.sv.vt.edu>, 1995.

Design

ELASTIC BUCKLING BEHAVIOR OF ORTHOTROPIC WEB PLATE WITH A LONGITUDINAL STIFFENER

S. J. Yoon¹, J. H. Jung², D. J. Ahn³

¹ Assistant Professor, Department of Civil Engineering, Hongik University
72-1, Sangsu-dong, Mapo-gu, Seoul, 121-791, KOREA

² Graduate Research Assistant, Department of Civil Engineering, Hongik University
72-1, Sangsu-dong, Mapo-gu, Seoul, 121-791, KOREA

³ Director, Dongshin Engineering, Co. Ltd.
181-1, Dongshin BD., Chamshil-dong, Songpa-gu, Seoul, 138-220, KOREA

SUMMARY: This paper presents the results of an elastic buckling analysis of orthotropic rectangular plate with a longitudinal stiffener under in-plane linearly distributed loads. The analytical solution for the longitudinally stiffened orthotropic web plate whose boundaries were assumed to be simply supported was derived in the previous work. In this study the edges of the web plate bounded by transverse stiffeners are assumed to be simply supported and other two edges are restrained against rotation and out-of-plane deflection by the flanges. The stiffener is modeled as a beam element and the torsional rigidity of stiffener is neglected. For the buckling analysis Rayleigh-Ritz method is employed. The upper limit of the buckling coefficient at various locations of stiffener is calculated by using the Lagrangian multiplier method. To verify the results obtained by using the ensuing equation, the orthotropic material properties are replaced with the isotropic ones and the results are compared with those in published document.

KEYWORDS: elastic buckling, orthotropic web plate, longitudinal stiffener, Rayleigh-Ritz method, Lagrangian multiplier method

INTRODUCTION

During the past few decades, many engineers have been investigating the behavior of fiber-reinforced plastic (FRP) structural members produced by the pultrusion process. As a result, pultruded beams and columns are increasingly being used in civil engineering field. The widespread applications of pultruded structural members demand the development of rational analysis method and design criteria. In order to establish the design criteria, there is an urgent need to understand the limit state of each pultruded structural members under various loading and boundary conditions.

A structural member focused in this paper is an orthotropic flexural member whose web is very slender. If the pure bending moment is applied to this member, the web local buckling may occur due to linearly distributed compressive loading. In order to prevent such a failure, a longitudinal stiffener can be located in the web. For the web plate, the edges bounded by

transverse stiffener, which are loaded edges, are usually assumed to be simply supported. Thus the limit condition depends on the boundary conditions of other two unloaded edges. If both unloaded edges are restrained by the flange, the lowest limit condition for the web buckling can be determined by assuming the unloaded edges of plate to be simply supported. Then the upper limit condition may be investigated by setting the unloaded edges of plate fixed. For the case of simply supported web plate the analytical solution was improved in the previous work [1].

In this paper, an analytical solution applicable to the buckling analysis of fiber-reinforced polymeric web plate with a longitudinal stiffener subjected to the in-plane linearly distributed loads is derived when the unloaded edges are fixed. For the equation of buckling analysis, the Rayleigh-Ritz method is employed. The upper limit of buckling strength of longitudinally stiffened web plate is evaluated by using the Lagrangian multiplier method.

THEORETICAL DERIVATIONS

Fig. 1 shows the longitudinally stiffened orthotropic plate under in-plane linearly distributed loads. It is assumed that the loaded edges are simply supported and the unloaded edges are fixed support. The stiffener, which is modeled as a beam element, is located at the distance y_0 from the edge under in-plane compressive forces and torsional rigidity of stiffener is assumed to be negligibly small.

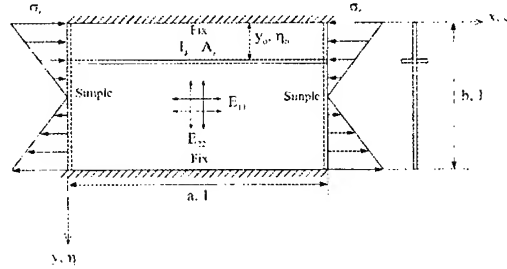


Fig. 1 Longitudinally stiffened orthotropic plate under in-plane linearly distributed loads

In Fig. 1 the in-plane linearly distributed loads can be expressed as [1]:

$$\sigma = \sigma_0(1 - c\eta) \quad (1)$$

In Eqn. 1, numerical factor c represents the distribution of in-plane loads. If $c=0$ then the uniform compression is applied, and if $c=2$ then the same magnitudes of triangularly distributed compressive and tensile stresses are applied.

Using the coordinate axes and nondimensionalized parameters $\xi (=x/a)$ and $\eta (=y/b)$ in Fig. 1, the deflection curve for buckled shape is chosen as [2]:

$$w = \sum_{m=1}^{\infty} \sum_{n=1}^{\infty} A_{mn} \sin m\pi\xi \left\{ \sin n\pi\eta + C_n\eta^3 + D_n\eta^2 + E_n\eta \right\} \quad (2)$$

In Eqn. 2, A_{mn} is the amplitude of deflection, and C_n , D_n , and E_n are defined as, respectively:

$$C_n = -n\pi \left\{ 1 + (-1)^n \right\} \quad D_n = n\pi \left\{ 2 + (-1)^n \right\} \quad E_n = -n\pi \quad (3 \text{ a,b,c})$$

Then the deflection curve of a longitudinal stiffener can be found by replacing η with $\eta_0 (y_0/b)$.

Since the longitudinal stiffener is modeled as a beam element, the buckled form of the system will be one of two types shown in Fig. 2.

In this paper two buckling equations are derived. One is derived by using the Rayleigh-Ritz method considering buckled shape in Fig. 2(a), which is a general case, and the other is developed for the special case in which the stiffener does not deflect when buckling occurs as shown in Fig. 2(b). In this case the buckling stress of plate is expected to reach its maximum value and for the derivation of equation the Lagrangian multiplier method is adopted [3, 4].

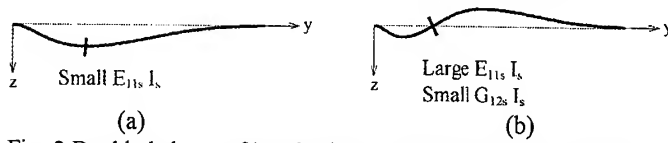


Fig. 2 Buckled shape of longitudinally stiffened plate in y-z plane

Buckling Strength of Longitudinally Stiffened Plate

Substituting the deflection curves into the basic energy equation of orthotropic plate [5], one can find the strain energy of bending of orthotropic plate (U_p), the strain energy of stiffener (U_s), and the work done for the plate (T_p) and the stiffener (T_s) by the applied forces. Then the total potential energy ($\Pi = U_p + U_s + T_p + T_s$) can be obtained as a function of buckling coefficient of orthotropic plate k_b , the plate aspect ratio ϕ , the flexural rigidity ratio γ , and the area ratio δ .

The buckling coefficient of orthotropic plate k_b is defined as [5]:

$$k_b = \frac{\sigma_0 t b^2}{\pi^2 \sqrt{D_{11} D_{22}}} \quad (4)$$

Therefore the buckling stress σ_{cr} can be calculated from the following equation:

$$\sigma_{cr} = k_b \frac{\pi^2 \sqrt{D_{11} D_{22}}}{b^2 t} = k_b \frac{\pi^2 \sqrt{E_{11} E_{22}}}{12(1 - \nu_{12} \nu_{21}) \left(\frac{b}{t}\right)^2} \quad (5)$$

According to the principle of stationary potential energy, the coefficients A_{mn} must be chosen to make the total potential energy being stationary. Using the Rayleigh-Ritz method, the minimization of total potential energy with respect to A_{mn} results in a set of simultaneous homogeneous linear equations represented by following equation:

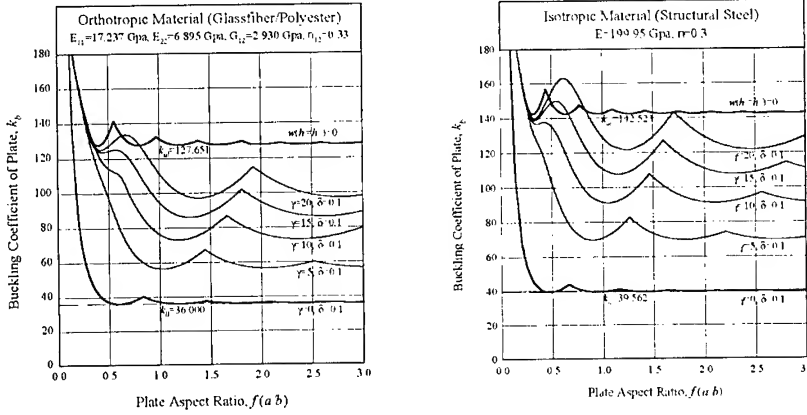
$$\begin{aligned} & A_{mn} \{Q_{mn} - k_b \phi^2 m^2 (a_n - c d_n)\} + \sum_{p=1}^{\infty} A_{mp} \{Q_{mnp} - k_b \phi^2 m^2 (a_{np} - c d_{np})\} \\ & + \left\{ \gamma m^4 - k_b \delta (1 - c \eta_0) \phi^2 m^2 \right\} \sum_{p=1}^{\infty} A_{mp} S_n S_p - c k_b \phi^2 m^2 \sum_{q=1}^{\infty} A_{mq} \frac{4nq}{(n^2 - q^2)^2} = 0 \end{aligned} \quad (6)$$

In Eqn. (6), $n+q$ are odd numbers, and all undefined variables are given in Appendix.

Since Eqn. (6) are homogeneous, the determinant of coefficient of A_{mn} must be vanished to get the solution other than the trivial one. In this study, the determinant is expanded up to ten terms, and it gives good approximation.

Using the numerical analysis technique such as the secant method, the buckling coefficient of plate k_b at each value of ϕ with a certain value of γ and δ is found, and the results are represented in a graphical form as shown in Fig.3. In order to verify the ensuing equation the

orthotropic material properties are replaced with isotropic ones, and the results are plotted in Fig. 3(b). The results obtained coincide with published ones [3].



(a) Orthotropic material [6]

(b) Isotropic material

Fig. 3 Buckling coefficient of longitudinally stiffened plate ($c=2$)

Limit Value of Buckling Strength of Longitudinally Stiffened Plate

So far it has been assumed that when buckling occurs the plate and longitudinal stiffener both deflect simultaneously as shown in Fig. 2(a). However if the stiffener has high flexural rigidity, it may happen that the plate buckles while the stiffener does not as shown in Fig. 2(b). When this happens, the junction of plate and stiffener behaves as a nodal line and the buckling stress of plate is expected to reach its maximum value.

In this case there is one more condition to be satisfied because the deflection at the junction of plate and stiffener is vanished. This additional condition can be expressed by:

$$\sum_{m=1}^{\infty} \sum_{n=1}^{\infty} A_{mn} S_n = 0 \quad (7)$$

In expression of the total potential energy, the strain energy of stiffener can be vanished since the stiffener does not deflect.

Using the same manner for more general case already mentioned in the previous section, the total potential energy of the system must be extremized by the amplitude A_{mn} , while A_{mn} is restricted to Eqn. (7). Employing the Lagrangian multiplier method [2, 3], following system of linear equations can be derived:

$$A_{mn} \{Q_{mn} - k_b \phi^2 m^2 (a_n - cd_n)\} + \sum_{p=1}^{\infty} A_{mp} \{Q_{mp} - k_b \phi^2 m^2 (a_{np} - cd_{np})\} - ck_b \phi^2 m^2 \sum_{q=1}^{\infty} A_{mq} \frac{4nq}{(n^2 - q^2)^2} + \lambda S_n = 0 \quad (8)$$

In this equation, λ is the Lagrangian multiplier which is the unknown factor and n, q are odd numbers.

Same as Eqn. (6), these simultaneous equations may be written in a matrix form and the determinant of coefficient matrix of constants A_{mn} and λ must be vanished in order to have a non-trivial solution. From this condition, the buckling coefficient of plate can be determined by using the same numerical technique mentioned above.

Using the ensuing equation, the maximum value of buckling coefficient of plate with a longitudinal stiffener with respect to the stiffener location is obtained when pure bending is applied ($c=2$) and the results are plotted with solid line in Fig. 4. This value indicates the upper limit of buckling coefficient of longitudinally stiffened plate because the unloaded edges are fixed support.

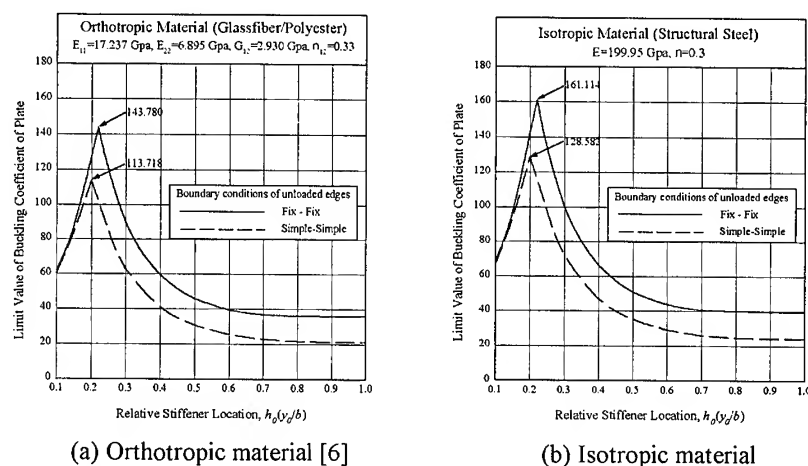


Fig. 4 Limit value of buckling coefficient of longitudinally stiffened plate ($c=2$)

In Fig. 4, dashed line represents the maximum buckling coefficient of plate when the unloaded edges are simply supported and this value indicates the lower limit of buckling coefficient of longitudinally stiffened plate because the unloaded edges can not restrain the rotation of plate at the edges.

In order to verify the ensuing equation the orthotropic material properties are replaced with isotropic ones and the results are plotted as shown in Fig. 4(b). Identical results in reference [2] are obtained.

DISCUSSIONS AND CONCLUSIONS

The analytical solution for the elastic buckling of orthotropic web plate with a longitudinal stiffener subjected to the linearly distributed compressive forces was derived. In this paper the loaded edges of the plate were assumed to be simply supported and the unloaded edges were assumed to be fixed support. Using the ensuing equation, the upper limit of buckling strength of longitudinally stiffened plate was suggested when the plate was subjected to the linearly distributed forces due to pure bending.

The maximum buckling strength of longitudinally stiffened plate of which the unloaded edges were fixed was evaluated when the stiffener was located at the distance $0.22b$ from the compression edge, while it was found for the simply supported plate when the stiffener was located at the distance $0.2b$ from the compression edge.

In practical case, the unloaded edges of web plate are elastically restrained by adjacent flanges. Therefore the elastic restraining effect between the plate components of flexural member on the web buckling needs to be further investigated.

REFERENCES

1. J. H. Jung, S. J. Yoon, and S. K. Cho, "Buckling strength of orthotropic rectangular plate with a longitudinal stiffener under in-plane linearly distributed loads", *Journal of Korean Society of Steel Construction, KSSC*, Vol.10, No.3, 1998, pp. 393-406.
2. K. C. Rokey and D. M. A. Leggett, "The buckling of a plate girder web under pure bending when reinforced by a single longitudinal stiffener", *Proceedings of Institution of Civil Engineers*, Vol.21, 1962, pp. 161-188.
3. S. P. Bulson, *The Stability of Flat Plates*, American Elsevier Publishing Company Inc., New York, 1969.
4. B. Budiansky and P. C. Hu, "The lagrangian multiplier method of finding upper and lower limits to critical stresses of clamped plates", *National Advisory Committee for Aeronautics*, Technical Note No.848, 1946.
5. S. G. Lekhnitskii, *Anisotropic Plates*, S. W. Tsai and T. Cheron (Trans.), Gordon and Breach, Second Printing, New York, 1984.
6. MMFG, *Extern Fiberglass Structural Shapes Design Manual*, Morrison Molded Fiberglass Company, Bristol, Virginia, 1989.

APPENDIX

$$\phi = \frac{a}{b}, \gamma = \frac{E_{11}I_s}{\sqrt{D_{11}D_{22}}b}, \delta = \frac{A_s}{bt}$$

$$a_n = \frac{1}{2} + a_{nn}, \quad b_n = \frac{1}{2} + b_{nn}, \quad c_n = \frac{1}{2} + c_{nn}$$

$$a_{np} = np\pi^2 \left\{ \frac{2}{15} - \frac{(-1)^n}{30} - \frac{(-1)^p}{30} + \frac{2(-1)^{n+p}}{15} \right\} - \frac{1}{\pi^2} \left\{ \frac{n}{p^3} + \frac{p}{n^3} \right\} \left\{ 4 + 2(-1)^n + 2(-1)^p + 4(-1)^{n+p} \right\}$$

$$b_{np} = \left\{ \frac{2}{15} - \frac{(-1)^n}{30} - \frac{(-1)^p}{30} + \frac{2(-1)^{n+p}}{15} \right\} - \frac{1}{\pi^2} \left\{ \frac{1}{p^2} + \frac{1}{n^2} \right\} \left\{ 4 + 2(-1)^n + 2(-1)^p + 4(-1)^{n+p} \right\}$$

$$c_{np} = -\frac{1}{np\pi^2} \left\{ 4 + 2(-1)^n + 2(-1)^p + 4(-1)^{n+p} \right\}$$

$$d_{np} = np\pi^2 \left\{ \frac{1}{280} - \frac{(-1)^n}{280} - \frac{(-1)^p}{280} + \frac{(-1)^{n+p}}{168} \right\} + \frac{1}{\pi^2} \left[\frac{n}{p^3} \left\{ 2 - 2(-1)^p - 6(-1)^{n+p} \right\} + \frac{p}{n^3} \left\{ 2 - 2(-1)^n - 6(-1)^{n+p} \right\} \right] - \frac{24}{\pi^2} \left[\frac{n}{p^5} \left\{ 1 + (-1)^n - (-1)^p - (-1)^{n+p} \right\} + \frac{p}{n^5} \left\{ 1 + (-1)^p - (-1)^n - (-1)^{n+p} \right\} \right]$$

$$S_n = \sin n\pi\eta_0 + C_n\eta_0^3 + D_n\eta_0^2 + E_n\eta_0$$

$$Q_{mn} = m^4 a_n \sqrt{\frac{E_{11}}{E_{22}}} + 2\nu_{21} \phi^2 m^2 n^2 b_n \sqrt{\frac{E_{11}}{E_{22}}} + \phi^4 n^4 c_n \sqrt{\frac{E_{22}}{E_{11}}} + 4\phi^2 m^2 n^2 b_n \frac{G_{12}(1 - \nu_{12}\nu_{21})}{\sqrt{E_{11}E_{22}}}$$

$$Q_{mnp} = m^4 a_{np} \sqrt{\frac{E_{11}}{E_{22}}} + 2\nu_{21} \phi^2 m^2 np b_{np} \sqrt{\frac{E_{11}}{E_{22}}} + \phi^4 n^2 p^2 c_{np} \sqrt{\frac{E_{22}}{E_{11}}} + 4\phi^2 m^2 np b_{np} \frac{G_{12}(1 - \nu_{12}\nu_{21})}{\sqrt{E_{11}E_{22}}}$$

STACKING SEQUENCE OPTIMIZATION FOR BUCKLING OF LAMINATED PLATES BY THE COMPLEX METHOD

Xilu Zhao¹ and Yoshihiro Narita²

¹ Fuji Technical Research Inc., 1-19-17 Tennocho, Hodogaya-ku, Yokohama 240, JAPAN:
zhao@olive.ocn.ne.jp

² Department of Mechanical Engineering, Hokkaido Institute of Technology, 7-15, Maeda, Teine-ku,
Sapporo 006-8585, JAPAN: narita@hit.ac.jp

SUMMARY: This paper proposes an optimal design method to maximize critical buckling loads of laminated composite plates. The buckling loads are calculated by a modified Ritz method for generally laminated plates with arbitrary boundary conditions. A complex method, one of the effective mathematical design approaches, is used to find the buckling loads that are maximized with respect to fiber orientation angles of the plate. Numerical examples demonstrate the effectiveness of the present combination of buckling analysis and optimal design method in determining the optimal stacking sequence of laminated plates.

INTRODUCTION

Due to the increasing demand for light-weight composite structures, buckling analysis of the composite plate elements currently constitutes one of important considerations in the composite structural design. Many research reports have appeared dealing with the buckling analysis and such previous efforts were summarized in a book [1] compiled by Turvey and Marshall.

Composite materials, particularly laminated fiber composites, are known as *tailored materials*, which imply that structural behavior can be optimized with respect to the fiber orientation angle and laminate thickness. From that point of view, a number of technical papers have been published to make use of such advantage for better buckling performance. Development of the optimal design application to composites is found in a recently published textbook [2]. The previous studies on plate buckling were however constrained to certain boundary condition and limited stacking sequence, and to the authors' best knowledge there are no approaches to make possible the comprehensive coverage that includes general boundary conditions and stacking conditions.

The authors' previous paper [3] demonstrated the effectiveness of combination of a modified Ritz method [4] and an optimization technique called a complex method [5]. In the present paper, our approach in the previous vibration optimization [3] is extended to the optimal buckling design of laminated composite plates. It is explained that the proposed Ritz method can accommodate arbitrary boundary conditions of rectangular plates. An application procedure of the complex method is then explained. Numerical results are presented for optimal solutions of laminated plates with different aspect ratios and boundary conditions.

ANALYTICAL MODEL AND METHOD

Figure 1 presents a rectangular plate having dimension of $a \times b \times h$ (thickness), and an origin of the coordinate system is located at the center of the plate. Constraints with respect to transverse deformation along the four edges are taken to be free, simply supported and clamped conditions. These conditions are denoted by F, S and

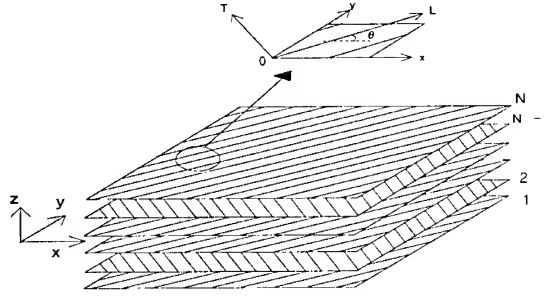


Fig.1 Laminated composite rectangular plate and coordinate system

C, respectively, and can be assumed independently along each of the edges. The overall boundary condition of the plate is written by the four capital letters, where the first letter is a condition along the edge of $x=-a/2$, the second is along $y=b/2$, the third is along $x=a/2$ and the fourth is along $y=b/2$. For example, the CSFF plate has the boundary condition of Clamped-Simply supported-Free-Free edges denoting edges in counter-clockwise direction from $x=-a/2$.

As shown in Fig.1, a laminated plate is composed of N number of unidirectional fibrous composite layers. The stress and strain relation is given in each layer by

$$\begin{Bmatrix} \sigma_L \\ \sigma_T \\ \tau_{LT} \end{Bmatrix} = \begin{bmatrix} Q_{11} & Q_{12} & 0 \\ Q_{12} & Q_{22} & 0 \\ 0 & 0 & Q_{66} \end{bmatrix} \begin{Bmatrix} \epsilon_L \\ \epsilon_T \\ \gamma_{LT} \end{Bmatrix} \quad (1)$$

where the matrix elements are given by

$$Q_{11} = \frac{E_L}{1 - \nu_{LT}\nu_{TL}}, \quad Q_{22} = \frac{E_T}{1 - \nu_{LT}\nu_{TL}}, \quad Q_{12} = \frac{\nu_{TL}E_L}{1 - \nu_{LT}\nu_{TL}}, \quad Q_{66} = G_{LT} \quad (2)$$

with E_L and E_T are moduli of longitudinal elasticity in the L and T directions, respectively, G_{LT} is a shear modulus and ν_{LT} is a Poisson's ratio. Relation (1) can be transferred to

$$\begin{Bmatrix} \sigma_x \\ \sigma_y \\ \tau_{xy} \end{Bmatrix} = \begin{bmatrix} \bar{Q}_{11} & \bar{Q}_{12} & \bar{Q}_{16} \\ \bar{Q}_{12} & \bar{Q}_{22} & \bar{Q}_{26} \\ \bar{Q}_{16} & \bar{Q}_{26} & \bar{Q}_{66} \end{bmatrix} \begin{Bmatrix} \epsilon_x \\ \epsilon_y \\ \gamma_{xy} \end{Bmatrix} \quad (3)$$

where the stresses and strains are given with respect to the x and y axes [6]. If one considers the linear buckling theory for a generally laminated thin plate, the strain energy is expressed by

$$U = \frac{1}{2} \iint_A \begin{Bmatrix} \epsilon \\ \kappa \end{Bmatrix}^T \begin{bmatrix} A & B \\ B & D \end{bmatrix} \begin{Bmatrix} \epsilon \\ \kappa \end{Bmatrix} dA \quad (4)$$

where

$$\{\epsilon\} = \left\{ \frac{\partial u_0}{\partial x}, \frac{\partial v_0}{\partial y}, \frac{\partial u_0}{\partial y} + \frac{\partial v_0}{\partial x} \right\}^T, \quad \{\kappa\} = \left\{ -\frac{\partial^2 w_0}{\partial x^2}, -\frac{\partial^2 w_0}{\partial y^2}, -2\frac{\partial^2 w_0}{\partial x \partial y} \right\}^T \quad (5)$$

and the sub-matrices are

$$[A] = \begin{bmatrix} A_{11} & A_{12} & A_{16} \\ A_{12} & A_{22} & A_{26} \\ A_{16} & A_{26} & A_{66} \end{bmatrix}, [B] = \begin{bmatrix} B_{11} & B_{12} & B_{16} \\ B_{12} & B_{22} & B_{26} \\ B_{16} & B_{26} & B_{66} \end{bmatrix}, [D] = \begin{bmatrix} D_{11} & D_{12} & D_{16} \\ D_{12} & D_{22} & D_{26} \\ D_{16} & D_{26} & D_{66} \end{bmatrix} \quad (6)$$

The u_0 and v_0 are the in-plane displacements of a point in the middle plane in the x and y directions, respectively, and w_0 is the out-of-plane displacement (deflection). The A_{ij} , B_{ij} and D_{ij} are the stretching, stretching-bending and bending stiffness, respectively, over the total thickness of the plate [6].

The potential energy due to the applied in-plane load is

$$W = \frac{1}{2} \iint_A \{Y\}^T \begin{bmatrix} N_x & N_{xy} \\ N_{xy} & N_y \end{bmatrix} \{Y\} dA \quad \text{with} \quad \{Y\} = \left\{ \frac{\partial w_0}{\partial x} \quad \frac{\partial w_0}{\partial y} \right\}^T \quad (7)$$

where N_x and N_y are normal loads applied along x and y axes, respectively, and N_{xy} is a set of shear loads along the four edges.

For the sake of simplicity, non-dimensional quantities are introduced as

$$\xi = \frac{x}{a}, \eta = \frac{y}{b} \quad (\text{non-dimensional coordinates}), \quad \alpha = \frac{a}{b} \quad (\text{aspect ratio}),$$

$$D_0 = \frac{E_T h^3}{12(1 - \nu_{LT} \nu_{TL})} \quad (\text{reference stiffness}), \quad d_{ij} = \frac{D_{ij}}{D_0} \quad (\text{non-dimensional stiffness}) \quad (8)$$

The next step in the Ritz method is to assume the displacements

$$u(\xi, \eta) = \sum_{i=0}^{M-1} \sum_{j=0}^{N-1} p_{ij} X_i(\xi) Y_j(\eta), \quad v(\xi, \eta) = \sum_{k=0}^{M-1} \sum_{l=0}^{N-1} q_{kl} X_k(\xi) Y_l(\eta), \quad w(\xi, \eta) = \sum_{m=0}^{M-1} \sum_{n=0}^{N-1} r_{mn} X_m(\xi) Y_n(\eta) \quad (9)$$

where p_{ij} , q_{kl} and r_{mn} are unknown coefficients and $X_i(\xi), \dots, Y_n(\eta)$ are the functions modified that any kinematical boundary conditions are satisfied at the edges [4]. After substituting Eqs.(9) into the energies (4) and (7), the stationary value is obtained by

$$\frac{\partial}{\partial p_{ij}} (U + W) = 0, \quad \frac{\partial}{\partial q_{kl}} (U + W) = 0, \quad \frac{\partial}{\partial r_{mn}} (U + W) = 0 \quad (\bar{i} = 0, 1, 2, \dots; \bar{j} = 0, 1, 2, \text{ and } \bar{n} = 0, 1, 2, \dots) \quad (10)$$

Then the eigenvalue equation that contains the buckling parameter λ is derived as

$$\begin{bmatrix} K_{ij\bar{j}} & K_{kl\bar{j}} & K_{mn\bar{j}} \\ K_{kl\bar{k}} & K_{mn\bar{k}} & \\ \text{sym} & K_{mn\bar{m}\bar{n}} & \end{bmatrix} - \lambda \begin{bmatrix} 0 & 0 & 0 \\ 0 & 0 & 0 \\ \text{sym} & L_{mn\bar{m}\bar{n}} & \end{bmatrix} \begin{bmatrix} p_{ij} \\ q_{kl} \\ r_{mn} \end{bmatrix} = 0 \quad (11)$$

where the first matrix is the stiffness matrix that contains the elements $K_{ij\bar{j}}, \dots, K_{mn\bar{m}\bar{n}}$ and the second matrix is the initial stress matrix that has $L_{mn\bar{m}\bar{n}}$. Equation (11) is a set of linear simultaneous equations in terms of the coefficients $\{p_{ij}, q_{kl}, r_{mn}\}$, and λ is the nondimensional buckling loads (eigenvalues) defined by

$$\lambda = - \left(\frac{a^2}{D_0} \right) N_x \quad (\text{buckling parameter for uniaxial, biaxial and compression-tension loads})$$

$$\lambda = -\left(\frac{a^2}{D_0}\right)N_{xy} \quad (\text{buckling parameter for shear load}) \quad (12)$$

The analytical procedure developed thus far is a standard routine of the Ritz method, and the modification is explained next so as to incorporate arbitrary edge conditions into the displacements. Unlike the traditional approach, the present approach introduces a kind of polynomials that include "boundary indices" [4] added to satisfy the kinematical boundary conditions. They are used in such a way as $B_i=0$ for F (free edge), 1 for S (simply supported edge) and 2 for C (clamped edge). To the CSFF plate, for instance, $B_1=2$, $B_2=1$ and $B_3=B_4=0$ are applied. With such boundary indices B_i 's, the method of Ritz can accommodate arbitrary sets of the boundary conditions.

OPTIMIZATION TECHNIQUE

The present design problem is formulated by imposing constraints on the design variables as $-90^\circ \leq \theta_i \leq 90^\circ$ (hereafter [°] is omitted) in the form

$$\text{Find } \bar{\theta} = [\theta_1, \theta_2, \dots, \theta_i, \dots, \theta_N]. \text{ To Maximize } \lambda = \lambda(\theta) \quad (13)$$

Subject to $(-90 \leq \theta_i \leq 90)$

where λ is the buckling parameter that represents the critical buckling load and N is a number of layers.

In the complex method [5], a "complex" is a set of K points in the N dimensional space ($K > N+1$) and geometrically these points form a kind of geometry whose vertices are given by the K point. In practically applying the complex method, an initial complex may be generated as

$$\theta_i^1 = 180(r_i^1 - 0.5), \theta_i^2 = 180(r_i^2 - 0.5), \dots, \theta_i^j = 180(r_i^j - 0.5) \text{ for } i=1, 2, \dots, N \quad (14)$$

where r_i^j 's are uniform random numbers given in the interval [0,1]. The superscript j ($j=1, 2, \dots, K$) attached to r_i and θ_i indicates the sequential number of vertex in the complex. It is sometimes useful to determine the initial complex by considering physical meaning of the problem.

In the subsequent optimization process, the following specific points are defined among the vertices θ^i ($j=1, 2, \dots, K$). The minimum point is defined as

$$f(\theta^h) = \min_j \{f(\theta^j)\} \quad (15)$$

which gives the lowest value of the object function. The next minimum point is

$$f(\theta^s) = \min_j \{f(\theta^j) \mid j \neq h\} \quad (16)$$

which has a smallest object function except for θ^h . The maximum point is given by

$$f(\theta^t) = \max_j \{f(\theta^j)\} \quad (17)$$

to yield the largest value among the vertices. The center θ^0 of a sub-complex, formed by subtracting the minimum point from the full complex, is given by

$$\theta^0 = \frac{1}{K-1} \left(\sum_{j=1}^K \theta^j - \theta^h \right) \quad (18)$$

in the subset of $(K-1)$ vertices. With these specific points thus defined, a reflection point θ^r with respect to the θ^0

$$\theta^r = (1.0 + \alpha)\theta^0 - \alpha\theta^h \quad (19)$$

is determined, where α is a coefficient of reflection used to accelerate the convergence and is given as $0 < \alpha < 2$ in the present case. Then the minimum point is replaced by the reduction point, and these steps are repeated until the solution satisfies the convergence criterion.

NUMERICAL RESULTS AND DISCUSSION

Numerical examples are presented for the conditions:

- (a) Constraint conditions are F: free, S: simple support and C: clamp, and their combinations are arbitrary along the four edges.
- (b) The material constants for the graphite/epoxy composite are [6]
 $E_1=138.0\text{Gpa}$, $E_2=8.96\text{Gpa}$, $G_{12}=7.10\text{Gpa}$, $\nu_{12}=0.30$
- (c) The laminated plate considered has eight layers and the fiber orientation angles are denoted by $[\theta_1/\theta_2/.../\theta_8]$ ($-90 \leq \theta \leq 90$). The number of design variables is therefore eight. The thickness of each layer is taken to be equal and is not used as a design variable.
- (d) A modified Ritz method explained above is employed by using 8x8 solutions to calculate the buckling parameters. The analysis is applicable to various loading patterns such uniaxial, biaxial, compression-tension, positive and negative shear loads, but the results for uniaxial compression are presented here.
- (e) The number of vertices used in the complex optimization process is chosen to be fourteen.

Table 1 presents the optimal solutions of fiber orientation angles and buckling parameters for eight-layered plates. These optimized values are obtained by the complex method where eight design variables $\theta_1, \theta_2, \dots, \theta_8$ are independently assumed. Ten different sets of boundary conditions are calculated in the examples that are denoted by four capital letters of F, S and C, and are listed in such order that the optimized buckling loads λ_{opt} become greater. The optimized fiber orientation angles $\theta_1, \theta_2, \dots$ and θ_8 are rounded to the integer and written in the brackets. Similarly, the optimal solutions are listed in Table 2 for the rectangular plate ($a/b=1.5$).

Variations of the fiber orientation angles are plotted for layer sequence of the CSFF, CCFF, CSFS and CCFS square plates in Fig.2, and it is seen that the optimized fiber angles are almost in the form of symmetric angle-ply sequence of $[(45/-45)_2]_s$. For comparison, the buckling parameters λ_{45} are presented for $[(45/-45)_2]_s$ plates in Table 1 and 2. The relative difference

$$(\text{Difference}) = (\lambda_{opt} - \lambda_{45}) / \lambda_{opt} \times 100 \quad (\%) \quad (20)$$

are also given in the tables. Comparison of λ_{opt} and λ_{45} indicates that the optimal fiber angles tend to be diagonally cross-ply $[(45/-45)_2]_s$, and the difference between λ_{opt} and λ_{45} gets smaller as the plates are more constrained along the edges. In fact, the values of λ_{opt} and λ_{45} are almost identical for the SCFC and CCFC plates with aspect ratio $a/b=1$ and 1.5.

CONCLUSIONS

A stacking sequence optimization is studied for maximizing the critical buckling loads of laminated plates with various boundary conditions. Analytical method and optimization technique using the complex method are summarized. In numerical examples, the optimal fiber angles of eight-layered plates are found to be nearly $[(45/-45)_2]_s$ as the plates are constrained more along the edges.

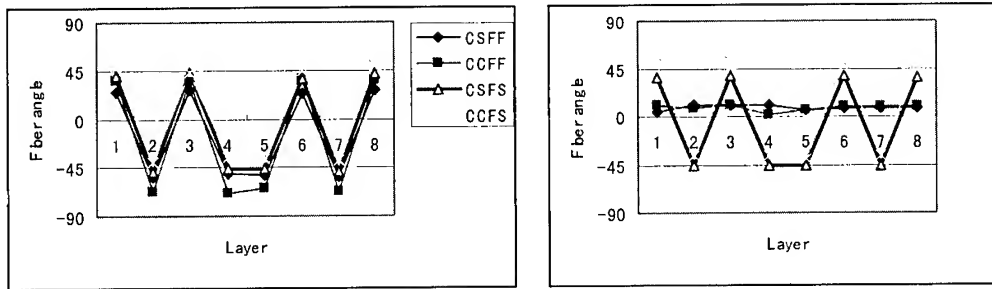
(a) Square plate ($a/b=1$)(b) Rectangular plate ($a/b=1.5$)

Fig.2 Variations of the optimal fiber orientation angles in the eight layers.

Table 1. Optimal solutions of eight-layered square plates with various boundary conditions and comparison with $[(45/-45)_2]_s$ plates ($a/b=1$).

Boundary	$[\theta_1/\theta_2/\theta_3/\theta_4/\theta_5/\theta_6/\theta_7/\theta_8]$	λ_{opt}	λ_{45}	D iff. (%)
CFFF	$[0/0/0/0/0/0/0/0]$	2.465	0.641	74.0
CSFF	$[25/-53/26/-51/-52/23/-54/26]$	3.892	3.117	19.9
SCFF	$[42/-51/45/-51/-52/44/-51/44]$	5.275	5.114	3.1
CCFF	$[36/-68/35/-69/-64/37/-68/35]$	5.521	5.120	7.3
SSFS	$[39/-49/47/-50/-49/42/-49/41]$	11.03	10.88	1.4
CSFS	$[40/-49/43/-46/-46/37/-49/41]$	11.04	10.89	1.4
SCFS	$[47/-41/49/-40/-40/48/-41/48]$	15.23	15.12	0.7
CCFS	$[49/-40/43/-36/-37/44/-39/49]$	15.36	15.22	0.9
SCFC	$[48/-43/44/-43/-42/46/-44/47]$	17.10	17.08	0.1
CCFC	$[46/-43/46/-42/-43/45/-43/46]$	17.17	17.16	0.1

Table 2. Optimal solutions of eight-layered rectangular plates with various boundary conditions and comparison with $[(45/-45)_2]_s$ plates ($a/b=1.5$).

Boundary	$[\theta_1/\theta_2/\theta_3/\theta_4/\theta_5/\theta_6/\theta_7/\theta_8]$	λ_{opt}	λ_{45}	D iff. (%)
CFFF	$[0/0/0/0/0/0/0/0]$	2.466	0.685	72.2
CSFF	$[4/10/10/10/6/8/7/8]$	2.831	1.820	35.7
SCFF	$[55/-55/53/-56/-57/53/-55/55]$	1.960	1.830	6.6
CCFF	$[10/8/10/2/6/9/9/9]$	3.016	2.435	19.3
SSFS	$[43/-50/44/-49/-52/43/-50/44]$	4.785	4.748	0.8
CSFS	$[36/-45/38/-45/-46/38/-45/36]$	5.072	4.956	2.3
SCFS	$[49/-37/52/-41/-41/53/-37/49]$	6.935	6.827	1.6
CCFS	$[50/-37/52/-36/-39/50/-36/51]$	6.955	6.829	1.8
SCFC	$[44/-43/48/-43/-43/46/-43/45]$	7.733	7.722	0.1
CCFC	$[47/-41/48/-43/-42/49/-41/47]$	7.786	7.776	0.1

OPTIMAL DESIGN FOR THE MAXIMUM FREQUENCY OF A RECTANGULAR PLATE WITH ADDITIONAL FRP SHEETS

Yoshihiro NARITA¹, Yoshiki OHTA² and Tomonori KAKUDATE³

¹ *Department of Mechanical Engineering, Hokkaido Institute of Technology, 7-15 Maeda,
Teine-ku, Sapporo 006-8585, JAPAN: narita@hit.ac.jp*

² *Department of Mechanical Engineering, Hokkaido Institute of Technology: ohta@hit.ac.jp*

³ *Graduate student, Hokkaido Institute of Technology: q99102@hit.ac.jp*

SUMMARY: This paper presents an analytical method to study vibration of an isotropic metal plate having some additional FRP reinforcement sheets. An extension of the method is also discussed to consider the optimal design of the plate. The analysis is based on a Ritz method that takes arbitrary boundary conditions into account. Numerical examples show that the approach provides very accurate natural frequencies and is applicable to optimization for the vibration behavior of plate-like components by adding FRP sheets with certain fiber orientation angle.

KEYWORDS: Optimal Design, Maximized Frequency, Rectangular Plate, Reinforcement, Bonded FRP Sheet, Stepped Thickness, Free Vibration,

INTRODUCTION

Recently, a technique has been developed to increase stiffness and strength additionally to already existing structures. This reinforcement is made possible by bonding the fiber reinforced plastic (FRP) sheets on the surface of structures [1]. This technique has been widely used because of its cost performance and easiness of the operation. Although this was utilized mainly to concrete structures in civil engineering, it is now equally applicable to metal structures.

Such reinforced plate-like structure can be considered as a plate with stepped thickness. Some papers were published dealing with vibration of isotropic plates with stepped thickness, e.g., in Ref. [2], but the literature on plates partly laminated by composite sheets has not been found because such applications were impractical in the past. Due to the newly developed technique mentioned above, however, the importance of analyzing vibration of plates partly laminated with FRP sheets has increased considerably.

Based on the technical demand, the present paper proposes a method of analysis to study vibration of such reinforced plate-like structure, i.e., a rectangular plate with additional unidirectional FRP sheets on the surface. A Ritz method is used to calculate natural frequencies of the plates with arbitrary boundary conditions. In numerical examples, the

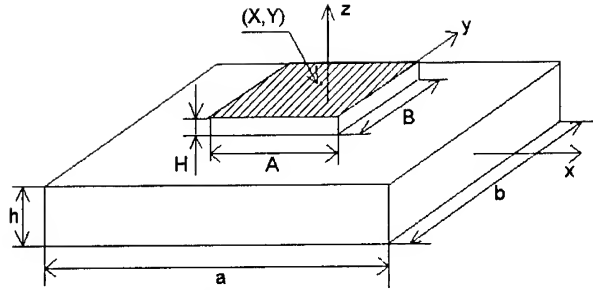


Figure 1. Rectangular isotropic plate having additional FRP sheets on both surfaces.

feasibility for optimization is considered to design the maximum fundamental frequency of the rectangular plate. The attached location and fiber orientation angle of the unidirectional sheets are design variables in the optimization. Numerical results clarify the effect of increasing the fundamental frequencies of the plate, and the feasibility is confirmed for optimizing the vibration behavior of the metal plate with use of additional FRP sheets.

ANALYTICAL METHOD

Figure 1 shows an isotropic rectangular plate, e.g., metal plate such as aluminum, that has a pair of unidirectional FRP sheets on both surfaces. A unidirectional FRP sheet shown on the upper surface in the figure is symmetrically attached at the same location on the bottom surface. The dimension of the base plate is given by $a \times b \times h$ (thickness) and that of an attached sheet is by $A \times B \times H$ (thickness). The origin of the global coordinates is located in the center of the base plate. The center location (X, Y) and the fiber orientation angle of the attached sheet is arbitrary on the plate.

Analytical method used here is a Ritz method, one of the energy approaches, that is chosen due to its wide applicability. By use of the classical plate theory, the strain energy for the plate system is given by

$$U = \frac{1}{2} \int_{vol} (\sigma_x \epsilon_x + \sigma_y \epsilon_y + \tau_{xy} \gamma_{xy}) dv + \frac{1}{2} \int_{FRP1} (\sigma_x \epsilon_x + \sigma_y \epsilon_y + \tau_{xy} \gamma_{xy}) dv + \frac{1}{2} \int_{FRP2} (\sigma_x \epsilon_x + \sigma_y \epsilon_y + \tau_{xy} \gamma_{xy}) dv \quad (1)$$

where the first term represents the energy of the base plate and the second and third terms do those of upper and lower additional sheets, respectively. The integral regions are then given by

$$\int_{vol} dv = \int_{-\frac{a}{2}}^{\frac{a}{2}} \int_{-\frac{b}{2}}^{\frac{b}{2}} \int_{-\frac{h}{2}}^{\frac{h}{2}} dx dy dz, \quad \int_{FRP1} dv = \int_{X-\frac{A}{2}}^{X+\frac{A}{2}} \int_{Y-\frac{B}{2}}^{Y+\frac{B}{2}} \int_{\frac{h}{2}}^{\frac{h}{2}+H} dx dy dz, \quad \int_{FRP2} dv = \int_{X-\frac{A}{2}}^{X+\frac{A}{2}} \int_{Y-\frac{B}{2}}^{Y+\frac{B}{2}} \int_{-\frac{h}{2}-H}^{-\frac{h}{2}} dx dy dz \quad (2)$$

The expressions above include the energy due to stretching motion. It is assumed here that two FRP sheets on both surfaces are symmetrically bonded, and therefore the bending motion can be uncoupled from the stretching motion in the present problem. This allows us to consider only the bending (out-of-plane) vibration that has lower frequency values. After integrating over the thickness, the strain energy due to bending is rewritten as

$$U = \frac{1}{2} \int_{A_{vol}} \{\kappa\} [D_{ij}] \{\kappa\}^T dA + \frac{1}{2} \int_{A_{FRP}} \{\kappa\} [D_{ijFRP}] \{\kappa\}^T dA \quad (3)$$

where $\{\kappa\}$ is a curvature vector and $[D_{ij}]$ and $[D_{ijFRP}]$ are stiffness matrices given by

$$\{\kappa\} = \left\{ -\frac{\partial^2 w}{\partial x^2} \quad -\frac{\partial^2 w}{\partial y^2} \quad -2\frac{\partial^2 w}{\partial x \partial y} \right\}$$

and

$$[D_{ij}] = \begin{bmatrix} D_{11} & D_{12} & 0 \\ D_{12} & D_{22} & 0 \\ 0 & 0 & D_{66} \end{bmatrix}, \quad [D_{ijFRP}] = 2 \begin{bmatrix} D_{11FRP} & D_{12FRP} & D_{16FRP} \\ D_{12FRP} & D_{22FRP} & D_{26FRP} \\ D_{16FRP} & D_{26FRP} & D_{66FRP} \end{bmatrix} \quad (4)$$

The stiffness matrix for the FRP sheet is doubled because of the symmetrically attached two sheets. The kinetic energy due to bending vibration is defined by

$$T = \frac{1}{2} \left(\int_{A_d} \rho_d \left(\frac{\partial w}{\partial t} \right)^2 dv + \int_{FRP1} \rho_{FRP1} \left(\frac{\partial w}{\partial t} \right)^2 dv + \int_{FRP2} \rho_{FRP2} \left(\frac{\partial w}{\partial t} \right)^2 dv \right) \quad (5)$$

and by assuming sinusoidal time variation $w = \sin t$, the maximum kinetic energy is obtained.

By using the nondimensional quantities

$$\xi = 2x/a, \quad \eta = 2y/b \quad (\text{nondimensional coordinates}), \quad \alpha = a/b \quad (\text{aspect ratio})$$

$$\delta_x = A/a, \quad \delta_y = B/b \quad (\text{sheet size ratio}), \quad \bar{h} = H/h \quad (\text{thickness ratio}),$$

$$\bar{\rho} = \rho_{FRP} / \rho_0 \quad (\text{mass ratio}), \quad d_{ij} = D_{ij} / D_0, \quad \bar{d}_{ij} = D_{ijFRP} / D_0 \quad (\text{stiffness ratio}), \quad (6)$$

$$\Omega = \omega a^2 (\rho_0 h / D_0)^{1/2} \quad (\text{frequency parameter}), \quad D_0 = E_0 h^3 / 12(1 - \nu_0^2) \quad (\text{reference stiffness})$$

with E_0 and ν_0 being Young's modulus and Poisson's ratio, respectively, of the base plate, the maximum strain and kinetic energies (3) and (5) are expressed by

$$U_{\max} = \frac{1}{2} \left(\frac{2}{a} \right)^4 D_0 \frac{ab}{4} \left(\int_{A_d} \{\kappa\} [d_{ij}] \{\kappa\}^T d\xi d\eta + \int_{A_{FRP}} \{\kappa\} [\bar{d}_{ij}] \{\kappa\}^T d\xi d\eta \right) \quad (7)$$

and

$$T_{\max} = \frac{1}{2} D_0 \frac{ab}{4} \left(\frac{2}{a} \right)^4 \frac{\Omega^2}{16} \left(\int_{A_d} w^2 dA + 2\bar{\rho} \bar{h} \int_{A_{FRP}} w^2 dA \right) \quad (8)$$

respectively, where

$$\{\kappa\} = \left\{ \frac{\partial^2 w}{\partial \xi^2} \quad \alpha^2 \frac{\partial^2 w}{\partial \eta^2} \quad 2\alpha \frac{\partial^2 w}{\partial \xi \partial \eta} \right\}, \quad [d_{ij}] = \begin{bmatrix} d_{11} & d_{12} & 0 \\ d_{12} & d_{22} & 0 \\ 0 & 0 & d_{66} \end{bmatrix}, \quad [\bar{d}_{ij}] = 2 \begin{bmatrix} \bar{d}_{11} & \bar{d}_{12} & \bar{d}_{16} \\ \bar{d}_{12} & \bar{d}_{22} & \bar{d}_{26} \\ \bar{d}_{16} & \bar{d}_{26} & \bar{d}_{66} \end{bmatrix} \quad (9)$$

The areas for the integrals are defined by

$$\int_{A_d} dA = \int_{-\frac{a}{2}}^{\frac{a}{2}} \int_{-\frac{b}{2}}^{\frac{b}{2}} dx dy = \int_{-1}^1 \int_{-1}^1 \frac{ab}{4} d\xi d\eta, \quad \int_{A_{FRP}} dA = \int_{\xi_1 - \frac{a}{2}}^{\xi_1 + \frac{a}{2}} \int_{\eta_1 - \frac{b}{2}}^{\eta_1 + \frac{b}{2}} \frac{ab}{4} dx dy = \int_{\xi_1 - \delta_x}^{\xi_1 + \delta_x} \int_{\eta_1 - \delta_y}^{\eta_1 + \delta_y} \frac{ab}{4} d\xi d\eta \quad (10)$$

where (ξ_1, η_1) is the center of the FRP sheet. The transverse amplitude is assumed by

$$w(\xi, \eta) = \sum_{m=0}^{\infty} \sum_{n=0}^{\infty} C_{mn} X_m(\xi) Y_n(\eta) \quad (11)$$

where C_{mn} are unknown coefficients, and the functions X_m and Y_n are

$$X_m(\xi) = \xi^m (\xi + 1)^{BC_1-1} (\xi - 1)^{BC_2-3} \quad Y_n(\eta) = \eta^n (\eta + 1)^{BC_3-2} (\eta - 1)^{BC_4-4} \quad (12)$$

where $BC_1 \sim BC_4$ are the boundary indices [3] which are added to satisfy the kinematical boundary conditions and are used in such a way as $BC_i=0$ for F (free edge), 1 for S (simply supported edge) and 2 for C (clamped edge). The integer i denotes edges ($i=1$ is an edge along $\xi=1$, 2 is along $\xi=-1$, 3 is along $\eta=1$ and 4 is along $\eta=-1$). To the CSFF plate, for instance, $BC_1=2$, $BC_2=1$ and $BC_3=BC_4=0$ are applied. With the boundary indices BC_i 's and Eqs.(12), the method of Ritz can accommodate arbitrary sets of the edge conditions.

After minimizing $F=T_{max}-U_{max}$ with respect to C_{mn} , one obtains the frequency equation

$$\begin{aligned} & \left[d_{11} I_{1,m\bar{m}n\bar{n}}^{(2200)} + \alpha^4 d_{12} I_{1,m\bar{m}n\bar{n}}^{(0022)} + 4\alpha^2 d_{66} I_{1,m\bar{m}n\bar{n}}^{(1111)} + \alpha^2 d_{12} (I_{1,m\bar{m}n\bar{n}}^{(0220)} + I_{1,m\bar{m}n\bar{n}}^{(2002)}) \right. \\ & + \bar{d}_{11} I_{2,m\bar{m}n\bar{n}}^{(2200)} + \alpha^4 \bar{d}_{12} I_{2,m\bar{m}n\bar{n}}^{(0022)} + 4\alpha^2 \bar{d}_{66} I_{2,m\bar{m}n\bar{n}}^{(1111)} + \alpha^2 \bar{d}_{12} (I_{2,m\bar{m}n\bar{n}}^{(0220)} + I_{2,m\bar{m}n\bar{n}}^{(2002)}) \\ & + 2\alpha \bar{d}_{16} (I_{2,m\bar{m}n\bar{n}}^{(1210)} + I_{2,m\bar{m}n\bar{n}}^{(2101)}) + 2\alpha^3 \bar{d}_{26} (I_{2,m\bar{m}n\bar{n}}^{(1012)} + I_{2,m\bar{m}n\bar{n}}^{(0121)}) \\ & \left. - \frac{\Omega^2}{16} (I_{1,m\bar{m}n\bar{n}}^{(0000)} + 2\bar{\rho}\bar{h} I_{2,m\bar{m}n\bar{n}}^{(0000)}) \right] \{C_{mn}\} = 0 \end{aligned} \quad (13)$$

where I 's are integrals defined by

$$I_{1,m\bar{m}n\bar{n}}^{(pqrs)} = \phi_{0,m\bar{m}}^{(pq)} \cdot \phi_{0,n\bar{n}}^{(rs)}, \quad I_{2,m\bar{m}n\bar{n}}^{(pqrs)} = \phi_{1,m\bar{m}}^{(pq)} \cdot \phi_{2,n\bar{n}}^{(rs)} \quad (14)$$

$$\begin{aligned} \phi_{0,m\bar{m}}^{(pq)} &= \int_{-1}^1 \frac{d^p X_m(\xi)}{d\xi^p} \frac{d^q X_{\bar{m}}(\xi)}{d\xi^q} d\xi, \quad \phi_{1,m\bar{m}}^{(pq)} = \int_{\xi_1-\delta}^{\xi_1+\delta} \frac{d^p X_m(\xi)}{d\xi^p} \frac{d^q X_{\bar{m}}(\xi)}{d\xi^q} d\xi, \\ \phi_{2,n\bar{n}}^{(rs)} &= \int_{\eta_1-\delta}^{\eta_1+\delta} \frac{d^r Y_n(\eta)}{d\eta^r} \frac{d^s Y_{\bar{n}}(\eta)}{d\eta^s} d\eta \end{aligned} \quad (15)$$

Equation (13) is a set of linear simultaneous equations in terms of the coefficients C_{mn} , and the eigenvalues Ω may be extracted by using existing computer subroutines.

NUMERICAL RESULTS AND DISCUSSIONS

Frequency parameters can be calculated by using Eq.(13), and accuracy of the solutions should be tested. The base isotropic plate is assumed to be aluminum and the material constants are taken to be $E_0=70.6$ GPa, $\nu=0.34$ and $\rho=2700$ kg/m³. The constants of a pair of attached sheets are those of Graphite/epoxy composite

G/E material: $E_L=138$ GPa, $E_T=8.96$ GPa, $G_{LT}=7.1$ GPa, $\nu_{LT}=0.30$ and $\rho=1600$ kg/m³

that result in $\bar{\rho} = \rho/\rho_0 = 0.6$.

Table 1 presents a convergence study for the frequency parameters Ω (lowest five modes) of aluminum square plate ($\alpha=1$) having a pair of square sheets ($\alpha=x=y=0.25$) located in the center ($X,Y)=(0,0)$. The thickness ratio \bar{h} is 0.1, and the fiber orientation angle in the sheet is $\theta=30^\circ$. The boundary condition of plate is simply supported along the entire edges. It is clearly seen that the frequencies monotonically decrease from above as the number of terms is increased in Eq.(11), and the fundamental frequency converges with the four significant figures when the terms $M=N=10$ in the series are taken. Based on the test results, the frequencies are calculated hereafter by using the $M \times N = 10 \times 10$ solutions.

Table 1. Convergence study of aluminum square plate with FRP sheets on both surfaces

$$(\alpha = 1, \delta_x = \delta_y = 0.5, (X, Y) = (0, 0), \bar{h} = 0.1, \bar{\rho} = 0.6)$$

	Ω_1	Ω_2	Ω_3	Ω_4	Ω_5
4	20.17	49.51	49.96	80.67	139.19
6	20.13	49.39	49.88	80.35	100.28
8	20.09	49.39	49.82	80.24	98.99
10	20.08	49.39	49.77	80.20	98.97
12	20.08	49.38	49.74	80.19	98.97

Table 2. Comparison of frequency parameters for stepped isotropic plate (isotropic base plate and attached same isotropic material sheets), $(\alpha = 1, \delta_x = \delta_y = 0.25, (X, Y) = (0, 0), \bar{h} = 0.1, \bar{\rho} = 1)$

	Ω_1	Ω_2	Ω_3	Ω_4	Ω_5	Ω_6
Present	20.59	49.90	83.16	105.0	106.7	131.6
Irie [2]	20.43	49.84	83.36	105.3	105.9	131.6

The solution accuracy is also validated by comparison of the present values with those of an isotropic stepped plate, i.e. a plate composed of base plate and attached sheet, both of the same isotropic material. Table 2 compares with solutions of Irie et al.[2] and the agreement is excellent for all the results compared. The validity of the analytical method is thus confirmed.

Figures 2-4 present frequency variations for the fundamental mode of square plate ($=1$) versus the fiber orientation angle of the attached FRP sheet ($\bar{h}=0.1$). Curves are given for different location (X, Y) of the attached sheet and it is observed how the fundamental frequencies are affected by the location and fiber orientation angle of the attached sheet.

Figure 2 shows the frequencies of the simply supported square plate (SSSS plate) with a pair of the square attached sheet ($x=y=0.5$). Among five different locations of the sheet, the fundamental frequency for the central sheet $(X, Y)=(0, 0)$ is highest for all and it is noted that the frequency value is not affected by the angle. In contrast, a plate with sheet on the corner $(X, Y)=(0.5, 0.5)$ gives lowest value showing a wave-like variation. The difference between the maximum and minimum values in the figure is less than 4 percent. Results for the same condition are presented in Fig.3, except that the sheet has a rectangular shape ($x=1, y=0.25$). As the long sheet is moved from bottom $(X, Y)=(0, -0.875)$ to the center $(0, 0)$, the maximum point of each curve shifts from $=42^\circ$ to 0 but again the difference is minor.

Figure 4 presents the frequencies of the cantilever square plate (CFFF plate) with the square attached sheet ($x=y=0.25$). Because the fundamental mode is a simple bending motion with no nodal line, the attached sheet with $=0$ adjacent to the clamped edge ($x=-1$), i.e. $(X, Y)=(-0.5, 0)$ and $(-0.5, -0.5)$, yields the maximum frequency. The case of sheets at the free end, $(X, Y)=(0.5, 0)$ and $(0.5, 0.5)$, give lowest identical results. The difference between the maximum and minimum values in the figure is more than 20 percent.

REFERENCES

1. Y. Iba, et al., *J. Jpn. Soc. Comp. Mat.* (in Japanese), Vol.25, 1999, pp.73-78.
2. T. Irie, G. Yamada and H. Ikai, *Int. J. Mech. Sci.*, Vol.22, 1980, pp.767-777.
3. Y. Narita, Y. Ohta, G. Yamada and Y. Kobayashi, *AIAA J.*, Vol.30, 1992, pp.790-796.

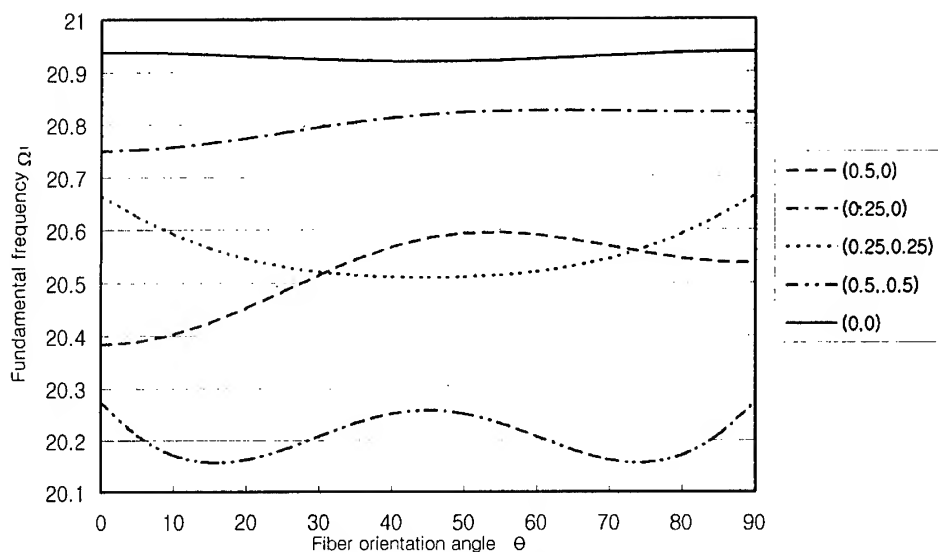


Figure 2. Variations of fundamental frequencies Ω_1 for the SSSS plate with square sheets.

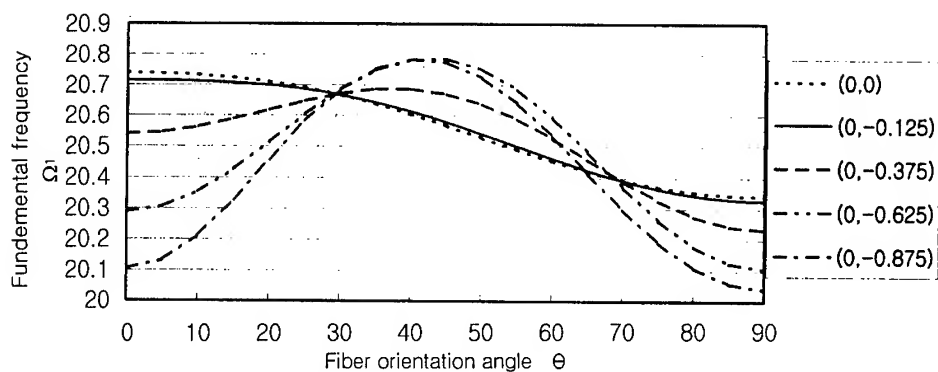


Figure 3. Variations of fundamental frequencies Ω_1 for the SSSS plate with rectangular long sheets

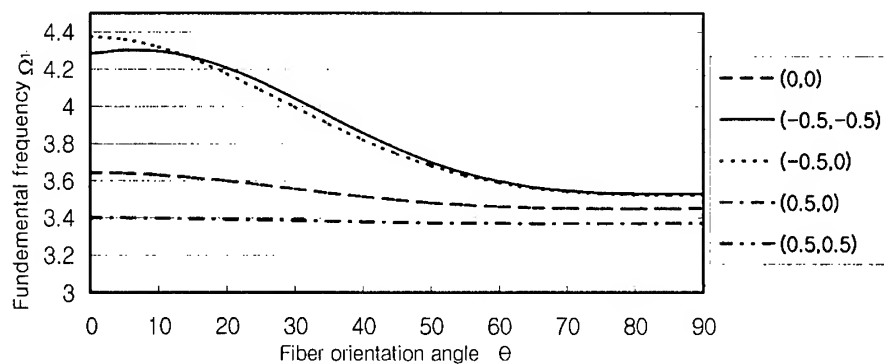


Figure 4. Variations of fundamental frequencies Ω_1 for the CFFF plate with square sheets

Optimal Design of Laminate Composites with Gradient Structure for Weight Reduction

Sung Ki Back¹, Tae Jin Kang¹ and Kyung Woo Lee²

¹*Department of Fiber and Polymer Science, Seoul National University*

San 56-1, Shinlim-dong, Kwanak-ku, Seoul, 151-742 Korea : Email: taekang@plaza.snu.ac.kr

²*Division of Fashion and Textiles, Dong-A University*

Hadan-2-Dong 840, Saha-gu, Pusan, 604-714 Korea : Email: kwlee@mail.donga.ac.kr

SUMMARY: In an effort to construct a structure under the design principle of minimal use of materials for maximum performances, a discrete gradient structure has been introduced in laminate composite systems. Using a sequential linear programming method, the gradient structure of composites to maximize the buckling load was optimized in terms of fiber volume fraction and thickness of each layer. Theoretical optimization results were then verified with experimental ones. The buckling load of laminate composite showed maximum value with the outmost [0°] layer concentrated by almost all the fibers when the ratio of length to width (aspect ratio) was less than 1.0. But when the aspect ratio was 2.0, the optimum was determined in a structure where the thickness and fiber volume fraction were well balanced in each layer. From the optimization of gradient structure, the optimal fiber volume fraction and thickness of each layer were proposed. Experimental results agreed well with the theoretical ones. Gradient structures have also shown an advantage in the weight reduction of composites compared with the conventional homogeneous structures.

KEYWORDS: laminate composites, gradient structure, weight reduction

INTRODUCTION

The desire to make new material and/or structures with better performance than current ones has continued from man's earliest days. Engineering design is a process for structuralization of required functions. There are two approaches to embodiment of new functions starting from a certain material. One is the direction of affording new intrinsic properties to the material itself, and the other is the direction of achieving new functions by way of new structuralization process and/or new method of structure control starting from common materials.

With increasing use of fiber-reinforced composites in various fields, especially in the weight sensitive fields such as aerospace industries, the concern about new structuralization of composites have been rapidly increased in recent years. This has not only accelerated the development of new material systems but also advanced the optimal design of composite materials. Recently many researches have been reported on the subject of structural optimization.

Schmit and Farshi[1,2] reported a method for the optimum design of laminated composite plates for minimum weight, subjected to multiple in-plane loading conditions.

A cracked fiber reinforced angle-ply laminate composites were analyzed using fracture mechanics by Wang and Karihaloo[3,4]. The solution of the formulated min{max}

optimization problem was obtained by the bound-formulation method and mathematical programming[5].

Riche et al.[6-7] used discrete ply angles as a design variable in the optimum design of composite laminates with respect to buckling load.

Todoroki et al.[8] proposed an object-oriented approach to optimize composite laminated plate stiffness with discrete ply angles.

Hu and Lin[9] investigated the buckling resistance of symmetrically laminated plates with a given material system and subjected them to uniaxial compression with respect to the fiber orientations by using a sequential linear programming method[10] together with a simple move-limit strategy.

Okamoto[11,12] put forward new concepts of engineering design. He proposed many promising designs, for example, inhomogeneous composites in cylindrical tube structures, functionally graded materials/structures, multi-functional composites, and intelligent composites which changed their own properties and/or grew and changed their shapes, adapting to their environment.

In the present investigation, the buckling optimization of laminate composites with different fiber volume fractions and thicknesses of each layer was performed using a sequential linear programming method, together with a simple move-limit strategy. The critical buckling loads of composites were calculated using the bifurcation buckling analysis, implemented in the ABAQUS[13] finite element program. And post-buckling analysis was followed on the basis of results of buckling optimization. Firstly, the calculation of the fiber volume fraction of each layer in given composite systems and optimization procedures are briefly reviewed. Then the associate optimal results are presented, together with the most useful conclusions obtained from this study.

ANALYSIS

Finite Element Analysis

The laminate plates were modeled using nine-node isoparametric laminate shell elements with six degrees of freedom for a node(three displacements and three rotations).

Model Geometry and Boundary Conditions

The buckling loads and post buckling strengths of the laminate composites subjected to a uniaxial compressive load N_x in the x direction per unit length applied at the top edge of the laminate composite in the x direction were analyzed. The aspect ratio had the values of 0.5 and 2.0, respectively. The total thickness of the composite was 2.4 mm. The fiber volume fraction of each layer was between 0% and 70%. We considered the boundary conditions that prevented out movements in the y and z directions, v and w, but allowed in-plane movement, u with no rotations on the top of the model. At the bottom, all displacements and rotations were prevented.

Determination of Buckling Load

A system of non-linear algebraic equations in the incremental form of finite element analysis is expressed as

$$[K_t]d\{u\} = d\{p\} \quad (1)$$

where $[K_t]$ is the tangent stiffness matrix, $d\{u\}$ is the incremental nodal displacement vector and $d\{p\}$ is the incremental nodal force vector. Within the range of elastic behavior, it is well known that when the deformation of a structure is small, the non-linear theory leads to the same critical load as the linear one. Consequently, if only the buckling load is to be determined, the calculation can be greatly simplified by assuming that the deformation is small. The linearized formulation gives a tangent stiffness matrix in the following expression:

$$[K_t] = [K_l] + [K_e] \quad (2)$$

where $[K_L]$ is a linear stiffness matrix and $[K_\sigma]$ is a stress stiffness matrix. If a stress stiffness matrix $[K_\sigma]_{ref}$ is generated according to a reference load $\{p\}_{ref}$, for another load level $\{p\}$,

$$\text{we have } \{p\} = \lambda \{p\}_{ref} \quad ; \quad [K_\sigma] = \lambda [K_\sigma]_{ref} \quad (3)$$

When buckling occurs, the external loads do not change, i.e. $d\{p\}=0$. Then the bifurcation solution for the linearized buckling problem may be determined from the following eigenvalue equation:

$$([K_L] + \lambda_{cr} [K_\sigma]_{ref}) d\{u\} = 0 \quad (4)$$

where λ_{cr} is an eigenvalue and $d\{u\}$ becomes the eigenvector defining the buckling mode. The critical load $\{p\}_{cr}$ can be obtained from $\{p\}_{cr} = \lambda_{cr} \{p\}_{ref}$.

EXPERIMENTS

A basic materials characterization of unidirectional lamina aims to establish their intrinsic elastic and strength properties to predict the buckling load and post buckling strength of laminated composites. Comparisons of theoretical buckling optimization results with experimental results were performed.

RESULTS AND DISCUSSTION

In this study, the objective of the optimization problem is to maximize the buckling load by optimizing the structure of composites. Based on the sequential linear programming method, for each iteration the current linearized optimization problem becomes:

Maximize

$$N_{xcr}(\underline{x}) \approx N_{xcr}(\underline{x}_0) + \nabla N_{xcr}(\underline{x}_0)^T \delta \underline{x} \quad (5)$$

subject to:

$$0 \leq x_k \leq 70 \quad \text{if } x_k \text{ is the fiber volume fraction of laminate composite} \quad (6)$$

$$0 \leq x_k \leq 1.0 \quad \text{if } x_k \text{ is the thickness ratio of each layer of laminate composite} \quad (7)$$

$$-r_k \times q \times 0.5^s \leq (x_k - x_{k0}) \leq r_k \times q \times 0.5^s \quad (8)$$

where N_{xcr} is the critical buckling load, \underline{x}_0 is a solution obtained in the previous iteration, and r_k and q are the size and the reduction rate of the move limit. The move limit should gradually approach zero as the iterative process of the sequential linear program method continues. In this study, the value of r_k was 35 for fiber volume fraction and 0.5 for thickness ratio of each layer. But these r_k values could be changed with respect to the types of the solutions in the sequential linear programming. And q was selected $0.9^{(N-1)}$, where N is a current iteration number.

In order to control the oscillation of the solution, a parameter 0.5^s is introduced to the move limit, where s is the number of sign change of the derivatives $\partial N_{xcr} / \partial x_k$ that has taken place before the current iteration. The value of s increases by 1 if the sign of $\partial N_{xcr} / \partial x_k$ changes. Whenever oscillation of the solution occurs, the range of the move limit is reduced to half of its current value, so this increases the solution convergent rate very rapidly. In above linearized optimization problem, the $\nabla N_{xcr}(\underline{x}_0)$ and $\delta \underline{x}$ can be expressed as follow:

$$\nabla N_{xcr}(\underline{x}_0) = \begin{Bmatrix} \partial N_{xcr}(\underline{x}_0) / \partial x_{10} \\ \partial N_{xcr}(\underline{x}_0) / \partial x_{20} \\ \vdots \\ \partial N_{xcr}(\underline{x}_0) / \partial x_{n0} \end{Bmatrix} \quad (9)$$

$$\delta \underline{x} = \begin{Bmatrix} x_1 - x_{10} \\ x_2 - x_{20} \\ \vdots \\ x_n - x_{n0} \end{Bmatrix} \quad (10)$$

The $\partial N_{scr}(\underline{x}_0) / \partial x_{k0}$ term in Equation (9) may be approximated by using a forward finite difference method with the following form:

$$\frac{\partial N_{scr}}{\partial x_{k0}} \approx \frac{[N_{scr}(x_{10}, x_{20}, \dots, x_{k0} + \Delta x_k, \dots, x_{n0}) - N_{scr}(\underline{x}_0)]}{\Delta x_k} \quad (11)$$

Hence, to determine the value of $\partial N_{scr} / \partial x_{k0}$ numerically, two bifurcation buckling analyses to compute $N_{scr}(\underline{x}_0)$ and $N_{scr}(x_{10}, x_{20}, \dots, x_{k0} + \Delta x_k, \dots, x_{n0})$ are needed in each iteration. In this study, the value of Δx_k was selected to be 0.01. Most optimization results were achieved within 16 iterations.

6-2. Aspect Ratio Effect on Buckling Behavior

In our investigation we chose the aspect ratios of laminate composites to be 0.5 and 2.0, respectively. That is because there are two ranges of the aspect ratio: for the aspect ratio below 1.0, the buckling loads of the angle ply laminate composites are almost less than those of the unidirectional composites; for the aspect ratio over 1.0, conversions appear between the unidirectional composites and the angle ply laminate composites. The aspect ratios of 0.5 and 2.0 were chosen to represent the two aspect ranges, respectively. In case of aspect ratio 0.5, the buckling loads of all laminate composites are less than that of the unidirectional composite. But in case of aspect ratio 2.0, the buckling loads of various laminated composites are surrounding that of the unidirectional composite. In case that the aspect ratio was larger than 1.0, the tendency of buckling behavior was almost similar to that for the aspect ratio of 2.0.

6-3. Optimized Structure of Laminate Composites

In our study, buckling load is also the objective function for laminate composites. When the total thickness and initial gross fiber volume fraction of laminate composites are determined, the fiber volume fraction of each layer can be calculated step by step from the outmost layer. And the thickness and fiber volume fraction of each layer were design variables to be optimized using the sequential linear programming method.

Buckling optimization was performed between 20% and 50% of the gross fiber volume fraction for every increment of 2.5%.

For the aspect ratios of 0.5, $[0]_4$, $[0/90]_s$, $[90/0]_s$ and $[0/90/0]_s$ composites were selected and for the aspect ratio of 2.0, $[0]_4$, $[0/90]_s$, $[90/0]_s$, $[0/90/0]_s$ and $[\pm 53/0/90]_s$ were selected. Especially, $[\pm 53/0/90]_s$ composite was selected because when $\theta = 53^\circ$, among the $[\pm 0/0/90]_s$ composites, the buckling load had the maximum value.

For the aspect ratios of 0.5, $[0]_4$, $[0/90]_s$ and $[0/90/0]_s$ composites were optimized when the fibers were reinforced to the maximum amount, up to about 70%, in the outer layer aligned in the 0° direction. For example, when the gross fiber volume fraction was 50%, $[0]_4$ composite with aspect ratio of 0.5 had the optimized structure where the thickness ratios of layer were 0.71, 0.29, respectively and fiber volume fractions of layer were about 70%, 0%, respectively. But in case of $[90/0]_s$ composites, the fiber of the lamina in the 0° direction was not reinforced maximally, but the layer of 0° direction was widely distributed. For the aspect ratio of 2.0, the optimal results are rather complex. $[0]_4$ composite showed an optimal structure similar to those for the aspect ratios of 0.5, for which the fibers were reinforced to the maximum amount for the outer layer. But the optimal structures of the $[0/90]_s$ and $[90/0]_s$ composites showed

that the fibers were optimally reinforced for each layer. The thickness ratio of each layer was not significantly different for all gross fiber volume fractions. In the case of $[0/90]_s$ composites, the thickness ratio of the outer layer was between 0.23 and 0.20 for all gross fiber volume fractions and in the case of $[90/0]_s$ composites, the thickness ratio of the outer layer was between 0.11 and 0.14 for all gross fiber volume fractions. The $[0/90/0]_s$ and $[\pm 53/0/90]_s$ composites showed the optimal structures where the thickness of each layer is similar to that of the $[0]_4$ composite, but fibers were reinforced to the maximum amount in the outer layer and to the minimum amount in the most inner layer. The thickness of each layer varied. For example, when the gross fiber volume fraction was 50%, the $[0/90/0]_s$ composite with the aspect ratio of 2.0 had the optimized structure when the thickness ratios of layers were 0.23, 0.48 and 0.29, and the fiber volume fractions were about 70%, 70% and 0%.

In the post buckling analysis, because the post buckling analysis was performed on the basis of buckling optimization results, most results fundamentally showed similar tendency to the result of buckling analysis.

6-4. Weight Reduction of Composites

To verify the weight save by composites with gradient structures in compared with the composites with conventional homogeneous composites, buckling loads and post buckling strengths of optimized composites in the range of gross fiber volume fraction between 20% and 50% and those of homogeneous composites in the range of gross fiber volume fraction of 20% and 70% were computed for every 2.5% increment of the gross fiber volume fraction. In the laminate composites with homogeneous structures, the $[0]_4$ composites showed the largest buckling load. As the gross fiber volume fraction increases, the optimal buckling load also increases for homogeneous composites as well as for the composites with optimal gradient structures. For example, for the aspect ratio of 0.5, when the gross fiber volume fraction of $[0]_4$ composites was 50%, the buckling load was about 125 kN for the homogeneous composite, but the same buckling load can be obtained with 30% of the gross fiber volume fraction by optimizing the structure.

For the $[0/90]_s$ and $[0/90/0]_s$ composites, the optimum structures were similar to that of the $[0]_4$ composites but the reduction of the fiber volume was much larger than that obtained by the $[0]_4$ composites. But for the aspect ratio 2.0, the $[90/0]_s$ composites showed the largest weight reduction effect. As a result, they showed 15-30% reduction of fiber volume fraction.

In the post buckling analysis, most results showed similar weight reductions to those for the buckling analysis.

CONCLUSIONS

Buckling optimization for laminate composites with gradient structure was performed under a uniaxial compressive loading condition with respect to the thickness and fiber volume fraction of each layer. Post-buckling analysis was also performed for the laminate composites. For verification purpose, experiments were performed and compared with predicted optimal structures. From this study, the following conclusions were made.

1. Analyses showed that the buckling load and post-buckling strength increase as the gross fiber volume fraction increases for both the gradient-structured and homogeneous composites.
2. Experiments were in good agreement with the optimization results obtained using the sequential linear programming method.
3. Optimization results of laminate composites were affected by the aspect ratio. For the aspect ratio of 0.5, the optimum was obtained when the volume of fiber was maximized in the out-most layer. However, for the aspect ratio of 2.0, the optimum needs balanced values between the thickness and fiber volume fraction in each layer. Especially, in cases

of $[0/90]_5$ and $[90/0]_5$ composites, in spite of the increase of the gross fiber volume fraction, the thickness ratio of the outer layer did not increase significantly and the fiber volume fraction of the inner layer increased as the gross fiber volume fraction increased.

4. Gradient structures also had an advantage over conventional homogeneous structures by saving fiber volumes in the composite systems. For the laminate composite with gradient structure the fiber volume was reduced by 15-30% and the weight of composite by 6-12% as compared to the conventional homogeneous composites.

REFERENCES

1. L. A. Schmit Jr. and B. Farshi, "Optimum Laminate Design for Strength and Stiffness", Int. J. Num. Meth. Engng., Vol. 7, 1973, pp. 519-536
2. L. A. Schmit Jr. and B. Farshi, "Optimum Design of Laminated Fiber Composite Plates", Int. J. Num. Meth. Engng., Vol. 11, 1977, pp. 623-630
3. J. Wang and B. L. Karihaloo, "Optimum in situ Strength Design of Composite Laminates. Part I: In situ Strength Parameters", J. Compos. Mater., Vol. 30, 1996, pp. 1314-1337
4. J. Wang and B. L. Karihaloo, "Optimum in situ Strength Design of Composite Laminates. Part II: Optimum Design", J. Compos. Mater., Vol. 30, 1996, pp. 1338-1357
5. N. Olhoff, "Multicriterion Structural Optimization via Bound formulation and Mathematical Programming", Struct. Optimiz., Vol. 1, 1989, pp. 11-17
6. R. L. Riche and R. T. Haftka, "Optimization of Laminate Stacking Sequence for Buckling Load Maximization by Genetic Algorithm", AIAA J., Vol. 31, No. 5, 1993, pp. 951-957
7. R. T. Haftka and J. L. Walsh, "Stacking Sequence Optimization for Buckling of laminated Plate by Integer Programming", AIAA J., Vol. 30, 1992, pp. 814-819
8. A. Todoroki et al., "Object-Oriented Approach to Optimize Composite Laminated Plate Stiffness with Discrete Ply Angles", J. Compos. Mater., Vol. 30, 1996, pp. 1020-1041
9. H. T. Hu and B. H. Lin, "Buckling Optimization of Symmetrically Laminated Plate with Various Geometries and End Conditions, Composites Science and Technology, Vol. 55, 1995, pp. 277-285
10. O. C. Zienkiewicz and J. S. Chubb, "Shape Optimization and Sequential Linear Programming, in Optimum Structural Design, Theory and Application", ed. R. H. Gallagher and O. C. Zienkiewicz, John Wiley, New York, 1973, pp. 109-126
11. H. Okamoto, "A Dialogue on Biomimetic Design for Natural Technology", Biomimetics, Vol. 2, 1994, pp. 1-13
12. H. Okamoto, "Biomimetic Fiber Reinforced Composites", Proc. 4th Japan International SAMPE Symposium, Sep. 25-28, 1995, pp. 627-632
13. ABAQUS, Hibbit, Karlsson & Sorenson Inc. 1080 Main Street, Providence, Rhode Island, USA

PROPERTY TAILORING OF CFRP LAMINATES BY INTERLEAVING

Toshio Tanimoto

*Department of Materials Science & Ceramic Technology
Shonan Institute of Technology
1-1-25 Tsujido-Nishikaigan, Fujisawa, Kanagawa 251-8511, Japan*

SUMMARY: The effect of interleaf layers incorporated between laminae on the mechanical properties of quasi-isotropic carbon/epoxy laminates was investigated. Two kinds of laminates, with and without interlayers, were compared in this study. Static and fatigue tests in tension were performed on both laminates. It is shown that introducing the interleaf layers remarkably improved the ultimate tensile load and tension fatigue resistance of the laminates. The interlayers delayed the onset of interlaminar delamination from the free edge and impeded the progression of interlaminar delamination until final failure. Discussion is made on how these interlayers work in enhancing the interlaminar toughness and thus improving the mechanical properties of $[0/\pm 45/90]_s$ carbon/epoxy laminates. In order to enhance the static load carrying capability without reducing elastic modulus, geometry of interleaf films to be incorporated at the flat surfaces of interlayers was investigated from the viewpoint of optimum interfacial properties. Discussion is also made on the optimum interleaf width in case the interleaf films were placed only in a limited local area near free edges, in order to tailor the interfacial properties and thus improve the fatigue resistance of quasi-isotropic carbon/epoxy laminates.

KEYWORDS: Interleaf layers, Tensile properties, Fatigue, Carbon/Epoxy laminate, Quasi-isotropic laminate, CFRP, Interfacial Properties, Delamination.

INTRODUCTION

Carbon fiber reinforced plastics (CFRP) have been widely used as a structural material. In general, fiber orientation angle of each lamina in these laminates is variously chosen in order to tailor a material which meets the particular requirement for the material properties in arbitrary direction of laminate. Quasi-isotropic lamination, in which the laminate consisted of laminae with fiber orientation of 0° , $+45^\circ$, -45° and 90° to loading axis, is most commonly employed in the actual application. However, quasi-isotropic carbon/epoxy laminates are known to develop the interlaminar stress concentrations near the free edge region. These laminates have a strong tendency to delaminate near the edges when subjected to axial in-plane loading as shown in Figure 1. This greatly reduces not only the static tensile properties of the laminate, but also the fatigue properties under cyclic loading. This has

prompted many studies for the improvement of the free-edge delamination resistance of laminates, and various solutions have been proposed for this purpose, namely toughening of the matrix [3], stitching [4,5], edge-cap reinforcement [6,7], notched edges [8], discrete critical ply [9], and interleaving [2,10-16]. Among these solutions, interleaving is a very simple technique to manufacture the laminate, and it gives high interlaminar toughness to the laminate. Delamination suppression concepts using interleaf films have demonstrated a good potential for significantly increasing both the static strength and the fatigue life of laminates susceptible to delaminations[2,12-16].

This paper summarizes the author's investigation which was performed to reduce the free edge interlaminar stresses in the laminate by incorporating interleaf films between plies and thus to improve the mechanical properties of these materials. In our previous work[2], we have shown that these laminates exhibit a high vibration damping capability. Loss factor values for these CFRP/interleaf laminates, which were measured in cantilever beam tests, are 5 to 50 times as large as that for conventional CFRP. In this paper, discussion is provided on the mechanical properties of the interleaved quasi-isotropic carbon/epoxy laminate, $[0/\pm 45/90]_s$, with a special emphasis on the optimum design of interply locations to incorporate the interleaf films for the particular requirement such as static strength, elastic modulus, fatigue resistance and so on. In addition, the optimum interleaf width, in case the interleaf films are placed only in a limited local area near free edges, is investigated from the viewpoint of the fatigue resistance of quasi-isotropic carbon/epoxy laminates.

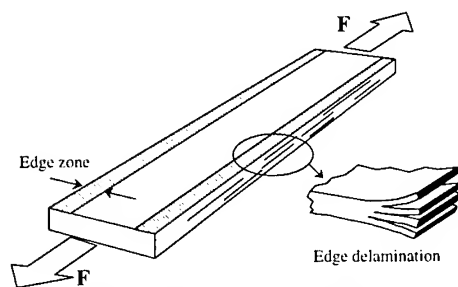


Fig.1: Free-edge delamination.

SPECIMEN PREPARATION AND EXPERIMENTAL METHOD

The specimens were fabricated from unidirectional carbon/epoxy prepreg sheet (T800/#2500, TORAY Industries, Inc.) and polyethylene based interleaf films. The interleaf films were approximately 70 μ m thick and were sandwiched between thermo-adhesive surface layers. CFRP laminates with interleaf films were produced using a vacuum bagging/autoclave curing technique. After cutting and lay-up of the required stacking sequence, the laminates were cured in an autoclave for three hours at 130°C. A postcure process was conducted for melting the thermo-adhesive surface layer of the interleaf film.

The various laminates with different interply locations were prepared for the present work. The Type I specimen is a conventional CFRP laminates with symmetric $[0/\pm 45/90]$ lay-up, which has no interleaf layer. Type II through Type IV were the CFRP laminates with interleaf films where the incorporation location of the interleaf is varied in each type. Type II has one interleaf film placed in its middle interlayer (90/90 interlayer). In Type III interleaf films were incorporated in every interlayer. Type IV has two interleaf films where the interleaf films were incorporated at $-45/90$ interlayer.

Type I₂ and Type IV₂ in Figure 2 show the quasi-isotropic carbon/epoxy laminates with sixteen layers. The number of layers is twice as large as above-mentioned specimen and lamination is double repetition for each angle layer. Subscript 2 signifies this type of laminates. The tension test was conducted at a speed of 0.5mm/min. Tension fatigue tests were performed by an electro-hydraulic fatigue testing machine at the frequency of 10Hz. Cyclic stress ratio, R, representing a ratio of minimum stress to maximum stress was fixed to 0.1 for the tension fatigue tests. The specimens were also prepared in which the interleaf films were placed only in a limited local area near the free edges. The ratio of interleaf width placed near the free edges to the specimen width (let it be called edge interleaf width ratio) were changed in the three different ways, 25%, 50% and 75% (see Figure 3).

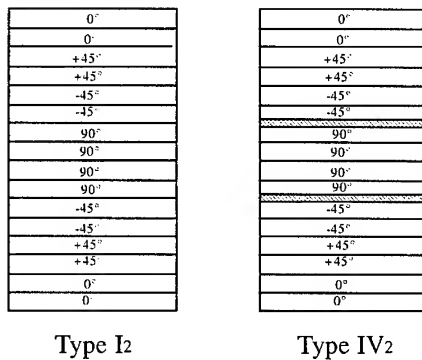


Fig.2 Stacking sequence for 16-ply CFRP/interleaf laminates.

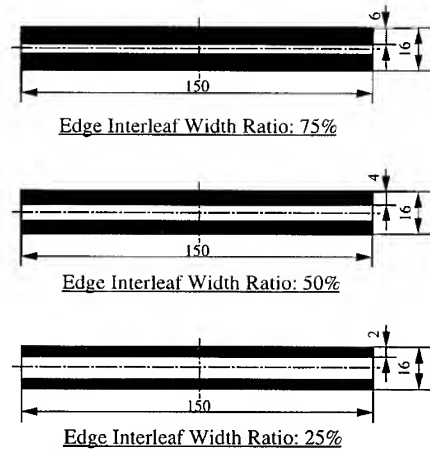


Fig.3 Geometry of interleaf film in each edge interleaf width ratio.

EXPERIMENTAL RESULTS AND DISCUSSION

Tensile Properties

Tensile test result is shown in Table 1 for the quasi-isotropic carbon/epoxy laminates with sixteen layers. The ultimate load (UL) value of Type IV₂ was 30.2 kN and is 15% larger UL value, in comparison with the conventional CFRP value, 26.3 kN. The coefficient of variation (CV), which is related to the tensile strength reliability, is also listed in Table 1. The CV value for CFRP/interleaf laminate, Type IV₂ is much lower than that for the laminate without interleaf layer, Type I₂. This result suggests that the CFRP/interleaf laminates have high reliability, in regard to the tensile strength.

Table 1 Tensile properties of CFRP/interleaf laminate with 16 layers.

	Ultimate load UL (kN)	Load ratio UL/UL(Type I)	Coefficient of variation Cv (%)
Type I ₂	26.3	1.00	4.0
Type IV ₂	30.2	1.15	0.6

The fracture mode for CFRP/interleaf laminates was found to be quite different from that for conventional CFRP. In conventional CFRP, the delaminations between -45° and 90° angle layers were generated at about 80% load of UL. The ultimate failure occurred in a catastrophic fashion with multiple longitudinal splits (broom straw effect). Ultrasonic C-scan inspection

and fracture appearance have shown that the fracture process is remarkably different in each laminate [12]. Dominant failure mode in CFRP/interleaf laminates depends strongly upon the location of interlayer, in which the interleaf films are incorporated. That means, the failure mode in CFRP laminate is changeable by choosing the most appropriate interplies to incorporate the interleaf films. Experimental results showed that interleaf film incorporated at the $-45/90$ interlayer can suppress the delamination damage in the CFRP laminate. On the other hand, an interleaf film is effective for suppressing the multiple splitting in the 0° angle layer, when it has been sandwiched between 0° and $+45^\circ$ layers [12].

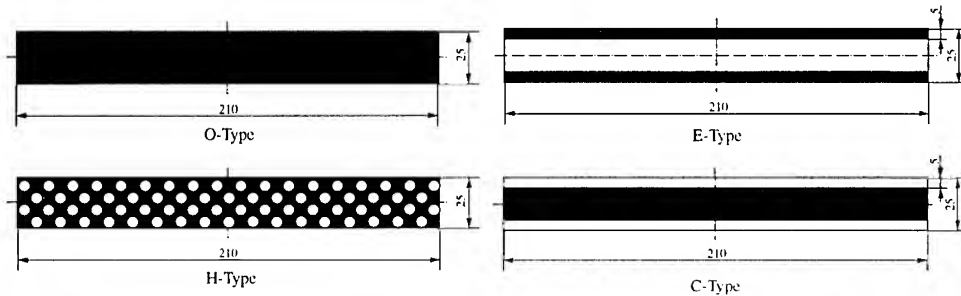


Fig.4 Geometry of Interleaf Film in Each Type.

According to our previous work [14], it was observed that increasing the number of interleaf films results in a decrease in tensile modulus. This fact may be an inherent demerit in this delamination-suppression method. In order to overcome this problem, authors attempted to change the geometry of interleaf film [14,16]. Geometry of interleaf films in flat tensile specimens was thus changed in the four different ways, as shown in Figure 4. In O-Type specimen, interleaf film was placed over the whole flat area of the specimen. Interleaf film of H-Type has open holes punched in equal distance. In E-Type, interleaf film was incorporated only in a very narrow area near the free edge. In C-Type, interleaf film was placed only in the central area of the specimen. Table 2 shows tensile test results for Type II specimen in case where the geometry of interleaf films is changed variously. Subscript for the type of specimen signifies the geometry of interleaf, as explained above. Type II_H and Type II_C has shown to decrease slightly the ultimate load values of the specimen, in comparison with conventional CFRP, Type I. However, improvement in tensile properties is observed in Type II_E. The elastic modulus is apparently improved by these local reinforcements. Particularly, Type II_E can enhance not only the static load carrying capability but also elastic modulus. This point is extremely important in practical application of this concept.

Table 2 Effect of Geometry of Interleaf Film on Tensile Properties.

specimen	Ultimate load (kN)	Elastic modulus (GPa)
Type I	24.7	53.8
Type II _E	25.9	57.0
Type II _H	23.2	55.4
Type II _C	22.6	55.1

Fatigue Properties

The interleaf films were placed not over the whole width of the specimen flat area, but only in a limited local area near the free edges. The edge interleaf width ratio, representing a ratio of

interleaf width placed near the free edges to the specimen width, were changed in the three different ways, 25%, 50% and 75% (see Figure 3).

Figure 5 shows comparisons of the tensile fatigue properties for Type II CFRP/interleaf laminates with different edge interleaf width ratios. As a result, the tensile fatigue strengths of Type II CFRP/interleaf laminates for edge interleaf width ratios of 25%, 50%, 70% and 100% were significantly higher in any cases than that of the conventional CFRP laminates without interleaf layers (edge interleaf width ratio of 0%). From the viewpoint of the fatigue resistance, the optimum edge interleaf width ratio in Type II CFRP/interleaf laminates was found to be 75%. The Type II CFRP/interleaf laminates can enhance not only the static load carrying capability but also the fatigue resistance under tensile fatigue, as a result of suppressing the onset and propagation of delamination damage.

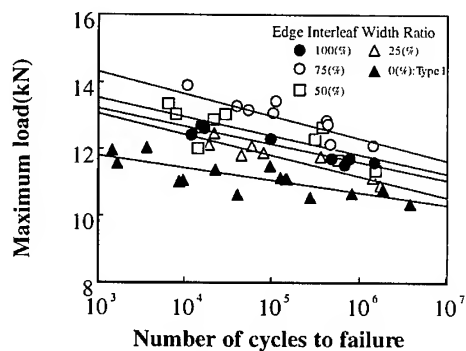


Fig. 5 Comparison of tensile fatigue properties for Type II CFRP/interleaf laminates with different edge interleaf width ratios.

Author's previous work [14] also indicated that visco-elastic properties of interleaf material affects significantly the fatigue fracture process in CFRP/interleaf laminate. When the CFRP/interleaf laminate is subjected to cyclic loading, ductility of interleaf material in service temperature, which reflects the glass transition temperature of the interleaf material will probably be a key in fatigue performance.

CONCLUDING REMARKS

Delamination-suppression concept by use of interleaf layers is concluded to have a good potential for significantly increasing both static strength and fatigue life of delamination-susceptible laminates. Optimum interleaf design such as determinations of adequate interlayers to be sandwiched and interleaf width near free edges, and probably selection of the most appropriate interleaf material with different glass transition temperatures corresponded to the actual application, is the most important key issues for a successful application of this concept.

REFERENCES

1. C. T. Sun and S. G. Zhou, Failure of quasi-isotropic composite laminates with free edges, *J. Reinforced Plast. Composites*, **7**, 515-557 (1988).
2. T. Tanimoto and T. Morii, Mechanical properties and fracture mechanism of quasi-isotropic carbon/epoxy laminates with different stacking sequence, *Proc. 3rd Japan SAMPE Symp. Exhibit.*, 368-373 (1993).
3. T. K. O'Brien, M. Rigamonti and C. Zanotti, Tension fatigue analysis and life prediction for composite laminates, *Int. J. Fatigue*, **11**, 379-393 (1989).
4. C. T. Sun, L. A. Minery and C. J. Jib, A study of stitching as a thickness-directional reinforcement in graphite/epoxy lamination, *ASTM STP 876*, 371-385 (1986).
5. W. S. Chan and E. Dan Jumbo, A comparison of the structural behavior of laminates made of knitted non-woven fabric and laminate made of conventional unidirectional tapes, *SAMPE J.*, **22**, (1986).
6. R. Y. Kim, Prevention of free-edge delamination, *Proc. 28th National SAMPE Symp.*, (1983).
7. W. E. Howard, T. Gossard Jr. and R. M. Jones, Reinforcement of composite laminate free-edges with U-shaped caps, *AIAA Paper No.86-0972*, (1986).
8. C. T. Sun and G. D. Chu, Reducing free edge effect on laminate strength by edge modification, *J. Compos. Mater.*, **25**, 142-161 (1991).
9. E. W. Y. Lee and W. S. Chan, Delamination arrestment by discretizing the critical ply in a laminate, *AIAA Paper No.89-1403*, (1989).
10. W. S. Chan, C. Rogers and S Aker, Improvement of edge delamination strength of composite laminates using adhesive layers, *ASTM STP 893*, 266-285 (1986).
11. P. A. Lagace, R. L. Mong and C. W. Kuhlmann, Suppression of delamination in a gradient stress field in graphite/epoxy laminates, *Proc. ICCM-9*, 705-713 (1993).
12. T. Tanimoto, J. Fujimoto, T. Tamura, K. Todome, M. Adachi, Y. Suzuki and K. Kauchi, Static and fatigue properties of CFRP/damping-material laminates, *AIAA Paper No.91-0931*, (1991).
13. T. Tanimoto, T. Morii, J. Fujimoto and T. Tamura, Improvement of mechanical properties of quasi-isotropic carbon/epoxy laminates by use of interleaf films, *Proc. ICCM-9*, 714-721 (1993).
14. T. Tanimoto, Suppression of interlaminar damage in carbon/epoxy laminates by use of interleaf layers, *Scripta Metallurgica et Materialia*, **31**, 1073-1078 (1994).
15. T. Tanimoto, Improving the fatigue resistance of carbon/epoxy laminates with dispersed-particle interlayers, *Acta Mater.*, Vol. 46, No.7, 2455-2460 (1998).
16. T. Tanimoto, Enhanced fatigue resistance in carbon/epoxy laminates by use of interleaf layers, *Proc. ICCM12*, Paper No. 1130 (1999).

THE EFFECT OF NEGLECTING THE LONGITUDINAL MOMENT TERMS IN ANALYZING $[90,0,90]_r$ TYPE LAMINATES WITH INCREASING ASPECT RATIO

DUK HYUN KIM¹, BONG KOO HAN², JI HYUN PARK³, DONG HEE LEE³

¹Korea Composites, 97 Gugidong, Chongrogu, Seoul, 110-011 Korea, E-mail :
Yamcha@chollian.net

²Professor, Seoul National University of Technology, Seoul, Korea, E-mail :
bkhan@duck.snut.ac.kr

³Graduate Student, Department of Structural Engineering, Do. E-mail :
superman@bularm.snut.ac.kr
and dbhue202@bularm.snut.ac.kr

SUMMARY: The most of the design engineers for construction has academic background of bachelors degree. Theories for advanced composite structures are too difficult for such engineers and some simple but accurate enough methods are necessary. The senior author has reported that some laminate orientations have decreasing values of D_{16} , B_{16} , D_{26} and B_{26} stiffnesses as the ply number increases. For such plates, the fiber orientations given above behave as special orthotropic plates and simple formulas developed by the senior author can be used [1,3]. Most of the bridge and building slabs on girders have large aspect ratios. For such cases further simplification is possible by neglecting the effect of the longitudinal moment terms(M_x) on the relevant partial differential equations of equilibrium. In this paper, the result of the study on the subject problem is presented.

KEYWORDS: simple method, influence of neglecting M_x , large aspect ratio, finite difference method, special orthotropic plate.

INTRODUCTION

The future of material industry will depend on if and when the conventional construction materials are replaced by advanced composite materials. If composite materials are used for construction, the quantity is huge : in tons, not in kilos or pounds. Composite materials can be used economically and efficiently in broad civil engineering applications when standards and processes for analysis, design, fabrication, construction and quality control are established.

The problem of deteriorating infrastructures is very serious all over the world. The U.S. Civil Engineering Research Foundation(CERF) report,"High-Performance Construction Material and System : An Essential Program for America and its Infrastructure," published in April, 1993, in collaboration with several organizations, cities, U.S. Department of Transportation figures as follows : A. 230,000 of the nations(U.S.A.) 575,000 bridges are structurally deficient or obsolete.

B. 143,000 of these bridges are more than 50 years old and unsuitable for current or projected traffic.

C. Traffic delays alone will cost the country 50 billion dollars per year in lost work time and fuel by the year 2005.

Steel girders become rusty. The reinforcing bars embedded in concrete beams or slabs are subject to corrosion caused by electro-chemical action. Underground fuel tanks are under similar condition. In 1979, the U.S. Bureau of Standards(NIST) study showed that yearly loss caused by corrosion related damages mounted to 82 billion dollars, about 4.9% of GNP. About 32 billion dollars could be saved if existing technologies were used to prevent such losses[1].

These figures are in the United States of America, where various federal, state, and other agencies are doing their best in maintaining such structures in good condition. The issue of deteriorating and damaged infrastructures and lifelines has become a critically important subject in the United States as well as Japan and Europe. The problem in developing nations, where degree of construction quality control and maintenance are in question, must be much more profound[1,2].

The advanced composite materials can be effectively used for repairing such structures. Because of the advantages of these materials, such repair job can fulfill two purposes :

A. Repair of existing damage caused by corrosion, impact, earthquake, and others.

B. Reinforcing the structure against anticipated future situation which will require increasing the load beyond the design parameters used for this structure. Before making any decision on repair work, reliable non-destructive evaluation is necessary. One of the dependable methods is to evaluate the in-situ stiffness of the structure by means of obtaining the natural frequency. By comparing the in-situ stiffness with the one obtained at the design stage, the degree of damage can be estimated rather accurately.

The reinforced concrete slab can be assumed as a $[0,90,0]$ type special orthotropic plate as a close approximation, assuming that the influence of B_{16} , B_{26} , D_{16} and D_{26} stiffnesses are negligible. Many of the bridge and building floor systems, including the girders and cross-beams, also behave as similar special orthotropic plates. Such plates are subject to the concentrated mass/masses in the form of traffic loads, or the test equipments such as the accelerator in addition to their own masses. Analysis of such problems is usually very difficult.

The most of the design engineers for construction has academic background of bachelors degree. Theories for advanced composite structures are too difficult for such engineers and some simple but accurate enough methods are necessary.

The author has reported that some laminate orientations such as $[\alpha, \beta]_r$, $[\alpha, \beta, \gamma]_r$, $[\alpha, \beta, \beta, \alpha, \alpha, \beta]_r$ and $[\alpha, \beta, \beta, \gamma, \alpha, \alpha, \beta]_r$ with $\alpha = -\beta$, and $\gamma = 0^\circ$ or 90° , and with increasing r , have decreasing values of B_{16} , B_{26} , D_{16} and D_{26} stiffnesses. Most of the civil and architectural structures are large in sizes and the numbers of laminae are large, even though the thickness to length ratios are small enough to allow to neglect the transverse shear deformation effects in stress analysis. For such plates, the fiber orientations given above behave as special orthotropic plates and simple formulas developed by the senior author[1,3] can be used. Most of the bridge and building slabs on girders have large aspect ratios. For such cases further simplification is possible by neglecting the effect of the longitudinal moment terms(M_x) on the relevant partial differential equations of equilibrium[5]. In this paper, the result of the study on the subject problem is presented. Even with such assumption, the special orthotropic plate with boundary conditions other than Navier or Levy solution types, or with irregular cross section, or with nonuniform mass including point masses, analytical solution is very difficult to obtain. Numerical method for eigenvalue problems are also very much involved in

seeking such a solution.

The method of vibration analysis used is the one developed by the senior author. He developed and reported, in 1974, a simple but exact method of calculating the natural frequency of beam and tower structures with irregular cross-sections and attached mass/masses[7]. Since 1989, this method has been extended to two-dimensional problems with several types of given conditions and has been reported at several international conferences. This method uses the deflection influence surfaces. The finite difference method is used for this purpose, in this paper.

METHOD OF ANALYSIS

Vibration Analysis

In this paper, the method of analysis given in detail, in the senior author's book[1] is briefly repeated.

The magnitudes of the maximum deflection at a certain number of points are arbitrarily given as

$$w(i, j)(1) = W(i, j)(1) \quad (1)$$

where (i, j) denotes the point under consideration. This is absolutely arbitrary but educated guessing is good for accelerating convergence. The dynamic force corresponding to this(maximum) amplitude is

$$F(i, j)(1) = m(i, j)[\omega(i, j)(1)]^2 W(i, j)(1) \quad (2)$$

The "new" deflection caused by this force is a function of F and can be expressed as

$$w(i, j)(2) = f\{m(k, l)[\omega(i, j)(1)]^2 W(k, l)(1)\} = \sum_{\Delta(i, j, k, l)} \{m(k, l)[\omega(i, j)(1)]^2 W(k, l)(1)\} \quad (3)$$

where Δ is the deflection influence surface. The relative (maximum) deflections at each point under consideration of a structural member under resonance condition, $w(i, j)(1)$ and $w(i, j)(2)$, have to remain unchanged and the following condition has to be held :

$$w(i, j)(1) / w(i, j)(2) = 1 \quad (4)$$

From this equation, $\omega(i, j)(1)$ at each point of (i, j) can be obtained. But they are

not equal in most cases. Since the natural frequency of a structural member has to be equal at all points of the member, i.e., $\omega(i,j)$ should be equal for all (i,j) , this step is repeated until sufficient equal magnitude of $\omega(i,j)$ is obtained at all (i,j) points. However, in most cases, the difference between the maximum and the minimum values of $\omega(i,j)$ obtained by the first cycle of calculation is sufficiently negligible for engineering purposes. The accuracy can be improved by simply taking the average of the maximum and the minimum, or by taking the value of $\omega(i,j)$ where the deflection is the maximum. For the second cycle, $W(i,j)(2)$ in

$$w(i,j)(3) = \mathcal{A}m(i,j)[\omega(i,j)(2)]^2 W(i,j)(2), \quad (5)$$

the absolute numerics of $W(i,j)(2)$ can be used for convenience.

Finite Difference Method(F.D.M)

The method used in this paper requires the deflection influence surfaces. F.D.M is applied to the governing equation of the special orthotropic plates,

$$D_1 \frac{\partial^4 w}{\partial x^4} + 2D_3 \frac{\partial^4 w}{\partial x^2 \partial y^2} + D_2 \frac{\partial^4 w}{\partial y^4} = q(x,y) - kw + Nx \frac{\partial^2 w}{\partial x^2} + Ny \frac{\partial^2 w}{\partial y^2} + 2Nxy \frac{\partial^2 w}{\partial x \partial y} \quad (6)$$

where $D_1 = D_{11}$, $D_2 = D_{22}$, $D_3 = (D_{12} + 2D_{66})$.

The number of the pivotal points required in the case of the order of error Δ^2 , where Δ is the mesh size, is five for the central differences. This makes the procedure at the boundaries complicated. In order to solve such problem, the three simultaneous partial differential equations of equilibrium with three dependent variables, w , M_x , and M_y , are used instead of Eq.(6) with $N_x=N_y=N_{xy}=0$ [4,5].

$$\frac{\partial^2 M_x}{\partial x^2} - 4D_{66} \frac{\partial^4 w}{\partial x^2 \partial y^2} + \frac{\partial^2 M_y}{\partial y^2} = -q(x,y) + kw(x,y) \quad (7)$$

$$M_x = -D_{11} \frac{\partial^2 w}{\partial x^2} - D_{12} \frac{\partial^2 w}{\partial y^2} \quad (8)$$

$$M_y = -D_{12} \frac{\partial^2 w}{\partial x^2} - D_{22} \frac{\partial^2 w}{\partial y^2} \quad (9)$$

If F.D.M is applied to these equations, the resulting matrix equation is very large

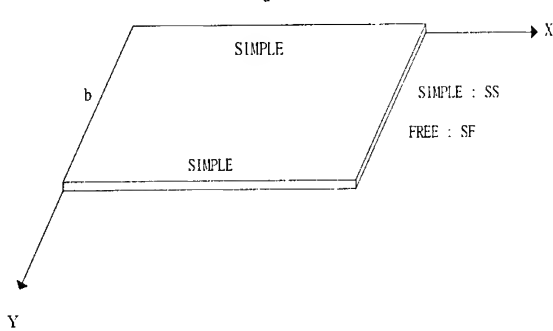
in sizes, but the tridiagonal matrix calculation scheme used by Kim, D. H. [4,5,6] is very efficient to solve such equations. Since one of the few efficient analytical solutions of the special orthotropic plate is Navier solution, and this is good for the case of the four edges simple supported, F.D.M is used to solve this problem. The result is satisfactory as expected.

By neglecting the M_x terms, the sizes of the matrices needed to solve the resulting linear equations are reduced to two thirds of the "non-modified" equations[5].

NUMERICAL EXAMINATION

Structure Under Consideration

The plate considered is as shown in Fig.1.



$a = nb$, $n = \text{an integer, } 1 \sim 5$.
 $b = 3\text{m}$.

Fig. 1. Plate under consideration.

The material properties are :

$E_1 = 67.36 \text{ Gpa}$, $E_2 = 8.12 \text{ Gpa}$,
 $G_{12} = 3.0217 \text{ Gpa}$, $\nu_{12} = 0.272$,
 $\nu_{21} = 0.0328$, $r = 1$.

Ply thickness = 0.005 m.

Orientation : $[90^\circ, 0^\circ, 90^\circ]$.

The stiffnesses are (in GPa) :

$D_{11} = 2929$, $D_{22} = 18492$, $D_{12} = 627$
 and $D_{66} = 849$.

Loading, $q = 286.65 \text{ N/m}^2$.

Numerical Results

In order to study the influence of M_x on the equilibrium equations, two cases are considered :

Case A : w , M_x , and M_y are considered.

Case B : w and M_y are considered, i.e., M_x is neglected.

F.D.M. is used to obtain w , M_x , and M_y , and the method by Kim, D.H., is used to obtain the natural frequency. The result is as shown in Tables 1 to 5.

Table 1. Deflection at the center of the plate(SS)

Aspect Ratio (b : a)	Case	δ
1:1	A	0.1434E-01
	B	0.1525E-01
	A/B	0.9403
1:2	A	0.1698E-01
	B	0.1643E-01
	A/B	1.0335
1:3	A	0.1654E-01
	B	0.1648E-01
	A/B	1.0036
1:4	A	0.1647E-01
	B	0.1648E-01
	A/B	0.9994
1:5	A	0.1648E-01
	B	0.1648E-01
	A/B	1.0000

Table 2. Moment M_y at center of the plate(SS)

Aspect Ratio (b : a)	Case	M_y
1:1	A	0.2873E+03 *
	B	0.3016E+03
	A/B	0.9526
1:2	A	0.3329E+03
	B	0.3217E+03
	A/B	1.0348
1:3	A	0.3235E+03
	B	0.3225E+03
	A/B	1.0031
1:4	A	0.3223E+03
	B	0.3225E+03
	A/B	0.9994
1:5	A	0.3225E+03
	B	0.3225E+03
	A/B	1.0000

Table 3. Moment M_x at the center of the plate (SS)

Aspect Ratio (b : a)	Case	M_x
1:1	A	0.4676E+02
	B	0.2804E+02 *
	A/B	1.6676
1:2	A	0.1268E+02
	B	0.1156E+02
	A/B	1.0969
1:3	A	0.1038E+02
	B	0.1095E+02
	A/B	0.9480
1:4	A	0.1088E+02
	B	0.1093E+02
	A/B	0.9954
1:5	A	0.1094E+02
	B	0.1093E+02
	A/B	1.0009

Table 4. Natural frequency (SS)

Aspect Ratio (a : b)	Natural Frequency (rad/sec)		Case A/ Case B
	Case A	Case B	
1	0.3879841	0.3540070	1.0960
2	0.2328229	0.2259199	1.0303
3	0.1823675	0.1789838	1.0189
4	0.1548738	0.1527856	1.0137
5	0.1369551	0.1355045	1.0107

Table 5. Natural frequency (SF)

Aspect Ratio (a : b)	Natural Frequency (rad/sec)		Case A/ Case B
	Case A	Case B	
1	0.2783243	0.2795208	0.9957
2	0.2018968	0.20235530	0.9977
3	0.1663077	0.1665625	0.9985
4	0.1446715	0.1448391	0.9988
5	0.1297479	0.1298688	0.9991

CONCLUSION

Most of the bridge and building slabs have plate aspect ratios large than 2. For such cases, design analysis becomes much simpler if influence of the longitudinal moment(M_x) terms on the relevant differential equations of equilibrium can be neglected. The result of the study on this subject is presented in this paper.

The result of numerical examination is quite promising.

Plates with all edges simple supported (SS), the ratios of the natural frequencies and the deflections at the center of the uniformly loaded plate are :

a/b	1	2	3	4	5	a/b	1	2	3	4	5
δ_A/δ_B	0.9403	1.0335	1.0036	0.9996	1.0000	ω_A/ω_B	1.0960	1.0303	1.0189	1.0137	1.0107

For SF case,

a/b	1	2	3	4	5	a/b	1	2	3	4	5
δ_A/δ_B	0.9824	0.9979	1.0000	1.0000	1.0000	ω_A/ω_B	0.9957	0.9977	0.9985	0.9988	0.9991

It is concluded that, for all boundary conditions, neglecting M_x terms is acceptable if the aspect ratio(a/b)is equal to or larger than 2. This conclusion gives good guide-line for design of bridge and building slabs on main girders, for which the aspect ratio is larger than, at least, five.

REFERENCES

1. D.H.Kim, Composite Structures for Civil and Architectural Engineering, E & FN Spon, London, 1995.
2. D.H. Kim, "Composite materials for repair and rehabilitation of buildings and infrastructures", Plenary Lecture at The Third Int'l Symposium on Textile Composites in Building Construction, Seoul, Korea, 1996.
3. D. H. Kim, "A simple method of analysis for the preliminary design of particular composite laminated primary structures for civil construction", J. Materials Processing Technology, 55, Elsevier, London, 1995, pp 242~248.
4. D. H. Kim, "Analysis of triangularly folded plate roots of umbrella type", Proc. 16th Congress of Applied Mechanics, Tokyo, Japan. 1965.
5. D. H. Kim, "The effect of neglecting the radial moment terms in analyzing a finite sectional plate by means of finite differences", Proc. Int. Symposium on Space Txchnology and Sciences, Tokyo, Japan, 1967.
6. D. H. Kim, "Tridiagonal scheme to solve super large size matrices by the use of computer", J. Korean Society of Civil Engineers, Vol. 15-1, 1967.
7. D. H. Kim, "A method of vibration analysis of irregularly shaped structural members", Proc. Int. Symposium on Engineering Problems in Creating Coastal Industrial Sites, Seoul, Korea, 1974.

Application (1)

OPTIMAL DESIGN OF THE COMPOSITE AEROSTATIC SPINDLE

Kyung Geun Bang, Po Jin Kim and Dai Gil Lee

*Department of Mechanical Engineering, Korea Advanced Institute of Technology
373-1, Kusong-dong, Yusong-gu, Taejeon 305-701, KOREA: kgb@cais.kaist.ac.kr*

SUMMARY: Low rotational inertia and high damping ratio of spindle shafts as well as high natural frequency are indispensable for the stable operation of high speed aerostatic spindles. Conventional stainless steel spindles are not appropriate for very high-speed operation because of their high rotational inertia and low damping ratio. In this study, aerostatic spindles were designed and manufactured with carbon fiber/epoxy composite, and their characteristics were evaluated through modal testing and compared to those of a conventional stainless steel spindle of comparable power rating

KEYWORDS: composite spindle, composite shaft, aerostatic bearing, optimal design, critical speed and static deflection.

INTRODUCTION

In the current manufacturing field, the reduction of machining time of high precision products is demanded for improving the productivity [1]. High precision air spindles operated at high speed are widely used in the manufacturing of high precision units such as computer hard disks, dental drills, polygon mirrors of the laser scanner etc. Air spindles can be rotated at very high speed with low heat generation because the viscosity of air used is much lower than other liquid lubricants. However, the unstable operation of stainless steel aerostatic spindle frequently occurs due to the high rotational inertia and low damping ratio of stainless steel shafts.

Although air enables very high speed rotation of the spindle, the damping characteristics of aerostatic spindle are poor than those of hydrostatic spindles due to the low viscosity of air. The studies on the stable operation of air spindles at high-speed rotation have been performed by many researchers. In 1854, Hirn suggested the air as the fluid for lubrication of bearing [2]. Gross experimentally discovered the characteristics of whirling and the start of unstable operation [3]. Larson found that the start point of the unstable operation was higher when the supplied pressure was high or the clearance of the bearing was small [4]. Taniguchi investigated the operating characteristics according to the number of supply holes, the supplied pressure and the clearance of bearings [5]. Blondeel modeled aerostatic air bearings as a control system with feedback loop and investigated the dynamic stability of aerostatic bearing through frequency analysis [6].

In order to prevent the unstable operation of steel air spindles, expensive machining of non-circular bearing section and additional equipment for the active control are required. Another possibility of improvement of aerostatic spindles is to employ high specific stiffness material with high damping for the spindle shaft. Since carbon fiber-epoxy composite has high specific stiffness (E/ρ), high specific strength (S/ρ), low coefficient of thermal expansion (C.T.E.) and good damping property, aerostatic spindles whose shaft are made of carbon fiber composite may result in weight-reduction, stable operation and thermal stability. Lee [7] and Choi [8] applied carbon fiber epoxy composites to high-speed spindles with ball bearing and found that the static and dynamic characteristics were improved in comparison with conventional steel spindles.

In this study, the aerostatic spindles with built-in type motor of 1.5 kW was designed and manufactured with carbon fiber composite and its characteristics were compared with the conventional steel spindle.

DESIGN OF THE COMPOSITE AEROSTATIC SPINDLE

The carbon fiber aerostatic spindle was designed based on the dimensions of a conventional steel spindle of 1.5 kW power rating. Table 1 shows the specifications of the conventional steel aerostatic spindle.

Table 1. Specifications of the aerostatic spindle.

Shaft outer diameter (mm)	25
Shaft length (mm)	210
Bearing clearance (μm)	15
Max. radial load capacity (N)	80
Max. radial stiffness (MN/m)	6

Since the static and dynamic characteristics of aerostatic bearings are largely dependent on radial stiffness, the radial stiffness of the aerostatic bearing whose specification was listed in Table 1 was measured with respect to radial displacement. The apparatus for measuring the radial stiffness is shown in Fig. 1.

When the supplied pressure into the aerostatic bearing was from 0.2 MPa to 0.9 MPa, the displacement at the nose of the shaft was measured with an inductive gauging sensor as the weight was increased from 5 N to 80 N with increment of 5 N. The aerostatic bearings were assumed to have linear spring stiffness of k as shown in Fig. 2. The relationship among the radial stiffness k of the aerostatic bearing, applied load W , and the deflection δ_{tot} at the nose was derived in Equation (1) using simple bending theory of beams.

$$k = \frac{W[(L+b)(2a+L)+2a^2]}{(L^2-b^2)\left(\delta_{\text{tot}} + \frac{Wa^3}{EI_1}\right) + \frac{W(L-b)}{6EI_2}[2a^2L^2 - 2ab(a+L)(2b+L) - b^3(b+L+4a)]} \quad (1)$$

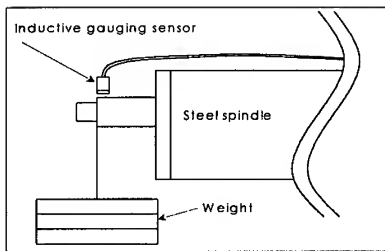


Fig. 1. Schematic diagram of test for measuring the radial stiffness of the aerostatic bearing.

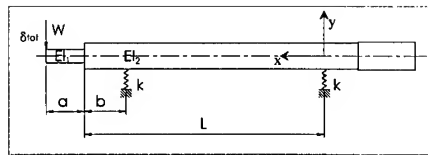


Fig. 2. The model of the shaft and the aerostatic bearing.

The radial stiffness of the aerostatic bearing calculated by Equation (1) is shown in Fig. 3 in which the radial stiffness of the bearing increases as the supplied pressure increased until 0.7 MPa and then saturated. Therefore, for the design of the composite shaft, the radial stiffness was assumed to be 6 MN/m at the applied pressure of 0.7 MPa.

Since the composite shaft was designed for stable rotating at high speed rather than high torque transmission capability, the composite shaft was designed to increase the bending natural frequency of the system because the required torque of very high speed spindle is negligibly small of 1 Nm order. The bending natural frequencies of the composite aerostatic spindle were calculated with ANSYS 5.3, a commercial FEM software. The composite shaft and the aerostatic bearing were modeled using one-dimensional beam elements and equivalent spring elements, respectively as shown in Fig. 4. The FEM analysis was performed varying the thickness of the composite shaft from 1 mm to 12.5 mm when the outer diameter was constant. The first, second and third natural frequencies of the composite spindle and the steel spindle calculated are shown in Fig. 5, Fig. 6 and Fig. 7, respectively. The first and second mode shapes are translatory rigid and conical rigid modes, respectively and the third mode is bending mode.

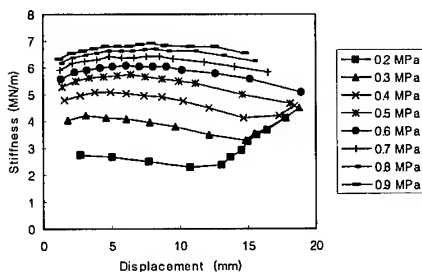


Fig. 3. The radial stiffness of the aerostatic bearing w. r. t. displacement when the applied pressure is from 0.2 MPa to 0.9 MPa.

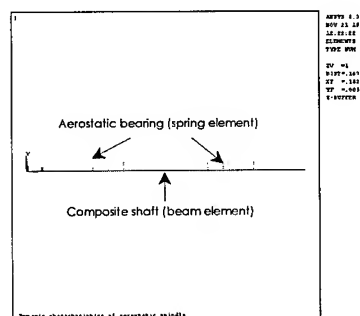


Fig. 4. The model of the composite shaft and aerostatic bearing for FE analysis.

Since the very high speed aerostatic spindle for high-precision machining of electronics components is normally operated in the speed range between 40,000 rpm (670 Hz) and 100,000 rpm (1670 Hz), the second natural frequency is most important. As shown in Fig. 5, the hollow section rather than the solid section is beneficial to both the composite shaft and

the steel shaft because the second natural frequencies of the spindle become higher when the thickness of the shaft is properly thin. However, hollow steel shafts are hardly used for aerostatic spindle due to the difficulty of precision boring of long stainless steel shaft. On the contrary, it is very easy to manufacture hollow composite shafts using mandrels. In this study, the thickness of the composite shaft was determined to be 3 mm with the stacking sequence of $[\pm 15]_n$. The unidirectional composite shaft was not employed to give some torsional rigidity to the shaft.

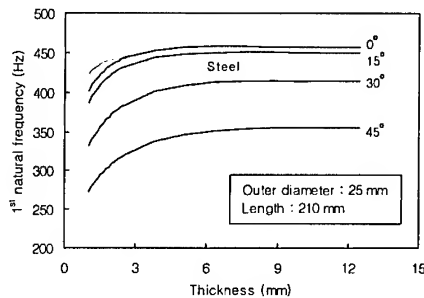


Fig. 5. Fundamental natural frequency of the composite aerostatic spindle and the steel aerostatic spindle w. r. t. thickness of the shaft.

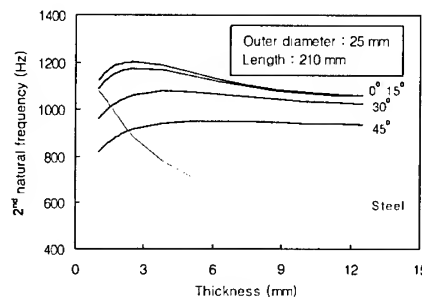


Fig. 7. 2nd natural frequency of the composite aerostatic spindle and the steel aerostatic spindle w. r. t. thickness of the shaft.

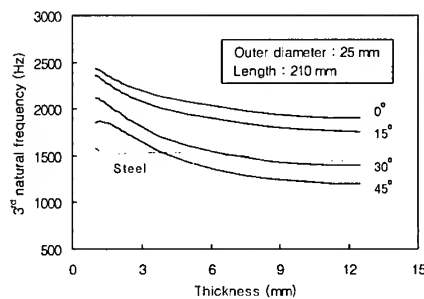


Fig. 6. 3rd natural frequency of the composite aerostatic spindle and the steel aerostatic spindle w. r. t. thickness of the shaft.

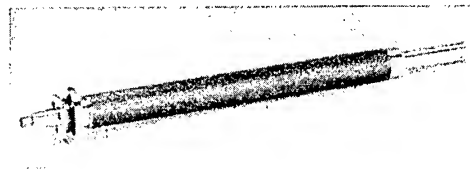


Fig. 8 Photograph of the composite shaft.

MANUFACTURE OF THE COMPOSITE AEROSTATIC SPINDLE

The composite shaft was cured by vacuum bag degassing autoclave molding after the carbon fiber-epoxy prepreg (Table 2) was stacked on the steel mandrel. The cured composite shaft was roughly ground to fit the required dimensions approximately. After adhesively

joining the composite shaft to the tool mounting steel sleeve and to the rotor of a motor, the composite shaft and the steel sleeve were precisely ground to the exact dimensions. The composite shaft and the steel sleeve were adhesively joined with epoxy adhesive (IPCO9923 of National Starch Co.). The adhesive was cured for 2 hours under 80°C at 0.6 MPa. Fig. 8 shows the manufactured carbon fiber composite shaft.

Table 2. Properties of the unidirectional carbon fiber-epoxy composite material (USN125, SKC Co.)

Tensile modulus (GPa)	131.6
Transverse modulus (GPa)	8.2
Shear modulus (GPa)	6.1
Tensile strength (GPa)	1.78
Transverse strength (MPa)	50
Shear strength (MPa)	88
Density (kg/m ³)	1560

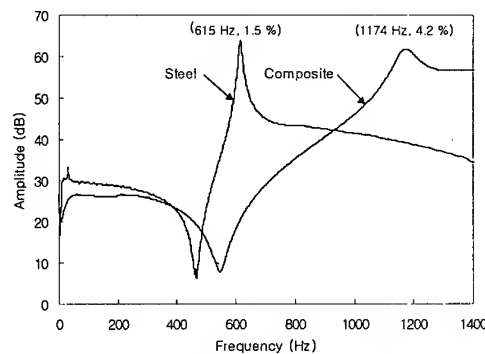


Fig. 9. Amplitude of the acceleration for the steel and composite aerostatic spindle w. r. t. the frequency.

PERFORMANCE EVALUATION OF THE COMPOSITE AEROSTATIC SPINDLE

The dynamic characteristics of the manufactured composite aerostatic spindle were evaluated through measuring natural frequency and damping ratio in modal testing. The stability at high-speed rotation was evaluated through operating test under no load.

Fig. 9 shows the second natural frequency response curves of the composite aerostatic spindle and the steel aerostatic spindle obtained through modal testing. From the results of Fig. 9, it was concluded that the second natural frequency and damping ratio of the composite aerostatic spindle was higher than those of the steel aerostatic spindle. Also, the real operating test of the spindles was performed to investigate the stability of the spindle with respect to rotating speed and found that the vibration and noise of the composite aerostatic spindle during high speed operation were less than those of the steel aerostatic spindle. The dynamic characteristics of the composite aerostatic spindle and the steel aerostatic spindle are listed in Table 3.

Table 3. Performance comparisons of the composite aerostatic spindle and the steel aerostatic spindle.

	Steel spindle	Composite spindle
Spindle section shape	Solid	Hollow
Mass (kg)	1.11	0.37
Rotational moment of inertia (kgm ²)	9.14×10^{-5}	3.32×10^{-5}
Second natural frequency (rpm)	36,900	70,440
Loss factor (%)	1.5	4.2

CONCLUSION

In this study, an aerostatic spindle was designed and manufactured with carbon fiber epoxy composite material to increase the natural frequency and to reduce the rotational inertia of the shaft of the spindle. The mass and rotational inertia of the composite spindle were 33 % and 36 %, respectively of the steel spindle with comparable power rating. The second natural frequency which encompasses the operating range of aerostatic spindles and damping ratio were 1.9 times and 2.8 times, respectively of the steel spindle.

REFERENCES

1. M. Weck and A. Koch, "Spindle-Bearing Systems for High-Speed Applications in Machine Tools", *Ann. CIRP*, Vol. 42(1), 1993, pp. 445-448.
2. G. Hirn, "Sur les Principaux Phenomenes qui Present les Frottements Mediate", *Soc. Ind. Mulhouse Bull*, Vol. 26, 1854, pp. 188-277.
3. W. A. Gross, "Investigation of Whirl in Externally Pressurized Air-Lubricated Journal Bearings", *J. Basic Eng. Trans. ASME*, Vol. 84, 1962, pp. 132-138.
4. R. H. Larson and H. H. Richardson, "A Preliminary Study of Whirl Instability for Pressurized Gas Bearings", *J. Basic Eng. Trans. ASME*, Vol. 84, 1962, pp. 511-520.
5. O. Taniguchi, "Experimental Study on Instability of Externally Pressurized Air Journal Bearing", *JSME Int. J.*, Vol. 33, 1967, pp. 997-1004.
6. E. Blondeel, R. Snoeys and L. Devrieze, "Dynamic Stability of Externally Pressurized Gas Bearings", *J. Lub. Tech. Trans. ASME*, Vol. 102, 1980, pp. 551-519.
7. D. G. Lee, H. C. Sin and N. P. Suh, "Manufacturing of a Graphite Epoxy Composite Spindle for a Machine Tool", *Ann. CIRP*, Vol. 34, 1985, pp. 365-369.
8. J. K. Choi and D. G. Lee, "Manufacture of a Carbon Fiber-Epoxy Composite Spindle-Bearing System for a Machine Tool", *Composite Structures*, Vol. 37, 1997, pp. 241-251.

HEALTH MONITORING SYSTEM OF COMPOSITE LAMINATED STRUCTURES USING VIBRATION DATA

Takaomi INADA¹, Yoshinobu SHIMAMURA², Akira TODOROKI²,
Hideo KOBAYASHI² and Haruo NAKAMURA²

¹Graduate student of Tokyo Institute of Technology,

O-okayama 2-12-1, Meguro-ku, Tokyo 152-8552, Japan: tinada@ginza.mes.titech.ac.jp

²Department of Mechano-Aerospace Engineering, Tokyo Institute of Technology

SUMMARY: This paper presents a damage identification method for advanced composite structures using vibration data. Delamination identification of a graphite-epoxy laminated beam using natural frequency change and response surfaces was conducted. Response surfaces were used for approximation of the natural frequency change in delaminated graphite-epoxy beams. In order to identify the delamination sizes and locations, an objective function was made from response surfaces and the natural frequencies of the delaminated graphite-epoxy beam. By minimizing the objective function, we can predict the delamination size and location easily and inexpensively. As a result, it is shown that there are good agreements between actual and predicted delamination sizes and locations.

KEYWORDS: Health monitoring, Delamination identification, Natural frequency change, Response surface

INTRODUCTION

Recently, composite laminated structures have been applied to many structures of vehicles. Since interlamina strength of composite laminated structure is relatively low, internal damage, such as delamination, can be easily induced in service. In order to assess integrity of the damaged structures, it is necessary to identify the size and location of the damage nondestructively.

Health monitoring systems using piezoelectric materials have been investigated to localize and quantify the damage [1-4]. In these systems, piezoelectric materials are often used as actuators and sensors for vibration tests. Since modal parameters of damaged structures change from that of undamaged structures, the damage can be easily detected by its change. Among the modal parameters, modal strain distribution is effective to localize damage [5,6], but measurement of modal strain distribution is expensive since it needs many sensors on the structure. On the contrary, natural frequencies are often used for damage inspection because they are global parameters and can be measured easily with a few sensors [1,2]. However, natural frequency change of structures induced by damages is complicated, and localization

and quantification of the damage are quite difficult. For this reason, backpropagation neural network (BNN) is often used. BNN is, however, time-consuming for teaching and the regression results cannot be validated by using a statistical testing.

The present study proposes a delamination identification method using natural frequency change and response surfaces. In our method, response surfaces are used for approximations of the natural frequencies, and delaminations are identified by solving optimization problem. In order to show effectiveness of the present method, delamination identification of a graphite-epoxy cantilever beam was conducted in the analysis. As a result, it is shown that there are good agreements between actual and predicted delamination locations and sizes.

HEALTH MONITORING SYSTEM USING VIBRATION DATA

Health monitoring systems using piezoelectric materials have lately attracted attention. In the present study, we propose a conceptual model of health monitoring system for graphite-epoxy beam as shown in Fig.1. In this system, modal parameters of the beam are specified by vibration tests using piezoelectric materials. Among the piezoelectric materials, PZT is often used for actuators and PVDF is often used for sensors. Sine sweep method is suitable for excitation of the beam and the frequency response function can be obtained easily, however, it takes for hours. From the measured frequency response function, modal parameters (natural frequencies, damping, etc.) are extracted, and delamination identification is conducted by delamination identification technique on the personal computer. It has already confirmed that the natural frequencies of the beam measured by this system are well agreed with the result of conventional modal analysis method using impulse hammer excitation [7].

Owing to the presence of delamination, the natural frequencies of a Graphite-epoxy cantilever beam are changed from that of an intact state. Accordingly, presence of delamination can be easily detected by the natural frequency change. The natural frequency change of a delaminated structure, however, is complicated and localization and quantification of the delamination are quite difficult. In order to complete the health monitoring system, delamination identification technique from the natural frequency change must be developed immediately.

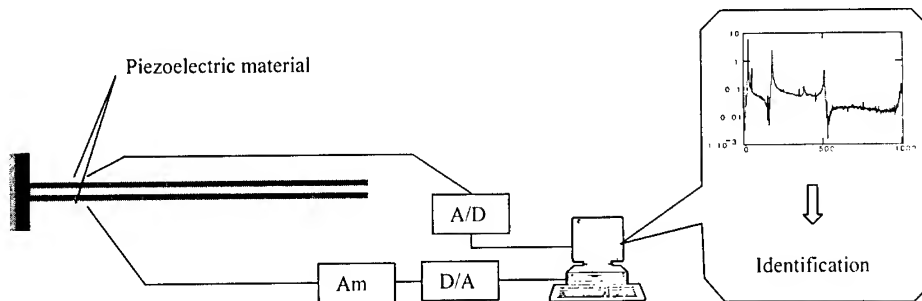


Fig.1 Health monitoring system for graphite-epoxy cantilever beam

DELAMINATION IDENTIFICATION OF A CANTILEVER BEAM

Analytical model

In order to identify the size and location of a delamination from the natural frequency change, we have to estimate the relationship between the natural frequencies and the delamination sizes and locations. An analytical model used to calculate the natural frequency change of delaminated beams is shown in Fig.2 [1,2]. In the model, the cantilever beam is divided into four Euler beams and the natural frequencies are obtained as a result of eigenvalue problem. The stacking sequence is $[0/90/90/0]_s$, and delamination is located on the midplane of the graphite-epoxy beam. The length of the beam is 0.25m, and the thickness of the beam is 0.0015m. Material properties of graphite-epoxy ply used for the analysis are: $E_1=157\text{GPa}$, $E_2=10.0\text{GPa}$, $\nu_{12}=0.27$. Although the model does not include bending and extensional coupling terms, it has been shown that the natural frequencies calculated from this model are well agreed with the experimental results [1,2].

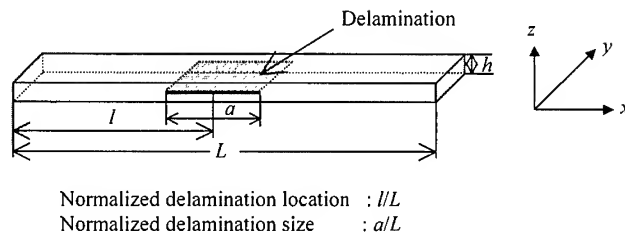


Fig.2 Analytical model of a graphite-epoxy cantilever beam with a delamination

Identification procedure

Backpropagation neural network (BNN) is often used for identifying the size and location of delamination. BNN is, however, time-consuming for teaching and we cannot validate the regression results by using a statistical testing. In the present study, we propose an identification method using response surfaces and optimization.

Response surfaces of natural frequencies

It is easy to calculate many data sets from analytical models. It is, however, difficult and expensive to calculate many data sets for general complicated structures. In order to reduce the calculation cost, we adopt response surface methodology (RSM) to complement many data sets from a few data sets that are calculated from analysis. RSM is a method to get an approximate expression of relation between variables and responses, which consists of surface regression by least squares method and design of experiments.

The quadratic polynomial response surface of two variables is expressed as follows.

$$y = \beta_0 + \beta_1 x_1 + \beta_2 x_2 + \beta_3 x_1^2 + \beta_4 x_2^2 + \beta_5 x_1 x_2 \quad (1)$$

In Eqn 1, y is the natural frequency, x_1 is the delamination size and x_2 is the delamination location. To calculate the coefficients β , least squares method are used. First, we tried to use a fourth order polynomial to approximate natural frequency change of first mode, a fifth order polynomial to approximate natural frequency change of second mode and a sixth order polynomial to approximate natural frequency change of third mode. The natural frequency change, however, was complicated and we could not obtain good approximate results. In order to improve approximate accuracy, we used three response surfaces to approximate natural frequency change of individual mode. That is, we divide the feasible region for the delamination size and location into three regions, and approximated natural frequency change separately (See Fig. 3).

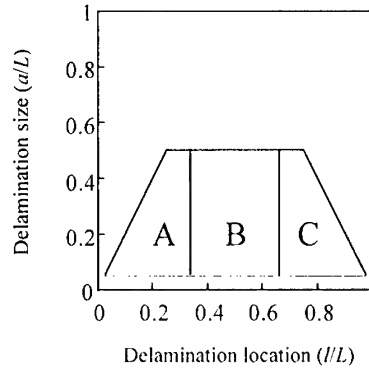


Fig.3 Divided feasible region for the delamination size and location

Delamination identification using optimization

As mentioned above, we can calculate approximate expressions of natural frequency change of the cantilever beams with various delamination sizes (x_1) and locations (x_2) using response surfaces. Now, we define these response surfaces as $\{\Omega_1(x_1, x_2), \Omega_2(x_1, x_2), \Omega_3(x_1, x_2)\}$ on individual regions, and the natural frequencies of a graphite-epoxy cantilever beam which are supposed to be delaminated as $(\omega_1, \omega_2, \omega_3)$. In order to identify the delamination size and location of the graphite-epoxy beam, we make an objective function on individual regions as follows.

$$F = \sum_{i=1}^3 \{\omega_i - \Omega_i(x_1, x_2)\}^2 \quad (2)$$

By minimizing the objective function F , we can identify the delamination size and location on individual regions. From the three candidates, the global minimum is decided. When the function F is globally minimized at (\hat{x}_1, \hat{x}_2) , \hat{x}_1 means expected delamination size and \hat{x}_2 means expected delamination location. We used the conjugate gradient method to minimize the function F . Since there are many local minimums in the function, we used random initial values of x_1, x_2 and calculated the local minimums for these initial values on individual regions.

Identification results

Fig.4-(a) shows the relationship between actual and predicted delamination size. Fig.4-(b) shows the relationship between actual and predicted delamination location. In each figure, horizontal axis means actual value, and vertical axis means predicted value. A diagonal line in each figure means agreement between actual and predicted value. These data sets used for identifying delamination were calculated from an analytical model shown in Fig.2. The data

sets used to identify delamination were not used for making the response surfaces of the natural frequencies. Though there are a few errors in Fig.4-(a), we can almost predict the delamination sizes. On the contrary, accuracy of the prediction of delamination locations is not enough, since there is a tendency to predict an opposite side against the midspan of the beam within $0.4 \leq l/L \leq 0.6$.

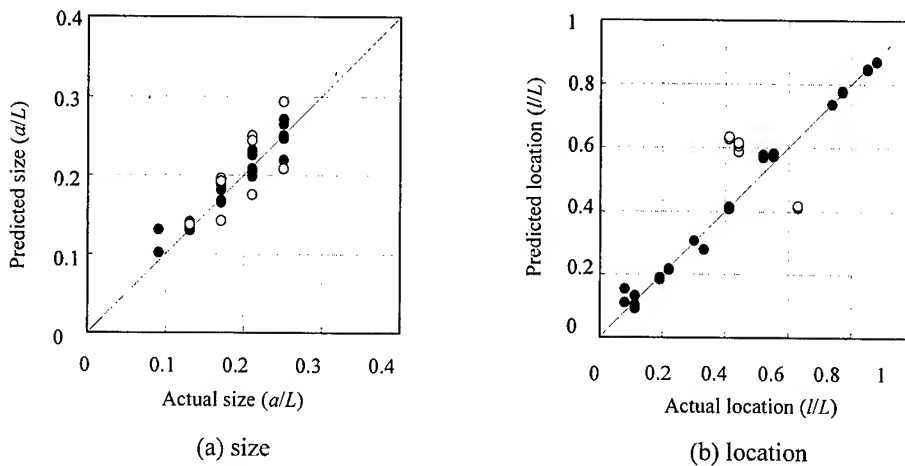


Fig.4 Comparison between actual and predicted delamination

In practical use, it is not so important to identify delamination size and location precisely, and it is desirable to obtain identification results simply and quantitatively. For this reason, we classified delamination sizes and locations into levels as shown in Table 1.

For simplicity we define the identification reliability as follows.

$$\text{Reliability (\%)} = \frac{\text{The number of data identified in the same level as the actual one}}{\text{The total number of data}} \times 100$$

According to the above definition, the reliability of delamination size is 92.9% and location is 81.0%. It is evident that the present delamination identification method is effective to identify delamination sizes and locations.

Table 1 Classification of delamination sizes and locations

Delamination size		Delamination location	
Level	Range	Level	Range
1	$0 \leq a/L < 0.1$	1	$0 \leq l/L < 0.2$
2	$0.1 \leq a/L < 0.2$	2	$0.2 \leq l/L < 0.4$
3	$0.2 \leq a/L < 0.3$	3	$0.4 \leq l/L < 0.6$
		4	$0.6 \leq l/L < 0.8$
		5	$0.8 \leq l/L < 1$

CONCLUSIONS

The present paper describes the delamination identification method of graphite-epoxy laminated structures using natural frequency change and response surfaces. Delamination identification of a graphite-epoxy cantilever beam was conducted to confirm efficiency of the present method. As a result, it is shown that there are good agreements between actual and predicted delaminations. The present delamination identification method is easy and inexpensive because of adopting the response surfaces. Since natural frequencies can be simply measured by vibration tests with piezoelectric materials, smart structures with the function of health monitoring can be constructed easily by using the proposed delamination identification method.

REFERENCES

1. A. C. Okafor, K. Chandrashekhara and Y. P. Jiang, "Delamination prediction in composite beams with built-in piezoelectric devices using modal analysis and neural network", *Smart Mater. Struct.*, 5, 1996, pp.338
2. A. S. Islam and K. C. Crag, "Damage detection in composite structures using piezoelectric materials", *Smart Mater. Struct.*, 3, 1994, pp.318
3. C. H. Keilers, Jr. and F. Chang, "Identifying Delamination in Composite Beams Using Built-In Piezoelectrics: Part II-An Identification Method", *J. Intell. Matls. Sys. & Struct.*, 6, 1995, 664
4. H. Luo and S. Hanagud, "PVDF SENSOR AND ITS APPLICATIONS IN DELAMINATION RESPONSE DETECTION", *AIAA*, 97-1218, 1997, pp.720
5. A. K. Pandey, M Biswas and M. M. Samman, "DAMAGE DETECTION FROM CHANGES IN CURVATURE MODE SHAPES", *J. Sound and Vibration*, 145(2), 1991, pp.321
6. C. P. Ratcliffe, "DAMAGE DETECTION USING A MODIFIED LAPLACIAN OPERATOR ON MODE SHAPE DATA", *J. Sound and Vibration*, 204(3), 1997, PP.505
7. T. Inada, Y. Shimamura, A. Todoroki, H. Kobayashi and H. Nakamura, "Damage Identification in Smart Composite Beam With Piezoelectric Patches", *Proc. of The First Asian-Australasian Conference on Composite materials (ACCM-1)*, Vol.2, 1998, pp.621

DESIGN STRENGTH OF PULTRUDED UNIVERSAL SECTION COLUMNS

S. J. Yoon¹, S. K. Jeong², S. K. Cho³

¹Professor, Department of Civil Engineering, Hongik University 72-1, Sangsu-dong, Mapo-gu, Seoul 121-791, KOREA: sjyoon@wow.hongik.ac.kr

²Graduate Research Assistant, Department of Civil Engineering, Hongik University 72-1, Sangsu-dong, Mapo-gu, Seoul 121-791, KOREA: g98311306@wow1.hongik.ac.kr

³Full-time Instructor, Department of Civil Engineering, Seoul National University of Technology 172 Gongneung-dong, Nowon-Gu, Seoul, 139-743, Korea

SUMMARY: Due to the increase of using composite materials in construction fields, many companies are currently producing fiber-reinforced polymeric structural members in a various section configurations. Thus, there is an urgent need to understand the mechanical behavior of these materials under various loading conditions. This paper presents the results of local buckling analysis of fiber-reinforced thermosetting plastic universal section columns. The transcendental equation for the local buckling behavior of universal section column is derived based upon the classical orthotropic plate theory. The interaction between the plate components is taken into account in the derivation. The finite element analysis is also performed for the simulation of local buckling behavior of columns. Based on the results of the investigation, the minimum local buckling coefficient with respect to the ratio between the plate elements is shown graphically so that the local buckling strength of the universal section columns could be estimated.

KEYWORDS: fiber-reinforced thermosetting plastic, orthotropic, local buckling, interaction, universal section, closed-form, finite element

INTRODUCTION

The use of new materials such as structural composites in civil engineering is much more increased as the special demands of construction fields, rehabilitation and strengthening of existing structures. In particular, fiber-reinforced polymeric (FRP) composite materials are widely used due to the attractive material properties such as lightweight, high specific strength and stiffness, electro-magnetic transparency, corrosion resistance, and tailorability to a variety of desired cross section. Through the pultrusion process, this material has competition with the conventional construction materials such as concrete and steel even in costs. However, in use of this material, engineers may face with an urgent problem due to the absence of reliable design criteria. Therefore, the study on the behaviors of pultruded material to establish the design criteria is necessary. This paper involves both theoretical and numerical studies of

pultruded universal section columns. The universal section is unique column section allows for the addition of cross members at any height and in either direction for piping or cable supports as shown in Fig. 1. The results are used to find the equation for the local buckling strength of thin-walled universal section columns. The graphical form of results generated using the given mechanical properties [1] are presented for a design aid.

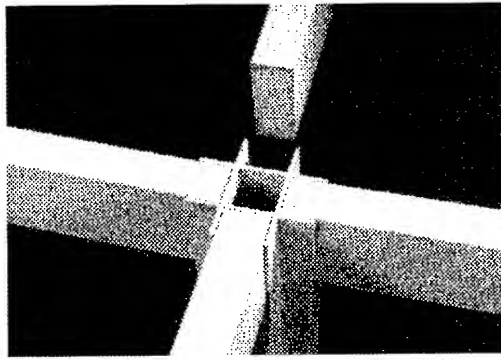


Fig. 1 The use of universal section column [1]

LOCAL BUCKLING OF MEMBERS

Consider a short universal section column of length L that is composed of 4 rectangular orthotropic elastic plates meeting at a common junction as shown in Fig. 2. The governing differential equation for the buckling behavior of a rectangular orthotropic plate is given by following Whitney (1987) [2] using the dimensionless parameters $\xi = x/L$ and $\eta = y/L$ [3].

$$s^4 \lambda_1^4 \frac{\partial^4 w}{\partial \xi^4} + 2s^2 \lambda_2^2 \frac{\partial^4 w}{\partial \xi^2 \partial \eta^2} + \frac{\partial^4 w}{\partial \eta^4} + \pi^2 s^2 \lambda_1^2 k \frac{\partial^2 w}{\partial \xi^2} = 0 \quad (1)$$

where

$$s = \frac{b}{L}, \quad \lambda_1 = \left(\frac{D_{11}}{D_{22}} \right)^{\frac{1}{4}}, \quad \lambda_2 = \left(\frac{D_{12} + 2D_{66}}{D_{22}} \right)^{\frac{1}{2}}, \quad k = \frac{ph^2}{\pi^2 \sqrt{D_{11}D_{22}}} \quad (2-1,2,3,4)$$

If the boundary condition of loaded edges is assumed to simple support, the solution of equation (1) may be taken in the form:

$$w = (A_1 \cosh \alpha \eta + A_2 \sinh \alpha \eta + A_3 \cos \beta \eta + A_4 \sin \beta \eta) \sin m\pi \xi \quad (3)$$

where A_1 , A_2 , A_3 , and A_4 are constants which must be determined from the boundary conditions along the unloaded edges. The letter m denotes the number of half-sine waves along the longitudinal direction of the plate components. The parameters α and β can be shown to have the forms, respectively:

$$\alpha = m\pi s \lambda_2 \sqrt{1 + \sqrt{1 - \left(\frac{\lambda_1}{\lambda_2} \right)^4 \left(1 - \frac{k}{m^2 s^2 \lambda_1^2} \right)}}, \quad \beta = m\pi s \lambda_2 \sqrt{-1 + \sqrt{1 - \left(\frac{\lambda_1}{\lambda_2} \right)^4 \left(1 - \frac{k}{m^2 s^2 \lambda_1^2} \right)}} \quad (4-1,2)$$

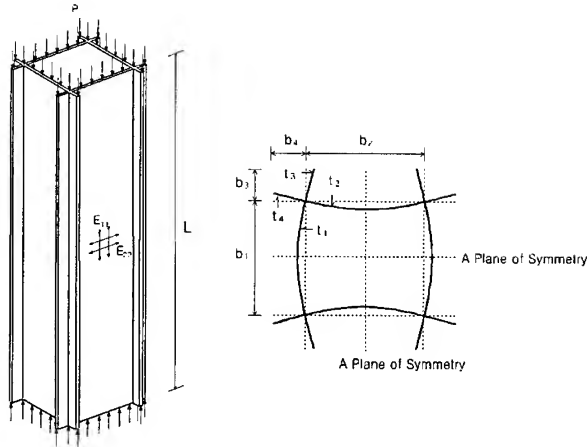


Fig. 2 Orthotropic universal section column under uniform compression

The characteristic equations for the buckling of plate having following boundary conditions at its unloaded edges are taken in the form [3]:

$$\text{Simply supported and a plane of symmetry: } SSy = \alpha\beta(\alpha^2 + \beta^2) \cosh \frac{\alpha}{2} \cos \frac{\beta}{2} \quad (5-1)$$

$$\text{Fixed support and a plane of symmetry: } FSy = -\alpha\beta(\alpha \sinh \frac{\alpha}{2} \cos \frac{\beta}{2} + \beta \cosh \frac{\alpha}{2} \sin \frac{\beta}{2}) \quad (5-2)$$

$$\text{Simply supported and free: } SFr = (\alpha^2 + \beta^2) \{ \beta \chi^2 \sinh \alpha \cos \beta - \alpha \psi^2 \cosh \alpha \sin \beta \} \quad (5-3)$$

$$\text{Fixed support and free: } FFr = -2\alpha\beta\chi\psi - \alpha\beta(\chi^2 + \psi^2) \cosh \alpha \cos \beta - (\beta^2 \chi^2 - \alpha^2 \psi^2) \sinh \alpha \sin \beta \quad (5-4)$$

For the local buckling analysis of a thin-walled compression member composed of fiber-reinforced plastic, following assumptions (Bulson, 1969) [4] at a common junction are needed in addition to the basic assumptions for the classical orthotropic plate theory:

- Out of plane deflection is zero,
- Plate components are connected rigidly at a common junction so that the rotation angles of each plate are identical,
- Sum of the moment at each plate component is zero.

Substituting equation (3) into the boundary conditions of each plate element, 16 linear homogeneous simultaneous equations are obtained. In order to get the solution other than the trivial one, the determinant of coefficient matrix must be vanished. The determinant of 16×16 matrix can be expanded by fourth-order minors using the Laplace expansion. Each minor represents the characteristic equation for the buckling of plate having aforementioned boundary conditions at its unloaded edges. Therefore we can obtain the transcendental closed-form of instability equation for a universal section column:

$$\left(\frac{SSy}{FSy} \right)_1 + \frac{1}{\delta_2 \omega_2^3} \cdot \left(\frac{SSy}{FSy} \right)_2 + \frac{1}{\delta_3 \omega_3^3} \cdot \left(\frac{SFr}{FFr} \right)_3 + \frac{1}{\delta_4 \omega_4^3} \cdot \left(\frac{SFr}{FFr} \right)_4 = 0 \quad (6)$$

Subscripts in equation (6) denote the number of plates, δ_i ($i = 2, 3, 4$) means the width ratio between the plate i and plate 1 (b_i/b_1) and ω_i means the thickness ratio between the plate 1 and plate i (t_i/t_1). Since the buckling stress of each component could be assumed to be the same, we can find the buckling coefficient that can evaluate the buckling strength using Timoshenko's expression [5]:

$$\sigma = k_i \cdot \frac{\pi^2 \sqrt{E_{11} E_{22}}}{12(1 - \nu_{12} \nu_{21})} \left(\frac{b_{\perp}}{t_i} \right)^2, \quad (i = 1, 2, 3, 4) \quad (7)$$

From the equation (6), the minimum buckling coefficient k_i of universal section is calculated through the numerical analysis technique for the various values of b_2/b_1 and b_3/b_1 as shown in Fig. 3. The orthotropic material properties used to draw Fig. 3 are taken from MMFG (1989)[1]. If orthotropic material properties in equation (6) are replaced with isotropic ones, we may obtain the graph as shown in Fig. 4. The results are identical with those given in Bulson (1955) [6]:

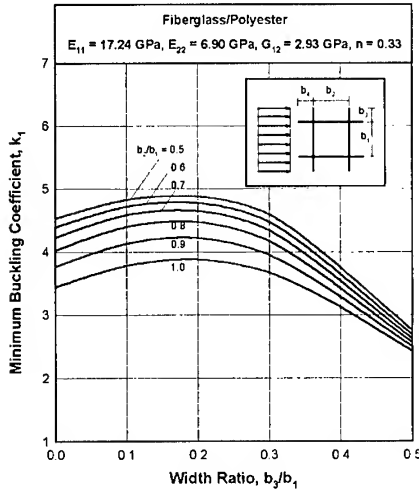


Fig. 3 Minimum local buckling coefficient of orthotropic universal section column

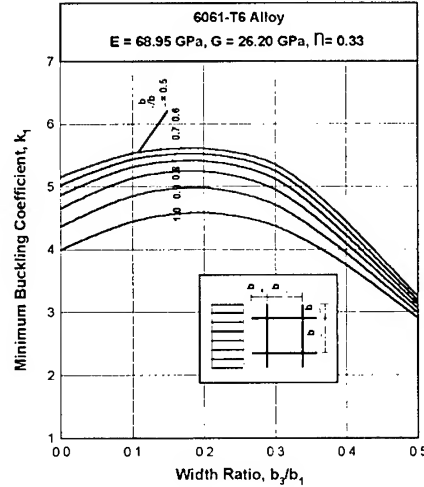


Fig. 4 Minimum local buckling coefficient of isotropic universal section column

FINITE ELEMENT ANALYSIS

To estimate the local buckling load of pultruded universal section column, the finite element analysis (FEM) was also performed using GTSTRUDL [7]. The finite element used in this analysis is a stretching bending hybrid quadrilateral (SBHQ) element. This element has five degrees of freedom (DOF) per node as shown in Fig. 5. The element is a combination of a plane stress element and a plate bending element. This element can be used in a buckling analysis, since the plane stress formulations allow in-plane loads to be considered and the plate bending formulations allow bending effects to be considered. Total of three column specimens are modeled to perform the local buckling analysis and one entire section of the column with

buckled mode shape after performing finite element analysis is shown in Fig. 6. Element dimension is 25.4 mm \times 25.4 mm and uniform thickness $t=5.08$ mm for all columns.

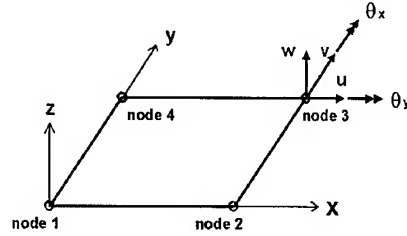
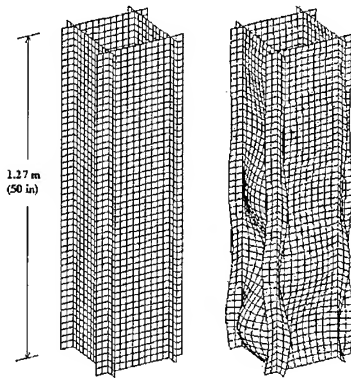


Fig. 5 SBHQ plate element with DOF at node 3

In the analysis, the boundary conditions of the column ends were modeled as follows:

- (1) Rotation due to bending allowed at both ends;
- (2) Rotation due to torsion restrained at both ends;
- (3) Out of plane deflection restrained at both ends;
- (4) Axial deflection allowed at loaded end but restrained at the other end.

The results of analysis are presented in Table 1, and compared with analytical solution.



Specimen dimension:

$$b_1 = b_2 = 25.4 \text{ cm}$$

$$b_3 = b_4 = 5.08 \text{ cm}$$

$$t = 5.08 \text{ mm}$$

Material properties:

$$E_{11} = 17.237 \text{ GPa} (2500 \text{ ksi})$$

$$E_{22} = 6.895 \text{ GPa} (1000 \text{ ksi})$$

$$G_{12} = 2.930 \text{ GPa} (425 \text{ ksi})$$

$$\nu_{12} = 0.33$$

Buckling load:

$$P_{cr} = 83.4 \text{ kN} (18.8 \text{ kips})$$

Total of 2400 elements.

Fig. 6 Finite element model with buckled shape

A unit load is applied at each node on the loaded end of the column in a manner similar to that described in reference [8].

Table 1 Comparison of buckling loads in kN (kips)

Column height	$b_1 = 25.4 \text{ cm (10 in)}$ $b_3 = 2.54 \text{ cm (1 in)}$			$b_1 = 25.4 \text{ cm (10 in)}$ $b_3 = 5.08 \text{ cm (2 in)}$			$b_1 = 25.4 \text{ cm (10 in)}$ $b_3 = 7.62 \text{ cm (3 in)}$		
	FEM	CLOSED FORM	Diff (%)	FEM	CLOSED FORM	Diff (%)	FEM	CLOSED FORM	Diff (%)
0.76 m (30 in)	76.65 (17.23)	81.86 (18.40)	6.36	84.53 (19.00)	91.25 (20.51)	7.36	88.40 (19.87)	92.14 (20.71)	4.06
1.02 m (40 in)	76.03 (17.09)	79.46 (17.86)	4.31	84.08 (18.90)	88.93 (19.99)	5.45	86.98 (19.55)	91.07 (20.47)	4.49
1.27 m (50 in)	75.45 (16.96)	79.10 (17.78)	4.61	83.42 (18.75)	88.67 (19.93)	5.92	85.42 (19.20)	91.42 (20.55)	6.57

CONCLUSION

This paper presents a closed-form solution for the local buckling analysis of fiber-reinforced polymeric universal section column subjected to uniform compression edge loading. From the presented local buckling equation, the numerical results shown in graphical form for the practical range of cross sections and material properties are presented. As shown in the figure, if the plate width ratio (b_3/b_1) is increased, the buckling stress also increases. The buckling stress is the maximum at the range of $b_3/b_1 = 0.15 \sim 0.25$. When the width of outstanding portion of the universal section is increased, the buckling strength falls under that of basic rectangular box section. Therefore, it is adverse if the outstanding flange width is wider than one-third of the web depth.

To verify the solution presented in this study, also the graphical results of minimum buckling coefficient of isotropic, such as structural aluminum alloy, columns are obtained. They are identical to those reported by Bulson (1955)[6].

The finite element method is used to find the buckling load and buckled mode shape. The finite element analysis results differ by 4 to 8% from the closed-form solution. Thus, the finite element analysis results may be useful for both the prediction of local buckling loads and/or the preliminary design of FRP structural shapes under compression.

REFERENCES

1. MMFG, *Extern fiberglass structural shapes design manual*, Morrison Molded Fiberglass Company, Bristol, Virginia, 1988.
2. J. M. Whitney, *Structural analysis of laminated anisotropic plates*, Technomic Publishing Co. Inc., Lancaster, Pennsylvania, 1987.
3. S. J. Yoon, S.H. Chae, "Local buckling strength of rectangular compression members composed of orthotropic thin plate elements" *Journal of Civil Engineering, KSCE*, Vol. 18, No. I-2, 1998, pp.161-172.
4. P. S. Bulson, *The stability of flat plates*, American Elsevier Publishing Company Inc., New York, 1969.
5. S. P. Timoshenko and J.M. Gere, *Theory of elastic stability*, 2nd ed., McGraw-Hill Book Co., Inc., New York, 1961.
6. P. S. Bulson, "Local instability problems of light alloy struts", The Aluminum Development Association, *Research Report No. 29*, London, 1955.
7. GTSTRUDL, *GTSTRUDL user's manual*, Latest Revision, K. May, GTICS Systems Laboratory, Georgia Institute of Technology, Atlanta, Georgia. 1999.
8. S. J. Yoon, "Local buckling of pultruded I-shape columns", *Ph.D. Thesis*, Georgia Institute of Technology, Atlanta, Georgia, 1993.
9. S. J. Yoon, D. Scott, A. Zureick, "An experimental investigation of the behavior of concentrically loaded pultruded columns" *Proc., 1st Int. Conf. on Advanced Composite Materials in Bridges and Structures*, Quebec, Canada, 1992, pp.309-317.

CORRELATION BETWEEN DAMAGE BEHAVIOR AND ELECTRICAL RESISTANCE CHANGE IN CFRP AND CFGFRP COMPOSITES

D. Y Song¹, J. B. Park¹, T. Yamane¹, N. Takeda¹ and A. Kitano²

¹*Komaba Open Laboratory, The University of Tokyo*

*4-6-1 Komaba, Meguro-ku, Tokyo 153-8904, Japan : song@compmat.rcast.u-tokyo.ac.jp,
jbpark@compmat.rcast.u-tokyo.ac.jp, takeda@compmat.rcast.u-tokyo.ac.jp*

²*Composite Materials Research Lab., Toray Industries Inc.*

*1515 Ohazatsutsui, Matumae-cho, Iyo-kun, Ehime Prefecture, Japan : Akihiko-
Kitano@nts.toray.co.jp*

SUMMARY: This paper studies the correlation between the mechanical damage and the change of electrical resistance for unidirectional CFRP and CFGFRP (Carbon Fiber/Glass Fiber Reinforced Plastics) composites. This study is performed using experimental and numerical methods, and the results of two methods are compared. The change of electrical resistance is measured under the condition of simple tension and loading-unloading, and the failure process of two types of CFRP is investigated using an optical microscope. A Monte Carlo simulation is performed to predict the change in electrical resistance due to strain and damage (fracture) of carbon fibers. Through these works, it is revealed that the change of electrical resistance had a close relation with the damage process and there is a good agreement between experimental and predicted results.

KEYWORDS: CFRP, CFGFRP, carbon fiber, electrical resistance, failure behavior, Monte Carlo simulation

INTRODUCTION

The electrical resistance of conductive wires changes proportionally according to the change of cross section area and length. This means that the change in electrical resistance of conductive wire is affected by its mechanical deformation and damage. So, to understand the main reason of the change of electrical resistance in CFRP, which consists of conductive carbon fibers and non-conductive epoxy matrix, the damage accumulation mechanism should be considered seriously. According to the existing fracture theory of composite, the stress distribution of composites is significantly affected by fracture modes such as matrix-fiber interface debonding, fiber breakage and matrix crack. In this study, two types of carbon fibers with different electromechanical properties were selected. And simple tension and loading-unloading tests and failure progress observation using an optical microscope were carried out for CFRP and CFGFRP hybrid

composites. Moreover, using the shear-lag theory and Weibull distribution of fiber strength, a Monte Carlo simulation is performed for prediction of the change in electrical resistance due to strain and fiber fracture. The predicted results were compared with the experimental results in order to check the validity of the numerical model.

EXPERIMENT AND ANALYSIS

Test Materials and Experimental Procedure

Two types of carbon fiber (PAN based Torayca T700S and M46J of diameter 7 and 5 μ m, tensile strength 4.9 and 4.21GPa, Young's modulus 230.3 and 436.1GPa, ultimate elongation 2.1 and 1%, respectively) and E-glass fiber (diameter 13 μ m, tensile strength 1.47GPa, Young's modulus 76GPa) were used as raw materials for CFRP and CFGFRP composites. The electrical resistivity of T700S and M46J carbon fibers was 16.2 and 9.7 $\mu\Omega$ m, respectively. Composite laminates were fabricated by carbon and glass fibers and epoxy matrix (the curing conducted at 130°C and 3.92MPa for 2hrs). The electrodes for measuring electrical resistance of CFGFRP were prepared by inserting thin conductive wires between CFRP and GFRP prepreg sheets during layup process. The electrodes of CFRP were attached at the surface of the specimen. The dimensions of specimens were 160mm in length, 30mm in width (where, the thickness of CFGFRP and CFRP were 0.6–0.95mm and 0.1mm, respectively). The volume fractions of carbon fibers in the CFGFRP and CFRP were about 9–15 and 60%, respectively. Tensile tests were conducted at the crosshead speed of 0.5 mm/min. The electrical resistance was measured using two-probe DC method. A constant current of 1mA was applied on the composites, and the change in electrical resistance due to loading was plotted simultaneously with stress and strain.

Numerical Analysis

Monte Carlo simulation approach was used to evaluate quantitatively the correlation between mechanical damage and electrical resistance change in composites. For this analysis, the shear lag analysis method was used to calculate the stress distribution of composites. The simulation was carried out according to the following procedure: at first, the tensile strength of each fiber element was assigned using two-parameter Weibull distribution. Then, the nodal displacement of proposed model is calculated by finite difference method based on successive over relaxation algorithm for unit displacement, u_o (Fig.1). From this displacement, the tensile stress of fiber element and the shear stress of matrix element are obtained using the following Eq.1:

$$\sigma_{i,j} = E \frac{u_{i,j} - u_{i,j-1}}{\Delta x}, \quad \tau_{i,j} = G \frac{u_{i+1,j} \text{ (or } u_{i,j+1}) - u_{i,j}}{\Delta x} \quad (1)$$

Whether the fiber elements will break or not is determined by comparing their tensile stresses to the assigned fiber strengths, and the debonding behavior of matrix elements is reviewed by

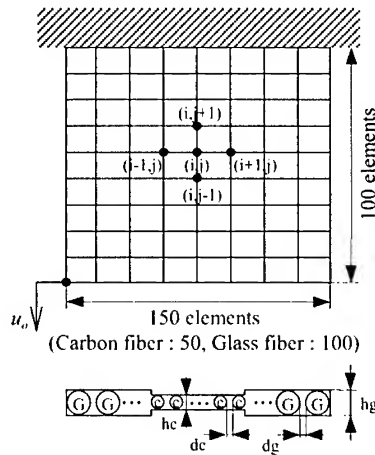


Fig.1 2-D analysis model for CFRP and CFGFRP composites

comparing their shear stresses to interfacial shear strengths. If debonding occurs between fiber and matrix, the fiber is assumed to slide on the matrix with a constant frictional stress [1]. Also, if there is the breakage in fiber and/or matrix elements, the nodal displacement is calculated again considering the change of the surrounding element and applying the state function (C_1 , C_2 and C_3) in Eq.2.

$$U_{i,j} = \frac{1}{C_1 + C_2 C_3 \Delta X^2} [U_{i,j-1} + U_{i,j+1} + C_2 \Delta X^2 (U_{i+1,j} + U_{i-1,j})] \quad (2)$$

where, $U_{i,j}$ is the dimensionless displacement ($U_{i,j} = u_{i,j} / \xi$, $\xi = \sqrt{(EAd/Gh)}$ [1]), and C_1 , C_2 and C_3 are the state functions which represent the fracture state of fiber and matrix elements. d is the distance between fibers, E and A are the modulus and cross-sectional area of the fibers. h is the thickness of the composite. G is the shear modulus of the matrix. $\Delta X = \Delta x / \xi$ is the dimensionless length (Δx : the length of a fiber element). These procedures are repeated until no new breakage occurs. If no new break occurs, the composite apparent stress and strain were determined. The relative change of the electrical resistance in the composite can be determined using Eq.3.

$$\frac{\Delta R}{R_0} = \frac{R - R_0}{R_0} = \frac{(1 + \epsilon)}{(1 - \nu \epsilon)^2} \frac{N}{(N - N_f)} - 1 \quad (3)$$

where, R is the electrical resistance of the fiber bundle with fractured fibers of N_f , N is the number of fibers, R_0 is the initial resistance of the fiber bundle, ϵ and ν are the strain and Poisson's ratio of fibers, respectively. These procedures were repeated until the stress drops, i.e. the fracture of composites.

RESULTS AND DISCUSSION

Relations of Stress/Strain and Change in Electrical Resistance/Strain

Figures 1 and 2 show the stress/strain and electrical resistance change/strain curves obtained from

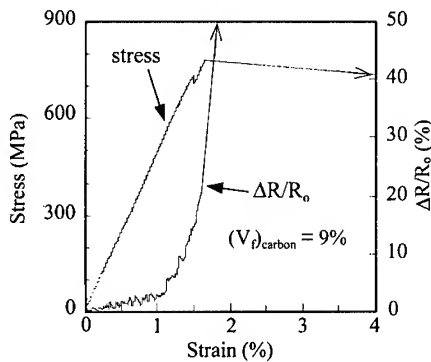


Fig. 1 Stress vs. strain, resistance vs. strain curve of CFGFRP-T700S

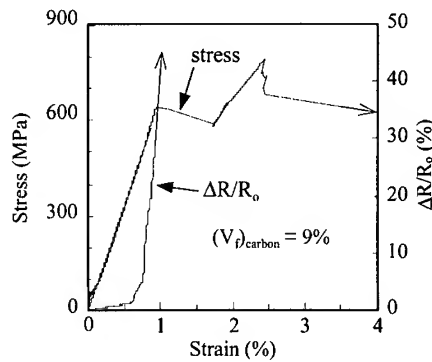


Fig. 2 Stress vs. strain, resistance vs. strain curve of CFGFRP-M46J

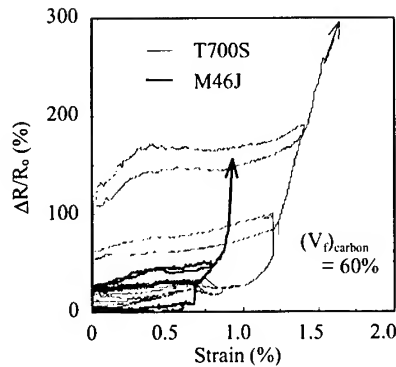


Fig. 3 The change in electrical resistance/strain under repeated loading and unloading : CFRP

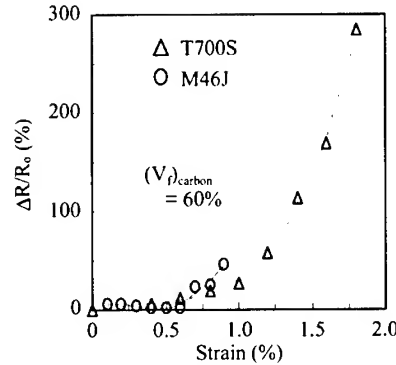


Fig. 4 The comparison of residual resistance change : CFRP

tensile tests of CFGFRP. For T700S, the stress increases linearly up to 1.5% strain, and then shows a sudden drop due to the failure at the interlayer between carbon and glass layers. After 1.7% strain when carbon fibers were fractured, the specimen supported stress up to about 4% strain owing to the presence of glass fibers. In the case of M46J, the stress decreases temporarily after the failure of carbon fiber layer but increases again until about 2.5% strain. At this time, the interfacial debonding and/or matrix cracks in glass fiber layers were hardly observed unlike as T700S. This seems to be due to the difference of the stress/strain behavior of M46J and T700S. On the other hand, the change in electrical resistance of T700S increases almost linearly up to about 1% strain. But after 1% strain the electrical resistance increases more steeply in non-linear shape, and increases extensively near 1.8% strain. This is attributed to the deformation, cracking and breakage of carbon fiber respectively [2-4]. For M46J, the entire tendency of electrical resistance is similar to T700S, but after linear increase of resistance, its change is more rapid than that of T700S. This difference of electrical resistance change seems to be related to the different failure mechanisms of T700S and M46J.

Figure 3 shows the electrical resistance/strain curves of CFRP lamina under repeated loading and unloading test. When the strain was removed, electrical resistance decreased, but did not return along the initial line and left some permanent change in electrical resistance. Figure 4 shows the increase of residual electrical resistance with the applied maximum strain. The residual electrical resistance of CFRP depended upon the maximum strain applied (this behavior was also identified for CFGFRP composites). This means that the change in the internal structure and the fractured number of carbon fibers owing to the applied loads affect the residual resistance of CFRP. These facts suggest that the CFRP and CFGFRP have the ability to memorize the maximum strain applied in the form of residual electrical resistance.

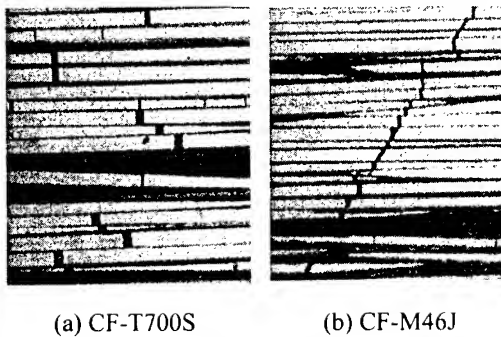


Fig. 5 Fracture appearances just before fracture

Optical Observation of Failure Process

Figure 5 shows the photos of fracture appearances observed on the surfaces of CFRP specimens just before failure. For CF-T700S, fiber breakage occurred randomly on the whole surface and fiber/matrix debondings were easily observed at the broken fiber ends. This is due to the shear stress concentrations generated by the fiber breakage. Pull-out fibers were significantly observed on the fractured section of the specimen and their lengths are relatively large. For CF-M46J, the initial crack occurred at the stress level nearly equal to that of CF-T700S, but this crack rapidly propagated across the specimen in connection with the breakage of neighboring fibers by subsequent loading. Furthermore, fiber/matrix debonding was hardly observed. The overall crack propagation path is almost straight and perpendicular to the load direction. This is probably due to the relatively strong adhesion of the fiber/matrix interface. Considering these results and the difference in the behavior of resistance change, there should be a close relation with failure process and electric resistance change.

Comparison between Simulation and Experimental Results

The input data and material constants used in the simulation are shown in Table 1. Figure 6 shows the comparison between the experiment and simulation for CFRP. There's reasonable agreement with the simulation and experimental results. And, Fig. 7 shows the simulation examples of stress/strain, fracture density of carbon fiber, and relative resistance change for CFGFRP. The electrical resistance in this example shows the same tendency to the experiment. It has the linear increase up to about 1.3% strain, more steep non-linear increase up to 1.8%, and drastic increase near fracture strain (see Fig. 1). Considering these results, it is possible to evaluate the damage state in the structure by comparing simulation results to the measured results during and after loading.

Table 1. Input data used in the simulation

Materials	Carbon fiber		Glass Fiber	Epoxy
	T700S	M46J		
Young's modulus of fiber, E(GPa)	230	436	76	3.5
Cross-sectional area of fiber, A(μm^2)	38.5	19.6	200.9	
Shear modulus of matrix, G(GPa)				1.3
Distance between fibers, d(μm)	2.16	1.55	7.50	
* Weibull scale parameter, σ_0 (GPa)	4.9	4.2	1.2	
* Weibull shape parameter, m	5.5	5.5	10	
* Interfacial shear strength, τ_i (MPa)				30
* Friction stress at interface, τ_f (MPa)				15
* Fiber element length, Δx (μm)	7	5	13	
Thickness of composite, h (μm)	23	23	23	

* These were assumed by considering Refs. [6-8]

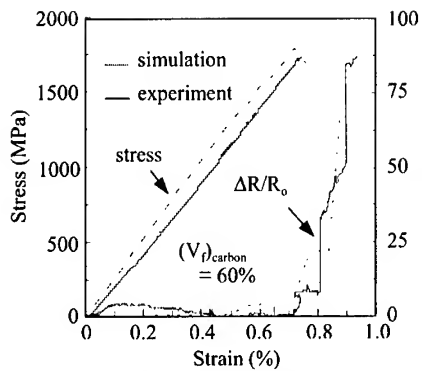


Fig. 6 Comparison of simulation and experimental result : CFRP -M46J

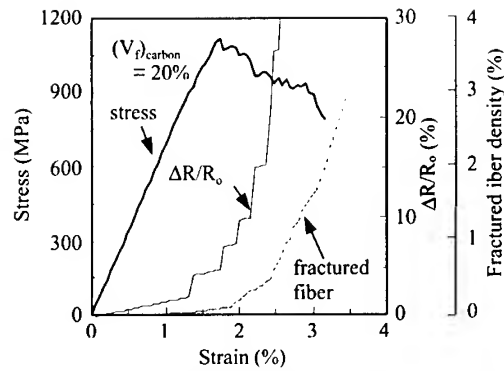


Fig. 7 A simulation example : CFGFRP - T700S

CONCLUSIONS

The relationship between the mechanical damage and the change in electrical resistance in CFRP and CFGFRP hybrid composites was experimentally investigated and numerically simulated. Test results revealed that the change in the electrical resistance was closely related with the failure mechanisms. The predicted results by a Monte Carlo simulation showed reasonable agreement with the experimental results. Therefore, by comparing the simulation results to the measured result of electrical resistance, it is possible to evaluate the damage state quantitatively during and after loading.

REFERENCES

1. J.Yuan et al, "A Note on the Monte Carlo Simulation of the Tensile Deformation and Failure Process of Unidirectional Composites", *Comp. Sci. Tech.*, Vol. 52, 1994, pp.197.
2. N. Muto et al., "Foreseeing of Fracture in CFGFRP Composites by Measuring Electrical Resistance", *J. Jpn. Soc. Compos. Mater.*, Vol 18, No.3, 1992, pp.144.
3. K.Schulte and H. Wittich, "The Electrical Response of Strained and/or Damaged Polymer Matrix Composites", *Proc. ICCM Vol.10*, 1995, pp.349.
4. X. Wang and D. D. L. Chung, "Eletromechanical Behavior of Carbon Fiber", *SPIE Conf. Vol. 3324*, 1998, pp.242.
5. H. Hukuda, "Monte Carlo Simulation of the Strength of Hybrid Composites", *J. Compo. Mater.*, Vol. 16, 1982, pp.371.
6. J.Aveston and J. M. Sillwood, "Synergistic Fibre Strengthening in hybrid Composites", *J. Mater. Sci.*, Vol. 11, 1976, pp.1877.
7. M. Shioya and A. Takaku, "Estimation of Fiber and Interfacial Shear Strength by using a Single-Fibre Composite", *Comp. Sci. Tech.*, Vol. 55, 1995, pp.33.
8. M. R'Mill et al, "Estimation of Weibull Parameters from Loose-Bundle Tests", *Comp. Sci. Tech.*, Vol. 56, 1996, pp.831.

Design and manufacture of a composite end effector for large LCD glass handling robots

Je Hoon Oh¹, Dai Gil Lee¹, and Hyun Surk Kim²

¹ *Department of Mechanical Engineering, ME3221, Korea Advanced Institute of Science and Technology, 373-1, Kusong-dong, Yusong-gu, Taejon 305-701, KOREA: dglee@kaist.ac.kr*

² *Meerae Engineering Corporation, 54-2, Mok-ri Dongtan-myon, Hwaseong-gun, Kyungki-do, 445-810, KOREA*

SUMMARY: In this work the end effector for robots that handle large LCD glass panels was designed and manufactured using carbon/epoxy composite and honeycomb. Box type sandwich structure was employed to reduce the shear effect arising from the low modulus of honeycomb. In order to determine the optimum structural shape of the composite robot end effector, a commercial finite element software, ANSYS was used along with an optimization routine when the end effector was subjected to both the self-weight and the weight of the LCD glass panel. Also, the static and dynamic characteristics of the composite robot end effector were measured and compared with those of the aluminum robot end effector.

KEYWORDS: LCD glass panel, End effector, Glass handling robot, Optimum design, Sandwich structure

INTRODUCTION

Industrial robots are increasingly employed in clean room environment semiconductor industries to eliminate contamination from human workers. As the size of glass panel, a part of LCD, increases, the payload and stiffness of robots are required to increase accordingly. Recently, the thickness of aluminum robot end effector for loading and unloading of large glass panels has been increased much to reduce the deflection caused by the weight of large glass panels. However, the thickness increase of the aluminum end effector requires large working space of glass panel storage cassettes, which reduces the number of panels loaded in one cassette and therefore, reduces the productivity. When the height of storage cassettes is increased to increase the number of glass panels to be loaded, the size of the robot should be also increased, which requires larger motors to give the same acceleration. Therefore, the design and manufacture of slim but stiff end effectors have become important as the size of glass panels increases.

Since composite materials have high specific stiffness, high specific strength, high damping and low coefficient of thermal expansion, they have been widely used in aircraft and spacecraft structures as well as in conventional structures such as drive shafts, machine tool spindles, guide rollers, and the nozzle dam for a steam generator [1-5]. The structure of a robot should have both high specific stiffness and high damping in order to increase positional

accuracy and dynamic performance. The specific modulus and damping capacity of carbon/epoxy composite materials are several times larger than those of conventional metals [6]. Therefore, the carbon/epoxy composite material is a promising material for the end effector that requires lightweight and high stiffness to minimize the deflection due to the self-weight and the weight of glass panels.

In this work, a light end effector that can be used for loading and unloading large glass panels, parts of LCD, was designed and manufactured using carbon/epoxy composite and honeycomb, in order to reduce the deflection due to self-weight of the end effector and weight of the glass panel without sacrificing stiffness of the end effector. The box type sandwich structure whose two side walls and top and bottom faces were reinforced, was employed to reduce the shear effect arising from the low modulus of honeycomb structure. In order to determine the optimum shape of the composite end effector, the finite element analysis in combination with an optimization routine was performed using ANSYS, a commercial finite element software, when the end effector was subjected to both the self-weight and the weight of the glass panel. Also, the static and dynamic characteristics of the composite robot end effector such as the static deflection, natural frequency and damping were measured and compared with those of a comparable aluminum robot end effector.

DESIGN OF THE COMPOSITE END EFFECTOR

Fig. 1 shows the typical robot system used for loading and unloading glass panels into a cassette. The robot that has three degrees of freedom (r , θ , and z), is composed of a base, arm, wrist block and end effector. The end effector for the single arm can be used directly for the dual arm because the configuration of end effector for the dual arm is the same as that of end effector for the single arm shown in Fig. 1. The end effector is mounted on the wrist block located at the end of the second arm using six bolts. Fig. 2 shows the configuration of composite end effector. Two vacuum chucks are located on the end effector to secure the glass panel on the end effector. The glass panel is loaded on the ten cone-shaped pins mounted on the end effector, to prevent the glass panel from being scratched by the surface of end effector. An infrared sensor is used to detect the existence of the glass panel on the end effector.

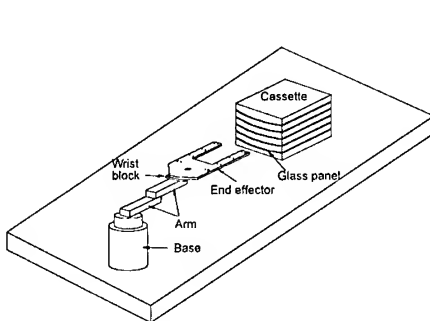


Fig. 1. Typical robot system for loading and unloading glass panels.

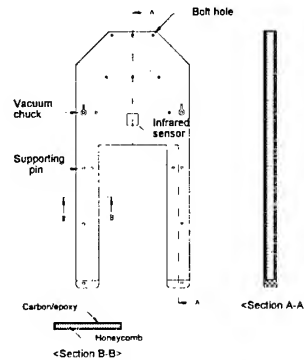


Fig. 2. Configuration of the composite end effector. (Sectional views are exaggerated for clarity.)

The total deflection δ_{total} of the end effector due to the weight of glass panel and the self-weight of the end effector is expressed as follows:

$$\delta_{total} = \delta_{panel} + \delta_{self-weight} \quad (1)$$

where δ_{panel} and $\delta_{self-weight}$ are deflections due to the weight of glass panel and self-weight, respectively. The total thickness Δ required by the end effector when the glass panel is loaded, is given by

$$\Delta = \delta_{total} + t_{end-effector} \quad (2)$$

where $t_{end-effector}$ is the thickness of the end effector. As the total thickness required by the end effector increases, the pitch between the stacked panels increases, which reduces the number of glass panels loaded in one cassette. Thus, the total thickness Δ required by the end effector must be minimized to improve productivity.

In order to reduce the total thickness Δ required by the end effector, not only the end effector should be slim but also have high bending stiffness with low weight. The sandwich structure composed of carbon/epoxy face material and Nomex honeycomb was employed for the end effector to increase bending stiffness and decrease self-weight. The sidewalls were reinforced to reduce the shear deformations arising from the low rigidity of honeycomb structure. The unidirectional carbon/epoxy prepreg and Nomex honeycomb used in this work were USN 125 and HRH-10-1/8-4.0 manufacture by Sunkyung Chemicals (Suwon, Korea) and Hexcel Composites (USA), respectively. The material properties used in this work are listed in Table 1.

Table 1 Mechanical properties of carbon/epoxy, honeycomb and glass panel

	Carbon /epoxy (USN125)	Honeycomb (HRH-10- 1/8-4.0)	Glass panel
E_1 (GPa)	128.0	-	57.5 ^a
E_2 (GPa)	8.0	-	57.5 ^a
G_{12} (GPa)	4.5	-	-
G_{23} (MPa)	-	32.4	-
G_{13} (MPa)	-	59.3	-
ν_{12}	0.30	-	0.2
X_T (MPa)	1900	-	-
Y_T (MPa)	60	-	-
S (MPa)	75	-	-
Density (kg/m ³)	1550	64	2440

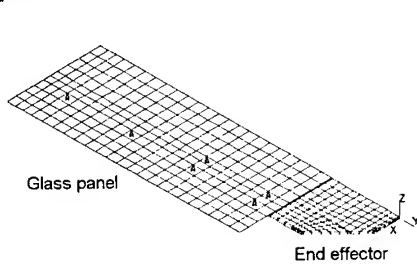
^a property measured by vibration test.

Table 2 Determined optimum design variables

Design variables	Values
Core thickness t_h (mm)	6.0
Face thickness t_c (mm)	2.0
Stacking angle ($\pm \theta$)	14.5
Length l_1 (mm)	1010.0
Length l_2 (mm)	440.5
Width w_1 (mm)	90.0
Width w_2 (mm)	135.0
Width w_3 (mm)	90.0

The stacking angle, thickness of the face and core, and dimensions of the end effector were determined through finite element analyses along with optimization routine. During analyses of the end effector, only a half of the end effector was modeled due to its symmetry. The holes for bolts and supporting pins were not modeled in detail to keep the finite element model simple. The face, the core and the loaded glass panel were modeled using multi-layered 8-node shell elements, 20-node quadrilateral solid elements and 8-node structural shell elements, respectively. Since the stacking angle and ply thickness can be assigned in the

multi-layered shell element of ANSYS 5.3, it is suitable for modeling of composite material. Fig. 3 shows the finite element model used for the analysis. As shown in Fig. 3, the nodes on the end effector located at the supporting pin positions were coupled in the z direction with the corresponding nodes on the glass panel. For the boundary condition, all the displacements of nodes corresponding to the location of bolts were fixed and the gravitational acceleration was applied to both the end effector and the loaded glass panel.



The symbol \bullet represents node coupling positions

Fig. 3. Finite element model used for the analysis.

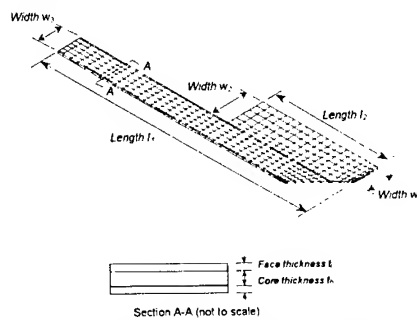


Fig. 4. Geometric design variables.

The design optimization module within ANSYS 5.3 was used to optimize the end effector. The optimization module minimized the total thickness Δ required by the end effector with glass panel when the design was subjected to constraints imposed on the design variables. The selected design variables for the optimization were the thickness of the honeycomb for the core (t_h), thickness of the carbon/epoxy for the faces (t_c), stacking angle of the carbon/epoxy ($\pm \theta$), length l_1 , length l_2 , width w_1 , width w_2 , and width w_3 . Fig. 4 shows the geometric design variables used in the analysis. The optimization technique used in the analysis was the subproblem approximation method and the first order method offered by the optimization module of ANSYS. From the results of the optimization, the optimum design variables were determined as shown in Table 2.

Although the structural failure by the applied loads seldom occurs in the stiffness-designed structure including the end effector, the failure index was also calculated using Tsai-Wu failure criterion to investigate the possibility of failure. The calculated maximum failure index was 0.02, which occurred near the bolted region.

MANUFACTURE OF THE COMPOSITE END EFFECTOR

The composite end effector was manufactured using the prepreg lay-up method and autoclave vacuum bag degassing process. In order to prevent the thermal deformation due to temperature difference, the symmetric stacking sequence was employed in the manufacturing process. Fig. 5 shows the manufacturing sequence for the end effector. First, the top and bottom faces were manufactured with stacking sequence of $[\pm \theta]_s$. As shown in Fig. 5(a), the two sidewalls of bottom face were also reinforced to reduce shear effects arising from the low modulus of honeycomb. The core was fabricated by bonding the carbon/epoxy face to the 6mm Nomex honeycomb using film adhesive as shown in Fig. 5(b). Then the prepreg tailored to the appropriate size was wrapped on the core as shown in Fig. 5(c). In order to spread the seam line through the surface, the core was turned upside down in every step of stacking.

After curing the end effector, two edges and six holes for bolts were machined using a diamond-cutting wheel and a tungsten carbide drill, respectively. The machined areas were filled with nylon edge closures. The total stacking sequence of the composite end effector was

$\left[\left\{ \left(\theta / -\theta / -\theta / \theta \right)_{2T} \right\}_S / C_{48} / \left\{ \left(-\theta / \theta / \theta / -\theta \right)_{2T} \right\}_T \right]$. Fig. 6 shows the manufactured composite end effector before machining. The aluminum end effector that had the same dimensions as the composite end effector was also manufactured to compare the static and dynamic characteristics with those of the composite end effector. The weight of the composite end effector was 21.5N, while the aluminum end effector weighed 43.6N. Therefore, the composite end effector had only 49% weight of the aluminum end effector.

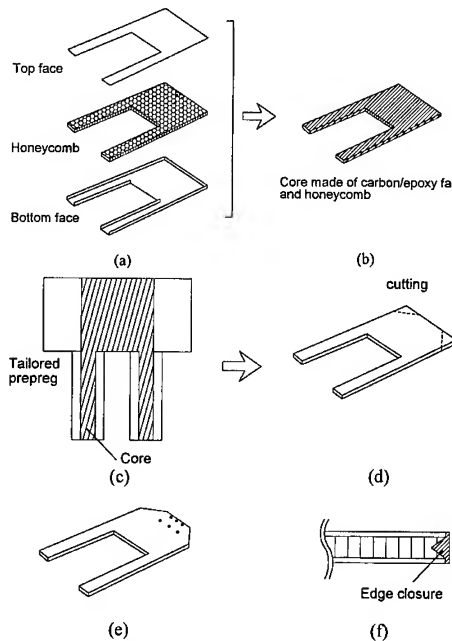


Fig. 5. Schematic diagram of the manufacturing sequence for the composite end effector.

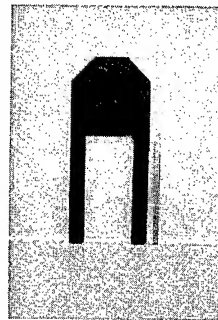


Fig. 6. Photograph of the composite end effector. (Right bar is a 600mm long scale)

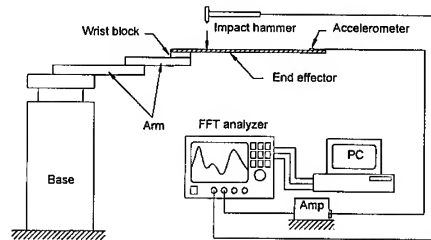


Fig. 7. Schematic diagram of the experimental set-up for vibration test

STATIC AND DYNAMIC CHARACTERISTICS OF THE COMPOSITE END EFFECTOR

The static and dynamic tests of the end effectors were performed to compare the characteristics of the composite end effector with those of the aluminum end effector. In order to measure the static deflection due to both the self-weight and the weight of glass panel, the composite and aluminum end effector were placed on the precision surface plate and the deflection was measured by a dial gauge. In case of the composite end effector, the static deflection due to the self-weight and the total deflection were 1.55mm and 2.52mm, respectively, whereas, in case of the aluminum end effector, those were 3.06mm and 4.87mm, respectively. The static stiffness of the composite end effector was 95% higher than that of the aluminum end effector.

The dynamic characteristics of the composite and the aluminum end effectors were measured by giving an impulse at the top surface of the end effector after assembling the end effector into the robot. The vibration signal measured by an accelerometer (B&K 4374) at the end of the end effector was processed by a FFT signal analyzer (B&K 2032) to get frequency response. Fig. 7 shows the schematic diagram of vibration test and Fig. 8 shows the frequency

response of the composite and the aluminum end effectors. The natural frequencies and damping ratios of the composite end effector at the first and second modes were 14.9 Hz, 20.0 Hz and 0.032, 0.031, respectively, whereas those of the aluminum end effector were 10.2 Hz, 16.8 Hz and 0.0088, 0.0060, respectively. From the experimental results, it was found that the fundamental natural frequency and damping ratio of the composite end effector were 1.5 and 3.6 times, respectively, compared with those of the aluminum end effector.

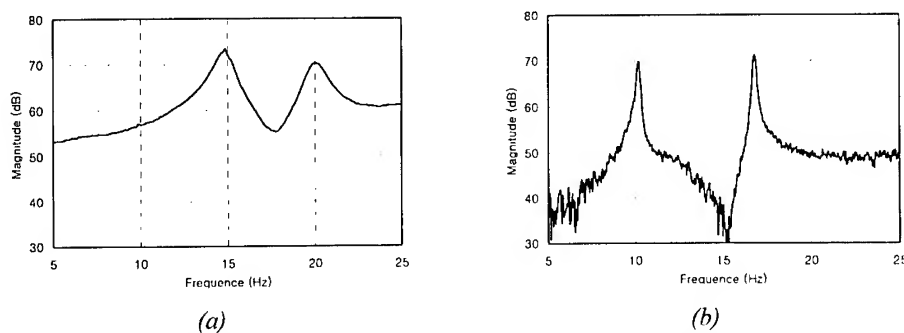


Fig. 8. Impulse frequency responses of (a) the composite end effector and (b) the aluminum end effector.

CONCLUSIONS

In this work, a composite end effector for manipulating large LCD glass panels was developed using carbon/epoxy composite material and honeycomb. Finite element analysis was used along with the optimization routine to design the composite end effector. The manufactured composite end effector had only 49% weight of the aluminum end effector. From the static and dynamic tests, it was found that the static stiffness of the composite end effector was 95% higher than that of the aluminum end effector, and the fundamental natural frequency and damping ratio of the composite end effector were 1.5 and 3.6 times higher, respectively, compared with those of the aluminum end effector.

REFERENCES

1. J. H. Oh, Y. G. Kim and D. G. Lee, "Optimum bolted joints for hybrid composite materials," *Composite Structures*, Vol. 38, 1997, pp.329-341.
2. D. H. Cho, D. G. Lee and J. H. Choi, "Manufacture of one-piece automotive drive shafts with aluminum and composite materials," *Composite Structures*, Vol. 38, 1997, pp.309-319.
3. D. G. Lee, H. C. Sin and N. P. Suh, "Manufacturing of a graphite epoxy composite spindle for a machine tool," *Annals CIRP*, Vol. 27, 1985, pp.365-369.
4. K. G. Bang, J. K. Choi, H. S. Kim and D. G. Lee, "Development of guide rollers using electroplated carbon fiber-epoxy composite for thin polymer film processing," *Composite Structures*, Vol. 38, 1997, pp.321-328.
5. J. H. Oh, D. G. Lee and T. R. Kim, "Composite nozzle dam in the steam generator of a nuclear reactor," *Composite Structures*, Vol. 38, 1997, pp.203-213.
6. C. Reugg and J. Habermair, "Composite propeller shafts design and optimization," *3rd International Conference on Composite Materials, Advanced Composite Materials*, Vol. 2, 1980, pp.1740-1755.

TEMPERATURE EFFECT ON IMPACT RESPONSES OF CARBON FIBRE/EPOXY COMPOSITE LAMINATES

M.S. Sohn¹, X.Z. Hu¹ & J.K. Kim²

¹ Department of Mechanical and Materials Engineering, The University of Western Australia,
Nedlands, 6907, WA, Australia: min@mech.uwa.edu.au and xhu@mech.uwa.edu.au

² Department of Mechanical Engineering,
The Hong Kong University of Science and Technology,
Clear Water Bay, Kowloon, Hong Kong: mejkkim@ust.hk

SUMMARY: Instrumented impact tests have been performed to study the impact responses of carbon fibre/epoxy composite laminates at the following temperatures; -60°C, room temperature, 90°C and 130°C. The composite laminates contained short Kevlar fibres that were reinforced between the continuous carbon fibre layers. A digital camera was used to record impact-induced damage on the front and back faces of impact. Load-time history diagrams were used to assess the impact damage resistance, while cross-sectional fractographs were used to quantitatively evaluate the sub-surface delamination area. The result shows that the short Kevlar fibre reinforcement contributed considerably to the improvement in delamination resistance of laminates.

KEY WORDS: carbon fibre composite, epoxy matrix, short Kevlar fibre reinforcement, impact damage resistance, cross-sectional fractography, temperature effect.

INTRODUCTION

Thermoset matrix materials (e.g., epoxy, polyester) used in fibre-reinforced composite laminates have distinct advantages over conventional metal alloys, such as the effective cost, easy shapability and high chemical resistance. It, however, is well known that the resistance to plastic deformation and fracture toughness of these matrix materials vary depending on temperature and strain rate due to their viscoelastic natures. Quasi-static mode-I and -II interlaminar fracture toughnesses, G_{Ic} and G_{IIc} , respectively, have been shown to increase with increasing temperature in the range from -60°C to 120°C for carbon fibre composites with different types of matrix [1,2]. The impact damage property of composite laminates is also influenced by temperature [3].

The effects of temperature and moisture on the ductility of epoxy resin and the damage size of carbon fibre composite laminates were studied [4]. It is shown that the resin ductility and the damage size increased with the increase of temperature. However, when the composites were made with a rubber modified resin, a reversed behaviour was observed due to the additional energy-absorption mechanisms associated with the modified resin [5]. Both the incipient energy and the damage size were reduced with increasing temperature.

The current investigation aims at understanding the effect of temperature on low-velocity impact responses and damage mechanisms of the carbon fibre/epoxy composite laminates with and without short Kevlar fibre reinforcement introduced between the continuous carbon fibre layers.

MATERIALS AND EXPERIMENTS

NCT301 carbon fiber/epoxy prepregs (supplied by Newport Adhesives and Composites) were used to prepare the composite laminate specimens. The prepreg cloth has the weight per area of 300 g/m^2 and consists of 48k yarns. The fibre volume percentage of the prepreg before curing was about 65%. Ten-ply composite laminates were prepared by hand-lay up with a stacking sequence of $[0/90]_5$. During the lay-up process, short Kevlar fibres of 15 mm in length with two different weight fractions of 0.8 wt % and 0.4 wt % were introduced on one side of each prepreg layer. The composites were cured following the manufacturer's instruction based on the compression moulding technique. The composite laminates were then cut into the final size of $100 \times 100 \text{ mm}^2$.

Low-energy impact tests were conducted on a Dynatup 8250 drop-weight impact machine. An impact load was applied onto the centre of specimen with a test window 75 mm in diameter using an impactor having a hemispherical nose of 12.7 mm in diameter. Two different impact energies, 15J and 20J, were used at four different temperatures; -60°C , room temperature (RT), 90°C and 130°C .

IMPACT RESPONSES DUE TO TEMPERATURE EFFECT

The load-time (P-t) diagrams were obtained from the instrumented impact machine. Figure 1 shows the P-t diagrams obtained at different temperatures at an impact energy of 15J for the composite laminates without and with Kevlar fibres of 15 mm in length at 0.8 wt %. It is noted that the curves obtained at 20J were similar to those at 15J. The total impact response time was quite consistent for all composite laminates between 6.3 and 6.7 msec. It is interesting to note that the load drops in the rising portion of the curve became less prominent with increasing temperature for all composites studied. The ratios of absorbed energy over the total impact energy were in the range from 0.43 to 0.55 without any particular trend regardless of whether the composites contained short Kevlar fibres or not.

The incipient load, P_i , and the peak load, P_m , taken from the P-t diagrams are plotted as a function of temperature as shown in Figs. 2 and 3. The P_i and P_m values obtained at 20J were in general higher than those obtained at 15J. The P_i values were approximately constant between -60°C and 90°C and dropped significantly at 130°C , confirming the result of a previous study [3]. This temperature is equivalent to the prepreg cure temperature recommended by the manufacturer. The P_m values are shown in the same trend as the P_i results. The above observation is a reflection of degradation of the matrix mechanical properties at an elevated temperature due to the viscoelastic behaviour of the epoxy resin.

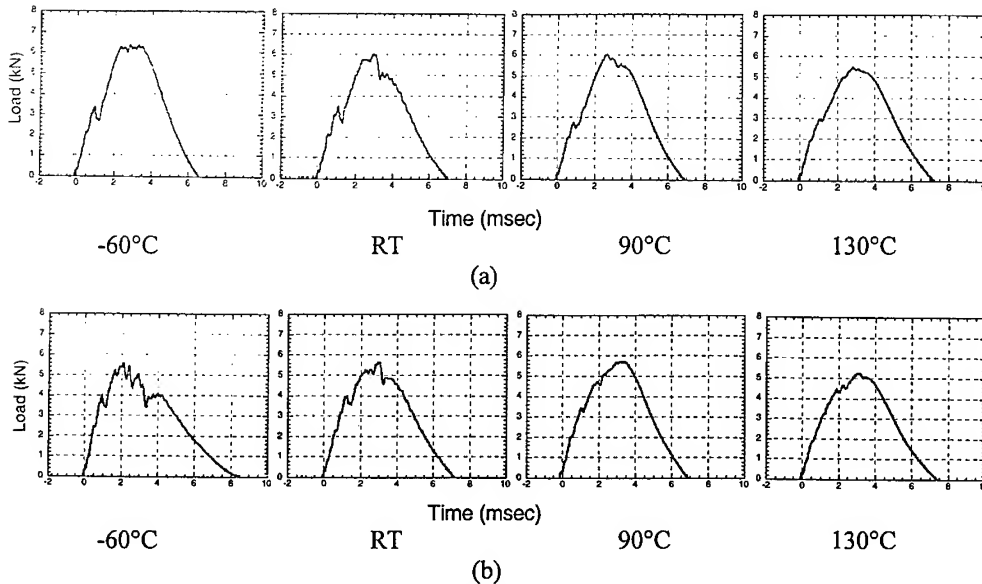


Fig. 1. Load-time diagrams of carbon fibre/epoxy composite laminates impacted at 15J; (a) without and (b) with interlayers containing Kevlar fibres of 0.8 wt% and 15 mm in length.

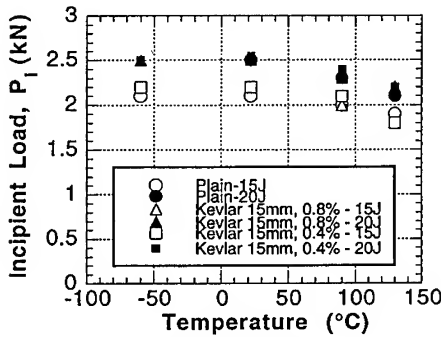


Fig.2. P_i vs. Temperature.

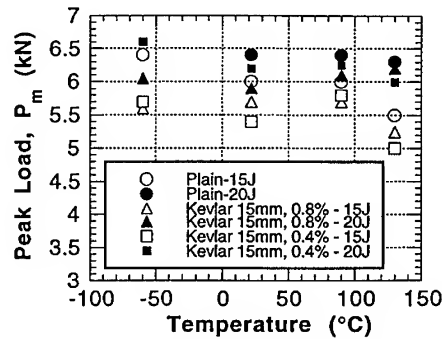


Fig.3. P_m vs. Temperature.

DAMAGE ASSESSMENT

Surface Damage Assessment

The front and back faces of the composite specimens after impact were examined. Figure 4 shows the photographs of the front and back faces of typical specimens containing Kevlar fibres. The extent of damage produced at the front face varied with temperature. The composites impacted at -60°C showed an indent with some fractured fibres within the indent crater (Fig. 4(a)), while those impacted at 130°C exhibited a major crack running in the transverse direction with some splitting along the fibre axis of top layer (Fig. 4(b)). The extent and shape of damage produced at RT and 90°C were intermediate between the above two extremes occurred at -60°C and 130°C .

The damage exhibited at the back face was push-out type fracture [6]. As shown in Fig. 4(c) and (d), the damage became less extensive with the increase of temperature. The damage produced at -60°C contained extensive delaminations and distinct fibre/matrix splitting along the fibre axis of bottom layer. The damage created at 130°C was much smaller in size than that at -60°C . The large damage size at a low temperature is mainly attributed to the brittleness of epoxy resin promoted by the low temperature. Therefore, the impact load can be transferred through the thickness of laminates more efficiently than for a ductile matrix. On the other hand, the high ductility of matrix at an elevated temperature led to more fracture on the front face of impact than that on the back face. The matrix material in a rubbery state above T_g absorbed the rest of the impact energy. The upward movement of the fibres on the top ply, as shown in Fig. 4(b), is a damage pattern explaining the increased ductility of the epoxy matrix material.

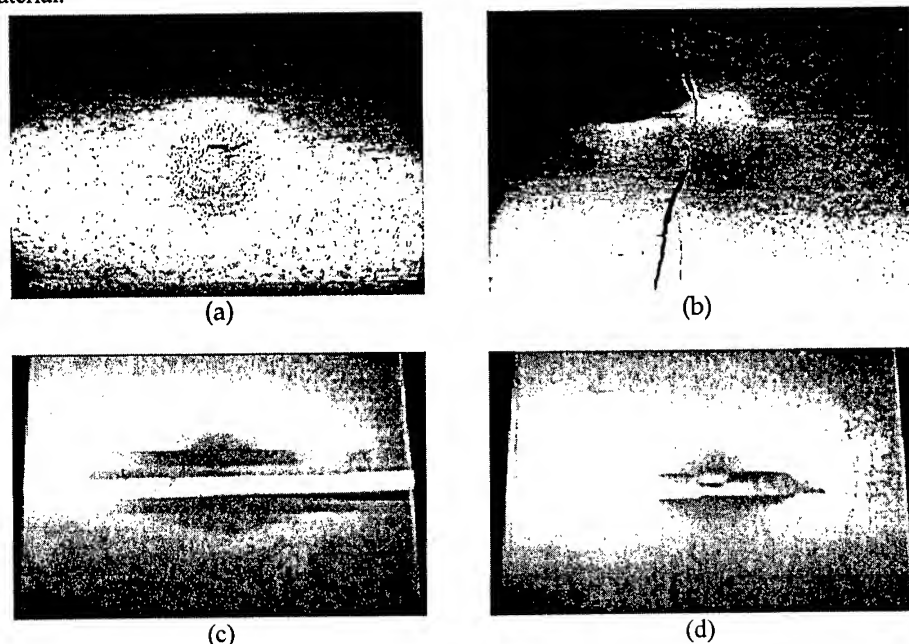


Figure 4. Damage patterns produced at front and back faces of the composites with 0.8 wt% Kevlar fibres of 15 mm in length: (a) front face of impact (-60°C); (b) front face (130°C); (c) back face (-60°C) and (d) back face (130°C);.

Cross-Sectional Fractography

Cross-sectional fractography was performed to measure the delaminated areas produced at the individual laminar interfaces of the composites impacted at 20J. The specimens were sectioned through the impact region by about 1.5 mm in width. The edges of specimens were polished down to $1\text{ }\mu\text{m}$ using a diamond paste. The optical microscope equipped with a micro-size scale was used to measure the delamination size at each interface. Table 1 shows the total delaminated areas measured for different temperatures. The control specimens presented the largest delamination areas for all temperatures studied, without showing a particular trend over the temperature range. The delamination areas of the composites containing interlayers were much smaller than those for the control, and decreased with increasing the temperature. This trend is closely related to the delamination area formed at the

bottom (9th) interface, as shown in Table 2, which was the largest portion of the total delaminated area.

Table 1. Total delaminated area (mm²) measured by cross-sectional fractography.

	plain	Kevlar 15mm, 0.8 wt %	Kevlar 15mm, 0.4 wt %
-60°C	-	2528	2888
R.T.	2654	1707	1878
90°C	3796	2008	1832
130°C	2480	1488	1180

Table 2. Delaminated area (mm²) at bottom interface.

	plain	Kevlar 15mm, 0.8 wt %	Kevlar 15mm, 0.4 wt %
-60°C	-	920	920
R.T.	917	733	884
90°C	896	704	448
130°C	600	420	440

Short Kevlar fibres are known to be effective to resist delamination in composites[7]. It promotes crack bridging between the adjacent plies of the laminate under quasi-static loading conditions and increase impact energy absorbing capability. This is the main mechanism to resist delamination fracture during impact. Physical properties and failure mechanisms of Kevlar 49 used in this study are known not to be affected by the temperature in the range from -60°C to 130°C [8].

The scanning electron micrograph shown in Fig. 6 depicts the typical Kevlar fibre fracture produced at RT under impact energy of 25J. The longitudinal splitting of fiber surface and peel-off as well as fine fibrillation took place during impact, as often found under quasi-static loading. The failure mechanisms of Kevlar fibre supports the additional energy absorption mechanism in the carbon fibre composite during impact.



Figure 6. Kevlar fracture under impact energy of 25J at room temperature.

SUMMARY

The low-velocity impact responses of the carbon fibre/epoxy composite laminates without and with short Kevlar fibres have been investigated at a range of temperatures between -60°C and 130°C . The total delamination area of the control laminate is much larger than that of the composite with interleaves. The damage area for the composite with interleaves decreases with increasing temperature.

The extent of damage on the front and back faces of impact produced at different temperatures appears to be considerably distinct due mainly to the viscoelastic nature of epoxy resin matrix. The composites impacted at -60°C showed an indent with limited fibre fracture, whereas those impacted at 130°C exhibited a major crack running transversely along with significant fibre splitting along the fibre axis of top layer.

ACKNOWLEDGEMENT

The authors thank the Australian Research Council (ARC) for continuous support of this project through the ARC Postdoctoral Research Fellowship of the first author (MSS). MSS was a visiting scholar to Hong Kong University of Science & Technology when the impact experiments were carried out.

REFERENCES

1. P. Davies and M.L. Benzeggagh, "Interlaminar mode-I fracture testing", In Applications of Fracture Mechanics to Composite Materials, ed. K. Friedrich, Elsevier Science, Amsterdam, 1989, pp.81-112.
2. P.J. Hines, B. Brew, R.A. Duckett and I.M. Ward, "Failure mechanisms in carbon fibre-reinforced poly(ether sulphone), Comp. Sci. & Tech. 43, 1992, pp. 37-47.
3. Y. Hirai, H. Hiroyuki and J.K. Kim, "Impact response of woven glass-fabric composites – II. Effect of temperature" Comp. Sci. & Tech. 58, 1998, pp.119-128.
4. M.L. Karasek, L.H. Strait, M.F. Amateau and J.P. Runt, "Effect of temperature and moisture on the impact damage", J. Compos. Technol. Res. 17, 1995, 11-16.
5. J.K. Kim, C. Baillie, J. Poe and Y.W. Mai, "Fracture toughness of CFRP with modified epoxy matrices", Comp. Sci. Tech. 43, 1992, 283-297.
6. K.J. Bowles, "The correlation of low-velocity impact resistance of graphite fibre reinforced composites with matrix properties", Composite Materials: Testing and Design (8th Conference), ASTM STP 972, Philadelphia, 1988, pp. 124-142.
7. M.S. Sohn and X.Z. Hu, "Comparative study of dynamic and static delamination behaviour of carbon fibre/epoxy composite laminates", Composites 26, 1995, pp.849-858.
8. R.J. Morgan, C.O. Pruneda and W.J. Steele, "The relationship between the physical structure and the microscopic deformation and failure processes of poly(p-phenylene terephthalamide) fibres", J. Polym. Sci.: Polym. Phys. Ed., 21, 1983, 1757-1783.

SMC / RTM

EFFECT OF BOUNDARY CONDITION TYPE ON MOLD FILLING IN RTM PROCESS

A. Shojaei¹, S. R. Ghaffarian¹ and S. M. H. Karimian²

¹*Polymer Engineering Department, Amirkabir University of Technology, P. O. Box
15875-4413, Tehran, Iran: S7432942@cic.aku.ac.ir*

²*Aerospace Engineering Department, Amirkabir University of Technology, P. O. Box
15875-4413, Tehran, Iran*

SUMMARY: The boundary condition (BC) type influences the RTM process parameters such as mold filling time and pressure distribution inside the mold. Major goal of this study is to highlight the BC effects on process cycle and process parameters. Numerical simulation of mold filling showed that mold filling time with specified pressure is less than that of specified flow rate BC. Application of partial vacuum at flow front reduces mold filling time for specified inlet pressure BC, and reduces pressure build up for specified flow rate BC. Also, a change in inlet BC from specified flow rate to certain pressure during mold filling affects the filling time.

KEYWORDS: inlet boundary condition, specified flow rate, specified pressure, flow front boundary condition, vacuum level, boundary condition transition.

INTRODUCTION

RTM is a complex process which involves various parameters in designing process cycles. Optimization of process parameters such as inlet pressure, inlet flow rate, inlet resin temperature, mold wall temperature, reaction kinetics, vent and gate location, etc. are very important and can help designer to obtain low cost process, high performance product, and rapid process, specially for high volume production. Optimization of these parameters through experiment will be costly and time consuming. Modeling and simulation of the process can have a major role in reduction of such experiments. In this respect, research works in the simulation of the RTM process have been very active in recent years and different simulation softwares have been developed [1,2].

Proper choice of boundary conditions (BCs) such as inlet, flow front, mold wall BCs, etc. can influence the process cycle parameters. Primary goal of this article is the study of BC effects on RTM process during mold filling. For this, effect of inlet and flow front BCs on pressure distribution inside the mold during mold filling, and filling time are investigated through the numerical simulation. Constant flow rate, constant pressure and combination of them are considered as inlet BC. Also, effect of vacuum level is investigated as flow front BC on pressure distribution and mold filling time. Although, we are carrying out simulation of 3-D and nonisothermal systems, to highlight the importance of BC on process cycle in RTM for the time being, results of simplified flow will be discussed.

FLOW MODELING

In modeling of mold filling in RTM, several assumptions should be made to simplify the problem. These include, negligible fiber deformation, negligible capillary effect, no inertia effects due to low Reynolds number, Newtonian fluid and etc. Under these situations Darcy's law can be used as a governing momentum equation for mold filling as follows [1]:

$$\vec{v} = -\frac{k}{\mu} \frac{dp}{dx} \quad (1)$$

where k , μ , p , and \vec{v} are permeability, viscosity, pressure, and x-component of superficial velocity vector, respectively. $\frac{d\vec{v}}{dx}$ is the continuity equation for incompressible fluid in 1-D.

CONTROL VOLUME APPROACH AND NUMERICAL FORMULATION

The entire domain of the mold is discretized to a specified number finite elements. Each finite element is divided into two sub-control volumes with equal sizes, i.e. divided from its middle. (Fig. 1)

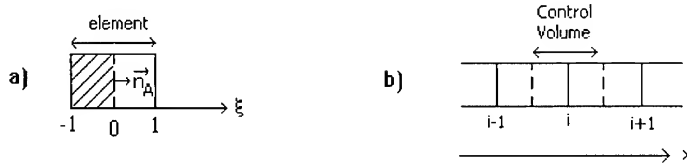


Fig. 1(a) sub-control volume in an element in local coordinate
(b) control volume in linear elements

Using linear shape functions, pressure is approximated within the element as:

$$p = p_1 N_1 + p_2 N_2 \quad (2)$$

$$N_1^e = \frac{1}{2} - \frac{\xi}{2} \quad N_2^e = \frac{1}{2} + \frac{\xi}{2} \quad \xi = \frac{2x - (x_i + x_j)}{x_j - x_i} \quad (3)$$

where p_i is nodal pressure, and N_i^e is the element shape function in local coordinate. Subscripts i and j denote the first and second nodes for an element in global coordinate. Integration of continuity equation over a control volume and using the divergence theorem and Darcy's law [1], we have:

$$\iint_s \frac{1}{\mu} [n_x] k \frac{dp}{dx} ds = 0 \quad (4)$$

where n_x is the x component of unit vector normal to the surface of control volume. Derivative of pressure with respect to the global coordinate is derived using the chain rule and the shape functions. Substituting derivatives of pressure into Eqn 4 yields

$$\iint_s \frac{1}{\mu} [n_x] k \frac{1}{x_j - x_i} < 1 \quad -1 > \left[\frac{p_1}{p_2} \right] ds = 0 \quad (5)$$

By considering constant cross sectional area for the mold, Eqn 5 for a control volume is converted to the following form.

$$\frac{1}{x_{i+1} - x_i} p_{i+1} - \left(\frac{1}{x_i - x_{i-1}} + \frac{1}{x_{i+1} - x_i} \right) p_i + \frac{1}{x_i - x_{i-1}} p_{i-1} = 0 \quad (6)$$

where the variables in this equation have already been defined. Eqn 6 is basically the mass balance equation for a control volume (i) in 1-D flow. This equation which is applied to all control volumes in solution domain results in a system of equations. This system of equations is solved using a tri-diagonal solver.

BOUNDARY CONDITIONS

There are two boundary conditions for the 1-D flow. One is the flow front and the other is at the inlet gate. Boundary conditions at the inlet gate are: i) specified pressure and ii) specified flow rate. In practical situation, if one starts with constant flow rate BC, after a certain time, inlet boundary condition may change to specified pressure due to pressure build up at the inlet [3]. At the flow front, we use both atmospheric pressure, and partially vacuum.

RESULTS

In this study, the filling of the 1-D mold shown in Fig. 2 will be simulated at various boundary conditions.

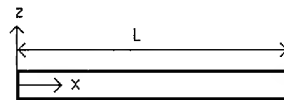


Fig. 2 Mold geometry

Typical values of the processing and material parameters for RTM are taken from the literature and are given in Table 1.

Table 1 Typical values for RTM process from the literature [1,3,4]

Variable	value
k	10^{-9} m^2
μ	0.45 Pa.s
v	$> 0.0001 \text{ m/s}$
L	1 m

To verify the accuracy of the numerical results to calculate the mold filling, we used analytical solution to calculate mold filling time (t_f) for the case of 1-D flow having both BC of specified flow rate ($t_f = L/v$) and specified pressure at the inlet ($t_f = \mu L^2 / 2 p_0 k$) from the literature [3], where t_f is the mold filling time, p_0 is the inlet pressure and the other variables have the usual definition. Table 2 shows good agreement between numerical and analytical results.

Table 2 Comparison of numerical and analytical t_f

Inlet BC	Analytical t_f (Sec)	Numerical t_f (Sec)	
		N.E. = 50	N.E. = 100
Specified flow rate; $v = 0.001 \text{ m/s}$	1000	990	995
Specified pressure; $P_0 = 4.5 \text{ bar}$	500	519.8	509.9

*N.E.= Number of Elements

Pressure distribution inside the mold at different filling steps (t_f) and mold filling time (t_f) are shown in Fig. 4 and Fig. 5 for specified flow rate BC and specified pressure BC at the inlet, respectively. As shown in Fig. 3 and Fig. 4, the pressure inside the mold is built up with the specified flow rate BC. Fig. 5 shows pressure distribution at different filling steps and mold filling time of specified pressure BC at the inlet for the two cases of inlet pressure. In Fig. 5-a, pressure at the inlet is the same as final maximum pressure (4.5 bar) at the end of mold filling for specified flow rate BC (Fig. 4). In the second case (Fig. 5-b) inlet pressure was chosen as which mold filling time is almost the same as specified flow rate BC ($t_f=995 \text{ sec}$). Comparison among these results show that filling time in the specified pressure at the inlet is less than the specified flow rate BC. On the other hand, if we need lower pressure at the inlet at a certain filling time, the specified pressure BC is the best choice.

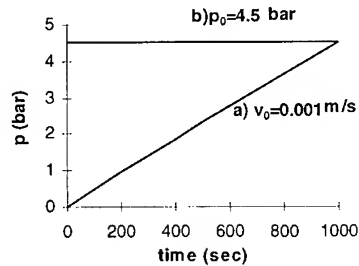
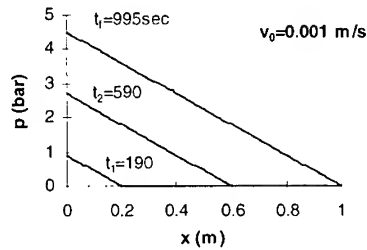
Fig. 3 Pressure build up at the inlet
a) Specified flow rate b) Specified pressure

Fig. 4 Pressure distribution with specified flow rate at different filling steps

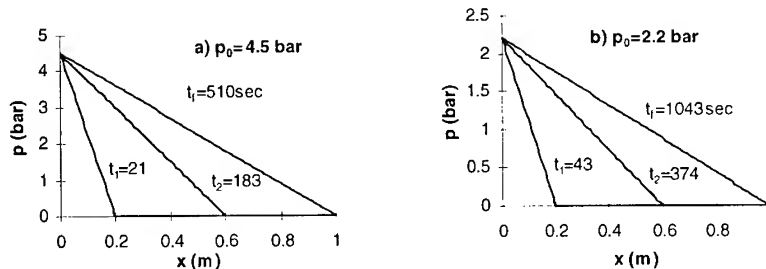


Fig. 5 Pressure distribution with specified pressure BC at different filling steps

In Fig. 6 pressure distribution at the end of mold filling for specified flow rate BC and vacuum level at the flow front have been shown. Using of partially vacuum at the flow front, mold filling time with specified flow rate BC doesn't change with respect to atmospheric pressure at the flow front, while as shown in the figure, pressure build up is reduced. Pressure build up reduction depends on vacuum level. Fig. 7 shows pressure distribution at the end of

mold filling for specified pressure BC and vacuum level at the flow front. In this case, mold filling time is reduced but reduction amount depends on inlet pressure and vacuum level.

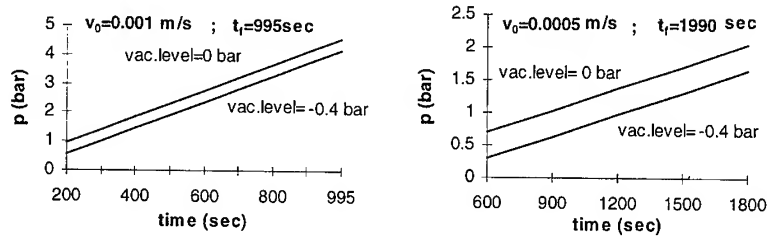


Fig. 6 Pressure build up at the inlet with specified flow rate BC and vacuum level at flow front

Effect of BC transition during filling in pressure distribution and mold filling time have been shown in Fig. 8 and Fig. 9. It is assumed that initial specified flow rate BC is v_0 and the pressure limit is p_0 . In Fig. 8 mold filling begins with specified flow rate BC at the inlet ($v_0 = 0.001$ m/s) but it is changed to specified pressure BC at the inlet ($p_0 = 1.5$ bar) when the pressure at the inlet builds up to p_0 and then, filling continues until the mold is filled. Fig. 9 shows mold filling time and pressure distribution inside the mold at the end of filling with and without BC transitions from specified flow rate ($v_0 = 0.001$ m/s) to different specified pressures ($p_0 = 1$ and 2.5 bar) at the inlet. As shown in the figure, if BC transition takes place at lower pressure at the inlet, the mold filling time will be longer.

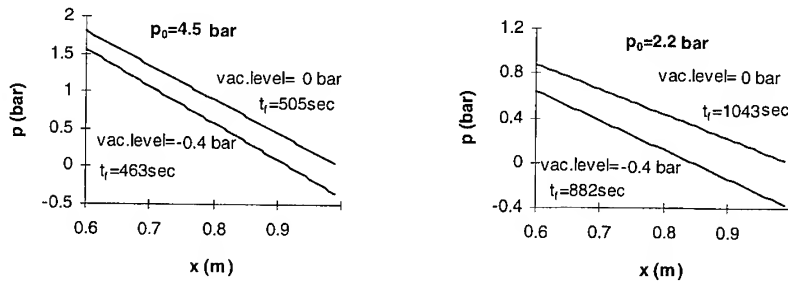


Fig. 7 Pressure distribution at the end of mold filling with specified pressure BC and vacuum level at flow front

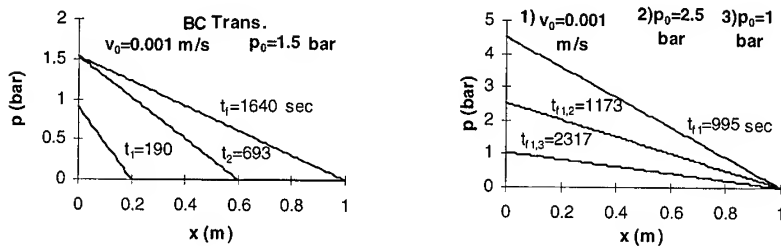


Fig. 8 Pressure distribution at different filling steps with BC transition

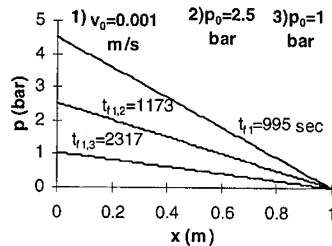


Fig. 9 Pressure distribution at the end of mold filling with BC transition

CONCLUSION

Process parameters such as pressure, vacuum, mold filling time can influence process cycle and quality of final part in RTM. For example, vacuum influences wetting and void formation[5], and high pressure can cause fiber mat deformation[6]. On the other hand, low mold filling time is desirable for fast cycle. For a high volume production process, fast cycle with good product quality is desirable. Proper choice of BC can help to select a convenient process to reach above goals. Numerical results showed that there is a pressure build up with specified flow rate BC, and mold filling time is longer than that of the specified inlet pressure BC at the inlet. Application of partially vacuum level at the flow front reduces pressure build up for specified flow rate BC and reduces mold filling time for specified inlet pressure BC. Also, BC transition makes the mold filling time, to increase but reduces final maximum inlet pressure at specified flow rate BC. In incoming work, we will extend this approach to complicated 3-D geometry.

REFERENCES

1. W. B. Young, "Three Dimensional Nonisothermal Mold Filling Simulation in Resin Transfer Molding", *Polymer Composites*, Vol. 15, 1994, pp. 118-127.
2. R. Guavin and F. Trochu, "Key Issues in Numerical Simulation for Liquid Composite Molding Processes", *Polymer composites*, Vol. 19, 1998, pp. 233-239.
3. Z. Cai, "Simplified Mold Filling Simulation in Resin Transfer Molding", *J. Comp. Materials*, Vol. 26, 1992, pp. 2606-2629.
4. S. G. Advani, "Flow and Rheology in Polymer Composites Manufacturing", Chapter 8, Amsterdam, Elsevier Science BV, 1994.
5. Y. T. Chen, H. T. Davis and C. W. Macosko, "Wetting of Fiber Mats for Composites Manufacturing: I. visualization Experiments", *AIChE J.*, Vol. 41, 1995, pp. 2261-2273.
6. K. Han, L. Trevino, L. J. Lee and M. Liou, "Fiber Mat Deformation in Liquid Composite Molding. I: Experimental Analysis", *Polymer composites*, Vol. 14, 1993, pp. 144-149.

A New Technique to Determine In-Plane Permeability of Fiber Preforms : Gas Flow Method

Byung-Sun Hwang¹, Moon-Kwang Um^{1*} and Isaac M. Daniel²

^{1, 1*} Korea Institute of Machinery and Materials, Composite Materials Group
66 Sangnam-dong, Changwon, 641- 010, South Korea
: hbs@kmail.kimm.re.kr, umk1693@kmail.kimm.re.kr

² Robert R. McCormick School of Engineering and Applied Science
Center for Intelligent Processing of Composites
Northwestern University, Evanston, IL 60208, USA : imdaniel@nwu.edu

SUMMARY: Resin flow plays a crucial role in many composite manufacturing processes. The most important parameters used in modeling and designing mold filling are the permeability of the fibrous preform, which is a kind of flow conductance and a property of the reinforcement, and the viscosity of the resin. The extent of chemical reaction, or degree of cure, is also important and causes change of resin viscosity during mold filling.

To determine the permeability of fiber preforms, many researchers have been using liquid flow analysis. In this study, a new scheme to obtain permeability using gas flow is proposed. In conventional liquid flow methods, radial propagation of the polymer into a porous medium is measured and used to determine permeability, whereas in the gas flow method the flow rate for several different preform geometries is measured and used. The effectiveness of the gas flow method was verified by comparing it with conventional methods.

KEYWORDS: resin flow, in-plane permeability, gas flow method

INTRODUCTION

Resin flow and cure are essential parts of the composite manufacturing process. Crucial parameters affecting resin flow are the permeability of the reinforcement and viscosity of the resin. Many studies related to permeability have been performed. Most of them are concentrated on unidirectional fiber beds where flow is perpendicular or parallel to the fiber direction [1-3]. However, in woven and textile fabrics, a complex flow consisting of resin flow perpendicular and parallel to the fiber direction is typical. There are many theoretical, numerical and experimental studies considering microscopic flow through unidirectional fiber beds, whereas experimental studies considering macroscopic flow are mainly reported for woven fabrics or random mats due to the complexity of the geometry [4-6]. In almost all studies, permeability was quantified by measuring the flow front with liquid infiltration. In this study a new technique to determine permeability using gas flow is proposed and verified. In this method, mass flow rates are measured for two different rectangular preforms (Fig.1) and permeability is obtained by comparing them with analytic relations accompanied by numerical calculation. Most errors encountered in permeability measurements are due to edge effects in one-dimensional flow and deformation of the test mold due to the injection pressure

and preform compaction [7-8]. Edge effects can be minimized by special treatment of the edge region or by adopting a two-dimensional flow. Mold deformation can be minimized by using the gas flow technique, because the injection pressures used are lower than those used in liquid flow methods.

NUMERICAL SOLUTION FOR GAS FLOW

Governing Equation and Mass Flow Rate: The governing equation of gas flow through porous media at low Reynolds number can be derived by applying Darcy's law to the law of mass conservation during gas flow [9]

$$\nabla \cdot (\rho_g \bar{u}_D) = \nabla \cdot (\rho_g [K] \nabla P / \mu_g) = 0 \quad (1)$$

where \bar{u}_D is the Darcian velocity, $[K]$ the permeability tensor of the reinforcement, P the pressure, ρ_g is the gas density and μ_g the gas viscosity. We assume that the gas flow through a porous medium of a given fixed geometry is fully developed and regarded as quasi-steady which can neglect the unsteady term in the mass conservation. The gas is assumed as an ideal gas. If measurements are performed at constant temperature and pseudo-pressure ($\bar{P} = P^2 / 2$) are defined, the nonlinear governing equation becomes linear

$$\nabla \cdot ([K] \nabla \bar{P}) = 0 \quad (2)$$

In general, permeability shows orthotropic behavior and with two principal values (K_1, K_2) for in-plane flow. If the orthotropic permeability is transformed into an isotropic one through coordinate transformation, the governing equation takes a simple Laplace form.

$$x = x_0, y = \alpha^{-0.5} y_0, \alpha = K_2 / K_1 (K_2 < K_1) \quad (3)$$

where x_0, y_0 are coordinates before transformation and x, y coordinates after transformation.

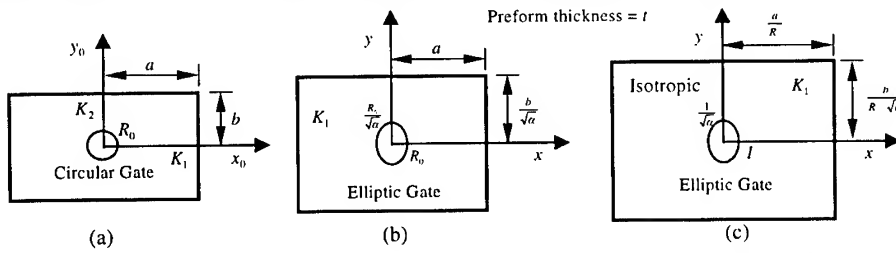


Fig.1 Geometry for flow rate measurement, (a) original orthotropic preform, (b) transformed isotropic preform, (c) normalized isotropic preform

The geometry considered in this study for permeability measurement is shown in Fig.1. The flow through a rectangle with a circular gate changes into flow through a rectangle with an elliptic gate. This transformation changes the governing equation (Eq.2) as follows

$$\nabla^2 \bar{P} = 0 \quad (4)$$

The relation between mass flow rate and flow parameters is needed to quantify permeability of the preform using gas flow. Mass flow rate of gas (\dot{M}) through the rectangular boundary can be calculated by the following equation if the pressure along the inner and outer boundaries is constant. Integration with the original coordinates is changed into that with transformed coordinates.

$$\dot{M} = \int_{\Gamma} \rho_{g,\Gamma} \bar{u}_D dA = \frac{\rho_{g,\Gamma} t}{\mu_{g,\Gamma}} \int_{\Gamma} (K_1 \frac{\partial P}{\partial x_0} dy_0 + K_2 \frac{\partial P}{\partial y_0} dx_0) = \sqrt{\alpha} \frac{K_1 \rho_{g,\Gamma} t}{\mu_{g,\Gamma}} \int_{\Gamma} (\frac{\partial P}{\partial x} dy + \frac{\partial P}{\partial y} dx) = \sqrt{\alpha} \frac{K_1 \rho_{g,\Gamma} t}{\mu_{g,\Gamma}} \int_{\Gamma} \nabla P dl \quad (5)$$

where A is a cross-sectional area of the boundary, Γ represents the preform boundary, $\rho_{g,\Gamma}$ is the density of gas at the inlet or outlet boundary, $\mu_{g,\Gamma}$ is the viscosity of the gas at the boundary, t is the preform thickness, K_1 is the major principal direction permeability and l is

an integration variable along the boundary (Γ) in the transformed coordinate system.

By replacing the above equation with the pseudo-pressure gradient(\bar{P}) and applying the principle of superposition,

$$\dot{M} = \sqrt{\alpha} K_1 \frac{t}{\mu_{g,r}} \frac{\rho_{g,r}}{P_{g,r}} \int_{\Gamma} \nabla \bar{P} dl = \sqrt{\alpha} K_1 \frac{t}{\mu_{g,r}} \frac{\rho_{g,r}}{P_{g,r}} \frac{P_{in}^2 - P_{out}^2}{2} \int_{\Gamma} \nabla \bar{P}_1 dl \quad (6)$$

where $P_{g,r}$ is the pressure at the boundary, \bar{P}_{in} , \bar{P}_{out} are the inlet and outlet pseudo-pressures, P_{in} , P_{out} are the inlet and outlet absolute pressures and \bar{P}_1 means that the difference of pseudo-pressures between the inlet and outlet is one ($\bar{P}_1 = \bar{P}_{in} - \bar{P}_{out} = 1$). By applying the ideal gas law ($\rho/P = 1/ZRT$) to the above equation, a simplified form is derived and it is used to determine permeability from the experimentally measured mass flow rate

$$\dot{M} = \sqrt{\alpha} K_1 \frac{t}{\mu_{g,r}} \frac{1}{ZRT} \frac{P_{in}^2 - P_{out}^2}{2} F_{unit} \quad \text{where } F_{unit} = \int_{\Gamma} \nabla \bar{P}_1 dl \quad (7)$$

where Z is the compressibility factor, R is the gas constant and T the absolute temperature. Values for the compressibility factor, gas constant and gas viscosity are readily found in reference 10. The compressibility factor depends on temperature and pressure, whereas gas viscosity depends primarily on temperature. We define the integral term in Eq.7 as the non-dimensional unit of mass flow rate (F_{unit}). This non-dimensional mass flow rate depends on the geometry of the flow field. For a simple geometry with a one-dimensional flow field an analytic solution exists, whereas there is no analytic solution for a two-dimensional flow geometry like that of Fig.1, even though there exists an approximate one obtained by a complex variables approach for isotropic permeability [11]. Therefore, a numerical approach was tried to obtain the solution for the two-dimensional case.

Determination of Mass Flow Rate: a) 1-Dimensional Flow: Analytic Solution

One-dimensional gas flow can be produced using line gate injection and the mass flow rate is easily derived as follows

$$\dot{M} = K_1 \frac{1}{\mu_{g,r}} \frac{1}{ZRT} \frac{P_{in}^2 - P_{out}^2}{2} \frac{bt}{a} \quad (8)$$

where b is the width of the fabric, and a is the flow region fabric length. Equation 8 can be directly used to determine permeability in one of the principal directions. Normally, the flow pattern of one-dimensional flow is simple, but it is not easy to eliminate the edge effects near mold walls, which may cause significant error.

b) 2-Dimensional Flow: Numerical Solution: Two-dimensional radial flow is frequently used for determining in-plane permeability, because the two principal permeabilities (K_1, K_2) can be obtained simultaneously. For two-dimensional flow, the non-dimensional unit mass flow rate (F_{unit}) is determined numerically. A numerical scheme of the boundary element method (BEM, [12]) was used for determining the permeability of a rectangular porous medium with an elliptic gate, in which the permeability is isotropic. By using BEM the effort in mesh generation and the calculation time can be reduced in comparison with the finite element method (FEM) or finite difference method (FDM). More accurate mass flux values can be obtained than those obtained by the FEM or FDM because BEM calculates mass flux on the very boundary. In this study, the linear boundary element was selected for its accuracy and relative simplicity in node generation. For a hollow cylinder, the numerically determined flux was compared with the analytic result to check the accuracy [13]. The flux difference between the two results was less than 0.01%. This shows that the linear element is accurate enough for our purpose.

F_{unit} has a non-dimensional form. It means that the same result is obtained for cases

with geometric similarity and identical boundary conditions.

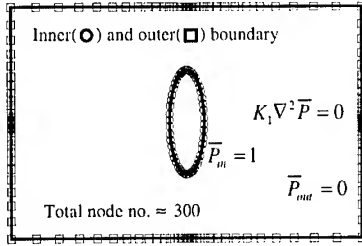


Fig.2 Example of node distribution used in boundary element analysis

Therefore, the geometry of Fig. 1 (b) can be further transformed into the one of Fig. 1 (c) by dividing the whole length scale by the inlet hole radius (R_0). The elliptic type governing equation (Eq.4) requires the following boundary conditions

- Outer Boundary : $\bar{P}_{out} = 0$
- Inner Injection Gate : $\bar{P}_{in} = 1$

(9)

An example of node distribution used in flux calculation is shown in Fig.2. To increase the accuracy, nodes were distributed based on the flux and its change. Flux differences in the inner and outer boundaries were compared and they were found to be less than 0.02%.

The ranges of width (b) and length (a) of the geometry, selected by considering the desired flux change and adaptability of boundary conditions, are

$$10 \leq a/R_0, b/(\sqrt{\alpha}R_0) \leq 40 \quad (10)$$

Curve-Fit of Non-Dimensional Unit Mass Flow Rate:

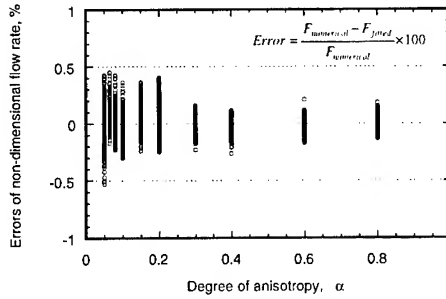


Fig.3 Errors between fitted and calculated non-dimensional mass flow rates

The non-dimensional unit flow rate obtained numerically can be easily accessed by fitting it to a suitable functional form. The basic form of the function originates from the conduction shape factor used in heat transfer analysis [13]. This form is valid for rectangular geometry with a circular hole with isotropic thermal conductivity. The deviation can be adjusted by applying correction functions (F_{mod1} , F_{mod2}).

$$F_{unit} = (F_b + F_{mod1}) \cdot F_{mod2} \quad \text{at } 0.05 \leq \alpha < 0.18 \quad \text{OR} \quad F_{unit} = F_b \cdot F_{mod2} \quad \text{at } 0.18 \leq \alpha < 1 \quad (11)$$

$$F_b = 2\pi / \left[\ln \left[y_2 \cdot \left\{ A + B \cdot \exp(C \cdot (x/y_2)^D) \right\} \right] \right]$$

$$F_{mod1} = E \cdot \exp\left(G \frac{x}{y_2}\right) + H \cdot \exp\left(I \frac{y_2}{x}\right), F_{mod2} = 100 / (99.947 + 0.62142 \cdot \alpha - 0.71422 \cdot \alpha^2)$$

$$x = a/R_0, y_2 = b/(R_0 \sqrt{\alpha})$$

$$A = -1.12599 + 2.40381 \cdot \alpha^{0.14490}, B = 1.38275 - 2.54396 \cdot \alpha^{0.12112}$$

$$C = -1.75089 - 0.02369/\alpha, D = 1.58318 + 2.22008 \times 10^{-3}/\alpha$$

$$E = -0.01569 + 4.54195 \times 10^{-3}/\alpha, G = 0.232$$

$$H = -0.06485 - 1.56319 \cdot \exp(31.992 \cdot \alpha), I = -0.89982 - 6.61435 \cdot \alpha$$

F_{mod1} is used to enhance the accuracy for low degrees of anisotropy and F_{mod2} is used for reducing the fluctuation of fitted values as the degree of anisotropy increases. The curve fit errors are calculated from the numerical results. They are given in Fig.3. As can be seen in the figure, the error is small enough not to affect the results.

DETERMINATION OF PERMEABILITY

The procedure for determining permeability is described in Fig. 4. First, preform shapes for measuring flow rate should be determined. An approximate degree of anisotropy ($\alpha_a = (\text{min or flow front} / \text{major flow front})^2$) is determined by the flow fronts of liquid flow

(Fig.5). From an approximate degree of anisotropy, two shapes which have a flow rate ratio (length and width direction) of approximately 0.1 and 10 are selected using non-dimensional unit flow rate. A flow rate ratio of 0.1 is used for generating a K_1 direction dominant flow and a ratio of 10 is used for K_2 direction dominant flow. The inlet pressures at the given flow rate are measured for these shapes (Fig.6). Using Eq.7, the permeability (K_1) and degree of anisotropy (α) are determined through the iteration.

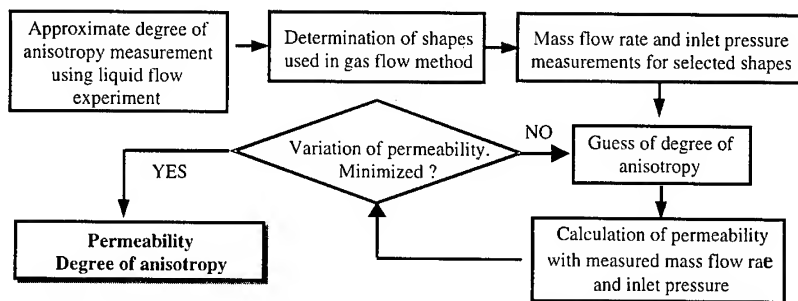


Fig.4 Flow chart for determination of permeability by gas flow method

EXPERIMENTAL VERIFICATION

Conventional Liquid Flow Method: Mold filling experiments using glass fabric (HEXCEL, Fiberglass fabric 7500) and silicone oil (Clearco, PSF350CS) were performed with varying injection pressures. The viscosity of silicone oil which is dependent on temperature only is

$$\mu = 0.0201 \cdot \exp(813/T) \quad \text{Pa} \cdot \text{sec} \quad (12)$$

where T is the absolute temperature. The experimental setup is shown in Fig.5. The mold consists of two parallel plates with the reinforcement placed between them. Silicone was driven to flow through the preform by pressurizing the nitrogen gas in the reservoir. The resin pressure at the inlet gate was monitored with a pressure transducer and the resin fronts were recorded by a video camera. From the resin fronts and the inlet pressure, the permeability was determined by the procedure of Adams *et al.*[4]. Adam's flow equation was modified to consider variable pressure injection. The average principal permeabilities K_1 and K_2 determined in each experiment were found to be $2.6 \times 10^{-10} \text{ m}^2$ and $8.3 \times 10^{-11} \text{ m}^2$, respectively.

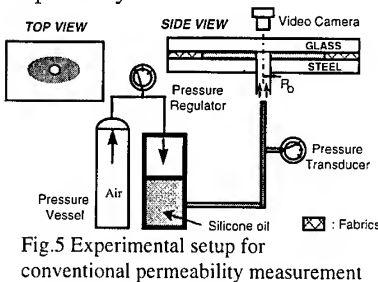


Fig.5 Experimental setup for conventional permeability measurement

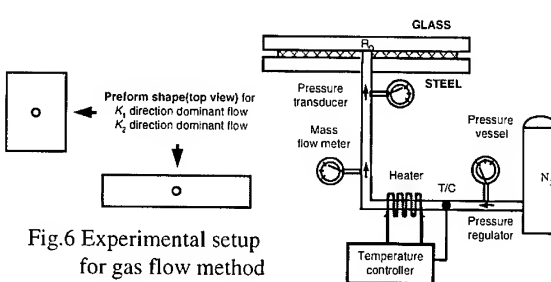


Fig.6 Experimental setup for gas flow method

Gas Flow Method: Mass flow rates using the same glass fabric and Nitrogen gas were measured for two geometries. The viscosity of Nitrogen gas was fitted from the data given in reference 10 and the compressibility factor (Z) and gas constant (R) are

$$\mu = 2.8463 \times 10^{-6} + 5.3406 \times 10^{-8} T - 1.053 \times 10^{-11} T^2 \quad \text{Pa} \cdot \text{sec} \quad (13)$$

$$Z = 0.9998 \quad R = 296.8 \quad \text{J}/(\text{kg} \cdot \text{K}) \quad (14)$$

The experimental setup is given in Fig.6. The same mold was used as in liquid flow method. Nitrogen gas was driven to flow through the preform from the reservoir. To control a mass

flow rate, a flowmeter was used. The pressure developed at the inlet gate is quite small because the viscosity of nitrogen is very small. To prevent a gas temperature drop due to throttling, a small capacity heater (20 watts) was used. Experimental results are given in Table 1. Gas viscosity was determined from the measured mold temperature. The approximate degree of anisotropy (α_a) for determining the preform shape was 0.4. Two different preform shapes were used in the measurements, one for K_1 direction dominant flow and the other for K_2 direction dominant flow. Finally, following the procedure illustrated in Fig.4, the average principal permeabilities were obtained as $K_1 = 2.8 \times 10^{-10} \text{ m}^2$ and $K_2 = 8.4 \times 10^{-11} \text{ m}^2$, respectively. Two measurement results were compared and they showed good agreement (Fig.7). There is some scatter in permeability caused by the non-uniformity generated in the preform pattern itself and the stacking procedure.

	EXP No.	Temperature °C	Inlet gage pressure (P_{in}) Pa
Shape 1 K_1 direction dominant flow	1	24.3	168
	2	24.7	160
	3	24.1	154
Shape 2 K_2 direction dominant flow	1	24.4	177
	2	24.5	165
	3	24.3	159

$R_f = 6.35 \text{ mm}$, $v_f = 0.41$, $P_{atm} = 1.013 \times 10^5 \text{ Pa}$,
Preform thickness = 2.41 mm
Mass flow rate = $9.67 \times 10^{-6} \text{ kg/sec}$ at 21.1 °C, 1 atm
Shape 1: $2a \times 2b = 171 \times 260 \text{ mm}$
Shape 2: $2a \times 2b = 337 \times 101 \text{ mm}$

Table 1 Measured data for gas flow method

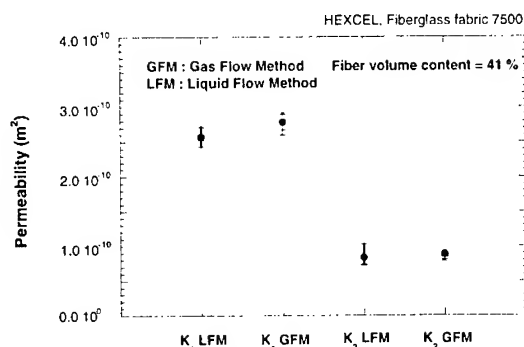


Fig.7 Comparison of measured permeabilities

CONCLUSIONS

A new method, the gas flow method, is proposed for measuring permeability in reinforcement preforms used in liquid injection molding. The governing equation of gas flow through a porous medium was derived and linearized. An expression was derived for mass flow rate for rectangular preforms. A boundary element method was incorporated to calculate the flux for a given geometry and boundary conditions. The proposed gas flow method was tested experimentally and verified by comparing results with those obtained by the conventional liquid flow method. The latter was modified to account for varying injection pressure. The gas flow method has the additional advantages that it is not hindered by edge effects and that the effect of mold deformation is minimized because of the low gas pressures.

REFERENCES

1. R. E. Larson and J. J. L., Higdon, *J. Fluid Mech.*, **178**, 119 (1987).
2. B. T. Astrom, R. B. Pipes and S. G. Advani, *J. Compos. Mater.*, **26**, 1351 (1992).
3. L. Skartsis, J.L. Kardos and B. Khomami, *Polym. Eng. Sci.*, **32**, 221 (1992).
4. K. L. Adams, W. B. Russel and L. Rebenfeld, *Int. J. Multiphase Flow*, **14**, 203 (1988).
5. A. W. Chan and S. T. Hwang, *Polym. Eng. Sci.*, **31**, 1233 (1991).
6. M.-K. Um and S.-K. Lee, *Polym. Comp.*, **20**, (1999).
7. L. Trevino, K. Rupel, W. B. Young, M. J. Liou and L. J. Lee, *Polym. Comp.*, **12**, 20 (1991).
8. R. S. Parnas, K. M. Flynn and M. E. Dal-Favero, *Polym. Comp.*, **18**, 623 (1997).
9. M. Kaviany, *Principles of Heat Transfer in Porous Media*, Springer-Verlag (1991).
10. W. M. Rohsenow and J. P. Hartnett, *Handbook of Heat Transfer*, McGraw-Hill (1973).
11. M. J. Balcerzak and S. Raynor, *Int. J. Heat Mass Transfer*, **3**, 113 (1961).
12. C. A. Brebbia, *The Boundary Element Method for Engineers*, Pentech Press (1980).
13. F. M. White, *Heat Transfer*, Addison-Wesley (1984).

Modeling of Void Formation during Resin Transfer Molding Process

Seong Taek Lim¹, Moon Koo Kang², and Woo Il Lee²

¹*Opto-mechatronics Laboratory, Samsung Electronics, Suwon, Kyungki-Do,
442-742, KOREA : stlim912@sec.samsung.co.kr*

²*Department of Mechanical Engineering, Seoul National University
San 56-1, Shillim-dong, Kwanak-gu, Seoul 151-742, KOREA : wilee@snu.ac.kr*

SUMMARY: During the filling process of the RTM, the injected resin displaces the air and impregnates the dry preform. Inside the fiber preform, there exist two distinguishable regions according to their pore sizes, which are inter-tow and intra-tow region. Due to the pore size difference, the capillary force and the flow resistance become different considerably between the two regions, which causes the retarded impregnation and the entrapment of the tiny air voids. The formed voids are undesirable due to their detrimental effects on the performance of the final products. In this study, some mathematical models on the void formation were developed. The derived void formation models were described as a function of the capillary number, which corresponded to the experimental results of other researchers. In order to predict the three dimensional void distributions inside the thicker parts, the void models were extended to the three dimensions. The three dimensional void formation models were embedded in the three dimensional RTM mold filling simulation program. The predicted three dimensional void distribution was validated by the experiments using the unsaturated polyester resin and the plain weave fabric, where the void contents were measured by investigating the polished specimen with a microscope and a CCD camera after curing.

KEYWORDS: RTM, Void Formation, Capillary Number, Impregnation.

INTRODUCTION

During the filling process of the RTM, the existence of the considerable heterogeneity in the pore size distribution causes the mechanical entrapment of the air void. In the intra-tow region, the viscous resistance and the capillary force are much larger than those in the inter-tow region because its pores are very small compared with those of the inter-tow region. Due to the differences of the viscous resistance and the capillary force, the flow speed of the resin at microscopic level in the intra- and the inter-tow region becomes different to some extent. If the resin flow in one region precedes that in the other, it is more probable that the resin fails to drive out the air in the region left behind. This incomplete impregnation often results in the formation of flow-induced air voids [1-4].

The resin flow in the inter-tow region, i.e. the macro-flow which forms apparent flow front is mainly driven by the inlet pressure and the resin flow in the intra-tow region, i.e. the micro-flow by the resin pressure surrounding the intra-tow region and the capillary pressure. If the

macro-flow in the channel driven by the inlet pressure is fast enough to outrun the micro-flow inside the tow, more vacant spaces are generated inside the fiber tows at flow front region. If this rapid macro-flow meets relatively high permeable spots in the inhomogeneous fiber tows, the cross-flow inside the fiber tows occurs, which makes the dry spots inside the fiber tows (see Fig. 1). The more the macro-flow outruns the micro-flow, the more the micro-voids are formed inside the fiber tows. Therefore the major cause of the micro-void formation is the irregularity of the pore size inside the fiber tows combined with the flow velocity difference between the macro-flow and the micro-flow [1, 2].

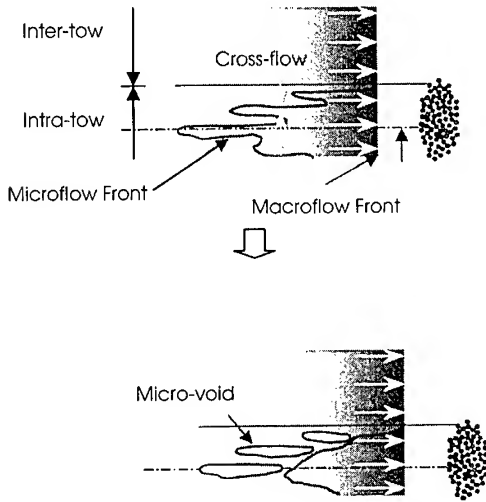


Fig. 1 Formation of the micro-voids.

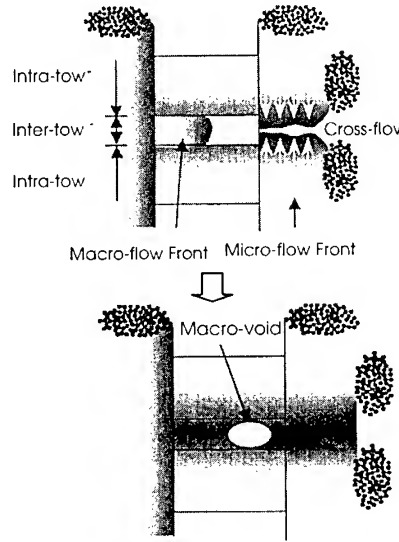


Fig. 2 Formation of the macro-voids

If the macro-flow between the fiber tows is so slow that the micro-flow driven by the capillary force overtakes the macro-flow, the macro-pores might be surrounded by already wet fiber tows at flow front region. Then the capillary driven cross-flow along the fiber tow normal to the macro-flow wraps up the vacant channel, which leads to the formation of the macro-voids (see Fig. 2). In case of the plain weave fabrics used in this study, the cross-flow occurs in the fiber tows normal to the macro-flow. In case of non-woven unidirectional stitched mat, the nylon stitches that bind the fiber bundles together cause the cross-flow [1]. As the difference between the macro-flow speed and the micro-flow speed is larger, the size of the macro-void, i.e. the macro-void content is increased.

MODELING OF THE FORMATION OF THE MACRO- AND MICRO-VOID

The probability of the macro- and the micro-void formation induced by the resin flow are increased, as the speed difference between the macro- and the micro-flow is larger. Consider the resin flow along the fiber tows illustrated in Fig. 3. In this figure, complicated three dimensional flows through the dual scale porous media are simplified into one dimensional macro- and micro-flow in a small cell whose characteristic length is L . In this situation, the elapsed time for the macro- and the micro-flow to reach the characteristic length L can be written as

$$\Delta t_M = \mu L / \left(K^M \left| \frac{dP_r}{dn} \right| \right) \quad (1.a) \quad \Delta t_m = \left(L - \left(P_c / \left| \frac{dP_r}{dn} \right| \right) \ln \left(1 + \left(\left| \frac{dP_r}{dn} \right| / P_c \right) L \right) \right) / \left(\frac{K^m}{\mu} \left| \frac{dP_r}{dn} \right| \right) \quad (1.b)$$

where Δt_M and Δt_m are the elapsed time of the macro- and the micro-flow respectively to

reach the characteristic length L , K^M and K^m are the permeability of the inter-tow and the intra-tow region respectively in the flow direction, $\left| \frac{dP_r}{dn} \right|$ is the local pressure gradient in the flow direction induced by the inlet pressure and P_c is the capillary pressure.

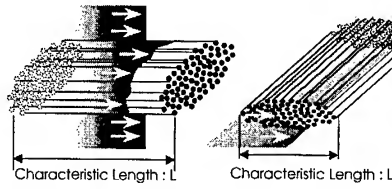


Fig. 3 Simplified one dimensional macro- and micro-flow in the small cell with the characteristic length of L during the filling process of the RTM with the dual scale porous media.

According to the relative magnitude between Δt_M and Δt_m , it is determined where the air voids are formed. If Δt_M is larger than Δt_m , the macro-voids are more probable to be formed in the inter-tow region. On the other hand, if Δt_m is larger than Δt_M , the micro-voids are to be formed in the intra-tow region. First consider the case that the macro-flow leads the micro-flow. The probability of the micro-void formation inside the fiber tow is proportional to the ratio of the unfilled volume inside the fiber tow to the total volume of a small cell. This can be written as

$$f_v^m \propto V_{unfilled} / V_{total} \quad (2)$$

where f_v^m represents the micro-void fraction, $V_{unfilled}$ is the unfilled volume inside the fiber tow in a small cell and V_{total} is the total volume of a small cell. In the simplified one dimensional flow mentioned above, this unfilled volume ratio can be evaluated through the followings.

$$V_{unfilled} / V_{total} = f_T (L_m - L_m^{imp}) / L_m = f_T (1 - L_m^{imp} / L_m) \quad (3)$$

where f_T is the fiber tow ratio which is equal to $(1 - \phi_M)$, L_m is the characteristic length of a small cell for the micro-void formation and L_m^{imp} is the impregnation length by the micro-flow inside the fiber tow during the time for the macro-flow to reach the characteristic length L_m . Also the ratio of the impregnation length to the characteristic length L_m^{imp} / L_m can be approximated with the mean flow velocities in each region.

$$L_m^{imp} / L_m \approx (\bar{u}_m \Delta t_M) / (\bar{u}_M \Delta t_M) = \bar{u}_m / \bar{u}_M \quad (4)$$

where \bar{u}_m and \bar{u}_M denote the mean velocity of the micro- and the macro-flow respectively advancing the characteristic length L_m .

$$\bar{u}_M = L_m / \Delta t_M \quad (5.a) \quad \bar{u}_m = L_m / \Delta t_m \quad (5.b)$$

If the Eqs. (1) - (5) combined, the micro-void fraction can be expressed as

$$f_v^m = f_{v,\infty}^m f_T \left(1 - \frac{K^m}{K^M} \left(L_m / \left(L_m - \left(P_c / \left| \frac{dP_r}{dn} \right| \right) \ln \left(1 + \left(\left| \frac{dP_r}{dn} \right| / P_c \right) L_m \right) \right) \right) \right) \quad (6)$$

where $f_{v,\infty}^m$ is the coefficient of the proportionality of the Eq. (2), which means the asymptotic value of the micro-void fraction against the fiber tow, not against the whole, when the macro-flow exceeds the micro-flow far enough.

Likewise the macro-void fraction can be derived the same way as the micro-void fraction, when the micro-flow leads the macro-flow. The probability of the macro-void formation between the fiber tows is proportional to the unfilled volume ratio in a small cell and thereby the macro-void fraction can be modeled as the following equation.

$$f_v^M = f_{v,\infty}^M f_c \left(1 - \frac{K^M}{K^m} \left(\left(L_M - \left(P_c / \left| \frac{dP_r}{dn} \right| \right) \ln \left(1 + \left(\left| \frac{dP_r}{dn} \right| / P_c \right) L_M \right) \right) / L_M \right) \right) \quad (7)$$

where f_v^M is the macro-void fraction, f_c is the channel ratio which is equal to ϕ_M , L_M is the characteristic length of a small cell for the macro-void formation and $f_{v,\infty}^M$ is the coefficient of the proportionality, which means the asymptotic value of the macro-void fraction against the channel, not against the whole, when the micro-flow outruns the macro-flow fairly. the capillary pressure in the unidirectional fiber tows can be stated as [4]

$$P_c = (4\gamma \cos \theta / d_f) (V_f / (1 - V_f)) \quad (8)$$

Using the Eqs. (6), (7) and (8), the final equations for the macro-void formation and the micro-void formation are as follows. First for the micro-void formation, the model can be described as

$$f_v^m = \Pi_1^m [1 - (K^m / K^M) \{1 / (1 - (\Pi_2^m \cdot Ca)) \ln(1 + \Pi_2^m \cdot Ca)\}] \quad (9)$$

where

$$\Pi_1^m = f_{v,\infty}^m f_T \quad (10.a) \quad \Pi_2^m = \{d_f L_m (1 - V_f^m)\} / \{4K^{eff} V_f^m\} \quad (10.b) \quad Ca = (\mu U) / (\gamma \cos \theta) \quad (10.c)$$

Also for the macro-void formation,

$$f_v^M = \Pi_1^M [1 - (K^M / K^m) \{1 / (\Pi_2^M \cdot Ca) \ln(1 + \Pi_2^M \cdot Ca)\}] \quad (11)$$

where

$$\Pi_1^M = f_{v,\infty}^M f_c \quad (12.a) \quad \Pi_2^M = \{d_f L_M (1 - V_f^m)\} / \{4K^{eff} V_f^m\} \quad (12.b) \quad Ca = (\mu U) / (\gamma \cos \theta) \quad (12.c)$$

As is seen from the Eqs. (9) and (12), the models for the formation of the micro- and the macro-voids have two dimensionless constants Π_1, Π_2 and the dimensionless number Ca which is the capillary number modified with the contact angle θ . The constant Π_1 is related to the maximum void content and the constant Π_2 includes the characteristic length L and etc., which depend on the fiber reinforcement structures. That is, if the fiber reinforcement type and the process parameters related to that (e.g. *fiber volume fraction*) are specified during the RTM filling process, the two dimensionless model constants Π_1, Π_2 are fixed. Therefore the only variable is the capillary number Ca which represents the ratio of the viscous force to the surface tension force.

Total Void Contents in Three Dimensional Resin Flow

A unit cell is introduced in order to estimate the total void contents from the void contents in the two major directions (*in-plane and through-thickness*) for the dual scale porous media (plain weave fabric in this study, see Fig. 4). The unit cell originates from the unit of the weave pattern of the fabrics. In the Fig. 4, the characteristic length of the unit cell in the in-plane direction $L|^{in-plane}$ can be measured and the characteristic length in the through-thickness direction $L|^{thick}$ is approximated from the information about the ratio of the mold cavity thickness to the number of the stacked layers (mm/layer). If the characteristic lengths of the unit cell are determined, the representative time scale in the in-plane and the through-thickness direction should be determined. The representative time scale is the minimum required time for the macro- or the micro-flow to advance the characteristic length in each

direction, which can be written as

$$\Delta t|^{in-plane} = \min[\Delta t_M|^{in-plane}, \Delta t_m|^{in-plane}] \quad (13.a)$$

$$\Delta t|^{thick} = \min[\Delta t_M|^{thick}, \Delta t_m|^{thick}] \quad (13.b)$$

where $\Delta t|^{in-plane}$ and $\Delta t|^{thick}$ are the representative time scale of the in-plane flow and the through-thickness flow respectively. $\Delta t_M|^{in-plane}$, $\Delta t_m|^{in-plane}$, $\Delta t_M|^{thick}$ and $\Delta t_m|^{thick}$ can be obtained from the Eq. (1) with the characteristic length $L|^{in-plane}$ and $L|^{thick}$

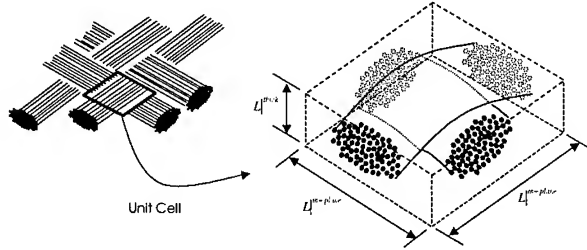


Fig. 4 A unit cell for the comparison of the time scale between the in-plane and the through-thickness flow for the plain weave fabric.

The total void contents can be estimated from the simple relations as follows.

$$f_v^m|^{total} = w_{||} f_v^m|^{in-plane} + w_{\perp} f_v^m|^{thick} \quad (14.a) \quad f_v^M|^{total} = w_{||} f_v^M|^{in-plane} + w_{\perp} f_v^M|^{thick} \quad (14.b)$$

where

$$w_{||} = \Delta t|^{thick} / (\Delta t|^{in-plane} + \Delta t|^{thick}) \quad (15.a) \quad w_{\perp} = \Delta t|^{in-plane} / (\Delta t|^{in-plane} + \Delta t|^{thick}) \quad (15.b)$$

EXPERIMENTS AND NUMERICAL RESULTS

In order to show the validity of the developed three dimensional void formation model, three dimensional RTM mold filling experiment was conducted. The mold geometry is shown in Fig. 5. The resin was injected at constant pressure of 3.0 atm. The vinylester resin (Aerotran 50437-8, Ashland Chemical) and the plain weave fabrics (Hankuk Fiber, WR 860A) were used. The macro-void contents were measured by investigating the cured specimen microscopically after the end of the filling. The macro-void contents at eight cross-sections randomly chosen were averaged to yield a data point. Three different zones were investigated as shown in Fig. 6, where the measured data were compared with the numerical results later.

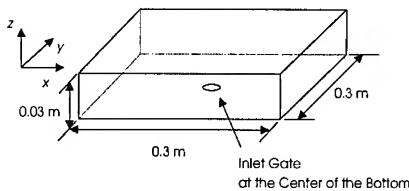


Fig. 5 Mold geometry for the three dimensional void formation experiment.

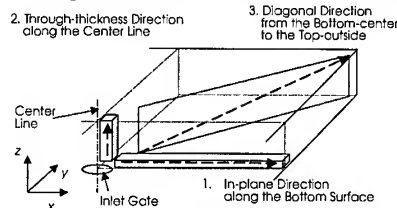


Fig. 6 Three zones to be investigated for the measurements of the air voids.

The three dimensional void formation was simulated with the Eqs. (9) - (15). In Fig. 7, the numerical results for three dimensional macro-void formation are shown. Only a quarter is displayed because of the symmetry of the geometry. The macro-void fraction around the inlet gate is about zero percent, where the global flow velocity is higher and the macro-flow

exceeds the micro-flow. As the mold is filled, the resin flows more slowly because the pressure gradient at the flow front decreases and hence the macro-flow gets to compete the micro-flow. As the micro-flow leads the macro-flow, the macro-voids are formed and those contents are increased.

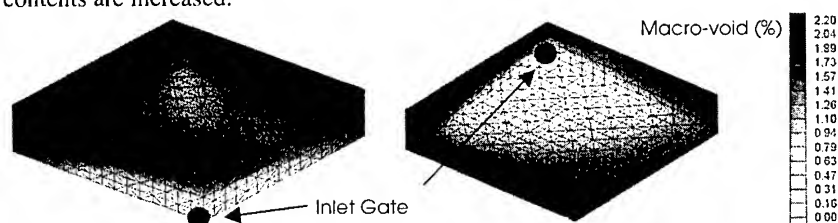


Fig.7 Macro-void distribution about the experimental geometry. The upper is the view from the top and the lower is from the bottom. Only a quarter is displayed due to the symmetry of the geometry.

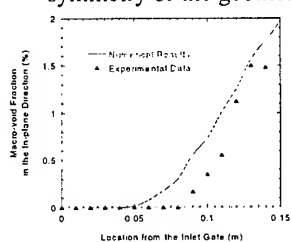


Fig. 8 Comparison between the numerical results and the experimental data in the in-plane direction.

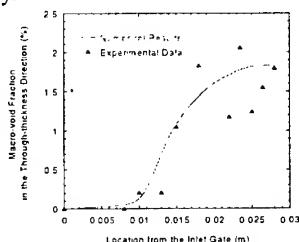


Fig. 9 Comparison between the numerical results and the experimental data in the through-thickness direction.

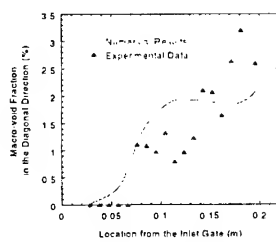


Fig. 10 Comparison between the numerical results and the experimental data in the diagonal direction.

In Figs. 8-10, the numerical results and the experimental data were compared in the three different zones illustrated in Fig. 6. Comparatively close agreement was found.

CONCLUSIONS

Mathematical models on the void formation during the RTM were developed, which was described as a function of the capillary number. The models were incorporated in the RTM simulation program that predicted the three dimensional void distributions. The simulation results were compared with the experimental data from the three dimensional RTM filling experiment.

REFERENCES

1. Patel, N., Rohatgi, V., and Lee, L.J., Micro Scale Flow Behavior and Void Formation Mechanism During Impregnation Through a Unidirectional Stitched Fiberglass Mat, *Polym. Compos.*, 1995, **35**, 837-851.
2. Chen, Y.T., Davis, H.T., and Macosko, C.W., Wetting of Fiber Mats for Composites Manufacturing: II. Air Entrapment Model, *AIChE J.*, 1995, **41**, 2274-2281.
3. Sadiq, Thomas, A.K., Parnas, R.S., and Advani, S.G., Experimental Investigation of Flow in Resin Transfer Molding, *24th International SAMPE Technical Conference*, 1992, 660-674.
4. Lim, S.T., A Study on the Three Dimensional Resin Transfer Mold Filling Process, Ph.D. Thesis, Seoul National Univ., 2000.

NOVEL SENSOR DEVELOPMENT FOR RESIN FRONT DETECTION IN RTM

Shinya MOTOGI¹, Kenjiro YAMAGISHI² & Takehito FUKUDA¹

¹*Department of Intelligent Materials Engineering, Osaka City University
3-3-138 Sugimoto Sumiyoshi-ku Osaka 558-8585, Japan
smtg@mech.eng.osaka-cu.ac.jp*

²*Research Institute, Ishikawajima-harima Heavy Industries
1 Shin-nakahara Isogo-ku Yokohama 235-8501, Japan
yamagishi@zai6.mech.eng.osaka-cu.ac.jp*

SUMMARY: A new dielectric type sensor is developed for detection of the position of resin front in RTM. Comb shape electrodes etched on a thin polyimide film form a dielectric sensor which can be set in the die of RTM, then permittivity response changes with the wet length of the electrodes with resin. This simple physics can be utilized as sensing mechanism of the resin front position in RTM. It is found that the high frequency permittivity linearly changes with the wet length but the dielectric loss factor does not. Specific conditions exist for stable and linear response of the sensor with progress of the resin front in particular resin and preform systems. The sensor can also be used as a cure monitoring sensor after filling of the resin, and as a damage sensor of the material in service.

KEYWORDS: Resin front sensor, Dielectric sensor, Dielectric permittivity, Smart RTM.

INTRODUCTION

Resin transfer molding (RTM) is now expected to be a promising manufacturing technology of advanced composite materials for the next generation because of its high cost performance in making complex shape parts. It is comparatively easy to make 3-dimensionally curved and/or twisted parts, and the fiber volume fraction can be up to as high as 60%; therefore, the strength requirement meets well with the RTM fabricated composite parts. But unfortunately, the present level of the RTM technique is rather low because it is still based on try-and-errors. For improvement of the RTM performance, the smart technology for RTM is strongly required.

RTM processing is divided into three stages: a near net shape preform of fibers is made and set to a cavity of the mold, and melt resin is injected to fill completely the cavity and then the composite is cured at elevated temperature. There are many factors which influence the performance of the RTM fabricated composite parts, e.g., temperature, resin flow, void content, thermal residual stresses etc. The resin filling stage is effectively a penetrating process of resin into preform, therefore it is now widely accepted that the flow is described by

Darcy's law with the analogy of liquid flow through porous media. Darcy's law is a constitutive equation and a mechanics version of Fourier's law relating the heat flux and the temperature gradient. It says that the average velocity v of the resin penetrating the fiber preform is given by

$$v_i = -\frac{K_{ij}}{\mu} \frac{\partial P}{\partial x_j} \quad (1)$$

where P is the pressure, μ is the viscosity of the resin and K_{ij} is the permeability tensor. This last quantity depends on the volume fraction and geometry of the fibrous preform and also on the wettability of the fiber with the resin. Therefore the measurement of value of the permeability tensor is extremely important for simulation of filling stage of RTM process. Such simulation is of course necessary for automation and control as well as better understanding of molding process, i.e., for the smart manufacturing. But the exact and precise measurement of the permeability tensor may be extremely laborious task using e.g., the so-called short-shot technique, and the data has in general large scatter. Automation and process control of RTM using simulation technique might be an indispensable key technology for the development of RTM technique.

This paper describes the development of a new type sensor for RTM processing. The sensor is a dielectric measuring device which is effectively a pair of comb shape electrodes made of copper printed on a flexible board (in fact, it is a rather thin polyimide film). The dielectric response of matter in the vicinity of the electrodes is measured upon application of alternating voltage, therefore the response changes with wet length of the sensor with liquid (in this case, the melt resin). If we can make a long sensor, and set it to the cavity of RTM mold, it can give an information of the position of the penetrating resin front. Because the information can be a continuous one, we can measure very precisely and locally the value of permeability.

Moreover, the same sensor can serve as a cure monitoring device at the curing stage after the filling of the resin. The sensing principle (the dielectric loss measurement) is now widely accepted as a standard and robust but sensitive technique for degree of cure of resin.

DIELECTRIC SENSOR

We developed a new dielectric sensor whose electrodes shape is shown in Fig.1. This is non other than a longer version of already commercially available dielectric sensor developed e.g., by Micromet Inc. and other companies. But these conventional sensors can only be used for cure monitoring purpose not as a resin front sensor. Cure monitoring dielectric sensor monitors dielectric response change of contacting resin when the whole length of its electrodes are wet by the resin. On the other hand, when a long electrodes are contacting with melt resin, its dielectric response also changes.

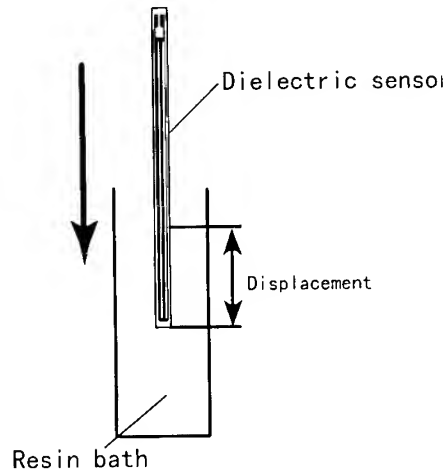


Fig.1 Sensor response test.

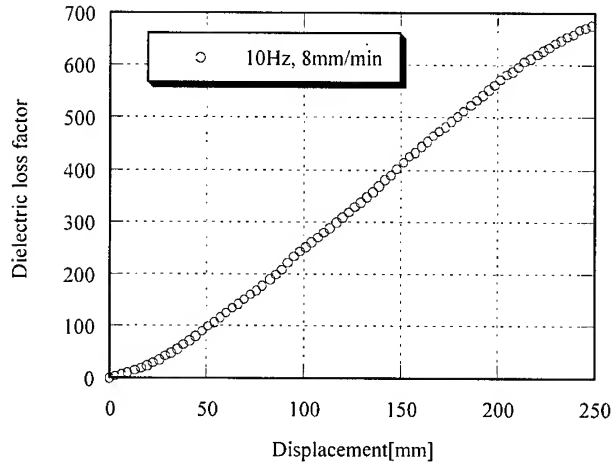


Fig.2 Relationship between the dielectric loss factor measured by the dielectric sensor and displacement.

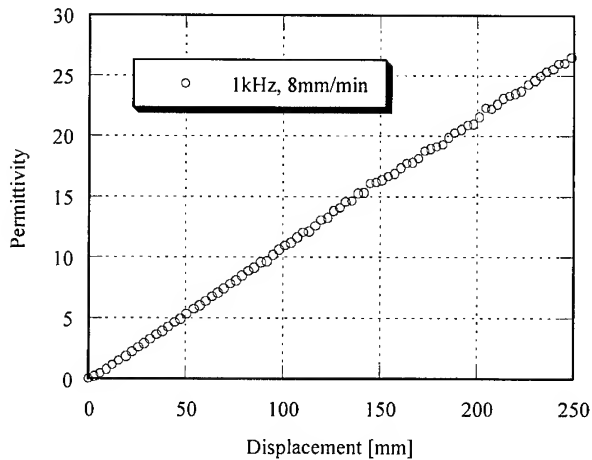


Fig.3 Relationship between the permittivity measured by the dielectric sensor and displacement.

This is the sensing mechanism of the resin front in RTM. The response change is essentially continuous, therefore we can obtain precise information on the resin front position by this new sensor.

We conducted a sensor response test in order to check the response characteristics of the sensor whose electrode is 10mm wide and 250mm long. The sensor is sunk into melt resin with constant speed, and the dielectric response is measured. Figure 2 is the dielectric loss factor, on the other hand Fig.3 is the permittivity. These two quantities are, respectively, the imaginary and the real part of the complex permeability. The figures show relative change in specific quantities (loss factor and permittivity divided by the vacuum permeability). The

frequencies shown in these figures are those of electric field subjected on the two electrode of the sensor. We tested several speeds of sinking, and up to 50mm/min. the linearity of 1kHz was kept in permittivity response. The permittivity at 1kHz was then selected as indicating quantity for our new sensor.

RTM FLOW FRONT MONITORING

We fabricated a simple RTM mold. A plate of three sensors array is set on the lower mold, and glass cloth preform is used because of easy insulation of sensor electrodes and visual observation of the resin front. Carbon fiber preform can be used with thin insulating layer on the sensor surface. A resin reservoir tank is connected and set at the atmospheric pressure, but resin flow is induced by vacuum suction from the other end (Fig.4). The upper mold is made of a thick glass plate through which the resin front can be observed.

The flow experiments are conducted with the mold vertically set in order to avoid the three dimensional distribution of the resin front (Fig.5). The flow is two dimensional in the early stage as is seen from Fig.5, but it gradually becomes one dimensional as the flow progresses. The resin used here is an epoxy of room temperature cure.

Figure 6 is a comparison between the visual observation through upper mold and the center sensor output. The correspondence is excellent, which shows that our new sensor is well capable of monitoring the resin front.

Figure7 indicates a two dimensional flow front pattern drawn by the sensor output. At every 30 seconds, front positions on the three sensor are connected simply by straight lines, but early two dimensionality and later one

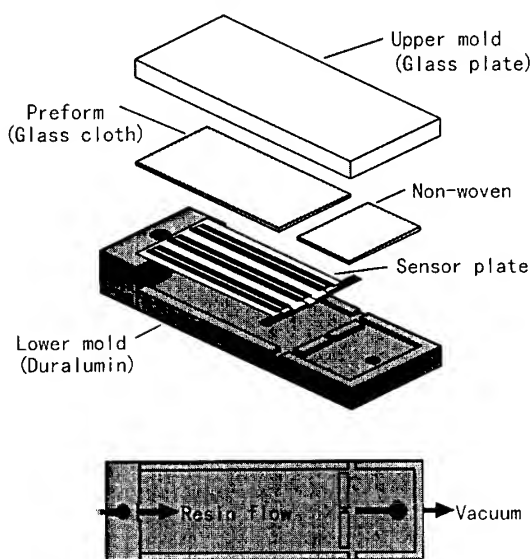


Fig.4 Configuration of the mold.

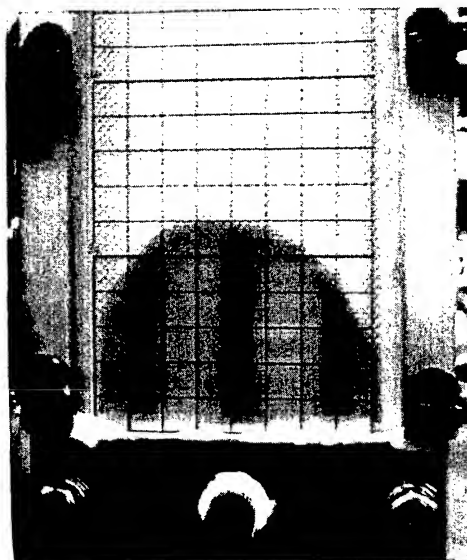


Fig.5 Photograph of resin front progress.

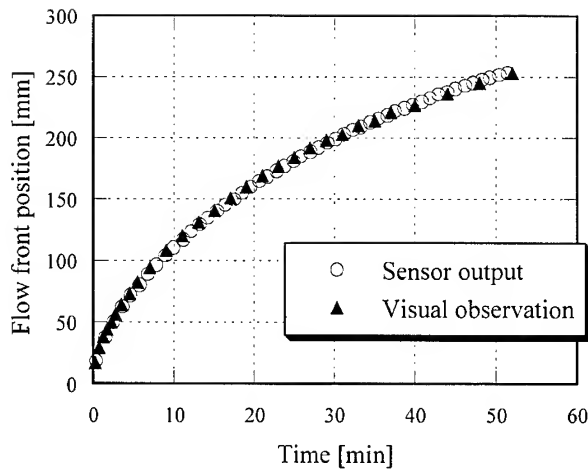


Fig.6 comparison of resin flow-front progress between sensor output and visual observation.

dimensionality of the flow can be clearly recognized.

The sensor base is, in this experiment, GFRP plate for the ease of preparation, but thin flexible base is also available which can easily be set in curved molds. Real molds are in general made of metals, then we cannot see the inside flow. Our new sensor is expected to work in such invisible situation, which leads to the real smart manufacturing of RTM.

The preform used is 8 layers of plain woven glass cloth whose warp direction is set to that of the mold (flow direction). However preform setting can have much variety in real situation, then we tested the case where the warp direction set to the 30° from the mold direction. Figure 8 shows the flow pattern obtained from sensor output. Comparing the visual observation, we confirmed that the three sensors array can detect correctly the resin front also in such case.

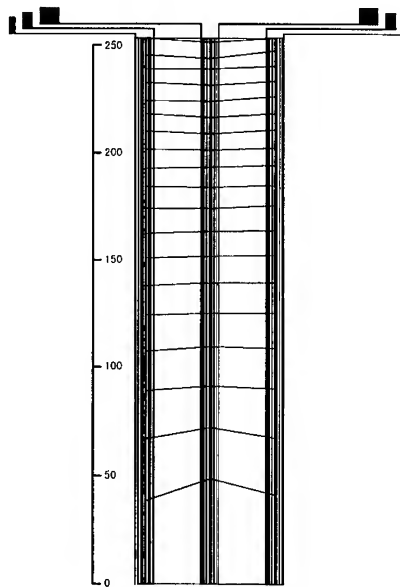


Fig.7 Two dimensional flow front progress at every 30 seconds drawn by sensor output.

CURE MONITORING

The new sensor is essentially a dielectric sensor whose original function is the cure monitoring of resin. Our new sensor was set on an autoclave bagging just below the prepreg stack of GFRP. Figure 9 shows a comparison of the cure responses between our new sensor

and conventional sensor. The ordinate is the log ion viscosity which is calculated from the loss part of the dielectric response, and it is widely accepted as an indicator of the degree of cure of resin. The absolute values of log ion viscosities of new sensor and the conventional sensor are different, however the minimal and saturation characteristic are the same in these two sensors. The minimal point is considered to indicate the gelation point, and the saturation corresponds to the completion of cure. This figure clearly shows that our new sensor can be used also as a cure monitoring sensor.

DAMAGE MONITORING

We are in course of extending our new sensor as a damage sensor using ultrasonics. This completes development of a new sensor which has three functions: i.e., resin front sensor in filling stage, cure monitoring sensor in curing stage, and damage sensor when the material is in use. Such sensor can be called as a whole life sensor.

CONCLUSION

We developed a new type resin front sensor for smart RTM technology. The new sensor has also the cure monitoring capability of resin. It can be extended to have damage monitoring capability.

References omitted.

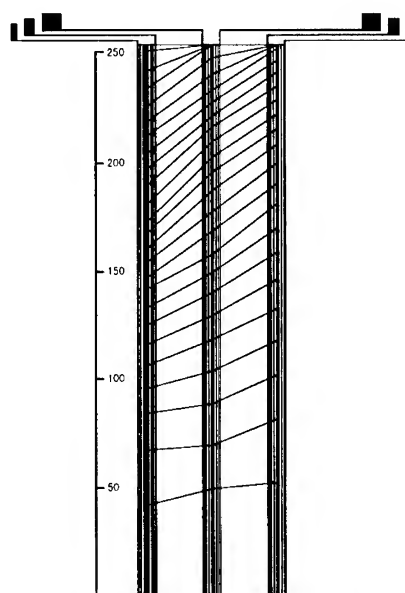


Fig.8 Two dimensional flow front progress at every 30 seconds drawn by sensor output in case of 30° setting of the warp.

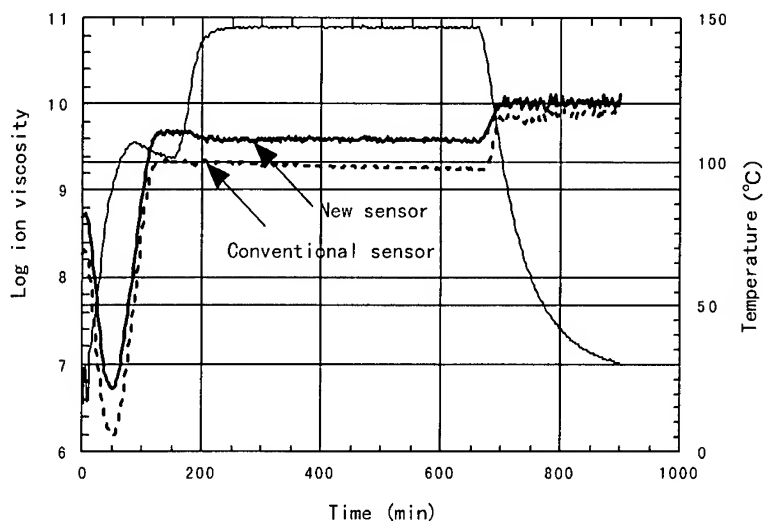


Fig.9 Comparison of cure monitoring ability between newly developed sensor and commercially available sensor.

A STUDY ON THE MANUFACTURING OF SCREW ROTORS USING RTM PROCESS

Jin Ho Choi¹, Jung Do Suh² and Dai Gil Lee²

¹*School of Transport Vehicle Engineering, Gyeongsang National University, 900, Gazwa-dong, Chinju-si, Kyongnam, KOREA, 660-701: jh_choi@nongae.gsnu.ac.kr*

²*Department of Mechanical Engineering, Korea Advanced Institute of Science and Technology, ME3221, 373-1, Kusong-dong, Yusong-gu, Taejon-shi, KOREA 305-701: dglee@kaist.ac.kr*

SUMMARY: Screw rotors are widely used for air compressors in heat pumps, air-conditioners and super chargers of automobiles etc. They are composed of female and male rotors which have complex helical shapes. Since the helical shapes of screw rotors are manufactured usually by high cost machining process due to long machining time with dedicated machine tools. In this work, the screw rotors for air-compressors were manufactured with chopped carbon fiber reinforced epoxy composite materials by resin transfer molding process using separable molds for the easy unloading of helical shape products.

KEYWORDS: screw rotor, screw compressor, RTM, separable mold

INTRODUCTION

Screw compressors have been employed in various industries due to their advantages over conventional reciprocating piston-type compressors: they can be operated with various working fluids which are gases, dry vapors or multi-phase mixtures. Consequently, they are used in air compressors, heat pumps, refrigeration-plants, super chargers of automobiles etc. Since screw compressors do not have reciprocating parts, they can be operated at high speed with less noise and vibration, which results in productivity improvement, compact size, long-life reliability and easiness in maintenance. The manufacturing of screw rotors with conventional materials such as aluminum and steel requires dedicated tools and sophisticated CNC milling process. The long machining time and complex process result in high production cost, which restricted the wide application of screw type compressors despite of their advantages.

The manufacturing difficulties of screw compressors can be solved if the screw rotors are manufactured with composite materials by RTM (Resin Transfer Molding) process because the RTM process enables complex and integrated parts to be produced in one operation. The RTM process is a closed mold process in which molds, pre-placed with fiber preform, are clamped to form composite components. Resin mixture is transferred into a cavity through injection ports at a relatively low pressure (less than 0.69 MPa). The RTM process offers the low production cost of composite parts with large size and complex shape [1].

Fiber reinforced composite materials have been widely used in spacecraft and aircraft

structures because they have high specific modulus, high specific strength and good characteristics in damping. Recently, the application of these materials are extended in sports equipment such as tennis racquet, golf club as the prices of these materials became lower.

In this work, screw rotors were manufactured with carbon fiber reinforced epoxy composite materials using RTM process. Chopped carbon fiber of 3 mm length and epoxy type resin were used as reinforcement and matrix, respectively. The molds were made of aluminum with separable 4-pieces for the easy unloading of helical shaped products.

MANUFACTURING OF CARBON FIBER EPOXY SCREW ROTORS

Shape of the screw compressor

The screw compressor is a rotary type positive displacement compressor whose operation principle is the same as that of a piston type compressor [2].



(a) Suction (b) Compression 1 (c) Compression 2 (d) Discharge

Fig. 1 The operation procedure of a screw compressor

In this study, the asymmetrical screw rotors of 164.2 mm length composed of female rotor and male rotor were manufactured. The female rotor of 42.0 mm radius and male rotor of 46.9 mm radius had 6 teeth and 4 teeth, respectively. The cell volume, which is a closed volume between rotors and housing, varies along the rotation of rotors. Fig. 1 shows the compression process and variation of the cell volume. The shape of housing covers serves as both suction and discharge valves. The screw rotor has complex section profile and large helix angle for enhanced performance. Fig. 2 shows the section profiles which are combination of curves such as epi-trochoid, arc, epi-cycloid, and arc-evolute [3].

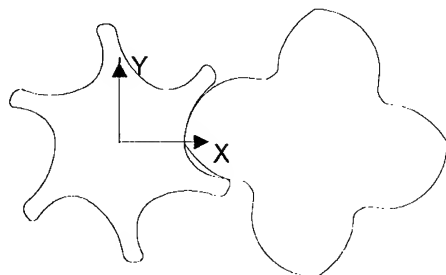
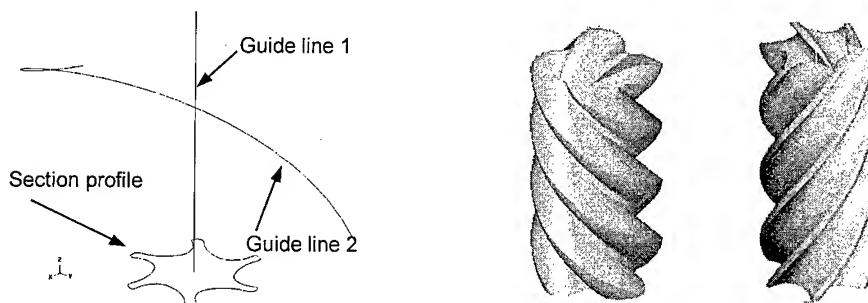


Fig. 2 The meshing of screw rotors

Mold for the screw rotors

The section profile of the screw rotor was obtained as discrete point data by C-programming with the distance in neighboring points kept less than 0.5 mm. Then the data were converted into the script format used in CAD system by C-programming. The script format was the section profiles of the screw rotors formed by the connection of discrete points using spline curves as shown in Fig. 2. The script file was read by the Mechanical Desktop (Auto-desk Co.) [4], a CAD software for machinery design, and saved in the format of IGES (Initial Graphics Exchange Specification) for Mastercam (CNC software Co.) [5]. A helix curve and a center-line of a screw rotor were used as the guide line for the generation of swept helical surface of the screw rotor. Fig. 3 (a) shows both the section profile of the screw rotor and the two guide lines, which are composed of a straight line and a helix curve. Fig. 3 (b) shows the three dimensional helical surface obtained by the sweep surface generation function of the Mastercam.



(a) The profile of the female rotor and two guide lines (b) Helical surfaces of screw rotors
Fig. 3 The surface modeling of screw rotors

The mold for the screw rotors was made of aluminum with separable 4-pieces for easy unloading of the products. The mold was machined with ball-end mills using a CNC milling machine. Fig. 4 shows one part of the helical mold for the male rotor. Fig. 5 (a) shows the assembled shape of the four-piece mold and Fig. 5 (b) shows the cover plates of the mold, which have grooved shapes like rotor profiles. The cover plates work as resin flow ports and vents. Resin mixture flows from resin port along the grooves which form ring gate system, and fills up the screw shaped cavity. The vent system had a clearance of 0.5 mm.

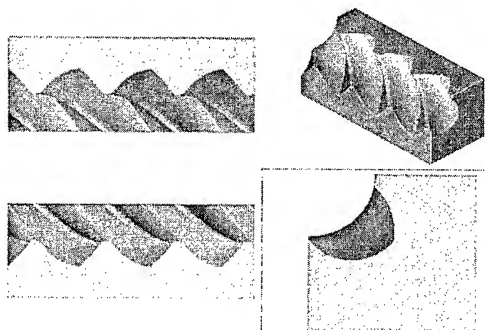
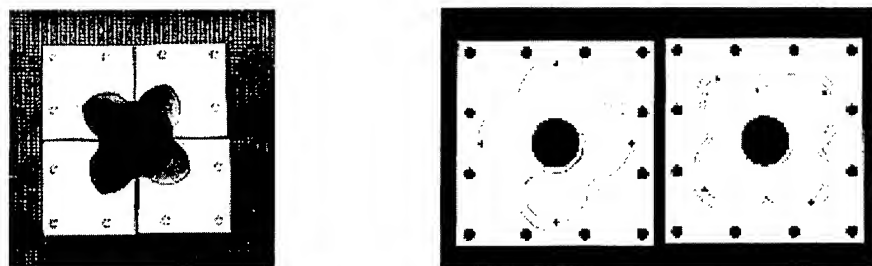


Fig. 4 A piece of helical mold for a male rotor



(a) helical parts of molds consist of four pieces (b) Cover parts of molds

Fig. 5 Mold parts for RTM of a screw rotor

Materials and RTM process

The resin system for the RTM process should have long pot life and low viscosity less than 1000 cPs during injection process for adequate wetting [6]. Since the compressed air in screw compressor rises from room temperature at inlet to 150°C at outlet due to nearly adiabatic compression, resins for the application of screw compressor rotors should have little degradation until 150°C. The low shrinkage of resin during curing process is essential for the precision of products. In this study, an epoxy resin system (IPCO 2434/2310, National Starch & Chemical Co.) was used, whose properties are shown in Table 1.

Table 1 Properties of IPCO 2434/2310

Mixed viscosity	Density	Pot life	Shrinkage	Mix ratio
1000 cPs	1.12 / 1.10	50 min	0.001 cm/cm	100 : 20

The strength and stiffness of composite materials are dependent on reinforcements which are usually glass, carbon or aramid fibers. Since screw rotors are exposed in chemicals, such as lubricant oil of high temperature, the chemical resistance of fiber is also important. Therefore, chopped carbon fiber of 3 mm was used for reinforcement because carbon fiber has high specific stiffness and good chemical resistance. The properties of the carbon fiber used are shown in Table 2.

Table 2 Properties of the carbon fiber

Tensile strength	Tensile modulus	Elongation	C.T.E.	Length
3528 MPa	245 GPa	1.5 %	$-0.1 \times 10^{-3} / ^\circ\text{C}$	3 mm

The RTM apparatus is composed of a resin bath, a mold and resin flow lines. The resin in the bath was agitated with a manual agitator during vacuum applying period to break bubbles produced. Then pressure was applied to the resin bath to inject the resin from the resin bath into the mold. A core made of aluminum 6061T6 as shown in Fig. 6 was inserted in the mold before resin injection. The core had a role to transmit the motor power to the screw rotors and reduced the shrinkage of the composite rotor by decreasing the resin volume. It had stepped sections for bearing mounting and knurling sections for secure joining with composite materials. The knurling size of 1.5 mm was used to enhance joining characteristics [7].

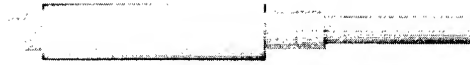


Fig. 6 A core of a screw rotor

Fig. 7 shows the RTM apparatus and the RTM procedure for manufacturing screw rotors is as follows.

- (1) Cleaning molds with acetone or MEK (methyl ethyl ketone)
- (2) Spraying mold-release (Release-All #30 of Airtech Co.)
- (3) Filling up the mold with reinforcement and the aluminum core.
- (4) Mixing of epoxy resin and hardener in the resin bath.
- (5) Agitation with applying pressure and vacuum alternately.
- (6) Resin injection into the mold using the air pressure in the resin bath.
- (7) Curing and demolding of the products.

During the resin transfer process, the air pressure of 6 atm was applied in the resin bath. The resin flow rate was controlled by the control valve installed between the resin bath and the mold. Resin transferred through PVC pipe line, 8 mm in diameter, from the resin bath to the mold. The control valve and the valve installed at the end of the vent were closed during the curing process to prevent growing of bubbles.

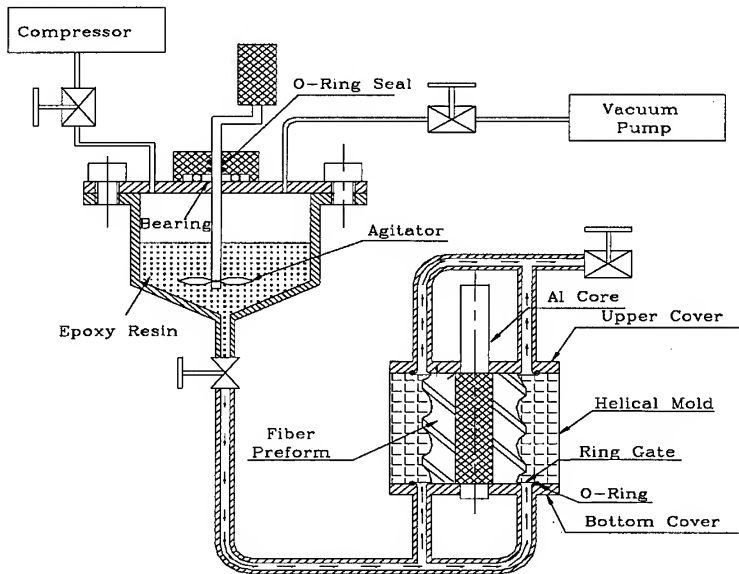


Fig. 7 The apparatus for RTM process



Fig. 8 The composite screw rotors manufactured by RTM process

CONCLUSIONS

Since the manufacturing of helical shape screw rotors with conventional materials such as aluminum and steel requires dedicated tools and sophisticated CNC milling process, which requires long machining time with high production cost, the screw rotors for air compressors were successfully manufactured with chopped carbon fiber epoxy composite materials by RTM (Resin Transfer Molding) process because the RTM process enables complex and integrated parts to be produced in one operation. The molds were made of aluminum with separable 4-pieces for the easy unloading of the helical shaped products.

ACKNOWLEDGMENT

This work was partially supported by the BK21 project of Korean Government.

REFERENCES

1. T. G. Gutawski, "Advanced Composites Manufacturing", John Willy & Sons Inc., 1997, pp.396-399.
2. N. Stosic and K. Hanjalic, "Development and Optimization of Screw Machines with a Simulation Model," *Journal of Fluid Engineering*, Vol. 119, 1997, pp.659-663.
3. F. L. Litvin and P. H. Feng, "Computerized Design, Generation and Simulation of Meshing of Rotors of Screw Compressor," *Mech. Mach. Theory*, Vol. 32, No. 2, 1997, pp.137-160.
4. H. C. Kim, "Mechanical desktop [MDT]", HanBaek press, 1998, <http://www.autodesk.com/>.
5. S. C. Jonathon Lin and F.C. Tony Shiue, "Mastercam version 7", Scholar's Int. Publishing Corp., 1998, <http://mastercam.com/>.
6. S.T. Peters, "Handbook of composites 2nd ed.", Chapman & Hall, 1998, pp.433-456.
7. Y. G. Kim, K. S. Jeong and D.G. Lee, "A Study on the Composite Screw Rotors for Superchargers," *Composite Structures*, Vol. 32, 1995, pp.575-581.
8. P. K. Mallic, "Composites Engineering Handbook", Marcel Dekker Inc., 1997, pp.51-100.

Textile Composites

PREDICTION OF ELASTIC MODULI OF WOVEN COMPOSITE BY USING ARTIFICIAL NEURAL NETWORK

DING Xin and YI Honglei

*College of Textiles, Dong Hua University, 1882 Yanan Road (west)
Shanghai 200051, PR China: xding@dhu.edu.cn*

SUMMARY: Artificial neural networks (ANNs) have been proven an ideal tool to solve non-linear problems based on historical data and it is applied, in this study, to predict elastic moduli of woven composites. Defined by nine structural parameters, multi-layer woven fabrics (MWFs) were used as reinforcement for the composite, of which elastic moduli were the desired property to be approached in both longitudinal and transverse directions. 64 pairs of data were obtained corresponding to the fiber architecture of MWFs and the elastic moduli of the composite. A three-layer neural network was developed and trained with 48 pairs of obtained data by using a modified back propagation algorithm. Performances of the developed network were assessed with the remaining 16 pairs of data. It was demonstrated that the network could perform a function mapping between fiber architecture and composite performance with errors within given range.

KEYWORDS: multi-layer woven fabric, artificial neural network, back propagation, woven composite, structural parameter, elastic modulus

INTRODUCTION

Multi-layer woven fabrics (MWFs) are three-dimensional textile structures consisting of two or more layers woven fabrics, with corresponding warp and filling yarns, jointed together in the thickness direction by binding yarns. Because of their great potential in net-shape manufacturing and excellent structural integrity, MWFs have been applied as three-dimensional reinforcement for advanced composites. Due to structural complexity of MWFs, to understand the contribution of reinforcement to the properties of woven composites, it is desirable to apply a suitable modeling technique instead of traditional ones to avoid too complicated analyses.

Artificial neural networks (ANNs) have been proven an ideal tool to develop models directly from historical data and some successive applications have been reported in the literature[1-3]. They are data processing systems that can give human-brain-like performances in a digit computer. ANNs are characterized by a large number of neuron-like processing elements connected together in a certain way. With weighted connections between the elements, the network can be trained to contain "Knowledge" in a learning process. A well-developed network is expected to give correct responses that simulated system could give and, therefore, it could be an effective modeling technique to build a relationship between fiber architecture of reinforcement and performances of composite.

In addition to fiber, matrix and their interface, mechanical properties of composite reinforced by MWFs are primarily influenced by yarn properties (count and cross sectional shape), fiber volume fraction (warp, filling and binding densities) and fiber orientation (binding pattern, layers of fabric, etc). Determined by these primary parameters, fiber architecture determines geometric and mechanical properties of reinforcement and, consequently, performances of composites. To quantitatively represent fiber architecture of MWFs, several structural parameters are presented in this study. It is hoped that these parameters could be used, by means of ANNs, to predict elastic moduli of woven composites.

STRUCTURAL PARAMETERS OF MWFs

According to different binding patterns, fiber architecture of MWFs can be classified into two groups: angle interlock and orthogonal interlock[4], the later is focused in this study. For orthogonal interlock structures, binding warps are in 90° to the fabric plane. According to the binding thickness, which describes number of fabric layers jointed by a binding thread, the fiber architecture can further be divided into through-the-thickness binding and layer-to-layer binding. Although there are a number of parameters determining fiber architecture of MWFs, it has been demonstrated that six parameters are sufficient to fully describe the binding pattern and its variations[5]. They are: groups of binding warp along the thickness direction (K_b), number of fabric layers (n_f), number of fillings in a weave repeat that a binding thread interlacing in the thickness and the lengthwise directions (n_{fi} , n_{fl}), minimum number of fabric layers by moving a binding warp up or down to the nearest one (S_f) and minimum number of fabric layers by moving a binding warp in the thickness direction along the i -th filling column until it reaches the same level of the other one in the $(i+n_f/2)$ -th filling column (S_l). Further investigation[6] discovers that, among those six parameters, only three of them are independent. In other words, once three out of six afro-mentioned parameters are known, fiber architecture of MWFs can be determined. In this study, parameters n_{fi} , S_f , and K_b are chosen to represent the fiber architectures, as illustrated in Fig.1. The numbers inside the square brackets under each pattern represent n_{fi} , S_f , and K_b respectively.

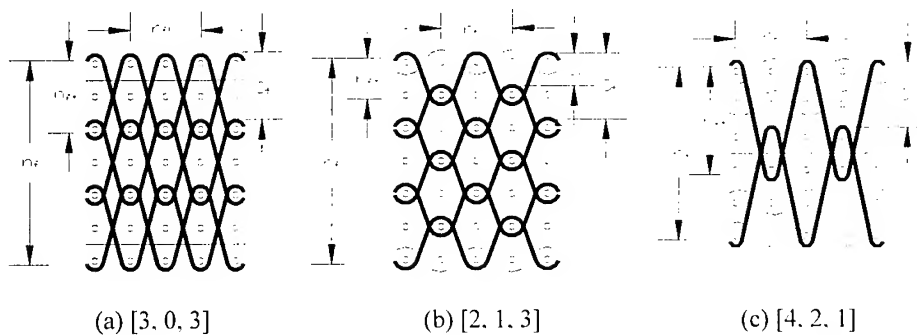


Fig.1 Schematic diagram of MWFs

In addition to the three parameters representing the binding patterns, from the point of view of contributions of reinforcement to mechanical properties of woven composites, six additional parameters are required. They are: densities of warp and filling (P_f , P_w), their counts (N_f , N_w) and deformation coefficients of yarns cross section (λ_f , λ_w). Totally, nine structural parameters are necessary to fully represent the fiber architecture of MWFs and their influences on woven composite.

BACK PROPAGATION NETWORK

Back propagation network (BP net) is a multi-layer feed forward ANN introduced by Rumelhart et al[7] in 1986. It is composed of an input layer, an output layer and in between hidden layer(s). In each layer, there is a number of processing elements, neurons, containing given transfer function. The neurons in adjacent layers are jointed by connection weights. Fig.2 schematically shows a typical BP net with a single hidden layer. The number of neurons in the input layer, N_0 , equals to the number of input parameters and that in the output layer, N_m , is equivalent to the output parameters. The number of neurons in the hidden layer should be determined empirically during the process of network development.

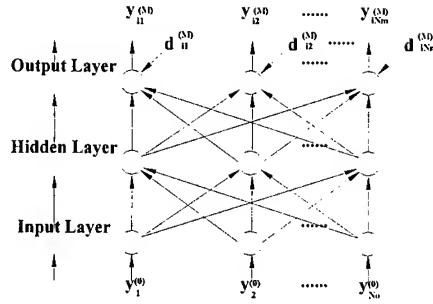


Fig.2 A typical BP net

Before performing simulation, a BP net must be trained in a learning process with known data sets in pairs of input and output. There are two stages in this process: a forward pass and a backward pass. In the former stage, the net is presented with training inputs. With the transfer functions and connection weights in consecutive layers, the input data are processed gradually to present the net's responses at the output layer. Once expected outputs are failed to obtain, i.e. the difference between the net outputs and the target ones (training outputs) exceed the set values, the error estimates of the output neurons are computed in the backward pass. In this stage, the thresholds and the connection weights of each layer are then adjusted in order to reduce the error. Layer by layer the errors are propagated back to the input layer. This process is repeated until the errors associated with the net outputs compared with the target ones converge to an acceptable level.

In a M -layer BP net, the output of the j -th neuron in the k -th layer, $y_j^{(k)}$, can be determined in terms of the corresponding input, $y_j^{(k-1)}$:

$$y_j^{(k)} = f\left(\sum_{i=1}^{N_{k-1}} w_{ij}^{(k-1)} y_i^{(k-1)} - \theta_j^{(k-1)}\right) \quad j=1, 2, \dots, N_k, \quad k=1, 2, \dots, M \quad (1)$$

where, $w_{ij}^{(k-1)}$ is the connection weight between the i -th neuron in the $(k-1)$ -th layer to the j -th neuron in the k -th layer. $\theta_j^{(k)}$ is the corresponding threshold. N_k is the number of elements in the k -th layer and $f(\cdot)$ the transfer function. In this study, logarithmic hyperbolic activation function is applied in the hidden layers and linear function in the output layer:

$$\text{In the hidden layer:} \quad f(x) = 1 / (1 + e^{-x}) \quad (2a)$$

$$\text{In the output layer:} \quad f(x) = x \quad (2b)$$

As explained previously, a number of known data sets of inputs $Y_1^0, Y_2^0, \dots, Y_l^0$ and corresponding outputs $D_1^M, D_2^M, \dots, D_l^M$ are required to train a BP net in order to obtain a relationship between them. The input/output relationship is, in fact, contributions of the connection weights. The evaluation of the weights follows the principle that the function $E(w)$ should be minimum:

$$E(w) = \sum_{i=1}^I \|Y_i^M - D_i^M\|^2 \quad (3)$$

Corresponding to the net inputs $Y_i^0 = [y_{i1}^{(0)}, y_{i2}^{(0)}, \dots, y_{iN_m}^{(0)}]$, the net will generate its outputs $Y_i^M = [y_{i1}^{(M)}, y_{i2}^{(M)}, \dots, y_{iN_m}^{(M)}]$. Then comparisons are made between the net outputs and the target ones $D_i^M = [d_{i1}^{(M)}, d_{i2}^{(M)}, \dots, d_{iN_m}^{(M)}]$. If $E(w)$ is less than the desired value, the learning process is terminated and the trained BP net is ready for applications.

The learning process is actually the process of adjustments to the connection weights and the thresholds. The adjustments to the connection weights are performed as following:

$$\Delta w_{ij}^{(k-1)}(t+1) = \eta \cdot \Delta w_{ij}^{(k-1)}(t) + (1-\eta) \cdot \alpha(t) \cdot G_y^{(k-1)}(t) \quad (4)$$

$$G_y^{(k-1)}(t) = -\partial E / \partial w_{ij}^{(k-1)}(t) \quad (5)$$

where, $\Delta w_{ij}^{(k-1)}(t)$ is the increment of the connection weight in the t -th iteration. η ($0 < \eta < 1$) is the momentum factor and $\alpha(t)$ the learning rate. The adjustments of the threshold will follow the same procedures.

In order to increase the convergent speed of the BP net in learning processes, variable learning rate is sometimes preferable. In this study, a learning strategy suitable for non-linear models is adopted[8].

$$\alpha(t+1) = \begin{cases} K_I \cdot \alpha(t) & \lambda = 1 \\ 0.618 \cdot K_I(t) & \lambda = -1 \end{cases} \quad (6)$$

$$\lambda = \text{sign}[G_y^{(k-1)}(t) \cdot G_y^{(k-1)}(t-1)] \quad (6a)$$

$$\text{sign}[x] = \begin{cases} 1 & x > 0 \\ -1 & x \leq 0 \end{cases} \quad (6b)$$

where, K_I is the incremental factor chosen in the range $1 < K_I < 1.618$.

Relying on the gradient of error variation at the output, the BP net can perform the adaptive adjustment of learning rate in the learning process with Eqn.6 and its supplements. If the gradient directions of two successive updates are opposite (i.e. $\lambda = -1$), indicating too fast the learning rate or too large the step size, then the step size should be reduced. On the other hand, if the gradient directions of two successive updates are the same (i.e. $\lambda = 1$), which means too slow the learning rate, then the step size should be increased.

PREDICTION OF ELASTIC MODULI OF WOVEN COMPOSITE

Woven composites with MWFs of E-glass as reinforcement and polyester resin as matrix were involved in the study. The fiber architectures of the MWFs represented by the nine structural parameters are those described in the previous section of this paper. Mechanical properties of the components are: for E-glass, $E_f = 68.7\text{GPa}$, $\nu_f = 0.22$ and for polyester matrix, $E_m = 2.45\text{GPa}$, $\nu_m = 0.44$. The fiber volume fraction of the composites was 0.7. Elastic moduli of the composites, E_x and E_y , were obtained in both lengthwise and transversal directions. 64 pairs of data set were organized in the form that the structural parameters as inputs and the

elastic moduli as outputs. These data were used to train the BP net in the learning process and, also, to examine the net performances.

A three-layer BP net with one hidden layer was developed. There were nine neurons at the input layer corresponding to the nine structural parameters of MWFs and two neurons at the output layer for the elastic moduli of the composite. The number of neurons at the hidden layer should be determined during the net development. In general, more the neurons at hidden layers, faster the convergent speed of a net, however, less the generalization ability. In other words, with an increase in neurons at hidden layers, a BP net will increase its ability to memorize the characters of learning samples instead of giving correct responses to inputs other than training data. Therefore, with sufficient convergent speed and response precision, it is desirable to choose a small scale net structure.

Among the 64 available data sets, 48 were chosen to train the PB net and to optimize the net parameters. The remaining 16 pairs of data set would be used to assess the performances of the net to simulate the situation when the net was facing the data it had never seen before. According to the experiences, the initial learning rate was set 0.01, the momentum factor 0.9 and the tolerance of output error 0.01. In addition, 180 neurons at the hidden layer were chosen after consideration to the convergent speed and prediction precision of the net. The incremental factor $K_f = 1.005$ was also determined empirically.

After 5,236 training iterations, as shown in Fig.3, the sum-square-error defined by Eqn.3 reduces to the tolerant value, 0.01, indicating the accomplishment of the learning process.

To assess the performances of the trained BP net, the remaining 16 pairs of testing data were applied. The net outputs (predicting values) were compared with the target ones, the elastic moduli of the woven composite. It is illustrated in Fig.4 that two groups of data are in very good agreements with the correlation coefficient 0.99.

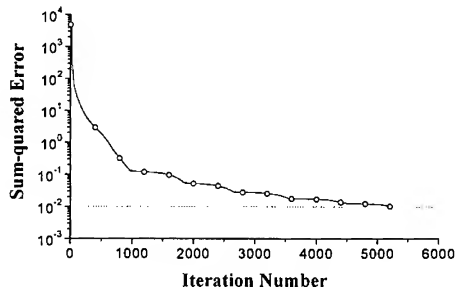


Fig.3 Variation of error estimate

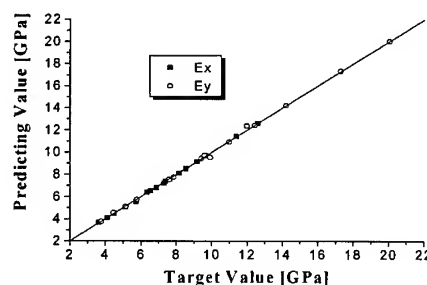


Fig.4 Prediction value vs. target value

CONCLUSION

It is well known that performances of textile composites depend on their fiber architecture. To build a relationship between them, however, complicated model developments and analyses are often required. In this study, ANNs were applied to approach the problem of predicting mechanical properties of MWF's reinforced composites by referring to the fiber architecture. Nine structural parameters were used to define the fiber architecture of MWFs and used as inputs to the BP net. Two output parameters were elastic moduli of the woven composite in both lengthwise and transversal directions. 64 pairs of testing data were then obtained. A three-layer BP net was developed and trained with the testing data and a relationship was

developed between the fiber architecture of MWFs and mechanical properties of the woven composite. Then the developed net was applied to predict elastic moduli of woven composite of defined fiber architecture. Very good agreements between predicting values and the target ones proved the validity of the current approach.

REFERENCES

1. Y.Akoi and O.I.Byon, "An Application of Neural Network to Identification of Boundary Conditions of CFRP Laminated Plates", *Proc. of the Joint Canada-Japan Workshop on Composites*, 1996, pp.129-132.
2. F.Pynckels, P.Kiekens, S.Sette and L.Van Langenhove, "Use of Neural Nets for Determining the Spinnability of Fibers", *J.Text.Inst.*, Vol.86, 3, 1995, pp.425-437.
3. M.C.Ramesh, R.Rajamanickam and S.Jayaraman, "The Prediction of Yarn Tensile Properties by Using Artificial Neural Networks", *J.Text.Inst.*, Vol.86, 3, 1995, pp.459-469.
4. B.N.Cox and G.Flanagan, "Overview of Textiles - Hand Book of Analytical Methods for Textile Composites", *NASA Contract Report 4750*, March 1997.
5. DING Xin and YI Honglei, "The Structural Characteristics of Orthogonal Interlock Woven and Their Effect on the Fiber Volume Fraction of Reinforcement", *Journal of Tianjin Institute of Textile Science and Technology*, Vol.17, 4, 1998, pp.15-19.
6. YI Honglei and DING Xin, "On the Representation of Multi-Layer Woven Structure", *Journal of China Textile University*, Vol.16, 3, pp.14-16.
7. D.E.Rumelhart, G.E.Hinton and R.J.Williams, "Learning Internal Representations by Error Propagation - Parallel Distributed Processing", MIT Press, Cambridge, USA, 1986.
8. YI Honglei and DING Xin, "A New Approach towards Optimizing Network Training Parameters for BP Adaptive Learning Rate Algorithm", accepted by *SAMPE Journal*.

INTER-LACED FIBERS / LIGHT-CURING RESIN COMPOSITE STRUCTURES

N. Akkus¹, G. Verchery², Y. Kanemoto¹, M. Kawahara¹ and A. Hurez²

¹Tokyo Metropolitan University, Faculty of Engineering
1-1 Minami-osawa, Hachioji-shi, Tokyo, 192-0397 JAPAN
nihat@mech.metro-u.ac.jp, *kawahara@mech.metro-u.ac.jp*

²ISAT, LRMA, 49 Rue Mademoiselle Bourgeois,
B.P. 31, 58027 Nevers, FRANCE

Georges.Verchery_isat@u-bourgogne.fr, *a.Hurez@iutlecreusot.u-bourgogne.fr*

SUMMARY: Design and testing of 2 dimensional FRP structures using light-curing resin is presented. The structures can be described as formed of girders spaced by skew ribs. The present study was limited to plane structures with two girders and ribs as 45° roving are positioned along the girders and the ribs so that fibers are interlaced at the joints between ribs and girders. Several deposition paths were designed. They differ by interlacing and proportions of fiber in girders and ribs. T-glass fibers impregnated in light-curing resin were placed in an open die for the manufacturing of the test pieces. Light curing was performed in 20min. by using 600W metal-halide lamp with the light wavelength of 380 to 800nm. Overall stiffness and strength of the structures were investigated in bending and local deformations were measured with the strain gages. Finite element modeling of four-point bending test for some test pieces has been carried out using beam elements to predict the deflection and the strains. Discussions were directed to the comparison of the results of the various designs.

KEYWORDS: Fiber inter-lacing, light-curing resin, FRP structural parts, bending, FE modeling

INTRODUCTION

Composite structural parts manufactured from fibers have been used in the industry to produce mechanical parts in which lightness and high strength are required. High pressure vessels, rotating shafts, robot arms, and other sports and leisure goods can be shown as examples of application of the composite fibers. Recently, many composite design works are underway for Japanese supersonic transport airplane and some truck containers are produced by Toray company[1] of Japan. In a previous work Chen and Tsai[2] studied grid structures to analyze and optimize the design of composite structures utilizing unidirectional continuous fibers. Tsai and Liu[3] also studied low cost square composite grids to make two or three-dimensional parts. Fibers impregnated in resins are very strong under tension loads, however, very low compression and bending strength makes the application of the fibers very limited in the industrial area. Thus, it is difficult to manufacture of two or three-dimensional parts, which work under several type of loading such as bending and compression.

Two-dimensional parts with interlaced joints were prepared to improve bending and compression strength of the fibers in the present study. Test pieces were prepared using GFRP

roving impregnated in light curing resin. An open die was used for manufacturing of the test pieces. Roving were directed to follow certain path in which the same roving passed through upper girder, ribs and lower girder. This made the fibers face different type of loads. Light curing process was performed by using metal-halide lamp, after deposition of fibers into open die. Overall stiffness and strength of the structures were investigated in bending and FEM simulations. Local deformations were measured with the strain gages. Discussions were directed to the comparison of the results of the various designs. Experimental results revealed that the overall stiffness of the two-dimensional test pieces are improved by interlaced joints.

DESIGN AND ANALYSIS OF INTERLACED JOINTS

Test pieces with a shape shown in Fig.1 were prepared to evaluate the bending stiffness of the two-dimensional structural parts produced by unidirectional continuous fibers. A test piece can be divided in to three main sections, which are the upper girder, ribs and lower girder. The most simply design is to produce the girders first by using a number of roving and then add ribs between upper and lower girder by another number of roving. But in this case, the strength in joints between girders and ribs will be equal to that of resin strength, which is very low if compared to tensile strength of fiber. Thus several deposition paths given in Fig. 2 are proposed in the present study to improve the strength in joints. The unidirectional continuous fiber were directed to go between girders and ribs so that the same continuous fiber can be loaded compressive load while passing on the upper girder, and tensile load while passing trough lower girder. Thus, depending on the place, the same fiber is forced to undergo compression and tension loads by passing through ribs.

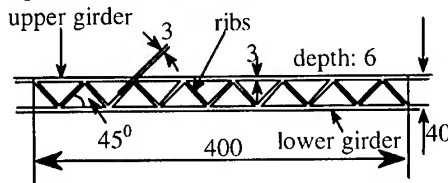


Fig. 1 Shape of interlaced and light cured resin composite structure

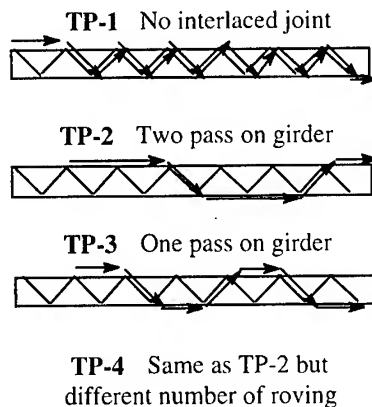


Fig. 2 Simplified deposition paths of test pieces with and without interlaced joints produced from unidirectional continuous fibers

Four-type of test pieces were manufactured to understand the advantages of the new design. In the first design, which is the simplest one, the deposition direction of the roving was not changed between upper and lower girder. This design had no interlaced

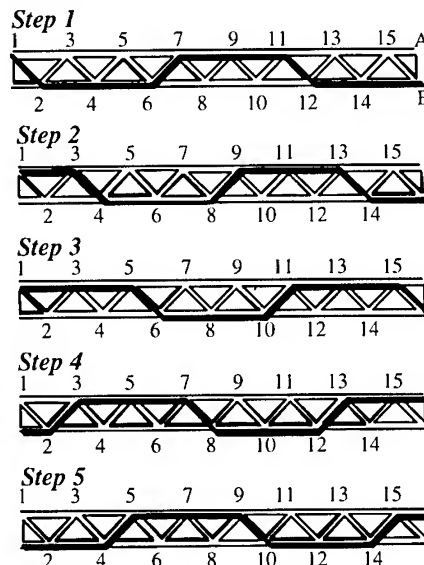


Fig. 3 Roving deposition path of design 2 (TP-2)

joints between girder and ribs. The test piece was prepared to compare the strength of the interlaced test pieces with the one without interlaced joints. In the second design, the deposition direction of the roving was changed after every two block between upper and lower girder to make interlaced joints. The third design was similar to the second design but the deposition direction of the roving was changed after each block between upper and lower girder. In the forth design the number of the roving in upper and lower girder was increased to 6.5 and roving in the ribs were decreased to 2. Table 1 indicates some properties of four types of test pieces. As an example of interlaced joint design, roving deposition path of design 2 (TP-2) is shown in Fig. 3. This design was created by considering that the upper and lower girder need higher strength than that of ribs. Thus, when a set of deposition shown in the Fig. 3 was performed, the test piece has 2 roving in the upper and lower girder and 1 roving in the ribs. The roving deposition path from step 1 to 5 was repeated 3 times to obtain a test pieces whose roving ratio of girders and ribs were 6:3:6.

Table 1. The manufacturing properties of test pieces

	Roving in girders and ribs	Joint type	Deposition path
TP-1	6.0:3.0:6.0	resin only	no pass
TP-2	6.0:3.0:6.0	interlaced	2 pass on girder
TP-3	6.0:3.0:6.0	interlaced	1 pass on girder
TP-4	6.5 : 2.0 : 6.5	interlaced	2 pass on girder

Prediction of tension and bending stiffness by FEM

An analysis was developed to predict tension (A_{eq}) and bending (D_{eq}) stiffness from the component stiffness. A half-pattern of the beam was modeled as the assembly of three beams (Fig. 4). The global stiffness matrix was derived, then loads for pure tension and pure bending were applied. From the response to these loads, formulas for the equivalent tension and bending overall stiffness were obtained and are shown hereafter. It appears from these formulas, than both the tension and bending stiffness of the components (girders and ribs) have an effect on the overall stiffness.

Tension stiffness:

$$A_{eq} = 2 \frac{A_1 A_2 h^2 + 12 A_1 D_2 \cos^2 \theta + 6 A_2 D_1 \cos \theta}{A_2 h^2 + 12 D_2 \cos^2 \theta}$$

Bending stiffness:

$$D_{eq} = \frac{1}{2} A_1 h^2 + 2 D_1 + D_2 \cos \theta$$

where:

A_1 : tension stiffness of parts 1 and 3

A_2 : tension stiffness of part 2

D_1 : bending stiffness of parts 1 and 3

D_2 : bending stiffness of part 2

θ : angle between the girders and the ribs.

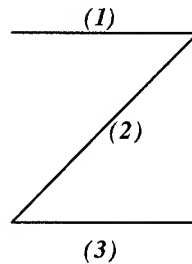


Fig. 4 Three beam model of the half pattern

EXPERIMENTAL

Preparation of the test pieces

T-glass roving, RST-220PA, which had 6400x13mic fiber in a bundle, was used as roving. Table 2 shows material properties of GFRP roving. An open die was employed to lay out unidirectional continuous fibers in predefined paths. Fibers first impregnated in a resin bath with light curing resin then deposited in the die grooves. A new type of vinyl ester resin, LC-720, manufactured by Showa Kobunshi Polymer Co. of Japan, was used as matrix resin base for roving. After deposition, test pieces were placed 30cm distance from 600W metal halide lamps with light range of 380 to 800nm, which provided visible to near-infrared light as the source of the curing light. The light exposure time was 20min for all test pieces. The photo of light curing process is shown in Fig. 5.

Table 2 Material properties of GFRP

E_L (GPa)	85.5
E_T (GPa)	12.6
G_{LT} (GPa)	14.8
ν	0.26
σ_B (GPa)	2.87

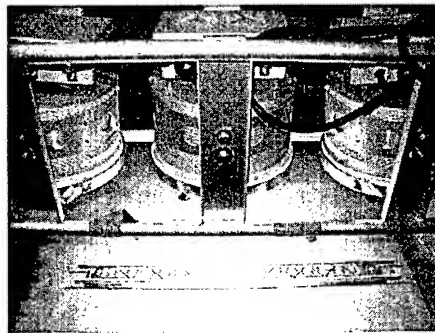
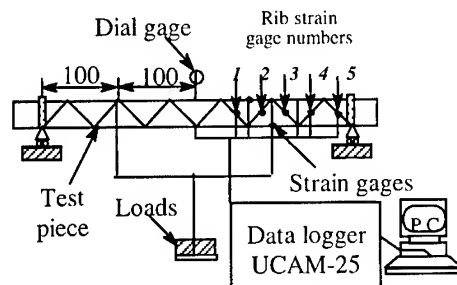


Fig. 5 Photo of the open die and test piece during light curing process

Bending test experiments

Four-point bending tests were conducted to understand the overall stiffness of the produced part. Illustration of the four-point bending test equipment is shown in Fig. 6. A double hook



Dimensions are in mm
Fig. 6 illustration of test piece and four-point bending test equipment

was used to apply gradually increased bending loads until collapse of the test pieces. Deflections were measured by a dial gage located in the center of the test piece. Attentions were paid to place hooks and supports on the interlaced joints in all experimental tests. The support and hook span was 400 and 200mm, respectively. Strain gages were used to obtain strain values at the upper and lower girders and ribs at several locations. The measured values of deflection and strains then were sent to a microcomputer via data logger.

RESULTS AND DISCUSSIONS

Overall stiffness of test pieces

Interlaced joints were utilized to improve overall stiffness of the two-dimensional composite structure. Figure 7 shows load vs. deflection relationship of all 4 types of test pieces. Test Piece 1 (TP-1), which had no interlaced joints, was broken around 200N with very low

deflection value if compared with interlaced test pieces. The second and third test pieces (TP-2 and TP-3) which had the almost the same design except pass length, were broken under almost the same loads. But TP-3 was stronger than TP-2, which had higher deflection value. The strongest test piece was TP-4, which had the highest number of roving in the girders and less in the ribs if compared with the other test pieces.

Finite element modeling of four point bending test for cases TP-2, TP-3 has been carried out using beam elements (48 elements along each girder and 4 elements along each skew rib). Rough estimates for material parameters were used. It may be considered that uncertainties for these values are about 20 – 30%. As a result of the calculations, deflection value was found 4.6mm at the middle point of the test pieces under 1000N load, which was between 4.2 – 5.2mm in experimental results.

Local deformations in the test pieces

Figure 8 shows load vs. strain values of TP-2. This figure reveals that upper and lower girders are subjected to higher straining in a single test piece if compared with the ribs. The straining of the rib is also different in each rib. This implies that the number of roving should be well defined to increase the overall stiffness and reduce the weight of the test pieces. This can be achieved by changing deposition path of the test pieces.

Figure 9 compares the tensile and compression strains of girders of three test pieces, all of which had interlaced joints. In this figure TP-4, which had higher number of roving in the girders, shows the less straining in case of tensile strains. Comparing compression strains, TP-4 also shows higher straining which reveals less compression strength. And generally all compression strains are higher than that of tensile stresses. Two reasons can be thought for this: 1-The hook, used to apply loads, were close to the strain gage in the upper girder, making the local deformations higher in the upper girder. 2-Tensile stresses mostly resisted by fibers whereas compression stresses resisted by resin. The compression stress of the resin is less than tensile stress of the fibers. This may satisfy the highest tensile and lowest compression strains in TP-4 whose fiber volume fraction was less than the other test pieces. (Girders: 6.5 roving, ribs: 2 roving, pass: 2). Tension strains in

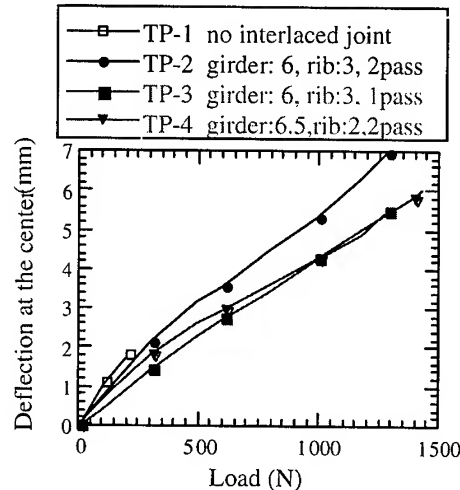


Fig. 7 Load-deflection curves of interlaced composite test pieces

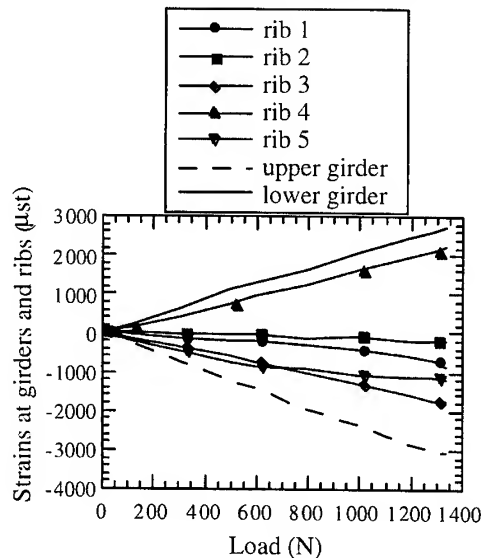


Fig. 8 Strain variation of the TP-2 at girders and ribs under gradually increased

girders and ribs under gradually increased

the lower girder were also calculated by FEM and to be found around $2800\mu\text{st}$ under the load of 1000N (compared to $2000\mu\text{st}$ – $2500\mu\text{st}$ for experiments). This result illustrates a rather good agreement between analysis and experiment.

Comparing TP-2 with TP-3 reveals that TP-2 has higher tensile strength and less compressive strength than TP-3. Longer fiber length may be the reason for the lower compressive strength. This indicates that length of the fibers on the girders should be well designed since buckling can be easy occur under compression loads if the length is unnecessarily long. Rib strains in Fig. 10 are mostly affected by the strength of girders. Comparing Fig. 9 with Fig. 10, it can be seen that ribs of stronger girders have less tensile straining.

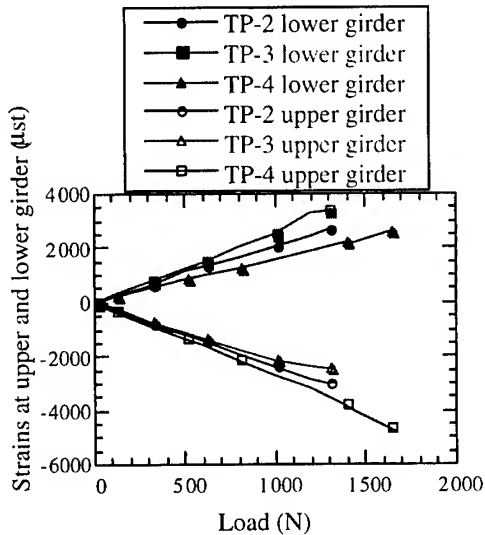


Fig. 9 Comparison of the upper and lower girder strains of interlaced test pieces

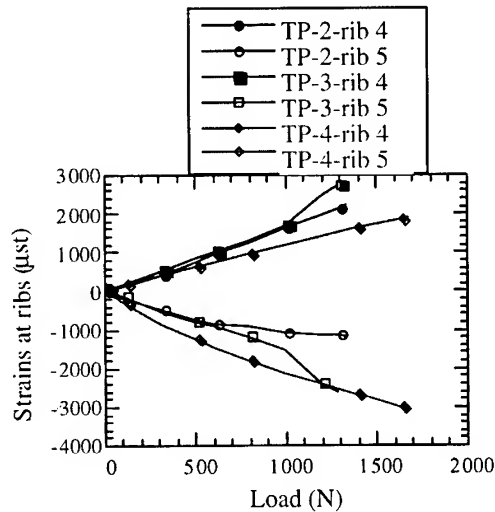


Fig. 10 Comparison of rib strains of Interlaced test pieces

CONCLUDING REMARKS

Two-dimensional parts with interlaced joints were tested to understand bending and compression strength of the fibers in the several designs in the present study. Test pieces were produced using T-glass fiber impregnated in light-curing resin. The experimental results indicated that interlaced joints are very effective to increase overall stiffness of the structures. Stronger girders with higher number of roving yield better stiffness if compared with the test pieces, which had lesser fiber in the girders. The very primary results obtained from FEM simulation of bending tests showed rather good agreement with experiments. Thus, using FEM, more improvement is expected in the future designs of the test pieces with increased overall stiffness.

REFERENCES

- 1 T. Sekido, "FRP Application to Truck Bodies" ,*Proceedings of 7th Euro-Japanese Symposium on Composite Materials and Transportation*, 1999.
- 2 H. Chen and S. W. Tsai, "Analysis and Optimum Design of Composite Grid Structure", *J. of Composite Materials*, Vol. 30, 1996, pp. 503
- 3 K. K. S. Liu and S. W. Tsai, "Low Cost Square Composite Grid", *Stanford University*, Unpublished work.

PHASE SHIFT EFFECT ON THE STRESS DISTRIBUTION FOR SATIN WEAVE COMPOSITES

Kyeongsik Woo, Seunguk Paik, and Youngwook Seo

*Department of Structural Systems & CAE, Chungbuk National University
Cheongju, Chungbuk, 361-763, KOREA:kw3235@cbucc.chungbuk.ac.kr*

SUMMARY: In this study, the stacking phase shift effect on the effective property and stress distribution was investigated for eight-harness satin weave textile composites. Simple and reverse stacking configurations with tow phase shifts were modeled by unit cells and repeating boundary conditions were applied at the outer surfaces. Multi-field macro-elements were used to consider the micro-structural details and to effectively reduce computation efforts. Results were analyzed to investigate the variation of the effective modulus and the stress distribution according to the manner how the adjacent tows were arranged. The changes in the failure initiation at the resin and tows were also examined.

KEYWORDS: Satin weave composites, phase shift, unit cell, repeating condition, periodicity vector, macro-element.

INTRODUCTION

Woven textile composites have several advantages over conventional tape laminates. The advantages mostly come from the fiber tow architecture which, however, is very complex and often makes the analyses very formidable. The fiber tow geometry of the 'planar' woven composites is very three dimensional as shown in Fig. 1. The unit cell of the eight-harness satin weave includes a large region and a three-dimensional analysis with discrete modeling often requires huge computer memory. Because of this, previous works have been focused mostly on predicting effective properties (eg, [1-3]). Few works were performed to predict the detailed stress distribution at the micro-structural level.

The eight-harness satin weave has a warp face and a fill face. In Fig. 1, the fill face is shown where fill tows are aligned mostly in the upper side. When putting layers together, the layers can be stacked simply, putting the different faces together, or symmetrically, the like faces together. The perfectly simple or symmetric stacking is highly ideal. The layers are, in reality, stacked with phase shifts in the planar direction. The phase shift effect for eight-harness satin weaves was studied by Avery [3] for two-dimensional satin weave configurations. A full three-dimensional stress analysis was performed by Clinton [4] for eight-harness satin weave unit cells. The configurations were, however, limited to the simple and symmetric stacking.

In this study, the tow phase shift effect on the effective modulus and stress distribution was investigated for eight-harness satin weave composites. Unit cells with tow phase shifts were

modeled for simple and reverse stacking configurations. The repeating boundary conditions were derived and at the outer surfaces of the unit cells. To reduce the computer memory requirement, multi-field macro-elements were employed and the detailed stress distributions were calculated by block-wise post-processing [5]. The analyses were focused on the variation of effective modulus and the stress distribution as the adjacent tow arrangement changed. The effects on the failure initiation at the resin and tows were also investigated.

UNIT CELL MODELING

Eight-harness satin weave composites exhibit a periodic pattern as can be seen in Fig. 1. The periodicity can be identified as a unit cell which is the minimum repeating block. The definition of the unit cell includes not only the geometric repeating but also the boundary and load conditions.

A unit cell model for a layer of eight-harness satin weave composites is shown in Fig. 2. The unit cell can be represented by periodicity vectors \vec{r}_1 , \vec{r}_2 , and \vec{r}_3 .

$$\vec{r}_1 = a(\hat{i} - 3\hat{j}), \quad \vec{r}_2 = a(3\hat{i} - \hat{j}), \quad \vec{r}_3 = 2a(\hat{i} + \hat{j}) \quad (1)$$

where a indicates the width of the tows. A point P at the outer boundary orthogonal to the x- or y-axis must have a corresponding point Q at the boundary which satisfies the following relation.

$$\vec{x}_P + \vec{r}_\alpha = \vec{x}_Q \quad (\alpha = 1, 2, \text{ or } 3) \quad (2)$$

With the periodicity vectors, the repeating boundary is divided into 3 sections. For these, the repeating boundary conditions are derived.

In this study, a uni-axial tensile load (ϵ_0) was assumed to apply to the unit cells in the x-direction to simulate the uni-axial tension test. In this case, the boundary conditions are

$$\begin{aligned} u(\vec{x}_P) + \epsilon_0 r_{\alpha 1} &= u(\vec{x}_Q) \\ v(\vec{x}_P) - \bar{v}_{\alpha 1} \epsilon_0 r_{\alpha 2} &= v(\vec{x}_Q) \\ w(\vec{x}_P) &= w(\vec{x}_Q) \end{aligned} \quad (3)$$

where $r_{\alpha 1}, r_{\alpha 2}$ are the x- and y-component of \vec{r}_α , respectively. Note that the displacement boundary conditions are completely determined by the corresponding component of the periodicity vector. Boundary conditions for other loading cases can be derived similarly.

CONFIGURATION

Fig. 3 shows schematically the stacking phase shifts in the x- and y-directions. In the figure, the upper layer was shifted against the lower layer by the amount of Δx and Δy . The shift can be represented by the following vector.

$$\vec{s} = \Delta x \hat{i} + \Delta y \hat{j} \quad (4)$$

Note that when the shift vector reaches to one of the periodicity vectors, the configuration returns to the original one. Thus, the range of the shifts Δx and Δy are limited by the periodicity vectors.

As mentioned previously, a conventional finite element analysis for eight-harness satin weave unit cells is very difficult due to a huge memory requirement. When several layers are included in the unit cells, the analysis becomes simply impractical. In this study, multi-field macro-elements were used to reduce the computational efforts.

Fig. 4 shows a macro-element mesh for a two-layer unit cell model. In this study, one macro-element was assumed to take one tow width region of a layer. Thus, the two-layer unit cell was modeled with 16 macro-elements. The numbers in the Figure indicates the sub-element types which modeled the micro-structures discretely. To consider the phase shifts in the analyses, changes were made only for the sub-element meshes and the types numbers of the macro-element mesh. The figure shows the phase shift of $\Delta x = \Delta y = a$.

The satin weave unit cell contains tows and resin pockets. The tows in return consist of fiber and resin. The properties used in this study are [4]

$$\begin{aligned} E_{11} &= 273 \text{ GPa}, E_{22} = E_{33} = 7.65 \text{ GPa}, \nu_{12} = \nu_{13} = 0.231, \nu_{23} = 0.244 \\ G_{12} &= G_{13} = 5.37 \text{ GPa}, G_{23} = 3.03 \text{ GPa} \\ X &= 3450 \text{ MPa}, Y = Z = 65.3 \text{ MPa}, S_{12} = S_{13} = 34.5 \text{ MPa}, S_{23} = 24.1 \text{ MPa} \end{aligned}$$

for tows, and

$$E = 9.17 \text{ GPa}, \nu = 0.11, X = 38.5 \text{ MPa}, S = 20.19 \text{ MPa}$$

for resin pockets. The tow properties were transformed to the global coordinate system for each integration point. The tow waviness ratio, defined as the period of the wavy region divided by the layer thickness (h/λ), was assumed to be $1/3$.

NUMERICAL RESULTS

This section discusses the variation of the effective modulus and the stress for the two-layer configurations of eight-harness satin weave composites with phase shifts.

Fig. 5 shows the effective modulus variation for the simple and reverse stacking configuration. In the figure, the considered shifts were indicated. The right-most data point corresponds to the phase shift of $\vec{s} = 0.5\vec{r}_3$. The results with the phase shift to $-\vec{r}_3$ direction were identical to that of $+\vec{r}_3$ direction. The figure shows that the effective modulus E_{xx} varied as the phase shift changed. The modulus was the smallest when the adjacent layers were simply stacked and the tows were in-phase, while it was the largest when the layers were symmetrically stacked without phase shift. This was consistent to the plain weave composites and ascribed to the extension-bending coupling of warp tows [6,7]. However, only a $1/4$ region of the unit cell contained wavy warp tows in the x-direction for eight-harness satin weaves. As a result, the variation in the effective modulus was small: 6% for the simple stacking and 4% for the reverse stacking.

Fig. 6 shows the variation of the maximum failure index under tensile loading by the maximum stress theory. The applied nominal stress was 55.7 MPa ($=0.1\% \text{ strain} \times E_{xx, \Delta t = 0}^{\text{simple}}$). Under the tensile loading, the σ_{13} was important stress component for tows. In the case of the resin pockets, the failure index distributions were significantly larger than those of the tows for all components. The failure indices for σ_{33} and σ_{13} components were discussed herein.

Figure 6(a) shows the σ_{33} failure index for the reverse stacking. When the shift was small, large failure index distributions occurred for the resin due to the compressive interaction between the tows of the adjacent layers. The shearing interaction was self-eliminating and it resulted in much smaller σ_{13} failure indices as can be seen in Figure 6(b). As the phase shift increased, however, the shearing was less constrained and the σ_{13} failure index became larger. When the layers were simply stacked and the tows in-phase, the intra-layer shear interaction was adding. This resulted in large values of the failure indices for the resin and for the fill tows as shown in Figure 6(c). In this case, matrix cracking in the fill tows would be expected to occur after early resin pocket failures. For the other phase shift cases, the fill tows had decreased failure indices.

CONCLUSION

In this study, the phase shift effect was investigated for eight-harness satin weave composites. Two-layer simple and reverse stacking configurations were modeled by unit cells. The repeating pattern in the model was represented by periodic vectors from which the repeating boundary conditions were derived. For efficient computation, multi-field macro-elements were used and the phase shifts between the layers were considered by changing the sub-element meshes. Results showed that the effective modulus was dependent on the stacking phase shift but the variation was small. The failure index distribution showed a much larger variation as the phase shift changed. For the fill tows, the failure index was significantly increased when the layers were stacked simply and in-phase. As expected, the index was very large at the resin pocket where an early failure initiation was suggested to occur for all configurations considered.

REFERENCES

1. T. Ishikawa and T. W. Chou, "In-Plane Thermal Expansion and Thermal Bending Coefficients of Fabric Composites", *Journal of Composite Materials*, Vol. 17, 1983, pp. 92-104.
2. T. Ishikawa and T.W. Chou, "One-dimensional Micromechanical Analysis of Woven Fabric Composites", *AIAA Journal*, Vol. 21, 1983, pp. 1714-1721.
3. W. Avery and C. Herakovich, "A Study on the Mechanical Behavior of a 2-D Carbon-Carbon Composite", *VPI&SU Interim Report 66*, 1987.
4. C. Chapman, "Prediction of Moduli and Strength Woven Carbon-Carbon Composites Using Object-Oriented Finite Element Analysis", *Ph.D. Dissertation*, Texas A&M University, 1997.
5. K. Woo and J. D. Whitcomb, "A Post-processor Approach for Stress Analysis of Woven Textile Composites", *Composites Science and Technology* (in press).

6. M. Ito and T. W. Chou, "Elastic Moduli and Stress Field of Plain-Weave Composites under Tensile Loading", *Composites Science & Technology*, Vol. 57, 1997, pp. 787-800.
7. K. Woo and J. D. Whitcomb, "Effects of Fiber Tow Misalignment on the Engineering Properties of Plain Weave Textile Composites", *Composite Structures*, Vol. 37, 1997, pp. 343-355.

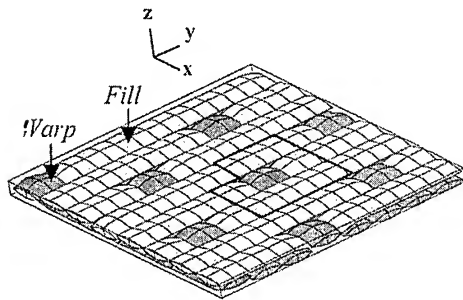


Fig. 1 Tow architecture of eight-harness satin weave composites.

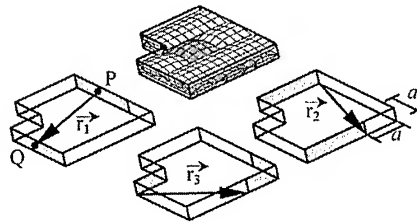


Fig. 2 A unit cell and periodic boundaries.

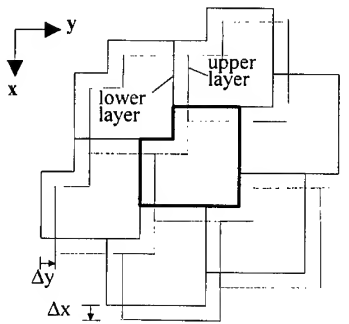


Fig. 3 Phase shifts between adjacent layers.

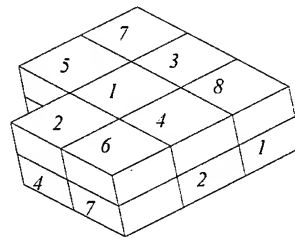


Fig. 4 Macro-element mesh. The numbers indicate sub-element mesh types. The present mesh modeled the case for $\Delta x = \Delta y = a$.

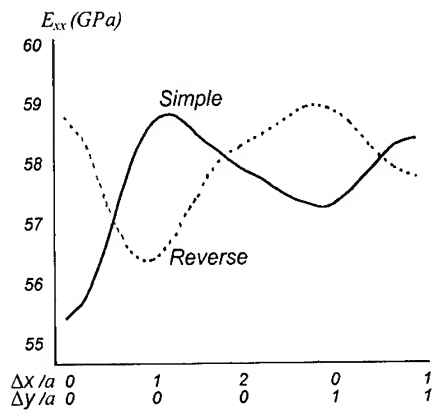
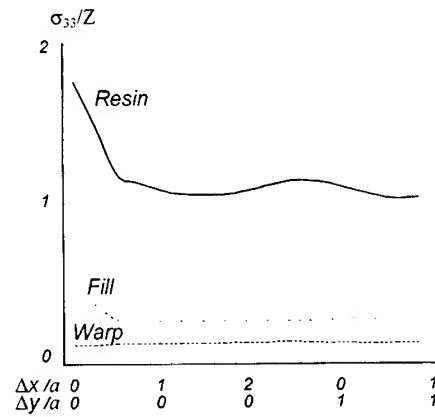
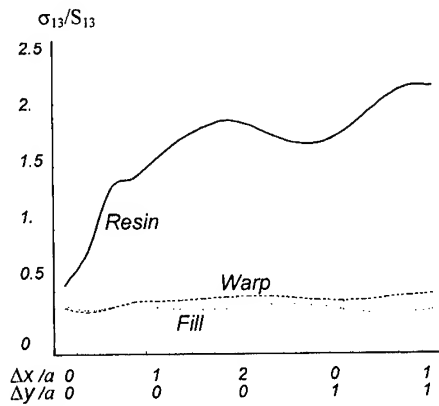


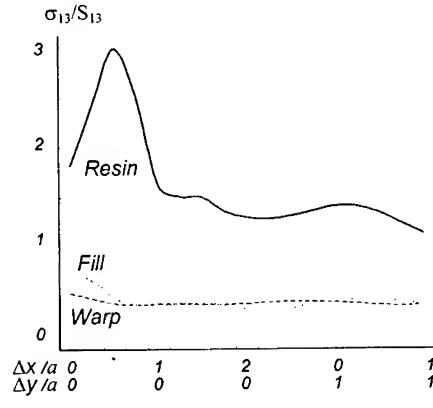
Fig. 5 Variation of E_{xx} for two-layer eight-harness satin weave composites.



(a) σ_{33} (reverse stacking)



(b) σ_{13} (reverse stacking)



(c) σ_{13} (simple stacking)

Fig. 6 Variation of maximum failure index by stress theory.

DEEP-DRAWING SIMULATION OF KNITTED FABRIC COMPOSITE MATERIALS BY THE HOMOGENIZATION METHOD CONSIDERING MICRO-MACRO COUPLING EFFECT

Naoki Takano¹, and Masaru Zako¹

¹ *Department of Manufacturing Science, Osaka University
2-1 Yamada-oka, Suita, Osaka 565-0871, Japan: takano@mapse.eng.osaka-u.ac.jp*

SUMMARY: A novel continuum-based simulation of deep-drawing process of knitted fabric composite materials considering the micro-macro coupling effects is presented. The nonlinearity due to the large deformation of the microstructure is considered using the mathematical homogenization method. The periodicity of the microstructure after the large deformation is carefully considered both theoretically and experimentally. The homogenized constitutive law under the large deformation is expressed by the fully anisotropic material model, which is calculated by the homogenization method. As the results of the deep-drawing simulation, not only the macroscopic quantities such as the deformation, strain, stress and stiffness but also the microscopic quantities were obtained. The predicted microscopic deformation was compared with the experimental result, and both agreed very well.

KEYWORDS: knit, deep-drawing, microstructure, large deformation, homogenization method, micro-macro, process simulation

INTRODUCTION

Processing of composite materials and its simulation are the important topics, and therefore there have been many studies taking experimental, theoretical and numerical approaches. This paper discusses the deep-drawing of textile composite materials such as the knitted fabric composite materials. We can find some pioneering literatures describing the experimental investigation of the deep-drawing of woven and knitted fabric composite materials [1,2]. Concerning the simulation of deep-drawing process, the draping simulation using the mapping algorithm and the shaping simulation were studied [3,4]. However, they could be applied to only plain woven fabrics, and most of the works considered only the shearing and rotation at the cross-point of the fabrics and the stretching of the fabrics was neglected. For more complex microstructures such as the knitted fabric composite materials, a novel computational method has to be developed. The temperature effect is also important, and therefore the properties of matrix resin should be accurately considered in the simulation for composite materials with complex microstructures. It is a matter of course that the classical rule of

mixture or Eshelby's equivalent inclusion method can not predict the macroscopic homogenized properties for arbitrary complex microstructures.

To solve above-mentioned various problems involved in the previous simulations of deep-drawing of textile composites, a novel computational method based on the mathematical homogenization method is proposed. The homogenization method was firstly developed in 1970s by many applied mathematicians in France, Italy, Russia or U.S.A. [5]. Recently, there are many studies on the application of the homogenization method to the nonlinear problems of composite materials such as the damage propagation [6], visco-elasto-plasticity [7] and the large deformation problems [8]. In the deep-drawing simulation presented in this paper uses the authors' formulation of the homogenization method applied to the micro-macro large deformation problem [8]. The outline of the formulation is described in the next section. Because this formulation is based on the continuum mechanics, very complex deformation can be analyzed and the properties of both fiber and matrix resin are considered rigorously.

The large deformation of the knitted fabric composite materials under biaxial loading conditions are analyzed first. The nonlinear homogenized properties are calculated. Then, the deep-drawing simulation is carried out. Some important and original results are presented. Also the comparison of the microscopic deformation between the simulation and the experiment is shown briefly.

OUTLINE OF THE FORMULATION OF THE HOMOGENIZATION METHOD

The textile composite materials have very complex microstructures. The microstructures are arrayed periodically for both woven and knitted fabric composite materials. The authors [8,9] have investigated deeply on the periodicity of the microstructures of knitted fabric composite materials. It was revealed by experimental work that the condition of the periodicity is satisfied even after the large deformation for small region in the structure. The fact that the periodicity holds for small region means that the deformation is uniform in this small region.

Define the macroscale x and microscale y satisfying the relation of $y=x/\varepsilon$ where ε is the scale ratio. The real displacement considering the microscopic heterogeneity can be described by the summation of the homogenized displacement and the perturbed displacement due to the heterogeneity as Eq.(1).

$$\dot{u}_i^\varepsilon = \dot{u}_i^H(x) + \dot{u}_i^1(x) = \dot{u}_i^H(x) + \varepsilon \dot{u}_i^1(y) \quad (1)$$

Based on the above-mentioned experimental results, the displacements of the homogenized structure and the microstructure are carefully described theoretically. The macroscopic displacement is approximated by the homogenized displacement, and the microscopic one is described as follows:

$$U_i^{\text{micro}}(y) = \dot{u}_i^\varepsilon(y) = \frac{\partial \dot{u}_i^H(x)}{\partial x} y + \dot{u}_i^1(y) \quad (2)$$

By substituting the resolved displacement, Eq.(1), into the governing equation expressed in the updated-Lagrangian form, and using the averaging principle with taking the limit of $\varepsilon \rightarrow 0$ [8-10], we can derive the microscopic equation as follows:

$$\int_Y \frac{\partial \delta u_i^1(y)}{\partial Y_j} (C_{ijmn} + \delta_{im} S_{jn}) \frac{\partial \dot{u}_m^H(y)}{\partial Y_n} dY = \int_Y \frac{\partial \delta u_i^1(y)}{\partial Y_j} (C_{ijkl} + \delta_{ik} S_{jl}) dY \quad (3)$$

A unique solution of the microscopic equation (3) exists under the periodic boundary condition. The solution of Eq.(3) is the characteristic deformation, which bridges the perturbed displacement and the gradient of the homogenized displacement. The macroscopic equation and the homogenized properties are derived as follows:

$$\int_{\Omega} \frac{\partial \delta u_i^H(x)}{\partial X_j} (C_{ijkl}^H + S_{ijkl}^H) \frac{\partial u_k^H(x)}{\partial X_l} d\Omega = \int_{\Gamma_i} \delta u_i^H t_i d\Gamma \quad (4)$$

$$C_{ijkl}^H = \frac{1}{|Y|} \int_Y \left(C_{ijkl} - \frac{\partial \chi_m^{kl}}{\partial Y_n} C_{ijmn} \right) dY \quad (5)$$

The strain and stress (2nd Piola-Kirchhoff stress) in the microstructure are calculated by the following equations:

$$\dot{E}_{ij}^{\text{micro}}(y) = \frac{1}{2} \left(\frac{\partial u_i^H}{\partial X_j} + \frac{\partial u_j^H}{\partial X_i} + \frac{\partial u_i^1}{\partial Y_j} + \frac{\partial u_j^1}{\partial Y_i} \right) \quad (6)$$

$$\dot{S}_{ij}^{\text{micro}}(y) = C_{ijkl} \dot{E}_{kl}^{\text{micro}}(y) \quad (7)$$

The microscopic stress is in self-equilibrium under the condition of the periodicity, and the macroscopic stress is defined as the average of the microscopic stress within a microscopic unit cell (or RVE), which is in equilibrium with the external forces under the macroscopic constraints. This point is very important in the strictness with the theory of mechanics, which can not be obtained by other homogenizing procedure. See Ref. [8] for more detail.

LARGE DEFORMATION OF A KNITTED FABRIC COMPOSITE MATERIAL UNDER BIAXIAL LOADING CONDITIONS

The finite element model of the microscopic unit cell of a knitted fabric composite material is shown in Fig. 1. The reinforcing cloths are supposed to be symmetrically laminated. Hexahedral elements are used. The number of elements and nodes are 5792 and 6665, respectively. As the constituents, aramid fiber and polypropylene are used.

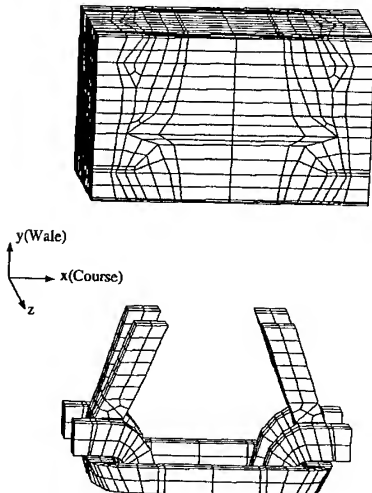


Fig.1 Microstructure model

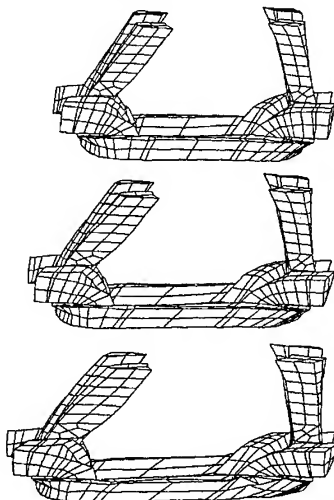


Fig.2 Deformation under biaxial loading
(top: strain 20%, middle: 30%, bottom: 40%)

Some representative biaxial loading conditions are considered so that they can cover the various combinations of biaxial tension and shearing loadings. The loading increments are assumed to be monotonic. Fig. 2 is one example of the biaxial loading analyses under combined tension in course direction and shearing deformation. The deformation of the microstructure satisfies the periodic condition, and the microscopic stress is in self-equilibrium. The biaxial loading condition is put on the macroscopic model, which is not shown here due to the limitation of pages. In such cases like Fig. 2, the simple stress-strain curve can not be drawn. Hence, the 21 parameters of the stress-strain tensor were calculated. Fig. 3 shows E_{xxxx} and E_{xxyy} , where x denotes the course direction and y denotes the wale direction. E_{xxyy} is nonzero only when the orthogonality is lost. Fig. 3 tells us that the orthogonality is lost for the knitted fabric composite materials under shearing deformation. The proposed computational method is a unique method that can provide the anisotropic properties under the large deformation.

Fig. 3 is stored as the nonlinear material database for the following deep-drawing simulation. As mentioned above, only some representative loading cases are analyzed, and simple linear interpolation is used to build up the database.

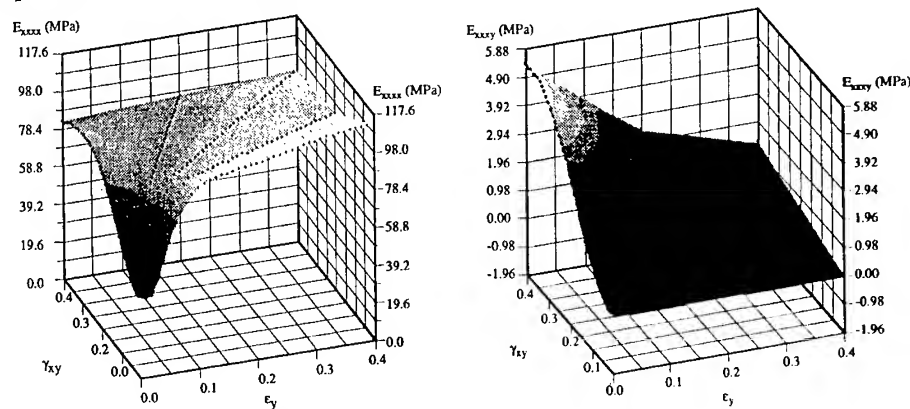


Fig. 3 Database of nonlinear material properties under biaxial large deformation

DEEP-DRAWING SIMULATION

In the deep-drawing simulation, geometrical nonlinearity, material nonlinearity and contact are considered macroscopically. Since the material nonlinearity comes from the microscopic large deformation, it is expressed numerically by the pre-calculated material database in Fig. 3. The usage of the database enables us to simulate the micro-macro coupling phenomena during the deep-drawing process by a standard personal computer. Otherwise, a huge amount of computer memory is required for this kind of micro-macro coupled nonlinear analysis.

Spherical punch is assumed. The process is assumed to be isothermal at 443K. Therefore, the Young's modulus of the matrix resin was measured experimentally. Fig. 4 shows the deformation when the stroke is 27mm. The deformed microstructures are also shown. The variation of the microscopic deformation leads to the distribution of the stiffness in the deep-drawn product. Fig. 5 shows the distribution of the stiffness which is expressed as the component of the stress-strain tensor. E_{xxyy} is nonzero in some region where shearing deformation is large. The distribution of the stiffness must be considered in the evaluation of the strength, for instance, of the deep-drawn product.

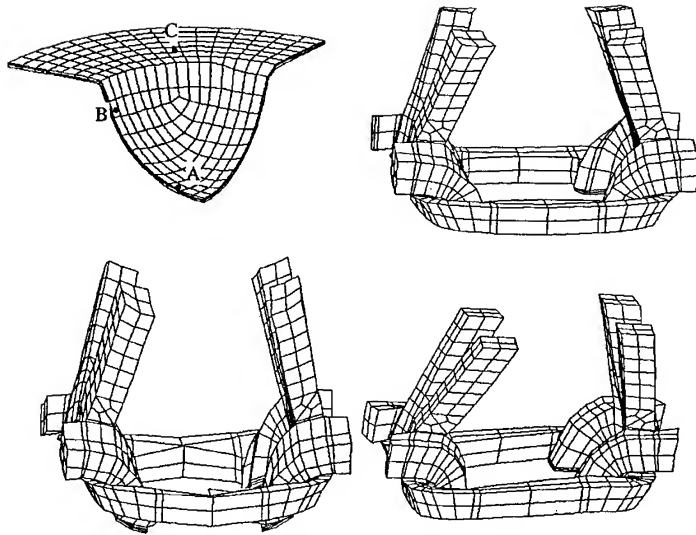


Fig. 4 Macroscopic and microscopic deformation
(A: top right, B: bottom left, C: bottom right)

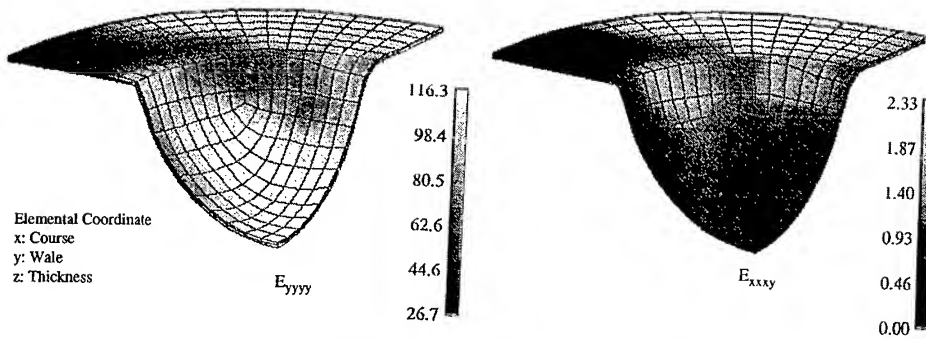


Fig. 5 Distribution of stiffness, E_{yyyy} and E_{xxyy}

Fig. 6 and Table 1 show the comparison of the microscopic deformation between the simulation and the experiment. Both results are coincident very well.

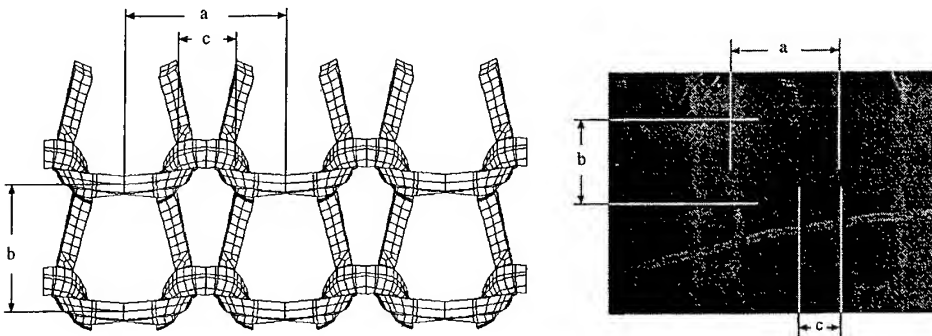


Fig. 6 Representative dimensions for the comparison between simulation and experiment

Table 1 Comparison between simulation and experiment

		$\frac{b}{a}$	$\frac{c}{a}$
Initial		0.57	0.31
Deep-drawn	Simulation	0.78	0.36
	Experiment	0.77	0.39

CONCLUDING REMARKS

Using the formulation of the mathematical homogenization method applied to large deformation problem, a novel continuum-based simulation of deep-drawing of a knitted fabric composite material was presented. To reduce the computational cost, a simplified micro-macro coupled analysis procedure was proposed. Then, the deep-drawing simulation was carried out by a personal computer (CPU: Pentium II, 450Mhz) in 18 minutes. The homogenized constitutive law under biaxial stress states was expressed numerically by the homogenization method. The predicted largely deformed microstructures were coincident with the experimental results. The proposed deep-drawing simulation is useful for the design and control of the deep-drawing process, and also useful for the design of the microstructure.

Acknowledgment - The authors are grateful for the help of Dr. Y.Ohnishi (Osaka University) and Prof. K.Nishiyabu (Osaka Prefectural College of Technology).

REFERENCES

1. K.Nishiyabu, *Proc. 4th Japan International SAMPE Symposium*, 1995, pp.795-800.
2. T.C.Lim, S.Ramakrishna and H.M.Shang, *Abstracts of ACCM-I*, 1998, Paper No.409.
3. O.K.Bergsma, "Three Dimensional Simulation of Fabric Draping - Development & Application-", Delft University Press, 1996.
4. J.L.Billoet and A.Chrouat, *Proc. ICCM-12*, 1999, Paper No.1172 (CD-ROM).
5. J.M.Guedes and N.Kikuchi, *Comput. Methods Appl. Mech. Eng.*, 83, 1990, pp.143-198.
6. N.Takano, Y.Uetsuji, Y.Kashiwagi and M.Zako, *Modelling Simul. Mater. Sci. Eng.*, 7, 1999, pp.207-231.
7. S.Jansson, *Int. J. Solids Struct.*, 29-17, 1992, pp.2181-2200.
8. N.Takano, Y.Ohnishi, M.Zako and K.Nishiyabu, *Int. J. Solids Struct.*, in press.
9. N.Takano, Y.Ohnishi, M.Zako and K.Nishiyabu, *Proc. 6th Japan International SAMPE Symposium*, 1999, pp.525-528.

Processing (1)

SILICA NANOPARTICLES FILLED POLYPROPYLENE: EFFECTS OF IRRADIATION GRAFTING OF SILICA ON THE TENSILE PROPERTIES OF COMPOSITES

Minzhi RONG¹, Mingqiu ZHANG², Yongxiang ZHENG¹ and Hanmin ZENG²

¹*Materials Science Institute, Zhongshan University, Guangzhou 510275, P. R. China:
cesrmz@zsulink.zsu.edu.cn*

²*Laboratory of Polymeric Composite and Functional Materials, The Ministry of Education of
China, Zhongshan University, Guangzhou 510275, P. R. China: ceszmq@zsulink.zsu.edu.cn*

SUMMARY: A viable method has been developed to improve the strength and toughness of polymer with the addition of small amount of modified inorganic nanoparticles (typically less than 3% by volume), which is much lower than the content required by the conventional particulate filled composites, using direct compounding techniques. Through irradiation grafting polymerization, nanoparticles agglomerates become microcomposites comprised of nanoparticles, grafted and homopolymerized polymer and thus strong interfacial interaction can be established easily between the nanoparticles and the matrix. Both the strong nanoparticles agglomerates and interface is responsible for the improving of tensile properties. The chemical interaction between monomers and nanoparticles during irradiation procedure, fracture mechanism of this nanocomposites during tensile, as well as morphological changes induced by the addition of nanoparticles are also discussed.

KEYWORDS: silica, nanoparticles, irradiation grafted, mechanical compounding, nanocomposites, reinforcement, tensile behavior.

INTRODUCTION

Polymer nanocomposites are attracting considerable attention owing to their unique properties resulted from nano-scale microstructure characterized by the large fraction of the filler atoms that reside in the interface and lead to a strong interfacial interaction. With respect of enhancement of polymers through the addition of nano-inorganic particles, nanocomposites might attain a significant improvement in rigidity and reinforcement at a filler content far less

than comparable glass or mineral reinforced polymers in case the ultra-fine phase dimension were kept after compounding with matrix materials. As such, they are much lighter in weight, transparent and easier to be processed than conventional inorganic particulates filled polymers [1, 2].

However, a homogeneous dispersion of nanoparticles in polymer matrices has been proved a very difficult task due to the strong tendency for nanoparticles to agglomerate. To break down nanoparticles agglomerates and to produce nanostructured composites, most of works mainly focus on the approaches of in-situ polymerization of monomers at presence of nanoparticles, such as the sol-gel process [2] and intercalation polymerization technique [3]. All of these methods utilize the kinetic and thermodynamic control. Although the nano-scale dispersion of particles have been obtained, both sol-gel process and intercalation polymerization technique are found to be not applicable to most of the technically important polymers because neither a suitable monomer nor a compatible polymer-silicate solvent system is always available. In addition, a large amount of commercial available nanoparticles is not layered inorganic substances, the extensive utilization of which could not be solved by intercalation polymerization. Further, the above approaches are characterized by complex polymerization procedures and special conditions, therefore, the simple direct mixing of nanoparticles with melted polymers by conventional processing techniques is still required in certain situation where in-situ polymerization approaches above mentioned are not applicable and a mass production of nanocomposites with cost effectiveness is required.

In this paper a new methods utilizing irradiation surface modification of nanoparticles and mechanical mixing was developed to overcome the defeats existing in each method. The essential issue is that the nanoparticles were modified by irradiation graft polymerization firstly, then the grafted nanoparticles are mechanically mixed with plastic as usual. Owing to the low molecular weight nature, the monomers can penetrate into the aggregated nanoparticles easily and react with the activated sites of the nanoparticles. The surface of the primary particles not only outside but also inside the agglomerates will be covered by grafted polymer or homopolymer. In other words, the gap between nanoparticles will be filled with grafting macromolecular chains; thus, the agglomerates will become much stronger. In addition, the surface of the nanoparticles will also become hydrocarbon that is compatible with matrix resin in some degree. When the pre-grafted nanoparticles are mechanically mixed as usual with thermoplastic polymer, a different structure and properties of composites should be obtained due to thermodynamic change on nanoparticles surface. Different grafting polymers could bring about different miscibility between the particles and matrix as well as properties of agglomerates; consequently, composite's structure and properties could be adjusted, which implies a concept of materials and interface design. The purpose of this paper is to show how efficiently the mechanical performance of the nanocomposites can be improved by the above approach. Polypropylene and silica are chosen as matrix and filler respectively, the chemical interactions between monomers and nanoparticles during irradiation procedure, fracture mechanism of this nanocomposites during tensile, as well as morphological changes induced by the addition of nanoparticles are also discussed in detail.

EXPERIMENTAL DETAILS

Materials

General purpose isotactic PP homopolymer (F401, MI=8.5g/10min and 6.7g/10min) provided by Guangzhou Petroleum Chemical Co. was used as matrix in this test. Pyrogenic colloidal silica (Degussa 'Aerosol' 1380) of primary particle size 7nm was selected as the filler. Various commercial monomers: styrene, methyl methacrylate, butyl acrylate, ethyl acrylate, methyl acrylic acid, and vinyl acetate were used as grafting monomers without further purification.

Pregrafting of Nanoparticles by Irradiation

The nanoparticles was preheated at 120 °C for 5 hrs before being mixed with monomers to eliminate possible absorbed water on the surface of particles. Then the mixture of particles/monomer (100/20) and certain amount of solvent was irradiated by ^{60}Co -ray under atmosphere at a dose rate of 10^6 rad/hr at room temperature. After being exposed to a dose of 10 Mrad, the solvent was recovered and the dried residual powder could be compounded with thermoplastic directly by general processing techniques. The weight increase of inorganic substances by grafted polymers was obtained by two methods, weighting and TGA. The amount of grafted polymer by the two methods well agreed within experimental errors. Grafted polymers on grafted silica were obtained by treatment with 10-20% HF solution for 1-2 days to dissolve SiO_2 . ESCALAB ZZOI-XL electron spectroscopes for chemical analysis (ESCA) and Nicolet 5DX Fourier transform infrared spectroscope (FTIR) were also utilized to characterize the changes of nanoparticles surface.

Preparation of Composites and Testing Procedure

Composites were prepared first by tumble mixing preweighted quantities of polypropylene and grafted fillers, followed by compounding on a single screw extruder. The melt temperature was kept at 200 °C and screw speed was 25 r.p.m. The specimens for mechanical tests were machined from the compressing moulding plaques (65×45×3 mm) of extrudates. The volume fraction of the filler, V_f was computed from the known weights of polymer matrix, fillers and polymer introduced by irradiation. The reinforcement effects will be examined with tensile tests, which were carried on dumbbell shaped specimens with an LWK-5 testing machine at room temperature and at a crosshead speed of 10 mm/min. The fractured surfaces were observed by Hitachi S-520 scanning electron microscopy (SEM).

RESULT AND DISCUSSION

Grafted polymer molecular weight and its interaction with the nanoparticles

Fig. 1a shows the C 1s spectra of PS/ SiO_2 blend, which can be deconvoluted into two components, with one at 285.1 eV and the other around 282.3 eV, representing the binding energy (BE) of C-C or C-H and aromatic ring respectively. Comparatively, another two peaks

appear on the spectra of SiO₂ grafted by PS (SiO₂-g-PS) in addition to above two peaks remaining (Fig. 1b), implying chemical interaction between the SiO₂ and grafted polymers. The appearance of a high-BE peak in C 1s spectra of PS reveals that some of carbon atoms become more electron-poor after grafted on the surface of SiO₂. If bonds of Si-O-C were present, the ether oxygen atom has a strong electron-withdrawing effect on the carbon atom of PS, resulting in a decrease in the electron density of the PS chain. On the other hand, the appearance of low-BE C 1s peak can be attributed to the formation of Si-C bonds thus causes the attached carbon atom to be electron-rich. Therefore, it can be ruled out that PS is chemically connected with SiO₂ through Si-O-C and Si-C bonds. In the FTIR spectra of unextractable or grafted PS polymers, there is hydrogen bond from interaction of -OH groups, which can not be present by PS homopolymers, proving the existence of Si-O-C bonds also. These PS bonded on the surface of SiO₂ must be beneficial to the improvement of interface adhesion in the composites.

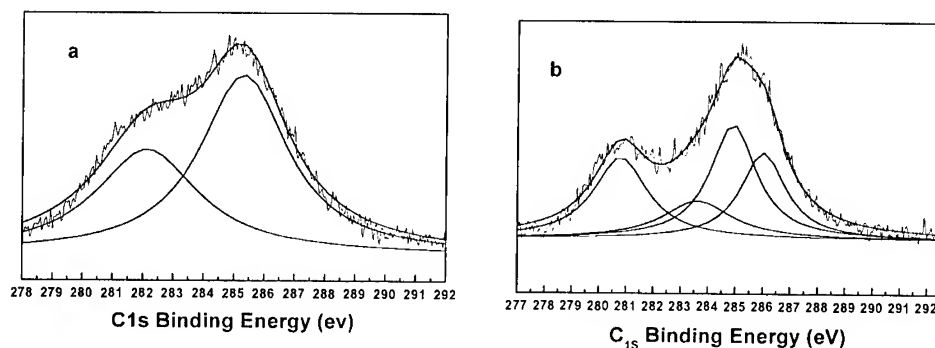


Fig. 1 C 1s spectra of SiO₂/PS blend (a) and SiO₂-g-PS (b)

Effect of different structure design on the tensile properties of composites

All composites showed a typical yield point from which tensile yield strength at maximum load, σ_y , was calculated (Fig. 2). Other quantities such as elongation at break (ϵ_b) and Young's modulus (M_T) were also measured for systems containing different monomers grafted particles (Table 1). These results clearly indicate both the reinforcing and toughening effect of nanoparticles

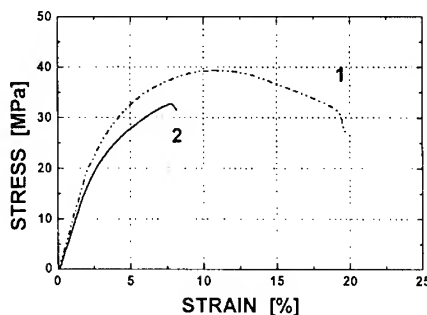


Fig. 2 Typical stress-strain curves of PP (MI: 6.7 g/10min) composites filled with nano-scale particles: (1) SiO₂-g-PS; (2) neat PP

on polymeric material can be brought into full play as expected, indicating that the weakness resulted from aggregating behavior of nanoparticles has been eliminated by the structure design via irradiation grafted particles. On the other hand, the nature of agglomerates and interface between the agglomerates and matrix can

be changed by the different grafting monomers, as a result, the mechanical properties of composites can be purposely adjusted according to the interphase theory.

There are great number of parameters affecting the tensile strength of particulate composites, such as filler volume fraction, the particle shape and size, the nature of matrix, and the adhesion between particles and matrix. Among these factors, the interface adhesion is of cardinal importance and markedly influences the tensile strength of filled polymers [4]. In the case of poor interface, the tensile strength generally decreases with increasing filler loading due to the dewetting phenomena at matrix-filler interface, which leads to falling of the volume fraction of matrix carrying the load [5]. Tensile strength is generally enhanced when interfacial adhesion is improved. This can be ascribed to better stress transfer at the interface between the matrix and the filler [6]. These models can also be used to explain the effect of grafting polymer on the tensile properties of nanoparticles filled composites. The interdiffusion and entanglement of the grafting polymer segments with the polypropylene macromolecules may lead to a good physical anchoring between the complex agglomerates and PP matrix. Therefore, except the PEA, all other grafting polymers exhibit improving effect on the tensile yield strength of composites at very low content of the fillers. The higher molecular weight of PP matrix seem to be entangled more effectively with the complex agglomerates, leading to a higher tensile yield strength (compared Fig. 2 with Table 1). Kendall and Sherliker [7] reported the effect of polymer molecular weight on colloidal silica filled thermoplastic polymers and observed similar phenomena.

Young's modulus and elongation to break also showed improvement in comparison with neat polypropylene, while the interphase feature plays an important role on these properties. The increase of the stiffness is obviously due to the higher modulus of the particles ($E_{\text{silica}}=70$ GPa). The determination of the modulus is based on the linear slope of the stress-strain curve, which was in a range of low stress. In this low stress region, the formation of a relatively compliant layer at the interface (for PBA, PVA, and PEA) tends to hinder the complete stress transfer, thus mask the stiffness of the filler particles. On the other hand, the elongation at break, ϵ_b , showed more complicated relationship with the interface behavior because both the interface viscoelastic deformation and matrix yielding contribute to the value of ϵ_b (Table 1).



Fig. 3 SEM fractograph of tensile fracture surface for SiO_2 -g-PS (1.96 vol. %) filled PP (MI=6.7 g/10min)

The toughness of the composites can be characterized by the area under the stress-strain curves (A). On the basis of tensile test, the PP incorporated with grafted SiO_2 exhibit improving toughness except of SiO_2 -g-PEA filled system. Generally, the local plastic deformation or drawing of matrix was considered as main energy absorption process in particulate filled polymer systems. The SEM fractograph of tensile fracture surface showed some evidence of plastic deformation (Fig. 3). The presence of microfibrils circles around agglomerates must absorb a considerable amount of the energy during the tensile test. The overlap of these deformation circles revealed that the yielding process has propagated and pervades over the entire matrix in the deformation zone.

this propagation could be modeled as percolation phenomenon. The microdeformation

process of the fibrils circles may be ascribed to the void formation due to debonding, as well as the matrix plastic deformation through shear yielding. At the beginning of deformation, the agglomerates act as stress concentrators, and the stress field is disturbed by dispersed particles. Then shear bands occur because there is a maximum shear stress component under an angle 45° , and the yielding process propagates through thin ligaments between the agglomerates, in which a plain-strain to plain-stress transition take place due to the percolation phenomena. Once the debonding is initiated at the both side of the agglomerates in parallel direction to the applied stress (i.e., at the poles), the shear stress state is locally relieved and the deformation circles form due to the contraction of matrix.

Table 1 Mechanical properties of PP filled with different polymers grafted SiO_2 (3.31 vol.%)

Grafted polymer	Neat PP	PS	PBA	PVA	PEA	PMMA	PMA
σ_y , MPa	32.03 (0.52)	34.14 (1.5)	33.31 (0.7)	32.96 (1.2)	26.78 (2.7)	35.17 (0.8)	33.88 (1.2)
M_T , GPa	0.746 (0.10)	0.916 (0.1)	0.853 (.03)	0.811 (0.1)	0.875 (.03)	0.890 (1.0)	0.845 (0.1)
A, MPa	2.17	2.43 (.12)	3.27 (.49)	2.34 (0.3)	0.81 (.21)	3.24 (.34)	2.88 (.59)
ϕ , %	11.7 (2.6)	9.34 (0.7)	12.63 (1.4)	9.98 (0.9)	4.56 (0.7)	11.96 (1.3)	11.94 (0.1)

Note: PS: polystyrene

PBA: polybutyl acrylate

PVA: polyvinyl acetate

PEA: polyethyl acrylate

PMMA: polymethyl methacrylate

PMA: polymethacrylic acid

ACKNOWLEDGMENT

The Key Programs of the Ministry of Education of China (Grant: 98069), and the Natural Science Foundation of Guangdong (Grant: 990277) are gratefully acknowledged. Dr. Rong is grateful to the Pilot Program for Young Ph.D. of the Natural Science Foundation of Guangdong (Grant: 974072).

REFERENCES

1. Dagni, R. C&EN 1992, 23.18
2. Novak, B. M. Adv. Mater. 1993, 5, 422
3. Giannelis, E. P. Adv. Mater. 1996, 8, 29
4. Pukanszky, B. Composites 1990, 21, 255
5. Quazi, R. T.; Bhattacharya, S. N.; Kosior, E. J. Mater. Sci. 1999, 34, 607
6. Demjen, Z.; Pukanszky, B. Polym. Comps. 1997, 18, 741
7. Kendall K.; Sherliker, F. R. Brit. Polym. J. 1980, 12, 111

The Deciding Method of Drill Tool Life based on Estimation of Hole Damage in PWB made of GFRP

H. Inoue¹ T. Hirogaki², E. Aoyama³ and T. Katayama⁴

¹ Faculty of Engineering, Aichi University of Technology,
50-2 Manori, Nishihasama-cho Gamagohri, Aichi 443-0047, Japan

² Faculty of Engineering, University of Shiga Prefecture,
2500 Hassaka-cho, Hikone, Shiga 522-8533, Japan:hirogaki@mech.usp.ac.jp

³ Faculty of Engineering, Doshisha University,
Kyotanabe, Kyoto, 610-0321, Japan:eaoyama@mail.doshisha.ac.jp

⁴ Faculty of Engineering, Doshisha University,
Kyotanabe, Kyoto, 610-0321, Japan:tkatayama@mail.doshisha.ac.jp

SUMMARY: When drilling a printed wiring board (PWB), internal damaged zone around the drilled hole occurs. This damaged zone strongly affects the durability of a PWB. For this reason, we proposed a method for determining the drill's life by studying the relationship between the extent of damaged zone and the number of drilled hole. The experimental equation for the drill's life are obtained from the upper relationship.

Keywords: Tool wear, Small diameter drilling, Printing wiring board, Internal damaged zone of drilled hole, Drill's life, limit number of drilled hole

1. INTRODUCTION

Currently, PWBs made of glass fiber reinforced plastic (GFRP) are widely used as circuit boards for electronic devices. With the current trend in downsizing electronic devices, a circuit formed on a PWB is required to have a higher packaging density and reliability. When using a pin-insertion packaging method for integrated circuit (IC) parts on a PWB, the following problems occur: 1. There is a surface roughness on the inner wall of the drilled hole (1-4); 2. A bending of drilled path(5); and 3. The extent of internal damage around the drilled hole (6,7).

Concerning the first problem, it is impossible to make a same surface roughness for the inner wall of a drilled hole because of the glass fiber reinforced composite material used for PWBs. The second problem comes from the installation condition and the rigidity of the drill, the quality of the cutting edge of the drill bit, and the inconsistent wear of cutting edge. Therefore, the problem does not always occur in the same manner. Regarding the third problem, the internal damage around a drilled hole expands as the cutting edge of drill bit wears. The internal damaged zone expands with an increased number of drilled hole. This internal damage around a drilled hole decreases the real hole distance for setting hole distance and also cause of the generation of the

ion migration, which possibly causes disconnection when the PWB is used as an electronic circuit. As a result, the internal damage prevents us from increasing the number of holes per area and, furthermore, largely affects the durability, which is the reliability, of the product.

At this point, we focused on internal damage around the drilled hole. We examined the drill's life by determining the limit number of drilled hole. This was accomplished by observing the relationship between the extent of the damaged zone and the number of drilled hole. The wear condition of the drill bit was observed and defined.

2. SPECIMENS USED FOR THE DRILLING AND THE DRILLING METHOD

Two specimens were used for the drilling. One was a heat-resistant glass-cloth epoxy resin laminate of eight layers, 1.6-mm thick in total, sandwiched between copper films. The other was a glass cloth-reinforced epoxy resin plate of one ply, 0.2-mm thick, made of the same materials as the former specimen. The latter is for the purpose of observing any internal damage taking place around the drilled hole. For drilling, a numerically controlled (NC) drilling machine (Hitachi Seiko, ND-1H) was used. The two specimens were considered as one set, and when drilling both specimens simultaneously, the number of drillings was counted as one. The drilling was conducted by stacking three sets of specimens sandwiched between an aluminum plate on top and a paper base phenolic laminated sheet on bottom. The drill used was a carbide step drill on the market with a 1-mm diameter by two-step plane grinding. The number of drilled hole was determined to be 30,000 times, which would completely wear out the drill bit. And both the spindle speed and the feed rate are changed on drilling the PWBs.

3. OBSERVATION OF THE INTERNAL DAMAGE AROUND THE DRILLED HOLE AND THE WEAR OF DRILL BIT

3.1 Observation of the internal damage around the drilled hole

An example of the internal damage that took place around the drilled hole at various conditions of drilling is shown in Fig. 1. The damage zone was observed by means of transmitted light placed. The black portion around the drilled hole in the figure represents the internal damage. The extent of damaged zone increases as the number of drilled hole increases. But the shape of damaged zone is not same for the each drilled hole. This depends on the relative position of the drill bit against the direction of the glass fiber bundle.

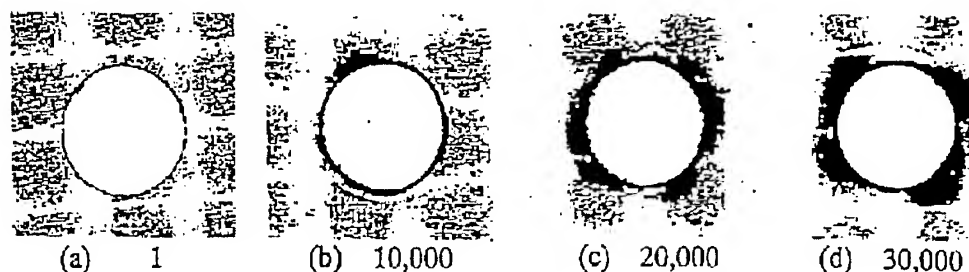


Fig. 1 Experimental results of internal damage around the drilled hole.
(Number means the number of drilled hole)

From that, the extent of the internal damage was defined as the maximum width of the internal damaged zone as shown in the figure2. That is, the maximum width of the internal damaged zone (L) is obtained by the difference between the radius of the maximum damaged zone and the radius of the drilled hole.

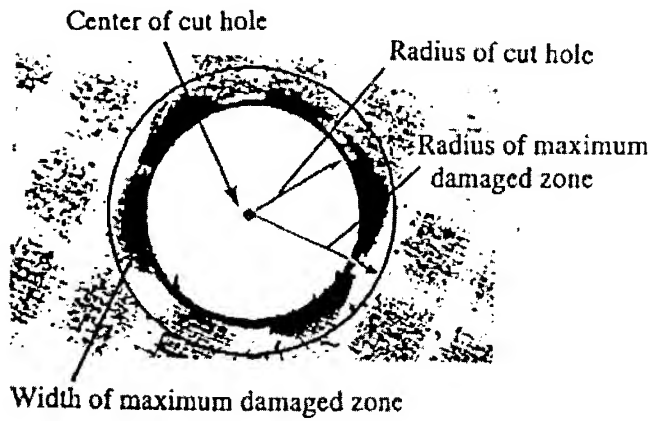


Fig.2 Definition of maximum width for internal damaged area

3.2 Observation of the wear of a drill bit

As the drill used in this study was a carbide step drill of two-step plane grinding, the shape of flank face is a trapezoidal shape. On the other hand, the wear of a drill generally progresses by the abrasive wear when it is used for cutting glass fiber reinforced plastic material (8,9).

wear. From this, the progress of the drill-bit wear can be estimated by observing the change in shape of the trapezoidal flank face, which is considered to reflect the progress of the flank wear.

4. THE DECISION METHOD OF DRILL'S LIFE

4.1 The relationship between the extent of the internal damage around the drilled hole and the number of drilled hole

An example of the relationship between the maximum width of the internal damaged area, around the drilled hole and the number of drilled hole is shown in Fig.3. The figure shows their relationship when the spindle speed was 20,000 rpm. The figure shows the number of drilled hole at which the maximum width of the internal damaged zone steeply increased. This was observed under other drilling conditions. When drilling PWBs, it is desirable to have as little internal damage around the drilled hole as possible. The limit numbers of drilled hole for all drilling conditions to be occurring just before the maximum width of the internal damaged zone steeply increased show the table.1.

The wear of a cutting tool generally taking place in the cutting FRP material is similar to the abrasive wear, and the abrasive wear depends on the cutting length. Therefore, by replacing the change of drilling conditions, such as the feed rate and the number of drilled hole, with the change in the cutting length, which corresponds to the wear on the tip of the drill bit, the cutting length L

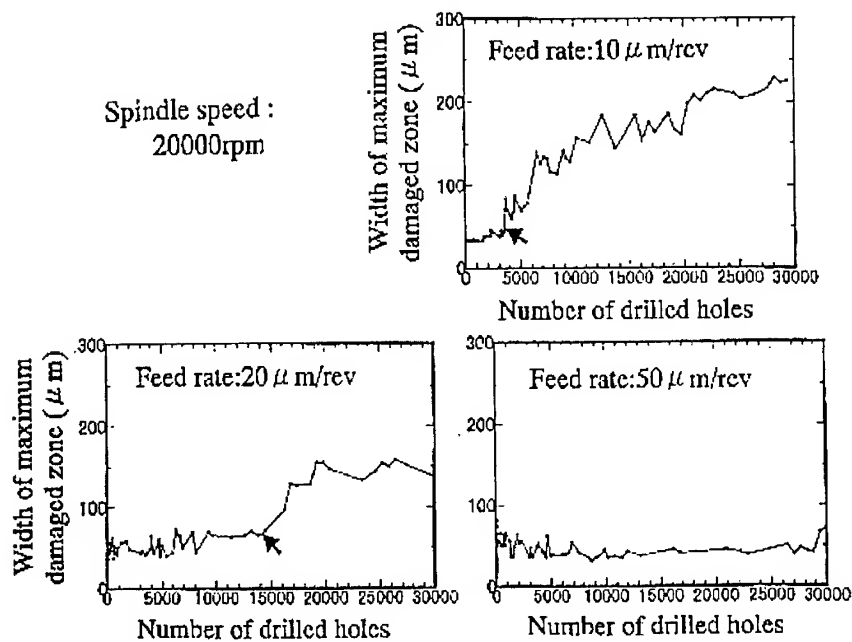


Fig.3 Relationship between width of maximum damaged area and number of drilled hole

is obtained by the following equation,

$$L = \pi D N t / f \quad \dots\dots\dots(1),$$

where L is the cutting length (m), D the drill diameter (m), t the thickness of the PWB, f the feed rate of the drill(m), and N the number of drilled hole. The cutting lengths on the Table.1 obtained by Eq. (1) . From Table.1 the limit number of drilled hole is strongly affected by the feed rate compare with the spindle speed.

Table.1 Limit number of drilled hole

Spindle speeds(rpm)	Feed rate(μ m/rev)	Limit number of drilled hole	Limit cutting length(m)
20000	10	3500	1979
	20	14500	4100
	50		
60000	10	1300	735
	20	11500	3251
	50		
80000	10	3200	1809
	20	16500	4665
	50		

4.2 The shape of the worn drill bit at the limit number of drilled hole

Based on the limit number of drilled hole obtained from Table.1 we drilled the PWBs and observed with scanning microscopy the shape of the drill bit at the limit number of drilled hole as well as before and after. The results are shown in Fig.4.

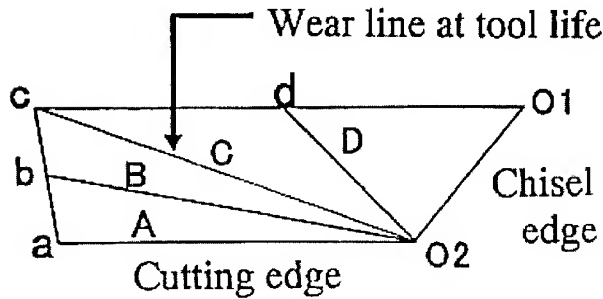


Fig.4 Schematic figure of flank face of worn drill

The shape of the flank face of the drill bit at the limit number of drilled hole has been changed with its cutting edge retreating to the c-O2 position from the original a-O2 position as shown in Fig.4. In other words, if the drill is used until its cutting edge retreats beyond the c-O2 position, the width of the internally damaged area around the drilled hole expands steeply. From that, this c-O2 line means the wear line at tool life.

Next, the cutting edge of the drill bit does not retreat parallel to the cutting edge, as does the tool wear in an orthogonal cutting. Instead, it retreats revolving around the chisel edge. Therefore, we decided to use the remaining area of the flank face of the drill bit in order to measure the progress of the wear that occurs at the outer edge of the drill bit. In other words, we defined the amount of wear taking place during the drilling as the worn area of flank face (Φ : %), which reveals how much the cutting edge decreases, as in the following equation:

$$\text{The worn area of flank face} = \{1 - (\text{the remaining area of the flank face}) / (\text{the original area of the flank face})\} \times 100 \dots (2)$$

Figure 5 shows the relationship between the cutting length and the worn area of flank face when the PWB are drilled on various number of drilled hole. This figure means the life curve for drill on this study.

From this Figure 5, next experimental equation is obtained:

$$\Phi = A \cdot \ln(L/B + 1) \dots (3),$$

where Φ is the worn area of flank face, L is the cutting length, A, B are the material constant (in this case, $A=23.26$, $B=148.4$).

On the equation (3), if the value of worn area of flank face is decided, cutting length (correspond the number of drilled hole) is easily calculated. The worn area of flank face of the drill bit when the drill bit is worn out obtained by Eq. (2) was approximately 60% under the conditions of this study.

5. CONCLUSION

In order to judge drill's life used for drilling a PWB, we focused on the extent of internal damage zone that takes place around drilled hole and proposed a method to estimate the drill's life from the relationship between the extent of the internal damage and the number of drilled hole. The results of the study are as follows:

- (1) The limit number of drilled hole was determined from the relationship between the extent of the internal damaged zone (the maximum width of the internal damaged zone taking place

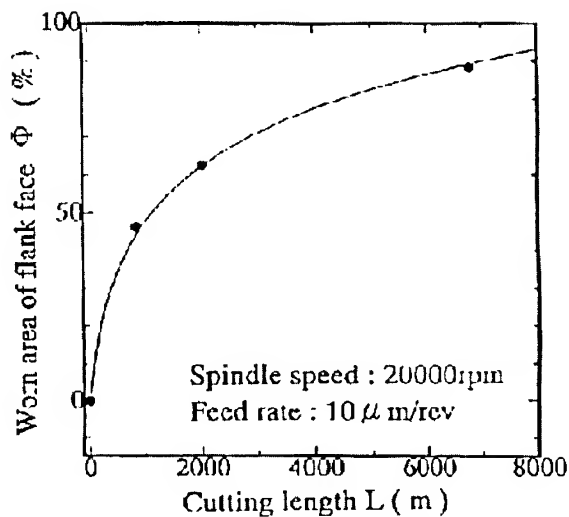


Fig.5 Relationship between worn area of flank face and cutting length

around the drilled hole) and the number of drilled hole.

- (2) The drill's life was defined according to the wear of the flank face of the drill bit at the limit number of drilled hole, and the relationship was clarified between cutting length, which corresponds to the number of drilled hole, and the wear of the drill bit.

REFERENCES

1. H. Inoue, S. Kondoh, T. Yasuhara, T. Kurashiki, K. Kariya and T. Yamaguchi, "Drilling of glass epoxy copper clad laminate" J. Textile Machinery Soc. Jpn., 47 (1994) p.T110
2. X. Wang, K. Nakayama and M. Arai, "Investigation on cutting of fiber reinforced composite material (1st report) J. Jpn. Soc. for Precision Engineering, 55 (1989) p.709
3. C. W. Wern, M. Ramulu and K. Colligan, "A study of the surface texture of composite drilled hole" J. Mat. Proc. Tech., 37 (1993) p.39
4. H. Ho-Cheng and C. K. Dharan, "Delamination during drilling in composite laminates" Trans. ASME, J. Eng. for Industry, 112 (1990) p.236
5. M. Hiranaka, H. Yokouchi, X. Li, K. Kaito and H. Tusaka, "Studies on bending at small hole drilling of printed wiring boards" J. Jpn. Soc. for Precision Engineering, 59 (1993) p.119
6. E. Aoyama, T. Hirogaki, H. Inoue, S. Gunjima, H. Nobe, Y. Kitahara and T. Katayama, "Study on drilled hole quality in small diameter drilling of GFRP" J. Soc. Materials Science Jpn., 45 (1996) p.522
7. H. Inoue, E. Aoyama, T. Hirogaki, K. Ogawa, H. Matushita, Y. Kitahara and T. Katayama, "Influence of tool wear on internal damage in small diameter drilling in GFRP" J. Composite Structures, 39 (1997) p.55
8. Y. Hasegawa, S. Hanasaki and S. Satonaka, "Characteristics of tool wear in cutting of GFRP" J. Jpn. Soc. for Precision Engineering, 44 (1978) p.36
9. Y. Hasegawa, S. Hanasaki and J. Fujiwara, "Characteristics of tool wear in cutting of GFRP" J. Jpn. Soc. Compos. Mater., 10 (1984) p.29

KINETIC STUDY ON THE THERMAL DEGRADATION OF PHENOLIC RESIN/SILICA HYBRID CERAMER NANOCOMPOSITES

C. C. M. Ma¹, J. M. Lin², and C. Y. Chen³

¹*Department of Chemical Engineering, National Tsing-Hua University, Hsinchu,
Taiwan, 300: ccma@che.nthu.edu.tw*

²*Department of Chemical Engineering, National Tsing-Hua University, Hsinchu,
Taiwan, 300: d857607@oz.nthu.edu.tw*

³*Department of Chemical Engineering, National Tsing-Hua University, Hsinchu,
Taiwan, 300: g883615@oz.nthu.edu.tw*

SUMMARY: The kinetic parameters of thermal degradation of the phenolic resin/silica hybrid ceramers with different mixing ratios were investigated. The activation energies of degradation were calculated from the methods of Kissinger, Friedman and Ozawa by a conventional dynamic thermogravimetric technique in nitrogen atmosphere at several different heating rates. The Kissinger's results exhibit that both pure phenolic resin and hybrid ceramers show two stages of degradation, but the activation energies of thermal degradation of ceramers in the first stage are all lower than that of phenolic resin. The results calculated by the Friedman and the Ozawa method are similar for phenolic resin and phenolic resin/silica hybrid ceramers. This indicates that the existence of silica in the phenolic resin does not affect the degradation mechanism of phenolic resin significantly.

KEYWORDS: ceramer, degradation, kinetics, sol-gel, hybrid nanocomposites

INTRODUCTION

Organic/inorganic hybrid ceramers fabricated through sol-gel methods have become a new kind of materials. They attract a lot of interests in the past decade. These materials combine both the advantages of organic and inorganic materials and are expected to possess new properties that individual organic or inorganic materials could not achieve [1]. These materials are termed "Ceramers" by Wilkes[2] or termed "Ormosils" by Schmidt[3]. These terms have been used in some related articles published in the international journals. Several polymers have been investigated to be the organic phase of the hybrids such as polyimides[4-5], polybutadiene and polydimethylsiloxane[6], phenolic resins[7], and so on.

Phenolic resin is one of the most used synthetic resins that are used in wide range of applications. In order to modify the thermal properties, silicon containing compounds have been used and the effects have also been discussed[8-10]. Furthermore, according to the concept for preparing hybrid ceramers, sol-gel method can also be used to derive inorganic ingredients into the phenolic resin and the effect on the physical properties have also been investigated[7,11]. Furthermore, phenolic resin is a kind of polymers that is used for the precursors of matrix of carbon/carbon composites[12-13]. In our previous study[14], the phenolic resin/silica ceramers have been utilized as the precursors to fabricate the carbon/carbon composites and the oxidation behaviors have been studied. The results show that the ceramer based carbon/carbon composites have better oxidation resistance. However, the thermal degradation of the hybrid ceramers has not been studied. Thus, in this study, the kinetics parameters of the degradation of phenolic resin/silica ceramers will be investigated by means of thermogravimeter analysis (TGA). Three analytical methods, Kissinger, Friedman and Ozawa methods will be used to obtain the kinetic parameters of the degradation.

EXPERIMENTAL

Materials and Preparation

The alkoxysilane used for the sol-gel system was tetraethyl orthosilicate (TEOS), supplied by Acros Organics Co., U. S. A. The ethanol supplied by the Shimadzu Chemical Co., Japan was used as the co-solvent of water and TEOS. The 35.0 wt% hydrochloric acid, supplied by the Union Chemical Works Ltd. Taiwan, was used as the catalyst. The resole-type phenolic resins were supplied by the Chang-Chun Plastics Co., Taiwan. The sol-gel solution used in this research contains 23.0 wt% of TEOS, 51.0 wt% of water, 25.0 wt% of ethanol and 1.0 wt% of HCl. The solution was stirred continuously at room temperature for 5 min and then mixed according to the desired ratios with phenolic resin. The mixtures were then stirred for 10 min to form homogeneous solutions. The mixing weight ratios of phenolic resin and sol-gel solutions selected in the study are 90/10, 80/20, 70/30 and 60/40, respectively. The uniform

mixed solutions were then heated at 70°C for 2 hrs to remove solvents and then cured at 180°C for 30 min. In order to complete the reaction, the cured samples were then postcured at 230°C for 24 hrs. The nomenclature of the hybrids used in this study is simplified as PXSY where P is phenolic resin, S is sol-gel solutions, X and Y are the weight ratios of each component. For example, P80S20 is the mixture of 80wt% phenolic resin and 20wt% of sol-gel solutions.

Characterization of phenolic resin/silica hybrid ceramers

Thermal degradation of the phenolic resin/silica hybrid ceramers was performed by a TGA (Dupont-951) from room temperature to 800°C with four heating rates (5, 10, 20, 40°C/min, respectively). The kinetic parameters for degradation were calculated by Kissinger, Friedman and Ozawa kinetic models.

RESULTS AND DISCUSSION

The Kissinger method[15] is a differential thermal analysis pattern. It involves obtaining the temperature values (T_m) at the peaks of the first derivative weight loss curves. The equation is:

$$\frac{E\beta}{RT_m^2} = An(1-\alpha)_m^{n-1} \exp(-E/RT_m) \quad (1)$$

where β is heating rate (°C/min), α is degree of degradation, T is temperature, k is rate constant, A is a preexponential factor of Arrhenius equation and E is the activation energy of thermal degradation. Assuming that $n(1-\alpha)_m^{n-1}$ is independent of β and nearly equal to unity for first-order reaction, eqn (1) could be rearranged and the following expression could be derived:

$$\frac{d[\ln(\beta/T_m^2)]}{d(1/T_m)} = -\frac{E}{R} \quad (2)$$

Therefore, the activation energy of thermal degradation can be determined from the plot of $\ln(\beta/T_m^2)$ versus $1/T_m$. Table 1 lists the activation energy of degradation of each system in the two stages. Figure 1 shows the comparison of maximum temperatures of both stages for different ceramer systems under heating rate of 10°C/min. For stage 1, the ceramer systems all show lower maximum temperatures than that of pure phenolic resin except 90/10 system; for stage 2, the ceramer systems all show higher maximum temperatures than that of pure phenolic resin except 60/40 system.

Table 1. The calculated activation energy of degradation by Kissinger's method.(kcal/mol)

	Ea (stage1)	Ea (stage2)
<i>Phenolic resin</i>	48.81	67.81
P90S10	37.43	65.47
P80S10	37.70	54.94
P70S30	34.12	63.43
P60S40	28.47	58.41

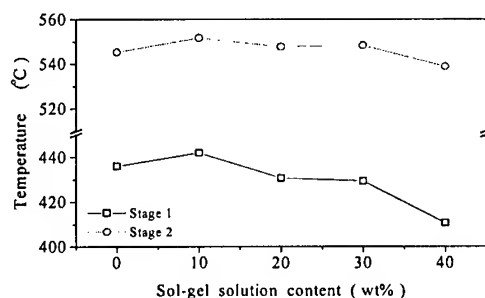


Figure 1. Comparison of the Kissinger's temperatures of different ceramer systems. (Heating rate: 10°C/min)

The Friedman method[16] is based on the intercomparison of experiments which were performed at different linear rates of heating. By using this method, it is possible to determine the activation energy of thermal degradation without knowing the kinetic equation. The equation is:

$$\ln\left(\frac{d\alpha}{dt}\right) = \ln\left[\beta\left(\frac{d\alpha}{dT}\right)\right] = \ln A + n \ln(1-\alpha) - \frac{E}{RT} \quad (3)$$

Thus the activation energy of thermal degradation for the whole range of conversions can be obtained by plotting $\ln[\beta(d\alpha/dT)]$ against $1/T$ for a constant α value. Table 2 is the summary of the activation energy of thermal degradation on fractional weight loss by Friedman's method.

Table 2. The activation energy of degradation on fractional weight loss by Friedman's method. (Unit: kcal/mole)

	5%	10%	15%	20%	25%
<i>Phenolic resin</i>	36.03	53.31	68.97	63.78	67.45
P90S10	38.15	31.98	64.09	64.80	80.70
P80S10	35.58	52.72	66.75	85.11	91.41
P70S30	35.99	47.33	70.78	73.85	81.16
P60S40	30.03	60.69	65.61	94.22	51.35

The Ozawa method[17], which is different from the Friedman method, is a integral technique to determine the activation energies directly from the weight loss against temperature curves

obtained at different heating rates. By assuming that A , $(1-\alpha)^n$ and E are independent of T while A and E are independent of α , the equation is shown as follow:

$$F(\alpha) = \int_0^\alpha \frac{d\alpha}{(1-\alpha)^n} = \frac{A}{\beta} \int_{T_0}^T \exp\left(\frac{-E}{RT}\right) dT \quad (4)$$

Taking the logarithmic form of the integration results of eqn(4), it gives:

$$\log F(\alpha) = \log(AE/R) - \log \beta + \log p(E/RT) \quad (5)$$

for $E/RT > 20$, then $\log p(E/RT)$ can be expressed as:

$$\log p(E/RT) \cong -2.315 - 0.4567E/RT \quad (6)$$

Therefore, the activation energies of thermal degradation can be obtained from the plot of $\log \beta$ against $1/T$ for a constant conversion and the slope of the line is $-0.4567E/R$. Table 3 shows the activation energy of degradation on fractional weight loss by Ozawa method.

Table 3. The activation energy of degradation on fractional weight loss by Ozawa method.
(Unit: kcal/mole)

	5%	10%	15%	20%	25%
<i>Phenolic resin</i>	29.80	35.68	63.83	62.76	62.30
P90S10	30.61	32.29	50.40	60.90	69.81
P80S10	32.19	40.95	56.57	68.95	76.60
P70S30	36.16	37.46	56.87	61.84	73.85
P60S40	25.68	48.64	67.10	78.97	65.18

CONCLUSIONS

The thermal degradation of the phenolic resin/silica hybrid ceramers with different mixing ratios was investigated by TGA techniques. The results were utilized to calculate the activation energies of thermal degradation by the methods of Kissinger, Friedman and Ozawa. The Kissinger results show that both pure phenolic resin and hybrid ceramers show two stages of degradation. The activation energies of thermal degradation of ceramers (28~37 kcal/mol) in the first stage are all smaller than that of phenolic resin (48.81 kcal/mole). This is due to the liberation of entrapped water and alcohol inside the phenolic resin. The results calculated by Friedman and Ozawa methods for phenolic resin and hybrid ceramers are similar.

ACKNOWLEDGEMENTS

This research was financially supported by the National Science Council of the Republic of China, under the Contract No. NSC-88-2216-E-007-013.

REFERENCES

1. G. L. Wilkes, B. Orler-B and H. H. Huang, "Ceramers - Hybrid Materials Incorporating Polymeric Oligomeric Species into Inorganic Glasses Utilizing a Sol-Gel Approach", *Abstracts of Papers of the American Chemical Society*, Vol.190, 1985, pp.109.

2. G. L. Wilkes, B. Orlor and H. H. Huang, "Ceramers - hybrid materials incorporating polymeric oligometric species with inorganic glasses by a sol-gel process. 2. effect of acid content on the final properties", *Polym. Bull.*, Vol.14, 1985, pp.557-564.
3. H. Schmidt, "New type of non-crystalline solids between inorganic and organic materials", *J. Non-crystal. Solids*, Vol.73, 1985, pp.681-691
4. A. Kioul and L. Mascia, "Compability of polyimide-silicate ceramers induced by alkoxysilane silane coupling agents", *J. Non-crystal. Solids*, Vol.175, 1994, pp.169-186
5. L. Mascia, Z. Zhang and S. J. Shaw, "Carbon fibre composites based on polyimide/silica ceramers: aspects of structure-properties relationship", *Composites Part A*, Vol.27, 1996, pp.1211-1221.
6. F. Surivet, T. M. Lam, J. P. Pascault and C. Mai, "Organic-inorganic hybrid materials. 2. Compared structure of polydimethylsiloxane and hydrogenated polybutadiene based ceramers", *Macromol.*, Vol.25, 1992, pp.5742-5751.
7. K. Haraguchi, Y. Usami and Y. Ono, "Preparation and characterization of hybrid materials composed of phenolic resin and silica", *J. Mater. Sci.*, Vol.33, 1998, pp.3337-3344.
8. General Electric Co., *U.S. Patent* 2,258,218, 1941.
9. Westinghouse Electric Corp., *U.S. Patent* 2,836,740, 1958.
10. Dow Corning Corp., *U.S. Patent* 2,842,522, 1958.
11. J. M. Lin, C. C. M. Ma, N. H. Tai, W. C. Chang and C. C. Tsai, "Carbon fiber reinforced phenolic resin/silica ceramer composites-processing, mechanical and thermal properties", *Polym. Compos.*, accepted, 1999.
12. W. C. Chang, N. H. Tai and C. C. M. Ma, "Dynamic-Mechanical Properties of Carbon-Carbon Composites", *J. Mater. Sci.*, Vol.30, 1995, pp.1225-1232.
13. C. C. M. Ma, N. H. Tai, W. C. Chang and Y. P. Tsai, "Morphologies, Microstructure and Mechanical-Properties of 2D Carbon/Carbon Composites During the Cvi Densification Process", *Carbon*, Vol.34, 1996, pp.1175-79.
14. J. M. Lin, C. C. M. Ma and W. C. Chang, "Silica containing carbon/carbon composites derived from novel phenolic resins/silica hybrid fabricated through the sol-gel Method oxidation kinetics and morphological properties", *Carbon*, revised, 1999.
15. H. E. Kissinger, "Reaction kinetics in differential thermal analysis", *Analy. Chem.*, Vol.29, 1957, pp.1702.
16. H. L. Frieman, "Kinetics of thermal degradation of char-forming plastics from thermogravimetry. Application to a phenolic plastic", *J. of Polym. Sci. Part C*, Vol.6, 1964, pp.183.
17. T. Ozawa, "A new method of analyzing thermogravimetric data", *Bull. Chem. Soc. Jpn.*, Vol.38, 1965, pp.1881.

Effects of Packing on the Fiber Orientation during Injection Molding of Short Fiber Composites

Seok Won Lee¹ and Jae Ryoun Youn²

*Department of Fiber and Polymer Science, Seoul National University
56-1, Shinlim-dong, Kwanak-gu, Seoul, Korea*

¹E-mail: *polyman2@snu.ac.kr*

²E-mail: *jaeryoun@gong.snu.ac.kr*

SUMMARY: A compressible flow analysis of the polymer melt is carried out to predict fiber orientation states in the packing stage as well as in the filling stage during injection molding. Tait's state equation is adopted to describe compressibility and modified Cross model is employed to consider non-Newtonian behavior of the polymer melt. Heat transfer and phase change due to cooling by the relatively cold mold wall are also considered. The 2nd order orientation tensor is introduced to describe 3-dimensional states of fiber orientation. It is possible to predict flow-induced fiber orientation by solving the equation of change of the orientation tensor with a suitable closure approximation. Flow and temperature fields are obtained by the hybrid FEM/FDM technique. Melt front is advanced by control volume method. Orientation fields are solved by the 4th order Runge-Kutta method. Fiber orientation develops mainly due to shear flow in the skin layer and due to stretching effect in the core layer. It turns out that the compressibility, which induces additional velocity gradients during packing, reduces development of the fiber orientation. Results are dependent upon the interaction coefficient between short fibers. The larger the interaction coefficient, the smaller the orientation development and the compressibility effect, and vice versa. Effects of compressibility are strong at the middle layer where fibers are moderately oriented. To predict orientation dependent mechanical properties, the orientation averaging for an arbitrary orientation is performed from the properties of a transversely isotropic unit cell. The compressibility reduces the axial modulus, and increases the transverse modulus. For thermal expansion coefficients, opposite results are observed. The larger the interaction coefficients, the less the effect of compressibility. The compressibility reduces anisotropy on the whole.

NUMERICAL AND EXPERIMENTAL ANALYSES OF ROLL FORMING FIBRE REINFORCED THERMOPLASTIC SHEETS

D. Bhattacharyya¹, R.J. Dykes¹, P.J. Hunter²

¹ *Centre for Composites Research, Private Bag 92019, University of Auckland,
Auckland, New Zealand.*

² *Department of Engineering Science, Private Bag 92019, University of Auckland,
Auckland, New Zealand.*

SUMMARY: Roll forming is a rapid manufacturing process which can be used to transform flat sheet material into useful profiled sections. This paper introduces the background theory and governing equations for the analysis of a steady state deformation process such as roll forming. Unique kinematic relations are developed that describe the rate of change of deformation in terms of the line speed of the sheet as well as higher order spatial derivatives. For this special case, the time dependence, usually associated with viscous materials, is eliminated allowing the problem to be formulated using a classic large strain approach. Equations of motion and constitutive laws are then outlined before a suitable finite element solution procedure is presented. The results of a 3-dimensional simulation are then briefly detailed. Finally, the limitations and suitability of the modelling procedure are discussed in the context real forming problems.

KEYWORDS: roll forming, finite element, numerical modelling, kinematic relations, strain rate, deformation zone.

INTRODUCTION

Roll forming is a rapid manufacturing technique which has traditionally been used to transform flat metallic sheet material into useful profiled sections. As shown in Fig 1, the process involves passing a flat sheet through a series of matched rolls that progressively deform strip into a uniform profile. Due to the speed and versatility of the process, it has found widespread appeal amongst various industries including automobile, construction, and aerospace. Recently the process has been adapted for continuous forming fibre thermoplastic (CFRT) sheets which offer a number of advantages of traditional materials.

The research that has been performed has concentrated on many of the practical aspects of the process such as roll scheduling, speed, and laminate architecture [1, 2] More recently Dykes *et al.* [3] have focused on the transitional deformation that the sheet undergoes prior contacting the forming rolls. This paper introduces the background theory for the computational analysis of CFRT materials in a steady state deformation. No attempt is made to cover the entire theory

which has been developed along the lines of other Lagrangian finite strain formulations. The unique aspects of the formulation are however highlighted, particularly the kinematic relationship for the strain rate tensor. Most of the other relationships pertaining to the stress equilibrium and finite stress tensors can be found elsewhere in [4] which provide an excellent account large strain finite element theory.

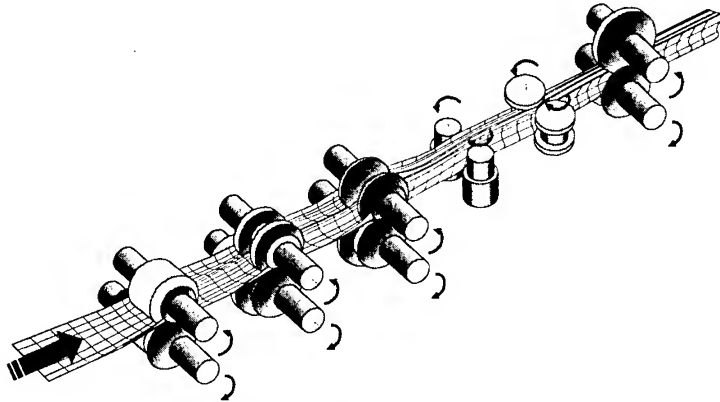


Fig. 1 A schematic illustration of the roll forming process

THEORY

The theory pertaining to the computational analysis of continuous fibre reinforced thermoplastic sheets is developed using a finite strain approach. This theory considers just two states a body possesses during the course of an arbitrary deformation: the reference (undeformed) configuration, and the current (deformed) configuration. This type of formulation, as it applies to roll forming, has been illustrated schematically in Fig 2. The analysis can be undertaken by initially considering a flat (undeformed) sheet. Sometime later, the same sheet assumes a deformed geometry as it progressively deforms through the forming rolls. By carefully considering the kinematics of the operation in relation to viscous nature of the material being considered allows a modified finite element scheme, not unlike those employed to solve hyper-elastic problems, to be utilised. The following theory is intended to expose the unique aspects of the computational theory that has been developed for this particular problem.

Kinematics of a steady state deformation

The key to analysing strain in a material undergoing large deformations is to establish two types of coordinate systems and develop a relationship between them. The first are fixed spatial coordinates (x,y,z) and the second (material coordinates) are embedded in the deforming body (v_1,v_2,v_3) . The kinematics of the deforming body can then be defined by the relationship between the reference x_i - coordinates and the material v_{iM} - coordinates in the deformation gradient tensor which is written as

$$F_{iM} = \frac{\partial x_i}{\partial v_{iM}} \quad (1)$$

Note the convention of a lower case letter and subscript for the deformed Cartesian coordinates and the upper case letter and subscript for the material coordinate v_{iM} . As shown in Fig. 2, the v_{iM} - coordinate directions are chosen to coincide with certain features of the undeformed fibre reinforced sheet: v_1 is aligned with the fibre directions, v_2 is aligned in the

plane of the sheet, and v_3 is normal to the sheet surface. In the undeformed sheet the v_M - coordinates form an orthogonal coordinate system.

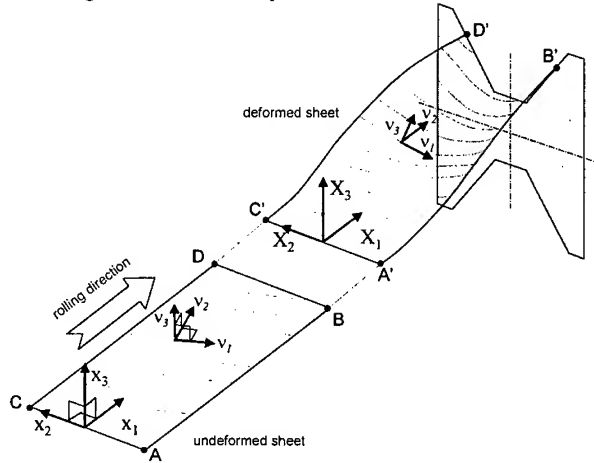


Fig. 2 The undeformed and deformed sheet with spatial (x_1, x_2, x_3) and material (v_1, v_2, v_3) coordinate systems. Note that the shaded region represents the cross-section of the circular female forming roll.

Establishing the deformation gradient for a particular configuration enables the usual strain and deformation tensors to be calculated. Typically, in viscous (or rate dependent) problems, these quantities are developed in terms of the current configuration using an Eulerian approach. This is primarily because fluids do not possess any natural reference state to which they return after any applied loads are removed. Here however, we develop the Lagrangian strain rate tensor \dot{E}_{MN} as the total time derivative of E_{MN} which leads to the following expression for strain rate

$$\dot{E}_{MN} = \frac{DE_{MN}}{Dt} = \frac{\partial E_{MN}}{\partial t} + \frac{\partial E_{MN}}{\partial x_i} v_i \quad (2)$$

v_i are the components of a velocity vector for a material particle at a fixed point in space on the deformed body referred to the x_i - coordinates. The first term on the right hand side of Eqn (2) is referred to as the local rate of change of E_{MN} and in the case of a steady state deformation this term is zero. The second term on the right hand side of Eqn (2) results from the particles changing position in space and is referred to as the collective rate of change of E_{MN} . Using the deformation gradient, the current velocity can be simply referred back to the undeformed configuration, which conveniently leads to a revised form of the strain rate tensor

$$\dot{E}_{MN} = \frac{\partial E_{MN}}{\partial X_R} V_R \quad (3)$$

Where V_R are the components of velocity of the undeformed sheet (i.e. related to the known line speed of the operation). It is emphasised that this description of strain rate is strictly limited to the case of a steady state deformation such as roll forming.

Finally, with regard to the kinematics, it is important to consider the interpolation of \dot{E}_{MN} in the context of a discretised finite element mesh. To ensure C_0 continuity of strain rate across element boundaries, interpolating functions of order 3 must be used. For this reason cubic-Hermite elements, shown in Fig 3, have been employed which allow the desired quantities to

be adequately interpolated. More will be said later regarding the complexities of specifying boundary conditions to such elements.

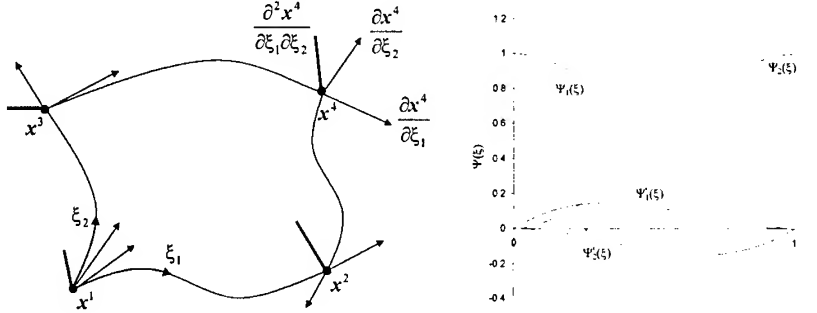


Fig. 3 2-dimensional cubic-Hermite element with a graph depicting the shape of the interpolating functions.

Constitutive Equation

The material law used in this analysis is based on the idealised fibre reinforced material model proposed by Spencer [ref]. Here we depart from convention and develop the law, not in terms of the usual Cauchy stress tensor, but rather the second Piola-Kirchhoff tensor which can be expressed as

$$T_{(v)}^{MN} = -p\delta^{MN} + T\delta^{M1}\delta^{1N} + 2V^R\eta_T \frac{\partial E_{MN}^{(v)}}{\partial v_s} \frac{\partial v_s}{\partial X_R} + 2V^R(\eta_L - \eta_T) \left(\delta^{M1}\delta^{1K} \frac{\partial E_{KN}^{(v)}}{\partial v_s} \frac{\partial v_s}{\partial X_R} + \delta^{N1}\delta^{1K} \frac{\partial E_{KM}^{(v)}}{\partial v_s} \frac{\partial v_s}{\partial X_R} \right) \quad (4)$$

The bracketed subscript indicates that the stresses are referred to the v_M - fibre coordinates. The Lagrangian multipliers p and T arise due to the constraints imposed on the material and need to be determined from the equilibrium equations. The terms η_L and η_T define the longitudinal and transverse viscosities respectively. As defined in the last section, the material derivatives define the rate of strain in the body.

Stress Equilibrium Equations

Large strain finite stress tensors, like the finite strain and deformation tensors described in the previous section, may be expressed in either spatial or material coordinate systems - and can be measured per unit area of deformed or undeformed material. In addition, all the stress tensors must obey the transformation laws required of a tensor quantity, meaning that components are not necessarily physical components of stress. Applying the principle of virtual work over an arbitrary volume Ω enables the equilibrium of the body to be expressed in terms of the following integral expression:

$$\int_{\Omega} T^{MN} x_N^k \delta v|_M d\Omega = \int_{\Omega} s \cdot \delta v d\Omega \quad (5)$$

where δv represents an arbitrarily small displacement, which satisfies compatibility as well as any displacement boundary condition specified on the surface $\delta\Omega$. The term $|_M$ denotes contravariant differentiation with respect to material coordinates while s denotes external tractions which act on the surface of the body. Notice that in this expression of the virtual work principal the stress components are referred to material v_M - coordinates while the displacement components are referred to the x_k - coordinates. Both boundary forces and acceleration terms have been neglected in Eqn (5).

Boundary Conditions

The boundary conditions applied in this analysis are somewhat simplified from the actual conditions encountered during forming. The prescribed nodal displacement boundary conditions used in the analysis are illustrated schematically in Fig 4. Higher order information is also prescribed along these boundaries. Prescribed shear and roll angles were applied to the leading edge of the sheet as shown in Fig 4. The choice of this type of boundary condition has a number of important implications which are discussed in the next section.

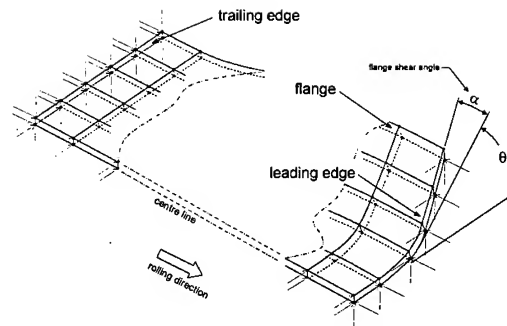


Fig. 4 A schematic illustration of the boundary conditions applied to the sheet

RESULTS AND DISCUSSION

Before presenting the results of the computational analysis it is worth briefly reviewing the main experimental findings as detailed in [3]. Fig. 5 shows the principal strains plotted over the undeformed surface of a $[0^\circ/90^\circ]$ laminate. A feature of the result is the in-plane shear deformation which increases through the deformation length.

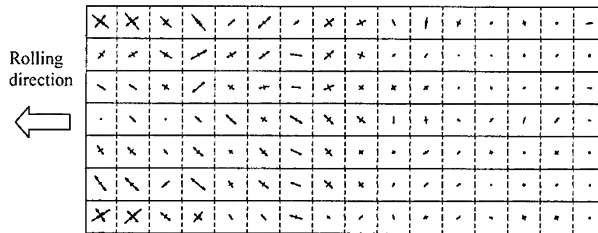


Fig. 5 Experimental grid strain pattern result for $[0^\circ/90^\circ]$ laminate

All of the roll forming simulations were undertaken using CMISS - a finite element analysis program developed at the University of Auckland. All models were run on a RS6600 work station and consumed no more than 720 seconds for the most computationally demanding model. The modelling parameters used in the analysis were as follows: roll angle = 20° , shear angle = 3° , and $V_0 = 5\text{m/min}$. The material parameters used in the analysis were taken as $\eta_L = 11.2\text{kPa.s}$ and as $\eta_T = 8.1\text{kPa.s}$. The Lagrangian multipliers arising from the dual kinematic constraints of fibre inextensibility and incompressibility were solved for explicitly using auxiliary interpolating functions. In general the conditions were adequately satisfied with calculated fibre strains exceeding no more than 0.02%. The stresses in the fibre direction have been plotted in Fig 6. The results show that almost all of the tension in the sheet is carried at the outer extremities of the flange. This narrow band of tension, which increases with X_1 , is a feature of the highly constrained idealised fibre reinforced material model and arose in a number of other off-axis forming simulations. One other notable feature, is the occurrence of compressive stresses in the web region of the sheet. In reality, these stresses result in localised fibre instabilities, or perhaps in the worst case, gross buckling of the sheet. Experimental evidence presented by [1] supports the existence of compressive stresses in the sheet. In-plane

shearing stresses were found to be an order of magnitude less than the fibre tensions while the hydrostatic pressure variation through the sheet was minimal.

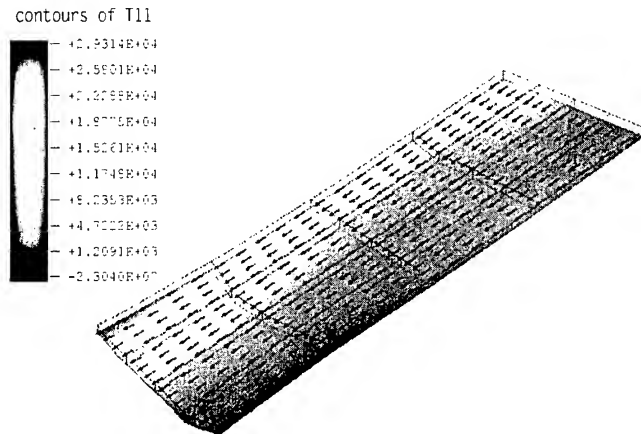


Fig 6. Contours of T^{11} plotted on the underside of the sheet.

One of the concerning aspects of the analysis is clearly the over constraining nature of the boundary conditions used in throughout the simulations. There is certainly the danger of over constraining the material or even inadvertently violating the kinematic material constraints detailed earlier on. Ideally the simulations would be performed on semi-continuous sheets where it might be possible to achieve a stress free condition at the trailing edge of the sheet. How this might be reconciled with the highly constrained nature of the material is an issue that would require considerable effort.

CONCLUSIONS

This paper has detailed the computational framework for the analysis of CFRT sheets in a steady state forming process such as roll forming. The kinematic equations describing the rate of deformation through the sheet have been developed using a large strain approach. A series of simulations have been conducted on unidirectional sheets identifying potentially problematic areas around the web of the sheet.

ACKNOWLEDGEMENTS

The authors gratefully acknowledge the support of the NZ Foundation for Research, Science and Technology. We also acknowledge the free supply of material from Mitsui-Toatsu (Japan).

REFERENCES

1. Mander, S.J., Panton, S.M., Dykes, R.J., Bhattacharyya, D., Roll forming of sheet materials. In Composite Sheet Forming, ed. D. Bhattacharyya, Chapter 9. Composite Materials Series. Elsevier, Amsterdam, 1997.
2. Mander, S. J., Bhattacharyya, D., 'Roll forming of fibre-reinforced thermoplastic composites', *Proceedings of ICCM-10*, Vol. III: Processing and Manufacturing. Whistler, B.C. Canada. pp. 413-420, 1995.
3. R.J. Dykes, D. Bhattacharyya, P.J. Hunter, Analysis of roll forming continuous fibre reinforced thermoplastic sheets, *Flow Processes in Composite Materials (FPCM-6)*, Plymouth, United Kingdom, July (1999).
4. Malvern, L.E., Introduction to the Mechanics of a Continuous Medium. Prentice-Hall, Englewood Cliffs, New Jersey, USA. (1969).
5. Rogers, T.G. 'Rheological Characterisation of Anisotropic Materials', *Composites*, Vol. 20 (1), pp. 21-27 (1989).

Processing (2)

PARTICULATE COMPOSITES BASED ON GROUND RUBBER TIRE AND POLYETHYLENE: MANUFACTURING OF POROUS PIPE AND EFFECTS OF DIFFERENT PEs ON MECHANICAL PROPERTIES AND LEAK RATE

G. H. Motlagh, S. R. Ghaffarian, N. Mohammadi, H. Nazokdast, M. H. Mahdavian

*Department of Polymer Engineering, Amirkabir University of Technology
424, Hafez Ave., Tehran, Iran*

SUMMARY: The paper presents the mechanical properties and leak rate of porous pipes made of different polyethylenes. The effects of PE type and MFI on these properties are investigated. A mixture of polyethylene as a matrix (binder), ground rubber tire (GRT) as a disperse phase and some additives are dry blended in a high speed mixer and then fed to a pipe extruder to form a porous pipe. Several types of polyethylene (HDPE, LLDPE and LDPE) with various MFI have been used in producing porous pipes. Some of the mechanical properties and leak rate of them are presented. The results demonstrate significant effect of type and content of PE on the mechanical properties whereas the MFI does not have a perceptible effect. To explain the latter observation, DSC analysis has been used and revealed that with increasing MFI, degree of crystallinity of end product increases. This confirms that in production of porous pipe, crystallization of matrix is kinetic control. In spite of mechanical properties, the leak rate is strongly depends on MFI of the PE. It was shown that for optimizing desirable mechanical properties and leak rate of a porous pipe for a special service conditions, binary blends of different grades of PE can be used.

KEYWORDS: porous pipes, ground rubber tire, GRT, polyethylene, mechanical properties leak rate, crystallization.

INTRODUCTION

Increasing legislation restricting the disposal of used tires and greater environmental consciousness have heightened the search for economical and environmentally sound methods of recycling discarded tires. Although a number of uses have already been examined [1,2], they are either uneconomical or do not utilize sufficient quantities of tires to represent a complete solution and new methods need to be explored. One area with the potential both to

be economical and to utilize large volume of used tires is the use of ground tires as fillers in polymer composites. In these systems tires are cryogenically or under the ambient condition, ground to a fine powder(100 to 600 μm), separated from the metal and polyester cord, and then compounded with thermoplastics, elastomers, or thermosets.

production of porous pipe is one of the application area of GRT which was invented by Turner in 1977 [3]. Porous pipe is made of GRT particles with smaller amount of polyethylene as binder to integrate them. The main application of porous pipes is subsurface irrigation but they are also used in water and sewage aeration and soil stabilizing. In subsurface irrigation they have many advantages specially water saving (having irrigation efficiency higher than 90%), increasing crop yield, continuous irrigation without surface watering and direct injection of nutrients to root zone.

In this work the effects of polyethylene type (HDPE, LLDPE and LDPE) and its melt flow index (MFI) on the mechanical properties and leak rate of porous pipe was studied. The properties of porous pipes involving binary blends of PEs were also examined.

EXPERIMENTAL

Materials

Different types of polyethylene which their properties are summarized in Table 1, one type of GRT having particle size distribution of 45 mesh: 18%, 60 mesh: 50%, 120 mesh: 30%, >120 mesh: 2% by weight, talc (as slip contact agent) and zinc stearate (as lubricant) were used in this study.

Table 1 Specifications of polyethylenes

PE Type	MFI (g/10 min), 190 °C :		Density (g/cc)	DSC Melting Point (°C)
	5 Kg	2.16 Kg		
HDPE 1	0.73		0.944	128
	1.8		0.946	131
	7.8		0.952	---
LLDPE 1		0.5	0.920	124
		3.8	0.928	127
LDPE 1		0.83	0.925	110
		5.4	0.926	112

Preparation of Porous Pipes

The composition consisting of 100 phr GRT, 35 phr polyethylene (unless otherwise stated), 4 phr talc, 0.5 phr zinc stearate were dry blended in a high speed mixer to obtain homogenized mixtures. These mixtures were fed to hopper of an unvented single screw extruder having barrel diameter of 19 mm, L/D= 24 and compression ratio of 2.3. Screw speed was set on 50 rpm and temperature of feeding, transition and metering zone adjusted on 170, 180, 190 °C. The pipe (outside diameter 15 mm, inside diameter 10 mm) was extruded through an annular

die maintained at 150 °C into the ambient while the water vaporized (originating from absorbed moisture in the GRT particles) and expanding bubbles of steam formed a network of pores extending from the bore to the surface of the porous pipe. Once the pipe formed and passed out of the die it was submerged in a chilled water bath held at about 18 °C to cool the hose and stabilizing the formed pores. After cooling the hose moved on a conveyor belt and under a top roller which was spaced apart from the conveyor so as to contact the hose on the conveyor. The distance between the conveyor and the top roller was so set that to insure

positive movement of the hose away from the extruder without applying any substantial tension force on the pipe to pull the pipe from the extruder.

Testing

To obtain tensile strength, elongation at break and tensile modulus, the tensile testing was carried out at room temperature on dumbbell shaped specimens cut from porous pipes in a Monsanto testing machine model 500 at a crosshead speed of 50 mm/min according to ASTM D412 die C. Compression testing was directly performed on porous pipes samples as per ASTM D2412 in an Instron Universal Testing Machine Model DY-26. Stiffness at 10, 20, 30% displacement was calculated according to Eqn 1 and average of them was defined as pipe stiffness and used in figures.

$$S = F / (D \cdot L) \quad (1)$$

Where S, F, D and L are stiffness, exerted compression force, displacement of specimen under compression force and length of specimen respectively.

For leak rate measurement all the pipes were pretreated with an internal water pressure of a few bar for 5 min to ensure the wetting of the pores.

Then the measurement was performed with the pipes 1.5 m long (4 piece per any composition) at a constant pressure of 1 bar throughout the length of the pipe. Registration of the leaking was started after the fixation of pressure for 5 min. The permeate was collected for 2 min. The leak rate was calculated from the Eqn 2.

$$J = V / (L \cdot t) \quad (2)$$

Where J, V, L, t are leak rate, volume of permeation, length of specimen and time of permeation respectively.

RESULTS AND DISCUSSION

Effect of Binder Content

To determine the effect that binder content has on leak rate and mechanical properties, several compositions consisting of variable amount of polyethylene were prepared. It is clearly seen in Fig. 1 that polyethylene content has a detrimental effect on the leak rate. Porous pipe involving more than 50 phr PE, almost losses its leaking. It is believe that insufficient amount of PE to fill the voids between the solid elastomer particles is mainly responsible for existing labyrinth passageways within the wall of the pipe so that the vaporized water can create them when the pipe leaves the die and enters to ambient. According to this process, increasing binder content while the amount of water incorporated to GRT particles is constant, decreases the voids and susceptibility of extruded pipe to foaming. More over, before the complete stabilization of the open pores during the cooling process, higher flow of the molten PE closes them.

As shown in Fig. 2 PE content has pronounced effect on tensile strength and slightly increases the elongation at break as well as pipe stiffness. The first observation can be related to the increase of continuous phase which mainly support the exerted tensile stress, while the latter mainly returns to the decrease of voids in the system.

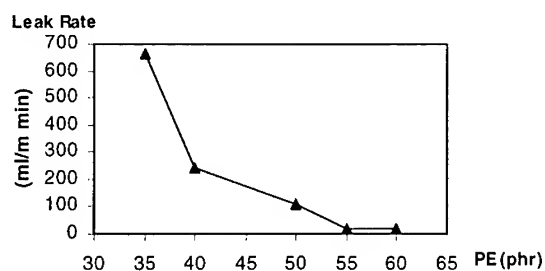


Fig. 1 Effect of PE content on leaking rate

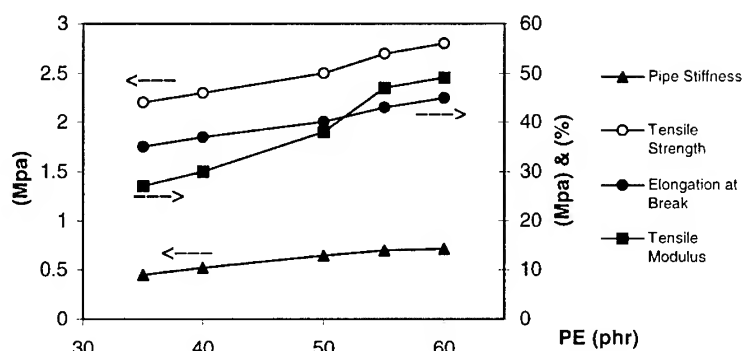


Fig. 2 Mechanical properties of porous pipe vs PE content

Effect of PE grade

Fig. 3 shows the properties of porous pipes consisting of different types of PE (HDPE, LLDPE, LDPE) having various MFI. The leak rate increases as MFI increases which is attributed to more porosity. In addition to this, it is almost independent of PE type.

For tensile strength this order is observed: HDPE > LLDPE > LDPE (Fig. 4). This is in agreement with order of crystallinity of them (DSC analysis was carried out on samples of these porous pipes and showed the same order for heat of fusion). Also as seen from Fig. 4 tensile strength is almost independent of MFI which is an unexpected result because of Fig. 3 which confirmed that porosity increases as MFI increases. Thus it should lead to decrease of mechanical properties particularly tensile strength. To interpretation of this phenomena DSC analysis was used for three couples of samples mentioned in Fig. 3. Obtained results revealed that the porous pipes including PE with higher MFI have greater heat of fusion compared to those with lower MFI (for example HDPE with MFI = 1.8 and HDPE with MFI = 0.73). This arises from the condition of porous pipe production, when the extruded pipe once leaves the die enters in the cooling bath. Consequently the crystallization of PE chains is restricted to time so that the lower molecular weight chains (higher MFI), due to their higher crystallization rate, can achieve more degree of crystallinity which has a pronounced effect on mechanical properties. So it can be concluded that crystallization behavior of PE in production of porous pipes is kinetic control. In addition higher MFI means easier flow and better coating of GRT particles which definitely result in better mechanical properties.

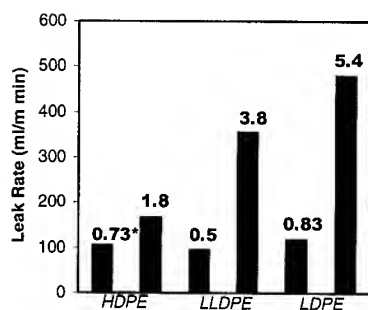


Fig. 3 Leak rate of porous pipes vs PE type MFI

*numbers are the MFI of virgin PE

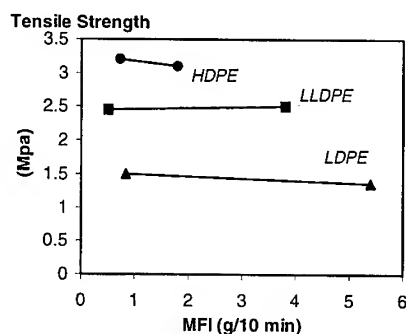


Fig. 4 Tensile strength of porous pipes vs PE type and MFI

Fig.5 shows the results of tensile modulus. It is strongly depends on the type of polyethylene which is obvious according to order of crystallinity (HDPE >LLDPE >LDPE). In addition increasing of tensile modulus versus MFI is noticeable. As was explained before the higher MFI would increase degree of crystallinity which causes enhancement of tensile modulus. Elongation at break significantly depends on type of polyethylene(HDPE >LLDPE >LDPE) which is seen in Fig. 6. It may be due to higher modulus of HDPE compared to others which can result in more transfer of load to elastomer particles to share in tensile deformation up to failure point. The similar behavior of LLDPE to HDPE can be related to this fact that failure mechanism of LLDPE is more ductile.

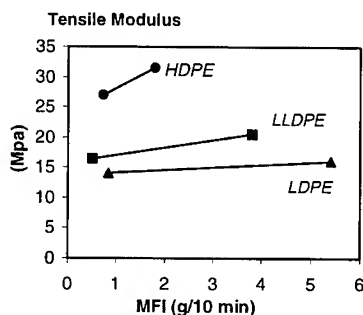


Fig. 5 Tensile modulus of porous pipe for different grades of PE

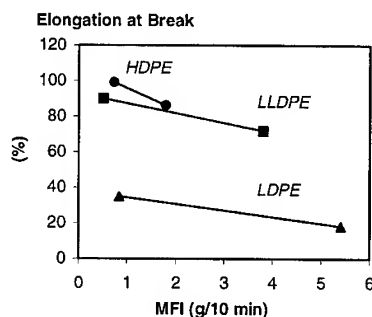


Fig. 6 Elongation at break of porous pipe for different grades of PE

Using Binary Blends of PE

Several porous pipes were produced by using of binary blends of LDPE, LLDPE and HDPE having various MFI. Test results demonstrated that the properties of each component is reflected in the final properties of the product as much as its relative amount in the binary blend. The properties of one of them is represented in Fig. 7 and 8. As seen with increasing the relative amount of LDPE ie poor component, the mechanical properties falls while the leak rate increases with respect to lower melt viscosity of LDPE.

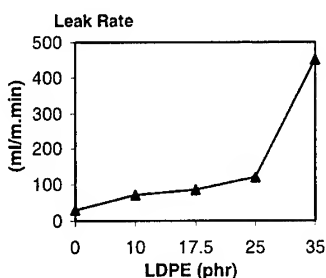


Fig. 7 Effect of relative composition of LDPE- 2 and HDPE- 1 on leak rate
(total amount of PE in composition is constant and equal to 35 phr)

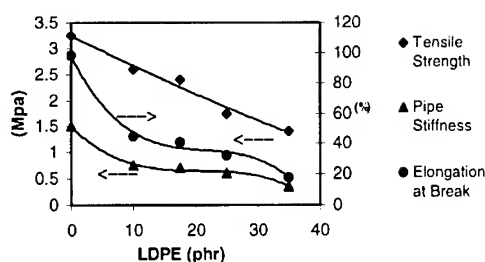


Fig. 8 Effect of relative composition of LDPE- 2 and HDPE- 1 on mechanical properties
(total amount of PE in composition is constant and equal to 35 phr)

CONCLUSION

Properties of polyethylene as a binder to integrate the GRT particles strongly determines the final properties of porous pipes. While type of PE (HDPE, LLDPE or LDPE) effectively changes the mechanical properties, MFI has noticeable effect on the leak rate. DSC results revealed that crystallization behavior of PE in porous pipe production is a kinetic control phenomena. For a determined type of PE, higher MFI means higher porosity and leak rate, whereas the mechanical properties remain almost constant. This result returns to enhancement of crystallinity of the final product consisting of PE with higher MFI which compensates the detrimental effect of higher porosity. Besides, PE having higher MFI can coat the surface of GRT particles better, which definitely improve the mechanical properties. For optimizing the flexibility and stiffness of a porous pipe suitable for a special service conditions, blends of different PE grades can be used.

ACKNOWLEDGMENTS

The authors are grateful to the Propagation and Development Organization of Agriculture Ministry (Tehran, Iran) for financial support of this project.

REFERENCES

1. F. G. Smith and W. B. Klingensmity, "Tires as a Consumer Source of Recycled Materials", *Meetings of the Rubber Division, Amer. Chem. Soc.*, Oct. 9-12, 1990
2. A. A. Hershaft, *Environ. Sci. Technol.*, Vol. 6, 1972, pp.412.
3. J. E. Turner, "Method for Extruding Porous Irrigation Pipe", *US Patent No. 4 028 288*, 1977.

RESISTANCE WELDING OF CARBON FIBRE REINFORCED THERMOPLASTIC COMPOSITE

Q. Yuan¹, M. Hou², Y.-W. Mai¹, and L. Ye¹

¹*Centre for Advanced Materials Technology (CAMT), Department of Mechanical & Mechatronic
Engineering J07, The University of Sydney, Sydney 2006, NSW, Australia*

²*Cooperative Research Centre for Advanced Composite Structures Ltd. 361 Milperra Road c/o Hawker De
Havilland, Bankstown 2200, NSW Australia*

SUMMARY: CF/PEI laminate was joined using a resistance welding technique. The heating element has a sandwiched structure, which consists of two GF/PEI prepregs covered on both sides of a stainless metal mesh. The mechanical properties of the welded flat panel were characterised by three-point bending, end-notched flexural, Charpy and falling weight impact tests. The results showed that failure occurred mainly inside the adherent laminates adjacent to the heating element in the form of delamination. Fracture surface analysis revealed that the material was deconsolidated in these layers due to the differential thermal expansion during the welding process. This deconsolidation defect could be reduced by increasing the hold pressure. Hence, the values of flexural strength and modulus of the welded laminates increased with hold pressure. The delamination area of the welded laminates decreased with increase of hold pressure.

KEYWORDS: Resistance welding, Thermoplastic Composite, Polyetherimide,

1. INTRODUCTION

Resistance welding is used to join parts together in the manufacture industries. Many studies have been done on resistance welding of thermoplastic composites [1-3]. One of the most common methods is using carbon fibre prepreg as a heating element to join carbon fibre reinforced composites, since carbon fibre prepreg keeps the material homogeneous and no new interface will be introduced into the bonding surface. However, during the preparation procedure some unavoidable defects, such as breakage of fibres and incomplete removal of matrix from fibre surface, can cause inhomogeneous heating in the bonding surface, leading to an incomplete bonding. This phenomenon is predominant in the welding of large area.

Metal mesh can be used as heating elements, because it can conduct electricity more uniformly than CF/resin prepreg or fabric. Taylor has used metal mesh to join CF/PEEK composite in 1991 [1]. It was found that the metal mesh has a big processing window and outstanding bond existed between the metal mesh and matrix.

Current leakage is identified as a main reason for incomplete bonding of large areas. Yang [5] using a single layer of GF/PEI prepreg co-consolidated on both sides of the metal mesh heating element to form a sandwiched heating element, in which the GF/PEI prepreg can effectively prevent any physical contact between metal mesh and carbon fibre in the adhered composite during the full welding process. The mechanical performance of their welded specimens in terms of lap shear and mode I interlaminar fracture toughness were equivalent to that of compression-molded benchmarks.

This work is focused on the mechanical properties of welded laminates. The deconsolidation problem during welding was examined. Impact properties of welding materials were studied using Charpy and falling weight impact tests. The damage area

was measured using ultrasonic C-scanning. Finally, a demonstration structures CF/PEI hinge was joined successfully using resistance welding technique.

2. EXPERIMENTAL WORK

2.1. Manufacture of Consolidate Laminate and Heat Element

CF/PEI laminates were manufactured by compression molding. CF fabric/PEI prepreg consists of 5H Satin woven fabric and has a resin content 44.1 wt%. The hot press conditions were 320 °C and 2 MPa for 10 minutes [4]. The thickness of the fully consolidated laminate was about 3.0 mm.

Two kinds of benchmark laminates were manufactured using the same processing conditions. One was the CF/PEI benchmark consisted of 22 CF/PEI of prepergs with a thickness of about 6.6 mm. The other was CF/GF/PEI benchmark laminates with a stacking sequence of $(CF_{10}/GF)_s$. The thickness of $(CF_{10}/GF)_s$ benchmark laminate was about 6.3 mm.

The heating element consists of a layer of metal mesh sandwiched between two layers of GF/PEI prepreg and was consolidated by compression. The metal mesh consists of stainless steel wire with a diameter of 25 μ m. The mesh dimensions were 30 μ m square.

2.2. Welding Process

Welding of sample with small area (25x220 mm) was carried out using an Instron 5567 universal testing machine. The welding conditions were: hold pressure 0.2 MPa, input current 30 A, and the welding time 32 s. [13]. Welding of samples with large welding area (100x220 mm) were carried out using a metal welding machine. Different holding pressures of 0.5, 1.0 and 2.0 MPa were used to study the effect of holding pressure on the mechanical properties of welded laminates. The input current was 100 A, and the welding time was 30 s.

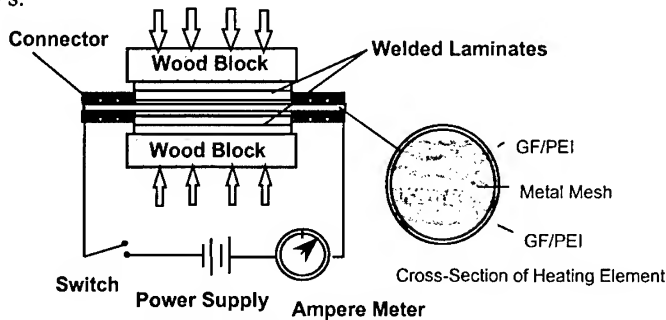


Figure 1 A schematic picture of resistance welding set-up

2.2. Characterisation of Mechanical Properties

Interlaminar fracture toughness was determined using End-Notched-Flexural (Mode II) tests according to Reference [8]. The maximum load value and the non-linearity load point value were used to calculate G_{IIC} . Three methods were used to calculate the value of G_{IIC} [6], which are experimental compliance calibration (Method A, $G_{IIC}=3ma^2P^2/2B$), the direct beam theory (Method B, $G_{IIC}=9a^2P\delta/(2B(2L^3+3a^3))$) and corrected beam theory (Method C, $G_{IIC}=9a^2P^2/16EB^2h^3$), where C is compliance, a is length of crack, P is load, B is width of sample, δ is displacement, L is the support span, E is the modulus.

Flexural properties of the laminate were determined by three-point bending test according to ASTM D790M-84.

Charpy impact test was carried out using an instrumented impact tester (ITR-200). The samples were cut from the small welded sample and the impact direction was normal to the surface of laminate. Falling weight impact test used the samples cut from the larger welded area panel. The dimensions of the specimen were 60x60 mm. The impact speed was 3.8 m/sec. Different impact energies were obtained by changing the masses of dart from 2 kg to 8 kg, (impact energy between 14.44 to 57.76 J). The impact dart had a hemispherical head with a radius of 5 mm. The specimen was laid on a support with 40 mm diameter hole. Above the specimen a disk with a 40 mm diameter hole was used to clamp the specimen. Once the laminate was impacted the dart was caught to prevent further impact.

2.3. Damage Analysis

The fracture surface of Charpy impacted specimens was analyzed by scanning electron microscopy. The delamination area of falling weight impacted laminates was determined by ultrasonic C-scan (KK&S Instruments Pty. Ltd). Scanning conditions were as follows: frequency 5 MHz, the step length 0.05 mm and amplitude 30 db.

3. RESULTS AND DISCUSSIONS

3.1. Interlaminar Flexural Toughness

The interlaminar fracture toughness of (CF/PEI₁₀GF)_s benchmark has higher G_{IIC} value than that of (CF/PEI₁₁)_s benchmark. The G_{IIC} value of welded laminate is the lowest amongst the three types of specimens that of both benchmarks.

Table 1. Interlaminar fracture toughness of welded laminate and benchmarks

	$G_{IIC,NL}$ (Method A)	$G_{IIC,NL}$ (Method B)	$G_{IIC,NL}$ (Method C)	$G_{IIC,Max}$ (Method A)	$G_{IIC,Max}$ (Method B)	$G_{IIC,Max}$ (Method C)
CF	1813	1559	1332	2874	2739	2111
Benchmark	±720	±615	±529	±673	±631	±494
GF	2071	1802	1713	3877	4339	3206
Benchmark	±288	±224	±238	±947	±655	±783
Resistance	1041	1007	670	1800	1862	1159
Welded*	±386	±369	±248	±908	±708	±585

G_{IIC} Unit: J/m², * Welded conditions: 30 A, Time 32 s. and 0.2 MPa, NL: non linearity load, Max: Maximum load

Three cracks were found in the welded specimens. The main crack remained in the initial crack layer (ie. between GF/PEI prepreg and CF/PEI prepreg). The other cracks existed in the adjacent layers of the welded surfaces. During the loading process failure occurred not only in the initial crack along the starting film, but also propagated in the adjacent layers. The adjacent layers during the welding process were partly melted, which led to residual stresses in these layers and the thermal expansion created some voids. These deconsolidation defects in turn led to a reduction in the interlaminar fracture toughness in mode II.

3.2. Charpy Impact Test

An instrumented three-point bending impact tester was used to determine the energy absorption capability of welded materials. It has been found that the welded specimen

had larger displacement than that of benchmarks, due to the delamination damage, which resulted in much higher energy absorption.

Table 2. Charpy properties of the welded laminate and benchmarks materials

Specimen	F_{Max} [N/mm ²]	E_{Fmax} [kJ/m ²]	E_{Total} [kJ/m ²]
CF Benchmark	26.15 ±0.95	18.85 ±0.72	36.26 ±2.77
GF Benchmark	29.51 ±1.95	25.10 ±5.43	72.43 ±29.40
Welded Laminate*	31.63 ±2.61	32.47 ±5.16	121.51 ±17.05

Weld conditions: 30A, Time 32seconds, 0.2MPa, E_{Fmax} : Energy absorption at maximum load, E_{Total} : Total energy absorption.

Different fracture mechanisms were observed through fracture surface analysis. For the CF/PEI benchmark laminate the failure mechanism is dominated by the brittle fracture of CF fibres. For benchmark containing glass fibre prepreg, besides fibre fracture, small amount of delamination was found between GF/PEI layer and CF/PEI layer, since the glass fibre has higher elongation than that of carbon fibre. However, the welded laminate broken into two pieces, along bending line, due to the delamination during the Charpy impact. The delamination does not occur in the welding surfaces, but in the adjacent layers.

3.3. Flexural Properties of Welded Laminates with Different Welding Pressure

The flexural strength of the welded laminate was lower than those of the benchmarks. (Table 3) The failure modes of benchmarks and welded laminate were found to be the same as the Charpy impact tests.

Table 3. Flexural properties of welded laminates and benchmarks tested by three-point bending test

	Holding Pressure [MPa]	Flexural Strength [MPa]	Flexural Modulus [GPa]
CF Benchmark	2.0	782.4 ±25.4	39.5 ±2.3
GF Benchmark	2.0	762.5 ±52.2	43.4 ±1.7
Welded Laminate	0.2	505.5 ±31.5	39.7 ±2.8
Welded Laminate	0.5	717.7 ±9.12	45.0 ±1.0
Welded Laminate	1.0	763.6 ±28.5	45.4 ±1.3
Welded Laminate	2.0	784.6 ±39.8	47.8 ±0.6

Comparing the consolidation pressure of 2.0 MPa used in the compression of benchmark samples, the hold pressure for the welding process was too low (only 0.2 MPa). It is assumed that a low hold pressure could be a reason of deconsolidation in the adjacent layers. To reduce this defect caused by thermal expansion, hold pressure must be increased. The effect of holding pressure on the flexural properties was studied using the welded laminates with different holding pressure (0.5, 1.0 and 2 MPa). It is clear that the flexural strength increased with holding pressure and much less delamination was found in samples welded with high hold pressures.

The flexural modulus of welded laminates also increased with hold pressure varying in a similar pattern as the flexural strength. At 2 MPa hold pressure, the flexural modulus of

the welded laminate was higher than those of both benchmarks. It seems that the metal mesh has increased the modulus of welded laminate.

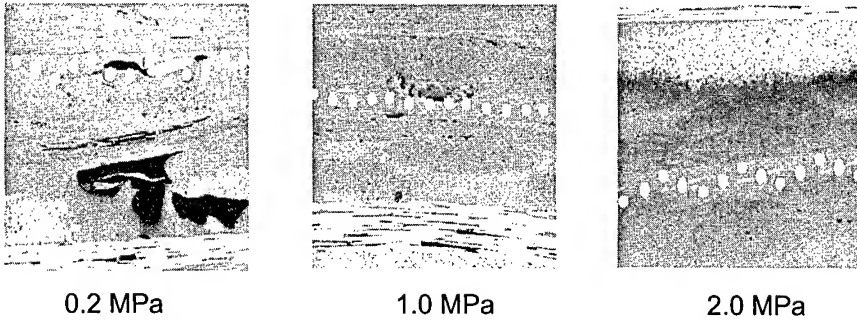


Figure 2 Cross-sections of welded laminates with different holding pressure

At lower hold pressure many cavities (voids) can be found in the adjacent layer. When the hold pressure was increased, the number of cavity was dramatically reduced.

3.4. Falling Weight Impact Properties

A falling weight impact test was used to measure the impact tolerance with different impact energy. It is clear that increasing impact energy led to increasing damage area. The welded laminate with 1MPa hold pressure has larger delamination area than those of benchmarks. However, if the hold pressure was increased to 2 MPa, the same pressure used in the compression molding, both welded and benchmark laminates have nearly the same damage area.

Table 4. Delamination area* of welded and benchmark laminates as a function of impact energy

	CF Benchmark	GF Benchmark	Welded Laminate	Welded Laminate	Welded Laminate
Impact Energy [J]	Pressure 2 [MPa]	Pressure 2 [MPa]	Pressure 0.5 [MPa]	Pressure 1 [MPa]	Pressure 2 [MPa]
29.4	-	-	79	-	-
44.1	60	77	84	90	79
58.8	95	97	85	-	-
73.5	182	175	116	-	-

Delamination area unit: mm²

It is interesting to note that the welded laminates have smaller delamination area than those of benchmarks under the highest impact energy. It seems that the metal mesh provide resistance to delamination at high energy levels.

4. Demonstration for Welding of Hinge with Front Spar

A real demonstration part was manufactured using resistance welding technique. The hinge and a short front spar were manufactured from a fabric CF/PEI prepreps by compression molding procedure. The welding conditions were 100 A current (power level: 126 kW/m²) and high pressure (4 MPa), and current time 35 s. The hold pressure was kept until the specimen cooled down below 50 °C. The welded hinge was polished and examined. No defect was found in the joint (Figure 3).

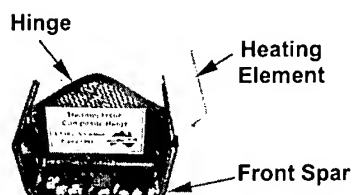


Figure 3 Demonstration of welded hinge and front spar

5. CONCLUSIONS

Carbon fibre reinforced thermoplastic PEI laminates can be joined using resistance-welding method with sandwiched heating element. Results of three-point bending and Charpy impact tests showed that in the adjacent layers of the heating element deconsolidation occurred during the welding process. This defect could be reduced or eliminated by using higher holding pressures. The flexural strength and flexural modulus of welded laminates were improved by increasing the holding pressure. The delamination area of welded laminates decreased with increasing holding pressure. A demonstration part has been archived using resistance welding technique.

6. ACKNOWLEDGEMENTS

This work was carried out as part of the Cooperative Research Center for Advanced Composite Structures (CRC-ACS) Research Program (Task 2.1.3 Alternative Prepreg Technology). The authors would like to thank all members of the Centre for Advanced Materials and Technology at the University of Sydney.

7. REFERENCES

1. N.S. Taylor and R. Davenport, Resistive implant welding of thermoplastic composite materials, Conference Proceedings of the 49th Annual Technical Conference ANTEC 91. 37, 1991, pp. 2038-2041.
2. C. Ageorges, L. Ye, Y.-W. Mai and M. Hou, Characteristic of resistance welding of lap-shear coupons Part III: Crystallinity, Composites –Part A: Appl. Sci. & Manufact. 29(8), 1998, pp. 921-932.
3. M. Hou, L. Ye and Y.-W. Mai, An experimental study of resistance welding of carbon fibre fabric reinforced polyetherimide (CF Fabric/PEI) composite materials, Appl. Comp. Mater. 6, 1999, pp.35-49.
4. M. Hou, L. Ye, H.J. Lee and Y.-W. Mai, Manufacture of a carbon-fabric reinforced polyetherimide (CF/PEI) composite materials.; Compos. Sci. & Techno. 58(2), 1998, pp. 181-190.
5. M.B. Yang, M. Hou, A. Beehag, Y.-W. Mai and L. Ye, Resistance welding of carbon fiber reinforced polyetherimide composites using metal mesh as a heating element CRC-ACS TM 99001 Feb. 1999.
6. L.A. Carlsson and J.W. Gillespie Jr., Mode II Interlaminar fracture of composite, Application of Fracture Mechanics to Composite Materials, Composite Materials Series 6, Ed: Friedrich K, 1989, pp. 113-157.

Cure monitoring of FW Pipe by Using EFPI Fiber Optic Sensors

Tatsuro Kosaka¹, Katsuhiko Osaka², Masaya Sando³ and Takehito Fukuda⁴

*Department of Intelligent Materials Engineering, Osaka City University
3-3-138 Sugimoto, Sumiyoshi-ku, Osaka, 558-8585, Japan*

¹*kosaka@mech.eng.osaka-cu.ac.jp*: ²*ohsaka@mech.eng.osaka-cu.ac.jp*
³*sando@zai6.mech.eng.osaka-cu.ac.jp*: ⁴*takehito@mech.eng.osaka-cu.ac.jp*

SUMMARY: Smart composites with sensor functions can be used for cure and health monitoring, and optical fiber sensors are suitable for FW molded composites. In this paper, internal strain measurements of FW pipe by embedding a EFPI optical fiber sensor were conducted. Some experiments were conducted to understand the relation between the internal strain and the curing state. It is found that the curing shrink can be measured by using a EFPI optical fiber sensor in the curing process of FW pipe. From the experimental results in the after curing process, it is concluded that the embedding configuration strongly affects on the sensor outputs. More detail researches are needed to reliable measurements of internal strains.

KEYWORDS: Smart composites, FW molded composites, Optical fiber sensor, Cure monitoring, Internal strain measurements

INTRODUCTION

Recently, many studies of smart composite materials, which added sensor and actuator functions to composite materials have been conducted[1], [2]. Smart composites with sensor functions can be used for cure and health monitoring. Cure monitoring technologies have merits of a decrease of curing time and a prevention of under-cure, and health monitoring technologies have merits of an improvement of reliability and a reduction of maintenance cost. There are many studies on cure and health monitoring of FRP laminates with embedded sensors[3], but there are few studies on those of FW (Filament Winding) molded composites. Optical fiber sensors have many advantages of small size, lightweight, high flexibility and so on, so it is expected that they are used as sensors for smart composites. Especially, optical fiber sensors are most suitable for embedding in FW molded composites.

In this paper, internal strain measurements of FW pipes by an embedded optical fiber sensor under cure were conducted. Dielectric parameters and a temperature of FW pipe were also measured to know the curing state and the temperature change. Some experiments were conducted to understand the relation between the internal strain and the curing state.

EXPERIMENT METHODS

Optical Fiber Sensor in This Experiment

A EFPI (Extrinsic Fabry-Perot Interferometer) optical fiber sensor was used in this study. EFPI optical fiber sensors are capable of providing precise, absolute, and perfectly linear measurements without stabilization means [4]. Figure 1 shows schematic diagram of the sensing part. The sensing part has an air gap and is covered with a silica tube. A phase difference between reflected lights from A and B was changed when the length of air gap was changed. In this experiment, FTI-Bus500 (FISO Technologies, Co. Ltd.) was used for the strain measurement device which obtained strain from the phase difference.

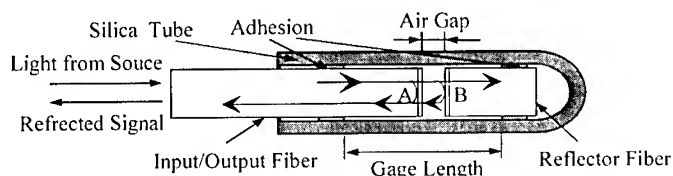


Fig.1 Schematic diagram of sensing part in EFPI optical fiber sensor

Experiment A: Internal Strain and Dielectric Parameters Measurements of FW Pipe

The embedding configuration of an optical fiber sensor and the dimensions of FW pipe are shown in Fig.2. A matrix resin of FW pipe was vinyl ester, RIPOXY R-802 (Showa High Polymer, Co. Ltd.) and reinforced fibers was E-glass (Nippon Sheet Glass, Co. Ltd.). The winding method was a helical winding at 45 degrees. An Optical fiber sensor was embedded in the middle plane of the thickness toward the length of FW pipe. The resin was cured at RT (26°C) for 20 hours in RT cure and at 110°C for 100 minutes in after-cure. The actual temperature was a little different from 26°C.

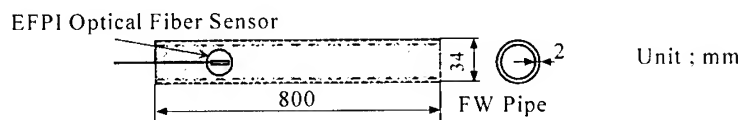


Fig.2 The embedding configuration of optical fiber sensor and the dimensions of FW pipe

The measurement system of internal strain and dielectric parameters of FW pipe is shown in Fig.3. In this experiment, after winding of fiber strands finished. The EFPI optical fiber sensor was connected to FTI-Bus500, and the internal strain outputs were collected by a personal computer through a serial line per 15 seconds. Eumetric100A (Micromet Instruments, Inc.) dielectric sensor system was used for the dielectric parameters measurements. The measurement cycle of the dielectric parameters was two minutes and the setting frequencies were 0.1Hz, 1 Hz, 10 Hz and 100 Hz. A thermo couple was used for temperature measurement with two minutes cycle. For cure monitoring of resin, the most important dielectric parameter is an ion viscosity, which indicates movability of the electric charges and dipoles in high polymer chains [5]. An ion viscosity is obtained from a permittivity and a loss factor, where the former is a real part of complex dielectric constant and the latter is an imaginary part. A dielectric sensor and a thermo couple were attached on the surface of FW pipe.

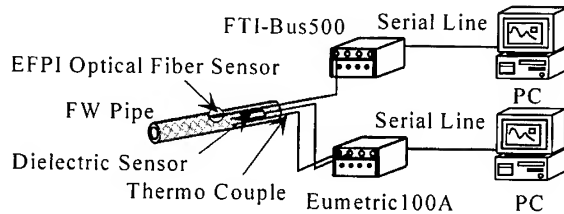


Fig.3 The measurement system of internal strain and dielectric parameters of FW pipe

Experiment B: Internal Strain and Dielectric Parameters Measurements of Resin

A EFPI optical fiber sensor, a dielectric sensor, and a thermo couple were put in resin which was filled in an aluminum cup. The curing condition and the measurement system were same as those of FW pipe.

EXPERIMENT RESULTS

The Results of Experiment A

The experimental results of the internal strain measurement and the relations among log ion

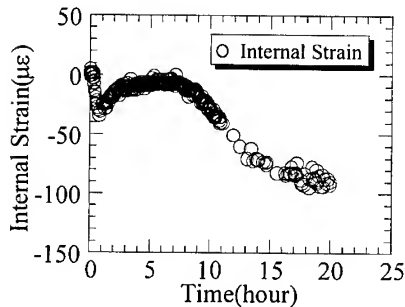


Fig.4 The relation between internal strain outputs and time in cure at RT

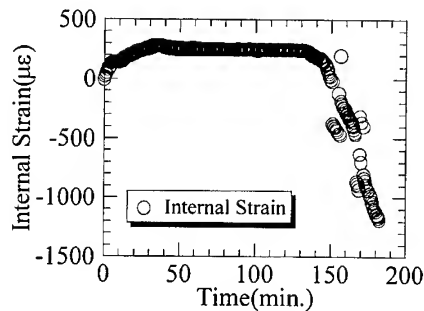


Fig.6 The relation between internal strain outputs and time in after-cure

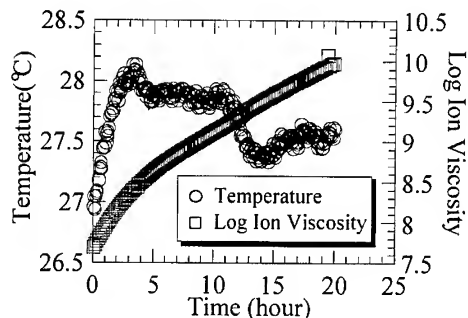


Fig.5 The relations among log ion viscosity, temperature, and time in cure at RT

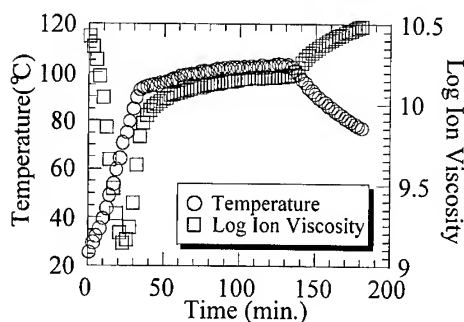


Fig.7 The relations among log ion viscosity, temperature, and time in after-cure

viscosity, temperature and time in the curing process at RT are shown in Fig.4 and Fig.5, respectively. After one hour from the beginning of measurement, the strain output and the temperature increased by almost $30\mu\epsilon$ and then became constant. After about 8 hours, the strain began to decrease, and then continued to decrease till the end. The temperature began to decrease after about 4 hours. The total strain in cure process of FW pipe was about $-80\mu\epsilon$ for 20 hours. The log ion viscosity continued to increase in the measurement, and did not converge to constant value.

Figure 6 and 7 show the experimental results in the after-curing process. The strain changed with the temperature change in after-curing process. When the temperature became 110°C , the internal strain became constant. In the cooling stage, the strain decreased by $1000\mu\epsilon$ in 25°C down, and then the strain will be about $-3300\mu\epsilon$ at RT. Four FW pipes were monitored and have almost similar behavior to each other. It shows that the measured strain behavior has reproducibility. The log ion viscosity fell down to minimum value, and then went up rapidly till the temperature became 100°C . After about 100 minutes, the log ion viscosity and the temperature reached constant values.

The Results of Experiment B

The internal strain and the relations among log ion viscosity, temperature and time in curing process at RT are shown in Fig.8 and Fig.9, respectively. For four hours from the beginning, the internal strain was constant, and then decreased till the end. The temperature began to

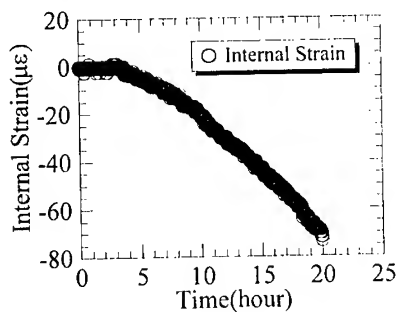


Fig.8 The relation between internal strain outputs and time in cure at RT

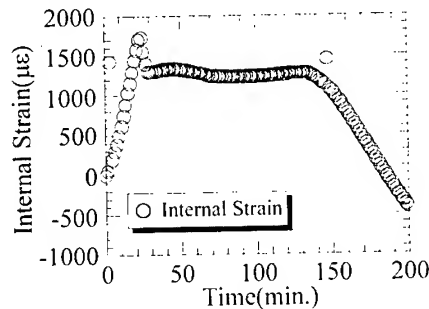


Fig.10 The relation between internal strain outputs and time in after-cure

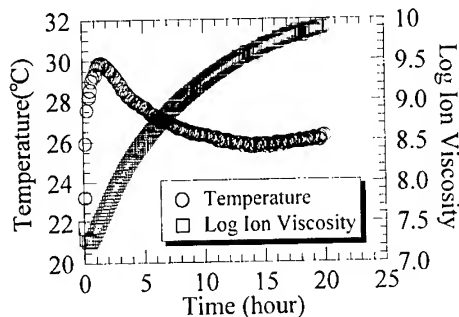


Fig.9 The relations among log ion viscosity, temperature, and time in cure at RT

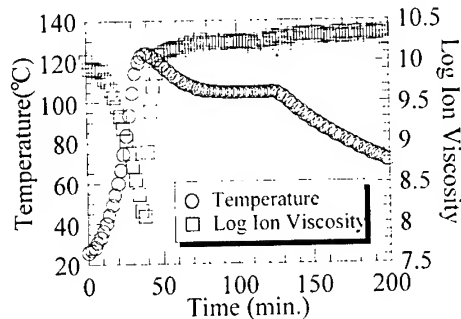


Fig.11 The relations among log ion viscosity, temperature, and time in after-cure

decrease after 1.5 hours and converged to constant value. The internal strain in after cure went up with rise in temperature and fell down rapidly by $500\mu\epsilon$ before the temperature reached to the maximum value, and then kept constant value before the cooling stage. In the cooling stage, the strain decreased by $1800\mu\epsilon$ in 40°C down, and then the strain will be about $-2500\mu\epsilon$ at RT. Figure 10 and 11 show the experimental results in the after-curing process. The behavior of log ion viscosity was similar to that of Exp. A.

DISCUSSIONS

The Behavior of Internal Strain Outputs in Curing Process at RT

From experimental results, the behavior of internal strain outputs of the optical fiber sensor in the FW pipe can be divided into three stages as follows:

Stage I : temperature increase, strain increase.

Stage II : temperature decrease, strain decrease.

Stage III : temperature is constant, strain decrease.

From experimental results of DSC (Differential Scanning Calorimeter) in Fig.12, it is found that the increase of temperature on the stage I is caused by the heat reaction of resin. The strain outputs in Exp.B showed constant values because the optical fiber sensor was not constrained by the resin which was liquid on the stage I. Thus, the increase of strain in the FW pipe is probably caused by thermal expansion of reinforcing fiber strands which constrain the optical fiber. On the stage II, the results of Exp.B (Fig.8) shows that the optical fiber is constrained by the fiber strands and the resin. It is thought that the temperature began to decrease because of the decrease of heat generation and the decrease of strain includes thermal and curing shrink. The starting time of the decrease of temperature curve is different from that of strain curve because their embedded positions are different. On the stage III, the temperature converged to constant value but the strain outputs continue to decrease and the ion viscosity continue to increase. The convergence of ion viscosity means the end of cure. Therefore, these facts indicate that the strain outputs show curing shrink and that cure reaction did not finished completely in 20 hours. It is concluded that a curing shrink can be measured by using an optical fiber sensor in the curing process of FW pipe.

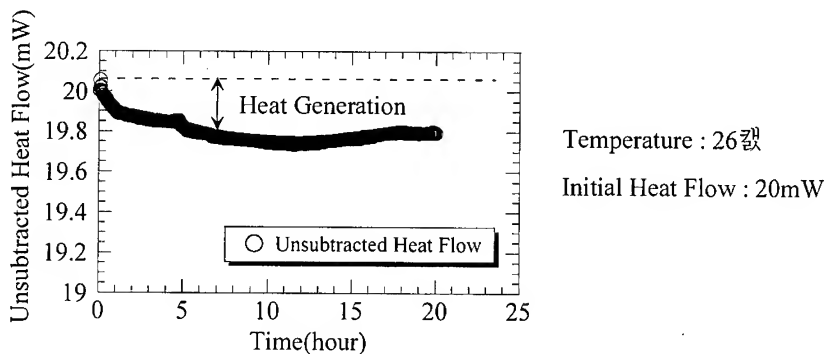


Fig.12 The experimental results of DSC

The Behavior of Internal Strain Outputs in After-curing process

In Exp.B, internal strain increased because of thermal expansion of the resin on heating stage. But the strain outputs of Exp.A increased up to 100°C with thermal expansion coefficient less than Exp.B. Thus, it is concluded that the optical fiber in the FW pipe was constrained by glass fiber strands after it became free from constraint by resin. In the cooling stage, thermal expansion coefficients obtained from Exp.A and Exp.B are almost same. It means that there was a resin rich region around the optical fiber sensor in FW pipe. Then, in this experiment, large thermal residual strain of optical fiber sensor in FW pipe was detected. These facts suggest that the embedding configuration affect the strain outputs of the optical fiber sensor. More detail investigations are needed to evaluate the effect of embedding configuration of optical fiber on the strain outputs.

CONCLUSIONS

The behavior of the EFPI optical fiber sensor embedded in the FW pipe was investigated in the curing process at RT and in the after-curing process. It is found that the curing shrink can be measured by using a EFPI optical fiber sensor in the curing process of FW pipe. From the experimental results in the after curing process, it is concluded that the embedding configuration strongly affects on the sensor outputs. More detail researches are needed to reliable measurements of internal strains.

REFERENCES

1. G. R. Powell, P. A Crosby, D. N. Waters, C. M. France, R. C. Spooncer, and G. F. Fernando, "In-situ cure monitoring using optical fibre sensors-a comparative study", *Smart Material Structure*, 7, 1998, 557-568
2. C. Doyle, A. Martin, T. Liu, M. Wu, S. Hayes, P. A. Crosby, G. R. Powell, D. Brooks and G. F. Fernando, "In-situ process and condition monitoring of advanced fibre-reinforced composite materials using optical fibre sensors", *Smart Material Structure*, 7, 1998, pp.145-158
3. K. Osaka and T. Fukuda, "Strain monitoring in curing of composites using EFPI sensor", *Proc. of the 44th International SAMPE Symposium and Exhibition*, 1999, pp. 1993-2004
4. C. Belleville and G. Duplain, "White-light interferometric multimode fiber-optic strain sensor", *Optic Letters*, Vol.18, No.1, 1993, pp.78-80
5. J. Mijovic, J. M. Kenny, A. Maffezzoli, A. Trivisano, F. Bellucci and L. Nicolais, "The principles of dielectric measurements for in situ monitoring of composite processing", *Composites Science and Technology*, 49, 1993, pp. 277-290

NUMERICAL SIMULATION OF SHEET MOLDING COMPOUND IN COMPRESSION MOLDING PROCESS

S.L.Yan¹ Z.G.Tang² M.Liu¹

¹ *Department of Mechanics, Huazhong University of Science and Technology
Wuhan, 430074, P.R. CHINA: liuning@public.wh.hb.cn*

² *Department of Engineering Structures and Mechanics, Wuhan University of Technology
Wuhan, 430070, P.R. CHINA: mechsoft@public.wh.hb.cn*

SUMMARY: Computer numerical simulation of sheet molding compound in compression molding flow is realized by finite element method. The programs of finite element numerical computing and result post analysis have been written. The compression mold filling process, pressing time and forming pressure needed of SMC in a closed mold are analyzed. Compression molding flow with different charge shapes of SMC are simulated and compared to each other. The most optimal charge shape to fill a rectangular mold is suggested. To simulate the compression molded flowing process of SMC by computer will be of theoretical significance to mold design and optimization of technological parameters.

KEYWORDS: sheet molding compound, compression molding flow, numerical simulation, finite element method.

INTRODUCTION

Sheet molding compound(SMC) is a kind of prepreg materials developed in the last few decades for molding process of resin matrix composites, It usually use chopped fibers as the reinforcement. For the fabricator, Because of providing an easy-to-handle dry molding material with a shorter forming cycle time, ideal for mechanized mass production and good stability of products quality, SMC products have been widely used in the fields of automobiles, buildings, chemical engineering, space navigation and so on. Simulating the compression molded flowing process by computer is an effective method for optimizing technological parameters and designing mold. It can also predicate the orientation of short fiber and help to control the quality of SMC products. In a word, the flow behavior of preoreg materials in mold has significant effects on ultimate product qualities. Analyzing the flow states of charge in different time step is very useful for avoiding appearance of faults in SMC products.

GHS MODEL AND DERIVATION OF GOVERNING EQUATION

Most SMC parts have a sheetlike geometry, with the thickness being much smaller than the other dimension of the part(see Fig.1). Making use of the feature, Heiber and Shen presented a

simplified model for simulating compression molding flow (generalized GHS model). The assumptions of the model are summed up as follow:

- (1) The mold is thin and flat in the z-direction, with an arbitrary shape in x-and y-direction.
- (2) The part thickness h is a slowly varying function x and y .
- (3) The molding compound is treated as an incompressible fluid which is isotropic in the x-y plane and whose viscosity only depends on strain rate, temperature and degree of cure.
- (4) There is no leakage at the edges of the mold.

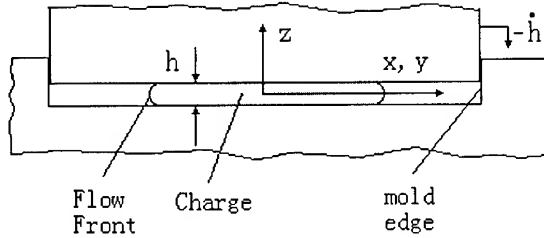


Fig.1 Nomenclature for model of compression molding

The molding compound is treated as a Generalized Newtonian Fluid, so we get Eqn.1:

$$\tau_{ij} = \eta \dot{\gamma}_{ij} \quad (1)$$

Where, $\tau_{ij}, \dot{\gamma}_{ij}$ is the stress tensor and stress rate tensor, the viscosity η is taken to be a function of the temperature T , the strain rate $\dot{\gamma}$ and the degree of cure C :

$$\eta = \eta(T, \dot{\gamma}, C) \quad (2)$$

For the charge thickness h , which is smaller compared to the other dimensions, many terms in the equations of motion are negligible. The equations of motion then reduced to

$$\frac{\partial P}{\partial x} = \frac{\partial \tau_{xy}}{\partial z}, \quad \frac{\partial P}{\partial y} = \frac{\partial \tau_{yz}}{\partial z} \quad (3)$$

Where, P is the fluid pressure of molding compound. Assuming u, v is the flow velocity of molding compound along the x-direction and y-direction respectively, we can find that the velocities on an arbitrary point are

$$u = \frac{\partial P}{\partial x} \int_{-\frac{h}{2}}^{\frac{h}{2}} \frac{z}{\eta} dz, \quad v = \frac{\partial P}{\partial y} \int_{-\frac{h}{2}}^{\frac{h}{2}} \frac{z}{\eta} dz \quad (4)$$

The average velocities are defined as

$$\bar{u} = \frac{1}{h} \int_{-\frac{h}{2}}^{\frac{h}{2}} u dz = -\frac{s}{h} \frac{\partial P}{\partial x}, \quad \bar{v} = \frac{1}{h} \int_{-\frac{h}{2}}^{\frac{h}{2}} v dz = -\frac{s}{h} \frac{\partial P}{\partial y} \quad (5)$$

Where

$$s = \int_0^{\frac{h}{2}} \frac{1}{\eta} \left(\frac{h^2}{4} - z^2 \right) dz \quad (6)$$

The continuity equation for an incompressible fluid is integrated across the gap height, and accounted for (5) we obtain the governing equation for the pressure distribution

$$\frac{\partial}{\partial x} \left(s \frac{\partial P}{\partial x} \right) + \frac{\partial}{\partial y} \left(s \frac{\partial P}{\partial y} \right) - \dot{h} = 0 \quad (7)$$

Where \dot{h} is the closure speed of the mold. The boundary conditions are

$$P|_{\Gamma} = 0, \frac{\partial P}{\partial x} \Big|_{\Gamma_x} = 0, \frac{\partial P}{\partial y} \Big|_{\Gamma_y} = 0 \quad (8)$$

Where, Γ is the free edge of molding compound, Γ_x is the mold edge which is vertical to the x-axis, and Γ_y is the mold edge which is vertical to the y-axis.

THOUGHT OF SIMULATION AND DESIGN OF FEM PROGRAM

Thought of Simulation

In general, the charge is placed in the mold with little or no initial contact at the mold boundary. During filling, parts of the charge come into contact with the boundary, and the mold-filling process is completed when the entire charge boundary coincides with the mold boundary. If we solve the equation (7) by a proper method, the pressure distribution is known at a certain instant of time. By equations (5), we obtain the fluid velocities and directions every where. Then the deformation and shape in the charge are known at the same instant.

The flowing process of molding compound in the mold is a nonlinear question. On the one hand the deformation of SMC is quite large when it is molded. On the other hand, the constitutive relation is nonlinear for the variation of the viscosity following the strain rate, temperature and degree of cure. So this paper adopts the finite element step-by-step computing method. That is, the molding process is divided into many time steps. The deformations of the charge are small at each time step, and $\dot{\gamma}$, T , C are approximately invariable, so the viscosity η of the charge is treated as a constant at each time step. Every time the calculated nodal coordinates are based on the previous result. We obtain the trace of motion at an arbitrary point, which reflects the charge flow regulation and the charge shape at the arbitrary time. Finally, we know the time and pressure that the mold is filled.

Finite Element Formulations

It is reasonable to take the viscosity η as a constant at each time step. The governing equation (7) then simplifies:

$$\frac{\partial^2 P}{\partial x^2} + \frac{\partial^2 P}{\partial y^2} = \frac{\dot{h}}{s} \quad (9)$$

Where

$$s = \frac{h^3}{12\eta} \quad (10)$$

The triangular elements are used here, and the nodal pressure P is treated as a essential variable within every element. The interpolation functions:

$$P^e(x, y) = \sum_{i,j,m} N_i(x, y) P_i^e = [N] \{P\}^e \quad (11)$$

Where $\{P\}^e = [P_i, P_j, P_m]$ is the nodal pressure matrix. $[N] = [N_i, N_j, N_m]$ is the shape function matrix,

The equation (5) gives the velocity

$$\begin{Bmatrix} \dot{u} \\ \dot{v} \end{Bmatrix}^e = -\frac{s}{h} \begin{Bmatrix} \frac{\partial}{\partial x} \\ \frac{\partial}{\partial y} \end{Bmatrix} P^e = -\frac{s}{h} [B] \{P\}^e \quad (12)$$

Where

$$[B] = \begin{bmatrix} \frac{\partial N_i}{\partial x} & \frac{\partial N_j}{\partial x} & \frac{\partial N_m}{\partial x} \\ \frac{\partial N_i}{\partial y} & \frac{\partial N_j}{\partial y} & \frac{\partial N_m}{\partial y} \end{bmatrix} \quad (13)$$

From (12), it is easy to be seen that the displacement are

$$\begin{Bmatrix} \Delta X \\ \Delta Y \end{Bmatrix}^e = \Delta t \begin{Bmatrix} \dot{u} \\ \dot{v} \end{Bmatrix}^e \quad (14)$$

Where Δt is the time step, Δx , Δy is the displacement in the x- or y-direction. To equation (9), we have function

$$\Pi^e = \int_{\Omega^e} \left[\frac{1}{2} \left(\frac{\partial P}{\partial x} \right)^2 + \frac{1}{2} \left(\frac{\partial P}{\partial y} \right)^2 + \frac{h}{s} P \right] d\Omega \quad (15)$$

Substituting

$$\left(\frac{\partial P}{\partial x} \right)^2 + \left(\frac{\partial P}{\partial y} \right)^2 = \left[\frac{\partial P}{\partial x} \frac{\partial P}{\partial y} \right] \left[\frac{\partial P}{\partial x} \frac{\partial P}{\partial y} \right]^T = \{P\}^T [B]^T [B] \{P\}$$

and(11) into (15),we have

$$\Pi^e = \frac{1}{2} \{P\}^T [k] \{P\} + \frac{h}{s} \int_{\Omega^e} [N] \{P\} d\Omega \quad (16)$$

in which

$$[k] = \int_{\Omega^e} [B]^T [B] d\Omega = [B]^T [B] A \quad (17)$$

is the element characteristic matrix. Taking into consideration $\frac{\partial \Pi^e}{\partial \{P\}} = 0$, we have

$$[k] \{P\}^e = \{F\}^e \quad (18)$$

$$\{F\}^e = -\frac{h}{s} \int_{\Omega^e} [N]^T d\Omega = -\frac{h}{s} \frac{A}{3} \{I\} \quad (19)$$

Where $\{F\}^e$ corresponds to equivalent nodal load matrix, and $\{I\} = [1 \ 1 \ 1]^T$ is unit matrix.

The global governing equation can be written.

$$[K] \{P\} = \{F\} \quad (20)$$

Program Design

The Program is divided into two parts. One is the finite element computing programs which include twelve program section- a main program and eleven subprogram. The other is the post analysis programs which may give the charts of computing result at each time step in the screen, The corrected global governing equations use the Crout direct method. The simulation of compression molding flow in a closed mold with the boundary is based on the boundary conditions (8) in the program. The automatic modification of boundary conditions is designed on the basis of the charge flowing front whether it encounters the mold boundaries.

EXAMPLE CALCULATION

As an example, we choose the original SMC charge size is $200 \times 300 \times 5$ mm. Taking one-fourth of charge for analysis because of symmetry. The in-plane dimension of the mold is assumed 280×400 mm. In computing, the viscosity η , the closure speed of the mold \dot{h} and the time step increment Δt are need to be inputted, which can be various on the basis of the actual situations at each time step. Now the paper assumes that the viscosity and the closure speed of mold are not various with the time in compression molding process, that is ,the constant temperature molding is considered in the example. The necessary computing constants are:

$$\eta = 3.0 \times 10^5 \text{ pa} \cdot \text{s} \quad \dot{h} = 0.1 \text{ mm/s}$$

The compression-molding flow and the compression mold filling process in a closed mold are implemented by computer simulation (as shown in Fig.2).

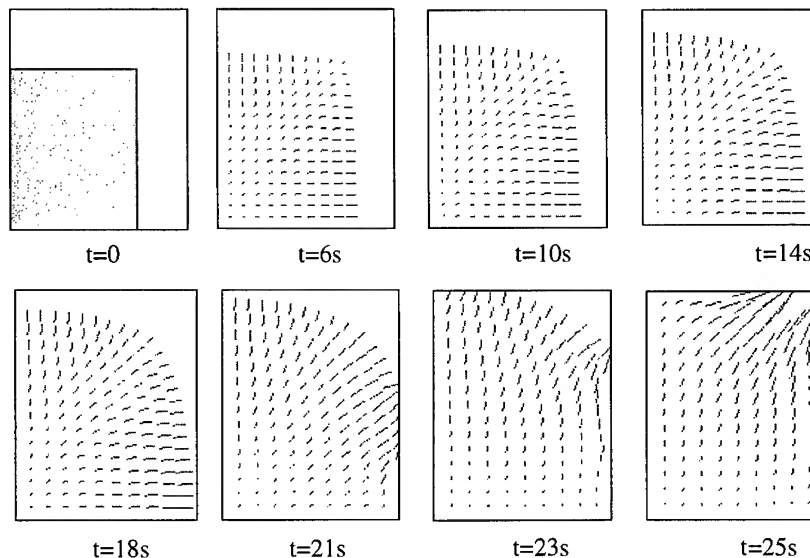


Fig.2 The compression mold filling process in closed mold

RESULT ANALYSIS AND DISCUSSION

We can extract the fact from the above example that the time of the compression mold filling is about 25s and the pressure at the last time step is 16MPa. It is necessary to point out that the temperature of compression mold filling process maybe vary when the actual SMC is compressed in a mold. However, once the variable relation of SMC viscosity with the time is found based on the temperature-time curve and the viscosity-temperature curve in a closed mold, the flow states at any time of the charge in the mold, the compression mold filling time and predictable forming pressure can be likely calculated. The research work of this paper shows that simulating the compression molding flow of charge and compression mold filling process of SMC products is can be realized. It will be of a certain theoretical function to mold design, to the placement of SMC charge and to the optimization of the technological parameters even though the further study and prove by experiments are waited for doing for the actual simulation of compression-molding flow.

ACKNOWLEDGMENTS

Financial assistance is provided by National Natural Science Foundation of CHINA, Grant No.19972049, and by Hubei Province Natural Science Foundation of CHINA, Grant No.99J073.

REFERENCES

1. C. A. Heiber and S. F. Shen, "A Finite Element/Finite Difference Simulation of the Injection mold Filling Process", *J. Non-Newtonian Fluid Mech.*, Vol.7, 1980, pp1-32.
2. C. C. Lee, F. Folgar and C.L. Turker, "Simulation of Compression Molding for Fiber-Reinforced Thermosetting Polymers", *J. Engineering for Industry*, Vol.106, 1984, pp. 114-125.
3. J. M. Castro and R. M. Griffith, "Sheet Molding Compound Compression-Molding Flow", *Poly. Eng. Sci.*, Vol.29, 1989, pp632-638.

Study on the Non-linear Creep Behavior of BMC

Satoshi Somiya¹ and Youichi Shirata²

¹ *Dept. of Mechanical Engineering, Keio University,
E-mail: somiya@ mech.keio.ac.jp
3-14-1 Hiyoshi Kouhoku-ku Yokohama 223-8522, JAPAN*
² *Graduated School of Keio University*

SURMARY: Creep behavior of FRP (BMC) was researched using three points bending method. As BMC have the durability of the size and deformation at high temperature condition, they were practically used in parts of machines and instruments operating over 100°C circumstance such as copy machines etc. When the machines have to be designed in more shiver conditions, visco-elastic deformation must be calculated and estimated. There are few reports and information for the visco-elasticity on FRP. In this research, creep compliance of BMC and its resin were measured. And the linearity of creep deformation was discussed using the master curves of creep compliance, which were drawn with superposing creep compliance curves. The linearity for the curves was realized but a few non-linear phenomena were found. It was found that the non-linear deformation was depended on two reasons and there were physical aging effect and chemical reaction in resin.

KEYWORDS: BMC, Bending creep behavior, After cure Effect, Physical aging

INTRODUCTION

Bulk Molding Compound (BMC) usually use in as parts of electric instrument in the high temperature circumstance but there are few reports and information for the visco-elasticity [1-4]. Used BMC concluded in 15% of fiber weight fraction. Creep behavior in a matrix and BMC (Wf=15%) have been researched under some temperature conditions from 60°C to 220°C using three point bending creep test machine. The creep compliance curves obtained by a virgin matrix resin and a virgin BMC showed non-linear creep but and it was recognized that creep phenomena showed a linear viscoelasticity as an Arrhenius-type after heat treatment. From these facts, two affective factors were pointed out. One is physical aging effect on creep deformation and the other one is after cure effect over cure temperature.

The master curves of resin and BMC after heat treatment, in comparison with that of virgin BMC, moved to the direction of a long time on the axis of physical time. It means that the viscoelastic behavior should be clearly constrained by the heat treatment.

EXPERIMENTAL METHODS AND MATERIALS

Three-point bending creep-test has been performed and the applied bending load was installed so as to produce the bending stress equal to 10% of the bending strength. The length of supports was 16 times of plate thickness. The creep tests have been performed under 9 kinds of

temperatures such as 60, 80, 100, 120, 140, 160, 180, 200 and 220°C. For the case of BMC, 5 test pieces have been tested.

BMC is Rosite-3550C, which is made by ASAHI GLASS CO., LTD. The matrix of this material consists of unsaturated polyester resin and calcium carbonate particles, in which fibers consist of chopped glass fibers with the weight fraction 15%. The glassy temperature is about 150°C. This material was molded at about 160°C. This material does not apply after cure treatment. The shape of a test piece is a strip with the thickness 5-mm, width 10-mm and length 100-mm.

CREEP BEHAVIOR OF BMC

The creep behavior of matrix resin of BMC

Under 60°C to 120°C air circumstance conditions, creep test have been done and creep compliance curves were obtained. Using them on each temperature, the master curve of creep compliance was drawn. On Fig 1, the vertical axis and horizontal axis show the creep compliance values and physical time respectively. This figure shows the compliance curve increases rapidly rising temperature and an elapsed time. However for example under the 120°C condition, the value of creep compliance reached for a long time has been recognized to be saturated with decreasing a extent of the increment. The result in such a region being neglected, superposing curves has been shown a smooth line. From the relationship between shift factors and temperature to make master curve it confirmed that the compliance of BMC matrix represents an Arrhenius' linearity. However strictly speaking on a master curve, in the case of testing for a long time it should be found to be in off-position from the linearity.

Because the temperature acts for a long time in spite of that lower than the glass-transition temperature, the influence of the physical aging behavior is considered on changing characteristics of physical properties. Therefore under the molding temperature 160°C, heat treatment at 120°C has been performed for 100min and 1000min. Fig.2 shows the master curves of creep compliance at different aging time for aged matrix. Increasing the value of creep compliance with a time, these show the same tendency in the case of virgin matrix, the value at the same physical time decreased by physical aging time. This means that physical aging affected to arrest the progress the visco-elastic deformation under loading. And also the change of creep compliance curve for a long time not expressing non-linear deformation like

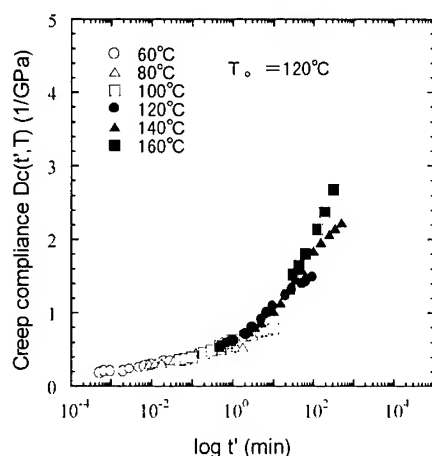


Fig.1 Master curve of creep compliance on resin matrix of BMC

that for virgin matrix. It has been confirmed that, master curves of aged matrix moving to the right-hand side namely to a long time side on the axis of physical time, the heat treatment results in decomposition for the inter-molecular behavior to be under constraint.

Creep behavior in BMC

Creep compliance of BMC was calculated from dispersed data by the statistical method introduced in the preceding report[4]. The mean values of creep compliance values obtained by some specimens at creep real time were used in this report. The testing temperature conditions have been used at 9 kinds of temperatures from 60 to 220°C. Over the temperature at 160°C, it was higher than the molding temperature but sometime this material used in such temperature condition without the after cure treatment. Then, in this research, the high temperature conditions over the molding temperature were applied. Fig.3 shows the creep compliance of BMC. Increasing temperature, creep values rose up with the passing of creep time. Moreover being obtained from moving a group of curves deduced for different test temperatures on the time axis, the superposition leads to an apparent master curve of BMC. Fig.4 shows the master curve of BMC (see solid circle) and to compare the difference of pure resin, the master curve (see open circle) of resin material too. Quantities of shift for each temperature used in drawing up Fig.5. Generally in the case of plotting a shift factor by using an inverse absolute temperature as a parameter, the result showing a straight line represents producing Arrhenius type deformation. From these facts, creep deformation of BMC material has been recognized to be Arrhenius' one similar to that of the matrix. The master curve of BMC shows a viewpoint of lower compliance values and moving to the direction of a long time on the axis of physical time. These facts can be estimated to be influenced by a mixture of fibers. Under the temperature at 160°C, non-linear behavior in the long term region of creep curve were observed as same as the case of virgin resin. It might be depended on the same reason as physical aging of matrix resin. Moreover besides these characteristics, it has been noticed to form a flat part in the center of the curve. As a reason of this forming, it has been considered to be chemical reaction between remained active monomers. Because above the glassy temperature, physical aging phenomenon does not occur. This is thought that the change results from producing the "After cure treatment effect" due to heat in the testing process. Therefore, it has been tried to produce decomposition from the beginning with performing after cure before testing.

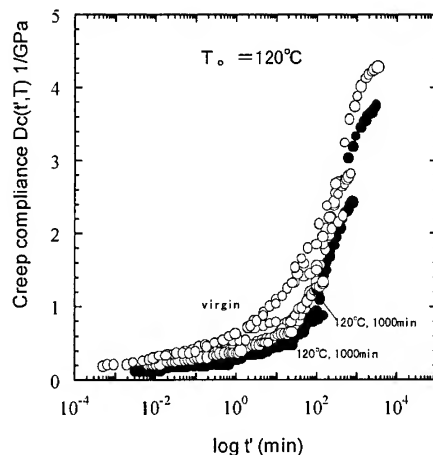


Fig.2 Effect of Physical aging treatment on master curves of creep compliance on resin matrix of BMC.

The influence of after cure on a creep behavior

To research the effect of "After cure" on visco-elasticity of BMC, the change of creep phenomenon of the matrix resin by the heat treatment have been researched. Fig. 6 shows experimental test results for resin matrix and BMC materials aged for 100 min and 1000min. at 220°C. By the study on this group of curves it is recognized that these curves are increasing uniformly in the tested range, like that of resin matrix. non-linear deformation behavior is decreased due to after cure treatment. From an estimation that the end of a creep compliance curve in the range of about 160°C is deviated from the master curve so as to show non-linear behavior, this reason should be considered to be curing phenomena promoted by thermosetting resin material. It has been confirmed that performing after cure over the glass transition temperature results in making more stable physical properties.

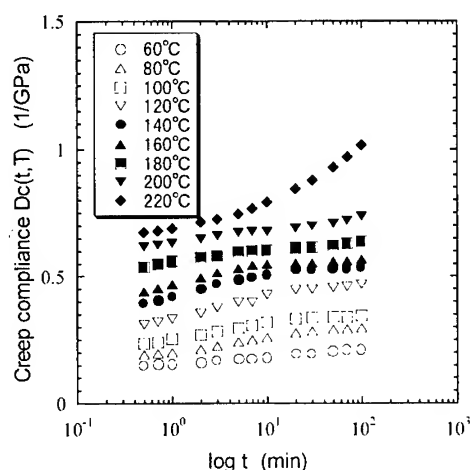


Fig.3 Creep compliance curves on each temperature of BMC

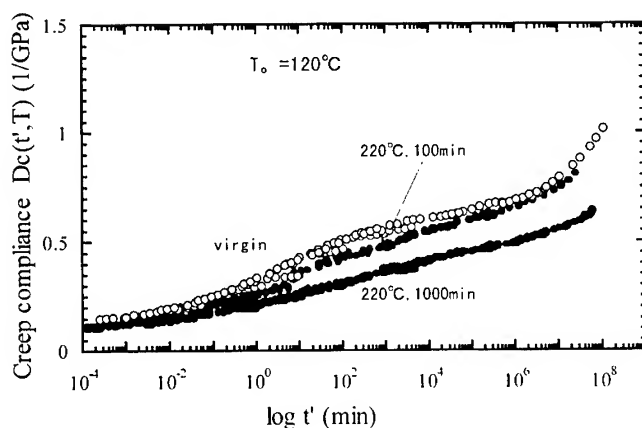


Fig.4 Master curves of creep compliance superposing creep compliance curves obtained for virgin resin matrix and BMC

To make clear the reasons of non-linearity on the master curve of BMC at near 160°C, the specimens were prepared and treated at 220°C for 100min and 1000min as same as matrix resin. Fig.7 indicates the master curves of BMC evaluated from the result as shown in Fig.6. It has been confirmed that the master curve of after cure treated BMC shows lower compliance in comparison with that of virgin BMC. And also the curves shifted to the direction of a long time on the axis of physical time, so that the viscoelastic behavior should be clearly constrained by the heat treatment. These facts have revealed that even for materials like BMC containing a great many fibers and calcium carbonate, the viscoelastic behavior depends on the properties of resin unconditionally and as a result sharply depends on the change of resin materials due to heat treatment etc.

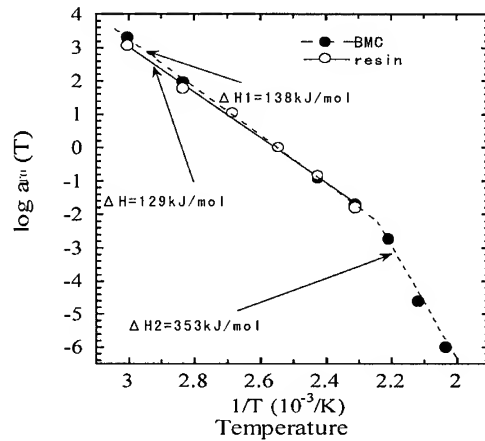


Fig.5 Shift factors of creep phenomena BMC and its resin matrix on Arrhenius plotting

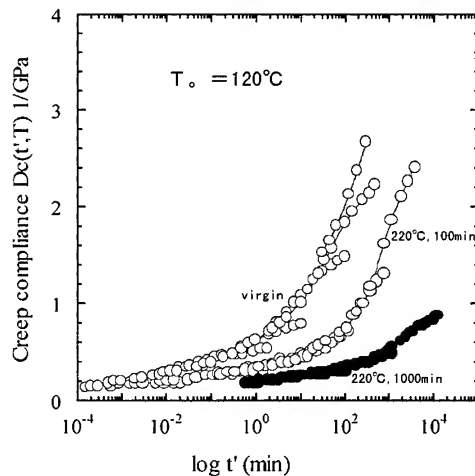


Fig.6 Effect of after cure treatment on resin matrix of BMC

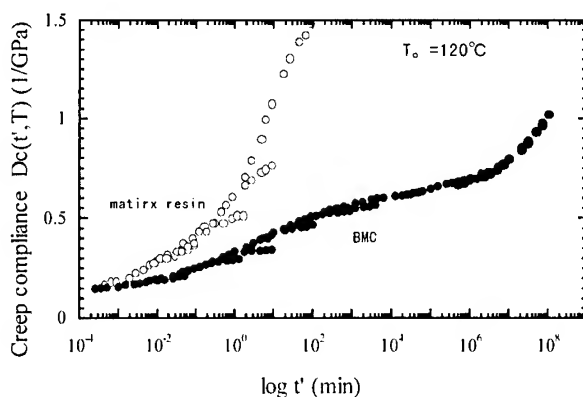


Fig.7 Effect of After cure treatment on creep compliance master curves of BMC

Conclusions

The non-linear creep behavior of BMC and its matrix resin has been investigated. The results are as follows.

1) It is recognized that the creep phenomena of BMC and the matrix of BMC in consequence of Arrhenius type. Moreover under glassy temperature condition with longer testing time, non-linearity has been observed. With physical aging treatment for matrix resin, non-linearity behavior was distinguished and any creep compliance curve for different temperature has revealed Arrhenius' deformation behavior. It has been recognized that the master curve is shifted to the direction of a long time on the axis of physical time, which means hard to produce viscoelastic deformation.

2) The non-linearity on the master curve of a virgin BMC was found over the molding and glassy temperature. From the result of similar creep tests for aged BMC, like that of virgin material, possibility of drawing up a master curve in consequence of Arrhenius' shift factor has been cleared. It has been recognized that the master curve, in comparison with that of virgin BMC, shows a shift to the direction of a long time on the axis of physical time, so that the viscoelastic behavior should be clearly constrained by the heat treatment. It is confirmed that the non-linearity on the master curve of a virgin BMC must depended on the change of physical properties of matrix resin of BMC by the chemical reaction in remained active monomer.

Acknowledgments

The authors are much indebted to Mr. Norifumi Minowa, ASAHI MATEX CO. for assistance.

Reference

- [1] S. K. Ha and G. S. Springer., J. Composite Materials, 23, 1130.(1989).
- [2] D.H.Mgyyen and A.A. Ogal.J.Thermoplastic Composite Materials., 4.83.(1991).
- [3] M.Kasamori, T. Ootuka, M.Shinpo and Y. Miyano.. J. The Society of Material Science,41,465(1992).(in Japanese)
- [4] S.Somiya and H.Kimura, J. material System,13,127,(1994).(in Japanese)

MMC (1)

FABRICATION OF TiAl MATRIX COMPOSITE BY REACTIVE FORMING PROCESS

Makoto Kobashi¹, Hiroki Muto², Naoyuki Kanetake³, Takao Choh⁴

¹ *Department of Materials Processing Engineering, Nagoya University
Furo-cho, Chikusa-ku, Nagoya 464-8603, JAPAN
kobashi@numse.nagoya-u.ac.jp*

² *Graduate School of Nagoya University*

³ *Department of Materials Processing Engineering, Nagoya University
kanetake@numse.nagoya-u.ac.jp*

⁴ *Department of Materials Processing Engineering, Nagoya University
choh@numse.nagoya-u.ac.jp*

SUMMARY: A new processing route, by which both the combustion synthesis and the compressive forming were carried out simultaneously, was developed to fabricate titanium aluminide (TiAl) or TiAl matrix composite. Elemental powders (titanium and aluminum powders) were blended, compacted and heated to ignite the combustion reaction. Immediately after the combustion reaction, the synthesized TiAl was compressed to reduce the porosity and to give it a specific shape. The level of the temperature rise during the combustion reaction was increased by blending the B₄C powder with the [Ti+Al] elemental powder, whereas it was reduced by blending the TiC powder. By blending the B₄C powder, TiB₂ and TiC particles were produced in the TiAl matrix, and the TiAl matrix composite with low porosity (<2%) was obtained.

KEYWORDS: combustion reaction, TiAl, B₄C, plastic deformation

INTRODUCTION

Combustion synthesis utilizes the heat of reaction between elemental powders to form a bulk of ceramics or intermetallics. The advantages of using combustion synthesis are; (1) the final products can be formed in a short time (within several seconds), (2) a minute quantity of energy is required to ignite the reaction since the reaction propagates throughout the specimen once ignited, and (3) a special equipment, such as a large furnace, is not required. However, the pores tend to remain in the specimen after the reaction. Applying compressive deformation immediately after the combustion

reaction (reactive forming process) is one of the solutions to remove the pores. Furthermore, the reactive forming process makes it possible to deform the ceramics or intermetallics, which are difficult to be deformed at ambient temperature, into a desirable shape.

In this work, elemental powders of titanium and aluminum were blended (this will be denoted as the [Ti+Al] powder blend) and heated to ignite the combustion reaction. The TiAl was then pressed immediately after the combustion. The following aspects were investigated to obtain the basic knowledge about the reactive forming process.

- (1) Microstructure of the combustion synthesized specimen
- (2) Relation between the formability and the temperature of the specimen
- (3) Effect of the compressive deformation on reducing the porosity

EXPERIMENTAL PROCEDURE

Titanium powder (99.9%pure, diameter: $<44\mu\text{m}$), aluminum powder (99.9%pure, diameter: $<44\mu\text{m}$), TiC powder (99%pure, diameter: $2\text{--}5\mu\text{m}$) and B_4C powder (99%pure, diameter: $10\mu\text{m}$) were used as the starting materials. These elemental powders were blended and compacted into a cylindrical shape ($15\text{mm}\phi \times 15\text{mm}h$). The compacted cylindrical powder was located in a compressive testing machine as is shown in Fig.1, and then heated by an acetylene flame in order to ignite the combustion reaction. The compressive pressure was applied to the specimen immediately after the combustion reaction. After compressing the specimen to a prescribed level, the specimen was cooled in the air. Three kinds of powder blends (specimen 1 through 3) were prepared for this experiment and both the starting powders and the final products are listed in Table 1.

Table 1 Starting powders and final products of the specimens used in this experiment

	STARTING POWDERS	FINAL PRODUCTS	VOLUME FRACTION OF CERAMIC PHASE
Specimen 1	Ti, Al	TiAl	0%
Specimen 2	Ti, Al, B_4C	TiAl, TiB_2 , TiC	20% (TiB_2 , TiC)
Specimen 3	Ti, Al, TiC	TiAl, TiC	20% (TiC)

Microstructure of the compressed specimen was observed by scanning electron microscopy (SEM) and energy probe microanalyzer (EPMA). Porosity of the specimen was also measured.

RESULTS AND DISCUSSION

Microstructure and Compressive Deformation

Cross sections of the specimens 2 and 3 after the combustion reaction are shown in Fig.2(a) and (b), respectively. In Fig.2(a) the formation of TiB_2 and TiC are visible, whereas TiC particles dispersed in the TiAl matrix are visible in Fig.2(b).

Figure 3 shows the compressive stress-strain curves of the specimen 1 through 3 measured immediately after the combustion reaction. As is clearly seen in Fig.3, the specimen 3 showed the higher resistance against the compressive load than monolithic TiAl (specimen 1). The TiC powder absorbed the heat of reaction and prevented the sharp increase in the temperature of the specimen during the combustion reaction. On the contrary, the stress-strain curve of the specimen 2 showed the lower resistance against the compressive load. By blending the B_4C powder, the reaction forming both TiB_2 and TiC took place and raised the temperature of the specimen during the combustion reaction. Therefore the fluidity of the specimen 2 was highly improved in comparison with the specimen 1.

Effect of Compression Level on the Porosity

The porosity of the specimen was measured after the compression. The results are shown in Fig.4. The porosity decreased in each specimen by increasing the compressive reduction. Since the initial porosity of the specimen 3 was high (more than 80%), the effect of compression to reduce the porosity was hardly observed by a small reduction (less than 30%). However, by compressing up to 80%, the specimen with low porosity (about 2%) could be obtained.

CONCLUSIONS

A new processing route, by which both the combustion synthesis and the compressive forming were carried out simultaneously, was developed to fabricate TiAl or TiAl matrix composite. TiC/TiAl matrix composite and $[\text{TiB}_2, \text{TiC}]/\text{TiAl}$ matrix composite was obtained by this process. By blending B_4C powders in the $[\text{Ti}+\text{Al}]$ elemental powders, compressive deformation of the specimen could be done with less applied force. The specimen with low porosity ($<2\%$) was obtained by this process.

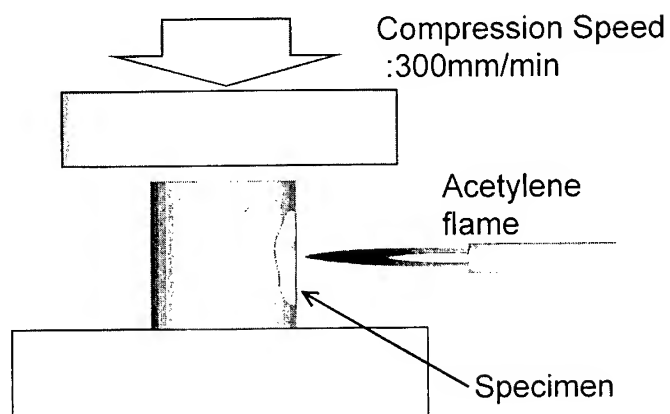


Fig.1 Schematic illustration of the experimental set-up

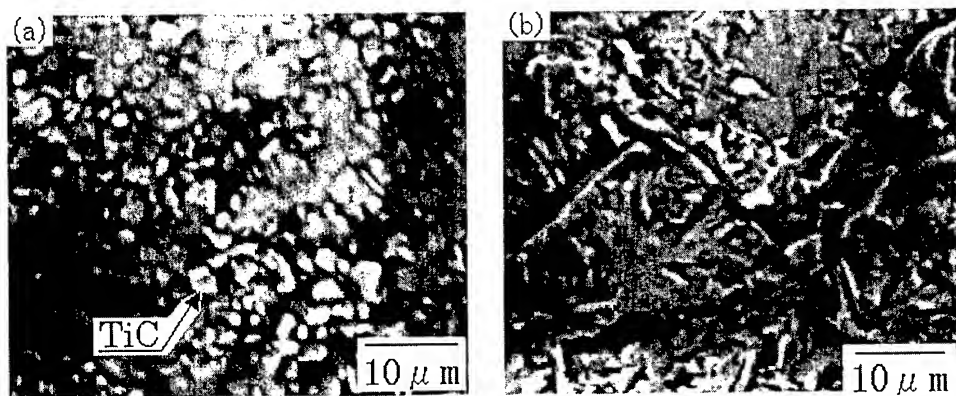


Fig.2 Secondary electron images of (a) specimen 2 and (b) specimen 3

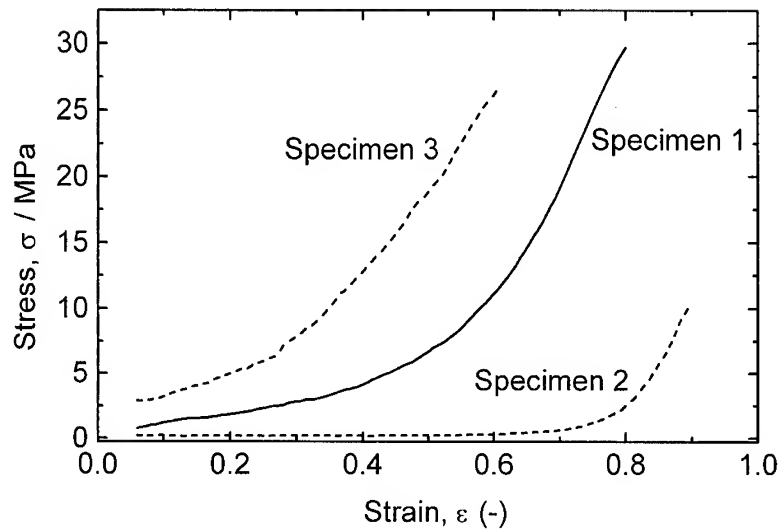


Fig.3 Compressive stress-strain curves of specimen 1 through 3 (Compressive deformation was applied immediately after the combustion reaction)

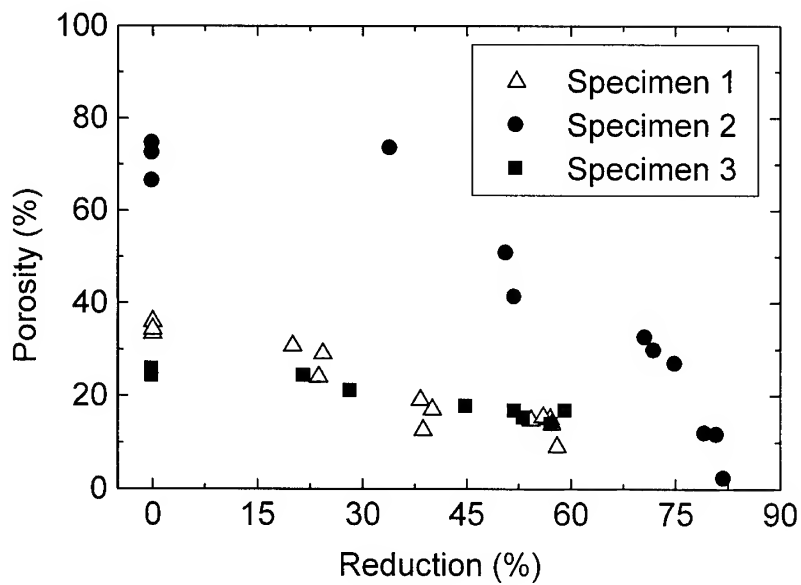


Fig.4 Relation between compressive reduction and porosity in the specimen

2-D SIMULATION OF FIBER ORIENTATION IN SHORT FIBER PREFORM

S.W. Jung¹, J.B. Nam², H.W. Nam¹ and K.S. Han¹

¹Department of Mechanical Engineering, Pohang University of Science and Technology
San 31, Hyoja-dong, Nam-gu, Pohang 790-784, Korea : sungwook@postech.ac.kr

²Technical Research Laboratories, Pohang Iron and Steel Co.
Pohang 790-785, Korea : pc543324@posco.co.kr

SUMMARY: The fiber orientation distribution (FOD) in a Al_2O_3 short fiber preform are analyzed by two-dimensional numerical simulation for its fabrication process. The preform is fabricated with vacuum forming method and the FOD cause the anisotropic characteristic of metal matrix composites made of it. The fabrication process can be separated according to fiber movement as stacking and rearranging. The simulation is performed for the stacking of fiber on the bottom of the vacuum molds using the FOD characteristic of axially symmetric to pressure direction. The simulation assume the cylindrical fibers as rectangular elements and model the stacking stage with the movement of fiber as drop, rotate, slide, and shift. The analysis result shows that the fiber orientation and volume fraction depend on fiber aspect ratio and the dominant orientation is horizontal directions.

KEYWORDS: fiber orientation distribution, volume fraction, short fiber, preform, simulation

1. INTRODUCTION

The mechanical properties of short fiber reinforced composites depend on fiber volume fraction, aspect ratio, and orientation[1]. There are good theoretical treatments for the effect of aspect ratio and volume fraction on the properties such as modulus and strength, but orientation is more difficult for a number of reasons. First, orientation is difficult to control. It is strongly influenced by processing methods and by local flow conditions in, for instance, injection-molded parts. As a result, changes in volume fraction and aspect ratio will change the degree of orientation. In addition it is difficult to determine the fiber orientation distribution (FOD) in real samples[2].

Many researches have been performed to analyze the orientation in composites. Most of them deal with the composites which fabricated without using fiber preform because the orientation change during the fabrication is predictable by simulating the flow of the fiber/matrix mixture[3]. In other processes which uses fiber preform in, for instance, squeeze casting or resin transfer molding process, the orientation study is few because the change of FOD during the process is negligible and the FOD can be easily assumed to be 2D or 3D random[4].

However, in real situation, the FOD is not simply 2D or 3D random. As the application of the composites increases, the needs of being able to understand the FOD more accurately is

increase. Since the FOD of preform determine that of composite, the simulation should be performed on the preform processing.

In this study, the FOD of short-fiber-reinforced metal matrix are studied by applying numerical simulation for its preform process. The simulation for preform fabrication is a new approach proposed in this study and performs two dimensionally while the real situation is 3-dimensional. Therefore, the simulation qualitatively analyzes fiber orientation and volume fraction of uniform composite for various fiber aspect ratio and hybrid composite for various mixture ratio of two different kind of fibers.

2. PROCESSING OF PREFORM

Fiber orientation is determined during preform fabrication process, because preforms are not deformed during the casting of MMCs[5]. The fiber preform in this study is fabricated with vacuum forming method as illustrated in Fig.1. Short fibers dispersed in water are trapped in a net on the bottom of the cylindrical mold and then pressurized by punch to vertical direction. The punch pressure induces rearrangement of the stacked fibers and thus increases volume fraction. But, the increase in volume fraction is limited because a large pressure can cause fiber breakage and as a result there is optimized punch pressure and corresponding fiber volume fraction[6]. Generally, the punch pressure is fixed in processing and the volume fraction is determined by the specification of fibers. If the fibers are brittle, the fiber aspect ratio(length to diameter, L/d) is one of the most important factor to determine volume fraction and orientation. As the aspect ratio increases, the fiber volume fraction decreases. Oppositely, as the ratio decreases, volume fraction increases. For example, the volume fraction preform made of Al_2O_3 with $L/d=50$ and $d=3\mu m$ are fabricated about 15vol.% that made of $L/d=1$ of Al_2O_3 particle fabricated about 50 vol.%.

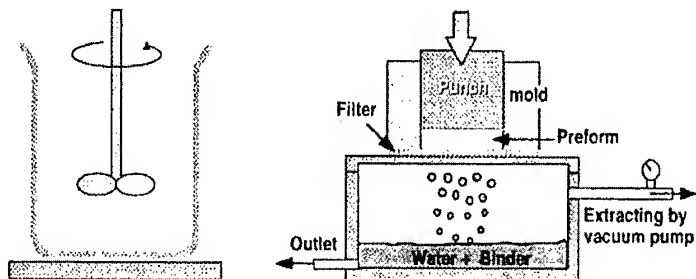


Fig. 1. Schematic diagram of preform fabrication

3. NUMERICAL SIMULATION

The numerical simulation performed two-dimensionally on the basis of the fact that the FOD of the preform is axially symmetric to z-direction (parallel to punch direction) and random to x,y-plane (normal to punch direction)[7]. The simulation represents fiber as a rectangular element which denoted by the position of four vertex points and analyze free stacking of fiber on the bottom of the mold. The stacking procedure consisted of the fiber movements of drop, rotate, slide, and shift which is determined by relative position with other fiber. The relative position of a fiber is checked by the extended line which connecting vertex points of a element as illustrated in Fig.3. The algorithm is shown in Fig.2.

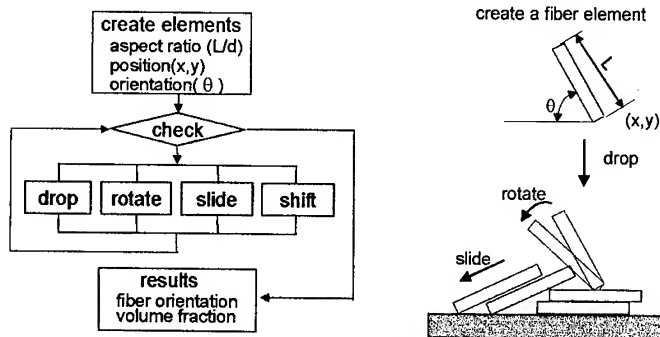


Fig.2. Algorithm of 2D simulation Schematic diagram fiber packing procedure

Creation of Fiber Elements: The first stage of the simulation is to create fiber element at x, y position with a slope and dimensions. Since the position of y which is sufficiently apart from the bottom and the fiber diameter are fixed, the variable of this stage becomes fiber length L , x -position and fiber orientation θ . These parameters can be determined from the position of four vertex points of rectangular elements. Simulation performed according to the fiber aspect ratio for several kinds of composites.

Drop : The created element moves downward with the orientation preserved until it contacts other elements on the bottom of the mold. The condition for drop is that there is no intersection point which is made by two of extended lines connecting vertex points of each elements within the domain of elements. For an example of Fig.3(a), the point P should not be inside of the domain of element ① and ② to drop.

Rotate and Slide: If an element contact with other elements more than one points, it rotate or slide according to the movement conditions. The condition for rotate is that the center of gravity C in the element is outside of contact points of A and B as illustrated in Fig.3(b). The rotation center will be point B because B is nearer to C than A .

The condition for sliding is that the element contacts more than two points with other elements and the x -position of gravity center C is located between two of the contact points, i.e., A and B . In addition, the slope of the element should steeper than 15° to overcome the friction force with the friction coefficient is 0.3.

Shift : There are many cause inducing simulation errors. The shift is one of virtual movement of element to avoid hanging. As shown in Fig.3(d), the rotating fiber with its gravity center is under the rotation center will hanging with infinitely rotating to clock and counter clock wise repeatedly. The is shifted to left side and continue to stacking movement of drop, rotate, and shift.

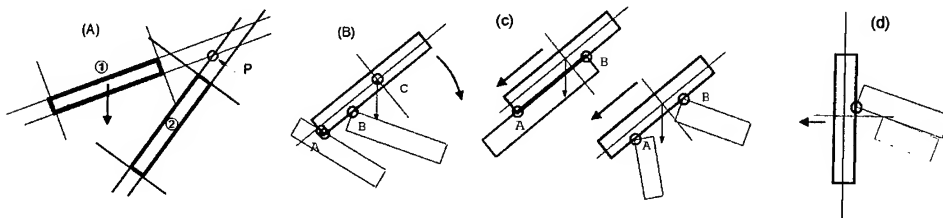


Fig.3. Conditions for the movement

4. RESULT AND DISCUSSION

Examples of simulation results for stacking of fibers are shown in Fig.4. The simulation is seem to be successful because fibers are not overlapped and the stacking shape is natural. The static stability analysis did not performed and as a result the stacking is unstable for gravity force. If the static analysis add, the stacking density, i.e, volume fraction, increases and the effects of punch pressure can be evaluated. But it requires rearrangement of stacked fibers and analysis of coupling effects between them and thus the computational time explosively increase. This study approaches the FOD with probability method using as many of fibers as possible and the stacking simulation without considering static stability seem to reasonable. Therefore, this study limits the simulation for the stacking of fibers without considering rearrangements.

Fig.5 shows the FOD of for the fiber of $L/d=3$ and $L/d=20$. The number of fiber used in the analysis is about 4000 to 5000 excluding fibers near the mold boundaries. The fiber created at the position of $-10L < x < 10L$ and $y=100L$ move toward $y=0$. As shown in Fig.5, fiber orientation is dominant to horizontal direction, i.e. $\theta = 0^\circ$ and symmetric to $\theta = 0^\circ$ which means the average of the FOD is $\theta = 0^\circ$. The comparison between the two FOD of fibers shows that the fiber of $L/d=3$ is more uniform than $L/d=15$. A large frequency of fiber orientation near $\pm 90^\circ$ is resulted because the fiber is represented rectangular elements. If the orientation of element is near to $\pm 90^\circ$ it rotate toward $\pm 90^\circ$ and as the L/d becomes smaller, the probability to rotate to $\pm 90^\circ$ is increase.

To get common characteristic of the FOD, we defined the FOD function as represented in Fig.6. The function is a simplified form of Fu and Lauke's equation as given by[8]:

$$g(\theta) = \frac{\{\sin \theta \cos \theta\}^n}{\int_{-90}^{90} \{\sin \theta \cos \theta\}^n d\theta}$$

where, n is the shape parameter which can be used to determine the shape of the distribution curve. As shown in Fig.6. the function well represent the simulated FOD.

Fig.7 shows the FOD and volume fraction of uniform fiber for various fiber aspect ratio. As the L/D increase, the FOD become more unidirectional with dominant orientation $\theta = 0^\circ$ and the volume fraction decreases. However, the change of the FOD and volume fraction becomes slower for a large aspect ratio with increasing fiber aspect ratio. From this we can expect that for a large aspect ratio, the FOD and the volume fraction of the preform is fixed if it fabricated without punch pressure.

Fig.8(a) is the FOD of the hybrid composite made of two kind of fibers of $L/d=3$ and $L/d=10$ for various mixture ratio. For convenience, we nominate $L/d=3$ elements as particle and other as fiber although the aspect ratio of particle is approximately 1 and fiber is much larger than 30 in real situation. As the portion of particle increase, the orientation of each component

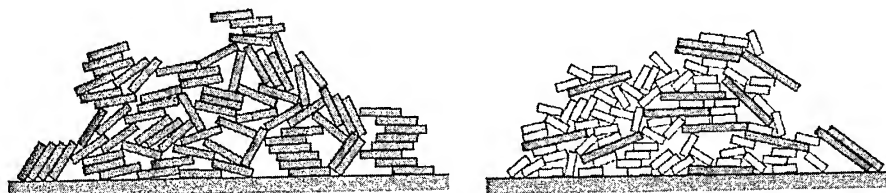


Fig.4. Examples of the simulation results for (a) uniform fibers ($L/d = 5$) (b) hybrid composite ($L/d = 3, L/d = 8$, mixture ratio = 2.5:1)

become uniforms. Fig.8 (b) shows the volume fraction of hybrid preform for various fiber aspect ratio and three kind of mixture ratio. They are always between that of particles and fibers and become closer to that of particle as expected. It is easily predictable that the FOD and the volume fraction of hybrid composite are mean value of each uniform if there are no coupling effects between fiber and particle. But the research as performed like this paper is desirable to evaluate further characteristic of hybrid composite which have coupling effects[9,10]. This study therefore suggests a new approach technique on fiber preform as a basic study to evaluate the mechanical properties of hybrid composite materials.

CONCLUSION

The following conclusion were obtained from the present study

1. The preform determine the FOD of the short fiber reinforced composite and the FOD can be analyzed by modeling the processing of the preform.
2. The fiber aspect ratio is one of major factor to determine the FOD and the volume fraction of the preform if the reinforced fibers are brittle. As the aspect ratio of fiber decreases, the FOD become uniform and volume fraction increases.
3. The FOD and the volume fraction of hybrid preform take mean value of the each component of fibers if there are no coupling effects between them.

REFERENCE

1. A.R.Clarke, G.Archenhold and N.C.Davidson, "A novel technique for determining the 3D spatial distribution of glass fibers in polymer composites", *Composite Science and Technology*, Vol.55, 1995, pp.75-91
2. J.S.Sirkids, A.Cheng and A.Dasgupta, "Image processing based method of predicting stiffness characteristics of short fiber reinforced injection molded parts", *Journal of Composite Materials*, Vol.28, No.9, 1994, pp.784-799
3. H.Henry De Frahan, V.Verleye, F.Dupret and M.J.Crochet, "Numerical prediction of fiber orientation in injection molding", *Polymer Engineering and Science*, Vol.32, 1992, pp.254-256
4. X. Jiang, Q. Gao and G. Kang, "Numerical simulation of microstructure and strength prediction for short-fiber-reinforced-metal-matrix composites", *Composite Science and Technology*, Vol.58, 1998, pp.1685-1695
5. J.I.Song, and K.S. Han, "Squeeze casting conditions of Al/Al₂O₃ metal matrix composites with variations of preform drying process", *Journal of Materials Science*, Vol. 31, 1996, pp. 2615-2621
6. G.Durrant and V.D.Scott, "The effect of forging on the properties and microstructure of saffil fiber reinforced aluminium," *Composite Science and Technology*, Vol.49, 1993, pp.153-164
7. S.W.Jung, S.Y.Kim and K.S.Han, "Image processing based analysis of elastic modulus on short fiber reinforced composites", *ACCM I*, 220-1~220-4, Osaka, Japan, 1998
8. S.Y. Fu, and B. Lauke "The elastic modulus of misaligned short-fiber-reinforced polymers," *Compos. Sci. Tech.*, Vol. 58, 1998, pp.389-400
9. S.Y. Fu, and B. Lauke "Characterization of tensile behavior of hybrid short glass fiber/calcite particle/ABS composites," *Composites Part A*, Vol. 29A, 1998, pp.575-583
10. S.F. Corbin, and D.S., Wilkinson, "The influence of particle distribution on the mechanical response of a particulate metal matrix composite," *Acta metall. mater.*, Vol.42, No.4, 1994, pp.1211-1318

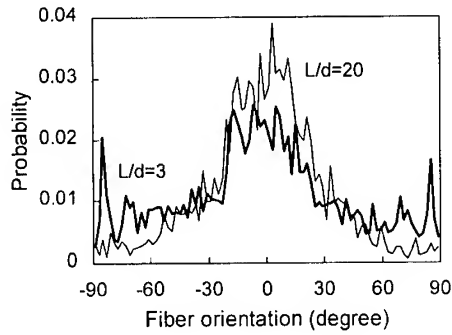


Fig.5. Comparison of the FOD between uniform preforms of $L/d=3$ and $L/d=20$ fibers.

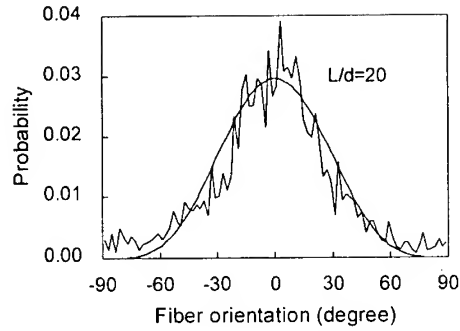


Fig.6. Fitting curve for the FOD of simulated preforms

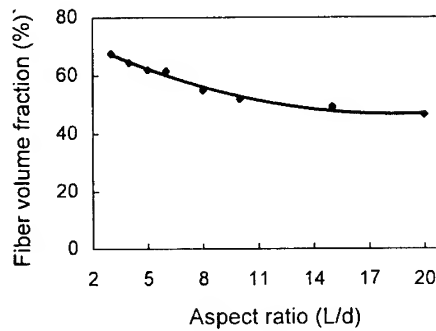
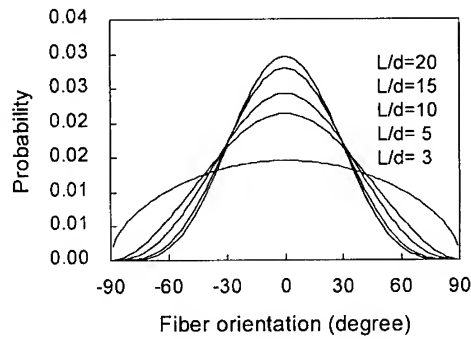


Fig.7. (a) The FOD and (b) the volume fraction of uniform preform for various fiber aspect ratio

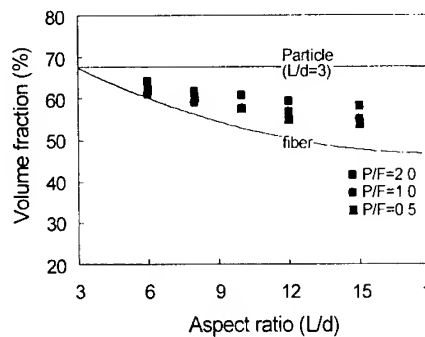
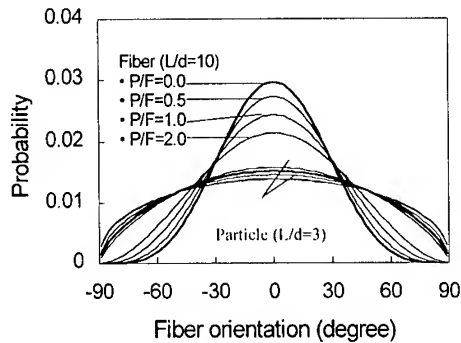


Fig.8. (a) The FOD and (b) the volume fraction of hybrid preform for various mixture ratio and fiber aspect ratio

Investigation on Corrosion Behaviour of Aluminum Metal Matrix Composite

M.J.Hadianfard¹, S.Jafari²

¹ Department of Material Science and Engineering Shiraz University, Shiraz, Iran

² Department of Material Science and Engineering Shiraz University, Shiraz, Iran

SUMMARY: The corrosion Behaviour of 6061 Aluminum alloy and 6061 Al - SiC composite in persian gulf water was investigated by using of electrochemical measurements on both 6061 Aluminum - Silicon carbide metal matrix composite and the unreinforced alloy in sea water. The corrosion behaviour of the materials in three different temperature were studied, and scanning electron microcope were used to determine microstructure of corrosion. The results are indicated that corrosion rate in MMCs is faster than corrosion rate in unreinforced alloy.

KEYWORDS: polarisation, composite, unreinforced, Aluminum

INTRODUCTION

Metal matrix composite (MMCs) are attractive materials because they combine high strength and stiffness with low density. Other advantages of them include high temperature strength, good shock resistance to thermal fatigue, high thermal conductivity and low coefficient of thermal expansion [1]. These properties lead to a range of current and potential uses in the aerospace, automotive and electronic industries. Many of application of MMCs can involve exposure to potentially corrosive environments. Despite the risk of corrosion attack, most of work on MMCs has concentrated on the Mechanical and the effect of processing route on the properties. Therefore a few investigation have been conducted on the effect of SiC reinforcement on the electrochemical polarisation characteristics of an aluminum alloy in a range of environment conditions [2,3]. This study tries to find better image from corrosion behaviour of MMCs.

Material Characterization and Experimental Method

Material used in this study were, a 6061 Al alloy and a 6061 alloy reinforced with 20wt%, 40µm SiC particles. The composition of the 6061 alloy is given in table (1)

Table (1) . chemical composition of 6061 alloy

Si=0.4 - 0.8	Cu= 0.15 - 0.4	Cr = 0.04 - 0.35
Zn = 0.25	Mg = 0.8 - 1.2	Mn = 0.15

The MMCs and unreinforced alloy were manufactured by identical processing method , including liquid metallurgy route , casting and hot extrusion.

The specimens were cut through the material with the shape of disc with diameter of 1 cm.

The specimens then mounted in epoxy resin , grounded and polished using SiC particle and diamond paste. In the last step before testing specimen were washed with distilled water and acetone to remove any dirt and dust from their surface.

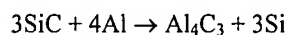
Polarisation test were carried out in the Persian Gulf water , for aeration , the air from atmosphere was pumped through the water solution was stirred by using of a magnetic stirrer. The specimen were immersed in the solution for at least 2h prior to referred . All potentials were referred to a saturated Calomel electrode (sce) which was introduced in to the cell via a luggin probe. A potentiostat galvanostat , model VII - PG with scan rate of 0.2 was used to record all polarisation curve and scanning electron microscope were used to study the microstructure of the material before and after exposure to sea water , to identify features of corrosion on the surface of the specimen. The electrochemical experiment were performed at room temperature , 40 °C and 60 °C

RESULT

The polarisation , curves are shown in figs 1,2 and 3 .Figure 1,2 show the cathodic and anodic polarisation of Al6061- SiC and Al6061 and figure 3 shows the anodic polarisation of Al6061 - SiC at 30 , 40, 60 °C .cathodic and anodic polarisation diagrams for 20wt% SiCp 6061 Al are compared with those for the unreinforced alloy in figure 1 and 2. Result from tests show that anodic and cathodic density on the MMCs is greater than unreinforced alloy. figure 3 is shown that anodic current density increase by increasing of temperature. on the other hand , increasing of temperature is causes of increasing corrosion rate in MMCs, Similar behaviour is observed for unreinforced alloy.

DISCUSSION

Anodic polarisation curves for 20wt% Al6061 - SiCp and Al6061 in aerated stirred sea water solution shows in figure 3 .The anodic current density on the MMCs was about an order of magnitude greater than the value measured for the unreinforced alloy. This behaviour may be attribute due to Aluminum carbide that is formed in interface between aluminum / silicon carbide in composite , the interface reaction can produce aluminum carbide according to following reaction:



for the reaction to proceed silicon must enter into aluminum as a solute atom and carbide should form between aluminum and SiC interface. Aluminum carbide is more active relative to aluminum , and therefore current density is increased due to presence aluminum carbide phase , and lead to faster corrosion rate in MMCs than unreinforced alloy [4,5].

The cathodic polarisation curves showed regions of diffusion controlled of oxygen , since diffusion is limited current being larger for the MMCs than the unreinforced alloy

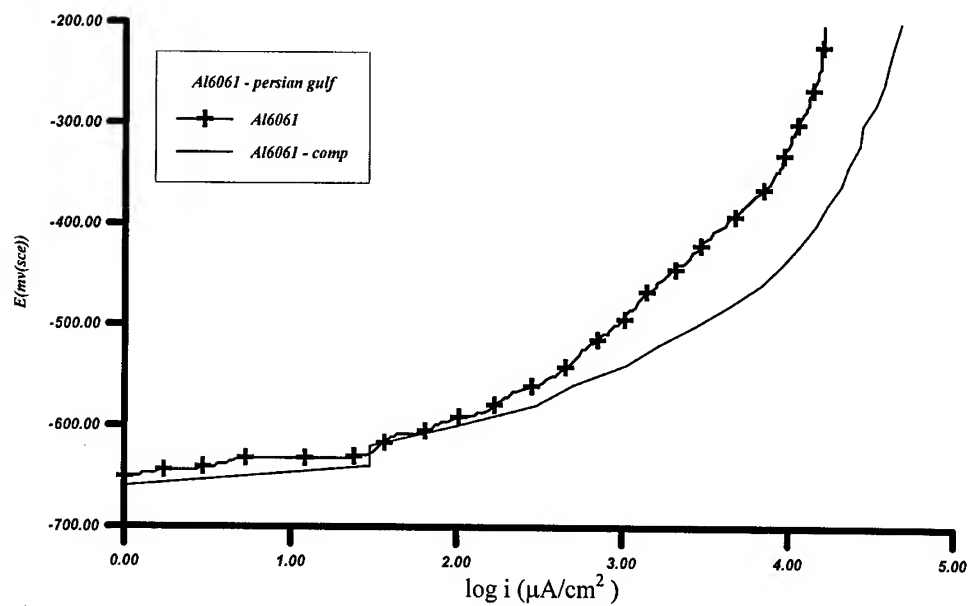


Figure 1, anodic polarisation of Al6061-SiC and Al6061, in stirred and aerated Persian Gulf water

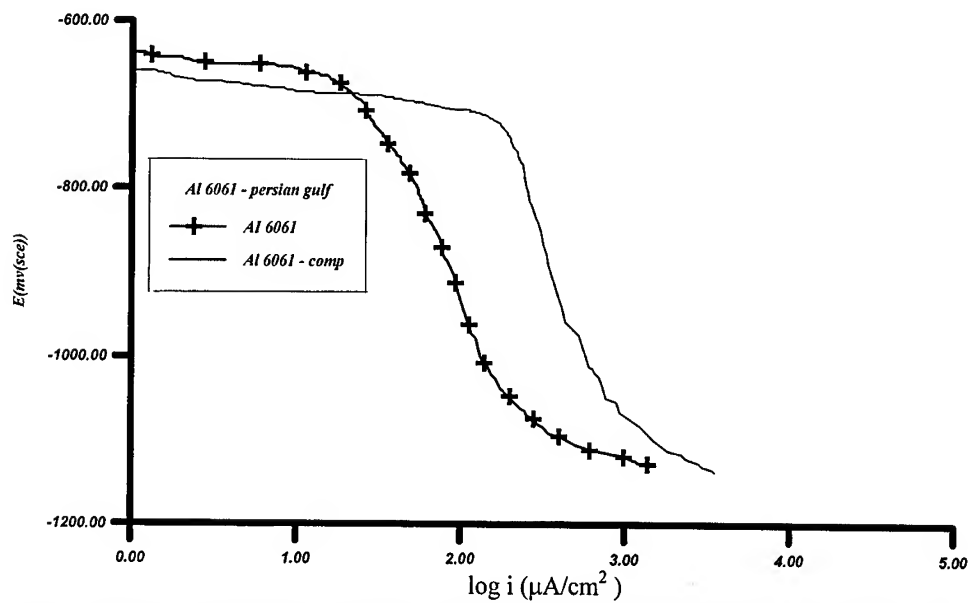


Figure 2, cathodic polarisation of Al6061-SiC and Al6061, in stirred and aerated Persian Gulf water

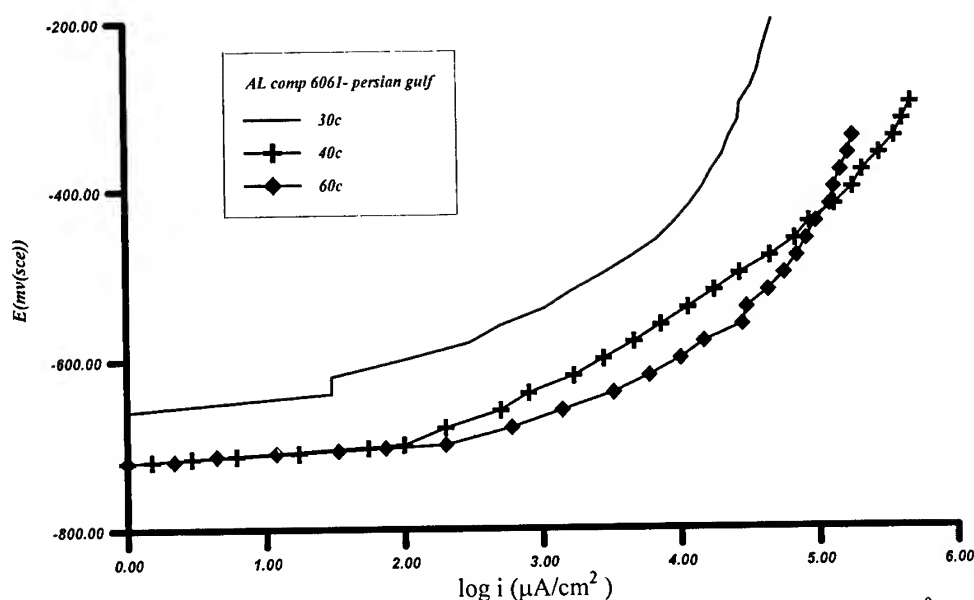


Figure 3, anodic polarisation of Al6061- SiC in persian gulf water at 30 , 40, 60 °c

The corrosion potential measured for the 20wt% SiCp / 6061Al is slightly lower than the value of aluminum alloy in sea water solution. Therefore in first region cathodic curve of unreinforced alloy. In the second region, the cathodic curve of MMCs is greater than cathodic curve of unreinforced alloy. Since the oxide film forms on aluminum and aluminum alloy is dielectric, cathodic reaction may take place only at points where this oxide film is weak. In homogenates and reinforcing particle can act as barriers for producing continuous oxide film and providing path for electrical current. In addition in the cause of SiC particle, they produce metal / particle interface with higher conductivity compare to the oxide film and they help cathodic reactions to take place easier and faster, therefore cathodic current density is observed higher in the MMCs compare to the unreinforced alloy.[6,7]

Effect of temperature is shown in figure 3 in this figure anodic current density increase by increase of temperature. That is due to increase rate of anodic and cathodic reaction on the MMCs, because of increasing of temperature.

Comparison between behaviour of MMCs and unreinforced alloy with increasing temperature show that rate of increase of current density in the MMCs is greater than unreinforced alloy. That is happening because protective film formed on the MMCs relative to unreinforced alloy. due to presence of SiC particle in the MMCs The protective film on the MMCs is heterogeneities. on the other hand protective film formed on the unreinforced alloy is more uniform than protective film formed on the MMCs and consequently corrosion rate in MMCs is greater than unreinforced alloy with increasing of temperature.[8]

figure 4 show the effect of exposure to water on the microstructure of MMCs. Result of microscopic investigation shows while, surface of unreinforced alloy corroded uniformly. the surface of the MMCs was corroded locally at the same environment condition. Electron microscope from surface of the MMCs indicates that interface between SiC particles and matrix alloy were attack more than other points, and it is provides further reason for production of less corrosion resistance phase at interface of the composite.

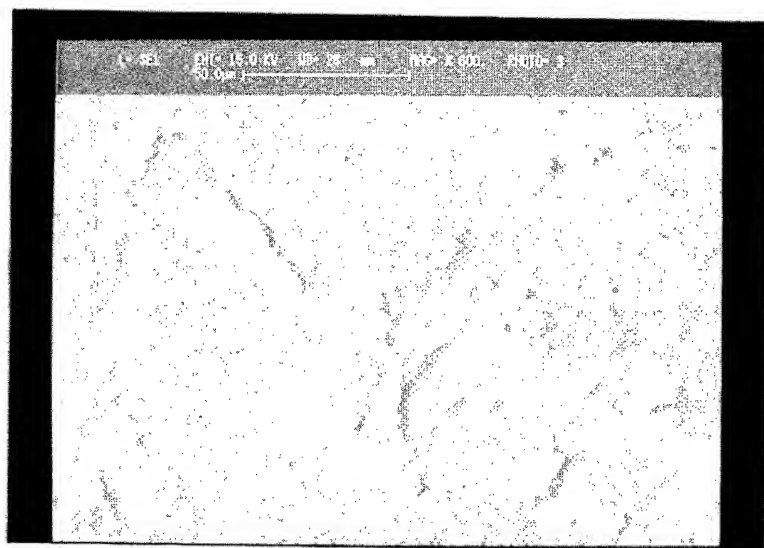


Figure. 4 the microstructure of MMCs after exposure to the sea water

CONCLUSIONS

- 1) Introduce of SiC particles to 6061 alloy enhanced the corrosion rate of composite relative to the matrix material (aluminum 6061)
- 2) Electrochemical studies showed that the corrosion potential of the composite is more negative compared to the matrix alloy.
- 3) Increasing of the application temperature enhanced the corrosion rate of the composite due to increase of anodic and cathodic reaction.

REFERENCES

- 1- B.Terry,G.Gones, "Metal Matrix Composite",Current Development & Trends in Industrial Research & Application, Elsevier Advanced Technology ,1990
- 2- J.R. Uinson, R.L Sierakowski, V87, The Behavior of Structure Composed of Composite Material, Martinus Nijhoff ,Boston, 1987, 321P.
- 3- BhaGwan, D.A, J. Broutman, Analysis and Performance of Fiber Composite , Wiley Interscience , New york ,1990 ,449p.

4- 30- Z. X. Guo , B. Derby , “Solid State Fabrication & Interface of Fiber Reinforced Metal Matrix Composite” , Progressin Material Science ,Vo39 , pp411-495,1995

5-23-T.R. Sehrecengost, B.A Show, R. G. Wendt, and W.C Moshier, “Nonequilibrium Alloying of Graphite- Reinforced Aluminum Metal Matrix Composite”, NACE International, pp842-849,1993

6-M.A , Denise , D. taylor, “Corrosion of Metal Matrix Composites, Naval ship Research Development center”, Corrosion Science ,Vol35 ,1990,pp859-863.

7-L.H. Hihara, R.M Iatanision,”Corrosion of Matrix Composites, International Materials, Reviews”. vol 39, 1994, pp239- 245.

8-T.R. Sehrecengost, B.A Show, R. G. Wendt, and W.C Moshier, “Nonequilibrium Alloying of Graphite- Reinforced Aluminum Metal Matrix Composite, NACE International,VOL36 ,1993, pp 842-849.

INDUCTION HEATING OF METAL MATRIX COMPOSITES FOR THIXOFORMING

S. S. Ahn¹, C. G. Kang², and H. H. Jo³

¹*School of Mechanical Engineering, Pusan National University*

San 30, Changjun-dong, Kumjung-gu, Pusan 609-735 KOREA:la134@hanmail.net

²*School of Mechanical Engineering, Pusan National University*

San 30, Changjun-dong, Kumjung-gu, Pusan 609-735 KOREA:cgkang@hyowon.pusan.ac.kr

³*Korea Institute of Research Technology*

472, Ka Jwa 4dong, Seo-gu, Incheon 404-254 KOREA:johh@kitech.re.kr

SUMMARY: This paper is concerned with the microstructure characterization of reheated A357 aluminum alloys reinforced with 5, 10, 15 vol.% of SiC particle reinforcements. To obtain the uniform dispersion of reinforcements, particulate reinforced metal matrix composites (PMMCs) were fabricated by mechanical stirring method mixed by electromagnetic stirring. Reheating conditions of PMMCs for thixoforming are introduced by experimental method and in reheating process of PMMCs, the effects of reinforcements dispersion state are drawn by experiments. In case of particle size, 14 μm , at 5, 10 vol.%, the minute globular microstructures was obtained in 582, 583 °C which was same or higher than A357 by 1 °C, but at 15 vol.%, reheating temperature of PMMCs was higher than A357 by 13 °C and in case of 25 μm , similar results were obtained. The effects of reinforcements dispersion state were invalid during reheating process of PMMCs. As reinforcements dispersed uniformly, the total reheating time of PMMCs was short and reheating temperature of the last reheating step was low.

KEYWORDS: electromagnetic stirring, reheating process, thixoforming

INTRODUCTION

Recently it is important subject to improve fuel efficiency in the transportation fields like automobiles, vessels, and aircraft and so on because of global environmental preservation. To better fuel efficiency and improve problems with environmental pollution, it is essential to lighten, improve minimize parts. Especially in case of auto engine parts, known materials such as Al, Mg and Cu alloys can't satisfy ratio of modulus of elasticity, ratio of strength, fatigue strength, wear resistance, corrosion-resistance and stability of measurements. Therefore, the research about metal matrix composites (MMC) is being performed. Fabricating methods of MMC are powder metallurgy [1][2], to apply method of forging melted metals with whisker and short fibers [3][4], to use mechanical and electromagnetic stirring [5][6]. In case of forging melted aluminum with particulate reinforcements, it is possible to manufacture

complicated shapes of PMMC parts, but it is difficult to acquire products with uniform dispersion of reinforcements because of difference of density between matrix and reinforcement. In case of PMMC by melt forging method, even though reinforcement disperse uniformly, joining strength of surface between reinforcement and matrix is not good and segregation exists, so it makes mechanical properties lower. To solve those problems, necessity of studies of semi-solid forming about MMC rises. Uniform dispersion is very important because of thermal unequalness by difference of heat transfer coefficient between reinforcement and matrix in reheating process to manufacture parts of MMC by semi-solid forming. So it is going to be suggested to fabricating PMMC by combined methods of electromagnetic and mechanical stirring for uniform dispersion of reinforcements. The reheating conditions of PMMCs which reinforced by 25, 14 μm SiCp are introduced by experimental method and the changes of reheating condition by the effects of reinforcement dispersion state are drawn in experiments.

EXPERIMENTS

The tool for fabricating PMMCs

In this study fabricating tools were designed and manufactured in person for fabricating PMMCs and they are shown in Fig.1. To melt matrix A357, a high frequency furnace was used and rotating movement of the furnace was possible for pouring melted metals into the graphite mold. It is possible for the furnace to be heated desired temperature quickly compared with a electric furnace, and it is easy to keep fabricating temperature fixed. The stirring tool is composed of three parts. One is a driving motor and control part for moving impeller up and down, another is cover part for protecting vibration of the impeller and minimizing contact with atmosphere and the other is a driving motor and control part for forming torque of the impeller. The driving motor for forming torque is D.C motor and RPM changes according to input voltage in control parts. In this equipment, moving impeller for stirring up and down is controlled easily and in cover part using buffer springs and heat-resistance material has several functions such as inserting thermo-couple for measuring exact temperature, guide for impeller rotation, role of bearing and so on.

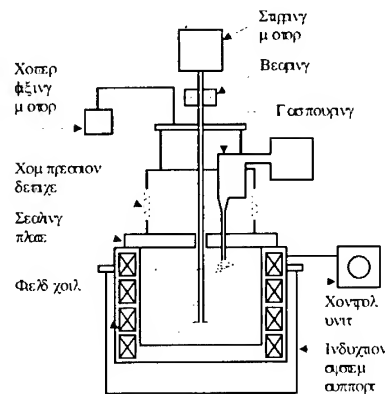


Fig.1 Schematic diagram to fabricate the metal matrix composites

Fabrication of PMMCs

The proper amount(750~780)g of matrix A357 alloy was washed with acetone put into the graphite crucible in induction furnace, heated over liquid temperature(615°C), and melted completely(over 630°C). After oxidation films by contact with atmosphere were removed, the cover fixing motor was driven for making the cover in cover in contact with the crucible. After driving the stirring impeller, melted matrix was keep in 595°C(solid fraction 40%) and stirred for a minute to obtain uniform flow. SiCp made by Showa Denko Company in Japan

was preheated up to 400°C in the electric furnace, and 10g of it was injected into the matrix per a minute. Stirring impeller was coated with Fiber Frax Coating Cement made by Carborundum Company in the United States, and preheated up to 500°C for protecting decrease of temperature by contacting with the matrix. After injection of reinforcements, the impeller was driven regularly for 15 minutes, moved up and down to obtain uniform dispersion and then melted PMMC was poured into the graphite mold. It cooled down in the mold for a minute and then was quenched in the water. V_f , volume fraction of reinforcements, is defined as a ratio of reinforcement volume to whole volume of matrix and reinforcements and the equation is as follow.

$$V_f = \frac{\frac{M_p}{\rho_p}}{\frac{M_m}{\rho_m} + \frac{M_p}{\rho_p}} \times 100\% \quad (1)$$

where, M_p , M_m , ρ_p and ρ_m are the weight of reinforcements, the weight of matrix, the density of reinforcement and the density of matrix, respectively. The size of fabricated PMMC billet are 40mm in the distance across and 180~200mm in the height. Reheating billets for thixoforming was machined by $d \times l = 40 \times 50$ (mm).

Reheating of PMMCs

The process of reheating is divided with three steps and by controlling heating and keeping time in each step, uniform heating can be obtained [7]. In this study, reheating temperature was set with three steps as shown in Fig.2 and reheating condition for fine globular microstructure was drawn from experiments.

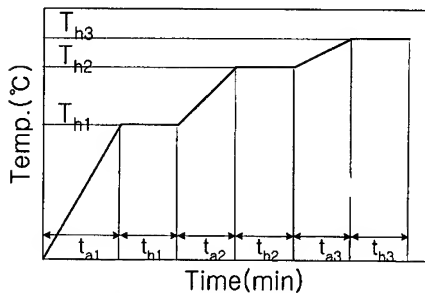


Fig.2 Schematic diagram of reheating condition to obtain semi-solid material

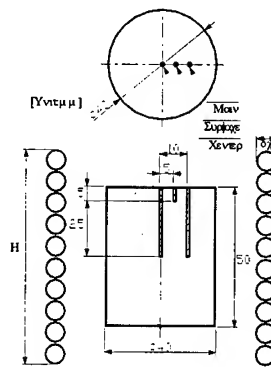


Fig.3 Thermocouple positions to measure the temperature during reheating process

Reheating experiments were performed using the 20kW induction furnace and the microstructure was observed after reheating and then quenching. As shown in Fig.3, to measure temperature of reheating billets, holes with Φ 2mm in center, surface and main was drilled. CA type thermo-couple were put into the holes and difference between real heating temperature and setting temperature. The main was set as input temperature of the 20kW induction furnace.

RESULTS AND DISCUSSION

The reheating conditions drawn from experiments according to the volume fraction are shown in Table 1 and 2. The difference of PMMC's and A357 reheating temperature is about $\pm (0\sim 2)^{\circ}\text{C}$ in volume fraction 5 and 10%, but in 15%, in case of particle size. 14 μm , over 13°C , and 25 μm , over 11°C , a suitable specimen shape for thixoforming and a globular microstructure are obtained and commonly whole reheating time of PMMC is set 9 minutes shorter than time of A357 alloy by 1 minute. Globular microstructure of matrix in each part of specimen was done quickly around 575°C by effect of different reinforcement conductivity and whole reheating time decreased. If heat gradient by reinforcement in reheating occurs, output of power increases to maintain regular time for heating, and relatively, globular speed of matrix with high conductivity is faster, therefore the whole reheating time decreases. The temperature profiles of each points in reheating PMMC are shown in Fig.4 and 5.

Table 1 Reheating conditions of metal matrix composites for thixoforming (SiCp 14 μm)

Vol %	Test Specimen(mm)	Heating time $t_a(\text{min})$			Heating temp. $T_h(^{\circ}\text{C})$			Holding time $T_h(\text{min})$		
		t_{a1}	t_{a2}	t_{a3}	T_{h1}	T_{h2}	T_{h3}	t_{h1}	t_{h2}	t_{h3}
0	$\Phi 40 \times 150$	3	2	1	451	576	582	1	1	2
5		3	1	1	501	575	582	1	2	1
10		3	1	1	501	575	583	1	2	1
15		3	1	1	501	575	595	1	2	2

Table 2 Reheating conditions of metal matrix composites for thixoforming (SiCp 25 μm)

Vol %	Test Specimen(mm)	Heating time $t_a(\text{min})$			Heating temp. $T_h(^{\circ}\text{C})$			Holding time $T_h(\text{min})$		
		t_{a1}	t_{a2}	t_{a3}	T_{h1}	T_{h2}	T_{h3}	t_{h1}	t_{h2}	t_{h3}
0	$\Phi 40 \times 150$	3	2	1	451	576	582	1	1	2
5		3	1	1	501	575	580	1	2	1
10		3	1	1	501	575	582	1	2	1
15		3	1	1	501	575	593	1	2	2

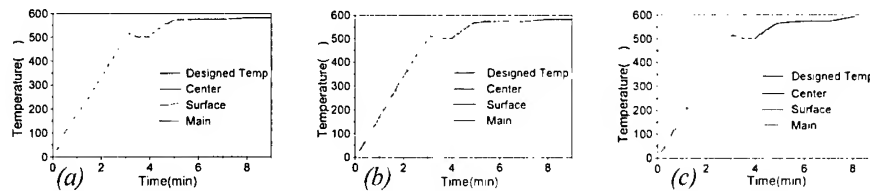


Fig.4 Temperature profiles during reheating process of metal matrix composites (SiCp 14 μm)
(a) 5 vol.% (b) 10 vol.% (c) 15 vol.%

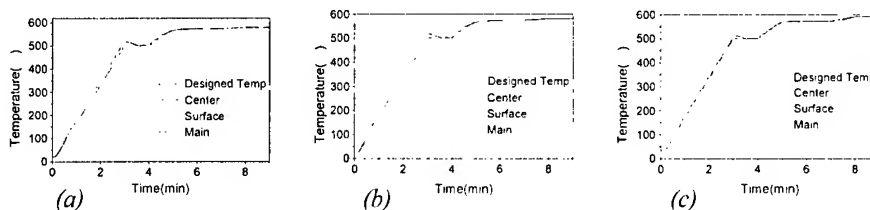


Fig.5 Temperature profiles during reheating process of metal matrix composites (SiCp 25 μm)
(a) 5 vol.% (b) 10 vol.% (c) 15 vol.%

The main and center part is heated similarly with setting temperature but in surface, temperature deviation increases commonly at 2~6 minutes and at last step, decreases about 0~5°C. The microstructures of reheating PMMC are shown in Fig.6 and 7. Uniform globular microstructure about 100 μm is observed without relation of observation parts and uniform dispersion of reinforcements is also observed. The reheating condition according to dispersion state in reheating PMMC is shown in Fig.8. In case (b) that reinforcement dispersed uniformly, setting temperature of the last step in reheating was 580°C lower than case (a) by 12°C and the whole reheating time was 9 minutes lower than (a) by 3 minutes. And as shown in microstructure photograph, globularity is much minute and uniform than the case (a).

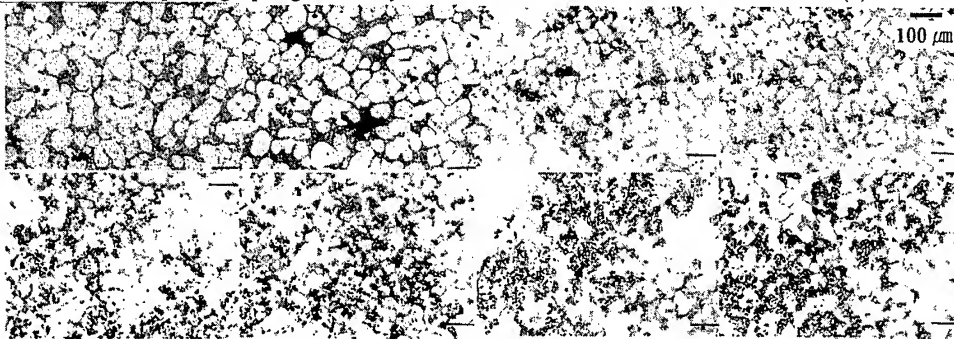


Fig.6 Microstructure of metal matrix composites after reheating process (SiCp 14 μm)
1.Center 2. Edge (a) A357 (b) 5 vol.% (c) 10 vol.% (d) 15 vol.%

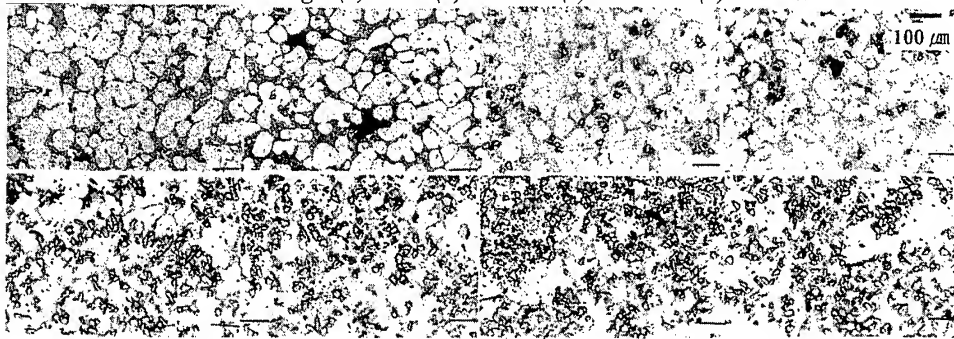


Fig.7 Microstructure of metal matrix composites after reheating process (SiCp 25 μm)
1.Center 2. Edge (a) A357 (b) 5 vol.% (c) 10 vol.% (d) 15 vol.%

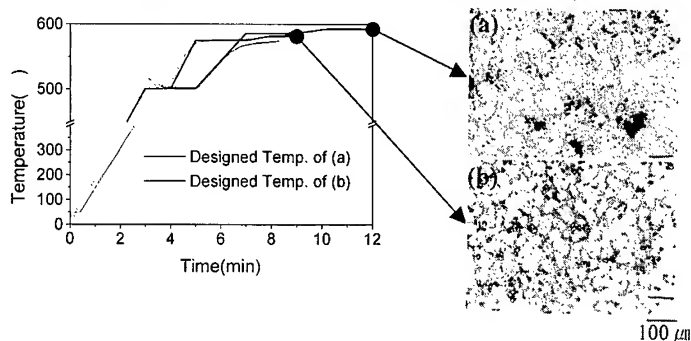


Fig.6 Temperature profile during reheating process and microstructure of PMMCs after reheating process (a) non-uniform dispersion state of reinforcements (b) uniform state

CONCLUSIONS

From the reheating experiments of metal matrix composites for thixoforming, the following conclusions are drawn.

- (1) The whole reheating time of PMMC is shorter than A357 by 1 minute.
- (2) In case of particle size, 14 μm , the difference of the reheating temperature between PMMC and A357 are about (0~1) $^{\circ}\text{C}$ at the volume fraction, 5,10% of reinforcements but at the volume fraction, 15% of reinforcements, the temperature of the last reheating step is higher than A357 over 13 $^{\circ}\text{C}$. In case of particle size, 25 μm , the difference of the reheating temperature of the last reheating step between PMMC and A357 is higher than A357 over 11 $^{\circ}\text{C}$.
- (3) The difference of the reheating temperature according to particle size of reinforcements is about (1~2) $^{\circ}\text{C}$, so no invalid difference is found.
- (4) The whole reheating time is shorter in PMMC with uniformly dispersed reinforcement than PMMC without uniformly dispersed reinforcement and the reheating temperature is lower at the last step.

ACKNOWLEDGEMENT

The authors wish to acknowledge the financial support of the Korea Research Foundation made in the program year of 1998

REFERENCES

- (1) V. V. Bhanu Prasad, B. V. R. Bhat, A. C. Rao, V. K. Varma, "Mechanism of Vacuum Hot Pressing of Metal Matrix Composites", *Proc. 10th International Conference on Composite Materials: (ICCM-10)*, Vol.2, 1995, pp.755 ~ 762
- (2) C. Stone, P. Tsakirooulos, "Spatial Distribution of Reinforcement in PM Al-4Cu/SiCp MMCs : Computer Simulation and Characterisation by EDX Analysis", *Proc. 10th International Conference on Composite Materials: (ICCM-10)*, Vol.2, 1995, pp.465 ~ 472
- (3) I. Tsuchitori, H. Fukunaga, "Fabrication of Particulate Rutile TiO₂/Al Composites by Squeeze Casting and Their Structural Characteristics", *J. Jpn. Inst. Light Metals*, Vol.43, NO.1, 1993, pp.26 ~ 32
- (4) T. Yamauchi, Y. Nishida, "Infiltration Kinetics of Al-12%Si Alloy into SiC Whiskers Preform", *J. Jpn. Inst. Metals*, Vol.58, No.12, 1994, pp.1436 ~ 1443
- (5) G. A. Rozak & J. J. Lewandowski, "Effects of Casting Conditions and Deformation Processing on A356 Aluminum and A356-20 Vol% SiC Composites", *J. Composites Mat.*, Vol.26, No. 14, 1992, pp.2076 ~ 2106
- (6) M. Hayashi, N. Tatsumoto, "Processing and Mechanical Properties of SiC Particel Dispersion Strengthened AC8A Composite by Agitation Casting", *J. Jpn. Foundrymen's Society*, Vol.65, No.11, 1993, pp.846 ~ 852
- (7) W. G. Cho, "A study of the Filling Behavior by Thixoforging Process with Aluminum Alloys", Pusan National University, Graduate School. M. Sc., 1998

Effect of SiC Whiskers on the Elastic Constants of SiC_w/2124Al Metal Matrix Composites

H.K.Jung¹, Y.M.Cheong¹, S.H. Kim¹, H.J.Ryu² and S.H.Hong²

¹Korea Atomic Energy Research Institute, PO Box 105, Yusong, Taejon 305-600, Korea

²Department of Material Science and Engineering, Korea Advanced Institute of Science and Technology, 373-1 Kusung-dong, Yusong-Ku, Taejon 305-701, Korea

SUMMARY : The effect of SiC whiskers on elastic stiffnesses was investigated to analyze the elastic behavior of SiC_w/2124Al metal matrix composites (MMCs). The SiC_w/2124 Al composites containing 10-30 volume % of SiC whiskers were fabricated by powder metallurgy process and followed by hot extrusion with ratio ranged 12:1-70:1. The elastic constants were measured by resonant ultrasound spectroscopy (RUS). The initial estimates of elastic stiffnesses for the RUS were calculated from the Mori-Tanaka approach using the aspect ratios of SiC whiskers. Young's moduli were calculated from the measured elastic stiffnesses. The results show that Young's moduli were significantly improved by increasing the volume fraction of SiC whiskers and were affected by both the SiC reinforcement and the matrix simultaneously with increasing the extrusion ration of the composites. The measured elastic stiffnesses indicate that the whisker redistribution induced by the extrusion process increases the anisotropy factor (C_{33}/C_{11}) in the transversely isotropic symmetry.

INTRODUCTION

Metal matrix composites(MMCs) are becoming an attractive materials for advanced aerospace and automobile components since their properties can be tailored through the addition of selected reinforcements. In particular, SiC whisker reinforced aluminum composites have been of special interest due to their high specific strength and specific modulus at room or elevated temperatures.[1] Short-fiber reinforced composites are most often manufactured in the form of short glass or ceramic fibers embedded in a polymer, metal or ceramic matrix and processed by conventional casting, infiltration or powder metallurgy technologies.

The RUS technique is a nondestructive technique based on ultrasonic excitation and the measurement of the mechanical resonant frequencies of a small sample having a regular shape. The mechanical resonant response of a solid is dependent on its elastic moduli, shape, and density. The resonant spectrum can be predicted based on these parameters. The resonant frequency spectrum is first calculated from an initial estimate for each of the elastic constants. The calculated spectrum is then compared with the measured ones, and a least square difference between the measured and predicted resonant frequencies is calculated and summed for all the spectral peaks to find a residual figure of merit.[2] The elastic constants that minimize a residual figure of merit are then considered to be the actual elastic constants of the material and can be obtained by RPR code programmed in Fortran according to the above procedure. The RUS technique has already been successfully applied to identify the complete elastic constants of many single crystal[3], intermetallic compounds[4], as well as boron-fiber-reinforced

aluminum composites.[5]

The present study has attempted to investigate the effect of microstructural parameters on the elastic moduli of SiC whisker reinforced 2124 Al matrix composites. Five elastic constants of SiC_w/2124 Al composites have been determined by the RUS measurement method. At the same time, the initial estimates of elastic constants for RUS have been obtained using the Mori-Tanaka theory considering the effective aspect ratio of the SiC whiskers. The effects of volume fractions and extrusion ratios of SiC whisker reinforcement on the elastic properties of the SiC_w/2124 Al composites have been discussed.

EXPERIMENTAL PROCEDURES

Fabrication of SiC_w/2124Al Composites

Atomized 2124 Al powders with an average diameter of 20 μm were used as the matrix material, and β -SiC whiskers were used as the reinforcements to fabricate the SiC_w/2124Al composite by the powder metallurgy process. The properties of the 2124 Al powders and SiC whiskers are given in Table 1. SiC_w/2124 Al composites with a nominal volume fraction of 10%, 20%, and 30% with SiC aspect ratio for a 25:1 extrusion ratio were fabricated. At the same time, 20 volume percentage SiC_w/2124 Al composites containing different whisker extrusion ratios of 12:1, 25:1, and 70:1 were also fabricated. The 2124Al powders and SiC whiskers were wet mixed in ethanol under ultrasonic stirring condition. The mixtures were dried for 10 hrs at 85 $^{\circ}\text{C}$ in an oven and then consolidated into the cylindrical ingots by vacuum hot pressing. The hot pressing chamber was evacuated to 1×10^{-5} Torr while heating the die up to 570 $^{\circ}\text{C}$. The consolidated ingots were hot extruded at 500 $^{\circ}\text{C}$ with different extrusion ratios of 12:1, 25:1, and 70:1. The microstructures of the SiC/2124Al composites were observed using optical microscopy. The aspect ratios of SiC whiskers in the composites were measured from the scanning electron micrographs (SEM) after etching in a 10% NaOH solution.

Table 1. Material properties of the 2124 Al matrix and the SiC whisker reinforcement

	2124 Al	SiC powder
Composition	Al-4.4Cu-1.5Mg-0.6Mn	monocrystal β -SiC
UTS	490 MPa	
YS	400 MPa	21 GPa
Young's Modulus	72 GPa	490 GPa
Elongation	10%	
Poisson's ratio	0.33	0.17
Density	2.77 g/cm ³	3.2 g/cm ³
Melting Point	683 $^{\circ}\text{C}$	2690 $^{\circ}\text{C}$
CTE (Coefficient of Thermal Expansion)	$23 \times 10^{-6}/\text{K}$	$4.5 \times 10^{-6}/\text{K}$

Measurements of Elastic Constants

Rectangular-parallelepiped specimens were cut by electric-discharge machining (EDM) from the extruded bar of SiC/2124 Al MMC. The machined specimens were finely polished to the dimensions of 2.0 mm x 2.5 mm x 3.0 mm. The longitudinal axis of the specimen, which represents 3-axis, were aligned parallel to the extrusion axis of the extruded bar.

For the measurement of elastic moduli by resonant ultrasound spectroscopy (RUS), the sample was lightly clamped between two piezoelectric transducers along one of its body diagonals.

One transducer was used for the generation and the other for the detection of ultrasonic vibrations. The excitation frequency varied over a range of 0.4 - 1.7 MHz. By sweeping the excitation frequencies, a large number of the lowest resonant frequencies of the sample were measured at room temperature. The measurement was repeated several times while the sample position with respect to the transducers was altered slightly each time. This practice ensured that all possible vibrational modes were detectable. For each of the specimens, the 30 lowest resonant frequencies were measured for the determination of the elastic constants using the RPR code programmed by Migliori et al.[6] The elastic constants were determined using the minimization algorithm of the difference with the typical root-mean-square (RMS) deviation of less than 0.23% between the measured and the calculated frequencies.

The initial estimates of elastic stiffness for the RUS were calculated using a program by D.C. Lagoudas et al.[7] based on the Mori-Tanaka (MT) theory. Before applying this model, the characteristics of reinforcement such as shape, aspect ratio, and orientation distribution as well as the material properties of constituent, should be considered to get more accurate elastic stiffness. In the SEM, the shape of the SiC whiskers could be approximated as cylinders to describe the behavior of MMCs.[8] The microstructural analysis revealed the average of the aspect ratios and the reinforcement orientation to be used in MT calculation.

RESULTS AND DISCUSSION

Effect of the SiC Microstructure on Elastic Constant

The role of whiskers can be inferred from the quantitative microstructural information on the average aspect ratio by the sample analysis of the longitudinal planes (1-3 plane) in the SEM micrographs. As the extrusion ratio increases, the average aspect ratio decreases because the extrusion process breaks the whisker. To apply the geometrical shape and misorientation of the reinforcement in the direction of the extrusion, the concept of effective aspect ratio was used to estimate the effective elastic constants. [8] It is meaningful to adopt the effective aspect ratio parameter in order to consider the whisker shape (i.e. aspect ratio for cylinder-shaped whiskers) and the orientation simultaneously. The average/effective aspect ratios for the three different extrusion ratios of the 20% SiC reinforcements are shown in Fig. 1. The elastic constants were measured in Table 2 under three conditions according to the assumed reinforcement shapes (sphere, average aspect ratio, effective aspect ratio). This explains the importance of composite microstructures for accurately determining the elastic properties.

Effect of the SiC Volume Fraction on Elastic Constant

Table 2 shows the results of five elastic stiffnesses measured by RUS technique. The C_{33} , which is the elastic stiffness along the extrusion axis, is higher than those perpendicular to the extrusion axis (C_{11} and C_{22}). The transversely isotropic symmetry was assumed to be reasonable for the extrusion bar. As the volume fraction of reinforcements increases, all elastic stiffnesses including shear and off-diagonal stiffnesses and the C_{33}/C_{11} ratio which represents the longitudinal-mode anisotropy, also increase. Because the whiskers are stiffer than the matrix and are aligned along the direction of extrusion (3-direction), we can expect $C_{33} > C_{11} \cong C_{22}$. It suggests that the anisotropy (C_{33}/C_{11}) attributed to its extrusion process has occurred with the whisker redistribution.

Young's moduli along directions 1, 2 and 3 are computed from the elastic compliance elastic stiffness, and relations $E_{ii} = 1/S_{ii}$, respectively, where S_{ij} denotes the component of the elastic

compliance expressed in the contracted notation using the inverse Hook's law $\varepsilon_y = S_y \sigma_y$. In

Table 2. Measured elastic stiffnesses of SiC_w/2124 Al composites with diferent SiC whisker volume fractions and different extrusion ratios by resonant ultrasound spectroscopy. (unit: GPa)

		Elastic Constants (Cij) with whisker reinforcement (Transversely Isotropic symmetry)							
		C11	C33	C23	C12	C44	C66	RMS Error %	C33/C11
10% volume fraction	S	125.5	134.0	58.8	61.4	33.0	32.0	0.225	1.07
	A	126.2	135.1	59.7	62.2	33.0	32.0	0.222	1.07
	E	126.1	135.0	59.6	62.1	33.0	32.0	0.222	1.07
20% volume fraction	S	142.9	157.3	62.0	66.9	39.6	38.0	0.165	1.10
	A	145.7	163.0	66.4	70.0	39.6	37.9	0.160	1.12
	E	145.7	163.0	66.4	70.0	39.6	37.9	0.160	1.12
30% volume fraction	S	162.1	183.4	66.2	71.5	47.0	45.3	0.210	1.13
	A	162.5	184.3	66.8	71.9	47.0	45.3	0.210	1.13
	E	162.5	184.3	66.8	71.9	47.0	45.3	0.210	1.13
12:1 Area reduction	S	137.1	147.1	59.6	62.8	38.3	37.2	0.198	1.07
	A=8.2	138.2	149.4	61.3	64.0	38.4	37.1	0.200	1.08
	E=6.07	138.0	148.9	61.0	63.8	38.4	37.1	0.199	1.08
25:1 Area reduction	S	142.9	157.3	62.0	66.9	39.6	38.0	0.165	1.10
	A=7.8	145.7	163.0	66.4	70.0	39.6	37.9	0.160	1.12
	E=6.27	145.7	163.0	66.4	70.0	39.6	37.9	0.160	1.12
70:1 Area reduction	S	142.3	159.6	61.8	66.4	39.9	38.0	0.134	1.12
	A=7.3	142.5	161.2	62.7	66.6	39.9	38.0	0.132	1.13
	E=6.36	142.5	161.2	62.7	66.6	39.9	38.0	0.132	1.13

S : Sphere (Aspect ratio=1), A : Average aspect ratio, E : Effective aspect ratio

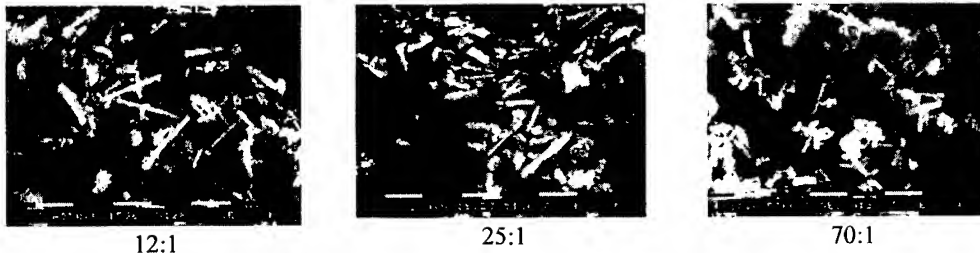


Fig. 1. Scanning Electron Micrographs for aspect ratios of SiC whiskers at 12:1, 25:1, and 70:1 extrusion ratios.

Fig. 2, the longitudinal Young's modulus, E_{33} , is greater than the transverse Young's modulus E_{11} or E_{22} because the redistribution of the reinforced whiskers along the extrusion direction may happen which could be explained with the effective aspect ratios shown in Fig. 1.. RUS shows the advantage of five independent elastic stiffnesses from one small specimen. It can be also found in Fig. 2 that the transverse Young's moduli, E_{11} and E_{22} , as well as the longitudinal Young's modulus, E_{33} , as a function of the volume fraction of reinforcements fall within bounds calculated from the rule of mixtures (ROM) and the Hashin-Shtrikman (H-S) model.[9]

Effect of Extrusion Ratio on Elastic Constant

It can be seen in Fig. 3 that there is an obvious increase in the longitudinal modulus (E_{33}) of these composites with increasing the extrusion ratio for a 20% volume fraction of SiC whiskers. It is reported that the extrusion process affects the redistribution of reinforcements, texture formation and the microcracks.[10] The extrusion process also tends to align the SiC whiskers along the extrusion direction as shown in X-ray pole figures constructed from (111) peak

intensity of SiC whiskers in SiCw/2124 Al composites.(Fig. 4). The higher extrusion ratio results in the greater texture of the matrix and more microvoids or microcracks due to the breakage of long whiskers. The effect of microvoids or microcracks and the texture of the matrix can be ignored during the hot extrusion.[10] We can reach a conclusion that the redistribution of reinforcements plays a major role in the elastic constants of the composites. The anisotropy (E_{33}/E_{11}) of Young's modulus increased by increasing the extrusion ratio because the degree of misorientation of the reinforcement decreased.

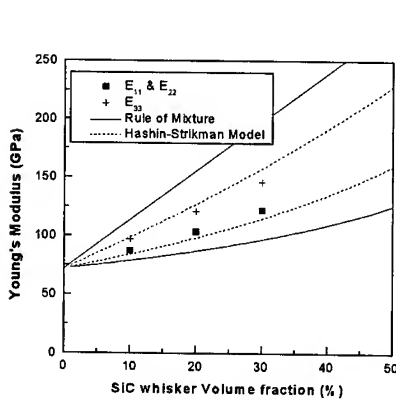


Fig. 2. Variation of Young's moduli of 25:1 extrusion ratio SiC_w/2124 Al composites by varying the volume fraction of SiC whiskers

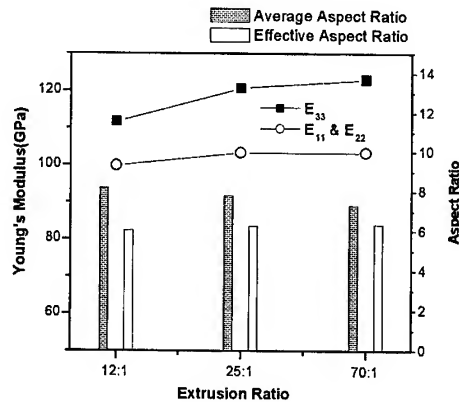


Fig. 3 Variation of Young's moduli and aspect ratios of 20 volume % SiC_w/2124 Al composites by varying the extrusion ratios.

The relationship between the aspect ratios and the Young's modulus is shown in Fig. 3. A significant decrease in the average aspect ratios with the extrusion ratios would be considered to break the long whiskers by the extrusion process. The longitudinal effective aspect ratios show the linear trend with the increments of extrusion ratios to consider the misorientation of whisker at the same time. Also, the transverse effective aspect ratios show the inverse linear effect with the increments of extrusion ratios, which suppress the increment of the transverse Young's Modulus. The slight increase in Young's modulus for the 70:1 extrusion ratio results from both the hardening effect of the redistribution of SiC whiskers and the softening effect of the recrystallization of the matrix.[11] The parameter of effective aspect ratio seems to be useful for describing the elastic modulus and mechanical properties related with the directional alignment of whiskers.

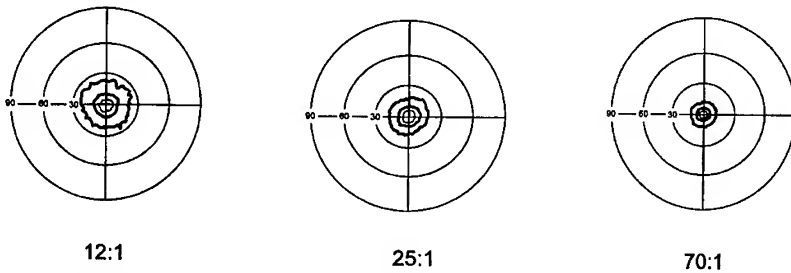


Fig. 4. X-ray pole figures constructed from (111) peak intensity of SiC whiskers in SiCw/2124 Al composites extruded with ratios 12:1, 25:1, and 70:1.

CONCLUSIONS

1. RUS has been applied successfully to measure the elastic constants using the initial moduli calculated by the Mori-Tanaka model. The simple and useful parameter of effective aspect ratios was used to calculate the effective elastic constants by simultaneously considering the shape and orientation of the reinforcement.
2. The longitudinal and transverse elastic moduli (E_{11} and E_{33}) increased linearly with increasing the volume fraction of SiC whiskers. Although the Young's modulus has been known as one of the microstructure-insensitive material properties, the modulus of the composite material is known to be dependent on the aspect ratio and alignment of SiC whiskers.
3. The increase of extrusion ratio caused an increase of longitudinal Young's modulus due to the alignment of whisker reinforcements, while may not affect the transverse Young's modulus due to the breakage of long whiskers. The volume fraction of SiC whiskers showed a significant effect on the elastic constants, and the aspect ratio and alignment of the SiC whiskers caused anisotropy in the moduli of the metal matrix composite.

ACKNOWLEDGEMENTS

This research was supported by a long-term nuclear research program by the Minister of Science and Technology and by the Korea Research Foundation(01 E 0472).

REFERENCES

1. R.K. Everett and R.J. Arsenault, Metal Matrix Composites: Mechanisms and properties, Academic Press, San Diego, 1991.
2. A. Migliori and J. Sarrao, Resonant Ultrasound Spectroscopy, John Wiley & Sons, Inc., 1997.
3. P.S. Spool, J.D. Maynard, M.J. Pan, D.J. Green, J.R. Hellmann, T. Tanaka, Appl. Phys. Lett. Vol. 70, No. 15, 1959, 1997.
4. F. Chu, T.E. Mitchell, B. Majumdar, D. Miracle, T.K. Nandy and D. Banerjee, Intermetallics 5, 147, 1997.
5. H. Ledbetter, C. Fortunko and P. Heyliger, J. Appl. Phys. 78(3), 1542, 1995.
6. A. Migliori, J.L. Sarrao, W.M. Visscher, T.M. Bell, M.L. Lei, Z. Fisk and R.G. Leisure, Physica B 183, 1, 1993.
7. A.C. Gavazi and D.C. Lagoudas, Compu. Mech., 7, 13, 1990.
8. H. J. Ryu, H.K. Jung and S. H. Hong, 12th International Conference on Composite Materials, Paris, France, Jul. 5. 1999.
9. Z. Hashin and T. Shtrikman, J. Mech. Phys. Solids 11, 127, 1963.
10. J.C. Lee and K.N. Subramanian, "Young's modulus of cold and hot rolled (Al_2O_3)p-Al composite," J of Mater. Sci. 29, 4901, 1994.
11. H. K. Jung, S. H. Hong, "Analysis of Dynamic Elastic Properties of SiC/Al Metal Matrix Composites using Resonant Ultrasound Spectroscopy, Ph. D. Thesis, KAIST, 2000.

MMC (2)

PROCESSING AND MICROSTRUCTURE OF MAGNESIUM ALLOY MATRIX COMPOSITES

Gen Sasaki¹, Shunsuke Hara², Makoto Yoshida², Jin Pan², Nobuyuki Fuyama³, Toshio Fujii³ and
Hideharu Fukunaga²

¹ Hiroshima Univ. Dept. of Mech. Eng., 1-4-1 Kagamiyama, Higashi-Hiroshima 739-8527, Japan,
E-mail: gen@ipc.hiroshima-u.ac.jp

² Hiroshima Univ. Dept. of Mech. Eng., 1-4-1 Kagamiyama, Higashi-Hiroshima 739-8527, Japan

³ Western Hiroshima Pref. Industrial. Res. Inst., 2-10-1, Aga-minami, Kure, Hiroshima, 737-0004 Japan

SUMMARY: SiC and $\text{Al}_{18}\text{B}_4\text{O}_{33}$ particle/whisker reinforced AZ91D (Mg-9%Al-1%Zn) alloy matrix composites were prepared by compo and squeeze casting process. Some composites were fabricated under the semi solid condition. The strength of the composites was estimated and the deciding factors of the mechanical properties were investigated from the microstructure. The oxidation of SiC surface improved the wettability with AZ91D. In the $\text{Al}_{18}\text{B}_4\text{O}_{33}$ and oxidized SiC particles/AZ91D composites prepared by compocasting process, particles dispersed uniformly in the matrix without any segregation and coalescence and has a good tensile strength. The interfacial reaction in $\text{Al}_{18}\text{B}_4\text{O}_{33}$ particle and whisker/AZ91D composite prepared by compo and squeeze casting was very little owing to the uniform reaction layer between the whisker and the matrix. The reaction layer is MgAl_2O_4 with spinel structure. The interfaces of $\text{MgAl}_2\text{O}_4/\text{Al}_{18}\text{B}_4\text{O}_{33}$ have well coherent and seem to have good bonding strength. The bending strength of $\text{Al}_{18}\text{B}_4\text{O}_{33}$ /AZ91D alloy composite is stable for the heat treatment up to 600 °C.

KEYWORDS: SiC, $\text{Al}_{18}\text{B}_4\text{O}_{33}$, Mg alloy, Compo casting, Squeeze casting, Microstructure, interface, Strength

INTRODUCTION

Magnesium alloys are being watched for the next generation materials because of the lightweight and the recyclables. Furthermore, magnesium alloys are good for the relative strength, the size stability, the machinability and the shielding materials against electromagnetic wave. As their mechanical and thermal properties are less than those of aluminum alloy, the combination with ceramic reinforcements is needed. In actual, SiC, Al_2O_3 particles and carbon fiber are mainly investigated for the reinforcement of the magnesium alloy [1-5]. These composites are usually prepared by the casting process because of the conventional technique. But the kind of the investigated reinforcement and the fabrication technique are very few. Furthermore, the studies on the investigation of the controlling factor of the mechanical properties were still unknown.

In this study, in order to obtain $\text{Al}_{18}\text{B}_4\text{O}_{33}$ and oxidized SiC reinforced magnesium alloy matrix composites prepared by the compo and the squeeze castings having good mechanical properties, the deciding factors for the mechanical properties were investigated by the microstructure observation.

EXPERIMENTAL PROCEDURE

SiC particle (GC1000, Showa Denko Co., particles size: less than $13\text{ }\mu\text{m}$) and $\text{Al}_{18}\text{B}_4\text{O}_{33}$ particle/whisker (ALBOLEX PC-8 and M-12, Shikoku Chemicals Co., particle size: less than $8\text{ }\mu\text{m}$, whisker size: $10\text{--}30\text{ }\mu\text{m}$ in length and $0.5\text{--}1.0\text{ }\mu\text{m}$ in diameter) were used for the reinforcements of the composites. SiC particles were heat-treated in air at 1000°C for 4 h in order to improve the wettability for Mg alloy. AZ91D alloy was used for the matrix of the composites. SiC particle/AZ91D and $\text{Al}_{18}\text{B}_4\text{O}_{33}$ particle/AZ91D composites were prepared by compocasting. The particles were poured into the molten metal at 580°C and 630°C and then stirred by the blade for 10 min. This temperature corresponds with the solid fractions of 33 and 0 %, respectively. The volume fraction of the reinforcement in the composites was 5 vol. %. $\text{Al}_{18}\text{B}_4\text{O}_{33}$ whisker/AZ91D composites were prepared by squeeze casting process at the preform temperature of 750°C , metal poring temperature of 570°C and 750°C (solid fractions: 50 and 0%) and a pressure of 100MPa. The volume fraction of the reinforcement in the squeeze casting composites was 25 vol. %. The tensile strength and the density of all composites were measured at the room temperature. The bending strength of heat-treated $\text{Al}_{18}\text{B}_4\text{O}_{33}$ whisker/AZ91D composites prepared by squeeze casting was estimated. Microstructure and fracture structure were observed by scanning and transmission electron microscopy (SEM and TEM).

RESULTS AND DISCUSSION

Table 1 shows the tensile strength and the density of SiC particle and $\text{Al}_{18}\text{B}_4\text{O}_{33}$ particle/whisker reinforced AZ91D composites prepared by compo and squeeze casting. Some composites were fabricated under the semi solid condition. The strength of SiC particle/ AZ91D composites prepared by the conventional and the semi-solid compo casting are 143 and 133MPa, respectively. The densities are 1.93 and 1.77 g/cm^3 , respectively. Although the density decreased drastically by using the semi solid processing, the degradation of the strength was little. The strength and density of $\text{Al}_{18}\text{B}_4\text{O}_{33}$ particle/ AZ91D composites prepared by the semi-solid compo casting is 160 MPa and 1.81 g/cm^3 . On the other hand, the strength of the $\text{Al}_{18}\text{B}_4\text{O}_{33}$ whisker/AZ91D composites prepared by squeeze casting increase 197 to 207 MPa by the use of the semi solid condition

Table 1 Tensile strength and density of SiC and reinforced AZ91D matrix composites prepared by compocasting and squeeze casting processes.

Processing	Solid fraction (fs) (%)	Reinforcement (Vf (%))	Density (g/cm^3) (Porosity(%))	Tensile strength (MPa)
Compo-casting	0	SiC particle(5)	--- (0)	143
	33	SiC particle (5)	1.77 (8.1)	133
		$\text{Al}_{18}\text{B}_4\text{O}_{33}$ particle (5)	1.81 (5.3)	160
Squeeze casting	0	$\text{Al}_{18}\text{B}_4\text{O}_{33}$ whisker (25)	--- (0)	197
	50	$\text{Al}_{18}\text{B}_4\text{O}_{33}$ whisker (25)	--- (0)	207

SiC reinforced composites

Figure 1 shows the microstructure of the heat-treated SiC particles in air before casting. Particles are equiaxed with $10\ \mu\text{m}$ in average diameters and have some squarish. The shape of the particles is very similar to that of the as-received particles in SEM observation. But there is a thin and uniform oxide layer with 10nm on the surface of the particles, which was identified as SiO_2 . Oxidized particles are miscible with the molten AZ91D alloy easily in compocasting process. This layer seems favorable for improve the wettability of SiC particles for the molten AZ91D.

Figure 2 is the microstructure of the oxidized SiC/AZ91D composites prepared by the compo casting. SiC particles disperse uniformly in α phase in the matrix. No segregation and coalescence of the particles were observed. The porosity of the composites is almost zero. The composite seems to have an ideal microstructure. The grain sizes of β phase in the composites prepared by the conventional and the semi solid process are about 100 and $20\text{--}30\ \mu\text{m}$, respectively. A little degradation of the strength by use the semi solid process causes the combination of the refinement of the grain size and the high porosity.

Figure 3 is the fracture surface of the composite by the tensile testing. Many SiC particles and the dimple patterns of matrix were observed on the surface. Composites tend to fracture in the matrix and along the interface between SiC particle and matrix. The strength of the composites depends on the strengths of the matrix and this interface.

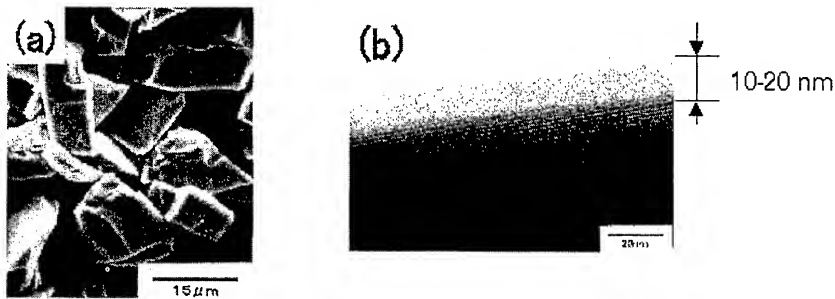


Fig.1 SiC particles oxidized at 1000°C for 4h in atmosphere. (a) and (b) SEM and TEM images, respectively.

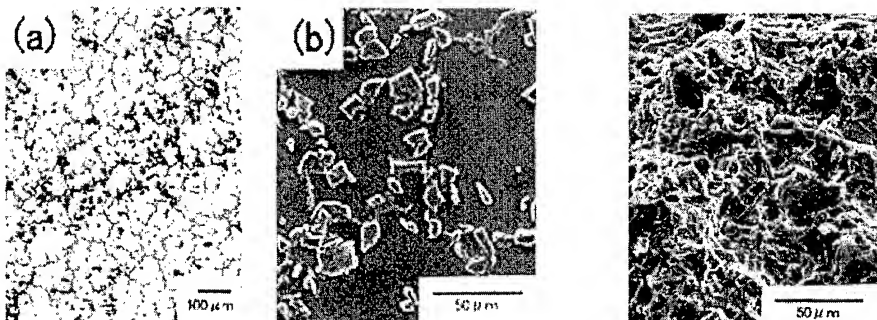


Fig.2 Microstructure of SiC particle/AZ91D composites prepared by the compo casting. (a) optical microscopy image and (b) SEM image.

Fig. 3 SEM image of fracture surface of SiC particle/AZ91D composites prepared by the compo casting.

$\text{Al}_{18}\text{B}_4\text{O}_{33}$ particle/whisker reinforced composites

Figure 4 is the microstructure of $\text{Al}_{18}\text{B}_4\text{O}_{33}$ particle/AZ91D matrix composite prepared by the semi solid compo casting. $\text{Al}_{18}\text{B}_4\text{O}_{33}$ particles distribute uniformly in the matrix without segregation and coalescence. But the composites have many holes, and the porosity of the composite is 5.3%. This is caused by the semi solid processing. Figure 5 is the crack propagation in the composites. Crack tends to propagate in the matrix and the particle. The particles used in this study are the coalescence of the nanometer-sized particles. The strength of the particle seems to have very week strength. The tensile strength '160MPa' of the composite depend on the strength of the matrix and the particle, and the porosity in the composites.

Figure 6 shows the relationship between the bending strength and the heat treatment temperature in AZ91D and AC8A (Al-12%Si-1%Mg alloy) matrix composites. The strength of as cast AC8A matrix composites is 730 MPa and highest compared with heat-treated composites. As increasing heat-treated temperature, the bending strength decreased. The degradation of the strength causes the chemical attraction of the whisker. As increase the heat-treatment temperature and time, the reaction products ' MgAl_2O_4 ' produce partially at the interface between and the matrix, so that the whisker become to thin and have some irregularities. On the other hand, the highest bending strength of AZ91D matrix composite is 610 MPa at 500°C. As increasing heat treatment temperature above 600°C, the strength decreased gradually. Obviously, AZ91D matrix composite have high strength at high temperature compared with AC8A composite and have a good thermal stability.

Figure 7 is the microstructure around the interface between the whisker and matrix in $\text{Al}_{18}\text{B}_4\text{O}_{33}$ whisker/AZ91D composites prepared by the conventional squeeze casting. The whisker attraction seems to be very little. In figure 7(b), there is a uniform reaction layer between and Mg matrix with a thickness of 20-30nm. The reaction layer is MgAl_2O_4 . The interfaces of $\text{MgAl}_2\text{O}_4/\text{Al}_{18}\text{B}_4\text{O}_{33}$ have well coherent, and seem to have good interface strength. Figure 7(c) shows the interface between whisker and the matrix in composites heat-treated at 700°C for 1h. Although some anomalous growths of the reaction products are observed in here and there, this uniform reaction layer prevents a further reaction of the whisker with the matrix. The composite interfaces seem to be stable after the heat treatment. As the $\text{Al}_{18}\text{B}_4\text{O}_{33}$ whisker is single crystal and have good strength, cracks propagate in the matrix and the interface between whisker and the matrix.

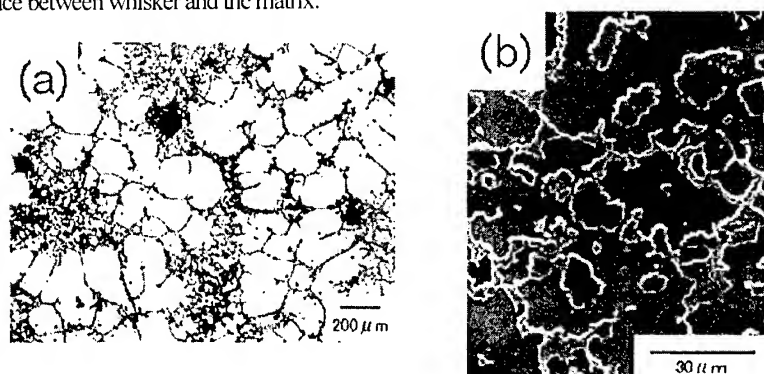


Fig.4 Microstructure of $\text{Al}_{18}\text{B}_4\text{O}_{33}$ particle/AZ91D composites prepared by the compocasting. (a) optical microscopy image and (b) SEM image.

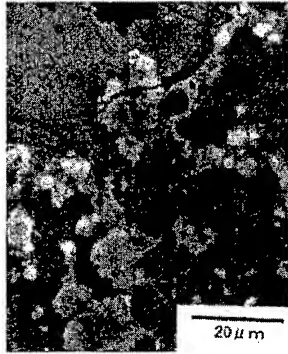


Fig.5 SEM image of crack propagation of $\text{Al}_{18}\text{B}_4\text{O}_{33}$ particle/AZ91D composites prepared by the compocasting.

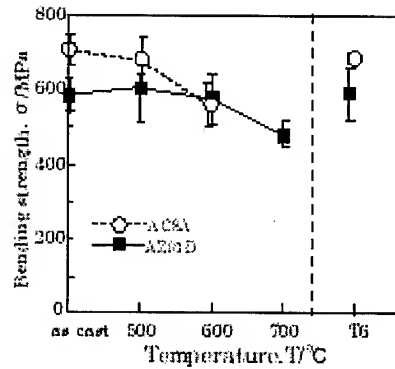


Fig.6 Bending strength of $\text{Al}_{18}\text{B}_4\text{O}_{33}$ particle/AZ91D composites heat-treated at different temperature. That of AC8A (practical aluminum alloy) matrix composites is reference.

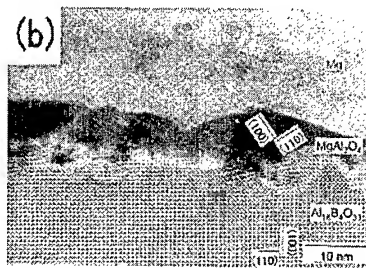
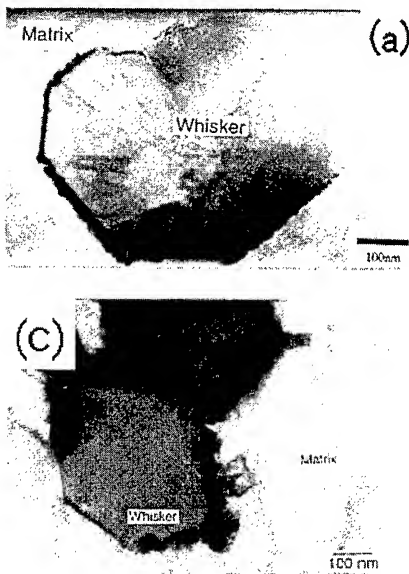


Fig.7 TEM images of the interface between $\text{Al}_{18}\text{B}_4\text{O}_{33}$ and Mg in the $\text{Al}_{18}\text{B}_4\text{O}_{33}$ whisker/AZ91D composites prepared by the squeeze casting. (a) and (b) are the as-cast, and (c) is the heat-treated at 700°C for 1h.

CONCLUSION

SiC and $\text{Al}_{18}\text{B}_4\text{O}_{33}$ particle and whisker/AZ91D composites were prepared by compo and squeeze casting. Some were fabricated by semi-solid processing. The strength and the microstructure of the composites were investigated in order to clarify the controlling factor of the mechanical properties.

(1) The oxidation of SiC surface improved the wettability with AZ91D alloy. Oxidized SiC and as received $\text{Al}_{18}\text{B}_4\text{O}_{33}$ particles in composites prepared by compocasting dispersed uniformly in the matrix. Cracks in SiC particle/AZ91D composites tend to propagate at the interfaces between SiC and matrix, whereas in $\text{Al}_{18}\text{B}_4\text{O}_{33}$ particle/AZ91D composites propagate in $\text{Al}_{18}\text{B}_4\text{O}_{33}$ particle.

(2) The interfacial reaction in $\text{Al}_{18}\text{B}_4\text{O}_{33}/\text{AZ91D}$ alloy composite prepared by compo and squeeze casting was very little owing to the uniform reaction layer between the whisker and the matrix. The thin reaction layer is MgAl_2O_4 with spinel structure and prevents the direct reaction between $\text{Al}_{18}\text{B}_4\text{O}_{33}$ and matrix. The interfaces between MgAl_2O_4 and $\text{Al}_{18}\text{B}_4\text{O}_{33}$ have well coherent. These interfaces seem to have good bonding strength. The bending strength of $\text{Al}_{18}\text{B}_4\text{O}_{33}/\text{AZ91D}$ alloy composite is stable for the heat treatment up to 600°C .

ACKNOWLEDGEMENTS- This work is supported, in partly, by a Grant-in-Aid No. 09650749 from the Ministry of Education, Science, Sports and Culture of Japan.

REFERENCES

1. D. M. Lee, B. K. Suh, B.G. Kim and C. H. Lee: *Mat. Sci. Tech.*, 13(1997), 590
2. H. Kaneda, and T. Cho: *J. Japan Inst. Light Metals*, 46, 7(1996) 321
3. J. Kiehn, E. Bohn and K.U. Kauner: *Key Eng. Mat.*, 127-131(1997) 861
4. G. Sasaki, L. J. Yao, M. Yoshida, J. Pan and H. Fukunaga: *J. Japan Inst. Metals*, 63, 5(1999) 577
5. M. Yoshida, S. Takeuchi, J. Pan, G. Sasaki, N. Fuyama, T. Fujii and H. Fukunaga: *Adv. Composite Mater.* 8,3(1999), 259

SYNTHESIS OF A COPPER MATRIX COMPOSITE AND SIMULTANEOUS BONDING WITH ALUMINUM VIA COMBUSTION REACTION IN Ti-B SYSTEM

Yong-Jai Kwon¹, Makoto Kobashi², Naoyuki Kanetake³, and Takao Choh⁴

¹ Department of Materials Processing Engineering, School of Engineering,
Nagoya University, Nagoya 464-8603, Japan: h982202d@mblox.media.nagoya-u.ac.jp

² kobashi@numse.nagoya-u.ac.jp

³ kanetake@numse.nagoya-u.ac.jp

⁴ choh@numse.nagoya-u.ac.jp

SUMMARY: The synthesis of the titanium diboride reinforced copper matrix composite and simultaneous bonding between the synthesized composite and aluminum via the combustion reaction in copper-titanium-boron system were experimentally investigated. In this process, the heat generated by the combustion reaction in copper-titanium-boron system was used for the bonding process as well as the synthesis process of the copper matrix composite. As a result of the combustion reaction, titanium diboride particles were formed in the copper matrix. The exothermic reaction among the elemental powders was initiated at about 1370K, which was nearly equal to the melting point of copper. The aluminum rod ranged from 20 to 60 mm in length was bonded with the copper matrix composite synthesized at the preheating temperature of 438K.

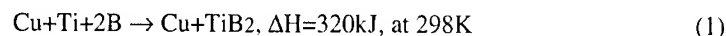
KEYWORDS: Combustion Synthesis, Bonding, Copper Matrix Composite, Titanium Diboride (TiB₂), Aluminum

INTRODUCTION

Combustion synthesis, also known as self-propagating high-temperature synthesis (SHS), is gaining an attention as a technique for synthesizing refractory materials⁽¹⁾. In this process, once a highly exothermic reaction is initiated at one end of a reactant which consists of the constituent elements by heating a small region of the reactant, the generated reaction spontaneously and continuously propagates throughout the whole reactant in the form of a combustion wave, with converting it into a product. As this process has many attractive advantages, such as high purity of the products, time and energy-savings process, and the possibility of synthesizing relatively complex materials, it has been used for the production of ceramics⁽²⁾, intermetallic compounds⁽³⁾, and composites⁽⁴⁾.

In this study, the synthesis of a titanium diboride (TiB₂) reinforced copper matrix composite and simultaneous bonding with aluminum via the combustion reaction in copper-titanium-boron system was experimentally investigated. Figure 1 shows the schematic

illustration of this study. As the compacted reactant composed of copper, titanium and boron powders was heated by an ignitor, it turns into the titanium diboride reinforced copper matrix composite by the combustion reaction among the starting powders, with generating the high reaction energy⁽⁵⁾ shown in eq. (1).



Such the high reaction energy generated by the combustion reaction can be used for the bonding process with aluminum as well as the synthesis process of the copper matrix composite. Figure 2 shows the adiabatic temperature (T_{ad}) in a wide variety of the volume fractions (V_f) of titanium diboride for the combustion reaction in copper-titanium-boron system. In the case of 60vol%TiB₂, it can be seen that the adiabatic temperature reaches up to about 2650K by the combustion reaction.

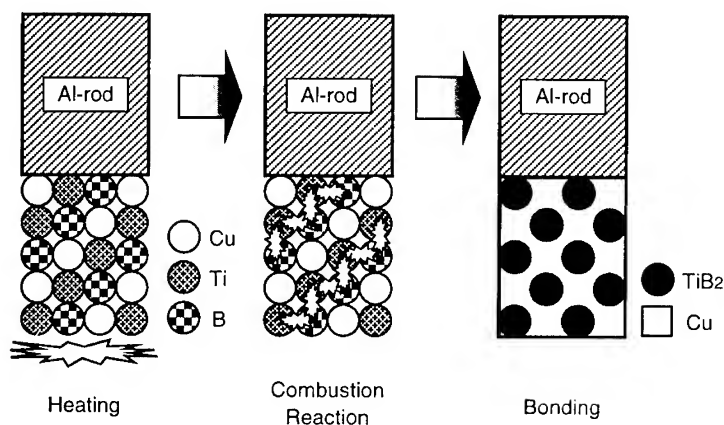


Fig. 1 Schematic illustration of this study.

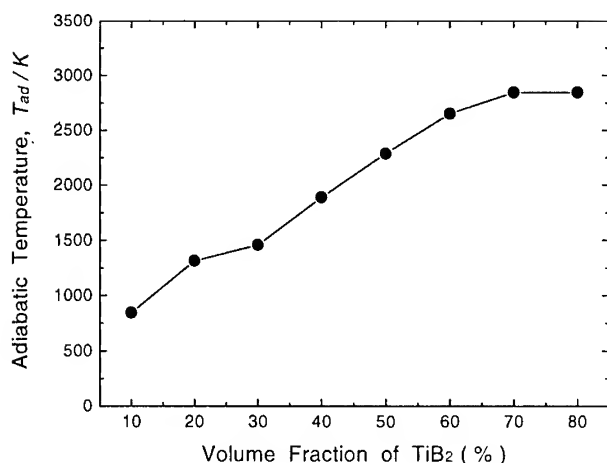


Fig. 2 Adiabatic temperature (T_{ad}) in a wide variety of the volume fractions (V_f) of titanium diboride for the combustion reaction in copper-titanium-boron system.

EXPERIMENTAL PROCEDURE

The copper powder (particle size: $-177\mu\text{m}$, purity: 99.9%), titanium powder (particle size: $-44\mu\text{m}$, purity: 99.9%) and boron powder (particle size: $-44\mu\text{m}$, purity: 99%) were used as the starting powders. On the assumption that all the titanium and boron are turned into titanium diboride (TiB_2) in copper during the combustion reaction, these powders were mixed with the mole ratio of $\text{Cu}:\text{Ti}:\text{B}=1.5:1:2$, which turns into the copper matrix composite with the titanium diboride of 60vol% after the combustion reaction. The powder mixture was pressed into cylindrical shape in a uniaxial press by the pressure of 196MPa. The diameter and height of these compacted reactants were approximately 15mm and 20mm, respectively. The pure aluminum rod was used for the bonding process. The diameter of the aluminum rod was 15mm and the length ranged from 20 to 60mm.

The specimens were set in the experimental apparatus like shown in Fig. 3. The combustion reaction was ignited from the bottom surface of the compacted reactant by the ignitor in an argon gas atmosphere. The pressure was 0.05MPa for the bonding process. The preheating temperature ranged from room temperature to 438K, which was controlled by the heater for preheating.

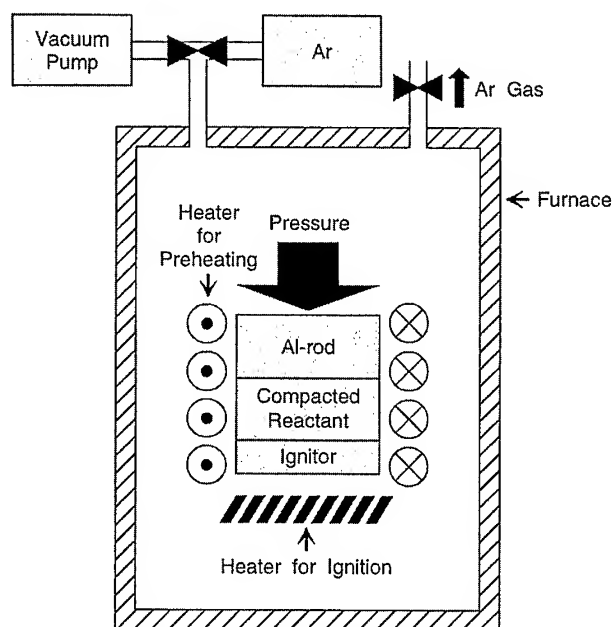


Fig. 3 Schematic illustration of the experimental apparatus.

RESULTS AND DISCUSSION

An X-ray diffraction (XRD) analysis was carried out to identify the phases present after the combustion reaction. Figure 4 shows X-ray diffraction patterns of the powder mixture and composite synthesized by the combustion reaction in 1.5Cu-Ti-2B system. For the X-ray

diffraction pattern after the combustion reaction, the only peaks of copper and titanium diboride were observed without the peaks of unreacted titanium and boron. This result suggests that all the titanium and boron turned into the titanium diboride during the combustion reaction.

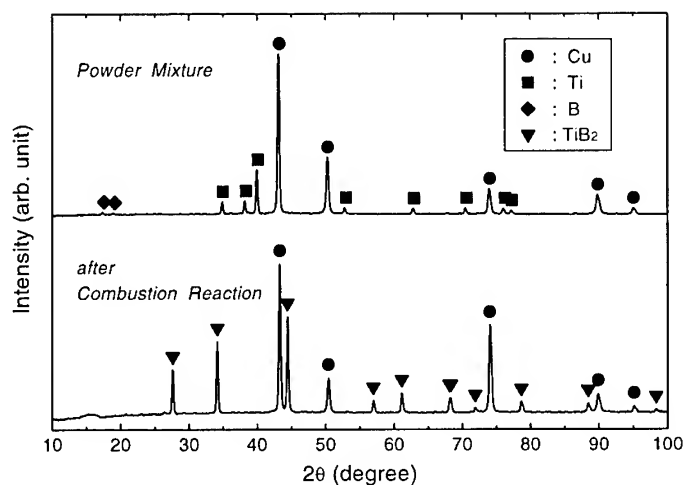


Fig. 4 X-ray diffraction patterns of the powder mixture and composite synthesized by the combustion reaction in 1.5Cu-Ti-2B system

The microstructure of the composite synthesized by the combustion reaction in 1.5Cu-Ti-2B system is shown in Fig. 5. The microstructure of the synthesized composite consisted of the copper matrix (brighter part) and the titanium diboride reinforcement (darker part). It can be seen that the titanium diboride particles formed by the combustion synthesis were uniformly dispersed in the copper matrix. The unreacted titanium and boron powders were not observed.

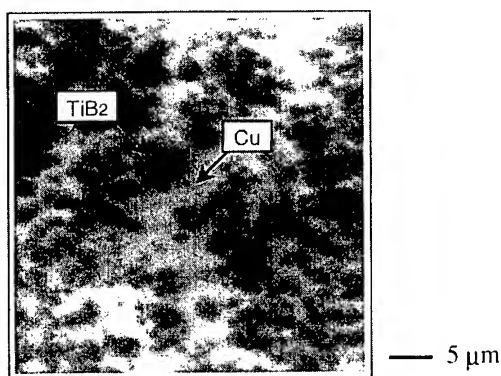


Fig. 5 SEM micrograph of the copper matrix composite synthesized by the combustion reaction in 1.5Cu-Ti-2B system.

In order to investigate the ignition temperature of the combustion reaction, the differential thermal analysis (DTA) was carried out. Figure 6 shows the differential thermal analysis curve of the compacted reactant with the mole ratio of Cu:Ti:B=1.5:1:2. After the endothermic reaction begins at approximately 1360K, the highly exothermic reaction among the elemental powders was observed at approximately 1370K. It is believed that the combustion reaction in this system initiated after the melting of copper, as this temperature is nearly equal to the melting point of copper.

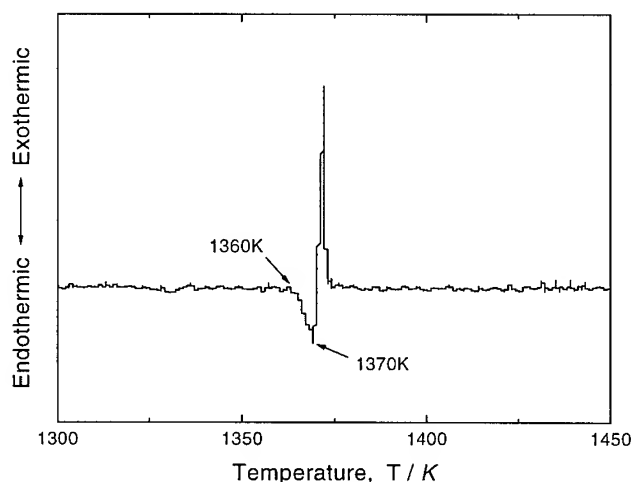


Fig. 6 Differential thermal analysis curve of the compacted reactant with the mole ratio of Cu:Ti:B=1.5:1:2.

The results of the bonding experiments of the copper matrix composite and aluminum rod are shown in Table 1. In the case of the preheating at room temperature, the aluminum rod ranged from 20 to 40 mm in length was successfully bonded with the copper matrix composite. As the preheating temperature increases to 438K, the longer aluminum rods (50 and 60 mm) were also successfully bonded with copper matrix composites. These results indicate that the preheating of the specimens has an effect on the bonding process.

Table 1 Results of the bonding experiments of the copper matrix composite and aluminum rod by the combustion reaction in 1.5Cu-Ti-2B system.

Length of Aluminum Rod (mm)	Preheating Temperature (K)	
	R. T.	438
20	O	O
30	O	O
40	O	O
50	×	O
60	×	O

CONCLUSIONS

1. The composite synthesized by the combustion reaction in copper-titanium-boron system consisted of copper (matrix) and titanium diboride particle (reinforcement).
2. The exothermic reaction in the compacted reactant with the mole ratio of Cu:Ti:B=1.5:1:2 was initiated at approximately 1370K, which is nearly equal to the melting point of copper.
3. The bonded specimens of the copper matrix composite and aluminum were obtained by the combustion synthesis in copper-titanium-boron system. The aluminum rod ranged from 20 to 60 mm in length was successfully bonded with the copper matrix composite synthesized by the combustion reaction at the preheating temperature of 438K.

REFERENCE

1. Z. A. Munir and U. Anselmi-Tamburini, "Self-propagating exothermic reaction: the synthesis of high temperature materials by combustion", *Mater. Sci. Rep.*, Vol.3, 1989, pp.277-365.
2. J. B. Holt and Z. A. Munir, "Combustion synthesis of titanium carbide: theory and experiment", *J. Mater. Sci.*, Vol.21, 1986, pp.251-259
3. K. A. Philpot, Z. A. Munir, and J. B. Holt, "An investigation of the synthesis of nickel aluminides through gasless combustion", *J. Mater. Sci.*, Vol.22, 1987, pp.159-169
4. A. Saidi, A. chrysanthou, J. V. Wood, and J. L. F. Kellie. "Characteristics of the combustion synthesis of TiC and Fe-TiC composites", *J. Mater. Sci.*, Vol.29, 1994, pp.4993-4998
5. I. Barin, F. Sauert, E. Schultze-Rhonhof, and W. S. Sheng. "Thermochemical data of pure substances", VCH, Vol.2, 1993, pp.1523.

Study on Technology for Manufacturing MMC by V-EPC Method

CUI YIHUA, TAO JIE and WO DINGZHU

Nanjing University of Aeronautical & Astronautics, Nanjing, P. R. China

SUMMARY: In this paper steel fiber/ZL109 matrix composites are prepared by V-EPC method, which is usually used for casting normal metals & alloys. The most important evaporative patterns are manufactured by putting the surface-treated (zinc plating) and mechanically fixed steel fiber into EPMMA-EPS foam. This kind of pattern is then buried in dry sand (without binder), and the melted aluminum is cast in the evaporative pattern. The mechanical properties of the prepared samples are tested, the microstructure and the fracture surfaces of the samples are also observed. The results show that the mechanical fixing method can be used for fiber perform, the optimum casting speed: $3\sim 4\text{Kg/s}$; vacuum degree: $-0.025\sim -0.04\text{MPa}$. The influencing factors for preparation of pattern and the effect of casting parameters on the properties of FRM are also analyzed in this paper.

KEYWORDS: V-EPC; metal matrix composite; evaporative pattern; perform

Fiber reinforced metal matrix composites (FRM) have been the representative of modern composites materials because of their excellent high-temperature properties, high specific strength and specific modulus, heat and electric transmission and so on. However, the complicated technologies and the high cost of production have limited the fields of their applications for a long period of time. Available methods for manufacturing MMC such as compression casting, vacuum casting, powder metallurgy^[1-3], have many disadvantages and demerits. For example, each method needs high investment for equipment but cannot produce complicated shaped products. All of the finished products with good surface can only be obtained by second processing. To develop new technology for FRM has been the popular topic in recent years.

Vacuum evaporative pattern casting (V-EPC), a common method to produce castings such as steel, iron, copper and etc. is carried out by putting evaporative pattern made up of expanded polystyrene (EPS) and reinforcing fiber into dry sand without any binder. Then mold under conditions of slight vibration and vacuum; pour melted metals or alloys into the pattern without any core and riser. Vacuum degree and vibration are kept during process of pouring and solidifying, then the original pattern is taken place by melted alloys, and thus an FRM casting is formed.

V-EPC method for manufacturing FRM has the following advantages:

- 1) It can make FRM with good surface and precise dimension. A special refractory coating which assures the smooth finish of FRM is applied in advance on the surface of perform. The size precision of the perform also assures that of FRM.
- 2) The shape of FRM is unlimited, especially fit for complex shape. The shape of pattern determines the finished shape of FRM, and also the distribution and the content of reinforcement

are variable freely.

3) The cost of FRM and investment of equipment are lower than that of existing methods.

4) V-EPC needs not second processing.

For the sake of the ripe technology in producing normal alloys and metals by V-EPC, there are two important problems to be solved to manufacture FRM by this method: ①How to prepare perform, that is how to put the reinforcing fibers into EPS and constantly keep their state when casting and solidifying. ②Infiltrating process of alloys, also how to control the parameters and assure the alloys to infiltrate completely.

In this paper, the preparation of pattern is introduced and the casting parameters are optimized with example of steel fiber reinforced ZL109 alloys.

1. Experimental details

The reinforcing fiber adopted in this experiment was steel fiber net with diameter of 110um, 150um, 300um and the matrix was ZL109 alloy with composition of 11.96wt% Si, 0.26wt% Fe, 0.96wt% Cu, 1.3wt% Ni, 85.52wt% Al.

1.1. Pattern fabrication

EPMMA-EPS co-polymerized resins were chosen for making original foaming grains whose properties were shown in Table 1.

Table 1 Properties of EPMMA-EPS co-polymerized resins

Appearance	Grain size	Apparent density	Volatile content	Foaming multiple
White grain	300-400um	0.54-0.65g/cm ³	12-15%	35

The pre-foamed grains were obtained by putting the original foaming grains into boiling water for 5-10 minutes, then dried, ripened and screened. The steel fiber net was treated in advance with zinc-plating and machined into 150mm× 100mm.The volume fraction of fiber in perform was computed according to the following formula:

$$V_f = \pi \rho_f d_f^2 k_f / 2t$$
 (1)

where, ρ_f is the weft density of steel fiber net; d_f is the fiber diameter; k_f is length ratio of fiber before and after bent; t is interlayer distance.

Fiber perform was fabricated from steel fiber net by mechanical fixing method and mixed with pre-foaming grains. Compressed the fiber perform into foaming mold, put it into boiling water for 10-12minutes and then drew the pattern, bond the pattern and a foam-runner, an ideal pattern was prepared.

Soaked the pattern with coatings, the typical prescription for them were showed in Table 2.

Table 2 Prescription for coating

Zircon Powder	Quartz powder	Binder	Suspended additive	Hardener	Water
100	6.0	50.0	4.0-6.0	2.2-3.0	100-130

1.2. Molding and casting

Put the prepared pattern into a special sand box and filled the box with dry sand without any binder and water, then covered it with a piece of PE film with diameter of 0.02mm, started the vibrator and vacuum machine, the molding processing was accomplished.

Through monitoring and controlling the vacuum degree within the sand box, cast the melting ZL109 alloy under temperature of 750-770°C, cooled down the castings and cleaned them up, plates of 20mm thickness were produced to machine as flexural strength specimens.

The microstructures of above specimens were observed by metallograph and the flexural fracture surfaces of them were examined in the scanning electron microscope (SEM).

2. Results and analysis

2.1. Observations of microstructure and flexural fracture surface

The typical metallgraph of the samples is shown in Fig.1. As can be seen, the steel fibers are oriented almost randomly in two dimensions in ZL109 alloy, such defects as openings, holes, inclusions are seldom found. The white or light points in Fig 2. are the corrosion-resistant silicon elements of high content in ZL109. Fig.3 is a single steel fiber section, where a clear layer of coating is about 3μm thickness, also a good interface between the coating and steel fiber is formed which shows that the coating is well-combined with ZL109 matrix. The flexural property data in Table 3 indicate that steel fibers have played a reinforcing role in ZL109 alloy and similarly state that V-EPC can be used to manufacture FRM.

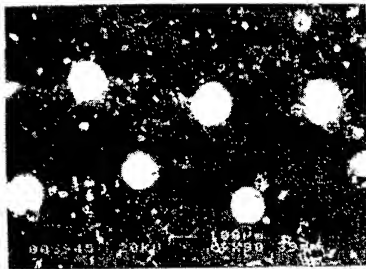


Fig.1 Microstructure of FRM

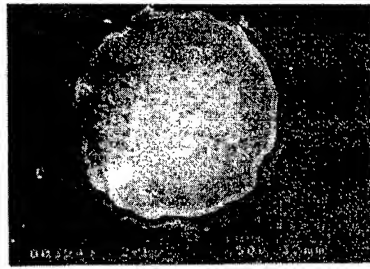


Fig.2 A single fiber section of FRM

Table 3 Flexural strength data of FRM

Fiber diameter/μm	Volume content of fiber			
	0	5	10	15
110	215	228	254	271
150	215	227	237	268
300	215	218	232	266

The flexural fracture surface of FRM is shown in Fig.3. It is obvious that the fracture plane is parallel to that of the matrix, displaying shear fracture characteristics. However, interface disintegration is clearly formed between the fiber and the matrix. Few alloys is adhered to the

surface of the fibers, on the other hand, the fracture matrix nearby presents toughness fracture characteristics. So a weak combination interface is formed when steel fiber is treated by zinc plating. This conclusion is also testified by the flexural strength data in Table 3. The flexural strength of FRM is only improved 25% when it is reinforced with 15vol% steel fiber.

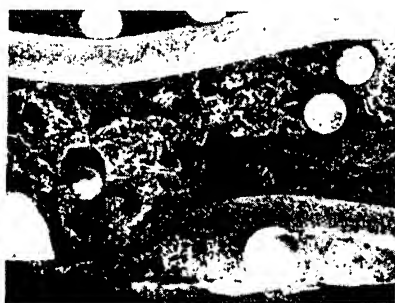


Fig.3 Flexural fracture surface of FRM

2.2. Discussion

(1) Pattern

The preparations of pattern are of importance to manufacture FRM by V-EPC method especially the type of resins for foaming, coatings, and fabrication of fiber perform. Foam resins chosen for V-EPC should completely be taken place by melting alloys without any remains; otherwise a good interface could not be obtained, which will worsen the properties of FRM. Normal EPS used for packaging cannot be used for V-EPC because it will give off a lot of smoke ($1200-1500\text{cm}^3/\text{g}$) when gasified. The smoke given off by EPMMA-EPS when gasified is only $200-400\text{cm}^3/\text{g}$, few remains is left. Coatings are the second vital to the preparations of pattern. Coatings can prevent the castings from adhering to the sand, raise the surface strength and overall stiffness of pattern and keep it in good shape when casting. Qualified coatings must possess good properties of daubing-up, ventilating and strength. The prescription in Table 3 had been proved to be suitable for making FRM which has good surface.

How to prepare fiber perform is equally important. Good perform should keep the fibers inside it in stable state when the foam is gasifying. The mechanical method, which is carried out by putting the fiber into framework and locating it, can successfully be applied in V-EPC process. Meanwhile, the limitations of this method is also obvious, it cannot manufacture FRM when fiber content is more than 25%. Under this circumstance, it is difficult to control the tiny distance between fiber layers. To make such FRM, the diameter, the warp and weft density of fibers should strictly be limited.

(2) Casting parameters

Casting parameters will directly affect the properties of prepared FRM; these parameters include casting temperature, casting speed, vacuum degree within casting mold.

① Casting temperature : Casting temperature is a key parameter to manufacture FRM with full shape, clear outline and perfect structure. V-EPC process for casting FRM needs higher temperature compared to casting common castings because higher temperature can improve the fluidity of alloy and compensate the temperature dropping caused by energy absorbing of foam and fibers. Test results show that castings can acquire the best quality when casting temperature is between 730°C and 740°C . In higher temperature elements are easy to lose, which will decrease the properties of FRM, increase holes content. While in lower casting temperature .the

fluidity of alloy will drop and many defects such as holes, openings will increase, the properties of FRM will also weaken.

② Casting speed : Low casting speed may give rise to sand box collapse while fast speed will cause alloy to overflow from runner, the sealed film to burn, vacuum system to be destroyed and result in disorder filling. For castings of not more than 20 Kg, the optimum speed is 3-4Kg/s.

③ Vacuum degree within mold : During casting, there is a distinct decrease in vacuum degree within the mold because the sealed film will be destroyed and pattern will gasify (see in Fig.4). Under the same seal condition, the vacuum degree in the mold will drop $0.01 \sim 0.03$ MPa, so it is very important to choose original vacuum degree, higher vacuum degree will cause sand to bind each other and fibers to be deformed and perform to be destroyed. When excessive vacuum degree is applied, the alloy can even flow along the mold; this will prevent the gases from removing and bring many defects in the castings. On the contrary; lower vacuum degree will prohibit gas produced by pattern from excluding and alloy sprinkle is easy to happen. When vacuum degree is controlled between -0.025 MPa and -0.040 MPa, the filling of alloy is very smooth and steady and the best quality is easy to acquire.

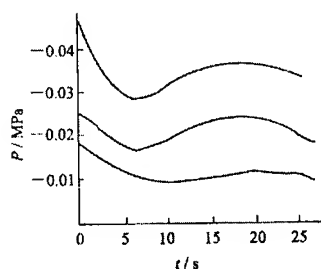


Fig.4 Vibrations of vacuum degree during casting

3. Conclusions

- 1) V-EPC method can successfully be used for manufacturing FRM.
- 2) Mechanical fixing may be applied to prepare perform.
- 3) The optimum parameters for manufacturing steel fiber/ZL109 by V-EPC are:
casting temperature; $730-740^{\circ}\text{C}$; casting speed: $3-4\text{Kg/s}$; vacuum degree $-0.025 \sim -0.040$ MPa.
- 4) The interface of steel fiber/ZL109 is weak when steel fibers are treated by zinc plating.

REFERENCES

1. Hack J E Page R A, Leverant G R. Tensile and fatigue behavior of aluminum oxide fiber reinforced magnesium composites. Metallurgical Transaction A. 1984,15A(7):pp1389-1405
2. Kchara S. Materials and manufacturing process. 1991.51
3. Koch.P. Annual review—pressure die casting Giesserei 72 No 18(September 1985)pp521-524
4. Clyne, T.W. and Mason, J.F. Metal Trans A 18A(1987)pp1519-1529
5. Z.ZHANG,S.LONG and H.M.FLOWER. Light alloy composite production by liquid metal infiltration. Composites, Vol 25,No.5,1994.pp380-385

THERMAL PROPERTIES OF HIGH VOLUME FRACTION SiC PARTICLE REINFORCED Al MATRIX COMPOSITES

Hyo S. Lee and Soon H. Hong

*Department of Materials Science and Engineering, Korea Advanced Institute of
Science and Technology, 373-1 Kusung-dong, Yusung-gu, Taejon, 305-701, Korea
shhong@sorak.kaist.ac.kr*

SUMMARY: Thermal conductivity and coefficient of thermal expansion (CTE) of 50~71 vol% SiC particle reinforced Al matrix composites were investigated for possible application as electronic packaging material. 50~71vol% SiC particulate preforms were fabricated by ball milling & pressing method, which consisted of the wet mixing of SiC particles, binder, distilled water and followed by cold pressing. 50~71vol% SiCp/Al composites were fabricated by pressure infiltration casting process. Thermal conductivity of SiCp/Al composites decreased from 177W/mK to 123W/mK and coefficient of thermal expansion decreased from 10ppm/K to 6ppm/K with increasing the volume fraction of SiC particles from 50% to 71%. The measured CTEs of SiCp/Al composites were in good agreement with the calculated CTEs based on the Turner's model. The measured thermal conductivities were lower than the calculated thermal conductivities based on the Maxwell's model at higher volume fraction of SiC particles due to an agglomeration of SiC particles, remaining SiO₂ and residual pores.

KEYWORDS: SiCp/Al composite, SiC particulate preform, pressure infiltration casting process, electronic packaging, thermal conductivity, coefficient of thermal expansion

INTRODUCTION

Metal matrix composite(MMCs) have been recently developed for electronic packaging applications due to their attractive combination of physical properties, manufacturing flexibility and relatively inexpensive cost. One unique advantage of metal matrix composites is a capability to tailor the thermal properties, such as thermal conductivity and coefficient of thermal expansion(CTE), through a proper control of reinforcement and matrix. In addition, the manufacturing flexibility of metal matrix composite by various processes allows easy fabrication of complicated shaped parts [1-3].

Metal matrix composites for electronic packaging applications have been actively investigated since late 1980's and several electronic packaging components have been commercialized using MMCs [4-5]. It is important to increase the volume fraction of reinforcement above 50% for electronic packaging applications so as to reduce the coefficient of thermal expansion comparable to that of alumina substrate or semiconductor such as silicon and gallium arsenide,

which coefficient of thermal expansion is ranged 6~7ppm/K. It is possible to apply the high volume fraction SiCp/Al composites to heat sink materials such as heat spreader, microwave housing, microwave lids in electronic packaging applications.

In this study, the 50~71vol% SiCp/Al composites were fabricated by pressure infiltration casting process of pure Al matrix into α -type SiC particulate preforms. The thermal conductivity and the coefficient of thermal expansion of 50~71vol% SiCp/Al composites were characterized with varying microstructure and volume fraction of SiC particles using laser flash method and thermomechanical analysis.

EXPERIMENTAL PROCEDURES

High volume fraction over 50vol% SiC particulate preforms were prepared by wet ball milling of unimodal or bimodal sizes of SiC particles, consisted of 48 μ m and 8 μ m, in diameter with 0~3wt% of SiO₂ as inorganic binder and 1wt% of cationic starch as organic binder in distilled water. The wet milled mixtures were consolidated into cylindrical preforms by cold pressing with 1.2MPa at room temperature. The consolidated SiC particulate preforms were dried and followed by calcination at 1100°C for 4h. The distribution of SiC particles and residual inorganic binders in SiC particulate preforms were observed by scanning electron microscope.

Pure Al melt was infiltrated into SiC particulate preforms to fabricate SiCp/Al composites by pressure infiltration casting process, which was performed by infiltration of Al melt heated 700~900°C into SiC particulate preforms preheated to 750 °C by applying a pressure ranged 10~70MPa for 30 seconds. Densities of SiCp/Al composites were measured by the Archimedes water immersion method. Thermal conductivities of SiCp/Al composites were measured by laser flash method and coefficients of thermal expansion were measured by thermomechanical analysis (TMA). Electrical conductivities of SiCp/Al composites were measured by 4-point probe method.

RESULTS AND DISCUSSION

Fabrication Process and Microstructure of High Volume Fraction SiCp/Al Composites

The 50~71vol% SiC particulate preforms were fabricated by the ball milling and pressing method consisted of mixing, compaction, drying and calcination processes. The maximum allowable volume fraction was sensitively dependent on the size of SiC particles. SiC particulate preforms containing up to 60vol% SiC were fabricated using an unimodal size of 48 μ m SiC particles, while, SiC particulate preforms containing 60 to 71vol% could be fabricated using bimodal sizes of SiC particle consisted of 48 μ m and 8 μ m by effectively filling the space of larger particles with smaller ones. Two step drying process consisted of natural drying at 25°C for 36h and forced drying at 100°C for 12h was performed in order to prevent the micro-cracking of SiC particulate preform during the drying process. In order to investigate the effect of inorganic binder, the surface of SiC particulate preforms was analyzed by XRD after calcination at 1100°C for 4h. Fig. 1(a) shows the XRD analysis of SiC particulate preform after calcination at 1100°C for 4h and the arrow mark indicates the (101) peak of cristobalite SiO₂ located at the interface of SiC particles as shown in Fig. 1(b). It is known that the formation of cristobalite SiO₂ allows bonding between SiC particles, which increases the strength of SiC particulate preforms [6-8]. The pressure infiltration casting

process of SiCp/Al composites consists of the infiltration of Al melt heated 700–900°C into porous SiC particulate preforms under high pressure. The Al melt was fully infiltrated into SiC particulate preforms at 800 °C above 50MPa as shown in Fig. 2(a) and 2(b). The microstructures of SiCp/Al composites with varying volume fraction of SiC particles are shown in Fig. 3(a)–3(c). The 50vol% SiCp/Al and 59vol% SiCp/Al composites were consisted of unimodal SiC particle size of 48 μ m. The 71vol% SiCp/Al composites were consisted of bimodal SiC particle sizes of 8 μ m and 48 μ m. In 71vol% SiCp/Al composites, the smaller SiC particles of 8 μ m were agglomerated between the larger SiC particles of 48 μ m as shown in Fig. 3(c). The relative densities were measured as 99%, 99% and 97% for 50vol%, 59vol% and 71vol% SiCp/Al composites, respectively.

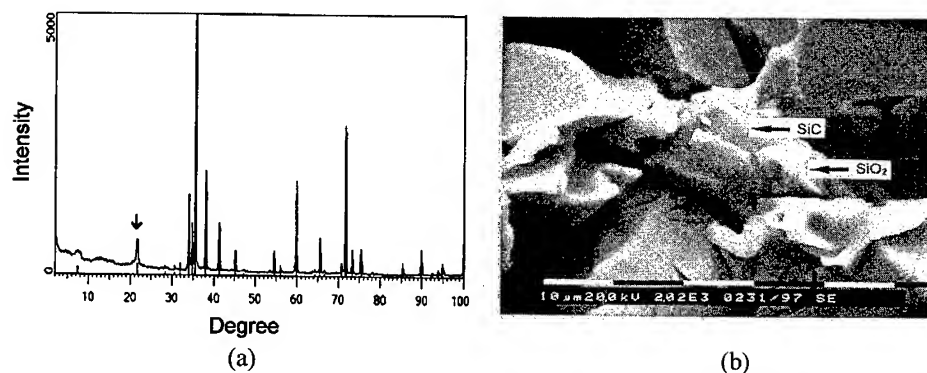


Fig. 1. Analyses of 71vol% SiC particulate preform. (a) XRD analysis of 71vol% SiC particulate preform after calcination at 1100 °C for 4 hours. The arrow indicates the (101) peak from SiO₂, cristobalite having tetragonal structure, (b) SiO₂, cristobalite observed at the interfaces of 71vol% SiC particles.

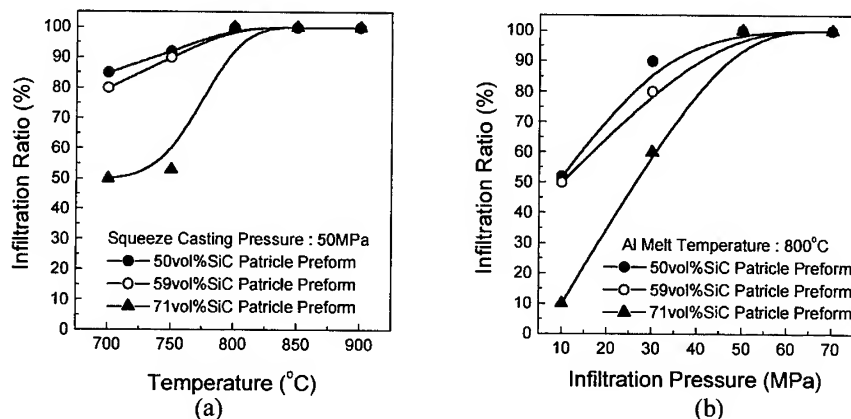


Fig. 2. Variation of infiltration ratio of Al matrix into SiC particulate preforms. (a) With varying the Al melt temperature, (b) with varying the infiltration pressure.

Thermal Properties of High Volume Fraction SiCp/Al Composites

The coefficient of thermal expansion could be estimated with varying the volume fraction of reinforcement by Turner's model [9]. Considering the constraint due to thermal expansion of

each component in Turner's model, the coefficient of thermal expansion is represented as following Eq. (1) ;

$$\alpha_c = \frac{V_r K_r \alpha_r + V_m K_m \alpha_m}{V_r K_r + V_m K_m} \quad (1)$$

where α_c , α_r , and α_m are coefficients of thermal expansion of composite, reinforcement and matrix, respectively, V_r is volume fraction of reinforcement and K_r and K_m are bulk moduli of reinforcement and matrix, respectively.

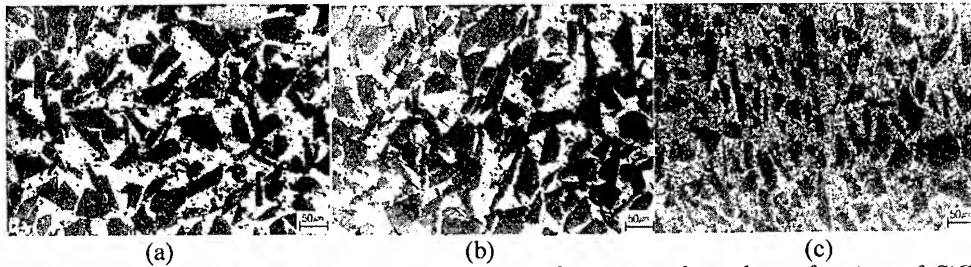


Fig. 3. Microstructures of SiCp/Al composites with varying the volume fraction of SiC particles. (a) 50vol% SiCp/Al composite containing unimodal size of 48 μ m SiC particles, (b) 59vol% SiCp/Al composite containing unimodal size of 48 μ m SiC particles and (c) 71vol% SiCp/Al composite containing bimodal sizes of 8 μ m and 48 μ m SiC particles.

The thermal conductivity could be estimated with varying the volume fraction of reinforcement by Maxwell's model [10]. Maxwell's model predicts the overall thermal conductivity of the mixture by considering the random distribution of spherical reinforcement in matrix as shown in Eq. (2) ;

$$k_c/k_m = \frac{2 - 2V_r + (1 + 2V_r)k_r}{2 + 2V_r + (1 - V_r)k_r} \quad (2)$$

where k_c , k_r and k_m are thermal conductivities of composite, reinforcement and matrix, respectively, V_r is volume fraction of reinforcement.

Fig. 4 shows the variation of thermal properties of SiCp/Al composites with increasing the volume fraction of SiC particle. The solid line and the dotted line in Fig. 4(a) are the theoretically calculated values of the coefficient of thermal expansion with varying the volume fraction of SiC particle based on the rule-of-mixture and Turner's model, respectively. The experimental values of the coefficient of thermal expansion ranged 6~10ppm/K agreed well with the theoretical values based on Turner's model in Fig. 4(a). The experimental values of the thermal conductivity agreed with the theoretical values based on the rule-of-mixture and Maxwell's model at 50vol% and 59vol% SiCp/Al composites was shown in Fig. 4(b). The thermal conductivity decreased from 177W/mK to 172W/mK with increasing the volume fraction of SiC particles from 50vol% to 59vol%. However, the measured thermal conductivities of 71vol% SiCp/Al composites were much lower than the theoretical value of 123W/mK based on Maxwell's model. It is suggested that the lower thermal conductivity in 71vol% SiCp/Al composites is due to an agglomeration of smaller SiC particles and remaining inorganic SiO₂ binders. The remaining inorganic binder also decreases the thermal conductivity of SiCp/Al composites because of its lower conductivity which is about 1.1~1.4W/mK. In addition, the agglomeration of smaller SiC particles prevents the infiltration of Al melt into SiC

preforms. The incomplete infiltration of Al melt causes the formation of residual pores at the interfaces of SiC particles and Al matrix, which decreases the density of SiCp/Al composites. The relative density of 71vol% SiCp/Al composites were measured as 97%, which is lower than that of 50~59vol% SiCp/Al composites. Therefore, the complete infiltration of Al melt was much prominent with increasing volume fraction of SiC particles. Fig. 5(a) shows the variation of thermal conductivity and electrical conductivity with varying SiC particle volume fraction in SiCp/Al composite. The electrical conductivity of SiCp/Al composite containing over 70vol% SiC particles decreases rapidly as shown in Fig. 5(a). The average interparticle spacing between SiC particles for 50vol% SiCp/Al composites was measured as $5.7\mu\text{m}$ and was decreased to $2.3\mu\text{m}$ for 71vol% SiCp/Al composite as shown in Fig. 5(b).

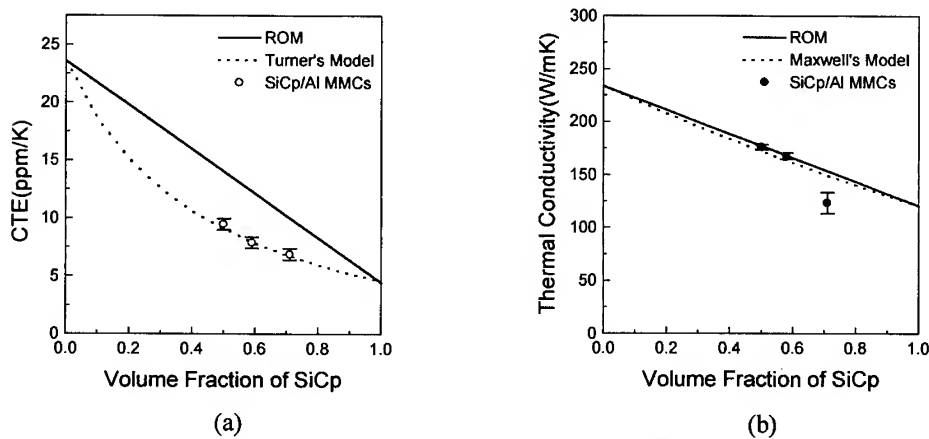


Fig. 4. The variation of thermal properties of SiCp/Al composites with increasing the volume fraction of SiC particle. (a) Coefficient of thermal expansion, (b) thermal conductivity.

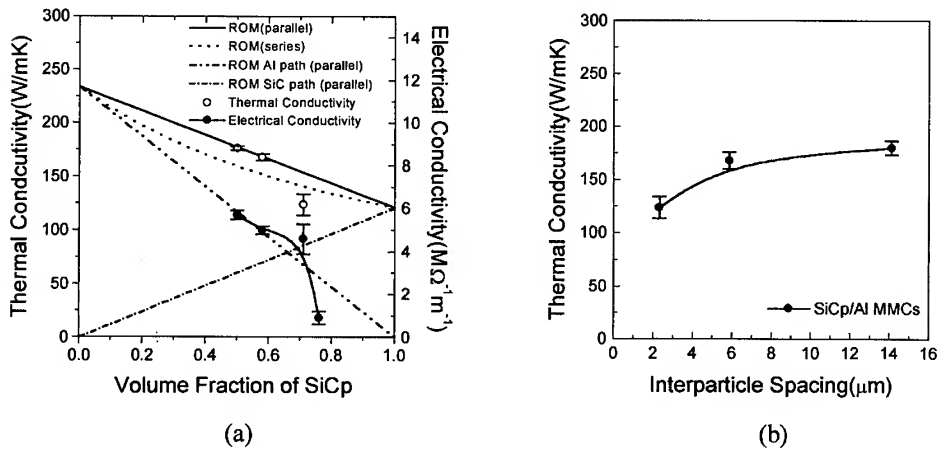


Fig. 5. Thermal conductivity and CTE of SiCp/Al composites with increasing the volume fraction of SiC particle. (a) Thermal conductivity and electrical conductivity with increasing the volume fraction of SiC particle, (b) thermal conductivity with increasing the interparticle spacing.

Thermal conductivity is sensitive to the path of Al matrix phase. Besides, as the volume fraction of SiC particles increased, the amount of residual pores increased due to inadequate infiltration of Al melt. As the result, the measured thermal conductivity was much lower than the calculated thermal conductivity of SiCp/Al composites.

CONCLUSIONS

1. 50~71vol% SiC particulate preforms were successfully fabricated by the ball milling and pressing method. The SiC particulate preforms containing a maximum of 60vol% SiC particle could be fabricated using an unimodal size of 48 μ m SiC particles. The SiC particulate preforms containing over 70vol% could be fabricated using bimodal sizes of SiC particle, consisted of 48 μ m and 8 μ m, by effectively filling the space of larger particles with smaller ones.
2. 50~71vol% SiCp/Al composites were successfully fabricated by fully infiltrating Al melt into SiC particulate preforms at 800 °C above 50MPa. The relative densities of SiCp/Al composites decreased from 99% to 97% with increasing the volume fraction of SiC particles from 50% to 71%.
3. The SiCp/Al composites decreased from 10ppm/K to 6ppm/K with increasing volume fraction of SiC particle ranged from 50% to 71%, which agreed well with the theoretical values based on Turner's model without regard to the remaining inorganic binders and the residual pore.
4. The thermal conductivity of SiCp/Al composites decreased from 177W/mK to 123W/mK with increasing volume fraction of SiC particles ranged from 50% to 71%, which agreed well with the theoretical values up to 70vol% SiC particle. However, the thermal conductivity of 71vol% SiCp/Al composite was measured much lower than the theoretical value due to the remaining inorganic binders, the residual pore and the discontinuous matrix phase.

REFERENCES

1. Guillermo L. Romero and Joe L. Martinez Jr., *International J. of Microcircuits and Electronic Packaging*, vol. 18, no. 3, 1995, pp. 246.
2. J. Sadanandam, G. Bhikshamaiah and M. K. Jain, *J. of Mater. Sci. Let.*, vol. 11, 1992, pp. 1518.
3. M. Okumura, Y. Koyo, T. Ito, K. Yoshizaki, H. Yamashita and T. Fujiwara, *Proceeding of International SAMPE Electronic Conference*, vol. 6, 1992, pp. 285.
4. M. K. Premkumar, W. H. Hunt and R. R. Sawtell., *JOM*, July, 1992, pp. 24.
5. C. Zweben, *JOM*, July, 1992, pp. 5.
6. Jeng-Maw Chiou and D. D. L. Chung, *J. of Mater. Sci.*, vol. 28, 1993, pp. 1135.
7. Ralph K. Ileler, "The chemistry of silica(solubility, polymerization, colloid and surface properties and biochemistry)", A Wiley-Interscience Publication, 1987.
8. Jeng-Maw Chiou and D. D. L. Chung, *J. of Mater. Sci.* vol. 28, 1993, pp. 1447.
9. W. D. Kingery, H. K. Bowen and D. R. Uhlmann, *Introduction to Ceramics*, 1975.
10. D. R. Poirier and G. H. Geiger, *Transport Phenomena in Materials Processing*, TMS, 1994, pp. 188.

STRENGTHENING OF PARTICULATE METAL MATRIX COMPOSITES DUE TO GRAIN BOUNDARIES

M.J. Hadianfard

*Department of Materials Science and Engineering
Shiraz University, Shiraz, Iran
hadianfa@succ.shirazu.ac.ir*

SUMMARY: The effect of 10,15 and 20 volume percent of SiC reinforcement particulate on grain structure of a 6061 Al alloy were investigated by optical and electron microscope. The strength of 6061 Al plane alloy and the composite materials were also measured, and contribution of the particles to strengthening of the materials due to effect of particles on grain structure of the matrix alloy were discussed. The results show reinforcing particles have a considerable affect on grain size and strength of the matrix.

KEYWORDS: Metal Matrix- Composite- Aluminum- Grain- Strengthening

INTRODUCTION

Metal matrix composites combine metallic and ceramic properties to produce attractive mechanical properties such as high strength and modulus and low sensitivity to surface flaw. The strengthening of metal matrix composites have been the subject of many investigations [1-3]. One method has been used to explain the strengthening of MMC_s is based on change in the microstructure of the matrix metal due to introduce reinforcing particles in to the matrix [3,4]. A part of the effect of reinforcement phase is occurring on the grain structure of the matrix.

The objectives of the current work is to find effects of reinforcement particles on grain structure of matrix and contribution of this effect on strength of the composites.

EXPERIMENTAL PRODUCER

Materials and Heat Treatment

A 6061 aluminum alloy and there composite materials consisting of 6061 Al alloy with, 10, 15 and 20 volume percent of SiC particles were used for this investigation.

The SiC particles with angular shape and average size of 18.3 μm and aspect ratio of 1.77 were used for reinforcing 6061 Al alloy. All tested materials were produced by liquid metallurgy consisting of casting and hot extrusion. Prior to testing specimens were heat treated to peak-aged condition (T6) by heating at 530°C for 1.5 hours, cold water quenching , natural aging at room temperature for 24 hours, and artificial aging at 175°C for 8 hours [5].

Metallography and Electron Microscopy Examination

To study distribution of reinforcing particles and microstructure of the materials optical and SEM electron microscope were used. For preparation of metallurgical specimens, their surface were polished up to 1/4 μM diamond paste and then etched with suitable solution. Since observation of grain structure of 6061 Al alloy is difficult and it becomes more difficult when SiC particle added to the matrix, several etchant solution were examined. In addition the etching process were not completely reproducible even with successful solutions. For measurement of grain size from each materials 3 specimens and on each specimen 5 field were selected, the measurement were carried out by lineal intersection method according to ASTM E112 standard.

Tensile Test and Microhardness Tests

On each materials three repeated tensile tests were conducted. Tensile testing was performed using an Instron machine. Microhardness tests were carried out on polished surfaces of specimens using a Vickers Micro-hardness testing machine with an applied load of 100g and loading time of 15s. For each specimen 10 measurements within the matrix and away from any particles were obtained.

RESULTS

Metallographic observations show that all of the tested materials have almost uniform grain size with small variation in the size of their grain. The variation in the grain size of unreinforced alloy is higher than variation in the composite materials, the grain size uniformity almost increased with increasing reinforcement volume percent.

The result of grain size measurement on the plane alloy and composite materials indicates that while average grain size of plane alloy is 75 μM , average grain size of 10, 15 and 20 volume percent composites are 35, 27 and 23 μm respectively. This results show increase in volume percent of reinforcing particles leads to decrease grain size of the matrix alloy. Figure 1 shows grain structure and particle distribution of the 15 vol% composite material.

Investigation of the composite structures by electron microscope shows a large number of particles are laying on the grain boundary areas or very near to these areas. In addition many of particles are observed on grain corner and grain edge of the matrix alloys in the all tested specimens figures 2 and 3 are show the interaction of reinforcing particles and grain boundaries.

The result of microhardness tests is shown that microhardness of plane alloy was 126 VHN and composite materials had hardness of 134, 137 and 139 VHN for 10, 15 and 20 vol % composites respectively. This results indicate that matrix hardness increase with increasing reinforcing particles, even in points far from the particles.

The results of tensile tests shows while unreinforced 6061 Al alloy presents 275 MPa as a yield strength composite materials present 317, 329 and 341 MPa for 10, 15 and 20 volume percent composite respectively. These result clearly shows reinforcing of 6061 Al alloy with SiC particles raised its yield strength. Addition in yield strength of 6061 Al alloy increased with increasing the volume fraction of the particles.

DISCUSSION

The result of metallography and electron microscopy investigations show that SiC particles have an strong effect on grain size and grain structure of the aluminum alloy. The effect of ceramic particles on grain boundary of the matrix alloy is largely dependent on surface energy between particles and matrix (γ_{pm}), wetting angle between these two phase and grain boundary specific energy (γ) when a particle with given size and shape intersects with a grain boundary, the particle effectively removes a region of boundary, therefore the total energy of system decreases; thus the particle make an angle to the boundary which is function of γ_{pm} and γ [6,7]. As a result of this interaction a drag force is produced by the particle, which is controls grain boundary movement and grain size. It is shown that the drag force is changing with particle shape and aspect ratio [6]. In the case of a non spherical particle with

aspect ratio of "a" when the particle meets a grain boundary with angle of 90° the drag force is calculated [6] as:

$$F_d = \pi r \gamma [(1+2.14a)/(\pi a^{1/2})] \quad (1)$$

when r is radius of a spherical particle with the same volume .

From this relation can be seen that the pinning force which is produced by a single particle is function of aspect ratio of particle. the pinning pressure (P) produced by particles on grain boundaries is also function of particle volume fraction (V_f). The pinning force at which point the drag force reaches a maximum is calculated [6] as:

$$P = (1.2 \gamma V_f^{3/2})/r \quad (2)$$

For 10, 15 and 20 volume percent of particles with average radiuses of r and matrix with grain boundary energy of γ , maximum drag pressures are $5.56 \gamma/r$, $7.3 \gamma/r$ and $8.84 \gamma/r$ respectively. It is seen pressure is increased with increasing V_f but the rate of increase, reduces with further increase in volume percent of particles. the same trend is observed from metallugraphy tests . The experimental results show effect of addition of 10 volume percents of ceramic particles on grain size of matrix is very large but the effect of the second 10 percent of particles is much less than the effect of the first 10 percent of them. The effect of reinforcing particles on grain size of matrix (D) is calculated by Miller et al. [8] as:

$$D = 2r [(1-V_f)/V_f]^{1/3} \quad (3)$$

In the present case the average diameter of reinforcing particle ($2r$) can be assumed as $10.45 \mu\text{m}$, therefore for 10, 15 and 20 volume percent of particles , calculated grain sizes are 21.74 , 18.6 and $16.6 \mu\text{m}$ respectively. Although these results are much smaller than measured grain size in all tested composite materials but they show similar trend with experiment and indicate that grain size decreases with increasing volume percent of particles.

The effect of grain size on strength of an alloy can be calculated by Hall-Petch equation [9] from which:

$$\Delta\sigma = K_y D^{-1/2} \quad (4)$$

where K_y is constant and for Al alloy is equal to $0.1 \text{ MNm}^{-3/2}$ [8]. This value is 11.5 MPa , 16.9 MPa and 20.8 MPa for unreinforced alloy, 10, 15 and 20 volume percent composites respectively. Therefor strengthening value which is produced by particles over the matrix alloy due to change in grain size of the matrix is 5.4 MPa , 7.7 MPa and 9.3 MPa for 10, 15 and 20 volume percent particles.

Comparison these values with the results of tensile test shows grain boundary strengthening is produced 5.3% , 5.8% and 6% of strength of 10, 15 and 20 volume percent composites respectively. the contribution of the grain size in strengthening of composites over plane alloy is 12.6%, 10.7% and 9% for 10, 15 and 20 volume percent composites respectively. The results of microhardness tests also show hardness of matrix in composites are much higher than hardness of the matrix in plane alloy. A part of this increase in hardness can be attributed to decrease in grain size of the composite materials. The other parts of strengthening in MMCs over plane alloy may be related to other change in microstructure of the materials such as, generation of high dislocation density [10], effect of ceramic particles on precipitate particles [5] and effect of ceramic/matrix interfaces.

CONCLUSION

Since composite system likes to decrease its internal energy, by reducing grain boundary areas, a great number of reinforcing particles accumulates on grain boundaries and near to the grain boundary areas. They produce a drag force to decrease grain areas and grain sizes. The increase in grain sizes of the matrix increases with an increase in volume fraction of the particles. A decrease in the grain size of the material lead to increase in its strength and

therefore particles contribute in to the strengthening of the composite material. by effect on grain structure of the materials.

ACKNOWLEDGMENT

Author wish to thank the office of research council of Shiraz University for financial support through grant number of 75-EN-964-570

REFERENCES

1. C.G. Boehlert, B.S. Majumdar, Krishnamurthy, and D.B. Miracle, Metall and Mate. Trans. A, 1997, Vol. 28A, pp 309-323.
2. J. Yang, S.M. Pickard, C. Cady, A.G. Evans and R. Mehrabian. Acta. Metall. Mater., 1991, Vol. 39, pp. 1863-1869.
3. C. Vorturries and T.W. Hall, J. Mat. Sci., 1991 Vol. 26, pp. 424-249.
4. F.J. Humphreys, Dislocation-Particles Interactions. in Dislocation and Properties of Real Materials, Pub. Institute of Metals, London. 1985, pp. 175-205.
5. M.J. Hadianfard, J. Healy and Y.W. Mai. J. Mat. Sci. 1993, Vol. 28 , pp 3668-3669.
6. F.J. Humphreys and M. Hatherly in "Recrystallization and Related Annealing Phenomena", 1996, Pergamon Press.
7. D.A. Porter and K.E. Easterling. Phase Transformations in Metals and Alloys. Van Nostrand and Reinhold (UK).co. Ltd, 1983
8. W.S. Miller and F.J. Humphreys, in Fundamental Relationship Between Microstructure & Mechanical Properties of Metal Matrix Composites. Edited by P.K. Liaw and M.N. Gungor, TMS, 1990, pp 175-202.
9. Mc Elary and Z.C. Sckopiak, Int. met. Rev. 1972., Vol. 17, pp 175-202.
10. R.J. Arsenault and N. Shi., Mater. Sci. Engng., 1986. Vol. 81, pp 175-187.

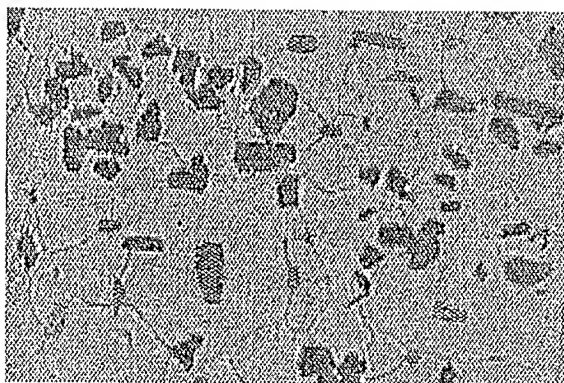


Fig. 1 Grain Structure of 15 vol % composite

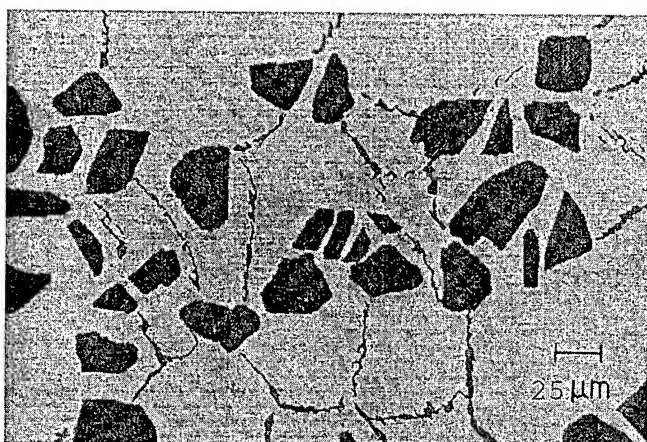


Fig. 2 Optical photograph showing interaction of reinforcing particles with grain of the matrix

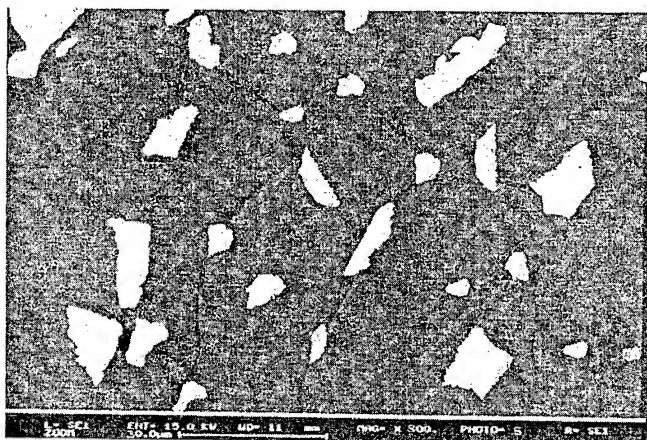


Fig. 3 Electron microscopic photograph showing interaction of reinforcing particles with grain of the matrix

EVALUATION OF HOT CORROSION RESISTANCE OF Al_2O_3 AND YAG BY COMPUTER SIMULATION

Akihiko Otsuka¹, Yoshiharu Waku¹, Kuniyuki Kitagawa² and Norio Arai²

¹ Japan Ultra-high Temperature Materials Research Institute (JUTEMI)
Okiube 573-3, Ube, Yamaguchi 755-0001, JAPAN:otsuka@jutem.co.jp

² Research Center for Advanced Energy Conversion, Nagoya University, Furo-cho,
Chikusa-ku, Nagoya 464-8603, Japan:narai@mhlab.nuce.nagoya-u.ac.jp

SUMMARY: The chemical stability of Al_2O_3 and $\text{Y}_3\text{Al}_5\text{O}_{12}$ (YAG) in a complex atmosphere of H_2O , CO_2 , H_2 and CO has been analyzed using the computer simulation based on the principle of minimizing the Gibbs free energy of the system. On the basis of thermodynamic calculations, the upper temperature limits of these materials for long-term use were predicted. The calculation result shows the main decomposition Al_2O or Y_2O gases increases with the increases in the temperature and partial pressure of corrosive gases. However, the partial pressure of the reaction product gases is less than 1 ppm in total at 1500°C in pure H_2 and CO . In the CH_4 combustion fields, Al_2O_3 can be used at up to about 2000°C and YAG at up to about 1900°C . Therefore, these materials are considered to pose no serious problems in long-term use below these temperatures.

KEYWORDS: chemical stability, Al_2O_3 , YAG, thermodynamic calculation.

INTRODUCTION

Ceramics and ceramics-matrix composites are being developed for a variety of high-temperature applications. Oxide ceramics have higher potential to maintain mechanical properties in oxidizing atmospheres than non-oxide ceramics. In addition to an understanding of mechanical properties at high temperatures, knowledge of the chemical properties as a function of temperature is essential for component design and property prediction.

Recently, a new eutectic composite of oxide ceramics has been developed in Al_2O_3 - $\text{Y}_3\text{Al}_5\text{O}_{12}$ (YAG), and it was found to be a promising candidate material for structural applications at high temperature, such as gas turbine components. This eutectic composite has a new microstructure, in which single crystals Al_2O_3 and YAG are three-dimensionally and continuously connected and finely entangled without grain boundaries. This composite is thermally stable at 1700°C in air for 1000 hours and has the following properties [1-3]:

- 1) Compressive creep strength at 1600°C and strain rate of 10^{-4} sec^{-1} are about 13 times higher than those of sintered composites under the same composition.
- 2) Flexural strength at room temperature can be maintained almost up to the melting point of about 1820°C .

A Detailed understanding of hot corrosion resistance in combustion gases is important to enable us to apply this material to aero gas turbines and power generation systems with non-cooled turbine blades operating at temperatures above 1500°C . In the present study, the

chemical stability of Al_2O_3 and YAG in an atmosphere containing water (H_2O), carbon dioxide (CO_2), hydrogen (H_2) and carbon monoxide (CO) was examined as a function of temperature by means of thermo-chemical simulations. On the basis of thermodynamic calculations, upper temperature limits of these materials for long-term use in an exhaust gas atmosphere during the CH_4 -combustion are predicted.

EQUILIBRIUM CALCULATIONS

All of the equilibrium calculations were performed using the computer program ChemSage. This program was originally developed by Eriksson [4] and it has been described in detail elsewhere [5,6]. This computer program is based on the principle of minimizing the Gibbs free energy of the system. The equilibrium compositions, including both condensed phases and vapor species, were determined for different input quantities of C, H, N, O. The thermodynamic data for all relevant species except for the Al-Y-O, Al_2O_3 - Y_2O_3 systems were obtained from the standard sources such as JANAF Thermochemical Tables [7]. The thermodynamic data for Al-Y-O and Al_2O_3 - Y_2O_3 were taken from the work of J.Gröbner [8] and Z.Jin [9]. All the calculations were done at the Japan Fine Ceramic Center (JFCC).

EQUILIBRIUM CALCULATION RESULTS

(1) Stability of Al_2O_3 and YAG in an H_2O or CO_2 atmosphere

The equilibrium calculations show that Al_2O_3 is the only condensed phase existing in the equilibrium with H_2O and CO_2 ; no liquid phase is formed as a result of the reaction of Al_2O_3 with H_2O nor CO_2 gas. Such gaseous species as AlO_2 , AlO , Al , Al_2O_2 , and Al_2 are the predominant reaction products. Figures 1 and 2 show the equilibrium partial pressures of these predominant gases for the system in Al_2O_3 - H_2O and Al_2O_3 - CO_2 , respectively (total pressure is 1 atm). In case of Al_2O_3 - CO_2 system, the thermodynamic calculations predicts the formation of AlC gas but its equilibrium partial pressure is negligibly low (less than 1.5×10^{-24} atm at 2000°C).

YAG is the only stable condensed species in an H_2O or CO_2 atmosphere and the major gaseous products are YO_2 , AlO_2 , AlO , YO and Al . The equilibrium partial pressures of these species as a function of temperature (total pressure 1 atm) are shown for the YAG- H_2O system in Fig. 3. Figure 4 also shows the equilibrium partial pressures for the YAG- CO_2 system as a function of temperature. These calculation results show that the thermodynamic stability of YAG in an H_2O or CO_2 atmosphere is slightly poorer than that of Al_2O_3 . However, the partial pressure of the reaction product gases is less than 1 ppm in total. In general, if the total pressure of the reaction product gases is less than 10^{-6} atm (less than 1 ppm), it poses no serious problems of the degradation of structural material for long-term use [10]. From above discuss, it is predicted that Al_2O_3 and YAG are thermodynamically stable up to 2000°C in the H_2O or CO_2 atmosphere.

(2) Stability of Al_2O_3 and YAG in H_2 and CO atmosphere

The equilibrium calculations show that Al_2O_3 is also the only condensed phase in the equilibrium with H_2 or CO ; no liquid Al is formed as the result of the reaction of Al_2O_3 with gases. Such gaseous species as Al_2O , Al , AlO , Al_2O_2 , Al_2 and AlO_2 , and Al_2O , Al , AlO , Al_2O_2 and AlO_2 are the predominant reaction products in the systems of Al_2O_3 - H_2 and Al_2O_3 - CO , respectively. Figure 5 shows the equilibrium partial pressures for these species for the Al_2O_3 - H_2 system as a function temperature. The equilibrium partial pressure of Al_2O is larger than 10^{-6} atm over the temperature of 1540°C . Therefore, the upper temperature limit of this material for long-term use is expected to be 1540°C in the pure H_2 atmosphere. Figure 6 also shows the equilibrium for the Al_2O_3 - CO system as a function of temperature. The upper

temperature limit expected is 1620°C, and it is higher than that for the $\text{Al}_2\text{O}_3\text{-H}_2$ system. On the other hand, the gaseous species Al_2O , Al , YO , AlO , AlO_2 , Y , Al_2 , Y_2O_2 and Y_2O , and Al , Al_2O , YO_2 , YO and AlO are the predominant reaction products in the systems of $\text{YAG-H}_2\text{O}$ and YAG-CO , respectively. Figures 7 and 8 show the equilibrium partial pressures as a function temperature of these species in these systems, respectively. The equilibrium partial pressure of Al_2O is higher than 10^{-6} atm in H_2 gas over the temperature of 1640°C and in CO gas over 1730°C.

(3) Stability of Al_2O_3 and YAG in CH_4 combustion gases

Figures 9 and 10 show the 3-D diagrams of the total equilibrium pressure of the reaction product gases for Al_2O_3 and YAG as a function of the equivalence ratio (ϕ) during CH_4 combustion and the temperature ranging 1000-2000°C. The equivalence ratio (ϕ) is given as the fuel-to-air ratio, with the total hydrocarbon content normalized to the amount of oxygen (O_2). The upper temperature limit increases with the decrease in ϕ (lean-burn). The effect of the total system pressure of CH_4 combustion gases ($\text{H}_2\text{-CO-H}_2\text{O-CO}_2\text{-N}_2$) on the equivalence of Al_2O_3 and YAG for three pressure levels of 1, 4 and 10 atm is shown in Figs. 11 and 12 as the function of temperature. The total gas pressure of the reaction product gases at the system pressure of 1 atm is slightly larger than that at 10 atm. The total pressure of the system has negligibly small effect on the stability of Al_2O_3 and YAG in the CH_4 combustion gas atmosphere. YAG can therefore be used up to about 1900°C. Al_2O_3 is also stable during both fuel-lean burn and fuel-rich combustion at the high temperatures.

CONCLUSION

The stability of Al_2O_3 and YAG in the CH_4 combustion gas atmosphere has been examined from thermodynamic considerations using the computer simulation. Al_2O_3 and YAG are stable up to 2000°C in the pure H_2O or CO_2 atmosphere. On the contrary, H_2 and CO gases are corrosive for Al_2O_3 and YAG at high temperatures. The system pressure has negligibly small effects on the stability of Al_2O_3 and YAG in CH_4 combustion gas environment. YAG can be used up to about 1900°C in this CH_4 combustion atmosphere. Al_2O_3 is stable during both fuel-lean burn and fuel-rich combustion at high temperatures.

ACKNOWLEDGEMENT

The authors wish to thank Dr. Satoshi Kitaoka, Japan Fine Ceramics Center (JFCC), for his helpful comment of this study.

REFERENCES

1. Y. Waku, H. Ohtsubo, N. Nakagawa and Y. Kohtoku, "Sapphire matrix composites reinforced with single crystal YAG phases," *J. Mater. Sci.*, Vol.31, 1996, pp.4663-4670.
2. Y. Waku, N. Nakagawa, T. Wakamoto, H. Ohtsubo, K. Shimizu and Y. Kohtoku, "High temperature strength and thermal stability of unidirectionally solidified $\text{Al}_2\text{O}_3/\text{YAG}$ eutectic composite," *J. Mater. Sci.*, Vol.33, 1998, pp.1217-1225.
3. Y. Waku, N. Nakagawa, T. Wakamoto, H. Ohtsubo, K. Shimizu and Y. Kohtoku, "A ductile ceramic eutectic composite with high strength at 1873 K," *Nature*, Vol.389, 1997, pp.49-52.
4. G. Eriksson and K. Hack, "ChemSage: A Computer program for thermochemical application calculations," *User Aspects of Phase Diagrams*, 1991, pp.287-294.
5. E. Köenigsberger, E. Schuster, H. Gamsjäger, C. God, K. Hack, M. Kowalski and P.J. Spencer, "Thermochemical data and software for the optimization of processes and

materials," Netsu Sokutei, Vol.19, pp.135-144.

6. G. Eriksson and K. Hack, "ChemSage-A computer program for the calculation of complex chemical equilibria," Met. Trans. B. Proc. Metallurgy, Vol.21, 1990, pp.1013-1023.

7. Chase, et al.: JANAF Thermochemical Tables, 3rd ed., Part I and II. J. Phys. Chem. Ref. Data, Vol.14, 1985, Suppl.1 1.

8. J. Gröbner, H.L. Lukas and F. Aldinger, "Thermodynamic calculation of the quasibinary Al_2O_3 - Y_2O_3 system and the Y-Al-O Ternary system," Z. Metallkd. Vol.87, 1996, pp.268-273.

9. Z. Jin and Q. Chen, "An assessment of the $\text{AlO}_{1.5}$ - $\text{YO}_{1.5}$ system," Calphad Vol.19, 1995, pp.69-79.

10. A. K. Misra, "Thermodynamic analysis of chemical stability of ceramic materials in hydrogen-containing atmosphere at high temperature," NASA Contractor report 4271, 1990.

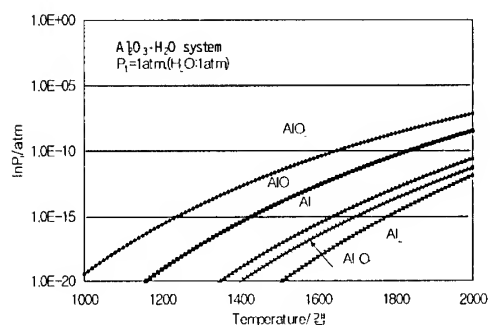


Fig.1. Equilibrium partial pressure of AlO_2 , AlO , Al , Al_2O_2 and Al_2O for Al_2O_3 - H_2O system at 1 atm.

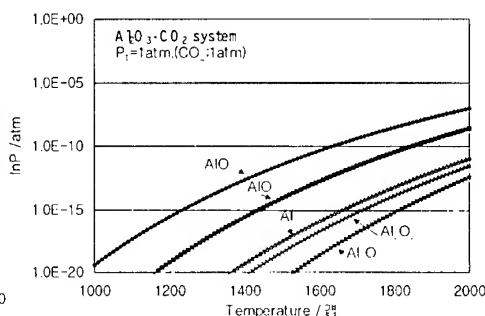


Fig.2. Equilibrium partial pressure of product gases for Al_2O_3 - CO_2 system at 1 atm.

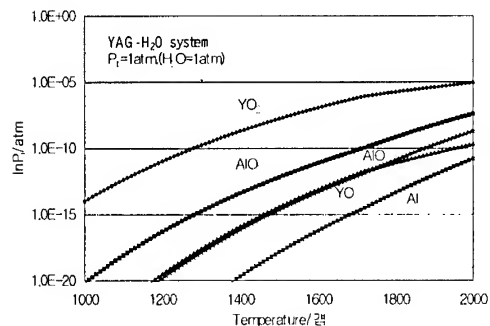


Fig.3. Equilibrium partial pressure of product gases for YAG- H_2O system.

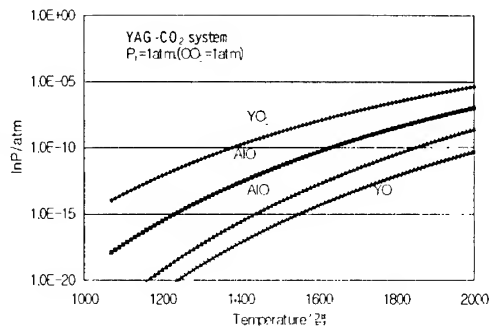


Fig.4. Equilibrium partial pressure of product gases for YAG- CO_2 system.

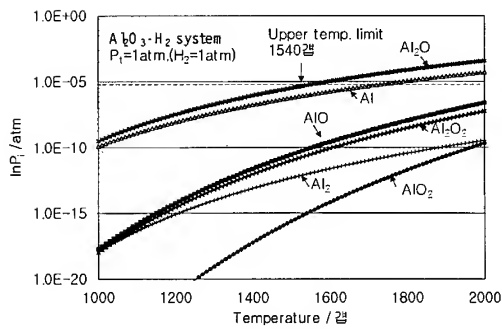


Fig.5. Equilibrium partial pressure of product gases for $\text{Al}_2\text{O}_3\text{-H}_2$ system.

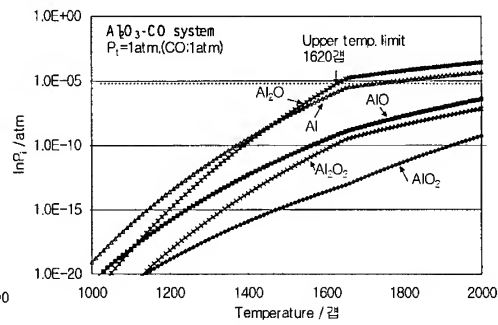


Fig.6. Equilibrium partial pressure of product gases for $\text{Al}_2\text{O}_3\text{-CO}$ system.

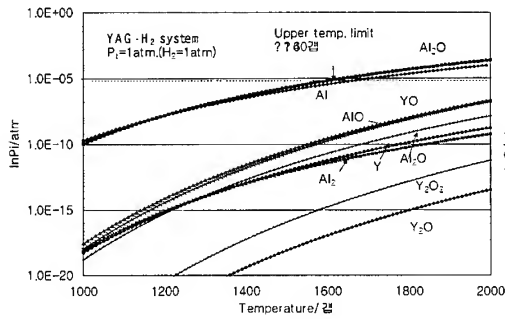


Fig.7. Equilibrium partial pressure of product gases for YAG-H_2 system.

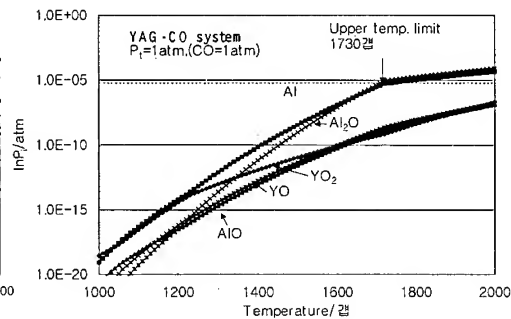


Fig.8. Equilibrium partial pressure of product gases for YAG-CO system.

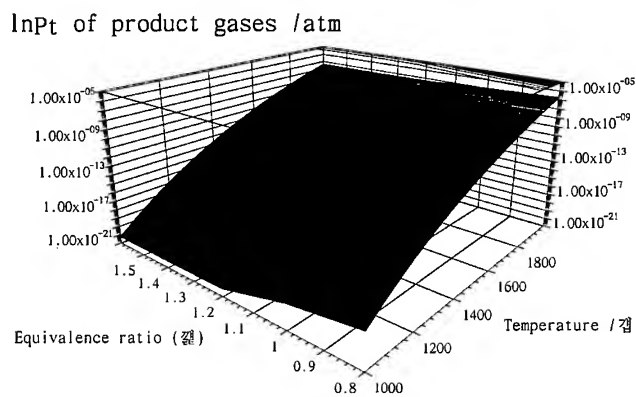


Fig.9. Equilibrium total pressure of reaction product gases for Al_2O_3 as a function of CH_4 combustion equivalence ratio (ϕ).

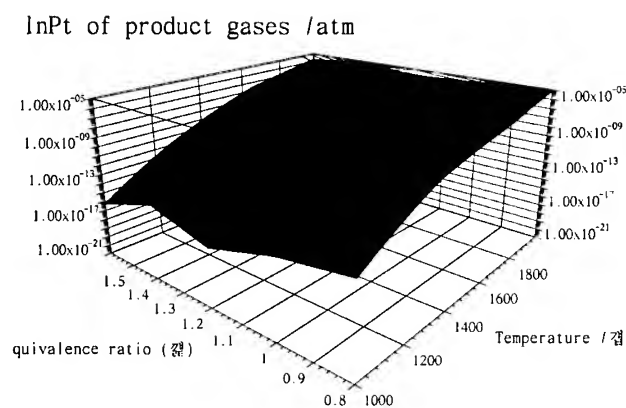


Fig.10. Equilibrium total pressure of reaction product gases for YAG as a function of CH_4 combustion equivalence ratio (ϕ).

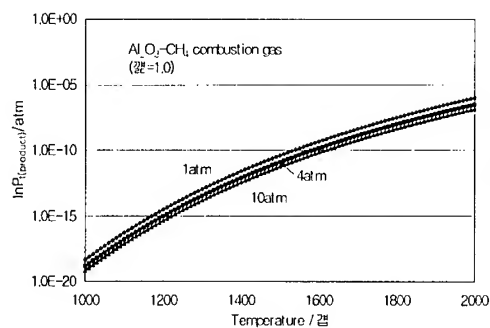


Fig.11. The effect of system pressure of CH_4 combustion on equilibrium of Al_2O_3 .

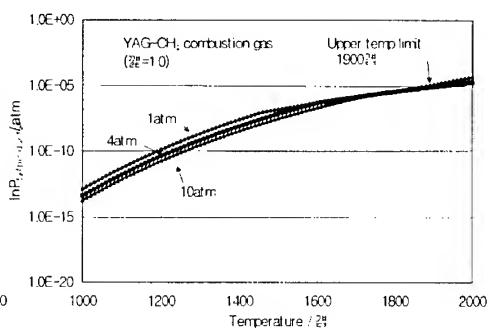


Fig.12. The effect of system pressure of CH_4 combustion on equilibrium of YAG.

MMC (3)

A STUDY ON THE IMPACT ABRASION PERFORMANCE OF THE $\text{Al}_2\text{O}_3/\text{Al-9Si}$ MMC AND ITS SPEED-DEPENDENCY BY SINGLE PENDULUM SCRATCH METHOD

Xiao-jun Bai, Jiang-bo Sha, He-xiang Zhu, Ge-cheng, Yuan, Zou-jian, Li and Qiang Zeng

*Department of Materials Science and Engineering, Guangdong University of Technology, 729 E. Dongfeng
Road, Guangzhou, 510090 China: tieqili@gdut.edu.cn*

SUMMARY: Impact abrasion test by single pendulum scratch method is one of the methods for investigating the work and wear performance of the spares under dynamic moving conditions. The present work studies the impact abrasion resistance of the $\text{Al}_2\text{O}_3/\text{Al-9Si}$ MMC. The resistance to impact abrasion was found to depend on the impact speed significantly. At an impact speed of 3m/s, it decreases with the increase in Al_2O_3 fiber volume fraction on the volume fraction range between 10 and 25 percent. The resistance to 4m/s impact abrasion, however, maximized at the volume content of 20percent, though it is higher than the resistance to 3m/s impact abrasion for all the studied Al_2O_3 content. SEM studies of the worn surface reveal two concurrent mechanisms, namely the serious plowing and the pullout of the Al_2O_3 short fibers.

KEYWORDS:: Impact abrasion, $\text{Al}_2\text{O}_3/\text{Al-9Si}$ MMC, Impact speed effect

INTRODUCTION

The movement of many spares, such as the piston and the brake, has clear dynamic moving character at the stage of either the starting, the ending or the change of the speed. The corresponding abrasion behavior can not be revealed through common laboratory wear tests, for example, the pin-on-disk or the sand rubber abrasion wheel tests, and so on. An alternative is the tests based on the impact abrasion, with the single pendulum scratch method [1-4] being adopted in this work. The impact abrasion process was simulated and carried out by a single event of a stylus with impact energy scratching through the materials surface, and the energy dissipated of stylus was used to describe the dynamic wear behavior of a material scratched.

With respect to the anti-wear materials, MMCs metal matrix composites are wear-resistant materials with the potential of ranges of applications. It has been shown through in studies on the friction coefficient, the lost weight ratio and the wear mechanism that the reinforcement phase results in improvements, which depends on the percentage, the particle size and the type of reinforced phase. [5-10].

In this paper, the single pendulum scratch testing in SiCp reinforced Al alloy matrix MMCs [9,10] has been carried out. The specific energy, dynamic hardness and the feature of surface scratch properties were examined proving the advanced abrasion resistance of the MMCs

compared to the neat matrix materials. The tribology mechanism of the MMC materials was analyzed in depth.

EXPERIMENTAL

Material and Specimen

The materials used in this work were the Al-9Si matrix alloy reinforced with the Al_2O_3 short fiber. The volume fraction was either 10%, 20% or 25%. The Al_2O_3 short fiber ranges from 20 to 100micron in length and 3 to 10micron in radius. The three materials were squeezing cast, then treated by T6 technology (aqueous solution treated at 515 degree C for 4 hours, water cooled and aged at 205 degree C for 6 hours), and then machined into the block specimen of $40 \times 5 \times 3 \text{ mm}^3$. The specimen was grounded with the sand papers up to #800 to obtain the smooth surface for the impact abrasion tests.

Fig. 1 shows the single pendulum scratch testing device, which was modified based on a common impact test machine. The impact speed at the moment when the diamond stylus contacted the specimen was controlled by the initial angle of the pendulum. The impact speeds 3m/s and 4m/s were thus corresponding to the angle, theta, of 90 and 130 degrees, respectively. The length of the pendulum employed in this work is 477mm. After the pendulum was released from the chosen initial angle, the stylus scratched the specimen surface and an arc-shaped groove was left. The length of groove, L, and the energy dissipated, E, was then recorded. The specific energy, e, defined by the ratio between energy dissipated E and the volume V of loss materials at the scratched trace ($e=E/V$), was calculated. The specimen holder can be adjusted up and down to change the distance between stylus and specimen surface so that a series of length of scratched trace and the energy dissipated could be obtained. The critical specific energy, e_c , was then obtained. The detailed method to measure and calculate the specific energy and V was reported in references [3,7]. The surface of the scratched specimens was examined with SEM.

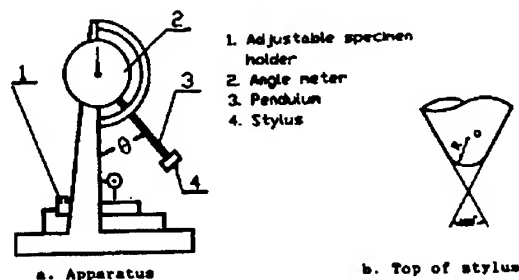


Fig.1. Schematic diagram of single pendulum scratch device

RESULTS AND DISCUSSION

Microstructure of $\text{Al}_2\text{O}_3/\text{Al-9Si}$

The axis of Al_2O_3 short fibers tends to be perpendicular to the direction of the applied squeezing pressure. Fig.2 shows the microstructure of the two perpendicular planes of the 20% $\text{Al}_2\text{O}_3/\text{Al-9Si}$. It can be seen that most of Al_2O_3 are distributed uniformly in the matrix and are perpendicular to the squeezing direction (Fig. 2a). On the transverse worn surface (Fig.2b), a large amount of Al_2O_3 fibers can be seen as the radial cross-section.

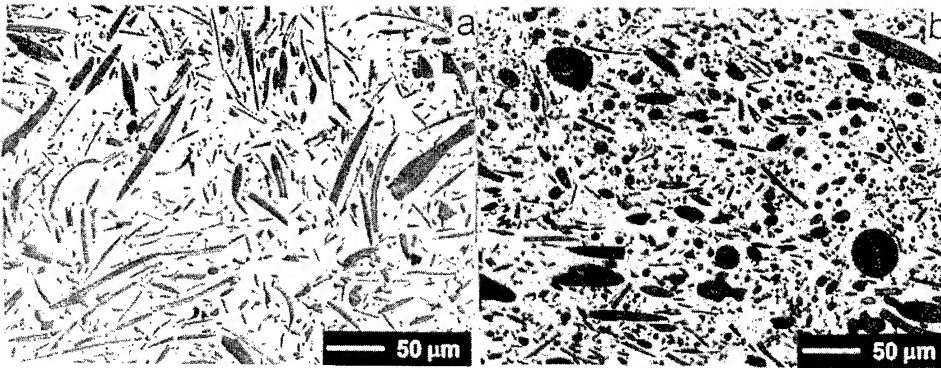


Fig.2. Optical micrograph of the microstructure in 20%Al₂O_{3f}/Al-9Si
Plane (a) perpendicular and (b) transverse to squeezing direction;

HB Hardness

After MMCs treated by T6 technology, the matrix is hardened obviously by the reinforced phase. As shown in Fig.3, the HB hardness increases linearly with the amount of volume fraction of Al₂O_{3f}, agreeing well with the literature results [5-10].

Determined of Critical Specific Energy e_c

For materials and the specific speeds, the specific energy varies with the scratch size or the volume of the lost material rather than being a constant. When the volume of lost material reaches a certain value, the specific energy has a relative steady value, which is corresponding to the critical specific energy e_c . Table 1 shows the original data of the energy consumption E , the length of groove L , the volume of lost material V , and the specific energy e , in the case of 10% Al₂O_{3f}/Al-9Si at 4m/s impact speed. The lost volume V equals $0.53 \cdot L \cdot A \cdot t$, where $A \cdot t$ is the maximal transverse cross section area of the grooves [5]. It is clear that the E value increases while the amount of lost materials increases, but the energy consumption for unit mass lost decreases. Figure 4 illustrates the relationship between e and V , showing a typical e versus V curve. The value of e corresponding to the relative steady region is 1.72 J/mm^3 , considered as critical specific energy e_c .

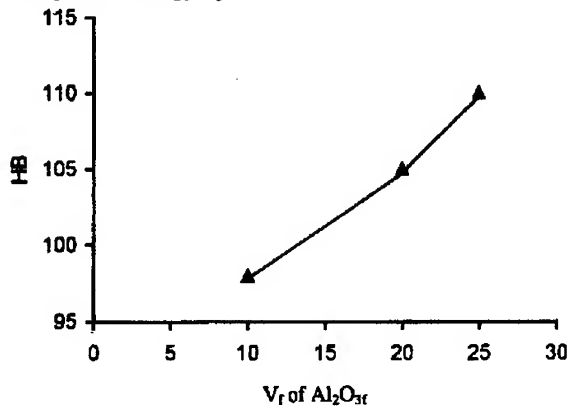


Fig. 3 HB hardness versus the volume fraction of Al₂O_{3f}

Table 1. Dates of energy consumption and size of groove

No.	E(J)	L(mm)	V(mm ³)	e(J/mm ³)
1	3.25	30.6	1.862	1.71
2	0.687	36	3.885	1.73
3	0.212	25	0.627	3.32
4	13.25	41	7.44	1.74
5	4.0	31	1.841	2.13
6	3.5	29	1.313	2.61
7	4.75	31	1.841	2.53
8	3	27	0.921	3.19

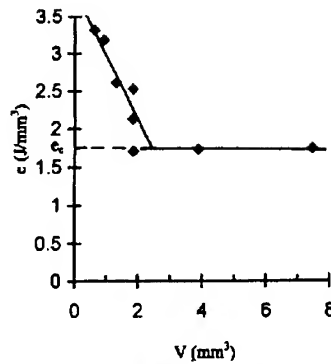


Fig.4 Relationship between e and volume of lose materials

Influence of Impact Speed on the Behavior of Impact Abrasion

After e_c is determined, the critical specific energy e_c is compared for each material in the cases of 3m/s and 4m/s impact speed and is shown in Fig.5. In the case of the 3m/s impact speed, the resistance of impact abrasion decreases (e_c decreases) with an increasing of volume fraction. The 20% $\text{Al}_2\text{O}_3/\text{Al-9Si}$ has the highest impact abrasion resistance value of 2 J/mm³ while the 25% $\text{Al}_2\text{O}_3/\text{Al-9Si}$ has the lowest value of 1.3 J/mm³ under the condition of 4m/s. On another hand, the behavior of impact abrasion is superior at higher speeds. It is clear that the effect of the impact speed on impact abrasion is very complicate and is to be analyzed qualitatively in the following section.

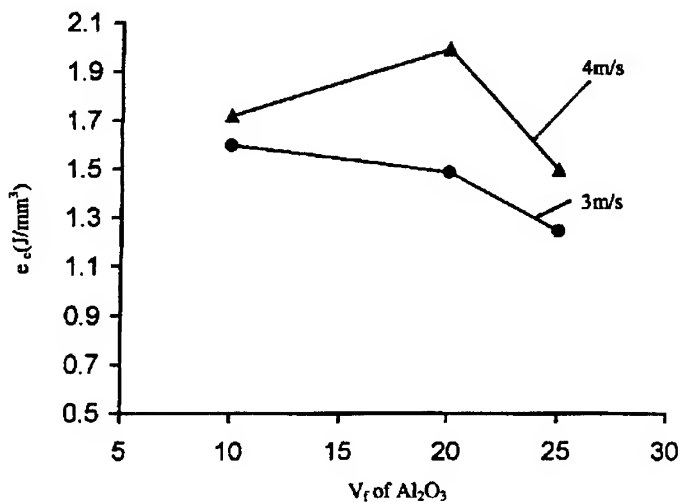


Fig.5 Variation of critical specific energy e_c versus impact speed

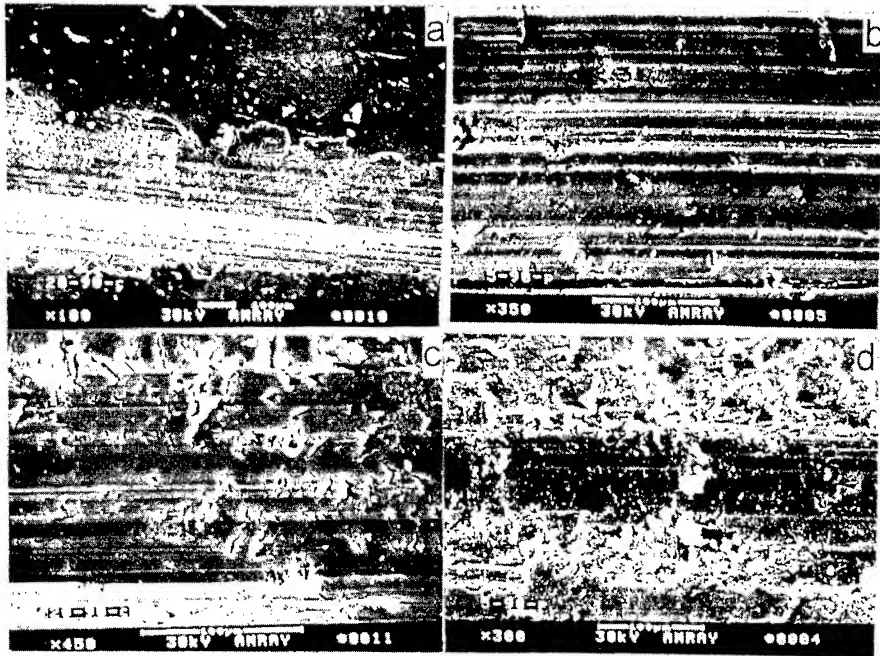


Fig.6 SEM photograph of the scratched traces:
(a) scratched groove; (b)plough, (c) single void and (d) voids group

Investigation of the Groove

The scratched traces on the surface of specimen were observed carefully with SEM (Fig. 6.a). On the two sides of the surface, debris are formed due to the stripping of the twisted Al_2O_3 short fiber, which accompanied also by part of the matrix materials. Smooth bottom of grooves means the typical shear rupture exist and is accompanied by ploughing in Fig 6(b). During scratching, the reinforcing Al_2O_3 short fibers are pulled out from the matrix either independently (Fig 6.c) or in association with some matrix materials (Fig 6.d), leaving single void or group of voids, respectively. If the Fig 6.c is compared with the Fig 6.d and Fig 2, the density of the voids can be seen lesser than that of the reinforced short fiber, indicating that only part of the Al_2O_3 had deformed cooperately with the matrix. This is just like the particle reinforced MMCs [11,12]. Actually, the matrix material without reinforced phase did not show the appearance of the voids because there is no separation between the reinforced phase and the matrix materials, revealing the difference in scratch mechanics between reinforced MMCs and matrix materials [11,12].

It is well known that according to traditional Archard's law and some investigations [5-10], the abrasive resistance of composites would be obviously higher than the matrix alloy. It should increase with an increasing amount of the reinforced phase because the hardness also increases. However, the expectation differs from the present results. This is believed to be due to details of the mechanics and metallurgy.

From mechanics, the impact abrasion is consisted of two characters that are impact and wear. During scratching, the stylus scratches the specimen surface, resulting in the deformation that leads to the compressive and shearing fracture, and would encounter resistance of the materials in front and two sides. The entire process resembles the mechanical cutting process

and has the obvious dynamic characteristics. The hardness was measured by the quasi-static loading. The parameter, which had been used as the judging parameter for the sliding wear with plough and adhere mechanics, can not describe the impact abrasion and the actual material abrasive behavior under the dynamic loading here. The mechanical properties affecting the impact abrasion must be the toughness, the strength, the materials response of the strain rate speed and the interface between reinforced phase and matrix. Therefore, the hardness is not the main factor for impact abrasion.

With respect to the metallurgy and damage considerations, the ability of the matrix to absorb the impact energy reduces due to the decrease in plasticity and in toughness. The metallurgical defects by reinforced phase may be also present. Though the extra impact energy could be consumed while the reinforced phases are pulled out from matrix, the impact abrasion may be improved only when the latter is prior to the former. The ideal phenomenon would be observed when there is good interfacial coherent at interface, uniform distribution of reinforcing phase without defects in matrix. Lastly, impact speed makes the materials turn to brittle behavior, which means the strength increases and toughness decreases with an increasing of impact speed, but its direct effect to impact abrasion is not clear and thus remains to be the subject of further research. As discussed above, at an impact speed, a very nice coordination between strength and toughness can make the materials advantageous in the impact abrasive behavior. In this work, the 10%Al₂O₃/Al-9Si may has the best coordination in the case of 3m/s impact speed, but the 20% Al₂O₃/Al-9Si dose in the case of 4m/s impact speed, for both cases corresponding to the highest resistance of impact abrasion, respectively. The quantitative model should be established for impact and sliding speed.

Conclusions

In the case of the 3m/s impact speed, with an increasing of volume fraction, the resistance of impact abrasion decreases (ϵ_c decreases). The 20% Al₂O₃/Al-9Si has the highest resistance of impact abrasion while the 25% Al₂O₃/Al-9Si has the lowest value under the condition of 4m/s. The impact abrasion behavior at 4m/s speed is prior to that of same materials at 3m/s speed case. The plastic deformation, the shear fracture, the ploughing and the separation of short fiber from matrix are the main characters and mechanics in the case of impact abrasion. The materials have advanced impact abrasive behavior while strength and toughness of materials coordinates very well.

REFERENCES

1. Vingsbo, O. and Hogmark, S., *Wear*, 1984, Vol.100, pp.489-502.
2. Bryggman, U., Hogmark, S. and Vingsbo, O., *Wear*, 1986, Vol.112, pp.145-162.
3. Bryggman, U., Hogmark, S. and Vingsbo, O., *ibid*, 1987, Vol.115, pp.203-210.
4. Kennsdy, F. E., *Journal of Lubrication Technology, Transactions of the ASME*, October 1982, Vol. 104, pp.582-588.
5. Liang, Y. N., Li, S. Z. and Li, S., *Wear*, 1994, Vol. 177, pp.167-173.
6. Liang, Y. N., Li, S. Z., Li, D. F., et al., *Wear*, 1996, Vol.199, pp.66-73.
7. Bhan, K. J., Mehrabian, R., *J. Metals*, 1982, Vol.32, pp.30-34.
8. Roy, M., Venkataraman, B., Bhanuprasad, V.V., *Metall. Tran.*, 1992, Vol.23A, pp.2833
9. Hosking, F. M., Portillo, F. F., Wunderlin, R., et al., *J. Mater. Sci.*, 1982, Vol.17, pp.477
10. Ma, Z. Y., et al., *Wear*, 1991, Vol.148, pp.287-293.
11. Liang, Y. N., Ma, Z. Y., Li, S. Z., et al., *Wear*, 1994, Vol.178, pp.9-15.
12. Sha, J. B., Zhu, H. X., Li, Z. J., et al., *Journal of Experimental Mechanics*, 1998, Vol.13(1), pp. 34-40.

Fabrication of A356 Aluminum Alloy Composites Reinforced with SiC Particulates by Vacuum Compo-casting Process

Kwangjun Euh¹, Woo Sang Kim², and Sunghak Lee¹

¹Center for Advanced Aerospace Materials
Pohang University of Science and Technology, Pohang 790-784, KOREA:
toto@postech.edu, shlee@postech.edu

²Technical Center, Daewoo Motor Co., Inchon, 403-714 KOREA

SUMMARY: The present study aims at investigating a vacuum compo-casting process for fabrication of A356 aluminum alloy composites reinforced with SiC particulates. At the stirring temperature of 610°C and the stirring speed of 400 rpm under a 10^{-2} torr vacuum, good quality Al-SiC_p composites having relatively homogeneous microstructure and sound Al/SiC interfacial bonding were obtained, although a small amount of micropores were present in the castings. The microstructures and mechanical properties of these composites were compared with those of commercial composites fabricated by Duralcan. Enhanced distribution of SiC particulates and reduction in the sizes of micropores were found in composites processed by vacuum compo-casting. In order to improve the mechanical properties of the A356 Al-SiC_p composites, minimization of micropores, fast cooling rate and homogeneous distribution of SiC particulates and eutectic Si particles were suggested.

KEYWORDS: Vacuum, Compo-casting, SiC, A356 Al, Composite

INTRODUCTION

Compo-casting is the most economical fabrication method of aluminum alloy composites reinforced SiC particulates. Al-Si alloys such as A356 aluminum alloy are used as the matrix to improve SiC/matrix interfacial properties and the fluidity of molten metal during casting [1,2]. A vacuum compo-caster is used to prevent the formation of pores, which is caused by the air intrusion during melting, and to minimize the formation of oxides. In vacuum compo-casting, the processes of melting, degassing, stirring, and casting can be carried out continuously [3]. The vacuum compo-casting is more suitable for mass production and commercialization than any other new techniques such as the *in-situ* process [4,5] and squeeze casting [6].

In this study, the parameters for fabrication of A356 Al-SiC_p composites by vacuum compo-casting were optimized. Vacuum compo-casting is specifically used because of its advantages in obtaining a homogeneous matrix and uniform distribution of SiC particulates

and in eliminating casting defects such as pores [3]. The parameters that were investigated included the microstructure and mechanical properties of these composites. The composites, which were processed under different conditions, were comparatively analyzed with respect to the distribution of reinforcements and the degree of casting defect occurrence.

EXPERIMENTAL

The material used in this study was A356 aluminum alloy manufactured by Duralcan, whose chemical composition is shown in Table 1. For comparison, the matrix compositions of A356 Al-SiC_p composites used for sand-casting and die-casting purposes are also shown in this table. SiC particulates with an average size of 17 μm were obtained from Washington Mill Co..

Table 1. Chemical compositions of the A356 Al ingot and the aluminum matrices of the Duralcan composites (wt.%)

Alloy	Si	Mg	Fe	Mn	Al
A356 Ingot	6.03	0.45	0.13	0.001	bal.
Duralcan (Sand-Cast)	7.2	0.35	0.2	0.03	bal.
Duralcan (Die-Cast)	9.7	0.39	0.81	0.39	bal.

The vacuum compo-caster was consisted of stirring/rotating system, temperature control system, vacuum systems, and charging system of SiC particulates. The A356 Al alloy was charged into a graphite crucible with an inner diameter of 300 mm, and was placed into the vacuum chamber, which was then evacuated at room temperature. The alloy was melted at 700°C under a vacuum of 10^{-2} torr. After the removal of oxides that floated on the molten metal, SiC particulates preheated at 300°C were charged into the molten metal as it was stirred at 610°C. The charging rate of the particulates was about 28 g/min (5.1 vol.%/min), and their volume fractions in the composites was kept at 15% and 20%. The stirring was carried out for 20 minutes at the optimum rotation speed of 400 rpm, after which the temperature was raised to 700°C to properly maintain the fluidity of the molten metal [7]. Ingots were manufactured by pouring the molten metal into a copper mold.

Heat-treatment was performed under T6 conditions to achieve a maximum hardness of the matrix. The Rockwell hardness (B scale) and tensile properties were tested for measuring the mechanical properties. Dimensions of round tensile specimens were a gauge length of 20 mm and a gauge diameter of 4 mm. The specimens were loaded at a constant crosshead speed of 0.5 mm/min at room temperature. The microstructures were examined with an optical microscope and a scanning electron microscope (SEM).

RESULTS AND DISCUSSION

Microstructure

Optical micrographs of the A356 Al composites reinforced with 15% and 20% SiC particulates are shown in Figures 1(a) and (b). The particulates are homogeneously distributed and there are no large pores; however, a small amount of micropores are present. The composite reinforced with 20% particulates shows an inferior distribution of particulates compared to the composite reinforced with 15% particulates. The interior of a residual

micropore consists of the agglomeration of SiC particulates. This is associated with the formation of micropores and the congregation of particulates around these micropores, which are caused by the pushing effect during solidification [8].

Optical micrographs of the three different cooling rates used during the solidification of melts, are shown in Figures 2(a)-(c). In the case of furnace cooling, coarse solidified grains were formed and SiC particulates were segregated along the grain boundaries (Figure 2(a)). Eutectic Si particles, which formed coarsely near SiC particulates can also be seen. For the slow cooling rate of 7°C/sec applied by using a 300°C preheated mold, solidified grains were smaller with an average grain size of 45 μm , SiC particulates were better distributed and eutectic Si particles were finer than those formed in furnace cooling (Figure 2(b)). When a fast cooling rate (19°C/sec) in an unheated mold was employed, an improved microstructure with an average grain size of 26 μm was obtained and SiC particulates were homogeneously distributed in the microstructure (Figure 2(c)). Thus, a fast cooling rate is recommended to obtain an optimized microstructure.

Figures 3(a)-(b) shows the microstructures Al-SiC_p composites of Duralcan, which were manufactured for sand-casting and die-casting purposes, respectively. The average size of SiC particulates contained in these composites is about 12 μm and their volume fractions are 20%. In comparison, the average size of SiC particulates in the composite materials produced during this study was 17 μm . Thus, the microstructures of these composites cannot be reasonably compared. However, it was observed that the volume fraction of micropores in the composites processed in this study (0.56%) was similar to those of the Duralcan composites manufactured for sand-casting (0.5%), but smaller than those made for die-casting (0.9%).

Pores also existed when the composites were fabricated under vacuum, but their sizes and numbers were reduced to a great extent, leaving only some micropores while eliminating large pores. The commercial composites with some micropores can be mostly used in the production of parts whose function is not seriously affected by micropores.

Hardness and Tensile Properties

Table 2 shows the Rockwell hardness data of the composites fabricated with slow and normal cooling rates, in comparison to those of the Duralcan Al-SiC_p composites made for sand-casting and die-casting. Under the T6 condition, the Duralcan composite manufactured for die-casting has the highest hardness, while the others have similar hardness values. This is because more eutectic Si particles are formed due to the higher content of Si in the die-casting Duralcan composite (Table 1).

This table shows the tensile test results of the A356-T6 composites reinforced with 15% and 20% SiC particulates as well as the Duralcan composites for comparison. The yield and tensile strengths are highest in the composite reinforced with 20% particulates at a fast cooling rate, followed by the composite reinforced with 15% particulates at a fast cooling rate and the sand-casting Duralcan composite, the composite fabricated with a slow cooling rate, and the die-casting Duralcan composite. Elongation of these composites decreases in the following order: the sand-casting Duralcan composite, the composites fabricated with fast cooling rate, the composite fabricated with slow cooling rate and the die-casting Duralcan composite. This indicates that elongation decreases as the amount of micropores increases, as shown in Figures 1(a)-(b) and 3(a)-(b). In particular, the Duralcan composite made for die-casting exhibits poor mechanical properties because it contains more micropores (0.9 vol.%), as shown in Figure

3(b). The composite reinforced with 20% particulates solidified with a fast cooling rate has a tensile strength of 317 MPa yield strength of 300 MPa, and elongation of 1.5%, showing excellent mechanical properties among the five composites. These improved mechanical properties, as compared to the commercial composites, are associated with a good distribution of SiC particulates and a reduction of micropores.

Table 2. Rockwell hardness test and tensile test data of the T6-treated Al-SiC_p composites

	17 μ m 15% (Fast Cooling)	17 μ m 15% (Slow Cooling)	17 μ m 20% (Fast Cooling)	Duralcan (Sand-cast)	Duralcan (Die-cast)
Hardness (RHB)	65.3	64.0	67.0	60.0	68.9
Yield Strength (MPa)	279	266	300	261	231
Tensile Strength (MPa)	280	269	317	277	233
Elongation (%)	1.7	1.4	1.5	1.8	1.2

When SiC particulates are large, the melt is easier to stir and the distribution of particulates is more uniform. However, the particulates may be separated from the matrix during final pouring. When particulates are small, stirring of the melt is more difficult because particulates are easily agglomerated, and thus a homogeneous distribution is quite difficult to achieve [9]. Consequently, the optimum size of particulates in achieving the most enhanced mechanical properties is about 10 to 20 μ m [9,10]. Eutectic Si particles formed adjacent to SiC particulates during casting process are brittle; therefore, they can deteriorate fracture properties.

Figures 4(a)-(d) shows SEM fractographs of fractured tensile specimens and indicates a mixed fracture mode of ductile rupture and cleavage. Ductile fracture dominates the rupture; however, dimples are shallower than those in other typical ductile materials. This is due to the presence of cleaved SiC or eutectic Si particles inside the dimples. The cleavage facet size of the composites processed in this study, shown in Figures 4(a)-(b), is larger than that of the Duralcan composite made for sand-casting, shown in Figure 4(c). This is due to the use of larger SiC particulates in the former composite. These observations indicate that cleavage facets are formed by SiC particulates or eutectic Si particles. In the Duralcan composite made for die-casting, as shown in Figure 4(d), cleavage fracture is predominant and the cleavage facet size is very large. Inclusions that might be present inside the pores can be found around large cleavage facets and thus, mechanical properties are deteriorated due to the presence of pores.

CONCLUSIONS

The distribution of SiC particulates depends on their charging rate, the amount of solid phase in the molten metal and the stirring speed. For the solid phase to be contained at about 20% in the molten metal, the temperature of the molten metal was determined to be 610°C. The composites with low residual pores were obtained under the following conditions: a SiC particulates charging rate of 28 g/min, an impeller rotating speed of 400 rpm and a pouring temperature of 700°C. The T6-treated composites with 20% volume fraction of SiC particulates processed in this study have shown better mechanical properties than those of the commercial composites manufactured by Duralcan with the same amount of SiC particulates. These composites have tensile strength of 317 MPa, yield strength of 300 MPa and elongation

of 1.5%. This is associated with the homogeneous distribution of SiC particulates and the reduction of micropores.

REFERENCES

1. K. F. Kobayashi, L. M. Hogan, *J. Mater. Sci.*, Vol.20, no.6, 1985, pp.1961-75.
2. M. Shamsuzzoha, L. M. Hogan, *Phil. Mag. A*, Vol.54, no.4, 1986, pp.459-77.
3. Z. Zhu, "Cast Reinforced Metal Composites", S. G. Fishman, A. Dhingra, eds., ASM International, Metal Park, OH, 1988, pp.93-100.
4. Martin Marietta Corp., US Patent 4 915 908, 1990.
5. R. T. Pepper, R. A. Penty, *J. Composite Mater.*, Vol.8, 1974, pp.29-37.
6. S. K. Hong, S. H. Hwang, J. C. Choe, I. M. Park, H. Tezuka, T. Sato, A. Kamino, "Materials Science Forum Their Physical and Mechanical Properties Proceedings of the 1996 5th International Conference on Aluminum Alloys", Transtec Publ. Ltd., Zurich, Switzerland, 1997, pp. 165-72.
7. D. J. Lloyd, *Composite Sci. Technol.*, Vol.35, 1989, pp.159-79.
8. P. K. Rohatgi, R. Asthana, S. Das, *Inter. Met. Rev.*, Vol.31, 1986, pp.115-39.
9. D. J. Lloyd, *Inter. Mater. Rev.*, Vol.39, 1994, pp.1-23.
10. D. J. Lloyd, B. Chamberlain, "Cast Reinforced Metal Composites", S. G. Fishman, A. Dhingra, eds., ASM International, Metal Park, OH, 1988, pp.263-69.

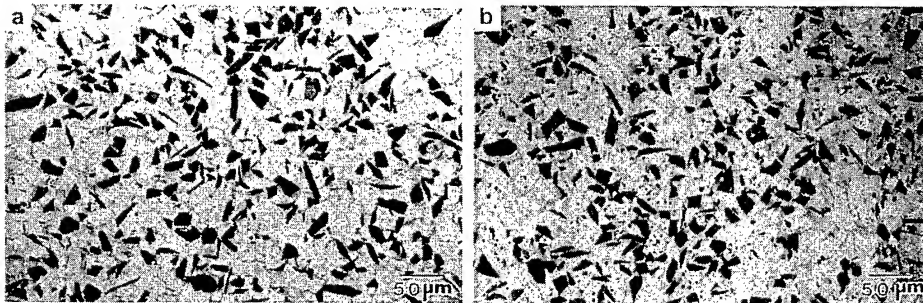


Fig. 1. Optical micrographs of the A356 Al-SiC_p composites reinforced with (a) 15 vol.% and (b) 20 vol.% SiC particulates

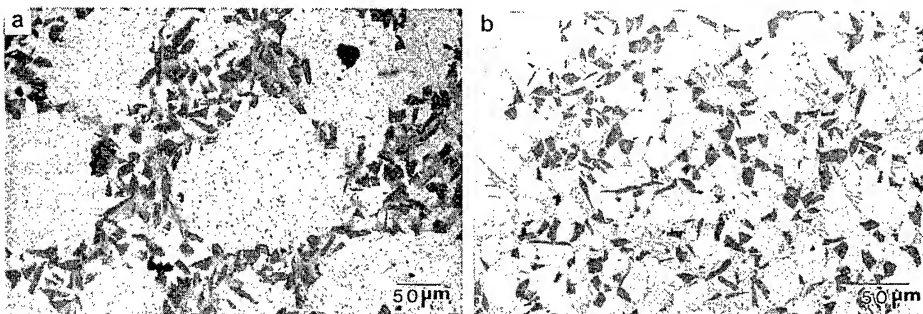


Fig. 2. Optical micrographs of the A356 Al-SiC_p composites processed with (a) furnace cooling, (b) slow cooling, and (c) fast cooling rates

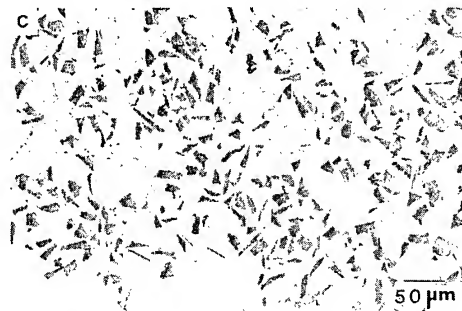


Fig. 2 (c) continued.

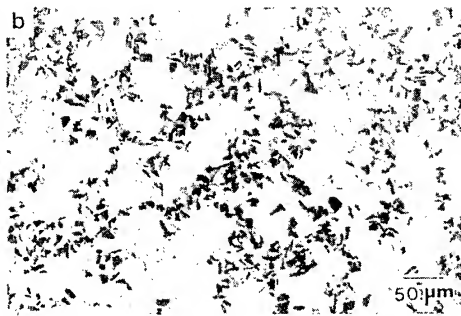
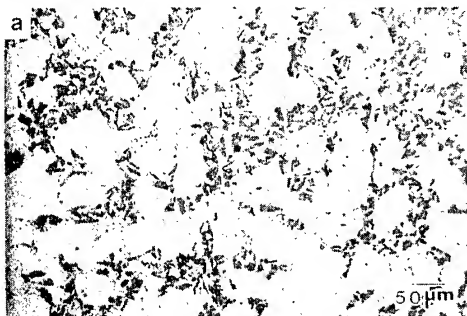


Fig. 3. Optical micrographs of the Al-SiC_p composites commercially processed for (a) sand-casting and (b) die-casting by Duralcan Co.

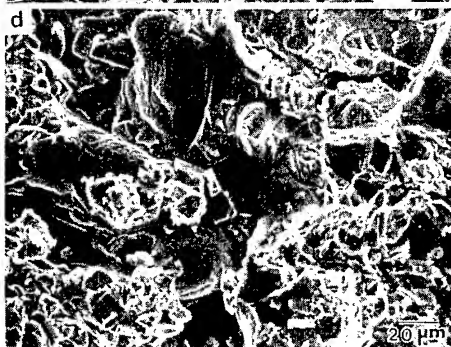
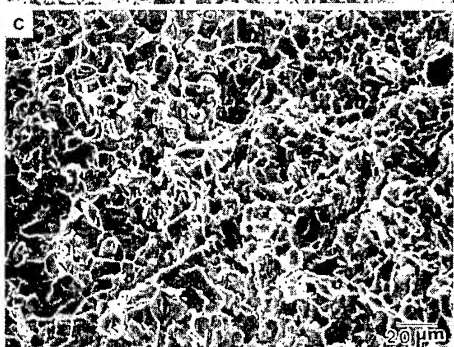
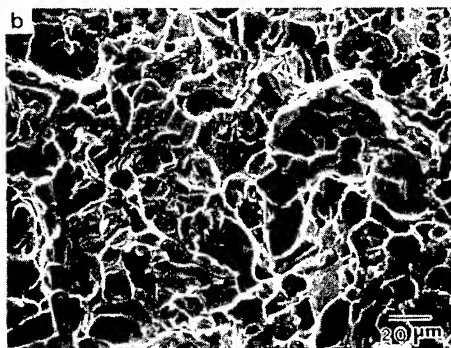
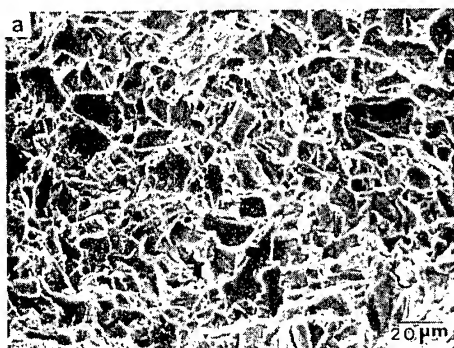


Fig. 5. SEM fractographs of fractured tensile specimens of the T6-treated Al-SiC_p composites reinforced with (a) 15 vol.% and (b) 20 vol.% SiC_p particulates and processed for (c) sand-casting and (d) die-casting by Duralcan Co.

CAVITY NUCLEATION AT INTERFACES IN SUPERPLASTIC METAL MATRIX COMPOSITES

H. Hosokawa ¹, H. Iwasaki ² and K. Higashi ³

¹ Graduate Student, Department of Metallurgy and Materials Science, College of Engineering, Osaka Prefecture University, Gakuen-cho, Sakai, Osaka 599-8531, Japan:
hosokawa@mtl.osakafu-u.ac.jp

² Department of Materials Science and Engineering, College of Engineering, Himeji Institute of Technology, Shosha, Himeji, Hyogo 671-2201, Japan:
iwasaki@mse.eng.himeji-tech.ac.jp

³ Department of Metallurgy and Materials Science, College of Engineering, Osaka Prefecture University, Gakuen-cho, Sakai, Osaka 599-8531, Japan:
higashi@mtl.osakafu-u.ac.jp

SUMMARY: Cavitation has been investigated in many aluminum alloy matrix composites. These show that cavities were nucleated at the interfaces. It has been showed stress concentrations are caused around particles during deformation. Cavitation reduces the performance of mechanical properties of the deformed specimens and leads to premature fracture. Therefore, it is important to investigate cavitation characteristics of these materials during deformation. In the present investigation, the particle size for cavity nucleation is investigated in high strain rate superplastic 20vol. %Si₃N₄/2124Al composite. It can be known that the particles, which are larger than that of the experimental minimum sizes, contain the possibility of cavity forming during deformation.

KEYWORDS: High strain rate superplasticity aluminum matrix composite, cavity forming, particle size

INTRODUCTION

Aluminum matrix composites are characterized by high specific modulus, high specific strength, high heat resistance and wear resistance at room temperature. The composites can be expected as structural materials. However, the composites have lower ductility than the matrix-alloys, resulting in a poor formability, which makes the final cost higher. Therefore, it is desired to improve low ductility of the composites for many structural applications.

It has demonstrated that many aluminum matrix composites show superplastic behavior [1-8]. These results indicate that ductility of the composites is improved and have possibility of superplastic forming. Superplastic behavior of composites is related to high strain rate sensitivity, m , or low stress exponent, n . The increase of m value (or the decrease of n value) increases resistance of development of necking. However, it is recognized that largest elongation doesn't coincide with high strain rate sensitivity, because cavitation behavior is also associated with elongation. Cavitation is an important factor influencing the

total elongation. Also, cavitation deteriorates the performance of mechanical properties after deformation. Therefore, it is important to investigate cavitation in aluminum matrix composites. It is recognized that cavitation in aluminum matrix composites is nucleated at the interfaces of matrix alloy and particles [9-15]. That is because the stress concentrations are caused around particles. If the stress concentration around particle is relaxed, no cavity nucleation is caused at the interfaces during deformation. Hence, it is important to investigate size of the particle that formed cavitation during deformation in order to obtain large elongation and to maintain the performance of mechanical properties after deformation.

In this investigation, the sizes of the particles, which formed cavities, have been investigated in aluminum matrix composites.

EXPERIMENTAL PROCEDURE

20vol. %Si₃N₄_p/2124Al composite was used, where *p* is particulate. These materials were prepared by following procedure. Aluminum matrix alloy powders and ceramic powders were mixed in an alcoholic solvent followed by drying. These mixed powders were sintered at 873 K with a pressure of 390 MPa. The billet was then extruded with a reduction ratio of 100:1. Tensile specimens were machined from the extruded bar. The tensile specimens had a length of 5 mm and a diameter of 2.5 mm.

Constant true stress tests were carried out in air at 773-793 K at superplastic condition. The specimens required about 1.8 ks to equilibrate at the test temperature prior to initiation of straining. A three-zone furnace was used in which the temperature was monitored and maintained constant to within ± 1 K. A tensile axis was selected to be parallel to the extrusion direction for all tests.

A metallographic investigation was carried out by using scanning electron microscope (SEM) and transmission electron microscope (TEM) before tensile tests. Furthermore, cavity formation at the particle/matrix interfaces was investigated by SEM. Quantitative metallographic measurements were conducted mechanically polished specimens with size distributions of particles being analyzed, assuming a spherical geometry.

RESULTS

Microstructure

A typical SEM microstructure of 20vol. %Si₃N₄_p/2124Al composite is shown in Figure 1. The particles were uniformly dispersed. The particle sizes were quantitatively measured for 20vol. %Si₃N₄_p/2124Al composite. The results are shown in Fig. 2, where the size interval is taken to be 0.1 μ m. The particle sizes were 0.2~ 2.5 μ m for 20vol. %Si₃N₄_p/2124Al composite. The peak particle size was 0.6~ 0.7 μ m, where the peak particle size is the particle size where the number of the particles is a maximum. Figure 3 also shows the TEM microstructure of the extruded sample. The structure consists of very fine grains with a mean size of 2.4 μ m and the particles were uniformly dispersed. The refinement of grains and uniform distribution of Si₃N₄ particles are fairly necessary and very important for obtaining the high strain rate superplasticity in the materials.

Cavitation

It is recognized that cavities were nucleated at the interfaces during large elongation in superplastic aluminum matrix composites because of accumulation of stress concentrations

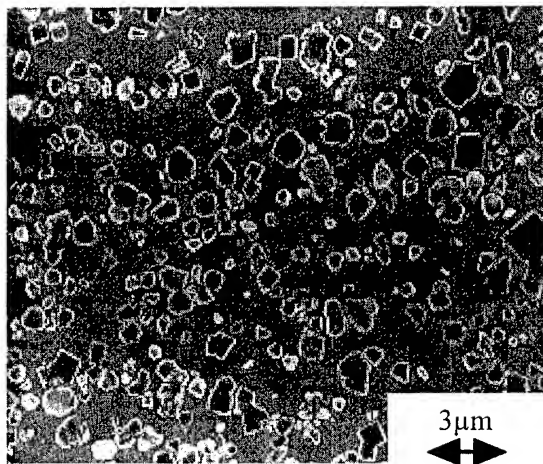


Fig. 1 A typical SEM microstructure of 20vol. % Si₃N₄/2124Al composite.

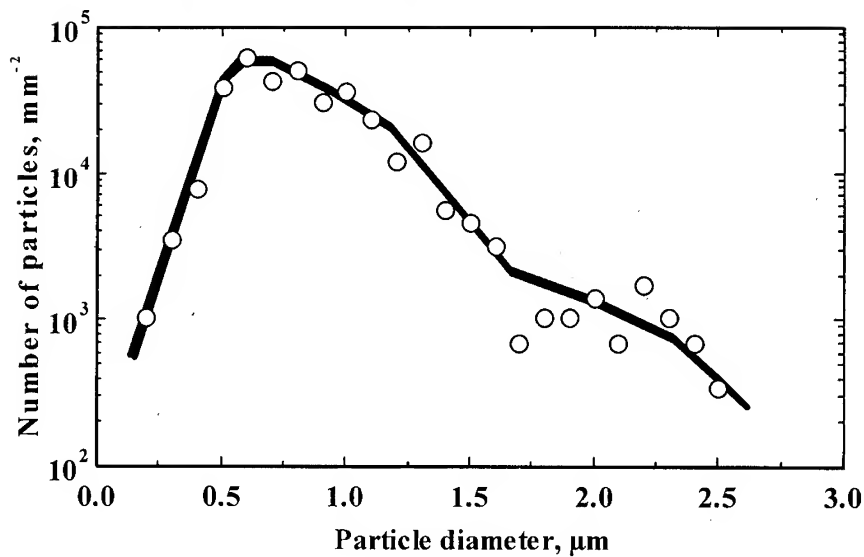


Fig. 2 Particle size distributions for 20vol. % Si₃N₄/2124Al.

around particles. Specimens pulled to any strain were observed by SEM, where the conditions in which cavity formation at the particle/matrix interfaces was investigated is the condition in which the deformation behavior is superplasticity. The conditions in present investigation are shown in Table 1. The values of strain rate sensitivity are over 0.5 in all investigated condition. Cavities formed during deformation are depicted in Figure 4. The cavities in Figure 4 are marked by arrows. Cavities were formed at the interfaces of metal matrix and particles. It is suggested that stress concentrations caused around particles during deformation. Size distributions of the particles formed cavities at the interfaces were



Fig. 3 A typical TEM microstructure of 20vol. %Si₃N₄p/2124Al composite.

experimentally investigated in all specimens, where the particles containing cavities over radius of 0.1 μm at the interfaces were considered the particles which formed cavities. The results are shown in Figure 4, where the size interval is taken to be 0.1 μm . The experimental minimum sizes of particles, which formed cavities, are 0.35, 0.59, 0.51 and 0.50 μm in No. 1, 2, 3 and 4, respectively. Therefore, it can be known that the particles, which are larger than the particles of the experimental minimum sizes, contain the possibility of cavity forming during deformation. It is considered that the critical particle sizes for cavity nucleation exist in aluminum matrix composites. In this investigation, when the particle sizes were less than a certain value, no cavitation was caused around particles. Therefore, it is important to reduce the size of the particles less than the minimum particle sizes in order to limit the damage due to the development of cavitation.

Table 1 Test condition of the investigated samples in aluminum matrix composites.

Sample No.	Temperature, K	Strain rate, s ⁻¹	Stress, MPa	Strain rate sensitivity
1	773	0.28	15	0.68
2	773	0.1	12	0.68
3	783	0.57	15	0.57
4	783	0.1	4	0.57
5	793	0.16	7	0.70

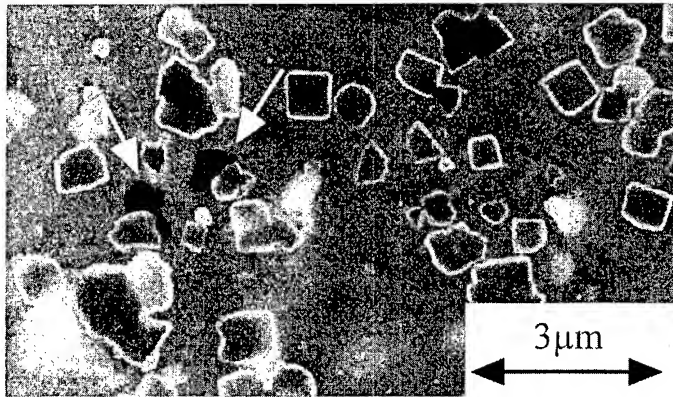


Fig. 4 Microstructure of sample of Si₃N₄/2124 Al composite deformed to $\epsilon = 0.24$ at 773 K under constant true stress of 12 MPa . The arrows indicate cavities.

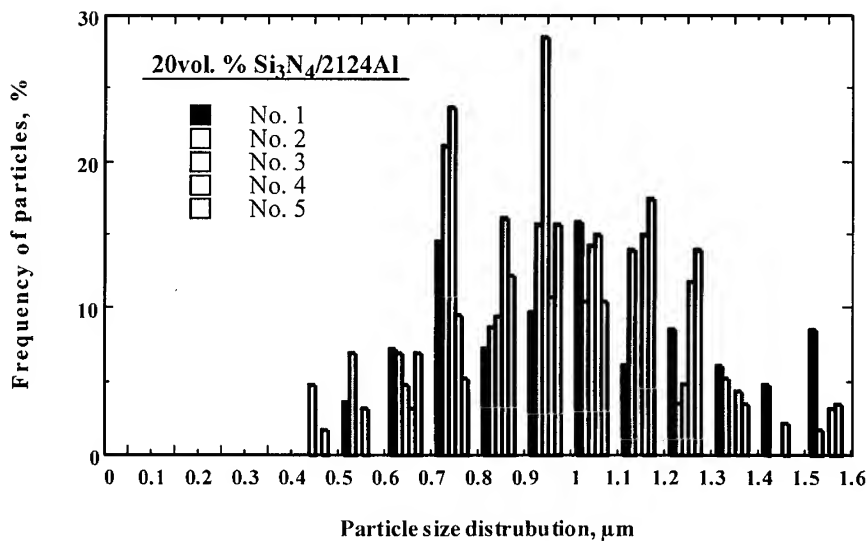


Fig. 5 Particle size distributions which formed cavity nucleation in Si₃N₄/2124Al.

CONCLUSIONS

Cavitations reduces the performance of mechanical properties of the deformed specimens and leads to premature fracture. Therefore, it is important to investigate cavitation characteristics of these materials during deformation. Cavity nucleation site was investigated in aluminum matrix composites; results are shown as follows.

(1) Cavitation is caused at the interfaces, because the stress concentrations were caused

around particles.

- (2) The particle sizes, which nucleated cavities, were investigated under the condition exhibiting high strain rate sensitivity. When the particle sizes were less than a certain value, no cavitation was caused around particles.

Acknowledgment - The authors (H. Iwasaki and K. Higashi) gratefully acknowledges the financial support of the Ministry of Education Science and Culture of Japan as a Grant-in-Aid.

REFERENCES

1. M. Mabuchi, K. Higashi and T.G. Langdon, *Acta Metall. Mater.* **42**, 1739 (1994).
2. M. Mabuchi and K. Higashi, *Mater. Sci. Eng.* **A179/A180**, 625 (1994).
3. M. Mabuchi and K. Higashi, *Mater. Trans. JIM* **35**, 399 (1994).
4. M. Mabuchi and K. Higashi, *Mater. Trans. JIM* **36**, 420 (1995).
5. M. Mabuchi and K. Higashi, in *Key Eng. Mater.* edited by G.M. Newaz, H. Neber-Aeschbacher and F.H. Wöhlbier (Trans Tech Publications, Zürich, Switzerland, 1995), vol. 104-107, p. 225.
6. M.W. Mahoney and A.K. Ghosh, *Metall. Trans.* **18A**, 653 (1987).
7. J. Pilling, *Scripta Metall.* **23**, 1375 (1989).
8. K. Higashi, T. Okada, T. Mukai, S. Tanimura, T.G. Nieh and J. Wadsworth, *Scripta Metall.* **26**, 185 (1992).
9. M. Mabuchi, H. Iwasaki, K. Higashi and T.G. Langdon, *Mater. Sci. Tech.* **11**, 1295 (1995).
10. H. Iwasaki, M. Mabuchi, K. Higashi and T.G. Langdon, *Mater. Sci. Eng.* **A246**, 117 (1998).
11. H. Iwasaki, M. Mabuchi, K. Higashi and T.G. Langdon, *Mater. Sci. Forum* **170-172**, 537 (1994).
12. H. Iwasaki, M. Takeuchi, T. Mori, M. Mabuchi and K. Higashi, *Scripta Metall. Mater.* **31**, 255 (1994).
13. H. Iwasaki, M. Mabuchi and K. Higashi, *Mater. Sci. Tech.* **12**, 505 (1996).
14. H. Iwasaki, T. Ohtani, T. Mori, M. Mabuchi, K. Higashi and S. Tanimura, *Mater. Sci. Res. Inter.* **1**, 31 (1995).
15. K. Higashi and M. Mabuchi, *Mater. Sci. Eng.* **A176**, 461 (1994).
16. R. Raj and M.F. Ashby, *Metall. Trans.* **2**, 1113 (1971).
17. R. Raj and M.F. Ashby, *Acta Metall.* **23**, 653 (1975).
18. G.L. Roy, J.D. Embury, G. Edward and M.F. Ashby, *Acta Metall.* **29**, 1509 (1981).
19. M. Mabuchi and K. Higashi, *J. Mater. Res.* **13**, 640 (1998).
20. G.L. Roy, J.D. Embury, G. Edward and M.F. Ashby, *Acta Metall.* **29**, 1509 (1981).
21. G. Bao, J.W. Hutchinson and R.M. McMeeking, *Acta Metall. Mater.* **39**, 1871 (1991).
22. J. Rosler, G. Bao and A.G. Evans, *Acta Metall. Mater.* **39**, 2733 (1991).

APPLICATION OF COMPOSITE MATERIALS IN HYUNDAI MOTOR COMPANY

Sung Chul Kim¹, Chi Hoon Choi², Tae Won Hwang³, Won Suk Cho⁴

^{1,4} Materials Research Team, ^{2,3} Polymeric Materials Research Team,
Research & Development Division for Hyundai Motor Company & Kia Motor Company
772-1, Changduk-Ri, Namyang-Myun, Whasung-Gun, Kyunggi-Do, KOREA

SUMMARY: Hyundai Motor Company has developed and demonstrated various applications of metal matrix composites and polymeric matrix composites. Examples of applications of metal matrix composites(MMCs) are a piston, a damper pulley hub, a brake disk, a con-rod, etc. Both ceramic particles and short fibers were used as the reinforcements for MMCs and the matrix alloys were mainly aluminum alloys. To make proto parts and test specimens, various fabrication methods including squeeze casting, stir casting, PrimexTM process, etc, were adopted. Some MMC parts showed the feasibility of mass production. Thermoset polymeric composite parts were applied for low volume vehicles using hand layup, resin transfer molding and sheet molding compound. Thermoplastic composites were also applied for automotive chassis and under-the-hood parts. Glass mat thermoplastic was used for bumper back beam and glass fiber reinforced polyamide 66 are used for many parts containing rocker cover, air intake manifold, fan and shroud and so on.

KEYWORDS: MMC piston, MMC con-rod, MMC brake disc, thermoplastics, thermosets

INTRODUCTION

Metal matrix composites (MMC) and polymeric composites reinforced with ceramic fibers or particles, due to their improved mechanical properties, economy of fabrication, and ability of near-net shaping are gaining popularity for potential applications in automotive engine components, structural automotive and aerospace components. Therefore, many automotive part producers are adopting MMC and polymeric composite to achieve higher power, better durability and lower emissions by either reinforcing the whole parts or selective regions. Hyundai Motor Company(HMC) has developed many kinds of parts with MMC and polymeric composites to pace with the increasing trend of application of lightweight materials for automotive parts. In this paper, some parts which were developed by HMC are introduced.

APPLICATIONS OF METAL MATRIX COMPOSITES

According to the shape of the reinforcement, MMC parts can be divided into two categories, the fiber and the particle reinforced material parts.

Ceramic Fiber Reinforced Material Parts

Short ceramic fibers are widely used as reinforcement for the aluminum alloys in many applications due to their cost-effectiveness, near-net shaping and the suitability for mass production. Various kinds of ceramic short-fiber MMCs were investigated at HMC and summarized in Table 1.

Table 1. Summary of Ceramic Fiber MMC Applications

Item	Description	Comment
Ceramic short fiber	Saffil TM (alumina 96%) Kaowool TM (alumina : silica = 1:1) Alborex TM (9Al ₂ O ₃ .2B ₂ O ₃) HTZ TM (alumina:silica:zirconia = 3:5:2)	Cost Comparison - Expensive - Intermediate cost - Intermediate cost - Cost-effective
Part Manufacturing Method	Squeeze casting	Casting machine - Ube HVSC TM (Japan) - Modified diecaster(Korea)
Part Application	Gasoline piston, Diesel Piston Damper pulley hub, Cylinder liner, etc	

The most famous application of ceramic fiber MMC is a piston. HMC has developed both MMC gasoline and diesel pistons. For both pistons, the top ring groove regions were reinforced with short ceramic fiber and fabricated by squeeze casting. The main objects of the reinforcement are different. In MMC gasoline piston, with the enhanced high temperature strength and wear resistance of MMC, top land height could be reduced by 20% compared with that of the conventional design. Reducing top land height of piston enables the reduction of raw emission, an approximately 20% reduction of raw emissions from MMC gasoline piston engine was verified by the engine test results.

The incumbent diesel piston uses Ni-resist iron in the top ring groove region to endure the high temperature wear condition. In MMC diesel piston, MMC was substituted for Ni-resist iron. Many advantages such as better durability, weight reduction, and cost-effectiveness were achieved. Figs.1 and 2 are the actual shape of the MMC diesel piston and the microstructure of MMC near the top ring groove.



Fig. 1 MMC diesel piston



Fig. 2 Microstructure of MMC

Full load engine tests for both MMC gasoline and diesel engine piston were completed and the durability of both pistons were affirmed.

Other applications such as MMC damper pulley hub and cylinder liner also have been developed. Figs. 3 and 4 show the proto MMC damper pulley hub and the engine block with MMC cylinder liner. The test results showed that the MMC damper pulley hub has the equivalent creep behavior of a cast iron hub, and the MMC cylinder liner is a possible substitute for the incumbent cast iron liner.

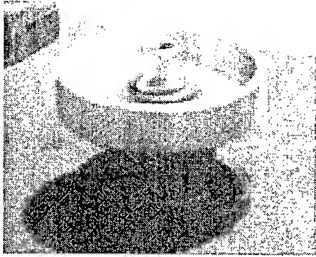


Fig. 3 MMC damper pulley hub

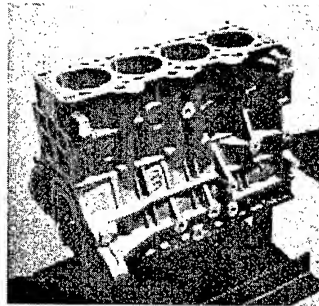


Fig. 4 Aluminum Engine block with MMC cylinder liner

Ceramic Particle Reinforced MMC Parts

The adoption of ceramic particle reinforced MMC parts such as brake discs and drum, propeller shaft, etc. are gradually increasing. As a wider range of reinforcement (10~70 vol%) is now possible in the ceramic particle reinforced MMCs, the wider application of ceramic particle MMC is growing. (Table 2)

Table 2. Summary of the Application of Ceramic Particulate Reinforced MMC

Item	Description	Comment
Ceramic Particle	SiC	Cost comparison
	Al ₂ O ₃	- more Expensive - Cost-effective
Part Manufacturing Method	Sand Casting Primex TM Pressureless Infiltration Primex TM Casting	Materials Source - Duralcan - AML(Advanced Material Lanxide)
Part Application	Vented Brake disc, Brake drum, Connecting rod, Cylinder liner, etc.	

The vented brake disk is the well known application of particle reinforced MMC and has been developed for a couple of automobiles of HMC. To cope with the requirement of higher maximum operating temperature, strength and stiffness, the fabrication method for high (≥ 30 vol. %) reinforcement content composite was required and the PrimaxTM pressureless metal infiltration process was found to be the most adequate one. The Primax processTM was also applied to making proto con-rods. The amount of particle reinforcement for the brake disk is more than 30 vol% and for the con-rod is more than 50 vol%. Figs. 5 and 6 show the proto brake disk and con-rod.

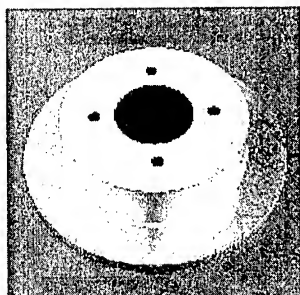


Fig. 5 Proto Brake disk



Fig. 6 Proto connecting rod

APPLICATIONS OF POLYMERIC COMPOSITE MATERIALS

The matrices of polymeric composites can be divided into two general categories ; thermosets and thermoplastics. Thermoset composites are usually compression molded and reinforced with relatively long glass fiber ($\leq 6\text{mm}$). Depending on the annual production volume of a vehicle there are some different molding techniques available such as hand layup, resin transfer molding (RTM), and sheet molding compound (SMC). On the other hand, thermoplastic composites are usually injection molded and reinforced with short glass fiber and/or mineral filler.

Thermosets

Body panels for a sports car are molded by vacuum-assisted RTM process. This application seems to be a good example of an emerging trend to reduce cost and weight for low volume vehicles. Some parts including hood, trunk lid, door, and floor panel are molded by nickel shell tooling to improve surface quality. The other ones are molded by using simple epoxy tooling. A Total of 112 kg of composite material is used in the car. The composite parts are shown in Fig. 7.

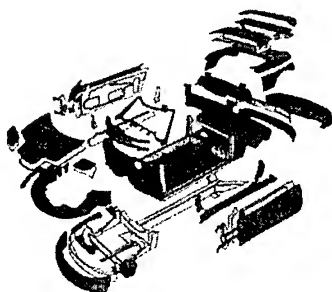


Fig. 7 Composite Parts Used in a Sports Car

Composite body panels for a lightweight vehicle based on a small car are molded by hand layup using soft epoxy tooling. High heat resistant unsaturated polyester is used as a matrix and carbon-glass hybrid type is used as a reinforcement in the composite. The total weight of the composite parts is more than 80 kg. Skin parts such as roof, fender, and side outer panel are one-piece whereas moving parts such as front door, rear door, and tailgate are two-piece parts. The hood assembly was made from low pressure SMC, so called LPMC, instead of hand layup in order to test feasibility of mass production. A standard density Class A LPMC

(specific gravity = 1.85) was used for the hood outer panel and a low density LPMC (specific gravity = 1.35) was used for the inner panel.

In the case of bus flap door, both outer and inner panels are made from SMC, and a pultruded composite is contained as reinforcement in some inner panels. A total of 125 kg of composite material is used in a bus. A sliding door panel was also made from the same material. These panels are conductive primer coated by a molding company, and then mounted on body-in-white and run through our company's paint shop.

SMC rocker cover for a new diesel engine has also developed. The weight of the cover is about 6.5 kg. In that case vinyl ester type matrix resin was used to improve chemical resistance as well as heat resistance.

Bus air conditioner cases on the roof use about 60 kg of composite that contains 35wt% of glass fiber mat. There are many kinds of specifications with different size varying with fan and blower number; therefore, hand layup is used as a cost-effective manufacturing process. Recently HMC have changed the molding method from hand layup to SMC for the purposes of common use and cost reduction.

Both head lamp reflectors and fog lamp reflectors for passenger cars are made from bulk molding compound (BMC) due to the needed higher stiffness, dimensional stability and heat resistance.

Thermoplastics

Long glass fiber reinforced polypropylene (PP), namely glass mat thermoplastic (GMT), is used for automotive parts. GMT is mainly used in chassis parts such as front end module, seat structure, and bumper back beam. We have also already developed bumper back beams for passenger cars. The weight of a GMT back beam is around 5.0kg and it is joined to a thermoplastic polyolefin outer skin. In the case of seat structure, a rear seat back prototype is in testing for a passenger car application. Other applications of GMT are the mud guard and the engine under cover which are used for buses and trucks.

Reinforced thermoplastics based on polyamide, called NylonTM, are increasingly used on under-the-hood parts. Polyamide 66 is commonly used as a matrix due to its low coefficient of friction, good dielectric properties, and excellent fatigue resistance. And higher loading of reinforcements and fillers is easy because of their excellent processability and adhesion. Short glass fiber is commonly used as reinforcement and it imparts higher mechanical properties and thermal stability to the composite parts.

In the case of plastic air intake manifold, a vibration welding method was recently adopted to produce the parts, rather than the more expensive lost-core process. A new concept module was applied to a part that integrates the rocker cover with air cleaner for a small passenger car. Polyamide 66 reinforced with 33% short glass fiber was used in the component.

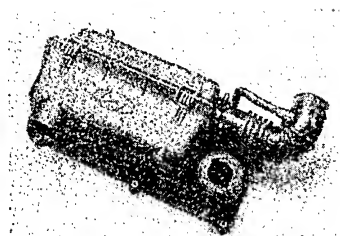


Fig. 8 Rocker Cover Module Used in a Passenger Car

Some characteristics of composite parts used in a passenger car are summarized in Table 3.

Table 3. Characteristics of composite parts used in a Passenger Car

No.	Part Name	Material	Weight (g)
1	Rear Bumper Backbeam	GMT	4,000
2	Head Lamp Reflector	BMC	760
3	Fog Lamp Reflector	BMC	200
4	Ouside Mirror Base Plate	PET-GF50	470
5	Ouside Mirror Frame	PA66-GF60	180
6	Rocker Cover	PA66-GF10+MF28	1,430
7	Intake Manifold	PA66-GF33	1,900
8	Engine Cover	PA66-GF33	1,100
9	Delivery Pipe	PA66-GF33	160
10	Accelerator Pedal	PA66-GF33	145
11	Fan & Shroud	PA66-GF17+MF21	1,670
12	Radiator End Tank	PA66-GF33	700
	Total		12,715

CONCLUSIONS

1. With ceramic short fiber reinforced MMC, pistons and the damper pulley hub, etc. have been demonstrated and some parts are in the final preparation step for mass production.
2. With ceramic particle reinforced MMC, the brake discs and the con-rod, etc. have been developed and continue to be evaluated actively these days.
3. The applications of polymeric composite parts are increasing rapidly

REFERENCES

1. Taewon Lim, "Fabrication and Mechanical Behaviour of Aluminum Matrix Composite Materials", *Ph.D. dissertation, New York state University*, Nov., 1990.
2. A.R. Baker, "Developments in materials for Pistons", *Materials and design*, Vol. 9, No. 1, 1998.

3. Tommy J. Bedwell, "MMC Pistons a solution for 1990's High Output Diesel", *SAE 890595*, 1989.
4. Alexandre Afonso, "Development of Fiber Reinforced Aluminum Alloy for Diesel Piston Applications", *SAE 910632*, 1991.
5. F.K. Chi, "Elevated Temperature Mechanical Properties of Squeeze Cast Metal Matrix Composites for Diesel Pistons", *SAE 930183*, 1993
6. H.W. Nam, "Mechanical Properties and Fatigue Behaviour of HTZ/AC8A Metal Matrix Composites", *Journal of Korean Society of Metal Matrix Composites*, Vol.11, No. 5, 1998.
7. J. Querengaesser, "The Effect of Cranktrain Design on Powertrain NVH", *SAE 971994*, 1997.
8. A. James and T. Miller, "Performance Comparison of Plastic Composites with Metals for Vertical Body Panel Applications", *SAE Technical Paper 1999-01-0848*.
9. O.C.Zaske in "Handbook of Thermoset Plastics", S.H. Goodman ed., Noyes Publications, New Jersey, 1998, pp.97-168.
10. R.F. Jones, "Guide to Short Fiber Reinforced Plastics", Hanser, Munich, 1998, pp.25.
11. "Thermoplastics drive into the Future", *Reinforced Plastics*, Vol.42, No. 9, 1998, pp.46-50.

Adhesion & Coating

A STUDY ON ICE ADHESIVENESS TO NEWLY-DEVELOPED WATER-REPELLENT COATING

Hiroyuki SAITO¹, Goro YAMAUCHI², Kenichi TAKAI³, Chiemi NISHI⁴ and Toshinobu UEDA⁴

¹ *Nippon Telegraph and Telephone East Corporation*
UrbanNet Bldg 18F, 2-2-2 Otemachi, Chiyoda-ku, Tokyo, Japan: saito@mm.bch.east.ntt.co.jp

² *Daido Institute of Technology*
2-21 Daido-cho, Minami-ku, Nagoya, Japan: gyamauch@daido-it.ac.jp

³ *Sophia University*
7-1 Kioicho, Chiyoda-ku, Tokyo, Japan: takai@me.shophia.ac.jp

⁴ *NTT Advanced Technology*
3-9-11 Midoricho, Musashino-shi, Tokyo, Japan : hirec@ntt-at.co.jp

SUMMARY: Thick snow or ice adhering to the surface of an antenna used for radio communication can impede telecommunication, so methods to reduce the build-up of snow and ice are needed. We have studied the use of water-repellent coatings to prevent snow and ice sticking, and in this paper, we report our results of tests on ice adhesion and how it is affected by the contact angle, surface roughness and thermodynamics. And we obtained the results as following: (1) A water-repellent coating consisting of PTFE particles dispersed in polyvinylidene fluoride exhibited a contact angle of 150 degrees. (2) Ice adhesion was linearly proportional to the surface free energy of the water-repellent coating. (3) The higher the surface roughness of high wettability materials, the stronger the adhesion. The higher the surface roughness of water-repellent coatings, the weaker the adhesion.

KEYWORDS: Wettability, Water-repellent, Coating, Adhesion, Snow, Ice Wettability, Water-repellent, Coating, Adhesion, Snow, Ice

INTRODUCTION

Since thick snow or ice adhering to the surface of an antenna used for radio communication can impede telecommunication [1-3], methods to reduce the build up of snow and ice are needed. Various methods have been investigated, for example, the adhesion of ice to common rubber has been measured [4-6], and recently, a method that takes advantage of the physiochemical properties of material surfaces has attracted attention [6]. Snow or ice build-up is seen when the thin water layer on snow or ice particles adheres to a surface [6-8]. Therefore, a surface that has low wettability, i.e., a water-repellent surface, can prevent snow or ice sticking to antennas. Fluorocarbon, such as pure PTFE has been used to prevent snow or ice sticking, but their water-repellency is not good enough.

We have studied a new water-repellent coating and its application to prevent snow and ice sticking. In this paper, we report the results of our tests on ice adhesion and how it is affected by the contact angle, surface roughness and thermodynamic factors.

EXPERIMENTAL

Samples

Water-repellent coatings were made as follows. Fine particles of polytetrafluoro-ethylene (PTFE), which had perfluorinated terminal ends, an average molecular weight of 1000, and a particle size of about $1\ \mu\text{m}$, were dispersed and mixed into a 30 to 90 vol. % polyvinylidene fluoride (PVdF) resin by using a ball mill [9,10] to give a PTFE content ranging from 30-90 vol. %. The re-sulting mixture was sprayed onto an epoxy-resin-based fibre-reinforced plastic sub-strate $250 \times 350 \times 3\text{ mm}$. For comparison, we used samples of stainless steel (JIS SUS 304) and conventional PTFE. The surface roughness of samples was measured as ten point height of irregularities (R_z).

Measurement of The Contact Angle and Surface Free Energy

To measure the contact angle of each sample, we dropped a water droplet with volume of 4 mm^3 onto the sample surface [11] and measured the contact angle between the sessile water droplet and the sample using the CA-Z contact-angle measurement system manufactured by Kyowa Kaimen Kagaku Co., Ltd.

The same measurement was also made using bromonaphthalene and methyl iodide instead of water. The apparent surface free energies exhibited by the samples were determined in accordance with the extended Fowkes's equation [12].

Surface Observation

We used a scanning electron microscope (SEM), manufactured by JEOL Ltd., to observe the surface of the water-repellent coatings. Water droplets having diameters of about $10\text{--}50\ \mu\text{m}$ were then condensed onto the surface, and observed using an environmental SEM (ESEM), manufactured by Nikon Corp. The ESEM enables a secondary electron image to be observed in vacuum as low as about 1000 Pa [13].

Measurement of Ice Adhesion

To measure the shearing force at the interface between ice and sample, we used the experimental apparatus shown in Fig. 1. We developed this apparatus based on some references [14-16]. The sample was fixed on a movable stage (Fig. 1) installed in an isothermal reservoir whose temperature had been previously reduced to -5°C . The sample was left on the stage until its temperature reached that in the reservoir. A cylindrical block of ice (20 mm high, 25 mm in diameter) was produced from deionized water at -5°C . The bottom of the ice block was wetted by 0°C water. The ice block was then placed on the sample. As shown in Fig. 1, the ice block was connected to a transducer by using a PTFE cap and immobilized by a stainless wire. After 5 minutes of contact, the stage was moved horizontally at a speed of 2 mm/min and the shearing force was measured during the movement. No load was applied to the ice to make it adhere to the sample. That is, the only force on the ice was gravity.

RESULTS AND DISCUSSION

Contact Angle, Roughness and Surface Free Energy

As Fig. 2 shows, when the PTFE content in the coating was 60%, the contact angle was about 150 degrees, which is much larger than that for the conventional PTFE plate (110 degrees) and SUS304 (40 degrees). An example of a water droplet on a water-repellent coating that contains 80%PTFE is shown in Fig. 3.

The surface roughnesses of coatings are shown in table 1. The larger the PTFE content, the rougher the surface.

As shown in Fig. 4, the surface free energy decreased with increasing PTFE content. It was 10mJ/m^2 when the PTFE content was 80%, which is lower than that of conventional PTFE plate (21 mJ/m^2).

Surface Observation

As shown in SEM photographs of sample surfaces (Fig. 5), the PTFE particles projected from the surface. At PTFE content of 60% and above, almost the whole surface was covered with particles. Below 60%, some of the surface was not covered. This explains why the contact angle increased abruptly when the PTFE content reached 60%, where the coating can be considered to be a particulate composite of PTFE particles and PVdF binder. Additionally, most of the outer surface is composed of particles and air gaps [17-19]. Therefore, this coating has an extremely large contact angle according to Cassie's equation. In the 60%PTFE-40%air covering system (Fig. 6), the contact angle of that coating can be estimated by Cassie's equation [20-23]:

$$\cos \theta = t \cos \phi + (1-t) \cos \pi = 0.6 \cos 110^\circ + 0.4 \cos 180^\circ \quad (1)$$

Here, θ is the contact angle of the composites, ϕ is the contact angle of the PTFE and t is the coverage of the PTFE particles. The coverage of air is $1-t$, and the contact angle of air is considered to be π , so contact angle θ is 127 degrees. This equation is not enough to completely explain this large contact angle because the ends of the PTFE particles are not flat but hemispherical, and the actual coverage of PTFE particles on the outermost surface is less than 0.6 and that of air is more than 0.4.

An ESEM image of water droplets on the surface of the sample is shown in Fig. 7. The contact angle when the amount of PTFE was 60% was 140 degrees, even when the water droplet had a diameter twice the particle size, as shown in Fig. 7. This angle was substantially the same as that for a 4 mm^3 droplet. This result is consistent with that for a sample in which PTFE alone was deposited on a glass preparation [24]. The PTFE particles thus covered the surface of the coating.

Ice Adhesion

The relationship between the ice adhesion and the surface free energy of the coating was linear, as shown in Fig. 8. This result is consistent with Yoshida's results for the surface free energy of a solid material and the ice adhesion of roof coatings [6].

Figures 9 and 10 show the relationships between the surface roughness of the sample and the ice adhesion. Figure 9 shows the results obtained using SUS304 with a contact angle of 40 degrees, and Fig. 10 shows the results obtained using water-repellent coatings having a contact angle of 145 degrees.

The higher the surface roughness of the SUS304, the greater the adhesion. This is known as normal adhesion [25] and agrees with the experimental results for ice sticking reported by Landy[5] and Yoshida[6]. For the water-repellent coatings, the rougher the surface, the weaker the adhesion, as shown in Fig. 10.

We attribute the difference between the results for stainless steel (SUS304) and those for the water-repellent coatings to the difference in surface wettability. That is, for materials with

high wettability, such as stainless steel, as the surface becomes rougher, liquid penetration into the rough surface increases. This causes either the anchoring effect or the fastener effect, and the adhesion increases. In contrast, for materials with low wettability, such as a water-repellent coating, as the surface becomes rougher, liquid penetration decreases. Liquid water is still supported by the materials. As a result, the anchoring or fastener effect is smaller. Therefore, covering antennas with this water-repellent material having controlled surface roughness will reduce snow and ice adhesion to them.

CONCLUSION

Our study on water-repellent coatings and their effects on ice adhesion is summarized as the follows:

1. A new type of water-repellent coating consisting of perfluorinated PTFE particles dispersed in PVdF resin binder exhibited a contact angle of about 150 degrees. This extraordinarily high contact angle is attributed to the surface roughness and surface heterogeneity of the new material taking into account the existence of air between water and the new material in the high PTFE content resin.
2. The surface free energy of the water-repellent coatings has a linear relationship with the ice adhesion.
3. The larger the surface roughness of high wettability materials, the larger the adhesion. And the larger the surface roughness of water-repellent coatings, the smaller the adhesion. This difference is apparently based on the water-penetrating properties attributed to the difference in anchoring effect on rough surface.

ACKNOWLEDGEMENT

Hiroyuki SAITO thanks Miss Ayumi IIDA for her help of illustrating some figures.

REFERENCES

1. Saito, H., Yamauchi, G., Kenichi, T., Sugawara N., Hayashi Y., "Hydrophobic Paint for Reducing of Ice Accreting and Preventing Its Harmful Effects on Reflection", *The transactions of the institute of electronics, information and communication engineering*, J81C2, (1998)pp.342-349(in Japanese)
2. Asami, Y., and Matsumoto, T., *Denshi Joho Tsusin Gakkai Shi (The Transactions of The Institute of Electronics, Information and Communication Engineers)*, **74** (1991) pp.897-891.(in Japanese)
3. Yamauchi, G. and Ueda, T., *Kogyo Zairyo (Industrial Materials)*, **44** (1996) pp.42-46.(in Japanese)
4. Anderson, L., Golander, C., and Persson, S., *Journal of Adhesion Science and Technology*, **8** (1994) pp.117-121.
5. Landy, M., and Freiburger, A., *Journal of Colloid and Interface Science*, **25** (1967) pp.231-247.
6. Yoshida, M., *Nippon Setchaku Gakkai Shi (Journal of Adhesion Society of Japan)*, **30** (1994) pp.418-422.
7. Mizuno, Y. and Wakahama, G., *Teion Kagaku Butsurihen (Low Temperature Science)*, **38**(1980) pp.17-26.(in Japanese)
8. Mizuno, Y., and Wakahama, G., *Teion Kagaku Butsurihen (Low Temperature Science)*, **35**(1978) pp.133-135.(in Japanese)

9. Ueda, T., *Bousei Bousyoku Gijutu Happyou Taikai Yokousyuu (Preprint of Corrosion Protection Conference)* (1996) pp.188-189.
10. Kato, E., Sugimoto, Y., Kita, Y. and Ando, I., *Abstract of 14th International Symposium on Fluorine Chemistry* (1994) p.275.
11. Yamauchi, G., Takai, K., Saito, H. and Kojima, M., *Extended Abstract of The First Asian-Australasian Conference on Composite Materials vol.2* (1998) pp.609-613
12. Kitazaki, N. and Hata, T., *Nippon Setchaku Kyokai Shi (Journal of The Adhesion Society of Japan)*, **8** (1972) pp.131-139.(in Japanese)
13. Parra, R. E., *Microscopy Research and Technology*, **25** (1993) pp.362-366.
14. Shimizu, M., *Seppy (Snow and Ice)*, **54** (1992) pp.269-273.(in Japanese)
15. Tomabechi, T. and Ito, T., *Seppy (Snow and Ice)*, **56** (1994) pp.215-219.(in Japanese)
16. Murase, H., Kogure, H., Fujibayashi, T., Tamura, K and Haruta, N. , *Journal of Applied Polymer Science*, **54** (1994) pp.2051-2058.
17. Shibata, F. and Kawasaki, S., *Sen-i Gakkai Shi (Fiber)*,**44** (1988) pp.94-98.(in Japanese)
18. Hozumi, A., *Hyomen Gijutu (Surface Finishing)*, **47** (1996) pp.575-579.(in Japanese)
19. Saito, H., Takai, K. and Yamauchi, G., *NTT R&D*, **48** (1999) pp.337-343.(in Japanese)
20. Cassie, A. B. D. and Baxter, S., *Transactions of Faraday Society*, **40** (1944) pp.546-552.
21. Yamauchi, G., Miller, J. D., Takai, K., Saito, H and Takazawa, H., *Book of Abstracts, 14th European Chemistry at Interfaces Conference*,(1996) pp.37-41.
22. Handa, T., Saito, H. and Takazawa, H., *Zairyo-to-Kankyo (Corrosion Engineering)*, **45** (1996) pp.460-466.(in Japanese)
23. Yamauchi, G., Miller, J.D., Saito, H., Takai, K., Takazawa, H. and Ueda, T., *Materials Transactions of JIM*, **37** (1996), pp.721-726.
24. Saito, H., Takai, K. and Takazawa H., *Hyomen Gijutu (Surface Finishing)*, **46** (1995) pp.86-90.(in Japanese)
25. Nakao, K., *Hyomen Gijutu (Surface Finishing)*,**42**(1991) pp.964-968.(in Japanese)

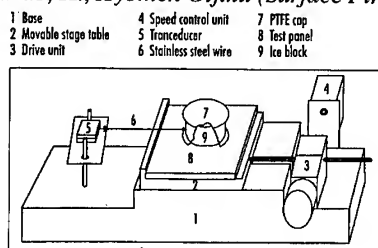


Fig.1 Schematic illustration of apparatus

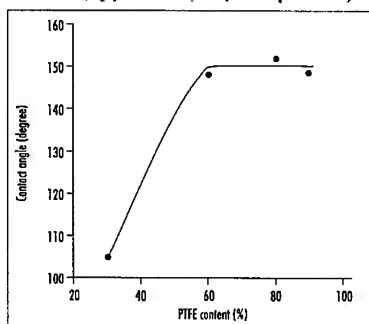


Fig.2 Relation between contact angle and PTFE content

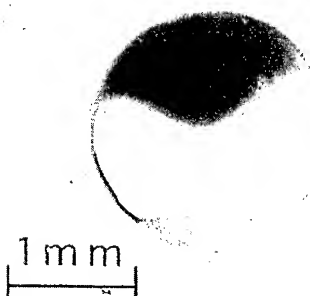


Fig.3 Water droplet on water-repellent coating

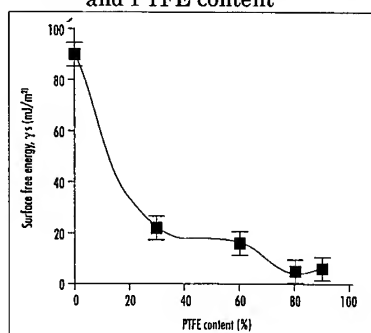


Fig.4 Relation between surface free energy and PTFE content

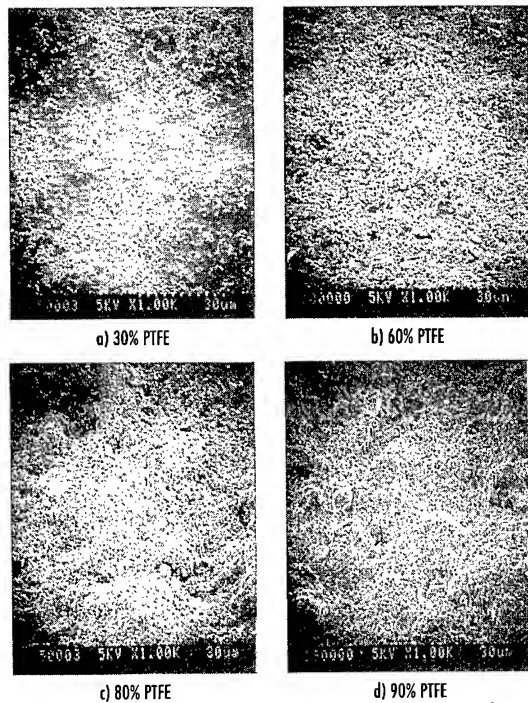


Fig.5 Surface views of the water-repellent coatings

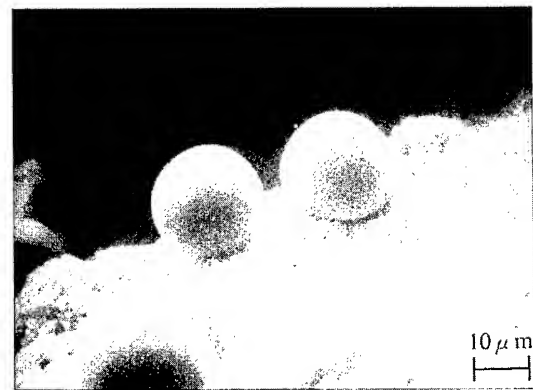


Fig.7 ESEM views of droplets on 60%PTFE coating

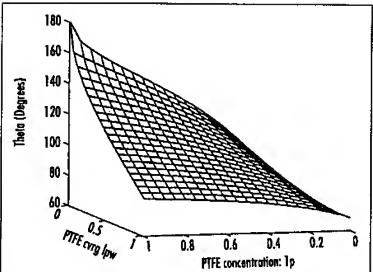


Fig.6 Relation of contact angle, PTFE concentration and its coverage

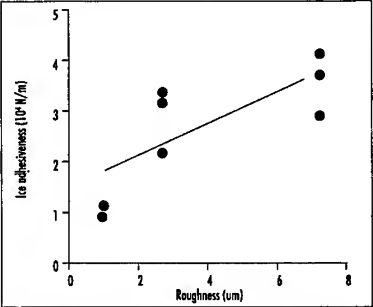


Fig.8 Relation between ice adhesion and surface free energy

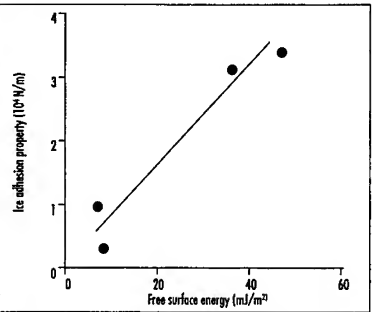


Fig.9 Relation between ice adhesion and the roughness of SUS surface

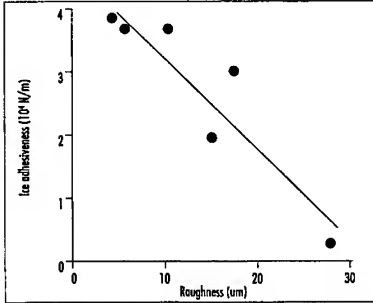


Fig.10 Relation between ice adhesion and the roughness of coating surface

A STUDY ON THE TENSILE LOAD BEARING CAPACITIES OF A CO-CURED DOUBLE LAP JOINT

Kum Cheol Shin¹ and Jung Ju Lee¹

¹*Department of Mechanical Engineering, Korea Advanced Institute of Science and
Technology 373-1, Kusong-dong, Yusong-gu, Taejon 305-701,
Korea: kcshin@imhp.kaist.ac.kr and jjlee@sorak.kaist.ac.kr*

SUMMARY: A co-cured joint requires neither any surface treatment onto the composite laminate nor additional adhesive joining process because the co-cured joining process is accomplished by the excess resin extracted from composite materials during consolidation. In this work, the tensile load bearing capacities of the co-cured double lap joint subjected to the tensile load was experimentally investigated. Co-cured joint specimens, which have several bond parameters such as bond length, surface roughness and stacking sequence of the composite laminate, were fabricated and tested. Failure mechanism of the co-cured double joint was cohesive failure by delamination at the 1st ply of the composite laminate. Finally the optimum values of several bond parameters were determined.

KEY WORDS: Co-cured double lap joint, Tensile load bearing capacity, Bond length, Stacking sequence, Surface roughness, Delamination.

INTRODUCTION

Since the conventional metal alloys are still those of the most important engineering materials compared to the advanced polymer composite materials, the joining between the metal alloys and polymeric composite materials is very useful for the fabrication of various engineering structures. The efficiency of the composite structures is largely dependent on the joint used rather than the structure itself [1]. A co-cured joint, whose curing and bonding processes are performed simultaneously, can be thought of as an adhesively bonded joint whose adhesive is the excess resin extracted from composite materials during consolidation. The co-cured joint has several advantages compared to the adhesively bonded joint because of manufacturing simplicity. The co-cured joint requires neither adhesive nor surface treatment of the composite laminate. Since the adhesive of the co-cured joint has the same material properties as the resin of the composite laminate, the analysis and design of the co-cured joint for composite structures becomes simpler compared to those of the adhesive joint which uses additional adhesive.

Jones *et al.* [2] performed shear test of the co-cured joint and reported the shear properties. Kim *et al.* [3] manufactured the co-cured stepped lap joints for the composite structures and

tested under the static and fatigue tensile loads. Choi and Lee[4] reported the torque capacities of the co-cured tubular lap joint with and without knurling of the pyramid type. Lee *et al.* [5] reported the static and dynamic torque capacities of the co-cured joints manufactured with respect to several bond parameters such as surface roughness, bond length and stacking sequence of the composite laminate. Cho *et al.* [6, 7] designed and fabricated the hybrid shaft by co-curing the composite materials to the aluminum. They measured vibration characteristics of the hybrid drive shaft by impulse-frequency responses and whirling tests. They calculated the residual thermal stress distribution along the length of the preloaded co-cured hybrid shaft by finite element method. The fatigue torque transmission capability of the co-cured hybrid shaft was experimentally investigated.

Table 1 Properties of the composite materials (USN150)

Longitudinal tensile modulus E_L , GPa	130
Transverse tensile modulus E_T , GPa	8
Shear modulus G_{LT} , GPa	6
Poisson's ratio ν_{LT}	0.28
Longitudinal tensile strength X' , MPa	1800
Transverse tensile strength Y' , MPa	60
Shear strength S , MPa	75
Ply thickness, mm	0.15
Density, kg/m^3	1560

Static and dynamic joint strengths of composite structures are dependent on the surface roughness of the adherends, stacking sequence of the composite laminate and bond length [8, 9]. In this work, co-cured double lap joint specimens, which have several bond parameters such as bond length, surface roughness and stacking sequence of the composite laminate, were fabricated and experimentally tested.

EXPERIMENT RESULTS

Table 1 shows the properties of the carbon/epoxy composite (USN150) produced by SK Chemicals. Figure 1 shows the dimensions of the co-cured double lap joint specimen. The stacking sequences of the composite laminates are $[\pm\theta]_{4S}$ ($\theta=0, 15, 30, 45^\circ$), where θ is called stacking angle. The specimens were cured without resin bleeder and peel ply to prevent the excess resin from bleeding under 0.7 MPa pressure [10]. Figure 2 shows a recommended cure cycle for the carbon/epoxy composite.

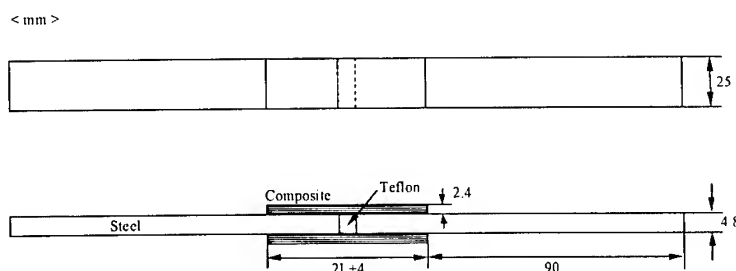


Fig. 1 Dimension and shape of the co-cured double lap joint specimen

Figure 4 shows the tensile load bearing capacity of the co-cured double lap joint with respect to stacking sequence of the composite laminate. The tensile load bearing capacities of the co-cured double lap joint decreased as the stacking angle increased. Figure 5 shows the tensile load bearing capacities of the co-cured double lap joint with respect to bond length. Irrespective of stacking sequence of the composite laminate, tensile load bearing capacities of the co-cured double lap joint increased but the rate of increase reduced when the bond length increased. Figure 6 shows the tensile load bearing capacities of the co-cured double lap joint with respect to surface roughness between the steel adherend and composite adherend. Tensile load bearing capacities of the co-cured double lap joint were little affected by surface roughness.

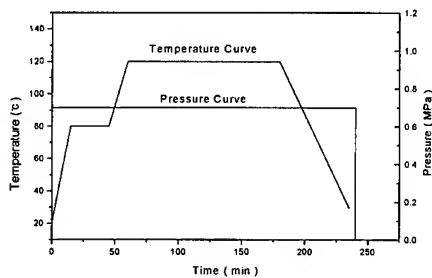


Fig. 2 Cure cycle for the carbon/epoxy composite

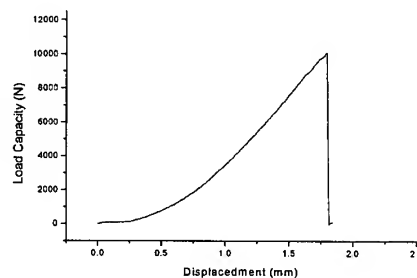


Fig. 3 Typical tensile load-displacement curve of the co-cured double lap joint

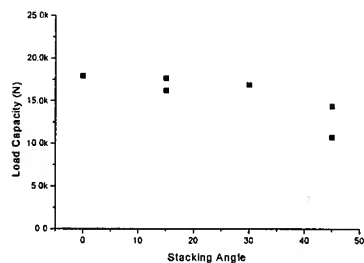


Fig. 4 Tensile load bearing capacities of the co-cured double lap joint w.r.t. stacking sequence

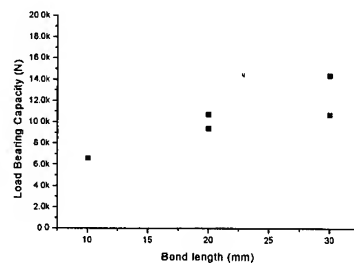


Fig. 5 Tensile load bearing capacities of the co-cured double lap joint w.r.t. bond length

The specimens were tested with a 10 kN MTS, a material testing system. The loading speed was 1.27 mm/min. Figure 3 shows the typical tensile load-displacement curve of the co-cured double lap joint. The failure mechanism of the co-cured double lap joint was cohesive failure by delamination at the 1st ply of the composite laminate.

CONCLUSIONS

In this work, the tensile load bearing capacities of the co-cured double lap joint was experimentally investigated and the optimum values of several bond parameters were determined. From the experimental investigations, the following conclusions were obtained:

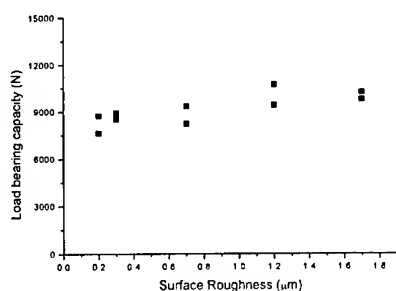


Fig. 6 Tensile load bearing capacities of the co-cured double lap joint w.r.t. surface roughness

1. The failure mechanism of the co-cured double lap joint was cohesive failure by delamination at the 1st ply of the composite laminate.
2. Tensile load bearing capacities of the co-cured double lap joint decreased as the stacking angle increased.
3. Tensile load bearing capacities of the co-cured double lap joint increased but the rate of increase reduced when the bond length increased.
4. Tensile load bearing capacities of the co-cured double lap joint were little affected by surface roughness.

REFERENCES

1. T. J. Reinhart(Eds.), Composites, ASM International, Metal Park, Ohio 44073, U.S.A., 1987.
2. R. M. Jones, W. K. Chiu and J. Paul, "Designing for the Damage Tolerant Bonded Joints," Composite Structures, Vol. 25, 1993, pp. 201-207.
3. H. S. Kim, S. J. Lee and D. G. Lee, "Development of a Strength Model for the Co-cured Stepped Lap Joints under Tensile Loading," Composite Structures, Vol. 32, 1995, pp. 593-600.
4. J. H. Choi and D. G. Lee, "Torque Capacity of Co-cured Tubular Lap Joints," Journal of Composite Materials, Vol. 31, No. 14, 1997, pp. 1381-1396.
5. S. W. Lee, D. G. Lee and K. S. Jeong, "Static and Dynamic Torque Characteristics of Composite Co-cured Single Lap Joint, Journal of Composite Materials, Vol. 31, No. 21, 1997, pp. 2188-2201.
6. D. H. Cho, D. G. Lee and J. H. Choi, "Manufacture of One-piece Automotive Drive Shafts with Aluminum and Composite Materials," Composite Structures, Vol. 38, 1997, pp. 309-319.
7. D. H. Cho and D. G. Lee, "Manufacturing of Co-cured Composite Aluminum Shafts with Compression during Co-curing Operation to Reduce Residual Thermal Stresses," Journal of Composite Materials, Vol. 32, No. 12, 1998, pp. 1221-1241.
8. D. G. Lee, K. S. Kim and Y. T. Im, "An Experimental Study of Fatigue Strength for Adhesively Bonded Tubular Single Lap Joints," Journal of Adhesion, Vol. 35, 1991, pp. 39-53.
9. Kum Cheol Shin and Jung Ju Lee, "A Study on the Strength of the Co-cured Joint," Proc. of the First Asian-Australasian Conference on Composite Materials: (ACCM-1), Vol. 1, 1998, pp. 425.

Effects of Strain Rates on Stress-Strain Behaviors in Adhesively Bonded Joints

Katsuhiko Osaka¹, Akinori Fujinami², Takao Wada³, Takehito Fukuda⁴ and Makoto Imanaka⁵

^{1,4} Department of Intelligent Materials Engineering, Osaka City University,
3-138, Sugimoto 3, Sumiyoshi-ku, Osaka 558-8585 Japan
E-mail: ohsaka@mech.eng.osaka-cu.ac.jp

takehito@mech.eng.osaka-cu.ac.jp
^{2,3} Graduate School of Osaka City University
E-mail: fujinami@zai6.mech.eng.osaka-cu.ac.jp
wada@zai6.mech.eng.osaka-cu.ac.jp

⁵ Department of Tech. Education, Osaka University,
4-698-1, Asahigaoka, Kashiwara-City, Osaka 582-8582 Japan
E-mail: imanaka@cc.osaka-kyoiku.ac.jp

SUMMARY: In the experiments, tensile tests of the bulk specimens made of an epoxy adhesive were performed at the various constant strain rates and the stress-strain curves were measured. And shear tests of bonded joint specimens consisting of ring-shaped adherends were also done under various loading rates and the stress-strain curves of their adhesive layers were measured. Furthermore, the stress-strain curves of adhesive layers in the butt joint specimens at various constant crosshead speeds were measured under tensile loading. From these experimental results, their equivalent stress-equivalent plastic strain relations were obtained and compared. And the effects of the strain rates on the stress-strain behaviors in adhesively bonded joints were examined.

KEYWORDS: Strain rate, Stress-strain curve, Adhesively bonded joint, Butt joint, Epoxy adhesive, Pure shear stress state

INTRODUCTION

Adhesive bonding has many attractive features in comparison with other joint techniques, such as bolting, riveting and so forth [1]. Chemical engineering works to develop high-performance adhesives are active and newly developed adhesives are in use. But structural adhesive bonding has a low reliability and is empirically designed [2]. Failure behaviors of bonded joints are more complicated than those of single material parts because they have many factors affecting them. The factors are, for example, combination of adherends and adhesives, form of bonded joints, curing state of adhesives, state of bonded surface and so forth. The stress-strain behavior of the adhesive is very important for the stress analysis of the joints. The adhesive designates remarkable viscoelastic nature. Therefore, it is expected that strain rates conspicuously affect its stress-strain behavior. However, it has not been clarified yet. The stress-strain curves of the bulk adhesives are usually used when the stress analysis of the bonded joints is performed. But it is predicted that the stress-strain behavior of the adhesive layer in the bonded joints differs from that of the bulk adhesives, because the deformation of the adhesive layer having a very thin thickness

is constrained extensively by the adherends.

In the present paper, the effects of the strain rates on the stress-strain behavior in adhesively bonded joints were investigated. In the experiments, tensile tests of the bulk specimens were performed at the various constant crosshead speeds and their stress-strain curves were measured. And shear tests of bonded joint specimens consisting of ring-shaped adherends were also done under various loading rates and the stress-strain curves of their adhesive layers were measured. Furthermore, the stress-strain curves of adhesive layer in the butt joint specimens at various constant crosshead speeds were measured under tensile loading. From these experimental results, their equivalent stress-equivalent plastic strain relations were obtained and compared. And the effects of the strain rates on the stress-strain behaviors in adhesively bonded joints were examined.

EXPERIMENTS

Specimens

The shape and dimensions of the bulk specimen are shown in Fig.1. They have been defined in JIS K7113. Fig.2 shows the shape and dimensions of the butt joint specimen. Its adhesive layer thickness is controlled to be nominally 0.3mm. The shape and dimensions of the pure shear specimen used for the shear tests are shown in Fig.3. The adhesive layer has a ring shape and bonds the adherends A and B as shown in the right side of the figure. The pure shear stress state in it is realized when the shearing loads are applied to the specimen as shown in the left side of the figure. The adhesive layer thickness is controlled to be nominally 0.5 mm. The materials used for the adherends of the butt joint and the pure shear specimens are a carbon steel for machine construction (JIS S45C). The adherend surfaces of the butt joint and pure shear specimens were treated for bonding by dry-polishing with 320-grade emery papers and washing with acetone. The adhesive used in the specimens is an epoxy one (Araldite Standard; Nagase-Chiba Inc.). The epoxy adhesive and curing agent were mixed at 1:1 in volume ratio with degassed below 10mmHg. The specimens were cured at 60°C for 48 hours in a constant temperature oven.

Measurement method

The uniaxial tensile tests of both the butt joint and bulk specimens were performed at the various constant crosshead speeds (V)=0.1mm/min, 1.0mm/min, 10mm/min and 50mm/min.

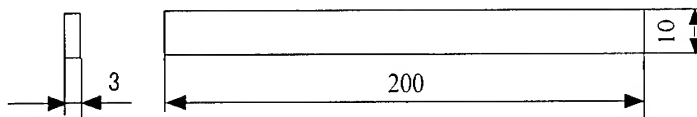


Fig.1 Shape and dimensions of the bulk specimen.

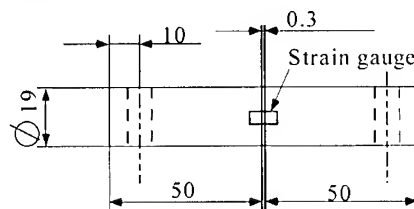


Fig.2 Shape and dimensions of the butt joint specimen.

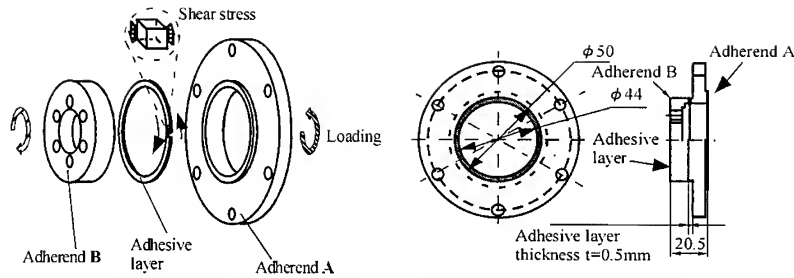


Fig.3 Shape and dimensions of the pure shear specimen.

The bulk specimens were also tested at $V=100\text{mm/min}$ in addition to these speeds. The strain of the bulk specimen was measured with the strain measurement system using a CCD camera. For the butt joint specimen, the strain of the adhesive layer was measured with the strain gauges bonded on the adhesive layer as shown in Fig.2. Since the measurement area of the strain gauge includes the adherends as shown in Fig.2, the strains of the adherends are included in the measured values. So, the strain of the adhesive layer was obtained by calculating from the measured values of the strain gauges. The shear tests of the pure shear specimen were performed at the constant rotating rates (R)= 0.4deg./min , 2.0deg./min and 12deg./min with a shear test machine designed in the authors' laboratory. The shear strain of the pure shear specimen was obtained from the relative shear displacement of the adherends A and B which was measured with a noncontact displacement sensor. All tests were performed in the room where the temperature was kept at 23°C .

RESULTS AND DISCUSSIONS

Stress-strain curves of the bulk specimens at the various strain rates

The stress-strain curves of the bulk specimens at various strain rates are shown in Fig.4. In the figure, the abscissa is the strain rate converted from the crosshead speed on the basis of the linear relation between them which has been confirmed by preliminary tests. The fracture stress and strain, the elastic modulus and the inclination of the stress-strain curve after the yielding point of all the specimens increase with the strain rate as shown in the figure.

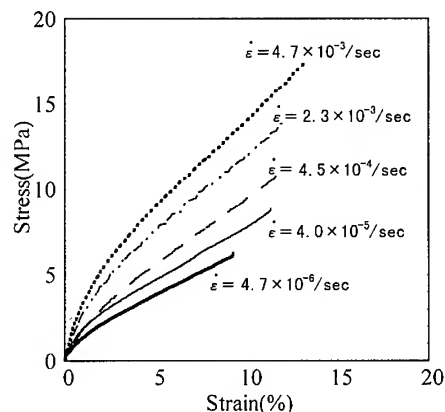


Fig.4 Stress-strain curves of the bulk specimens at various strain rates.

Stress-strain curves of the butt joint specimens at the various crosshead speeds

The relation between the strain of the adhesive layer and the crosshead displacement of the butt joint specimen at $V = 1.0\text{mm/min}$ is shown in Fig.5. The broken line indicates the elastic limit of the stress-strain curve. The strain rate is approximately constant before the elastic limit but increases rapidly after that. Therefore, in the tensile test of the butt joint specimen, it isn't constant after the elastic limit. Its value before the elastic limit is about two orders of magnitude smaller than that after the elastic limit. The stress-strain curves of the butt joint specimens are shown in Fig.6 with the parameter of the crosshead speed. From the figure, it is found that the elastic moduli and the yield points of all the specimens increase with the crosshead speed.

Shear stress-shear strain curves of the pure shear specimens at the various constant shear strain rates

It was confirmed that the relation between the shear displacement and the shear strain was linear in the shear test. Fig.7 shows the shear stress-shear strain curves of the pure shear specimens at the various constant shear strain rates ($\dot{\gamma}$). With the increasing strain rate, the elastic modulus increases but the failure strain decreases.

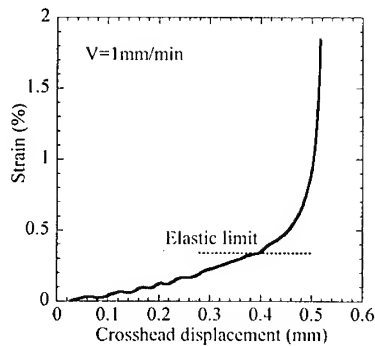


Fig.5 Relation between strain and crosshead displacement in the butt joint specimen.

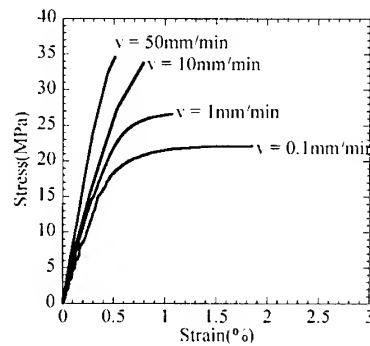


Fig.6 Stress-strain curves of the butt joint specimens at the various crosshead speeds.

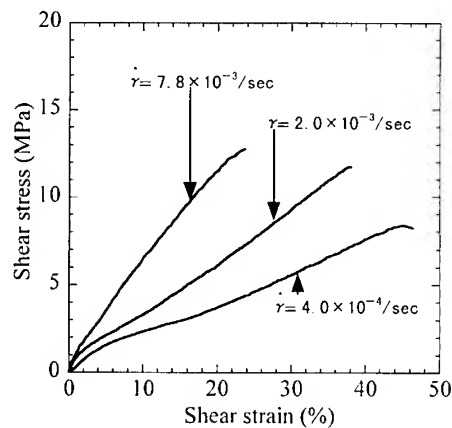


Fig.7 Shear stress-shear strain curves of the pure shear specimen at the various strain rates.

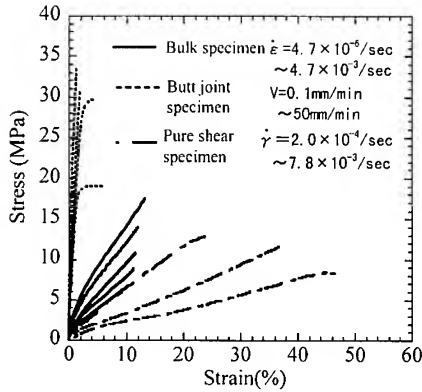


Fig. 8 Stress- strain curves of all the specimens.

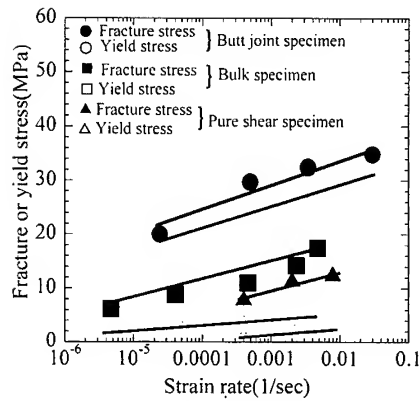


Fig. 9 Fracture and yield stresses of all the specimens.

Comparison of the stress-strain behaviors of the bulk, the butt joint and the pure shear specimens

Fig. 8 shows the stress-strain curves of all kinds of the specimens. The elastic moduli of the butt joint specimens are an order of magnitude higher than those of the bulk specimens. The apparent modulus of the butt joint specimen is higher than that of the bulk specimen, because the deformation of their adhesive layer is constrained by the adherends. But it is too high even if this effect is considered. Therefore, further investigation of the measured strains of the butt joint specimens is needed. Fig. 9 shows the fracture and the yield stresses of all kinds of the specimens. The ordinate is the stress and the horizontal axis is the strain rate designated by the logarithmic scale. For the butt joint specimens, the strain rate before the elastic limit is adopted for the abscissa. If the tensile test of the butt joint specimen at a constant strain rate is performed, the failure stress will designate the value between the yield and the fracture stress. Its cause is that the strength should be lower than that shown in the figure at the lower strain rates after the elastic limit. The fracture and the yield stresses of the butt joint specimens increase linearly with the increasing strain rate as shown in the figure. The difference between the fracture and the yield stresses of the butt joint specimen are smaller than that of the bulk and the pure shear specimens. Therefore, the degree of the work hardening of the butt joint specimen is smaller than that of the bulk and the pure shear specimen.

Equivalent stress-equivalent plastic strain curves of the bulk and the pure shear specimens

In order to compare the stress-strain behaviors between the bulk and the pure shear specimens, their equivalent stress-equivalent plastic strain ($\sigma_{eq} - \epsilon_{eq}$) curves are shown at almost the same order of equivalent plastic strain rate ($\dot{\epsilon}_{eq}$) in Fig. 10. The equivalent stress increment ($d\sigma_{eq}$) and the equivalent plastic strain increment ($d\epsilon_{eq}$) of the pure shear specimen under the pure shear stress condition are given by the following equations,

$$d\sigma_{eq} = \sqrt{3}d\tau \quad (1)$$

$$d\epsilon_{eq} = \frac{1}{\sqrt{3}} \left(d\gamma - \frac{d\tau}{G} \right) \quad (2)$$

where $d\tau$ and $d\gamma$ show shear stress and total shear strain increments, respectively. And G shows the shear modulus of elasticity. The $\sigma_{eq}-\epsilon_{eq}$ curves are calculated by integrating Eqs. 1 and 2. The strain rate range of the pure shear specimens ($2.3 \times 10^{-4}/\text{sec} \sim 4.5 \times 10^{-3}/\text{sec}$) is larger than that of the bulk specimens ($4.0 \times 10^{-5}/\text{sec} \sim 2.3 \times 10^{-3}/\text{sec}$). But, as shown in the figure, the difference in the slopes of the stress-strain curves of the pure shear specimens is larger than that of the bulk specimens. From these results, it is found that the $\sigma_{eq}-\epsilon_{eq}$ curve of the pure shear specimen is affected more than that of the bulk specimen by the strain rate. Therefore, the effects of the strain rate on the stress-strain relation are different between the pure shear and the bulk specimens.

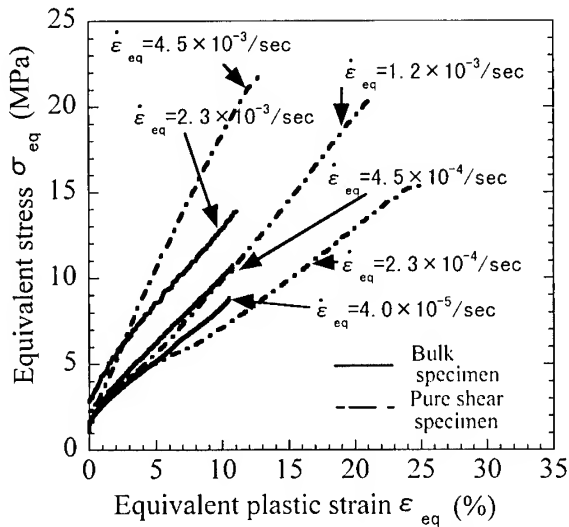


Fig.10 Equivalent stress-equivalent plastic strain curves of the bulk and the pure shear specimens.

CONCLUSIONS

In the present study, the effects of the strain rate on the stress-strain behavior of the adhesively bonded joint were investigated. The following conclusions were obtained.

1. The fracture and the yield stresses of three kinds of the specimens increase linearly with the strain rate in the semi-log graph.
2. The degree of the work hardening of the butt joint specimen is smaller than that of the bulk and the pure shear specimen.
3. The effects of the strain rate on the stress-strain relation are different between the pure shear and the bulk specimens.

REFERENCE

- [1] P. D. Chalkley, W. K. Chiu, Int. J. Adhesives, 13, 4, pp. 237-24 (1993).
- [2] P. Kurzmann and D. A. Klemme, J. of Adhesion, 7, 203 (1978).

EFFECT OF MICROSTRUCTURE ON THE ANODIC SURFACE MODIFICATION OF CARBON BLACKS

Soo-Jin Park¹, Jeong-Soon Kim¹ and Jae-Rock Lee¹

¹Advanced Materials Division, Korea Research Institute of Chemical Technology,
P.O. Box 107, Yusong, Taejeon 305-600, Korea: psjin@pado.kRICT.re.kr

SUMMARY: In this work, the effect of anodic surface treatments of carbon black on the development of microstructure has been studied. The experimental results show that the acidic and basic anode surface treatments on carbon blacks lead to an increase of the surface functional groups. It is observed that the acidic anode treatment on carbon blacks (ACB) increases the crystalline aggregation, resulting in increasing the crystallite size and the concentration of crystallite boundaries in a turbostratic structure. Meanwhile, the basic anode treatment on carbon black (BCB) is shown in decreasing of d_{002} and L_c in the XRD studies. It is then noted that basic surface functional groups on carbons establish more stable conditions than acidic one, which are characterized by disappearance of many dislocations and bent planes as well as by a shifting of planes in a more ordered condition.

KEYWORDS: anode surface treatment, carbon black, surface properties, microstructure.

INTRODUCTION

Carbon black plays so important a role in rubber compounding technology and in evaluating rheological, mechanical and processing behaviors. It is also well known that carbon black has been largely used in a reinforcing agent for pneumatic tire industry. The requirements for tire materials have become more and more specialized and diversified in recent years.

The degree of adhesion at interfaces in a compounding solid depends on the surface energy, active functional groups, energetically different crystallite faces, and so on. Wang et. al. (2) studied that the changes in the surface energy of carbon blacks due to graphitization were attributed to the growth of an organized microstructure. Obviously, more detailed investigations of the surface microstructure of carbon blacks are required in order to unveil the nature of the active sites centers and improve the understanding of elastomeric reinforcement by carbon blacks.

Until recently, x-ray diffraction (namely, XRD) has been the primary source of knowledge of the microstructure of carbon blacks. Measurements of average crystallite dimensions: the average interplanar spacing (d_{002}), the layer diameter (L_a) and the crystallite height (L_c) have been obtained. In 1960s, Heckman (1) pointed out that while XRD techniques are capable only of obtaining average values, there is evidence for a spread in the d_{002} and concluded that the nature of the indicated distribution of these spacing remains one of unresolved microstructure problems in carbon blacks.

While the anodic oxidation of carbon materials has been used to improve the adhesive properties of carbon surfaces to a polymer matrix to increase the interfacial adhesion,

resulting in growing final composite materials with a viewpoint of good mechanical properties and long durability (3).

In the present paper, the effect of anodic surface-treated carbon blacks on the pH, acid-base values and microstructure is investigated in terms of titration and XRD studies.

EXPERIMENTAL

Materials and Sample Preparation

Virginal carbon blacks denoted in VCB (N 220) were supplied by Korea Carbon Black Co. The VCB was treated with 35 wt.% H_3PO_4 (ACB) and 10 wt.% KOH (BCB) chemical solution. At this time, the electric current used in this work were 0, 1, 2, 3, 4, 5 A for 30 min. Prior to use following analysis, the residual chemicals used were removed by Soxhlet extraction by boiling with acetone at 80 °C for 2 h. Finally, the carbon blacks were washed several times with distilled water and dried in a vacuum oven at 90 °C for 12 h.

Surface Properties

The pH of the carbon blacks studied was measured according to ASTM D 1512 based on the boiling and sonic slurry method. The acid-base values of the carbon black surfaces were determined by Boehm's method (4). In the case of acid value measurement, about 0.1 g of the sample were added to 100 ml of 0.1 N NaOH solutions and shaking it for 24 h. Then, the solutions were filtered through membrane paper and titrated with 0.1N HCl solutions. Likewise, the base value was determined by converse titration.

Macrostructure

A wide-angle x-ray diffraction (XRD) patterns of these samples was obtained with a Rigaku Model D/MAX-B diffractometer equipped with a rotating anode and $\text{CuK}\alpha$ radiation ($\lambda = 0.15418$ nm) as the source for measuring the interlayer spacing (d_{002}) and crystallite size along the c-axis (L_c).

RESULTS AND DISCUSSION

Surface Properties

Table 1 shows the results of pH values of the carbon blacks before and after anodic surface treatments. Also, Fig. 1 can be seen that the treatments with electric currents influence the acid-base surface values of the carbon blacks studied. This seems to be a consequence of the variation of functional group of carbon black surfaces after treatments. While, it is noted that

Table 1. Results of pH of virgin and treated carbon blacks.

	Electric current [A]	pH		Electric current [A]	pH
VCB	0	7.01	BCB		
ACB	1	6.70		1	7.56
	2	6.68		2	7.76
	3	6.62		3	7.77
	4	6.57		4	7.82
	5	6.57		5	7.81

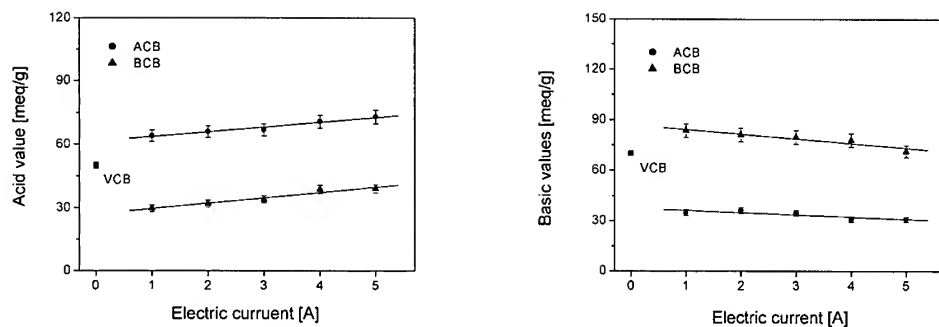


Fig. 1 Results of acid-base values of the virgin and treated carbon blacks.

the carbon manufactured at low process temperature below 800°C ; the surface functional groups of carbon are less stable and then develop acidic group, such as hydroxyl, carbonyl and carboxyl groups. On the other hand, when the process temperature is higher than 800°C , the surface functional groups are more stable and increase the basic oxide, such as pyrone and chromene groups. As a result, the pH and acid-base surface values of the ACBs with electric current sample show an immense decrease as compared with VCB. This result indicates that the acid-base reaction between basic carbon black and acidic chemical solution makes increases of micropore blockage of carbon black, and aggregate of the ACB which were heated at very high temperature (industrially manufactured at 1400°C , here). An expected behavior is given in the case of the polar basic carbon blacks (BCBs) with electric current on the carbon blacks in which slight changes of the pH and acid and base values are shown in Table 1 and Fig. 1.

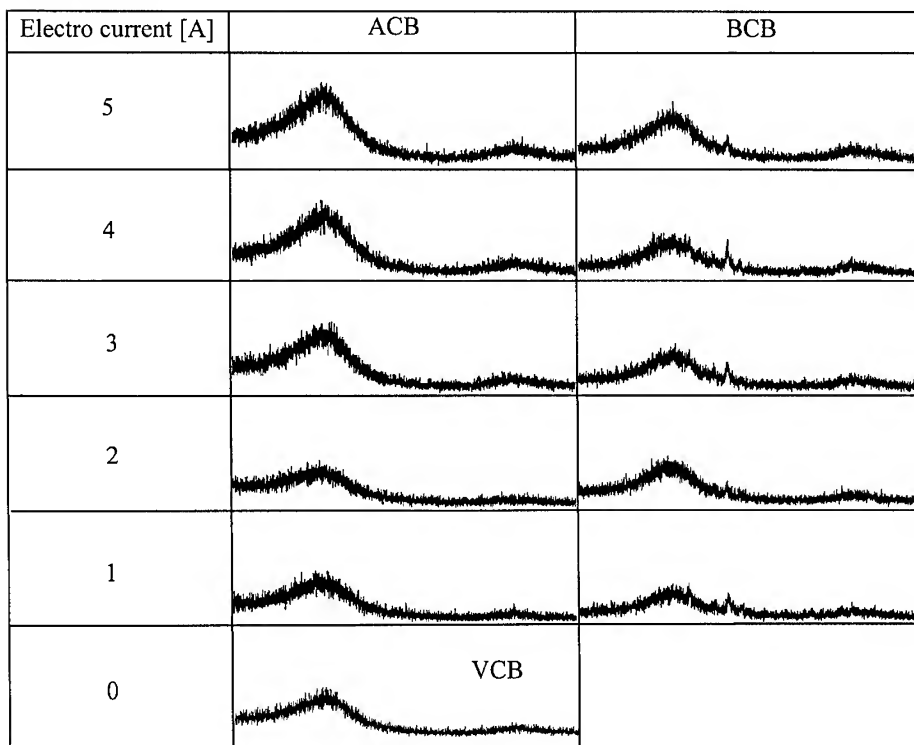


Fig. 2 Wide-angle diffraction patterns of virgin and treated carbon blacks.

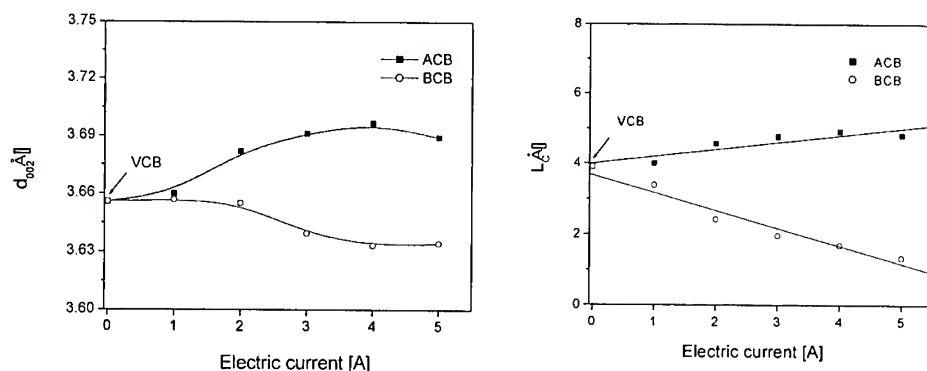


Fig. 3 d_{002} and L_c values of the virgin and treated carbon blacks.

Macrostructure

Fig. 2 displays the wide-angle XRD patterns of anodically surface-treated carbon blacks. Samples show broad diffraction peaks about $2\theta = 24^\circ$ and 43° that are related with the (002) and (10x) reflection, respectively. The location and broadness of two diffraction peaks indicate that carbon blacks have a coke like character with disordered carbonaceous interlayers. As the anodic surface treatments, the intensity of the original two peaks increases as shown in Fig. 2. This is indicative of the increase of crystallite.

Meanwhile, it is now widely recognized that XRD is a technique for knowing the detailed and precise microstructure, such as the interlayer spacing (d_{002}) and crystalline size along c-axis (L_c), of carbon blacks which are composed of small layers with same atomic positions as graphite within the layers. In this work, the Scherrer equation (1) was used to calculate L_c from the width of the (002) reflection, B:

$$L_c = \frac{K\lambda}{B \cos \theta} \quad (1)$$

in which K; the Scherrer constant ($=0.89$), $\lambda=0.154$ nm, B; the half-height width of the (002) diffraction line, and θ ; the Bragg angle.

Fig. 3 shows the effect of anodic surface treatment of carbon blacks on the interlayer spacing and crystalline size along c-axis. d_{002} and L_c values of ACB with electric current become slightly larger than that of the VCB. As mentioned above in Fig. 1, surface properties, it is clear that acidic anode treated carbon blacks (ACBs) lead to an increase of crystalline aggregation, resulting in increasing the crystallite size and the concentration of crystallite boundaries as a turbostratic structure. While, basic anode treatments on carbon blacks (BCBs) are shown in decreasing of d_{002} and L_c in the XRD studies. The result that basic surface functional groups establish more stable conditions, characterized by disappearance of many dislocations and bent planes as well as by a shifting of planes in a more ordered condition.

CONCLUSION

In this work, the effect of the acidic and basic anodic treatments has been investigated in the context of surface and microstructures studies. The experimental results show that acidic anode treatments on carbon blacks (ACBs) leads to an increase of crystalline aggregation.

resulting in increasing the acidic surface functional groups and the crystallite size and the concentration of crystallite boundaries in a turbostratic structure. A result of basic anode treatments on carbon blacks (BCB) is shown in decreasing of d_{002} and L_c in the XRD studies. It is concluded that basic surface functional groups establish more stable conditions, characterized by disappearance of many dislocations and bent planes as well as by a shifting of planes in a more ordered condition.

REFERENCES

1. F. A. Heckman, *Rubber Chem. Technol.*, Vol.38, 1964, p.1245.
2. M. J. Wang, S. Wolff, and B. Freund, *Rubber Chem. Technol.*, Vol.67, 1994, p.27.
3. S. J. Park and J. R. Lee, *J. Mater. Sci.*, Vol.33, 1998, p.64.
4. H. P. Boehm, *Adv. Catal.*, Vol.16, 1966, p.179.
5. M. A. Short and P. L. Jr. Walker, *Carbon*, Vol.1, 1963, p.3.

Interface (1)

RHEOLOGICAL CHARACTERIZATION OF INTERFACIAL INTERACTION IN PP/BaSO₄ COMPOSITES

Ke Wang^{1,2} Jing-Shen Wu¹ and Han-Min Zeng²

¹Department of Mechanical Engineering, Hong Kong University of Science and Technology,
Clear Water Bay, Kowloon, Hong Kong.; mewangke@ust.hk and mejswu@ust.hk

²Materials Science Institute of Zhongshan University, Guangzhou, P.R.China, 510275,.;
ceszhm@zsulink.zsu.edu.cn

SUMMARY A group of polypropylene (PP)/Barium sulfate (BaSO₄) composite samples with different interfacial modification were prepared, in which the fillers were pretreated with stearic acid, silane or polypropylene-g-maleic anhydride, respectively. The effects of filler surface treatment on the interfacial interaction between PP and BaSO₄ was characterized by means of torque rheometer, capillary rheometer and creep-recovery test. It was shown that both the viscosity and elasticity of the composites are dependent on the interfacial modification and the higher viscosity and elasticity are related to stronger interfacial adhesion, and vice versa. The results of rheological tests were conformed by scanning electron microscopy (SEM) observations.

KEYWORDS: polypropylene, barium sulfate, interfacial interaction, rheology

INTRODUCTION

The mechanical properties of filled polymers depend largely on the physical and chemical interactions at the interfaces. Although the deformation and damage processes involving fillers are affected by many factors such as their shape, size and size distribution, volume fraction, physical properties of fillers and matrix, etc., interfacial interaction is undoubtedly one of the most important factors [1,2]. There have been many methods can be applied for the enhancement of the dispersion of fillers in polymeric matrix and the polymer—filler interfacial interaction. Generally, an optimised interfacial bonding is often needed and the evaluation of interfacial feature is always fundamental for the material designing [3,4].

It is well known [5] that the rheological behavior of filled polymers strongly depends on parameters such as volume fraction, shape and size of particles, filler-filler and filler- matrix interactions and rheological measurements have been widely used in characterizing the viscoelastic properties of filled polymers. However, the quantitative characterization of the interfacial interaction in multiphase polymer systems by rheological measurement were explored only in recent years [6-9].

In the present study, the interfacial interaction of a polypropylene (PP)/barium sulfate (BaSO_4) composite was studied by means of several rheological methods, including torque analysis, capillary rheological analysis and creep-recovery tests. The results of rheological tests were compared with the direct morphological observations.

EXPERIMENTAL PROCEDURE

Materials The polypropylene used was a commercial homopolymer-F401 (MFI = 3.0 g/10min, $\rho=0.91 \text{ g/cm}^3$) supplied by Guangzhou Petrochemical Corp. (China). Barium Sulfate powder ($\rho = 4.4 \text{ g/cm}^3$, $\bar{d} = 1.5 \text{ }\mu\text{m}$) was provided by Qingdao Chemical Factory (China), which was calcinated at 400°C for at least 6 h to remove any contaminant or surface agent applied by the manufacturer. Silane coupling agent and stearic acid were supplied by Gaixian Chemical Factory and Changjiang Chemical Factory, respectively. A PP-g-MAH copolymer was prepared in our laboratory via melt reactive extrusion procedure. The MAH content was 0.66 % (w/w).

Sample preparation A two-step mixing process was employed to produce different polymer-filler interface adhesion. In the first step, four PP/ BaSO_4 master pieces with high filler load were prepared, in which the filler was treated with stearic acid, silane or PP-g-MAH, and then mixed with the PP resin on a two-roll mill at $170\text{--}180^\circ\text{C}$ for 15min and granulated. In the second step of mixing, a group of PP/ BaSO_4 composites containing 24 wt % of fillers was prepared by compounding the virgin PP with each of the master pieces using a co-rotating twin-screw extruder (ZSK-30) at a temperature range of $200\text{--}220^\circ\text{C}$ with a screw speed of 200rpm. The resultant composites were designated hereafter as C-SA, C-SI and C-MAH, respectively. For comparison, a control specimen was also prepared by a single extrusion of the virgin PP under the same condition without adding fillers. The composite of virgin PP and untreated BaSO_4 was also prepared for comparison, designated as C-0.

Rheological measurements The torque analysis was performed at 200°C with a torque rheometer (HAAKER Rheomix 600p) equipped with a pair of roller rotors. The volumes of sample were kept constant by carefully measure their melt density. The rotor rate was set either at 40 rpm or at 100 rpm. A capillary rheometer (Göttfert Rheograph 2003) was used to obtain shear viscosity and shear stress data at 200°C using a 1 mm diameter die with L/D 30:1 and 180° entrance angle. A HAAKE RS150 CS rheometer with parallel plate (25 mm diameter and 2 mm spacing) was used for creep-recovery study. The tests were conducted at 200°C .

Morphology observations

Direct observation of the dispersion of BaSO_4 and the interfacial adhesion were undertaken by scanning electron microscopy (JEL 6300) on cryo-fractured surfaces.

RESULTS AND DISCUSSION

Torque measurements are affect by the viscosity of the materials, test temperature, rotor rate, as well as the melt volume of the samples [10]. To ensure the results reliable, the volumes of the samples were carefully kept uniform and the tests were performed at two different rotor rates, i.e., 40 rpm and 100 rpm, respectively. Figure 1 shows the torque-time curves for the neat PP and the PP/ BaSO_4 composites. It can be seen that all the torque of the composite samples is higher than that of the neat PP, especially at high rotor rates. Among the composite studied, sample containing PP-g-MAH modified BaSO_4 (C-MAH) exhibited the highest torque value, and the C-

SI the second. The C-SA composite showed only slightly higher torque than the C-0. The data were collected in Table 1.

The results of the capillary rheological tests are in accordance with that of the torque analysis, except that the shear viscosity and shear stress of the C-SA is a little lower than that of the C-0, as shown in Figures 2 and 3, where the shear viscosity and shear stress of all PP/BaSO₄ composites were plotted against shear rate. The shear viscosity and shear stress of the composite samples with different filler surface treatment have an order as: C-MAH>C-SI>C-0>C-SA.

Creep-recovery test provided more information about the viscoelasticity of the composites. The experiment data include two phases: creep and recovery, as shown in Figure 4. The zero shear viscosity was measured in the creep phase by analysis of the stress-strain relationship; the results were listed in Table 1. The ranking of the zero shear viscosity in the present study is C-MAH>C-SI>C-0>C-SA>pure PP. The results are consistent with that of the torque analysis and capillary tests, i.e. treating the fillers with silane or functionalized PP can improve the melt viscosity of the PP/BaSO₄ composites. In the recovery phase, the elastic and viscous components in the rheological behaviour can be distinguished. The experimental results listed in Table 1 show that the C-MAH is most elastic r whilst pure PP most plastic.

The melt viscoelasticity of multiphase polymer systems has been proved to be related to the interfacial adhesion. In particulate filled polymer composites, the mobility of those matrix molecules neighbouring the filler particles may be restricted because of the polymer-filler interaction, which can be regarded as an interphase layer around the filler particles. The thickness of this interphase layer is dependent on the extent of the interaction and the "effective particle size" [7,8] increases along with the increase of the work of adhesion. Consequently, an increase in "effective particle size" decreases the "free" polymer volume, and in turn causes both the viscosity and the shear modulus to increase. On the other hand, the particles can act as crosslinking points, which reduce the tendency of inter-molecular slippage and result in improved elasticity.

In the C-MAH, the PP-BaSO₄ interface was modified by PP-g-MAH, which is a grafted copolymer with anhydride groups connected to the long hydrocarbon chain through covalent bond. The anhydride groups can interact strongly with the surface of BaSO₄ particles and the long hydrocarbon chain can entangle with PP macromolecules. Thus, the mobility of PP macromolecules is largely restrained, resulting in a pronounced increase in melt viscosity and elastic contributions to the total deformation. The silane (AMPTES) used in the present study can react with the BaSO₄ and reduce its surface energy, and modify its affinity with PP subsequently. Pukanszky and colleagues [3] reported that AMPTES is the most effective silane when compared with other seven silane coupling agents in terms of the interfacial interaction in particulate filled PP systems. However, the hydrocarbon chain of AMPTES is too short to entangle with PP chains, therefore, the melt of the C-SI is much less viscous and elastic than the C-MAH.

It is notable that the C-SA showed lowest viscosity and elasticity among the PP/BaSO₄ composites. Stearic acid is a non-reactive surfactant. It can be adsorbed onto the polar surface of fillers through its carboxyl group and with its hydrocarbon chain perpendicular to the surface of fillers, forming a coating layer that produce weak interactions between filler and matrix and improve the dispersion of fillers in matrix. The relatively low viscosity and elasticity are resulted from the reduced particle interaction and the lubricating effect of stearic acid layers.

The results obtained with our rheological studies were conformed by the direct observation on the fracture surfaces. Figure 5a to 5d show the SEM micrograph of the C-0, C-SA, C-SI and C-MAH, respectively. In Figure 5a, large BaSO₄ clusters and holes appear on the fracture surface, which shows that the filler particles were not well dispersed and the interfacial bonding between fillers and matrix was weak. When the fillers were treated with stearic acid (Figure 5b), improvements in the interfacial adhesion is observed whereas the particle agglomeration is still obvious. Good dispersion of the filler particles and better interfacial bonding are evident in the C-SI, in which the fillers were treated with silane (AMPTES), as shown in Figure 5c. Excellent adhesion between BaSO₄ particles and PP matrix was achieved when the interface was modified with PP-g-MAH. As can be seen in Figure 5d, all the filler particles are connected firmly with the matrix and no trace of debonding can be seen.

CONCLUSIONS

The rheological data suggest that once the polymer-filler interfacial interaction is enhanced through filler surface treatment, the fillers act as temporary physical crosslinking points, effectively restricting the motion of polymer chains. This in turn promotes the frictional resistance to sliding of polymer molecules, and thereby enhancing both the melt viscosity and elasticity. However, when the polymer-filler interfaces are modified with coupling agents like stearic acid, the weakened particle-particle interaction and the lubricating effect of stearic acid layers resulted in the decrease of viscosity.

ACKNOWLEDGEMENTS

The authors wish to thank the Research Grant Council (RGC) of Hong Kong for support of this work (HKUST 6105/97E). Technical supports from the Advanced Engineering Materials Facilities (AEMF) and the Materials Characterisation & Preparation Facilities (MCPF) at the Hong Kong University of Science and Technology (HKUST) are also acknowledged.

REFERENCES

1. M.Hancock, in: *Particulate-filled polymer composites*, Rotheron, R., Ed., Longman group limited, 1995.
2. B.Pukanszky, in *Polypropylene: Structure, Blends and Composites*, Karger-Kocsis, J., Ed., Vol 3, Chapman & Hall, 1995.
3. Z.Demjen, B.Pukanszky and J.Nagy, *Composites*, 29A, 323, 1998
4. J.S.Wu, D.M.Yu, Y.W.Mai and A.F.Yee, *J. Mater. Sci.*, 35, 1, 2000.
5. A.Y.Malkin, in: *Filled Polymers, I Science and Technology*, N.S.Enikolopyan, Ed., Springer-Verlag, 1990
6. P.R.Hornsby and A.Mthupha, *J. Mater. Sci.*, 29, 5293, 1994.
7. S.W.Shang, J.W.Williams and K-J.M.Söderholm, *J. Mater. Sci.*, 30, 4323, 1995.
8. N.A.Memon, *J. Polym. Sci., Polym. Phys.*, 36, 1095, 1998.
9. K.P.Menard, *Dynamic Mechanical Analysis : A Practical Introduction*, CRC Press LLC, 1999.
10. G.Schramm, *A Practical Approach to Rheology and Rheometry*, Gebruder HAAKE GmbH, 1994.

Table 1. Rheological data of PP and PP/BaSO₄ composites

Sample Code	Torque (Nm)		Zero Shear Viscosity ($\times 10^4$ Pa·s)	Elastic Recovery (%)
	40 rpm	100 rpm		
PP	2.44	6.43	1.16	1.57
C-0	2.66	7.30	1.56	6.16
C-SA	2.54	7.13	1.36	3.30
C-SI	2.80	8.21	1.73	6.23
C-MAH	3.07	8.76	1.92	25.12

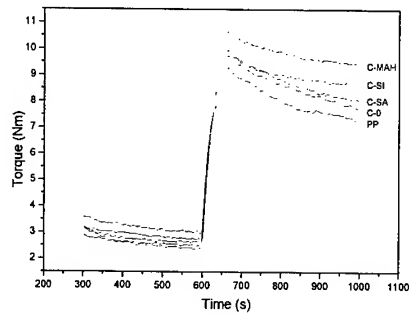


Figure 1. Torque-time curve

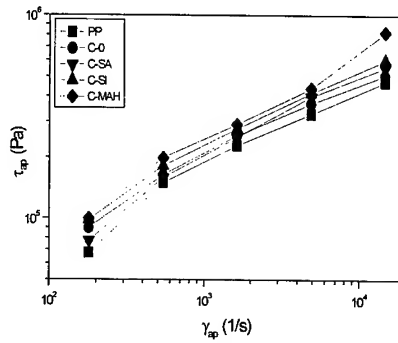


Figure 2. Shear stress-shear rate relationship

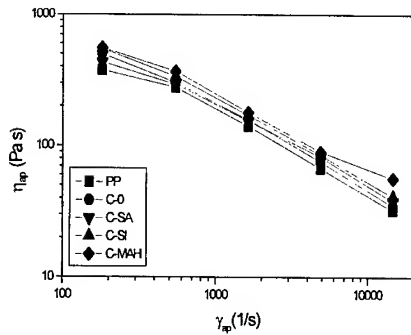


Figure 3. Shear viscosity-shear rate relationship

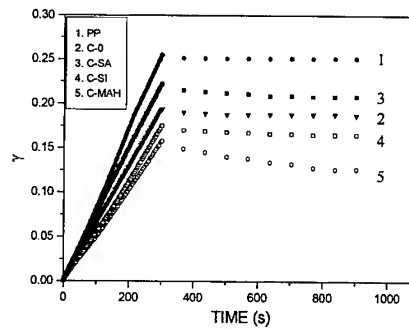


Figure 4. Creep-recovery curve

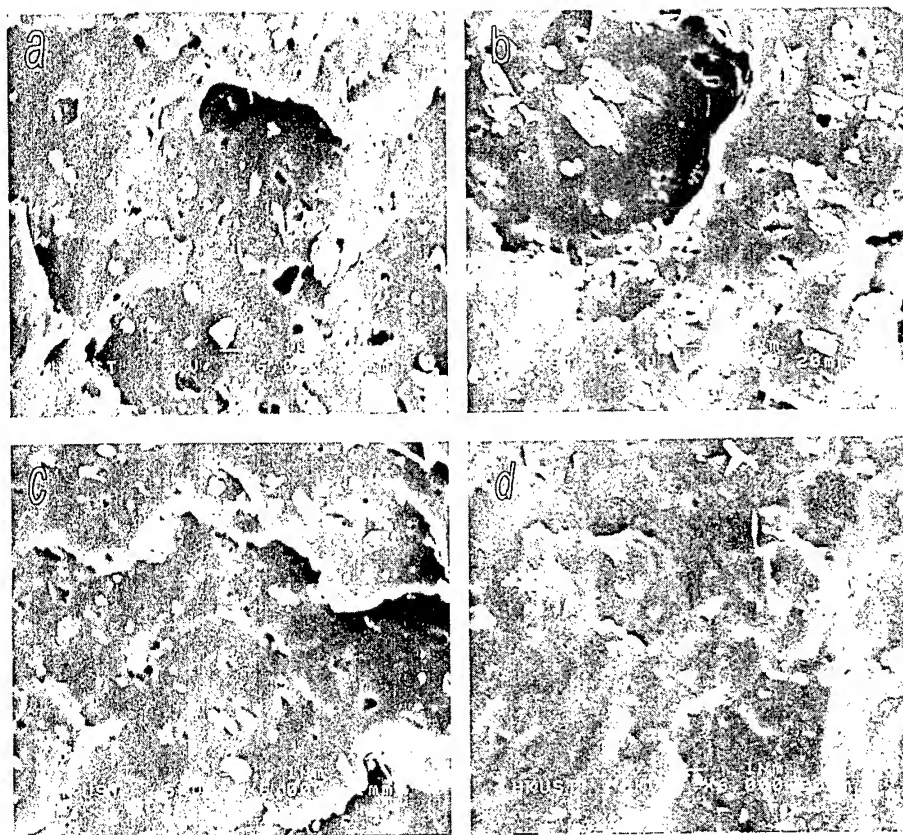


Figure 5. The morphology of PP/BaSO₄ composites:

(a) C-0; (b) (C-SA); (c) C-SI and (d) C-MAH.

THE INFLUENCE OF INTERPHASE CONDITION AND FIBER SHAPE ON THE TENSILE PROPERTIES OF SHORT-FIBER REINFORCED RUBBER

S. R. Ryu¹ and D. J. Lee²

*School of Mechanical Engineering, Yeungnam University
214-1, Dae-dong, Gyungsan, Gyungbuk 712-749, KOREA*

¹*Email : p9724401@chunma.yeungnam.ac.kr*

²*Email : djlee@yeungnam.ac.kr*

SUMMARY: The tensile properties of short nylon66 fiber reinforced Chloroprene rubber have been investigated as functions of interphase conditions, fiber content and fiber shape. The tensile moduli are significantly improved due to fiber content. The ultimate tensile strength exhibits a dilution effect at a low fiber content in each case. It is found that the interphase conditions and fiber shape have an important affect on the dilution ratio and critical fiber content. In this study, the combination of double coatings with bonding agent 402 and rubber solution becomes the best interphase model(E) in short-fiber reinforced rubber among many types. Compared with the regular short fiber with straight ends, the dumbbell shaped fiber shows the low dilution ratio and high tensile strengths. Also, the stress analysis near the fiber end carries out using 2-D FEA to confirm the dilution effect.

KEYWORDS: short-fiber reinforced rubber, dilution effect, dumbbell shaped fiber, interphase condition

INTRODUCTION

A considerable interest in short-fiber rubber composites has been generated recently due to the advantages in processing and improvements in their mechanical properties. The primary effects of short fiber reinforcement on the mechanical properties of rubbers include increased modulus, increased strength especially at high fiber volume fraction, decreased elongation at rupture, increased hardness at relatively low fiber volume fraction and possible improvements in cut, tear and puncture resistance. The properties of short-fiber reinforced rubbers depend on fiber aspect ratio(AR:length/diameter), fiber volume fraction, fiber dispersion, fiber orientation and fiber-matrix adhesion[1-3]. These materials have been utilized in some practical commercial uses such as hoses, V-belts, diaphragms, tires and gaskets. Derringer[4] used short fibers of rayon, nylon and glass in natural rubber to increase Young's modulus of vulcanizates. Moghe[5] reported the milling parameters that affect fiber orientation and its' influence on composite properties. This study deals with the influence of interphase condition, fiber end shape and fiber content in chloroprene rubber

composite, and the comparison of the stress distribution near the fiber end using 2-D FEA to show the difference of dilution effect.

EXPERIMENTAL PROCEDURES

The Chloroprene rubber used for this study was S-40V(ML₁₊₄ at 100°C; 48± 5) made by the DENKA Company of Japan. We also used carbon black(FEF, SRF), nylon 66 fiber as reinforcing materials and other ingredients of commercial grade quality. The formulation and mechanical properties of the test compound to check the influence of interphase condition are given in Table 1(type I). Also, the formulation and mechanical properties for the influence of fiber end geometry are given in Table 2(type II). We treated the fiber surface with bonding agent(Chemlok 402) and rubber solution by dipping method. A schematic representation of coated short-fiber surface(A-E) and short-fiber shape(F,G) is shown in Fig. 1.

The fabrication of reinforced rubber was according to ASTM D3182 and D3190. The mixes were prepared in a two-roll laboratory model of an open mixing mill(14") at a nip of 1.5 mm. The mixing time and number of passes were maintained in the same way for all cases. Orientation of the fiber in the rolling direction was achieved by a repeated passing of the uncured compound through a controlled nip. A square preform cutting from the uncured sheet was marked in the direction of the mill grain and vulcanized at 170°C in a hydraulic press heated platen at 1.5 times of its' respective optimum cure time(tc₉₀) based on data obtained from a rheometer. The test pieces were punched from the molded sheet [thickness=2mm(type I), 3mm(type II)] in the direction of the fiber orientation. The tensile properties were measured using an Autograph(Model AG-5000E) of Shimadzu tensile machine with a testing speed of 50mm/min. Typically, five specimens were used for a single evaluation at room temperature.

Table 1 Formulation of the reinforced rubber, and mechanical properties of rubber matrix and short-fiber(type I)

Ingredients	Phr*				Matrix	2 nd Inter-phase	1 st Inter-phase	Short-fiber
	Matrix	2 nd Inter-phase	1 st Inter-phase					
Polymer, S40-V	100	←	←	Tensile strength (MPa)	19.65	22.23	18.06	600
Stearic Acid	1	←	←	Tensile modulus (MPa)	3.66	11.58	22.20	2.0(Gpa)
Carbon Black, (FEF)	24	45	60	Elong.(%)	454	240	121	30
DOP	10	←	←	Hs(JIS A)	55	72	82	
Mg O	4	←	←	Fiber AR				265const
3P	1.5	←	←	Fiber Content (phr)				10, 20, 30
Sunnoc	2	←	←	Fiber Surface Treatment				Type A-E of Fig.1
MB	1	←	←					
ZnO	5	←	←					
TS	1	←	←					
NA22	1	←	←					
Sulfur	0.3	←	←	Characteristic Factor				Interphase , Fiber Content
Short-fiber	+ α	←	←					
SUM.	150.8+α							ø 15μm

phr* ; Parts per hundred grams of rubber

Table 2 Formulation of the reinforced rubber, and mechanical properties of rubber matrix and short-fiber(type II)

Ingredients	Phr*			Matrix	Interphase	Short-fiber
	Matrix	Inter-phase				
Polymer, S40-V	100	←	Tensile strength (MPa)	34	76.1	304.2
Stearic Acid	1	←	Tensile modulus (MPa)	13.11	31.45	845
Carbon Black, (FEF)	15	45	Elong.(%)	408	249	36
DOP	10	←	Hs(JIS A)	48	68	
Mg O	4	←				
3P	1.5	←				
Sunnoc	2	←	Fiber AR			10, 20
MB	1	←	Fiber Content(%)			3, 6, 10
ZnO	5	←	Fiber Surface Treatment			Type F, G of Fig. 1
TS	1	←				
NA22	1	←				
Sulfur	0.3	←	Characteristic Factor			Interphase, Fiber Content, Fiber Shape
Short-fiber	+ α	←				
SUM.	141.8+ α					\varnothing 0.45mm

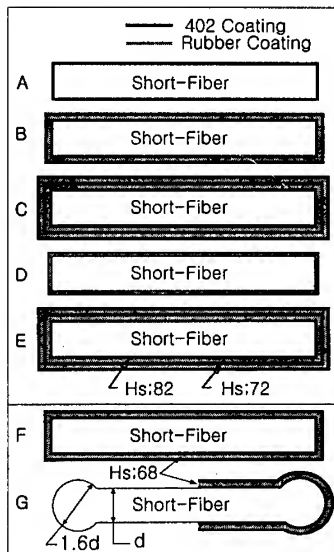


Fig. 1 Schematics of coated short-fiber surface(A-E) and short-fiber shape(F,G)

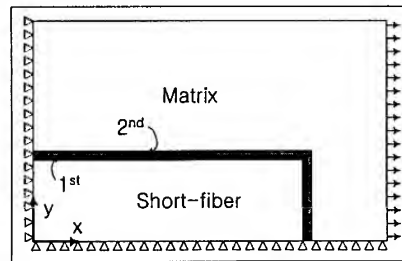


Fig. 2 2-D symmetric and loading boundary conditions

FINITE ELEMENT ANALYSIS

The influence of interphase condition and short-fiber end geometry was studied by axisymmetric FEA using PARTRAN. The 2-D multi-fiber model was used to develop the physical concepts. In the ideal case, where fibers were perfectly aligned, a single fiber axisymmetric model would nearly correspond to a 3-D model and fiber interactions can be accounted for by use of cell boundary constraint conditions[6]. The ARVE(aligned representative volume element) is shown in Fig. 2. The matrix is assumed to be

incompressible hyperelastic which is to follow the Ogden formulation[7] with eight constants. The short-fiber is assumed to be elastic. The chosen fiber AR and fiber content of the model is $AR=20$ and $V_f=6\%$. The PATRAN program has been used to create and mesh the geometries of the model and to generate an ABAQUS input file. In present analysis, 4 node shell elements are used.

RESULTS AND DISCUSSION

1. Tensile Properties

Our results(type I) for the tensile properties are summarized in Figs. 3-4. With a low fiber content, the tensile strength(σ_c) was dominated by the rubber and reinforcing fibers that acted as the network defects. As a result, σ_c decreased with the fiber content until a critical fiber level was reached. At higher fiber contents, σ_c became the fiber-dominating property and increased with the fiber content[1,8]. An initial drop of σ_c reaching a characteristic minimum around 10-20phr was derived from the dilution effect of the fibers, which weakened the rubber if its fiber content was not reinforced high enough to sustain the corresponding fraction of the tensile load. The critical fiber content level, at which strength of the reinforced rubber recovered, varied directly with the interphase conditions. The better interphase condition showed the lower critical fiber content and dilution ratio(σ_c/σ_{matrix}). It is believed the failure in short-fiber reinforced rubber is initiated at the fiber end/matrix interface as a result of the stress concentration. The tensile modulus(Young's modulus) was calculated from the initial slope of the stress-elongation curve. The modulus ratio(E_{fiber}/E_{matrix}) was 546, the tensile moduli(E_c) of the reinforced rubbers were significantly improved when compared to the virgin rubber. Tsai and Pagano[9] showed that the moduli for randomly oriented short-fiber polymer composites can be predicted approximately as Eqn 1. Fig. 4 shows the similar trend between predictive model and experimental data. And the tensile modulus increased with fiber content in each interphase and showed the highest in the case of double coatings, model E.

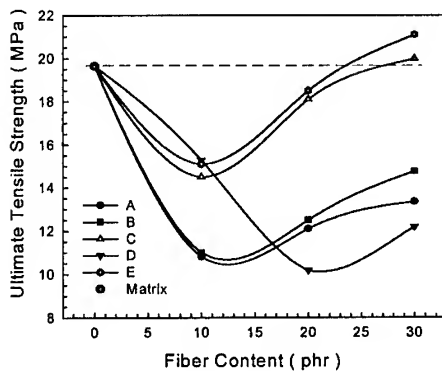


Fig. 3 Effects of interphase and fiber content on the tensile strength

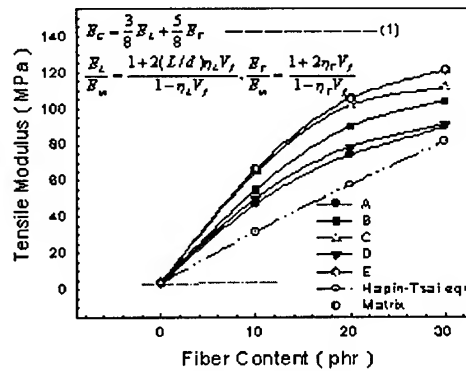


Fig. 4 Effects of interphase and fiber content on the tensile modulus

As the effects of fiber end geometry in tensile properties(type II), it is believe that the fiber end geometry plays an important role in fiber/matrix stress transfer mechanisms. The failure in regular short-fiber reinforced rubber is usually initiated at the fiber end/matrix interface as a result of the stress concentration caused by geometrical and material discontinuity. The tensile strength shows the dilution effect in all cases. However, the rubber with dumbbell shaped fiber shows the low dilution ratio and high tensile strength in same fiber content(Fig. 5). Also, the tensile modulus in the case of dumbbell shape fiber is slightly higher than one of common short-fiber(Fig. 6).

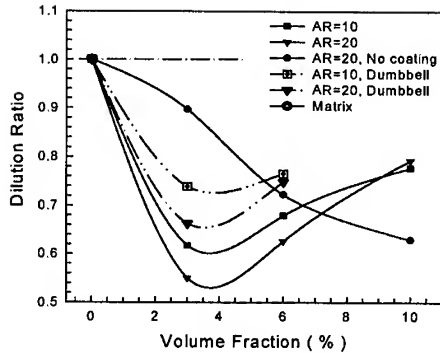


Fig. 5 Effects of fiber shape and fiber content on the dilution ratio

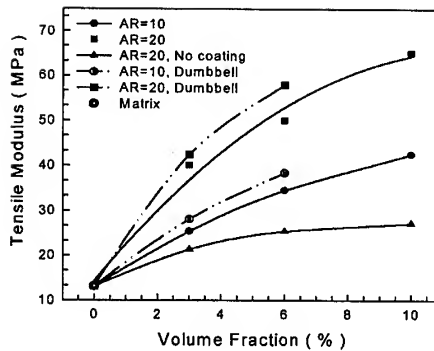


Fig. 6 Effects of fiber shape and fiber content on the tensile modulus

2. Stress Distribution

The 2-D FEA carried out for short-fiber/matrix systems up to extension ratio of 30%. The objective of this study is to obtain the stress distribution in the vicinity of fiber end. Therefore, the used short-fiber AR was 20. When the fiber/matrix interface is weak, interfacial bond failure may be initiated at the fiber tip and then propagated towards the center causing fiber/matrix debonding. A strong interface results in matrix yielding or cracking in the vicinity of fiber ends. Fig. 7 shows the stress distribution in the near the fiber end; (a) H-M-L (model E) is the case of hardness control of 1st, 2nd interphase, (b) L-L-L (model A-D) means the same hardness for 1st, 2nd interphase and matrix. It can be seen that the case of (a) interphase is stronger than (b) one.

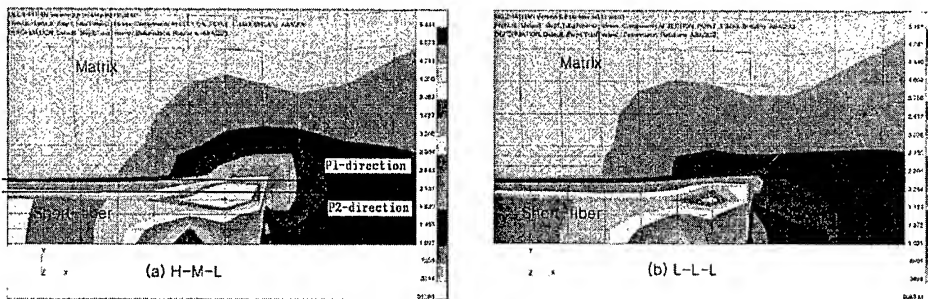


Fig. 7 Contour plots of shear stress distribution in near the fiber end

The stress profiles along the fiber longitudinal axis for cases of different interphase condition are shown in Fig. 8 (P1, P2 direction). Clearly, the case of hardness controlled interphase (a) showed higher stress level than interphase (b) in near the fiber end. So, it seems that interphase (a) makes to relax the stress concentration between strong fiber and weak matrix when the external load acts on the reinforced rubber. The axial stresses in the fibers having different end geometries from the fiber tip are shown in Fig. 9. The axial stress (σ_{xx}) in the matrix near the matrix/fiber boundary ahead of the spherical end is found to be lower than stress in front of flat end. This fact is of major importance since it can predict the prevention of interfacial debonding. In the case of weak interface, the load cannot be transferred to the fiber neither by a shear mechanism nor directly through the fiber tip. While the fiber with flat end loses its ability to bear load due to cessation of these two mechanisms of stress transfer, the fiber with spherical end continues to take part in the load bearing process by being

anchored in the matrix. Thus, the difference in load bearing capability between the two fiber end geometries increases with the interface deterioration.

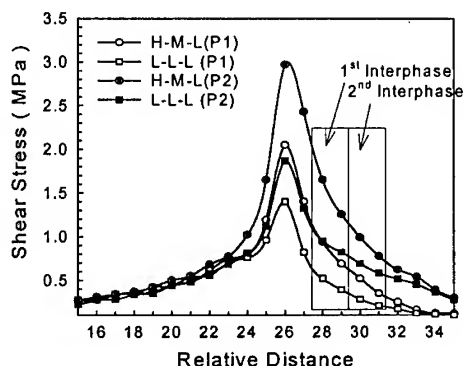


Fig. 8 Stress profiles along fiber and 1st inter-phase

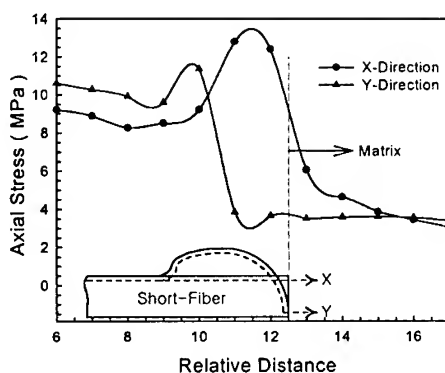


Fig. 9 Stress profiles along fiber (fiber geometry is shown at bottom)

CONCLUSION

The tensile properties of nylon66 short-fiber reinforced CR have been investigated as functions of interphase conditions, fiber content and fiber end shape. The ultimate tensile strength exhibits a dilution effect at low fiber content in each case. The better interphase condition shows the lower critical fiber content and dilution ratio. The rubber with dumbbell shaped fiber shows the low dilution ratio and high tensile strength in same fiber content. It is found that the interphase conditions and fiber shape have an important effect on the dilution ratio and critical fiber content. The tensile moduli are significantly improved due to fiber content. The combination of double coatings with bonding agent and rubber solution becomes the best interphase model(E) in short-fiber reinforced rubber. In the stress analysis near the fiber end, the case of hardness controlled interphase(E) shows higher stress level than the other. A spherical fiber end geometry reduces the probability of debonding initiation at the fiber end and the probability of its propagation towards the fiber center. The rubbers with dumbbell shaped fiber and double coatings in interphase have the most enhanced mechanical properties.

REFERENCES

1. L. A. Goettler, "Hand Book of Elastomers", Dekker., Inc., 1988, p.220, p.240.
2. A. Y. Coran, K. Boustany and P. Hamed, *Rubber Chem. Technol.*, Vol.47, 1974, p.396.
3. D. J. Lee and S. R. Ryu, *ICCM12, Paris*, 1999, Paper No. 26.
4. D. C. Derringer, *Rubber World*, Vol.45, 1996, pp.130-156.
5. S. R. Moghe, *Rubber Chem. Technol.*, Vol.49, 1976, p.1160.
6. D. J. Lee and H. G. Kim, *Intern. J. Polymeric Mater.*, Vol.28, 1995, p.69.
7. L. R. G. Treloar, "The Physics of Rubber Elasticity", Clarendon Press, 1975, p.323.
8. Y. Termonia, *J. of Polymer Science ; Part B*, Vol.32, 1994, p.975.
9. R. F. Gibson, "Principles of Composite Material Mechanics", MacGraw-Hill Inc., 1994, p.168.

COMPARISON OF INTERFACIAL PROPERTIES FOR ELECTRODEPOSITED CARBON FIBER/EPOXY COMPOSITES BY TENSILE/COMPRESSIVE FRAGMENTATION TESTS AND ACOUSTIC EMISSION (AE)

Joung-Man Park¹, Jin-Won Kim¹, Young-Min Kim¹, and Dong-Jin Yoon²

¹ Department of Polymer Science & Engineering, Research Center for Aircraft Parts
Technology, Gyeongsang National University, Chinju, Gyeongnam 660-701,
KOREA: jmpark@nongae.gsnu.ac.kr

² Nondestructive Evaluation Group, Korea Research Institute of Standards and Science
PO Box 102, Yusong-gu, Taejeon 305-600, KOREA: djyoon@kriss.re.kr

SUMMARY: Interfacial and microfailure properties of carbon fiber/epoxy matrix composites were evaluated using both tensile fragmentation and compressive Broutman tests with acoustic emission (AE). One monomeric and two polymeric coupling agents were used via the electrodeposition (ED). Both coupling agents exhibited higher interfacial shear strength (IFSS) improvements under tensile tests. However, polymeric coupling agent showed higher IFSS improvement than monomeric case under compressive test. The typical interfacial failure modes including fiber break, matrix cracking, and debonding were observed during tensile test, whereas diagonal slippage in fiber ends was observed during compressive test. For both the untreated and treated cases AE distributions were well separated under tensile testing, whereas AE distributions were rather closer under compressive tests because of the difference in failure energies between tensile and compressive loading. Under both loading conditions, fiber breaks occurred until yielding point. After yielding, much more AE events occurred from the interlayer failure in both the ED treated and the dipping cases.

KEYWORDS: micromechanical technique, electrodeposition (ED), fragmentation test, interfacial shear strength (IFSS), single fiber Broutman test, acoustic emission (AE), interfacial properties.

INTRODUCTION

Interfacial properties of carbon fiber/epoxy matrix composites were evaluated using both the tensile and the compressive fragmentation tests. The commonly used tensile fragmentation test was interested in the characteristics of the fiber/matrix interfacial transverse properties, in particular to know the matrix cracking and fiber breaking phenomena [1-4]. On the other hand, transversal interfacial properties of the fiber/matrix adhesion were obtained by means of the single fiber Broutman test. The single fiber Broutman test was used to investigate the fiber/matrix interface debonding and buckling behavior while subjecting to a transverse compressive stress [5-7]. The interfacial failure modes in the fiber/matrix were observed simultaneously using polarized-light microscope. During the Broutman testing, AE test monitored the fracture signals of microfailure sources, such as cracking of matrix, fracture of fiber, and debonding of the fiber/matrix interface. AE results were correlated with the interfacial shear strength (IFSS) trends coming from tensile and compressive fragmentation

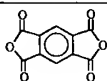
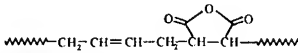
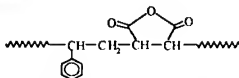
tests [5-7].

IFSS can be improved by an introduction of chemical functional groups via the oxidation of fiber surface, plasma or commercial coupling agent treatments. The ED method is a process that a film is deposited on a conductive carbon fiber surface from a dispersion of colloidal particles (or ions) in aqueous solution. Adsorption amount of coupling agents were compared as functions of treating time, concentration and temperature to obtain the optimized conditions. With the optimized treating processes, polymeric and monomeric coupling agents were deposited on carbon fibers with desired composition and thickness, respectively [4]. The frequently used micromechanical techniques to measure IFSS include the single fiber pull-out test, the fragmentation test (or called as a single-fiber-composites (SFC) test) etc [1-3]. The untreated, ED and the dipping carbon fibers/epoxy composites were compared simultaneously using tensile and compressive Broutman fragmentation tests with an aid of AE method.

EXPERIMENTAL

Materials. Carbon fiber was supplied from Tae Kwang Co. (TZ-307). Carbon fiber has a density of 1.8 g/cm³ and average diameter of 7.9 μm, respectively. Epoxy resin (YD-128, Kukdo Chemical Ind. Co.) based on diglycidyl ether of bisphenol A was used as a matrix. Polyoxypropylene diamine (Jeffamine) was used as curing agents to provide optimized flexibility for microspecimens. One monomeric and two polymeric coupling agents were used as shown in Table 1.

Table 1. Chemical Structure of Coupling Agents.

Type	Chemical Name	Chemical Structure	Solvent ³⁾
Monomeric	Pyromellitic dianhydride (PMDA) ¹⁾		Water (soluble)
Polymeric	Polybutadienemaleic anhydride (PBMA) ²⁾		Water (Soluble)
	Polystyrenemaleic anhydride (PSMA) ²⁾		Water (Partially soluble)

1) Aldrich Chemical Company Inc.; 2) Polysciences Inc.; 3) Deionized and doubly distilled water.

Methodologies

Single Fiber Strength and IFSS Measurements. Single carbon fiber tensile strength was obtained using about fifty specimens for statistical mean value. The fragmentation test using microspecimens was carried out to obtain IFSS using UTM and a specially designed strain fixture. Ultimate fragment lengths within the matrix were measured, and subsequent failure process was observed via a polarized-light microscopy. The relationship among fiber tensile strength σ_f , aspect ratio l/d , and IFSS, was given by Kelly-Tyson equation and Weibull statistics:

$$\tau_i = \frac{\sigma_{fu} \cdot d}{2l_c} \quad (1)$$

Where σ_{fu} is the tensile strength of the fiber at average critical length l_c , and d is the fiber

diameter. The compressive stress on a fiber can be transferred perfectly across the break from one the fiber fragment to the other due to the fact the fragments are still in contact with each other. It is evident that a critical fragment length, as defined by the tensile load transfer model, does not exist in compressive system. According to the compressive profile, τ_c , based also on the force balance,

$$\tau_c = \frac{\sigma_{fc} \cdot d}{2l_c} \quad (2)$$

Where critical length l_c is the original length of the fiber ($l_c = l_1$). σ_{fc} is the fiber stress at the point where the interfacial stress is insufficient to induce further fragmentation.

Preparation of Microspecimens. Tensile and Compressive Broutman microspecimens were made single fiber embedded in epoxy matrix in silicon mould as shown in figure 1.

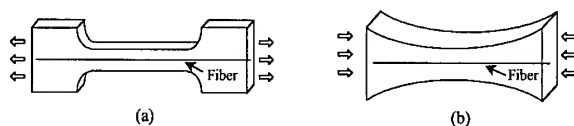


Fig. 1. Schematic illustrations showing for:

(a) Tensile dog-bone specimen; (b) Compressive Broutman specimen.

Fiber Surface Treatment by ED and Dipping. Untreated fifty carbon fibers were fixed with regular distance apart in rectangular acrylic electrolytic frame. The frame acted as an anode in itself and the cathode was made of an aluminum plate (Figure 2). Coupling agents were diluted to the 0.5 wt.% concentration with deionized distilled water. After anode frame and cathode bar were immersed into aqueous electrolyte solutions, voltage of 1.1 V was supplied to both electrodes by power source. Typical locating time and applied voltage were 10 minutes and 1.1 V, respectively. After ED treated, carbon fibers were dried at room temperature without further thermal treatment. For comparison, PMDA was dipped into diluted solution directly.

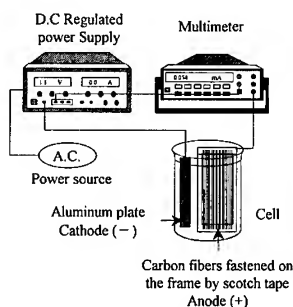


Fig. 2. Schematic Plot of ED system

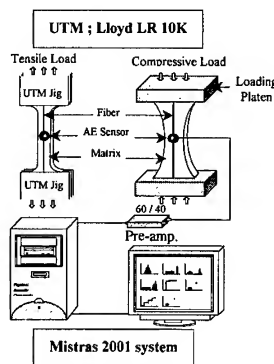


Fig. 3. Schematic Diagram of Instrumentation for AE

AE Measurement. Microspecimen was placed on the UTM for applying unidirectional tensile/compressive forces in figure 3. AE sensor was attached in the center of the specimen using vacuum grease couplant. After AE test, the number of fragment of fiber and the microfailure in the testing specimen were observed via the polarized-light microscopy. AE signals were detected using a miniature sensor (Resonance Type model, PICO by PAC) with peak sensitivity of 54 Ref V/(m/s)[-68 Ref V/mbar] and resonant frequency at 500 kHz. The

sensor output was amplified by 40 dB at preamplifier and passed through a band-pass filter with a range of 200 kHz to 750 kHz. The threshold level was set to 30 dB. Using in-built software AE waveforms and their fast *Fourier* transform (FFT) were analyzed.

RESULTS AND DISCUSSION

Microfailure Modes of Tensile/Compressive Specimens: Figure 4 showed photographs for tensile and compressive microfailure modes under polarized light microscope. Untreated fiber exhibited the debonding around fiber fracture and ED treated case exhibited cone shaped matrix crack, whereas in compressive specimen there were diagonal slippage based on transverse tensile stress, characteristic of the transverse properties of the interface.



Fig. 4. Polarized-light photographs of the carbon fiber failure modes under applied load: (a) Untreated (tensile); (b) ED treated (tensile); (c) ED treated (compressive).

Comparison of IFSS using Three Coupling Agents: Both monomeric and polymeric coupling agents showed significant improvements in IFSS under tensile fragmentation test as shown in figure 5. It is due to chemical and physical interdiffusion between coupling agent and epoxy matrix. On the other hand, in the compressive case polymeric coupling agents exhibited higher improved IFSS than the monomeric PMDA case. It may be because better wetting effect can contribute to affect favorably compressive IFSS. PMDA with dipping also exhibited the similar trend as ED case.

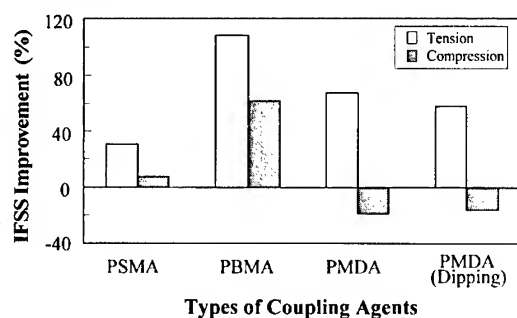


Fig. 5. Comparison of IFSS improvements depending on types of coupling agents.

AE Analysis with Microfailure Mechanisms and their Mechanical Properties. AE showed the interesting results in figure 6 as follows: there is well separation in tensile testing for both the untreated and coupling agents treated cases, whereas AE distributions are rather closer in compressive tests. It is because of the difference in fracture energies between the tensile and the compressive tests. Under both tensile and compressive conditions, fiber breaks occurred until yielding point. After yielding, much more AE events occurred from the interlayer failure in both the ED treated and the dipping cases, compared to the untreated case. Especially, AE amplitude from the interlayer microfailure in the dipping exhibited higher distributions than other ED treated cases. Ultimate stress in compressive loading exhibited much higher than that of tensile loading.

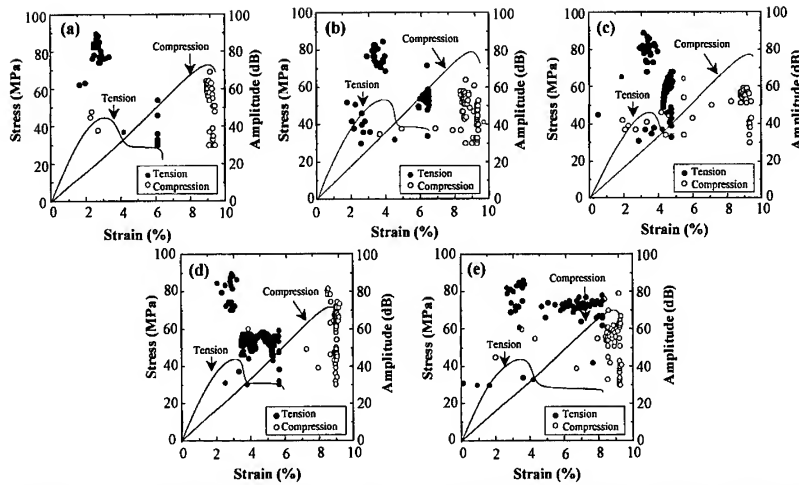


Fig. 6. Comparison of stress-strain curve and AE amplitude for carbon fiber/epoxy composite using tensile and compressive fragmentation tests: (a) Untreated; (b) PBDA; (c) PSMA; (d) PMDA; and (e) PMDA (dipping).

Figure 7 showed AE waveform and their FFT results. There were so many intermediate size waveforms coming from the interlayer failure in the ED and the dipping treated cases. Maximum AE voltages coming from waveform of fiber breaks under tensile tests were relatively larger than those under compressive tests. Characteristic frequencies for various microfailure modes were observed in the range of 500 Hz. In compressive test ED treated fiber waveform exhibited larger voltage than the untreated case. It may be due to the microfailure types and differing failure energies in compressive tests.

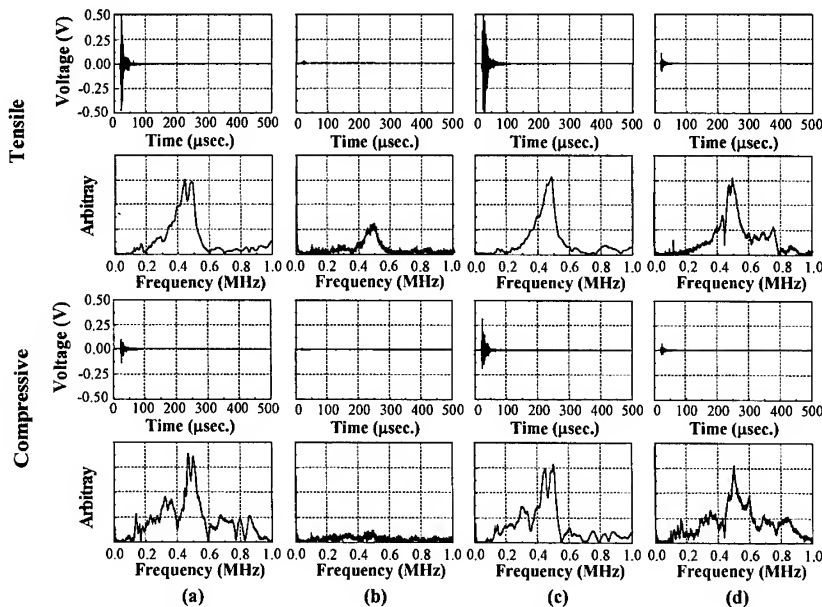


Fig. 7. AE waveforms and their FFT results in carbon fiber/epoxy composites under tensile and compressive tests: (a) Untreated fiber fracture; (b) Untreated matrix cracking; (c) ED treated fiber fracture; (d) ED interlayer failure.

CONCLUSIONS

Using monomeric and polymeric coupling agents, interfacial properties and their microfailure of carbon fiber/epoxy matrix composites were evaluated using both tensile and compressive Broutman fragmentation tests. AE test monitored the fracture signals of microfailure sources, such as cracking of matrix, fiber fracture, debonding, especially diagonal slippage of the broken fiber ends. For both the untreated and ED cases AE events were separated well under tensile testing, whereas AE distributions were rather closer under compressive tests. It is because of the difference in fracture energies between the tensile and the compressive tests. Under both tensile and compressive conditions, fiber breaks occurred until yielding point. After yielding, much more AE events occurred from the interlayer failure in both the ED treated and the dipping cases. Ultimate stress in compressive loading exhibited much higher than that of tensile loading. Maximum AE voltage for waveform of fiber break under tensile tests were relatively larger than those under compressive tests

ACKNOWLEDGEMENT: This study was supported financially by KoSEF through the Research Center for Aircraft Parts Technology (ReCAPT), Gyeongsang National University.

REFERENCES

- 1) J. M. Park, W. G. Shin, and D. J. Yoon, "Interfacial aspects of two basalt and SiC fiber reinforced epoxy composites using fragmentation technique and acoustic emission", *Composites Sci. & Technol.*, Vol. 59, 1999, pp. 355-370.
- 2) S. I. Lee, J. M. Park, D. W. Shin, and D. J. Yoon, "Interfacial properties of glass fiber/brittle-ductile dual matrix composites using by micromechanical technique and acoustic emission", *Polymer Composites*, Vol. 20, 1999, pp. 19-28.
- 3) J. M. Park, S. I. Lee, K. W. Kim, and D. J. Yoon, "Interfacial aspects of electrodeposited multi-fiber reinforced composites using electro-micromechanical techniques and acoustic emission," *Proc. of The 12th International Conference on Composite Materials: (ICCM-12)*, Vol. VI, 1999.
- 4) J. M. Park, Y. M. Kim, K. W. Kim, and D. J. Yoon, "Interfacial properties of electrodeposited carbon fibers reinforced epoxy composites using fragmentation technique and acoustic emission," *Proc. of The 6th International Conference on Composite Engineerings: (ICCE-6)*, 1999, pp. 645-646 .
- 5) J. R. Wood, H. D. Wagner, and G. Marom, "The compressive fragmentation phenomenon: using microcomposites to evaluate thermal stress, single fibre compressive strengths, Weibull parameters and interfacial shear strengths, *Proc. R. Soc. Lond. A*, Vol. 452, 1996, pp 235-252.
- 6) C. Ageorges, K. Friedrich, and J. Karger-Kocsis, "Fibre/matrix interface testing using the single fibre Broutman test," *Proc. of The 12th International Conference on Composite Materials: (ICCM-12)*, Paris, France, July 5-9, Vol. VI, 1999.
- 7) C. M. L. Wu, S. L. Bai, R. K. Y. Li, and Y. W. Mai, "Fiber fragmentation by twin-fiber bending beam," *Proc. of The 12th International Conference on Composite Materials: (ICCM-12)*, Vol. VI, 1999.

BIOMEDICAL APPLICATIONS OF POLYMER COMPOSITE MATERIALS

S. Ramakrishna

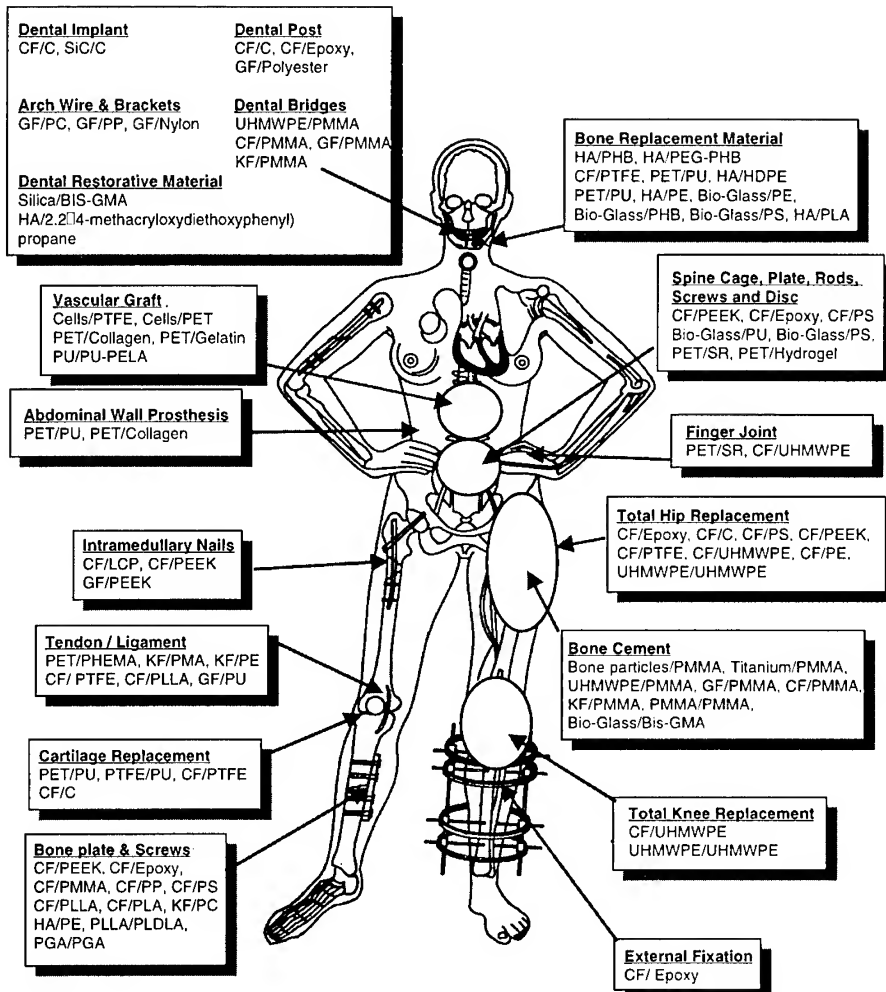
*Polymer and Textile Composites Laboratory,
Department of Mechanical and Production Engineering, National University of Singapore,
10 Kent Ridge Crescent, Singapore 119260; mpesr@nus.edu.sg*

SUMMARY: Polymer composite materials are gaining acceptance in biomedical engineering because of their tailorable manufacturing processes and mechanical properties comparable to those of the tissues of the human body. Aim of this research work is to design and develop implants with superior performance using polymer composite technologies. Current metallic bone plates used for treatment of bone fractures are not entirely satisfactory as they cause improper bone healing and loss of bone mass. This is attributed to large stiffness mismatch between the metallic bone plate and the bone. To address this problem, efforts have been made to develop a braided carbon fiber reinforced polyetheretherketone composite bone plate, which is less rigid and biocompatible. In dentistry, metallic posts are used to restore damaged teeth. Once again the high stiffness mismatch between the metal post and the dentine causes failure of dental restoration. Efforts have been made to design and develop a functionally graded composite dental post that eliminates the problems associated with commercial dental posts.

KEYWORDS: biomaterials, composite biomaterials, polymer composites, dental post, bone plate, fracture fixation

INTRODUCTION

Traditionally biomaterials made of polymers (polyethylene, polyurethane, polytetrafluoroethylene, polyacetal, polymethylmethacrylate, polyethylene terephthalate, silicone rubber, polysulfone, and polyetheretherketone), metals (stainless steel, cobalt-chromium and titanium alloys), and ceramics (alumina, zirconia, and bioglass) are commonly used to replace and/or restore the function of traumatized or degenerated tissues or organs. The estimated world market for biomaterials is around \$12 billion per year, with an average global growth between 7% to 12% per annum. Over the last few decades considerable progress has been made in understanding the interactions between the materials and the tissues. It has been recognized that for optimal interaction between a biomaterial and the host tissues, there should be surface as well as structural compatibility between them. Surface compatibility meaning the chemical, physical (including surface morphology), and biological suitability of an implant surface to the host tissues. Structural compatibility is the optimal adaptation to the mechanical behavior of the host tissues. Therefore, structural compatibility refers to the mechanical properties of the biomaterial, such as stiffness and strength, and



CF: carbon fibers, C: carbon, GF: glass fibers, KF: kevlar fibers, PMMA: Polymethylmethacrylate, PS: polysulfone, PP: Polypropylene, UHMWPE: ultra-high-molecular weight polyethylene, PLDLA: poly(L-DL-lactide), PLLA: poly(L-lactic acid), PGA: polglycolic acid, PC: polycarbonate, PEEK: polyetheretherketone, HA: hydroxyapatite, PMA: polymethylacrylate, BIS-GMA: bis-phenol A glycidyl methacrylate, PU: polyurethane, PTFE: polytetrafluoroethylene, PET: polyethyleneterephthalate, PEA: polyethylacrylate, SR: silicone rubber, PELA: Block co-polymer of lactic acid and polyethylene glycol, LCP: liquid crystalline polymer, PHB: polyhydroxybutyrate, PEG: polyethyleneglycol, PHEMA: poly(20hydroxyethyl methacrylate)

Fig.1: Various biomedical applications of polymer composite materials.

optimal load transmission at the implant/tissue interface. Many homogenous biomaterials mentioned above were found to be not meeting these requirements. Metals and ceramics are many times stiffer than most tissues of the human body. Polymers are too flexible and too weak to meet the mechanical demands of certain applications. Polymer composite materials are particularly attractive for biomedical applications because of their tailorable manufacturing process and properties comparable to those of the host tissues. By controlling the volume fractions, and local and global arrangement of reinforcement phase, the properties of an implant can be varied and tailored to suit the mechanical and physiological conditions of the host tissues. Polymer composites also display reasonable corrosion and wear

resistance and strength properties. More over the polymer composite materials are fully compatible with the modern diagnostic methods such as computed tomography (CT) and magnetic resonance imaging (MRI) as they are non-magnetic and produce no artifacts which is the case with metals and ceramics. As shown in **Fig. 1**, over the years a wide variety of polymer composite materials have been investigated for possible biomedical applications [1]. Polymer composite biomaterials are proposed for various applications such as artificial joints, fracture fixation implants/devices, bone replacement, dental restoration, instruments for correction and stabilization of spine deformities, vascular grafts, hernia patches,

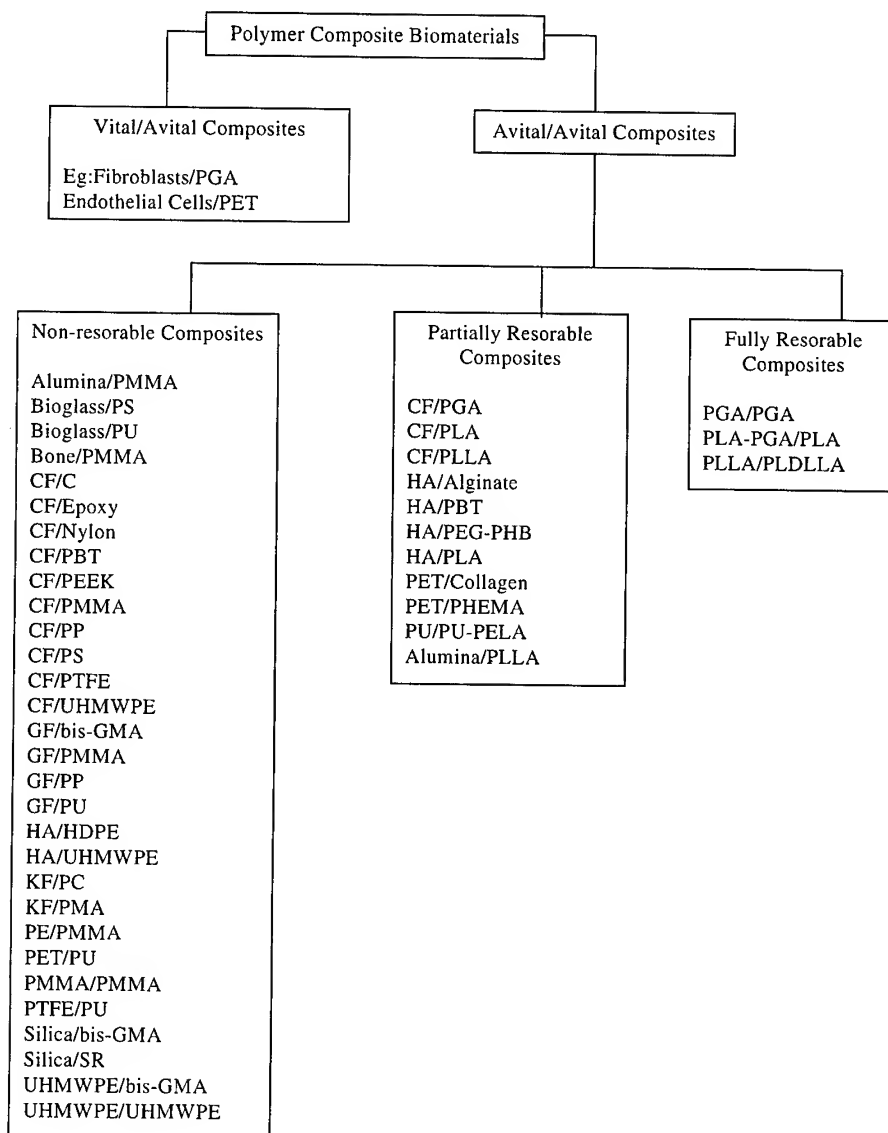


Fig.2: Classification of man-made polymer composite biomaterials.

tendon/ligament prostheses, artificial skin, cartilage repair prostheses, artificial limbs, etc. For the purpose of clarity, the various man-made polymer composite materials are classified into several sub-groups as shown in **Fig. 2**. The first sub-group is the 'vital/avital composites', which are made by combining living (or vital) cells with non-living (or avital) materials such as porous polymers. The vital/avital composites are in their infant stage of development. However, it is an area of intensive research worldwide and commonly known as 'tissue engineering' or 'cellular engineering'. Alternatively a composite material made of avital (non-living) matrix and reinforcement phases, is called 'avital/avital composite'. The avital/avital composites are analogous to polymer composites known to engineers. The avital/avital composites are further divided into non-resorbable, partially resorbable and fully resorbable composite biomaterials. The non-resorbable composites are designed not to degrade in *in vivo* (in side the body) environment. On the other hand the resorbable composites are intended to loose their mechanical integrity in *in vivo* conditions. The non-resorbable polymer composite materials are particularly promising for long-term implants, whereas the resorbable composites are suitable for short-term or transient implants. The reminder of this paper presents two examples of non-resorbable polymer composites i.e. carbon fiber reinforced polyetheretherketone (CF/PEEK) and carbon fiber reinforced epoxy (CF/epoxy) for possible applications as bone plates and dental posts respectively.

DEVELOPMENT OF BRAIDED CF/PEEK COMPOSITE BONE PLATE

In orthopedic surgery, often bone plate and screws as shown in **Fig. 1** are used to treat the diaphyseal (shaft of a long bone) fractures. Currently, bone plates made of stainless steel, Cr-Co alloy, and titanium alloy are commonly used. The elastic modulus of metals lies in the range from 110 GPa to 220 GPa, which is much higher than the 12~18GPa elastic modulus of human bone. It has been recognized that this stiffness mismatch results in 'Stress-Shielding' effect, which causes bone weakening. To overcome the shortcomings associated with the metal bone plates, researchers considered using polymer composite bone plates. Early studies mainly conducted on thermoset polymer based composites. Possible toxic effects of unused monomers and non-suitability to re-shape in the operating room made thermoset polymer composites not an obvious choice for bone plate applications. Recently researchers proposed thermoplastic polymer composite, CF/PEEK for bone plate application. Most of the work is confined to short fiber and unidirectional fiber reinforced composites. In this work first attempts were made to develop braided CF/PEEK composite bone plates as shown in **Fig. 3**.



Fig.3: Braided CF/PEEK composite bone plate.

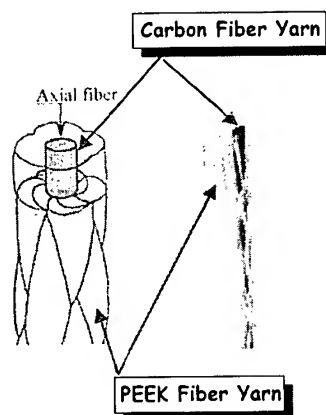


Fig.4: Schematic diagram of a micro-braided yarn

Since the PEEK material has a high melt viscosity, impregnation of braided carbon fiber fabrics with PEEK is a difficult task to achieve using conventional processes. To overcome this problem, first, the fibers of carbon and PEEK materials were braided into a single yarn (called 'micro-braided yarn') using a tubular braiding machine. **Fig.4** shows schematic diagram of a typical micro-braided yarn, with 3K carbon fibers as the core and PEEK fibers as the sheath. This special yarn was subsequently formed into flat braided fabrics using a flat braiding machine. Six layers of flat braided fabrics were hot pressed at 400°C for one hour to obtain a 2 mm thick bone plate. Microscopic examination of several cross-sections of the specimen revealed good impregnation of carbon fibers with the PEEK matrix.

Four point bending tests were conducted to evaluate the flexural properties. Stainless bone plate displayed 20 [Nm] bending moment and 1.9 [Nm/degree] bending stiffness. On the other hand, the CF/PEEK composite bone plate (55% fiber volume fraction) displayed 5 [Nm] bending moment and 0.3 [Nm/degree] bending stiffness (approximately 25% and 16% values of stainless plate, respectively). As a next step, the composite bone plate properties will be further optimized by changing the braiding angle, fiber yarn tow size, fiber volume fraction, and plate thickness. The micro-braided yarn technique appears to be suitable for making good quality thermoplastic composite bone plates.

DEVELOPMENT OF BRAIDED CF/EPOXY COMPOSITE DENTAL POST

Dental post, approximately 20mm long and 1mm diameter, is used to reinforce the tooth in case where the remaining tooth structure is small. It is placed inside the root canal and cemented to the dentine. Above the dental post, a core and crown assembly is formed (**Fig 5**). In addition to providing retentive support to core, the dental post also helps to direct forces of mastication apically along the length of the root (indicated by '13' in **Fig.5**). Traditionally posts made of stainless steel, Ni-Cr or titanium alloys are used, based on the assumption that the post should be rigid. Failures reported include corrosion of posts, bending or fracture of posts, loosening of post, core fracture and root fracture. This is mainly due to large stiffness mismatch between the metal post (230 GPa) and dentine (11 GPa), and also the stress concentration in the dentine. Finite element analysis suggested that an ideal post should have varying stiffness along its length. Specifically, the coronal end of the post (indicated by No 1 in **Fig 5**) should have higher stiffness for better retention and rigidity of the core, and the apical end of the post (indicated by No 13 in **Fig 5**) should have lower stiffness matching that of the dentine so as to overcome the root fractures due to stress concentration. A post with varying stiffness but no change in the cross-sectional geometry along its length is only possible by using functionally graded materials concept. Author's research team developed a patented technology to produce functionally graded composite dental posts (FGM composite posts) [2]. This new technology combines modified braiding and pultrusion processes. Initially carbon fiber yarns were braided with continuously varying braiding angle (**Fig.6**). Subsequent impregnation with epoxy resin resulted in FGM composite posts. The new posts are adequately rigid, resistant to corrosion and fatigue.

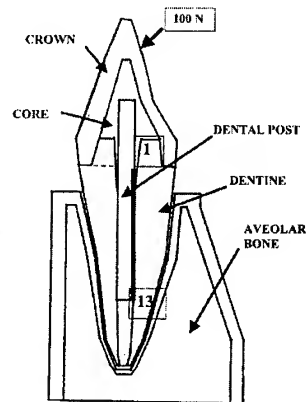


Fig.5: A dental post restored tooth.

To evaluate the benefits of FGM composite posts, a finite element study was carried out. For comparison purposes, tooth models restored with stainless steel and FGM composite posts were considered. The stainless steel post was modeled as isotropic material with uniform elastic modulus. The FGM composite post was modeled as transversely isotropic material with stiffness varying from 20 GPa at the apical end to 80 GPa at the coronal end in seven steps. A mastication load of 100N was applied at 45 degree to the longitudinal axis of tooth. Fig.7 shows the variation of normal stress and shear stresses at the post-dentine interface. The peak tensile and shear stresses for the FGM composite post were about half the values of those for conventional stainless steel dental post. The reduction in maximum tensile stress means that the tooth can sustain higher fatigue loads and thus reducing the chance of root fracture. The reduction of interface shear stress between the dental post and dentine also reduces the chance of post loosening, which constitutes major cause of dental restoration failures. Full scale experimental studies confirmed the findings of finite element studies. It can be stated

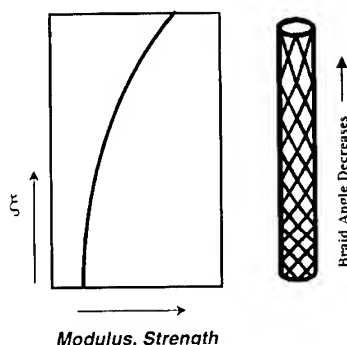


Fig.6: Braided CF/epoxy composite dental post with varying stiffness along the length.

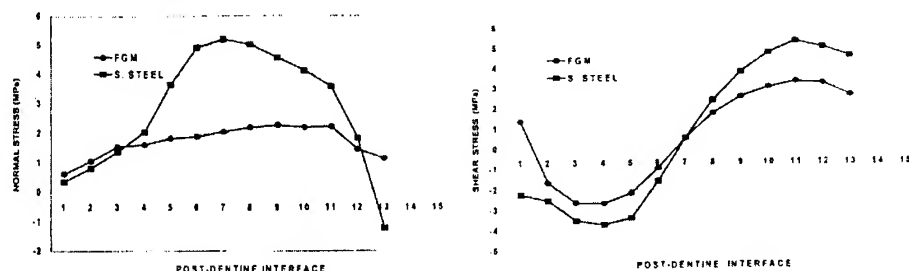


Fig.7: Normal and shear stress distributions along the post-dentine interface. As shown in Fig.5, the numbers 1 and 13 refers to coronal and apical ends respectively.

that the FGM composite dental post is functionally superior to conventional metallic posts.

CONCLUSIONS

Polymer composite are particularly attractive for biomedical applications because of their tailorable manufacturing processes and mechanical properties. The current research work clearly indicates that innovations in composites design and fabrication lead to better implants with improved performance.

REFERENCES

1. Ramakrishna, S., Mayer, J., Wintermantel, E. and Leong, K.W (2000) Biomedical applications of polymer composite materials: A review. Composites Science & Tehcnology (in press).
2. Ramakrishna, S., Ganesh, V.K., Teoh, S.H., Loh, P.L. and Chew, C.L. (1998). Fiber reinforced composite product with graded stiffness. Singapore Patent Application No. 9800874-1.

SILANE TREATMENT OF GLASS FIBER TO IMPROVE INTERFACIAL ADHESION BETWEEN GLASS FIBER AND UNSATURATED POLYESTER

Joong-Seong Jin¹, Soo-Jin Park¹, Jae-Rock Lee¹, and Yeung-Keun Kim²

¹ Advanced Material Division, Korea Research Institute of Chemical Technology
P.O. Box 107, Yusong, Taejeon 305-600, KOREA: psjin@pado.kRICT.re.kr

² Kangnam Industrial Co., Ltd., Sunggok, Ansan 425-110, Korea

SUMMARY: The effect of various silane coupling agent treatments of glass fiber surfaces has been studied in terms of the surface free energetics of fibers and the mechanical interfacial properties of composites. The γ -methacryloxy propyl trimethoxy silane (MPS), γ -amino propyl triethoxy silane (APS), and γ -glycidoxy propyl trimethoxy silane (GPS) were applied to the surface treatment of glass fiber. According to contact angle measurements based on the wicking rate of a liquid test, it is observed that silane treated glass fiber does lead to an increase in surface free energy, mainly due to the increase of its specific (or polar) component. Also, in the glass fibers-reinforced unsaturated polyester matrix system, a constant linear relationship is shown in both the interlaminar shear strength (ILSS) and the critical stress intensity factor (K_{IC}) on specific component, γ_s^{SP} , of surface free energy. It reveals that the hydrogen bonding which is one of specific component of surface free energy, between glass fibers and coupling agents plays an important role in improving the degree of adhesion at interfaces of composites.

KEYWORDS: glass fiber, silane treatment, surface free energy, contact angle, interlaminar shear strength (ILSS), critical stress intensity factor (K_{IC}).

INTRODUCTION

Since the innovation of the manufacturing techniques of polymeric composites, the performance of composites has been improved, and the study on interfacial adhesion of fiber and resin is also becoming important. When two materials are incompatible, it is often possible to bring about compatibility by introducing a third material that have intermediate properties between those of the other two. Organosilicone compounds are obvious choices as potential coupling agent for glass fiber-reinforced polymers since the silicone ends of the molecules are similar to glass, and organic groups on silicone could be synthesized for compatibility with organic polymers [1]. The usage of coupling agents can improve the interfacial adhesion and hence the resulting mechanical properties of composites [2]. When the silane coupling agents are introduced onto the glass fiber surface composites, two interfaces exist between glass fiber and polymer matrix: (a) the interface between glass fiber and silane coupling agents, and (b) the interface between silane coupling agents and polymer matrix. At the interface between the glass fiber and the silane coupling agent, the hydroxyl

groups of the silanes and those of the glass fiber surface can react with each other through siloxane bonding or hydrogen bonding.

It is generally accepted that the mechanical interfacial properties of fiber-reinforced composites depend strongly on the level of adhesion between fiber and matrix [3]. Interfacial adhesion cannot be achieved without intimate contact, i.e., unless the fiber surface contacts the resin in an intermolecular equilibrium distance level. In addition, suitable wetting of the fibers by the liquid polymeric matrix should occur when the fiber surface nature is well considered with that of the liquid polymeric surface with a viewpoint of the hydrophilic-hydrophobic properties or the specific (or polar)-London dispersive components of surface free energy [4].

In this work, we discuss the changes in interfacial adhesion after the presence of silane coupling agent in glass fiber-reinforced composites and their effect on mechanical interfacial and resulting mechanical properties for an unsaturated polyester resin based on matrix composites.

EXPERIMENTAL

Materials and Sample Preparation

The glass fabric (HD 324-01, 23× 23 count/inch) used in this study was supplied in the preheated state from Hyun-Dai Fiber Co. of Korea and unsaturated polyester (R-235, viscosity 2.8 poise) resin was ortho-phthalic acid type resin, which was supplied by Seiwon Chem. Co. of Korea. Silane coupling agents used in this study, γ -methacryloxy propyl trimethoxy silane (MPS), γ -amino propyl triethoxy silane (APS), and γ -glycidoxy propyl trimethoxy silane (GPS) supplied from Shinetsu Co. of Korea, were introduced to improve the interfacial adhesion of glass fiber-unsaturated polyester composites.

In this work, all of the silane coupling agents studied were prepared under constant condition in order to treat the glass surfaces. In those solution, cosolvent of methanol (95 wt.% in total solvent) and distilled water (5 wt.% in total solvent) was used, and the silane concentration was fixed at 0.2 wt.%. After the silane coupling agents were hydrolyzed at pH 4 for 1 h, the glass fiber was dipped in the hydrolyzed silane solution for 30 min. and it was dried at 110°C for 30 min. The composites made of 20 plies of silane-treated glass fabrics were prepared in a hot press at 20 atm and 100°C for 1 h with a vacuum bagging method [3]. The fiber volume fraction of bulk specimens was about 52± 2 % for all composites.

Table 1. The characteristics of wetting liquids used in this work

Wetting liquids	γ_L^L /mJ.m ⁻²	γ_L^{SP} /mJ.m ⁻²	γ_L^S /mJ.m ⁻²	η /mPa.s	ρ /g.cm ⁻³
n-hexane	18.4	0	18.4	0.33	0.661
Water	21.8	51	72.8	1	0.998
Diiodomethane	50.42	0.38	50.8	1.3	49.5

γ_L^L : London dispersive component of surface free energy, γ_L^{SP} : specific component of surface free energy, γ_L^S : total surface free energy, η : viscosity, ρ : density

Table 2. Contact angle determinations (in degree) on various silane-treated glass fibers

Wetting liquids	As received	MPS	APS	GPS
Water	86	68	74	78
Diiodomethane	49	52	50	50

Contact Angle Measurements

Contact angle measurements of glass fibers were performed using the Krüss Processor Tensiometer K 12 with fiber apparatus. About 2 g of glass fibers was packed into an apparatus, and then mounted indirectly to the measuring arm of the microbalance. The testing wetting liquids used for contact angle measurements were n-hexane, deionized water and diiodomethane. The surface free energy and their London dispersive and specific (or polar) component for the wetting liquids are listed in Table 1.

Mechanical Interfacial Properties

In this work, glass fiber-unsaturated polyester composites were characterized by mechanical interfacial properties, such as interlaminar shear strength (ILSS) and critical stress intensity factor (K_{IC}). The ILSS is tested in according to the ASTM D2344 procedure and span-to-depth of test specimens was 5:1. An analytical expression for K_{IC} may be characterized by single edge notched (SEN) beam fracture toughness test according to the ASTM E399.

RESULTS AND DISCUSSION

Contact Angle Measurements

Table 2 shows the contact angle data of glass fibers made with and without silane coupling agent treatments. As a result, the angles of water on various silane-treated glass fibers largely decreased as compared with the as received. As above mentioned, this is clearly found that the silane treatments lead to a change in fiber surface nature, resulting in increasing the hydrophilic properties.

In 1970's, Owens and Wendt [5] and Kaelble [6] proposed the method using geometric mean. Fig. 1 shows the results of surface free energies of the silane-treated glass fibers for two simultaneous liquids, e.g., water and diiodomethane [7-8]. As expected angle data, it is interesting to note that the total surface free energy, γ_s , of silane-treated glass fibers increases, while the London dispersive component, γ_s^L , remains a nearly constant. This surface free energy increase of silane-treated glass fibers can be attributed to the increasing of hydroxyl group, resulting in increasing hydrogen bonding between the glass fiber and the silane coupling agent, that is one of the specific component of surface free energies [4]. From the surface energetics of view, it is expected that increase of specific component of the surface free energy of silane-treated glass fibers play an important role in improving the degree of adhesion at interfaces between glass fibers and silane coupling agent.

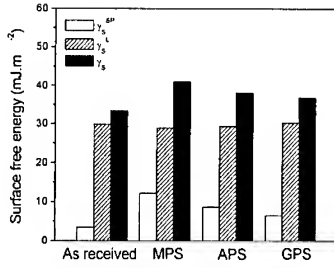


Fig. 1 Surface free energies (in mJ.m⁻²) of the various silane-treated glass fibers

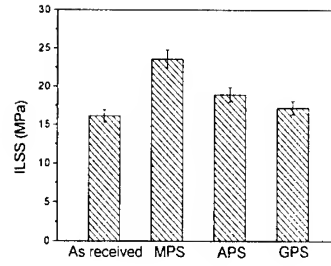


Fig. 2 ILSS of composites treated with various silanes

Mechanical Interfacial Properties

The degree of adhesion at interfaces between fiber and matrix may be measured by a short-beam test for the interlaminar shear strength (ILSS) of the mechanical behavior. For cross-section of the composites, the ILSS determined from three-point bending tests are calculated as follows:

$$ILSS = \frac{3F}{4bd} \quad (1)$$

where F (N) is the rupture force, b (m) the width of the specimen, and d (m) the thickness of the specimen

And the fracture toughness can be measured by a three point bending test for the critical stress intensity factor (K_{IC}) in according to the ASTM E399. For single edge notched (SEN) beam fracture toughness test, the value of K_{IC} is calculated as follows [9]:

$$K_{IC} = \frac{PS}{BW^{3/2}} f(a/W) \quad (2)$$

and

$$f(a/W) = \frac{3(a/W)^{1/2} [1.99 - (a/W)(1 - a/W)(2.15 - 3.93a/W + 2.7a^2/W^2)]}{2(1 + 2a/W)(1 - a/W)^{3/2}} \quad (3)$$

where P (kN) is the rupture force, S (cm) the span between the supports, and W (cm) the specimen width and thickness, respectively.

From the ILSS and K_{IC} results as shown in Fig. 2 and Fig. 3, the presence of silane coupling agent does lead to an increase of mechanical interfacial properties of the composites, which can be related to the effect of growing the degree of adhesion at interfaces between three elements in this system, i.e., fiber, matrix, and silane coupling agent.

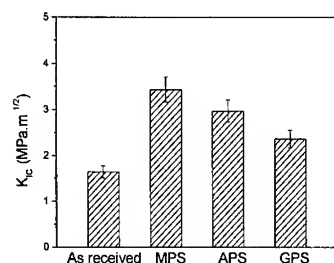


Fig. 3 K_{IC} of composites treated with various silanes.

CONCLUSION

The effect of silane coupling agent treatments on the fiber surface properties and the resulting mechanical behavior of the composites have been studied in terms of the surface energetics of fibers and the mechanical interfacial properties of composites. According to the experimental results, it reveals that the mechanical interfacial properties of composites, i.e., the ILSS and K_{IC} , are largely dominated by the specific component of surface free energy. These results could be explained by means of the increasing of hydroxyl group through siloxane bonding or hydrogen bonding at the interfaces between glass fibers and silane coupling agent. Consequently, the silane coupling agent plays an important role in improving the degree of adhesion at interfaces in a composites system.

REFERENCES

1. Edwin P. Plueddemann, *J. Adhesion Sci. Technol.*, Vol. 5, 1991, pp.261.
2. O. K. Johansson, et. Al., *J. Compo. Mater.*, Vol. 1, 1967, pp.278.
3. S. J. Park and M. S. Cho, *J. Mater. Sci. Let.*, Vol. 18, 1999, 373.
4. S. J. Park, "Interfacial Forces and Fields: Theory and Applications" (Ed. J. P. Hsu), Marcel Dekker, New York, 1999, pp.385.
5. D. K. Owens and R. C. Wendt, *J. Appl. Polym. Sci.*, Vol. 13, 1969, pp.1741.
6. D. H. Kaelble, *J. Adhesion*, Vol. 2, 1970, pp. 66.
7. W. Wu, "Polymer Interface and Adhesion", Marcel Dekker, New York, 1982.
8. S. J. Park, W. B. Park and J. R. Lee, *Polym. J.*, Vol. 31, 1999, pp.28
9. Chen, D. J. Hourston and W. B. Sun, *Eur. Polym. J.*, Vol. 31, 1995, pp.199.

Interface (2)

Effect of Interdiffusion on the Interfacial Adhesion of Polymer Coated Carbon Fibers

H. M. Kang ¹ and T. H. Yoon ¹

¹ *Department of Material Science and Engineering
Kwangju Institute of Science and Technology
1, Oryong-dong, Buk-gu, Kwangju 500-712, Korea:thyoon@kjist.ac.kr*

SUMMARY: The interfacial shear strength (IFSS) of carbon fibers with vinyl ester resin was investigated as a function of the structure of polymers for coating of carbon fiber. Poly(arylene ether phosphin oxide) (PEPO), Udel[®] P-1700, Ultem[®] 1000, poly(hydroxy ether) (PHE), carboxy modified poly(hydroxy ether)(C-PHE) and poly(hydroxy ether ethanol amine) (PHEA) were utilized for a coating of carbon fibers. Adhesion of polymers to carbon fibers was also evaluated in order to understand the adhesion mechanism. Interfacial shear strengths were measured via micro-droplet tests, and failure surfaces were analyzed by SEM. Diffusion between polymer and vinyl ester resin was investigated by inserting a piece of polymer film into vinyl ester resin, containing 33, 40 or 50% of styrene monomers. The solubility parameters of polymers were calculated and were correlated to the interfacial shear strength. The highly enhanced interfacial shear strength (IFSS) was obtained with PEPO coating, and marginally improved IFSS with PHE, Udel[®] and C-PHE coatings, but no improvement with PHEA and Ultem[®] coatings. Very high IFSS with PEPO coating can be attributed to excellent solubility and miscibility of PEPO in vinyl ester resin, but marginally high IFSS with PHE, C-PHE, Udel[®], PHEA and Ultem[®] may be due to limited solubility and/or miscibility in vinyl ester resin.

KEYWORDS: interfacial adhesion, vinyl ester resin, carbon fiber, polymer coating, micro-droplet test, solubility, miscibility

INTRODUCTION

Vinyl ester resin is one of the widely utilized thermoset resins for composite and coating applications due to their good electrical and mechanical properties, and excellent corrosion resistance [1-3]. Vinyl ester resins are prepared via esterification of polyfunctional epoxy resin with methacrylic or acrylic acid in order to provide vinyl end groups and addition of styrene monomers to reduce the viscosity of the resin. Thus, they have excellent processability and can be cured via free radical reaction, which are some of the attractive features of vinyl ester resins.

Recently, there has been an great interest in vinyl ester resins for infra-structural composites applications such as bridges due to their good processability and mechanical properties.

However, as expected, their inadequate adhesion to reinforcing fibers is a major hurdle to overcome for wide applications. Since performance of composites materials are strongly dependent on the interfacial adhesion between fibers and matrix resin [4-5], surface of reinforcing fibers has to be properly tailored to achieve maximum adhesion.

Polymer coatings for carbon fiber surface modification have received a great attention due to their advantages such as enhanced interfacial adhesion as well as improved toughness at the interface. Recently, poly(vinylpyrrolidone) [6-7], poly(arylene ether phosphine oxide) [8-9] and others [10] were successfully utilized to enhance the interfacial adhesion of carbon fiber to vinyl ester resin, or glass fiber to polyurethane, respectively. Improved adhesion and thus fatigue resistance and mechanical properties of composites with polymer coatings are attributed to good miscibility or compatibility of polymer coating with resin.

In this study, carbon fibers were coated with thermoplastic polymers in order to enhance the interfacial adhesion to vinyl ester resin. Diffusion behavior between polymers coating and vinyl ester resin was investigated via SEM analysis and correlated to the interfacial adhesion and the structure of polymers.

EXPERIMENTAL

Materials

The vinyl ester resin with 33 wt.% styrene (DERAKANE 441-400) was friendly donated by Dow Chemical, and styrene monomer (Junsei) and benzoyl peroxide (Aldrich) were purchased. Poly(arylene ether phosphine oxide) (PEPO) with molecular weight of 20,000 g/mole was synthesized in our laboratory as reported else where [11-12] and commercial polymers such as Udel[®] P-1700 and Ultem[®] 1000 were provided by Amoco and GE, respectively. Carboxy modified poly(hydroxy ether) (C-PHE) from Phenoxo Assoc. (Rock Hill, SC, U.S.A) and poly(hydroxy ether ethanalamine) (PHEA) from Dow Chemical and poly(hydroxy ether) (PHE) from Phenoxo Assoc., were also utilized. Unsized AS-4 carbon fibers from Hercules with an average diameter of 8 μm were used for polymer coating.

Interfacial adhesion study

Coating of carbon fibers with PEPO, Ultem[®] or Udel[®] was carried out by dipping a single carbon fiber into a 1wt.% solution in chloroform for 1 minute, followed by drying at 100°C for 12 hours. 2wt.% aqueous solution was utilized to coat carbon fiber by dipping for C-PHE. However, 2wt. % solution in THF or aqueous acetic acid for PHE and PHEA, respectively, was used for dip-coating of fibers, followed by drying at 100°C for 12 hours.

Micro-droplet specimens were prepared by the liquid method for vinyl ester droplet or film method for polymer droplets as described previously [8, 13]. Interfacial shear strengths of micro-droplets were measured with Instron 5567 at a speed of 0.3mm/minute. Since the loads from the test was so small, a micro-balance (BB 2400, Mettler) connected to a personal computer was utilized to measure debonding load. At least 30 specimens were tested and the results were averaged.

Diffusion Study

The samples for diffusion study were prepared from a piece of film and vinyl ester resin. The polymer films of 100-150 μm in thickness were prepared by compression molding and were cut into 3mm \times 6mm in size. An extra styrene monomer was added to DERAKANE 441-400 which already contained 33wt.% of styrene monomer to afford 40 and 50 wt.% styrene in

order to understand the role of styrene in diffusion. The specimens (3×6×15mm) for diffusion study were prepared by inserting polymer films into vinyl ester resin in silicon rubber mold, followed by curing at 130°C for 20min. The samples were cut in half so as to observe the diffused region in order to investigate diffusion behavior via SEM (JEOL-JSM 5800).

RESULTS AND DISCUSSION

Interfacial Adhesion

The interfacial adhesion of polymers to carbon fibers was evaluated in order to understand the adhesion mechanism between polymer coating and fiber. The prepared micro-droplet size was 40–80 μm . The interfacial shear strength with C-PHE could not be measured since it did not melt even at 400°C but degraded. The interfacial shear strength with PEPO was 66.7 ± 4.8 MPa, which was followed by Udel® (55.6 ± 4.3 MPa), PHE (55.2 ± 6.7 MPa), PHEA (53.2 ± 7.4 MPa) and Ultem® (45.0 ± 4.3 MPa).

The micro-droplets prepared from vinyl ester resin and polymer coated carbon fibers were ranged from 40 to 80 μm in length. As expected from polymer droplet study, PEPO coating exhibited higher interfacial shear strength of 52.5 ± 7.2 MPa than PHE (45.3 ± 8.3 MPa), Udel® (42.9 ± 5.7 MPa), and C-PHE (41.3 ± 6.4 MPa) coating. However, PHEA (30.5 ± 9.4 MPa) and Ultem® (29.7 ± 10.2 MPa) coated carbon fibers exhibited as low IFSS as those with as-received carbon fibers (29.1 ± 7.5 MPa).

Diffusion Study

SEM micrographs from PEPO/vinyl ester resin system provided different morphology from the rest of the samples. As shown in Figure 1, it was difficult to differentiate PEPO film from vinyl ester region, but only clue was surface roughness. However, the rough surface was not observed at 50wt % of styrene, suggesting that PEPO film completely dissolved in vinyl ester resin (before cure), and is completely miscible with vinyl ester resin (after cure), which could be due to strong interaction by phosphine moiety as reported [8, 14]. Therefore, highest IFSS with PEPO coating can be attributed to excellent solubility and miscibility of PEPO in vinyl ester resin, leading to complete inter-diffusion at the interface, and also to very good adhesion to carbon fiber which was demonstrated by PEPO droplet test.

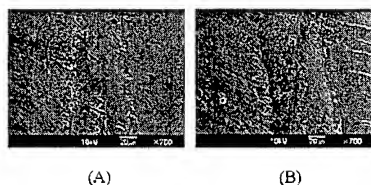


Figure 1. SEM micrographs of diffusion layer of PEPO/vinyl ester resin.
(A) 33wt.% styrene($\times 700$), (B) 40wt.% styrene($\times 700$)

As shown in Figure 2, the samples with Udel® film, however, exhibited a distinct film region and somewhat clear interface between the film region and the vinyl ester region even at 50% styrene. At 33wt % of styrene (Figure 2-A), the film region can be divided three parts: outer, inner and central part. The outer part has high roughness and shows small spheres which are believed to be formed by diffused vinyl ester resins. However, the inner part was fairly smooth, but spheres were also found, while the central part seem to be free of diffusion. As the styrene content increased to 40%, whole film was diffused by vinyl ester resin, leaving

spheres and rough surface. At 50%, an interface and spheres were still observed, but film region was distorted, indicating vinyl ester resin deformed Udel[®] film (Figure 2-C).

It is believed that Udel[®] film has limited solubility in liquid vinyl ester resin and reverse is also true, but once dissolved, Udel[®] seems to have good miscibility with cured vinyl ester resin. However, vinyl ester resins diffused into Udel[®] film (before cure), and forms spheres during the cure due to immiscibility with Udel[®]. High but inferior IFSS with Udel[®] coating to that with PEPO coating can be attributed to immiscibility of vinyl ester resin with Udel[®], and limited solubility of Udel[®] in vinyl ester resin.

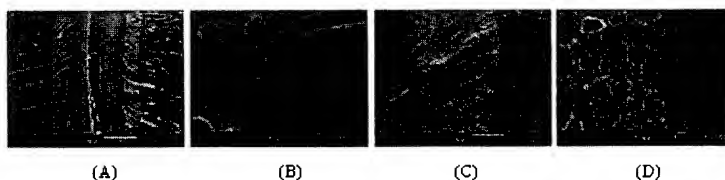


Figure 2. SEM micrographs of diffusion layer of Udel[®]/vinyl ester resin.

(A) 33wt.% styrene ($\times 500$), (B) 33wt.% styrene ($\times 10,000$),
(C) 50wt.% styrene ($\times 500$), (D) 50wt.% styrene ($\times 10,000$)

The Ultem[®] film region with sharp interface was observed. The diffused area of film region was very small; one tenth of total film width (Figure 3-A), and even at 50% of styrene only half of film was diffused. At the high magnification, small spheres were observed (Fig. 3-D) as seen in the diffused part of Udel[®] samples (Figure 2-B). Thus, it can be said that solubility of Ultem[®] in vinyl ester resin as well as that of vinyl ester resin in Ultem[®] is very limited. Moreover, Ultem[®] is not miscible in vinyl ester resin after being cured, as observed from Udel[®] samples. Therefore, very low IFSS with Ultem[®] coating can be explained by insolubility and immiscibility of Ultem[®] in vinyl ester resin, resulting in sharp interface and thus interfacial failure. In the micro-droplet samples, failure surface was relatively smooth except some spheres like particles, which suggests that low solubility of vinyl ester resin in Ultem[®] limited diffusion and thus only few aggregate of spheres.

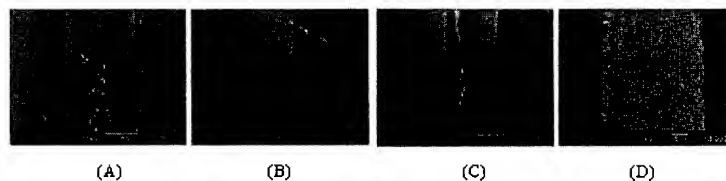


Figure 3. SEM micrographs of diffusion layer of Ultem[®]/vinyl ester resin.

(A) 33wt.% styrene ($\times 500$), (B) 33wt.% styrene ($\times 3,000$),
(C) 50wt.% styrene ($\times 500$), (D) 50wt.% styrene ($\times 3,000$)

The samples with PHE showed clear film region, but inter-diffused interface (or interphase) instead of sharp interface between film and vinyl ester region indicate good mutual solubility in each other (Figure 4-A). Spheres were also seen in the edge of film region, exhibiting immiscibility of diffused vinyl ester resin in the PHE region. At 40% of styrene, most of film was dissolved and whole film disappeared at 50% of styrene, suggesting good solubility of PHE in vinyl ester resin (Figure 4-B). Therefore, it can be said that solubility of PHE in vinyl ester resin was very good, possibly as good as PEPO, while miscibility of vinyl ester in PHE was inferior to that of PEPO, resulting in high, but inferior IFSS with PHE coating to that with PEPO coating.

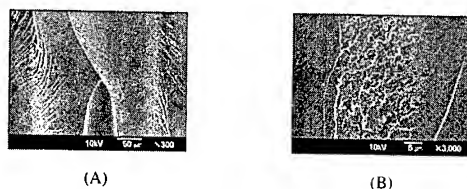


Figure 4. SEM micrographs of diffusion layer of PHE/vinyl ester resin.
(A) 33wt.% styrene ($\times 300$), (B) 50wt.% styrene ($\times 3,000$)

In C-PHE diffusion samples, inter-diffused interface (interphase), spheres in the film region and film region was observed even at 50% styrene. At 33% styrene, only the edge of film was diffused by vinyl ester, while whole film was diffused at 50% (Figure 5). However, major difference from other samples was mutual immiscibility between vinyl ester and C-PHE, showing spheres in inter-diffused region. Therefore, it can be said that spheres were formed not only by vinyl ester (dissolved into C-PHE) but also by C-PHE (dissolved into vinyl ester region). Relatively high IFSS with C-PHE coating can be attributed to good inter-diffusion, but limited solubility and immiscibility of C-PHE in vinyl ester provided inferior IFSS to PEPO.

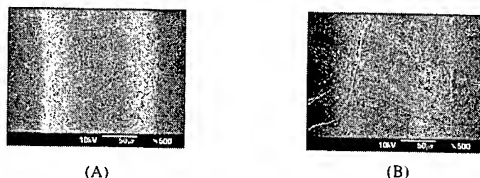


Figure 5. SEM micrographs of diffusion layer of C-PHE/vinyl ester resin.
(A) 33wt.% styrene ($\times 500$), (B) 50wt.% styrene ($\times 500$)

The samples with PHEA showed very narrow diffused region, but aggregate of spheres as observed from Udel[®] sample (Figure 6). As styrene content increased, inter-diffused layer slightly increased, but still very small. Therefore, it can be said that PHEA has very poor solubility and poor miscibility in vinyl ester resin, resulting in very low IFSS and smooth failure surface. PHEA, having similar chemical structure as PHE, exhibited very different diffusion behavior from PHE and C-PHE, which can be attributed to ethanolamine moiety in PHEA which is also responsible to high IFSS with PHEA droplet tests.

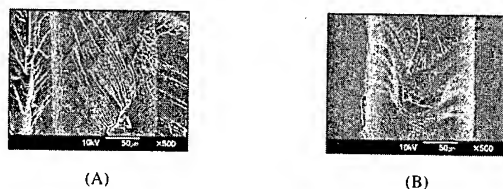


Figure 6. SEM micrographs of diffusion layer of PHEA/vinyl ester resin.
(A) 33wt.% styrene ($\times 500$), (B) 50wt.% styrene ($\times 500$)

CONCLUSIONS

The interfacial shear strength (IFSS) of PEPO with carbon fiber was highest, followed by Udel[®], PHE and PHEA, but no improvement was noticed with and Ultem[®]. Increased IFSS

with PEPO coating can be attributed to phosphine oxide group which provided strong adhesion not only to carbon fiber but also to vinyl ester resin. PEPO film exhibited excellent solubility and complete miscibility with vinyl ester resin, showing high IFSS, while Udel[®], PHE and C-PHE showed low solubility but good miscibility, resulting in marginally improved IFSS. However, Udel[®] and PHEA exhibited poor solubility in vinyl ester resin provided as same IFSS as control.

ACKNOWLEDGEMENT

This work was supported by the Brain Korea 21 Project.

REFERENCES

1. *Encyclopedia of Polymer Sci. & Eng.*, W. E. Daniels, ed., Chap. 17, John Wiley & Sons, New York, 1985
2. *International Encyclopedia of Composites*, S. M. Lee, ed., V6, VCH, New York, 1991
3. S. Ziaee, G.R. Palmese, *J. Polym.Sci. Part B*, Vol.37, pp. 725
4. V. Rao and L. T. Drzal, *Polym. Compos.*, Vol.12, 1991, pp. 48
5. L. H. Peebles, "Carbon Fibers", CRC Press, Inc., Florida, 1990
6. N.S. Broyles, K.N.E. Verghese, R.M. Davis, J.J. Lesko, J.S. Riffle, *Proc. ANTEC*, 1998, pp. 2240
7. H. Li, S. V. Davis, N. Broyles, K. E. Verghese, A. C. Rosario, M. Robertson, M. C. Flynn, J. J. Lesko, and J. S. Riffle, *Proc. Adhes. Soc. Annu. Meetings*, 1997, pp. 497
8. I. C. Kim, and T. H. Yoon, *J. Adhes. Sci. Technol.*, in press, 1999
9. M. B. Bump, S. A. Bedsaul, R. K. Jelen, M. A. F. Robertson, K. E. Verghese, J. J. Lesko, and J. S. Riffle, *J. Adhes.*, in press, 1999
10. N.S. Broyles, K.N.E. Verghese, R.M. Davis, H. Li, J.J. Lesko, J.S. Riffle, *Polymer*, Vol. 39, pp. 3417
11. C. D. Smith, H. Grubbs, F. Webster, A. Gungor J. P. Wightman and J.E. McGrath, *High Perf. Polym*, Vol.3, 1991, pp. 539
12. K. U. Jeong, I. Y. Park, I. C. Kim, and T. H. Yoon, *J. Appl. Polym. Sci.*, submitted, 1999
13. P. C. Commercon and J. P. Wightman, *J. Adhes.*, Vol.47, 1994, pp. 257
14. S. Wang, Q. Ji, C. Tchatchoua, A. R. Shultz and J. E. McGrath, *J. Polym. Sci.:Part B, Polym. Phys.*, Vol. 37, 1999, pp. 1849

MEASUREMENT OF INTERPHASE THICKNESS IN GLASS FIBRE COMPOSITES

Jang-Kyo KIM, Man-Lung SHAM and Jingshen WU

*Department of Mechanical Engineering,
Hong Kong University of Science & Technology,
Clear Water Bay, Kowloon, Hong Kong; mejkkin@ust.hk*

SUMMARY: Novel experimental techniques, including the nanoindentation and nanoscratch tests and the thermal capacity jump measurement based on differential scanning calorimetry (DSC), have been successfully employed to characterize the properties of the interphase between silane treated glass fibre and a vinylester resin. The nanoindentation test gave the interphase thickness approximately $1\mu\text{m}$ for all composites studied. The effective interphase thickness measured from the nanoscratch test varies between $0.8\mu\text{m}$ and $1.5\mu\text{m}$ depending on the type and concentration of silane agent. The higher was the silane agent concentration, the larger the interphase thickness. These values were consistent with those measured based on the heat capacity changes, in terms of both general trend and absolute quantity.

KEYWORDS: Interphase thickness; glass fibre-vinylester composite; nanoindentation test; nanoscratch test; heat capacity.

INTRODUCTION

The interphase formed between fibre and polymer matrix materials possesses chemical, physical and mechanical properties that are different from those of either bulk fibre or matrix. The interphase presents a transition region of which properties vary continuously between the bulk fibre and the matrix. The interphase may have a substantial thickness depending on the molecular conformation, the constituents involved, the ease of molecular motion, and most importantly, whether or not the fibres are treated with polymeric sizes and other coupling agents [1]. The interphase region is complicated by the interactions occurring between the silane and glass fibre surface. It is suggested that the polymeric and lubricant components of size dissolve into the surrounding resin and that the silane migrate to the fibre surface [2]. Although a great deal of research has been directed toward characterization of the interphase properties, including modulus and ductility, little has been well established. This is due to the experimental difficulties involved and the lack of appropriate techniques required for accurate measurements of the properties. In polymer matrix composites, the interphase is found to be significantly softer than the bulk matrix material [3,4]. The softer interphase than the bulk matrix is supported by the lower apparent fibre pull-out bond strength obtained for the silane treated glass fibre-polyester system [5]. Apart from the mechanical properties of interphase relative to the bulk matrix material, the effective thickness or width of interphase has also been of particular interest. For thermoset matrix composites, several novel

techniques have been devised to study the interphase with varying degree of success. They include the nanoindentation [3,4] and atomic force microscopy (AFM) [6].

The present study is a continuation of our on-going project on evaluation of the mechanical properties of glass woven fabric composites affected by silane coupling agent. To select optimum interfacial conditions that would provide balanced mechanical properties and fracture resistance, a series of mechanical test have been carried out in our previous work [7,8]. An attempt is made to characterize the properties of fibre-matrix interphase affected by different silane agents, based on novel experimental techniques, such as the nano-indentation and nano-scratch tests and the specific heat capacity jump measurements based on differential scanning calorimetry.

EXPERIMENTAL PROCEDURE

Materials and Specimens

An E-glass woven fabric reinforced vinylester matrix composites was employed in this study. The reinforcement and the matrix material used and the preparation of composite laminates were essentially the same as those previously reported [7,8]. For the nanoindentation and nanoscratch tests, composites of 4mm in thickness were cut into small pieces of approximately 10mm x 4mm, which were mounted in a resin mould, and the sample surface was polished using increasingly finer sand papers and was finally finished with aluminium oxide papers of 50nm in particle size

Nanoindentation and Nanoscratch Tests

All indentation and scratch tests were performed using an indenter. The indenter consists of an indenter head and an optical microscope connected to a video camera. The indenter head is made up of a three-sided pyramidal diamond with a Berkovich tip. All indentation experiments followed the recommended procedures [9] with multiple loading and unloading along the fibre-interphase-matrix. A series of indents were made 400nm apart, and to a constant indent depth of 60nm. The reduced elastic modulus, E_r , was calculated based on the equation:

$$E_r = \frac{\sqrt{\pi}}{2\beta} \frac{S}{\sqrt{A}} = \left(\frac{(1-\nu_i^2)}{E_i} + \frac{(1-\nu_s^2)}{E_s} \right)^{-1} \quad (1)$$

where A is the contact area, β is the geometric constant (= 1.034 for a triangular indenter) and S is the unloading stiffness at maximum load. E and ν are the modulus and the Poisson ratio; and the subscripts, i and s , refer to the diamond indenter and the specimen, respectively.

The scratch test involved moving the sample while being contact with the indenter tip. The tangential force option of the indenter was employed to measure continuously the indenter depth and the tangential force corresponding to a fixed normal force. A constant normal force, $W = 2.5\text{mN}$ was applied and the tangential (or friction) force, F , was recorded. The tangential force-displacement data were obtained at an interval of approximately 20nm, and the data were analyzed to plot the scratch depth versus scratch length and the coefficient of friction versus scratch length profiles. The coefficient of friction was calculated, $\mu = F/W$.

Specific Heat Capacity Jump Measurements

The effective thickness of interphase was also estimated from the consideration of differential heat capacity jump between the fibre-reinforced and unfilled reins in the glass transition region [10]. This method is based on the principle in that as the reinforcement content or fibre volume fraction

is increased, the jump in heat capacity, ΔC , in the glass transition region of resin is reduced. The volume fraction of this modified material (i.e. interphase), λ , is given as:

$$\lambda = 1 - \frac{\Delta C_f}{\Delta C_o} \quad (2)$$

where ΔC_f and ΔC_o are the specific heat capacity jumps for the fibre reinforced composite and neat resin, respectively. The volume fraction ratio of interphase and fibre can be related to the effective thickness of interphase, t , and λ by:

$$\frac{(t+r)^2 - r^2}{r^2} = \frac{(1-V_f)\lambda}{V_f} \quad (3)$$

where r and V_f are the fibre radius and fibre volume fraction, respectively. Rearrangement of equation (3) allows calculation of the effective thickness, t .

RESULTS AND DISCUSSION

Nanoindentation and Nanoscratch Test

Typical load-displacement curves of indentations made on the polished cross-section of specimen are shown in Fig. 1. The elastic modulus measured for a composite containing a silane agent is plotted along the matrix-interphase-fibre in Fig. 2. A transition region is observed between the fibre and matrix, which had indentation properties and load-displacement curves intermediate between fibre and matrix. The transition region can be regarded as the interphase, which was approximately $1\mu\text{m}$ for all specimens tested. It appears that the nano-indentation test was not sensitive enough to distinguish different surface treatments because of the limited spatial resolution of the technique and the finite distance between the adjacent indents.

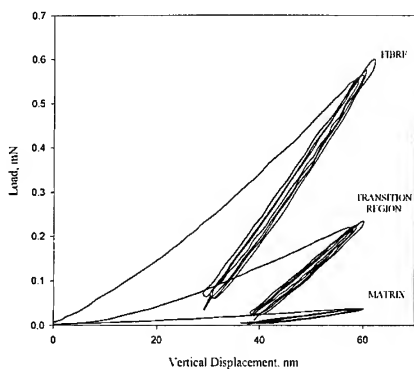


Fig. 1 Typical indentation load-displacement curves for fibre, matrix and the transition region.

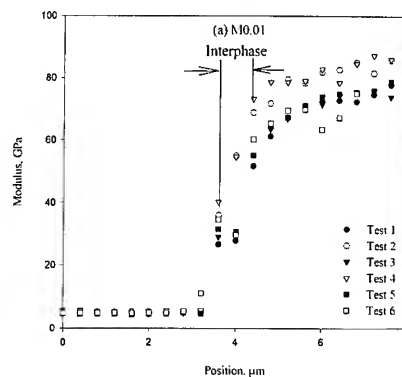


Fig. 2 Variation of elastic modulus across the matrix-interphase-fibre for composites with M0.01 silane treatment.

Fig. 3 presents typical coefficient of friction and scratch depth profiles. The vinylester matrix resulted in a higher coefficient of friction and a higher scratch depth than the fibre. Again, there was a transition region between the matrix and fibre, represented by the distance between Points A and B in Fig 3. These points are defined as the intersections of horizontal depth profiles with the two slant lines **a** and **b**, respectively. The thickness of the transition region estimated thereby was 3~4 μm , which is considered to be much larger than that obtained from the nano-indentation test, because it comprises not only the genuine interphase thickness, but also the region created by the finite width of the indenter tip. To separate the effect of indenter tip geometry, the interactions taking place between the indenter tip and the three composite components during the scratch process were carefully examined and divided into four stages.

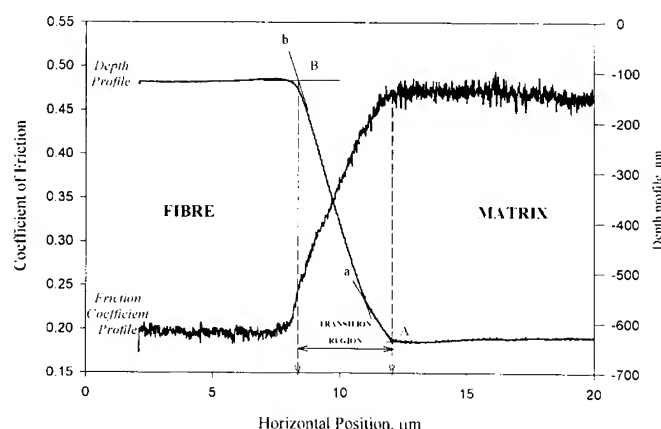


Fig. 3 Coefficient of friction and scratch depth profiles.

Fig. 4 illustrates the positions of the tip relative to the composite components at different stages. In Stage I, the scratch tip enters the matrix material and moves toward the interphase, and the depth profile remains constant. In Stage II, the scratch tip enters the interphase region with the scratch depth decreasing due to the slightly higher stiffness of the interphase than the matrix material. In Stage III, as the scratch tip enters the fibre, there is a sudden decrease in scratch depth because of the large change in stiffness. The large change in stiffness between the interphase and fibre is clearly manifested by the two distinct slopes of scratch depth profile, **a** and **b**, as shown in Fig. 3. In stage IV, the scratch depth profile becomes flattened as the whole tip moves into the fibre. The effective thickness of interphase was estimated taking into account the scratch tip geometry and the results are shown in Fig. 5. It varied between 0.8 μm and 1.5 μm depending on the type and concentration of silane agent. Of note is that the interphase thickness increased with increasing the methacryl silane concentration.

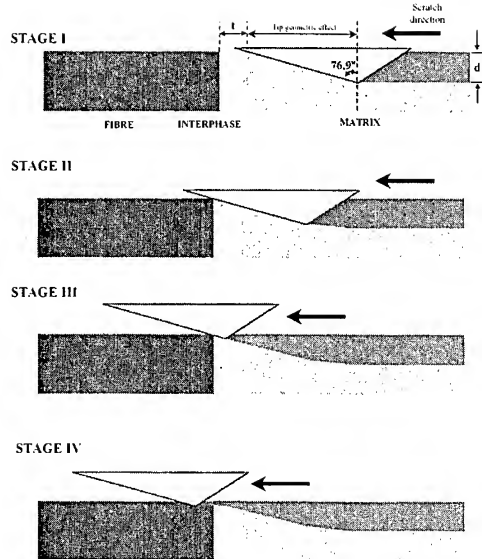


Fig. 4. Schematic illustrations of nanoscratch depth profiles at different stages.

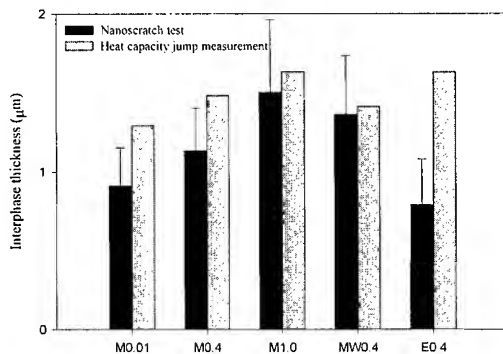


Fig. 5. Variations of effective interphase thickness with silane concentration determined from nanoscratch and heat capacity jump measurement.

Heat Capacity Jump Measurements

Typical specific heat capacity-temperature curves for the unfilled and reinforced vinylester matrix are showed in Fig. 6. The extent of heat capacity jump in the unfilled resin was much larger than those of fibre composites, which is clearly associated with the presence of inactive fibres as well as bound matrix material surrounding the fibre. The effective thicknesses of bound matrix material, i.e. interphase, is calculated and is presented in Fig. 5 for different silane treatments. It is interesting to note that the influence of fibre surface treatment on interphase thickness is consistent with the results from the nanoscratch test in both the qualitative and quantitative terms. The general trend was very similar between the two techniques, with the interphase thickness increasing with increasing the silane concentration. There is an exception, however, that for the composite

with epoxy silane treatment the heat capacity measurement gave much larger interphase thickness than the nano-scratch test. This observation suggests that the former method was more sensitive to a small change in chemical structure within the interphase region than the nanoscratch test.

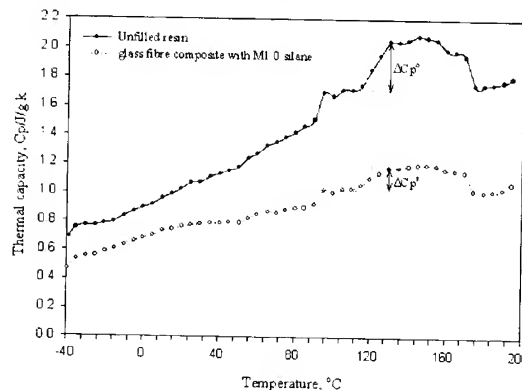


Fig. 6. Typical specific heat capacity curves at glass transition region of unfilled and fibre reinforced vinyl ester matrix.

CONCLUSION

Novel experimental techniques, including the nanoindentation and nanoscratch test and the heat capacity jump measurement, were successfully employed to in-situ measure the effective thickness of interphase region in glass fibre reinforced vinyl ester matrix composites. The following conclusions can be highlighted.

- i) The nanoindentation test gave the interphase thickness approximately $1\mu\text{m}$, although being unable to distinguish different silane agents applied.
- ii) The effective interphase thickness measured from the nanoscratch test and the heat capacity principle agree well in both the qualitative and quantitative terms.
- iii) The effective interphase thickness increased with increasing silane concentration, which is consistent with general perception. This observation supports the usefulness of the experimental techniques used in this study.

REFERENCES

1. J.K. Kim & Y.W. Mai, "Engineered Interfaces in Fiber Reinforced Composites" Elsevier Science, Oxford (1998).
2. F.R. Jones, *Key Eng. Mater.* **116-117** (1996) 41-60.
3. H.C. Tsai, A.M. Arocho & L.W. Gause, *Mater. Sci. Eng.* **A126** (1990) 295-304.
4. J.G. Williams, M.E. Donnellan, M.R. James & W.L. Morris, *Mater. Sci. Eng.* **A126** (1990) 305-312.
5. P.S. Chua, S.R. Dai & M.R. Piggott, *J. Mater. Sci.*, **27** (1992) 913-918.
6. K. Mai, E. Meader and M. Muhle, *Composites Part A*, **29A** (1998) 1111-1119.
7. Y. Hirai, H. Hamada & J.K. Kim, *Compos. Sci. Technol.*, **58** (1998) 91-104.
8. M.L. Sham, J.K. Kim & J.S. Wu, *Polym. Polym. Composites* **5** (1997) 165-175.
9. W.C. Oliver, G.M. Pharr, *J. Mater. Res.* **7** (1992) 1564-1583.
10. G.C. Papanicolaou, G.J. Messinis & S.S. Katakatsanidis, *J. Mater. Sci.* **24** (1989) 395-401.

ROLES OF CHEMICALLY MODIFIED CARBON BLACK SURFACES TO ENHANCE INTERFACIAL ADHESION BETWEEN CARBON BLACK AND ELASTOMER

Jeong-Soon Kim¹, Soo-Jin Park¹ and Jae-Rock Lee¹

¹*Advanced Materials Division, Korea Research Institute of Chemical Technology,
P.O. Box 107, Yusong, Taejeon 305-600, Korea: psjin@pado.kRICT.re.kr*

SUMMARY: Effect of chemical treatments, based on polar acidic and basic, and nonpolar oxidations, on the virgin carbon blacks had been studied in context of surface energetics and mechanical property studies. The surface energetics and mechanical properties of carbon blacks were measured using contact angle and adhesion-tearing energy, respectively. In this work, it was acidic and basic surface treatments led to an evolution of surface characteristics of the carbon blacks, resulting in improving the mechanical properties of carbon black/rubber composites. Particularly, it was found that the London dispersive component of the surface free energy derived from contact angle measurements was greatly correlated with the tearing energy of the composites.

KEYWORDS: chemical surface treatment, carbon black, surface properties, surface free energy, mechanical properties.

INTRODUCTION

Carbon blacks are the most widely used reinforcing fillers since they provide excellent reinforcement of general-purpose rubber at a relatively low cost. The macroscopic mechanical properties of the elastomer composites depend strongly on the characteristics of the intermolecular interaction between fillers and elastomer matrix. As a result of a vast amount of research, it is recognized that the size of primary particles, aggregate size distribution and surface activity of carbon black are the major governing parameters for the reinforcing ability in elastomer.

While, it is noted that good mechanical properties and long durability of the composites depend greatly on the reinforcing agent-rubber matrix interfacial adhesion, since the stress transferred from the matrix to the reinforcing agent would require strong adhesion at the interfaces of the constitutive elements rather than a high cohesive density. In addition, the degree of adhesion at interfaces of a solid depends on the surface energy, active functional groups, energetically different crystallite faces, and so on (1).

Among the methods very much in use to modify the surface characteristics of fillers, the grafting of functional molecules or polymers has largely a place of choice. Recently, Manna *et al.* (2) have shown that the modification of the surface of fillers by coupling agents results in an improvement of the filler/matrix interactions. Wu (3) reported that surface free energies

of semicrystalline solid were strongly related their crystalline structure. His data suggested that the transcrystallized polymer surfaces might have very high surface free energies due to increase of surface cohesive density.

In this work, the effect of polar acidic and basic, and nonpolar organic chemical surface oxidations on carbon blacks has been evaluated. Among them, the changes in surface properties, including surface energetics have been also investigated together with the mechanical tearing results obtained from the rubber compound composites.

EXPERIMENTAL

Materials and Sample Preparation

Virginal carbon blacks denoted in VCB (N220) was supplied by Korea Carbon Black Co. of Korea. The samples denoted in ACB, BCB, and NCB were prepared with 0.1 N H_3PO_4 , 0.1 N KOH, and C_6H_6 for the impregnation of functional groups on the carbon blacks, respectively. Prior to use following analysis, the residual chemicals used were removed by Soxhlet extraction by boiling with acetone at 80 °C for 2 h. Finally, the carbon blacks were washed several times with distilled water and dried in a vacuum oven at 90 °C for 12 h.

Compounding formulations are reported in Table 1. For the measurement of mechanical properties of filled vulcanizates, the compounds were cured under pressure at 160 °C for 60 min.

Surface Properties

Specific surface areas of the sample were determined by N_2 gas adsorption at 77 K with an automated adsorption apparatus (Micrometrics, ASAP 2400). Prior to each analysis, samples were outgassed at 298 K for 6 h to obtain a residual pressure of less than 10^{-3} torr.

Infrared spectra of the casting sample were measured with a FT-IR spectroscopy (Digital FRS-80, Bio-Rad). Scans were from 400 to 4000 cm^{-1} and required 40 s to be completed.

Surface Free Energy Measurement

Contact angles were measured using the sessile drop method on a Rame-Hart goniometer. About 5 μ l of wetting liquids on the specimen made from carbon composite support was used for each measurement at 20 °C. Reading within 5 s of drop formation was taken for the critical surface tension. And more than ten drops were tested for each of the carbon black surfaces studied. For this work, surface free energy (or surface tension) and London dispersive and

Table 1. Compounding formulations

Ingredients	Loading [phr]
Butadiene rubber ^a	100
Carbon black ^b	40
Zinc oxide	5
Stearic acid	2
Antidegradants ^c	1
Accelerators ^d	1
Sulfur ^e	2

a: KNB-35L (Kumho Petrochem.Co.of Korea)

b: N 220 (Korea Carbon black)

c: 2,2,4-trimethyl-1,2-dihydroquinone, Kumho Monsanto Co. of Korea)

d: N-oxydiethylene-2-benzothiazole sulfenamide, Kumho Monsanto Co. of Korea)

e: Midas 101 (Miwon Co. of Korea)

Table 2. Surface free energy characteristics of the testing liquids, measured at 20 °C

	γ_L^L [mJ/m ²]	γ_L^{SP} [mJ/m ²]	γ_L [mJ/m ²]
Water	21.8	51.0	72.8
Diiodomethane	50.42	0.38	50.8
Ethylene glycol	31.0	16.7	47.7
Glycerol	33.9	29.8	63.7

specific (or polar) components for the wetting liquids are shown in Table 2.

Mechanical Tearing Tests

Tearing energy (G_{MC}) which is one of the critical strain energy release rate (G_c) was characterized by split cantilever beam (SCB) tests for mechanical behaviors of rubber compound composites. Rectangular specimens with dimensions of about 100 mm long, 5 mm wide, and 5 mm thick were cut from a sheet that was manufactured by a two-roll mill technique. All tests were conducted at a crosshead displacement rate of 1 mm/min. For this geometry, the tearing energy G_{MC} is given by;

$$G_{MC} = \frac{2\lambda_s^2 F}{t} \quad (1)$$

where F is applied force, t width of the torn path and λ_s the linear swelling ratio.

RESULTS AND DISCUSSION

Fig. 1 shows the infrared spectra of the studied of carbon blacks at various angles of incidence. As the results of the absorption bands at 2923 cm⁻¹ and 3430 cm⁻¹ are, respectively, assigned to the C-H and C-OH stretching modes, these seem that the intensity of the asymmetric carboxylate-stretching region increases with an increase in acidic or basic surface treatment of carbon black. As a result of ACB, the absorption bands in the 1636 cm⁻¹ is probably associated with ring or double bond vibrations system. It is most due to a presence of conjugated double bonds of aromatic ring bands and double bond (C=C) vibrations with the

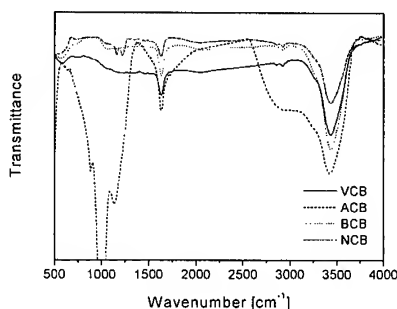


Fig. 1. FT-IR of the virgin and treated carbon blacks studied.

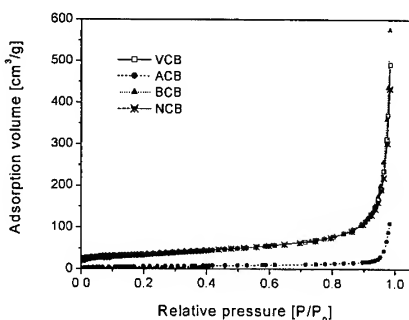


Fig. 2 Dependence of the relative pressure on the volume of N₂ adsorbed at 77K of the carbon blacks studied.

Table 3. Results of specific area values of virgin and treated carbon blacks

	S_{BET} [m ² /g]
VCB	112
ACB	18
BCB	118
NCB	114

is similar to that of carbon black untreated, resulting in no significant change in surface and adsorption properties. As the results of Table 3, the specific surface area of the ACB shows an immense decrease as compared with VCB. This result indicates that the strong acid-base reaction between basic carbon black and acidic chemical solution makes increases of micropore blockage of carbon blacks.

In order to obtain more detailed information about the physical properties of carbon black surfaces before and after chemical treatments, an analysis of the surface free energy is evaluated in the physical energetic studies divided by two components. The London dispersive, γ_s^L , and specific (or polar) components, γ_s^{SP} , of surface free energy of carbon blacks studied (subscript, S) are determined by measuring the contact angle of a variety of testing liquids (L) having known their London dispersive and specific components of surface free energy, as seen in Table 2.

For the interface between two polar liquids Owens (4) and Kaelble (5) expanded Fowkes formula (6) to obtain the following equation.

$$\gamma_{12} = \gamma_1 + \gamma_2 - 2\sqrt{\gamma_1^L \gamma_2^L} - 2\sqrt{\gamma_1^{SP} \gamma_2^{SP}} \quad (2)$$

Substituting Young's Equation and dividing by $\sqrt{\gamma_L^L}$, we get the following;

$$\frac{\gamma_L(1 + \cos\theta)}{2\sqrt{\gamma_L^L}} = \sqrt{\gamma_s^L} + \sqrt{\gamma_s^{SP}} \frac{\sqrt{\gamma_L^{SP}}}{\sqrt{\gamma_L^L}} \quad (3)$$

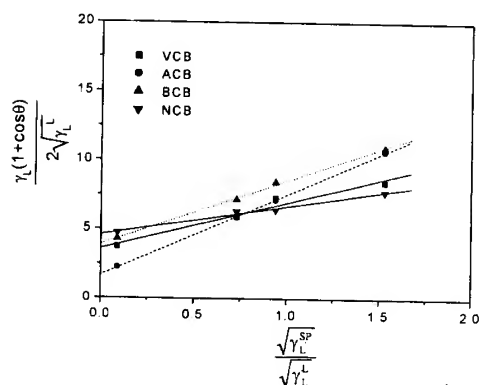


Fig. 3 Relationships between $\gamma_L(1 + \cos\theta)/\sqrt{\gamma_L^L}$ and $\sqrt{\gamma_L^{SP}}/\sqrt{\gamma_L^L}$ for the virgin and treated carbon blacks.

bands of C=O moieties. It is then noted that the C=C vibration increase in acidity is due to the $-\text{COOH}^+$ functionality, formed during the surface treatments, resulting in substantiating our spectral interpretation. Fig. 2 shows the adsorption isotherms of carbon black before and after chemical treatments. The adsorption isotherms on the carbon blacks studied are of type according to the BET classification. As a result, it can be seen that the adsorption behavior of carbon black treated by basic (BCB) and nonpolar (NCB) solution

In Fig. 3, this equation allows us that the linear relationship between $\gamma_L(1 + \cos\theta)/\sqrt{\gamma_L^L}$ and $\sqrt{\gamma_L^{SP}}/\sqrt{\gamma_L^L}$ is valid, when the contact angle (θ) is measured for various liquids having different values of γ_L , γ_L^L , and γ_L^{SP} . As shown in Fig. 4, London dispersive and specific components of surface free energies (or surface tensions) for the carbon blacks calculated by these procedures are illustrated. As the results, both acid and basic treatments on carbon blacks give maximum surface free energies, which are mainly due to their higher specific component (γ_s^{SP}). These specific

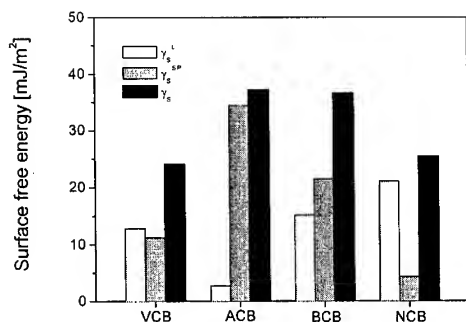


Fig.4 Results of surface free energy and their components of the virgin and treated carbon black specimens.

component increases of surface free energy can be attributed to the polar acidic and basic surface oxide groups on carbon blacks after acidic and basic chemical treatments, respectively. And particularly, the case of the polar basic (BCB) and nonpolar organic (NCB) treatments on the carbon blacks greatly appear to increase the London dispersive component in which slightly changes of surface functional groups, as listed in Table. 3.

The mechanical tearing test of rubber filled with carbon blacks is examined to obtain information about the consequence of the surface-modified carbon blacks on its reinforcing ability. In Fig. 5, the results of tearing energies measured in split cantilever beam (SCB) tests are shown. These results indicate that the tearing energies of the rubber compounds made of carbon blacks basic-treated (BCB) and nonpolar-treated (NCB) are higher than those of rubber compounds made of ACB, or even VCB. It is then found that the London dispersive component of the surface free energy of carbon blacks studied only leads to a good correlation with the G_c of rubber compound composites with a constant regression of coefficient ($R=0.9879$), as seen in Fig. 5. So, it is then recognized that increasing of γ_s^L of carbon blacks makes an important role in improving the degree of adhesion at interface between carbon black and hydrocarbon-based rubber matrix.

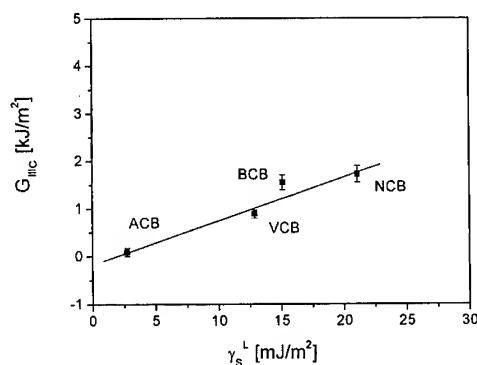


Fig. 5 Dependence of the tearing energy on the London dispersive component of surface free energy, γ_s^L of the virgin and treated carbon blacks studied.

CONCLUSION

It is observed that the chemical surface treatments (H_3PO_4 , KOH , and C_6H_6) on virgin carbon blacks lead to a change of the surface properties, including surface functionalities and surface free energy (γ_s^L) using FT-IR and contact angle measurements, respectively.

As experimental results, it is found that the developments of surface functional groups on acidic-treated carbon blacks derived from FT-IR analysis are largely related to the specific component of surface free energy determined from contact angle measurements. While, the specific surface areas obtained from BET adsorption studies are greatly correlated with the results of London dispersive component of surface free energy of carbon blacks. However, a significant advantage of compounding composites is gained by polar or nonpolar chemical treatment, resulting in improving the mechanical tearing energy.

This is a consequence of the increasing of London dispersive component of surface free energy of the carbon blacks studied in this work. Therefore, it is then concluded that the London dispersion component or specific surface area of carbon blacks makes an important role in an organic elastomer-based compounding composite system.

REFERENCES

1. S. J. Park, "Interfacial Forces and Field: Theory and Applications", (Ed. by J. P. Hsu), Marcel Dekker, New York, 1999, p.385.
2. K. Manna, A. K. Bhattacharyya, P. P. De, D. K. Tripathy, S. K. De, and D. G. Peiffer, *J. Appl. Polym. Sci.*, Vol.71, 1999, p.557.
3. S. Wu, *J. Polym. Sci., Part C*, Vol.34, 1971, p.19.
4. D. K. Owens and R. C. Wendt, *J. Appl. Polym. Sci.*, Vol.13, 1969, p.1741.
5. D. H. Kaelble and K. C. Uy, *J. Adhesion*, Vol.2, 1970, p.50.
6. F. M. Fowkes, *Ind. Eng. Chem.*, Vol.56, 1964, p.40.

MICROANALYSIS OF THE INTERFACE IN GLASS FIBRE – POLYMER MATRIX SYSTEMS

Z. H. Stachurski¹, A. Hodzic¹, and J. K. Kim²

¹*Department of Engineering, Faculty of Engineering and Information Technology,
The Australian National University, ACT 0200 Canberra, Australia.
zbigniew.stachurski@anu.edu.au*

²*Department of Mechanical Engineering, Hong Kong University of Science and Technology
Clear Water Bay, Kowloon, Hong Kong mejkkin@ust.hk*

SUMMARY: The properties of fibre-reinforced composite materials depend to a large extent on the nature of the interaction between the matrix and the fibre surface. We describe two techniques which are advantageous for characterisation of the interphase: (i) microdroplet test, and (ii) nanoindentation technique. A theoretical solution is derived for the shape of the droplet as a function of interfacial energy and it is compared with experimental data with good agreement. The use of the nano-scratch technique gives very detailed information about the width of the transition region and that of the true interphase region. Water ageing treatment and acetone washing of fibres has measurable effect on strength of adhesions and ultimate material properties.

KEY WORDS: nanoindentation, hardness, interphase width, droplet geometry, water aging

INTRODUCTION

The contact of a polymer melt with a solid surface (i.e. glass) results in the formation of a “gradient” interphase of finite width [1]. The presence of a coupling agent at the interface adds to the complexity and width of the interphase [2-4]. In addition to that, ingress of water or other solvents will extend the interphase layer even more.

In composite materials the loads are transferred from fibres to matrix through the fibre/matrix interface. Any understanding of toughness in composite materials is based on understanding of energy dissipation around a crack tip. As failure requires the separation of molecules, the fundamental failure process must occur in molecular scale regions of the order of nanometres, or more in the case of extended interphases. Micromechanical techniques prove useful for determination of the interfacial shear strength, although large discrepancies are reported, due to the fact that experimental (macroscopic) work of adhesion, W_E , is always greater than the theoretical work of adhesion, W_A , and because of inadequate characterisation of the interface [4-6].

In this paper we present theoretical analysis and experimental results on glass fibre – polymer resin interfaces, revealing more details about its behaviour and properties.

NANOINDENTATION AND NANOSCRATCH TECHNIQUE

Materials

Three composite matrix/fibre systems were investigated:

- (i) phenolic resin Resinox CL1916 mixed with 7 wt% AH1964F hardener,
- (ii) phenolic resin Resinox CL1880 mixed with 7 wt% H1196 hardener; and
- (iii) polyester resin Synolite 0288-T-1 mixed with 2.4 wt% methyl ethyl ketone peroxide as a catalyst.

The fibres were unidirectional 450 g/m² E-type glass, 20 µm in diameter. The panels were made and supplied by the Aeronautical and Maritime Research Laboratory (AMRL) in Melbourne.

Nano-Indentation Test

The apparatus used in this work was Nano Indenter II made by Nano Instruments, Inc. A detailed description of the instrument is available elsewhere [7]. A sample prepared for testing is mounted in the sample holder and positioned by the motorised precision table, visually controlled through the optical microscope. The Berkovich indenter is a three-sided triangular-based pyramidal diamond. Depths of indents were programmed to have a constant value of 30 nm. The indents were 210 nm wide. Each successive indent was displaced by 260 nm in order to avoid overlapping of plastic deformation zone onto neighbouring indents. The indents were made along a path of approximately 7 µm in the matrix and 7 µm in the fibre. Hardness of the material is calculated from the Eqn 1:

$$H = \frac{P}{24.5 h_c^2} \quad (1)$$

where: P is the load and h_c is the contact depth of the indent. Hardness values for polyester/glass systems are shown in Fig. 1. The hardness values range from approximately 9 GPa for the glass to less than 1 GPa in the matrix. The observed transition region between the matrix and the fibre has a similar character for the polyester and the phenolic systems [8]. This region shows material properties distinct from those of the matrix and the fibre. The width of the transition zone as revealed by this method is given in Table 1.

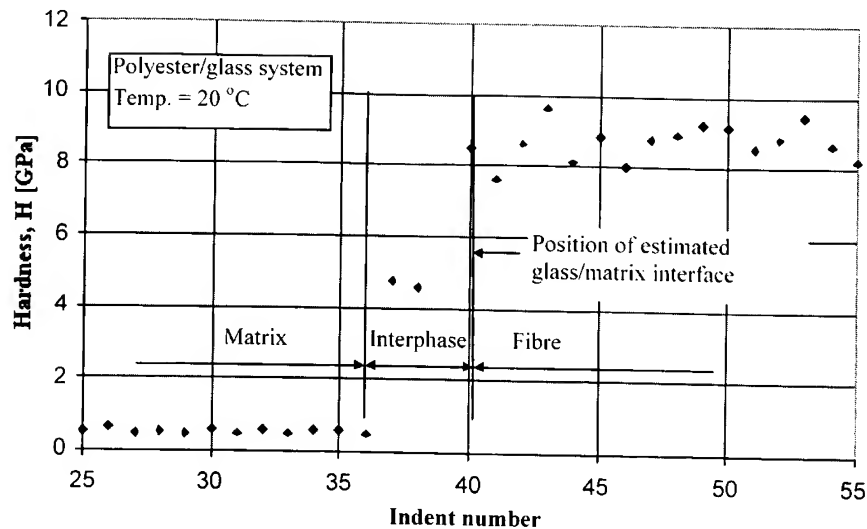


Fig. 1 Hardness measured by nano-indenter across the matrix/fibre interface.

Nanoscratch Test

The nano-scratch test involves moving a sample while being in contact with the diamond tip. The indenter tip is replaced by the scratch tip with the same geometry but oriented with the sharp edge into the direction of motion. The indenter scratches the surface of the sample in a straight line, traversing areas of matrix and fibre. The normal force is maintained at a constant value and the lateral force is measured from the deflection of the shaft and the lateral displacement. The ratio of these two forces is the coefficient of friction between the material of the indenter and that of the scratched material. The coefficient of friction indicates the resistance of the material to the tip penetration in the tangential direction. The depth of the indenter is also recorded, thus indicating the hardness of the surface being scratched. The profile depth is the penetrating depth of the tip in the material, influenced by the hardness of the scratched material. The method of determination of the width of the transition zone is shown in Fig.2, from which the interphase width is derived [8]. Aging in water has the effect of increasing the width of the interphase, as measured by the nano techniques in Table 1. The results show that 10 weeks aging has the effect of doubling the width (see Table 1).

Table 1. Width of interphase in polyester/glass system by nano-techniques

The Polyester/glass interphase width [μm] as measured by:	Dry conditions	Ten weeks in water
Nano-indentation test	0.78	1.3
Nano-scratch test $F_N=0.4$ mN	2	4.1
Nano-scratch test $F_N=1$ mN	2.1	5.1

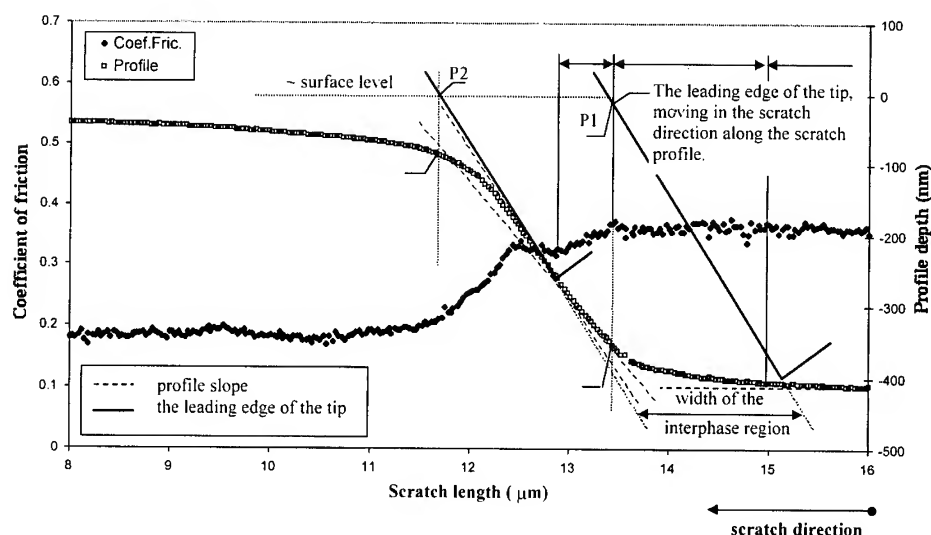


Fig. 2 Recording from a scratch test, showing friction and penetration into matrix and fibre. In this case the fibre is on the left-hand side with lower coefficient of friction. The position of the indenter, drawn to scale is indicated at P1 and P2.

PROPERTIES AND BEHAVIOUR OF MICRODROPLETS

Equilibrium Droplet Geometry

Consider a droplet of liquid formed on a solid fibre of radius, r . We assume that in an initial stage the droplet assumes a shape of perfect sphere of radius, R_0 . However, the presence of surface forces between the liquid and the fibre will spontaneously extend the droplet along the fibre. The final shape of the droplet will be determined by the principle of conservation of work and energy. We express the principle as follows:

$$W_d = \Delta E_s + \Delta E_p \quad (2)$$

where: W_d is the work done by the γ_{mf} surface forces to extend the droplet from its initial diameter, $2R_0$, to the extended length, L . ΔE_s is the energy stored in the form of surface energy due to an increase in the surface area of the droplet, and ΔE_p is the stored elastic energy due to increased pressure resulting from reduced radius of the droplet on extension. Thus:

$$W_d = \int_0^{2\pi r l} dF = (L - 2R_0)\pi r \gamma_{mf} \quad (3)$$

$$\Delta E_s = \gamma_m \Delta A_d \quad (4)$$

$$\Delta E_p = 2\gamma_m^2 \frac{V_d}{K} \left(\frac{1}{R^2} - \frac{1}{R_0^2} \right) \quad (5)$$

In Eqn 5 K is the bulk modulus of elasticity of the liquid. Substitution of Eqns 3-5 into Eqn 2, and solving for R , one obtains [9]:

$$R = \frac{1}{D} \left(\frac{r \gamma_{mf}}{2 \gamma_m} (A - E) - \frac{2 \gamma_m}{3 K} (E^3 - E) \right) \quad (6)$$

where: A , D and E are trigonometric functions. The radius of the fibre is of the order of 10^{-6} , the surface energies are of the order of 10^{-3} , whereas bulk modulus of liquids is of the order of 10^9 . Therefore, the second term on the right hand side in Eqn 6 is several orders of magnitude smaller than the first term, and can be neglected. The variation of R with conus angle ($= 2\phi$) and b , for a fixed value of $(\gamma_{mf}/\gamma_m) = 1.2$, is shown in a separate publication [9]. Here, a comparison of experimental results with the theoretical relationship is shown here in Fig. 3.

CONCLUSIONS

Aging has the effect of increasing the thickness of the interphase, contrary to the suggestion by some authors [10, 11]. In the case of polyester/glass system the result is a stronger bonding as measured by increased dF/dL in Fig. 4. However in the case of phenolic/glass system it has deleterious effect, as will be described in the presentation. The nano-indentation test detected degradation of the material properties and the extension of this region deeper into the matrix. The nano-indentation and nano-scratch techniques can be usefully employed to characterise the fibre/matrix interface. The micro-droplet results show that surface tension is not altered significantly by acetone washing or water aging. However the slope of force against length (Fig 4) does change with treatment, which means the mechanism of fracture is altered in conjunction with the increased width of the interphase.

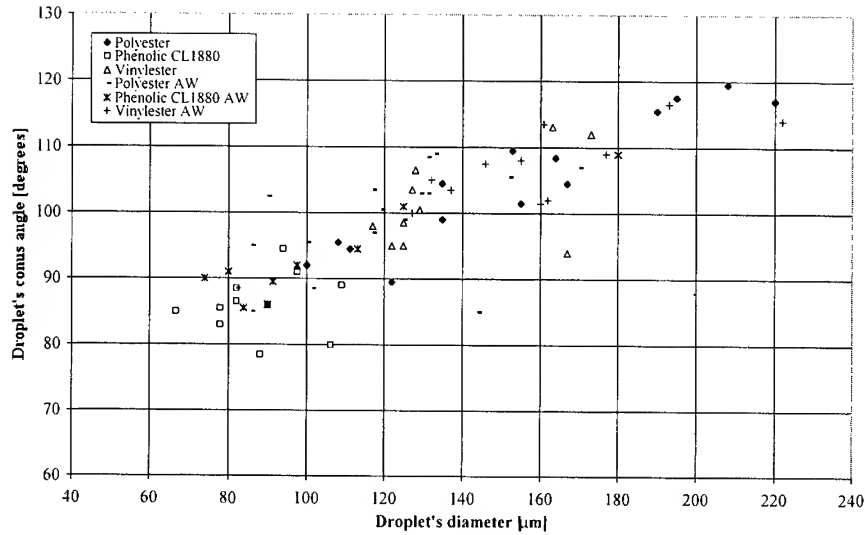


Fig. 3 A comparison of theoretical and experimental micro-droplet geometry in terms of resin and fibre properties (solid curve according to Eqn 6).

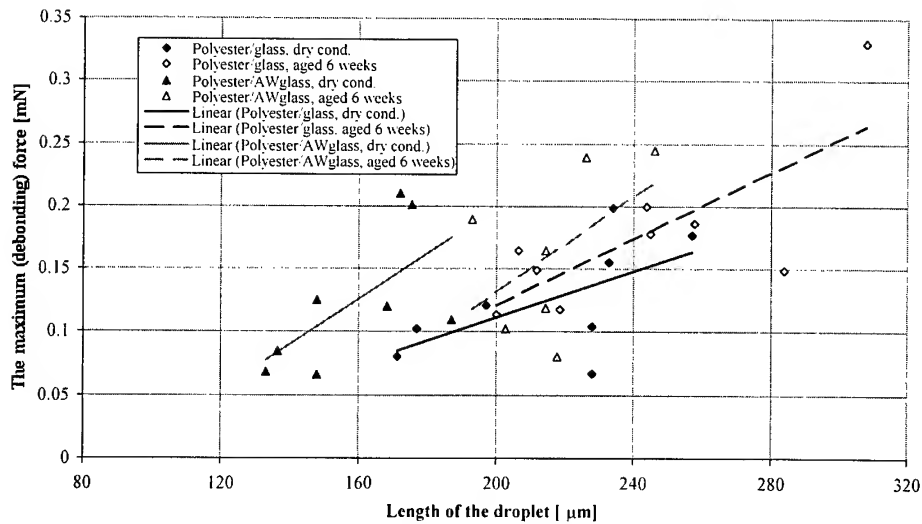


Fig. 4 The strength of the bond between micro-droplet and fibre for the epoxy/glass system, showing dependence on aging in water and acetone washing of fibres (AW).

REFERENCES

1. J. Baschnagel and K. Binder, "Interfacial properties of glassy polymer melts: a Monte-Carlo study", *Macromol. Symp.*, Vol.106, 1996, p.41.
2. L.T. Drzal, *SAMPE*, Vol. 19, 1983, p.7.
3. J.-F. Gerard and B. Chabert, "Introduction of tailored interphases in composite materials based on thermoset or on a semi-crystalline polymer matrix", *Macromol. Symp.*, Vol.108, 1996, p.137.
4. J.K. Kim and Y.W. Mai, "Engineered Interfaces in Fibre Reinforced Composites", Elsevier Science, New York, 1998.
5. E. Pisanova, V. Dutschk and B. Lauke, "Work of adhesion and local bond strength in glass fibre-thermoplastic polymer systems", *J. Adhesion Sci. Technol.*, Vol.12, 1998, p.305.
6. E.H. Andrews and A.J. Kinloch, *Proc. Roy. Soc.*, Vol. A332, 1973, p.385.
7. Bharat Bhushan, *Handbook of Micro/Nanotribology*, CRC Press, 1995.
8. A.Hodzic, J.K. Kim and Z.H. Stachurski, "Nano-indentation and nano-scratch of polymer – glass interfaces. Part I: Experimental and mechanical analysis", accepted for publication in *Polymer*.
9. A.Hodzic and Z.H. Stachurski, "Equilibrium shape of polymer micro-droplets on fibres", submitted for publication to *J. Coll. Interf. Sci.*
10. D.C. Phillips, T.M. Scott and N. Buckley, *Proc. 2nd Int. Conf. on Composite Materials*, Eds. B.N. Signorelli, K. Street and L. Phillips, AIME, New York, 1978, p.1544.
11. M.R. Piggott, "Why interface testing by a single-fibre methods can be misleading", *Comp. Sci. and Technol.*, Vol.57, 1997, p.965.

EFFECT OF SIZING AGENT ON GLASS FIBER/POLYMER MATRIX INTERFACIAL ADHESION OF COMPOSITES

Taek-Jin Kim¹, Soo-Jin Park¹ and Jae-Rock Lee¹

¹*Advanced Materials Division, Korea Research Institute of Chemical Technology
P.O. Box 107, Yusong, Taejeon 305-600, Korea: psjin@pado.krict.re.kr*

SUMMARY: Various surface treatments of glass fibers have been applied to promote the degree of interfacial adhesion between inorganic fibers and organic resins in glass fiber-reinforced plastics (GFRP). In this work, the effect of sizing agent on the final mechanical interfacial properties of GFRP was investigated by contact angle measurements at room temperature. For a series of sizing agents consisting of various film-forming resins, surface free energy and mechanical interfacial properties of GFRP were measured using tensiometer and short-beam flexural test, respectively. As a result, it was found that the sizing treatment strongly affected the surface free energy of the fibers, and consequently the fiber/matrix interfacial adhesion, resulting in improving final mechanical interfacial properties of the composites.

KEYWORDS: sizing, fiber/matrix adhesion, contact angle, surface free energy, interlaminar shear strength, fracture toughness.

INTRODUCTION

Glass fiber-reinforced plastics (GFRP) have been widely used in many applications due to their relatively good price/performance ratio and easy processability [1,2]. The high performance properties of these composite materials are not the sum of the properties of their components. The interfacial region between the fiber and the matrix is also considered of great importance. It is at the interfacial region where stress concentrations develop because of differences of thermal expansion coefficients between the reinforcement and the matrix-phase, loads applied to the structure and cure shrinkage in thermosetting matrices. The interphase can also serve as a nucleation site, a preferential adsorption site and a locus of chemical reactions. For these reasons, the interphase is considered a major fact affecting mechanical and various physical properties of GFRP [3-5].

During production of glass fibers, the fibers must be protected against fiber fracture and fuzz formation by a coating, which is called the "sizing" [6-7]. It is this sizing that also plays a crucial role in the degree of fiber/matrix adhesion, in optimum matrix/fiber stress transfer and, as a result, in the mechanical properties of GFRP.

In the past, the role of one essential component of the sizing, i.e. the silane coupling agent, received a lot of attention due to the pioneering work of Plueddemann [8]. While, the subject of silane chemistry and its interaction with both the glass surface and the matrix have been

extensively studied [9-12], little fundamental information of a predictive nature attesting to the relationship between sizing application and composite mechanical properties has been published.

In this work, a series of sized glass fibers having different range of surface free energies and solubilities in unsaturated polyester matrix were used for the investigation of interphase formation between glass fiber and matrix. The effects of the different sizings on interphase formation were quantified by measuring the surface free energies of sized glass fibers, the fiber/matrix adhesion and the composite mechanical properties.

EXPERIMENTAL

Materials and Sample Preparation

The glass fabric, HD 324-01 (23×23 count/inch, 246 g/m²) with desized surface by pre-heating was supplied by Hyun-Dai Fiber Co. of Korea. The polyvinyl alcohol (PVA), polyester and epoxy type resins were used as the film-former of a sizing agent. The proportion of components of sizing agent prepared by mixing was listed in Table 1. The glass fabric was dipped in each sizing agent and then dried at 120°C for 1 h to age the sizing agent. The coated glass fabric was allowed to stand still overnight under room temperature. The amount of the sizing composition applied to the glass fabric was about 0.8 wt. %.

Unsaturated polyester (R-235, specific gravity 1.11, viscosity 2.8 poise) matrix was orthophthalic acid type resin, which was supplied by Seiwon Chem. Co. of Korea. Methylethyl ketone peroxide (MEKPO) was selected as a hardener for the curing. The composites of sized glass fibers were prepared in a hot press at 20 atm and 100°C for 1 h with a vacuum bagging method. The fiber volume fraction of bulk specimens was about 52 % (±2 %) for all composites.

Contact Angle Measurements

Contact angle measurements of sized glass fibers were performed using the Krüss Processer Tensiometer K 12 with fiber apparatus. The sized glass fibers of 5 g was packed into an apparatus and then mounted indirectly to the measuring arm of the microbalance. The wetting liquids used for contact angle measurements were n-hexane, deionized water and diiodomethane.

Mechanical Interfacial Properties

Two types of composite mechanical properties were conducted to measure properties which are sensitive to the degree of adhesion of the fiber/matrix interphase. Short-beam shear test (ASTM D2344) were conducted on 20 ply laminates. The support span-to-depth ratio used was 5:1 with a corresponding specimen length to depth ratio of 7:1. The cross-head speed was

Table 1. Components of the sizing agent used in this work

Component	Weight percent
Film-former	5.0
γ-methacryloxy propyl trimethoxy silane	0.5
Glycerin	0.1
Formic acid	0.05
Water	up to 100

2.0 mm/min.

The critical stress intensity factor (K_{IC}) which is one of the fracture toughness parameters may be characterized by the single edge notched (SEN) beam fracture toughness test (ASTM E399) in three-point bending flexure. Notches were cut using a diamond wire saw, approximately half the depth of the specimen. A span-to-depth ratio of 4:1 and cross-head speed of 1mm/min were used.

RESULTS AND DISCUSSION

Contact Angle and Surface Free Energy Analysis

The method for measuring contact angles between a liquid and a fibrous material is a difficult process and complex, although several methods have been proposed to measure their wettability [13-15]. Chwastiak [16] introduced the procedure for wicking rate measurements by enclosing the fiber bundle in a glass tube so that the porosity is fixed for a given strand of fibers. In this work, the wettability of glass fibers determined by measuring the wicking rates either by the mass pickup technique or by the surface velocity method.

Table 2 shows contact angle data of the four glass fiber types. The contact angle in water is decreased in case of polyester and epoxy-sized glass fiber than in unsized fiber, while contact angle in diiodomethane is constant for most of the fibers except for epoxy sizing. As mentioned above, it can be suggested that sizing treatment of glass fiber leads to a change in fiber surface nature such as hydrophobic-hydrophilic properties.

In order to obtain more detailed information about the surface energetics of sized glass fibers, a surface free energy analysis can be evaluated in the surface energetic studies divided by two components i.e. the London dispersive and specific (or polar) components, which is important for evaluating the physical and mechanical properties [17,18].

In the early 1960s, Fowkes [19] introduced the concept of surface free energy, γ , which can be resolved into a London dispersive component (superscript L) and specific (or polar, SP) component:

$$\gamma = \gamma^L + \gamma^{SP} \quad (1)$$

where γ^L describes the London attraction of van der Waals force and γ^{SP} ascribes all other nondispersive component of physical interactions.

Owen and Wendt [20] and Wu [17] extended the Fowkes' concept using geometric mean, as follow:

$$\gamma_L (1 + \cos \theta) = 2(\gamma_L^L \cdot \gamma_S^L)^{1/2} + 2(\gamma_L^{SP} \cdot \gamma_S^{SP})^{1/2} \quad (2)$$

Table 2. Contact angle determination (in degree) on unsized and sized glass fibers

Wetting liquids	Unsized	PVA sized	Polyester sized	Epoxy sized
Water	85	81	70	73
Diiodomethane	61	60	64	54

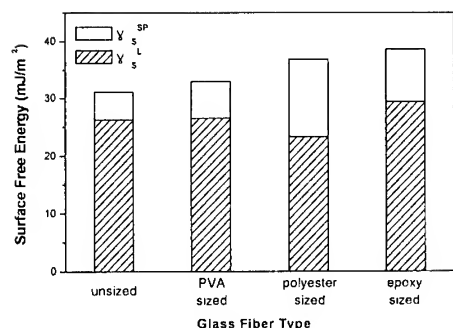


Fig. 1. Evolution of surface free energy of the sized glass fibers calculated from London dispersive/polar components

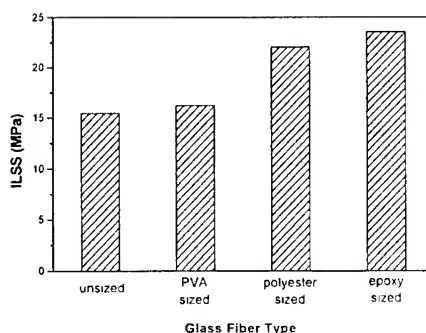


Fig. 2. ILSS of the sized glass fiber/unsaturated polyester composites

where the subscripts L and S represent the liquid and solid states, respectively.

In more practical relationship based on two simultaneous liquids of widely different properties on fiber surfaces, γ_s^L and γ_s^{SP} can be solved according to eq. (2). The results of surface free energies of unsized and sized glass fibers are shown in Fig. 1.

The four glass fiber types provide a range of total surface free energies from 31 to 39 mJ/m². The surface free energies of sized glass fibers increased as compared with the unsized one. The surface free energy of glass fibers is an indicator of thermodynamic wetting [21]. The unsized fibers have a low polar component of surface free energy, resulting in thermodynamically poor wetting. The epoxy sizing has the highest surface free energy (38.6 mJ/m²) of any of the fibers, and is expected to give the most favorable wetting conditions.

From the surface energetic point of view, it can be expected that increase of the surface free energy of fiber would be play an important role in improving the degree of adhesion at interfaces between sized fibers and matrix.

Interlaminar Shear Strength

Generally, the mechanical interfacial properties of GFRP depend strongly on the degree of adhesion between glass fiber and matrix. Interlaminar shear strength (ILSS) of composites was measured to determined the effect of sizings on their adhesion with the matrix. For a rectangular cross-section of the composites, the ILSS determined from three-point bending tests are calculated as follow:

$$ILSS = \frac{3F}{4bd} \quad (3)$$

where F is the rupture force, b the width of the specimen, and d the thickness of the specimen. Fig. 2 shows the ILSS of composites prepared with unsized and sized glass fibers. Base on the results of the surface free energy and ILSS, there is a strong correlation between ILSS and fiber surface free energy, with shear strength tending to be higher for the fibers with higher surface free energy. The polyester and epoxy sizings dissolve into matrix, allowing the silane-covered glass surface to interact or react with the matrix. Interaction between γ -methacryloxy propyl trimethoxy silane of fiber surface and matrix is due to its organic functional group which can react with the double bond of unsaturated polyester [22]. The lower ILSS is the

result of inadequate fiber/matrix interaction. The PVA sizing remained at the fiber/matrix interface and did not form an interphase, hindering stress transfer to the fiber.

Fracture Toughness

Fracture toughness is a critical property to resist crack propagation loaded from matrix to fiber, which ought to be considered in the evaluation of a composite material for a real application. For rectangular cross-section of composites, the fracture toughness of the composites can be measured by three-point bending test for the critical intensity factor (K_{IC}). For the single edge notched (SEN) beam fracture toughness test, the value of K_{IC} is calculated as follows:

$$K_{IC} = \frac{PL}{bd^{3/2}} Y \quad (4)$$

where P is rupture force, L the span between the supports, Y the geometry factor described in ASTM E399, and b and d the specimen width and thickness, respectively.

Fig. 3 shows the evolution of K_{IC} in flexure of the composites with each of the fiber types. As mentioned above, epoxy-sized fiber composites have high resistance for crack propagation due to high level of fiber/matrix adhesion.

A linear correlation between the surface free energies of glass fibers and both ILSS and K_{IC} of composites is shown in Fig. 4. This result indicates that the sizing surface free energy strongly affected the fiber/matrix interphase formation and consequently the fiber/matrix adhesion and composite mechanical interfacial properties.

CONCLUSION

The effect of sizing treatment on the fiber surface properties and interfacial adhesion of composites have been studied in terms of the fiber surface free energy and mechanical interfacial properties. As a result, composites produced with polyester and epoxy sizings developed an interphase which led to high mechanical interfacial properties of composites,

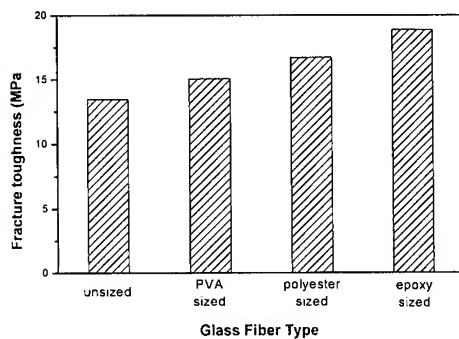


Fig. 3. Fracture toughness of the sized glass fiber/unsaturated polyester composites

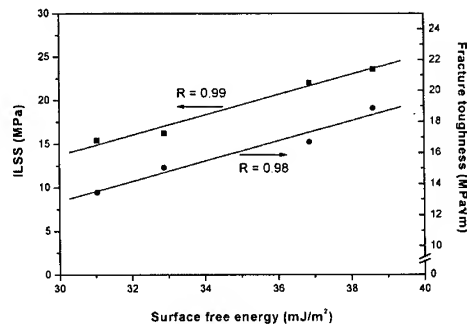


Fig. 4. Dependence of ILSS and fracture toughness on surface free energy of the sized glass fiber/unsaturated composites

while PVA sizing yielded low mechanical interfacial properties. In this work, the surface free energy of sized fibers provided desirable and predictive information on the degree of fiber/matrix interaction in a composite system.

REFERENCES

1. C. E. Knox, "Handbook of Composites", ed. by G. Lubin, van Nostrand Reinhold, New York, 1982.
2. P. K. Mallick, "Fiber-reinforced Composites", Marcel Dekker, New York, 1988.
3. T. Norita, J. Matsui, and H. S. Matsuda, "Composite Interfaces", ed. by H. Ishida and J. L. Koenig, Elsevier, New York, 1986.
4. J. L. Kardos, "Molecular Characterization of Composites Interface" ed. by H. Ishida and G. Kumar, Plenum Press, New York, 1985.
5. S. J. Park, "Interfacial Forces and Fields: Theory and Applications", ed. by J. P. Hsu, Marcel Dekker, New York, 1999.
6. K. L. Loewenstein, "The Manufacturing Technology of Continuous Glass Fibers", Elsevier, Amsterdam, 1983.
7. B. J. R. Scholtens, "The Interactions in Polymeric Composites", Kluwer, Dordrecht, 1993.
8. E. P. Plueddemann, "Silane Coupling Agents", 2nd ed., Plenum Press, New York, 1991.
9. C. H. Chiang and J. L. Koenig, *J. Colloid Interface Sci.*, Vol.83, 1981, p.361.
10. R. T. Graf, J. L. Koenig, and H. Ishida, *Anal. Chem.*, Vol.56, 1984, p.773.
11. E. T. Vandenberg, L. Bertilsson, B. Liedberg, K. Uvdal, R. Erlandsson, H. Elwing, and I. Lundstorm, *J. Colloid Interface Sci.*, Vol.147, 1991, p.103.
12. N. Suzuki and H. Ishida, *Macromol. Symp.*, Vol.108, 1996, p.19.
13. G. E. Hammer and L. T. Drzal, *Appl. Surf. Sci.*, Vol.4, 1980, p.340.
14. S. K. Li, R. P. Smith, and A. W. Neumann, *J. Adhesion*, Vol.17, 1984, p.105.
15. J. B. Donnet, M. Brendle, T. L. Dhami, and O. P. Bahl, *Carbon*, Vol.24, 1986, p.757.
16. S. Chwastiak, *J. Colloid Interface Sci.*, Vol.42, 1973, p.298.
17. S. Wu, "Polymer Interface and Adhesion", Marcel Dekker, New York, 1982.
18. S. J. Park, W. B. Park, and J. R. Lee, *Polymer J.*, Vol.31, 1999, p.28.
19. F. M. Fowkes, *J. Phys. Chem.*, Vol.66, 1962, p.382.
20. D. K. Owens and R. C. Wendt, *J. Appl. Polym. Sci.*, Vol.13, 1969, p.1741.
21. B. K. Larson and L. T. Drzal, *Composites*, Vol.25, 1994, p.711.

Polymer (1)

SILICA NANOPARTICLES FILLED POLYPROPYLENE: BRITTLE-DUCTILE TRANSITION AND DOUBLE PERCOLATION MECHANISM

Minzhi RONG¹, Mingqiu ZHANG², Yongxiang ZHENG¹ and Hanmin ZENG²

¹*Materials Science Institute, Zhongshan University, Guangzhou 510275, P. R. China:
cesrmz@zsulink.zsu.edu.cn*

²*Laboratory of Polymeric Composite and Functional Materials, The Ministry of Education of
China, Zhongshan University, Guangzhou 510275, P. R. China: ceszmq@zsulink.zsu.edu.cn*

SUMMARY: The present study about polypropylene filled with irradiation grafted nanoparticles shows the great effect of grafting surface modification on the fracture behavior of thermoplastic polymer. The mechanism involving double-percolation of stress volumes inside and around the dispersed phases is proposed. The influences of internal structure of agglomerates and their distribution in the matrix, as well as viscoelastic characteristics of interface phase were discussed. A strong interfacial interaction between both particles/matrix and particles/particles can be successively established by grafted polymers, which in turn induced more uniform dispersion of nanoparticles in polymer matrix. The toughness of polypropylene can be significantly improved with the addition of small amount of modified silica nanoparticles (typically less than 3% by volume).

KEYWORDS: silica, nanoparticles, irradiation grafted, nanocomposites, fracture behavior, double percolation.

INTRODUCTION

Incorporation of inorganic particulate fillers has been proved an effective way to improve mechanical properties, in particular, toughness of polymers. However, the typical filler contents needed for such an enhancement of performance are as high as 20% by volume [1, 2]. As a result of high particle loading, the processability of the compounds is inevitably

deteriorated and the weight of the end-products becomes much higher than neat plastics, which limit the applications of the materials in transportation subsegment, electrical and electronic industry, and appliance and equipment industry. The basic advantages of polymers - easy of processing and light weight are lost. Clearly, a composite with improved properties and lower particle concentration is highly desired. With regard to this, the newly developed nanocomposites would be a competitive candidate.

It has been proved that the agglomerate of nanoparticles is hardly to be checked by the limited shear force during mixing procedure and thus prevents a homogeneous dispersion in polymer melts characterized by high viscosity, even though the surface of particles has been modified by the coupling agent [3]. The so-called nanoparticles filled polymers can not exhibit reinforcing effects at lower content of particles, and sometimes provide properties even worse than conventional particle/polymer systems at comparable filler loading [4]. In this paper, a new surface modification, grafting polymerization by irradiation was introduced on the surface of nanoparticles, aiming at dispersion state improving of nanoparticles in thermoplastic polymer composites preparing by simply mechanical compounding. The fracture behavior was used to characterize the effect of surface grafting on the toughness of polypropylene, especially focusing on the interface effect and toughing mechanism.

EXPERIMENTAL DETAILS

Materials

General purpose isotactic PP homopolymer (F401, MI=8.5g/10min and 6.7g/10min) provided by Guangzhou Petroleum Chemical Co. was used as matrix in this test. Pyrogenic colloidal silica (Degussa 'Aerosol' 1380) of primary particle size 7nm was selected as the filler. Various commercial monomers: styrene, methyl methacrylate, butyl acrylate, ethyl acrylate, methyl acrylic acid, and vinyl acetate were used as grafting monomers without further purification.

Pregrafting of Nanoparticles by Irradiation

The nanoparticles was preheated at 120 °C for five hrs before being mixed with monomers to eliminate possible absorbed water on the surface of particles. Then the mixture of particles/monomer (100/20) and certain amount of solvent was irradiated by ^{60}Co γ -ray under atmosphere at a dose rate of 10^6 rad/hr at room temperature. After being exposed to a dose of 10 Mrad, the solvent was recovered and the dried residual powder could be compounded with thermoplastic directly by general processing techniques.

Preparation of Composites and Testing Procedure

Composites were prepared first by tumble mixing preweighted quantities of polypropylene and grafted fillers, followed by compounding on a single screw extruder. The melt temperature was kept at 200 °C and screw speed was 25 r.p.m. The specimens for mechanical tests were machined from the compressing moulding plaques (65×45×3 mm) of extrudates. The volume fraction of the filler, V_f was computed from the known weights of

polymer matrix, fillers and polymer introduced by irradiation. An XJJ-5 tester was used for unnotched Charpy and Izod impact strength. Fracture-toughness testing of the samples made use of a fracture mechanics test according to ASTM 5045-93, using single edge notched bending specimens (SENB) and a crosshead speed of 5 mm/min. The fractured surfaces were observed by Hitachi S-520 scanning electron microscopy (SEM). TEM was performed on ultrathin sections using Hitachi H-800 transmission electron microscopy.

RESULT AND DISCUSSION

Impact resistance and fracture toughness of nanocomposites

Fig. 1 showed the effects of untreated SiO_2 and polymer-grafted SiO_2 on the unnotched Izod impact strength of polypropylene. Both PS and PMMA grafted SiO_2 increased impact strength more effectively than untreated SiO_2 . However, in contrast to general brittle-tough transition behavior, a decrease of impact strength was observed with the further increase of filler above the loading corresponding to the maximum impact strength. The unnotched Charpy impact tests showed a similar behavior with the addition of polymer-grafted filler as Izod impact test (Fig. 2a), except that an impressive increase of impact strength by a factor of around 4 was observed at very low

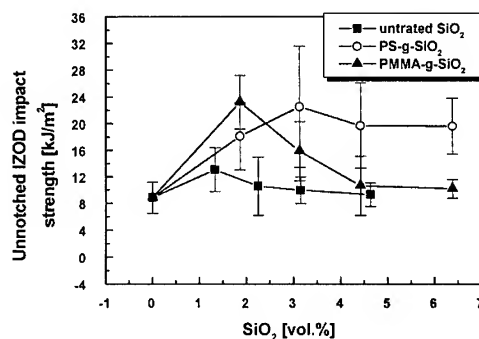


Fig. 1 Unnotched Izod impact strength of polypropylene ($MI=8.5$ g/10min) composites filled with various nano- SiO_2 as a function of filler loading

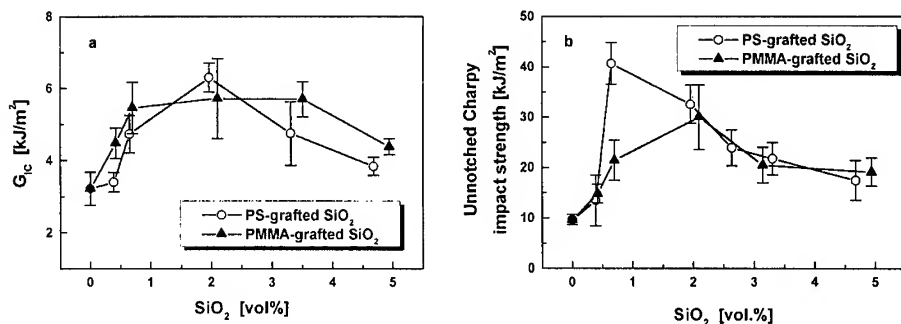


Fig. 2 Unnotched Charpy impact strength (a) and fracture toughness G_{IC} (b) of polypropylene ($MI=6.7$ g/10min) composites filled with various fillers as a function of filler loading

filler loading (0.65 vol. % for PS-grafted SiO_2). In considering the Izod and Charpy impact tests may be influenced by the sample geometry, the more serious SENB test was conducted to characterize the fracture properties of composites. It was observed that G_{IC} increases with increasing filler content before certain amount as shown in (Fig. 2b), then it tend to decreases with further incorporation of fillers. Evidently, the high content of grafted nanoparticles is detrimental to the impact properties and fracture toughness of nanocomposites.

The toughness improvement with modified silica compared with untreated silica is expected because the interdiffusion and entanglement between the modified polymer and matrix always exist, which is able to increased interfacial adhesion between the matrix and filler. The decreasing tendency of fracture toughness above certain loading of filler may be interpreted by constraints effects due to excess particles in presuming the uniform dispersion of filler, thus reducing the plastic deformation of matrix. It is reasonable that a competition exists between the inducing and restricting effect of fillers on the deformation of matrix, and the toughening of the composite depends on which of the two mechanisms predominates. From the results obtained here, it appears that it is latter mechanism that controls the system in slight high range of volume fraction of silica.



Fig. 3 SEM fractograph of SiO_2 -g-PS (1.96 vol. %) filled PP (MI=6.7 g/10min) for SENB fracture surface

Corresponding to the maximum G_{IC} value, the fracture surface of sample with 1.96 vol.% PS-grafted SiO_2 is accompanied by extensive plastic deformation zone, and shows microfibrils circles around agglomerates (Fig. 4). It can be noticed that these agglomerates have much larger size than the nanoparticles, implying that the aggregates of nanoparticles is still maintained even though their size has been greatly reduced in comparison to the nanoparticles without surface grafted modification (from 500nm to 100nm observed by TEM). However, there are some differences between these two aggregates structure. In the case without surface modification, the aggregates possess a friable and less-stable structure. During the impact test, the aggregates do not resist crack propagation as effectively as the polymer matrix and thus the impact strength is reduced [5]. With the grafting modification, the gap between nanoparticles will be filled with

grafting macromolecular chain; this must benefit the composites toughness.

It is noteworthy that these deformation circles has propagated and pervade over the entire matrix in the deformation zone (Fig. 3), which reveals the percolation behavior induced by composite particles. It should be noticed that the maximum value of impact strength and fracture toughness appear at very low content of filler (< 1~3 vol.%). Beside, the microphase structure of aggregates also influences the fracture behavior of composites. The significant decrease of impact strength when the content of modified polystyrenes increased from 10% to 30% can be used to prove the importance of distribution of primary particles in the composite particles consisting of aggregates and grafted particles (Table 1). On the other hand, the uniform dispersion of composite particles is also important as shown in Table 2. There is significant decrease in impact strength with increase of irradiation dose. It is assumed that

high irradiation dose can induce crosslink structure in modified polymers, which is in turn detrimental to the uniform dispersion of nanoparticles. All of these facts revealed that there exist some fracture mechanisms different from conventional single percolation concept suggested by Wu [6]. Here, a model of double-percolation is quoted to explain the phenomena, i.e., percolation of the shear yielded zones inside the dispersed phases (consisting of the nanoparticles, the grafting polymer on the nanoparticles and the homopolymer derived from the grafting monomer) due to the superposition of stress volumes around the primary particles, and percolation of the shear yielded zones throughout the matrix resin due to the superposition of stress volumes around the dispersed composite particles. According to the common law of scaling theory [7], such double percolation process must be beneficial to the low percolation threshold.

Table 1 Dependence of mechanical properties of polypropylene (MI=8.5 g/10min) composites filled with PS-grafted SiO₂ (content of SiO₂ = 3.31 vol.%) on content of styrene, σ_I unnotched Charpy impact strength, σ_y tensile yield strength, ϵ_b elongation at break, E Young's modulus, S_A the area under the stress-strain curve

Content of styrene	σ_y (Mpa)	E (Gpa)	ϵ_b (%)	σ_I (kJ/m ²)	S_A (Mpa)
Neat PP	32.65 (0.61)	0.896 (0.05)	9.50 (3.03)	8.70 (4.17)	2.12 (0.43)
10	32.92 (0.86)	0.828 (0.03)	9.88 (1.38)	29.5 (9.44)	2.83 (0.16)
20	34.14 (1.46)	0.916 (0.10)	9.34 (0.66)	19.8 (6.36)	2.43 (0.12)
30	32.74 (1.45)	0.836 (0.06)	8.67 (2.10)	13.62 (4.40)	2.07 (0.66)

Table 2 Dependence of mechanical properties of polypropylene (MI=8.5 g/10min) composites filled with PS-grafted SiO₂ (content of SiO₂ = 3.31 vol.%) on radiation dose, the symbols are same as Table 1

Radiation dose (Mrad)	σ_y (Mpa)	E (Gpa)	ϵ_b (%)	σ_I (kJ/m ²)	S_A (Mpa)
Neat PP	32.03 (0.52)	0.746 (0.10)	11.71 (2.58)	7.99 (1.64)	2.17
2	36.49 (2.45)	0.885 (0.08)	11.79 (1.01)	37.54 (12.68)	3.31 (0.06)
10	34.14 (1.46)	0.916 (0.10)	9.34 (0.66)	19.78 (6.36)	2.43 (0.12)
20	33.16 (1.73)	0.816 (0.06)	8.00 (0.96)	3.69 (2.63)	2.01 (0.29)

The influence of different grafted polymers on the fracture behavior

It is shown that interface adhesion due to the entanglement between the grafting polymer and matrix greatly influences the impact strength of nanocomposites (Table 3), which is consistent with the conventional particles filled composites. In case of poor interface adhesion, such as PMA grafted silica, the addition of filler result in great decrease in impact toughness

of PP. The PMA molecule chain containing carboxyl groups prefers to react with surface of SiO_2 filler containing hydroxyl groups rather than entangle with the matrix, consequently, the impact strength of composites exhibited even lower than the neat PP. In this case, the crack tend to propagate along the weaker interfacial regions, in other words, the interfacial regions do not resist crack propagation as effectively as the polymer matrix, and thus the impact strength is reduced. Nevertheless, there are not much difference between the other grafting polymers, indicating that strict miscibility matches between the grafting polymers and matrix is not required so long as the certain degree molecular entanglement taking place.

Table 3 Mechanical properties of PP filled with different polymers grafted SiO_2 (3.31 vol.%), the grafted rate (γ_g) and content of homopolymer (γ_h) is on the basis of particles

Grafted polymer	Neat PP	PS	PBA	PVA	PEA	PMMA	PMA
γ_g (%)	-	3.64	3.32	2.82	1.73	1.85	2.16
γ_h (%)	-	16.3	15.4	13.7	12.3	15.5	15.4
σ_i (kJ/m ²)	7.99 (1.64)	19.78 (6.4)	19.38 (6.4)	22.93 (0.8)	14.58 (6.6)	20.46 (0.5)	4.74 (0.6)

Note: PS: polystyrene

PBA: polybutyl acrylate

PVA: polyvinyl acetate

PEA: polyethyl acrylate

PMMA: polymethy methacrylate

PMA: polymethacrylic acid

ACKNOWLEDGMENT

The Key Programs of the Ministry of Education of China (Grant: 98069), and the Natural Science Foundation of Guangdong (Grant: 990277) are gratefully acknowledged. Dr. Rong is grateful to the Pilot Program for Young Ph.D. of the Natural Science Foundation of Guangdong (Grant: 974072).

REFERENCES

1. Dagni, R. C&EN 1992, 23,18
2. Novak, B. M. Adv. Mater. 1993, 5, 422
3. Xu, W.; Huang, R.; Cai B.; Fan, W. China Plastics, 1998, 12, 30
4. Sumita, M.; Tsukumo, Y.; Miyasaka, K.; Ishikawa, K. J. Mater. Sci. 1983, 18, 1758
5. Wang Y, Huang JS J Appl Polym Sci 1996: 60: 1779
6. Wu S Polymer 1985; 26: 1855
7. Zallen R The Physics of Amorphous Solids, Wiley: New York, 1983

THERMAL STABILITY AND MECHANICAL PROPERTIES OF DGEBA/TRIMETHYLOLPROPANE TRIGLYCIDYLETHER EPOXY BLENDS INITIATED BY CATIONIC LATENT CATALYST

Taek-Jin Kim¹, Soo-Jin Park¹, Jae-Rock Lee¹ and Sung-Kwon Hong²

¹Advanced Materials Division, Korea Research Institute of Chemical Technology,
P.O. Box 107, Yusong, Taejeon 305-600, Korea: psjin@pado.krict.re.kr

²Department of Polymer Science and Engineering, Chungnam National University,
Yusong, Taejeon 305-764, Korea

SUMMARY: The effect of blend composition ratio on thermal stability and mechanical properties of diglycidylether of bisphenol A (DGEBA)/trimethylolpropane triglycidylether (TMP) epoxy blend initiated by *N*-benzylpyrazinium hexafluoroantimonate (BPH) as a thermal latent catalyst was investigated. Latent properties of these systems were investigated by measuring the conversion using isothermal DSC. As a result, it was found that BPH could be excellent thermal latent catalyst for this blend system without any co-initiator. The thermal stability characterized from the initial decomposition temperature (IDT), the temperature of maximum weight loss (T_{max}), integral procedural decomposition temperature (IPDT) and the decomposition activation energies increased in DGEBA-rich compositions. This could be resulted from the existence of the long repeat unit and stable aromatic ring in the DGEBA. The mechanical properties were also discussed in terms of the fracture toughness (K_{IC}), flexural and impact tests for the blend composition studied.

KEYWORDS: epoxy blends, cationic latent catalyst, thermal stability, mechanical properties.

INTRODUCTION

Epoxy resins are one of the most important thermosetting polymers and have wide use as structural adhesives and matrix for fiber-reinforced composites due to their high modulus and thermal stability [1]. However, the highly cross-linked nature of cured epoxy produces an undesirable characteristics, i.e. brittleness and poor resistance to crack growth. The technology to toughen a cross-linked epoxy resin by the addition of rubber particles such as carboxyl-terminated acrylonitrile butadiene (CTBN) and amino-terminated acrylonitrile butadiene (ATBN) has been well known [2-6]. However, use of rubber as toughening agent leads to a significant reduction in modulus and heat-distortion temperature. For this reason, the blends of aromatic epoxy resin mainly based on bisphenol A and epoxy based on aliphatic polyol are interesting because aliphatic epoxy imparts flexibility and toughness to final product, reduces the viscosity of the initial mixture and aids the processability of the resin [7].

In recent years, cationic polymerization of epoxide has been studied intensively [8,9]. Cationic initiator is generally used as a complex, such as BF_3 -ether, BF_3 -amine, or SbF_6 -epoxide. This

complex overcomes the disadvantages of excessively rapid gelation, high hygroscopicity, and light instability [1]. Particularly, development of latent catalyst for cationic polymerization is desirable for enhancement of both the pot-life and handling of thermosetting resins [10,11]. Usually, the latent catalyst forms active species by external stimulation such as heat and photo-irradiation.

Although the curing reaction of the epoxy/cationic latent catalyst system has been described by many authors, there is less information when aliphatic epoxy resin is blended in the aromatic formulation. The objective of this work is to study the effect of trifunctional aliphatic TMP on the thermo-stable and mechanical behaviors of DGEBA initiated by cationic latent catalyst, i.e., *N*-benzylpyrazinium hexafluoroantimonate.

EXPERIMENTAL

Materials and Sample Preparation

The two types of epoxy resins used in this work were diglycidylether of bisphenol A (DGEBA, LY556 supplied by the Ciba-Geigy Co.) and trimethylolpropane triglycidylether (TMP, YH300 supplied by the Kukdo Chem. Co. of Korea). Cationic latent catalyst (*N*-benzylpyrazinium hexafluoroantimonate, BPH) was synthesized throughout the recent work [12]. Fig. 1 shows the structures of two resins and BPH.

The BPH of 1 wt.% was dissolved in DGEBA, and then TMP was added to the DGEBA/BPH mixture, ranging from 0, 20, 40, 60, 80 and 100 wt.%. All formulations were mixed at room temperature and degassed under a vacuum for 1 h to remove voids and residual organic solvents. The bubble-free mixture was poured into a stainless mold and cured at 70 °C for 30 min, 150 °C for 3 h, and finally postcured at 200 °C for 1 h.

Measurements

Latent properties of DGEBA/TMP/BPH blends were performed by the measurements of conversion as a function of reaction time using isothermal differential scanning calorimetry

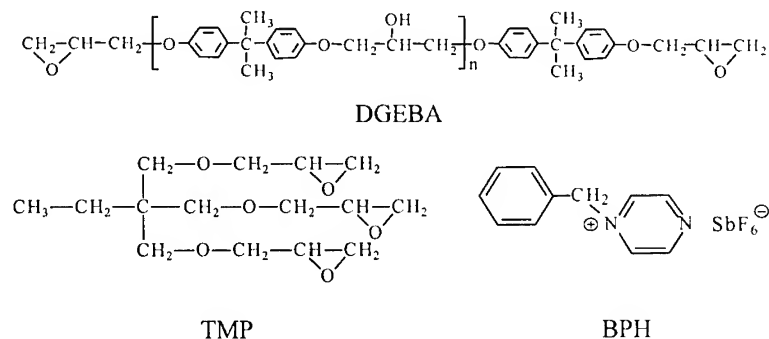


Fig.1. Chemical structures of DGEBA, TMP and BPH

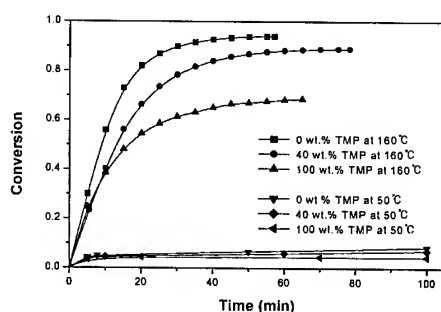


Fig. 2. Time vs. conversion curves of DGEBA/TMP at 160°C and 50°C

(DSC, Perkin Elmer DSC 6) at 50°C and 160°C.

The thermogravimetric analysis were performed in nitrogen using a TGA 951 DuPont analyzer at a heating rate of 10°C/min from 30 to 800°C to investigate the thermal stability of the cured resins.

The critical stress intensity factor (K_{IC}) which is one of the fracture toughness parameters may be characterized by single edge notched (SEN) beam fracture toughness test (ASTM E399) in three-point bending flexure. Notches with half the depth of the specimen were cut using a diamond wire saw. A span-to-depth ratio of 4:1 and cross-head speed of 1mm/min were used. Flexural properties were tested in according to ASTM D790. The flexural specimen with 25 mm wide, nominally 80 mm long specimens and tested at a span-to-depth ratio of 16:1. The impact strength is tested using the Izod method in according to the ASTM D256.

RESULTS AND DISCUSSION

Latent Properties of DGEBA/TMP/BPH Systems

Fig. 2 shows the conversion as a function of the time for the neat DGEBA, TMP and their mixture initiated by BPH using isothermal DSC. As the curing time proceeds, the conversion increases in the case of 160°C reaction temperature. However, the conversion notably in the 50°C reaction temperature shows no significant change with the process of the time. This results is due to the low temperature having a limiting factor prohibiting the activity of catalyst. As a result, these indicate that this systems including BPH have thermally stable latent properties at a given temperature condition in spite of the presence of external heat stimulation.

Thermal Stability

The thermal stabilities given by initial decomposition temperature (IDT), temperature of maximum rate of weight loss (T_{max}), and integral procedural decomposition temperature (IPDT) [13] decrease with increasing the concentration of TMP in blends, as shown in Table 1. This can be explained by the inherent chemical structures such as bulk side-group including long repeat unit and stable aromatic ring of DGEBA. It is noted that thermal degradation is progressed by the etherification, a sort of side reaction, and subsequently proceeded via dehydration and thermal oxidation, resulting in the scission of network chains [14,15].

Table 1. Thermal stabilities of DGEBA/TMP blends obtained by TGA

wt.% TMP	IDT [°C]	T _{max} [°C]	IPDT [°C]	E _a [kJ/mol]
0	344	449	576	114
20	338	442	558	82
40	330	437	539	72
60	309	426	504	67
80	291	416	491	56
100	283	402	448	55

This thermal degradation behavior is possible to measure the energy of activation for the decomposition of resins. Decomposed activation energy, E_a , is calculated from TGA curves by the integral method of Horowitz and Metzger [16], as follows:

$$\ln[\ln(1-\alpha)^{-1}] = \frac{E_a \theta}{RT_{\max}^2} \quad (1)$$

where a is decomposed fraction, T_{\max} temperature of maximum rate of weight loss, $\theta = T - T_{\max}$, and R gas constant.

From the slope for the plot of $\ln[\ln(1-a)^{-1}]$ vs. θ , the decomposed activation energy of the blend can be determined in the equation (1). As shown in Table 1, it is observed that the decomposed activation energy decreases in increasing the TMP composition, which can be influenced on the volume fraction of hard segment, such as aromatic ring, hydrogen bond, repeat unit, and thermal history [17,18]. Therefore, the results of activation energy are resulted from the chemical nature of the DGEBA.

Mechanical Properties

The fracture toughness can be measured by three-point bending test for the critical stress intensity factor (K_{IC}). For single edge notched (SEN) beam fracture toughness test, the value of K_{IC} is calculated as follows:

$$K_{IC} = \frac{PL}{bd^{3/2}} Y \quad (2)$$

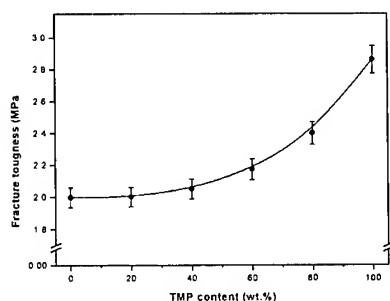


Fig. 3. Fracture toughness of DGEBA/TMP blend systems

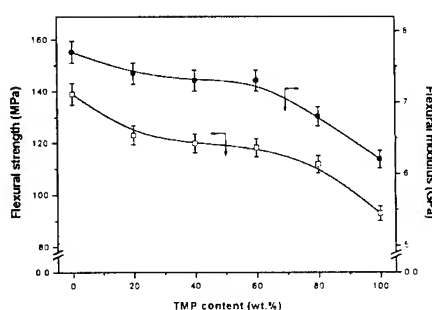


Fig. 4. Flexural strength and modulus of DGEBA/TMP blend systems

where, P is the rupture force, L the span between the supports, Y the geometric factor described ASTM E399, and b and d the specimen width and thickness, respectively.

Fig. 3 shows the evolution of K_{IC} in flexure of the DGEBA/TMP blend systems with the content of TMP. It is observed that fracture toughness of DGEBA increased with increasing the amount of TMP. For TMP content above 60 wt.%, a strong increase was noticed while slight increase was observed up to 40 wt.% of TMP. This results can be explained by means of a more flexible skeleton of TMP.

The flexural strength (σ_f) and the elastic modulus in flexure (E_b) for the DGEBA/TMP blends determined from three-point bending tests are calculated using the following equations:

$$\sigma_f = \frac{3PL}{2bd^2} \quad (3)$$

$$E_b = \frac{L^3}{4bd^3} \frac{\Delta P}{\Delta m} \quad (4)$$

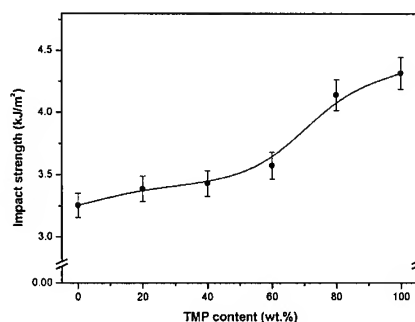
where P is load, L span length, b width of specimen, d thickness of specimen, ΔP change in force in the linear portion of the load-deflection curve and Δm change in deflection corresponding to ΔP

Fig. 4 shows the flexural strength and the elastic modulus as a function of TMP content. The flexural strength and modulus decrease with increasing the content of TMP, which is resulted from decrease of a compact hydrogen bond by the hydroxyl groups and a long repeat unit containing bulk side groups of DGEBA.

Meanwhile, it is noted that impact properties are directly related to overall toughness or ductility of the materials, which can be defined as the ability of the blend system to absorb applied energy. As an experimental result, the addition of TMP improves the impact strength and toughness of DGEBA/TMP blend system, as seen in Fig. 5. A stable brittle behavior increases when the chain flexibility increases, which can be correlated with results of K_{IC} data.

CONCLUSION

In this work, thermo-stable, and mechanical properties of DGEBA/TMP blend systems initiated by thermal latent catalyst have been investigated. The thermal stability of the



DGEBA-

Fig. 5. Impact strength for DGEBA/TMP blend systems

rich compositions containing long repeat unit, bulk side-group, stable aromatic ring structure and reactive hydroxyl functional group. However, the addition of TMP into DGEBA gave a improvement in fracture toughness such as K_{IC} and impact strength, which is results from the increase of aliphatic and flexible chain segments of TMP.

REFERENCES

1. C. A. May, "Epoxy Resins" Marcel Dekker, New York, 1988.
2. J. N. Sultan, R. C. Laible, F. J. McGarry, *J. Appl. Polym. Sci.*, Vol.6, 1971, p.127.
3. W. D. Bascom, C. O. Timmons, R. J. Jones, P. J. Peyser, *J. Appl. Polym. Sci.*, Vol.19, 1975, p.2545.
4. T. T. Wang, H. M. Zupko, *J. Appl. Polym. Sci.*, Vol.26, 1981, p.2391.
5. K. Yamanaka, Y. Takagi, T. Inoue, *Polymer*, Vol.30, 1989, p.1839.
6. L. Jayle, C. B. Bucknall, I. K. Partridge, J. N. Hay, A. Fernyhough, I. Nozue, *Polymer*, Vol.37, 1996, p.1897.
7. E. Espuche, J. Galy, J. F. Gerard, J. P. Pascault, H. Sautereau, *Macromol. Symp.*, Vol. 93, 1995, p.107.
8. S. D. Lee, T. Takata, and T. Endo, *Macromolecules*, Vol.29, 1996, p.3317.
9. I. I. Abu-Abdoun and A. Ali, *Eur. Polym. J.*, Vol.28, 1992, p.73.
10. J. V. Crivello and J. H. Lam, *J. Polym. Sci., Polym. Chem.*, Vol.18, 1980, p.1021.
11. J. Gu, S. C. Narang, and E. M. Pearce, *J. Appl. Polym. Sci.*, Vol.30, 1985, p.2997.
12. Y. C. Kim, S. J. Park, and J. R. Lee, *Polym. J.*, Vol.29, 1997, p.759.
13. G. H. Kwak, S. J. Park, J. R. Lee, and S. K. Hong, *Polymer(Korea)*, Vol.23, 1999, p.281.
14. D. J. Hourston and J. M. Lane, *Polymer*, Vol.33, 1992, p.1379.
15. L. H. Lee, *J. Polym. Sci.*, Vol.3, 1965, p.895.
16. H. H. Horowitz and G. Metzger, *Anal. Chem.*, Vol.35, 1963, p.1464.
17. S. L. Samuels and G. L. Wilkes, *J. Polym. Sci., Polym. Symp.*, Vol.43, 1978, p.149.
18. G. L. Wilkes, P. C. Moody, and M. R. Tant, *Polym. Eng. Sci.*, Vol.19, 1979, p.1029.

THERMAL AND MECHANICAL PROPERTIES OF POLY-(DIMETHYL-SILOXANE-ADIAMIDE) TOUGHENED NOVOLAC TYPE PHENOLIC RESIN

Feng-Yih Wang, Chen-Chi M.Ma*, and Chung-Chun Lee

*Department of Chemical Engineering, National Tsing Hua University,
Hsin-chu 30043, Taiwan.*

Email: ccma@che.nthu.edu.tw

TEL: 886-3-5713058 FAX: 886-3-5715408

SUMMARY : The miscibility, mechanical properties and thermal stability of the poly-(dimethyl-siloxane-diamide)(PDMSA) toughened novolac type phenolic resin were investigated. Differential scanning calorimetry (DSC) and infrared (IR) spectroscopy results show that there are strong intermolecular hydrogen bonding interactions existed between novolac type phenolic and PDMSA. DSC and IR results also revealed good miscibility within these modified novolac type phenolic blends. Results show that PDMSA can improve the toughness of novolac type phenolic resin. Intermolecular hydrogen bonding between novolac type phenolic resin and PDMSA can provide thermal stability and mechanical properties of the blends.

KEYWORDS: Novolac type phenolic resin, Intermolecular hydrogen bonding, Thermal stability, Mechanical properties.

INTRODUCTION

Phenolic resin has been widely used commercially in the applications such as paint, adhesives and composites due to its lower manufacturing cost, dimensional stability, and chemical resistance¹⁻³. Polysiloxane has been widely used in industry, due to its low glass transition temperature (T_g), low surface tension of wetting and low energy barrier of rotation. Polysiloxane causes lower glass transition temperature (T_g) and lower surface tension of wetting, due to lower energy barrier for rotation and soft segment of siloxane group. Consequently, polysiloxane can be used as a toughening agent for epoxy, phenolic and polyacrylate resin⁴⁻⁷. In this study, a novel method of blending the novolac type phenolic resin with poly-(dimethyl-siloxane-adiamide) (PDMSA) is proposed. The amide group of PDMSA would interact with the hydrogen-bonded of novolac phenolic resin and to improve the mechanical properties (including tensile strength, flexural modulus and notched Izod impact strength) of the modified phenolic resin⁵. The thermal stability of phenolic/PDMSA blend is also investigated in this study.

EXPERIMENTAL

Materials

The curing agent used is the bisphenol-A type epoxy resin, diglycidyl ether of bisphenol-A (DGEBA) (Epon-828, Shell Chemical Co., U.S.A.). The catalyst, 1,8-Diazabicyclo[5.4.0]-7-undecene (DBU), was purchased from the Lancaster Synthesis Ltd, U.S.A. Synthesis methods of novolac type phenolic resin and poly-(dimethyl-siloxane-adiamide) (PDMSA) were described as our paper⁽⁸⁾.

Sample Preparation

DGEBA epoxy was used as curing agent and DBU was used as catalyst. Various contents of PDMSA were blended with novolac type phenolic resin in THF. Compositions of cured samples are summarized in Table 1.

Table 1 Compositions of Curd Samples.

PDMSA Content (phr)	Phenolic (g)	SiNHCO (g)	Epoxy(g)	DBU (g)
1	30	0.3	15	0.6
3	30	0.9	15	0.6
5	30	1.5	15	0.6
7	30	2.1	15	0.6

Samples were put in an oven at 55°C for two hour and then the temperature was increased to 70°C overnight in vacuum. The postcured temperature was 150°C, and curing time was 5 hours, to ensure complete mixing of the polymer blend and to remove the residual solvent and water in the specimens completely. The preparation of the IR and TGA specimens are described as following: the phenolic/PDMSA blend was

prepared by mixing it with THF [1%(w/v)] at room temperature according to the designed composition. The mixed solution was stirred for 6~8 minutes and THF was evaporated slowly at 70°C under vacuum for one day.

Properties Measurements

Flexural modulus was measured according to ASTM D-256. The sample dimensions are 63mm×10mm×3mm, the span between the two supports was 50mm, and the crosshead speed was 1.3mm/min. The notched Izod impact strength was measured following the specification of ASTM D-256, its dimensions are 63mm×10mm×3mm.

The infrared spectrophotometer used was Perkin Elmer 842. The IR spectra was scanned at the range of 4000~400 cm⁻¹, and was utilized to study the intermolecular hydrogen bonding between phenolic resin and PDMSA. Thermogravimetric analysis (TGA) was conducted with a Dupont TGA951 from room temperature to 800°C using a heating rate of 10°C/min under nitrogen gas atmosphere.

Flame retardance was measured according to the UL-94 Standard⁹. Five specimens with the dimensions of 125±5mm long and 13.0±0.5mm wide were tested. Methane gas was supplied to the burner shell and the burner was adjusted to produce a blue flame of 20±1mm high. By applying the flame centrally to the middle point of the bottom edge of the specimen, the top of the burner is 10mm below the point of the lower end of the specimen and that distance was maintained for 10s. If only one specimen from one set of five specimens did not comply with the requirements, another set of five specimens has to be tested. The limited oxygen index (LOI) was tested according to ASTM D-2863.

RESULTS AND DISCUSSION

Molecular Structure Identification

The stretching peak of C=O functional group shifts from 1682 cm⁻¹ (Figure 1-a) to 1640 cm⁻¹ (Figure 1-c) that indicates that COOH reacts with NH₂ and CONH is formed. Figure 1-c shows the peaks of spectra 2690cm⁻¹ (CH₂), 827cm⁻¹ (Si-CH₂), 1251cm⁻¹ (Si-CH₃) and confirms the structure of poly-(dimethyl-siloxane adipamide). Figure 2 illustrates the hydrogen bonds existed in the polymer blends. The amide group of PDMSA appeared almost on the hydrogen-bonded figuration, corresponding to the PDMSA containing a high-density amide group which is more flexible in backbone than that of the phenolic resin. Both functional groups provide the opportunity to form intramolecular hydrogen bonding.

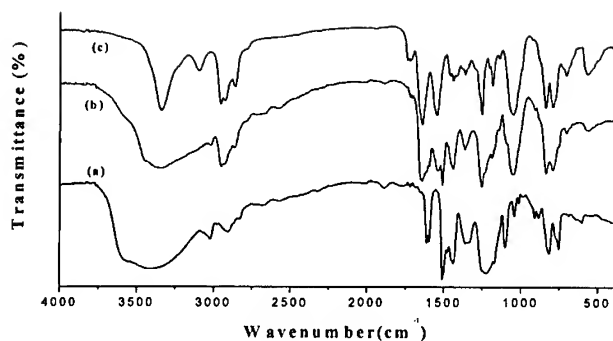


Figure 1 IR spectra: (a) adipic acid, (b) 1,3Bis(3-aminopropyl)-1,1,3,3 tetramethyl-disiloxane, (c) poly-(dimethylsiloxane adipamide).

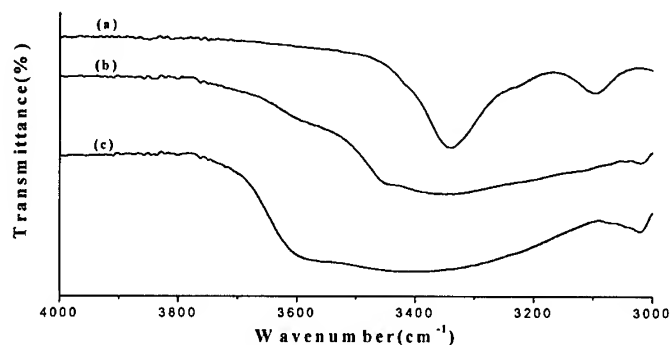


Figure 2 IR spectra: (a) Poly-(dimethylsiloxane adipamide), (b) phenolic/PDMSA (50/50), (c) phenolic resin.

Thermal Properties

Figure 3 illustrates the thermogravimetric analysis (TGA) results of the phenolic/PDMSA blend. PDMSA in the blend decomposed gradually at higher temperature than that of the phenolic resin. The decomposition temperature of the phenolic/PDMSA blend is above 400°C, indicating that the blend possesses good thermal stability.

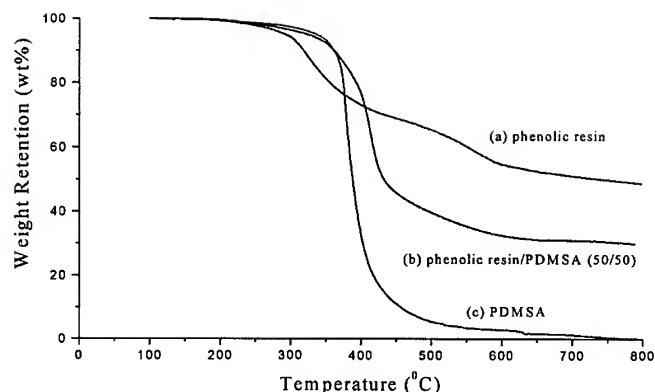


Figure 3 TGA of the phenolic/PDMSA copolymer at various compositions: (a) pure phenolic, (b) phenolic/PDMSA (50/50), (c) pure PDMSA.

The flame retardance of phenolic/PDMSA blends shows a high limited oxygen index (LOI) value (>35) and the UL-94 is V-1, as summarized Table 2. These values are maintained up to 7wt% PDMSA. The effect of PDMSA content on the flame retardance was insignificant since the phenolic resin is a high char-yielded material.

Table 2 The Flame Resistance of Modified Novolac type Phenolic Resin toughened by PDMSA.

PDMSA content (phr)	0	1	3	5	7
UL-94	V-1	V-1	V-1	V-1	V-1
Limited oxygen index (LOI)	35	35	35	35	35

Mechanical Properties

The flexural strength and modulus of the phenolic resin toughened by PDMSA are summarized in Table 3. Flexural strength and modulus show maximum values when PDMSA content is 5phr and then decrease gradually when PDMSA content is more than 5phr. This behavior can be interpreted when the soft segment of PDMSA is incorporated into the backbone of the phenolic resin. The soft segment of siloxane group will absorb any load applied first; hence, the flexural strength will be increased. However, when the PDMSA content is higher than 5phr, phase separation may occur and the flexural strength was decreased. The flexural strength of cured composite is higher than that of the uncured one. The flexural modulus of cured composites is comparable to the uncured one. The highest impact value is also occurred when the blend contains 5phr of PDMSA and a significant improvement in toughness was observed. The impact strength of the blended composite containing 5phr of PDMSA is 34% higher than that of the pure phenolic resin. When the PDMSA content is higher than 5phr, the impact strength is decreased because the phenolic resin and the PDMSA

become immiscible at a higher PDMSA content. A macrophase separation is formed in the modified phenolic resins instead of microphase separation. The notched Izod impact strength decreased with the increasing of PDMSA content. The cured composites show higher notched Izod impact strength than that of uncured one due to the reaction of cure is more complete.

Table 3. Mechanical Properties of PDMSA-modified Phenolic Resin

Specimen	Property	PDMSA Content (Phr)				
		0	1	3	5	7
Uncured specimen	Flexural strength (MPa)	29.43	32.53	39.42	49.85	41.89
	Fluxral modulus (MPa)	1261.6	1541.2	3399.2	4616.8	4166.1
	Notched Izod impact strength (kJ/m)	23.3	24.9	25.7	33.8	30.2
Cured Specimen	Flexural strength (MPa)	30.35	32.97	40.33	50.37	43.82
	Flexural Modulus (MPa)	1301	1562	3478	4665	4358
	Notched Izod impact strength (J/m)	25.4	26.6	29.6	34.8	31.7

CONCLUSIONS

The phenolic /PDMSA blend is a completely miscible system at low PDMSA content. The flexible siloxane chain of the PDMSA backbone penetrates into the rigid phenolic matrix, which serves as a good toughening agent for phenolic resin. Mechanical properties of modified novolac type phenolic resin show the highest values at blend contain 5phr PDMSA. The cured specimen shows higher mechanical properties than that of uncured one.

ACKNOWLEDGEMENTS

The authors gratefully acknowledge the financial support of the National Science Council, Taiwan. R.O.C., the contract No is NSC 88-CS-D-007-002.

REFERENCES

- 1.Y. Zaks, J. Lo, D. Raucher, and E. M. Pearce, *J. Appl. Polym. Sci.*, **27**, 913 (1982).
- 2.G. R. Bishop and P. A. Sheard, *Compos. Strut.*, **21**, 85 (1992).
- 3.C.C. M. Ma and W. C. Shih, U.S. Pat. 4,873,128 (Oct. 1989).
- 4.J. Hourston and Y. Zia, *J. Appl. Polym. Sci.*, **28**, 3745 (1983).
- 5.Brandrup and E. H. Immergut, *Polymer Handbook*, 3rd ed., John Wiley & Sons, New York (1989).
- 6.D. Bascon, R. Y. Ting, R. J. Moulton, C.K. Riew and Siebert, *J. Mater. Sci.*, **16**, 2657 (1981).
- 7.Shyu-Tzoo Lin and Steve K. Huang, *J. of Polym. Si. Part A: Polym Chem.*, **37**, 869-884 (1996).
- 8.Feng-Yih Wang and Chen-Chi M. M, *Polymer*.(revised),1999.
- 9.UL 94 Standard for Tests for Flammability of Plastic Materials for Parts in Devices and Appliances, 4th ed., Underwriters Laboratories, June 18, 1991.

A MECHANISTIC MODELLING OF THE GLASS TRANSITION TEMPERATURE OF A THERMOSET POLYMER

B.-G. Min

*Department of Polymer Engineering, Chungju National University
123, Geumdan-ri, Eryu-myun, Chungju, Chungbuk 380-702 KOREA:
Email@: bgmin@gukwon.chungju.ac.kr*

SUMMARY: The effect of elementary reactions on the development of the glass transition temperature (T_g) of a thermoset polymer has been analyzed quantitatively according to a proposed mechanistic model. The model was derived on the basis of the reaction mechanisms observed in the curing system and the assumption that the T_g has individual linear relationships with the degree of conversion of the elementary reactions. The conversions of elementary reactions during the cure were obtained experimentally by using near infrared spectroscopy (NIR). The T_g was measured on a differential scanning calorimeter(DSC). In addition, the overall conversion of the system was also obtained from DSC in a dynamic scanning mode for the purpose of comparison. The conversion-time data from the two different techniques were consistent. The proposed model successfully predicted the increases in T_g due to elementary reactions separately. The Di Benedetto equation and the viscoelastic model of Gan et al are also evaluated.

KEYWORDS: epoxy resin, kinetics, linear polymerization, crosslinking reaction.

INTRODUCTION

The glass transition temperature, T_g , of a linear polymer is generally well understood as a function of its molecular weight[1-3]. However, the T_g of a thermoset polymer is not clearly understood in terms of specific molecular factors, in spite of a considerable research effort[4-13]. The most common approach is to relate the T_g of a thermoset polymer to the overall conversion[9,11,12,14], although it is accepted that the variation in T_g is attributed to various molecular parameters such as molecular weight, stiffness of the cross-linked chains and free volume entrapped in the network[14]. In this study we show that the effects of the increasing molecular weight can be separated from those of the cross-linking and network formation. The increase of molecular weight is achieved by linear polymerization between epoxy and the cross-linking agent including branching, while the increase of the stiffness of the network chain and changes in free volume are functions of both the branching and cross-linking reactions. Therefore to separate the effects of the individual factors influencing T_g , we need to quantify the progress of the individual reactions(linear polymerization, and branching and cross-linking

reactions) as well as monitor the T_g . The former task has not been approachable with the DSC technique, which can only quantify the overall progress of the reaction by measuring the heat of reaction.

In a previous study of the reaction mechanisms we analyzed the individual reactions by monitoring the conversion of individual functional groups, including epoxy, primary and secondary amine, using near infrared spectroscopy[15]. The main reactions observed during the curing process of the system were epoxy-amine reactions. Assuming that no side reaction occurs in the stoichiometric DGEBA/DDS system, we can foresee that the primary amine-epoxy reaction would always result in a linear polymerization, and the secondary amine-epoxy reaction would always result in branching or cross-linking. We also found that the primary amine-epoxy reaction had priority up to gelation over the secondary amine-epoxy reaction. At the gel point (approximately 65% epoxy group conversion from NIR and DMTA measurements) most of the primary amine groups were consumed (95% conversion) whereas only 28% of the secondary amine groups were consumed. This observation implied that the increase of the molecular weight of the system by linear polymerization would be the main factor for the increase of T_g up to gelation. Above gelation the effect of increasing molecular weight by branching and cross-linking on T_g can be assumed to be negligible. Instead these reactions would increase the T_g by means of decreasing free volume and/or increasing the stiffness of the network chains. In this respect, the effect of molecular weight and the combined effects of free volume and chain stiffness can be expressed in terms of the extent of linear polymerization (primary amine-epoxy reaction) and cross-linking reaction (secondary amine-epoxy reaction including branching reaction) respectively. This approach is used below to derive an equation for relating T_g to conversions of elementary reactions.

THEORETICAL MODEL

The glass transition temperature of a cross-linked polymer can be expressed in a following form [8]:

$$T_g = T_{g0} + (\Delta T_g)_M + (\Delta T_g)_V \quad (1)$$

where T_{g0} is T_g of the unreacted monomer mixture, $(\Delta T_g)_M$ is the increase in T_g due to the increase of molecular weight, and $(\Delta T_g)_V$ is the increase in T_g due to the increase in cross-linking density. Based on the experimental observation in our DGEBA/DDS system, we find that $(\Delta T_g)_M$ is dependent only on the conversion of the linear polymerization reaction (the conversion of the primary amine-epoxy reaction) and $(\Delta T_g)_V$ is dependent only on the conversion of the cross-linking reaction (the conversion of the secondary amine-epoxy reaction). Therefore Eqn 1 can be written as follows:

$$T_g = T_{g0} + (\Delta T_g)_L + (\Delta T_g)_C \quad (2)$$

where $(\Delta T_g)_L$ and $(\Delta T_g)_C$ are the increases in T_g resulting from the conversion of the linear polymerization and the cross-linking reactions respectively. The number average degree of polymerization, \overline{X}_n increases with conversion of the linear polymerization reaction (α_L) [2,3]:

$$\overline{X}_n = (1+r)/[1-r(2\alpha_L-1)] \quad (3)$$

where r is the stoichiometric ratio of the reactant monomers. For $r=1$, Eqn 3 becomes:

$$\overline{X}_n = 1/(1 - \alpha_L) \quad (4)$$

Eqn 4 can be written in terms of molecular weight:

$$\overline{M}_n = M_0 / (1 - \alpha_L) \quad (5)$$

According to the Fox and Flory model, T_g of a linear polymer, $(T_g)_L$, can be expressed as:

$$(T_g)_L = T_{g0} + (\Delta T_g)_L = (T_{g^\infty})_L - K/\overline{M}_n \quad (6)$$

where $(T_{g^\infty})_L$ is the limiting T_g of linear polymer of infinite molecular weight, and K is constant. The substitution of Eqn 5 into Eqn 6 results in:

$$(T_g)_L = (T_{g^\infty})_L - K(1 - \alpha_L)/M_0 \quad (7)$$

When $\alpha_L = 0$, $(T_g)_L = (T_{g^\infty})_L - K/M_0$, $(T_g)_L = T_{g0}$ and therefore $K/M_0 = (T_{g^\infty})_L - T_{g0}$. By rearranging Eqn 7, $(T_g)_L$ can be expressed as a linear function of the conversion of linear polymerization, α_L , as follows:

$$(T_g)_L = T_{g0} + (\Delta T_g)_L = T_{g0} + \alpha_L [(T_{g^\infty})_L - T_{g0}] \quad (8)$$

We further assume that the $(\Delta T_g)_C$ in Eqn 2 also has a linear relationship with the degree of conversion of the cross-linking reaction. We write in analogy to Eqn 8:

$$(T_g)_C = T_{g0} + (\Delta T_g)_C = T_{g0} + \alpha_C [T_{g^\infty} - (T_{g^\infty})_L] \quad (9)$$

where α_C is the conversion of the cross-linking reaction, and T_{g^∞} is the maximum glass transition temperature of the system when $\alpha_L = \alpha_C = 1$. Substitution of Eqn 8 and 9 into Eqn 2 results in the following relationship:

$$T_g = T_{g0} + \alpha_L [(T_{g^\infty})_L - T_{g0}] + \alpha_C [T_{g^\infty} - (T_{g^\infty})_L] \quad (10)$$

T_{g0} , T_{g^∞} and $(T_{g^\infty})_L$ are usually known values or can be determined experimentally, and α_L and α_C can be measured for each sample.

EXPERIMENTAL

Materials and Sample Preparation

The epoxy resin used in this study was diglycidyl ether of bisphenol A (DGEBA; Epikote 8283, Shell chemicals, $M_n=380$), and the amine curing agent was 4,4'-diaminodiphenyl sulfone (DDS; Anchor chemicals, $M_n=248$). The sample preparation methods for the DSC and the NIR studies are already described in our advanced publication[15].

Data Collection

Samples of 15-20mg, obtained from the cured epoxy disks, were used to measure the glass transition temperatures (T_g 's) and the overall conversion, α , on a DSC-7 Differential Scanning Calorimeter. The residual heat of reaction for uncured DEGBA/DDS mixtures was used as a total heat of reaction. The overall conversion was calculated from the measured heat of the reaction according to the following equation[16]:

$$\alpha = (H_T - H_R)/H_T \quad (11)$$

where H_T is the total heat of the reaction for uncured samples and H_R is residual heat of the reaction for partially cured samples. More details about DSC methods for monitoring epoxy cure reactions can be found in a publication by Barton[16].

RESULTS AND DISCUSSION

The overall conversions, α , obtained from NIR and DSC measurements, are shown in Fig. 1 as a function of cure time. Although the values from NIR are slightly higher than those from DSC in the early stage of the cure, the overall contours of the graphs from the two different techniques are identical. Fig. 2 shows the T_g 's of the tested samples. The development of T_g with cure time is similar to that observed in the conversion-cure time curves shown in Fig. 1.

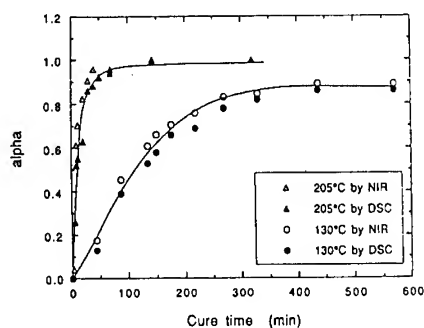


Figure 1. Plot of experimental conversion versus cure time.

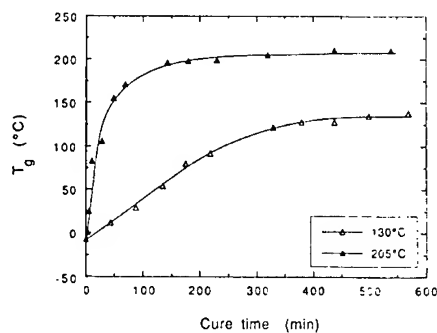


Figure 2. Plot of experimental T_g versus cure time.

Fig 3 shows the experimental results for conversion of primary amine (conversion of linear polymerization reaction, α_L) and secondary amine (conversion of cross-linking reaction, α_C) plotted as a function of α (overall epoxy group conversion). The linear polymerization dominates the process in the early stages of cure, while the cross-linking reaction does it in the later stages of cure. The cross-linking reaction is in fact not observed until at least $\alpha > 0.2$. Close to gelation ($\alpha = 0.65$) the linear polymerization is almost arrested ($\alpha_L = 0.95$) whereas the cross-linking reaction is still in its initial stages ($\alpha_C = 0.28$). In order to see the individual influence of the linear and the cross-linking reactions on T_g , we plotted T_g both as a function α_L and α_C in Fig. 4. Notice that up to approximately $\alpha_L = 0.8$, which corresponds to $\alpha = 0.4$, where the linear polymerization reaction dominates, T_g increases only by 40 °C. Above that T_g increases dramatically with increasing α_C . The rapid increase of T_g at $\alpha_L = 1$ is because the T_g continues to increase with increasing α_C even after the termination of the linear polymerization reaction.

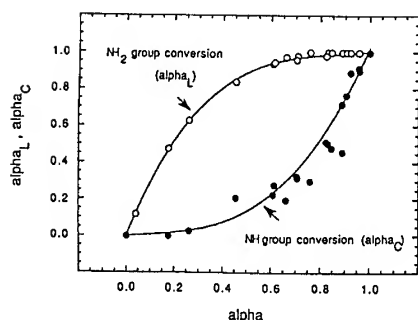


Figure 3. Experimental conversions of primary amine(linear polymerization) and secondary amine(crosslinking reaction) versus epoxy conversion

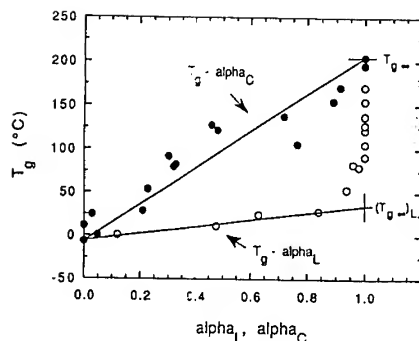


Figure 4. Plot of T_g against conversions of linear polymerization(α_L) and crosslinking reaction(α_C).

To analyze the results in terms of the proposed model (Eqn 10), it is necessary to determine the glass transition temperature, $(T_{g^{\infty}})_L$, for a linear DGEBA/DDS copolymer at $\alpha_L=1$. It can be estimated by extrapolation of the data shown in Fig 4, and we find it equal to 34°C. Other constants in Eqn 10 are known: $T_{g0}=-6^{\circ}\text{C}$ and $T_{g^{\infty}}=205^{\circ}\text{C}$ from Fig. 2. Using these data and the values for conversions from Fig. 3, Eqn 10 could be evaluated. It is shown in Fig. 5, together with experimental data for comparison. The agreement between theory and experiment is excellent considering that no adjustable parameters are used in Eqn 10. The degree of cross-linking reaction is a more critical factor for determining the T_g of cross-linked networks.

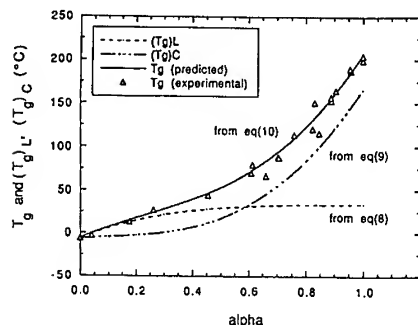


Figure 5. Plot of $(T_g)_L$, $(T_g)_C$ and T_g , predicted from the experimental values of α_L and α_C using Eqn 8, 9 and 10. Triangular points show experimentally obtained data.

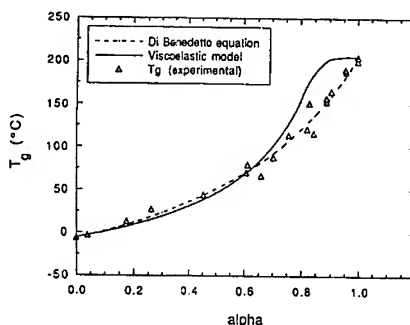


Figure 6. Comparison of T_g versus conversion data from Di Benedetto equation and viscoelastic model with experimental data.

The Di Benedetto equation is expressed in the following form[14]:

$$(T_g - T_{g0}) / T_{g0} = [(E_x / E_m - F_x / F_m) \alpha] / [1 - (1 - F_x / F_m) \alpha] \quad (12)$$

where E_x and E_m are lattice energies of the uncross-linked and cross-linked polymers respectively, F_x and F_m are the segmental mobilities of the same polymers, and T_g and T_{g0} have the same meaning as above. The fit of Di Benedetto equation to our experimental data is

shown in Fig. 6. Notice that the agreement is as good as that of our proposed Eqn 10. Eqn 12 has been found to fit well many other experimental systems[9,12].

A different approach to the relationship between T_g and overall conversion of network forming system was published by Gan et al[13]. Their final equation is as follows:

$$T_g = E_r / [R \ln \{C_1(1-\alpha)^\Phi + C_2\}] \quad (13)$$

where E_r is the activation energy for transition from the glassy to rubbery state, R is the universal gas constant, C_1 and C_2 are constants, α is the overall conversion and Φ is an exponent accounting for the effects of chain entanglement. The plot of Eqn 13 is also presented in Fig 6. It can be seen that the equation describes well the experimental data up to gelation only ($\alpha < 0.65$). Above gelation, the viscoelastic model overestimates the T_g .

CONCLUSION

The predicted T_g values using a proposed model were in good agreement with the experimental data, verifying the assumption made to derive the model. The proposed model is believed to be applicable to any thermoset system. In addition the Di Benedetto equation and the viscoelastic model were also evaluated. However, considering the fact that our model can predict T_g as a function of mechanistic reaction parameters, it can be used more practically for T_g estimation of a thermoset polymer.

REFERENCES

1. A. V. Tobolsky, "Properties and Structure of Polymers", Now York, Wiley, 1960.
2. T. G. Fox, and P. J. Flory, *J. Appl. Phys*, Vol.21, 1950, pp581.
3. T. G. Fox, and P. J. Flory, *J. Polym. Sci*, Vol.14, 1954, pp315.
4. K. Ueberreiter, and G. Kanig, *J. Chem. Phys*, Vol.18, 1950, pp399.
5. T. G. Fox, and S. Loshaek, *J. Polym. Sci*, Vol.15, 1955, 371.
6. T. G. Fox and S. Loshaek, *J. Polym. Sci*, Vol.15, 1955, 391.
7. H. D. Heinze, K. Schmieder, G. Schnell, and K. A. Wolf, *Rub. Chem. Technol*, Vol.35, 1966, pp776.
8. K. Horie, H. Hiura, M. Sawada, I. Mita, and H. Kambe, *J. Polym. Sci. part A-1*, Vol.8, 1970, pp1357.
9. H. E. Adabbo, and R. J. J. Williams, *J. Appl. Polym. Sci*, Vol.27, 1982, pp1327.
10. M. Cizmecioglu, A. Gupta, and R. F. Fedors, *J. Appl. Polym. Sci*, Vol.32, 1986, pp6177.
11. A. T. Di Benedetto, *J. Polym. Sci : part B*, Vol.25, 1987, pp1949.
12. A. C. Grillet, J. Galy, J. P. Pascault, and I. Bardin, *Polymer*, Vol.30, 1989, pp2094.
13. S. Gand, J. C. Seferis, and R. B. Prime, *J. Thermal. Analysis*, Vol.37, 1991, pp463.
14. L. E. Nielsen, *J. Macromol. Sci, Rev. Macromol. Chem*, Vol.C3, 1969, pp69.
15. B.-G. Min, Z. H. Stachurski, J. H. Hodgkin and G. R. Heath, *Polymer*, Vol.34, 1993, pp3620.
16. J. M. Barton, *Adv. Polym. Sci*, Vol.72, 1985, pp111.
17. S. Lunak, J. Vladyka, and K. Dusek, *Polymer*, Vol.19, 1978, pp931.

Polymer (2)

EPOXY RESIN CURED BY CATIONIC LATENT THERMAL CATALYST : EFFECT OF CATALYST ON THE PHYSICAL, THERMAL AND MECHANICAL PROPERTIES

Min-Kang Seo¹, Soo-Jin Park¹, Jae-Rock Lee¹ and Douk-Rae Lee²

¹*Advanced Material Division, Korea Research Institute of Chemical Technology
P.O. Box 107, Yusong, Taejeon 305-600, Korea: psjin@pado.kRICT.re.kr*

²*Department of Textile Engineering, Chonbuk National University,
Chonju, Chonbuk 561-756, Korea*

SUMMARY: In this work, to investigate the effect of catalyst on the thermal, and mechanical properties of epoxy system, an epoxy resin based on diglycidyl ether of bisphenol-A (DGEBA) was cured by cationic latent thermal catalysts i.e., N-benzylpyrazinium hexafluoroantimonate (BPH) and N-benzylquinoxalinium hexafluoroantimonate (BQH). Differential scanning calorimetry (DSC) was undertaken for thermal characterization of the epoxy system. Near-infrared (NIR) spectroscopy was employed to examine the cure reaction between the DGEBA and the cationic latent thermal catalyst used. It was characterized in terms of impact strength and fracture toughness (K_{IC}) for the mechanical tests. Phase morphology was studied by scanning electron microscopy (SEM) of the fractured surface of samples undergone by mechanical tests. As a result, the conversion and cure activation energy of DGEBA/BQH system were also higher than those of DGEBA/BPH system. The impact and K_{IC} values of DGEBA/BQH system were also superior to those of DGEBA/BPH system, as well as the morphology. This was due to the consequence of the effect of substituted benzene group of BQH catalyst, resulting in increasing the cross-link density and structural stability of the epoxy system studied.

KEYWORDS: diglycidyl ether of bisphenol-A (DGEBA), cationic latent thermal catalyst, cross-link density, structural stability, morphology

INTRODUCTION

A curing agent or accelerator is necessary to promote the ring-opening polymerization of one or more epoxide rings as the terminal groups of the resins. Generally, a curing agent involves the use of a cross-linker such as amine and diacid anhydride. However, they have some problems such as toxicity of amine combined with low heat resistance and the deterioration of electrical properties at high temperature and humidity, which requires energy consumption resulting in the long curing process at high temperature [1].

In recent years, it is being extended to the report that the catalyst curing agents of epoxy resins have been studied in substituting the amine or anhydride agents [2, 3]. Cationic catalyst is generally used as a complex, such as BF_3 -ether, BF_3 -amine, or SbF_6 -epoxide. These complexes overcome the disadvantage of excessively rapid gelation, high hygroscopicity, and light instability [4]. Particularly, development of latent catalyst for cationic polymerization is desirable for enhancement of both the pot-life and handling of thermosetting resins [5, 6].

With a focus on long term stability and electrical properties, cationic epoxy curing has been increasingly studied. Especially, cationic latent thermal catalysts are extremely important in the field of adhesive, paints, coating, molding resin, insulation materials, matrices for composite materials, and so on [7, 8].

N-benzylpyrazinium or N-benzylquinoxalinium salts have been shown to be excellent latent thermal initiator for epoxy resins [9]. These initiators are not hygroscopic and dissolve readily in epoxy resins and exhibit a long pot-life than the more commonly used BF_3 -4-methoxyaniline complex [10]. And the initiator activity of above salts can be enhanced by decreasing the nucleophilicity of the counterion, SbF_6^- , introducing an electron-donating substituent on the phenyl ring of the benzyl group [11].

In this work, two curing agents, i.e., N-benzylpyrazinium hexafluoroantimonate (BPH) and N-benzylquinoxalinium hexafluoroantimonate (BQH) are used as the cationic latent thermal catalyst to improve the property demands of epoxy system. And the mechanical properties are investigated to study the effect of substituted benzene group of the above catalysts carried out by impact and fracture toughness (K_{IC}) tests.

EXPERIMENTAL

Materials and sample preparation

Epoxy resin used in this study was diglycidylether of bisphenol-A ((DGEBA), YD-128 supplied from Kukdo Chem Co, of Korea). Epoxide equivalent weight of the DGEBA was 185-190 g/eq. The density was 1.16 g/cm^3 at 25°C . Cationic latent thermal catalysts used in this study were N-benzylpyrazinium hexafluoroantimonate (BPH) and N-benzylquinoxalinium hexafluoroantimonate (BQH). The chemical structures of DGEBA, BPH, and BQH were shown in Fig. 1.

The 1 wt.% of catalyst (BPH, BQH) was accurately weighted into a beaker and dissolved in acetone and the epoxy containing the catalyst was stirred for 10 min and degassed for 60 min before DSC and TGA measurements. Preparation of molded parts for mechanical tests are as

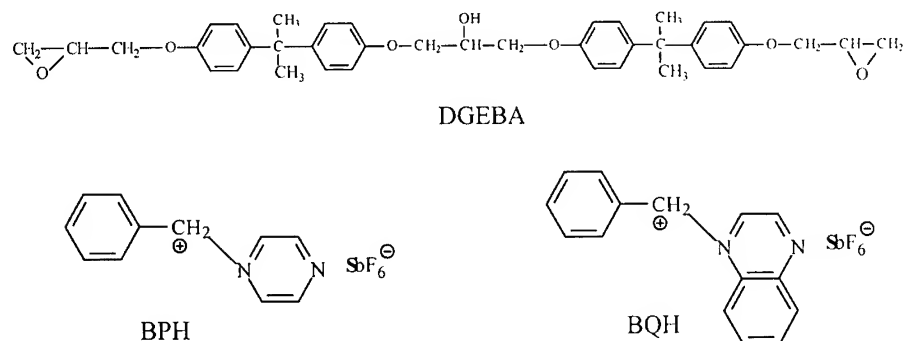


Fig. 1 Chemical structures of DGEBA, BPH and BQH.

follows: A silicon rubber spacer and steel plate were used as a mold to produce cured DGEBA/BPH and DGEBA/BQH mixture parts. And the mixture was formulated by mixing the epoxy resin at 65 °C. The reactant mixture was degassed in a vacuum oven at 60 °C before pouring it into the mold. And then the mixture was cured at 120 °C for 1 h, at 150 °C for 2 h and finally at 170 °C for 2 h in a convection oven.

Measurements

Latent properties of catalysts used were performed by the measurement of conversion as a function of curing time using isothermal DSC (Perkin Elmer Co., DSC-6) method. And DSC was also used in order to evaluate the cure activation energy (E_a) of the uncured samples. The samples were placed in aluminum sample pans and experiments were performed under a flow of dry nitrogen gas. Temperature scan were performed at different heating rate (2, 5, 10, and 20 °C/min) from room temperature to 350 °C.

A perstorp Analytical NIR System 6500 infrared spectrometer equipped with a lead sulfide detector was used to investigate the kinetics and cure behaviors of epoxy resins cured by BPH and BQH.

The Tinius Olsel Model 66 Izod Impact Tester was used for the measurement of impact strength of the cured samples. An analytical expression for K_{IC} may be characterized by single edge notched (SEN) beam fracture toughness test in three-point bending flexural and the SEN beam fracture toughness test was conducted on an Instron Model 1125 mechanical tester according to the ASTM E 339. Span-to-depth ratios of 4:1 and crosshead speed of 1 mm/min were used.

Scanning electron microscope (SEM) was used to investigate the fracture surface of impact test specimen.

RESULTS AND DISCUSSION

Fig. 2 shows the conversion of neat epoxy resin initiated by BPH and BQH as a function of curing time using isothermal DSC method. As the curing time proceeds, the conversion increases in the case of 180 °C reaction temperature. However, the conversion notably in the 50 °C reaction temperature shows no significant change with proceed of the time. This results is due to the low temperature having a limiting factor prohibiting the activity of catalysts. As a result, these indicate that this system including BPH or BQH have thermally stable latent properties at a given temperature condition in spite of the presence of external heat stimulation.

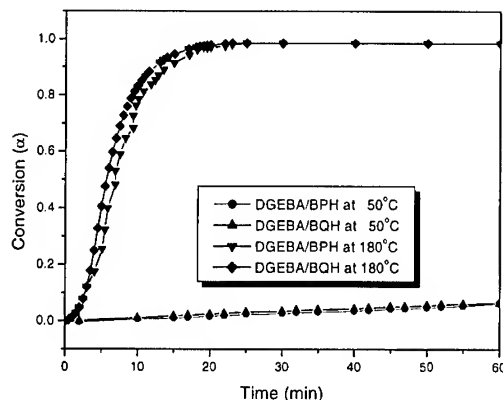


Fig. 2 Time-conversion curves of DGEBA/BPH and DGEBA/BQH system measured at 50 °C and 180 °C with curing time.

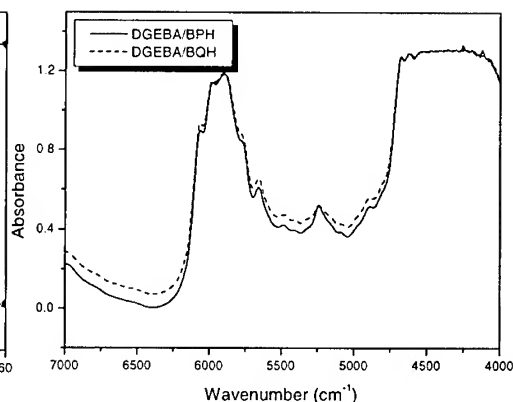


Fig. 3 Transmission spectra of uncured DGEBA/BPH and DGEBA/BQH system measured at room temperature.

Table 1 contains a list of major absorption peaks observed in this work, such as their molecular origin, and some relevant comments regarding their utility. The region from 4700 to 6500 cm^{-1} is the fingerprint section that contains specific information about the chemical structure of the resin, therefore, the section is useful for identification purpose. This zone contains the conjugated epoxy CH_2 deformation band at 4975 cm^{-1} , whose absorption intensity decreases during reaction and can therefore be used in the kinetic studied [12].

Fig. 4 shows the dynamic DSC curves for the cure of DGEBA initiated by BPH and BQH. From the exothermic peaks of DSC thermograms, these systems usually undergo more than one type of reaction, and above catalysts can be excellent latent initiator for epoxy resins without any co-initiator. These results show a similar behavior with that reported for epoxy-cured system made with aliphatic sulfonium salts [6]. Based on Gu's suggestion [6] and present DSC results, it may be considered that two separately initiated reactions occur.

The H^+SbF_6^- start the ring opening polymerization of epoxides by Lewis acid process. The presence of small exothermic peaks in the low temperature region may be the evidence of the reaction between epoxides and BPH or BQH, and the reaction between hydroxyl groups in DGEBA and BPH or BQH. From the results, it seems to be a consideration that the gelation begins with the initiated reaction between epoxides and catalyst or between hydroxyl groups and catalyst.

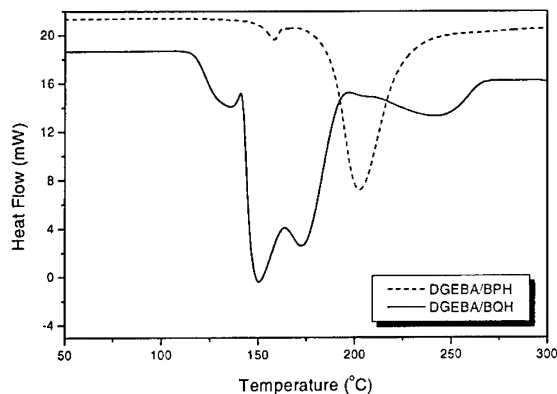


Fig. 4 DSC thermograms of uncured DGEBA/BPH and DGEBA/BQH samples.

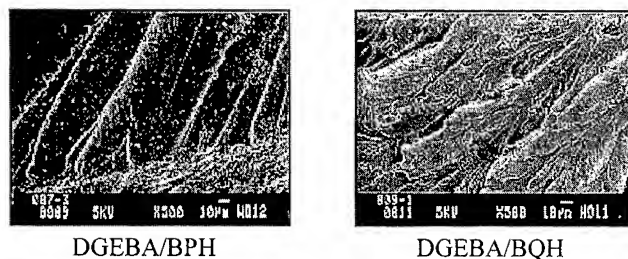


Fig. 5 SEM photographs of DGEBA/BPH and DGEBA/BQH samples after mechanical test.

The DSC scans at different heating rates allow us to determine the cure activation energy (E_a) of the overall process by Kissinger method [13].

$$\ln\left[\frac{\phi}{T_m^2}\right] = \ln\left[\frac{AR}{E_a}\right] - \frac{E_a}{RT_m} \quad (1)$$

where, ϕ is the heating rate, T_m the temperature of maximum exothermic peak, A the pre-exponential factor and R the gas constant.

The values of activation energy are 70 and 120 kJ/mol on DGEBA/BOH and DGEBA/BQH, respectively. This is probably due to the consequence of the effect of substituted benzene group that led to the increasing the cross-link density and structural stability of the epoxy system studied.

For the single edge notched (SEN) beam fracture toughness test, the value of K_{IC} is calculated by Eq 2 [14].

$$K_{IC} = \frac{P \cdot L}{b \cdot d^{3/2}} \cdot Y \quad (2)$$

where, P is the rupture force, L the span between the supports, Y the geometric factor described in ASTM E 399, and b and d the specimen width and thickness, respectively.

Table 2 represents the values of K_{IC} and impact strength of the DGEBA/BPH and DGEBA/BQH system. These results indicate that the K_{IC} and impact strength values of DGEBA/BQH system are much higher than those of DGEBA/BPH. As mentioned above, this result can be explained that it is probably due to the effect of substituted benzene group, which led to the ductile fracture properties, resulting in increasing the good resistance to the deformation and the crack initiation of epoxy system. And also, a good agreement can be found a SEM photographs of fracture surface in Fig. 5.

Table 2 Impact and K_{IC} values of DGEBA/BPH and DGEBA/BQH system

Composition	Impact strength [kg \cdot cm/cm]	Fracture toughness [K_{IC} , MPa \cdot m ^{1/2}]
DGEBA/BPH	1.2	2.6
DGEBA/BQH	1.5	3.3

CONCLUSIONS

In this work, we investigate the effect of catalyst on the cure kinetic and mechanical properties of epoxy system. As a result, the cure activation energy of DGEBA/BQH system was higher than that of DGEBA/BPH system. The impact and K_{JC} values of DGEBA/BQH system were also superior to those of DGEBA/BPH system, as well as the morphology. These results were due to the consequence of the effect of substituted benzene group of BQH catalyst, resulting in increasing the cross-link density and structural stability of the epoxy system studied.

REFERENCES

1. S. Inoue and T. Aida, "Ring-Opening Polymerization", McGraw, New York, 1967.
2. S. D. Lee, T. Takata, and T. Endo, *Macromolecules*, Vol.29, 1996, p.3317.
3. I. I. Abu-Abdoun, and A. Ali, *Eur. Polym. J.*, Vol.28, 1992, p.73.
4. C. A. May, "Epoxy Resins", 2nd Ed., Marcel Dekker, New York, 1988.
5. J. V. Crivello and J. H. Lam, *J. Polym. Sci., Polym. Chem.*, Vol.18, 1980, p.1021.
6. J. Gu, S. C. Narang, and E. M. Pearce, *J. Appl. Polym. Sci.*, Vol.30, 1985, p.2997.
7. H. Lee, K. Neville, "In Handbook of Epoxy Resins", McGraw-Hill, New York, 1967.
8. S. D. Senturia, N. F. Sheppard, Jr, "In Advances in Polymer Science", Vol.80, in epoxy resins and composites IV, Springer Verlag, Berlin, 1986, pp.1-47.
9. Y. C. Kim, S. J. Park, and J. R. Lee, *Polym. J.*, Vol.29, 1997, p.759.
10. K. Morio, H. Murase, H. Tsuchiya, and T. Endo, *J. Appl. Polym. Chem.*, Vol.32, 1985, p.5727.
11. J. A. Mcgown and L. J. Mathias, *Polym. Comp.*, Vol.18, 1997, p.348.
12. R. F. Goddu and D. A. Delker, *Anal. Chem.*, Vol.30, 1958, p.2013.
13. H. E. Kissinger, *Anal. Chem.*, Vol.29, 1957, p.1702.
14. M. C. Chen, D. J. Hourston, and W. B. Sun, *Eur. Polym. J.*, Vol.31, 1995, p.199.

THERMAL STABILITY AND CURE BEHAVIOR ON EPOXY/POLYURETHANE BLEND SYSTEM

Soo-Jin Park ¹, Joong-Seong Jin ¹, Jae-Rock Lee ¹, and Pyong-Ki Pak ²

¹ Advanced Material Division, Korea Research Institute of Chemical Technology
P.O. Box 107, Yusong, Taejeon 305-600, KOREA: psjin@pado.kRICT.re.kr

² Department of Textile Engineering, Chonbuk National University
Chonju, Chonbuk 560-756, Korea

SUMMARY: The effect of different epoxy resin (EP) and polyurethane (PU) blend composition ratios on thermal stability and cure kinetics were studied with TGA and DSC. In this work, 20 phr of DDM (4,4'-diamino diphenyl methane) was used as a curing agent for a epoxy resin and the content of EP/PU was varied within 100/0~100/60 phr. From the TGA results of EP/PU blend system, the thermal stability based on initial decomposition temperature (IDT), integral procedural decomposition temperature (IPDT) and decomposed activation energy (E_d) was investigated. The thermal stability decreased with increasing the amount of PU, up to 40 phr of PU. Conversion (α) and cure activation energy (E_a) were determined by dynamic and isothermal DSC. As a result, both α and E_a were increase at 40 phr of PU. These results could be explained by the increase in reactivity between the hydroxyl group in EP and isocyanate group in PU, resulting in an increase in the crosslinking density.

KEYWORDS: epoxy resin, polyurethane, conversion, activation energy,

INTRODUCTION

Epoxy resins (EP) are well known for some unique properties, including outstanding adhesion to most surfaces, high mechanical strength, and chemical resistance. They have been used as adhesives, coatings and resin matrices for advanced composites [1]. However, it is also well known that epoxy resins are rigid and brittle in nature, and have poor crack resistance in real applications [2-3]. In order to overcome these problems, a considerable amount of study has been done in the direction of toughening epoxies, with some research focused on introducing the interpenetrating polymer network (IPN) into epoxy resin [4-5].

Polyurethane (PU) elastomers are segmented copolymers consisting of "soft" segment domains derived from a macrodiol, and "hard" segment domains derived from a diisocyanate and a chain extender. Generally, the two segments are incompatible, resulting in microphase separation, which is primarily responsible for their excellent mechanical properties. The hard-segment structure, weight fraction, soft-segment structure, molecular weight, polydispersity, and crosslinking in either phase influence phase separation and copolymer properties [6].

The objective of this work is to study the with content of PU on the thermal stability and cure behavior using thermogravimetric (TGA) and differential scanning calorimeter (DSC).

EXPERIMENTAL

Materials and Sample Preparation

In this system studied, the epoxy resin was the diglycidyl ether of bisphenol A (YD-128 supplied by Kukdo Chem. Co. of Korea) and the viscosity of polyurethane (Adiprene supplied by Kangshin Ind. Co. of Korea) was 18,000 cps. Epoxide equivalent weight of the EP was 185-190 g.eq⁻¹ and the density was 1.16 g.cm⁻³ at 25 °C. The 4,4'-diamino diphenyl methane (DDM) was used to a curing agent for epoxy resin.

The content of EP/PU was varied within 100/0 ~ 100/60 phr in presence of 20 phr DDM. The EP was measured in a glass beaker and heated to melt at 50 °C for 30 min. After melting of epoxy resin, the PU was added into the beaker with DDM, and the reactants were homogenized by a strirer. And then samples were degassed in the vacuum oven at 60 °C. The homogeneous mixture was then poured into a mold and then cure cycle of a fully cured EP/PU blend system was 70 °C for 30 min, 140 °C for 2 h, and finally post-cured 200 °C for 1 h.

Analysis

Thermal stabilities were performed using a DuPont TGA-2950 and the samples (5 to 10 mg) were heated from 30 to 850 °C with the heating rate of 10 °C.min⁻¹. Cure behaviors on EP/PU blend system were measured using a TA Instruments DSC. Small sample quantities were then placed in hermetically sealed aluminum pans. Thermal equilibrium of the sample and reference holder was achieved in less than 1 min, and 30 ml.min⁻¹ of nitrogen gas was introduced into the DSC cell.

RESULTS AND DISCUSSION

Thermal Stabilities

From the TGA results, some factors of thermal stability including initial decomposition temperature (IDT), temperature of maximum rate of weight loss (T_{max}), and integral procedural decomposition temperature (IPDT) [7-8] have decreased values with increasing the content of PU, up to 40 phr of PU. But, at 40 phr of PU, they have increased, as shown in Table 1.

Thermal degradation is progressed by the etherfication, subsequently proceeded via dehydration and thermal oxidation, which results in the scission of network chains [9]. The behavior is possible to measure the energy of activation for the decomposition of resins. Decomposed activation energy, E_a , is calculated from TGA curves by integral method of Horowitz and Metzger [10], as follows:

Table 1. Thermal stability of EP/PU blend system of cured specimens

Compositions	IDT	T_{max} [°C]	$A^* \cdot K^*$	IPDT [°C]
100 : 0	315	394	0.5098	448
100 : 10	310	393	0.4907	431
100 : 20	303	389	0.4842	427
100 : 40	325	396	0.5172	454

100 : 60 301 388 0.4714 416

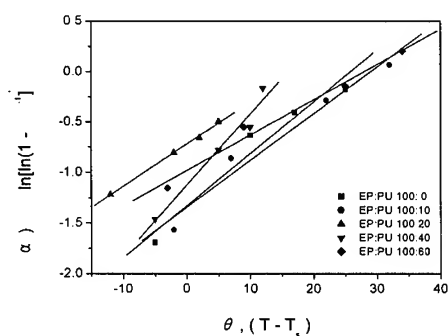


Fig. 1. Plots of $\ln[\ln(1-\alpha)^{-1}]$ vs. θ for thermally cured specimens

Table 2. Decomposed activation energies of EP/PU system of cured specimens

Compositions	$\ln[\ln(1-\alpha)^{-1}]$	$\theta [T-T_s]$	E_a/RT_s^2	$E_t [\text{kJ.mol}^{-1}]$
100 : 0	-1.6932	-5	-0.0520	183
	-0.6329	10		
	-0.4063	17		
	-0.1752	25		
100 : 10	-1.5689	-2	0.0461	165
	-0.8637	7		
	-0.2866	22		
	0.0650	32		
100 : 20	-1.2184	-12	0.0408	147
	-0.8068	-2		
	-0.6587	2		
	-0.4963	5		
100 : 40	-1.4647	-5	0.0525	192
	-0.7790	5		
	-0.5557	10		
	-0.1656	12		
100 : 60	-1.1561	-3	0.0351	130
	-0.5543	9		
	-0.1449	25		
	0.2023	34		

$$\ln[\ln(1-\alpha)^{-1}] = \frac{E_a \theta}{RT_{\max}^2} \quad (1)$$

where α is decomposed fraction, T_{\max} temperature of maximum rate of weight loss, $\theta = T - T_{\max}$, and R gas constant.

The plot of $\ln[\ln(1-\alpha)^{-1}]$ vs. θ are shown in Fig. 1. From slope of these straight lines, the decomposed activation energy of the blend is determined in Eq (1). As shown in Table 2, it is observed that the decomposed activation energy shows the highest value at 40 phr of PU. These results can be explained by the hydrogen bonding between hydroxyl group in EP and isocyanate group in PU

Cure Behaviors

In this study, the kinetic expressions derived from Ozawa's [11] method expression are used to investigate the cure behaviors. These expressions allow a calculation of the kinetic parameters through a relationship between the heating rates occurs. Ozawa's equation for cure behaviors is follow:

$$\log \phi = A' - 0.4567 \frac{E_a}{RT_p} \quad (2)$$

where ϕ is the heating rate, A' the constant, E_a the cure activation energy, R the gas constant, and T_p a temperature where the maximum conversion rate occurs based on DSC curve

Table 3 shows the values of cure activation energy obtained by Ozawa's method with content of PU. It clearly observed that the cure activation energies of EP/PU blends show maximum value in 40 phr of PU. From these results, it is expected that the addition of 40 phr of PU can lead to a more highly cross-linking in the EP/PU blend system.

Knowledge of the kinetic rate of curing and the rate change with temperature is important and useful for predicting the chemical conversion achieved after a cure schedule. In order to correlate the heat evolution in the DSC experiment to the epoxide conversion, it is necessary to assume that the heat released on reaction of an epoxide group is the same regardless of the type of epoxy or the nature of the reaction. The conversion rate, $d\alpha/dt$, as a function of time, t , was calculated from the rate of heat flow measured in isothermal DSC experimental, dH/dt , as follow:

$$\frac{d\alpha}{dt} = \frac{(dH/dt)_i}{\Delta H_{dyn}} = \frac{1}{H_i} \cdot \frac{\Delta H_i}{\Delta H_{dyn}} \quad (3)$$

where the average value of the total heat, ΔH_{dyn} developed during the dynamic DSC tests was taken as the basis for the ultimate fractional conversion, $\alpha=1$, and dH/dt is the differential value of heat time t .

Table 3. Activation energies obtained by Ozawa equation

Compositions	Kinetic factors	2 °C	5 °C	10 °C	20 °C	Cure activation energy, E_a [kJ.mol ⁻¹]
100 : 0	$1/T_p (\times 10^{-3})$	2.50	2.37	2.27	2.17	55.6
	$\log \phi$	0.301	0.699	1	1.301	
100 : 10	$1/T_p (\times 10^{-3})$	2.55	2.42	2.31	2.21	53.7
	$\log \phi$	0.301	0.699	1	1.301	
100 : 20	$1/T_p (\times 10^{-3})$	2.58	2.45	2.34	2.23	53.0
	$\log \phi$	0.301	0.699	1	1.301	
100 : 40	$1/T_p (\times 10^{-3})$	2.59	2.47	2.37	2.27	57.5

	$\log \phi$	0.301	0.699	1	1.301	
	$1/T_p (\times 10^{-3})$	2.62	2.50	2.38	2.28	
100 : 60	$\log \phi$	0.301	0.699	1	1.301	52.8

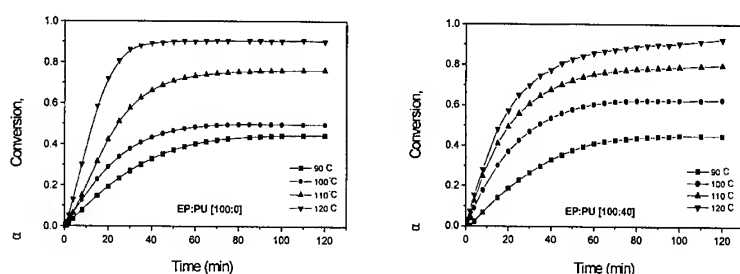


Fig. 2. Conversion as a function of time at different temperatures measured.

By partial integration of the Eq (3), the fraction conversion as a function of time was obtained.

$$\alpha = \frac{1}{H_t} \int_0^t \left(\frac{dH}{dt} \right) dt = \frac{\Delta H_t}{\Delta H_{dyn}} \quad (4)$$

Fig. 2 is shown the conversion (α) curves for the EP/PU blend system as a function of time in content of PU 0 and 40 phr. From the Fig. 2, α and cure reaction rate are increased with the increasing the cure temperature. And, α is decreased with increasing the PU to EP, up to 40 phr of PU. But, at 40 phr of PU, it is shown the maximum value. Up to 20 phr of PU, EP and PU can not completely react due to small quantities of PU and DDM less than stoichiometric ratio. These results are due to the increasing of crosslinking density between hydroxyl group in EP and isocyanate group in PU.

CONCLUSION

In this work, thermal stability and cure behavior of EP/PU blend system were studied using TGA and DSC. It reveals that presence of intermolecular hydrogen bonding between the hydroxyl group in EP and isocyanate group in PU makes an important role in increasing good network interlocking in the IPN formation. As the experimental results, the addition of 40 phr of PU in the blends appears to increase the thermal stability, such as IPDT and E_t , and crosslinking density.

REFERENCES

1. Varik, A. Ille, A. Vig, I. Czajlik, and I. Rusznak, *Radiat. Phys.Chem.*, Vol. 47, 1996, pp.457.
2. C. A. May, "Epoxy resins: Chemistry and Technology", 2nd Ed., Marcel Dekker, New York, 1988, pp.551.
3. J. D. LeMay, F. N. Kelly, "Structure and Ultimate Properties of Epoxy Reins" (Ed. K. Dusek), New York, 1986, pp.115.
4. S. J. Park, W. B. Park and J. R. Lee, *Polym. J.*, Vol. 31, 1999, pp.28.

5. L. H. Sperling and C. E. Carraher, *Polym. Mater. Sci. Eng.*, Vol. 60, 1991, pp.222.
6. W. Meckel, W. Goyert, and W. Wieder, "Thermosetplastic Elastomers" (Eds N. R. Legge, G. Holden, and H. E. Schroeder), Hanser, Munich, 1987, pp.13.
7. C. D. Doyle, *Anal. Chem.*, Vol. 33, 1961, pp.77.
8. G. H. Kwak, S. J. Park, J. R. Lee, and S. K. Hong, *Polymer(Korea)*, Vol. 23, 1999, pp.281.
9. D. J. Hourston and J. M. Lane, *Polymer*, Vol. 33, 1992, pp.1379.
10. H. H. Horowitz and G. Metzger, *Anal. Chem.*, Vol. 35, 1963, pp.1464.
11. T. Ozawa, *Bull. Chem. Soc. Jpn.*, Vol. 38, 1965, pp.1881.

Enhancing the fracture toughness of epoxy resins with amine terminated PES-CTBN-PES triblock copolymers

H. R. Kim¹, B. Y. Myoung¹, J. I. Yuck², T. H. Yoon¹

¹Department of Materials Science and Engineering
Kwangju Institute of Science and Technology, Kwangju, 500-712, KOREA:thyoon@kjist.ac.kr

²Agency for Defense Development
P.O. Box 35, Tae-Jon, KOREA

SUMMARY: PES-CTBN-PES tri-block copolymers were synthesized from amine terminated PES oligomers and commercial CTBN13 rubber, which was designed to have amine termination and the molecular weight of 15,000 g/mole. The copolymers were utilized to modify diglycidyl ether of bisphenol-A (DGEBA) epoxy resin, and loading of copolymer was varied from 5 to 40wt.%. Epoxy resins cured with 4,4'-diaminodiphenylsulfone (DDS) were subjected to the measurement of thermal properties, K_{IC} fracture toughness, flexural properties and solvent resistance, and also to SEM analysis in order to elucidate toughening mechanism. The copolymer toughening provided 2.2 MPa m^{0.5} of K_{IC} fracture toughness at 40% loading, but flexural properties were not deteriorated.

KEYWORDS: epoxy resin, block copolymers, fracture toughness, flexural properties, toughening

INTRODUCTION

Epoxy resins have been utilized in the high performance composites applications due to their excellent properties such as good mechanical and adhesive properties, excellent solvent resistance and dimensional stabilities. However, the major drawback of epoxy resin is inherent brittleness, resulting in the tremendous research on the improvement of poor toughness of epoxy resin (1). Epoxy resins can be modified with rubbers (2-3) thermoplastic polymers (4-7), and core/shell particles (8-9). However, incorporation of rubber deteriorated excellent thermal properties of epoxy resin, while thermoplastic polymer toughening decreased processability and core/shell had a problem of dispersability. Recently, a multi-phase modified systems, such as the ternary blends of rigid-rigid polymers and rigid-soft polymers with epoxies, have been investigated (10-12). These blends exhibited a synergistic effect, but showed some drawbacks such as limited solubility of thermoplastic and poor thermo-mechanical properties of rubber phase.

In this study, PES-CTBN-PES triblock copolymers were synthesized from amine terminated PES oligomers and commercial CTBN, and were utilized to toughen epoxy resins. K_{IC} fracture toughness, flexural properties, thermal properties and solvent resistance were evaluated, and SEM analysis was carried out to elucidate toughening mechanism. The properties of copolymer toughened epoxy resins were compared with those of samples

modified by blends of PES and CTBN.

EXPERIMENTAL

Synthesis and characterization of PES-CTBN-PES triblock copolymers

PES-CTBN-PES triblock copolymers were synthesized from commercial CTBN (1300x13, $M_n=3,200$ g/mol) and amine terminated PES oligomers ($M_n=5,500$ g/mol) which were prepared as previously reported in the literature (9). The triblock copolymers were designed to have amine end group and the molecular weight of 15,000g/mol. Intrinsic viscosity was measured in chloroform at 25°C using an Ubbelohde viscometer. The thermal behaviors were measured by a differential scanning calorimetry (DSC, TA 2010) and by a thermogravimetric analyzer (TGA, TA 2050) at 10°C/minute in air. The end group titration was performed with an Auto-titrator 670 (Metrohm) and the structure of copolymers was confirmed by the analysis of FT-IR (Perkin Elmer 2000).

Curing and Toughening of Epoxy Resins

DGEBA epoxy resin was cured with 4,4'-DDS, and toughened with amine terminated PES-CTBN-PES tri-block copolymer. The epoxy resins were also modified with PES/CTBN blend, or CTBN, and the ratio of PES/CTBN in a blend was 2:1. Epoxy resin was cured with DDS at 130°C for 5 hours and additional 2 hours at 220°C. If the tougheners were amine terminated, the amount of amine curing agent was carefully calculated not to upset the stoichiometry.

Properties of Toughened Epoxy Resins

The Tgs of the cured epoxy resins were measured by dynamic mechanical analyzer (DMA-983, TA Instrument) in a resonant mode at a amplitude of 0.2mm with a samples of 3x10x60mm and by differential scanning calorimetry (DSC, TA 2010) at a heating rate of 10°C/minute. The thermal stability of the samples were characterized by thermogravimetric analyzer (TGA, TA 2050) at 10°C/minute in air.

The plane strain fracture toughness (K_{IC}) of epoxy resin was measured with Single-Edge-Notched Bending (SENB, 3x6x40mm) specimens, following ASTM Standard D-5045-91. The samples were tested in 3-point bending mode with an Instron (Model 5567) at a cross-head speed of 12.5mm/minute. The fracture surface was analyzed with SEM (JEOL, JSM-5600) at 10kV in order to investigate the phase separation behaviors.

The flexural properties were measured with a specimen of 3x6x60mm at a 3-point bending mode, following ASTM D790M-86. The samples were tested with an Instron 5567 at a cross-head speed of 1.0mm/minute until failure occurred and 5 samples were tested.

RESULTS AND DISCUSSION

Characteristics of PES-CTBN-PES tri-block Copolymers

The molecular weights of amine terminated PES-CTBN13-PES copolymers were 17,072 g/mole by titration of amine end groups, while the intrinsic viscosity was 0.17dl/g. The Tg of copolymer was -27 and 160°C, and exhibited better thermal stability than CTBN. From FT-IR, disappeared broad O-H stretching of CTBN at 3400-3250 cm^{-1} and new peaks of C=O stretch absorption at 1650 cm^{-1} possibly from the amide bonds also support the formation of

copolymer.

Thermal behaviors of toughened epoxy samples

T_g of the toughened epoxy samples were -15 and 185°C with CTBN, -13 and 209°C with the blend of CTBN/PES(5.5k), and -12 and 217°C with 15k PES-CTBN13-PES copolymer at 20wt.% loading by DMA, compared to 223°C with control epoxy samples. The upper T_gs at around 185~217°C could be corresponding to the epoxy/PES phase, while the lower ones at around -15~-12°C could be attributed to the CTBN rubber. The TGA analysis indicated that PES-CTBN13-PES copolymer toughened epoxy sample showed much better thermal stability than CTBN or CTBN/PES blend toughened epoxy sample (Figure 1).

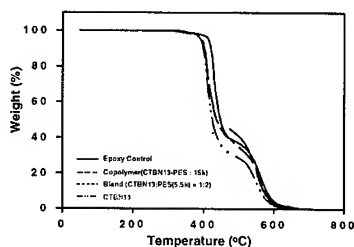


Fig. 1. TGA thermogram of toughened epoxy resins

Mechanical Properties of toughened epoxy resins

The maximum loading of CTBN was 20wt.% without utilizing solvent, which provided the K_{IC} fracture toughness of 1.2 MPa m^{0.5}, compared to 0.56 MPa m^{0.5} with the epoxy control sample (Figure 2). As expected, the epoxy resins toughened by the blends of CTBN/PES provided K_{IC} fracture toughness of 1.63 at 40wt.% loading. However, K_{IC} fracture toughness of PES-CTBN-PES copolymer toughened epoxy resins showed 2.21 MPa m^{0.5} at 40% and increased in two step manner; slowly at low loadings but rather rapidly at high loadings.

The flexural strength and modulus of control sample were 133MPa and 2.4GPa, respectively and decreased as the loading of toughener increased. The flexural properties did not decreased significantly with PES-CTBN13-PES copolymer, showing 120MPa and 2.1GPa at 40wt.% loading, compared to 105MPa and 1.8GPa with the blend of CTBN/PES (Figure 3). However, CTBN toughened epoxy samples showed a considerable drop in flexural strength and flexural modulus, providing 63MPa and 1.4GPa at 20wt%, which can be attributed to the soft rubber domain.

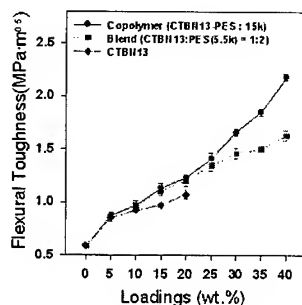


Fig. 2. K_{IC} fracture toughness of toughened epoxy resins

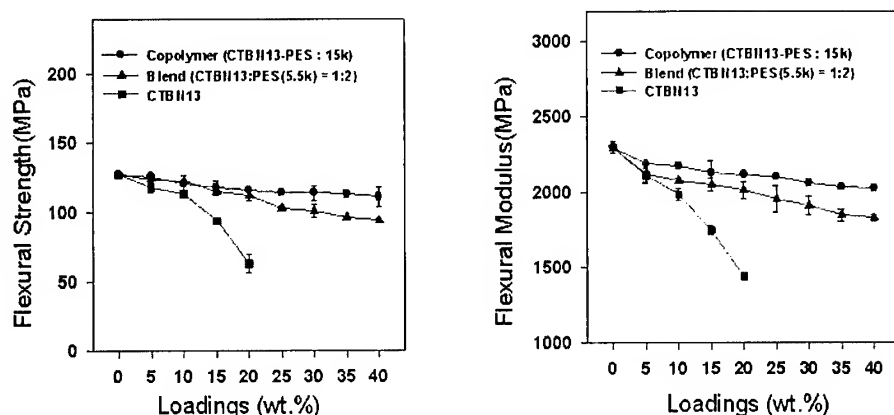
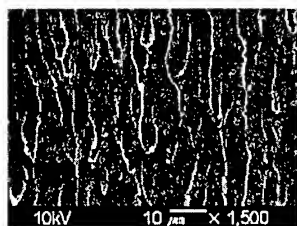


Fig. 3. Flexural properties of toughened epoxy resins

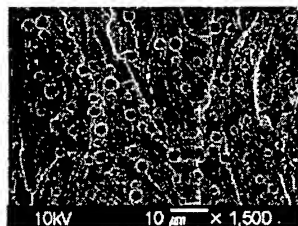
Fracture Surface Analysis by SEM

The epoxy control samples showed a featureless, shiny fracture surface, while the CTBN toughened epoxy samples showed a second. As the loading of CTBN increased up to 15wt.%, only the number of spheres increased, but the size was almost constant; 2-3 μm . At 20wt.% loading, however, the size of CTBN domain jumped to approximately 50 μm . Similar phase separation behavior was observed from the CTBN/PES blend toughened epoxy samples.

The fracture surface of PES-CTBN13-PES copolymer toughened epoxy samples showed good phase separation behavior; 0.5 μm spheres up to 20wt.% loading, but 5 μm spheres at 30 and 40wt.% loading (Figure 4). The copolymer toughened samples exhibited core/shell structure of second phase, which could be responsible for the highly enhanced fracture toughness, owing to the internal cavitation of CTBN core and ductile fracture of rigid PES shell. In addition to this, it can be attributed to the shear yielding of epoxy matrix and good interfacial adhesion between epoxy matrix and second phases.



(A)



(B)

Fig. 4. SEM micrographs of copolymer toughened epoxy resin (A:10%, B:40%)

CONCLUSIONS

Amine terminated PES-CTBN-PES triblock copolymers were synthesized from poly(arylene ether sulfone)s (PES) oligomers and commercial CTBN rubbers and utilized for the toughening of epoxy resins. The major finding are summarized as follow:

1. The amine terminated PES-CTBN-PES copolymers were successfully prepared, which were confirmed by end group titration, GPC, viscosity measurement, thermal analysis and FT-IR
2. The epoxy samples toughened with PES-CTBN-PES copolymers showed K_{IC} fracture toughness of $2.2 \text{ MPa m}^{0.5}$ at 40wt.% loading without loss of mechanical properties and thermal properties, compared with xxx and yyy with CTBN/PES blend and CTBN, respectively.
3. The remarkably enhanced fracture toughness with the amine terminated PES-CTBN-PES copolymer could be attributed to the internal cavitation of the rubbery core and ductile fracture of PES shell in the core (CTBN)/rigid shell(PES) second phase
- 4.

ACKNOWLEDGEMENT

This work was supported by the Brain Korea 21 Project.

REFERENCES

1. Bryan Ellis, *Chemistry and Technology of Epoxy Resins*, Chap. 3, Blackie Academic & Profession, New York, 1993
2. A. F. Yee and R. A. Pearson, *J. Mater. Sci.*, Vol. 21, 1986, pp. 2462
3. S. Kunz-Douglass, P. W. R. Beaumont and M. F. Ashby, *J. Mater. Sci.*, Vol. 15, 1980, pp. 1109,
4. T. H. Yoon, Duane B. Priddy Jr., Gregory D. Lyie and J. E. McGrath, *Macromol. Symp.* Vol. 98, 1995, pp. 673
5. J. L. Hedrick, I. Yilgor, M. Jurek, J. C. Hedrick, G. L. Wilkes and J. E. McGrath, *Polymer*, Vol. 32, 1991, pp. 2020
6. Bucknall C. B. and Gibert A. H., *Polymer*, Vol. 30, 1989, pp. 213
7. J. K. Kim and R. E. Robertson, *J. Mater. Sci.*, Vol. 27, 1992, pp. 161
8. S. K. Son, S. T. Kim, S. I. Hong, J. K. Kim, and C. R. Choe, *Polymer(Korea)*, Vol. 20, 1996, pp. 383
9. J. Y. Qian, R. A. Pearson, V. L. Dimonie, O. L. Shaffer and A. S. El-Aasser, *Polymer*, Vol. 38, 1997, pp. 21
10. S. T. Kim, J. K. Kim, C. R. Choe and S. I. Hong, *J. Mater. Sci.*, Vol. 31, 1996, pp. 3523
11. H. J. Sue and A. F. Yee, *J. Mater. Sci.*, Vol. 24, 1989, pp. 1447
12. J. Qin, A. S. Argon and R. E. Cohen, *J. Appl. Polym. Sci.*, Vol. 71, 1999, pp. 2319

Analysis (1)

CRIPPLING BEHAVIOR OF GRAPHITE/EPOXY COMPOSITE STRINGERS

Jin-Hwe Kweon

*Division of Aerospace and Mechanical Engineering, Gyeongsang National University
Research Center for Aircraft Parts Technology
900, Gazwa-dong, Chinju, Kyongnam 660-701, Korea: jhkwon@nongae.gsnu.ac.kr*

SUMMARY: A nonlinear finite element method for the crippling analysis of composite laminated stringers is presented. Composite stringer is idealized by the nine-node laminated shell element based on the first order shear deformation theory. The stiffness degradation by the local failure is simulated by the complete unloading method. A modified arc-length algorithm is incorporated into the nonlinear finite element method to trace the post-failure equilibrium path after local buckling. Finite element results are compared with those by experiments and show the excellent correlation. The parametric study is performed to assess the effect of the flange width and web height on the crippling and buckling stress of stringers.

KEYWORDS: Crippling, Local Buckling, Failure, Composite Stringer, FEM

INTRODUCTION

When a stringer consisting of thin web and flange is loaded in compression, the local buckling of the flange or web occurs prior to the global buckling or compressive catastrophe. Once the flange or web is locally buckled, external load is concentrated to the straight corner. The concentrated load induces the local failure at the corner, and the failure degrades the structural capability resisting to compression. As the results, stringer collapses at the much lower stress level than the material strength. This is the crippling failure. So far, only the experiment has been recommended as the method to evaluate the crippling stress of the composite stringer. Although several trials by the finite element method have been conducted[1-4], the effect of the progressive stiffness degradation was not included in the researches. The motive of this study is to investigate the applicability of the finite element method to calculate the crippling stress of the composite stringers.

To solve the crippling problem by finite element method, postbuckling and post-failure analyses are required. The nonlinear finite element formulation for the postbuckling analysis of composite shell by Jun and Hong[5] can be used for the crippling analysis of stringers. As for the progressive analysis after initial failure, various stiffness degradation methods have been presented.[6-9] Among them, the complete unloading model[7] is the most conservative stiffness degradation model. In addition to the failure model, when selecting the stiffness

degradation method, numerical method for the iteration should be considered. Previous study[10] on the post-failure analysis showed that the conventional arc-length method[11, 12] must be modified for postbuckling analysis when the complete unloading model is employed.

In this study, the crippling behavior of Z-section graphite/epoxy composite stringer is investigated by the nonlinear finite element method based on the updated Lagrangian formulation. For the finite element idealization, nine-node degenerated shell elements are used with the first order shear deformation theory. For the stiffness degradation after initial failure, complete unloading model is implemented into the finite element method. To trace the equilibrium path after failure, a modified arc-length method is introduced. Proposed finite element method is validated by the experimental result. Also, the parametric study to evaluate the effects of the flange width and web height on the crippling and local buckling stress of Z-section stringers is performed.

FINITE ELEMENT FORMULATION

Stiffness Degradation Model

The maximum stress method is employed as the failure criteria, because in which the failure modes can be clearly defined. To degrade the stiffness of the failed area, the complete unloading model[7] is used. In the model, the stress component corresponding to the failure mode of each layer is assumed to be completely unloaded and the stiffness to be zero. This stiffness degradation method shows the excellent performance for the brittle materials like the graphite/epoxy composite with the negligible plastic deformation. Also, this model most conservatively evaluates the load-carrying capacity after local failure of the structure.

Numerical Method for Complete Unloading Failure Model

Main difference of the present modified arc-length algorithm from the conventional arc-length scheme is the method to determine the arc-length. In the present modified arc-length method, the effect of the deformation by failure is considered when determining the arc-length, but not in the conventional arc-length method. A typical arc-length method without failure effect is presented by Crisfield[12]. The difference of the present arc-length method comes from the stiffness degradation method for progressive failure analysis. In the present method, the stress components are compared to the allowable values after the converging of iteration, and the stress and stiffness components corresponding to the failure mode are excluded instantaneously. Therefore, if failure occurs at a load step, corresponding unbalanced force arises due to the stress unloading, and consequently affects the deformation of the next load step. For the post-failure analysis, the effect of the deformation due to the failure-induced unbalanced force should be considered when determining the arc-length. For the incremental load parameter to have a real solution, the arc-length must allow the deformation corresponding to the failure-induced unbalanced force to occur. It means that not only the upper limit but also the lower limit of the arc-length should be set for the post-failure analysis.

In the present method, when a failure is detected by criteria, the failure-induced unbalanced force, $\{\Delta P_F\}$, the displacement for the force, $\{\Delta u_F\}$ and the arc-length corresponding to the displacement, Δl_F are calculated :

$$\Delta l_F = \sqrt{\{\Delta u_F\}^T \{\Delta u_F\}} \quad \text{with} \quad \{\Delta u_F\} = [K_T]^{-1} \{\Delta P_F\} \quad (1)$$

The arc-length by Eqn (1) is the lower limit of the arc-length. If no failure occur, then Δl_F and Δu_F will be zero. That seems to be a simple modification of the conventional method, but which is critical for the post-failure analysis based on the complete unloading model.

PROBLEM DESCRIPTION

Geometry and boundary conditions of the stringer are shown in Fig. 1. Effects of the flange width b_f and the web height b_w on the local buckling and crippling stress are investigated. To compare the results by present finite element method and experiment, the material properties of AS4/3502 graphite/epoxy composites are used: $E_1 = 18.5$ Msi, $E_2 = 1.64$ Msi, $G_{12} = 0.87$ Msi, $\nu_{12} = 0.3$, $X_T = 210$ ksi, $X_C = 210$ ksi, $Y_T = 7.5$ ksi, $Y_C = 29.9$ ksi, $S = 13.5$ ksi.

RESULTS AND DISCUSSION

Validation of Finite Element Analysis

Present finite element results are compared to the previous experimental data[2] in Table 1. The deviation of the finite element results from the averaged experimental values is within 10.3 % for the crippling stress and 11.4 % for the local buckling stress. The result demonstrates the present finite element algorithm can be widely used to calculate the crippling stress of the graphite/epoxy composite stringers. Figure 2 shows the load - shortening curves of the stringer by the finite element analysis and experiment when both the flange width and the web height are 1.25 inch. Finite element analyses are conducted for the stringer with and without consideration of the potted area, respectively. From the finite element results, it is proven that the potted area does not affect the local buckling and crippling stresses. However, the end shortening to the crippling becomes 12 % greater when the potted area is considered.

Buckling and Local Buckling Stress

Parametric study to evaluate the effect of the flange width and web height on the buckling and local buckling stress of the Z-section stringers was conducted. Stacking sequence considered is $[\pm 45/0/90]_s$. Buckling and local buckling stress distribution of stringers is given in Fig. 3. The figure shows the buckling stress of the stringer is very sensitive to the flange width variation, and the maximum value when b_f is about 0.5 inch.

The buckling stress has relation with the buckling mode shapes of the stringers. When the flange width is so small ($b_f \leq 0.25$ inch), the bending moment of inertia of the stringer becomes very small. The stringer behaviors like a simple plate. Initial buckling occurs as the global buckling as shown in Fig. 4(a), and the stress is not high. As the flange increases ($b_f = 0.5$ inch), the overall bending moment of inertia of the stringer increases. This means that the global buckling stress gets higher. On the contrary, as the flange width becomes bigger, effect of the constraint by the web becomes weak. Consequently, the local buckling stress of the flange becomes lower. Therefore, the global buckling of the stringer and the local buckling of the flange are coupled as shown in Fig. 4(b). In this case, initial buckling stress is higher than in the stringer showing the local buckling of flange. When the Z-section stringer has wide flange ($b_f \geq 0.75$ inch), the flange shows the local plate buckling. Corresponding boundary conditions can be approximated to be simply supported along the corner and free along the

other straight edge. Therefore, local buckling stress becomes very low, and occurs prior to global buckling or compression catastrophe. As shown in Fig. 4(c) and 4(d), corner of the stringer is still straight, not deflected into the out-of-plane direction.

Except for the stringer with 0.5 inch flange width which shows the combined buckling of local and global modes, the buckling stress is not sensitive to the variation of the web height. Overview on the results for the buckling stress of the Z-section stringer shows that the buckling stress has the maximum value when $b_f = 0.5$, $b_w = 1.0$ inch, and the corresponding buckling mode is the local-global combined one.

Crippling Stress

Effect of the flange width on the crippling stress is shown in Fig. 5. The crippling stress distribution shows some difference from that of the initial buckling stress when the flange width is bigger than 0.50 inch. The initial buckling stress shown in Fig. 3 has the maximum value at $b_f = 0.5$ inch and decreases drastically as the flange width increases or decreases. However, the crippling stress of the stringer with the flange width bigger than $b_f = 0.5$ inch is not sensitive as much as the local buckling stress and does not decrease so rapidly as the flange width increases. On the contrary, the strength of the stringer with the flange width smaller than the value, which is actually the compression strength after global buckling, shows the same trend as the buckling stress. This means that although the stringer showing global buckling may have the high initial buckling stress, the buckling directly results into the catastrophic failure because the whole stringer is bent by the global buckling. In the practical design of airframe, the stringer with wide flange showing the local buckling is frequently used. That is the reason why the crippling stress is accurately assessed for the weight-saving design of the stringer.

Similarly as in the buckling stress distribution, the crippling stress is less sensitive to the change of the web height. Even though there is a little difference according to the flange width, the stringers of web width $b_w = 1.0$ inch show the good performance to the compression load.

CONCLUSIONS

A finite element method based on the progressive stiffness degradation technique to characterize the crippling behavior of the composite stringers was presented. The finite element results were compared to previous test data for the validation, and very well correlated with the test results in the crippling and local buckling stress. Parametric study showed that the main factor affecting the crippling and local buckling behavior of Z-section stringer is flange width. On the other hand, web height does not affect so much. While the stringers of wide flange experienced the local buckling and crippling, the stringers with small flange width showed the global buckling and the buckling-induced collapse.

ACKNOWLEDGMENTS

This work was supported by grant No. 981-1003-020-2 from the Basic Research program of the KOSEF.

REFERENCES

1. E. E. Spier, "Stability of Graphite Epoxy Structures with Arbitrary Symmetrical Laminates", *Experimental Mechanics*, Vol.18, No.11, 1978, pp.401-408.

2. T. M. Wieland, J. Morton and J. H. Starnes, Jr., *Scale Effects in Buckling, Postbuckling and Crippling of Graphite-Epoxy Z-Section Stiffeners*, Report CCMS-92-25, VPI, 1992.
3. D. L. Bonanni, E. R. Johnson and J. H. Starnes, Jr., "Local Crippling of Thin-Walled Graphite-Epoxy Stiffeners", *AIAA Journal*, Vol.29, No.11, 1991, pp.1951-1959.
4. D. L. Bonanni, E. R. Johnson, and J. H. Starnes, Jr., *Local Buckling and Crippling of Composite Stiffener Sections*, Report CCMS-88-08, VPI, 1988.
5. S. M. Jun, and C. S. Hong, "Buckling Behavior of Laminated Composite Cylindrical panels under Compression", *Computers and Structures*, Vol.29, No.3, 1988, pp.479-490.
6. H. T. Hahn and S. W. Tsai, "On the Behavior of Composite Laminates after Initial Failures", *Journal of Composite Materials*, Vol.8, 1974, pp.834-855.
7. S. C. Chou, O. Orringer and J. H. Rainey, "Post-Failure Behavior of Laminates. I - No Stress Concentration", *Journal of Composite Materials*, Vol.1976, pp.371-381.
8. S. W. Tsai, *Composite Design*, Think Composite, 1988, Dayton, USA.
9. F. K. Chang and K. Y. Chang, "A Progressive Damage Model for Laminated Composite Containing Stress Concentrations", *Journal of Composite Materials*, Vol.21, 1987, pp.834-855.
10. J. H. Kwon, C. S. Hong and I. C. Lee, "Postbuckling Compressive Strength of Graphite/Epoxy Laminated Cylindrical Panels Loaded in Compression", *AIAA Journal*, Vol.33, No.2, 1995, pp.217-222.
11. E. Riks, "An Incremental Approach to the Solution of Snapping and Buckling Problems", *International Journal of Solids and Structures*, Vol.15, 1979, pp.529-551.
12. M. A. Crisfield, "A Fast Incremental/Iterative Solution Procedure That Handles Snap-Through", *Computers and Structures*, Vol.13, 1981, pp.55-62.

Table 1. Crippling and local buckling stress of $[\pm 45/0/90]_s$ stringers by finite element analysis and experiments[2].

No.	$b_f(\text{in})$	$b_w(\text{in})$	Area (in^2)	L (in)	Local Buckling Stress (ksi)				Crippling Stress (ksi)			
					FEM	Exp.	Exp. Aver.	Error* (%)	FEM	Exp.	Exp. Aver.	Error* (%)
111s	1.25	1.75	0.17	10	6.94	6.12 6.60	6.36	9.2	22.2	20.1 24.1	22.1	0.6
121s	1.00	1.75	0.15	10	10.1	8.94 9.02	8.98	13	25.8	27.9 22.8	25.4	1.7
131s	0.75	1.75	0.13	6	15.5	14.5 14.5	14.5	6.6	28.8	25.0 27.2	26.1	10.3
141s	0.50	1.75	0.11	6	19.1	16.8 17.5	17.2	11.2	31.1	28.9 28.4	28.7	8.4
211s	1.25	1.25	0.15	10	7.27	6.63 6.63	6.63	9.5	25.3	26.6 27.1	26.9	-4.6
221s	1.00	1.25	0.13	10	10.9	9.77 9.96 9.65	9.79	11.4	29.1	29.8 30.4 29.4	29.9	-2.6
231s	0.75	1.25	0.11	6	18.7	15.8 18.4 17.5	17.2	8.9	35.6	31.1 33.4 33.9	32.8	8.5
241s	0.50	1.25	0.09	6	31.8	28.7 29.8	29.3	8.8	38.1	36.3 36.6	36.5	4.5

* Error = $|FEM - Exp. / Exp. \times 100\%$

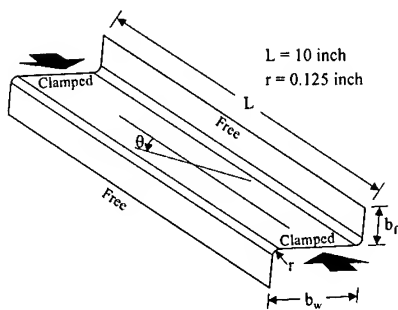


Fig. 1 Stringer Geometry and boundary conditions

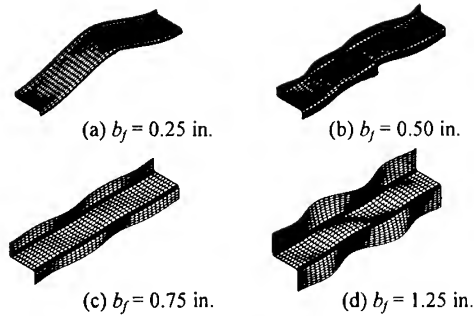


Fig. 4 Effect of flange width on buckling mode shape ($b_w = 1.75$ inch).

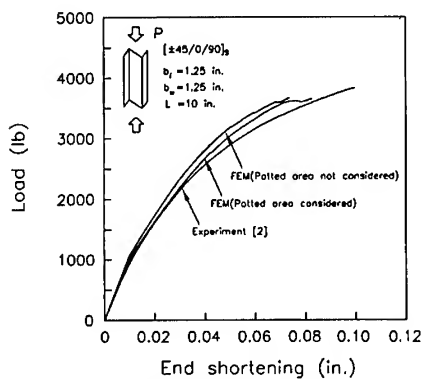


Fig. 2 Load-displacement curves by finite element method and experiment.

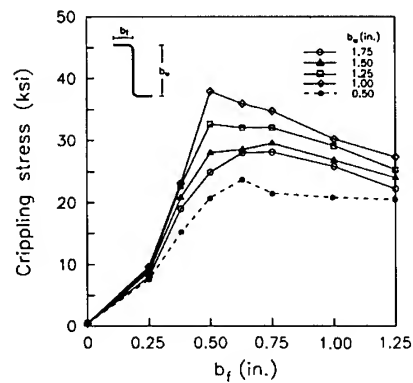


Fig. 5 Effect of flange width and web height on crippling stress.

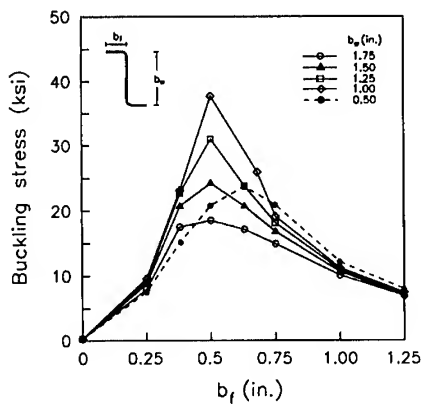


Fig. 3 Effect of flange width and web height on buckling stress.

PREDICTION OF DAMAGE GROWTH IN COMPOSITE LAMINATES BY FRACTURE SIMULATION METHOD BASED ON FEM

Yoshinobu SHIMAMURA¹, Akira TODOOROKI¹, Hideo KOBAYASHI¹,
and Haruo NAKAMURA¹

¹ *Department of Mechano-Aerospace Engineering, Tokyo Institute of Technology
O-okayama 2-12-1, Meguro-ku, Tokyo 152-8552, Japan: yshimamu@ginza.mes.titech.ac.jp*

SUMMARY: Recently, applications of integrated large composite structures have been attempted to many structures of vehicles. To improve the cost performance and reliability of the integrated composite structures, it is necessary to judge the structural integrity of the composite structures. In order to analyze the damage growth of composite laminates inexpensively, we have developed a fracture simulation technique using FEM with plane stress elements that includes both intralaminar and interlaminar fracture mechanisms. This approach does not require thickness-direction analysis. Analytical damage growth and stiffness degradation of CF/epoxy laminate with an open hole were compared with experimental results. As a result, it is shown that the proposed simulation method can roughly predict the damage growth and stiffness degradation of composite laminates.

KEYWORDS: Simulation, Damage Growth, Finite Element Method

INTRODUCTION

Recently, applications of integrated large composite structures have been attempted to many structures of vehicles. To improve the cost performance and reliability of the integrated composite structures, it is necessary to judge the structural integrity of the composite structures with defects that were found by nondestructive inspection. For the judgement, we need a fracture simulation technique of composite structures. Many researches on the fracture simulation method using FEM have been reported by now. The main objective in the studies, however, is to predict fracture strength of structures, and damage propagation of composite laminates has not been investigated in detail. Most of the researches carried out simulations considering only intralaminar fracture mechanisms, and did not consider delamination. Several papers have reported the delamination simulation [1][2][3][4], but all these reports require three-dimensional elements or quasi three-dimensional elements for FEM analysis. The analyses are very expensive and time-consuming.

In order to analyze the damage growth of composite laminates inexpensively, we have developed a fracture simulation technique using FEM with plane stress elements that includes

both intralaminar and interlaminar fracture mechanisms. For the intralaminar fractures, i.e. matrix cracking and fiber breaking, stiffness degradation of laminae is applied to the fractured laminae, and stress-strain matrices of elements are calculated based on the classical lamination theory. For the interlaminar fracture, i.e. delamination, stiffness degradation of elements based on improved lamination theory is applied to the delaminated elements. This approach does not require thickness-direction analysis. Analytical damage growth and stiffness degradation of CF/epoxy laminate with an open hole were compared with experimental results. As a result, it is shown that the proposed simulation method can roughly predict the damage growth and stiffness degradation of composite laminates.

SIMULATION PROCEDURE

Judgement of Intralaminar Fractures

Tsai-Hill criterion was adopted as a fracture criterion of intralaminar fractures.

$$\left(\frac{\sigma_L}{F_{Lt}}\right)^2 - \frac{\sigma_L \sigma_T}{F_{Lt}^2} + \left(\frac{\sigma_T}{F_{Lt}}\right)^2 + \left(\frac{\sigma_{LT}}{F_{LT}}\right)^2 = 1 \quad (1)$$

where σ_L , σ_T , σ_{LT} are longitudinal stress, transverse stress and shear stress, respectively, and F_{Lt} , F_{Lc} and F_{LT} are longitudinal tension strength, longitudinal compress strength and shear strength, respectively. If compressive stress components are involved, the corresponding compressive strength should be used.

Fiber breaking of the lamina is judged if $\sigma_L \geq F_{Lt}$ or $\sigma_L \leq F_{Lc}$, and matrix cracking of the lamina is judged if $F_{Lc} \leq \sigma_L \leq F_{Lt}$, where F_{Lc} is longitudinal compress strength. Stiffness degradation of the lamina that was judged as intralaminar fractures is as follows.

$$\begin{aligned} \text{Matrix cracking: } E_T^* &= \frac{1}{100} E_T, G_{LT}^* = \frac{1}{100} G_{LT} \\ \text{Fiber breaking: } E_L^* &= \frac{1}{100} E_L, E_T^* = \frac{1}{100} E_T, G_{LT}^* = \frac{1}{100} G_{LT}, \nu_{LT}^* = \frac{1}{100} \nu_{LT} \end{aligned} \quad (2)$$

where E_L , E_T , G_{LT} , ν_{LT} are longitudinal modulus, transverse modulus, shear modulus and major Poisson's ratio, respectively, and superscript * means degraded modulus.

Judgement of Interlaminar Fracture

In the present approach, delamination is regarded as stiffness degradation of plane stress elements of FEM. From the difference between total strain energy before and after delamination, we can estimate the total strain energy release rate G of the elements due to delamination. If strain components $\{\epsilon_1 \ \epsilon_2 \ \epsilon_6\}$ are unchanged before and after delamination, the total strain energy release rate G is expressed as

$$G = \left(\frac{1}{2} \epsilon^T D_{lam} \epsilon - \frac{1}{2} \epsilon^T D_{delam} \epsilon \right) \cdot St / S \quad (3)$$

where D_{lam} and D_{delam} are stress-strain matrices of the laminate without and with delamination, respectively, and S , t are the element area, element thickness, respectively [5]. It is assumed that longitudinal moduli of X direction and Y direction are calculated independently by using Whitcomb and Raju's method [6].

A criterion of delamination onset is described as

$$G > G_C \quad (4)$$

where G_C is the critical energy release rate.

Simulation Procedure

The simulation procedure is described as follows.

- (1) The D matrix is calculated based on the classical lamination theory.
- (2) Strain components of each element are determined by FEM analysis with 2-dimensional plane stress elements.
- (3) Stress components of each lamina are calculated using the classical lamination theory.
- (4) A fractured lamina or a delaminated element is estimated one by one according to Yamada's method [7].
- (5) Degradation of stiffness is applied to the fractured lamina or the delaminated element.
- (6) The above process is repeated until a given displacement is achieved.

In the simulation, triangle plane stress elements are adopted. In each element, an additional fracture is not judged after delamination for simplicity of calculation.

EXPERIMENTAL AND ANALYTICAL RESULTS

Using CFRP laminates of stacking sequence $[0_2/90_2]_S$ with an open hole, static tension tests were conducted under a displacement control. An extensometer was mounted on the specimens to measure a displacement over 50mm-gauge length. In order to observe delamination and matrix cracking, applied load was held and then unloaded at several steps. Ultrasonic inspection method (Hitachi AT5000) was used for the observation.

Damage propagation results obtained experimentally are shown in Fig. 1. In the first step, matrix cracking in 90° lamina emanated from the hole edges where the stress concentration occurred. Further increase of the displacement brought splitting in 0° lamina and local delamination between 0° lamina and 90° lamina.

Damage propagation analysis of the laminate with an open hole was conducted by using the proposed simulation method. In the analysis, a mesh division of 1952 nodes and 1068 elements was adopted, and a displacement was given at the upper edge of the mesh division. Material properties used in the analysis are listed in Table 1. In Table 1, subscripts L and T denote longitudinal and transverse, respectively.

Table 1 Material properties of CFRP

Longitudinal modulus, E_L	127.4 GPa
Transverse modulus, E_T	9.18 GPa

Shear modulus, G_{LT}	5.39 GPa
Major Poisson's ratio, ν_{LT}	0.34
Longitudinal tension strength, F_{Lt}	2370 MPa
Transverse tension strength, F_{Tt}	70 MPa
Shear strength, F_{LT}	75 MPa
Longitudinal compress strength, F_{Lc}	2370 MPa
Transverse compress strength, F_{Tc}	2370 MPa
Critical energy release rate, G_C	180 J/m ²

The results obtained from the analysis are shown in Fig. 1. Dark elements represent matrix cracking, and black elements represent delamination. Matrix cracking occurred 90° lamina from hole edges, and local delamination occurred between 0° lamina and 90° lamina from the splitting in 0° lamina. The profile of the analytical damage propagation agrees with the experimental one.

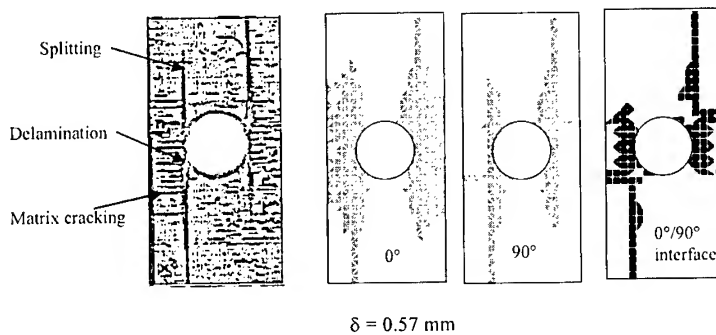


Fig. 1 Damage propagation in $[0_2/90_2]_S$ laminate

Fig. 2 shows experimental and analytical longitudinal stiffness degradation of the specimen. Solid line represents an experimental result and broken line represents an analytical result. The analytical result shows a good agreement with the experimental result.

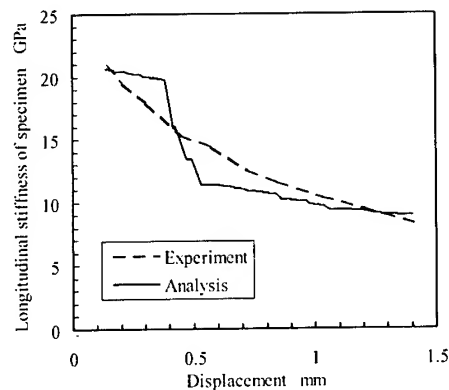


Fig. 2 Stiffness degradation of specimen

CONCLUSIONS

A FEM simulation method of damage propagation for composite laminates was proposed, and analytical results were compared with experimental results. As a result, it is shown that the simulation method can roughly predict damage propagation and stiffness degradation of composite laminates.

REFERENCES

1. Zako, M. and Tsujikami, T., "Development of Simulation Program for Delamination of Laminated Composite", *J.Soc.Mat.Sci.,Japan*, Vol. 43, No. 489, 1994, pp. 684-689 (in Japanese).
2. Chen, D.J., Chan, W.S. and Wang, B.P., "An Efficient Method to Simulate One- and Two-dimensional Delamination Growth in Composite Laminates", *Journal of Reinforced Plastics and Composites*, Vol. 15, 1996, pp. 944-957.
3. Rinderknecht, R. and Kröplin, B., "A Computational Method for the Analysis of Delamination Growth in Composite Plates", *Computers & Structures*, Vol. 64, No. 1-4, 1997, pp. 359-374.
4. Kamiya, S., Sekine, H. and Yagishita, Y., "Computational Simulation of Interlaminar Crack Extension in Angle-Ply Laminates Due to Transverse Loading", *Journal of Composite Materials*, Vol. 32, No. 8, 1998, pp.744-765.
5. Shimamura, Y., Todoroki, A., Kobayashi, H., Nakamura H. and Inada, T., "Inexpensive Simulation of Delamination Growth in Composite Plates by Using FEM with Two-dimensional Elements", *Proceedings of Computer Methods in Composite Materials VI*, Montreal, Canada, August 26-28, 1998, Hoa, S.V., De Wilde, W.P. and Blain, W.R., Eds, pp. 237-244.
6. Whitcomb, J.D. and Raju, I.S., "Analysis of Interlaminar Stresses in Thick Composite Laminates with and without Edge Delamination", *Delamination and Debonding of Materials, ASTM STP 876*, Johnson, W.S., Ed. American Society for Testing and Materials, Philadelphia, 1985, pp.69-94.
7. Miyoshi, T., Shiratori, M., Zako, M. and Sakata, S., "*Yuugenyoushou*", Jikkoushyuppan, Tokyo, 1976, pp.39-41 (in Japanese).

Effects of Mechanical Properties of Unidirectional Plies on Stress Analysis of Composite Structures

Mahmood M. Shokrieh¹ and Ashkan Bohlool²

¹Assistant Professor and ²Graduate Student
Mechanical Engineering Department
Iran University of Science and Technology
Narmak, Tehran, 16844, Iran

SUMMARY: In this article, the effects of variation of mechanical properties of unidirectional plies on stress analysis of composite structures are studied. Using differentiation technique, sensitivity coefficients are calculated. Also, the allowable magnitude of variation of mechanical properties of unidirectional plies and their effects on mechanical behavior of the structures are studied. Using a finite element technique, a method for calculation of sensitivity coefficients for nodal displacement, strain, stress and safety factor of the composite structure is established. A finite element program including a composite plane stress element is written which is able to calculate sensitivity coefficients.

As an example a plate with a hole under in-plane tensile loading is considered. Using the procedure established in this research, the variations of the stress state of the problem with respect to variation of mechanical properties of unidirectional plies is studied. Also the allowable variation of mechanical properties of unidirectional plies and their effects on mechanical behavior of the plate are calculated.

For a complicated structure the finite element analysis is performed only once and the sensitivity coefficients are calculated. Then, without using the finite element program, the variation in mechanical behavior of the structure with respect to variation of mechanical properties of unidirectional plies can be predicted by method presented in this study.

KEYWORDS: Sensitivity analysis, Finite Element, Composite Structure, Unidirectional Plies.

Introduction

In this research, the effects of change in mechanical properties of a unidirectional ply on the state of stress, strain and safety factor of a laminated composite has been studied. The main purpose is to establish a quality control criterion. Scatter in mechanical properties exists because of fabrication process of composites. This scatter causes changes in the state of stress, strain and safety factor in service of the component designed for a certain condition. Since the mechanical properties of a unidirectional ply are numerous in comparison with those of metals, it is difficult to predict the change in mechanical behavior of a component due to changes of mechanical properties of its unidirectional plies.

The sensitivity of design parameters of laminated composites due to changes of mechanical properties of unidirectional ply has been investigated for a flat plate using classical lamination plate theory in [1]. The mentioned study can give an initial

prediction for a simple plate, however for a more complicated structure with stress concentration, behavior of any point is affected by the whole structure. So, using classical lamination plate theory for sensitivity analysis of complicated structures is unsatisfactory. In this research, using finite element method., the sensitivity of design parameters of laminated composites with stress concentration due to changes of mechanical properties of constituent unidirectional plies is studied.

Finite Element Formulation of Laminated Composites

In this section an overview of finite element analysis of a laminated composite is presented [3-7].

Displacement, strain and stress fields

Let displacement vector, u , at any point in a typical element, e , with nodes i, j, \dots is approximated by a vector as a function of nodal displacements in the form of:

$$u \approx \hat{u} = \sum N_i a_i^e = [N_i, N_j, \dots] \begin{Bmatrix} a_i \\ a_j \\ \vdots \end{Bmatrix}^e = N a^e \quad \text{Eq. 1}$$

in which shape function N is a prescribed function of position and a^e is nodal displacement vector of element e . For instance, in the case of plane stress,

$$u = \begin{Bmatrix} u(x, y) \\ v(x, y) \end{Bmatrix}$$

presents the horizontal and vertical displacement of a point of the element and

$$a_i = \begin{Bmatrix} u_i \\ v_i \end{Bmatrix}$$

presents i 'th node displacement. Shape functions must be selected so that they present true displacement of element as closely as possible and satisfy convergence criteria [3].

For a known displacement at a point, the strain can be calculated as:

$$\varepsilon = S u \quad \text{Eq. 2}$$

where S is appropriate linear operator. Using Eq. 1, the above equation can be written as,

$$\varepsilon = B a^e = [B_i, B_j, \dots] \begin{Bmatrix} a_i \\ a_j \\ \vdots \end{Bmatrix} \quad \text{Eq. 3}$$

with:

$$B = S N \quad \text{Eq. 4}$$

In the case of plane stress, the strain-displacement relationship is as

$$\varepsilon = \begin{Bmatrix} \varepsilon_x \\ \varepsilon_y \\ \gamma_{xy} \end{Bmatrix} = \begin{Bmatrix} \frac{\partial u}{\partial x} \\ \frac{\partial v}{\partial y} \\ \frac{\partial u}{\partial y} + \frac{\partial v}{\partial x} \end{Bmatrix} = \begin{bmatrix} \frac{\partial}{\partial x} & 0 \\ 0 & \frac{\partial}{\partial y} \\ \frac{\partial}{\partial y} & \frac{\partial}{\partial x} \end{bmatrix} \begin{Bmatrix} u \\ v \end{Bmatrix} \quad \text{Eq. 5}$$

and B matrix is written as

$$B_i = S N_i = \begin{bmatrix} \frac{\partial N_i}{\partial x} & 0 \\ 0 & \frac{\partial N_i}{\partial y} \\ \frac{\partial N_i}{\partial y} & \frac{\partial N_i}{\partial x} \end{bmatrix} \quad \text{Eq. 6}$$

in which B_i is i 'th node strain shape function and matrix B is in the form of $B = [B_1 \ B_2 \ \dots]$.

Stress in material is defined using stress-strain relation. In the case of linear elastic behavior, material stress-strain relation is in the form of:

$$\sigma = \underline{D} \varepsilon \quad \text{Eq. 7}$$

where \underline{D} is suitable elasticity matrix [8]. Using Eq. 3, above equation can be written as:

$$\sigma = \underline{D} B a \quad \text{Eq. 8}$$

Stiffness matrix

Nodal displacements and applied forces in the finite element analysis are related using the following equation:

$$[K]\{a\} = \{f\} \quad \text{Eq. 9}$$

in which, $\{a\}$ represents the nodal displacement vector, $\{f\}$ is nodal force vector and $[K]$ is global stiffness matrix which is a function of mechanical properties, shape of body and element type. Global stiffness matrix is made up by assembling element stiffness matrices. Element stiffness matrix is defined as

$$K^e = \int_{V^e} B^T \underline{D} B d(\text{vol}) \quad \text{Eq. 10}$$

The integral bound in planar elements is element surface.

Solving equation system of Eq. 9, nodal displacements are obtained. Substituting nodal displacements in Eq. 3 and Eq. 8, strains and stresses are obtained.

Sensitivity Analysis Formulation and Finite Element Analysis

There are a few number of research in structural sensitivity analysis. For instance, Haug *et al* [9] have studied this topic in 1986. Considering equations mentioned in the previous section, it can be recognized that stress, strain, displacement and stiffness of each element are functions of stress-strain relationship, shape functions and strain-displacement relationship. So the response of the (stress,

strain and displacement) is implicitly related to the mechanical and geometrical properties. As a result of this dependency, scatter in mechanical properties causes variation stiffness matrix and in stress, strain, and displacement fields.

Let the mechanical properties to be design variable

$$\begin{aligned} K &= K(b) \\ f &= f(b) \end{aligned} \quad \text{Eq. 11}$$

where $b=[b_1, \dots, b_m]$ denotes design variable vector. Employing Eq 9:

$$[K(b)]\{a\} = \{f(b)\} \quad \text{Eq. 12}$$

So that, the nodal displacement vector is a function of design variables, i.e. $a=a(b)$. In most of the problems, a cost function, Ψ , which must be minimized (sometimes maximized) is considered. Generally cost function has the following form:

$$\psi = \psi(b, a(b)) \quad \text{Eq. 13}$$

Cost function is related to design variables (nodal displacement vector $a(b)$) in two ways, directly, and indirectly. In this study, design variable, b , is material properties, and cost function, Ψ , consists stress, strain, strength ratio and so on.

To study the variation of strain as a cost function due to changes of mechanical properties, consider Eqs 3 and 9:

$$\varepsilon = Ba = B(K^{-1}f) \quad \text{Eq. 14}$$

and for the stress consider Eqs 8 and 9:

$$\sigma = D_1 Ba = D_1 B(K^{-1}f) \quad \text{Eq. 15}$$

Employing chain rule, total derivative of Ψ with respect to b (i.e. sensitivity of Ψ with respect to b) is in the following form:

$$\frac{d\Psi}{db} = \frac{\partial \Psi}{\partial b} + \frac{\partial \Psi}{\partial a} \frac{da}{db} \quad \text{Eq. 16}$$

and by differentiating Eq. 12 with respect to b :

$$K(b) \frac{da}{db} = -\frac{\partial K(b)}{\partial b} a + \frac{\partial f(b)}{\partial b} \quad \text{Eq. 17}$$

solving above equations for da/db

$$\frac{da}{db} = K^{-1}(b) \left[-\frac{\partial K(b)}{\partial b} a + \frac{\partial f(b)}{\partial b} \right] \quad \text{Eq. 18}$$

substituting Eq. 18 in Eq 16 we get:

$$\frac{d\Psi}{db} = \frac{\partial \Psi}{\partial b} + \frac{\partial \Psi}{\partial a} K^{-1}(b) \frac{\partial}{\partial b} [f(b) - (K(b)a)] \quad \text{Eq. 19}$$

where tilde (\sim) indicates constant variable during differentiation. Above equation identifies $d\Psi/db$ completely and indicates the sensitivity of Ψ with respect to b .

The sensitivity of nodal displacement with respect to change of mechanical properties is

$$\frac{da}{dE_k} = K^{-1} \left[-\frac{\partial K}{\partial E_k} a + \frac{\partial f}{\partial E_k} \right] \quad \text{Eq. 20}$$

$E_k = E_x, E_y, E_s, \nu_x$

where $\partial K/\partial E_k$ is sensitivity of the stiffness matrix. Using Eq. 10 it can be calculated as

$$\frac{\partial K^e}{\partial E_k} = \int_{V^e} B^T \frac{\partial D}{\partial E_k} B d(\text{vol}) \quad \text{Eq. 21}$$

where $\partial D/\partial E_k$ is defined in references [1, 8].

As stated, the strain field can be calculated using the following equation:

$$\varepsilon = Ba \quad \text{Eq. 22}$$

in which, the matrix B is not a function of mechanical properties of unidirectional plies, and sensitivity of strain with respect to changes of mechanical properties of unidirectional plies is in the following form:

$$\frac{d\varepsilon}{dE_k} = BK^{-1} \left[-\frac{\partial K}{\partial E_k} a + \frac{\partial f}{\partial E_k} \right] \quad \text{Eq. 23}$$

$E_k = E_x, E_y, E_s, \nu_x$

On the other hand, sensitivity of the stress field due to changes of mechanical properties of unidirectional plies is calculated using the following equation:

$$\frac{d\sigma}{dE_k} = \frac{d}{dE_k} (D_1 Ba) = \frac{dD_1}{dE_k} Ba + D_1 BK^{-1} \left[-\frac{\partial K}{\partial E_k} a + \frac{\partial f}{\partial E_k} \right] \quad \text{Eq. 24}$$

$E_k = E_x, E_y, E_s, \nu_x$

The sensitivity of strength ratio [2] can be calculated by substituting the value of stress from Eq. 15 and the sensitivity of stress due to changes of mechanical properties of unidirectional plies from Eq. 24 in the equation of strength ratio used from references [1,8].

Case Study

After explanation of finite element formulation and the theoretical basis of the sensitivity analysis, a case study is presented in this section. Computer codes are written for calculating finite element analysis, calculations of sensitivity coefficients and performing evaluation or prediction. The finite element is written for 4-node laminated plane stress element and stores nodal displacement, stress, and strength ratio and their variation due changes of mechanical properties of unidirectional plies. The output files are used for predicting the allowable variations of mechanical properties.

In predicting the allowable variations of mechanical properties, maximum or minimum magnitudes of desired properties (i.e., stress and strength ratio) is given to the computer program and the allowable variations are calculated. In minimum

allowable variation, for each data, its weight function is calculated based on its sensitivity coefficients and mechanical properties. Then, using the calculated weight functions, allowable variation in mechanical properties is calculated. The computer program reports allowable variations in mechanical of all nodal points.

For evaluating properties, absolute or relative changes of mechanical properties are given to the computer program and for all nodal points, the resultant value of property is calculated. Moreover, the computer program reports minimum and maximum magnitudes of allowable mechanical properties.

A Rectangular Composite Plate with Stress Concentration

The application of the theoretical model presented by using the following example. Consider a rectangular composite plate with stress concentration (Fig. 1).

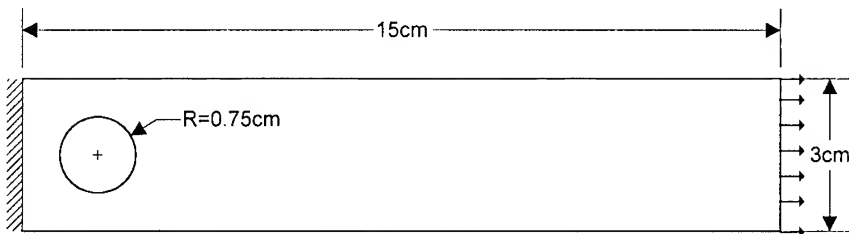


Fig. 1 A composite Plate with Stress Concentration

The material used for the modeling is assumed to be T300/5208 and the ply configuration of the plate is $[0/90]_s$. The model is clamped at the left side and a uniform distributed load is applied at the right side. The finite element model is shown in Fig. 2.

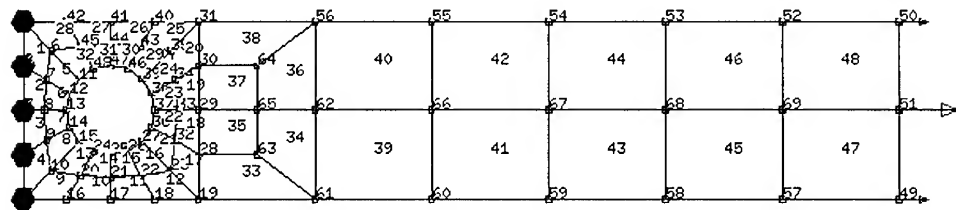


Fig. 2 Finite Element Model

The material properties of the unidirectional ply used for the analysis are as follows:

Table 1: Mechanical Properties of Unidirectional Ply	
E_x	181. GPa
E_y	10.3 GPa
E_s	7.17 GPa
ν_x	.28
X_T	1500. MPa
X_C	1500. MPa
Y_T	40. MPa
Y_C	246. MPa
S	68. MPa

After analysis, the smallest magnitude of the strength ratio is found to occur in layer #2 (90° layer) of element #15 and layer#3 (90° layer) of element #30 (upper and lower elements around hole) and is equal to 1.252. For studying the effects of changes of mechanical properties (E_x , E_y , E_s , ν_x) on the stress field and strength ratio, various models with different mechanical properties are analyzed using finite element method. The calculations are collected for layer #2 of element #30. The detail of the calculations and the results in form of graphs are presented in [8]. For instance for a 6.5% decrease in E_x , 6.5% decrease in E_y , and 7.0% decrease in E_t , the minimum strength ratio is equal to 1.040 and occurs at layer #2 of element #15. Also, for a 10.0% increase in E_s , X_c , and Y_c and 10.0% decrease in ν_x , X_t , and S , the minimum strength ratio is equal to 1.245 for layer #3 of element #30. The first and second examples are called case #1 and #2, respectively.

Now, using the computer program written in this study for the cases #1 and #2 the predicted strength ratios are 1.024 and 1.241, respectively. The results are summarized in Table 2. As shown in this table, it is clear that the difference between the results obtained by the finite element and sensitivity analysis are acceptable.

Table 2: Comparison Between Finite Element and Sensitivity Analysis

	Strength Ratio		Error %
	Finite Element Analysis	Sensitivity Analysis	
Case #1	1.040	1.024	1.5
Case #2	1.245	1.241	0.32

Another outcome of the present method is predicting the minimum distance to failure. It means, the method can predict a set of changes in mechanical properties which can reduce the strength ratio below 1 (failure initiation). For instance for the plate shown in Fig. 1, with the minimum strength ratio equal to 1.252, the following changes in the mechanical properties, shown in Table 3, reduces the strength ratio to 1.037. This magnitude of the strength ratio is very near to 1. It means that if the mechanical properties of unidirectional plies reduces to the following magnitudes the composite laminate fails.

Table 3: Critical Changes in Mechanical Properties

Mechanical Properties	Variation %
E_x	-6.70
E_y	+6.60
E_s	+0.06
ν_x	-0.05
X_T	-0.08
X_C	+0.05
Y_T	-7.07
Y_C	+0.02
S	-0.38

Summary

To calculate the strength ratio and predict the allowable variation of mechanical properties of unidirectional plies and the effects of that on mechanical

behavior of laminated composites a sensitivity analysis is performed. The results obtained, confirm the validity of the method presented in this research. It can be concluded that the method is reliable and can be used as a tool in predicting of mechanical behavior of composite laminates with stress concentrations due to changes of mechanical properties of its unidirectional plies. The method can be used instead of performing finite element analysis which is time consuming. In quality control process, if changes in mechanical properties of unidirectional plies are observed, without needs to a finite element program and using the computer program presented in this study the changes in mechanical behavior of the structure can be predicted.

Predicting the minimum distance to failure is another outcome of the method presented in this study. By having the mechanical properties of unidirectional plies t , the computer program can predict the magnitude of decrease or increase in mechanical properties which can result in failure of laminated composites.

References

- [1] Mahmood M. Shokrieh, and Ashkan Bohlool, "Sensitivity Analysis of Laminated Composite Materials due to Changes of Mechanical Properties of a Unidirectional Ply," Submitted to International Journal of Engineering, in Persian, 1999.
- [2] Stephen W. Tsai, "Introduction to mechanics of composites," Technomic, 1980.
- [3] O.C. Zienkiewicz and R.L.Taylor, "The Finite Element Method," Vol. 1, McGraw Hill, 1989.
- [4] O.C. Zienkiewicz and R.L. Taylor, "The Finite Element Method," Vol. 2, McGraw Hill, 1991.
- [5] R. D. Cook, D. S. Malkus, and M. E. Plesha, "Concepts and Application of Finite Element Analysis," John Wiley and Sons, 1989.
- [6] J.N. Reddy, "An Introduction to the Finite Element Method," 2nd Ed., McGraw Hill, 1993.
- [7] O.O. Ochoa and J.N. Reddy, "Finite element analysis of composite laminates," Kluwer Academic Publishers, 1992.
- [8] Ashkan Bohlool, "Sensitivity Analysis of Laminated Composite Materials due to Changes of Mechanical Properties of a Unidirectional Ply," M.Sc. Thesis, Mechanical Engineering Dept., Iran University of Science and Technology, 1999.
- [9] Edward j. Haug, Kyung K Choi and Vadim Komkov, "Design Sensitivity Analysis of Structural Systems," Academic Press Inc., 1986.

NONLINEAR ANALYSIS OF POSTBUCKLED STIFFENED PANELS MADE OF HEAT RESISTANT THERMOPLASTIC COMPOSITES (CF/PIXA) AND COMPARISON WITH EXPERIMENTS FOR SUPERSONIC COMMERCIAL TRANSPORT

Takashi Ishikawa¹, Masamichi Matsushima¹, Yoichi Hayashi²

¹: *Structures Division, National Aerospace Laboratory
6-13-1 Ohsawa, Mitaka, Tokyo 181-0015, JAPAN: isikawa@nal.go.jp*

²: *Tokyo Business Service Co. LTD
6-13-1 Ohsawa, Mitaka, Tokyo 181-0015, JAPAN*

ABSTRACT: Compression after impact (CAI) behavior of stiffened panels using T-shaped stringers made of heat resistant thermoplastic composites, CF/PIXA, was obtained by tests at room temperature and 180 deg. C. It is clarified that damage tolerance properties of CF/PIXA stiffened structure are so remarkable at room temperature that compression strengths are quite insensitive to relative impact energy. Its damage tolerance capability is also excellent at high temperature for High Speed Civil Transport structure. Linear and nonlinear buckling analyses based on simple models without delamination and interlaminar stresses were conducted using a finite element code. Nonlinear analysis considering deformed shape is the main focus of this paper. The results of strain and out-of-plane deformation agreed basically well with experimental results. In the case of prediction of the final strength, several points of improvements are identified. The present prediction provides the initial step to discuss possibility of post-buckling strength design at high temperature stiffened panels.

KEYWORDS: SST, FE Analysis, Weight Reduction, Thermoplastic Composites, Compressive Buckling, Postbuckling, Final Strength Prediction

INTRODUCTION

Weight reduction by composite materials is one the most important technical issues governing feasibility of commercially promising commercial Super-Sonic Transport (SST). Key requirements for such composites are thermal stability for long time duration at elevated temperature up to 177° C and excellent damage tolerance property to allow sufficient design critical strength values for light weight structures. One promising candidate composite material is carbon fiber (intermediate modulus fiber)/PIXA system. PIXA is a new high-temperature thermoplastic polyimide resin developed in Japan (by Mitsui Chemicals Co. LTD) and it comprises a family of similar resins. The major critical strengths as composite coupon levels were evaluated at room and elevated temperatures up to 230° C previously^{1,2} by the authors including compression strength after impact (CAI) using SACMA method at 6.7J/mm impact energy. Long term exposure tests at high temperature air followed by the same size OHC tests

as above have been being conducted³ by the other group in NAL, Japan. These basic tests demonstrated a great potential of this composite system for HSCT structure.

After acquisition of such coupon level strength data, the first step to the structure level damage tolerance evaluation was required at room and elevated temperatures. CAI tests of stiffened panels with T-shaped stringers fabricated by fusion bonding technique with special bonding film were chosen as the best compromise between desired property data and testing costs. The present paper will discuss such structural CAI properties in view of experimental behavior and a comparison of experiments with nonlinear numerical predictions using FEA. The first aim in this paper is to demonstrate excellent damage tolerant properties of the present stiffened panels and to determine test allowable values for a long term fatigue test of a model box of the same material under simulated temperature change. The second aim of this paper is to demonstrate predicting capability of the final strength of the panels by comparatively simple nonlinear FE analysis considering geometrical nonlinearity and ply level maximum stress.

DESCRIPTION OF TESTED MATERIAL

Among several heat resistant thermoplastic (H RTP) resins known to us, the family of PIX based on AURUM[®] polyimide resin are developed in Japan by the effort of Mitsui Chemicals Co. Ltd. Four types in the chronological order, PIX, PIXA, PI-SP and PIXA-M are developed and available in the market. Several properties of neat resin are listed in

TABLE 1 RESIN PROPERTIES OF PIX FAMILY

	PIX	PIXA	PI-SP	PIXA-M
	Crs.	Semi-Crs.	Non-Crs.	Non-Crs.
Crystallinity(Crs)	Crs.	Semi-Crs.	Non-Crs.	Non-Crs.
Gl. Trns. Tmp.(deg.C)	249	252	254	235
Tensile Modulus (GPa)	2.75	2.84	2.65	-
Tensile Strength(MPa)	92.2	89.2	91.2	83.4

Table 1. As stated before, material system selected in NAL H RTP structure project was CF(IM-7)/PIXA in accordance with a balance of material properties.

Test items conducted were UD tension and compressions, Open Hole Compression (OHC: 38×118.0×4.0^l, and 6.35^D), No Hole Compression (NHC: 25.4×105.4×4.0^l), and CAI tests in SACMA²⁾ method at 6.7J/mm impact. They were all conducted at room and elevated temperatures and up to 230 deg. C. Size and stacking sequence of all specimens are as follows: 101.6×152.4×4.0^l and {(45/0/-45/90)⁴/ sym.}, respectively. Results of these compression tests of quasi-isotropic coupons were reported in Ref.1. It should be noted that all dimensions quoted above are only nominal values in mm unit and that the actual values were measured for all the specimens. Elastic moduli and strengths obtained from unidirectional coupons at elevated temperatures will be used for numerical predictions of buckling behavior stated later.

DESCRIPTION OF STIFFENED PANELS FOR CAI TESTS

Outline of stiffened panel specimens made of CF/PIXA is described here. Two kinds of stiffened panels with one T-shaped stringer (1T) and with two T-shaped stringers (2T), similar to the author's previous work⁴ with four T, were fabricated by one supporting company, Fuji Heavy Industries Co. LTD (FHI), Japan, using fusion bonding technique with autoclaves. Shape and dimensions of the 1T and 2T panels are shown in Figs.1 and 2, respectively. In order to avoid later duplication of illustrations, strain and dial gage locations are also indicated in these drawings as much as possible. For both kinds, seven panels (01-07) were fabricated. A 2T

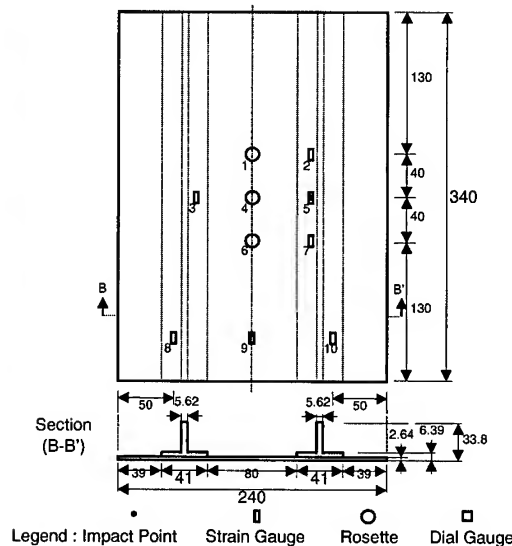
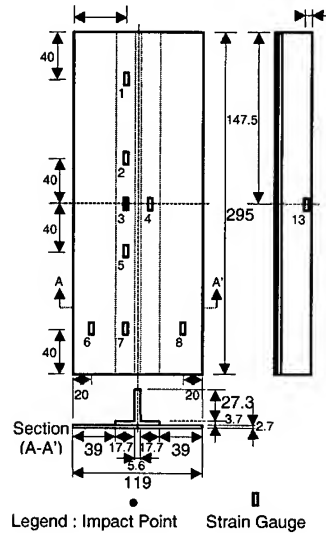


Fig.1 1T Panel Shape and Dimensions **Fig.2 2T Panel Shape and Dimensions**
(Same Gage Location All Panels) **(Different Gage Location in some Panels)**

panel has larger dimensions than 1T, although they are not sufficient in size to realize the unaffected local buckling state by peripheral supports. A size of an environmental chamber for the Instron machine used (1128) enforces these rather small sizes of the stiffened panels. The purpose of a 1T panel is to conduct a test under less effects of local inter-bay buckling.

For fusion bonding between skin and stiffeners, a thermoplastic polyimide film, Regulus PIXA-M by Mitsui Chem. Co. was utilized. Stacking sequences were (45/90/-45/0/0/45/90/-45/0)_{sym.}: 18 plies for skin, (45/0/-45/90/45/0/0/-45/0/0/-45/0/0/45/90/-45/0/45)_{sym.}: 36 plies for stringer web and (45/0/-45/90/45/0/0/-45/0/0/-45/0/0/45/90/-45/0/45/45/0/-45/-45/0/45): 24 plies for stringer attachment flange. They are identical regardless of stiffener numbers.

All panels were subjected to drop weight impact tests at the one leg center of an attachment flange with normalized energy level of 4 J/mm and 6.7 J/mm. All impacts were given to the specimens at room temperature by using an instrumented drop weight machine. Delaminated area in projection was measured by a ultrasonic C-scanner and small delamination areas are attributed to high fracture toughness of CF/PIXA. Relationships between delamination area and normalized impact energy were compared with the authors' previous data for CF/PEEK stiffened panels. The comparison indicates that CF/PIXA has more excellent impact resistance than CF/PEEK. This property can be ascribed rather to the used fusion bonding film.

One experimental difficulty in high temperature CAI tests of stiffened structures is how to clamp loading edges. Although we can rely on a potting agent at room temperature tests⁴, it is very hard to find a high-temperature potting agent. Instead of potting technique, clamping fixtures of stainless steel were developed for both types of panels. By tightening many screws, clamped boundary conditions at the loading ends were approximately realized, although one concern is a mismatch in coefficients of thermal expansion between CF/PIXA and steel. The present experience by the authors implies that this concern is not serious at least within 180 deg. C.

OUTLINE OF COMPRESSION TESTS AFTER IMPACT

Compression tests at room temperature and 180 deg. C were conducted for 1T-01,03,04, 2T-01,05,06,07 panels, and 1T-02,05, 2T-02,03,04 panels, respectively. In room temperature tests, data acquisition devices were normal strain gages, dial gages for out-of-plane deflections, an acoustic emission sensor network system for AE location identification and a Moiré-topography camera for obtaining out-of-plane deflection contour. Numbers of gages are 14 for 1T-01 and 30 for 2T-01 (in channels). In elevated temperature tests, the same high temperature grade gages as flat plate cases were used with a polyimide strain gage cement (PI-32). The gages were only data acquisition pick-ups except for AE trials at high temperature. Gage quantities were 14 for 1T-01 and 24 for 2T-02.

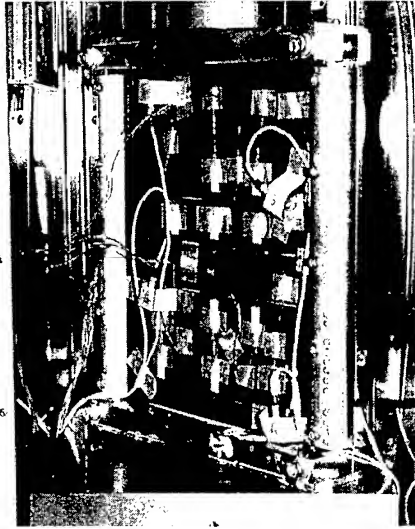


**Fig. 3 Photograph of High Temperature
CAI Test for 2T Panel**

Typical gage maps are already shown in Figs. 1 and 2

where some gages were glued in back to back locations. Gage #3 was placed on an impact indentation. Used data logger was an HP 3852A system. Acoustic emission sensors (PAC-R15) for universal purpose were tried in high temperature tests and it was verified that they worked at least in 180 deg. C.

Loading edge conditions were close to clamped owing to the stainless end platens described above. Stainless steel tubes with sharpened slits acting as knife-edges were installed along both side edges so that simply supported conditions were approximately realized. Compression load was applied by the Instron 1128 screw driven machine directly through an upper end platen. A photograph of an elevated temperature test of a 2T stiffened panel (02) is shown in Fig.3. Because of a shortage of width in the environmental chamber, it can be seen that the panel was placed diagonally to it. Also, acoustic emission sensors can be identified by lead wires. Due to such an arrangement, Moiré-topography pictures were not taken at all high temperature tests.

COMPARISON OF TEST RESULTS WITH FEA CALCULATIONS

Finite element buckling analysis was conducted for linear and nonlinear (postbuckling) behavior. Software package of NISA-II was used in the analysis. Quadrilateral laminate shell element of 8 node was selected as the base element. Loading and side edges were assumed as fixed and simply supported, respectively. Metallic end fixture was not incorporated into the model. Used material properties at room temperature and 180 deg. C are given in Table 2. Calculated buckling mode at RT is given in Fig.4. If we compare the experimental mode in Fig.5 and this numerical mode, extreme similarity can be found including slight skewness in the shape and small deflection in the lowest contour. Skewness is presumably brought by local asymmetry in stacking sequence in skin-attachment flange. Buckling mode taken by the Moiré camera for a different RT panel (2T-05) just before failure is shown in Fig. 5 where buckling stress is 228MPa. Four half waves of the out-of-plane deflection along the loading direction can be observed in the picture if examined carefully (the lowest one is difficult to be identified). Stress - out-of-plane deflection behavior of 2T-01 panel tested at room temperature is indicated

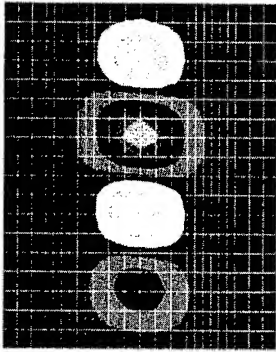


Fig. 4 Calculated Buckling Mode at RT

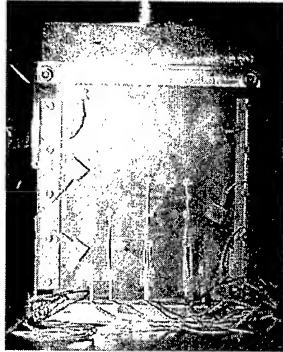


Fig. 5 Experimental Buckling Pattern for 2T-05

Table 2
Input Material Properties for
CF/PIXA UD Lamina for FEA

Temp. (deg.C)	RT	100	180	230
E_L (GPa)	152.4	152.4	152.4	152.4
E_T (GPa)	8.06	7.65	6.87	5.66
G_{LT} (GPa)	4.69	4.40	3.70	2.80
ν_{LT}	0.344	0.344	0.344	0.344
ν_{TT}	0.5	0.5	0.5	0.5

in Fig. 6 with nonlinear FEA results. It can be clearly seen that local buckling in a stiffener bay occurred at 257MPa in 2T-01 and that considerable increase in stress after buckling was observed before the final failure. A good correlation between nonlinear numerical analysis and experimental results can be found in the deflection. Comparison between numerical and experimental stress-strain relations is given in Fig. 7 for the same panel. Although agreement becomes worse than stress-deflection relation, qualitative similarity can be observed. Through such a comparison, a predictability of the final strength by numerical calculations can be suggested. A fact behind the suggestion is that the failure mode of CF/PIXA panel is not affected by the size of impact delamination. In other words, simple compression failure in postbuckling range mainly governs the final compression behavior of these CF/PIXA panels and skin-stiffener separation is well arrested by tough fusion bonding film.

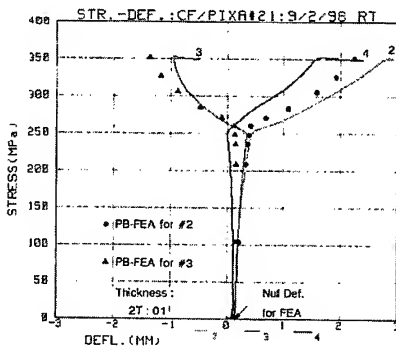


Fig. 6 Stress - Out-of-Plane Deflection Behavior in 2T-01 (RT at 4J/mm)

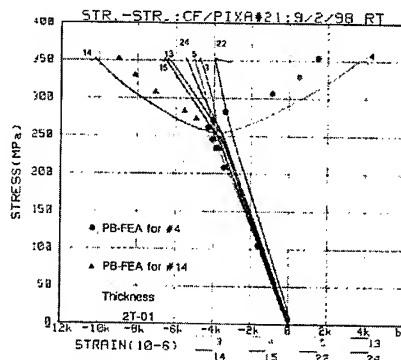


Fig. 7 Stress-Strain Behavior in 2T-01 (Room Temperature at 4J/mm)

Predicted final compression strengths of the panels based on UD compression failure strengths (F_c) at various temperature and the ply-level maximum stress criteria in the 1st 0° lamina from the surface (5th lamina) are shown in Fig. 8 with experimental results of RT and 180 deg. C. A curve indicated as 1.0 F_c was obtained directly by UD compressive strengths and one as 1.2 F_c was obtained by hypothetically increased compressive stress of 20%. A factor of 1.2 was chosen so as to coincide with RT experimental data. It can be seen that higher experimental data were obtained and that slight postbuckling behavior was observed. The theory predicts almost no postbuckling even if we assume 1.2 F_c . This is one point of improvement in theory.

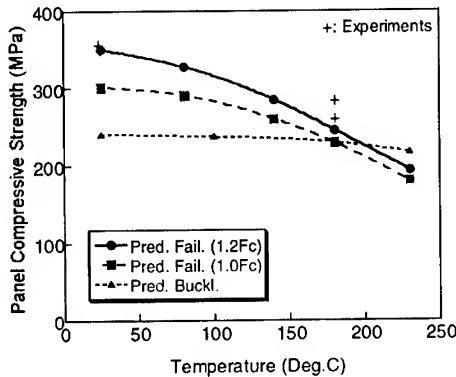


Fig.8 Comparison of Experimental and Predicted Compressive Strength of Panels

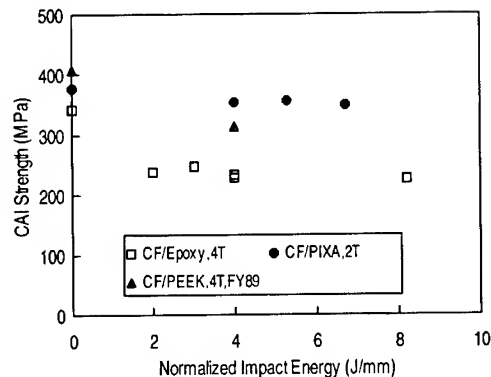


Fig.9 Relationships between CAI strengths and Normalized Impact Energy for Panels

Relationships between normalized impact energy and CAI strengths of stiffened panels at room temperature are shown in Fig. 9 by solid circles for CF/PIXA 2T. The previous results for several CF/PEEK and CF/Epoxy stiffened panels in Ref.4 are also plotted in this figure for reference. It can be understood that better quality panels of 2T shows remarkable insensitivity in CAI strength to impact energy. This insensitivity can be regarded as a proof of excellent damage tolerance of these CF/PIXA stiffened panels. Easier predictability of the final compressive strength is a by-product of this excellent damage arrest property.

CONCLUDING REMARKS

The following findings are obtained through the experiments and corresponding numerical analysis using simple FEA model for initial buckling prediction and nonlinear postbuckling behavior without a consideration of the delamination.

CF/PIXA stiffened panels demonstrate their excellent impact resistance at ambient temperature. Delaminated regions by impact were not triggers of the final failure in the present stiffened panel tests owing to excellent delamination evolution resistance of the present fusion bonding. Numerical calculations by FEA can predict well for linear buckling stresses, postbuckling deflection and postbuckling stress-strain behavior. Even in the current framework, prediction of the final strength will be possible if the above condition holds. Stiffened panels of 2T tested in room temperature exhibited substantial post-buckling behavior. The panels tested at high temperature also showed enough postbuckling behavior if fusion bonding is well accomplished.

References: 1. Ishikawa, T., Matsushima, M., Hayashi, Y., and Nakamura, H., "Strengths of Heat Resistant Thermoplastic Composites (IM-7/PIXA) for Future High Speed Civil Transport", *Proc. 5th Japan Int. SAMPE Symp.*, Tokyo, 1997, p.1137.
2. Ishikawa, T., Matsushima, M., Lim, E.K.G., Hayashi, Y. and Scott, M.L., "Compression after Impact (CAI) Behavior of CF/PIXA Stiffened Panels for HSCT Empennage", *Proc. 12th Int. Conf. Comp. Mat.*, Paris, France, July 1999 (in CD-ROM).
3. Shimokawa, T., Hamaguchi, Y., Kakuta, Y., Katoh, H., Sanda, T., Mizuno, H., and Toi, Y., "Effect of Isothermal Aging on Strength of High-Temperature Composite Materials for SST Structures", *Journal of Composite Materials*, Vol. 33, No.12, 1999, pp.1104-1108.
4. Ishikawa, T., Matsushima, M., and Hayashi, Y., "Improved Correlation of Predicted and Experimental Initial Buckling Stresses of Composite Stiffened Panels", *Composite Structures*, Vol. 26, No.1, 1993, pp. 25-38.

THREE DIMENSIONAL ANALYSIS OF ADHESIVELY BONDED COMPOSITE LAP JOINT

Seung Jo Kim¹, Hea Jin Yeo², Soon Wan Chung³ and Woo-Suck Han⁴

^{1,2,3} Department of Aerospace Engineering, Seoul National University
San 56-1, Shillim-dong, Kwanak-ku, Seoul, 151-742, Korea

¹ sjkim@snu.ac.kr, ² hjyeo@kr.ibm.com, ³ swchung@aeroguy.snu.ac.kr

² Currently working at Engineering Solutions, IBM Korea Inc.

⁴ Ecole des Mines de Saint-Etienne

158, cours Fauriel, 42023 Saint-Etienne, Cedex 2, France : han@emse.fr

SUMMARY: The three dimensional analyses of adhesively bonded composite single-lap joint are carried out by finite element method to calculate the stress concentration in the three dimensional deformation when the design variables are changed. Because the bond layer thickness is very thin and the stress gradient is large around the corner, fine meshes are needed for finite element modeling. To satisfy this requirement, the mesh models with large degree of freedom are solved by the multifrontal solver and the distributed parallel computing technique for memory and CPU time usage efficiency. For the numerical examples, firstly, 3-D solution of isotropic lap joint is compared with 2-D solution. And the composite lap joints are analyzed with various design variables, such as the type of adhesive spew and the difference of stiffness in two composite adherends. And the effects of the design variables are proposed with the results at the corners and the interface of adhesive and adherends.

KEYWORDS : lap joint, composite adherend, adhesive, three dimensional analysis, large degree of freedom, parallel computing, multifrontal solver, finite element method

INTRODUCTION

Adhesive lap joints[1] are capable of high structural efficiency and constitute a resource for structural weight saving because of the potential for elimination of stress concentrations which cannot be achieved with mechanically fastened joints like bolts and rivets. But, owing to a lack of reliable inspection method and a requirement for close dimensional tolerances in fabrication, aircraft structure designers have avoided the bonded construction in primary structures. But the advantage of this joint type becomes more important and the use of composite adherend is increasing specially.

For the analysis of adhesive single-lap joint, the linear elastic analysis which is assumed that both adhesive and adherend are linear elastic is performed usually.[2] Adams and Peppiatt[3] neglected the stress of adhesive and treated the adhesive as an infinite number of shear springs. Chen and Cheng[4] introduced the assumption that the stress of adhesive is constant through the thickness. And Sawa[5] analyzed the contact stress distributions between adherends and an adhesive in single-lap adhesive joints subjected to tensile loads as a two-

dimensional theory of elasticity. But because these researches offered the analytic method for the two dimensional problem, 3-D analysis is necessary to include all stress components under the general deformation. In particular, the composite material has the anisotropic property and therefore the 3-D analysis is required to obtain the sound results. And because the fine meshes are needed around the area with the large stress gradient, large degree of freedom is generated in 3-D analysis and the computing power for the analysis is essential. The objective of this paper is to perform the three dimensional analysis of adhesively bonded composite lap joint using the multifrontal solver and the distributed parallel computing technique[6]. The parallel computing is incorporated in the fast-networked 8-node PC system to work out the computing power issue. As the design variables of the lap joint structure, the spew fillet and the difference of stiffness between two composite adherends are chosen. And we make sure of the effects of the design variables through the numerical experiments.

COMPARISON OF 2-D AND 3-D ANALYSIS RESULTS

To address the features of the 3-D analysis of lap joint structure, the comparison between 2-D analysis and 3-D analysis is carried out using the isotropic aluminum adherends and epoxy adhesive. The sizes of adhesive and adherend are $10 \times 0.5 \times 5 \text{ mm}^3$ and $30 \times 2 \times 5 \text{ mm}^3$ respectively. The used model and loading/boundary conditions are shown in Fig.1.

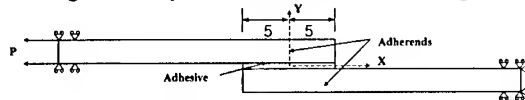


Fig.1. Loading and boundary condition of isotropic lap joint

The plane strain assumption is adopted for 2-D analysis and its results are compared with the average values of 3-D analysis results across the transverse direction(Z-direction). For the comparison, the stresses are calculated at the interface between the adhesive and the upper adherend along the longitudinal direction(X-direction). Fig.2 shows that the axial normal stresses(σ_{xx}) of two analyses are similar. But there are differences in the lateral normal stress(σ_{yy} , peel stress) and the shear stress(σ_{xy}).(Fig.3,4)

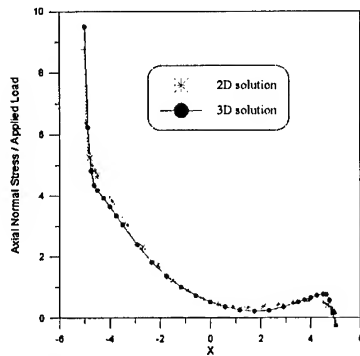


Fig.2. Comparison of axial normal stress

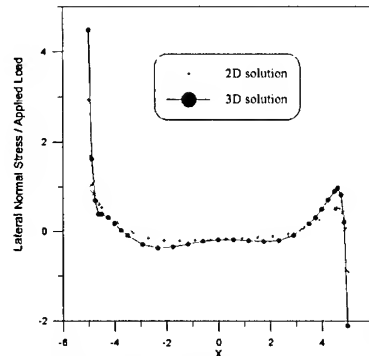


Fig.3. Comparison of lateral normal stress

Particularly, the difference at the corner($x = -5$) where stress singularity happens in the analytic solution, is prominent, it is because that the transverse deformation due to the Poisson's ratio increases the peel and the shear stress. Also the variation of σ_{xx} across the

width in 3-D analysis is shown in Fig.5 and it presents that the stress at the center($z = 0$) of width is larger than that at the boundary($z = 2.5$) around the corner.

Fig.6 and Fig.7 show stress distributions (σ_{xx} and σ_{xy}) along the thickness at the corner($x = -5$) respectively. 2-D solution accords with the analytic solution approximately in that σ_{xx} and σ_{xy} are zero at the adhesive and the lower adherend where the load does not apply. However, the stresses at the adhesive close to upper adherend have nonzero value in 3-D solution. This result is also inferred from the transverse deformation in 3-D analysis.

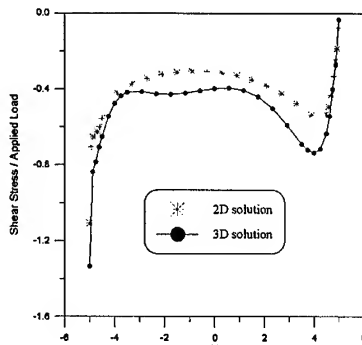


Fig.4. Comparison of shear stress

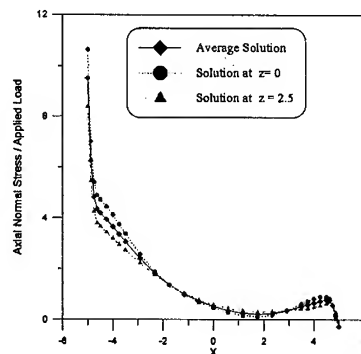


Fig.5. Axial normal stress across the width

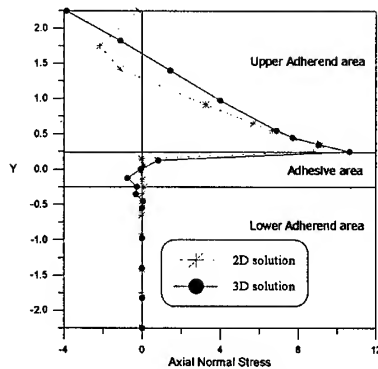


Fig.6. Axial normal stress along thickness at corner

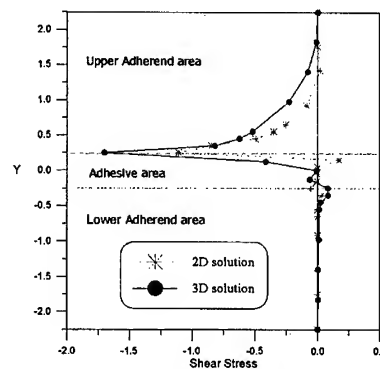


Fig.7. Shear stress along thickness at corner

ANALYSIS OF COMPOSITE LAP JOINTS

Design variables

The stress concentration of adhesively bonded joint occurs around the adhesive. And peel stress and shear stress at the corner affect the main influence to the damage of lap joint structure. Hence some design variables alleviating this stress concentration are considered in the numerical experiments. This study is based on Hart-Smith's research[7] on the design variables of composite lap joint structure. The sizes of used adhesive and adherends are the same in Fig.1 and the used D.O.F. is about 0.1 million. The stresses to come will be calculated at the joint centerline($z = 0$).

Type of adhesive spew

To lessen the stress concentration in the corner, the adhesive is spewed in manufacturing intentionally. In this research, we take account of two categories, one is the size of spew(the

region where the spew is contacted with the adherend) (Spew_A(Fig.8) and Spew_B(Fig.9)) and the other is the shape of spew(Case 1,2,3 (Fig.10)).

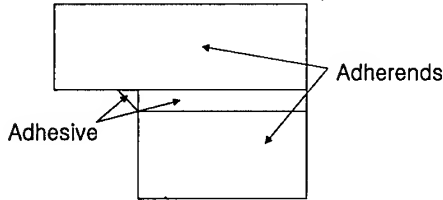


Fig.8. Spew_A type

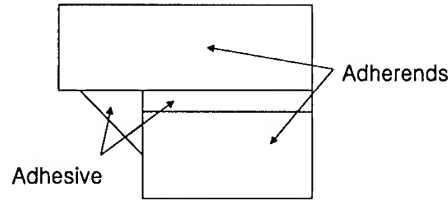


Fig.9. Spew_B type

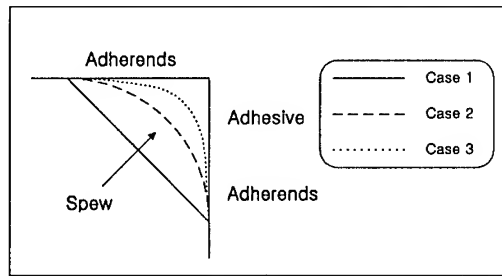


Fig.10. Models with variable spew depth

We use Epoxy and Boron/Al composite as adhesive and adherends. Their properties are shown in Table.1 and the loading/boundary conditions are the same as Fig.1.

Table 1. Material property of Epoxy and Boron/Al

Adhesive	E(GPa)		ν		G(GPa)	
Epoxy	1.284		0.49			
Adherend	E_1	E_2	ν_{12}	ν_{23}	G_{12}	G_{23}
Boron/Al	215	144	0.19	0.29	57.2	45.9
Graphite/Epoxy	206.9	5.171	0.25	0.0625	2.386	2.068

All results(σ_{yy} and σ_{xy}) are compared with that of the model without spew in Fig.11~14. From the figures, it can be seen that the size rather than the shape of spew is effective to reduce the stress concentration.

Effect of adherends stiffness unbalance

In this section, The influence of the stiffness unbalance is examined since two adherends have the different material property each other. While Graphite/Epoxy has high longitudinal stiffness, it is weak in the lateral loading. Hence it is investigated what changes happen when Boron/Al composite, whose E_1 and E_2 has the same order of magnitude, is used together.(Table 1) We classify the kind of adherend into three cases as follows for comparison.

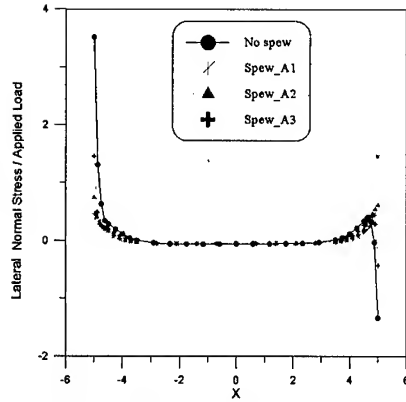


Fig.11. Lateral normal stress (Spew_A)

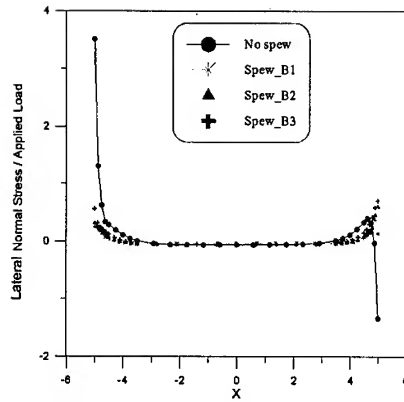


Fig.12. Lateral normal stress (Spew_B)

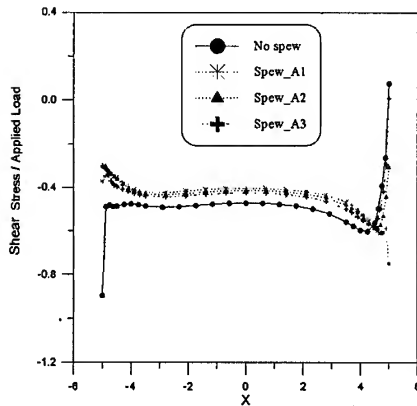


Fig.13. Shear stress (Spew_A)

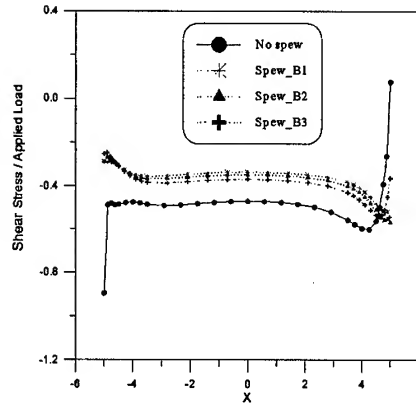


Fig.14. Shear stress (Spew_B)

Case-A : Graphite/Epoxy + Graphite/Epoxy
 Case-B : Graphite/Epoxy + Boron/Aluminum
 Case-C : Boron/Aluminum + Boron/Aluminum

Fig.15,16 show that σ_{xx} in Case-B is the average of σ_{xx} in other two cases on the whole but the stress around the corner approaches to the result in the case using the either of material only. On the other hand, when the difference of modulus (G_{12}, G_{23}) is large, the stress (σ_{xy}) depends mainly on the adherend with lower stiffness, that is Graphite/Epoxy composite. (Fig.17,18) Therefore, the decrease of stress at the corner ($x=5$ in Fig.18) is shown at the lower adherend but such decrease is not apparent at the upper adherend.

CONCLUSION

We analyzed the adhesively bonded composite lap joint by 3-D model with fine mesh and utilized the multifrontal solver combined with parallel computing technique to accomplish the required computing power. Through comparing 3-D solution with 2-D solution, it is found that the difference in peel stress and shear stress which affect the failure of structure primarily is not small. By the parametric study of the design variables, the following results can be obtained. The size of adhesive spew is more important than the shape of adhesive in reducing the stress concentration. And when the unbalance of adherends stiffness is large, the stress at

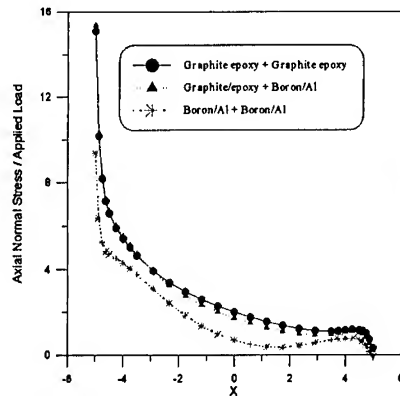


Fig.15. Axial normal stress at upper adherend

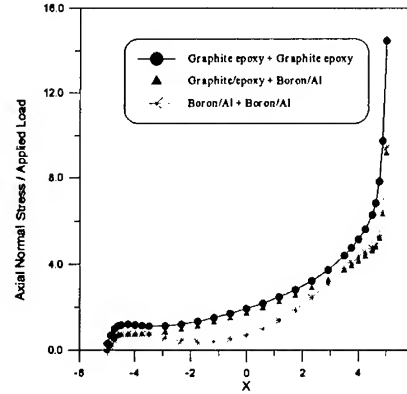


Fig.16. Axial normal stress at lower adherend

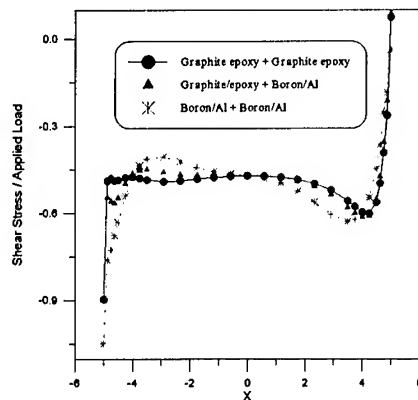


Fig.17. Shear stress at upper adherend

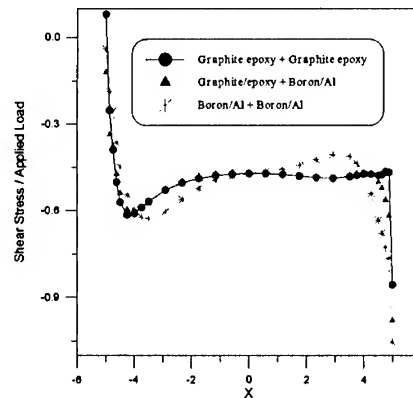


Fig.18. Shear stress at lower adherend

the interface is more susceptible to the adherend with lower stiffness. Finally, we suggest that the high precision analysis of 3-D composite lap joint is necessary to predict the failure at the corner more accurately.

ACKNOWLEDGEMENT

This paper is supported by Agency for Defense and Development(contract No.UD980011AD) and Ministry of Science and Technology(National Research Laboratory project).

REFERENCES

1. *Composite Material Handbook*, Vol.3, pp.5-3 ~ 5-19, NASA, 2 August 1996
2. F. L. Matthews, *Joining Fibre-Reinforced Plastics*, Chapter 5, Elsevier Applied Science, 1987
3. R.D. Adams and N.A. Peppiatt, *J. Strain Anal.*, 8, 134, 1973
4. D.Chen and S.Cheng, "An analysis of adhesive-bonded single-lap joints", *ASME Journal of Applied Mechanics*, Vol.50, pp.109-115, 1983
5. Toshiyuki Sawa, Katsuyuki Nakano and Hiroshi Toratani, "A two-dimensional stress analysis of single-lap adhesive joints subjected to tensile loads", *J. of Adhesion Sci. Technol.*, Vol.11, No.8, pp.1039-1062, 1997
6. J.H. Kim and S.J. Kim, "A multifrontal solver combined with graph partitioners", *AIAA Journal*, Vol.39, No.8, pp.964-970, 1999
7. L.J. Hart-Smith, "Adhesive bonded single lap joints", NASA Langley Contractor Report NASA CR-112237, 1973

Fatigue & Fracture (1)

FATIGUE LIFE ASSESSMENT OF REPAIRED PANELS WITH ADHESIVELY BONDED COMPOSITE PLATES

Hossein Hosseini Toudeshky¹, Hossein Shahverdi¹, Hamid Reza Daghyani²

¹ Aeronautical Eng. Dept., hosseini@cic.aku.ac.ir

² Mechanical Eng. Dept., hamid@cic.aku.ac.ir
Amirkabir University of Tech., Tehran 15914, Iran

SUMMARY: Fatigue crack extension behaviour of repaired aluminum plates is studied using the bonded composite patches. Variations of the stress intensity factor and the crack growth rate for both single-sided and double-sided repaired panels with the composite patches are investigated for different number of composite patch layers developing a three dimensional finite element method. The effect of the adhesive thickness on the stress intensity factor is studied. The results show that the stress intensity factor is decreased significantly in the double-sided repair. As the number of the composite patch layers in both single-sided and double-sided repaired panels are increased, the stress intensity factor and the crack growth rate are decreased. The effect of the adhesive thickness on the stress intensity factor depends on the number of the composite patch layers and the patch thickness.

KEYWORDS: Fatigue crack growth, Crack arrest, Stress intensity factor, Composite repair.

INTRODUCTION

One of the most challenging problems of the aging components in the aerospace industries is the way of their service life extension. If the component is cracked and the crack size is small relative to the size of the component, it is economic to arrest the crack growth using the bonded patches. Due to the high strength, high stiffness and light weight, fiber reinforced composites have an extensive application in repairing of aging components in aircraft. Patching the cracked panels in airplanes using single-sided repair is most often because only the outside surface of the cracked component is easily accessible.

The major concern in composite repair technology and remaining life assessment of repaired panels is the stress analysis and subsequent evaluation of stress intensity factor. Ratwani [1] and Rose [2] introduced analytical methods to characterize the behavior of cracked panels under various applied load conditions. Lu *et al.* [3] employed a closed form solution to assess the fatigue life of center-through cracked panels with adhesively bonded reinforcements. They concluded that Paris' law can be well employed to evaluate the reinforced cracked plates in

engineering practice. In the present study the stress intensity factors of repaired panels are evaluated developing three-dimensional finite element analyses. The effect of the number of composite layers of the patches and the adhesive thickness on the stress intensity factor and crack growth rate for both single-sided and double-sided repaired panels are investigated

Callinan *et al.* [4] developed an analytical solution to evaluate the stress intensity factor for both single-sided and double-sided repaired panels where the crack was located in a semi-infinite region, which is an upper estimation of K_I . They assumed that the patch was functioning as series of springs between the crack surfaces where the stress intensity factor varied linearly along the plate thickness, while the thickness of patch was in the same order of the cracked plate thickness.

EVALUATION OF STRESS INTENSITY FACTOR

The stress intensity factor can be calculated using nodal vertical displacements of the elements close to the crack tip in a finite element model of cracked panel as [4]:

$$V = C \frac{K_I}{E} f(r, \theta) \quad (1)$$

where C is a constant and depends on the state of stress defined as:

$$C = \begin{cases} 4 & \text{plane stress} \\ 4(1 - \nu^2) & \text{plane strain} \end{cases}$$

V is the vertical displacement of the nodes on the crack surface, (Fig. 1), K_I is the stress intensity factor, E is the Young's modulus, ν is the Poisson's ratio and $f(r, \theta)$ is a function depending on the coordinate of the grid. Using the extrapolation of nodal displacement values along the crack surfaces near the crack-tip, the stress intensity factor can be calculated as [5]:

$$K_I = \frac{2G}{k+1} \left(\frac{\pi}{2L} \right) [(4V_{B1} - V_{c2}) - (4V_{B1} - V_{c1})] \quad (2)$$

where;

$$k = \begin{cases} \frac{3 - \nu}{3 - 4\nu} & \text{plane stress} \\ 3 - 4\nu & \text{plane strain} \end{cases}$$

G is the shear modulus, L is the length of the element close to the crack tip, $V_{B1,2}$ and $V_{C1,2}$ are the vertical displacement components of the nodes shown in Fig. 1.

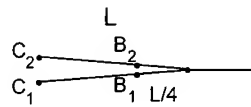


Figure 1. Schematic presentation of crack nodal arrangement.

FINITE ELEMENT MODELING

A wide range of three dimensional finite elements analyses (FEA) were performed for cracked panels. Figure 2 shows the geometry and loading of repaired cracked plates for both single-sided and double-sided repaired panels. The composite layers were patched in which the direction of fibers were considered perpendicular to the crack surfaces.

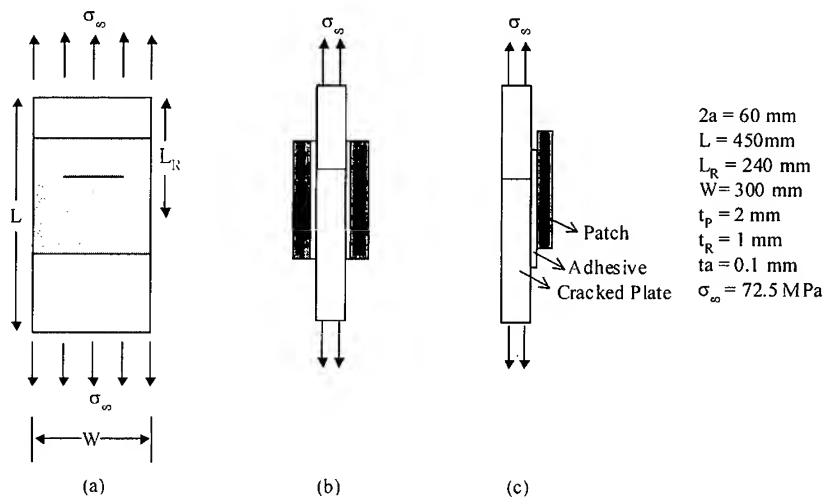


Figure 2: Geometry and loading of the repaired plates, a) upside view of a repaired cracked plate, b) double-sided repaired and c) single sided repaired

In the finite element modeling, the patches contained 1, 2, 4, 6, and 8 layers, respectively, and the thickness of each layer was 0.127 mm. The isoparametric solid elements with 20 grids were used and the crack-tip elements were modified to overcome the singularity problem. Due to the symmetric condition, a quarter of the plate was modeled. The finite element mesh configurations for the plate and the crack-tip are shown in Fig 3.

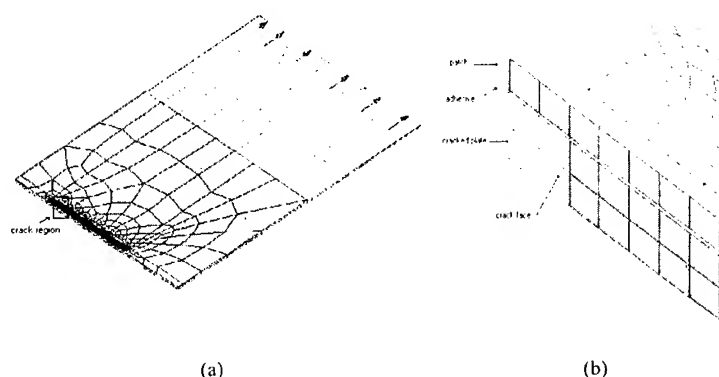


Figure 3: Finite element mesh configurations a) half of the plate. b) crack-tip

In this study the crack length was varied between 30 mm to 90 mm, therefore a fine mesh with the same elements sizes was considered along the crack length in the crack front. The increments of the crack length between the calculation steps were selected as $\Delta a = 5$ mm and for each new model the crack-tip elements were modified to overcome the singularity problem. For double-sided repaired plates three planes of symmetry were considered, therefore only 1/8 of the plate was modeled.

The mechanical properties of the aluminum plate and the composite patches are shown in table 1 and 2, respectively[6]. The adhesive and plate thickness were assumed to be 0.1 mm and 1 mm respectively.

Table 1: Mechanical properties of the aluminum plate and adhesive

Property	E (GPa)	ν
Al 2024-T3	72	0.3
Adhesive FM73	1.92	0.27

Table 2: Mechanical properties of the composite patches.

property (GPa)	E_1	E_2	E_3	G_{12}	G_{13}	G_{23}	ν_{12}	ν_{13}	ν_{23}
Gr/EP	138	9.7	9.7	6.9	6.9	3.2	0.3	0.3	0.49

Using the finite element analyses, the displacement fields around the crack-tip region were obtained, then using Eq. 2 the stress intensity factor were calculated. Due to the small thickness of the plates and patches, the plane stress condition was assumed.

Having the stress intensity factor, K for a cycle and assuming a constant amplitude loading, the service life of the cracked component is calculated by [6]:

$$N = \int_{a_0}^{a_f} \frac{da}{m(\Delta K)^p} \quad (3)$$

where N is the number of load cycles, p and m are material constants and, a_0 and a_f are initial and final crack length. The material constants in Eq. 3 for aluminum 2024 -T3 are: $m = 2.318$ and $p = 4.086 \times 10^{-7}$ [6].

To investigate the effect of the adhesive thickness, it was changed from 0.1 mm to 0.3 mm and the finite elements analyses were performed for different patch thickness.

RESULTS AND DISCUSSIONS

The variations of the stress intensity factor versus the crack length obtained from the finite element analyses for different number of composite patch layers are shown in Fig. 4 for unrepaired, single-sided and double-sided repaired plates. It is shown that in the double-sided repair (Fig. 4a), the stress intensity factor is decreased significantly in all number of composite patch layers. However, for single-sided repair, as the number of composite patch layers is increased the stress intensity factor is gradually increased. The comparison between the stress intensity factors shown in Fig. 4b and those obtained by Callinan *et al.* [4] indicates that their results are crack length independent and conservative, though, the FEA results from the present work indicates that as the number of patch layers is increased the stress intensity factor is increased towards the results obtained by Callinan *et al.* [4].

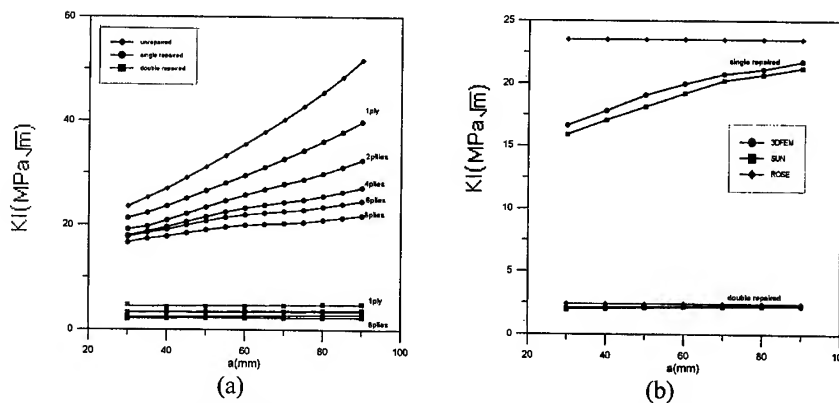


Figure 4: a) Variations of the stress intensity factor versus the crack length for different number of composite patch layers. b) Comparison of the stress intensity factors between the results of finite elements method and Callinan *et al.* [4] analysis.

The life cycles of the repaired plates under a cyclic load with constant amplitude are shown in Figure 5 for both double-sided and single-sided repaired plates. The results show that the life

cycle of the double-sided repaired plates are increased significantly. As the number of the patch layers is increased the life cycle of the component is increased .

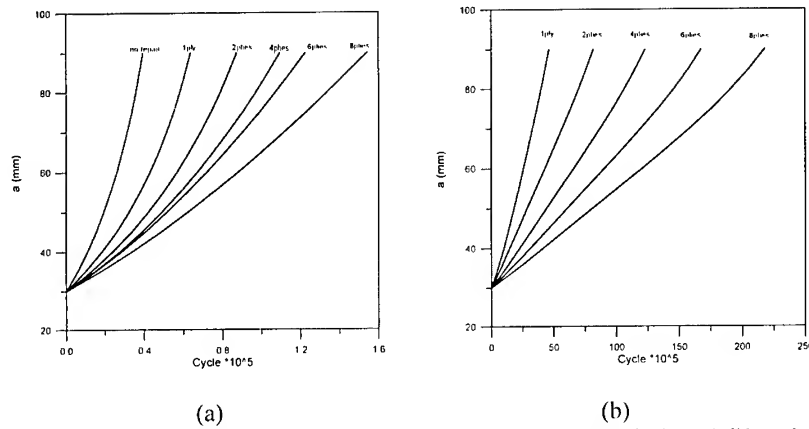


Figure 5: a) single-sided repaired panels life cycles. b) single-sided repaired panels life cycles

Typical results obtained for repaired panels with 8 layers composite patches and the adhesive thickness of $t_a = 0.1$ mm are compared with the results obtained for $t_a = 0.3$ mm in figure 6a. It is shown that the stress intensity factors obtained for $t_a = 0.3$ mm adhesive thickness is greater than

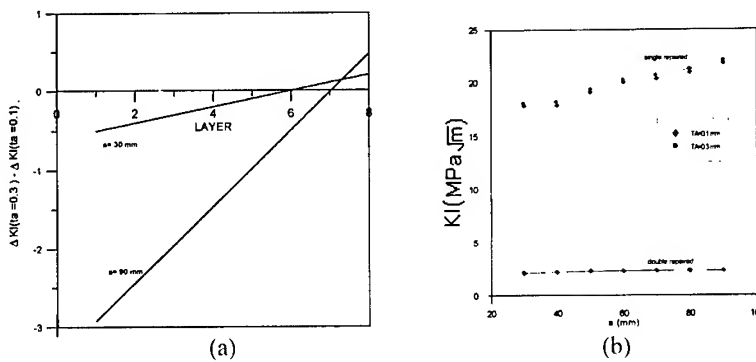


Figure 6: a) Comparison of the stress intensity factors of repaired panels between the adhesive thickness of 0.1 mm and 0.3 mm. b) Stress intensity factor variations versus number of patch layers for single sided repaired panels

those obtained for $t_a = 0.1$ mm. However, the effect of the adhesive thickness is not the same for all number of patch layers. As shown in Fig. 6b the stress intensity factors of the single-sided repaired plates with the number of patch layers less than 6 ($a=30$ mm) and adhesive thickness of 0.3 mm are smaller than those obtained for $t_a = 0.1$ mm. Therefore, One may conclude that the

stress intensity factor in repaired panels is influenced by mutual effects of adhesive thickness and number of patch layers.

CONCLUSION

Three dimensional finite elements analyses were performed for both single-sided and double-sided repaired panels to analyze the stress intensity factor and crack growth rate. The results show that as the number of the composite patch layers is increased in both single-sided and double-sided repaired panels, the stress intensity factor and the crack growth rate are decreased. It was shown that the results obtained by Callinan *et al.* for the analysis of repaired panels with a crack in a semi-infinite region are conservative, however, as the crack length is increased the Callinan *et al.* results are closer to the present finite element analyses. The effect of the adhesive thickness on the stress intensity factor in the single-sided repaired panels depends on the number of the composite patch layers and the adhesive thickness. If the adhesive thickness is increased, the stress intensity factor of the repaired panels with small patch thickness is decreased, but it is increased for large patch thickness.

REFERENCES

1. M. M. Ratwani, "Analysis of Cracked Adhesively Bonded Laminated Structures", *AIAA J.*, Vol.17, No. 4, 1979, pp. 988-994.
2. L. R. F. Rose, "A Cracked Plate Repaired by Bonded Reinforcements", *Int. J. Fract.*, Vol. 18, No. 2, 1982, pp. 135-44.
3. J. Lu, Y. Hu, and D. Ju, "An Assessing Method of Fatigue Life on Central-Through Cracked Plate with Adhesive Bounded Reinforcement", *Fatigue, Fracture, and Risk*, ASME, Vol. 215, 1991, pp. 135-140.
4. R. J. Callinan, L. R. F. Rose, and C. H. Wang, "Three Dimensional Stress Analysis of Crack Patching", *Advances in Fracture Research*, Vol. 4, 1997, pp. 2151-2158.
5. R. D. Cook, D. S. Malkus, and M. E. Plesha, "Concepts and Applications of Finite Element Analysis", Third Edition, John Wiley & Sons, New York, 1989.
6. M. R. Lena, J. C. Klug, and C. T. Sun, "Composite Patches as Reinforcements and Crack Arrestors in Aircraft Structures", *J. Aircraft*, Vol. 35, No. 2, pp. 318-323, 1998.

COMPLEMENTARITY OF THE EIGENVALUES IN THE THREE DIMENSIONAL WEDGES

Yongwoo Lee¹ and Seyoung Im²

¹Department of Mechanical Engineering, KAIST, Kusung-dong, Yusung-gu, TaeJön 305-701,
S. Korea : lyw@imhp.kaist.ac.kr

²Department of Mechanical Engineering, KAIST, Kusung-dong, Yusung-gu, TaeJön 305-701,
S. Korea : sim@kaist.ac.kr

SUMMARY : The eigenvalues of Williams' series expansion for generalized wedge problems, which include cracks, re-entrant corners, free edges, and cracks meeting with material interface, etc. are examined from the viewpoint of conservation laws like J -integral and M -integral. By use of the so-called two-state conservation laws or interaction energy, originally proposed by Eshelby and later treated by Chen and Shield, discussed is that the complementary pairs of eigenvalues exist in the J -integral sense and/or in the M -integral sense. Similar results are shown to hold for the eigenvalues of three dimensional wedges.

KEYWORDS : two-state conservation integral, J -integral, M -integral, three dimensional wedges, complementary relationship.

INTRODUCTION

The purpose of the present work is to examine the existence of a complementarity relationship among the eigenvalues in a generic isotropic wedge with the aid of the two-state conservation laws. The geometry of a generic wedge contains a variety of elements: free edges, cracks terminating at a material interface, and re-entrant edges of a thin film. It is found that an energetics property of the M -integral place a restriction upon the structure of asymptotic solutions in the eigenfunction series for these generic wedges in which the M -integral becomes path-independent. It turns out that this ensures the existence of a pair of complementary eigenvalues in the M -integral sense. For cracks in which the J -integral is conserved, similarly there exists a pair of complementary eigenvalues in the J -integral sense.

We first briefly review the two-state conservation laws from the J -integral and the M -integral[1]. We then define the complementary eigenvalues in the M -integral and in the J -integral sense, respectively. Subsequently we extend this complementary relationship to the problems of three dimensional generic wedges. Numerical examples are presented for illustration. Furthermore, applications of this complementarity, which have been reported in relation to analysis of thin films[2] and adhesive joints[3], are summarized.

TWO-STATE CONSERVATION LAWS

In this section, we discuss the two-state conservation laws by Chen and Shield[1]. For clarity, we restrict our attention to the plane strain problems, and assume that the material under consideration is isotropic.

Let u_α , σ_{ij} and ε_{ij} denote Cartesian components of a displacement vector, a stress and strain tensor, respectively. For the plane strain problems, we have the following governing equations in a two-dimensional domain:

$$\sigma_{\alpha\beta,\beta} = 0 \quad (\alpha, \beta = 1, 2) \quad (1.a)$$

$$\varepsilon_{\alpha\beta} = (u_{\alpha,\beta} + u_{\beta,\alpha}) / 2 \quad (1.b)$$

$$\sigma_{ij} = C_{ijkl} \varepsilon_{kl} \quad C_{ijkl} = \mu \delta_{ik} \delta_{jm} + \mu \delta_{im} \delta_{jk} + 2\nu \mu \delta_{ij} \delta_{km} / (1-2\nu) \quad (1.c)$$

where μ and ν are shear modulus and Poisson's ratio, respectively, and the comma indicates the partial differentiation with respect to the Cartesian coordinate x_i . For the plane problems, the J -integral[4,5] and the M -integral[6] may be written as:

$$J = \int_C (W n_i - t_i \frac{\partial u_i}{\partial x_j}) ds \quad (2.a)$$

$$M = \int_C (W n_i - t_i \frac{\partial u_i}{\partial x_j}) x_j ds \quad (2.b)$$

where n_j is the component of unit outward normal on the contour C ; W and t_i indicate the strain energy density and the traction component, given as $W = C_{ijkl} \varepsilon_{ij} \varepsilon_{kl} / 2$ and $t_i = \sigma_{ij} n_j$. In our discussion, we exclude the L -integral and the associated two-state integral because they are not connected to the present work in a pertinent way.

Consider two independent elastic states "A" and "B" for the plane problems. We suppose another elastic state "C", which is obtained by superposing the two equilibrium states "A" and "B". Then the path-independent integrals J and M are written as

$$J^C = J^A + J^B + J^{(A,B)} \quad (3.a)$$

$$M^C = M^A + M^B + M^{(A,B)} \quad (3.b)$$

where the superscripts A, B and C indicate the aforementioned elastic states, and $J^{(A,B)}$ and $M^{(A,B)}$ are given as

$$J^{(A,B)} = \int_C [C_{ijkl} \varepsilon_{ij}^A \varepsilon_{kl}^B n_i - (t_i^A \frac{\partial u_i^B}{\partial x_j} + t_i^B \frac{\partial u_i^A}{\partial x_j})] ds \quad (4.a)$$

$$M^{(A,B)} = \int_{\Gamma} [C_{ijkl} \varepsilon_{ij}^A \varepsilon_{kl}^B n_n - (t_i^A \frac{\partial u_i^B}{\partial x_n} + t_i^B \frac{\partial u_i^A}{\partial x_n})] x_n ds \quad (4.b)$$

The integrals $J^{(A,B)}$ and $M^{(A,B)}$ result from the mutual interaction between two elastic states A and B. These are conservation integrals for two equilibrium states, since the area integral version of these contour integrals vanishes identically for the domains with no singularities. In this context, these may be termed the two-state conservation laws, as in the preceding discussion.

We briefly summarize the structure of the asymptotic solutions in the form of eigenfunction series for the two dimensional wedge problem. The asymptotic solutions for the stress and displacement components for the present wedge may be written in the following power type eigenfunction of $z = x_1 + ix_2$ and $\bar{z} = x_1 - ix_2$ [2]:

$$\begin{aligned} \sigma_{\alpha\beta}^{(m)} &= \text{Re} \left[\sum_{\delta_n} \beta_n \sum_{k=1}^2 \{ C_{kn}^{(m)} (\Lambda_{\alpha\beta k} g_n'(z) + \Gamma_{\alpha\beta k} \bar{z} g_n''(z)) + C_{(k+2)n}^{(m)} (\bar{\Lambda}_{\alpha\beta k} g_n'(\bar{z}) + \bar{\Gamma}_{\alpha\beta k} z g_n''(\bar{z})) \} \right] \\ u_{\alpha}^{(m)} &= \frac{1}{2\mu^{(m)}} \text{Re} \left[\sum_{\delta_n} \beta_n \sum_{k=1}^2 \{ C_{kn}^{(m)} (p_{\alpha k}^{(m)} g_n(z) + q_{\alpha k} \bar{z} g_n'(z)) + C_{(k+2)n}^{(m)} (\bar{p}_{\alpha k}^{(m)} g_n(\bar{z}) + \bar{q}_{\alpha k} z g_n'(\bar{z})) \} \right] \\ \text{with } g_n'(z) &= z^{\delta_n}, \text{ and the non zero components of } \Lambda_{\alpha\beta k}, \Gamma_{\alpha\beta k}, p_{\alpha k} \text{ and } q_{\alpha k}: \end{aligned} \quad (5)$$

$$\begin{aligned} -A_{111} &= A_{221} = iA_{121} = 1, \quad A_{112} = A_{222} = 2, \quad \Gamma_{112} = -\Gamma_{222} = -i\Gamma_{122} = -1, \\ p_{11}^{(m)} &= -ip_{21}^{(m)} = -1, \quad p_{12}^{(m)} = ip_{22}^{(m)} = 3 - 4\nu^{(m)}, \quad q_{12} = -iq_{22} = -1 \end{aligned}$$

where δ_n is an eigenvalue and C_{kn} , short for $C_k(\delta_n)$, is the corresponding eigenvector; $\beta_n = \beta(\delta_n)$ represents the load parameter or the intensity of the elastic field associated with eigenvalue δ_n . Note that β_n is real for a real δ_n , but it is, in general, complex for a complex δ_n . For a complex δ_n , it is self-evident from the expression (5) that its conjugate $\bar{\delta}_n$ also belongs to the eigenvalues. For clarity, we assume that the imaginary part of complex δ_n is positive in the expression (5) since a complex eigenvalue δ_n and its conjugate $\bar{\delta}_n$ lead to the same eigenfunction. The superscript "(m)" indicates the m -th sector. We will omit the superscript "(m)" for simplicity unless it is needed for clarity to distinguish one sector from another.

For the generic composite wedge under consideration, the boundedness of the strain energy restricts the range of eigenvalue δ_n such that $\text{Re}(\delta_n) > -1$. The terms giving rise to a singular stress field near the vertex are represented by the eigenvalues $\bar{\delta}_s$ within the range $-1 < \text{Re}(\delta_s) < 0$.

For an arbitrary eigenvalue δ_l in equations (5), we first define its complementary eigenvalue δ_l^c in the M -integral sense such that

$$\delta_l^c + \delta_l = -2$$

It has been proved that δ_l^c is also an eigenvalue for the given wedge[2,7]. The elastic state for the complementary eigenvalue δ_l^c with the load parameter β_l^c , may be written as

$$\begin{aligned}\sigma_{\alpha\beta}(\delta_l^c) &= \text{Re}[\beta_l^c \sum_{k=1}^2 \{C_{kl} (A_{\alpha\beta k} g_{l_k}'(z) + \Gamma_{\alpha\beta k} \bar{z} g_{l_k}''(z)) + C_{(k+2)l} (\bar{A}_{\alpha\beta k} g_{l_k}'(\bar{z}) + \bar{\Gamma}_{\alpha\beta k} z g_{l_k}''(\bar{z}))\}] \\ u_{\alpha}(\delta_l^c) &= \frac{1}{2\mu} \text{Re}[\beta_l^c \sum_{k=1}^2 \{C_{kl} (p_{\alpha k} g_{l_k}(z) + q_{\alpha k} \bar{z} g_{l_k}'(z)) + C_{(k+2)l} (\bar{p}_{\alpha k} g_{l_k}(\bar{z}) + \bar{q}_{\alpha k} z g_{l_k}'(\bar{z}))\}] \quad (6)\end{aligned}$$

with l_k being the index indicating the eigenvalue δ_l^c , so that $g_{l_k}'(z) = z^{\delta_l^c}$ and

$$C_{kl} = C(\delta_l^c)$$

For cracks around which the J -integral becomes path-independent, in a similar way we can define the complementary eigenvalue δ_l^c in the J -integral sense for an arbitrary eigenvalue δ_l :

$$\delta_l^c = -1 - \delta_l$$

The singular stress for three-dimensional generic wedges has the following form:

$$\sigma_{ij} = r^{-\delta_l} \bar{\sigma}_{ij}(\theta, \phi; \delta_l) \quad (7)$$

where r is the distance from the singular vertex, $\bar{\sigma}_{ij}(\theta, \phi; \delta_l)$ determines angular variation of the stress; θ and ϕ are the spherical coordinates(see Fig. 1(b)).

For such three-dimensional generic wedges, we may extend the complementary relationship in the M -integral sense as follows:

$$\delta_l^c = -3 - \delta_l$$

NUMERICAL EXAMPLES

Bimaterial wedges under the plane strain condition are considered to obtain the eigenvalues(see Fig. 1(a)). By applying the near-field condition near the vertex, which consists of the traction free along the free surfaces and the traction and displacement continuity along the interface[2], the eigenvalues are computed for the free edge, the re-entrant edge of a thin film and the vertex of an adhesive lap joint. For a free edge case and a thin film, the material properties are $\alpha=1/2$ and $\beta=1/16$ where α and β are Dundurs' parameters and for an adhesive lap joint the material properties are $E_1=200 \times 10^3 \text{Mpa}$, $\nu_1=0.3$, $E_2=3.4 \times 10^3 \text{Mpa}$ and $\nu_2=0.35$.

The quarter-infinite crack in isotropic homogeneous solids is considered to obtain the eigenvalues for three dimensional wedges as shown in Fig. 1(b). The material properties are $E=1.0\text{MPa}$ and $\nu=0.3$. In case of three dimensional wedges, the eigenvalues are computed by means of the finite element technique by formulating a weak variational principle for the angular variation of displacements on a unit sphere about the singular point and discretizing it by dividing the image of the region on the sphere onto the $\theta\phi$ -plane[8].

The eigenvalues are tabulated in Table 1 for two-dimensional and three-dimensional cases. From this table, verified is the complementary relation $\delta_I^c + \delta_I = -2$ for the two-dimensional wedge and $\delta_I^c + \delta_I = -3$ for the three-dimensional wedge: that is, δ_I appears as a complementary pair.

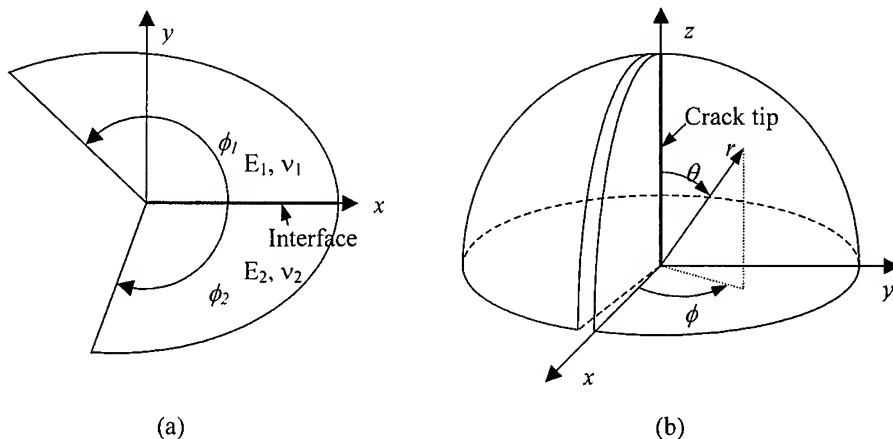


Fig. 1 The configurations near the vertex. (a) bimaterial wedge. (b) quarter-infinite crack.

CONCLUDING REMARKS

The existence of the complementarity relationships is linked to the conservation laws of the J and the M -integral. This type of relationship has been extended to the cases of three dimensional generic wedges, and an appropriate numerical example has been demonstrated.

ACKNOWLEDGEMENTS

The senior author gratefully acknowledges the support for this study from the Korean Science and Engineering Foundation(Grant No. 981-1004-025-2).

REFERENCES

1. F. H. K. Chen and R. T. Shield, "Conservation Laws in Elasticity of the J-integral type," *Z. Angw. Math. Phys.(ZAMP)*, Vol. 28, 1977, pp. 1-22.

2. S. Im and K-S Kim, "Application of the two-state M-integral for computing an intensity of a singular near-tip field for a generalized composite wedge," accepted for publication in *J. Mech. Phys. of Solids*, Vol. 48, 2000, pp. 129-151.
3. Y. Lee, N. S. Goo, and S. Im, "Application of two-state M-integral for analysis of adhesive lap joints," submitted to *Int. J. Num. Meth. Eng.*, 1999.
4. R. D. Eshelby, *The Continuum Theory of Lattice Defects*, Solid State Physics, **III**, eds., Seitz, F. and Turnbull, D., Academic Press, 1956.
5. J. R. Rice, "A Path Independent Integral and the Approximate Analysis of Strain Concentration by Notches and Cracks," *ASME J. Appl. Mech.*, Vol. 35, 1968, pp. 379-386.
6. J. K. Knowles and E. Sternberg, "On a class of Conservation Laws in a Linearized and Finite Elastostatics," *Arch. Rat. Mech. Anal.*, Vol. 44, 1978, pp. 187-211.
7. D. Leguillon and E. Sanchez-Palencia, *Computation of Singular Solutions in Elliptic Problems and Elasticity*, Masson(or John Wiley & Sons), New York, 1987.
8. Z. P. Bazant and L. F. Estenssoro, "Surface singularity and crack propagation in a half-space," *Int. J. Solids Structures*, Vol. 15, 1979, pp.405-426.

Table 1 Complementary pairs of the eigenvalues.

Free edge ($\phi_1=90^\circ$, $\phi_2=90^\circ$) ($\alpha = 1/2$, $\beta = 1/16$)	Re-entrant edge of a thin-film ($\phi_1=45^\circ$, $\phi_2=180^\circ$) ($\alpha = 1/2$, $\beta = 1/16$)	Vertex of a lap joint ($\phi_1=180^\circ$, $\phi_2=90^\circ$)	Three-dimensional quarter-infinite crack for symmetric deformation. ($\nu=0.3$)
$3.8401 \pm i 1.2160$	$2.5082 \pm i 0.1330$	$2.0000 \pm i 6.8554 \times 10^{-3}$	0.6808
$2.8272 \pm i 1.0243$	$1.5315 \pm i 0.1605$	$1.0000 \pm i 9.5562 \times 10^{-3}$	0.2146
$1.7977 \pm i 0.8662$	$0.6860 \pm i 0.3585$	$0.7139 \pm i 5.9644 \times 10^{-1}$	0.0040
$0.7947 \pm i 0.5065$	0.3325	0.0000	0.0003
0.0000	0.0000	-1.1125×10^{-4}	-0.4529
-0.1213	-0.4239	-3.2725×10^{-1}	-0.9990
-1.0000	-1.0000	-1.0000	-0.9998
-1.0000	-1.0000	-1.0000	-2.0002
-1.8787	-1.5761	-1.6728	-2.0010
-2.0000	-2.0000	-1.9999	-2.5471
$-2.7947 \pm i 0.5065$	-2.3325	-2.0000	-3.0003
$-3.7977 \pm i 0.8662$	$-2.6860 \pm i 0.3585$	$-2.7139 \pm i 5.9644 \times 10^{-1}$	-3.0040
$-4.8272 \pm i 1.0243$	$-3.5315 \pm i 0.1605$	$-3.0000 \pm i 9.5562 \times 10^{-3}$	-3.2146
$-5.8401 \pm i 1.2160$	$-4.5082 \pm i 0.1329$	$-4.0000 \pm i 6.8554 \times 10^{-3}$	-3.6808

COMPUTATIONAL ANALYSIS OF CRACK GROWTH IN SiC/SiC COMPOSITE CAUSED BY CREEP OF BRIDGING FIBERS

Hisashi Serizawa¹, Motooki Ando², Charles A. Lewinsohn³, and Hidekazu Murakawa¹

¹*Joining and Welding Research Institute, Osaka University*

11-1 Mihogaoka, Ibaraki, Osaka 567-0047, Japan: serizawa@jwri.osaka-u.ac.jp

²*Graduate School of Engineering, Osaka University*

2-1 Yamada-oka, Suita, Osaka 565-0871, Japan: ando@jwri.osaka-u.ac.jp

³*Pacific Northwest National Laboratory*

MSIN:P8-15, P.Obox 999, Richland, WA 99352, USA: charles.lewinsohn@pnl.gov

SUMMARY: In order to analyze crack propagation behavior in SiC/SiC composites, new computer simulation methods using time dependent interface elements were developed and applied to time-dependent crack growth in SiC/SiC composite under four-point bending test on single-edge-notched beam bend-bars. The time-dependent crack growth in SiC/SiC composite was simulated by two methods, in which the creep property was introduced into the interface elements according to : 1) the general method of FEM analysis and, 2) a new method making the best use of the potential function. In both cases, the stage-II slow crack growth of a general creep deformation was simulated. Furthermore, by using the new method, not only the stage-III crack growth but also transition phenomena from the stage-II to stage-III could be simulated. So the new method is considered to have the potential capability to demonstrate the time-dependent crack growth behavior in SiC/SiC composite.

KEYWORDS: SiC/SiC Composite, SiC Fiber, Creep, Finite Element Method

INTRODUCTION

Silicon carbide fiber reinforced silicon carbide composites (SiC/SiC composites) are promising candidates as high heat flux component materials, due to their potential of high-temperature properties, chemical stability and good oxidation and corrosion resistance [1]. From the point of view of safe design of the structures, it is very important to estimate the fracture strength and behavior of materials exactly. In many previous proposed methods for evaluation of the composites, however, the formation and propagation of cracks in the composites have been microscopically and statically analyzed [2], and the macroscopic and dynamic deformations have not been revealed sufficiently.

Recently a simple computer simulation method was developed [3], in order to simulate the fracture phenomena that can be considered as the formation of new surface with the crack propagation. Based on the fact that surface energy must be supplied for the formation of new

surface, a potential function representing the density of surface energy was introduced in the proposed finite element method (FEM) using interface elements. And it was reported that the time-dependent crack growth, in inert environments, in SiC/SiC composites is determined by the creep rate of the bridging fibers in the bridging zone of composites [2]. So, as an objective of this report, a new time-dependent interface element was developed for introducing the creep property of fibers into the interface element, and it was applied to analyze time-dependent crack growth, especially slow crack growth, of SiC/SiC composites.

INTERFACE POTENTIAL

In the case of ordinary crack propagation problems, a method using the interface element has been proposed [3]. The mechanical behavior of the crack, in other words, the formation and the propagation of the crack is governed by the interface potential ϕ per unit area of the crack surface. The requirements of the interface potential function are : 1) the surface energy γ , which is necessary to form the new surface as a material constant, and 2) a continuous function of opening displacement δ .

Among many functions satisfying these requirements, a Lennard-Jones type potential [4] may be employed and the potential energy ϕ is defined by the following equation.

$$\phi(\delta) \equiv 2\gamma \cdot \left\{ \left(\frac{r_0}{r_0 + \delta} \right)^{2n} - 2 \cdot \left(\frac{r_0}{r_0 + \delta} \right)^n \right\} \quad (1)$$

Where δ is the crack opening displacement and γ , n and r_0 are material constants. In particular, 2γ is the surface energy per unit area.

METHOD OF MODELING

In this research, the bridging zone was analyzed macroscopically, not microscopically. One interface element was assumed to represent many fibers and matrices in the bridging zone. The properties of the interface between fiber and matrix were assumed to be invariant, with respect to time or displacement. In other words, effective matrix properties were used to incorporate both the true matrix and the interface. Away from the cracked region, the composite was described by ordinary elements of FEM.

In order to characterize both fibers and matrices by one interface element, the interface potential ϕ was defined by the following equation as same as the simple rule of mixtures.

$$\phi \equiv \phi_f + \phi_m \quad (2)$$

$$\phi_f \equiv 2\gamma_f \cdot \left\{ \left(\frac{r_{f0}}{r_{f0} + \delta} \right)^{2n} - 2 \cdot \left(\frac{r_{f0}}{r_{f0} + \delta} \right)^n \right\} \quad (3)$$

$$\phi_m \equiv 2\gamma_m \cdot \left\{ \left(\frac{r_{m0}}{r_{m0} + \delta} \right)^{2n} - 2 \cdot \left(\frac{r_{m0}}{r_{m0} + \delta} \right)^n \right\} \quad (4)$$

Where subscripts of f and m indicate fiber and matrix, respectively. In this study, only the creep effect of fiber on the time-dependent crack growth was taken into account and the interface potential of fiber ϕ_f was assumed to have a time dependency. To introduce the creep effect, two methods according to: 1) the general method of FEM analysis and, 2) a new method making the best use of the potential function were applied.

THEORETICAL FORMULATION

General Method of FEM Analysis

In the general method of FEM analysis for creep deformation, total strain can be divided into elastic strain, plastic strain, creep strain and other strain, which is for example thermal strain. In the case of SiC/SiC composites, the deformation may be limited to be elastic and creep deformation, because of their brittleness. The strain of ordinary elements in FEM is equal to be the increment of displacement in the interface element. Then, for the interface potential of the fiber, the increment of displacement $\Delta\delta$ can be divided into the elastic increment $\Delta\delta^e$ and the creep increment $\Delta\delta^c$ according to following equation.

$$\Delta\delta \equiv \Delta\delta^e + \Delta\delta^c \quad (5)$$

Further, the creep increment $\Delta\delta^c$ was assumed to follow the classical Dorn's formalism [10] under the steady-state creep by the following equation.

$$\Delta\delta^c \equiv A \cdot \sigma^m \cdot \Delta t \quad (6)$$

Where A , σ , m and Δt are a constant describing the structure of the deformation, the applied stress of the interface element, the stress exponent and a time increment, respectively.

A New Method

In Eq.(3), there are three material constants, which are γ_f , r_{f0} and n . Among these constants, only r_{f0} has the same dimension as the total displacement δ . As written in the previous section, in general, the displacement δ is controlled by Eq.(6) during creep. So, in this research, to make the best use of the potential function, the material constant r_{f0} was assumed to have the time dependency and the increment of r_{f0} was defined to follow the next equation.

$$\Delta r_{f0} = B \cdot \sigma^m \cdot \Delta t \quad (7)$$

Where B is a constant, and the other parameters are the same as Eq.(6). So the interface potential energy of fiber ϕ_f becomes a function of both opening displacement δ and time t , and this is written as $\phi_f(\delta, t)$. Then the total interface potential energy is also described as $\phi(\delta, t)$, while the interface potential energy of matrix ϕ_m is a function of only the opening displacement.

MODEL FOR ANALYSIS

In this report, as an example of time-dependent crack growth in SiC/SiC composites, slow crack growth, which was obtained by loading single-edge-notched beam bend-bar specimens in four-point bending (Fig.1(a)), was examined. In this test, the crack propagated from the tip of the notch in the direction, which is parallel to the applied load. Experimental details are published elsewhere [2]. The reinforcements of the composites were 2-dimensional, plain-weave Hi-Nicalon fiber mats, which were stacked in the direction of thickness, and the matrices were deposited by chemical vapor infiltration.

To examine the validity of the proposed method using the time dependent interface element for the analysis of slow crack growth, the model shown in Fig.1(b) was analyzed as the plain strain problem. Because of the symmetry of the problem, only the half of the specimen was used. The time dependent interface model was arranged along the crack propagation path. In this analysis, only the mode-I type crack propagation parallel to y-axis in Fig.1(b) was taken into account according to the experimental results. The parameter n in Eq.(3) and (4) was assumed to be 6.

RESULTS AND DISCUSSION

Figure 2 shows an experimental result of the time-dependent crack growth in SiC/SiC composite reported in reference [2], where the temperature was 1200 °C, atmosphere was gettered Ar (< 20 ppm O₂), and applied load was 556 N. In this paper, the proposed method with the time dependent interface element was only applied to demonstrate the stage-II type slow crack growth. Therefore the area in the time-displacement curve, where the displacement was more than 0.06 mm, was compared with the calculation results since the rate of change of the displacement, with respect to time, was minimal. Accurate modeling of all stages of crack growth behavior must include a time-dependent term. The parameter m was assumed to be 1 according to reference [5] since the test was performed at high-temperature.

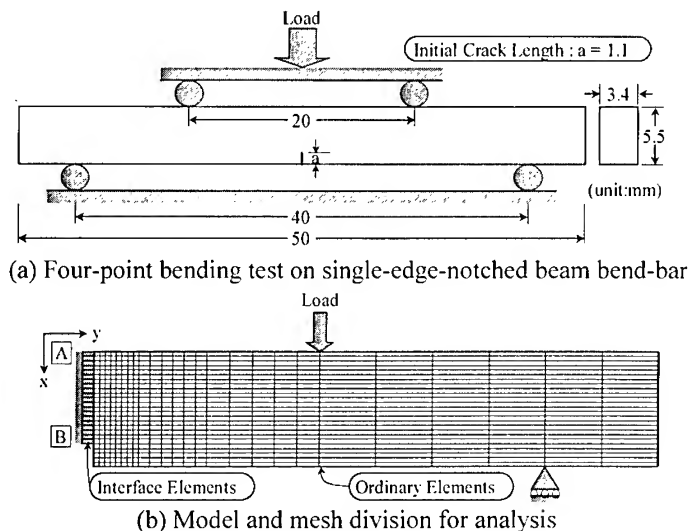


Fig.1 Schematic illustration of bending test and model for analysis

Figure 3 shows the experimental result and the calculation results using both the general method and new method. Although both calculation results simulated the stage-II slow crack growth, the result using the new method represented not only the stage-II slow crack growth but also the stage-III crack growth. So after this, the calculations using the new method under the different applied load were examined and discussed.

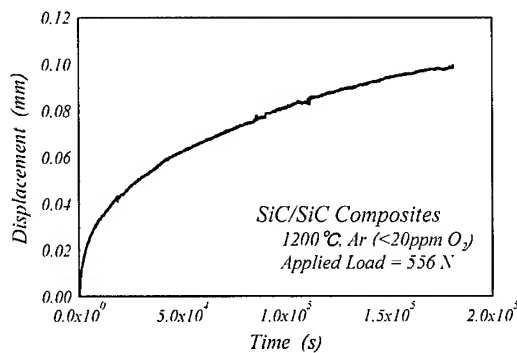


Fig. 2 Displacement-time curve during time-dependent crack growth in SiC/SiC composites [6]

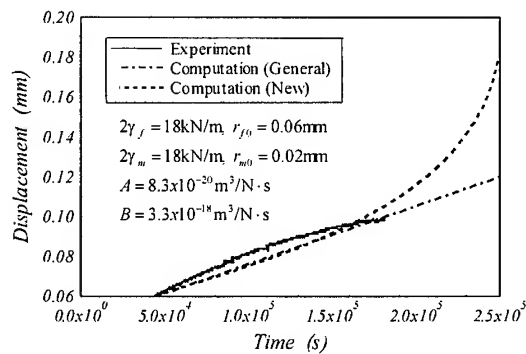


Fig. 3 Comparison between experiment and computation in time-dependent crack growth

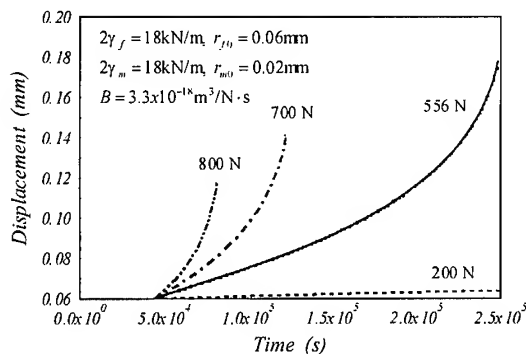


Fig. 4 Calculated displacement-time curves under various applied load.

The calculation results under various applied load using the new method were shown in Fig.4. The ends of curves indicate the fracture point of the specimen. The transition time from stage-II to stage-III decreased with increasing applied load, similar to the general creep deformation. Therefore, although the calculation result does not exactly represent the experimental behavior, the new method is considered to have the potential capability to demonstrate the time-dependent crack growth behavior in SiC/SiC composite. As the future work, the effect of fiber fracture and the effects of other parameters in Eq.(3) and (4) will be examined.

CONCLUSIONS

In order to analyze crack propagation behavior in SiC/SiC composite, a new computer simulation method using time dependent interface elements was developed and applied to time-dependent crack growth in composites. The conclusions can be summarized as follows.

- (1) The time-dependent crack growth in SiC/SiC composite was simulated by two methods, in which the creep property was introduced into the interface elements according to : 1) the general method of FEM analysis and, 2) a new method making the best use of the potential function. In both cases, the stage-II slow crack growth of a general creep deformation was simulated.
- (2) By using the new method, not only the stage-III crack growth but also transition phenomena from stage-II to stage-III could be simulated. So the new method is considered to have the potential capability to model all stages of time-dependent crack growth behavior in SiC/SiC composite.

ACKNOWLEDGEMENTS

This work was maintained by Core Research for Evolutional Science and Technology : Advanced Material Systems for Conversion of Energy.

REFERENCES

- 1 R. H. Jones, C. A. Lewinsohn, G. E. Youngblood and A. Kohyama, *Key Eng. Mater.*, Vols.164-165, 1999, pp.405.
- 2 C. A. Lewinsohn, C. H. Henager, Jr. and R. H. Jones, *Ceram. Trans.*, Vol.74, 1996, pp.423.
- 3 Z. Q. Wu, H. Serizawa and H. Murakawa, *Key Eng. Mater.*, Vol.166, 1999, pp.25.
- 4 A. Rahman, *Phys. Rev.*, Vol.136A, 1964, pp.405.
- 5 G. Boitier, J. L. Chermant and J. Vicens, *Key Eng. Mater.*, Vols.164-165, 1999, pp.317.
- 6 R. Bodet, J. Lamon, N. Jia and R. E. Tressler, *J. Am. Ceram. Soc.*, Vol.79[10], 1996, pp.2673.

FRACTURE ANALYSIS OF REPAIRED PANELS WITH ADHESIVELY BONDED COMPOSITE PLATES

Hamid Reza Daghyani¹, Siavash Eshaghi¹ and Hossein Hosseini Toudeshky²

¹ Mechanical Eng. Dept., hamid@cic.aku.ac.ir

² Aeronautical Eng. Dept., hosseini@cic.aku.ac.ir

Amirkabir University of Tech., Tehran 15914, Iran

SUMMARY: The stress intensity factor of a cracked plate is evaluated when repaired with single-sided and double-sided composite patches. A three layer technique is used in the finite element analyses and the results are compared with a three-dimensional finite element model. The results show that the stress intensity factor of an aluminum cracked plate is minimised when the fibre orientation of the patched layer is perpendicular to the crack face. The thickness of adhesive layer has minor effect on the stress intensity factor at the crack tip of the aluminum panel. An optimum dimensions for the patched plate is obtained when appropriate fibre orientation is used.

KEYWORDS: Cracked panels, Stress intensity factor, Composite repair.

INTRODUCTION

Repair of damaged components with adhesively bonded joints has been recognised as a cost-effective means in advanced aerospace structures. When a cracked panel is repaired, the stress state at the crack front is affected by the geometry conditions of the patched plate. Patching the cracked panels by single-sided repair is most often because only one face of a damaged component surface is accessible. A single-sided repair reduces the stress intensity factor at the crack tip, though produces out-of-plane bending effects. Several researchwork have been conducted to analyse the stress re-distribution at the crack tip of repaired structures. Ratwani [1] and Rose [2] carried out analytical studies to characterise the behaviour of cracked panels under various applied load conditions. Many numerical approaches have been conducted for the double-sided (symmetric) and single-sided (unsymmetric) repaired panels. In the single-sided repair, due to the bending effect induced on the repaired structure, a three dimensional analysis is often preferred. Chue *et al* [3] and Sun *et al*. [4] performed three-dimensional finite element analyses and found the stress intensity factor of cracked plates when repaired with composite layers.

Naboulsi and Mall [5] extended a three-layer model using Mindlin plate elements to evaluate the stress intensity factor of a cracked panel. The work of Daghyani *et al.* [6] showed that in a single-sided repair, the stress intensity factor at the free edge is higher than that in the regions close to the patch layer.

In the present study, the stress intensity factor of damaged panels with center-cracks is evaluated when subjected to in-plane loading, considering the effect of out-of-plane bending of composite patched plate for single-sided repair. The effects of geometry and the fibre orientation of the composite patch as well as the adhesive thickness on the stress intensity factor of the cracked plate is investigated.

FINITE ELEMENT MODELING

An aluminum plate containing a central through crack is adhesively repaired by unidirectional boron/epoxy composite patches. Fig. 1 shows typical single-sided and double-sided patch configurations. To evaluate the stress intensity factor of the cracked plate after repair, a three-layer model consisting of cracked plate, adhesive and composite patch is developed to provide an economical finite element model using two-dimensional Mindlin plate elements with the capability of transverse shear deformation. To evaluate the results of three-layer model, a three-dimensional finite element model (FEM) is used in which singular elements are employed at the crack front.

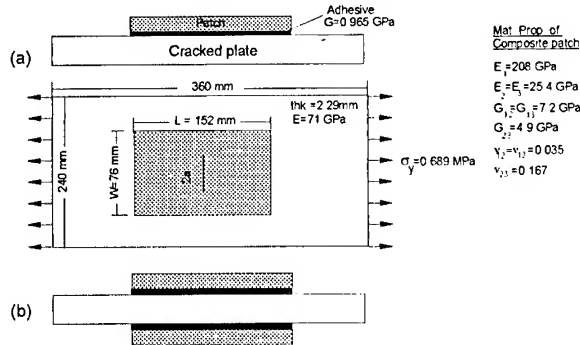


Fig. 1 Typical a) single-sided and b) double-sided patch configurations used in FEM.

In the Mindlin plate theory linear displacement field is considered along the plate thickness as follows:

$$\begin{aligned} U_x &= \bar{U}_x + Z\theta_y \\ U_y &= \bar{U}_y + Z\theta_x \\ U_z &= \bar{U}_z \end{aligned} \quad (1)$$

where \bar{U}_x , \bar{U}_y and \bar{U}_z are the mid-plane displacements along the x-, y- and z-directions respectively, θ_x and θ_y are the rotations of the cross-section along the x- and y-axis. The x and y

coordinates are in the plane of plate and z is in the thickness direction. Fig. 2 shows a three-layer model in two-dimensional finite element analysis.

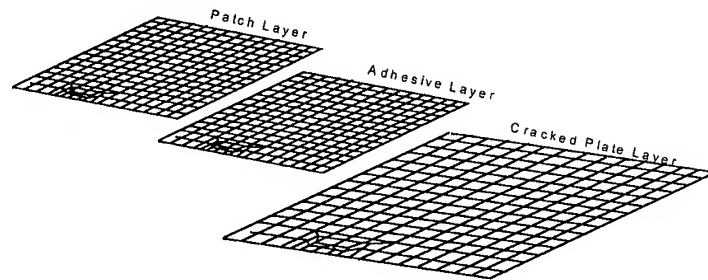


Fig. 2. Three-Layer model in two-dimensional finite element analysis.

Since in the single-sided repair a bending moment, M is induced on the cracked plate, the energy release rate, G_I can be evaluated considering the vertical displacement, V and the rotation of the point a shown in the Fig. 3 as follow:

$$G_I = \frac{1}{2\Delta c} F_y^b (V^a - V^{a'}) + \frac{1}{2\Delta c} M_x^b (\theta_x^a - \theta_x^{a'}) \quad (2)$$

Eq. 1 is rewritten as:

$$G_I = \frac{1}{\Delta c} F_y^b V^a + \frac{1}{\Delta c} M_x^b \theta_x^a \quad (3)$$

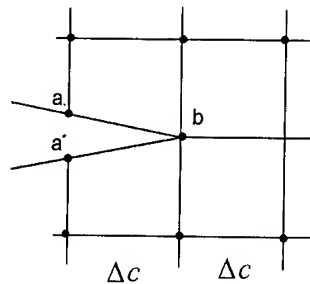


Fig. 3. Crack tip elements in three-layer model.

The stress intensity factor is calculated assuming plane strain state of stress at the near crack tip by:

$$K_I = \left(\frac{G_t E_p}{1 - \nu_p^2} \right)^{\frac{1}{2}} \quad (4)$$

where ν_p and E_p are Poisson's ratio and Young's modulus of aluminum plate, respectively. In the 3-D FEM, K_I at the crack tip is evaluated using crack tip opening displacement with a linear extrapolation along the nodal element line.

RESULTS AND DISCUSSIONS

The stress intensity factor of the repaired plate for the geometry and loading conditions shown in Fig. 1 calculated in the present study is compared with other research works in the literature as shown in Table 1. K_I is normalised with remote stress σ_o and crack length $2a$ as: $K = \frac{K_I}{\sigma_o \sqrt{\pi a}}$.

1. Normalised stress intensity factor at the mid-plane for single-sided repair of various research works.

Present study 3-Layer FEA	Present study 3-D FEA	Nabousi <i>et al.</i> 2-D	Sun <i>et al.</i> 2-D	Sun <i>et al.</i> 3-D	Chue <i>et al.</i> 3-D
0.6643	0.590	0.570	0.536	0.612	0.481

Sun *et al.* [4] used fine meshes at the crack tip of their 3-D model which resulted in an accurate K . The results of the 3-layer model of present study is well correlated to the work of Sun *et al.* [4]. Clearly, the 3-layer model is easy to model with less running time in the finite element analysis.

The effect of fibre orientation on K is shown in Fig. 4. The fibre angle, ϕ is zero, when it is parallel to the crack face, and $\phi = 90^\circ$ when it is perpendicular to the crack face. K decreases as ϕ increases from 0° to 90° . This means when the fibre orientation is perpendicular to the crack face, it prevents the opening of the crack, thus reduces the stress intensity factor of the cracked plate.

Fig. 5 exhibits the effect of patch dimensions on K in the repaired panel when the number of layers, $n = 6$ and $\phi = 90^\circ$. Keeping W as a constant and increasing the L , results in decreasing the K , while with a constant L , increasing the W results in rising the K in the cracked panel. A ratio of $L/W = 2$ seems to be the best dimensions of the patched layer.

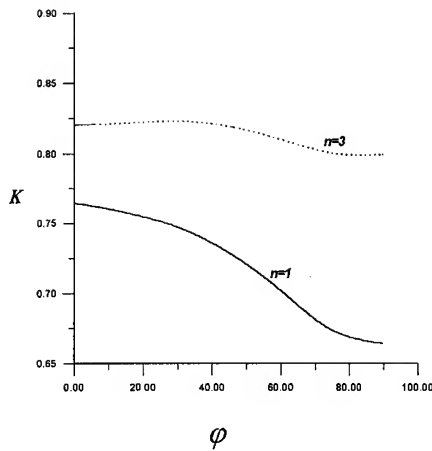


Fig. 4. Normalised stress intensity factor versus fiber angle φ .

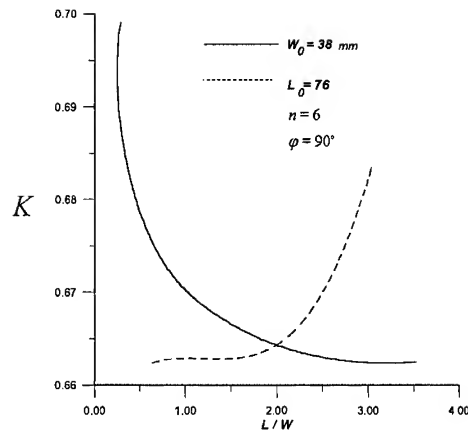


Fig. 5. Normalised stress intensity factor versus patch dimensions.

The variations of K as a function of adhesive thickness is shown in Fig. 6. The thickness of adhesive layer has minor effect on stress intensity factor of the cracked plate. The distribution of shear stress along the adhesive layer in the single-sided repair is illustrated in Fig. 7. Shear stress rises at the free edge of the patch and decreases along the adhesive layer, then increases again around the crack region due to the bending effect. However, the shear stress distribution of double-sided panel decreases sharply from the edge along the adhesive layer.

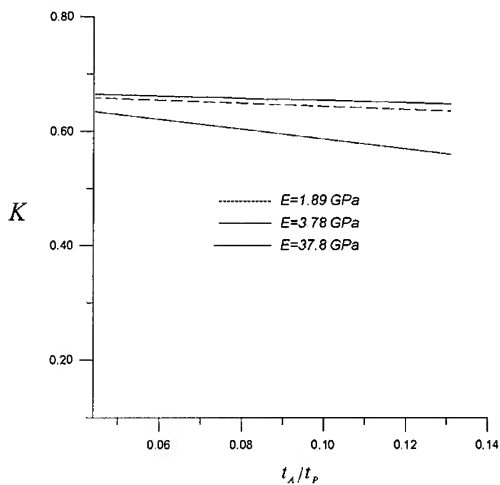


Fig. 6. Normalised stress intensity factor versus adhesive thickness.

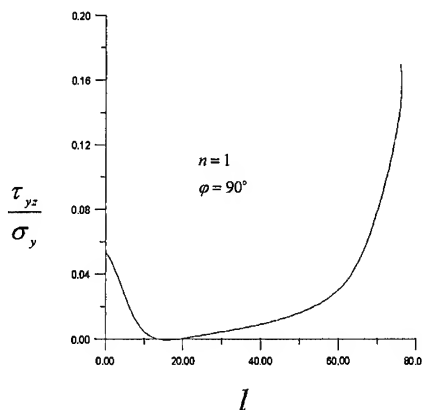


Fig. 7. Shear stress distribution for single sided repair along the bonded line, l .

CONCLUSION

A three-layer finite element model was developed for a cracked panel repaired with composite layers to calculate the stress intensity factor. The results of the three-layer model was compared with the three dimensional finite element analyses showing well correlation of the methods. The results show that in a single-sided repair when the direction of composite fibre is perpendicular to the crack face, the stress intensity factor, K approaches to its minimum value. Adhesive thickness showed minor effect on K . The stress intensity factor of single-sided crack decreases considerably when the ratio of the length to the width (L/W) of the patched layer is almost 2. The shear stress distribution of the single-sided and double-sided repair show different patterns around the cracked region due to the bending effect of the patch layer in single-sided repair.

REFERENCES

1. M. M. Ratwani, "Analysis of cracked adhesively bonded laminated structures", *AIAA J.*, 17, 1979, pp. 988-994.
2. L. R. F. Rose, "A cracked plate repaired by bonded reinforcements", *Int. J. Fract.*, 18, 1982 pp. 135-44.
3. Ch-W. Chue, I. Chang and J. Isai, "Bonded repair of a plate with inclined central crack under biaxial loading", *Composite Strucs.*, 28, 1994, pp. 39-45.
4. C. T. Sun, J. Klug, and C. Arendt, "Analysis of cracked aluminum plate repaired with bonded composite panels", *AIAA J.*, 34(2), 1996, pp. 369-374.
5. S. Naboulsi and S. Mall, S. "Modeling of a cracked metallic structure with bonded composite patch using the three layer technique", *Composite Strucs.*, 35, 1996, pp. 295-308.
6. H. R. Daghyani, H. Hosseini and S. Eshaghi, "Fracture Behaviour of Repaired Panels", *First Int., Conf., on Advanced Structural Eng. and Mech.*, Seoul, Korea, August 23-25, 1999, pp. 1291-1296.

Effects of Fiber Content on Strength and Damage for Notched FRP Plates under Static Load

Toshihiro Yamamoto¹ and Hiizu Hyakutake¹

¹*Department of Mechanical Engineering, Fukuoka University,
8-19-1 Nanakuma, Fukuoka 814-0180, Japan: yamamott@fukuoka-u.ac.jp*

SUMMARY: To develop a failure criterion for notched FRP plates based on the concept of severity near the notch root, the effects of fiber content on strength and damage initiation for notched glass fiber-reinforced polycarbonate plates subjected to tension were examined in this paper. The damage near the notch root was evaluated by measuring the luminance distributions during tests by using a CCD camera. The experiment shows that the initiation and growth of the damaged zone near the notch root were governed predominantly by notch-root radius, the maximum elastic stress at the notch root and fiber content. Closer observation in the damaged zone revealed that the process of microfracture depends on the fiber content. The deformation bands were observed in the matrix around the fiber for the specimen for which the weight percent of fiber is not greater than 10 %.

KEYWORDS: reinforced plastics, polycarbonate, notch, strength, damage, tension, luminance.

INTRODUCTION

Studying stress distribution near the notch root, Nisitani and Hyakutake [1] have obtained a failure criterion for notched bars under static load. The criterion is based on the concept of the severity near the notch root. The severity is determined by both the maximum elastic stress at the notch root and notch-root radius. Hyakutake et al. [2] have shown that the criterion is applicable to notched FRP plates of an orthotropic lamina.

For notched FRP plates the damage zone initiates and grows near the notch root prior to catastrophic fracture. The strength of notched FRP plates depends on the growth of damage. To evaluate quantitatively the damage near the notch root, we measured the luminance distributions by means of the luminance measurement technique with a CCD camera [3]. We have shown that the process of the damage initiation and growth near the notch root under static load can be explained on the concept of severity near the notch root [3].

The aims of the present study are to develop a failure criterion based on the concept of severity near the notch root for the initiation and growth of the damaged zone of notched FRP plates. An experimental program is presented which examines the effects of fiber content on strength and damage for notched plates of a short glass fiber-reinforced polycarbonate under static tension.

EXPERIMENTAL PROCEDURE

The material used was a glass fiber-reinforced polycarbonate (GF/PC). Idemitsu "Toughlon" PC was applied to the matrix. The plates of GF/PC were made by injection molding. The dimensions of the plates were 70 mm width, 270 mm long, and 3 mm thick. Photomicrographs of a transverse section of the GF/PC plate are shown in Fig. 1. The weight percent of E-glass fiber had the following four different values: 1, 10, 30 and 50 %. The diameter of a fiber is about 0.013 mm.

The nominal stress-strain curves of tension tests for unnotched GF/PC are represented in Fig. 2. It can be seen that the samples for which the fiber content is not greater than 10 % fails in a ductile manner, while the sample for which that is not less than 30 % fails in a brittle manner.

All specimens were cut from the plate, so that the principal direction of specimens coincided with longitudinal direction of the plate. Notched specimens having a constant width (= 20 mm) were notched in a U-shaped on both sides at the midpoint of their length. The notch-root radius had the following four different values: 0.25, 0.5, 1 and 2 mm. In addition, the notch depth ranged from 1 to 4 mm.

Tension tests were performed by an Instron-type testing machine at a constant cross-head speed of 0.5 mm/min in a temperature controlled room at 22°C. To evaluate the damage of notched FRP plate, we measured successively the luminance distributions near the notch root during test. To reveal the process of the luminance decline along with the increase of load, we observed the process of microfracture in the damaged zone near the notch root.

RESULTS AND DISCUSSION

There is considerable literature on the damage for notched FRP plates. Attempts to determine the damage for fiber-reinforced composite materials have used, for example, acoustic emission, X-ray radiography [4] and ultrasonic detection [5]. We observed the decrease of the luminance near the notch root [3]. It is evident that the decrease of luminance near the notch root was associated with irreversible damage and microfracture of composites.

Figure 3 shows the initiation and growth of the damaged zone near the notch root. There are three specimens with a constant notch-root radius (= 1 mm) but with different fiber content. The luminance distributions show the patterns with light and shade as shown in Fig. 3. The patterns correspond to the value of relative luminance (R.L.) that was made at four steps; 90, 85, 80 and 75 %. R.L. is the ratio of the luminance at a certain stress level to the luminance before testing. The damage is accumulated severely at the region where the value of relative luminance is small.

Figure 4 shows the relation between the area of the damaged zone for which $R.L. \leq 75\%$ and the maximum elastic stress σ_{max} . It is likely that the growth curve of damaged zone depends on the fiber content. As can be seen from Fig. 3 and 4, the configurations of the damaged zone near the notch root are determined by the maximum elastic stress, notch-root radius and fiber content.

To reveal the microfracture along with the luminance decline, we observed the transverse section of the damaged zone near the notch root. Typical examples of microfracture in the damaged zone are shown in Fig. 5. In the case of the specimen for which the fiber content is

10 % the deformation bands were observed in the matrix (PC) around the fiber as shown in Fig. 5(a). On the other hand, in the case of the fiber content is 30 % microcrack initiated at the end corner of a glass fiber. As shown in Fig. 5(b), several microcracks joined together in the range for which the value of R.L. is low. There were no deformation bands in the matrix.

The relation between the maximum elastic stress at brittle fracture, $\sigma_{\max,c}$ and notch-root radius ρ is shown in Fig. 6. The notch depth was varied from 1 to 4 mm for each specimen for which ρ is constant. It is evident that $\sigma_{\max,c}$ is governed by the notch-root radius for a constant fiber content. Furthermore, the $\sigma_{\max,c} - \rho$ curve for specimens for which the fiber content w is not greater than 10 % is differ the curve for specimens for which w is not less than 30 %. It seems likely that the fracture strength of notched specimens for which w is not greater than 10 % is governed by the strength of matrix materials.

CONCLUSIONS

To provide the experimental evidences of the validity of the failure criterion based on the concept of severity, tension tests on notched plates of a short glass fiber-reinforced polycarbonate were carried out for a wide range of fiber content. The initiation and growth of damage near the notch root were investigated by means of the luminance measurement technique using a CCD camera.

The initiation and the growth of the damaged zone near the notch root were governed by the maximum elastic stress at the notch root, notch-root radius and fiber content.

Closer observation in the damaged zone revealed that the process of microfracture depends on the fiber content. The deformation bands were observed in the matrix around the fiber for the specimens for which the weight percent of fiber w is not greater than 10 %. On the other hand, the microcracks initiated at the end corner of a glass fiber for the specimens for which w is not less than 30 %.

The fracture strength and fracture behavior of a short glass fiber-reinforced polycarbonate was discussed in terms of the mechanical properties and yield behavior of the matrix material, PC.

REFERENCES

1. H. Nisitani and H. Hyakutake, "Condition for Determining the Static Yield and Fracture of a Polycarbonate Plate Specimen with Notches", *Eng. Fract. Mech.*, Vol. 22, 1985, pp. 359-368.
2. H. Hyakutake, H. Nisitani and T. Hagio, "Fracture Criterion of Notched Plates of FRP", *JSME Inter. J.*, Vol. 32, 1989, pp. 300-306.
3. T. Yamamoto and H. Hyakutake, "Damage of Notched FRP Plates under Static Loads", *Trans. Jpn. Soc. Mech. Eng.*, Vol. 63, 1997, pp.780-786.
4. C.E. Bakis, H.R. Yih, W.W. Stinchcomb and K.L. Reifsnider, "Damage Initiation and Growth in Notched Laminates Under Reversed Cyclic Loading", *Composite Materials*, ASTM STP 1012, P.A. Lagace (ed.), ASTM, 1989, pp. 66-83.
5. H. Kaczmarek, "Ultrasonic Detection of Damage in CFRPs", *J. Compos. Mater.*, Vol. 29, 1995, pp.59-95.

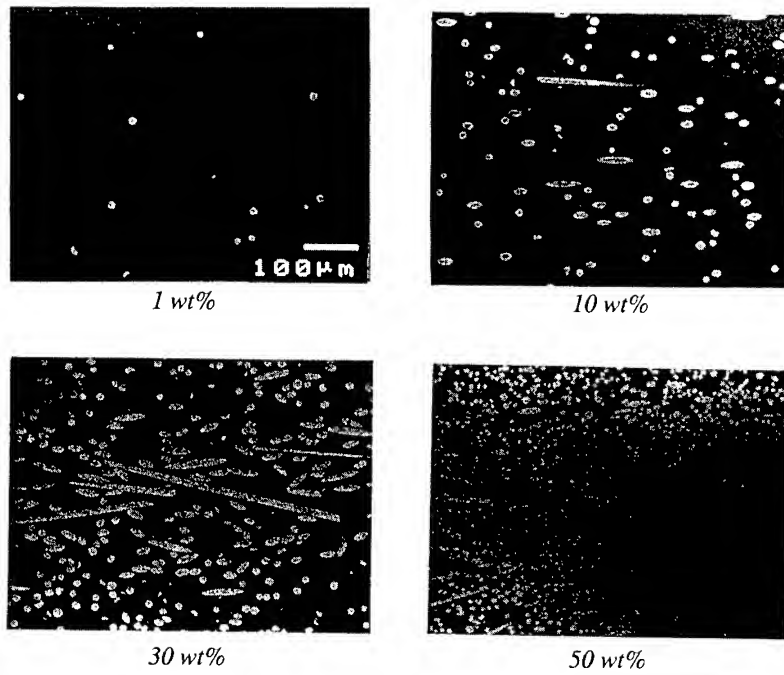


Fig. 1 Photomicrographs showing a transverse section of the GF/PC plates

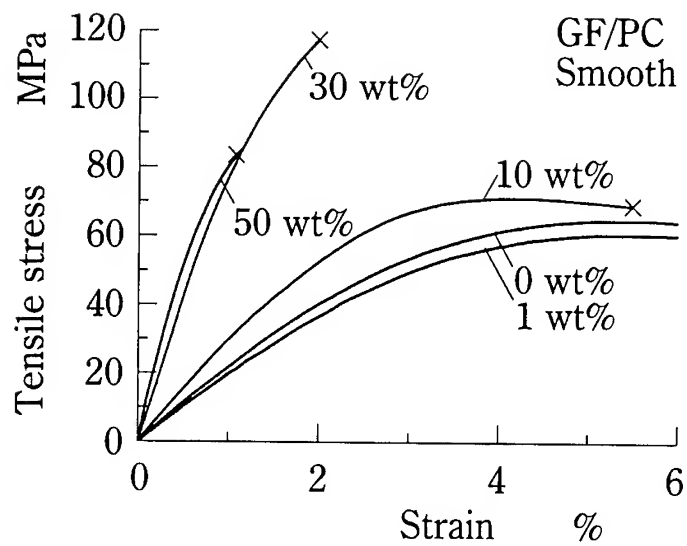


Fig. 2 Tensile stress-strain curves of unnotched specimens

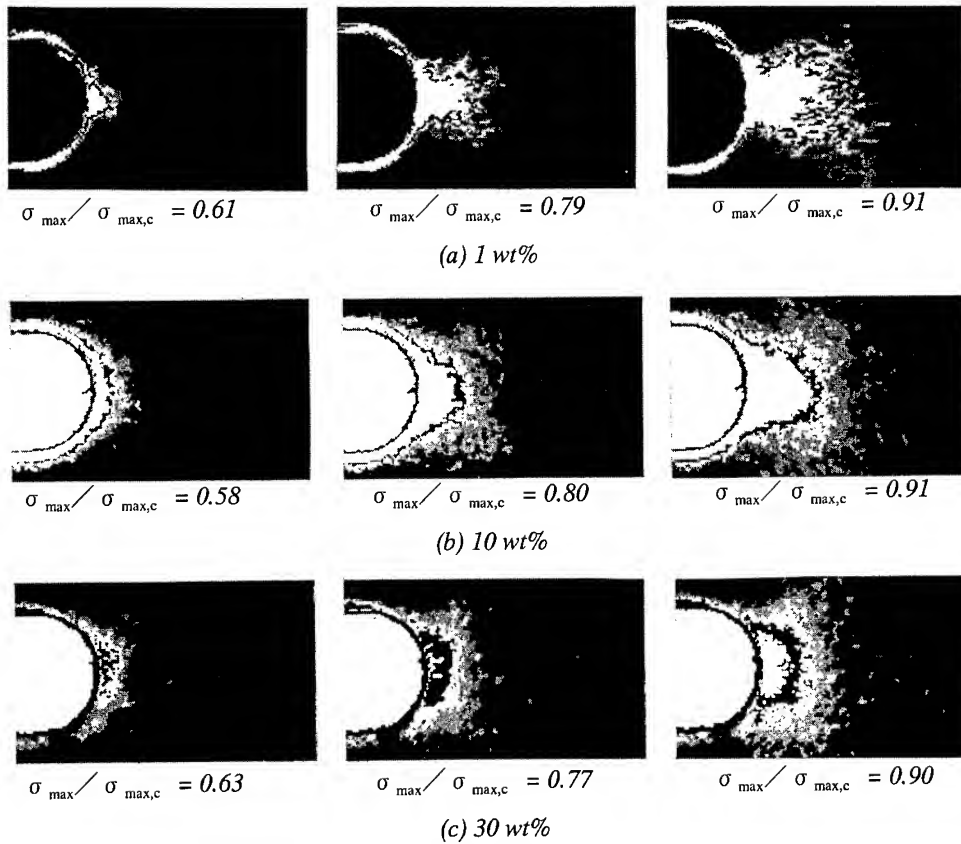


Fig. 3 Luminance distribution near the notch root

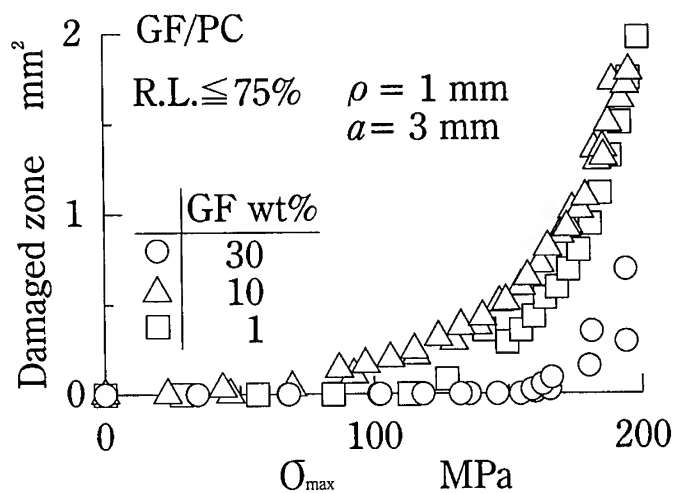


Fig. 4 Growth of the area of damaged zone

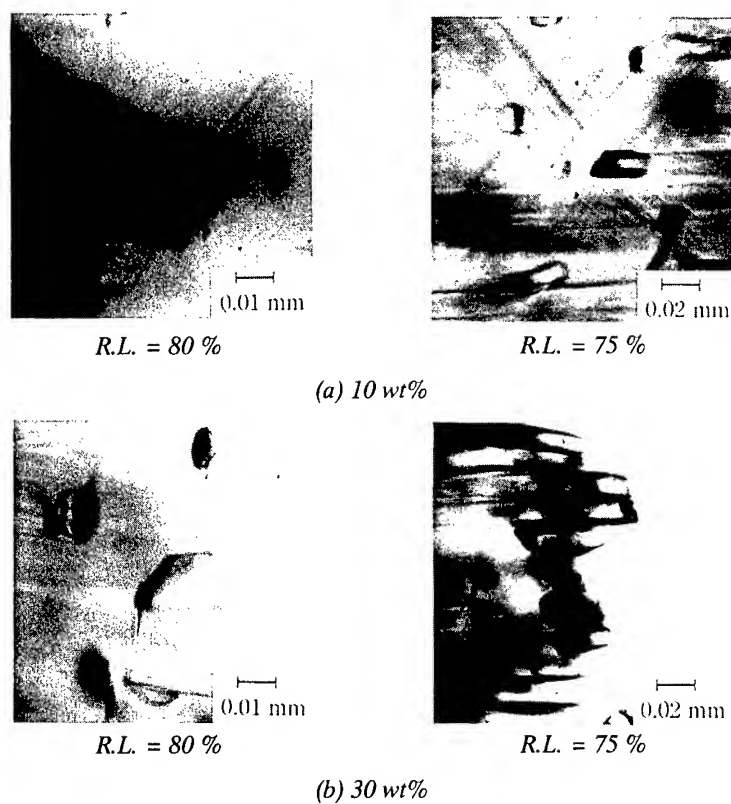


Fig. 5 Microfracture in the damaged zone

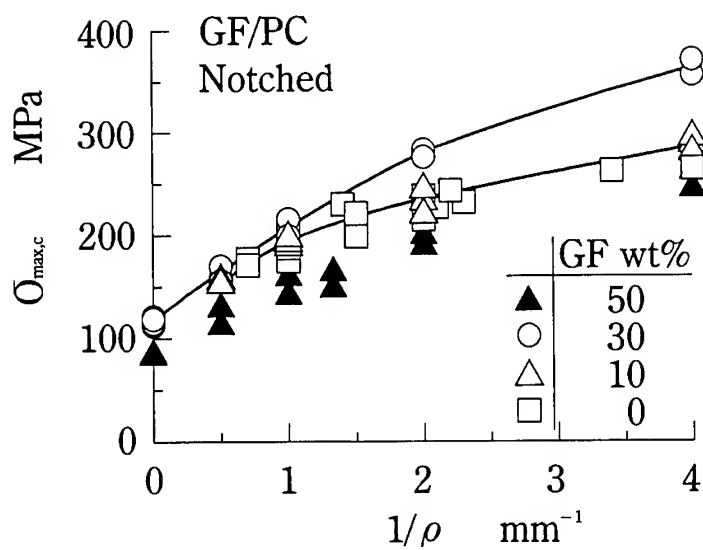


Fig. 6 Maximum elastic stress at fracture, $\sigma_{\max,c}$ versus notch-root radius ρ

CHARACTERIZATION OF LOW CYCLE FATIGUE FOR WOVEN FABRIC COMPOSITES (BELOW THE FREEZING POINT)

Masaru Zako¹, Naoki Takano¹, Tetsusei Kurashiki¹, and Hirokazu Moriki²

¹ *Department of Manufacturing Science, Graduate School of Engineering, Osaka University
2-1, Yamadaoka, Suita, Osaka, 565-0871, JAPAN: zako@mapse.eng.osaka-u.ac.jp*

² *Graduate Student at Department of Manufacturing Science, Osaka University, JAPAN*

SUMMARY Low cycle fatigue test for woven glass fiber / vinyl ester composites has been performed at the room temperature and below the freezing point. Fatigue characterization is discussed through an In-situ observation of the microscopic damage propagation during the fatigue test by means of SEM. The result shows that the fatigue life tends to increase with the decrease of the temperature, and the difference in the fatigue lives is very significant at high stress amplitude. The occurrence and the propagation of the transverse crack in the fiber bundle depend on the temperature. It was expected that the reason for the above-mentioned differences lies in the temperature dependency of the mechanical property of the vinyl ester resin. To prove it, the damage propagation has been analyzed by finite element method based on damage mechanics. In this paper, the numerical and experimental results are described.

KEYWORDS: Woven Fabric Composites, Below the Freezing Point, Low Cycle Fatigue, In-situ Observation, FEM, Damage Mechanics

INTRODUCTION

It is very important for the design of textile composites structure, such as some parts of artificial satellites and ships, working under extreme environmental conditions, to investigate the fatigue behavior below the freezing point. Some technical reports mentioned that the mechanical behavior of FRP at the room temperature and below the freezing point is completely different [1][2]. The difference relies in the temperature dependency of the mechanical properties of FRP. As for the woven fabric composites, where multi-axial stress states appear even under uni-axial load, and where damages such as matrix crack and delamination take place, the evaluation of the mechanical behavior is even more complicated. The development of the damage in woven fabric composites is influenced by the temperature dependency of the mechanical properties of resin. Furthermore, the data on fatigue characteristic of woven fabric composites below the freezing point have not been completely established and this issue is still under investigation.

In this study, low cycle fatigue tests for the woven glass fiber/ vinyl ester composite have been carried out at 293K, 273K and 213K. Fatigue characterization is discussed by an In-

situ observation of the microscopic damage propagation during the fatigue test by means of a scanning electron microscope (SEM).

Moreover, we have already developed a numerical simulation program to evaluate the mechanical behavior of woven fabric composites based on the damage mechanics [3][4]. To investigate the differences in the damage modes under each temperature, the damage behavior has been analyzed by the above-mentioned simulation program. In the finite element model of woven fabric composites, the heterogeneity is considered due to different nature of the fiber bundle and matrix, and the temperature dependency of the mechanical property of the vinyl ester is taken into consideration. In this paper, the numerical and experimental results are described.

LOW CYCLE FATIGUE TEST

Test Specimens and Experimental Setup

Test specimens were cut out of a glass fiber lamina sheet. The lamina was fabricated by the hand-lay up method, using vinyl ester resin (supplied from Showa polymer Co. LTD.: R-806) reinforced by E-glass woven cloth fabric (supplied from Asahi fiberglass Co. LTD.: MS250). The geometry and structure of the test specimen for In-situ SEM observation and the structure of the woven cloth lamina are shown in Fig.1. The shape of specimen is rectangular. Aluminum tabs are glued at the end parts of the specimen. The woven density of the cloth is as fine as 4 bundles / 3.0 mm.

The experimental equipments for In-situ SEM observation are shown in Fig.2. Testing device is composed of an electro hydraulic servo-type fatigue tester, SEM and liquid nitrogen

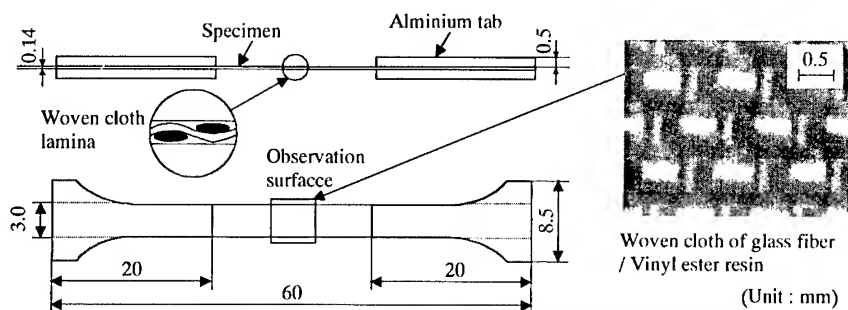
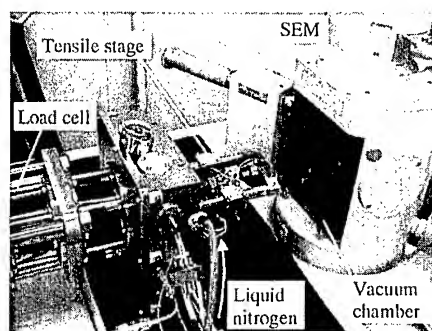
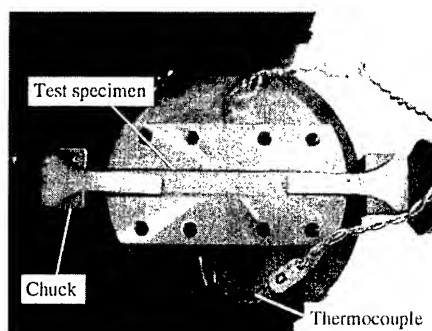


Fig.1 Geometry of specimen and structure of woven FRP



(a) Fatigue tester with SEM



(b) Tensile stage

Fig.2 Overview of the experimental equipments

vessel. In-situ observation can be performed by inserting the tensile stage into vacuum chamber of SEM. For the experiments below the freezing point, the tensile stage is cooled by the liquid nitrogen vessel. Tension-tension fatigue test is carried out by stress control. The frequency was set to 0.2Hz so that we can avoid the effect of frictional heat by cyclic load.

Results of Fatigue Test

Figure 3 shows the relation between stress amplitude and number of cycles to failure at each temperature. The fatigue life tends to increase with the decreasing of the temperature, and the difference of the fatigue life is very significant at high stress amplitudes. To perceive this difference in detail, the damage development is investigated by In-situ SEM observation. Matrix crack has occurred at the cross over point of the fiber bundles on the upper surface of the specimen as shown in Fig.4. The SEM images of crack propagation are recorded by a video camera, and the maximum length of the crack is measured. The results, for the cases of fatigue stress amplitude of 155 and 142 MPa at each temperature, are shown in Fig.5. After failure, the specimen is taken out and cut in the center of its width, and the damage state is investigated by SEM observation for the cross sections of specimens. Figure 6 shows the cross sectional images of fiber bundle in a damaged specimen. It is noted that the out-of-plane deformation becomes larger at the cross over parts of the fiber bundle. This is due to the flattening of fiber bundles parallel to loading direction under on-axis tensile load. On the other hand, the fiber bundle perpendicular to the loading direction suffered from transverse cracks at the center and edge parts in the case where the test was conducted at 293K. However, for test

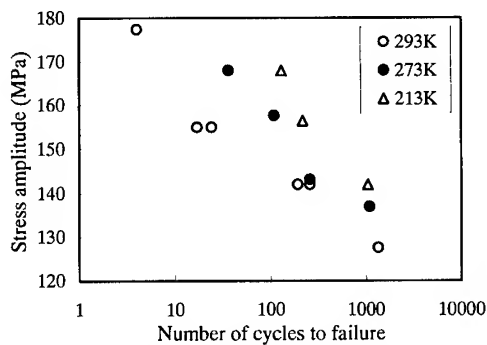


Fig.3 S-N diagram at each temperature

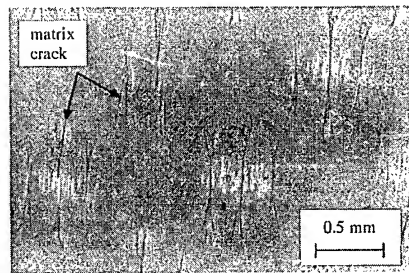
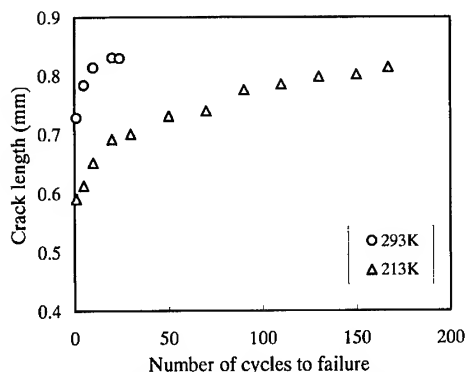
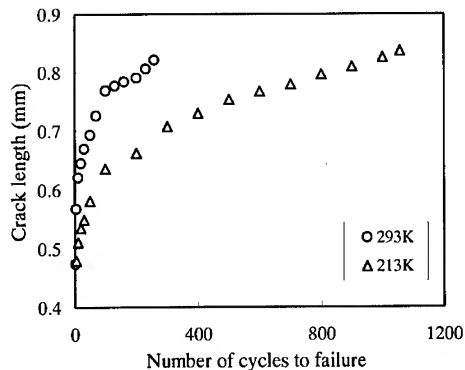


Fig.4 SEM image at the surface of damaged specimen (At 293K, stress amplitude 155MPa, $N/N_f = 1$)



(a) Case of stress amplitude 155MPa



(b) Case of stress amplitude 142MPa

Fig.5 Crack propagation on fatigue life at each stress amplitude

done at 213K, only one transverse crack appeared at the center part of the bundle.

In Fig.5, we can see that the tendency of crack development can be almost approximated to two straight-line parts. In the first part, it is supposed that the interfacial delamination develops at the cross over point of fiber bundles, and the development of delamination is influenced by the location of the transverse cracks. Therefore, it is very important to perceive the occurrence location and the number of transverse cracks.

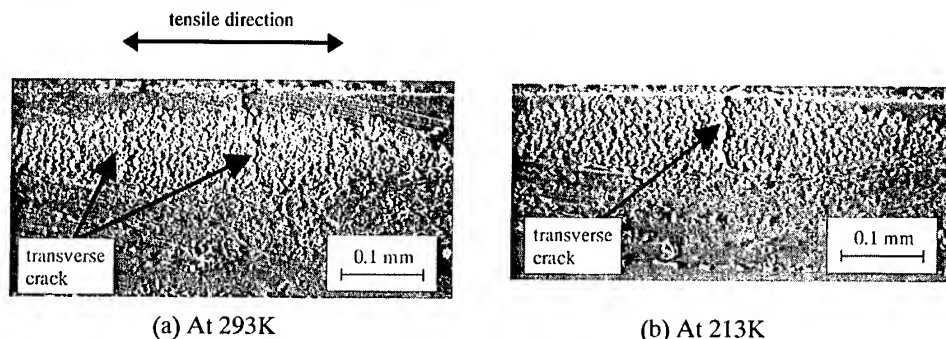


Fig.6 Cross sectional images of fiber bundle in damaged specimen

FEM ANALYSIS BASED ON DAMAGE MECHANICS

Analytical Procedure

It is expected that the reason for the above-mentioned differences of damage lies in the temperature dependency of the mechanical properties of the vinyl ester resin. To investigate this assumption, a tensile test was carried out, on a specimen made of vinyl ester resin, at different temperature conditions. Temperature dependency of Young's modulus and tensile strength are shown in Fig.7. In this figure, and for easier comparison, the values of the Young's modulus E and tensile strength F at temperature T are normalized by the value at $T=293\text{K}$, then plotted against the temperature. It is revealed that the Young's modulus and tensile strength tend to increase with the decrease of temperature.

The mechanical behavior of woven fabric composites under on-axis tensile load can be analyzed by finite element method based on damage mechanics [3][4]. In order to grasp the

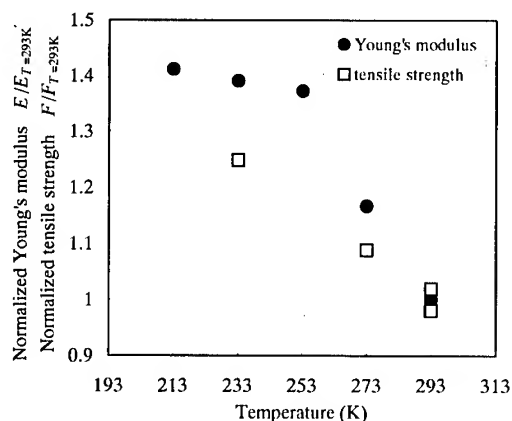


Fig.7 Temperature dependency of Young's modulus and tensile strength for vinyl ester

microscopic damage, woven fabric composite is treated as a heterogeneous body composed of fiber bundle and matrix. The fiber bundle is treated as anisotropic model. Matrix is simulated by isotropic model. Figure 8 shows a SEM image through which the volume fraction of fiber was determined. The temperature dependency of the mechanical properties of the vinyl ester is also taken into consideration. The occurrence of damage can be predicted by using the conventional criterion of Hoffman. The constitutive equation can be obtained by the characterization of the damage mode by Murakami's damage tensor [5]. The detail of its derivation are reported in ref.[4].

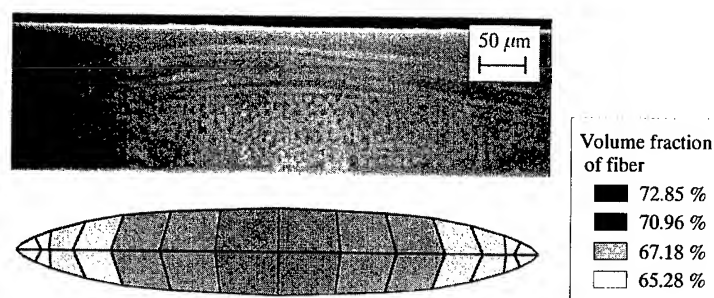


Fig.8 Distribution of volume fraction of fiber in a fiber bundle

Results of Numerical Analysis

Figure 9 shows the deformation and damage states of woven fabric composite at 293K. In this figure, the thin black parts indicate the damaged elements judged by Hoffman's criterion. A transverse crack occurs at the center of bundle because of the decreasing of the interfacial bonding force between fiber and resin due to the high volume fraction of fiber. The cracks also appear at the edge parts of fiber bundle at 293K. On the other hand, at 213K, the non-occurrence of cracks at the edge parts of bundle is due to the increase of mechanical properties. These results derive the differences in the fatigue lives at each temperature.

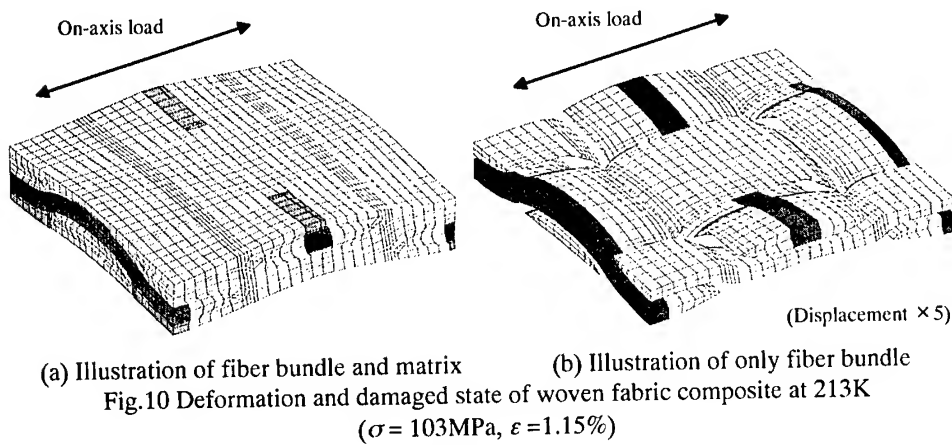
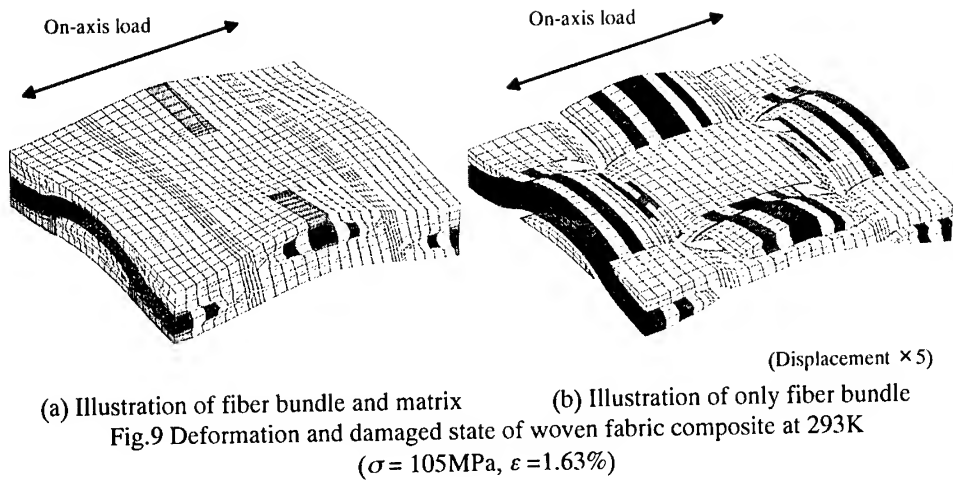
CONCLUDING REMARKS

Low cycle fatigue test for woven fabric composites has been carried out at the room temperature and below the freezing point. The results showed that the fatigue life tends to increase with the decrease of the temperature, and the difference in the fatigue lives is very significant at high stress amplitudes. The occurrence and propagation of the transverse crack in the fiber bundle depend on the temperature.

Furthermore, the mechanical behavior of composites under uni-axial static tensile load has been also analyzed by finite element method based on damaged mechanics. The numerical results show that the fiber bundle perpendicular to the loading direction suffered from transverse cracks at the center and edge parts at room temperature. Below the freezing point, however, only one transverse crack appeared at the center part of the bundle. From both experimental and numerical studies, it has been proved that the temperature must be taken into consideration as one of the mean factors controlling the low cycle fatigue behavior.

ACKNOWLEDGEMENT

We would like to express our thanks to Dr. Kazuaki Nishiyabu (Osaka Prefectural College of Technology, JAPAN) and Dr. Yasutomo Uetsuji (Kyoto Institute of Technology, JAPAN) for their cooperation.



REFERENCES

1. Atsushi Inoue, Toru Fujii and Hiroshi Hayakawa, "Effect of temperature on low cycle fatigue of a glass fabric composite under tension/tension biaxial loading", *Proc. of 28th FRP Symposium*, (Soc. Mater. Sci., Japan) II-15A, 1999, pp.115-116.
2. Tadayoshi Kawada, Shuichi Machida, Bodo Fiedler, Masaki Hojo, Shojiro Ochiai and Satoshi Matsuda, "Comparison of interlaminar fracture behaviors between carbon fiber reinforced plastics and alumina fiber reinforced plastics with a common matrix in air and in liquid nitrogen", *Proc. of 1999 Annual Meetings of JSME/MMD*, (Soc. Mech. Eng., Japan), 1999, pp.423-424.
3. Masaru Zako and Yasutomo Uetsuji, "AE simulation based on finite element analysis of damage propagation for fiber reinforced composite materials", *Proc. of The First Asian-Australasian Conference on Composite Materials: (ACCM-1)*, Vol.2, 1998, pp.643
4. Yasutomo Uetsuji and Masaru Zako, "Damage analysis of woven fabric composite materials", *J. Soc. Mat. Sci., Japan*, Vol.48, No.9, 1999, pp.1029-1034.
5. S.Murakami, *J.Applied Mechanics*, 55, 1988, pp.280

Fatigue & Fracture (2)

MODELLING OF THE CLOSURE EFFECT IN ANISOTROPIC DAMAGED MATERIAL USING THE CONCEPT OF LOADING MODE IN THE FRAMEWORK OF DAMAGE MECHANICS :

A. Thionnet⁽¹⁺²⁾, J. Renard⁽²⁾

(1) Université de Bourgogne - Département IEM - BP 47870 - 21078 Dijon Cedex FRANCE

(2) École Nationale Supérieure des Mines de Paris - Centre des Matériaux P. M. Fourt -
UMR CNRS 7633
BP 87 - 91003 Evry Cedex FRANCE

ABSTRACT : Damage decreases the mechanical characteristics of materials and also modifies their thermal properties. However these modifications can disappear when the microcracks are closed. We propose a model of this phenomenon for the thermomechanical behavior of strongly anisotropic materials. The aim of this work is to adapt the concept of loading mode in Fracture Mechanics to Damage Mechanics and to include it explicitly in the equations. This allows to obtain a thermomechanical behavior respecting rigorously all the criterions, notably the continuity and the deactivation of each modulus that are necessary for the consistency of the modeling of the damage phenomenon. In particular, contrary to the other ways of modeling, it simulates the Poisson effect restoration and according to case studies does restore or does not restore the shear modulus without adding a friction law on the microcracks.

INTRODUCTION

This study is an extension of a previous work [1]. In the present work, the recovery of the thermomechanical properties of a strongly anisotropic microcracked material due to the closing of the microcracks is discussed. In addition, it is a generalization showing how to take into account the unilateral character of the damage in tensorial, vectorial or scalar laws using two internal variables deduced from Fracture Mechanics.

HYPOTHESES AND FRAMEWORK

It is difficult to model the damage because in general its geometry depends on the solicitation. Here, we avoid this difficulty by supposing that the geometry of the damage spreads into preferential directions. Thus, the proposed study is very appropriate for strongly anisotropic materials like unidirectional composites. For this reason, we illustrate our study (§-VIII) considering a laminate structure of unidirectional carbon/resin oriented plies. The other hypotheses made on the microcracks are the following :

- all of them have the same geometry, form a diffuse network and are supposed to be plane when no stress is applied;
- if the microcracks are closed, the contact between their lips is considered to be without friction;
- they generate no residual stress field. As a consequence, no energy is kept inside the material;
- without solicitation, they are plane and contained in the plane $(O, \vec{e}_1, \vec{e}_3)$ of the $(O, \vec{e}_1, \vec{e}_2, \vec{e}_3)$ cartesian frame;

- the appearance of microcracks and their spreading are quasi-simultaneous phenomena. Thus, the present study analyzes the multiplication of the microcracks rather than their propagation.

A model of a physical phenomenon is written in a way to be thermodynamically coherent. For this reason, the local state hypothesis is used. It indicates that a finite number of variables, the state variables, are sufficient to describe the representative volume element equivalent to the damaged material. The evolution of these variables verifies the Second Principle of Thermodynamics.

The work is carried out in the framework of small perturbations allowing large heat fluctuations, using Damage Mechanics and Thermodynamics of Continuous Media. We assume that the stress fields are within the $(O, \vec{e}_1, \vec{e}_2)$ plane. The tensors are written using Voigt notation : thus, a second-order tensor t (stress or strain) is reduced to $t = (t_1, t_2, t_6)$. As a consequence of the previous hypothesis, we limit the description of the cracks to the plane. Thus the third component of the tangential plane perpendicular vector, at each point along the crack, is zero.

STATE VARIABLES

We use a scalar damage variable which quantitatively defines the phenomenon and two other internal scalar variables, m and r , which describe it geometrically [1]. The macroscopic strain (ϵ) and the temperature (T) complete the description of the equivalent material volume element.

The m and r variables have been derived from the experimental observations of Purslow [2] [3] and from the theoretical works of Andrieux [4], Allen et al. [5] and Lee et al. [6] :

- m describes the opening of the microcracks. From the solicitation mode in Fracture Mechanics, we choose :
 - $m = 1$ when all along the lips the normal (respectively, tangential) jump displacement is non zero (respectively, zero);
 - $m = 2$ when all along the lips the tangential (respectively, normal) jump displacement is non zero (respectively, zero).

The variation of m from 1 to 2 describes the in-between configurations;

- r describes the amplitude of the opening of the lips of the microcracks.

The expression of m and r depending on macroscopic variables are given [7] and updated in section VII which deals with identifications.

VECTORIAL DESCRIPTION OF THE CHANGE IN THE GEOMETRY OF THE MICROCRACKS

In previous works [8] based on Talreja's studies [9], within the microscopic scale, the microcracks have a constant geometry and are defined by a vector perpendicular to their location. In the present work, this geometry may evolve. Thus, taking into account the hypotheses (§-II), at the macroscopic scale, the whole network is described by a single vector whose orientation does not explicitly depend on the value of the damage variable [7] :

$$\vec{V} = (V_T(\alpha, m, r), V_N(\alpha, m, r), 0) = f(\alpha) (U_T(m, r), U_N(m, r), 0)$$

where $f(\alpha = 0) = 0$.

Considering the microscopic description and the definition of the m and r variables [7] [1]:

- $U_T(m = 1, r) = 0 \forall r$;
- $U_N(m = 2, r) = 0 \forall r$.

For a zero strain state, in order to keep continuous behaviour while the lips are closing the conditions are [7] [1] :

$$\bullet U_T(m, r = 0) = 0 \forall m; \quad (\text{Eq. 4a})$$

$$\bullet U_N(m, r = 0) = 0 \forall m. \quad (\text{Eq. 4b})$$

STATE FUNCTION AND STATE LAWS

The state function ψ is written as a polynomial function of degree 2 in terms of the strain tensor components under the following classic form. The temperature dependence is taken into account through the coefficients of this polynomial function. Then, the stress and the entropy are given by the following expressions :

$$a) \sigma = C(\theta, \alpha, m, r) \varepsilon + k(\theta, \alpha, m, r)$$

$$= [C^0(\theta) + f^2(\alpha) \{ C^N(\theta) U_N^2(m, r) + C^T(\theta) U_T^2(m, r) + C^{NT}(\theta) U_N(m, r) U_T(m, r) \}] \varepsilon + k(\theta, \alpha, m, r)$$

$$b) -s = 1/2 C_{ij}'(\theta, \alpha, m, r) \varepsilon_i \varepsilon_j + k_i'(\theta, \alpha, m, r) \varepsilon_i + G'(\theta, \alpha, m, r)$$

$$= 1/2 [C_{ij}^0(\theta) + f^2(\alpha) \{ C_{ij}^N(\theta) U_N^2(m, r) + C_{ij}^T(\theta) U_T^2(m, r) + C_{ij}^{NT}(\theta) U_N(m, r) U_T(m, r) \}] \varepsilon_i \varepsilon_j$$

$$+ [k_i^0(\theta) + f^2(\alpha) \{ k_i^N(\theta) U_N^2(m, r) + k_i^T(\theta) U_T^2(m, r) + k_i^{NT}(\theta) U_N(m, r) U_T(m, r) \}] \varepsilon_i$$

$$G_0'(\theta) + f^2(\alpha) \{ G_N'(\theta) U_N^2(m, r) + G_T'(\theta) U_T^2(m, r) + G_{NT}'(\theta) U_N(m, r) U_T(m, r) \}.$$

(The character " ' " represents the derivative with respect to temperature).

$$C^0(\theta) = \begin{pmatrix} 2A_1(\theta) & A_3(\theta) & 0 \\ A_3(\theta) & 2A_2(\theta) & 0 \\ 0 & 0 & 2A_4(\theta) \end{pmatrix}, C^N(\theta) = \begin{pmatrix} 2B_1(\theta) & B_3(\theta) & 0 \\ B_3(\theta) & 2B_2(\theta) & 0 \\ 0 & 0 & 2B_4(\theta) \end{pmatrix},$$

$$C^T(\theta) = \begin{pmatrix} 2C_1(\theta) & C_3(\theta) & 0 \\ C_3(\theta) & 2C_2(\theta) & 0 \\ 0 & 0 & 2C_4(\theta) \end{pmatrix}, C^{NT}(\theta) = \begin{pmatrix} 0 & 0 & D_1(\theta) \\ 0 & 0 & D_2(\theta) \\ D_1(\theta) & D_2(\theta) & 2D_3(\theta) \end{pmatrix},$$

$$k^0(\theta) = \begin{pmatrix} a_1(\theta) \\ a_2(\theta) \\ 0 \end{pmatrix}, k^N(\theta) = \begin{pmatrix} b_1(\theta) \\ b_2(\theta) \\ 0 \end{pmatrix}, k^T(\theta) = \begin{pmatrix} c_1(\theta) \\ c_2(\theta) \\ 0 \end{pmatrix}, k^{NT}(\theta) = \begin{pmatrix} 0 \\ 0 \\ d_1(\theta) \end{pmatrix}.$$

CLAUSIUS-DUHEM INEQUALITY. COMPLEMENTARY LAWS

Using the Clausius-Duhem inequality :

- we write the damage evolution law [1, 8] ;
- we built up the thermal diffusion tensor K :

$$K(\theta, \alpha, m, r) = K^0(\theta) + f^2(\alpha) \{ K^N(\theta) U_N^2(m, r) + K^T(\theta) U_T^2(m, r) + K^{NT}(\theta) U_N(m, r) U_T(m, r) \}.$$

$$K^0(\theta) = \begin{pmatrix} 2e_1(\theta) & 0 & 0 \\ 0 & 2e_2(\theta) & 0 \\ 0 & 0 & 2e_3(\theta) \end{pmatrix}, K^N(\theta) = \begin{pmatrix} 2f_1(\theta) & 0 & 0 \\ 0 & 2f_2(\theta) & 0 \\ 0 & 0 & 2f_3(\theta) \end{pmatrix},$$

$$K^T(\theta) = \begin{pmatrix} 2g_1(\theta) & 0 & 0 \\ 0 & 2g_2(\theta) & 0 \\ 0 & 0 & 2g_3(\theta) \end{pmatrix}, K^{NT}(\theta) = \begin{pmatrix} 0 & h_1(\theta) & 0 \\ h_1(\theta) & 0 & 0 \\ 0 & 0 & 0 \end{pmatrix}.$$

IDENTIFICATIONS AND EVIDENCE OF THE UNILATERAL EFFECT OF DAMAGE

Expressions of m and r

Using a similar procedure to the pure mechanical case [1], we show that m and r can be written as functions of ϵ , θ and α . The following definitions enable us to verify the conditions defined in section IV (Eqs. 3-4) :

$$\begin{cases} \text{if } \epsilon_2 \geq 0 : m(\epsilon, \theta, \alpha) = \frac{2\epsilon_6^2 + \frac{\epsilon_2^2}{n^2(\theta, \alpha)}}{\epsilon_6^2 + \frac{\epsilon_2^2}{n^2(\theta, \alpha)}} \text{ and } r(\epsilon, \theta, \alpha) = r(\epsilon) = \sqrt{\epsilon_2^2 + \epsilon_6^2} \\ \text{if } \epsilon_2 < 0 : m(\epsilon, \theta, \alpha) = 2 \text{ and } r(\epsilon, \theta, \alpha) = r(\epsilon) = \sqrt{\epsilon_6^2} \end{cases}$$

where $n(\theta, \alpha) = \epsilon_2^c(\theta, \alpha) / \epsilon_6^c(\theta, \alpha)$; $\epsilon_2^c(\theta, \alpha)$ and $\epsilon_6^c(\theta, \alpha)$ are the failure strains of the equivalent material depending on a priori the temperature and on the damage.

Other identifications and evidence of the unilateral effect of damage

Some of the coefficients in the equation laws can be easily identified [1, 7]. Finally :

$$\begin{aligned} C &= C^0(\theta) + \\ f^2(\alpha) &\left[U_N^2(m, r) \begin{pmatrix} 2B_1(\theta) & B_3(\theta) & 0 \\ B_3(\theta) & 2B_2(\theta) & 0 \\ 0 & 0 & 0 \end{pmatrix} + U_T^2(m, r) \begin{pmatrix} 0 & 0 & 0 \\ 0 & 0 & 0 \\ 0 & 0 & 2C_4(\theta) \end{pmatrix} \right. \\ &\quad \left. + U_N(m, r)U_T(m, r) \begin{pmatrix} 0 & 0 & D_1(\theta) \\ 0 & 0 & D_2(\theta) \\ D_1(\theta) & D_2(\theta) & 2D_3(\theta) \end{pmatrix} \right] \\ k &= k^0(\theta) + f^2(\alpha) \left[U_N^2(m, r) \begin{pmatrix} b_1(\theta) \\ b_2(\theta) \\ 0 \end{pmatrix} + U_N(m, r)U_T(m, r) \begin{pmatrix} 0 \\ 0 \\ d_1(\theta) \end{pmatrix} \right] \end{aligned}$$

$$G = G_0(\theta) + f^2(\alpha) \{ G_N(\theta)U_N^2(m, r) + G_{NT}(\theta)U_N(m, r)U_T(m, r) \}$$

$$K = K^0(\theta) + f^2(\alpha) \left[U_N^2(m, r) \begin{pmatrix} 2f_1(\theta) & 0 & 0 \\ 0 & 2f_2(\theta) & 0 \\ 0 & 0 & 2f_3(\theta) \end{pmatrix} + U_N(m, r) U_T(m, r) \begin{pmatrix} 0 & h_1(\theta) & 0 \\ h_1(\theta) & 0 & 0 \\ 0 & 0 & 0 \end{pmatrix} \right]$$

$m = 2$ means that the microcracks are closed and gives $U_N = 0$. This enables us to recover the initial properties of the virgin material except for the shear modulus on which the opening or closing of the microcracks has no influence. Thus, except for this quantity, when the microcracks are closed, the stress/strain relation and the thermal diffusion tensor (Eq. 11) of the damaged material ($f(\alpha \neq 0) \neq 0$) are identical to those of the virgin material ($f(\alpha = 0) = 0$). The unilateral effect of the damage is therefore completely taken into account.

APPLICATION

The unilateral effect of damage can be significantly observed through the mechanical behavior. For this reason, we apply the model when the temperature is constant and equals the reference temperature. The material under study is a carbon/epoxy composite. The volume element experimentally [10] and numerically tested is a thin plane plate. The loading is uniaxial and applied in the same direction as the axis of the specimen. Two stacking sequences are studied: $[0^\circ_2, 90^\circ_2]_s$ and $[60^\circ_2, 90^\circ_2]_s$. For each one, we show the curves ϵ_T/σ_L and ϵ_L/σ_L and the damage evolution in each ply of the laminate (figs. 1 and 2; ϵ_T is the transversal strain, ϵ_L is the longitudinal strain and σ_L is the longitudinal applied stress).

On the $[0^\circ_2, 90^\circ_2]_s$ ϵ_T/σ_L curve and on the $[60^\circ_2, 90^\circ_2]_s$ ϵ_L/σ_L curve, we clearly observe the difference between the damaged and the restored slope. For $[0^\circ_2, 90^\circ_2]_s$ the last slope is exactly equal to the initial one because the crossing between traction and compression coincides with the complete closing of the microcracks lips of the 90° ply. For $[60^\circ_2, 90^\circ_2]_s$ the restored slope is weaker than the initial slope because the shear modulus of the 60° ply (that is never recovered) acts in the global rigidity of the laminate (however this difference is not substantial on the diagram).

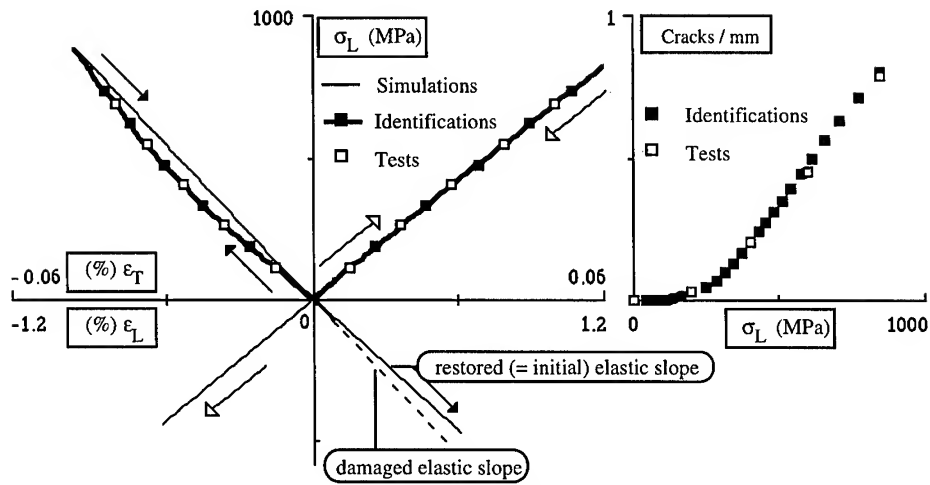
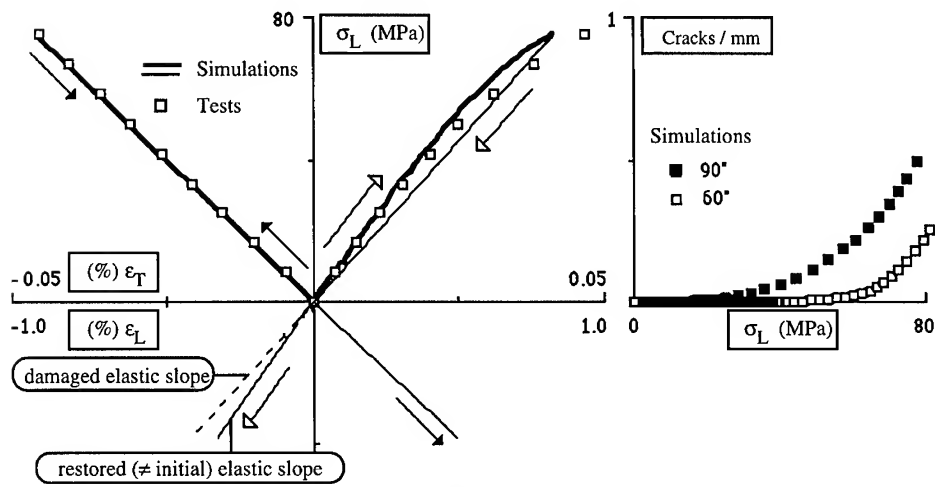
CONCLUSION

The microscopic vectorial description of a diffuse network of identical microcracks has allowed to define at the macroscopic scale, using two scalar variables m and r , a new concept for Damage Mechanics as already exists for Fracture Mechanics : the solicitation mode. Moreover, these two internal variables that take into account the geometry of the microcracks, model the unilateral damage effect. After studying the pure mechanical case in previous works, here we generalize the model for all thermomechanical properties.

If the definitions and the use of m and r are very easy and efficient, it is necessary to point out that this is the result of the plane character of the modelling. To extend the definition of the m variable in the tridimensional case, it would be difficult to take Fracture Mechanics as basis. In fact, if we define $m = 3$ to model the "third-mode" as in Fracture Mechanics, we can see discontinuities which will be not easy to solve.

REFERENCES

1. Thionnet, A., Renard, J., 1999, Modelling unilateral damage effect in strongly anisotropic materials by the introduction of the loading mode in Damage Mechanics, *International Journal of Solids and Structures* (in press)
2. Porslow, D., 1981, Some fundamental aspects of composites fractography, *Composites*, vol. 12, oct., p. 241-247
3. Porslow, D., 1986, Matrix fractography of fibre-reinforced epoxy composites, *Composites*, vol. 17, oct., p. 289-303
4. Andrieux, S., 1983, Un modèle de matériau microfissuré. Applications aux roches et aux bétons, Thèse, Université Paris VI, France
5. Allen, D.H., Harris, C.E., Groves S.E., 1987, A thermomechanical constitutive Theory for elastic Composites with distributed Damage. Part I and II, *International Journal of Solids Structures*, vol. 23, n° 9, p. 1301-1318
6. Lee, J.W., Harris, C.E., Allen, D.H., 1989, Internal State Variable Approach for Predicting Stiffness Reduction in Fibrous Laminated Composites with Matrix Cracks, *Journal of Composite Materials*, vol. 23, p. 1273-1291
7. Aussedat, E., Thionnet, A., Renard, J., 1995, Comportement en compression des composites par une définition du mode de sollicitation en mécanique de l'endommagement, *Compte Rendu de l'Académie des Sciences de Paris*, t. 321, série IIb, p. 533-540
8. Thionnet, A., Renard, J., 1993, Meso-macro approach to tranverse cracking in laminated composites using Talreja's model, *Composites Engineering*, vol. 3, n°9, p. 851-871
9. Talreja, R., 1985, Transverse Cracking and Stiffness Reduction In composite Laminates, *Journal of Composites Materials*, vol. 19, p. 355-375
10. Jeggy, T., 1990, Modélisation des dégradations des plaques trouées en carbone/époxy sous chargements biaxiaux quasi-statiques, Thèse, Ecole Centrale de Paris, France

fig. 1 : $[0^\circ_2, 90^\circ_2]_s$ fig. 2 : $[60^\circ_2, 90^\circ_2]_s$

Effect of Circular Hole Notch on Notched Strength Characteristics of Al7075/CFRP Layered Composites

Joon-Soo PARK¹, Han-Ki YOON², Sang-Pill LEE³ and Akira KOHYAMA⁴

¹ Institute of Advanced Energy, Kyoto University

Gokasho, Uji, Kyoto 611-0011, JAPAN:jspark@iae.kyoto-u.ac.jp

² Dept. of Mechanical Engineering, Dong-Eui University

24 Kaya-dong, Pusanjin-gu, Pusan 614-714, Korea:hkyoon@hyomin.dongui.ac.kr

³ Institute of Advanced Energy, Kyoto University

Gokasho, Uji, Kyoto 611-0011, JAPAN:splee@iae.kyoto-u.ac.jp

⁴ Institute of Advanced Energy, Kyoto University

Gokasho, Uji, Kyoto 611-0011, JAPAN:kohyama@iae.kyoto-u.ac.jp

SUMMARY: CARALL (Carbon fiber reinforced aluminum laminates) was fabricated in the autoclave by stacking CFRP laminate, adhesive film and Al7075. The mechanical properties of three samples i.e. Al7075, CFRP, and CARALL were investigated as a function of size in circular holes. Theoretical approach to analyzing mechanical behaviors near the circular hole notch was carried out to compare with experimental results. It was found that the abrupt strength reduction of CFRP was prevented by the adhesive bonding of Al7075. From the consideration of modified point stress failure criterion, predicted results was well consistent with the experimental one.

KEYWORDS: CARALL (carbon fiber reinforced aluminum laminates), circular hole notch, point stress failure criterion, characteristic length, notched tensile strength

INTRODUCTION

In the last decade, aluminum alloys has been used in aerospace industry, because of its lightweight, reliance and economical efficiency. Recently, the amount of fiber reinforced composites, including Kevlar and CFRP (Carbon Fiber Reinforced Plastics) is gradually increased since it has anti-corrosion, strength, and anti-fatigue properties. But, fiber reinforcement composites also have some defects such as lower anti-impact property, high absorbability, and lower thermal impact property. Therefore, the advanced laminate materials, which stacks with aluminum thin plates and fiber reinforced composites have been developed to improve their disadvantages.[1]~[6]

There are several methods in the processing and assembling for the fabrication of the laminate composites capable of applying to the aerospace industry. One is mechanical joining method such as a riveting and a bolting and the other is chemical bonding method using an adhesive such as an epoxy. It was well known that mechanical joining method prefers to chemical bonding method due to its reliance. However, the drilling on the surface of a beac plate

depreciates its strength. Consequently, the characteristic of strength reduction in the material must be clarified for the safety design of airplane.

In this study, the tensile notch strength and the fracture condition of the CARALL (Carbon fiber reinforced aluminum laminates) with circular notch, which are made of Al7075 aluminum alloy and CFRP, were investigated.

EXPERIMENTAL PROCEDURE

In this study, Al7075/CFRP layered composites were called CARALL. The CARALL was made with the aluminum alloy (Al7075-T6 a clad sheet, Alcoa Co., USA), the unidirectional carbon laminates (F584-4, Hexel Co., USA) and the adhesive film (FM300M, Cytec Co., USA) so as to evaluate its tensile characteristics. The thickness of Al7075-T6 sheet and CFRP sheet were 1.54 mm and 1.1 mm, respectively. A CFRP sheet used in this composite was composed of the carbon prepreg of 8 plies. The carbon laminate, which comprises 8 plies was also fabricated for the comparison. In order to improve the adhesive performance of aluminum plates and carbon prepregs, the phosphoric acid anodizing pretreatment was performed on the surface of aluminum plates prior to fabrication. The fabrication process of the CARALL was as follows. 1) A parting agent film was previously laid on a work plate. 2) The layered specimens were positioned on the parting agent film. 3) The part agent film and breed were laid on the specimen. 4) We pushed the work plate at the inside of the autoclave. The temperature was elevated up to 177°C at an interval of 2.5°C/min under the pressurized condition of 0.3 MPa. The pressure holding time was 90 min. The mechanical properties of the each specimen were conducted by the material testing system (MTS-810) in room temperature. Crosshead speed was 1.0 mm/min. Table 1 shows the results of the tensile tests.

Table 1 Mechanical properties of Al7075, CFRP and CARALL

	Al707-T6	CFRP		CARALL	
		0°	90°	0°	90°
Elastic modulus (GPa)	69.8	136.1	8.5	99.9	24.8
Shearing modulus (GPa)	26.2	5.9	-	12.5	-
UTS (MPa)	573.7	2013.5	40.5	1334.0	152.8
Poisson's ratio	0.33	0.3	0.01	0.3	0.01

To examine the relationship between the notch tensile strength and the fracture condition in CFRP, Al7075-T6 and CARALL, the circular notch was machined on the composites, as shown in Fig. 1. We decided the plate widths – w = 24 mm, 48 mm - and the ratios of notch size to plate width in the specimens – (ϕ/w) were 0.05, 0.1, 0.2, 0.3, 0.4. The widths of the composite plates (w) were 24 mm and 48 mm, respectively.

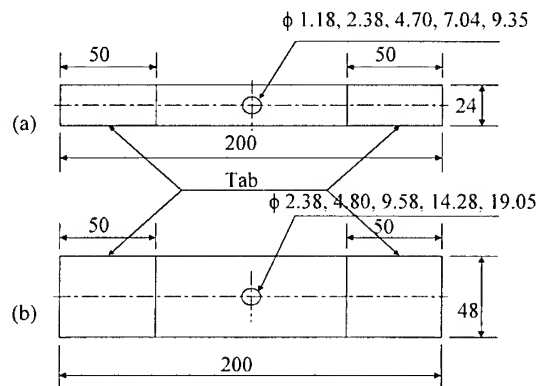


Fig. 1 Configuration of test specimen (unit : mm)

TEST RESULTS & DISCUSSION

The results of notch tensile test Table 2 Experimental results of notch tensile strength

The tensile test of Al7075, CFRP and CARALL composites were summarized in the Table 2. The ultimate tensile strength of unnotched Al7075, CFRP, CARALL were 573.7, 2013.5 and 1334.0 MPa respectively. The notch tensile strengths, σ_N , were gradually decreased with the increasing of circular notch diameter, $2R$. Especially, the CFRP has higher notch sensitivity than those of another materials, because of its unidirectional properties. When $2R/W$ is 0.4, the strength ratio of unnotched and notched tensile specimen for CFRP, σ_N/σ_0 , was changed from 0.35 to 0.36. Those values of CFRP were too low, compared to those of Al7075 and CARALL. In cases of Al7075 and CARALL, the strength ratios of unnotched and notched tensile specimen, σ_N/σ_0 , were 0.72 and 0.55 respectively. From the series of the test results, it is found that the notch sensitivity of CFRP was too high even though it has the high ultimate tensile

strength. On the contrary, the ultimate tensile strength of Al7075 is low, but slightly decreases due to a notch. The high strength of CFRP and the notch insensitivity of Al7075 can be simultaneously obtained by using CARALL.

Material	W (mm)	$2R$ (mm)	$2R/W$	σ_N (MPa)	$\sigma_{N\infty}$ (MPa)	$\sigma_{N\infty}/\sigma_0$
Al7075 ($\sigma_0=570$ MPa)	24	1.18	0.05	521	522	0.92
		2.38	0.10	500	505	0.89
		4.70	0.20	455	476	0.83
		7.04	0.29	388	430	0.76
		9.35	0.39	337	410	0.72
	48	2.38	0.05	517	518	0.91
		4.80	0.10	495	500	0.88
		9.58	0.20	441	461	0.81
		14.28	0.30	392	437	0.77
		19.05	0.40	336	412	0.72
CFRP ($\sigma_0=2014$ MPa)	24	1.18	0.05	944	946	0.47
		2.38	0.10	847	856	0.43
		4.70	0.20	821	857	0.43
		7.04	0.29	645	715	0.36
		9.35	0.39	581	706	0.35
	48	2.38	0.05	1204	1207	0.60
		4.80	0.10	1005	1016	0.50
		9.58	0.20	781	817	0.41
		14.28	0.30	666	742	0.37
		19.05	0.40	598	733	0.36
CARALL ($\sigma_0=1334$ MPa)	24	1.18	0.05	1136	1139	0.85
		2.38	0.10	911	921	0.69
		4.70	0.20	846	884	0.66
		7.04	0.29	682	757	0.57
		9.35	0.39	604	734	0.55
	48	2.38	0.05	930	932	0.70
		4.80	0.10	865	873	0.66
		9.58	0.20	773	809	0.61
		14.28	0.30	657	732	0.55
		19.05	0.40	591	725	0.54

Prediction of notch tensile strength

Whitney and Nuismer[7][8] suggested two models, the point stress failure criterion and average stress failure criterion, which were based on the distribution of normal stress in the near of the notch. It assumes that the failure of specimens occurs when the normal stress or the average stress at a constant distance (d_0), far from a notch, is equal to the failure strength of the unnotched specimens. Failure conditions were expressed as Equation (1) and (2).

$$\sigma_y(R + d_0, 0) = \sigma_0 \quad (1)$$

$$\frac{1}{a_0} \int_R^{R+a_0} \sigma_y(x, 0) dx = \sigma_0 \quad (2)$$

Where, R is the radius of circular notch, d_0 and a_0 are the characteristic lengths from circular notch under each stress condition. Whitney and Nuismer supposed that the characteristic

length was a material constant which is not related with the size of notch but evaluated the notch strength of glass/epoxy and graphite/epoxy composites with a circular notch and crack. However, Pipes *et al.*[9] and Kim *et al.*[10] described the relation between characteristic length, d_0 , and the ratio of a circle diameter to a plate width, $2R/W$ as shown in the equation (3) and evaluated the notch strength of glass/epoxy composites.

$$d_0 = k^{-1} \left[\frac{2R}{W} \right]^m \quad (3)$$

Where, k is the notch sensitive coefficient concerned with $2R$ and W , m is the coefficient showing the change of characteristic length. Kim *et al.* represented the exponential relationship of the characteristic length, d_0 , to the circular notch sizes in the glass/epoxy composites and modified the Whitney and Nuismer's equation to the equation (4).

$$\frac{\sigma_{N\infty}}{\sigma_0} = \frac{2}{[2 + \eta^2 + 3\eta^4 - (K_{T\infty} - 3)(5\eta^6 - 7\eta^8)]} \quad (4)$$

$$\eta = \frac{1}{(1 + 2^m R^{m-1} W^{-m} k^{-1})}$$

The relationship of the characteristic length, d_0 , to the circular notch sizes in Al7075, CFRP and CARALL was shown in Fig. 2. According to the test results in Fig. 2, the exponential curve corresponded to each condition was drawn by using of the equation (3). Therefore, k and m in above equation (3), concerned about the transition of the characteristic length were decided, as shown in Table 3. In the results of notch strength test, the notch sensitive coefficient (k) of Al7075 is higher than CARALL, which is higher than CFRP. Even though the same material, the notch sensitive coefficient (k) of a specimen with the width of 48 mm was higher than one with the width of 24 mm.

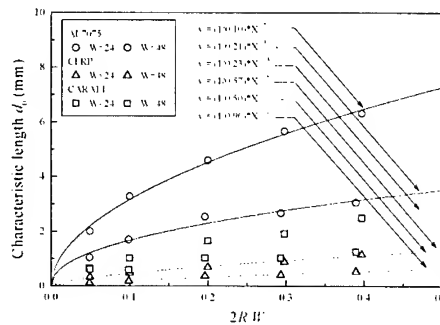


Fig. 2 Relationship between characteristic length and $2R/W$

Table 3 The coefficient values of characteristic length in Al7075, CFRP and CARALL.

	Al7075		CFRP		CARALL	
	$W=24\text{mm}$	$W=48\text{mm}$	$W=24\text{mm}$	$W=48\text{mm}$	$W=24\text{mm}$	$W=48\text{mm}$
K	0.21	0.10	0.96	0.50	0.57	0.23
M	0.46	0.52	0.72	0.72	0.38	0.64

Relationships among experimental results, modified equation (4) results, Whitney equation(1) results are shown in Fig. 3. The each symbol indicated that the ratio of $(\sigma_N/\sigma_0)_{PRE}$ to $(\sigma_N/\sigma_0)_{EXP}$. Where, the ratio of notched tensile strength to unnotched tensile strength, $(\sigma_N/\sigma_0)_{PRE}$ was calculated by theoretical equation, and $(\sigma_N/\sigma_0)_{EXP}$ was also obtained by the experiment. It can be regarded that the results calculated by modified equation were better agreement with experiment results, rather than that of Whitney equation. If (σ_N/σ_0) was high or low, the results calculated by Whitney equation were not good agreement with the experimental results, because the Whitney equation considered the characteristic length to the material constant.

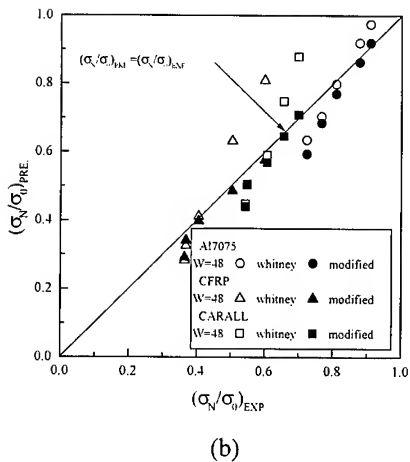
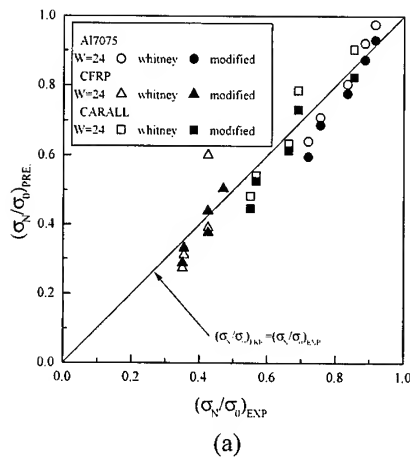


Fig. 3 Comparison of test results with point stress criterion and modified point stress criterion; (a) $w=24$ mm and (b) $w=48$ mm

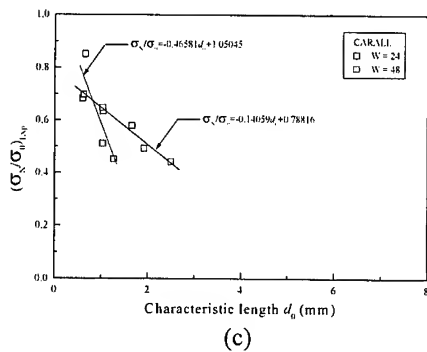
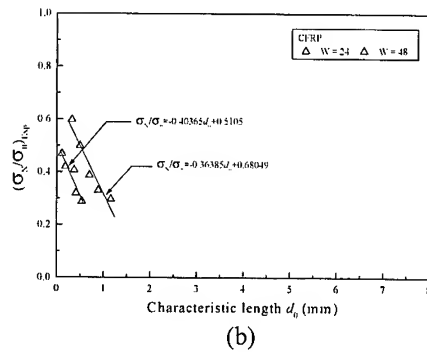
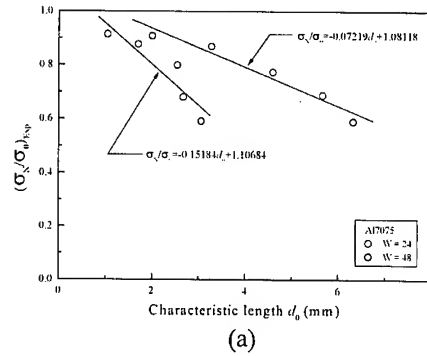


Fig. 4 Relationship between notched strength and characteristic length; (a) Al7075, (b) CFRP and (c) CARALL

The relationships of ease σ_N/σ_0 to characteristic length were shown in Fig. 4. In this figure, (a) is concerned with Al7075; (b) is concerned with CFRP; (c) is concerned with CARALL. The relationship of σ_N/σ_0 to characteristic length (d_0) is inverse. The slope of regression curve on each condition at the equation (5). The notch tensile strength of all composites intends to decrease with increasing the notch size. As shown in the equation (5), CFRP has the lowest slope coefficients. However, the slope coefficients increase with increasing the width of the specimen. Even if CARALL has the lowest slope coefficient in the width of 24 mm.

$$\begin{aligned}
&\text{Al7075} \quad W = 24 \text{ mm} : \sigma_N / \sigma_0 = -0.1518d_0 + 1.1068 \\
&\quad \quad \quad W = 48 \text{ mm} : \sigma_N / \sigma_0 = -0.0723d_0 + 1.0812 \\
&\text{CFRP} \quad W = 24 \text{ mm} : \sigma_N / \sigma_0 = -0.4037d_0 + 0.5105 \\
&\quad \quad \quad W = 48 \text{ mm} : \sigma_N / \sigma_0 = -0.3639d_0 + 0.6805 \\
&\text{CARALL} \quad W = 24 \text{ mm} : \sigma_N / \sigma_0 = -0.4658d_0 + 1.0505 \\
&\quad \quad \quad W = 48 \text{ mm} : \sigma_N / \sigma_0 = -0.1406d_0 + 0.7882
\end{aligned} \tag{5}$$

CONCLUSION

In this study, CARALL composite was fabricated by stacking CFRP laminate, adhesive film and Al7075, using the autoclave. The effects of the circular notch on the notch tensile strength of the CARALL and its components were investigated. The usefulness of the Whitney and modified failure criteria was also examined. The results were as follow:

- 1) The lamination of AL7075 sheets suppressed a sudden decrease in the notch tensile strength of CFRP
- 2) The characteristic length (d_0), was changed depending on the notch sizes as well as the materials.
- 3) The notch sensitive coefficient (k) was highest in CFRP. And it was lowest in Al7075. In the same material, the specimen with the width of 48mm had higher notch sensitive coefficient than that with the width of 28 mm.
- 4) The results predicted by the modified equation is a good agreement with the experiment results, rather than that by the Whitney equation.

REFERENCES

1. C. T. Lin and P. W. Kao, "Fatigue delamination growth in carbon fiber-reinforced aluminum laminates", *Composites*, Vol.27A, 1996, pp. 9.
2. R. Marissen, "Flight simulation behaviour of aramid reinforced aluminum laminates (ARALL)", *Engineering Fracture Mechanics*, Vol.19, 1984, pp. 261
3. J. W. Gunnink and L. B. Vogelsang, "Arall laminates structures : toward the supportable and durable aircraft", *20th International SAMPE Technical Conference*, Vol.20, 1988, pp. 605.
4. C. T. Lin, P. W. Kao and F. S. Yang, "Fatigue behavior of carbon fiber-reinforced aluminum laminates", *Composites*, Vol.22, 1991, pp.135.
5. C. T. Lin and P. W. Kao, "Effect of Fiber Bridging on the Fatigue Crack Propagation in Carbon Fiber-Reinforced Aluminum Laminates", *Materials Science & Engineering*, Vol.A190, 1995, pp. 65.
6. C. T. Sun, A. Dicken and H. F. Wu, "Characterization of Impact Damage in ARALL Laminates", *Composites Science and Technology*, Vol.49, 1993, pp.139.
7. J. M. Whitney and R. J. Nuismer, "Stress Fracture Criteria for Laminated Composites Containing stress Concentrations", *J. Composites Materials*, Vol.8, 1974, pp. 253~265
8. R. J. Nuismer and J. M. Whitney, "Uniaxial Failure of Composite Laminates Containing Stress Concentrations", *ASTM STP 593*, 1975, pp. 117~142.
9. R. B. Pipes and J. W. Gillespie, "Superposition of the Notched Strength of Composite Laminates", *Polymer Engineering and Science*, Vol.19, No.16, 1979, pp. 1151~1155.
10. J. K. Kim, N. Takeda and T. Shioya, "Fracture Criteria of Polymer Matrix Composite with Circular Hole", *Proceeding of 69th Annual Meeting. The Japan Society of Mechanical Engineers*, Vol. A, 1992.

FRACTURE TOUGHNESS AND INTERFACIAL STRUCTURE OF PP/WOOD COMPOSITES

T.Q. Li^{1,2,3}, R.K.Y. Li² and H. M. Zeng³

1. *Department of Materials Science and Engineering, Guangdong University of Technology, 729 E. Dongfeng Road, Guangzhou, 510090 China: tieqili@gdut.edu.cn*
2. *Department of Physics and Materials Science, City University of Hong Kong, 83 Tat Chee Avenue, Kowloon, Hong Kong: aprkyl@cityu.edu.hk*
3. *Laboratory of Polymeric Composite and Functional Materials, The State Educational Commission of China, Zhongshan University, Guangzhou 510275, China*

SUMMARY: The dynamic fracture toughness and the interfacial structure of polypropylene/wood flour (PP/Wood) composites were studied to reveal the nature of impact resistance of the composites. It was shown that the notched Izod impact resistance of the PP/wood compounds is not necessarily lower than the matrix resin. The strain energy release rate and the fracture toughness of the PP/Wood blends was found to increase with not only the filler content and average size but also the interfacial modifier content. Comparison of the fracture parameters with the results of crystalline morphology reveals the effect of the interfacial structure in determining the interfacial stress transfer under the dynamic loading rates and thus the impact resistance of the PP/wood blends.

KEYWORDS: polypropylene; wood flour; fracture toughness; interfacial structure; crystalline morphology; skin-core structure.

INTRODUCTION

The past decade has seen a growing interest in developing natural fiber reinforced thermoplastics. Because the natural fibers are currently provided mostly in forms that contain discontinuous cellulosic fiber [1], the traditional extruder compounding processes are still competitive. It is especially true in the case of the wood flour reinforced polypropylene (PP/Wood) systems, which are economically competitive.

Unfortunately, the decreased in impact strength was frequently reported for the PP/Wood composites. To improve the impact resistance of the PP/wood composites, efforts were made to modify matrix polymer with either elastomers or a High-Impact Propylene (HIPP) [2-4]. The impact modifications in these ways, however, were usually achieved at the price of stiffness. The potential increase in impact resistance according to the results on discontinuous long-fiber reinforced polypropylene [5] had not been observed, though the positive contribution of a stronger interface may well be implied in the experimental data of PP/Wood with maleated elastomers [2]. Obviously, the nature of the impact resistance in these systems should be further studied based on the fracture mechanics methods and also through comparison with the materials morphology.

EXPERIMENTAL

PP/wood blends studied in this report were compounded with a twin-screw extruder and then injection-molded into plates. The matrix resin was either a tough copolymer (EPS30R, MI=1.8g/min) or a commercial recycled PP (RPP). The wood flour was either the commercial 100mesh filler for phenolics or the sieve-fractionated grades of the sawdust. The compounds had been prepared to cover a wide range of the impact fracture behaviors. The maleic-anhydride grafted PP was applied during extrusion compounding when necessary to study the effects of interfacial interaction. Both traditional Izod impact tests (ASTM D256-93a) and drop weight dart Charpy tests [6] were performed at the 1.45m/s rate on a instrumented model of the Ceast equipment. LEFM was found to be suitable for characterizing the dynamic fracture of the blends in the Charpy tests. The critical stress intensity factor, K_{Ic} , and the stress release rate, G_c , were calculated based fracture mechanics [7, 8]. The crystalline morphology of the injection-molded plates was analyzed through X-ray methods.

RESULTS AND DISCUSSION

Notched Izod Impact Strength

Figure 1 and 2 illustrate the notched Izod impact strength of the wood composite based on the recycled PP and that of the blends based on the virgin copolymer, respectively. From Figure 1, it can be seen that the Izod strength tends to increase with filler content in MA-g-PP-containing blends but does the opposite in blends without the additive. The MA-g-PP had changed the dependence of the Izod strength on filler content. The additive had made the wood filler to contribute positively to the Izod impact strength.

From Figure 2, it can be seen that the Izod strength of the PP/100mesh wood flour composite increases with MAPP content until the latter reaches 5phr. At the MAPP content of 2.5phr, the Izod strength increases with the filler particle size. The dependence on filler particle size and interfacial modifier content agrees with the result of discontinuous glass fiber reinforced PP [5]. The potential role of the interfacial modification by MA-g-PP seems to be positive to the Izod impact strength.

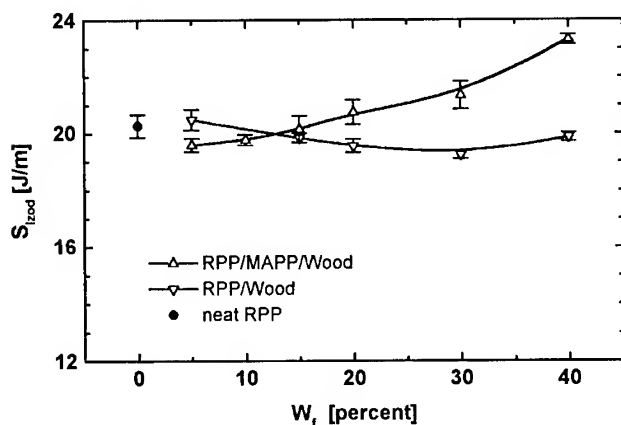
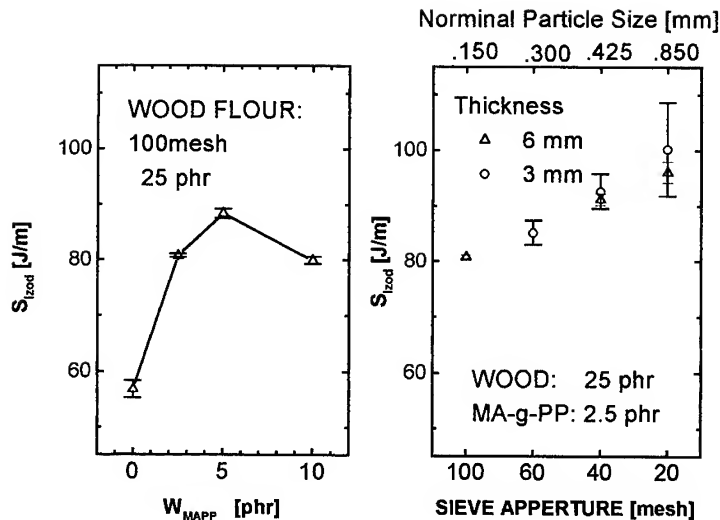


Figure 1. Izod impact strength of RPP blends with 20mesh sawdust



(a) Effects of MAPP Content (b) Effects of Particle Size

Figure 2. Izod impact strength of EPS30R/Wood blends

Fracture Toughness of the PP/Wood composites based on RPP

Figure 3 and 4 shows the critical energy release rate, G_c , and the critical stress intensity factor, K_{Ic} , respectively, of the RPP blends with the 20mesh sawdust. It can be seen that the dynamic fracture energy G_c increase considerably with filler content in the blends modified with MA-g-PP but remains almost unchanged in blends without the modifier. The fracture toughness, K_{Ic} , increases more significantly in blends with MA-g-PP, leading to K_{Ic} value that is even higher than that of the neat resin. It is the reinforcing role of the fillers that had resulted in the increasing trend of fracture resistance.

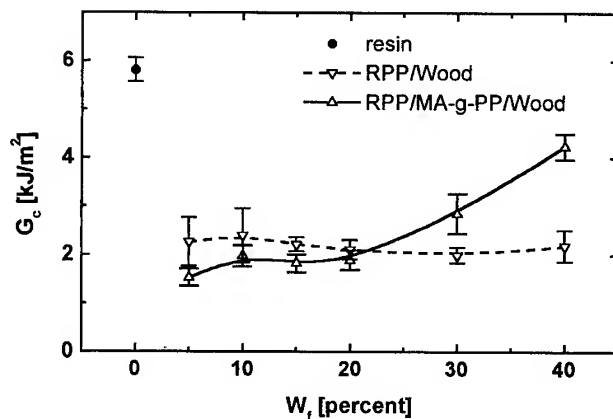


Figure 3. Fracture energy G_c of the RPP blends with 20mesh sawdust

Relationship between Fracture Toughness and Interfacial interaction

Figure 5 shows the fracture energy in the wood blends with the tough EPS30R matrix. As shown in Figure 5.a, G_c increases with the MA-g-PP content when the 100mesh wood flour was used as reinforcement. When the MA-g-PP content is fixed at 2.5phr, an increase in filler particle size results in increasing fracture energy. The results are in good agreement with the expected behavior of short fiber reinforced composites. A strong interface may well contribute to the fracture resistance if the interfacial and/or interphasial deformations are important mechanisms during the fracture.

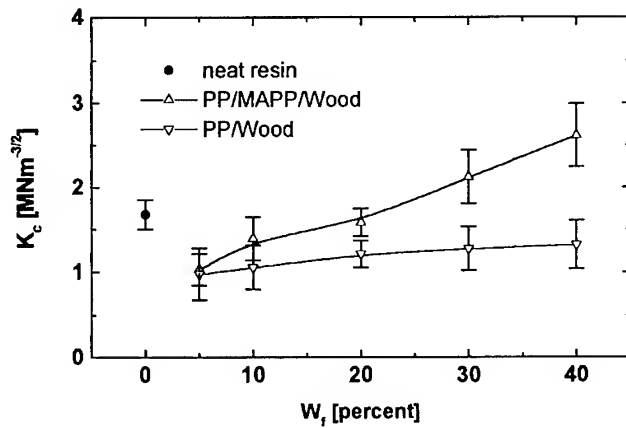
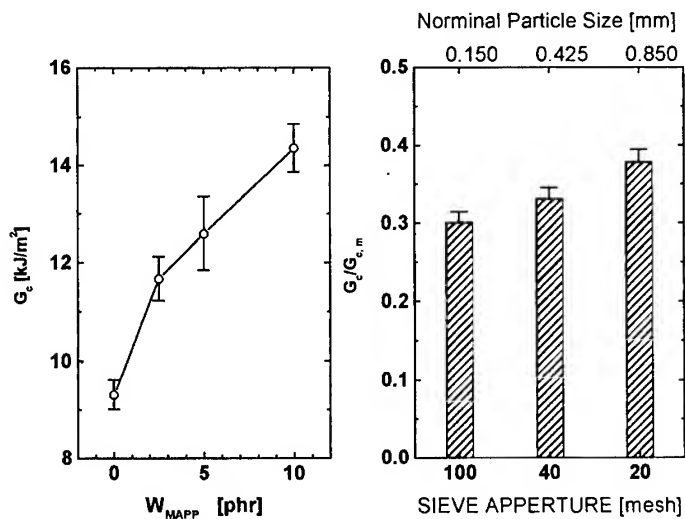


Figure 4. Fracture toughness K_c of the RPP blends with 20mesh sawdust



(a) Effects of MA-g-PP content

(b) Effects of particle size

Figure 5. Fracture energy of EPS30R blends containing 25phr wood flour

The morphology results shed more lights on the nature of dynamic fracture resistance found in these specimens. The Wide Angel X-ray Diffraction analyses suggest that the matrix PP consist of both alpha and beta phase crystallites, the latter being rich in the surface layer of one half millimeter (Figure 6). The relative content of the beta phase decreases with the increasing MA-g-PP content. The decrease indicates that the less stable beta crystalline form should not be responsible for the higher fracture energy in the MA-g-PP-containing wood blends. The increasing fracture energy should then result from the stronger interfacial interaction during the impact tests, rather than any change in matrix morphology. Factually, the pullout of single fibers and the defibrillation of the wood particles, which are undoubtedly energy-absorbing mechanisms, were typical fractographic features. A strong interface can then be benefit for the dynamic fracture resistance while playing the reinforcing role.

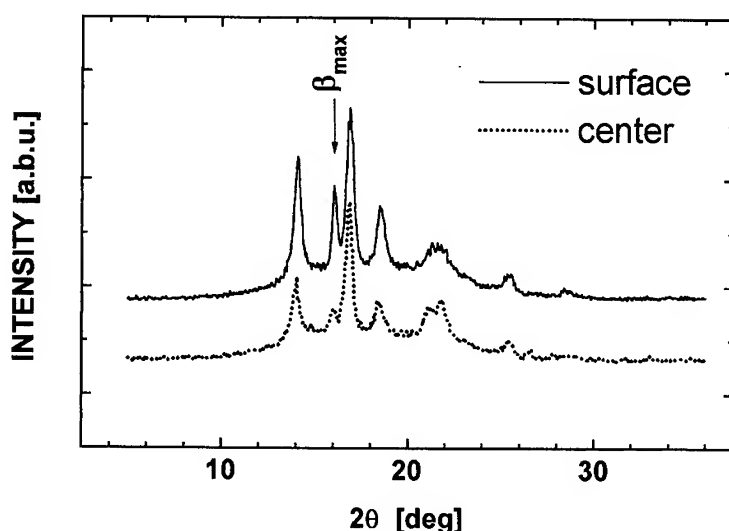


Figure 6. WAXD scans of the EPS30R/100mesh wood flour blend

The WAXD analyses also explain the dependence of K_{IC} and G_c on filler content in the blends based on the less tough RPP matrix. As shown in Figure 7, the relative content of the beta phase PP, indicated by the relative reflection intensity of the beta phase maximum over the alpha phase (040) peak, increases with the filler loading except for the composite with the highest 40 percent wood. The quantity of the MA-g-PP-containing blends is always less than the composite with the same filler loading but containing no MA-g-PP. It would be interesting to compare the figure with the dependence of G_c (Figure3) and K_{IC} (Figure4) on filler loading. The change of the beta phase content with the filler loading resembles that of G_c only in the system with MA-g-PP. the beta phase is known to be less stable and corresponding to lower yielding stress [9, 10]. In agreement with the results in the EPS30R blends, the difference in the beta phase content itself can not be the reason of the complex relative ranking of G_c . On another hand, filler loading affect the fracture toughness of MA-g-PP composites more considerably but has weaker effects on the beta phase content. The stronger dependence of K_{IC} on filler loading at the presence of MA-g-PP thus originates unambiguously from the stronger interfacial interaction during the impact tests.

Moreover, it seems that the wood filler tend to induce beta phase crystallites, at least in the surface layer and the effect is reduced by the MA-g-PP. The chemical reactions during processing are thus important for further understanding of the wood composite and also for a proper design of the interface.

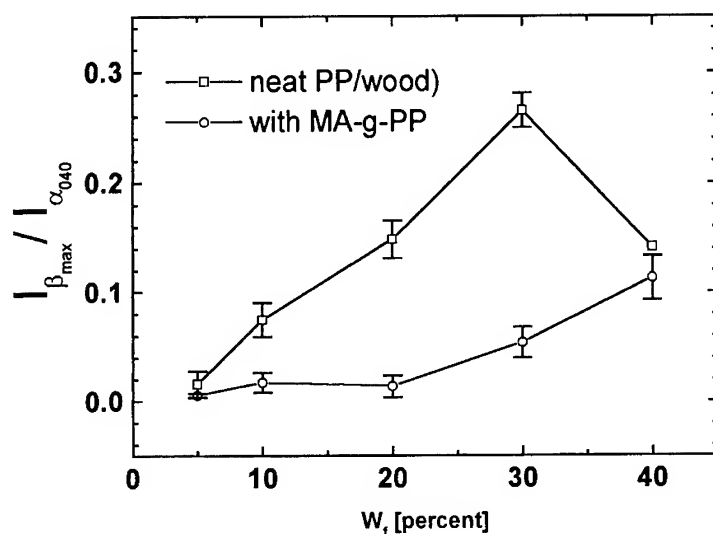


Figure 7. Intensity ratio of the beta phase maximum over the alpha phase (040) reflection Of the RPP blends with 20mesh sawdust

REFERENCES

1. Bledzki, A. K., Gassan, J., "Composite reinforced with cellulose based fibers", *Prog. Polym. Sci.*, 1999, Vol.24, pp. 221-274
2. Oksman, Kristiina. Clemons, Craig, "Mechanical properties and morphology of impact modified polypropylene-wood flour composites", *Journal of Applied Polymer Science*, 1998, Vol. 67, pp. 1503-1513
3. Dingova, E. Djiporovic, M. Miljkovic, J. "Effects of EPDM modification on some properties of polypropylene-wood flour composite", *Materials Science Forum*, Vol. 282-283, 1998, pp. 303-308
4. Park, B.-D. and Balatinecz, J. J., "Mechanical properties of wood-fiber/toughened isotactic propylene composites", *Polym. Compos.*, Vol.18, 1997, pp. 79-89
5. Karger-Kocsis, in *Polypropylene: Structure, blends, and composites*, Edited by J. Karger-Kocsis, Chapman & Hall, London. 1995, pp.142 - 201
6. Tam, W. Y., Cheung, T., Li, R. K. Y., "An investigation of the Impact Fracture Characteristics of EPR Toughened Polypropylene", *Polymer testing*, Vol.15, 1996, 363-379
7. Plati, E. and Williams, J. G., "The determination of the fracture parameters for polymer in impact", *Polym. Eng. Sci.*, 1976, Vol.15, pp.470-477
8. Mai, Y-W., "Discussion of impact fracture parameters in ductile polymers", *Polym. Commun.*, 1989, Vol.30, pp.330
9. Zhang, Xiaodong and Shi, Guangyi, "Effect of converting the crystalline form from α to β on the mechanical properties of ethylene/propylene random and block copolymers", *Polymer*, 1994, Vol.35, 5067 - 5072

Mixed Mode Impact Fracture Toughness and Rate Dependent Fracture Behavior of Interlayer-Toughened Carbon-Fiber/Epoxy Composite Laminates

Noriyo HORIKAWA¹, Takayuki KUSAKA², Masayoshi MASUDA³, Shinichi ADACHI⁴

¹Department of Mechanical Engineering, Ritsumeikan University,
1-1-1, Noji-Higashi, Kusatsu 525-8577, JAPAN:fme30024@se.ritsumei.ac.jp

²Department of Mechanical Engineering, Ritsumeikan University,
1-1-1, Noji-Higashi, Kusatsu 525-8577, JAPAN:kusaka@se.ritsumei.ac.jp

³Graduate Student, Ritsumeikan University,
1-1-1, Noji-Higashi, Kusatsu 525-8577, JAPAN:rm130959@se.ritsumei.ac.jp

⁴Undergraduate Student, Ritsumeikan University,
1-1-1, Noji-Higashi, Kusatsu 525-8577, JAPAN:rm000962@se.ritsumei.ac.jp

SUMMARY: Mixed mode impact fracture toughness of the interlayer-toughened carbon-fiber/epoxy composite laminates, T800H/3900-2 (Toray), which is a newly developed composite system having a tough 'interlayer' containing fine polyamide particles, was investigated by using MMF (Mixed Mode Flexure) specimen and SHPB (Split Hopkinson Pressure Bar) system. The strain rate dependence of fracture behavior was also studied from both macro- and microscopic aspects to clarify the mesoscopic fracture mechanism of the material. The experimental results showed that the crack path was inside the toughened interlayer during the initial stage of crack growth, however, it moved from the toughened interlayer to the carbon/epoxy base lamina during the propagation stage of crack growth. The impact fracture toughness for the toughened interlayer was about 38 % lower than the maximum value under static loading. The impact fracture toughness for the carbon/epoxy base lamina was about 30 % lower than the maximum value under static loading.

KEYWORDS: Delamination, Mixed mode, Fracture toughness, Rate dependence, Impact strength, Interlayer-toughened composite

INTRODUCTION

In many cases, CFRPs (Carbon Fiber Reinforced Plastics) are used as laminated plates or shells. Hence the delaminations play a critical role in the catastrophic failure of the composite structure. Recently, various composite systems were developed to improve the damage tolerance for delamination. The 'interlayer' toughened composite system is one of the highest-performance composite developed for large-sided commercial aircraft [1]. Excellent CAI (Compression After Impact) performance was come off by containing fine polyamide particles between the plies of the material.

The evaluation of rate dependence is very important to fully characterize the fracture

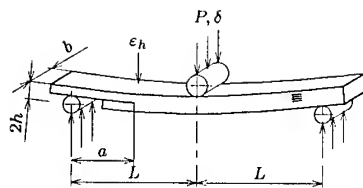


Fig. 1 MMF specimen for estimating mixed mode interlaminar fracture toughness of composite laminates.

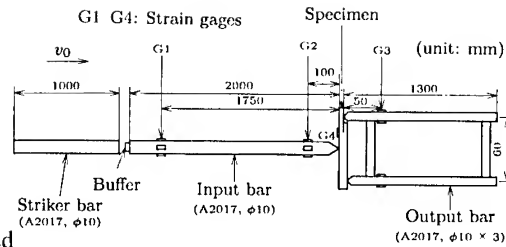


Fig. 2 Schematic drawing of the impact MMF testing apparatus using SHPB technique.

behavior of composite materials, because the mechanical properties of matrix resin is usually sensitive to strain rate [2]. The authors, therefore, studied the rate dependence of modes I and II fracture behaviors of various composites [3-6]. However, the characterization of mixed mode fracture behavior and its rate dependence is rather important, because the failure caused by delaminations usually occurs by mixed mode loading [7,8]

In this study, the effects of loading rate on mixed mode interlaminar fracture toughness of the interlayer toughened carbon-fiber/epoxy composite laminates were, therefore, investigated over a wide range of loading rate from quasi-static to impact. The microscopic fracture morphology was also discussed on the basis of the results of microscopic observation.

EXPERIMENTAL PROCEDURE

Material

The interlayer-toughened carbon-fiber/epoxy composite system, T800H/3900-2 (Toray), which is a newly developed composite system having tough 'interlayer' containing fine polyamide particles, was investigated in this study. Unidirectional panels of T800H/3900-2 were fabricated with autoclave under the prepreg manufacturer's recommended cure cycle. The volume fraction of carbon fibers was about 54%. The thickness of the panels was about 3.1 mm. A 8μm thick polyimide film was inserted at the mid-plane of the panels prior to processing to provide the starter slit. The panels were machined to coupon specimens of 5-6 mm in width using a diamond blade.

Experimental Procedure

The MMF (Mixed Mode Flexure) specimen was employed to measure the mixed mode fracture toughness (critical energy release rate), G_C , as shown in Fig.1. The displacement rate, $\dot{\delta}$, was varied from 8.3×10^{-7} to 6.2×10^0 m/s to study the effects of loading rate. A screw-driven testing machine was used for quasi-static MMF tests ($\dot{\delta} = 8.3 \times 10^{-7} - 8.3 \times 10^{-3}$ m/s; 0.05-500 mm/min). A SHPB (Split Hopkinson Pressure Bar) system was used for impact MMF tests ($\dot{\delta} = 2.2 \times 10^0 - 6.2 \times 10^0$ m/s), as shown in Fig. 2. In impact MMF tests, a ramped incident stress wave [9] was used for suppressing the flexural vibration of the specimen [10].

Data Reduction

On the basis of static compliance method, the mode I energy release rate, G_I , and the mode II energy release rate, G_{II} , can be given by the following equations for MMF specimen [11];

$$G_I = \frac{24C}{b(2L^3 + 7a^3)} (M_U - M_L)^2, \quad G_{II} = \frac{18C}{b(2L^3 + 7a^3)} (M_U + M_L)^2, \quad (1)$$

where M_U and M_L were bending moments applied to the upper and lower beams of the cracked region of the specimen, respectively. b , $2L$, a and $C (= \delta / P)$ are the width, length, bending span, crack length and compliance of the specimen. Applying the principle of superposition, the mixed mode energy release rate, G , can be given by the following equation;

$$G = G_I + G_{II} \quad (2)$$

Substituting $M_U = Pa / 2$ and $M_L = 0$ to Eqn (1), the mixed mode energy release rate, G , and its critical value, G_C , can be given by

$$G = \frac{21P^2 a^2 C}{2b(2L^3 + 7a^3)}, \quad G_C = \frac{21P_C^2 a_C^2 C_C}{2b(2L^3 + 7a_C^3)}, \quad (3)$$

where P_C , a_C and C_C are the critical values of the load, crack length and compliance of the specimen, respectively [11]. The ratio of the mode I energy release rate, G_I , to the mode II energy release rate, G_{II} , is equal to 4/3 theoretically, which means the contribution of the mode I energy release rate, G_I , is higher than that of the mode II energy release rate, G_{II} .

Assuming the surface strain of the specimen, ϵ , was proportional to the load, P , the mixed mode energy release rate, G , and its critical value, G_C , can be given by

$$G = \frac{21\epsilon^2 a^2 C}{2bD^2(2L^3 + 7a^3)}, \quad G_C = \frac{21\epsilon_C^2 a_C^2 C_C}{2bD_C^2(2L^3 + 7a_C^3)}, \quad (4)$$

where ϵ_C and D_C are the critical values of the strain, ϵ , and the strain coefficient, $D (= \epsilon / P)$, of the specimen, respectively. In this study, the mixed mode fracture toughness, G_C was calculated by Eqn (3) for quasi-static tests and by Eqn (4) for impact tests, respectively.

The onset of macroscopic crack growth was determined by the 5 % offset technique. The critical compliance, C_C , was determined from the load-displacement relation. The critical strain coefficient, D_C , was, however, approximated to be equal to the initial strain coefficient, D_0 [4, 6]. The critical crack length, a_C , was evaluated by the following equation;

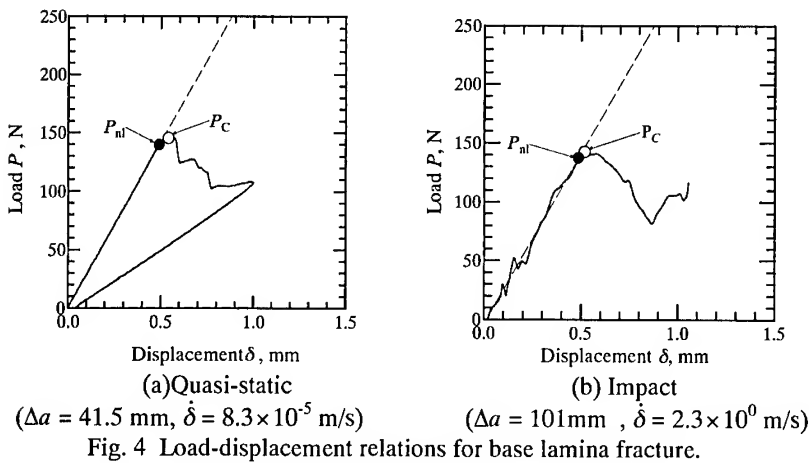
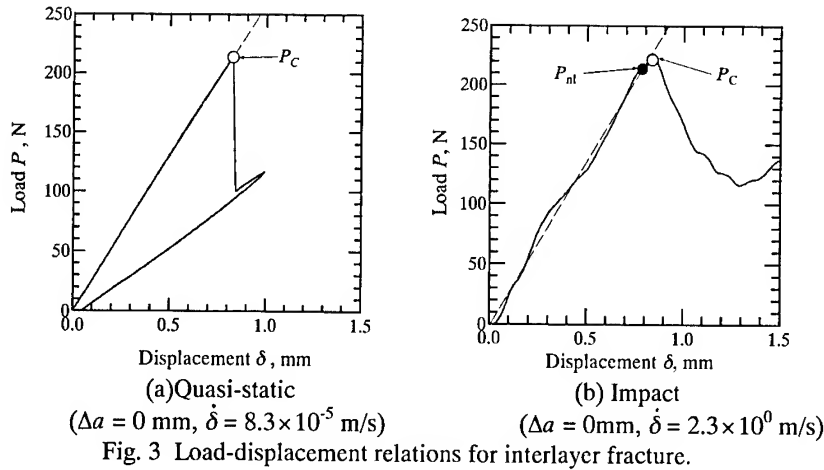
$$a_C = \sqrt[3]{\frac{C_C}{C_0} a_0^3 + \frac{2}{7} \left(\frac{C_C}{C_0} - 1 \right) L^3}, \quad (5)$$

where a_0 is the initial crack length of the specimen.

RESULTS AND DISCUSSION

Load-Displacement Relation

Figures 3 and 4 show the typical relationships between the reaction force, P , and the displacement, δ , of the loading point in quasi-static and impact fracture tests at the crack extension, $\Delta a = 0$ mm and $\Delta a = 41.5$, 101 mm, respectively. Figures 3(a) and 4(a) indicate the results of quasi-static fracture test. Figure 3(b) and 4(b) indicate the results of impact fracture



test. The open and solid circles represent the critical value of the load, P_c , and non-linear point, P_{nl} , of the load-displacement relation, respectively. The thin dashed line represents the initial slope of load-displacement relation under static loading.

The load-displacement relations shown in Figs. 3 (a) and (b) were similar to those of the neat epoxy resin, because the crack path was inside the toughened interlayer during the initial stage of crack growth. The load-displacement relations shown in Figs. 4 (a) and (b) were different from those in Figs. 3 (a) and (b); the load-displacement relation was non-linear before the onset of crack growth at quasi-static loading rates. This tendency was similar to the mode I results reported by the authors [12].

Fracture toughness

Figure 5 shows the relationships (R-curves) between the mixed mode fracture toughness, G_C , and the crack extension, Δa . The solid and open circles represent the quasi-static and impact results, respectively.

The mixed mode fracture toughness, G_C , was very high at the initial stage of crack growth. However, it decreased to a constant value with crack extension. The results of SEM observation indicated that the crack path was inside the toughened interlayer during the initial

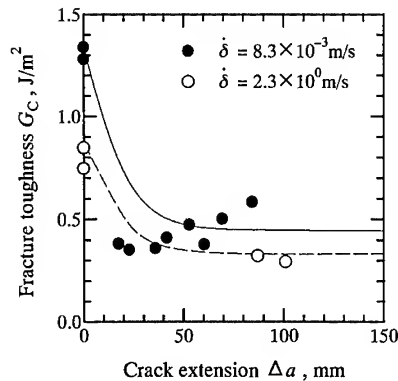


Fig. 5 Rate dependence of crack resistance curves.

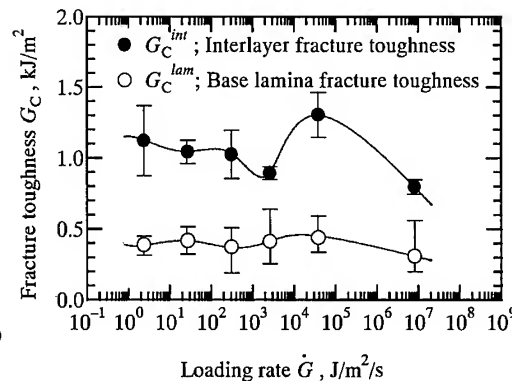


Fig. 6 Rate dependence of mixed mode interlaminar fracture toughness.

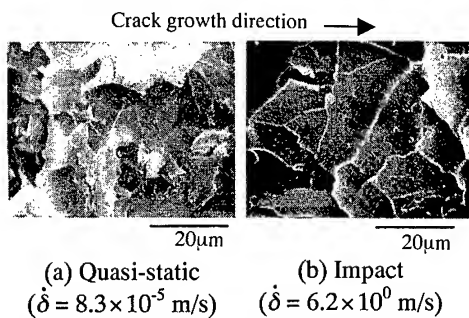


Fig. 7 SEM photographs of mixed mode interlayer fracture surface.

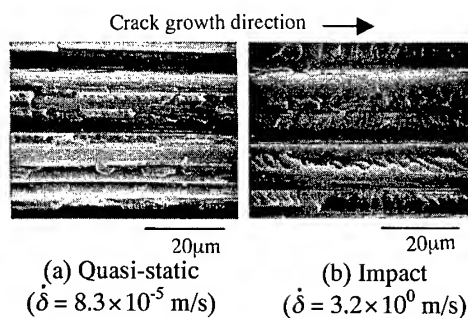


Fig. 8 SEM photographs of mixed mode base laminar fracture surface.

stage of crack growth, however, it moved from the toughened interlayer to the carbon/epoxy base lamina during the propagation stage of crack growth. The above tendency was similar to the mode I results [12].

Figure 6 shows that the relationship between the mixed mode fracture toughness (critical energy release rate), G_C , and the loading rate (time derivative of energy release rate), \dot{G} . The solid and open circles show the fracture toughness for the interlayer fracture, G_C^{int} , and for the base lamina fracture, G_C^{lam} , respectively.

For the interlayer fracture, the impact fracture toughness, $G_C^{int} = 800 \text{ J/m}^2$, was about 38 % lower than the local maximum value, $G_C^{int} = 1300 \text{ J/m}^2$, at quasi-static loading rates. For the base lamina fracture, the impact fracture toughness, $G_C^{lam} = 310 \text{ J/m}^2$, was about 30 % lower than the local maximum value, $G_C^{lam} = 440 \text{ J/m}^2$, at quasi-static loading rates. The above tendency was somewhat different from the mode I results [12], though the contribution of mode I component is higher than that of mode II component in MMF specimen.

Fracture Morphology

Figures 7 and 8 show the SEM photographs of the typical interlayer and base lamina fracture surface under the quasi-static and impact loading, respectively.

In the case of interlayer fracture, many fine cracks were observed on matrix resin and the edges of matrix resin were relatively rough under quasi-static loading, as shown in Fig. 7(a). However, a few fine cracks were observed on matrix resin and the edges of matrix resin were relatively smooth under impact loading, as shown in Fig. 7(b).

In the case of base lamina fracture, the carbon fibers were clearly observed on the fracture surface under quasi-static loading, as shown in Fig.8 (a). However, the ratio of the carbon fibers embedded in the resin was higher under impact loading, as shown in Fig. 8(b). In addition, the hackle pattern, peculiar to mode II fracture, was observed in Figs. 8 (a) and (b). These results were similar to the modes I and II results reported by the authors [4, 6, 12].

CONCLUSION

- (1) The crack path moved from the toughened interlayer to the fiber/matrix base lamina with the crack extension regardless of loading rates.
- (2) The interlayer and base lamina fracture toughness had local maximum values at the quasi-static loading rate.
- (3) The impact fracture toughness for interlayer and base lamina fracture was lower than their local maximum values under quasi-static loading.
- (4) The mixed mode fracture surface was similar to the mode I fracture surface.

REFERENCES

1. N. Odagiri, H. Kishi and M. Yamashita, "Development of TORAYCA Prepreg P2302 Carbon Fiber Reinforced Plastic for Aircraft Primary Structural Materials", *Adv. Compos. Mater.*, Vol.5, 1996, pp.249-252.
2. A. J. Kinloch, R. J. Young, *Fracture Mechanics of Polymers*, Chaps. 6, 8, 1983, Elsevier.
3. T. Kusaka, M. Hojo, Y.W. Mai, T. Kurokawa, T. Nojima and S. Ochiai, "Rate Dependence of Mode I Fracture Behavior in Carbon-Fiber/Epoxy Composite Laminates", *Compos. Sci. Tech.*, Vol.58, 1998, pp.591-602.
4. T. Kusaka, M. Hojo, T. Kurokawa and S. Ochiai, "Rate Dependence of Mode II Interlaminar Fracture Toughness of Interlayer-Toughened Carbon-Fiber/Epoxy Laminates", *Trans. Jpn. Soc. Mech. Eng.*, Ser. A., Vol.64, 1998, pp.1152-1159.
5. T. Kusaka, M. Hojo, T. Kurokawa and S. Ochiai, "Rate Effects on Mode I Interlaminar Fracture Toughness in Carbon-Fiber/Epoxy Composite Laminates", *Proc. of The First Asian-Australasian Conference on Composite Materials:(ACCM-1)*, Vol.2, 1998, pp.713.
6. T. Kusaka, M. Hojo and S. Ochiai, "Rate-Dependent Mode II Interlaminar Fracture Behavior of Carbon-Fiber/Epoxy Composite Laminates", *Mater. Sci. Res. Int.*, Vol.5, 1999, pp.98-103.
7. P. Sriram, Y. Khourchid, and J. Hooper, "The Effect of Mixed-Mode Loading on Delamination Fracture Toughness", *Composite Materials: Testing and Design (Eleventh Volume)*, *ASTM STP 1206*, 1993, pp.291-302.
8. J. R. Reeder, "A Bilinear Failure Criterion for Mixed-Mode Delamination", *Composite Materials: Testing and Design (Eleventh Volume)*, *ASTM STP 1206*, 1993, pp.303-322.
9. K. Ogawa and F. Sugiyama, "A New Application of Split Hopkinson Pressur Bar", *Plasticity and Impact Mechanics (ed. by N.K. Gupta)*, New Age, New Delhi, 1996, pp.466-483.
10. M. Masuda, S. Adachi and T. Kusaka, *Proc. 24th Composite Materials Symposium*, 1999, pp.155-156.
11. J. G. Williams, "On the Calculation of Energy Release Rate for Cracked Laminates", *Int. J. Fract.*, Vol.36, 1988, pp.101-119.
12. T. Kusaka, M. Hojo, T. Kurokawa and S. Ochiai, "Rate Dependence of Mode I Interlaminar Fracture Toughness of Interlayer-Toughened Carbon-Fiber/Epoxy Laminates", *Trans. Jpn. Soc. Mech. Eng.*, Ser. A., Vol.63, 1997, pp.2359-2365.

COMPOSITE PATCHING TECHNIQUE FOR THE EXTENSION OF FATIGUE LIFE OF AIRCRAFT

Wiedae Kim¹, Kyungdon Youn², and C.T.Sun³

¹Department of Aerospace Engineering, Pusan National University
Keumjung-ku, Pusan, 609-735, KOREA, :wdkim@hyowon.pusan.ac.kr

²Department of Aerospace Engineering, Pusan National University
Keumjung-ku, Pusan, 609-735, KOREA, :kdyoun@hyowon.pusan.ac.kr

³School of Aeronautics and Astronautics, Purdue University
1282 Grissom, West Lafayette, IN. 47907, :sun@ecn.purdue.edu

SUMMARY: Composite patching technique is widely used in aircraft to extend the fatigue life effectively with low repair cost. Composite patch repair has advantages to the conventional rivet repair method. It is cost-effective, reliable, and has high strength and longer fatigue life. One of the hot issues in composite patching is to reduce the thermal residual stresses between composite patch and aluminum surface which occurs after bonding of composite patch. In this paper, one of the way which can reduce the thermal residual stress is shown. The static strength and fatigue life are measured by experiments. For this study, the edge crack patching and center crack patching cases are adopted for different curing cycles. The ultrasonic C-scan method is used to detect the crack propagation and debonding area of the specimen. For the analysis, three layer Mindlin plate elements are used, and Paris' law is adopted to predict the fatigue life of composite patch specimen. The experimental and analysis results for fatigue life show good agreement.

KEYWORDS: composite patch, thermal residual stress, thermal mismatch, fatigue life, debonding area, three layer technique, patch strength.

INTRODUCTION

Composite patching technique is widely used in aircraft to extend the fatigue life effectively with low repair cost[1,2]. Composite patch repair has advantages to the conventional rivet repair method. It is cost-effective and reliable, and has high strength and longer fatigue life. In rivet repair, a number of rivet holes are drilled which increases repair cost. Around these holes, the secondary cracks may initiate and propagate leading to corrosion problem, and the situation goes worse and worse. In composite repair, it is easy to repair the cracks and is cost-effective. It can also remove the secondary crack propagation and corrosion problem by sealing the crack surface, and more reliable repair can be obtained. One of the hot issues in composite patching is to reduce the thermal residual stresses between composite patch and aluminum surface which occurs after bonding of composite patch. In this paper, one of the way which can reduce the thermal residual stress is shown. The static strength and fatigue life are measured by experiments and those are compared with the results by finite element analysis.

The edge crack and center crack patching cases are studied for different curing cycles. The ultrasonic C-scan method is used to detect the crack propagation and debonding area of the specimen. For the analysis, three layer Mindlin plate elements are used, and Paris' law is adopted to predict fatigue life of composite patch specimen. The most important and difficult point lies on the surface treatment of the bonding surfaces. Without proper procedure of surface treatment, a good bonding performance can not be expected. The effect of ill-conditioned surface treatment is also discussed. With these experimental and analytical results, more reliable composite repair technique is proposed, and application areas are discussed.

EXPERIMENTS

Experimental Procedures

For the preparation of specimen, aluminum 2024-T3 plate was cut by water jet in appropriate size as in Fig. 1, and 13mm edge and center crack was also cut by water jet. The sharp crack was made by fatigue loading by Instron machine. For composite patch, four plies of unidirectional AS4/3501-6 was cured by autoclave and cut accordingly. The cracked aluminum plate and composite patch was bonded and cured using FM73 adhesive. The performance of patch strongly depends on the condition of surface treatment and caution should be made on this point[3]. To investigate the effects of curing cycles on the fatigue life, three different curing conditions, case A: 121°C(250 °F)/1 hour, case B: 104 °C(220 °F)/0.5 hour and 82 °C(180 °F)/4 hours, case C: 82 °C(180 °F)/8 hours, were selected. Fatigue test are performed under 6Hz and zero stress ratio condition. The applied load is 25KN for edge crack case and 34KN for center crack case.

Experimental Results

To measure the crack length, optical microscope is used. The static strength of patch specimen was increased about thirty percents compared with non-patch specimen, and the fatigue life of patch specimen was also increased four or five times compared with non-patch case as shown in Fig. 2. These show the effectiveness and possibility of composite patching technique in cracked pannel. Among three different curing cycles, the case C, which has the lowest curing temperature, shows the longest fatigue life. This implies that the curing cycle, which can minimize the thermal residual stress, is best for the extension of fatigue life of patching structure. The lower the curing temperature, the longer the fatigue life is. The ultrasonic C-scan method is used to investigate the crack propagation and debonding area. If the bonding surface is not properly cleaned, the debonding area is increased and the fatigue life is also dramatically decreased.

FINITE ELEMENT ANALYSIS

For the prediction of fatigue life by finite element method, the Mindlin plate elements in ABAQUS are used in composite, adhesive, and aluminum layer, respectively. The half model and three layer model are shown in Fig. 3 and Fig. 4, respectively. The used material property data is represented in Table 1. To combine these three layers, appropriate constraint equations are used between mid-surfaces and bonded-surface nodes. The effective temperature concept is used to apply the temperature loading conditions. To calculate the stress intensity factor, the modified crack closure method is adopted combining the strain energy release rate concept. As is well known, the single side patching produces out-of-plane bending effects, and the stress intensity factor should be modified to include the translation and rotation effects, which was

used in Ref.[4,5]. When the patch is bonded on aluminum surface, the neutral plane of patch specimen no longer exists on the neutral plane of aluminum. And, therefore, the value of the stress intensity factor can be affected whether the stress is selected at mid surface or free surface of aluminum. To account for this effect, the root mean square value of stress intensity factor is also considered. For the prediction of fatigue life, Paris' law is adopted and the three different stress intensity factors are used in this calculation. These results are compared with experimental result.

The analysis results for edge crack are compared in Fig. 5, and the solid square(Nexp2) and the blank square(Nexp1) are experimental results of fatigue life for case B(higher temperature curing) and the case C(lower temperature curing), respectively. When the free surface stress is used in the calculation of stress intensity factor, the fatigue life is over-predicted(circles). If the mid-surface stress is used, the fatigue life is too much under-estimated(stars). The root mean square concept(triangles) is best compared with experimental results. For center crack case, the analysis procedure is the same as in edge crack case, and the results in Fig. 6 shows similar pattern as in edge crack case.

CONCLUSIONS

In this paper, the effect of thermal residual stress on fatigue life in composite patch specimen was studied for different curing cycles experimentally, and those results were compared with analysis results. Three different concepts in the calculation of stress intensity factors were also compared to show the effective way in the calculation of fatigue life. The key factor determining the performance of patch structure is the appropriate surface treatment. Emphasis should be made in this procedure. The composite patch repair can effectively extend the fatigue life of cracked panel and can be widely used in aging aircraft. The low temperature curing cycle which can minimize the thermal residual stress is much better than high temperature curing cycle. In finite element analysis, the effective temperature concept is useful to have a reasonable result. The root mean square concept in the calculation of stress intensity factor shows better agreement with experimental result.

REFERENCES

1. A.A. Baker and R. Jones, "*Bonded Repair of Aircraft Structure*", Martinus Nijhoff Publishers, Dordrecht, The Netherlands, 1988
2. E. Belason, "Fatigue and Static Ultimate Tests of Boron/Epoxy Doublers Bonded to 7075-6 Aluminum with Simulated Crack", *18th Symposium of the International Conference on Aeronautical Fatigue*, Melbourne, Australia, 1995
3. M. R. Lena, "Repair and Reinforcement of Cracked Aluminum Plates with Adhesively Bonded Composite Patches", M.S. Thesis, Purdue University, 1995
4. J.Klug, X.X.Wu, and C.T.Sun, "Efficient Modeling of Delamination Growth in Composite Laminates Using Plate Elements", *Symposium on the Durability of Composite Materials*, 1994, pp.177-189
5. J.Klug, S.Maley, and C.T.Sun, "Characterization of Fracture and Fatigue of Bonded Composite Repairs", *Proceedings of the First joint DOD/FAA/NASA Conference on Aging Aircraft*, 1997

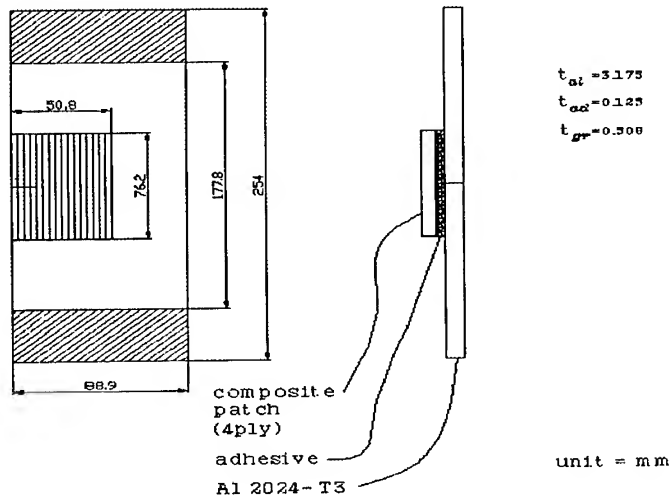


Fig. 1 Dimension of composite patch specimen with edge crack

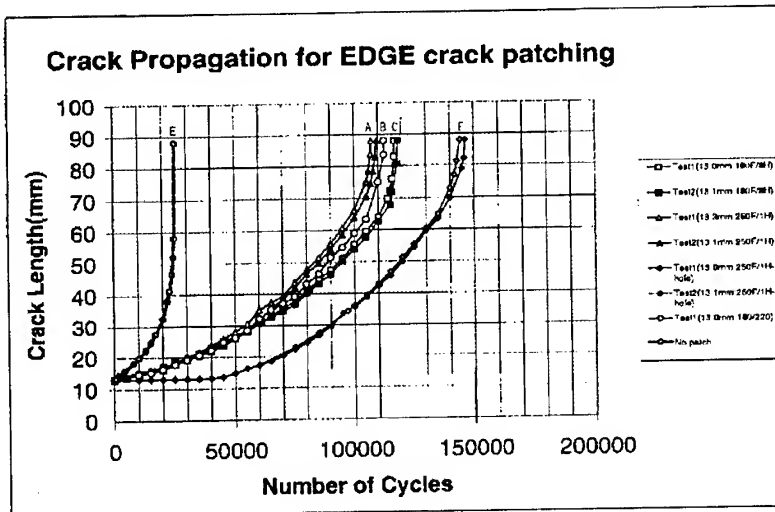


Fig. 2 Comparison of fatigue life and crack growth of edge crack patching for different curing cycles(6Hz, R=0, 24KN)

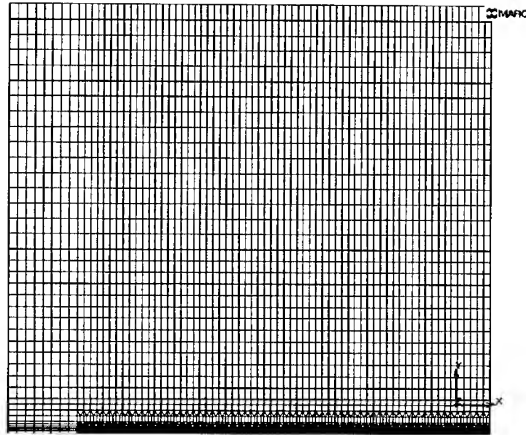


Fig. 3 Finite element modeling by Mentat

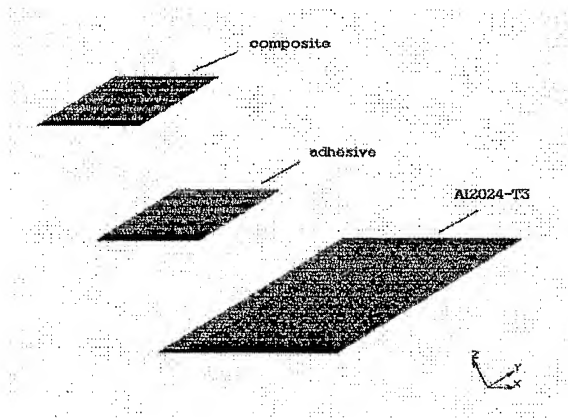


Fig. 4 Finite element model of three layers(patch, adhesive, aluminum)

Table 1 Mechanical properties of materials used in the analysis

	Gr/Ep (unidirection)	Al	FM73
E_1 (Gpa)	10.3	72	1.9
E_2 (Gpa)	142		
G_{12} (Gpa)	7.2		
G_{13} (Gpa)	3.2		
G_{23} (Gpa)	7.2		
ν_{12}	0.27	0.3	0.27
$\alpha_{11}((^{\circ}\text{C})^{-1} \times 10^{-6})$	1.5×10^{-6}	12.8×10^{-6}	
$\alpha_{22}((^{\circ}\text{C})^{-1} \times 10^{-6})$	-0.4×10^{-6}		
$\alpha_{33}((^{\circ}\text{C})^{-1} \times 10^{-6})$	1.5×10^{-6}		

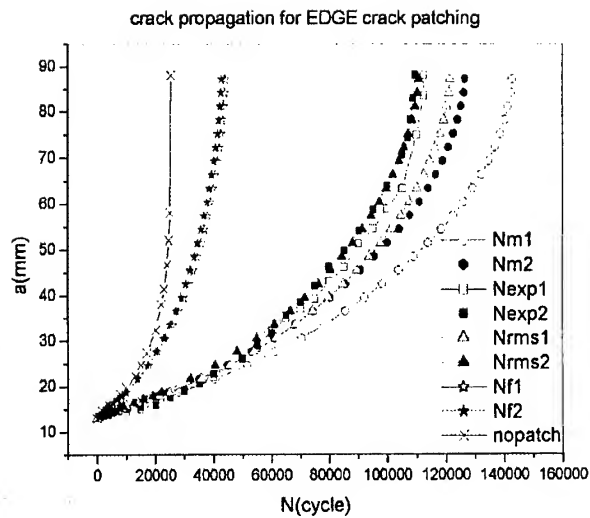


Fig. 5 Comparison of fatigue life between test and analysis results for edge crack (exp:experiment, rms:root mean square, m:mid-surface, f:free surface)

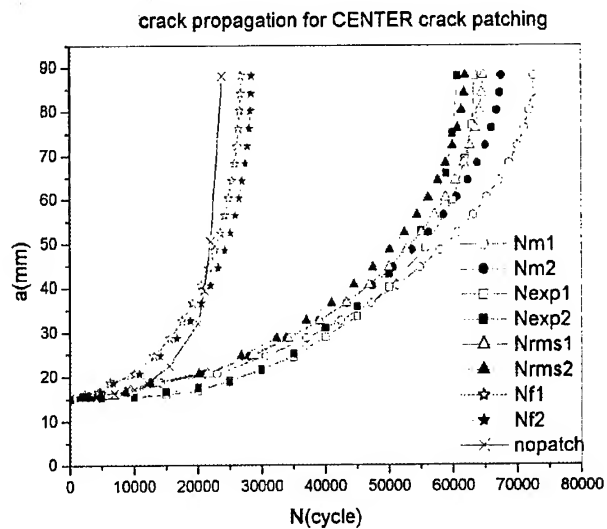


Fig. 6 Comparison of fatigue life between test and analysis results for center crack (exp:experiment, rms:root mean square, m:mid-surface, f:free surface)

MORPHOLOGICAL ASPECTS OF CRACKING UNDER CYCLIC LOADING

Refat a. I. El-Sheikhy

*Department of Concrete Research, Housing & Building Research Center
87 Tahrir street, Dokki, Giza, P.O. Box 1770, Egypt :hbrc@idscl.gov.eg*

SUMMARY: This paper discusses the directional assessment of crack growth rate under fatigue loading. Crack growth rate for mode I, mode II, and mixed modes under both tension and compression are studied using the application of the directional volumetric-distortional strain energy density theory, \bar{S}_{vd} . In case of mode I the applied fracture factor is the maximum volumetric strain energy density factor $\bar{S}_{v \max}$. The minimum distortional strain energy density factor, $\bar{S}_{d \min}$ is applied for mode II cracks. In the cases of mixed modes, directional combination of both maximum volumetric and minimum distortional strain energy density factors is applied in the form of $\bar{S}_{v \max-d \min}$. The crack propagation direction is predicted for all modes. The final fracture path during fracture process is predicted using the technique of directional crack path. In the case of mixed mode cracks under shear and compression stresses, the effect of friction between the surfaces of cracks is taken into consideration. Comparison between the current study and available data of previous studies is carried out, recording the best results. An experimental study is made using steel samples of SS400 JIS code Japanese specifications.

KEYWORDS: Fatigue, directional volumetric-distortional fracture theory, , mixed mode cracks, crack growth path.

INTRODUCTION

The aim of this work is to introduce a new application of the directional fracture approach, to predict the fracture direction, effective stress intensity factors, crack growth rate and the final fracture path during fracture initiation and propagation processes for cracks under mixed-mode conditions of fatigue loading. The new application is a new version of the directional volumetric-distortional strain energy density criterion S_{vd} which was proposed previously by El-Sheikhy [1]. Some researches studied the problem of mixed mode cracks according to the minimum total strain energy density criterion S_{\min} proposed by Sih [4] and the maximum dilatational strain energy density criterion T_{\max} -criterion proposed by Theocaris [7]. These criteria were presented according to the so-called vector-like quantity approach proposed by Sih which considered that cracks may behave like vectors, but in the calculations this approach considered only the scalar quantities of these vectors. The current approach

considers that the cracks behave as full vectors, considering the directions and quantities of the fracture factors used to determine the fracture aspects of the cracks. In addition, the S_{\min} theory considered the total strain energy density in studying of cracks under mode I, mode II, and mixed modes. The T -criterion used only the dilatational component of the strain energy density. Other criteria used only the distortional component of strain energy density as in the case of the $S_{d\min}$ -criterion. These criteria can be successfully used to study one mode and be a failure to study the other modes. For example, if we checked the validity of the T_{\max} criterion for a mode I crack only, we will achieve a good success, but in the case of mode II it fails completely according to the influence of the T_v factor at the crack tip. So, it cannot determine the mixed mode successfully. For the $S_{d\min}$ -criterion, we will find the opposite case, where it can determine the aspects of mode II and fail in the case of mode I. So in the case of mixed mode we cannot depend on just one component of strain energy density. In addition, these theories depend on the vector-like quantity approach [1], [4].

In the current criterion we studied a mode I crack under fatigue loading using the dilatational component ($\bar{S}_{v\max}$). Also, the study include mode II fatigue crack using distortional component ($\bar{S}_{d\min}$) and mixed mode cracks using (\bar{S}_{vd}) which represents the directional summation of the vectors of both (\bar{S}_{vi}) and (\bar{S}_{din}) at their directions, considering the fracture direction of each mode as an intrinsic material parameter. At any crack inclination angle to the applied load β , this criterion is used to determine the effective stress intensity factors and the final trajectory of the crack growth using the automatic directional crack-trajectory technique presented by the first author with a newly developed computer model [3]. The criterion is studied for both the cases of plane strain and plane stress conditions. Some examples are introduced using a constant-amplitude cyclic loads with different values of both mean stress and the ratio of minimum to maximum stress levels, $R = \sigma_{\min}/\sigma_{\max}$. An experimental investigation was carried out to verify the criterion [1], recording a good agreement. The comparisons with other theories [4], [7] conclude that the new version of the \bar{S}_{vd} -criterion gives the best results.

APPLICATION OF DIRECTIONAL VOLUMETRIC-DISTORTIONAL STRAIN ENERGY DENSITY THEORY

Mode I

(1) A crack under mode I will extend in the direction of the maximum volumetric strain energy density, $S_{v\max}$, when:

$$\frac{\partial \bar{S}_{vi}}{\partial \theta} = 0 \quad \& \quad \frac{\partial^2 \bar{S}_{vi}}{\partial \theta^2} \leq 0 \quad (1)$$

(2) Crack propagation will initiate when the fracture factor of $S_{v\max}$ reaches a critical quantity.

Mode II

(1) A crack under either clockwise and counter clockwise shear stresses will extend in the direction of the minimum distortional strain energy density $S_{d\min}$ under the conditions,

$$\frac{\partial \bar{S}_{din}}{\partial \theta} = 0 \quad \& \quad \frac{\partial^2 \bar{S}_{din}}{\partial \theta^2} \geq 0 \quad (2)$$

(2) It will initiate the propagation when $S_{d\min}$ reaches the critical value.

Mixed Mode

(1) A crack under mixed-mode tension or compression will extend in the direction of:

$$(\bar{S}_{vd}) = (\bar{S}_{vi}) + (\bar{S}_{dn}) \quad (3)$$

(2) It will start the extension when (\bar{S}_{vd}) reaches the critical value.

Where : (\bar{S}_{vd}) = directional volumetric-distortional strain energy density factor for mixed modes.

$K_I = \sigma (\pi a)^{0.5} \sin^2 \beta$ stress intensity factor for mode I.

(\bar{S}_{vi}) = directional volumetric strain energy density factor for mode I.

$(\bar{S}_{vi}) = [K_I^2 \cos^2 \theta / 2] / (9\psi \pi r)$ (plane stress)

$(\bar{S}_{vi}) = [K_I^2 (1 + \nu) \cos^2 \theta / 2] / (9\psi \pi r)$ (plane strain.)

$\psi = E / [3(1 - 2\nu)]$

K_{II} = stress intensity factor for mode II = $\sigma (\pi a)^{0.5} \sin \beta \cos \beta$.

(\bar{S}_{dn}) = directional distortional strain energy density factor for mode II.

$(\bar{S}_{dn}) = [K_{II}^2 / 12G\pi r] [4(\nu^2 - \nu + 1) \sin^2 \theta / 2 + 3 \sin \theta / 2 \sin \theta \cos 3\theta / 2 + 0.75 \sin^2 \theta + 3 \cos^2 \theta / 2 - 3 \cos \theta / 2 \sin \theta \sin 3\theta / 2]$ (plane strain.)

G = shear modulus = $E / [2(1 + \nu)]$

FATIGUE PHILOSOPHY IN THE DIRECTIONAL FORM

The commonly used fatigue crack growth equation is

$$(\Delta a / \Delta N) = C (\Delta K_I)^m \quad (4)$$

where a is half crack length, N is number of cycles, C and m are constants.

which includes the stress amplitude only. Sih [4], Badaliance [6], and Lam [7] used the strain energy density factor which includes both the stress amplitude and mean stress value. They used the scalar form of strain energy density in their quantitative assessment.

$$(\Delta a / \Delta N) = C (\Delta S_{min}) \quad (5)$$

The current study includes a directional and qualitative assessment using the directional fracture approach. This approach can predict the fracture direction under fatigue loading for uniaxial and multiaxial cases with great success. Mixed mode fatigue cracking cannot be studied under either compression-compression or compression-tension. This because of the difficulties faced in these cases using the scalar form of the strain energy density. On the other hand, total strain energy density factor does not have enough sensitivity to predict the fracture direction. Other researchers [4] tried to use the T-criterion which used the dilatational strain energy factor. From [1-3], it is clear that this factor fails completely to predict the fracture direction of mode II. Then it fails to predict any of mixed modes. In addition, the friction effect between crack surfaces in the case of mixed mode under compression cannot be considered. For mode I the dilatational factor can easily predict the fracture direction of mode I while the distortional factor cannot predict it. In the case of mode II distortional factor succeeds in prediction of the fracture direction while the dilatational factor fails to predict it.

PREDICTION OF CRACK GROWTH RATE

Using the directional volumetric-distortional strain energy density theory, the following relations are developed to predict crack growth rate:

Mode I crack

The dilatational strain energy density factor is developed to be

$$(\Delta \bar{a} / \Delta N) = C (\Delta \bar{S}_{vi \max}) \quad (6)$$

$$\Delta \bar{S}_{vi \max} = \bar{S}_{vi \max}^{\max} - \bar{S}_{vi \max}^{\min} \quad (7)$$

where: $(\bar{S}_{v1})_{\max} = [(K_I^2)_{\max} \cos^2 \theta_{1cr} / 2] / (9\psi \pi r)$ (plane stress) (8)

$(\bar{S}_{v1})_{\max} = [(K_I^2)_{\max} (1 + \nu) \cos^2 \theta_{1cr} / 2] / (9\psi \pi r)$ (plane strain). (9)

$(\bar{S}_{v1})_{\min} = [(K_I^2)_{\min} \cos^2 \theta_{1cr} / 2] / (9\psi \pi r)$ (plane stress) (10)

$(\bar{S}_{v1})_{\min} = [(K_I^2)_{\min} (1 + \nu) \cos^2 \theta_{1cr} / 2] / (9\psi \pi r)$ (plane strain). (11)

for: $\theta_{1cr} = 0.0^\circ$, $\beta = 90^\circ$ for infinite plate with central crack subjected to tensile normal stress, crack length (2a)

$$K_{I\max} = \sigma_{\max} \sqrt{\pi a} \quad (12)$$

$$K_{I\min} = \sigma_{\min} \sqrt{\pi a} \quad (13)$$

Mode II crack

The distortional strain energy density factor is applied for fatigue as

$$(\Delta \bar{a} / \Delta N)_{II} = C (\Delta \bar{S}_{dII\min}) \quad (14)$$

$$\Delta \bar{S}_{dII\min} = \bar{S}_{dII\min}^{\max} - \bar{S}_{dII\min}^{\min} \quad (15)$$

where for the plane strain case,

$$(\bar{S}_{dII\min}^{\max}) = \frac{[(K_{II}^2)_{\max} / 12G\pi r]}{0.75 \sin^2 \theta_{IIcr} + 3 \cos^2 \theta_{IIcr} / 2 - 3 \cos \theta_{IIcr} / 2 \sin \theta_{IIcr} \cos 3\theta_{IIcr} / 2 +} \quad (16)$$

$$(\bar{S}_{dII\min}^{\min}) = \frac{[(K_{II}^2)_{\min} / 12G\pi r]}{0.75 \sin^2 \theta_{IIcr} + 3 \cos^2 \theta_{IIcr} / 2 - 3 \cos \theta_{IIcr} / 2 \sin \theta_{IIcr} \cos 3\theta_{IIcr} / 2 +} \quad (17)$$

for $\beta = 0$, pure shear acting on infinite plate with central crack (crack length = 2a).

$$(K_{II})_{\max} = \tau_{\max} (\pi a)^{0.5}, \quad \beta = 0.0^\circ \quad (18)$$

$$(K_{II})_{\min} = \tau_{\min} (\pi a)^{0.5}, \quad \beta = 0.0^\circ \quad (19)$$

Mixed mode cracks

In the case of mixed mode which is a combination of mode I and mode II, the fracture factor used is (\bar{S}_{vd}) ,

where $(\bar{S}_{vd}) = (\bar{S}_{v1}) + (\bar{S}_{dII})$ (20)

For mixed mode tension-shear

$$(\bar{S}_{vd}) = \{[(S_{v1}) + (S_{dII}) \cos \theta_{IIcr}]^2 + [S_{dII} \sin \theta_{IIcr}]^2\}^{1/2} \quad (21)$$

For mixed mode compression-shear

$$(\bar{S}_{vd}) = \{[-(S_{v1}) + (S_{dII}) \cos \theta_{IIcr}]^2 + [S_{dII} \sin \theta_{IIcr}]^2\}^{1/2} \quad (22)$$

Then the relation developed for crack growth rate for mixed mode is,

$$(\Delta \bar{a} / \Delta N) = C (\Delta \bar{S}_{vd}) \quad (23)$$

$$\Delta \bar{S}_{vd} = \bar{S}_{vd}^{\max} - \bar{S}_{vd}^{\min} \quad (24)$$

where for mixed mode under tension,

$$(\bar{S}_{vd})^{\max} = \{[(S_{v1})_{\max} + (S_{dII})_{\min} \cos \theta_{IIcr}]^2 + [S_{dII\min}^{\max} \sin \theta_{IIcr}]^2\}^{1/2} \quad (25)$$

$$(\bar{S}_{vd})^{\min} = \{[(S_{v1})_{\min} + (S_{dII})_{\min} \cos \theta_{IIcr}]^2 + [S_{dII\min}^{\min} \sin \theta_{IIcr}]^2\}^{1/2} \quad (26)$$

$$K_{I\max} = \sigma_{\max} \sqrt{\pi a} \sin^2 \beta, \quad \beta \neq 90^\circ \quad (27)$$

$$K_{I\min} = \sigma_{\min} \sqrt{\pi a} \sin^2 \beta, \quad \beta \neq 90^\circ \quad (28)$$

$$(K_{II})_{\max} = \sigma_{\max} (\pi a)^{0.5} \sin \beta \cos \beta, \quad \beta \neq 0.0 \quad (29)$$

$$(K_{II})_{\min} = \sigma_{\min} (\pi a)^{0.5} \sin \beta \cos \beta, \quad \beta \neq 0.0 \quad (30)$$

while for mixed mode under compression,

$$(\bar{S}_{vd})^{\max} = \{[-(S_{v1})_{\max} + (S_{dII})_{\min} \cos \theta_{IIcr}]^2 + [S_{dII\min}^{\max} \sin \theta_{IIcr}]^2\}^{1/2} \quad (31)$$

$$(\bar{S}_{vd})^{\min} = \{[-(S_{v1})_{\min} + (S_{dII})_{\min} \cos \theta_{IIcr}]^2 + [S_{dII\min}^{\min} \sin \theta_{IIcr}]^2\}^{1/2} \quad (32)$$

$$K_{I \max} = -\sigma_{\max} \sqrt{\pi a \sin^2 \beta}, \beta \neq 90^\circ \quad (33)$$

$$K_{I \min} = -\sigma_{\min} \sqrt{\pi a \sin^2 \beta}, \beta \neq 90^\circ \quad (34)$$

$$(K_{II})_{\max} = \sigma_{\max} (\pi a)^{0.5} \sin \beta (\cos \beta - \mu \sin \beta), \quad \beta \neq 0.0 \quad (35)$$

$$(K_{II})_{\min} = \sigma_{\min} (\pi a)^{0.5} \sin \beta (\cos \beta - \mu \sin \beta), \quad \beta \neq 0.0 \quad (36)$$

The crack growth equation for mixed mode under tension is

$$[\Delta a / \Delta N] = \left\{ \left[[\Delta a / \Delta N]_I + [\Delta a / \Delta N]_{II} \cos \theta_{nc} \right]^2 + [\Delta a / \Delta N]_{II}^2 \sin^2 \theta_{nc} \right\}^{1/2} \quad (37)$$

while the relation for mixed mode under compression

$$[\Delta a / \Delta N] = \left\{ \left[-[\Delta a / \Delta N]_I + [\Delta a / \Delta N]_{II} \cos \theta_{nc} \right]^2 + [\Delta a / \Delta N]_{II}^2 \sin^2 \theta_{nc} \right\}^{1/2} \quad (38)$$

It is essential to remember that the stress intensity factor range includes both mean stress, $\bar{\sigma}$, and stress amplitude $\Delta \sigma$ whether the above equations include both $(K_{I \max}^2 - K_{I \min}^2)$ and $(K_{II \max}^2 - K_{II \min}^2)$, which can be represented in the following forms:

$$(K_{I \max}^2 - K_{I \min}^2) = 2(K_{I \max} - K_{I \min})(K_{I \max} + K_{I \min})/2 \quad (39)$$

$$(K_{II \max}^2 - K_{II \min}^2) = 2(\Delta K_{II})(\bar{K}_{II}) \quad (40)$$

where $(\Delta K_I) = \Delta \sigma \sqrt{\pi a}$ and $(\bar{K}_I) = \bar{\sigma} \sqrt{\pi a}$.

FRACTURE DIRECTION

By direct application of the hypotheses of the current theory, the direction of crack propagation can be predicted for all modes [1]. The fracture angle for mode I always equals zero, while the fracture direction of mode II is not equal to zero and it depends on material properties. The fracture directions of mixed modes can be predicted from the equations (41), (42) or Figs. (1,2) respectively.

$$\theta_c = -\tan^{-1} \left[(S_{dn}^I \sin \theta_{nc}) / (S_{v1}^I + S_{dn}^I \cos \theta_{nc}) \right] \quad (41)$$

$$\theta_c = \tan^{-1} \left[(S_{v1}^I - S_{dn}^I \cos \theta_{nc}) / (S_{dn}^I \sin \theta_{nc}) \right] + 90 \quad (42)$$

CRACK PATH TECHNIQUE

During the crack extension process, the geometry of the material will be changed due to the change in crack length (2a) and crack angle (β). The actual new crack length will be equal to the original crack length plus the crack extension increment which will be $[2(a + r)]$. However, the two active points of the crack are now moved to the new crack tips at which stress concentration zones and plastic core regions exist. The effective crack length is therefore assumed to be the line between these two new tips. Hence, the effective crack length becomes equal to a_1 and its inclination to external applied stress β_1 equals to $\beta_0 + \Delta \beta$. Then, calculations can now be made considering the new effective crack length and its new crack angle. Figures (3 - 6) and the following equations represent this problem [1]:

Cracks Under Tension

The fracture increment length will be:

$$r_I + r_{II} \cos \theta_{nc} = r \cos \theta_i \quad (43)$$

$$r_{II} \sin \theta_{nc} = r \sin \theta_i \quad (44)$$

Hence, the crack length (Fig. 13) will be

$$a_i = \left[(a_{i-1} + r_I + r_{II} \cos \theta_{nc})^2 + (r_{II} \sin \theta_{nc})^2 \right]^{1/2} \quad (45)$$

$$a_i = \left[(a_{i-1} + r \cos \theta)^2 + (r \sin \theta)^2 \right]^{1/2} \quad (46)$$

and the angle of the effective crack with respect to the loading axis will be

$$\beta_i = \beta_{i-1} + \Delta \beta \quad (47)$$

$$\Delta \beta = \tan^{-1} \left[(r \sin \theta) / (a_{i-1} + r \cos \theta) \right] \quad (48)$$

$$\Delta \beta \equiv \left[(r \sin \theta) / (a_{i-1} + r \cos \theta) \right] \quad (49)$$

Cracks Under Compression

The effective crack length is

$$a_i = \left[(a_{i-1} - r \cos(180 - \theta_i))^2 + (r \sin(180 - \theta_i))^2 \right]^{1/2} \quad (50)$$

and the angle of the effective crack to the loading axis will be

$$\beta_i = \beta_{i-1} - \Delta \beta \quad (51)$$

$$\Delta \beta = \tan^{-1} \left[(r \sin(180 - \theta_i)) / (a_{i-1} - r \cos(180 - \theta_i)) \right] \quad (52)$$

According to this technique the fracture path can be predicted during the fracture process till the final failure.

COMPARISONS

Comparisons have been carried out between the results of the current theory and the results of Sih [4] and Lam [7]. Sih [4] and Lam [7] used a total strain energy density factor in scalar form. The comparison is carried out for crack path examples under uniaxial loading [2] as shown in Fig. 7 and under biaxial [4] as shown in Fig. 8. From the comparison, the differences between the current theory and previous studies are clear. The current results are the closest to the experimental.

EXPERIMENTAL STUDY

Experimental program has been carried out using samples of high tensile steel SS 400 manufactured by a Japanese company according to Japanese specifications. The steel samples used are of dimensions 500 mm length, 70 mm width, and 10 mm thickness, with central slit cracks of length 20 mm emanating different inclination angles ($\beta = 0$ to 90°) to the loading direction. Uniaxial tension stress of low-cycle fatigue loading is applied using different values of amplitude and mean stress level. Figures 9 and 10 show the results of some test samples giving a good agreement with theoretical analysis.

CONCLUSIONS

As a general statement, the analysis of fatigue cracks depending on the directional fracture theory S_{vd} has better results than the old theory [4]. It is based on the fundamental analysis of strain energy density components of mode I, mode II and mixed modes. It is the only theory now available which can deal with mixed-mode cracks under compression, including the effect of friction between crack surfaces. In addition, it is the only theory which considers the effect of shear stress direction.

REFERENCES

1. El-Sheikhy, R. A. (1995). Ph. D. Thesis, Cairo University, Egypt.
2. El-Sheikhy, R. A. (1997). Proceedings of 5th International Conference on Biaxial/Multiaxial Fatigue and Fracture, Vol. II pp. 657-666, European Structural Integrity Society (Eds.), Poland.
3. El-Sheikhy, R. A. (1997). Proceedings of Worldwide ECCE Symposium on Computers in Practice of Building and Civil Engineering, Association of Finnish Civil Engineers RIL (Eds.), Finland.
4. Sih, G. C., Barthelemy, B. M. (1980). Engng Fracture Mech **13**, 439.
5. Badaliane, R. (1980). Engng Fracture Mech **13**, 657.
6. Lam, Y. C. (1993). Engng Fracture Mech **16**, 429.
7. P. S. Theocaris and N. P. Anderianopoulos, (1988), Eng Frac. Mech **30**, 1.

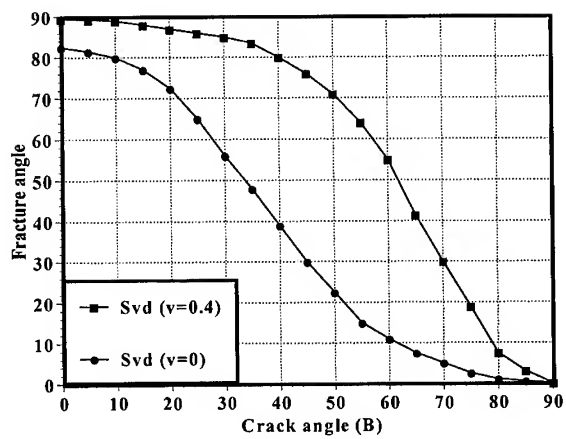


Fig. 1. Fracture direction for tension

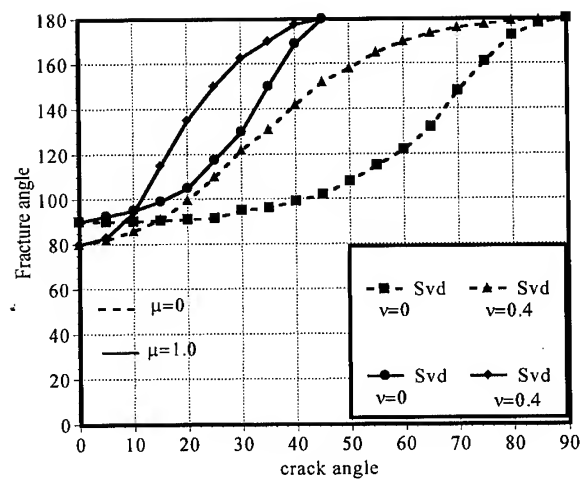


Fig. 2. Fracture direction for compression.

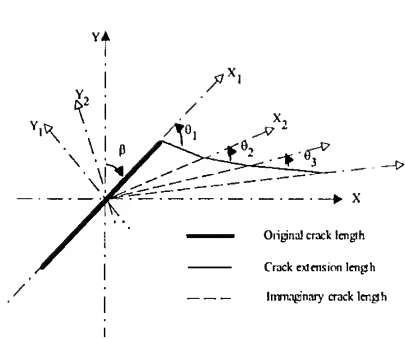


Fig. 3. . Crack propagation under tension .

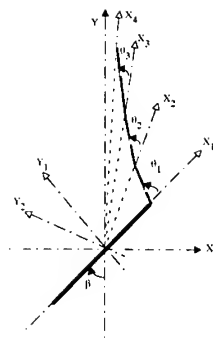


Fig. 4. Crack increments under comp

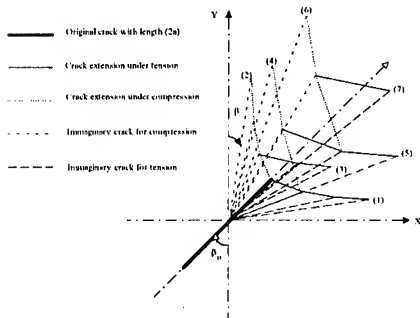


Fig. 5 Crack increments under tension-comp.

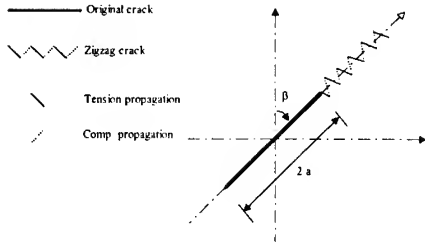


Fig. 6 Crack under low cycle fatigue extends as zigzag.

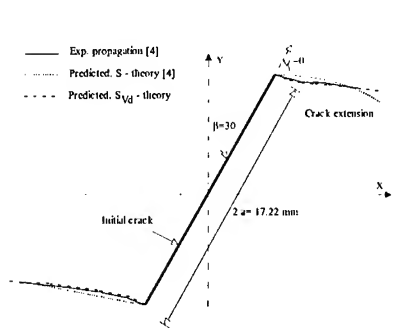


Fig. 7. Mixed mode crack path under tension.

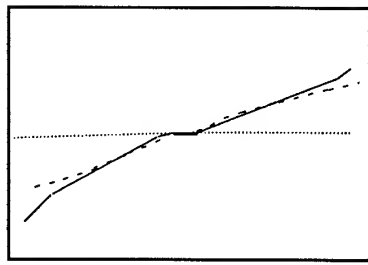


Fig. 8 Crack under biaxial fatigue (biaxial ratio $\lambda=1.0$)

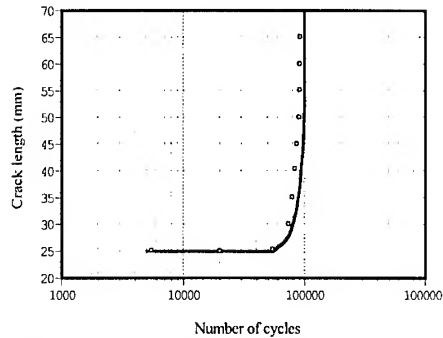


Fig. 9. Number of cycles for different crack length.

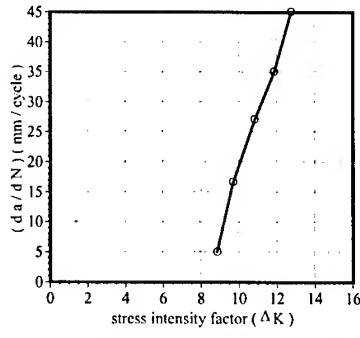


Fig. 10. Stress intensity factor at crack growth rate

Fatigue & Fracture (3)

FATIGUE STRENGTH OF FIBER-METAL LAMINATE: GLARE-3

M. Kawai¹, A. Hachinohe², H. Takakura², and K. Kato³

¹ *Institute of Engineering Mechanics and Systems, University of Tsukuba,
Tsukuba 305-8573, JAPAN: mkawai@kz.tsukuba.ac.jp*

² *Doctoral Program in Engineering, University of Tsukuba*

³ *Master's Program in Science and Engineering, University of Tsukuba*

SUMMARY: Anisotropic fatigue strength of the cross-ply fiber-metal laminate GLARE-3 under constant-amplitude loading conditions has been studied. Tension-tension fatigue tests were performed at room temperature on five kinds of plain coupon specimens $[0/90]_0$ with different off-axis angle θ . The off-axis fatigue strength became smaller as the off-axis angle became larger. The off-axis fatigue strength rapidly decreased for every off-axis angle in the intermediate range of the fatigue lifetime, and the S-N curve tended to approach a fatigue limit. A more excellent fatigue performance of GLARE-3 in comparison with the high strength aluminum alloy was observed only in the glass fiber directions (0° and 90°) and in the low fatigue lifetime range. The off-axis fatigue data plotted using the strength ratio were approximately represented by a single master S-N curve.

KEYWORDS: Fiber-Metal Laminate, GLARE, Cross-Ply Laminate, Off-Axis Fatigue Strength, S-N Relationships, GFRP, Aluminum-alloy

INTRODUCTION

GLARE is a fiber-metal laminate that consists of alternating layers of unidirectional glass fiber-reinforced composite (GFRP) prepregs and thin aluminum-alloy sheets [1, 2]. The GLARE laminate offers some superior mechanical properties, compared with either only GFRP laminates or monolithic aluminum-alloys. The aluminum-alloy skin sheets of the GLARE laminate protect the core GFRP; this surface protection compensates for the strength reduction of the inner GFRP layers against environmental attacks and impacts. A fiber-bridging mechanism impedes the growth and propagation of cracks in the aluminum-alloy layers under tensile fatigue loading conditions. In the GLARE laminate, little tensile residual stress remains in the aluminum-alloy layers after curing, since the glass-fiber has a positive thermal expansion coefficient in the fiber direction. This feature enables us to use the GLARE laminates in as-cured state and in practical stacking configurations.

The present study aims to examine the fatigue strength of the GLARE-3 laminate that includes cross-ply layers of GFRP, with a particular emphasis on the elucidation of the directional characteristics of the fatigue strength. For this purpose, tension-tension fatigue tests were

performed at room temperature using plain coupon specimens with different off-axis angles. To observe the effects of the different lay-up composition on the fatigue properties of GLARE laminates, the fatigue strength of the cross-ply GLARE-3 was compared with that of the unidirectional GLARE-2 [3].

EXPERIMENTAL

Material System and Specimens

The GLARE-3 laminate that consists of three layers of high-strength aluminum-alloy (2024-T3) sheets and two pairs of cross-ply layers of GFRP (Vetrotex R-glass/Fibredux 925). GLARE-3 was manufactured by Structural Laminates Company (SLC) using the autoclave method. The lay-up of the GLARE-3 laminate is schematically illustrated in Fig. 1.

The dimensions of the coupon specimens are as follows: the specimen length $L = 200$ mm; the gauge length $L_G = 100$ mm; the specimen width $W = 25$ mm; and the thickness $t = 1.45$ mm. The coupon specimens were cut from the cross-ply laminate $[0/90]_0$ in five different directions: the angles between the longitudinal and fiber directions are specified as $\theta = 0, 15, 30, 45$ and 90° . The type of the specimen is hereafter denoted as $[0/90]_0$.

Testing Procedure

To evaluate the tensile fracture strengths of the off-axis specimens $[0/90]_0$, the static tensile tests were first carried out at room temperature under a constant stroke rate of 1.0 mm/min. The longitudinal and lateral strains of the specimens were measured with two-element L-type rosette strain gages.

The tension-tension fatigue tests were then carried out under a load-control mode. The stress-ratio was kept at a constant value of 0.1. The tensile fatigue load was applied in a sinusoidal waveform with a frequency of 10 Hz. The fatigue lifetimes were measured in the cycle range up to 10^6 .

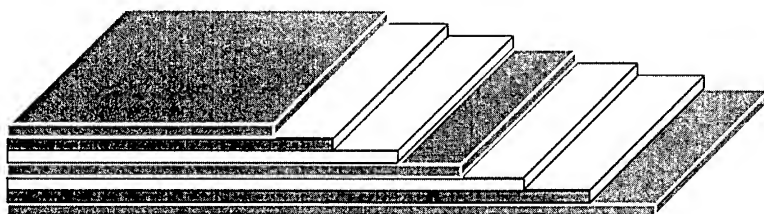


Fig. 1 Schematic illustration of the cross-ply GLARE-3 laminate

RESULTS AND DISCUSSION

Static Tensile Behavior

Fig. 2 shows the tensile stress-strain relationships for the off-axis specimens $[0/90]_0$ ($\theta = 0, 15,$

30, 45 and 90°) cut from the cross-ply laminate. The first quadrant of this figure exhibits the stress-strain responses in the loading direction ($\sigma_x - \epsilon_x$), and the second does the relationships between longitudinal stress and lateral strain ($\sigma_x - \epsilon_y$). The anisotropy of the stress-strain response of GLARE-3 is clearly observed from this figure. A significant non-linear response appears for every off-axis angle θ , which is due to the yielding of the aluminum-alloy layers. It is confirmed that the responses in the fiber directions $\theta = 0$ and 90° are in good agreement with each other. The Young's modulus E_x and Poisson's ratio ν_{xy} of the off-axis specimen $[0/90]_0$ are well described using the orthotropic elastic theory [4].

The off-axis tensile strengths of the specimens $[0/90]_0$ are shown in Fig. 3 as a function of the off-axis angle θ . It is obvious that the in-plane directional nature of the tensile strength of GLARE-3 is symmetrical with respect to the 45° -direction. The tensile strength of GLARE-3 is about 40% higher than that of the monolithic aluminum-alloy in the fiber directions, while it becomes smaller for the off-axis angle in the range $25^\circ \leq \theta \leq 45^\circ$. The anisotropy of the tensile strength of GLARE-3 can be described using the Tsai-Hill quadratic criterion [4].

Anisotropic Fatigue Behavior

The relationships between the maximum fatigue stress σ_{\max} and $\log N_f$ for all off-axis specimens $[0/90]_0$ of GLARE-3 are shown in Fig. 4. The tensile fatigue strength becomes smaller as the off-axis angle increases from 0° to 45° . The directional nature of the off-axis fatigue strength of GLARE-3 almost corresponds to that of the off-axis tensile strength.

In the cycle range $2 \times 10^3 < N_f < 10^5$, the fatigue strength rapidly decreases, regardless of the off-axis angle. The S-N relationships for all off-axis angles are almost horizontal in either shorter or longer fatigue lifetime ranges, i.e. $N_f < 2 \times 10^3$ or $N_f > 10^5$. The latter feature indicates the presence of the fatigue limits.

The fatigue strength of the off-axis specimen $[0/90]_0$ becomes higher than that of the monolithic aluminum-alloy (2024-T3) for the off-axis angles $\theta = 0^\circ, 15^\circ$ and 90° in the cycle range $N_f < 6 \times 10^3$. In the longer lifetime range $N_f > 6 \times 10^3$, however, the fatigue strength of GLARE-3 becomes lower than that of the aluminum-alloy for all off-axis angles.

In Fig. 4, the S-N relationships ($\sigma_{\max} - \log N_f$) for the cross-ply GLARE-3 are compared with those for the unidirectional GLARE-2 [3]. It is found that the S-N data for GLARE-3 are distributed in a relatively narrow band sited between the longitudinal and transverse S-N relationships for GLARE-2. This observation clearly indicates that the anisotropy of the fatigue strength of GLARE is significantly relaxed by the cross-ply lamination. The feature of the S-N relationship is common to these two types of GLARE laminates.

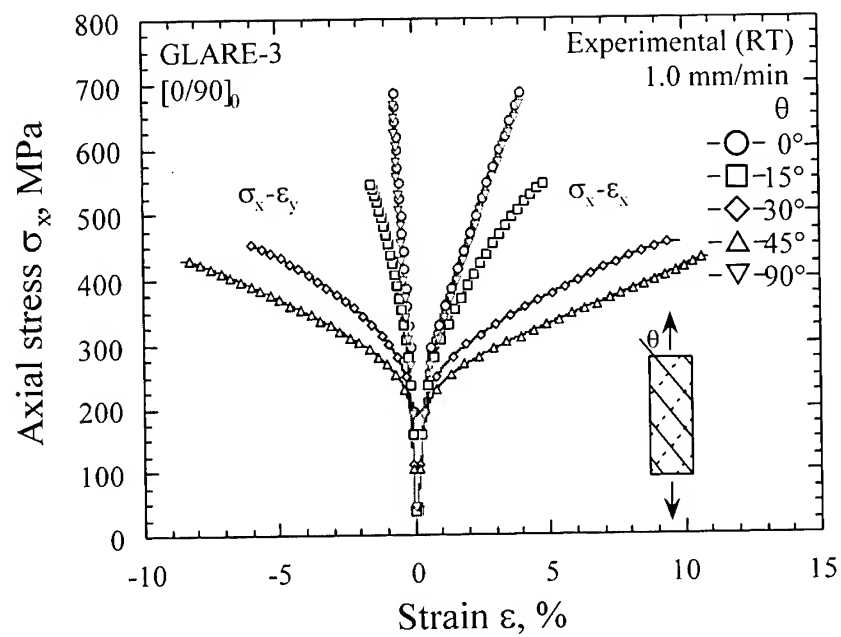


Fig. 2 Tensile stress-strain curves for various off-axis angles

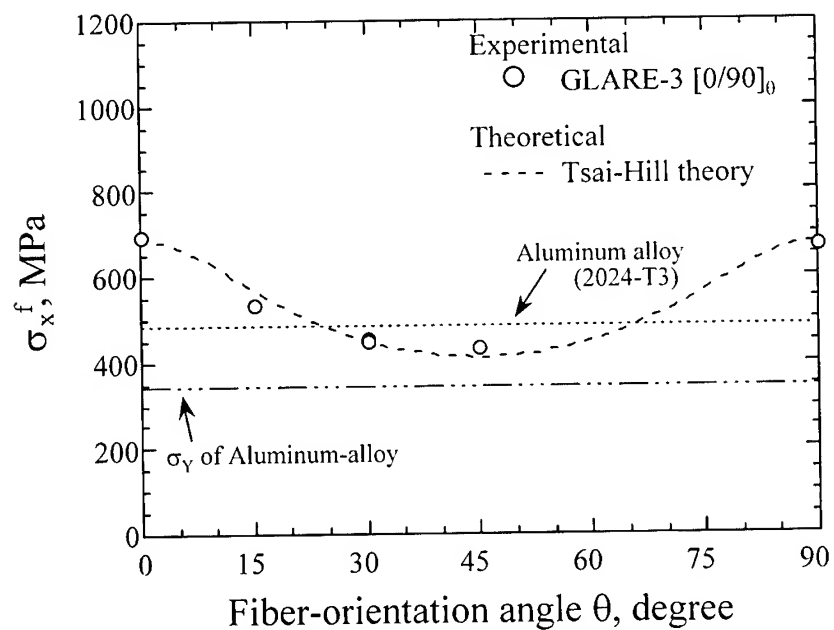


Fig. 3 Static tensile fracture stress as a function of the off-axis angle

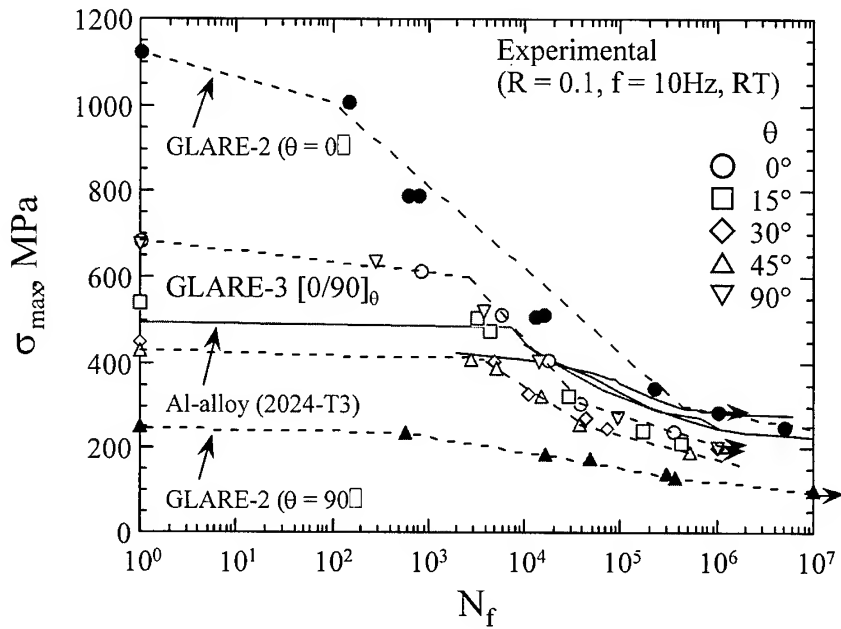


Fig. 4 Off-axis S-N relationships plotted using the maximum fatigue stress σ_{\max}

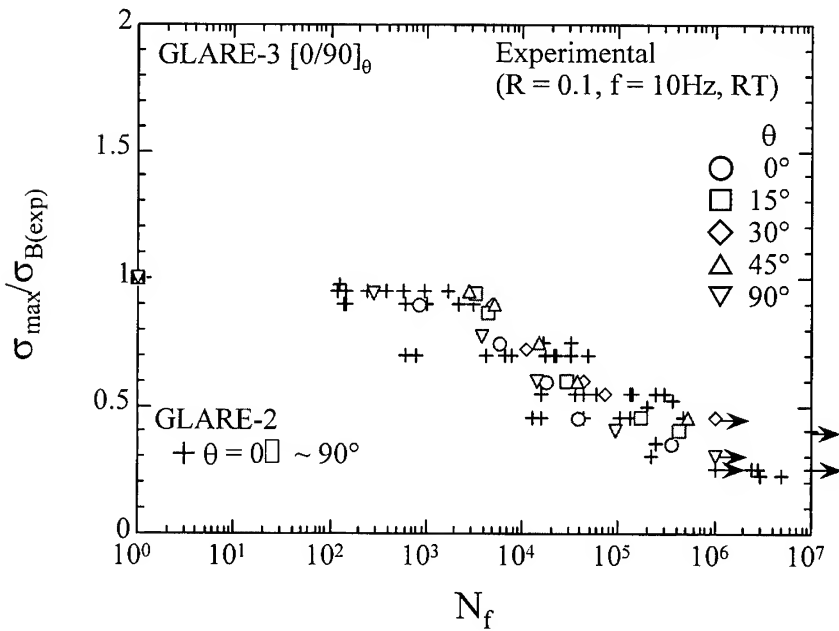


Fig. 5 Normalized off-axis S-N relationships plotted using the experimental strength ratio $\sigma_{\max} / \sigma_{B(\exp)}$

The S-N data for the cross-ply GLARE-3 are replotted in Fig. 5 using the experimental strength ratio $\sigma_{\max} / \sigma_{B(\text{exp})}$; $\sigma_{B(\text{exp})}$ denotes the experimental static tensile strength. This figure also includes the normalized S-N plots for the results on the unidirectional GLARE-2 using the symbol +. It appears in Fig. 5 that the normalized fatigue data points for GLARE-3 are randomly distributed in a relatively narrow band and no particular indication of the effect of off-axis angle can be read. This feature is found also in the plots for the unidirectional GLARE-2.

This result indicates that the experimental strength ratio $\sigma_{\max} / \sigma_{B(\text{exp})}$ is an effective parameter to cope with the directional nature of the fatigue strength of the cross-ply GLARE-3 and unidirectional GLARE-2. Also, the present study verifies that the non-dimensional effective stress defined in [3] is effective as a general measure for the anisotropic fatigue strength of the unidirectional and cross-ply GLARE laminates.

CONCLUSIONS

The characteristics of the anisotropic fatigue strength of the fiber-metal laminate GLARE-3 reinforced by the cross-ply GFRP layers were experimentally elucidated. The results obtained can be summarized as follows.

- (1) The tensile fatigue strength of the off-axis specimen $[0/90]_0$ becomes smaller as the off-axis angle θ increases from 0° to 45° .
- (2) The off-axis fatigue strength rapidly decreases in the cycle range $2 \times 10^3 < N_f < 10^5$, regardless of the off-axis angle.
- (3) The fatigue limit tends to appear in the S-N response for every off-axis angle.
- (4) The fatigue strength of GLARE-3 becomes higher than that of the monolithic high strength aluminum-alloy only for $\theta = 0^\circ$ and 90° in the low cycle fatigue range.
- (5) The experimental strength ratio is a useful parameter to handle the directional nature of the fatigue strength of GLARE-3.

REFERENCES

1. J.B. Young, J.G.N. Landry and V.N. Cavoulacos, *Composite Structures*, Vol. 27, 1994, pp. 457-469.
2. A. Asundi and A.Y.N. Choi, *J. Materials Processing Technology*, Vol. 63, 1997, pp. 384-394.
3. M. Kawai, K. Takumida, A. Hachinohe and Y. Kawase, *Transactions of JSME*, Vol. 64-627, 1998, pp.2847-2855.
4. D. Hull, *Introduction to Composite Materials*, Cambridge University Press, Cambridge, 1982.

Interactive Calculation of Stress Intensity Factors of Radial Cracks in Composite Plate by Mapping-Collocation Method

Seong-Kyun Cheong¹, Young-Bae Kim², Ho-Taek Yong³

¹ *Department of Mechanical Engineering, Seoul National University of Technology
172, Gongneung-dong, Nowon-gu, Seoul 139-743, Korea:skjung@duck.snut.ac.kr*

² *Department of Mechanical Engineering, Seoul National University of Technology
172, Gongneung-dong, Nowon-gu, Seoul 139-743, Korea:guzzi@bulam.snut.ac.kr*

³ *Department of Mechanical Engineering, Seoul National University of Technology
172, Gongneung-dong, Nowon-gu, Seoul 139-743, Korea:yonght@duck.snut.ac.kr*

SUMMARY: A computer code to interactively calculate the stress intensity factors for radial cracks in composite plate is developed in this paper. Complex function theory, mapping collocation method, and least square method are applied to formulate the problem. A computer code based on Lahey Fortran90 is developed and create 32-Bit Windows DLLs (Dynamic Link Library) in order to call the Fortran routines. Graphic User Interface (GUI) environments are constructed using Visual Basic. Entering the input data such as material properties, radius of a hole, crack length, and loading conditions, the stress intensity factors can be interactively obtained. Comparing the present results with those of the references, the present code and procedure seems to be guaranteed.

KEYWORDS: Stress Intensity Factors, Mapping-Collocation Method, Radial Crack, Composite Plate, Complex Function Theory, Interactive Calculation, Fortran90, Visual Basic

INTRODUCTION

Many researchers have numerically investigated the problems related to cracks [2~10]. To calculate the stress intensity factors, they use one of the various kinds of program languages, e.g., Fortran. However, the persons, who do not participate in research work, can neither understand the program nor use the results of papers. If the researchers develop the program which can interactively show the results of papers, it will be very useful to the persons.

The advantages of Windows-based Graphical User Interface are the quick interpretation of results and the interactive visual communication between users and computers. Although GUI program makes user use it more comfortably and easier, it requires much efforts to be developed.

In this study, a computer code based on Lahey Fortran90 and Visual Basic program is developed to calculate the stress intensity factors for radial cracks in isotropic or composite plate. Fortran is usually used to obtain the solution of scientific and technological problems. We also adopt it to analyze an infinite plate including cracks emanating from a hole. To

combine Fortran with Visual Basic, we use Dynamic Link Library (DLL) concept like Fig. 1. Fortran source code to be drawn up for solving a crack problem is complied to DLL file by Lahey Fortran90 compiler. Converting Fortran source code to DLL is supported by Lahey Fortran90 compiler and not Fortran77 compiler. We will utilize the modified mapping collocation algorithm [3, 4] and code it by Fortran language. Visual Basic program is used for user's convenience, that is, interactive environments and visualization of results.

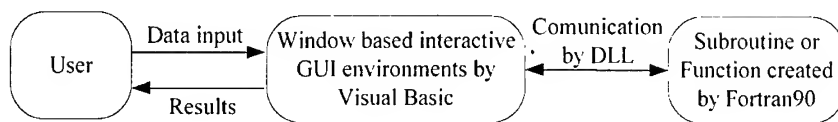


Fig. 1 Basic Concept

PROGRAM PROCEDURE

To construct interactive GUI program, we design interface part between user and computer such as Fig. 2. User can transmit information to program by only click and input number. For the purpose of helping user understand meaning of variable value, a picture frame is designed. Whenever events, for instance click or focus movement by pressing Tab-key, happen, the picture frame displays a different picture about such situations.

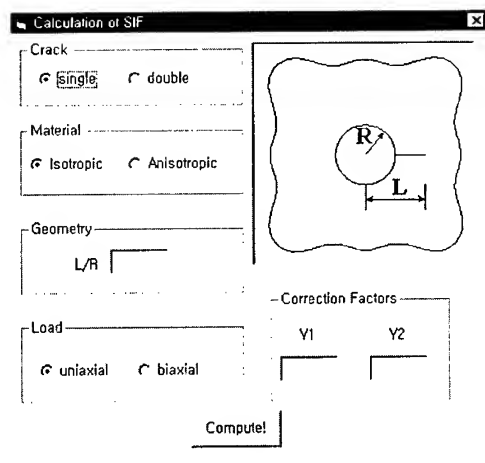


Fig. 2 Windows based GUI dialog box designed for interface between user and computer by the use of VB

All processes are expressed in Fig. 3 and important subroutines are summarized in Table 1. Program is limited to evaluate stress intensity factors of a single crack or double cracks emanating from a circular hole in infinite plate under biaxial loading. Users have to make a decision whether the problem is for a single crack or double cracks. Likewise, users have to decide whether the problem is for an isotropic or anisotropic material. If an isotropic material is chosen, the roots of characteristic [1] are set up for $s_1 = i$ and $s_2 = 0.99 i$ [3, 4]. If an anisotropic material is chosen, a dialog box requiring basic material properties, (E_1 , E_2 , ν_{12} , G_{12}) shows in a monitor. User determines whether laminate is symmetric or asymmetric and input the number of total layers (ELN), angle (ELA), and thickness (ELT) of each layer.

Program passes input variables into ABD_matrix subroutine to calculate effective modulus (E_x , E_y , ν_{xy} , G_{xy}) by using so called ABD-matrix algorithm in [12]. It returns results to Char_equation subroutine that computes the roots (s_1 , s_2) of characteristic equations. User inputs crack shape that is consisted of a single crack or double cracks, crack length from a center of a hole (L), the radius of a hole (R), and boundary conditions (uniaxial or biaxial loading) at infinity.

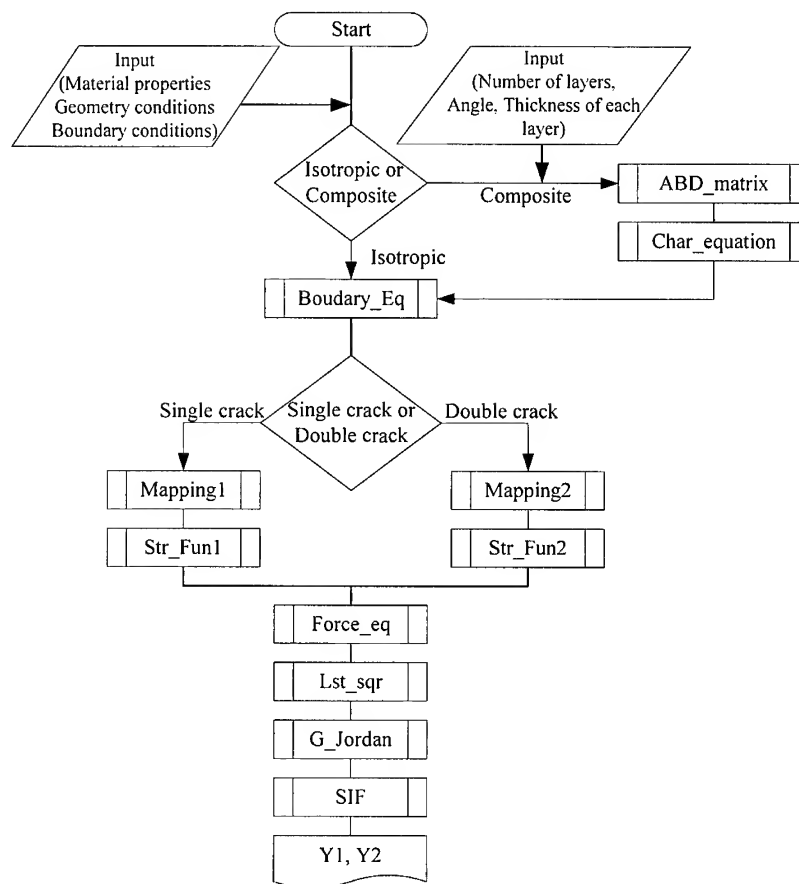


Fig. 3 Flow chart for calculating stress intensity factors for radial cracks emanating from a circular hole

We prepare Mapping1 subroutine and Mapping2 subroutine for considering a single crack and double cracks emanating from a hole. Input variables of mapping subroutine are the coordinate value (x , y) of collocation points in physical plane and outputs are the new coordinate values (ζ_1 , ζ_2) in ζ -plane. Mapping functions were proposed in [3~5] to describe a crack geometry. Mapping1 subroutine carries a single crack emanating from a hole and its exterior into the unit circle and its exterior in the ζ -plane. Mapping2 subroutine carries double cracks emanating from a hole and its exterior into the unit circle and its exterior in the ζ -plane. A stress function including unknown coefficients is set up by Str_fun1 or Str_fun2

subroutine. Employing stress function and resultant force boundary conditions, two matrices are constructed at Force_eq subroutine. Using least square method which was utilized by [8], unknown coefficients are determined at Lst_sqr and G_Jordan subroutine. SIF subroutine computes correction factors.

Table 1 Important subroutines in program

Main subroutine name	Description
ABD_matrix	Compute effective modulus
Char_equation	Calculate the roots of characteristic equation
Mapping_1	Define a mapping function for a single crack
Mapping_2	Define a mapping function for double cracks
Str_fun1	Define a stress function for a single crack
Str_fun2	Define a stress function for double cracks
For_Eq	Collocation of forces

THEORETICAL ALGORITHM

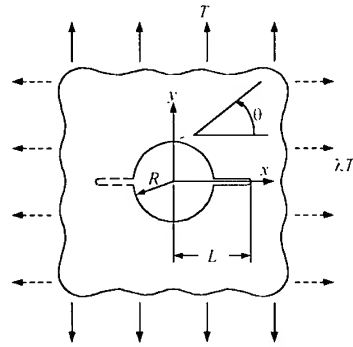


Fig. 4 Cracks emanating from a circular hole in an infinite plate under biaxial loading

We consider straight cracks or a crack emanating from a circular hole in an orthotropic infinite plate under uniaxial or biaxial loading as shown in Fig. 4. R is a radius of hole and L is a crack length emanating from a hole.

We utilize mapping functions which are used in [3], [4], and [5]. They carry the crack and its exterior into the unit circle and its exterior in the ζ -plane. Since $z = z_1 = z_2$ on the crack, the parameter planes ζ , ζ_1 and ζ_2 are coincided on the unit circle.

ζ_k for a single crack is as follows :

$$\zeta_k = \frac{2}{L} \left[\left(z_k - \frac{L}{2} \right) + \sqrt{z_k} \sqrt{z_k - L} \right] \quad (k = 1, 2) \quad (1)$$

ζ_k for double cracks is as follows :

$$\zeta_k = \frac{z_k}{L} \sqrt{\left(\frac{z_k y}{L} \right)^2 - 1} \quad (k = 1, 2) \quad (2)$$

The boundary conditions of the traction type may also be expressed as

$$f_1(s) + if_2(s) = i \int (X_n + iY_n) ds \quad (3)$$

$$= (1 + is_1)\phi_1(\zeta_1) + (1 + is_2)\phi_2(\zeta_2) + (1 + i\bar{s}_1)\overline{\phi_1(\zeta_1)} + (1 + i\bar{s}_2)\overline{\phi_2(\zeta_2)} + c$$

Where X_n and Y_n are the x and y components of forces exerted upon the edge per unit area. The bar notation is a conjugate symbol. $\phi_1(\zeta_1)$ and $\phi_2(\zeta_2)$ is unknown functions. From [2] we can define the relationship between $\phi_1(\zeta_1)$ and $\phi_2(\zeta_2)$

$$\phi_2(\zeta_2) = B\overline{\phi_1\left(\frac{1}{\zeta_2}\right)} + C\phi_1(\zeta_2) \quad (4)$$

Where

$$\overline{\phi_1\left(\frac{1}{\zeta}\right)} = \overline{\phi_1\left(\frac{1}{\bar{\zeta}}\right)}, \quad B = \frac{\bar{s}_2 - \bar{s}_1}{s_2 - \bar{s}_2}, \quad C = \frac{\bar{s}_2 - s_1}{s_2 - \bar{s}_2} \quad (5)$$

By considering boundary conditions at infinity, a stress function may be assumed for cracks emanating from a circular hole in an orthotropic infinite plate [3], [4], [6].

$$\phi_1(\zeta) = OD\zeta + OB(E - iF - DC)\frac{1}{\zeta} + \sum_{n=1}^{\infty} (a_n + ib_n)R \quad (6)$$

Where

$$R = (\zeta + 1)^{-n}, \quad O = L/4 \quad (\text{for a single crack})$$

$$R = \zeta(\zeta^2 + 1)^{-n}, \quad O = L/2 \quad (\text{for double cracks}) \quad (7)$$

a_n and b_n are real numbers to be determined and D, E, and F are roots of a simultaneous equations, which are based on introducing the condition that the stress components remain bounded at infinity. Truncating the unknown terms a_n and b_n in Eqn 6, the boundary conditions on the circular hole are satisfied with sufficient accuracy. Substituting Eqn 6 into Eqn 3, we can express the resultant forces by the function of $\phi_1(\zeta)$. The unknown terms a_n and b_n are determined by least square method.

The stress intensity may be evaluated directly from the stress functions $\phi_1(\zeta_1)$. The relation between the stress intensity factors and the stress functions can be expressed as [3].

$$K_I + \frac{K_{II}}{s_2} = 2\sqrt{2\pi/L} \left[\frac{s_2 - s_1}{s_2} \right] \phi_1'(1) \quad (8)$$

For convenience, we will introduce correction factors Y_I and Y_{II} defined by

$$Y_I = \frac{K_I}{T\sqrt{\pi L}}, Y_{II} = \frac{K_{II}}{S\sqrt{\pi L}} \quad (9)$$

DISCUSSION

The computer code to interactively calculate the stress intensity factors for radial cracks has been developed. To retain maximum flexibility in the variety of problems to be solved, the code has been written in a modular fashion.

Program to get correction factors consists of subroutines and modules. We minimize and visualize input variables. Anyone can gain the stress intensity factors interactively by using this program. Entering basic material properties (E_1 , E_2 , G_{12} , ν_{12}), geometry (radius of a hole, crack length), and boundary conditions (uniaxial or biaxial loading) at infinity, we can get stress intensity factors for radial cracks in an infinite plate under biaxial loading.

Comparing the present results with those of the references [7, 9, 10] as shown in Fig. 5, the present code and procedure seems to be guaranteed.

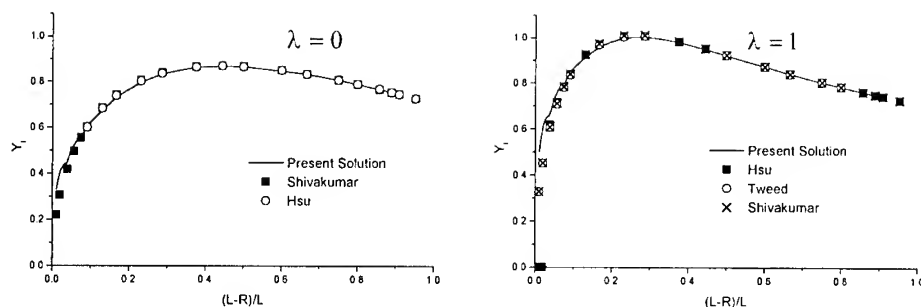


Fig. 5 Comparison of the present results with those of the references

REFERENCES

1. S. G. Lekhnitskii, *Anisotropic Plates*. Gordon and Breach. Science Publishers, 1968
2. Bowie O. L. and Fresse C. E., "Central crack in plane orthotropic rectangular sheet". *Int'l J. of Fracture mechanics*, Vol.8, 1972, pp.49-58.
3. S. K. Cheong and O. N. Kwon, "Analysis of a radial crack in cross-ply laminates under uniaxial Tension", *KSME Int. J.*, Vol. 11., No. 6, 1997, pp.650~656
4. S. K. Cheong and C. S. Hong, "Analysis of cracks emanating from a circular hole in an orthotropic plate under mixed mode deformation", *Engng Fracture Mech.*, Vol. 31, No. 2, 1988, pp.238~248
5. Cheong, S. K. and Hong, C. S., "Analysis of cracks emanating from a circular hole in [0n/90m]s laminates under various boundary conditions", *Engng Fracture Mech.*, Vol. 32, 1989, pp. 923~934
6. Bowie O. L., "Analysis of an Infinite plate containing radial cracks originating at the boundary of an internal circular holes", *J. Math. Physics*, Vol. 25, 1956, pp. 60~71
7. Hsu, Y. C., "The infinite sheet with cracked cylindrical hole under hole under inclined tension or in-plane shear", *Int. J. Fracture*, Vol. 11, 1975, pp. 571~581
8. Newman, J. C., Jr, "An improved method of collocation for the stress analysis of cracked plates with various shaped boundaries", *NASA Tech. Note D-6376*, 1971
9. shivakumar, V. and Forman, R. G., "Green's function for a crack emanating form a circular hole in an infinite sheet", *Int. J. Fracture*, Vol.16, 1980, pp.305~316
10. Tweed, J. and Rooke, D. P., "The elastic problem for an infinite solid containing a circular hole with a pair of radial edge cracks of different lengths", *Int. J. Engng Sci.* Vol. 14, pp. 925~933.
11. G. C. Sih and H. Liebowitz, "Mathematical Theories of Brittle Fracture: An Advanced Treatise", Vol. II., Academic Press, 1968
12. Robert M. Jones, "Mechanics of Composite Material". Scripta Book com. 1975

Microstructures and Fracture Characteristics of Reaction Sintered SiC/SiC Composites

S. P. Lee¹, Y. Katoh¹, W. Zhang¹, M. Kotani¹, A. Kohyama¹ and S. Suyama²

*1 CREST-ACE, JST, Tokyo, Japan and Institute of Advanced Energy, Kyoto University,
Gokasho, Uji, Kyoto 611-0011, JAPAN: splee@iae.kyoto-u.ac.jp; katoh@iae.kyoto-u.ac.jp;
wen@iae.kyoto-u.ac.jp; kotani@iae.kyoto-u.ac.jp; kohyama@iae.kyoto-u.ac.jp*

*2 Power & Industrial Systems R&D Center, Toshiba Corporation, 2-4, Suehiro-cho,
Tsurumi-ku, Yokohama 230-0045, JAPAN: shoko.suyama@toshiba.co.jp*

SUMMARY: In order to evaluate microstructural and fracture characteristics of SiC/SiC composites, electron microscopies including SEM, TEM and EDS, bending test and single-fiber push-out test have been conducted. SiC/SiC composites, which reinforced with the BN/SiC coated Hi-Nicalon fiber, have been fabricated by the reaction sintering process. It was found that the matrix portion of SiC/SiC composites comprised two sorts of phases depending on composition proportions of the silicon and the carbon, accompanying with the presence of the isolated silicon and the unreacted carbon. SiC/SiC composites also represented sufficient bending strength and fracture energy, even if the debonding between the interfacial coating layer and the Hi-Nicalon fiber occurred under the fabricating process.

KEYWORDS: Hi-Nicalon SiC fiber, SiC/SiC composites, Reaction sintering process, TEM analysis, Interfacial shear stress, Bending properties

INTRODUCTION

SiC/SiC composites have been considered to be the most potential candidate for fusion applications such as the fusion reactor and the first wall and advanced gas turbine engines. It has excellent high temperature strength, good fracture toughness compared with ceramic materials and low induced radioactivity under severe nuclear environments, etc. SiC/SiC composites have been fabricated by various techniques, including the chemical vapor infiltration (CVI), the precursor impregnation and pyrolysis (PIP), the hot pressing (HP) and the reaction sintering (RS). The major interest in recent works has been focused on the improvement of the fabricating process for high performance SiC/SiC composites and the evaluation of its mechanical properties¹⁻⁶. Recent development of high performance SiC fibers such as Hi-Nicalon, Hi-Nicalon type S and Tyranno SA, which possess the low oxygen content, the excellent high temperature stability and the weaving capacity, make it possible to promote various consolidation process of the matrix material at high temperature. One of the potential processes, the reaction sintering process has been recognized as an attractive technique because it offers high density, good air-tightness and lower cost productions. Several studies have shown that reaction sintered SiC/SiC composites have higher thermal conductivity ($\sim 50 \text{ W/m} \cdot \text{K}$), compared with those fabricated by PIP and CVI processes and possesses good first matrix cracking strength ($\sim 200 \text{ MPa}$)^{7, 8}. However, the residual silicon

phase generally remains in the matrix portion of reaction sintered SiC/SiC composites, since this composite is fabricated by infiltrating the molten silicon into a porous green preform, which is usually composed of SiC fiber bundles, SiC particles and carbon sources. Such residual silicon would lead to the deterioration in the radiation response and the creep resistance properties of SiC/SiC composites. Therefore, it is essential for the improvement of the reaction sintering process to control the appropriate reaction of carbon and silicon, based on the detailed analysis for the matrix microstructure of SiC/SiC composites. Unfortunately, there have been few studies to investigate the microstructure of reaction sintered SiC/SiC composites capable of contributing to the improvement of the reaction sintering process.

The purpose of the present work is to examine microstructures of reaction sintered SiC/SiC composites, which associate with the reaction of the carbon and the silicon and to evaluate its bending properties and interfacial fracture properties at the room temperature. The fracture mechanism of reaction sintered SiC/SiC composites is also investigated.

EXPERIMENTAL DETAILS

1. Material Fabrication

The reinforcement used in this experiment was a Hi-Nicalon fiber (Nippon carbon Co., Ltd). Filaments of Hi-Nicalon fiber, which BN and SiC coatings were applied by the chemical vapor deposition process, were prepared with the flat braided preform prior to the introduction of the matrix slurry. The matrix slurry was a mixture of SiC powder, carbon powder and water with some dispersant. The composition of SiC and carbon for the preparation of the matrix slurry was 10:3 at weight ratio. Average size of commercial SiC and carbon particles were 4 μm , 85 nm, respectively. SiC/SiC composites were fabricated by reaction sintering with the silicon melt, after the impregnation of the matrix slurry into the flat braided preform of Hi-Nicalon fiber. Fabricating temperature and its holding time inducing the molten silicon in vacuum atmosphere (6×10^{-2} Pa) were 1450 $^{\circ}\text{C}$ and 18 ks, respectively. The dimension of as-pressed SiC/SiC composites was $1 \times 10 \times 40 \text{ mm}^3$.

2. Microstructure analysis

The microstructure constituents of SiC/SiC composites fabricated by the reaction sintered process were analyzed with the scanning electron microscope and the energy dispersive spectrometer. The analysis of the transmission electron microscope was also carried out to examine fine carbon particle and isolated silicon in the matrix portion after the preparation of thin foil with the focused ion beam processing device. The fiber pullout and the interfacial delamination were also observed to explain the fracture mechanism of SiC/SiC composites.

3. Three point bending test and single fiber push-out test

In order to evaluate the performance of reaction sintered SiC/SiC composites, three point bending test was carried out at the room temperature. The dimension of the bending test sample, which is polished with diamond particles of 1 μm size, was $1 \times 4 \times 25 \text{ mm}^3$. The span length and the cross head speed were 18 mm and 0.5 mm/min, respectively. The bending strength was calculated from the maximum load, divided by the area of test sample.

The interfacial shear strength of reaction sintered SiC/SiC composites was investigated by an ultra-micro indentation test machine, which were loaded with a constant displacement rate. The indenter tip was the Berkovich pyramid with 68° . The single fiber push-out test was conducted at 90g-f for observing the debonding behavior of the selected fibers. The thickness of the specimen and the displacement rate used in this test were 75 μm and 0.2 $\mu\text{m/sec}$.

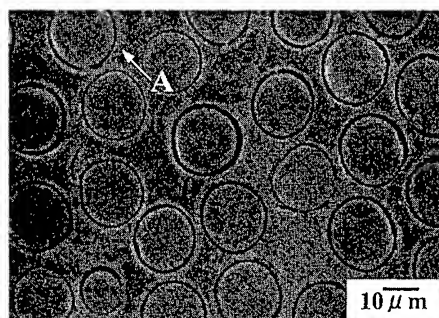
RESULTS AND DISCUSSION

1. Microstructure of reaction sintered SiC/SiC composites

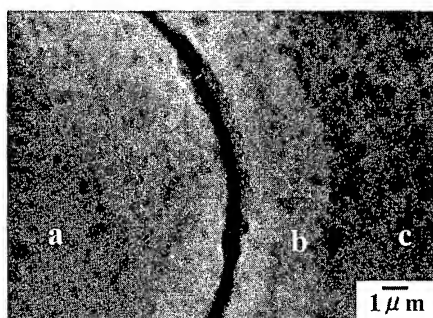
Fig. 1 shows SEM micrographs of SiC/SiC composites fabricated by the reaction sintering process. The composition of each portion displayed in Figure 1, which is identified by the EDS quantitative analysis, is also shown in Table 1. In this figure, two sorts of phases depending on composition proportions of the silicon and the carbon formed in the matrix portion of SiC/SiC composites. Especially, the white phases dominantly produced at the vicinity of fibers, as shown in Figure 1(b). It is obviously found from the results of the EDS analysis, the white phase has a higher concentration of the silicon, compared to that of the black phase and is approximate to the composition of Hi-Nicalon fiber. This is considered to be because the molten silicon reacting with the carbon easily flows between fibers in the reaction sintering process.

Table 1 Composition of each portion displayed in Fig.1, as identified by the EDS quantitative analysis.

	Si (at %)	C (at %)
a	38.57	61.43
b	44.85	55.15
c	29.36	70.64



(a) Microstructure



(b) Magnification of portion A in (a)

Fig. 1 SEM micrographs of reaction sintered SiC/SiC Composites

Fig. 2 shows TEM micrograph on the interfacial microstructure of reaction sintered SiC/SiC composites. Dense interfacial layers of the β -SiC and the boron nitride were observed in the interfacial region. The radial growth of β -SiC grains toward the left side in the micrograph was also revealed. The thickness of each interlayer deposited on the Hi-Nicalon fiber was

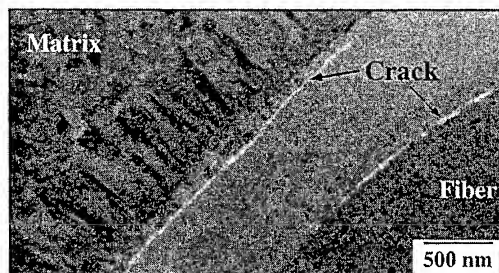


Fig. 2 TEM micrograph on the interfacial microstructure of SiC/SiC composites.

about $0.7\ \mu\text{m}$. It must be noted in this composite that an obvious crack occurs at the interface between the Hi-Nicalon fiber and the boron nitride or between the β -SiC and the boron nitride under the CVD process. Such the interfacial cracking is considered to result in the extensive delamination in the fracture mechanism of SiC/SiC composites, which will be discussed later.

Fig. 3 represents TEM micrographs on the matrix region of reaction sintered SiC/SiC composites. The corresponding electron diffraction pattern for the matrix region is also provided in this figure. The weak beam dark field images were determined by picking up parts of the $\langle 111 \rangle$ diffraction ring of β -SiC and the amorphous ring of the carbon, which is the nearest one from the spot, so that the grains in limited orientation are brightly imaged. It was found that the fine β -SiC phases smaller than SiC particle ($4.0\ \mu\text{m}$) used for the preparation of SiC/C matrix slurry created in the reaction sintered matrix due to the reaction of the molten silicon and the carbon. There are obviously amounts of unreacted carbons in the matrix region, as shown in Figure 3(c). Moreover, the isolated silicon phase is clearly observed in the matrix morphology of this composite, as displayed in Fig. 4. It can be concluded from these results that the morphology of the reaction sintered matrix is composed of the fine β -SiC phase, the unreacted carbon phase and the isolated silicon phase, which result from the difference of the matrix composition in reaction sintered SiC/SiC composites. In particular, the creation of isolated silicon phase in matrix region must be suppressed for the optimization of the conventional reaction sintering process, since the increase of silicon phases leads to the deterioration in the flexural strength of the reaction sintered matrix⁹. It should be therefore desirable to control the appropriate reaction of the carbon and the molten silicon capable of promoting the uniform microstructure of the crystallized SiC.

2. Evaluation of the interfacial shear stress

Fig. 5 shows the representative indentation curve of SiC/SiC composites obtained from the single fiber push-out test. As illustrated in an available literature¹⁰, the load gradually

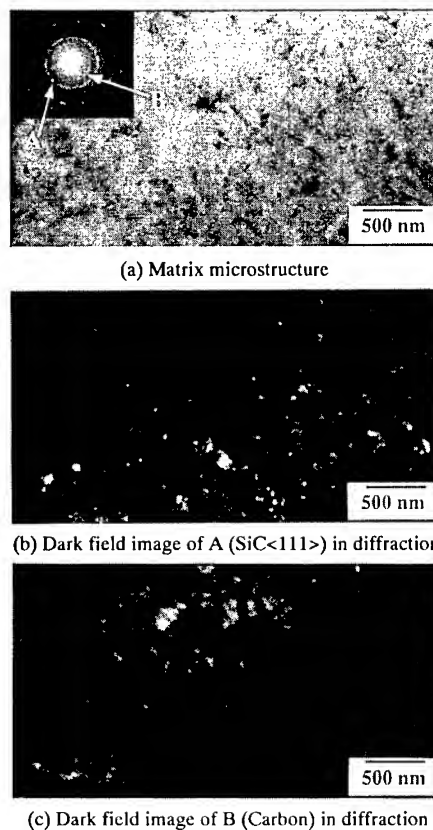


Fig. 3 TEM micrographs and diffraction pattern on the matrix region of SiC/SiC composites.

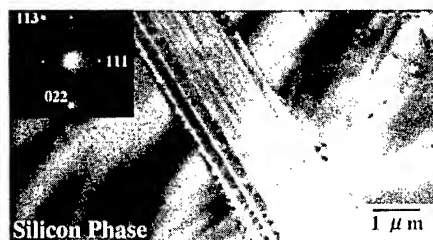


Fig. 4 Silicon phase detected on the matrix region of SiC/SiC composites.

increases to a push-out step, accompanying with an elastic deformation of the fiber and crack initiation along the interface between the fiber and the matrix. The load at a push-out step was used to determine the interfacial shear stress, because the pushing stress could be considered to overcome the interfacial shear stress. The interfacial shear stress can be defined as following.

$$\tau = P / \pi D t$$

where τ , interfacial shear stress, P , load at push-out, D , fiber diameter, t , specimen thickness. In this study, the average interfacial shear strength of SiC/SiC composites was about 50 MPa, even if the distribution of the interfacial shear stress is very large. In addition, this composite represented the lower resultant shear stress, compared to that of carbon coated SiC/SiC composites¹⁰. This is because the crack between the coating layers and the fiber occurs during the fabricating process.

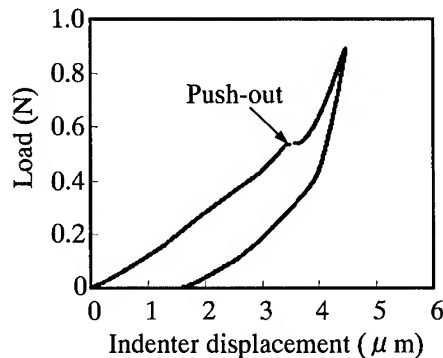


Fig. 5 Representative indentation curve of SiC/SiC composites obtained from the push-out test.

3. Evaluation of bending properties

The representative fracture behavior of SiC/SiC composites obtained from the three point bending test is shown in Fig. 6. It is clearly found that SiC/SiC composite represents noncatastrophical failure behavior, which displays a stable crack propagation beyond the maximum load. This is probably related to the variation of the crack propagation path associated with the interfacial delamination and the fiber fracture, because the crack continuously reinitiates on the tensile surface of subsequent fibers after the crack is arrested at the interface. Especially, the extensive interfacial fracture must be promoted in this composite system, since the debonding between the interfacial layer and the fiber occurred during the reaction sintering process. As shown in the fracture profile of Fig. 7, SiC/SiC composites dominantly represent pull-out of fibers and extensive interfacial delamination due to the constrain relaxation by the interfacial debonding. The bending strength and the fracture energy of SiC/SiC composites obtained from the bending test were about 330 MPa and about 3.2 kJ/m², respectively.

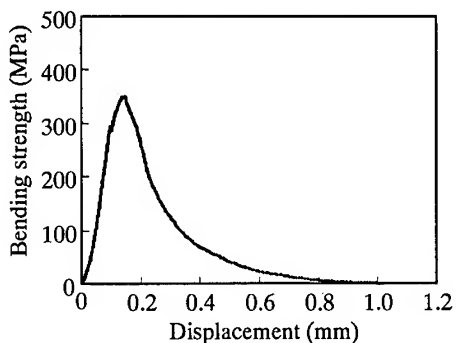


Fig. 6 Representative fracture behavior of SiC/SiC composites obtained from the bending test.

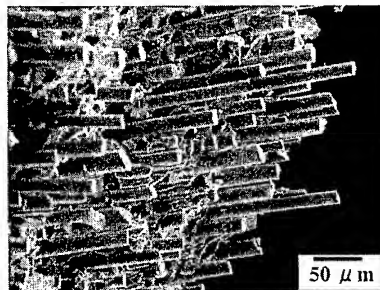


Fig. 7 Fracture profile of SiC/SiC composites.

CONCLUSION

1. Reaction sintered SiC/SiC composites comprised different kinds of phases in the matrix region, which depends on the composition of the silicon and the carbon. Furthermore, it was demonstrated from the results of TEM analysis that the isolated silicon and the unreacted carbon obviously existed in the matrix region.
2. Reaction sintered SiC/SiC composites represented the noncatastrophical failure behavior and the average fracture energy of about 3.2 kJ/m^2 . The average bending strength of SiC/SiC composite was about 330 MPa.
3. The debonding between the coating layer and the fiber occurred during the fabricating process became a critical point of the interfacial delamination, which related to fracture properties of Reaction sintered SiC/SiC composites.

ACKNOWLEDGMENTS

This study is supported by CREST-ACE (Core Research for Evolutional Science and Technology/Advanced Material Systems for Energy Conversion) program sponsored by Japan Science and Technology Corporation (JST).

REFERENCES

1. P. Fenici, A. J. Frias Rebelo, R. H. Jones, A. Kohyama, L. L. Snead, "Current status of SiC/SiC composites R&D", *J. Nucl. Mater.*, Vol. 258-263, 1998, pp.215-225.
2. C. A. Lewinsohn, M. L. Hamilton, G. E. Youngblood, R. H. Jones, F. A. Garner, S. L. Hecht and A. Kohyama, "Irradiation-enhanced creep in SiC: data summary and planned experiments", *J. Nucl. Mater.*, Vol. 253, 1998, pp.36-46.
3. C. Drollard and J. Lamon, "Fracture Toughness of 2-D Woven SiC/SiC CVI-Composites with Multilayered Interphases", *J. Am. Ceram. Soc.*, Vol. 79, 1998, pp.849-858.
4. N. Miriyala, P. K. Iiaw, C. J. McHargue and L. L. Snead, "The mechanical behavior of a Nicalon/SiC composite at room temperature and 1000 °C", *J. Nucl. Mater.*, Vol. 253, 1998, pp.1-9.
5. M. Takeda, Y. Kagawa, S. Mitsuno, Y. Imai and H. Ichikawa, "Strength of a Hi-NicalonTM/Silicon-Carbide-Matrix composite Fabricated by the Multiple Polymer Infiltration-Pyrolysis Process", *J. Am. Ceram. Soc.*, Vol. 82, 1999, pp.1579-1581.
6. S. Zhu, M. Mizuno, Y. Kagawa, J. Cao, Y. Nagano and H. Kaya, "Creep and Fatigue Behavior in Hi-NicalonTM-Fiber-Reinforced Silicon Carbide composites at High Temperature", *J. Am. Ceram. Soc.*, Vol. 82, 1999, pp.117-28.
7. T. Kameda, S. Suyama, Y. Itoh and Y. Goto, "Development of Continuous SiC Fiber-Reinforced Reaction Sintered SiC matrix Composites", *J. Jpn. Ceram. Soc.*, Vol.107, 1999, pp.327-334.
8. S. Suyama, Y. Itoh, T. kameda and A. Sayano, "Development of SiC Fiber Reinforced Reaction-Sintered SiC Matrix Composites", *The Second IEA/JUPITER Joint International Workshop on SiC/SiC Ceramic Composites for Fusion Applications*, 1997, pp.188-201.
9. S. Suyama, Y. Itoh, S. Nakagawa, N. Tachikawa, A. Kohyama and Y. Katoh, "Effect of Residual Silicon Phase on Reaction-Sintered Silicon Carbide", *The Third International Energy Agency Workshop on SiC/SiC Ceramic Composites for Fusion Structural Applications*, 1999, pp.108-112.
10. T. Hinoki, W. Zhang, A. Kohyama, S. Sato and T. Noda, "Effect of fiber coating on interfacial shear strength of SiC/SiC by nano-indentation technique", *J. Nucl. Mater.*, Vol. 258-263, 1998, pp.1567-1571.

Interlaminar Fracture of CF/EP Composite Laminates with Different Rubber Tougheners

Lin Ye and Keqin Xiao

Centre for Advanced Materials Technology
Department of Mechanical and Mechatronic Engineering
The University of Sydney, NSW 2006, Australia
ye@mech.eng.usyd.edu.au; xiao@mech.eng.usyd.edu.au

SUMMARY: In this study, core-shell rubber (CSR) and liquid rubber (LR) were used to modify the matrix toughness of unidirectional carbon fibre/epoxy composites. Double cantilever beam (DCB) and end notched flexure (END) tests were performed to evaluate the interlaminar fracture toughness. The CSR-modified epoxy shows an 18-fold increase in fracture toughness, and the LR-modified epoxy shows a 6-fold increase over the pure epoxy. Cavitation was identified as the main fracture mechanism for the CSR-modified epoxy while matrix plastic deformation ahead of the crack tip was the controlling energy dissipation mechanism for the LR-modified one. In the CSR- and LR-modified composites, the increase reduces to about 2-fold and 3-fold under the Mode I loading, respectively. The LR modification only obtains an increase of 50% in Mode II interlaminar fracture toughness of composite laminates, while the CSR modification reduces G_{IIc} by almost half. SEM observation of post-fracture surfaces of the specimens shows that the degree of plastic deformation of matrix is well related to the rating of fracture toughness of composites for these unmodified and modified composite laminates, and is the key factor controlling the interlaminar fracture toughness of composite laminates.

KEYWORDS: Interlaminar Fracture, Mode I and Mode II Fracture Toughness, Rubber-Modified Epoxies, Carbon Fibre/Epoxy Composite.

INTRODUCTION

Composite materials have undergone rapid development over the last decades and it is probably true to say that their usage pervades virtually every industrial sector. However, one major obstacle to the efficient application of continuous fibre reinforced thermosetting matrix laminates in advanced aerospace primary structures is the tendency for these materials to delaminate. Extensive research has been undertaken during the last few decades towards improving the interlaminar fracture toughness of carbon fibre/epoxy composites. Since interlaminar fracture toughness is controlled by the matrix properties, significant efforts have been concentrated on toughening thermosetting matrix resins with elastomers. It has been found that both the morphology and microstructures, such as the resin phase morphology, distribution of toughener particles, and the thickness of the interlaminar resin-rich region, are critical in effective toughening of high-performance composites [1-2]. The reproducibility of the mechanical properties of the composite is also found to depend greatly on how well the resin phase morphology is controlled [3-4]. Rubber-modified epoxies usually show up to a

20-fold increase in fracture toughness over the original bulk resin. However, such epoxies impart only a moderate improvement in Mode I interlaminar fracture toughness (G_{IC}) when used as a matrix material in unidirectional continuous fibre composites [5-6]. It has also been found that G_{IC} with a rubber-modified matrix is sometimes lower than that with an unmodified counterpart [7-8]. Ineffective rubber toughening in composites may be due to hindrance by the fibre phase, which limits the growth of the crack tip damage zone, and/or microcracking at the crack tip [5-8]. Under Mode II fracture, rubber modification often reduces interlaminar fracture toughness of composites, G_{IIIC} , [9]. However, the reason for this is not well understood.

In this study, three different resin systems, pure epoxy, LR-modified and CSR-modified epoxies, were used to make carbon fibre composites. Interlaminar fracture behaviour of composite laminates subjected to Mode I or Mode II loading was evaluated in order to establish relationships between fracture toughness of matrices and interlaminar fracture resistance of corresponding composite laminates. Fracture surfaces were examined using SEM to identify failure mechanisms of interlaminar fracture of pure epoxy composite and modified composites under different failure modes.

EXPERIMENTAL

The unmodified matrix resin was a standard DGEBA epoxy (Araldite F). The curing agent was piperidine. Two matrix tougheners were solid core-shell rubber (CSR, 0.4 μm in diameter) and CTBN 1300 \times 13 liquid rubber (LR). The proportion of these two matrix modifiers in the modified matrix resins was 15% by weight. A commercial SOLVENT 101 epoxy thinner was added to the degassed matrix resins in a ratio of 30% by weight to reduce their viscosity to an appropriate level for impregnation. The carbon fibre used in this study was Toray T300. Composite prepregs were fabricated from the carbon fibre tows and the diluted matrix resins using a two-axis winding machine. The unidirectional laminates were cured in an autoclave at 120°C for 16 hours. A constant pressure of 0.6 MPa is held throughout the cure cycle. The fibre volume fraction is 51.7, 50.3 and 48.2, respectively, for the pure epoxy, LR-modified and CSR-modified matrix composites. A Teflon film of 12.3 μm in thickness was inserted in the middle plane at one end of laminate to produce a pre-crack.

Mode I interlaminar fracture toughness was measured at room temperature using the double cantilever beam (DCB) test procedure at a crosshead rate of 2 mm/min. Five specimens were tested for each material system. G_{IC} was calculated using the modified beam theory expression (ASTM D-5528). Mode II interlaminar fracture toughness was evaluated at room temperature using the end-notched flexure (ENF) test procedures at the crosshead rate of 0.5 mm/min, and five specimens were tested for each material system. G_{IIIC} was obtained through the experimental compliance calibration method [10]. In order to evaluate the effect of the sharpness of pre-crack on Mode II interlaminar fracture toughness, a naturally grown crack was introduced. Specimens with the Teflon film pre-crack were loaded on the Instron testing machine at the crosshead rate of 0.5 mm/min. After an advance of about 10 mm, loading was stopped and the new crack front on the edge of the specimen was marked under the microscope.

RESULTS AND DISCUSSION

The fracture energy of the individual bulk matrices is 150 J/m², 930 J/m² and 2750 J/m²,

respectively, for the pure, LR-modified and CSR-modified epoxies. The major toughening mechanisms in the CSR-modified epoxy were rubber particle cavitation and dilation of the epoxy [11]. For the LR-modified epoxy, the improvement of fracture toughness is attributed to enhancement of capacity for plastic deformation of the epoxy, resulting from the dissolution of LR into the epoxy phase [12].

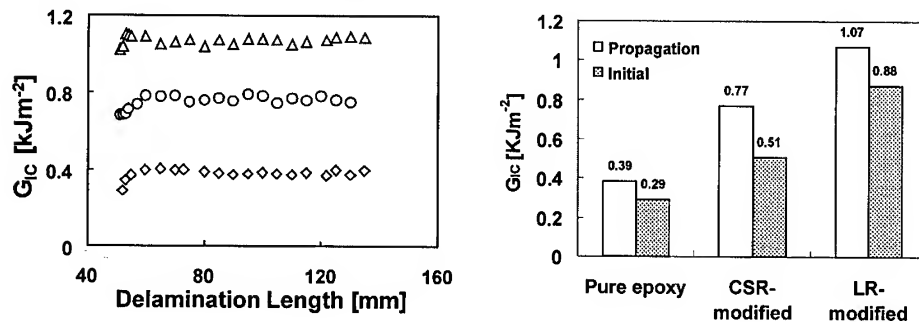


Fig. 1 Left: R-curves of Mode I tests: (◇) Pure epoxy, (○) CSR-modified epoxy and (△) LR-modified epoxy. Right: Effect of matrix resins on Mode I interlaminar fracture toughness.

Typical R-curves of composite laminates with three different resin systems under Mode I fracture are shown in Fig. 1. The initial value of Mode I interlaminar fracture toughness, G_{IC} (Initial), is defined at the first point where the crack was observed to move from the pre-crack tip at either of the specimen edges under the microscope, while G_{IC} (Propagation) is the plateau value of the R-curve. It is seen that G_{IC} increases from the pre-crack, and then quickly levels off within about 5 mm of crack advancement.

A comparison of G_{IC} (Initial) and G_{IC} (Propagation) for three composite systems with different matrices is presented in Fig. 1. It can be seen that both LR and CSR are effective in improving interlaminar fracture toughness of unidirectional composites. It is known that the CSR- and LR-modified epoxies show an increase in fracture toughness for 18-fold and 6-fold over the pure epoxy, respectively. However, in the composites, this increase reduces to about 2-fold and 3-fold, respectively, showing that toughness of the matrices do not completely transfer to improvement of fracture toughness of the composite materials. The result presented here is consistent with those reported in the literature. But it is interesting to note that LR is superior over CSR in enhancing the interlaminar fracture toughness of composites although the CSR-modified bulk epoxy has the highest fracture toughness. This result is reverse to the expectation if looking at the fracture toughness of a bulk matrix resin only.

SEM micrographs of Mode I fracture surfaces in Fig. 2 reveal that the rating of fracture toughness of composites for these three systems is well related to the degree of plastic deformation of the matrix resins and crack growth behaviour. For the pure epoxy matrix composite, the crack grows almost completely along fibre-resin interface, and fracture surfaces of matrix are relatively smooth. For the LR-modified epoxy composite, many plastic deformation bands are seen in the matrix. The crack clearly advances between the resin phase and fibres, but sometimes it goes through the resin phase, changing its path from one fibre-matrix interface to another. However, crack propagation occurs almost completely in the resin layer for the composite with the CSR-modified matrix. No plastic deformation band is observed in the matrix, and the matrix resin is less plastically deformed than that in the LR-

modified system. Rubber particle cavitation is observed (Fig. 2(d)), which provides an alternative energy absorption mechanism in this case, resulting in an improvement of fracture toughness of the CSR-modified matrix composite over the pure epoxy counterpart. However, extent of rubber cavitation is much less extensive than that in the bulk CSR-modified resin, because of constraint from the rigid fibres.

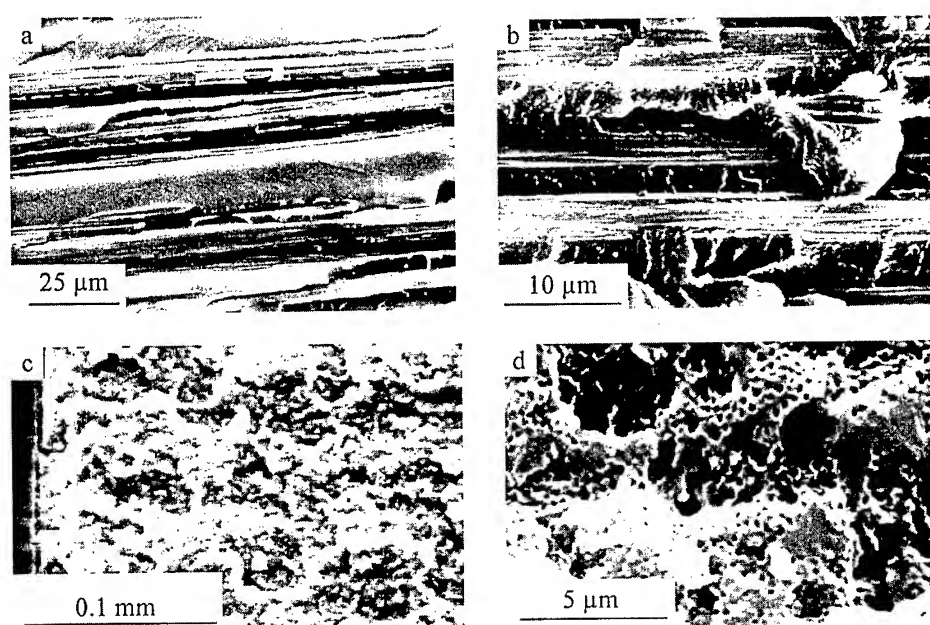


Fig. 2 Mode I fracture surfaces of laminates with different matrices: (a) pure epoxy, (b) LR-modified, (c) CSR-modified and (d) CSR-modified at a high magnification, showing rubber cavitation.

The effect of matrix systems on Mode II interlaminar fracture toughness of the composites is depicted in Fig. 3. Only a slight difference is observed between the two values of fracture toughness produced by a film pre-crack or a grown pre-crack. Thus it can be concluded that the pre-crack produced by the insert film is sharp enough to produce a minimum value of G_{IIC} . Interlaminar fracture toughness of composites under Mode II loading gives a different trend compared to that under Mode I, correlating with the matrix toughness. The LR modification obtains an increase of only 50% in G_{IIC} , while the CSR modification reduces G_{IIC} by almost half, compared to that of the pure epoxy system. It is found that with the increase in the matrix toughness, the ratio of G_{IIC}/G_{IC} decreases, being 2.68, 1.52 and 0.78, respectively, for the pure epoxy, LR-modified and CSR-modified laminates. This variation is consistent with that observed by Bradley et al [2].

The correlation of the Mode II fracture toughness with the matrix toughness can be explained using the morphology of fracture surfaces of the specimens, shown in Fig. 4. In the pure epoxy matrix laminate many zipper-like facets, usually called "hackles", can be seen. But the matrix is clearly plastically deformed to a greater extent under Mode II fracture (shear failure) than under Mode I fracture (Fig. 2(a)). As a result, the former produces a fracture toughness 1.5 times higher than the latter. Formation of the hackle pattern was studied in detail by Hibbs

et al [13] through in-situ observation of crack tip propagation in SEM. The morphology of the fracture surface for the LR-modified matrix composite is similar to that of the pure epoxy matrix composite, but having clearly more significant plastic flow in the matrix; this feature is responsible for the increase of G_{IIC} over the pure epoxy counterpart. Some other minor processes for energy absorption, such as fibre peeling, fibre breakage and imprint, are also found for both the pure epoxy and LR-modified composites. The global morphology of the fracture surface for the CSR-modified matrix composite is almost the same as that under Mode I in Fig. 2(c), and the matrix resin is less plastically deformed than that of the pure epoxy counterpart under Mode II in Fig. 4(a). As a result, G_{IIC} for the CSR-modified composite is lower than that for the pure epoxy composite.

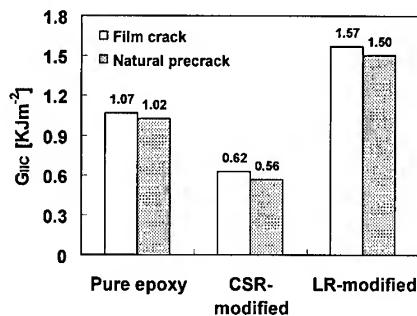


Fig. 3 Effect of matrix resins on Mode II interlaminar fracture toughness.

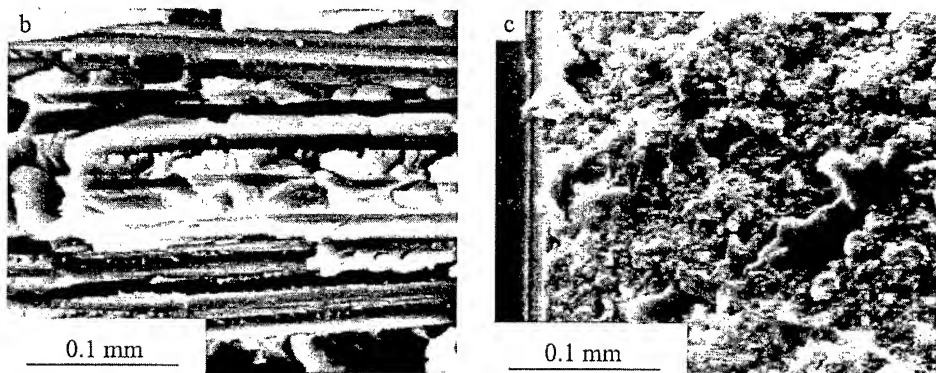


Fig. 4 Mode I fracture surfaces of laminates with different matrices: (a) pure epoxy, (b) LR-modified and (c) CSR-modified.

Poor toughening ability of CSR in the composite, especially under Mode II loading, can be explained from the difference of toughening mechanisms between the CSR-modified bulk epoxy and CSR-modified composite. For the CSR-modified bulk epoxy, the major energy absorption process is related to formation of the stress-whitened zone associated with rubber cavitation. The material is dilated in the area under the crack surface at least as deep as 0.2 mm (at some places reaching 0.8 mm), induced by rubber cavitation [14]. Although rubber cavities are also formed in the composite, the thickness of the resin layer in the composite is very thin. As a result, the volume dilation as the major energy absorption process in the CSR-

modified bulk epoxy is greatly suppressed in the composite.

CONCLUSIONS

Mode I delamination fracture toughness of composite laminates with LR-modified and CSR-modified matrices was found to increase by 200% and 100%, respectively. Mode II delamination fracture toughness with the LR-modified matrix increased by 50% over its pure epoxy counterpart, while a lower toughness value was obtained for the CSR-modified matrix composite. Plastic deformation of matrix and crack growth behaviour were identified as the key factors controlling the interlaminar fracture toughness of composites. The rating of delamination toughness of these three systems under both Mode I and Mode II could be well related to the capability of the plastic deformation of the bulk matrices.

The poor toughening ability of core shell rubber in the composite was attributed to suppression of the volume dilation process which is the major energy absorption process in the CSR-modified bulk epoxy. LR was identified to be more effective than CSR in improving G_{IC} and G_{IIC} of the composites, although fracture toughness of the CSR-modified epoxy was better than that of the LR-modified epoxy.

REFERENCES

1. N. Odagiti and H. Kishi, Polym. Preprint 33 (1992) 384.
2. W. L. Bradley, in "Application of Fracture Mechanics to Composite Materials", edited by K. Friedrich, Elsevier Applied Science, New York, (1989) p. 159.
3. D. S. Parker and A. F. Yee, J. Therm. Compos. Mater. 2 (1989) 2.
4. M. A. Hoisington and J. C. Seferis, in Pro. 6th American Society for Composites, New York, (1991) p. 53.
5. W. M. Jordan, W. L. Bradley and R. J. Moulton, J. Comp. Mater., 23 (1989) 923.
6. W. L. Bradley, Key Engng Mater., 37 (1989) 161.
7. D. L. Hunston, R. L. Moulton, N. J. Johnston and W. D. Bascomm, Toughened Composites, edited by N. J. Johnston, ASTM-STP-937, 1987, p. 74.
8. W. M. Jordan and W. L. Bradley, Toughened Composites, edited by N. J. Johnston, ASTM-STP-937, 1987, p. 95.
9. C. B. Bucknall, Advanced Composites, edited by I. K. Partridge, Elsevier Applied Science, New York, (1989) p. 145.
10. L. A. Carlsson, J. W. Gillespie and R. B. Pipes, J. Composite Materials, 20 (1986) 594.
11. Keqin Xiao and Lin Ye, Polym. Eng. Sci., in print, 2000.
12. Keqin Xiao and Lin Ye, submitted to Polym. Eng. Sci., 2000.
13. M. F. Hibbs and W. L. Bradley, Composites and Metal, edited by J. E. Masters and J. J., ASTM-STP-948, 1987, p.68.
14. Keqin Xiao, Fracture Toughness of Rubber-Modified Epoxies and Their Carbon Fibre Composites, PhD thesis, University of Sydney, NSW2000, Australia.

EFFECT OF PARTICLE DISPERSIBILITY ON THE FRACTURE BEHAVIOR OF ZrO_2/Ni COMPOSITE MATERIALS

Mitsugu Todo¹, Naoki Hanada¹, Kazuo Arakawa¹ and Kiyoshi Takahashi¹

¹ Research Institute for Applied Mechanics, Kyushu University, 6-1 Kasuga-koen, Kasuga,
Fukuoka 816-8580, Japan: tohdoh@riam.kyushu-u.ac.jp

SUMMARY: ZrO_2/Ni composite materials were fabricated by means of slip casting method to study the effects of composition and particle dispersibility on their deformation and fracture behavior. Their microstructures were examined using a laser microscope and image processing technique. The result showed that the compositions of the sintered materials were different from those of the compacts. The results of bend fracture testing exhibited that composition has significant influence on the fracture properties of the composites with sufficient dispersibility, whereas there is little effect on the properties with insufficient dispersibility. Relationship between the microscopic characteristics and the macroscopic fracture properties is discussed on the basis of those results of microscopies, image analysis and fracture testing.

KEYWORDS: Metal Matrix Composite, Fracture Toughness, Bending Strength, Image Processing

INTRODUCTION

Ceramics/metal composite material has attracted industrial attention as a structural material that possesses favorable mechanical properties of both base materials, that is, high heat resistibility of ceramics and high fracture toughness of metal [1]. However, relationship between the microstructure and mechanical properties of this type of composite material has not been well understood yet. For example, ZrO_2/Ni composites exhibited superb tensile mechanical properties at high temperatures up to 800°C [2]. It is also known that the composition and particle dispersibility of the material are important factors controlling its mechanical properties [3].

In the present study, six types of ZrO_2/Ni composite material having three kinds of composition and two kinds of particle dispersibility were fabricated using slip casting method [4]. Microstructures of the materials were analyzed using laser microscopy and digital image processing. Effects of the composition and particle dispersibility on their bending fracture properties and mode I fracture toughness were investigated on the basis of the results of mechanical testing and image processing.

EXPERIMENTAL

Material and specimen

ZrO_2/Ni composite materials were made of ZrO_2 and Ni powders by slip casting method [4]. Aqueous slips containing mixtures of the ZrO_2 and Ni powders were prepared with a deflocculant. Three different compositions chosen were $ZrO_2/Ni = 20/80$, 35/65 and 50/50 in

volume fraction. The slips were then stirred for three days to obtain sufficient dispersibility and for 10 minutes to obtain insufficient dispersibility. Compacts were formed by pouring the stirred slips into plastic frames set on gypsum molds. The compacts were dried for a couple of days and then pressureless sintered at 1400°C for two hours in flowing argon atmosphere. Six different types of ZrO₂/Ni composite material are hereafter denoted by 20/80-G, 20/80-B, 35/65-G, 35/65-B, 50/50-G and 50/50-B where G and B imply sufficient and insufficient dispersibility, respectively.

Specimens for bend testing were carefully cut out of the sintered materials using a low speed cutting machine. Two types of the bend specimens are shown in Figs.1. A diamond saw 0.3 mm thick was used to introduce a notch for each of the fracture toughness test specimens as shown in Fig.1(b).

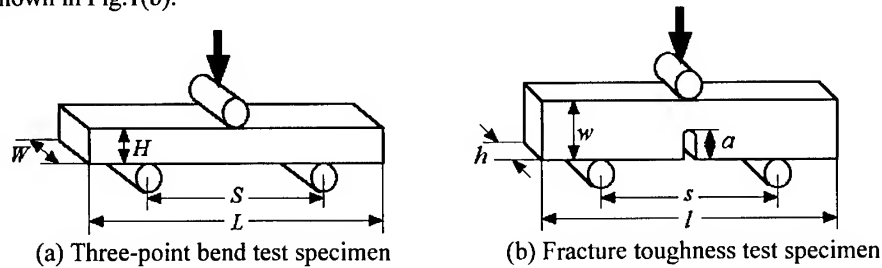


Fig.1 Bend test specimens

Observation and analysis of microstructure

Microstructures of the prepared materials were observed on their polished surfaces using a laser microscope. Microphotographs were saved as digital images and the thresholdings of the images were obtained by means of a digital image analysis software on a personal computer. Areal ratios of Ni to ZrO₂ were then obtained by analyzing the thresholding images. The volume fractions of Ni and ZrO₂ were determined on the basis of the areal ratios obtained.

Bending fracture testing

Three point bend testing of the specimens shown in Figs.1 was performed at a loading rate of 0.1 mm/min using a servohydraulic testing machine. Load-time and loading-point displacement were recorded in a sampling interval of 200 msec using a digital recorder. In the fracture toughness testing, crack-tip strain was also measured to detect initiation of unstable crack growth.

As a first approximation, nonlinear stress-strain relation of the ZrO₂/Ni composite materials was evaluated using the following procedure. For the initial linear portion of the load-displacement curve, from the classical beam theory, the relation between load, P , and displacement, δ , is given by:

$$P = \frac{4H^3WE}{S^3} \delta \quad (1)$$

where H and W are the specimen thickness and width, respectively, as shown in Fig.1(a). S is the span length and E is the bending modulus. Thus the modulus, E , of the material can be evaluated by comparing Eq.1 and the load-displacement curve. Using the E value, the linear stress-strain relation can be expressed as:

$$\sigma = E\varepsilon \quad (2)$$

If it is assumed that the stress-strain relation for the nonlinear part of the P - δ curve can be approximated by:

$$\sigma = E_0 \varepsilon^n \quad (3)$$

the P - δ relation is given by:

$$P = \frac{2E_0 I_n}{(S/2)^{2n+1}} \left(\frac{2n+1}{n} \right)^n \delta^n, \quad I_n = \left(\frac{2W}{n+2} \right) \left(\frac{H}{2} \right)^{n+2} \quad (4)$$

The bending strength, σ_b , was assumed to be equivalent to the maximum stress and the bending fracture energy, U_b , was defined as the area under the load-displacement curve up to the maximum load divided by the cross sectional area of the specimen.

Critical mode I strain energy release rate, G_{Ic} , was evaluated as a mode I fracture toughness to assess resistance to fracture initiation. G_{Ic} is given by:

$$G_{Ic} = \frac{U_c}{hw\phi(x)}, \quad x = a/w \quad (5)$$

$$\phi = \frac{A + 18.64}{dA/dx}$$

$$A = \frac{16x^2}{(1-x)^2} (8.9 - 33.717x + 79.616x^2 - 112.952x^3 + 84.815x^4 - 25.672x^5)$$

where h , w and a are the specimen thickness, width and the crack length, respectively, as shown in Fig.1(b). The critical fracture energy, U_c , was evaluated as the area under load-displacement curve up to the critical point that could be detected from crack-tip strain response.

RESULTS AND DISCUSSION

Microstructure analysis

Laser microphotographs of 50/50-G and 50/50-B are shown in Figs.2. In Figs.2, the bright regions are distributed Ni particles and the dark region is ZrO_2 . Fig.2(a) shows good particle dispersibility in 50/50-G, on the other hand, agglomerations of Ni are observed in 50/50-B. Those agglomerations were also seen in 20/80-B and 35/65-B. It should be noted that from Fig.2(a), the volume fraction of Ni seems to be less than that of ZrO_2 , although Ni and ZrO_2 were mixed into the slip in the ratio 50/50.

An example of thresholding of an image of 20/80-G is shown in Fig.3. The composition estimated by image analysis was $ZrO_2/Ni = 35/65$, indicating that the composition of the sintered material was different from that of the compact. The results of the image analysis exhibited that for all the materials, the volume fraction of ZrO_2 in the sintered material was larger than that in the compact. Expansion of ZrO_2 due to void formation at the interfaces of crystals is considered to be the main reason.

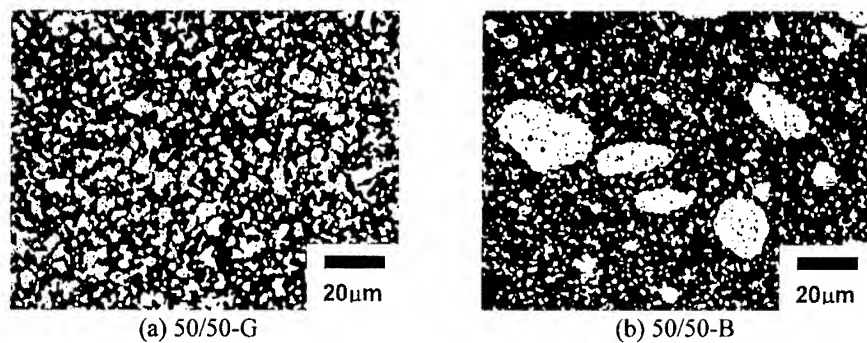


Fig.2 Microstructures of 50/50-G and 50/50-B composites.

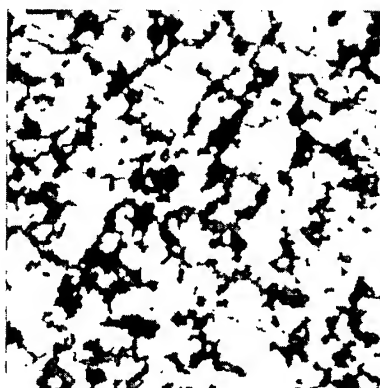


Fig.3 Thresholding of an image of 20/80-G.

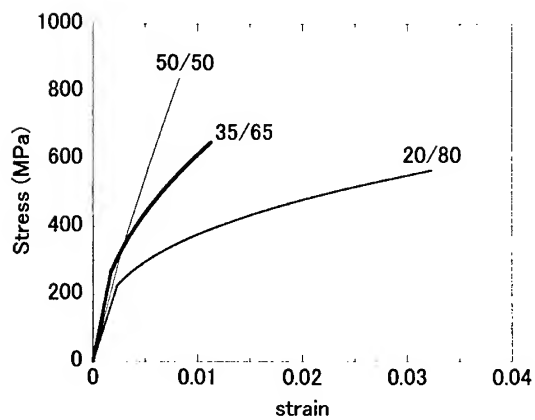


Fig.4 Stress-strain curves of the G-types.

Bending properties

Stress-strain relations for the G-types are shown in Fig.4. It is seen from Fig.4 that the nonlinearity caused by plastic deformation of Ni was reduced as the ZrO_2 content increased.

Bending strengths are shown in Fig.5. For the G-types, the strength increased as the ZrO_2 content increased. On the contrary, for the B-types, effect of the ZrO_2 content was not observed, implying that the Ni agglomerations control the strength of the B-type materials. Bending fracture energies are shown in Fig.6. The fracture energy of 20/80-G was the largest due to the effect of plastic deformation of Ni. For the G-types, the fracture energy decreased as the content of brittle ZrO_2 increased as expected. For the B-types, as seen in the results of the strength measurement, the fracture energy was independent of the ZrO_2 content.

Mode I fracture toughness

Mode I fracture toughnesses, G_{Ic} , are shown in Fig.7. It is interesting to see that G_{Ic} of 20/80-G was almost equivalent to that of 50/50-G. Although the largest energy dissipation due to plastic deformation of Ni is expected during the initiation of crack growth in 20/80-G, 50/50-G may have a different type of toughening mechanism such as additional energy dissipation due to microcrack formation generated from voids at the interfaces of ZrO_2 crystals. It is also seen that the B-types exhibited lower fracture toughness than the G-types. It thus appears that the Ni agglomerations in the B-type materials lower their toughness. 35/65-G exhibited the lowest G_{Ic} value of all the G-types, implying that toughening mechanisms such as plastic deformation of Ni and microcracking in ZrO_2 are less effective in this material than in the other G-types.

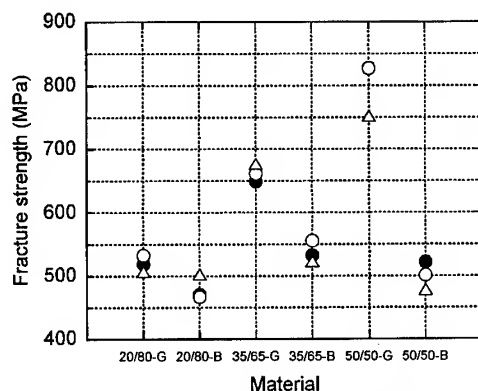


Fig.5 Bending fracture strength of the ZrO_2/Ni composites.

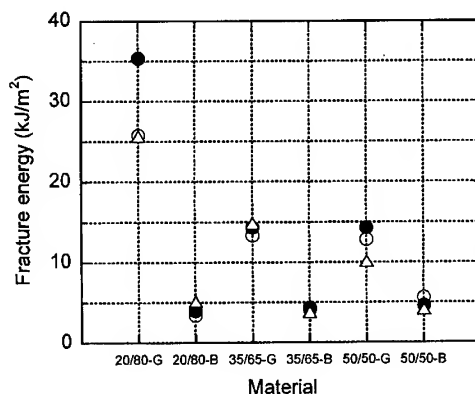


Fig.6 Bending fracture energy of the ZrO_2/Ni composite materials.

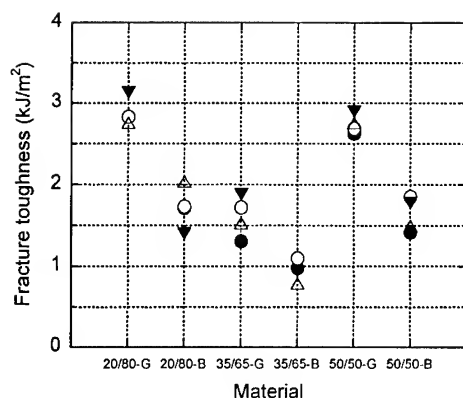


Fig.7 Mode I fracture toughness of the ZrO_2/Ni composite materials.

CONCLUSIONS

Six different types of ZrO_2/Ni composite materials were fabricated. Microstructure analysis was performed using a laser microscope and a technique of image analysis. Three-point bend tests were carried out to evaluate bending mechanical properties and mode I fracture toughness. Following conclusions are obtained:

- (1) The compositions of the sintered materials are different from that of the compacts. Void formation at the interfaces of ZrO_2 crystals is considered to be the main reason.
- (2) Existence of Ni agglomerations in this type of composite material lowers its bending strength and fracture energy.
- (3) Additional energy dissipation due to microcracking in the vicinity of crack-tip increases the fracture toughness of 50/50-G.

REFERENCES

1. I.A. Ibrahim, F.A. Mohamed and E.J. Lavernia, "Particulate Reinforced Metal Matrix Composites - A review," J. Mater. Sci., Vol.26, 1991, pp.1137-1156.
2. T. Ogawa, K. Arakawa, K. Takahashi, H. Takebe and K. Morinaga, "Temperature Effect on Deformation and Fracture Behaviors of ZrO_2/Ni Composite Materials," J. Soc. Mater. Sci. Japan, Vol.43, No.494, 1994, pp.1463-1468.
3. N. Hanada, M. Todo, K. Arakawa and K. Takahashi, "Study on the Deformation and Fracture Behavior of ZrO_2/Ni Composites," Proc. JSMS Composites-28, 1999, pp.29-32.
4. H. Takebe and K. Morinaga, "Fabrication of Zirconia-Nickel Functionally Gradient Materials by Slip Casting and Pressureless-Sintering," Mater. Manufact. Processes, Vol.9, No.4, 1994, pp.721-733.

SHEAR DEFORMATION BEHAVIOR IN SEMI-SOLID STATE OF A HIGH STRAIN RATE SUPERPLASTIC Si₃N₄/Al-Mg-Si COMPOSITE

Hajime Iwasaki¹, Takasuke Mori¹, Mamoru Mabuchi², and Kenji Higashi³

¹*Department of Materials Science and Engineering, College of Engineering,
Himeji Institute of Technology, Shosha, Himeji, Hyogo 671-2201, Japan:
iwasaki@mse.eng.himeji-tech.ac.jp*

²*National Industrial Research Institute of Nagoya, Hirate-cho, Kita-ku,
Nagoya 462-8510, Japan : mabuchi@nirin.go.jp*

³*Department of Metallurgy and Materials Science, College of Engineering,
Osaka Prefecture University, Gakuen-cho, Sakai, Osaka 599-8531, Japan*

SAMMARY: This paper describes shear deformation behavior in a wide temperature range of 683 ~ 893K and at $2 \times 10^{-3} \sim 3 \text{ s}^{-1}$ for a high strain rate superplastic Si₃N₄/Al-Mg-Si composite. The experimental results showed that the dominant deformation mechanism is dislocation creep at 683 ~ 773 K and superplastic flow at 813 ~ 863 K, respectively. In a superplastic region, the shear strain to failure was significantly increased by the presence of a liquid phase. At 873 ~ 893 K, high m of about 1 is attained. The deformation in this temperature range is likely to be the lubricated flow in a semi-solid state containing a continuous intergranular liquid phase. However, ductility is low in this range because of decohesion at boundaries with a thick liquid phase of the order of ~ 10 μm .

KEYWORDS: Deformation behavior, Seim-solid state, Shear test, Metal matrix composite

INTRODUCTION

Deformation behavior in a semi-solid state at the early states of melting has been investigated by compressive creep tests [1-4]. It was shown from the compressive tests that the deformation mechanism in a semi-solid state is grain boundary sliding accommodated by cavitation in the liquid phase for the copper containing a liquid bismuth [2]. For the compressive tests, however, because a liquid phase is squeezed out of boundaries experiencing compressive stresses in a very short time [2], it is difficult to investigate deformation in a semi-solid state under the condition where a liquid phase is not squeezed out. Recently, deformation behavior of an Al-5wt.%Mg alloy was investigated by shear tests in a wide temperature range containing a solid state and a semi-solid state [5]. Deformation in a semi-solid state under the condition where a liquid phase is not squeezed out can be investigated by the shear tests. The shear tests in the Al-Mg alloy revealed that deformation behavior at the early states of melting in a semi-solid state under the condition where a liquid is not squeezed out is divided into two deformation processes from the viewpoint of distribution of a liquid

phase; deformation in a semi-solid state containing a discontinuous intergranular liquid and deformation in a semi-solid state containing a continuous intergranular liquid [5]. The deformation mechanism of the latter is the lubricated flow by a liquid phase and that of the former is a transition from dislocation creep in a solid state to the lubricated flow in a semi-solid state containing a continuous intergranular liquid.

Recently, it was pointed out that a liquid phase plays an important role in high strain rate superplasticity [6-8]. For example, a maximum elongation is attained at the temperature close or slightly above the partial melting temperature [9-12]. However, too much liquid causes a rapid decrease in elongation [13]. This suggests that mechanisms of deformation and fracture are strongly affected by the volume and distribution of a liquid phase. To date, however, there are few data about deformation behavior in a wide temperature range including a semi-solid state containing a large volume of a liquid phase for high strain rate superplastic metal matrix composites because tensile tests can not be carried out in a semi-solid state containing a large volume of a liquid phase. In the present investigation, shear tests are carried out over a wide temperature range of 683 ~ 893 K, including temperatures below and above the partial melting temperature, for a $\text{Si}_3\text{N}_4/\text{Al-Mg-Si}$ composite exhibiting high strain rate superplasticity. Based on the results of the shear tests, deformation characteristics are investigated in three ranges; dislocation creep in a solid state, superplasticity containing a liquid phase or not, and deformation related to the liquid flow.

EXPERIMENTAL PROCEDURE

An Al-Mg-Si (6061) alloy matrix composite was processed by powder metallurgy and hot extrusion, which are similar to the fabrication methods for the high strain rate superplastic Al-Mg-Si alloy matrix composite in the previous paper [10]. The Al-Mg-Si alloy powder and 20 vol.% of Si_3N_4 particulates with less than 1 μm in diameter were mixed ultrasonically in an alcohol solvent and then dried and compressed in vacuum at 873 K for 20 min under a pressure of 390 MPa. The compressed billets were extruded at 773 K using a reduction ratio of 100 : 1. The grain size of the composite was 2.1 μm .

Double shear specimens were machined from the as-extruded composite. All tests were conducted double-shear conditions, using specimens having twin gauge lengths 2.5 mm long and 3 mm in diameter, in a strain rate range of $2 \times 10^{-3} \sim 3 \text{ s}^{-1}$ and in a temperature range of 683 ~ 893 K. The test temperature range includes temperatures below and above the partial melting temperature. The specimens required about 1.8 ks to equilibrate at the test temperature prior to initiation of testing. The deformed specimens were rapidly quenched to investigate the microstructure. The quenched specimens were mechanically polished by silicon-carbide papers. A differential scanning calorimeter (DSC) experiment was carried out for the as-received material of 13.6 mg in weight to investigate the partial melting temperature. The DSC run started at room temperature, ended at 873 K and was made with a constant heating rate of 10 K/min.

RESULTS

The result of the DSC experiment is shown in Fig. 1. The sharp endothermic peak is attributed to partial melting at the matrix/reinforcement interfaces [10,14]. Partial melting at the interfaces has been evidenced by in-situ TEM observation [14]. The partial melting temperature estimated from the sharp endothermic peak is 832 K. The shear stress - shear strain curves at 713, 843 and 883 K are shown in Fig. 2, where the shear rate is 1.7 s^{-1} .

The shear strain to failure at 843 K is much larger than those at 713 and 883 K, indicating that large elongation is attained at the temperature slightly above the partial melting temperature.

The variation in shear stress as a function of shear strain rate at 683 ~ 893 K is shown in Fig. 3. The shear stresses are determined at a small shear strain of $\gamma = 0.05$ because there is no aggregation of a liquid phase at a small strain ≤ 0.1 [5]. It can be seen that the strain rate sensitivity, m ($=\Delta \ln \tau / \Delta \ln \dot{\gamma}$, where $\dot{\gamma}$ is the shear strain rate and τ is the shear stress), is low at low strain rates $< 2 \times 10^{-1} \text{ s}^{-1}$, however, the value increases with increasing strain rate at all the testing temperatures. A maximum value of m at each temperature is about 0.2 at 683 ~ 773 K, 0.3 ~ 0.5 at 813 ~ 863 K and about 1 at 873 ~ 893 K. For many high strain rate superplastic metal matrix composites [6,10,11], a value of m is 0.3 ~ 0.5. Therefore, it is suggested that high m of 0.3 ~ 0.5 at 813 ~ 863 K is related to superplasticity and high m of about 1 at 873 ~ 893 K is related to the liquid flow. It has been reported that for metal matrix composites, the presence of threshold stress gives rise to a low value of m in a low strain rate range for dislocation creep [15-23] and superplasticity [24-26]. The experimental results in the present investigation revealed that at 873 ~ 893 K, a value of m in a low strain rate range of less than 1 s^{-1} is much lower than unity, though a value of m in a high strain rate range of more than 1 s^{-1} is about unity. This suggests the presence of threshold

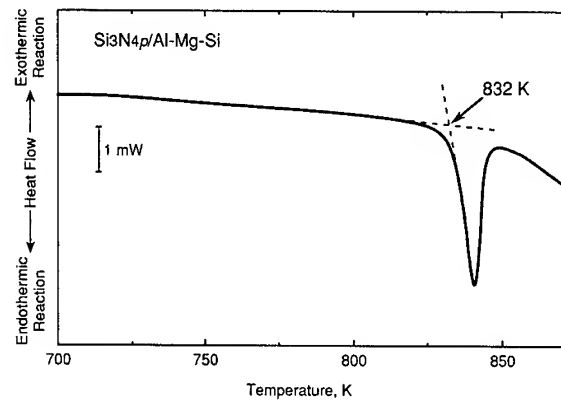


Fig. 1 The result of the DSC experiment, showing that the partial melting temperature is 832 K.

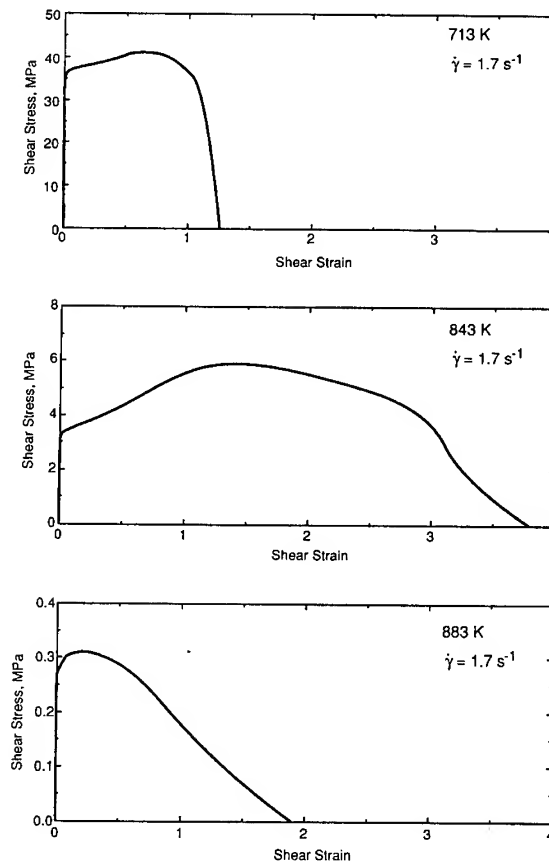


Fig. 2 The shear stress - shear strain curves at 713, 843 and 883 K.

stress in deformation related to liquid flow, though the origin of threshold stress is not clear.

The variation in shear strain rate as a function of the inverse temperature at 683 ~ 773 K is shown in Fig. 4, where the shear strain rate is determined at $(\tau - \tau_{th})/G = 7 \times 10^{-4}$ (where τ_{th} is the shear threshold stress and G is the shear modulus). The temperature range of 683 ~ 773 K is below the partial melting temperature and a maximum value of m is about 0.2.

A threshold stress was determined by extrapolation to zero strain rate for a line which the data give as τ vs $\dot{\gamma}^m$ on a double-linear scale [17]. The activation energy for deformation at 683 ~ 773 K, which is measured from the slope in Fig. 4, is 112 kJ/mol. This activation energy value is close to that for lattice diffusion of aluminum (= 142 kJ/mol [27]), indicating the deformation process is controlled by lattice diffusion of the matrix.

When $(\tau - \tau_{th})/G$ is constant, the activation energy for superplasticity can be given by [28]

$$Q = \frac{\Delta \ln [\dot{\gamma} (d/b)^p]}{\Delta \ln (1/T)} \quad (1)$$

where Q is the activation energy for superplasticity, b is Burgers vector, d is the grain size, p the grain size exponent and T is the absolute temperature. Many theoretical models on superplasticity [29-31] predict $p = 2$. Recently, it was shown [32] that the grain size exponent is experimentally about 2 for high strain rate superplasticity in the $\text{Si}_3\text{N}_4/\text{Al-Mg-Si}$ composite. Hence, p was taken to be 2 in the present investigation. The variation in $\dot{\gamma}(d/b)^2$ as a function of the inverse temperature at 813 ~ 863 K is shown in Fig. 5, where the shear strain rate is determined at $(\tau - \tau_{th})/G = 5 \times 10^{-4}$. The temperature range of 813 ~ 863 K includes the temperatures below and above the partial melting temperature. The partial melting temperature is superimposed as a dotted line in Fig. 5. The activation energy value at 813 ~ 823 K is 168 kJ/mol, which is close to that for lattice diffusion of aluminum. However, a value at 833 ~ 863 K is 1033 kJ/mol, which is much larger than that for lattice diffusion of aluminum. It should be noted that the activation energy value significantly increases at the partial melting temperature and the activation energy value at temperatures above the partial melting is much larger than that for lattice diffusion of the matrix. The same trend was found for many aluminum matrix composites exhibiting high strain rate superplasticity [28]. In addition, such a significant increase in the activation energy has been found at a temperature slightly above the solidus temperature for the Al-Mg alloy with a large grain size [5]. Therefore, it is suggested that the significant increase in the activation energy is attributed to the presence of a liquid phase.

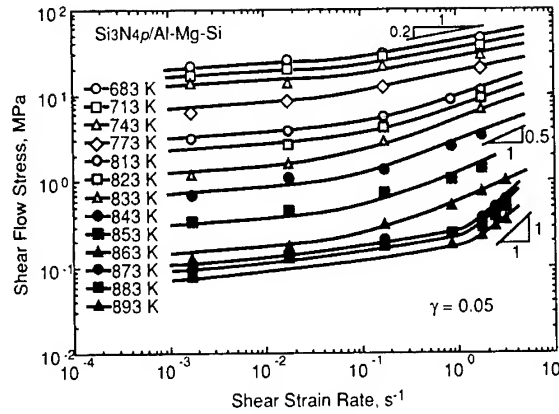


Fig. 3 The variation in shear stress as a function of shear strain rate at 683 ~ 893 K.

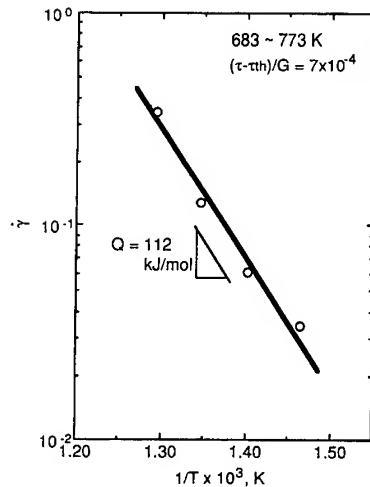


Fig. 4 The variation in shear strain rate as a function of the inverse temperature at 683 ~ 773 K.

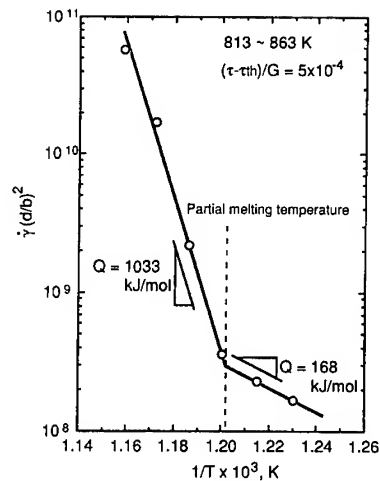


Fig. 5 The variation in shear strain rate as a function of the inverse temperature at 813 ~ 863 K.

The variation in shear strain rate as a function of the inverse temperature at 873 ~ 893 K is shown in Fig. 6, where the shear strain rate is determined at $(\tau - \tau_{th}) = 0.3$ MPa. The temperature range of 873 ~ 893 K is above the partial melting temperature and a maximum value of m is about 1. From Fig. 6, the activation energy at 873 ~ 893 K is 56 kJ/mol. If the deformation is controlled by viscosity of a liquid phase, the activation energy for the deformation is expected to be in agreement with that for viscosity of a liquid phase. However, the measured value of the activation energy at 873 ~ 893 K is larger than that for viscosity in the melt pure aluminum ($= 16.5$ kJ/mol [33]).

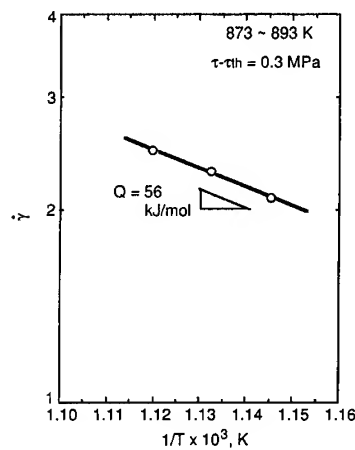


Fig. 6 The variation in shear strain rate as a function of the inverse temperature at 873 ~ 893 K.

CONCLUSIONS

It is conclusively demonstrated from the experimental results that the dominant deformation mechanism is dislocation creep at 683 ~ 773 K, superplastic flow at 813 ~ 863 K and lubricated flow at 873 ~ 893 K. In the range of superplastic flow, a liquid phase is contained at 833-863 K. It is likely that the lubricated flow in a semi-solid state at 873 ~ 893 K is affected by a solid phase configuration.

REFERENCES

1. M.C.Roth, G.C.Weatherly and W.A.Miller, *Acta metall.*, 28, 841 (1980).
2. B.L.Vaandrager and G.M.Pharr, *Acta metall.*, 37, 1057 (1989).
3. G.M.Pharr, P.S.Godavarti and B.L.Vaandrager, *J. Mater. Sci.*, 24, 784 (1989).
4. B.Baudelet, M.C.Dang and F.Bordeaux, *Scripta metall. mater.*, 26, 573 (1992).
5. H.Iwasaki, T.Mori, M.Mabuchi and K.Higashi, *Acta metall.*, 46, 6351 (1998).
6. M.Mabuchi, K.Higashi and T.G.Langdon, *Acta metal. mater.*, 42, 1739 (1994).
7. M.Mabuchi and K.Higashi, *Philos. Mag. Lett.*, 70, 1 (1994).
8. K.Higashi, T.G.Nieh and J.Wadsworth, *Acta metall. mater.*, 43, 3275 (1995).
9. K.Higashi, T.G.Nieh, J.Wadsworth and M.Mabuchi, *Scripta metall. mater.*, 32, 1079 (1995).
10. M.Mabuchi and K.Higashi, *Mater. Trans. JIM*, 35, 399 (1994).
11. M.Mabuchi and K.Higashi, *Mater. Sci. Eng.*, A179/A180, 625 (1994).
12. M.Mabuchi, H.Iwasaki, K.Higashi and T.G.Langdon, *Mater. Sci. Tech.*, 11, 1295 (1995).
13. M.Mabuchi, H.Iwasaki, H.-G.Jeong, K.Hiraga and K.Higashi, *J. Mater. Res.*, 12, 2332 (1997).
14. J.Koike, M.Mabuchi and K.Higashi, *Acta metal. mater.*, 43, 199 (1995).
15. V.C.Nardone and J.R.Strife, *Metall. Trans. A*, 18A, 109 (1987).
16. K.-T.Park, E.J.Lavernia and F.A.Mohamed, *Acta metal. mater.*, 38, 2149 (1990).
17. A.B.Pandey, R.S.Mishra and Y.R.Mahajan, *Acta metal. mater.*, 40, 2045 (1992).
18. G.G.-Doncel and O.D.Sherby, *Acta metal. mater.*, 41, 2797 (1993).
19. S.Ranganath and R.S.Mishra, *Acta mater.*, 44, 927 (1996).
20. A.B.Pandey, R.S.Mishra, A.G.Paradkar and Y.R.Mahajan, *Acta mater.*, 45, 41297 (1997).
21. D.C.Dunand and A.M.Jansen, *Acta mater.*, 45, 4569 (1997).
22. Y.Li and F.A.Mohamed, *Acta mater.*, 45, 4775 (1997).
23. Y.Li and T.G.Langdon, *Acta mater.*, 45, 4797 (1997).
24. R.S.Mishra, T.R.Bieler and A.K.Mukherjee, *Acta metal. mater.*, 43, 877 (1995).
25. M.Mabuchi and K.Higashi, *Philos. Mag. A*, 74, 887 (1996).
26. F.A.Mohamed, *J. Mater. Sci.*, 18, 583 (1983).
27. H.J.Frost and M.F.Ashby, *Deformation-Mechanism Maps*, Pergamon Press, Oxford, (1982), p. 21.
28. M.Mabuchi and K.Higashi, *Scripta mater.*, 34, 1893 (1996).
29. A.K.Mukherjee, *Mater. Sci. Eng.*, 8, 83 (1971).
30. R.C.Gifkins, *Metall. Trans. A*, 7A, 1225 (1976).
31. B.Burton, *Philos. Mag. A*, 48, L9 (1983).
32. M.Mabuchi and K.Higashi, *J. Mater. Res.*, 13, 640 (1998).
33. *Metal Data Book*, 2nd ed., Maruzen, Tokyo, (1984), p. 15.

Author Index

- Adachi, S., 617
Ahn, D. J., 95
Ahn, S. S., 309
Akkus, N., 211
Alibiglu, A., 921
Ando, M., 571, 733
Aoki, K., 1129
Aoyama, E., 237
Arai, N., 353
Arakawa, K., 663
Asagumo, R., 999, 1245
Asano, Y., 1117
Avril, S., 1283
Back, S. K., 113
Back, U. C., 1135
Bai, X. J., 361
Bang, K. G., 135
Bhattacharyya, D., 251
Bohlool, A., 535
Byon, O. I., 1167
Byun, J. H., 1265
Chan, S. L. I., 707
Chang, S. H., 929
Chen, C. Y., 243
Cheong, S. K., 645
Cheong, Y. M., 315
Cho, H. D., 1079
Cho, J. M., 1271, 1277
Cho, M. H., 965
Cho, S. H., 1271, 1277
Cho, S. K., 147
Cho, W. S., 379
Choe, C. R., 41
Choh, T., 291, 329
Choi, C. H., 379
Choi, H. S., 1091
Choi, J. H., 197
Choi, J. K., 929
Choi, L., 753
Choi, M. H., 915
Choi, N. S., 1155
Choi, S. B., 819
Choi, W. C., 683, 765
Chou, S. S., 1219
Chun, H. J., 799, 909, 1091
Chung, S. W., 549
Crasto, A. S., 33
Cui, Y. H., 335
Daghyani, H. R., 557, 577, 961
Daniel, I. M., 179
Ding, X., 205
Dong, S., 747
Dykes, R. J., 251
El-Sheikhy, R. A. I., 629, 973
Eshaghi, S., 577
Eslami, M. R., 921
Euh, K. J., 367
Farmanzad, F., 961
Fujii, T., 323, 1027, 1227
Fujinami, A., 399
Fukuda, H., 1187
Fukuda, T., 77, 191, 271, 399, 887, 1085, 1097, 1117, 1129
Fukunaga, H., 323
Funabashi, M., 1213
Fuyama, N., 323
Ghaffarian, S. R., 173, 259
Goo, N. S., 955
Guo, H. Y., 1289
Ha, S. K., 1303
Hachinohe, A., 639
Hadianfard, M. J., 303, 347
Hahn, H. T., 1, 1199
Hamaguchi, Y., 1245, 1257
Han, B. K., 125, 831
Han, D. Y., 11
Han, J. H., 881, 843
Han, K. S., 297, 849, 1019
Han, S. H., 1079
Han, W. S., 549, 1283
Hanada, N., 663
Hanzawa, S., 701
Hara, S., 323
Hawong, J. S., 1135
Hayashi, Y., 543
Higashi, K., 373, 669
Hinoki, T., 721, 739
Hirata, Y., 1013
Hirogaki, T., 237
Hodzic, A., 463
Hojo, M., 987
Hong, C. S., 715, 943, 1123, 1147
Hong, K. N., 1079
Hong, S. H., 315, 341, 1239
Hong, S. K., 483
Horikawa, N., 617
Hosokawa, H., 373
Hou, M., 265
Hu, H. T., 901
Hu, W. Y., 787
Hu, X. Z., 165
Hunter, P. J., 251
Hurez, A., 211
Huysmans, G., 1193
Hwang, B. S., 179
Hwang, J. H., 1019
Hwang, T. K., 943
Hwang, T. W., 379
Hwang, W., 1019, 1053
Hyakutake, H., 583
Im, K. H., 683
Im, S. Y., 565
Imanaka, M., 399
Inada, T., 141, 1047
Inoue, A., 1027
Inoue, H., 237
Ishikawa, T., 543
Itabashi, M., 1187
Iwamoto, M., 793, 1013
Iwasaki, A., 1047
Iwasaki, H., 373, 669
Jabbari, E., 961
Jafari, S., 303

Jang, P. S., 799	1147	Kudo, A., 1167
Jayaraman, K., 1173	Kim, C. K., 831	Kurashiki, K., 793, 1013
Jeon, H. C., 849	Kim, C. U., 943	Kurashiki, T., 589
Jeong, S. K., 147	Kim, C. W., 831	Kusaka, T., 617
Jeong, S. R., 781	Kim, D. H., 125, 875	Kwak, M. K., 857, 1103
Ji, K. H., 955	Kim, H. R., 515	Kweon, J. H., 523
Jin, J. S., 437, 509	Kim, H. S., 159	Kwon, I. B., 1079
Jo, H. H., 309	Kim, J. H., 819	Kwon, Y. J., 329
Ju, J. S., 1271	Kim, J. K., 165, 451, 463	Lara-Curzio, E., 721
Jun, E. J., 17	Kim, J. S., 405, 457	Lee, C. C., 489
Jung, H. K., 315, 1239	Kim, J. W., 425	Lee, C. H., 949
Jung, J. H., 95	Kim, K. S., 683, 715, 753, 765,	Lee, D. G., 135, 159, 197, 929
Jung, S. W., 297	1239	Lee, D. H., 125
Kageyama, K., 1007, 1059,	Kim, M. S., 1079	Lee, D. J., 419
1109	Kim, P. J., 135	Lee, D. R., 503
Kakudate, T., 107	Kim, R. Y., 33	Lee, G. S., 875
Kanai, M., 1109	Kim, S. C., 379	Lee, G. W., 1141
Kanemitsu, M., 993	Kim, S. H., 315	Lee, H. J., 1135
Kanemoto, Y., 211	Kim, S. J., 549, 955	Lee, H. S., 341
Kanetake, N., 291, 329	Kim, S. T., 1091	Lee, I., 843, 875, 881
Kang, C. G., 309	Kim, T. J., 469, 483, 753	Lee, J. H., 781
Kang, H. M., 445	Kim, W. D., 623	Lee, J. J., 395
Kang, M. K., 185	Kim, W. S., 367	Lee, J. K., 781
Kang, T. K., 113	Kim, Y. B., 645	Lee, J. R., 405, 437, 457, 469,
Kang, Y. C., 707	Kim, Y. K., 437	483, 503, 509, 727
Kang, Y. K., 863	Kim, Y. M., 425, 915	Lee, J. W., 1295
Karimian, S. M. H., 173	Kimpara, I., 1007, 1059, 1109	Lee, K. W., 113
Katayama, T., 237	Kishimoto, H., 733	Lee, S. B., 863
Kato, K., 639	Kitagawa, K., 353	Lee, S. H., 367, 1155
Katoh, H., 1245, 999	Kitano, A., 153	Lee, S. J., 1277
Katoh, Y., 651, 689, 721, 739,	Kobashi, M., 291, 329	Lee, S. P., 605, 651, 721
747, 759, 733	Kobayashi, H. 529, 141	Lee, S. W., 249, 909
Kawada, H., 1141	Kobayashi, M., 1065	Lee, W. I., 185
Kawahara, M., 211	Kobayashi, S., 981	Lee, Y. S., 915
Kawai, M., 639, 1233	Kohyama, A., 605, 651, 689,	Lee, Y. W., 565
Kawakami, H., 1027	721, 733, 739, 747, 759	Lewinsohn, C. A., 571
Kawasaki, Y., 1097	Kondo, K., 949	Li, G. H., 695
Kazama, T., 1233	Koo, B. Y., 1147	Li, R. K. Y., 611
Kemmochi, K., 771	Kosaka, T., 77, 271, 1071, 1097,	Li, T. Q., 611
Kim, B. H., 1265	1117	Li, Z. J., 361
Kim, B. S., 1265	Kotani, M., 651, 689, 759	Lim, S. T., 185
Kim, C. G., 715, 943, 1123,	Kouzeli, M., 47	Lin, J. M., 243

Lin, W. P., 901	Nam, J. B., 297	Renard, J., 597
Liu, J. S., 1289	Narita, Y., 101, 107, 869	Rew, Y. H., 1295
Liu, H. Y., 57	Naruse, H., 1059	Roh, H. Y., 965
Liu, K. K. S., 11	Nazokdast, H., 259	Rong, M. Z., 231, 477
Liu, M., 277	Ni, Q. Q., 793, 1013	Rossoll, A., 47
Luo, R., 677	Nishi, C., 389	Ryu, C. H., 915
Luo, Y. W., 1251	Nishiwaki, M., 811	Ryu, C. Y., 1147
Ma, C. C. M., 243, 489	Nishiyabu, K., 1193	Ryu, H. J., 315
Mabuchi, M., 669	Nozawa, T., 721, 739, 747	Ryu, S. R., 419
Mahdavian, M. H., 259	Nygren, R. E., 683	Sadighi, M., 895
Mai, Y. W., 57, 265	Ochiai, S., 987	Saito, H., 389
Makuta, Y., 949	Ofuji, K., 887	Sakai, A., 999
Marchi, C. S., 47	Ogisu, T., 1065	Sakamoto, D., 1085
Masuda, M., 617	Oh, I. K., 881	Sanbongi, S., 1245
Masuko, Y., 1233	Oh, J. H., 159, 1123	Sando, M., 271
Matsubara, T., 701	Oh, J. T., 1053	Sasaki, G., 323
Matsuda, S., 987	Ohsawa, I., 1109	Sato, N., 23
Matsushima, M., 543	Ohta, Y., 107, 837, 869	Sato, Y., 1257
Min, B. G., 495	Okabe, Y., 805, 1071	Schwab, S. T., 747
Mironov, V., 41	Okamura, K., 689	Sekine, N., 1161
Miserez, A., 47	Okubo, K., 1027	Seo, J. W., 819
Miyano, Y., 1161	Osaka, K., 271, 399, 1097,	Seo, K. M., 863
Mizuno, H., 1245	1117	Seo, M. K., 503, 727
Mohammadi, N., 259	Oshima, N., 1085, 1129	Seo, Y. W., 217
Mollenhauer, D. H., 87	Otsuka, A., 353	Serizawa, H., 571
Mori, T., 669	Paik, S. U., 217	Setiawan, K., 1205
Moriki, H., 589, 1047	Pak, P. K., 509	Sha, J. B., 361
Mortensen, A., 47	Pan, J., 323	Shahverdi, H., 557
Motlagh, G. H., 259	Pandita, S. D., 1193	Shakeri, M., 921
Motogi, S., 191, 811, 1129,	Park, B. J., 1271, 1277	Sham, M. L., 451
1179	Park, H. C., 683, 1019, 1053,	Shen, F., 1033
Motoyama, T., 1179	1103	Shimada, A., 1059
Murakami, A., 987	Park, J. B., 153	Shimamura, Y., 141, 529, 1041,
Murakawa, H., 571	Park, J. H., 125, 1199	1047
Murayama, H., 1059	Park, J. M., 425	Shimokawa, T., 999, 1245
Muto, H., 291	Park, J. S., 605, 943	Shin, K. C., 395
Myoung, B. Y., 515	Park, M., 41	Shin, S. J., 11 03
Nakada, M., 1161	Park, S. H., 765	Shinbo, S., 1233
Nakagaki, M., 937	Park, S. J., 405, 437, 457, 469,	Shirata, Y., 283
Nakamura, H., 141, 529, 1245	483, 503, 509, 727	Shojaei, A., 173
Nakayasu, H., 993	Park, S. S., 1295	Shokrieh, M. M., 535
Nam, H. W., 297	Ramakrishna, S., 431	Shon, M. Y., 1295

Snead, L. L., 747	Um, M. K., 179	Yoon, D. J., 425
Soemardi, T. P., 1205	Vautrin, A., 63, 1283	Yoon, H. K., 605
Sohn, M. S., 165	Verchery, G., 211	Yoon, K. D., 623
Somiya, S., 283	Verpoest, I., 1193, 1251	Yoon, K. J., 857, 1103
Song, D. Y., 153, 1065	Wada, T., 399	Yoon, S. J., 95, 147
Stachurski, Z. H., 463	Wakayama, Y., 869	Yoon, T. H., 445, 515
Suh, J. D., 197	Waku, Y., 353	Yoon, Y. B. 1303
Suh, S. S., 1199	Wang, F. Y., 489	Yoshida, M., 323
Sumita, M., 825	Wang, J., 11	Youchision, D. L., 683
Sun, C. T., 65, 623	Wang, K., 413	Youn, J. R., 249
Sung, D. U., 715, 1123	Wang, W. X., 701	Yuan, G. C., 361
Susuki, I., 1257	Wang, Y. M., 1289	Yuan, Q., 265
Suwa, H., 771	Watanabe, T., 1187	Yuck, J. I., 515
Suyama, S., 651	Weber, L., 47	Zako, M., 223, 589
Suzuki, T., 1109	Wo, D. Z., 335	Zeng, H. M., 231, 413, 477, 611
Tai, N. H., 1219	Woo, K. S., 217	Zeng, Q., 361
Takahashi, K., 663	Wu, J. S., 451, 413	Zhang, H., 825
Takai, K., 389	Wu, Y. C., 695	Zhang, L., 695
Takakura, H., 639	Wu, Y. D., 937	Zhang, M. Q., 231, 477
Takano, N., 223, 589	Xia, M., 771	Zhang, W., 651, 747, 759
Takao, Y., 701	Xiao, K., 657	Zhao, M., 1289
Takashima, M., 1141	Xiao, Y., 1257	Zhao, X., 101
Takawa, T., 887	Yamagishi, Y., 191	Zheng, Y. X., 231, 477
Takeda, N., 153, 805, 981, 1065, 1071	Yamaguchi, K., 1007	Zhu, H. X., 361
Tamura, H., 1245	Yamamoto, T., 583	Zhu, Z. H., 787
Tanaka, Y., 1041	Yamane, T., 153	
Tang, Z. G., 277	Yamasaki, T., 811	
Tani, J., 843	Yamauchi, G., 389	
Tanimoto, T., 119	Yan, S. L., 277	
Tao, J., 335	Yan, X., 825	
Tay, T. E., 1033	Yang, J., 753	
Terada, K., 981	Yang, W., 739	
Thionnet, A., 597	Yang, Y. C., 849	
Todo, M., 663	Yashiro, S., 1071	
Todoroki, A., 529, 141, 1041, 1047	Ye, L., 265, 657	
Toudeshky, H. H., 557, 577	Ye, M., 695	
Tsai, S. W., 11, 1161	Yeh, M. K., 1219	
Tsuda, H., 999	Yeo, H. J., 549	
Ueda, T., 389	Yi, H. L., 205	
Uenoya, T., 1227	Yonemori, T., 1161	
	Yong, H. T., 645	
	Yoo, J. S., 715	